Lecture Notes in Electrical Engineering 371

Vo Hoang Duy
Tran Trong Dao
Ivan Zelinka
Hyeung-Sik Choi
Mohammed Chadli *Editors*

AETA 2015: Recent Advances in Electrical Engineering and Related Sciences

Springer

Lecture Notes in Electrical Engineering

Volume 371

About this Series

"Lecture Notes in Electrical Engineering (LNEE)" is a book series which reports the latest research and developments in Electrical Engineering, namely:

- Communication, Networks, and Information Theory
- Computer Engineering
- Signal, Image, Speech and Information Processing
- Circuits and Systems
- Bioengineering

LNEE publishes authored monographs and contributed volumes which present cutting edge research information as well as new perspectives on classical fields, while maintaining Springer's high standards of academic excellence. Also considered for publication are lecture materials, proceedings, and other related materials of exceptionally high quality and interest. The subject matter should be original and timely, reporting the latest research and developments in all areas of electrical engineering.

The audience for the books in LNEE consists of advanced level students, researchers, and industry professionals working at the forefront of their fields. Much like Springer's other Lecture Notes series, LNEE will be distributed through Springer's print and electronic publishing channels.

More information about this series at http://www.springer.com/series/7818

Vo Hoang Duy · Tran Trong Dao
Ivan Zelinka · Hyeung-Sik Choi
Mohammed Chadli
Editors

AETA 2015: Recent Advances in Electrical Engineering and Related Sciences

Springer

Editors
Vo Hoang Duy
Faculty of Electrical and Electronics Engineering
Ton Duc Thang University
Ho Chi Minh City
Vietnam

Tran Trong Dao
MERLIN
Ton Duc Thang University
Ho Chi Minh City
Vietnam

Ivan Zelinka
Electrical Engineering and Computer Science
VŠB—Technical University
Ostrava, Poruba
Czech Republic

Hyeung-Sik Choi
Division of Mechanical
Korea Maritime and Ocean University
Busan
Korea (Republic of South Korea)

Mohammed Chadli
Université de Picardie Jules Verne
Laboratoire MIS
Amiens
France

ISSN 1876-1100 ISSN 1876-1119 (electronic)
Lecture Notes in Electrical Engineering
ISBN 978-3-319-27245-0 ISBN 978-3-319-27247-4 (eBook)
DOI 10.1007/978-3-319-27247-4

Library of Congress Control Number: 2015956138

Printed on acid-free paper

This Springer imprint is published by SpringerNature
The registered company is Springer International Publishing AG Switzerland

Preface

The Proceedings of AETA 2015, which you are holding in your hands, consist of selected papers from 10 different but related areas of modern engineering. The modern world is based on vitally important technologies that merge electronics, cybernetics, computer science, telecommunications, and physics together. Since the beginning of our technologies, we have been confronted with numerous technological challenges such as finding the optimal solution to various problems including controlling technologies, power sources construction, robotics, etc. Technological development of these and related areas has had and continues to have a profound impact on our civilization and on our future lifestyle.

Therefore, this proceedings book containing articles of the international conference AETA 2015, edited by Ivan Zelinka (Czech Republic), Vo Hoang Duy (Vietnam), Tran Trong Dao (Vietnam), Hyeung-Sik Choi (Korea), and Mohammed Chadli (France), is a timely volume to be welcomed by the community focused on telecommunication, power control, and optimization as well as the computational science community and beyond.

The book consists of 10 topic areas of selected papers such as telecommunication, power systems, robotics, control system, computer science, and more. Readers can find interesting papers on different topics that reflect the modern approach to interesting problems. All selected papers represent interesting ideas and state-of-the-art overviews.

Participations were carefully selected and reviewed, hence this book certainly is one of the few that discusses the benefits from intersection of those modern and fruitful scientific fields of research. We hope that this book will be an instructional material for senior undergraduates and entry-level graduates. The book can also be a resource material for practitioners who want to apply the discussed topics to solve real-life problems in their challenging applications. The important part of this book is the participation of two keynote speakers from the Russian Federation and Korea.

The decision to organize the AETA conference and to create this book was based on the fact that the technologies mentioned above, their use, and impact on life is an interesting area that is under intensive research from many other branches of

science today. The book contains simplified versions of experiments with the aim to show how, in principle, problems of power systems can be solved.

It is obvious that this book does not encompass all aspects of the discussed topics due to the limited space and time of the conference. Only the main ideas and results of selected papers are reported here. The authors and editors hope that the readers will be inspired to do their own experiments and simulations, based on the information reported in this book, thereby moving beyond the scope of it. For these reasons, we believe that this book will be useful for scientists and engineers working in the above-mentioned fields of research and applications.

At the end we *would like to thank* Ton Duc Thang University (Ho Chi Minh City, Vietnam), VŠB—Technical University (Ostrava, Czech Republic), Korea Maritime and Ocean University (Korea) and CIMEC Lab. (Korea) for their interest and strong support in the AETA conference organization. Also, *many thanks* to Springer publishing company for its highly professional, precise, and quick production process. Without all of this, it would be impossible to organize a successful conference with European and Asian participants.

This conference was supported by the Ton Duc Thang University (Ho Chi Minh City, Vietnam) and VŠB—Technical University (Ostrava, Czech Republic) and by the research groups NAVY (http://navy.cs.vsb.cz/) and MERLIN (http://merlin.tdt.edu.vn/) and CIMEC Lab.

Vietnam — Vo Hoang Duy
Vietnam — Tran Trong Dao
Czech Republic — Ivan Zelinka
Korea — Hyeung-Sik Choi
France — Mohammed Chadli
September 2015

Contents

Part I Keynote

SDN Based Wireless Heterogeneous Network Management 3
Choong Seon Hong, S.M. Ahsan Kazmi, Seungil Moon and Nguyen Van Mui

Hidden Attractors in Fundamental Problems and Engineering Models: A Short Survey 13
Nikolay V. Kuznetsov

Part II Telecommunication

Experimental Study on the Effects of External Interference on Slot Scheduling Based MAC Protocols in Wireless Sensor Networks 29
Chi Trung Ngo, Hoon Oh and Minh Thuy Pham

Performance Analysis of a Hybrid Efficient and Reliable MAC Scheme for Vehicular Ad Hoc Networks in Safety Applications 41
VanDung Nguyen, Oanh Tran Thi Kim and Choong Seon Hong

Wireless Information and Power Transfer for Full Duplex Relaying Networks: Performance Analysis 53
Tam Nguyen Kieu, Dinh-Thuan Do, Xinh Nguyen Xuan, Tan Nguyen Nhat and Hung Ha Duy

A Multi-channel MAC Protocol with Power Control for Wireless Ad Hoc Networks 63
Duc Ngoc Minh Dang, Quynh Tu Ngo, Hanh Ngoc Dang and Choong Seon Hong

A Novel Compressed Sensing Approach to Speech Signal Compression 75
Tan N. Nguyen, Phuong T. Tran and Miroslav Voznak

Optimization of Mobility Control in Mobile Wireless Networks for Energy Saving 87
Phuong T. Tran

Utilizing the Neural Networks for Speech Quality Estimation Based on the Network Characteristics 99
Jan Rozhon, Miroslav Voznak, Filip Rezac and Jiri Slachta

Bit Error Rate Performance of Clipped OFDM Signals Over Fading Channel 111
Dang Le Khoa, Huynh Quoc Anh, Nguyen Huu Phuong and Hiroshi Ochi

Part III Computer Science

Machine Learning Based Phishing Web Sites Detection 123
Huu Hieu Nguyen and Duc Thai Nguyen

Simulation and Optimization of a Non-linear Dynamic Process Using Mathematica 133
Tran Trong Dao, Vo Hoang Duy, Ivan Zelinka, Luu Minh Tung and Pham Nhat Phuong

Personality Disorders Identification in Written Texts 143
Petr Saloun, Adam Ondrejka, Martin Malčík and Ivan Zelinka

Part IV Power System

Compare Different Recent Methods and Propose Improved Method for Risk Assessment of Damages Due to Lightning 157
Quyen Huy Anh, Le Quang Trung and Phan Chi Thach

An Improvement Forward Floating Search Algorithm for Feature Selection in Power System Transient Stability Classification 167
Ngoc Au Nguyen, Huy Anh Quyen, Trong Nghia Le and Thi Thanh Binh Phan

Technical Efficiency and Recommendations for Overcurrent Relay Protection Setting 175
Tran Hoang Quang Minh

Enhanced Fault Ride-Through Capability of DFIG Wind Turbine Systems Considering Grid-Side Converter as STATCOM 185
Tan Luong Van and Van Cuu Ho

The Solar Collector and Thermal Storage System Using High Temperature Oil 197
Nguyen Dao, Nguyen Quang Dung and Nguyen Bon

Solving Bi-Objective Short-Term Cascaded Hydrothermal Scheduling Problem Using Modified Cuckoo Search Algorithm 213
Thang Trung Nguyen, Tuan Van Duong, Dieu Ngoc Vo and Bao Quoc Nguyen

A Backtracking Search Algorithm for Distribution Network Reconfiguration Problem 223
Thuan Thanh Nguyen, Hiep Ngoc Pham, Anh Viet Truong, Tuan Anh Phung and Thang Trung Nguyen

Part V Power Electronics

A Study on the Firing Angle at the Mode Conversion to Improve the Output Characteristics of the Double Converter for Urban Rail DC Power Supply 237
Sung Woo Han, Seung Sam Seo, Jin Han Lee, SeongGyu Kim, Min Kim and Gi Sig Byun

A Synchronization Method for Three-Phase Grid-Connected Inverters Using Levenberg-Marquardt Technique 249
Tran Quang Tho, Pham Huu Ly, Truong Viet Anh and Le Minh Phuong

Improved Control Strategy of Three-Phase Four-Wire Inverters Using Sliding Mode Input-Ouput Feedback Linearization Under Unbalanced and Nonlinear Load Conditions 261
Tan Luong Van, Le Minh Thien Huynh, Tran Thanh Trang and Duc Chi Nguyen

Part VI Materials

The Structural Characteristics of ZnO Nanorods for Flexible Gas Sensor Grown by Hydrothermal Method 275
JaeHeon Ock, JaeHyeon Oh, HyunMin Lee, SangHyun Kim and Nakwon Jang

SiO_2 Powder: A Novel Solution for Improving Spatial Color Uniformity of White LED Lamps 283
Nguyen Doan Quoc Anh, Yu-Nan Liu, Hsin-Yi Ma and Hsiao-Yi Lee

Optical Fiber-Coupled Compact Terahertz Transceiver Module 293
Hyeon Sang Bark, Young Bin Ji, Dong Woo Park, Sam Kyu Noh, Seung Jae Oh and Tae-In Jeon

Study of a Novel Secondary Lens for LED Fishing Lamps 299
Thieu Quang Tri and Nguyen Doan Quoc Anh

Part VII Motor Control

Sliding Mode Observer for Induction Motor Control 313
Chau Dong, Pavel Brandstetter, Huu Hau Vo and Vo Hoang Duy

MRAS Observers for Speed Estimation of Induction Motor with Direct Torque and Flux Control. 325
Hau Huu Vo, Pavel Brandstetter and Chau Si Thien Dong

Application of Servo Controller Design for Speed Control of AC Induction Motors Using Polynomial Differential Operator. 337
Dae Hwan Kim, Pandu Sandi Pratama, Phuc Thinh Doan, Sea June Oh, Van Tu Duong, Jung Hu Min, Young Seok Jung and Sang Bong Kim

Servo Controller Design for Speed Control of BLDC Motors Using Polynomial Differential Operator Method 353
Trong Hai Nguyen, Jin Woo Lee, Hak Kyeong Kim, Thien Phuc Tran, Yeon Wook Choe, Viet Tuan Dinh and Sang Bong Kim

Optimal Tuning of PI Controller for Vector Control System Using Hybrid System Composed of GA and BA 367
Dong Hwa Kim, Chau Dong, Cong Thinh Tran and Vo Hoang Duy

Part VIII Control System

Vehicle Side-Slip Angle and Lateral Force Estimator Based on Extended Kalman Filtering Algorithm. 377
Chih-Keng Chen and Anh-Tuan Le

Motion Control System Design for a Barge Type Vessel Moored by Ropes 389
Anh-Minh D. Tran, Jung-In Yoon and Young-Bok Kim

A Novel Advanced Controller for Robust Stability of High Order Plants with Time-Delay and Uncertainty 399
Ho Pham Huy Anh and Nguyen Ngoc Son

A Stable Lyapunov Approach of Advanced Sliding Mode Control for Swing up and Robust Balancing Implementation for the Pendubot System 411
Cao Van Kien, Nguyen Ngoc Son and Ho Pham Huy Anh

Tuning PID Controllers for Unstable Systems with Dead Time Based on Dual-Input Describing Function Method 427
Yeon Wook Choe

Cross-Coupling Synchronous Velocity Control for an Uncertain Model of Transformer Winding System Using Model Reference Adaptive Control Method 441
Van Tu Duong, Jae Hoon Jeong, Nam Soo Jeong, Min Saeng Shin, Tan Tien Nguyen, Gi Sig Byun and Sang Bong Kim

Comparing Convergence of PSO and SFLA Optimization Algorithms in Tuning Parameters of Fuzzy Logic Controller 457
Duc-Hoang Nguyen and Manh-Dung Ngo

MIMO Robust Servo Controller Design Based on Internal Model Principle Using Polynomial Differential Operator 469
Sang Bong Kim, Dae Hwan Kim, Pandu Sandi Pratama, Jin Wook Kim, Hak Kyeong Kim, Sea June Oh and Young Seok Jung

Design and Control Automatic Chess-Playing Robot Arm 485
Nguyen Duy Anh, Luong Thanh Nhat and Tran Van Phan Nhan

Adaptive Controller Design for Mechanical Transmission Systems with Backlash 497
Nguyen Duy Anh, Tran Ngoc Cong Thuong and Nguyen Tan Tien

Image Processing for Smoke Detection Based on Embedded System . . . 509
Thao Phuong Thi Nguyen and Hoanh Nguyen

Second Order Sliding Mode Control Design for Active Magnetic Bearing System 519
Van Van Huynh and Bach Dinh Hoang

Optimizing the CRI Method by Improving the Implication Step in MISO Fuzzy Expert Systems 531
Thoai Phu Vo

Model Predictive Control Nonlinear System of Active Magnetic Bearings for a Flywheel Energy Storage System 541
Yao-Wen Tsai, Phan Van Duc, Viet Anh Duong, Nguyen Cong Trang and Trung Dung Chu

Observer-Based Output Feedback Control Design for Mismatched Uncertain Systems 553
Van Van Huynh and Minh Hoang Quang Tran

Single and Multi Chaos Enhanced Differential Evolution on the Selected PID Tuning Problem 563
Roman Senkerik, Michal Pluhacek and Ivan Zelinka

Part IX Robotics

A Study on the Dynamics of Marine Umbilical Cable for Underwater Vehicle 575
The-Vu Mai, Hyeung-Sik Choi, Joon-Young Kim, Dae-Hyeung Ji, Hyun-Joong Son and Ngoc-Huy Tran

Adaptive Backstepping Control Design for Trajectory Tracking of Automatic Guided Vehicles 589
Pandu Sandi Pratama, Jae Hoon Jeong, Sang Kwun Jeong, Hak Kyeong Kim, Hwan Seong Kim, Tae Kyeong Yeu, Sup Hong and Sang Bong Kim

Obstacle Avoidance Control for Four Wheels Independent Steering Automatic Guided Vehicles 603
Pandu Sandi Pratama, Amruta Vinod Gulalkari, Jin Wook Kim, Chung Hwan Lee, Tae-Kyeong Yeu, Sup Hong, Hak Kyeong Kim and Sang Bong Kim

Steering and Diving Control of a Small-Sized AUV 619
Ngoc-Huy Tran, Hyeung-Sik Choi, Ngoc-Duc Nguyen, Sung-Won Jo and Joon-Young Kim

Design and Implementation of Dynamic Positioning Control System for USV 633
Ngoc-Huy Tran, Hyeung-Sik Choi, Ji-Youn Oh and Sang-Ki Jeong

Study on Mechanical Structure Design for Innovative Multi-function Assistive Mobile Robot 645
Vo Hoang Duy, Tran Trong Dao, Nguyen Thanh Quang and Ngoc-Bich Le

Object Following Controller Design for Four Wheel Independent Steering Automatic Guided Vehicle 655
Amruta Vinod Gulalkari, Pandu Sandi Pratama, Jae Hoon Jeong, Hak Kyeong Kim and Sang Bong Kim

Walking Gait Planning Using Central Pattern Generators for Hexapod Walking Robot 671
Dong Bo Sheng, Hung Nguyen Huy, Pandu Sandi Pratama, Hak Kyeong Kim, Vo Hoang Duy and Sang Bong Kim

Diameter-Adjustable Controller Design of Wheel Type Pipe Inspection Robot Using Fuzzy Logic Control Method 685
Husam Hasan Aldulaimi, Trong Hai Nguyeni, Pandu Sandi Pratama, Hui-Ryong Yoo, Dong Kyu Kim, Vo Hoang Duy and Sang Bong Kim

Development of RFECT System for In-line Inspection Robot for Unpiggable Natural Gas Pipeline 697
Jae-Ha Park, Hui-Ryong Yoo, Dae-Kwang Kim, Dong-kyu Kim, Sung-Ho Cho, Hak-Joon Kim and Sung-Jin Song

Research on Design and Simulation of an Automatic Car Painting System in Thaco-Kia Company 709
Tri Cong Phung and Duy Anh Nguyen

On-line Training Solution to Modify the Inverse Kinematic Approximation of a Robot Manipulator 721
Bach H. Dinh

A Research on Designing, Manufacturing and Controlling of a Motion Simulation System for Containers 731
Nguyen Duy Anh, Tran Ngoc Hoang and Kim Hwan Seong

Design and Control Humanoid Hand to Implement Hand Shaking Task Applied for Service Robot 745
Tri Dung Nguyen, Tan Tien Nguyen and Thien Phuc Tran

Study on an Automatic Solution for Container Transporting at Tan Thuan Port 757
Minh Doan Vu Hoang, Tan Tung Phan and Tan Tien Nguyen

A Study on Moving Direction and Surge Velocity Control of a Carangiform Fish Robot Driven by Flexible Pectoral Fins 769
Van Anh Pham, Khac Anh Hoang, Tan Tien Nguyen and Tuong Quan Vo

Precise Position Control of Shoes-Upper for Screen Printing Machine Using SCARA Robot 779
Trong Hieu Bui, Anh Tuan Bui and Thanh Huy Phung

A Study on Controllers Design of a 3-Joint Carangiform Fish Robot in 3D Environment 791
Khac Anh Hoang, Van Anh Pham, Tan Tien Nguyen and Tuong Quan Vo

Decentralized Motion Control for Omnidirectional Mobile Platform—Tracking a Trajectory Using PD Fuzzy Controller 803
Thanh Luan Bui

Part X Mechanical Engineering

Data Processing Assessment of the Comfort of Passengers on Board for Small Passenger Boat 823
Nguyen Anh Tuan and Tat-Hien Le

Development of a New Clutch Featuring MR Fluid with Two Separated Mutual Coils 835
Quoc Hung Nguyen, Le Dai Hiep, Bui Quoc Duy and Seung-Bok Choi

Estimation of Static Hydrodynamic Coefficient in Waves Using Static Drift Test 845
M.J. Jeon, D.H. Lee, D.M. Lee, V.M. Nguyen and H.K. Yoon

Part XI Computational Mechanics

Calibrating a Fracture Criterion for a Numerical Simulation of Warm-Incremental Forming Process 857
Le Van Sy

Building Structure Parameter Identification Using the Frequency Domain Decomposition (FDD) Method 869
Phuoc Nguyen Van

Airfoil Selection for Fixed Wing of Small Unmanned Aerial Vehicles 881
Ngo Khanh Hieu and Huynh Thien Loc

Application of the Dung's Microscopic Damage Model to Predict Ductile Fracture of the Deep Drawn Aluminum Alloy Sheets 891
Hao H. Nguyen, Trung N. Nguyen and Hoa C. Vu

Implementation and Application of Dung's Model to Analyze Ductile Fracture of Metallic Material 903
Hao H. Nguyen, Trung N. Nguyen and Hoa C. Vu

Author Index 915

Part I
Keynote

SDN Based Wireless Heterogeneous Network Management

Choong Seon Hong, S.M. Ahsan Kazmi, Seungil Moon and Nguyen Van Mui

Abstract The proliferation of novel network access devices and demand for high quality of service by the end users are proving to be insufficient for existing wireless heterogeneous networks, due to their inflexible and expensive equipment as well as complex and non-agile control plane. This article presents an architecture vision to address the challenges placed on future heterogeneous networks. Software defined networking is emerging as a solution for decoupling the control plane. Furthermore, it enables network function virtualization and network programmability which is very promising for meeting the high demands of end user. In this article, we present an SDN based management framework for cognitive heterogeneous networks. Moreover, we discuss the architectural changes, its control function and its interaction in detail. The proposed management framework enables optimal power control, resource allocation, interference management and provides end to end quality of service for its user.

Keywords Software defined networks · Cognitive radio networks · Hetrogenous networks · Network management

C.S. Hong (✉) · S.M. Ahsan Kazmi · S. Moon · N. Van Mui
Department of Computer Engineering, Kyung Hee University, 446-701 Seoul, Korea
e-mail: cshong@khu.ac.kr

S.M. Ahsan Kazmi
e-mail: ahsankazmi@khu.ac.kr

S. Moon
e-mail: moons85@khu.ac.kr

N. Van Mui
e-mail: nvmui@khu.ac.kr

V.H. Duy et al. (eds.), *AETA 2015: Recent Advances in Electrical Engineering and Related Sciences*, Lecture Notes in Electrical Engineering 371,
DOI 10.1007/978-3-319-27247-4_1

1 Introduction

The modern wireless communication has empowered us in optimizing our operations, economics, health and all the modern industries. Life without it is beyond imagination due to our broad dependencies over the wireless networks. We gather, analyze and share a huge amount of information among different entities to have a productive life which was not possible before the advent of modern communication networks. In the last two decades wireless communication has evolved at a very rapid pace to keep up with the expectations and requirements of the users.

Cellular communication falls among the category which has received the most popularity among the wireless networks. The first generation of cellular networks started off with analog communication primarily for voice communication. The second generation was dominated by digital voice and a small amount of data communication while the third generation which was initially focused to increase the number of users in the network but observed a tsunami of data communication in the networks [1]. Today we have Third Generation Partnership Project (3GPP) Long Term Evolution (LTE), state of the art fourth generation cellular network. Our 4G standard along with voice carrying capability enables richer and real time data networks. Currently it is providing broadband services to 50 million users around the globe and is expected to support two billion users by end of 2018 [2]. New features are being analyzed and added in the latest release of LTE standard (release 13) to enhance the overall efficiency of the network [3]. This trend of data traffic in cellular networks is hopeful to grow even more because of the bandwidth hungry applications and proliferation of modern communication gadgets i.e. smart phones, tablets, smart watches, e-health, Internet gaming and etc. The mobile traffic has increased 66 times from 2009 to 2014 with an annual rate of increase of 131 % [4]. On the other hand, the data rates from third to fourth generation technology has increased only by 55 % annually [5]. This shows us the need to further investigate and develop new techniques to improve the current cellular networks.

One of the most recent and promising direction for enhancing the capacity of the network is the installation of small cells under the coverage of existing cellular network. This novel paradigm with different cell sizes is known as heterogeneous networks (HetNets). Additionally, there has been a significant amount of work claiming the effective and efficient use of installing a cognitive radio network (CRN) under the existing cellular network in [6, 7]. Furthermore, academic and industrial communities has started active research activities on the fifth generation (5G) communication technologies to meet the goals for future wireless networks. Various programs by different organizations are launched aimed at potential key technologies of 5G namely 5GNOW and METIS under European Telecommunications Standards Institute (ETSI) to meet the cellular requirements beyond 2020 [8]. The 5G standard keeping in view the trend of growth in traffic is investigating and providing guidelines for future cellular network. 5G is expected to handle 1000 times more data volume per unit area, 10–100 times higher number of connected devices, latency reduced to five times with guaranteed data rates up to multiple

gigabit per second and battery life about 10 times longer than current state of the art [9]. According to [10], legacy cellular networks are not designed to handle such requirements so major changes are required to adopt the future cellular requirements. According to [11], one of the most promising aspect would be dense installation of small cells forming multiple HetNets which would play a vital part in fulfilling the requirements of future cellular networks.

Management of network in future HetNets will become one of the biggest and crucial challenge for efficient performance of the network. This broadly includes number of users per cell, small-cell placement, interference among cells, handover during mobility, scalability of networks, heterogeneous technologies and their interoperability issues and user association. If the future HetNet architecture can handle these tasks efficiently, goals of 5G network can be achieved. We in this article will consider the management of HetNets from Software defined networking (SDN) point of view.

Coordination and cooperation will play a vital role in operations especially with the dense small cells deployment as envisioned for 5G networks [12]. The existing LTE system has been designed to run as a distributed system where each cell takes all its decision. This distributed practice without taking into account neighbors information will cause serious inefficiencies in terms of performance. Thus, coordination of control plane is required to efficiently carry out network operations [4]. The concept of an SDN controller has revolutionized the network world especially in wired domain which primarily decouples the control and data plane. This concept looks very promising for the wireless and mobile communication domain and a number of studies are being conducted to adopt the SDN paradigm in mobile networks [12, 13]. Similarly, in [14], a central coordinator (standardized by 3GPP) is used, namely femto management system (FMS) to cooperate femto-cells within geographical proximity in order to allocate resources while protecting them from interference. The biggest challenge in central coordination is the message passing which consumes a significant amount of bandwidth in back-haul if a completely centralized solution is used. However, small cells are typically low power cheap devices and can be connected via broadband services through Internet to coordinate and cooperate. This saves significant bandwidth which would be used for message passing if back-haul is used. Furthermore, an analysis performed on a macro-cell with 20 micro-cell with 50 clients holding 10 flows claims that only 500 Mbps bandwidth was found suitable for layer 1 coordination and considering the advances in the communication world this bandwidth is not very high especially in fiber communication [15].

The rest of the article is organized as follows: Section 2 discusses the current and future HetNet architecture. In Sect. 3, we provide the SDN based management framework and its functions which will help in achieving the goals for the future HetNet architecture. Section 4, finally concludes this article.

2 Legacy and Future HetNet Architecture

The existing or the legacy HetNet typically consists of multiple small cells under the coverage of a macrocell as shown in Fig. 1. These small cells can be categorized in terms of their transmission power levels, cell range, access techniques, modulation techniques, sensing capabilities and etc. Some typical examples include micro, femto, pico, cognitive and WiFi transmitter as shown in Fig. 1. In the existing HetNets, coordination among different cells is typically done at the bases station in order for the network to operate efficiently. However in the existing HetNets, the number of small cells in a network are very scarce so coordination overhead among different cells is relatively less which will not be the case for the future. This makes management of HetNets a very important aspect for future wireless HetNets.

The main motivation for dense installation of small cells comes from the fact that increasing the number of macrocells is costly and ineffective since around 50 % of voice calls and 70 % of data usage currently takes place indoors where up to 20 dB penetration loss reduces the outdoor to indoor signal strength [13]. Therefore, installing indoor small cells increases the efficiency of the network if managed properly. Additionally, the novel wireless technologies i.e., device to device communication (D2D), massive multi input multi output (MIMO), cognitive radio network (CRN), millimeter-wave band communication and etc. will also be a part of future HetNets along with dense installation of small cells as shown in Fig. 1. This makes management of HetNets very vital especially for interference, networking congestion and spectrum allocation problems. The use of different functional network devices like switches, routers which is making the network architecture much more complex and difficult to handle. Some recent studies address dynamic infrastructure and flexible allocation of network resource on demand which calls for a new management framework as the existing cellular management framework was not designed for these HetNets.

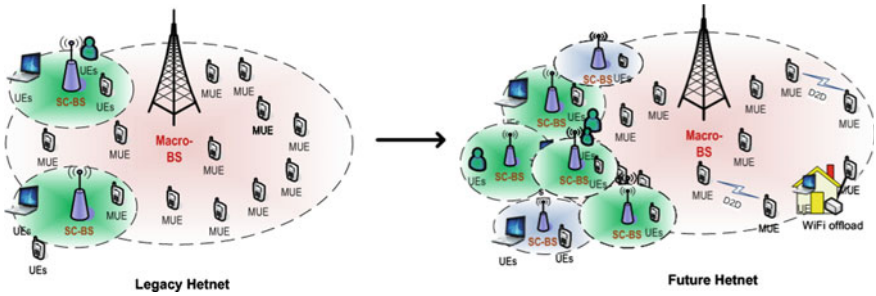

Fig. 1 Evolution of HetNet architecture

3 SDN Based Management Framework

Software-defined Network (SDN) with OpenFlow protocol which provides a dynamic and flexible network architecture to help todays static network evolve into an extensible service delivery. SDN refers to a network infrastructure in which control plane is separated from physical topology. The SDN enables us to develop a centralized traffic engineering, power control and spectrum selection protocol that needs to communicate among end-users, base-stations and SDN controller to achieve higher data delivery throughput, higher reliability and energy efficiency with excellent capability of spectrum utilization.

The SDN controller can have a number of functions depending upon the network operator policy both as internal or as an external application (using an application programmable interface (API) for external applications). The advantage of using SDN in heterogeneous networks is that incumbent devices (BSs, CPEs, SUs, Mesh routers, Mobile ad hoc Users) are re-designed to communicate with SDN controller so that their network policies are updated on the fly, leading to maximization of agency interoperability. Therefore, all networking devices have an agent installed in it to coordinate and cooperate among cells. The communication between the SDN controller and the agents can use the API concept as in [8]. However, the Open Network Foundation (ONF) is working on the OpenFlow extension standardization for wireless and mobile networks [13].

In this article, we would present an SDN based management framework proposed specifically for heterogeneous cognitive networks as shown in Fig. 2.

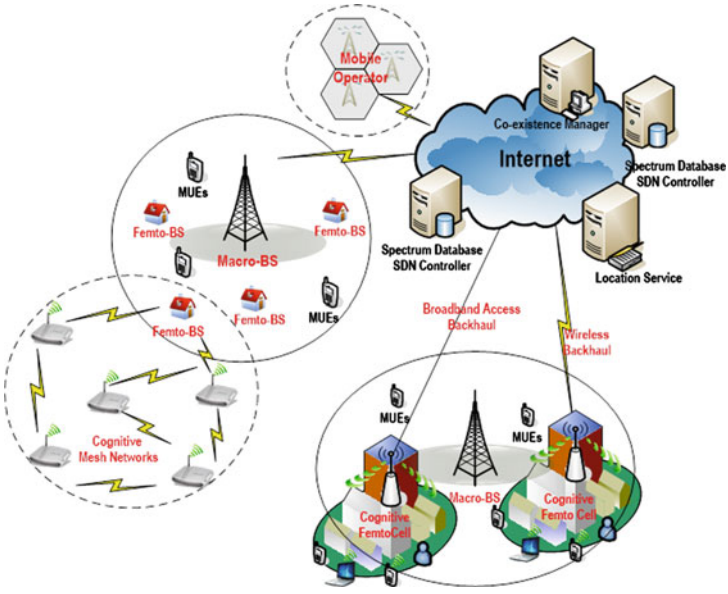

Fig. 2 Overview of a SDN-based heterogeneous cognitive network

The core functions and the working of the framework is discussed in detail. The proposed framework will provide a network resource optimization framework and efficient control mechanism based on SDN for such cognitive heterogeneous networks. It can provide centralized traffic engineering, power control and spectrum selection protocol that needs to communicate among end-users, BSs and SDN controller to achieve higher data delivery throughput, higher reliability and energy efficiency with excellent capability of spectrum utilization. The design of SDN-based cognitive heterogeneous networks necessitates substantial modification in the Physical layer and MAC layer software modules and couples with Routing Protocol. We do strongly claim that the framework would show high performance in a large number of cognitive applications, particularly for those emergency applications requiring high data rate, reliability, mobility and reduced end-to-end delay but spectrum shortage and short coverage such as vehicular, battlefield surveillance, disaster recovery, medical care, radioactive leakage detection, etc.

The framework separates control and data plane to obtain interoperability and scalability and provide sufficient services to each different kinds of user. SDN Controller can optimize the whole heterogeneous network by jointly considering:

1. Power Optimization Control and Interference mitigation: Based on information from spectrum database and co-existence Manager, SDN Controller optimally allocates transmission powers to each users and base station in the network to mitigate interference. Moreover, both users and base stations in the network adjusts its power in order to save energy and protects primary users.
2. Resource Allocation: Due to self-coexistence of multiple wireless radio access networks, SDN controller must perform the resource allocation optimization to maximize overall throughput. Each user/basestation can use a range of contiguous channels (i.e. channel bonding) to increase its capacity.
3. End-to-End QoS: SDN controller dynamically monitors a connection and allocate more channels or transmission power for related-users to ensure end-to-end QoS.

3.1 Controller Plane Architecture and Functions

In this section we discuss about the control plane architecture and the core functions which are build over the SDN controller as shown in Figs. 3 and 4. In Fig. 3, we can see that base stations are attached to the SDN controller which include both the licensed and unlicensed base station with heterogeneous capabilities. Furthermore, we describe the functionalities in detail for the SDN controller.

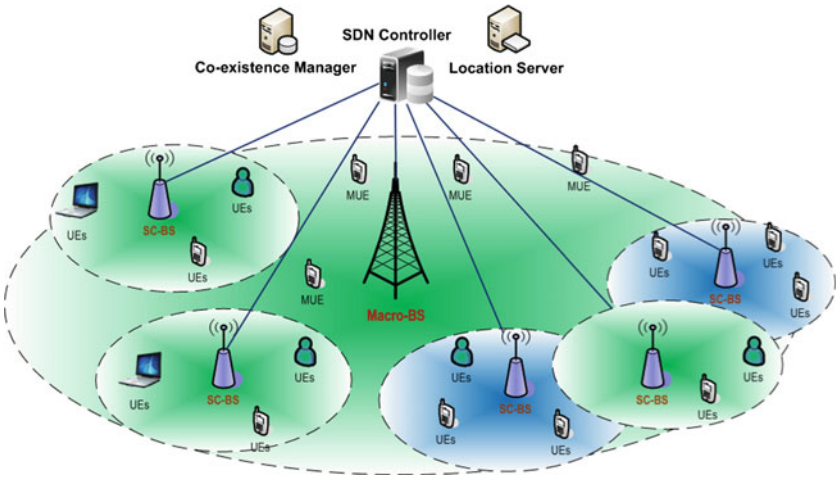

Fig. 3 Control plane architecture

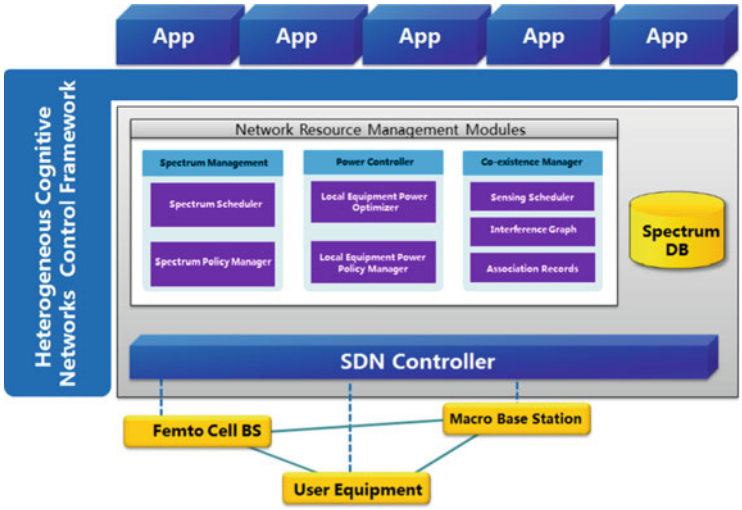

Fig. 4 SDN controller architecture for SDN-based heterogeneous CRN

3.1.1 Spectrum Management

1. Spectrum Scheduler (SS): It schedules spectrum hole usage in time, space to deploy co-existence of multiple small cells i.e., femtocells for different network operators.
2. Spectrum Policy Manager (SPM): It stores and updates meaningful data and policy-related radio parameters including protected channel numbers,

geo-location and contour of a base station, geo-location of cellular sites, terrain curvatures of the service region, maximum EIRP on allowed cellular channels, antenna height and gain, propagation models, interference scenarios, mobile devices and their geo-locations, transmission power and operating channels. SPM regularly updates information from broadcasters, regulators and service providers. The database can be pulled by or pushed directly/in-directly via BS to cognitive devices.
3. Spectrum Allocation Optimizer (SPO): It dynamically perform spectrum allocation optimization based on geo-location of cognitive devices, demand for bandwidth per each end-user, spectrum policies. SPO will adjust spectrum prices and broadcast to end-users.

3.1.2 Power Controller Manager

1. Local Equipment Power Optimizer (LEPO): It is based on power policies and strategies, LEPO optimally calculates transmission power ranges for end-users per spectrum hole.
2. Local Equipment Power Policy Manager (LEPM): It stores and updates the policy-related power parameters from broadcasters, regulators and cellular service providers. LEPM will make power strategies for each secondary system using spectrum holes for co-existence and incumbent protection.
3. Local Equipment Power Controller: It dynamically adjust transmission power levels in each users power ranges to support mobility and increase energy efficiency.

3.1.3 Coexistence Manager

1. Sensing Scheduler (SS): As multiple spectrum bands are available but due to the limited number of network interface per user, SS must optimally schedule the time and frequency to perform sensing at each end-user.
2. Interference Mitigator (IM): Based of analyzing the spectrum behavior and the performance metric of user devices, IM makes access strategies on each band for each user device to mitigate interference.
3. Route Manager (RM): Based on spectrum policies and power strategies, and end-user demands, RM calculates the feasible routes with the different costs and utilities for each user.
4. QoS Manager (QoSM): After establishing connection, QoSM will ensure end-to-end QoS for that connection by requesting more bandwidth to SPO for backhaul link. QoSM dynamically monitors the end to end user demands and provide services.

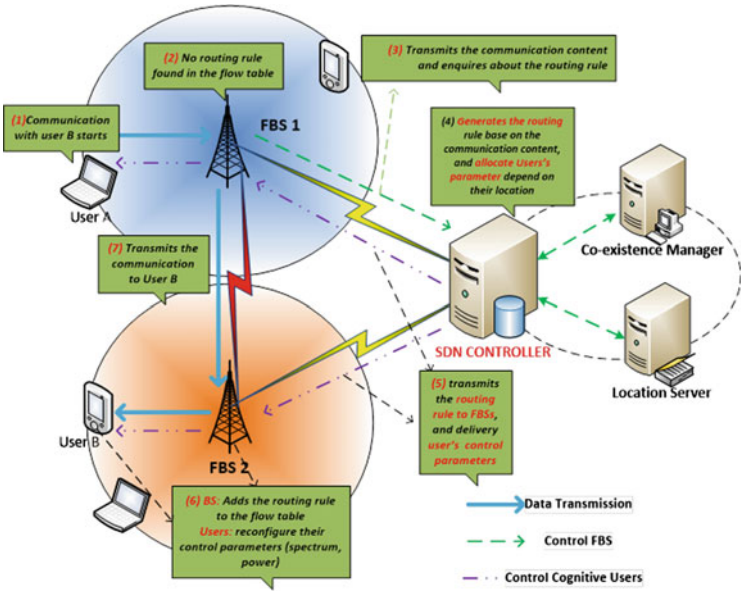

Fig. 5 Scenario: control plane interaction

3.2 Scenario: Control Plane Interaction

This section describes a scenario of control plane interaction between a cognitive user-device A connected to a femto base station 1 (FBS 1) and wants to communicate to cognitive user-device B which is connected to FBS 2 as shown in Fig. 5. Initially, user A sends request to its FBS 1 which is forwarded to the SDN controller for evaluation and allocation of power and channel. The SDN controller after evaluation send a route reply which consists of the route and the user's control parameters to concerned FBSs which installs the route in its table for future routing. Finally, FBS 1 transmits which initiates the actual exchange of data transmission as shown in Fig. 5.

4 Conclusion

The tremendous growth in wireless world due to the introduction of smart devices and associated bandwidth-hungry applications is forcing the service providers to enhance their existing network capabilities. The service providers need to support a high-capacity, agile, low-cost solution to ensure both user satisfaction and their profitability. This article introduces an SDN based framework for heterogeneous networks with network control capabilities to allow optimal power control, resource allocation, interference management and end to end quality of service.

Acknowledgments This research was supported by Basic Science Research Program through National Research Foundation of Korea (NRF) funded by the Ministry of Education (NRF-2014R1A2A2A01005900).

References

1. Fettweis G, Alamouti S (2014) 5 g: personal mobile internet beyond what cellular did to telephony. IEEE Commun Mag 52(2):140–145
2. Brown G (2013) White paper: converging telecom and it in the lte ran
3. Nam W, Bai D, Lee J, Kang I (2014) Advanced interference management for 5 g cellular networks. IEEE Commun Mag 52(5):52–60
4. Cisco (2010) Cisco visual networking index: forecast and methodology 2009 to 2014. Cisco White Paper
5. Hu R, Qian Y (2014) An energy efficient and spectrum efficient wireless heterogeneous network framework for 5 g systems. In: IEEE Commun Mag 52(5):94–101
6. Nguyen MV, Hong CS, Lee S (2012) Cross-layer optimization for congestion and power control in ofdm-based multi-hop cognitive radio networks. IEEE Trans Commun 60(8): 2101–2112
7. Nguyen MV, Hong CS, Lee S (2013) Joint rate adaption, power control, and spectrum allocation in ofdma-based multi-hop crns. IEICE Trans Commun E96-B(1)
8. ChihLin I, Rowell C, Han S, Xu Z, Li G, Pan Z (2014) Toward green and soft: a 5 g perspective. IEEE Commun Mag 52(2):66–73
9. METIS (2013) Scenarios, requirements and kpis for 5 g mobile and wireless system. ICT-317669 METIS Project
10. Chen S, Zhao J (2014) The requirements, challenges, and technologies for 5 g of terrestrial mobile telecommunication. IEEE Commun Mag 52(5):36–43
11. Bhushan N, Li J, Malladi D, Gilmore R, Brenner D, Damnjanovic A, Sukhavasi R, Patel C, Geirhofer S (2014) Network densification: the dominant theme for wireless evolution into 5 g. IEEE Commun Mag 52(2):82–89
12. Boccardi F, Heath R, Lozano A, Marzetta T, Popovski P (2014) Five disruptive technology directions for 5 g. IEEE Commun Mag 52(2):74–80
13. Wang C-X, Haider F, Gao X, You X-H, Yang Y, Yuan D, Aggoune H, Haas H, Fletcher S, Hepsaydir E (2014) Cellular architecture and key technologies for 5 g wireless communication networks. IEEE Commun Mag 52(2):122–130
14. Chandrasekhar V, Andrews JG, Gatherer A (2008) Femtocell networks: a survey. IEEE Commun Mag 46(9):59–67
15. Gudipati A, Perry D, Li LE, Katti S (2013) Softran: software defined radio access network. In: Proceedings of the second ACM SIGCOMM workshop on Hot topics in software defined networking. 1em plus 0.5em minus 0.4em ACM, pp 25–30

Hidden Attractors in Fundamental Problems and Engineering Models: A Short Survey

Nikolay V. Kuznetsov

Abstract Recently a concept of self-excited and hidden attractors was suggested: an attractor is called a *self-excited attractor* if its basin of attraction overlaps with neighborhood of an equilibrium, otherwise it is called a *hidden attractor*. For example, hidden attractors are attractors in systems with no equilibria or with only one stable equilibrium (a special case of multistability and coexistence of attractors). While coexisting self-excited attractors can be found using the standard computational procedure, there is no standard way of predicting the existence or coexistence of hidden attractors in a system.In this plenary lecture the concept of self-excited and hidden attractors is discussed, and various corresponding examples of self-excited and hidden attractors are considered. The material is mostly based on surveys [1–4].

Keywords Hidden attractor · Self-excited attractor · Hidden oscillation · System with no equilibria · System without equilibria · Multistability · Coexistence of attractors · 16th Hilbert problem · Aizerman and Kalman conjectures · Aircraft control system · Phase-locked loop · Chua circuit

International Conference on Advanced Engineering - Theory and Applications, 2015 (Ho Chi Minh City, Vietnam), plenary lecture.

N.V. Kuznetsov (✉)
Faculty of Mathematics and Mechanics, Saint-Petersburg University,
St. Petersburg 198504, Russia
e-mail: nkuznetsov239@gmail.com

N.V. Kuznetsov
Department of Mathematical Information Technology,
University of Jyväskylä, 40014 Jyväskylä, Finland

V.H. Duy et al. (eds.), *AETA 2015: Recent Advances in Electrical Engineering and Related Sciences*, Lecture Notes in Electrical Engineering 371,
DOI 10.1007/978-3-319-27247-4_2

1 Analytical-Numerical Study of Oscillations

An oscillation dynamical system can generally be easily numerically localized if the initial data from its open neighborhood in the phase space (with the exception of a minor set of points) lead to a long-term behavior that approaches the oscillation. Such an oscillation (or a set of oscillations) is called an attractor, and its attracting set is called the basin of attraction (i.e., a set of initial data for which the trajectories tend to the attractor).

When the theories of dynamical systems, oscillations, and chaos were first developed researchers mainly focused on analyzing equilibria stability, which can be easily done numerically or analytically, and on the birth of periodic or chaotic attractors from unstable equilibria. The structures of many physical dynamical systems are such that it is almost obvious that attractors exist because the trajectories can not tend to infinity and the oscillations are excited by an unstable equilibrium (see, e.g., the Rayleigh [5], Duffing [6], van der Pol [7], Tricomi [8], Beluosov-Zhabotinsky [9], and Lorenz [10] systems). This meant that scientists of that time could compute such attractors by constructing a solution using initial data from a small neighborhood of the equilibrium, observing how it is attracted and, thus, visualizes the attractor. In this *standard computational procedure*, computational methods and the engineering notion of a *transient process* were combined to study oscillations.

2 Self-excited and Hidden Attractors

From a computational perspective, it is natural to suggest the following classification of attractors, which is based on the connection of their basins of attraction with equilibria in the phase space:

Definition 1 [2, 4, 11, 12] An attractor is called a self-excited attractor if its basin of attraction intersects with any open neighborhood of a stationary state (an equilibrium), otherwise it is called a hidden attractor.

The first well-known example of a visualization of chaotic attractor in a dynamical system from the work of Lorenz [10] corresponds to the excitation of chaotic attractor from unstable equilibria. For classical parameters the Lorenz attractor is self-excited with respect to all three equilibria and could have been found using the standard computational procedure (see Fig. 1). Note that the chaotic attractor in the Lorenz system with other parameters may be self-excited with respect to zero unstable equilibrium only, and the possible existence in the Lorenz system of a hidden chaotic attractor is an open problem.

At the same time in the generalized Lorenz system $\dot{x} = -\sigma(x - y) - ayz$, $\dot{y} = rx - y - xz$, $\dot{z} = -bz + xy$ hidden chaotic attractors can be found [4, 13, 14] (see Fig. 2). For negative $a < 0$ the system corresponds to the Rabinovich system, which describes the interaction of plasma waves and was considered in 1978 [15, 16]; for

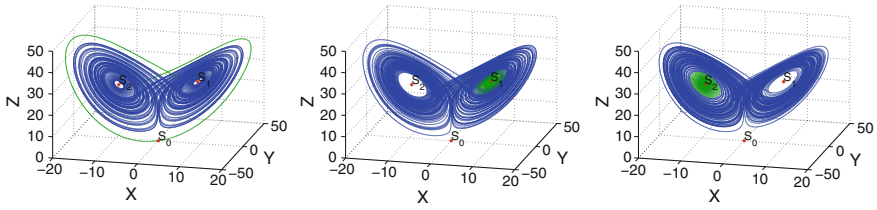

Fig. 1 Numerical visualization of the classical self-excited chaotic attractor in the Lorenz system $\dot{x} = 10(y - x)$, $\dot{y} = 28x - y - xz$, $\dot{z} = -8/3z + xy$. The attractor is self-excited respect to all three equilibria: it can be visualized by trajectories that start in small neighborhoods of any of unstable equilibria $S_{0,1,2}$. Here the separation of trajectory into transition process (*green*) and approximation of attractor (*blue*) is rough

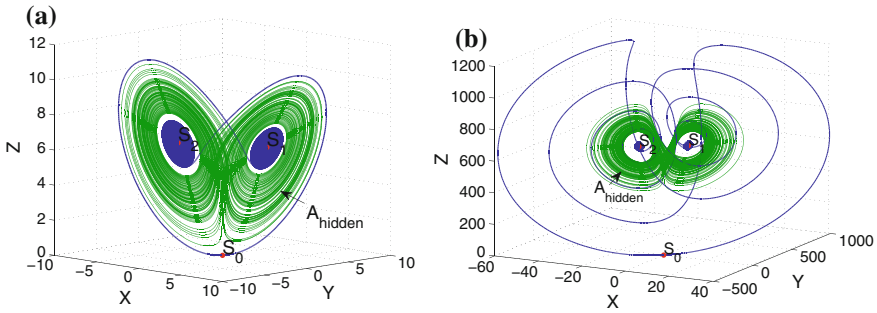

Fig. 2 Numerical visualization of hidden attractor (*green trajectory*) in the generalized Lorenz system. Outgoing separatrices of the zero saddle equilibrium are attracted to the stable equilibria$S_{1,2}$ (*blue trajectories*). **a** $r = 6.8$, $a = -0.5$, $\sigma = ra$, $b = 1$, **b** $r = 700$, $a = 0.0052$, $\sigma = ra$, $b = 1$

positive $a > 0$ it corresponds to the Glukhovsky-Dolghansky system, which describes convective fluid motion and was considered in 1980 [17]; also it describes a rigid body rotation in a resisting medium and the forced motion of a gyrostat (see [18]).

The basin of attraction for a hidden attractor is not connected with any equilibrium. For example, hidden attractors are attractors in systems with no equilibria or with only one stable equilibrium (a special case of the multistability and coexistence of attractors). Note that multistability can be undesired in various practical applications. At the same time the coexisting self-excited attractors in multistable systems (see, e.g. various examples of multistable engineering systems in famous book [19], and recent physical examples in [20]) can be found using the standard computational procedure, whereas there is no standard way of predicting the existence or coexistence of hidden attractors in a system.

For nonautonomous systems, depending on the physical problem statement, the notion of self-excited and hidden attractors can be introduced with respect to the stationary states of the system at the fixed initial time or the corresponding system

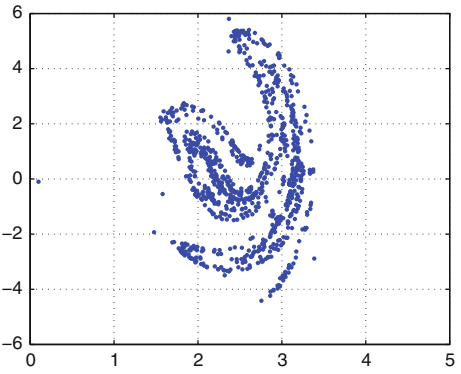

Fig. 3 An attractor in forced Duffing oscillator $\ddot{x} + 0.05\dot{x} + x^3 = 7.5\cos(t)$ is self-excited with respect to the zero equilibrium of unperturbed system (without $7.5\cos(t)$)

without time-varying excitations. For example, one of the classical examples of self-excited chaotic attractors was numerically found by Ueda in 1961 [21] in a forced Duffing system $\ddot{x} + 0.05\dot{x} + x^3 = 7.5\cos(t)$. To construct a self-excited chaotic attractor in this system (Fig. 3) it was used a transient process from the zero equilibrium of the unperturbed autonomous system (i.e., without $\cos(t)$) to an attractor in the forced system. If the discrete dynamics of system are considered on a Poincare section, then we can also use stationary or periodic points on the section that corresponds to a periodic orbit of the system (the consideration of periodic orbits is also natural for discrete systems). Note that if the attracting domain is the whole state space, then the attractor can be visualized by any trajectory and the only difference between computations is the time of the transient process.

One of the first well-known problems of analyzing hidden periodic oscillations arose in connection with the second part of Hilbert's 16th problem (1900) [22] on the number and mutual disposition of limit cycles in two-dimensional polynomial systems (see, e.g. resent results [2, 23–25] on visualization of nested limit cycles in quadratic systems: $\dot{x} = \alpha_1 x + \beta_1 y + a_1 x^2 + b_1 xy + d_1 y^2$, $\dot{y} = \alpha_2 x + \beta_2 y + a_2 x^2 + b_2 xy + d_2 y^2$).

Later, in the 1950s–1960s, the study of the well-known Aizerman's and Kalman's conjectures on absolute stability led to the discovery of the possible coexistence of a hidden periodic oscillation and a unique stable stationary point in automatic control systems. In 1957 Kalman stated the following [26]: "*If $f(e)$ in Fig. 1 [see Fig. 4] is replaced by constants K corresponding to all possible values of $f'(e)$, and it is found that the closed-loop system is stable for all such K, then it is intuitively clear that the system must be monostable; i.e., all transient solutions will*

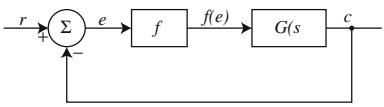

Fig. 4 Nonlinear control system. $G(s)$ is a linear transfer function, $f(e)$ is a single-valued, continuous, and differentiable [26]

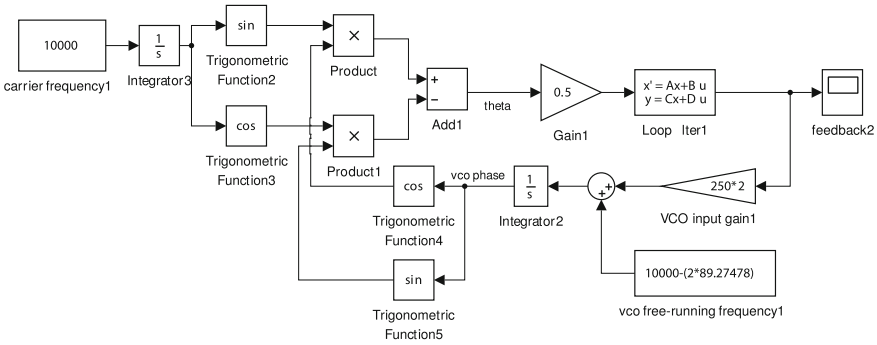

Fig. 5 Model of two-phase PLL with lead-lag filter in MATLAB Simulink. Lead-lag loop filter with the transfer function $H(s) = \frac{1+s\tau_2}{1+s(\tau_1+\tau_2)}$, $\tau_1 = 0.0448$, $\tau_2 = 0.0185$ and the corresponding parameters $A = -\frac{1}{\tau_1+\tau_2}$, $B = 1 - \frac{\tau_2}{\tau_1+\tau_2}$, $C = \frac{1}{\tau_1+\tau_2}$, $D = \frac{\tau_2}{\tau_1+\tau_2}$

converge to a unique, stable critical point." Kalman's conjecture is a strengthening of Aizerman's conjecture [27], which considers nonlinearities belonging to the sector of linear stability. Note that these conjectures are valid from the standpoint of simplified analysis such as the linearization, harmonic balance, and describing function methods (DFM), what explains why these conjectures were put forward. Nowadays various counterexamples to these conjectures (nonlinear systems where the only equilibrium, which is stable, coexists with a hidden periodic oscillation) are known (see [28–35]; the corresponding discrete examples are considered in [36, 37]).

Similar situation with linear stability and hidden oscillations occur in the analysis of aircrafts and launchers control systems with saturation [38, 39]. In [40] the crash of aircraft YF-22 Boeing in April 1992,[1] caused by the difficulties of rigorous analysis and design of nonlinear control systems with saturation, is discussed and the conclusion is made that *"since stability in simulations does not imply stability of the physical control system (an example is the crash of the YF22), stronger theoretical understanding is required"*.

Corresponding limitations, caused by hidden oscillations, appear in simulation of various phase-locked loop (PLL) based systems [2, 41–48]. PLL was designed to synchronize the phases of local oscillator and reference oscillator signals. Next example shows that the use of default simulation parameters in MATLAB Simulink for the study of two-phase PLL in the presence of hidden oscillation (see Fig. 5) can lead to the conclusions concerning the stability of the loop and the pull-in (or capture) range.[2] In Fig. 6 the model in Fig. 5 simulated with relative tolerance set to "1e-3" or smaller does not acquire lock (black color), but the model with default parameters (a relative tolerance set to "auto") acquires lock (red color). The same

[1] http://www.youtube.com/watch?v=M6sy-fxIhF0.

[2] See discussion of rigorous definitions in [48, 49].

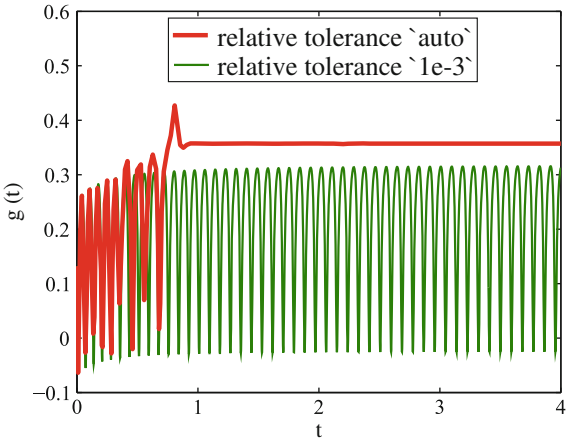

Fig. 6 Simulation of two-phase PLL. Loop filter output $g(t)$ for the initial data $x_0 = 0.1318$ obtained for default "auto" relative tolerance (*red*)—acquires lock, relative tolerance set to "1e-3"(*green*)—does not acquire lock

problems are also observed in SIMetrics SPICE model [41, 45, 46]. From a mathematical point of view, the above case corresponds to the existence of semi-stable periodic trajectory or co-existence of unstable and stable periodic trajectories (here the stable one is a hidden oscillation) [2, 41, 50, 51]. Therefore, if the gap between stable and unstable periodic trajectories is smaller than the discretization step, the numerical procedure may slip through the stable trajectory [45, 47].

Attractor in the *systems without equilibria* are the hidden attractors, according to the above definition. Systems without equilibria and with hidden oscillations appear naturally in the study of various electromechanical models with rotation and electrical circuits with cylindrical phase space. One of the first examples is from paper [52], published in 1902, in which Sommerfeld analyzed the vibrations caused by a motor driving an unbalanced weight and discovered the so-called Sommerfeld effect (see, e.g., [53, 54]). Another well-known chaotic system with no equilibrium points is the Nosè–Hoover oscillator [55–57]. An example of hidden chaotic attractor in electromechanical model with no equilibria was reported in a power system in 2001 [58]. Recent examples of hidden attractors in the systems without equilibria can be found, e.g. in [59–67].

After the concepts of hidden chaotic attractors was introduced first in connection with discovery of the first hidden Chua attractors (see Fig. 7) [11, 12, 68–74], the hidden chaotic attractors have received much attention. Recent examples of hidden attractors can be found in [59–61, 63, 75–112]).

See also *The European Physical Journal Special Topics: Multistability: Uncovering Hidden Attractors*, 2015 (see [113–124]).

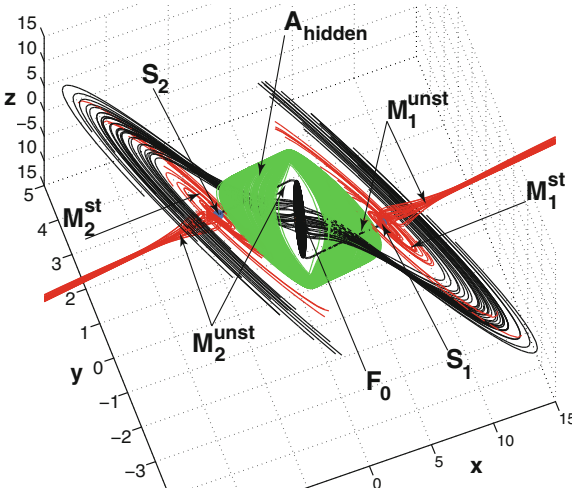

Fig. 7 Hidden chaotic attractor (*green*) in Chua circuit: $\dot{x} = \alpha(y - x - m_1 x - \psi(x)), \dot{y} = x - y + z, \dot{z} = -(\beta y + \gamma z), \psi(x) = (m_0 - m_1)\mathrm{sat}(x)$. Locally the stable zero equilibrium F_0 attracts trajectories (*black*) from stable manifolds $M^{st}_{1,2}$ of two saddle points $S_{1,2}$; trajectories (*red*) from the unstable manifolds $M^{unst}_{1,2}$ tend to infinity; $\alpha = 8.4562$, $\beta = 12.0732$, $\gamma = 0.0052$, $m_0 = -0.1768$, $m_1 = -1.1468$

Acknowledgments This work was supported by Russian Scientific Foundation (project 14-21-00041, sec. 2) and Saint-Petersburg State University (6.38.505.2014, sec. 1).

References

1. Leonov GA, Kuznetsov NV (2011) Analytical-numerical methods for investigation of hidden oscillations in nonlinear control systems. IFAC Proc Vol (IFAC-PapersOnline) 18(1):2494–2505
2. Leonov GA, Kuznetsov NV (2013) Hidden attractors in dynamical systems. From hidden oscillations in Hilbert-Kolmogorov, Aizerman, and Kalman problems to hidden chaotic attractors in Chua circuits. Int J Bifurcat Chaos 23(1):1330002
3. Kuznetsov N, Leonov G (2014) Hidden attractors in dynamical systems: systems with no equilibria, multistability and coexisting attractors. IFAC Proc (IFAC-PapersOnline) 19:5445–5454
4. Leonov G, Kuznetsov N, Mokaev T (2015) Homoclinic orbits, and self-excited and hidden attractors in a Lorenz-like system describing convective fluid motion. Eur Phys J Special Topics 224(8):1421–1458
5. Rayleigh JWS (1877) The theory of sound. Macmillan, London
6. Duffing G (1918) Erzwungene Schwingungen bei Veranderlicher Eigenfrequenz. F. Vieweg u. Sohn, Braunschweig
7. van der Pol B (1926) On relaxation-oscillations. Philos Mag J Sci 7(2):978–992
8. Tricomi F (1933) Integrazione di unequazione differenziale presentatasi in elettrotechnica. Annali della R. Shcuola Normale Superiore di Pisa 2(2):1–20

9. Belousov BP (1958) A periodic reaction and its mechanism. In: Collection of short papers on radiation medicine for 1958. Medical Publications, Moscow (in Russian)
10. Lorenz EN (1963) Deterministic nonperiodic flow. J Atmos Sci 20(2):130–141
11. Leonov GA, Kuznetsov NV, Vagaitsev VI (2011) Localization of hidden Chua's attractors. Phys Lett A 375(23):2230–2233
12. Leonov GA, Kuznetsov NV, Vagaitsev VI (2012) Hidden attractor in smooth Chua systems. Physica D 241(18):1482–1486
13. Leonov G, Kuznetsov N, Mokaev T (2015) Homoclinic orbit and hidden attractor in the Lorenz-like system describing the fluid convection motion in the rotating cavity. Commun Nonlinear Sci Numer Simul 28:166—174. doi:10.1016/j.cnsns.2015.04.007
14. Kuznetsov N, Leonov GA, Mokaev TN (2015) Hidden attractor in the Rabinovich system. arXiv:1504.04723v1
15. Rabinovich MI (1978) Stochastic autooscillations and turbulence. Uspehi Physicheskih 125 (1):123–168
16. Pikovski AS, Rabinovich MI, Trakhtengerts VY (1978) Onset of stochasticity in decay confinement of parametric instability. Sov Phys JETP 47:715–719
17. Glukhovskii AB, Dolzhanskii FV (1980) Three-component geostrophic model of convection in a rotating fluid. Academy of Sciences, USSR, Izvestiya, Atmospheric and Oceanic Physics 16:311–318
18. Leonov GA, Boichenko VA (1992) Lyapunov's direct method in the estimation of the Hausdorff dimension of attractors. Acta Applicandae Mathematicae 26(1):1–60
19. Andronov AA, Vitt EA, Khaikin SE (1937) Theory of Oscillators (in Russian). ONTI NKTP SSSR (trans: Pergamon Press, 1966)
20. Pisarchik A, Feudel U (2014) Control of multistability. Phys Rep 540(4):167–218
21. Ueda Y, Akamatsu N, Hayashi C (1973) Computer simulations and non-periodic oscillations. Trans IEICE Jpn 56A(4):218–255
22. Hilbert D (1901–1902) Mathematical problems. Bull Amer Math Soc (8):437–479
23. Leonov GA, Kuznetsova OA (2010) Lyapunov quantities and limit cycles of two-dimensional dynamical systems. Analytical methods and symbolic computation. Regular and Chaotic Dynamics 15(2–3):354–377
24. Leonov GA, Kuznetsov NV, Kuznetsova OA, Seledzhi SM, Vagaitsev VI (2011) Hidden oscillations in dynamical systems. Trans Syst Control 6(2):54–67
25. Kuznetsov NV, Kuznetsova OA, Leonov GA (2013) Visualization of four normal size limit cycles in two-dimensional polynomial quadratic system. Diff Equ Dyn Syst 21(1–2):29–34
26. Kalman RE (1957) Physical and mathematical mechanisms of instability in nonlinear automatic control systems. Trans ASME 79(3):553–566
27. Aizerman MA (1949) On a problem concerning the stability in the large of dynamical systems. Uspekhi Mat. Nauk (in Russian) 4:187–188
28. Pliss VA (1958) Some Problems in the theory of the stability of motion. Izd LGU, Leningrad (in Russian)
29. Fitts RE (1966) Two counterexamples to Aizerman's conjecture. Trans IEEE AC-11(3):553–556
30. Barabanov NE (1988) On the Kalman problem. Sib Math J 29(3):333–341
31. Bernat J, Llibre J (1996) Counterexample to Kalman and Markus-Yamabe conjectures in dimension larger than 3. Dyn Continuous Discrete Impulsive Syst 2(3):337–379
32. Leonov GA, Bragin VO, Kuznetsov NV (2010) Algorithm for constructing counterexamples to the Kalman problem. Dokl Math 82(1):540–542
33. Bragin VO, Vagaitsev VI, Kuznetsov NV, Leonov GA (2011) Algorithms for finding hidden oscillations in nonlinear systems. The Aizerman and Kalman conjectures and Chua's circuits. J Comput Syst Sci Int 50(4):511–543
34. Leonov GA, Kuznetsov NV (2011) Algorithms for searching for hidden oscillations in the Aizerman and Kalman problems. Dokl Math 84(1):475–481
35. Kuznetsov NV, Leonov GA, Seledzhi SM (2011) Hidden oscillations in nonlinear control systems. IFAC Proc Vol (IFAC-PapersOnline) 18(1):2506–2510

36. Alli-Oke R, Carrasco J, Heath W, Lanzon A (2012) A robust Kalman conjecture for first-order plants. In: Proceedings of IEEE Control and Decision Conference (2012)
37. Heath WP, Carrasco J, de la Sen M (2015) Second-order counterexamples to the discrete-time Kalman conjecture. Automatica 60:140–144
38. Andrievsky BR, Kuznetsov NV, Leonov GA, Pogromsky AY (2013) Hidden oscillations in aircraft flight control system with input saturation. IFAC Proc Vol (IFAC-PapersOnline) 5 (1):75–79
39. Andrievsky BR, Kuznetsov NV, Leonov GA, Seledzhi SM (2013) Hidden oscillations in stabilization system of flexible launcher with saturating actuators. IFAC Proc Vol (IFAC-PapersOnline) 19(1):37–41
40. Lauvdal T, Murray R, Fossen T (1997) Stabilization of integrator chains in the presence of magnitude and rate saturations: a gain scheduling approach. In: Proceedings of IEEE Control and Decision Conference, vol 4, pp 4404–4005
41. Kuznetsov N, Leonov G, Yuldashev M, Yuldashev R (2014) Nonlinear analysis of classical phase-locked loops in signal's phase space. In: IFAC Proc Vol (IFAC-PapersOnline) 19:8253–8258
42. Kuznetsov N, Kuznetsova O, Leonov G, Neittaanmaki P, Yuldashev M, Yuldashev R (2014) Simulation of nonlinear models of QPSK Costas loop in Matlab Simulink. In: 2014 6th International Congress on Ultra Modern Telecommunications and Control Systems and Workshops (ICUMT), 2015 January, IEEE, pp 66–71
43. Kuznetsov N, Kuznetsova O, Leonov G, Seledzhi S, Yuldashev M, Yuldashev R (2014) BPSK Costas loop: simulation of nonlinear models in Matlab Simulink. In: 2014 6th International Congress on Ultra Modern Telecommunications and Control Systems and Workshops (ICUMT).2015 January, IEEE, pp 83–87
44. Kudryasoha EV, Kuznetsova OA, Kuznetsov NV, Leonov GA, Seledzhi SM, Yuldashev MV, Yuldashev RV (2014) Nonlinear models of BPSK Costas loop. In: ICINCO 2014 - Proceedings of the 11th International Conference on Informatics in Control, Automation and Robotics, vol 1, pp 704–710
45. Kuznetsov N, Kuznetsova O, Leonov G, Neittaanmaki P, Yuldashev M, Yuldashev R (2015) Limitations of the classical phase-locked loop analysis. In: International Symposium on Circuits and Systems (ISCAS), IEEE (2015), pp 533–536 http://arxiv.org/pdf/1507.03468v1.pdf
46. Best R, Kuznetsov N, Kuznetsova O, Leonov G, Yuldashev M, Yuldashev R (2015) A short survey on nonlinear models of the classic Costas loop: rigorous derivation and limitations of the classic analysis. In: American Control Conference (ACC), IEEE, pp 1296–1302 http://arxiv.org/pdf/1505.04288v1.pdf
47. Bianchi G, Kuznetsov N, Leonov G, Yuldashev M, Yuldashev R (2015) Limitations of PLL simulation: hidden oscillations in SPICE analysis. In: arXiv:1506.02484 (2015) http://arxiv.org/pdf/1506.02484.pdf, http://www.mathworks.com/matlabcentral/fileexchange/52419-hidden-oscillations-in-pll (accepted to IEEE 7th International Congress on Ultra Modern Telecommunications and Control Systems)
48. Leonov G, Kuznetsov N, Yuldashev M, Yuldashev R (2015) Hold-in, pull-in, and lock-in ranges of PLL circuits: rigorous mathematical definitions and limitations of classical theory. In: IEEE Transactions on Circuits and Systems—I: Regular Papers (http://arxiv.org/pdf/1505.04262v2.pdf)
49. Kuznetsov N, Leonov G, Yuldashev M, Yuldashev R (2015) Rigorous mathematical definitions of the hold-in and pull-in ranges for phase-locked loops. In: 1st IFAC Conference on Modelling, Identification and Control of Nonlinear Systems, IFAC Proceedings Volumes (IFAC-PapersOnline), pp 720–723
50. Shakhtarin B (1969) Study of a piecewise-linear system of phase-locked frequency control. Radiotechnica and electronika (in Russian) 8:1415–1424
51. Belyustina L, Brykov V, Kiveleva K, Shalfeev V (1970) On the magnitude of the locking band of a phase-shift automatic frequency control system with a proportionally integrating filter. Radiophys Quantum Electron 13(4):437–440

52. Sommerfeld A (1902) Beitrage zum dynamischen ausbau der festigkeitslehre. Z Ver Dtsch Ing 46:391–394
53. Blekhman I, Indeitsev D, Fradkov A (2007) Slow motions in systems with inertially excited vibrations. IFAC Proc Vol (IFAC-PapersOnline) 3(1):126–131
54. Eckert M (2013) Arnold sommerfeld: science, life and turbulent times 1868–1951. Springer
55. Nose S (1984) A molecular dynamics method for simulations in the canonical ensemble. Mol Phys 52(2):255–268
56. Hoover W (1985) Canonical dynamics: equilibrium phase-space distributions. Phys Rev A 31:1695–1697
57. Sprott J (1994) Some simple chaotic flows. Phys Rev E 50(2):R647–R650
58. Venkatasubramanian V (2001) Stable operation of a simple power system with no equilibrium points. In: Proceedings of the 40th IEEE Conference on Decision and Control. vol 3, pp 2201–2203
59. Wei Z, Wang R, Liu A (2014) A new finding of the existence of hidden hyperchaotic attractors with no equilibria. Math Comput Simul 100:13–23
60. Pham VT, Jafari S, Volos C, Wang X, Golpayegani S (2014) Is that really hidden? The presence of complex fixed-points in chaotic flows with no equilibria. Int J Bifurcat Chaos 24 (11):1450146
61. Pham VT, Rahma F, Frasca M, Fortuna L (2014) Dynamics and synchronization of a novel hyperchaotic system without equilibrium. Int J Bifurcat Chaos 24(06):1450087
62. Pham VT, Volos C, Gambuzza L (2014) A memristive hyperchaotic system without equilibrium. Sci World J 04:368986
63. Pham VT, Volos C, Jafari S, Wei Z, Wang X (2014) Constructing a novel no-equilibrium chaotic system. Int J Bifurcat Chaos 24(05):1450073
64. Tahir F, Jafari S, Pham VT, Volos C, Wang X (2015) A novel no-equilibrium chaotic system with multiwing butterfly attractors. Int J Bifurcat Chaos 25(04):1550056
65. Vaidyanathan S, Volos CK, Pham V (2015) Analysis, control, synchronization and SPICE implementation of a novel 4-D hyperchaotic Rikitake dynamo system without equilibrium. J Eng Sci Technol Rev 8(2):232–244
66. Cafagna D, Grassi G (2015) Fractional-order systems without equilibria: the first example of hyperchaos and its application to synchronization. Chin Phys B 24(8):080502
67. Chen G (2015) Chaotic systems with any number of equilibria and their hidden attractors (plenary lecture). In: 4th IFAC Conference on Analysis and Control of Chaotic Systems. http://www.ee.cityu.edu.hk/∼gchen/pdf/CHEN_IFAC2015.pdf
68. Leonov GA, Kuznetsov NV (2009) Localization of hidden oscillations in dynamical systems (plenary lecture). In: 4th International Scientific Conference on Physics and Control. http://www.math.spbu.ru/user/leonov/publications/2009-PhysCon-Leonov-plenary-hidden-oscillations.pdf
69. Kuznetsov NV, Leonov GA, Vagaitsev VI (2010) Analytical-numerical method for attractor localization of generalized Chua's system. IFAC Proc Vol (IFAC-PapersOnline) 4(1):29–33
70. Kuznetsov N, Vagaitsev V, Leonov G, Seledzhi S (2011) Localization of hidden attractors in smooth Chua's systems. In: International Conference on Applied and Computational Mathematics, pp 26–33
71. Kuznetsov NV, Kuznetsova OA, Leonov GA, Vagaytsev VI (2011) Hidden attractor in Chua's circuits. In: ICINCO 2011 - Proceedings of the 8th International Conference on Informatics in Control, Automation and Robotics, vol 1, pp 279–283
72. Leonov GA, Kuznetsov NV (2012) IWCFTA2012 Keynote speech I - Hidden attractors in dynamical systems: from hidden oscillation in Hilbert-Kolmogorov, Aizerman and Kalman problems to hidden chaotic attractor in Chua circuits. In: IEEE 2012 Fifth International Workshop on Chaos-Fractals Theories and Applications (IWCFTA), pp 15–17
73. Kuznetsov N, Kuznetsova O, Leonov G, Vagaitsev V (2013) Analytical-numerical localization of hidden attractor in electrical Chua's circuit. Inform Control Autom Robot Lect Notes Electr Eng 174(4):149–158

74. Leonov G, Kiseleva M, Kuznetsov N, Kuznetsova O (2015) Discontinuous differential equations: comparison of solution definitions and localization of hidden Chua attractors. In: 1st IFAC Conference on Modelling, Identification and Control of Nonlinear Systems, IFAC Proceedings Volumes (IFAC-PapersOnline), pp 418–423
75. Kiseleva M, Kuznetsov N, Leonov G, Neittaanmaki P (2013) Hidden oscillations in drilling system actuated by induction motor. IFAC Proc Vol (IFAC-PapersOnline) 5:86–89
76. Kiseleva M, Kondratyeva N, Kuznetsov N, Leonov G, Solovyeva E (2014) Hidden periodic oscillations in drilling system driven by induction motor. IFAC Proc Vol (IFAC-PapersOnline) 19:5872–5877
77. Leonov GA, Kuznetsov NV, Kiseleva MA, Solovyeva EP, Zaretskiy AM (2014) Hidden oscillations in mathematical model of drilling system actuated by induction motor with a wound rotor. Nonlinear Dyn 77(1–2):277–288
78. Leonov GA, Kuznetsov NV (2014) Hidden oscillations in dynamical systems. 16 Hilbert's problem, Aizerman's and Kalman's conjectures, hidden attractors in Chua's circuits. J Math Sci 201(5):645–662
79. Leonov GA, Kuznetsov NV (2013) Prediction of hidden oscillations existence in nonlinear dynamical systems: analytics and simulation. Adv Intell Syst Comput AISC 210:5–13
80. Leonov GA, Kiseleva MA, Kuznetsov NV, Neittaanmäki P (2013) Hidden oscillations in drilling systems: torsional vibrations. J Appl Nonlinear Dyn 2(1):83–94
81. Kiseleva M, Kondratyeva N, Kuznetsov N, Leonov G (2015) Hidden oscillations in drilling systems with salient pole synchronous motor. In: 1st IFAC Conference on Modelling, Identification and Control of Nonlinear Systems, IFAC Proceedings Volumes (IFAC-PapersOnline), pp 418–423
82. Sprott J, Wang X, Chen G (2013) Coexistence of point, periodic and strange attractors. Int J Bifurcat Chaos 23(5):1350093
83. Wang X, Chen G (2013) Constructing a chaotic system with any number of equilibria. Nonlinear Dyn 71:429–436
84. Zhusubaliyev Z, Mosekilde E (2015) Multistability and hidden attractors in a multilevel DC/DC converter. Math Comput Simul 109:32–45
85. Wang Z, Sun W, Wei Z, Zhang S (2015) Dynamics and delayed feedback control for a 3d jerk system with hidden attractor. Nonlinear Dyn
86. Sharma P, Shrimali M, Prasad A, Kuznetsov NV, Leonov GA (2015) Controlling dynamics of hidden attractors. Int J Bifurcat Chaos 25(04):1550061
87. Dang XY, Li CB, Bao BC, Wu HG (2015) Complex transient dynamics of hidden attractors in a simple 4d system. Chin Phys B 24(5):050503
88. Kuznetsov A, Kuznetsov S, Mosekilde E, Stankevich N (2015) Co-existing hidden attractors in a radio-physical oscillator system. J Phys A Math Theor 48:125101
89. Pham VT, Volos C, Jafari S, Wang X, Vaidyanathan S (2014) Hidden hyperchaotic attractor in a novel simple memristive neural network. Optoelectron Adv Mater Rapid Commun 8(11–12):1157–1163
90. Li C, Sprott JC (2014) Coexisting hidden attractors in a 4-D simplified Lorenz system. Int J Bifurcat Chaos 24(03):1450034
91. Wei Z, Moroz I, Liu A (2014) Degenerate Hopf bifurcations, hidden attractors and control in the extended Sprott E system with only one stable equilibrium. Turk J Math 38(4):672–687
92. Pham VT, Volos C, Vaidyanathan S, Le T, Vu V (2015) A memristor-based hyperchaotic system with hidden attractors: Dynamics, synchronization and circuital emulating. J Eng Sci Technol Rev 2:205–214
93. Chen M, Yu J, Bao BC (2015) Finding hidden attractors in improved memristor-based Chua's circuit. Electron Lett 51:462–464
94. Chen M, Li M, Yu Q, Bao B, Xu Q, Wang J (2015) Dynamics of self-excited attractors and hidden attractors in generalized memristor-based Chua's circuit. Nonlinear Dyn. doi:10.1007/s11071-015-1983-7
95. Wei Z, Zhang W, Wang Z, Yao M (2015) Hidden attractors and dynamical behaviors in an extended Rikitake system. Int J Bifurcat Chaos 25(02):1550028

96. Burkin I, Khien N (2014) Analytical-numerical methods of finding hidden oscillations in multidimensional dynamical systems. Differ Equ 50(13):1695–1717
97. Wei Z, Zhang W (2014) Hidden hyperchaotic attractors in a modified Lorenz-Stenflo system with only one stable equilibrium. Int J Bifurcat Chaos 24(10):1450127
98. Li Q, Zeng H, Yang XS (2014) On hidden twin attractors and bifurcation in the Chua's circuit. Nonlinear Dyn 77(1–2):255–266
99. Zhao H, Lin Y, Dai Y (2014) Hidden attractors and dynamics of a general autonomous van der Pol-Duffing oscillator. Int J Bifurcat Chaos 24(06):1450080
100. Lao SK, Shekofteh Y, Jafari S, Sprott J (2014) Cost function based on Gaussian mixture model for parameter estimation of a chaotic circuit with a hidden attractor. Int J Bifurcat Chaos 24(1):1450010
101. Chaudhuri U, Prasad A (2014) Complicated basins and the phenomenon of amplitude death in coupled hidden attractors. Phys Lett A 378(9):713–718
102. Pham VT, Volos C, Jafari S, Wang X (2014) Generating a novel hyperchaotic system out of equilibrium. Optoelectron Adv Mater Rapid Commun 8(5–6):535–539
103. Kingni S, Jafari S, Simo H, Woafo P (2014) Three-dimensional chaotic autonomous system with only one stable equilibrium: analysis, circuit design, parameter estimation, control, synchronization and its fractional-order form. Eur Phys J Plus 129(5)
104. Li C, Sprott J (2014) Chaotic flows with a single nonquadratic term. Phys Lett A 378(3):178–183
105. Molaie M, Jafari S, Sprott J, Golpayegani S (2013) Simple chaotic flows with one stable equilibrium. Int J Bifurcat Chaos 23(11):1350188
106. Jafari S, Sprott JC, Pham VT, Golpayegani SMRH, Jafari AH (2014) A new cost function for parameter estimation of chaotic systems using return maps as fingerprints. Int J Bifurcat Chaos 24(10):1450134
107. Jafari S, Sprott J (2013) Simple chaotic flows with a line equilibrium. Chaos Solitons Fractals 57:79–84
108. Dudkowski D, Prasad A, Kapitaniak T (2015) Perpetual points and hidden attractors in dynamical systems. Phys Lett A 379(40–41):2591–2596
109. Wei Z, Yu P, Zhang W, Yao M (2015) Study of hidden attractors, multiple limit cycles from hopf bifurcation and boundedness of motion in the generalized hyperchaotic rabinovich system. Nonlinear Dyn
110. Zhusubaliyev ZT, Mosekilde E, Rubanov VG, Nabokov RA (2015) Multistability and hidden attractors in a relay system with hysteresis. Physica D: Nonlinear Phenomena
111. Bao B, Hu F, Chen M, Xu Q, Yu Y (2015) Self-excited and hidden attractors found simultaneously in a modified Chua's circuit. Int J Bifurcat Chaos 25(05):1550075
112. Danca MF, Feckan M, Kuznetsov N, Chen G (2016) Looking more closely to a Rabinovich-Fabrikant system. Int J Bifurcat Chaos (accepted)
113. Shahzad M, Pham VT, Ahmad M, Jafari S, Hadaeghi F (2015) Synchronization and circuit design of a chaotic system with coexisting hidden attractors. Eur Phys J Spec Topics 224 (8):1637–1652
114. Brezetskyi S, Dudkowski D, Kapitaniak T (2015) Rare and hidden attractors in Van der Pol-Duffing oscillators. Eur Phys J Spec Topics 224(8):1459–1467
115. Jafari S, Sprott J, Nazarimehr F (2015) Recent new examples of hidden attractors. Eur Phys J Spec Topics 224(8):1469–1476
116. Zhusubaliyev Z, Mosekilde E, Churilov A, Medvedev A (2015) Multistability and hidden attractors in an impulsive Goodwin oscillator with time delay. Eur Phys J Spec Topics 224 (8):1519–1539
117. Saha P, Saha D, Ray A, Chowdhury A (2015) Memristive non-linear system and hidden attractor. Eur Phys J Spec Topics 224(8):1563–1574
118. Semenov V, Korneev I, Arinushkin P, Strelkova G, Vadivasova T, Anishchenko V (2015) Numerical and experimental studies of attractors in memristor-based Chua's oscillator with a line of equilibria. Noise-induced effects. Eur Phys J Spec Topics 224(8):1553–1561

119. Feng Y, Wei Z (2015) Delayed feedback control and bifurcation analysis of the generalized Sprott B system with hidden attractors. Eur Phys J Spec Topics 224(8):1619–1636
120. Li C, Hu W, Sprott J, Wang X (2015) Multistability in symmetric chaotic systems. Eur Phys J Spec Topics 224(8):1493–1506
121. Feng Y, Pu J, Wei Z (2015) Switched generalized function projective synchronization of two hyperchaotic systems with hidden attractors. Eur Phys J Spec Topics 224(8):1593–1604
122. Sprott J (2015) Strange attractors with various equilibrium types. Eur Phys J Spec Topics 224 (8):1409–1419
123. Pham V, Vaidyanathan S, Volos C, Jafari S (2015) Hidden attractors in a chaotic system with an exponential nonlinear term. Eur Phys J Spec Topics 224(8):1507–1517
124. Vaidyanathan S, Pham VT, Volos C (2015) A 5-D hyperchaotic Rikitake dynamo system with hidden attractors. Eur Phys J Spec Topics 224(8):1575–1592

Part II
Telecommunication

Experimental Study on the Effects of External Interference on Slot Scheduling Based MAC Protocols in Wireless Sensor Networks

Chi Trung Ngo, Hoon Oh and Minh Thuy Pham

Abstract An energy-aware timely and reliable data transmission is one of the most critical requirements in designing slot scheduling based MAC protocols for applications in industrial fields. A time slot size affects two conflicting goals, reducing energy consumption and increasing the reliability of data transmission, thereby requiring an optimized time slot size. A time slot size should be determined in the presence of the signal interference by Wi-Fi, Bluetooth and other sensor nodes operating at the 2.4 GHz band. In this paper, we employ two different interference models that account for different types of interference sources to determine the optimal size of a time slot. The experimental study with a simple network testbed is conducted. In addition, the effectiveness of using the well-known Clear Channel Assessment mechanism in the radio chip is examined under the high interference environment.

Keywords Interference · Slot scheduling based MAC protocol · Wireless sensor networks

1 Introduction

The workforces working in industrial fields are highly susceptible to the hazardous environment or unexpected accidents. These hazards can be avoided or detected early for the timely measures if a server gathers and analyzes data from the working

C.T. Ngo · H. Oh (✉)
Department of Electrical Engineering and Computer Science,
University of Ulsan, Ulsan, South Korea
e-mail: hoonoh@ulsan.ac.kr

C.T. Ngo
e-mail: chitrung218@gmail.com

M.T. Pham
Faculty of Electrical and Electronics Engineering, Ton Duc Thang University,
No. 19 Nguyen Huu Tho Street, District 7, Ho Chi Minh City, Vietnam
e-mail: minhthuy285@gmail.com

V.H. Duy et al. (eds.), *AETA 2015: Recent Advances in Electrical Engineering and Related Sciences*, Lecture Notes in Electrical Engineering 371,
DOI 10.1007/978-3-319-27247-4_3

premises and then sends messages to warn workers of the situation. In this context-aware service, a wireless sensor network (WSN) can be used as a network platform where sensor nodes equipped with sensor modules that can sense thermal, gas, oxygen, smoke, flame, etc. use multi-hop communication to send sensed data to a server.

One of the most critical requirements for such service is a timely and reliable data transmission, thus so far there have been some proposed slot scheduling based MAC protocols that target a reliable and real-time data transmission such as TreeMAC [1], I-MAC [2], WirelessHART [3]. TreeMAC assigns non-overlapping frames to all nodes in a WSN where each frame consists of three slots. The slots are reused by the nodes every three depths in a tree topology. Meanwhile, I-MAC allocates slots to each node in a distinct manner since it targets a small control network. It tries to enhance a reliable data transmission by using RTS, CTS, and ACK when transmitting data. Since the time-varying channel is frequency-dependence, WirelessHART assigns each communication link between two sensors a time slot and frequency channel, which guarantees the collision-free for data transmission. In order to increase the transmission reliability it employs a frequency hopping technique and channel backlist which records frequency channels which are not allowed to use due to the significantly affected by interferences. These protocols require strict time synchronization and the size of slot should be big enough to transmit and receive one data packet.

However, besides inevitable phenomena such as fading and the intervention of some obstacles, the radio interference by WLAN [4], Bluetooths, and other sensor nodes also induces the unstable data communication. These interferences cause link breakage and data collision. Furthermore, in the environment with high interference if a slot size is small, a node may not have enough time to send data; however, increasing the slot size can violate the requirement of timely data transmission.

Therefore, investigating the impact of interference on data transmission between sensor nodes in slot scheduling based MAC protocols are essential in finding solutions to improve their robustness against interference as well as to increase energy efficiency. In this paper, we conduct experiments on testbed using Kmote for these purposes. We employ one sensor node acting as an interference node to generate the controlled interference signal which interferes with data transmission between other two sensor nodes. Its duty is to generate customized and repeatable interference patterns using different interference models, e.g. bursty interference and semi-periodic interference proposed in [5]. The performance is evaluated in terms of packet delivery ratio, energy consumption and missed timely delivery ratio.

The rest of the paper is organized as follows. In Sect. 2, we present the network model. The interference model used to generate interference signal is described in Sect. 3. We discuss the experimental results in Sect. 5. Finally, we make concluding remarks in Sect. 6.

2 Network Model

In slot scheduling based MAC protocols, the WSN consists of a control server (hereafter referred to as a *sink node*) which is wall-powered and a number of sensor nodes (hereafter referred to as *nodes*) which are battery-powered. Every node is equipped with at least one sensor module and required to generate one data packet that includes the sensed information every cycle and forwards it to the sink node within a specified time bound depending on the requirement of a specific application. Each node is assigned a pair of sending and receiving time slots to transmit data to an upstream node towards the sink and to receive data from a downstream node, respectively.

Since only one data transmission within the allocated time slot of a node is made, it is sufficient to consider a simple network model with three nodes placed within their transmission range each other to evaluate the impact of interference on the data transmission between two sensor nodes in slot scheduling based MAC protocols.

3 Interference Model

To generate the interference patterns that can be generated repeatedly and changed on a needed basis, we employ a signal generation method that uses a special test mode of the radio chip [6]. The characteristic of interference signal is modeled by using two simple interference models, *bursty interference* and *semi-periodic interference* [5].

3.1 Bursty Interference

The bursty interference model that models the characteristics of Wi-Fi or Bluetooth transmissions is used to generate the continuous blocks of the interference period and the spacing period, each having uniformly distribution. Since there is no one-to-one matching between 802.15.4 and Wi-Fi channels, for example, channel 1 of Wi-Fi just overlaps with channels 11, 12, 13, 14 of 802.15.4 as shown in Fig. 1, the Wi-Fi signal can be seen as the background noise in WSNs. The Wi-Fi interference signal as the background noise can be the unmodulated signal that is generated from a sensor node by changing the register value of the radio chip (e.g. CC2420_MDMCTRLI for CC2420) [6]. Note that the power spectrum of the unmodulated signal is highly concentrated at the center frequency.

Furthermore, the duration of the Wi-Fi traffic depends on the time span of data exchange between two Wi-Fi devices and a number of Wi-Fi devices generating the traffic. Therefore, in order to model the randomly continuous on/off periods of the

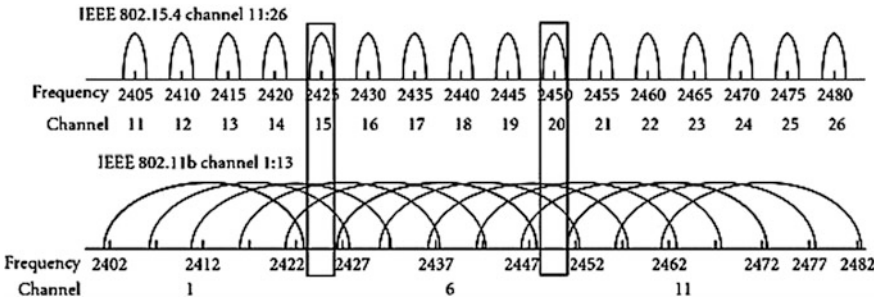

Fig. 1 Channel assignment in 2.4 GHz band

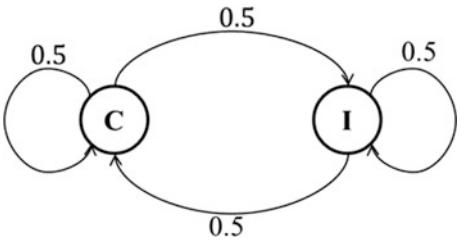

Fig. 2 Markov process to model the on/off periods of the interference transmission

interference transmission, a simple two-state discrete Markov process can be used as depicted in Fig. 2. In this figure, C and I denote the clear channel state and the interference state, respectively. The state transition condition is determined by a Bernoulli random variable 0.5. We can obtain a time period $T(C)$ and $T(I)$ which indicate the time duration that the process stays at state C and I, respectively, as follows:

$$T(C) = T(I) = R(x) \times S \tag{1}$$

where, $R(x)$ is a random number which is uniformly distributed in $[1, x]$ and S is used to scale the burstiness of the interference, namely $S \in [1, 2]$ and $S \in [5, 10]$ for short and long interference transmission, respectively. For example, given $x = 50$ and $S = 5$, assuming that the process changes from state C to state I where we obtain $R = 30$, the length of the interference period will be determined by $30 \times 5 = 150$ ms.

3.2 Semi-periodic Interference

The semi-periodic interference can be modeled by the continuous blocks of interference with small duration for interference signal generation and variable spacing,

which corresponds to the periodic data transmission of sensor nodes in other WSNs coexisting with the current one. Since this is an internal interference operating at the same 802.15.4 channel, we can use the randomly-modulated signal generated from a sensor device as the internal interference signal [6]. The characteristic of the modulated signal is that its power spectrum spreads out evenly across the channel bandwidth

Using the same two states C and I as described above, the process to generate the semi-periodic interference pattern is given as follows. The process changes in alternation of these two states in which states I and C last for $T(C)$ and $T(I)$, respectively, which are determined as follows.

$$T(I) = (1 + r) \times \alpha \times P \tag{2}$$

$$T(C) = (1 + r) \times (1 - \alpha) \times P \tag{3}$$

where, r is a random number which is uniformly distributed in [0, 0.3], P is the fixed time period, and $\alpha \in (0, 1)$ is the interference rate. It is worth noting that since the semi-periodic interference is caused by the periodic data transmission of sensor nodes, P should be selected such that the length of interference period, $T(I)$, is appropriately equal to the period of data transmission in the reality.

4 Calculation of Minimum Time Slot Size

In this section, we analyze the minimum time slot size which is enough to transmit one data packet without the effect of interference since it is one of the factors determining the timely data transmission. The minimum time slot size, T_s (i.e., one hop packet delay) can be computed as follows:

$$T_s = t_{ts} + 2t_{xm} + 2t_{pm} + t_{tr} \tag{4}$$

where, t_{ts} (transfer time at the sender): The time taken to generate a message and transfer from the buffer of the microcontroller into the buffer of the radio chip transceiver; t_{xm} (transmission time at the sender): The time taken to transmit the message; t_{rm} (receiving time at the receiver) = t_{xm}: The time taken to receive the message; t_{pm} (processing time at the sender and receiver): The time taken to process the message; and t_{tr} (transfer time at the receiver): The time taken to transfer the received message from the radio chip buffer to the microcontroller buffer.

In order to calculate values of these parameters we have to know the total size of the frame format when it is transmitted between the microcontroller and the radio chip as well as when it is transmitted over the medium. Now, we analyze the detail of the frame format at the MAC layer and the CC2420 radio layer (the radio chip CC2420 is used in this paper). Since the MAC layer uses the frame format defined by the IEEE 802.15.4 standard in order to be compatible with the IEEE 802.15.4

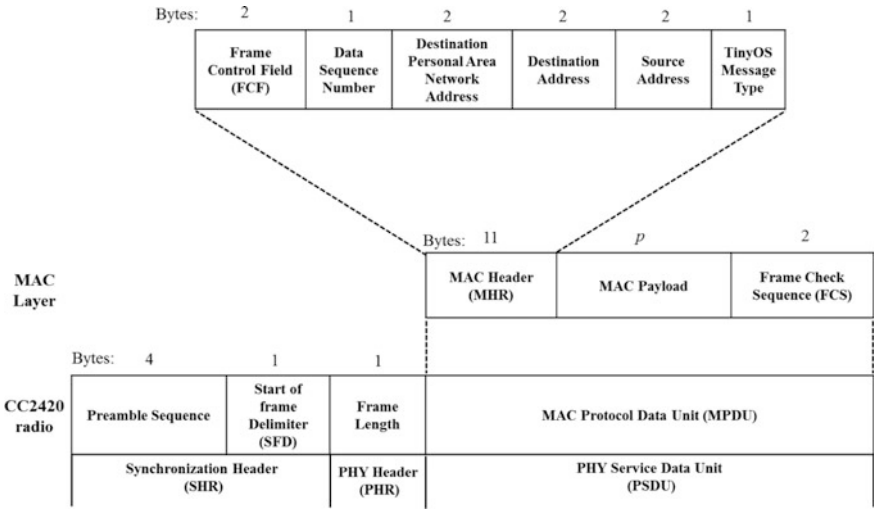

Fig. 3 Schematic view of the frame format at the MAC layer and the CC2420 layer

CC2420 radio. Therefore, as shown in Fig. 3 the MAC frame has MAC header of 11 bytes consisting of Frame Control Field (FCF) of 2 bytes, Data Sequence Number (DSN) of 2 bytes, destination Personal Area Network (PAN) address of 2 bytes, destination address of 2 bytes, source address of 2 bytes, and TinyOS message type of 1 byte. The MAC payload can contain the maximum size of 115 bytes and the MAC footer contains Frame Check Sequence (FCS) of 2 bytes. When the MAC frame is forwarded to the CC2420 radio, another 6 bytes are added in front of the MAC frame for transmission preamble and frame delimiter when the message is transmitted over the medium to the destination.

Assuming that payload at the MAC layer is p bytes. At the sender side, a MAC frame of $(11 + p)$ bytes (i.e. size(MHR) + p) is transferred from the microcontroller into the buffer of the radio chip, while at the receiver side a MAC frame of $(13 + p)$ bytes (i.e. size(MHR) + size(FCS) + p) is transferred from the buffer of the radio chip into the microcontroller. The total size of a frame when it is transmitted over the medium becomes size(SHR) + size(PHR) + size(MHR) + p + size(FCS).

The message transfer times t_{ts} and t_{tr} between the microcontroller and the radio chip are determined by the speed of the SPI interface interconnecting them, while the transmit time t_{xm} is determined by the transmission speed of the radio chip. In particular, the speed of the SPI interface on a mote equipped with the MSP430 microcontroller and the radio chip CC2420 can support a maximum rate of 500 Kbps. The transmission speed of CC2420 is 250 Kbps. Nevertheless, the SPI transfer speed is achieved about 173.91 Kbps in practice since the TinyOS interface to the SPI bus introduces a large control overhead [7].

Thus, based on the size of the frame format at each layer and the SPI speed, the practical values of t_{ts}, t_{tr}, and t_{xm} are computed as follows.

$$t_{ts} = \frac{(size(MHR) + p) \times 8}{173.91 \times 10^3} = (11 + p) \times 0.046\,\text{ms} \tag{5}$$

$$t_{tr} = \frac{(size(MHR) + size(FCS) + p) \times 8}{173.91 \times 10^3} = (13 + p) \times 0.046\,\text{ms} \tag{6}$$

$$t_{xm} = \frac{(size(SHR) + size(PHR) + size(MHR) + size(FCS) + p) \times 8}{250 \times 10^3} = (19 + p) \times 0.032\,\text{ms} \tag{7}$$

Finally, assigning the values of Eqs. (7)–(9) to Eq. (6) and ignoring t_{pm}, we get T_s as follows.

$$T_s = 2.32 + 0.156 \times p\,\text{ms} \tag{8}$$

5 Experimental Evaluation

5.1 Network Setup

We conducted experiments on a simple testbed of Kmote motes running TinyOS 2.1.2 as shown in Fig. 4. We evaluate the impact of interference on data transmission. Two nodes act as a source and a destination, while the remaining one plays a role as an interference node which generates the interference signal. The source

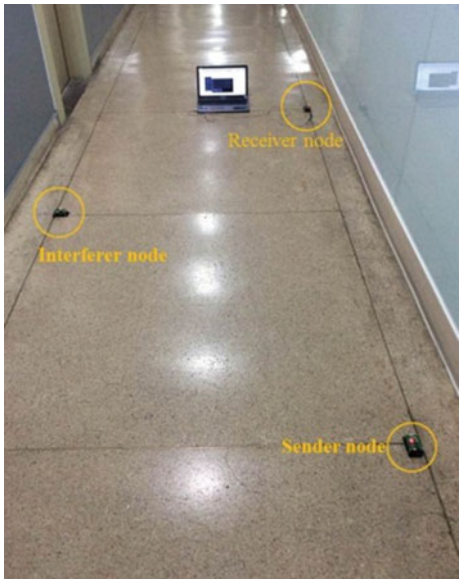

Fig. 4 Testbed configuration

generates a data packet of p bytes every T_r seconds and sends it to the destination within the assigned time slot of T_s. For convenience, we keep the radio chip of the destination turned on.

The Kmote is equipped with Texas Instrument's MSP430 ultra-low power 8 MHz microcontroller and Chipcon's CC2420 wireless transceiver as in Fig. 5. The microcontroller has 10 kB RAM and 48 kB of flash memory with a transmission rate of 250 Kbps in 2.4 GHz ISM band, which is compliant with the PHY layer of IEEE 802.15.4. The current draw of Kmote, excluding the radio, is 1.8 mA in active mode and 5.1 μA when in sleep mode. The CC2420 radio consumes 23 mA in receiving/listening mode, 8 mA when transmitting at level 3 (−25 dBm), 21 μA in idle mode, and 1 μA in sleep mode. Other experimental parameters and their values are given in Table 1.

The reliability of data transmission is assessed by *packet delivery ratio* (PDR) and *missed timely delivery ratio* (MTDR) and energy efficiency by *energy consumption per packet* (ECPP). PDR is given the ratio of the number of packets received successfully at a destination to the number of packets generated at a source. ECPP is given the ratio of the totally consumed energy to the number of packets received successfully at a destination. To measure the energy consumption of a sensor mote, we count the amount of time that each node has spent in a particular operation mode: sleep, idle, receiving or transmitting. Then, energy consumption is calculated by multiplying the cumulative time stayed at a mode and the consumed power to operate the radio in that mode, considering a battery of 3 V. MTDR is given the ratio of the number of packets that cannot be sent within the time slot size to the number of packets generated at a source.

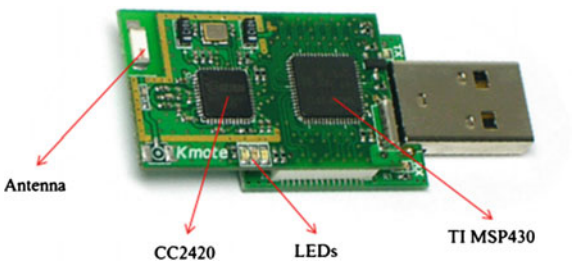

Fig. 5 The key components of Kmote

Table 1 Experimental Parameters

Parameters	Values
Experimental time	1800 s
Transmission power level	3 (−25 dBm)
x in Eq. (1)	50
S in Eq. (1)	5
P in Eq. (2)	87
α in Eq. (2)	0.2
T_r	1 s
p	100 bytes

5.2 Experimental Study

5.2.1 Effect of Time Slot Size

From the Eq. (8), we get the minimum time slot $T_s = 17.9 \approx 18$ ms for payload of $p = 100$ bytes. Thus, the performance is examined with varying time slot size starting from 18 to 26 ms under the bursty interference and semi-periodic interference. The experimental results are given in Figs. 6 and 7.

In general, the increase in time slot size enhances the reliability of packet delivery. This is because a node has a difficulty in finding the channel free if the time slot size is small and interference is high. In particular, referring to Fig. 6, as time slot size increases from 18 to 26 ms, the missed timely delivery ratio decreases by about 24 and 8 % for bursty interference and semi-periodic interference, respectively. Similarly, packet delivery ratio is shown in Fig. 7.

Furthermore, it is shown that bursty interference degrades the reliability of packet delivery more significantly than semi-periodic interference. It makes sense

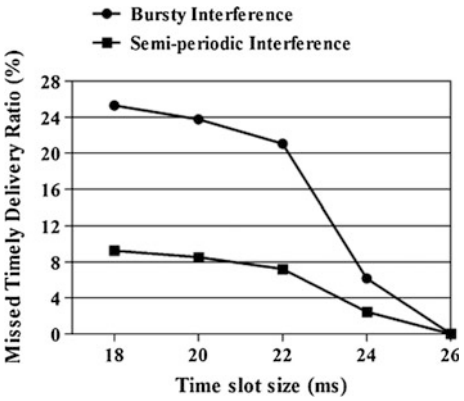

Fig. 6 Missed timely delivery ratio with varying slot size

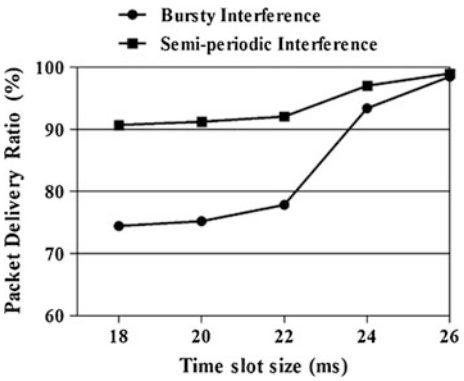

Fig. 7 Packet delivery ratio with varying time slot size

because the bursty interference model generates interference signal longer. However, under the semi-periodic interference model, interference does not take effect with the big slot size of 24 ms, while it lowers PDR with less than 22 ms.

5.2.2 Effect of Clear Channel Assessment (CCA)

As shown in Fig. 6, the missed timely delivery ratio is almost zero when $T_s = 26$ ms. This means that the time slot size of 26 ms is sufficient for transmitting and receiving one data packet of 100 bytes under the interference. Therefore, we fix the time slot size to 26 ms blank;to evaluate the effectiveness of using CCA. The experimental results are shown in Figs. 8 and 9.

Generally, the reliability of packet transmission and energy efficiency are enhanced with the use of CCA under both inference models. In particular, we can see that in Fig. 8 the gap of packet delivery ratio between two bar graphs is about 10 % in case of bursty interference model. This implies that the CCA mechanism

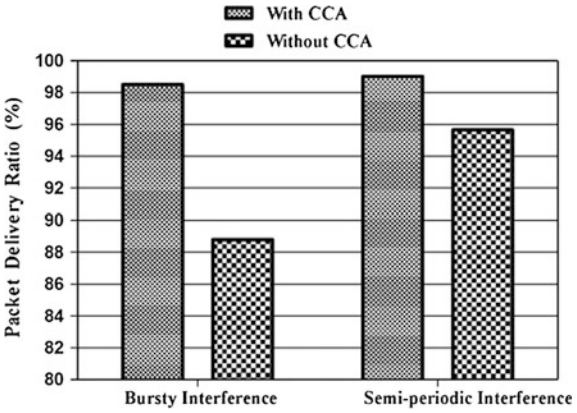

Fig. 8 Packet delivery ratio with/without CCA (*slot size* = 26 ms)

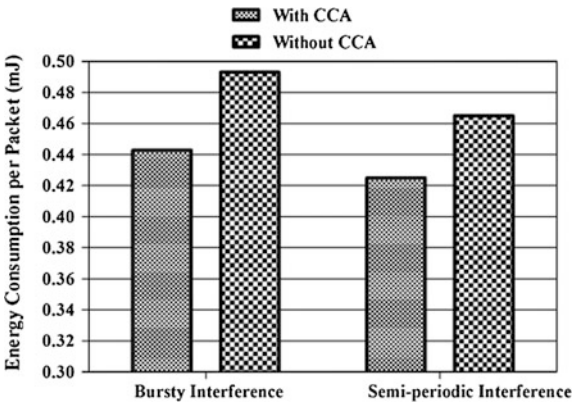

Fig. 9 Energy consumption per packet with/without CCA (*slot size* = 26 ms)

can decrease the probability of data packet collision gracefully. Consequently, the use of CCA can improve energy efficiency by about 0.05 and 0.04 mJ in the bursty inference and semi-periodic inference model, respectively as shown in Fig. 9.

6 Conclusion

We conducted experiments on testbed using the Kmote motes to evaluate the impact of different interference models on data transmission. The effect of slot size variation, the CCA mechanism were studied by examining the performance metrics that account for packet delivery ratio, missed timely packet delivery ratio and energy consumption. Through these experiments, we could identify that the appropriate selection of the time slot size and the use of the CCA mechanism are of great importance to secure data transmission reliability as well as to enhance the energy efficiency of slot scheduling based MAC protocols in wireless sensor networks.

Acknowledgement This research was supported by Basic Science Research Program through the National Research Foundation of Korea (NRF) funded by the Ministry of Education, Science and Technology (2013R1A1A2013396).

References

1. Wen-Zhan S, Renjie H, Shirazi B, LaHusen R (2009) TreeMAC: localized TDMA MAC protocol for real-time high-data-rate sensor networks. In: PerCom 2009. IEEE international conference on pervasive computing and communications, 9–13 March 2009, pp 1–10. doi:10.1109/percom.2009.4912757
2. Oh H, Van Vinh P (2013) Design and implementation of a MAC protocol for timely and reliable delivery of command and data in dynamic wireless sensor networks. Sensors 13 (10):13228–13257
3. WirelessHART specification (2007)
4. IEEE Standard for Information Technology-Telecommunications and Information Exchange Between Systems-Local and Metropolitan Area Networks-Specific Requirements-Part 11 (2007). Medium Access Control (MAC) and Physical Layer (PHY) Specifications
5. Boano C, Voigt T, Tsiftes N, Mottola L, Römer K, Zúñiga M (2010) Making sensornet MAC protocols robust against Interference. In: Silva J, Krishnamachari B, Boavida F (eds) Wireless sensor networks, vol 5970. Lecture Notes in Computer Science. Springer, Berlin, pp 272–288
6. Boano CA, Zhitao H, Yafei L, Voigt T, Zu X et al (2009) Controllable radio interference for experimental and testing purposes in wireless sensor networks. In: LCN 2009. IEEE 34th conference on local computer networks, 20–23 Oct 2009, pp 865–872. doi:10.1109/lcn.2009.5355013
7. Suriyachai P, Roedig U, Scott A (2009) Implementation of a MAC protocol for QoS support in wireless sensor networks. In: PerCom 2009. IEEE international conference on pervasive computing and communications, 9–13 March 2009, pp 1–6. doi:10.1109/percom.2009.4912839

Performance Analysis of a Hybrid Efficient and Reliable MAC Scheme for Vehicular Ad Hoc Networks in Safety Applications

VanDung Nguyen, Oanh Tran Thi Kim and Choong Seon Hong

Abstract Safety applications are the highest priority services in the Vehicular Ad Hoc NETworks (VANETs). To support the highest priority service, the Medium Access Control (MAC) protocol is designed to provide efficient broadcast. Compared to IEEE 1609.4, a new multi-channel MAC for VANET (HER-MAC) is proposed which is more reliable in safety applications. In this paper, we propose an analytical model to evaluate the performance of HER-MAC protocol under non-saturation condition through the packet delivery ratio. We also describe two MAC access schemes for HER-MAC protocol: safety application packets using TDMA access scheme and safety application packets using Distributed Coordination Function (DCF). Simulation results show that safety application packets using TDMA access scheme has higher packet delivery ratio and more reliability than safety application packets using distributed coordination function.

Keywords VANET · MAC · HER-MAC · A multi-channel MAC

1 Introduction and Related Works

One of the major goals of the Intelligent Transportation System (ITS) is to improve the quality, effectiveness and safety the future transportation systems. Vehicular Ad Hoc Networks (VANETs) are an important component ITS. VANETs are designed to enable communication between vehicles and vehicles or vehicles and

V. Nguyen · O.T.T. Kim · C.S. Hong (✉)
Department of Computer Engineering, Kyung Hee University,
446-701, Seoul, Korea
e-mail: cshong@khu.ac.kr

V. Nguyen
e-mail: ngvandung85@khu.ac.kr

O.T.T. Kim
e-mail: ttkoanh@khu.ac.kr

V.H. Duy et al. (eds.), *AETA 2015: Recent Advances in Electrical Engineering and Related Sciences*, Lecture Notes in Electrical Engineering 371,
DOI 10.1007/978-3-319-27247-4_4

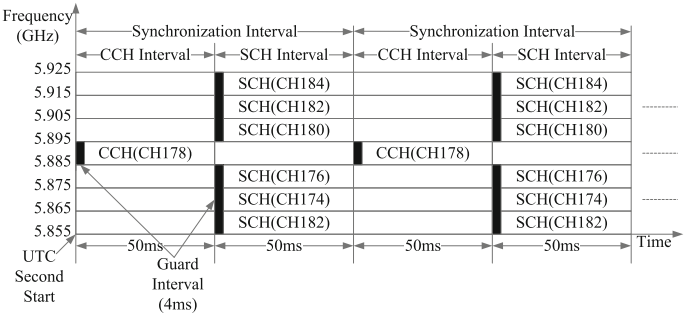

Fig. 1 Frequency channel layout of a 5.9 GHz WAVE system

infrastructures. Each vehicle is equipped with a radio interface, called on-board unit (OBU). Beside, along the road, to connect to the Internet, the roadside units (RSUs) are distributed. Based on RSUs and OBUs, VANETs consist of two communication types: vehicle-to-vehicle (V2V) and vehicle-to-RSU (V2R). They aim to increase a variety of safety applications and non-safety applications, and provide comfort to drivers and passengers. Safety applications are the most important message [1]. They have the very strict delay demand and high priority. Non-safety applications are more throughput-sensitive instead of delay-sensitive.

In year 1999, to support vehicular communications, the Federal Communication Commission (FCC) of the U.S gas approved 75 MHz bandwidth at 5.850–5.925 GHz frequency band for ITS wireless communications. It is divided into seven channels, as shown in Fig. 1. One of the seven channels is assigned the Control Channel (CCH), i.e. CH 178, which can only provide safety relevant applications and system control and management with high priority. Service Channels (SCHs) use other six channels, mainly supporting the non-safety relevant applications.

Due to characteristic of the VANET, such as high speed, unstable communication link, and network partitioning, information transfer becomes inevitably challenging. Compared to other wireless networks, VANETs suffer from some unique feature, such as high node mobility, topology dynamics and frequent link breakage. The effectiveness of traffic safety applications using VANETs depends upon the performance of Medium Access Control (MAC) protocol. The main challenge for design of MAC protocol for VANETs is to achieve reliable delivery of messages within the time limit even when the density of vehicles varies rapidly in the network.

Recently, IEEE 802.11p [2] and IEEE 1609.4 [3] have been proposed for VANETs. Based on the standard draft of IEEE 802.11p, VANETs employ the technique of dedicated short-range communication (DSRC) for enhancement of the driving safety, as well as, comfort of automotive drivers. In IEEE 802.11p, the broadcast service suffers from hidden terminal problem. This reason is that no request to send/clear to send (RTS/CTS) packets are exchanged before transmission of

broadcast messages and no acknowledge message is sent back to the source node. The IEEE 1609.4 standard draft is considered to be a default multichannel MAC standard for VANETs, which defines a multichannel wireless radio operation mode, including the interleaving operation of the CCH and SCH, priority access parameters, and other characteristic of MAC and PHYs. In IEEE 1609.4, nodes broadcast safety messages or negotiate the SCHs on the CCH during the Control Channel Interval (CCHI). In the Service Channel Interval (SCHI), nodes switch to the negotiated SCHs for their non-safety messages transmissions. This scheme has a high contention during the CCHI and the SCHI resources cannot be utilized during this interval.

The HER-MAC protocol [4] allows vehicle nodes to broadcast their safety messages in the reserved time slot to improve the reliability. Compared to IEEE 1609.4, HER-MAC protocol is more reliable in the safety message broadcast, efficient in the service channel utilization. In this paper, we propose an analytical model to evaluate the performance of HER-MAC protocol under non-saturation condition through the packet delivery ratio. We also describe two MAC access schemes for HER-MAC protocol: safety application packets using TDMA access scheme and safety application packets using Distributed Coordination Function (DCF).

The rest of this paper is organized as follows: Sect. 2 gives the analytical model of HER-MAC protocol in safety applications. Performance evaluations are drawn in Sect. 3. Section 4 finally concludes this paper.

2 Analytical Model of HER-MAC Protocol in Safety Applications

In our analytical model, we consider the CCH is divided into two parts: reservation period (T_{re}) and contention period (T_{con}), as shown in Fig. 2. In this paper, we use two access schemes to transmit safety application packets in HER-MAC. In the first scheme, we use TDMA access scheme and re-transmission mechanism for safety message broadcast, as shown in Fig. 2. Safety application packets using distributed coordination function is considered in the second scheme. DCF is a carrier sense multiple access with collision avoidance scheme with binary slotted exponential backoff, as shown in Fig. 5. Since safety application packets are sent by broadcast mechanism, the vehicle nodes will not send any acknowledgement for the received safety messages. The sender does not detect the failure of the safety transmission and there is no re-transmission. The Markov chain model is proposed to obtain the stationary probability τ_e that a node transmits a safety application in an arbitrary time slot. We divide packet transmissions into 2 types: safety application and WSA/RES packet transmissions on the CCH. There are N vehicle nodes in the network, the packet arrival rate of safety application and service packet in Poisson manner at each node are λ_e and λ_s. The packet arrival rate of safety application and

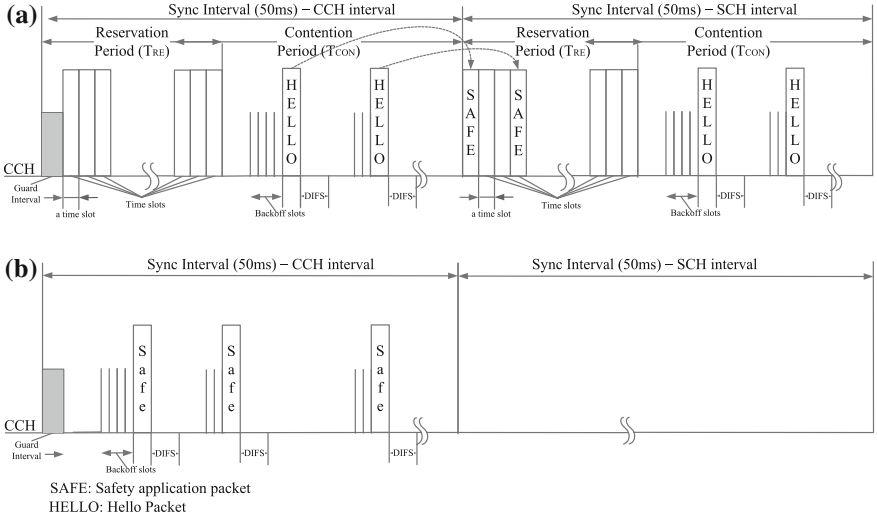

Fig. 2 The analytical model of safety application broadcast in case 1. **a** The operation of the HER-MAC protocol in safety applications. **b** The operation of the IEEE 1609.4 in safety applications

WSA/RES packet at each node are $2\lambda_e$ and $2\lambda_s$ because there are two queues with the same arrival rate during the CCHI: SCCHI and SCHI queues, referred detail in [5].

2.1 *Case 1: Safety Application Packet Uses TDMA Access Scheme*

In this case, HER-MAC protocol uses TDMA access scheme and retransmission mechanism to transmit a safety application. Each node will broadcast a SAFE packet to reserve an Emgslot on reservation period. If a node reserved an EmgSlot successfully, it can broadcast its safety application packet during its reserved EmgSlot without any any collision. Each node must transmit a SAFE packet in its time slot on the reservation period. Each SAFE packet is divided into five main fields: a ID, a serviced slot, the IDs of neighbor nodes, the time slot of each neighbor node, safe applications, as shown in Fig. 3. Based on each SAFE packet is transmitted on the reservation period, if all neighbor nodes confirm a ID and serviced EmgSlot of contended node, this node will occupy successfully an EmgSlot. Otherwise, a node

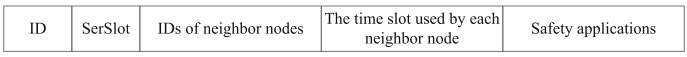

Fig. 3 Frame format of SAFE packet

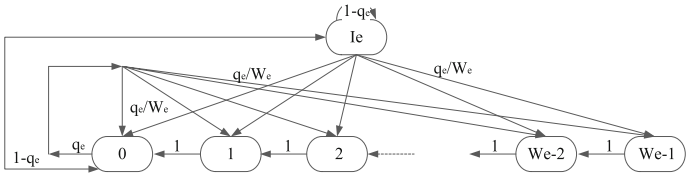

Fig. 4 Markov chain of safety application or HELLO packet broadcast

occupied unsuccessfully EmgSlot. If nodes do not reserve EmgSlots successfully, nodes will broadcast HELLO packets to reserve Emgslots in the next sync interval, as shown in Fig. 2. In this scheme, we consider each node has only a safety application packet to broadcast in the CCHI.

Because HELLO packet broadcast and safety application broadcast use the same mechanism, we use the same Markov chain for both safety application and HELLO packet broadcast depicted in Fig. 4. We assume the payload of HELLO packet and safety application packet both have the same length.

Let $b_e(t)$ be the stochastic process representing the backoff window size for a given node at slot time t, respectively, p_e be the probability collision, W_e be the contend window (CW), I_e be the idle state with an empty buffer and q_e be the probability of at least one HELLO or safety application packets in the buffer. This statistical model of q_e will be discussed later.

Let $b_{e,k} = \lim_{t\to\infty}\{b_e(t) = k\},\ 0 \le k \le W_e - 1$ be the stationary distribution of the Markov chain. From the Markov chain, it is clear that the probability τ_e that a node transmits a HELLO or safety application packet in an arbitrary time slot can be expressed as

$$\tau_e = b_{0.0} = \left[\frac{1-q_e}{q_e} + \frac{W_e+1}{2}\right]^{-1} \tag{1}$$

Let p_e be the collision probability when more than node transmit at the same time slot, we have

$$p_e = 1 - (1-\tau_e)^{N-1} \tag{2}$$

The packet delivery radio (PDR) of the safety application packet in IEEE 1609.4 is

$$PDR_{1609} = \frac{P_{ssuc}}{N\tau_e} = (1-\tau_e)^{N-1} \tag{3}$$

Consequently, based on (1) and (2), variables τ_e and p_e can be solved by the numerical methods as in [6]. Note that $0 \le \tau_e \le 1$ and $0 \le p_e \le 1$. In every time slot during the safety application or HELLO packet interval, let P_{esuc}, P_{ecol}, P_{eidle} and P_{ebusy} be the probability of successful transmission, collision transmission, a idle channel, a busy channel, respectively.

$$\begin{cases} P_{ebusy} = 1 - (1 - \tau_e)^N \\ P_{eidle} = (1 - \tau_e)^N \\ P_{esuc} = N\tau_e(1 - \tau_e)^{N-1} \\ P_{ecol} = P_{ebusy} - P_{esuc} \end{cases} \tag{4}$$

Let T_{esuc}, T_{ecol} and σ be the time the channel is busy because of the successful transmission of HELLO or safety application packet, the channel is idle, and a slot time.

$$T_e = T_{esuc} = T_{ecol} = T_{HELLO} + \delta + T_{DIFS} = T_{safe} + \delta + T_{DIFS} \tag{5}$$

where δ is a propagation time. Each state maybe a successful transmission, a collision or the medium is idle. The expected time spent per state E_s.

$$\begin{aligned} E_s =& (1 - P_{ebusy})\sigma + P_{ebusy} \cdot (1 - P_{esuc}) \cdot T_e \\ &+ P_{ebusy} \cdot P_{esuc} \cdot P_{ecol} \cdot T_e + P_{ebusy} \cdot P_{esuc} \cdot (1 - P_{ecol}) \cdot T_e \end{aligned} \tag{6}$$

From the average slot time E_s, the probability q_e can be approximated as

$$q_e = 1 - e^{-2\lambda_e . E_s} \tag{7}$$

In HER-MAC protocol, if nodes did not reserve EmgSlots successfully, nodes will broadcast HELLO packets to reserve Emgslots in the next sync interval. The HER-MAC uses a frame (100 ms) to transmit concurrently HELLO and safety applications. However, the IEEE 1609.4 only uses one sync interval (50 ms) to transmit safety applications. After one sync interval (50 ms), in HER-MAC protocol, the average number of node transmitted unsuccessfully HELLO packet is $N_2 = N.p_e$. By replacing N_2 for N in (2), we can solve variables τ_{e2} and p_{e2}. The PDR of the safety application packet in the second sync interval is $PDR_2 = (1 - \tau_{e2})^{N_2 - 1}$. The PDR of HELLO packet of HER-MAC protocol through a frame is

$$PDR_{HER-MAC} = 1 - (1 - PDR_{1609})(1 - PDR_2) \tag{8}$$

2.2 Case 2: Safety Application Packet Uses Distributed Coordination Function

For analyze transmission of safety application packet, we use Markov chain of safety application packet in case 1 because the transmission of safety application packets are independent of transmission of WSA/RES packets. Now, we analyze transmission of WSA/RES packets. Let $b_s(t)$ and $s_s(t)$ be the stochastic process representing the backoff window size and backoff state for a given node at slot time

t, respectively. Following [7], let m be the maximum backoff state, be the value such that $W_{max} = 2^m W$. W_i is maximal contention window (CW) of the ith backoff state, where $i \in (0, m)$, and $W_i = 2^i W$. Let p_s be the probability of collision that more than one node transmits in a single slot and q_s be the probability at least one new WSA/RES packet in the buffer. Then, the bidimensional process $s_s(t)$, $b_s(t)$ can be modeled with a discrete-time Markov chain, as shown in Fig. 6.

Let $b^s_{i,k} = \lim_{t\to\infty}\{s_s(t) = i, b_s(t) = k\}$, $0 \le i \le m$, $0 \le k \le W_i - 1$ be the stationary distribution of the Markov chain. From the Markov chain and [8], it is clear that

$$\begin{aligned} b_{0.0} &= \frac{2(1-p_s)(1-2p_s)q_s}{q_s[(W_s+1)(1-2p_s)+W_s p_s(1-(2p_s)^m)]+2(1-q_s)(1-p_s)(1-2p_s)} \\ \tau_s &= \frac{b_{0,0}}{(1-p_s)} = \frac{2(1-2p_s)q_s}{q_s[(W_s+1)(1-2p_s)+W_s p_s(1-(2p_s)^m)]+2(1-q_s)(1-p_s)(1-2p_s)} \end{aligned} \tag{9}$$

So p_e and p_s is the collision probability when more than one node transmits at the same time slot, based on (2) and (6) we have

$$\begin{aligned} p_e &= 1-(1-\tau_e)^{N-1}(1-\tau_s)^N \\ p_s &= 1-(1-\tau_s)^{N-1}(1-\tau_e)^N \end{aligned} \tag{10}$$

Consequently, based on (1)–(9), (10), variables τ_e, p_e, τ_s and p_s can be solved by the numerical methods as in [6]. Note that $0 \le \tau_e \le 1$, $0 \le p_e \le 1$, $0 \le \tau_s \le 1$ and $0 \le p_s \le 1$.

In each time slot, let P^e_{suc} and P^s_{suc} be the probabilities of successful transmission for emergency and service packet. A channel is collision with probabilities P^e_{col} and P^s_{col} and channel is idle with P^e_{idle} and P^s_{idle}. We have

$$\begin{cases} P_b = 1-(1-\tau_e)^N(1-\tau_s)^N \\ P_{idle} = (1-\tau_e)^N(1-\tau_s)^N \\ P^e_{suc} = N\tau_e(1-\tau_s)^N(1-\tau_e)^{N-1} \\ P^s_{suc} = N\tau_s(1-\tau_e)^N(1-\tau_s)^{N-1} \\ P^e_{col} = (1-\tau_s)^N(1-(1-\tau_e)^N - N\tau_e(1-\tau_e)^{N-1}) \\ P^s_{col} = (1-\tau_e)^N(1-(1-\tau_s)^N - N\tau_s(1-\tau_s)^{N-1}) \\ P^{es}_{col} = P_b - P^e_{suc} - P^s_{suc} - P^e_{col} - P^s_{col} \end{cases} \tag{11}$$

Let T_{WSA}, T_{RES}, T_{ACK} and T_{safe} denoted the time for transmitting a WSA, RES, ACK, safety application packet, and we assume that $T_{WSA} = T_{RES}$ and $T_{safe} = T_{WSA}$. T_{SIFS} and T_{DIFS} are the SIFS time and DIFS time, respectively.

The duration of a free time slot, the duration of a transmission collision and the duration for a successful reservation are T_{idle}, T_{col} and T_{suc}, respectively. Then from Fig. 5, we have

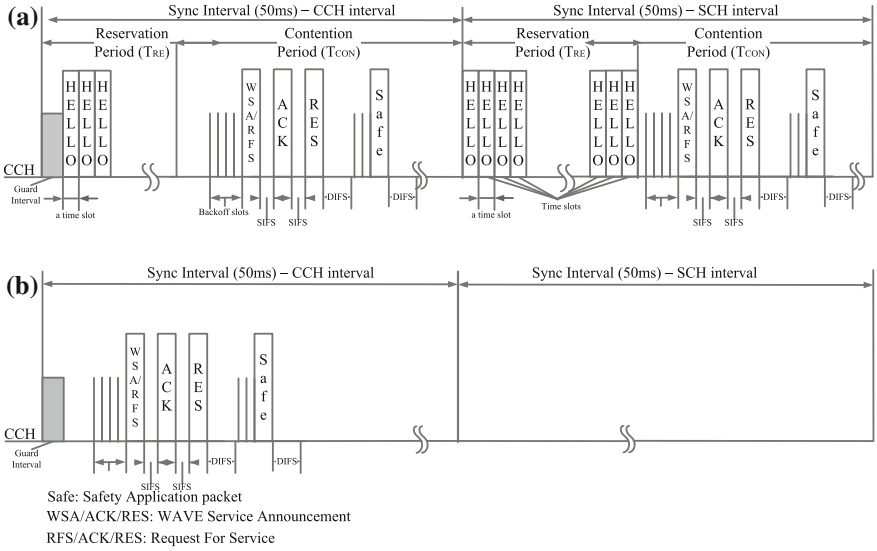

Fig. 5 The analytical model of safety application broadcast in case 2. **a** The operation of the HER-MAC protocol in safety applications. **b** The operation of the IEEE 1609.4 in safety applications

$$\begin{cases} T_{idle} = aSlotTime \\ T^s_{col} = T_{WSA} + \delta + T_{DIFS} \\ T^s_{suc} = T_{WSA} + + T_{RES} + 2 * T_{SIFS} + T_{ACK} + 3 * \delta + T_{DIFS} \\ T^e_{suc} = T^e_{col} = T_{SWT} + \delta + T_{DIFS} \end{cases} \tag{12}$$

The expect time spent per state E_s is given

$$E_S = (1 - P_b)\sigma + P^e_{suc}T^e_{suc} + P^s_{suc}T^s_{suc} + P^e_{col}T^e_{col} + P^s_{col}T^s_{col} + P^{e,s}_{col}\max(T^e_{col}, T^s_{col}) \tag{13}$$

From the average slot time E_s, the probability q_e and q_s can be approximated as

$$q_e = 1 - e^{-2\lambda_e . E_s} \tag{14}$$

$$q_s = 1 - e^{-2\lambda_s . E_s} \tag{15}$$

The packet delivery ratio (PDR) of the safety application packet in IEEE 1609.4 can be calculated as

$$PDR_{1609} = \frac{P^e_{suc}}{N\tau_e} = (1 - \tau_e)^{N-1}(1 - \tau_s)^N \tag{16}$$

The safety application packets in the HER-MAC protocol are transmitted twice and the successful transmission in the CCHI is the same with the IEEE 1609.4

(Eq. 16). During the SCHI, HER-MAC protocol, the safety application and SWA/RES packets are transmitted on the CCH. The PDR of the safety application packet also is the same with the IEEE 1609.4. Then, we have the PDR of the safety application packet in the HER-MAC protocol through a frame is

$$PDR_{HER-MAC} = 1 - (1 - PDR_{1609})^2 \tag{17}$$

3 Performance Evaluation

In this section, we validate our model using the event-driven simulation program written in Matlab. We consider a segment of a two-way vehicle traffic highway (20 m × 1000 m). The values of the parameters used to obtain the numerical results for both the analytical model and simulation runs, are summarized in Table 1. We fix the safety application and HELLO packets arrival rate λ_e at 50 pks/s, service arrival rate λ_s at 200 pks/s and vary the number of nodes N or the content windows W_s to evaluate the PDR of safety applications.

In case 1, all nodes have to reserve the EmgSlots in order to broadcast a safety application packet. If a node did not reserve the EmgSlot successfully and it has some safety application packets to broadcast, a node will attempt to reserve the EmgSlot in next sync interval. In Fig. 7a, when a number of nodes increases, the collision probability at the same time slot also increase, and thus, it takes a long time to finish the EmgSlot reservation for all nodes. In IEEE 1609.4, it uses one sync interval to exchange safety application packets. However, the HER-MAC uses two sync interval to exchange them. As variable W_e increase, the packet delivery ratio also increases respectively. PDR with 50 nodes in the HER-MAC keeps interval between 96 and 98 %, but in the IEEE 1609.4 it keeps interval 76 and 83 %. Because the probability τ_e decreases when the W_e increases, the collision probability at the same time slot also increases.

Table 1 System parameter for simulations

Parameter	Value	Parameter	Value
Data rate of each channel	6 Mbps	λ_s	50 pkts/s
WSA	100 bytes	λ_e	200 pkts/s
Safety application	100 bytes	ACK	14 bytes
HELLO	100 bytes	RES	14 bytes
Slot time σ	13 μ_s	SIFS	32 μ_s
Propagation time δ	1 μ_s	DIFS	58 μ_s
Number of SerSlots M	5	W_e	8
W_s	16	–	–

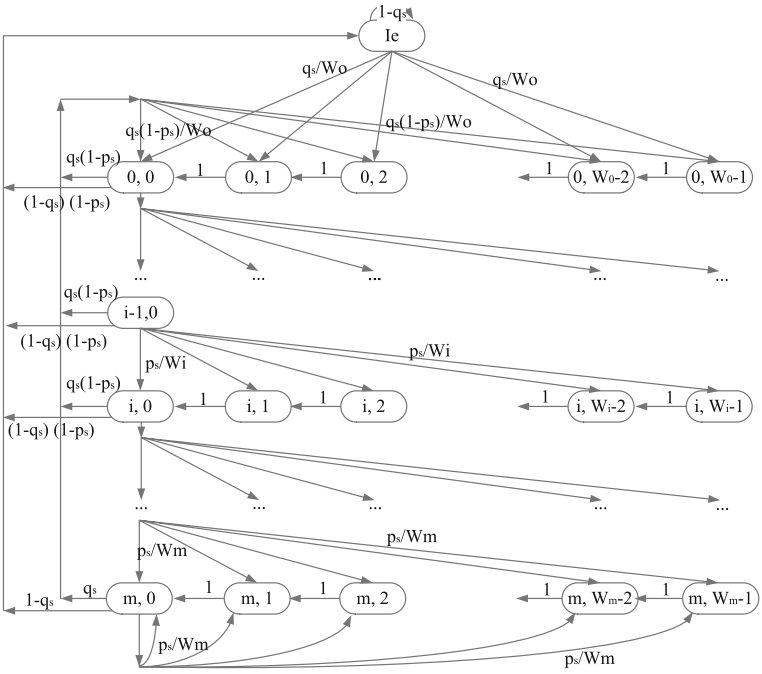

Fig. 6 Markov chain of the WSA or RES transmission

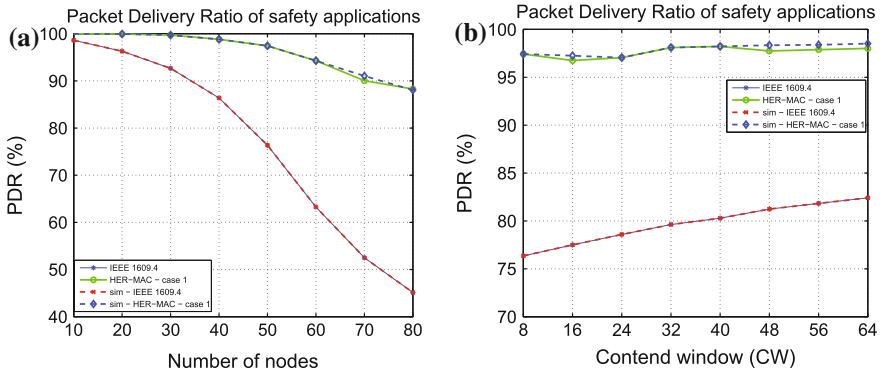

Fig. 7 Safety application packets use TDMA access scheme. **a** Packet delivery with variable nodes. **b** Packet delivery ratio with variable W_es

In case 2, the safety application and WSA/RES packets transmit concurrently on the same sync interval. The collision probability when more than one node transmits at the same time increases if the number of nodes increases. The number of node affects to collision probability p_e and PDR. The PDR in HER-MAC is greater

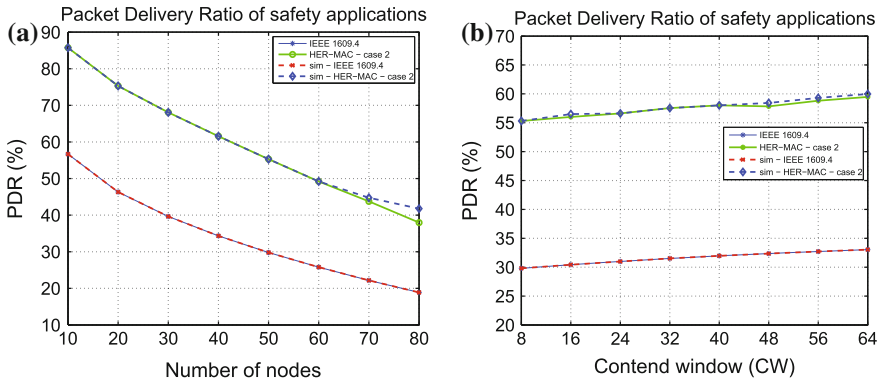

Fig. 8 Safety application packets use distributed coordination function. **a** Packet delivery with variable nodes. **b** Packet delivery ratio with variable W_es

about 1.86 times than in IEEE 1609.4, as shown in Fig. 8a. In other case, the content window W_e affects to the probability τ_e. Consequently, the collision probability p_e and PDR will increase when the W_e increases, as shown in Fig. 8b.

In case 2, if a node has a safety application packet, it will attempt to transmit on the contention period. Because both safety application and WSA/RES packets concurrently transmit on the contention period, the probability of successful safety transmission will be decreased. Unlike case 2, a safety application will be transmitted separately from WSA/RES packet in case 1. Due to safety application is transmitted in a node's time slot on the reservation period, safety application packets using TDMA access scheme more reliability and efficient than safety application packets using distributed coordination function.

4 Conclusion

In this paper, we describe an analytical model to evaluate the performance of HER-MAC protocol compared to IEEE 1609.4 in safety application. The safety application packet can transmit by using two MAC access schemes. In the first scheme, if a node has a safety application packet, it will send a HELLO packet to reserve an EmgSlot on reservation period. After a node reserved successfully an EmgSlot, it will transmit a safety application packet through its reserved EmgSot in next sync interval. In the second scheme, the safety application and WSA/RES packets transmit concurrently and both of them use distributed coordination function. In both of two schemes, the PDR in HER-MAC protocol is greater than in IEEE 1609.4. The performance results show that the safety application packets using TDMA access scheme more reliability and efficient than safety application packets using distributed coordination function.

Acknowledgments This research was one of KOREN projects supported by National Information Society Agency (15-951-00-001).

References

1. Xu Q, Mak T, Ko J, Sengupta R (2004) Vehicle-to-vehicle safety messaging in DSRC. In: Proceedings of the 1st ACM international workshop on vehicular ad hoc networks. 1em plus 0.5em minus 0.4em ACM, pp 19–28
2. Wireless lan medium access control (MAC) and physical layer (PHY) specifications amendment 6: Wireless access in vehicular environments, 2010
3. IEEE Standard for Wireless Access in Vehicular Environments (WAVE) Multi-channel Operation, 2010
4. Dang DNM, Dang HN, Nguyen V, Htike Z, Hong CS (2014) Her-MAC: a hybrid efficient and reliable MAC for vehicular ad hoc networks. In: IEEE 28th International Conference on Advanced Information Networking and Applications (AINA), 2014, pp 186–193
5. Dang DNM, Hong CS, Lee S, Huh E-N (2014) An efficient and reliable MAC in VANETs. IEEE Commun Lett 18(4):616–619
6. Bianchi G (2000) Performance analysis of the IEEE 802.11 distributed coordination function. IEEE J Sel Areas Commun 18(3):535–547
7. Wang Q, Leng S, Fu H, Zhang Y (2012) An IEEE 802.11 p-based multichannel MAC scheme with channel coordination for vehicular ad hoc networks. IEEE Trans Intell Transp Syst 13 (2):449–458
8. Daneshgaran F, Laddomada M, Mesiti F, Mondin M (2008) Unsaturated throughput analysis of IEEE 802.11 in presence of non ideal transmission channel and capture effects. IEEE Trans Wirel Commun 7(4):1276–1286

Wireless Information and Power Transfer for Full Duplex Relaying Networks: Performance Analysis

Tam Nguyen Kieu, Dinh-Thuan Do, Xinh Nguyen Xuan, Tan Nguyen Nhat and Hung Ha Duy

Abstract Energy harvesting (EH) based on ambient radio frequency (RF) has recently become advanced method to prolong the lifetime of the wireless networks. This paper deals with energy harvesting architecture of the full duplex relaying networks. By applying time switching based relaying (TSR) protocol and Amplify-and-Forward (AF) scheme, we derive the closed-form expression of the outage probability and hence compute the optimal throughput. An important result can be seen clearly that the time fraction in TSR impacts on the optimal throughput. Finally, numerical results show an efficient relaying strategy in full duplex cooperative networks.

Keywords Energy harvesting · Full duplex · Two way relaying network · Time switching-based protocol · Throughput

T.N. Kieu (✉) · T.N. Nhat · H.H. Duy
Faculty of Electrical and Electronics Engineering, Ton Duc Thang University,
No. 19 Nguyen Huu Tho Street, District 7, Ho Chi Minh City, Vietnam
e-mail: nguyenkieutam@tdt.edu.vn

T.N. Nhat
e-mail: nguyennhattan@tdt.edu.vn

H.H. Duy
e-mail: haduyhung@tdt.edu.vn

D.-T. Do · X.N. Xuan
Department of Electronics and Communications Engineering,
Ho Minh City University of Technology and Education, 1 Vo van Ngan Street,
Thu Duc District, Ho Chi Minh City, Vietnam
e-mail: dodinhthuan@gmail.com

X.N. Xuan
e-mail: xuanxinhspkt@gmail.com

V.H. Duy et al. (eds.), *AETA 2015: Recent Advances in Electrical Engineering and Related Sciences*, Lecture Notes in Electrical Engineering 371,
DOI 10.1007/978-3-319-27247-4_5

1 Introduction

Applications of renewable energy in the next generation wireless networks will be bring huge benefits for continuing operation in mobile equipments. Among other energy sources such as solar and wind power, power extracted from radio-frequency (RF) signals in ambient transmitters can be considered as replacements for traditional wired power grids. Such energy harvest from the natural environment is a promising approach to prolong the lifetime of energy constrained wireless networks such as cellular networks or wireless sensor networks. Simultaneous wireless information and power transfer technology (SWIPT) becomes appealing candidate since it realizes both useful information and energy from RF signals at the same time, and thus potentially offers great convenience to mobile equipments. Varshney first proposed the idea of transmitting information and energy simultaneously in [1]. Using relay to facilitate RF energy harvest and information transfer has also drawn significant attention, which is able to extend the transmission range and increased capacity for system. In [2], the authors studied the throughput performance of an amplify and-forward (AF) relaying system for both time-switching and power-splitting protocols.

More importantly, relaying network is an effective way to combat the performance degradation caused by fading, shadowing, and path loss. Full duplex (FD) relay network has the potential to realize the successful information exchange of two sources and more spectral efficiency than conventional half-duplex (HD) technique. When comparing to the HD mode, the FD mode has higher capacity in practical channel conditions. Alternatively, the FD mode can tolerate high loop interference power while achieving the same capacity as the half-duplex mode. The main disadvantage of FD communication is the self-interference from own node transmission, which is much larger than signal of interest from the distant node. To help the communication node that can transmit and receive signals over the same frequency band, many techniques of suppressing self-interference have been proposed in [3–5]. Unfortunately, the self-interference is residual due to limit technique. The residual interference still decreases the system performance. In fact, [6] indicates that the full-duplex mode is an attractive choice for fixed relays provided that the loop interference power is maintained at a tolerable level. The authors in [7] presented power allocation strategy to maximize the sum-rate of FD-two-way relaying system under realistic residual self-interference.

Recently, a few research trends have been conducted in FD relay system in context of the SWIPT scheme. In [8], the throughputs are analyzed for three relay control schemes, including the maximum relay, optimal relay, and target relay. Analytical expressions for outage probability and ergodic capacity are also presented for these considered relay control schemes. Later in [9], the authors consider two cases depending on the number of antennas used for harvesting and demonstrated that employing both relay antennas for energy harvesting is always beneficial, compared to the HD relaying architecture, results indicate that FD relaying can substantially boost the system throughput. The author in [10] analyzed

performance of two-way relaying networks under non-ideal hardware where is linear affected by impairment levels. However, no work related optimal throughput has considered the application of one-way FD relaying in RF energy harvesting systems.

Therefore, in this paper, we analyze the outage probability of full-duplex relaying with novel ability of energy harvesting and information transfer. Based on the analytical expressions, the optimal throughput and energy harvesting time are studied.

The remainder of this paper is organized as follows. Section 2 describes the system model of the EH enabled FD two-way relaying network. Section 3, the outage probability and throughput analysis. Simulation results are presented in Sect. 4. Finally, conclusion of Sect. 5 is drawn in this paper.

2 System Model

Let us consider a wireless dual-hop relay network with AF protocol system illustrated in Fig. 1, in which the destination node can be received at long distance thanks to relay node. The system consisting of three nodes, source node is denoted by S and destination node is denoted by D and one relay node R. Each node has two antennas, one of them is responsible for signal transmission and other is responsible for signal reception. The cooperative relay is assumed to be an energy constrained device so that it must harvest energy from the source, and use that energy to amplify and forward the source information to the destination node. We assume that the link between two sources doesn't exist due to the deep shadowing effect.

The interference cancellation mechanism is adopted to mitigate the self-interference. As the self-interference can not be eliminated completely, certain amount of self-interference remains. The residual self-interference channel at R is denoted by $\widetilde{h}_R$. Let d_j, $j = 1, 2$ denote the distance between $S - R$ link and $R - D$ link respectively and h_j, $j = 1, 2$ denote the channel coefficients between $S - R$ link and $R - D$ link respectively.

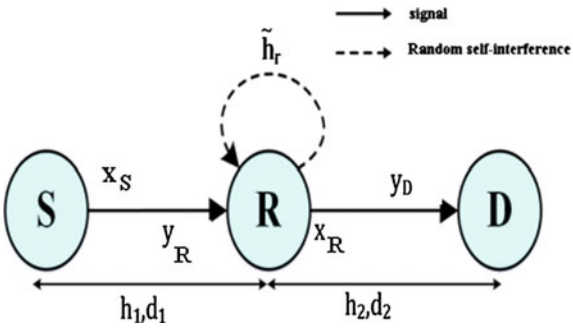

Fig. 1 System model of one way full duplex relaying

The scheme used in this investigation is the Time Switching-based Relaying (TSR) protocol as derived in [2]. The main parameters of protocol are expressed in Fig. 2.

Based on the TSR protocol proposed in [2], the communication process is divided into two phases. In the first phase, the energy transfer from the source to the relay with a duration of $\alpha T, (0<\alpha<1)$ and the second phase, the remaining time, $(1-\alpha)T$ is used to transmit information, in which α is time switching coefficient and T is time for the considered signal frame (Fig. 3).

During the energy harvesting phase, the received signal at the relay as

$$y_R = \sqrt{\frac{P_S}{d_1^m}} h_1 x_S + n_R \tag{1}$$

where P_S is the source transmission power, which is the same in the two sources,n_R is the additive white Gaussian noise at R with zero-mean and variance of σ_n^2.

Regarding wireless received power, the harvested energy at the relay is given by [2]

$$E_h = \eta \alpha T \frac{P_s |h_1|^2}{d_1^m} \tag{2}$$

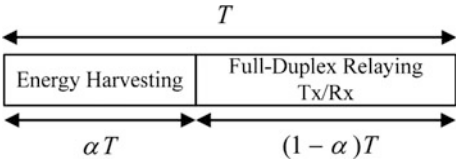

Fig. 2 Illustration of the parameters of TSR protocol

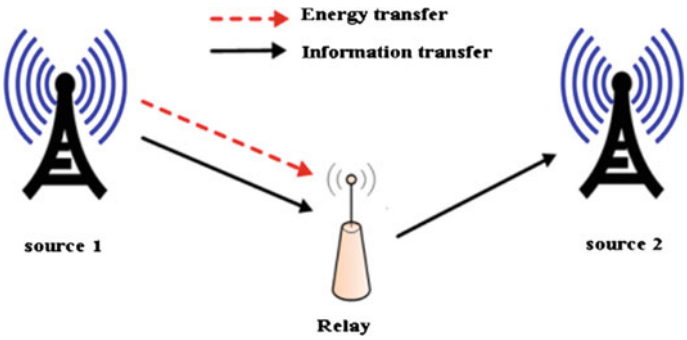

Fig. 3 One way relaying network for simultaneous wireless information and power transfer

where m is the path loss exponent, η is the energy conversion efficiency, h_1, h_2 are the channel coefficients between source-relay link and relay-destination link respectively.

In the information transfer phase, assume that the source node transmits respective signal x_S to R and R re-transmits signal x_r to the destination node. x_j, $j = S, R$. They have unit energy and zero–mean, i.e., $E\left[\left|x_j\right|^2\right] = 1$ and $E\left[x_j\right] = 0$. Therefore, the received signal at the relay under self-interference source is rewritten as

$$y_R = \sqrt{\frac{P_S}{d_1^m}} x_S h_1 + \widetilde{h}_R x_R + n_R \tag{3}$$

where $\widetilde{h}_R$ is the residual self-interference factor at R.

We suppose R receives y_R and in the next timeslot, R uses the harvested energy to amplify y_R. Hence the magnification of the prior received signal, x_R, is

$$x_R = G\sqrt{P_R} y_R \tag{4}$$

where G is the amplification factor of R.

Based on AF relaying scheme at R, according to [11] the amplification factor is given by

$$G^{-1} = \sqrt{\frac{P_S}{d_1^m}|h_1|^2 + P_R\left|\widetilde{h}_R\right|^2 + \sigma_n^2} \tag{5}$$

It is worth noting that harvested power then help operation for the next hop transmission, P_R is given by

$$P_R = \frac{E_h}{(1-\alpha)T} = \mu P_S \frac{|h_1|^2}{d_1^m} \tag{6}$$

where μ is defined as $\mu \triangleq \frac{\alpha\eta}{1-\alpha}$.

Next, we obtain the received signal at destination as

$$y_D = \frac{h_2}{\sqrt{d_2^m}} x_R + n_D \tag{7}$$

where n_d is Gaussian noise at destination node.

Substituting (4), (6) into (7), we calculate the received signal as

$$y_D(\kappa) = \underbrace{\frac{h_2}{\sqrt{d_2^m}} G\sqrt{P_R}\frac{h_1\sqrt{P_S}}{\sqrt{d_1^m}}x_S}_{signal} + \underbrace{\frac{h_2}{\sqrt{d_2^m}} G\sqrt{P_R}\widetilde{h}_R x_R}_{RSI} + \underbrace{\frac{h_2}{\sqrt{d_2^m}} G\sqrt{P_R}n_R + n_D}_{noise} \quad (8)$$

In the above equations, the instantaneous received SINR at S_j through R is determined as

$$\gamma_{\mathrm{OW}} = \frac{E\left\{|signal|^2\right\}}{E\left\{|noise|^2\right\} + E\left\{|RSI|^2\right\}} \quad (9)$$

By simple replacement, we obtain new formula as

$$\gamma = \frac{\frac{P_S|h_1|^2 P_R|h_2|^2}{d_1^m d_2^m P_R\left|\widetilde{h}_R\right|^2}}{\frac{\sigma_n^2 P_S|h_1|^2}{P_R\left|\widetilde{h}_R\right|^2 d_1^m} + \frac{P_R|h_2|^2}{d_2^m} + \sigma_n^2} \quad (10)$$

We assume that the channel gains $|h_1|^2, |h_2|^2$ are independent and identically distributed (i.i.d.) exponential.

3 Outage Probability and Throughput Analysis

In this section, we analyze the outage probability of full-duplex one-way relaying with energy harvesting and information transfer. Based on that analytical expressions, the throughput of scheme is derived and the optimal amount of time for harvesting energy α is also achieved.

3.1 Outage Probability Analysis

The outage probability of FD relaying network is calculated as

$$P_{out} = \Pr(\gamma \le Z) \quad (11)$$

where R is target rate and $Z = 2^R - 1$.

Proposition 1 *The outage probability of the energy harvesting enabled two way full duplex relay is derived as*

$$P_{out} = \Pr\left\{ \frac{\frac{P_S|h_1|^2 P_R|h_2|^2}{d_1^m d_2^m P_R \left|\widetilde{h}_r\right|^2}}{\frac{\sigma_n^2 P_S|h_1|^2}{P_R\left|\widetilde{h}_R\right|^2 d_1^m} + \frac{P_R|h_2|^2}{d_2^m} + \sigma_n^2} < Z \right\}$$
$$= 1 - \int_0^{1/\mu Z} 2\sqrt{\frac{d_1^m d_2^m Z\left(\frac{\sigma_n^2}{\mu} + \sigma_n^2 y\right)}{\lambda_s \lambda_d (P_S - \mu P_S Z y)}} \times K_1\left(2\sqrt{\frac{d_1^m d_2^m Z\left(\frac{\sigma_n^2}{\mu} + \sigma_n^2 y\right)}{\lambda_s \lambda_d (P_S - \mu P_S Z y)}}\right) \frac{1}{\lambda_r} e^{-\frac{y}{\lambda_r}} dy \tag{12}$$

where $\lambda_s, \lambda_d, \lambda_r$ *are the mean value of the exponential random variables* $h_1, h_2, \widetilde{h}_R$, *respectively and* $K_1(x)$ *is Bessel function defined as (8.423.1) in* [12]

Proof We denote $x = |h_1|^2|h_2|^2$ and $y = \left|\widetilde{h}_R\right|^2$ then we have:

$$P_{out} = \begin{cases} \Pr\left\{ x < \frac{d_1^m d_2^m Z\left(\frac{\sigma_n^2}{\mu} + \sigma_n^2 y\right)}{P_S - \mu P_S Z y} \right\}, & y < \frac{1}{\mu Z} \\ 1, & y > \frac{1}{\mu Z} \end{cases} \tag{13}$$

Interestingly, the cumulative distribution function of x is calculated by

$$F_x(a) = \Pr(x < a) = 1 - 2\sqrt{a/\lambda_s \lambda_d} K_1\left(2\sqrt{a/\lambda_s \lambda_d}\right) \tag{14}$$

and y can be modeled with probability distribution function $f_y(b) = (1/\lambda_r)e^{(b/\lambda_r)}$ then the **Proposition 1** is achieved after some simple manipulations.

3.2 Optimal Throughput Analysis

In the Proposition 1, the outage probability at the scheme, when the relay harvests energy from the source signal and uses that power to amplify and forward the source signal to the destination is a function of the energy harvesting time α, and exchange when α increase from 0 to 1. In the delay-limited transmission protocol, the transmitter is communicating at a fix transmission rate R bits/s/Hz is and

$(1-\alpha)T$ is the effective communication time. Therefore, the throughput of system is obtain as

$$\tau = (1 - P_{out})R\frac{(1-\alpha)T}{T} \tag{15}$$

Unfortunately, it is difficult to derive optimal throughput mathematically but we can obtain the optimal value by simulation as presented in the next section.

4 Numerical Results

In this section, we use the derived analytical results to provide the outage probability, optimal throughput, optimal energy harvesting time. We set the source transmission rate $R = 3,\ 4,\ 5$ (bps/Hz), and hence the outage SINR threshold is given by $Z = 2^R - 1$. The energy harvesting efficiency is set to be $\eta = 1$, the path loss exponent is set to be $m = 3$. For simplicity, we set the distance $d_1 = d_2 = 1$. Also, we set $\lambda_s = \lambda_d = 1; \lambda_r = 0.1$.

It can be seen from Fig. 4, the outage probability of different scenarios of time allocation is α. The outage probability is 1 when $\alpha = 0$, $\alpha = 1$ and so-called the worst performance of the system. The outage is minimum at approximate $\alpha = 0.75$, $R = 3$. As we can observe, the analysis curves provide a strictly agreement with simulation curves.

As your observation, Fig. 5 examines the impact of energy harvesting time α on the optimal throughput of systems. The throughput is maximum at approximate $\alpha = 0.36$, $R = 4$, and $\tau \approx 1.45$ can be called the optimal value. The throughput increases as α increases from 0 to optimal value α, however it starts decreasing as α increases over its optimal value. This is because for the values of α smaller than the

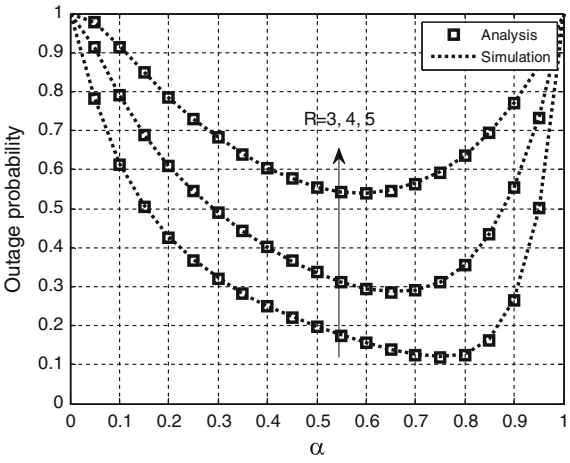

Fig. 4 Outage probability of FD energy-aware relaying network

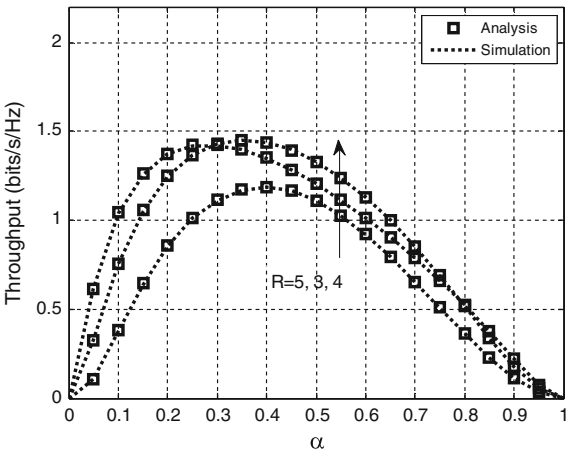

Fig. 5 Optimal throughput of FD relaying

optimal α, there is less time for information transmission. Consequently, less time for forward the signal and smaller values of throughput are observed at the destination node due to outage probability increases. On the other hand, for the values of α greater than the optimal α, more time is wasted on energy harvesting and less time is available for information transmission. As a result, smaller throughput results at the destination node due to smaller value of $(1 - \alpha)$.

5 Conclusion

In this paper, we have proposed a full duplex relaying network with wireless energy harvesting and information transfer protocol, where an energy constrained relay node harvests energy from the received RF signal and uses that harvested energy to forward the source signal to the other sources. In order to determine the achievable throughput, analytical expressions for the outage probability and the optimal value of energy harvesting time in TSR protocol can be found by simulation.

References

1. Varshney LR (2008) Transporting information and energy simultaneously. In: Proceedings of IEEE international symposium on information theory (ISIT), pp 1612–1616
2. Nasir AA, Zhou X, Durrani S, Kennedy R (2013) Relaying protocols for wireless energy harvesting and information processing. IEEE Trans Wireless Commun 12(7):3622–3636
3. Popovski P, Yomo H (2006) Bi-directional amplification of throughput in a wireless multi-hop network. In: Proceedings of vehicular technology conference, vol 2. Melbourne, Australia, May 7–10, pp 588–593
4. Louie RH, Li Y, Vucetic B (2010) Practical physical layer network coding for two-way relay channels: performance analysis and comparison. IEEE Trans Wireless Commun 9(2):764–777

5. Rankov B, Wittneben A (2006) Achievable rate regions for the two-way relay channel. In: Proceedings of IEEE international symposium on information theory. Seattle, WA, USA, pp 1668–1672
6. Riihonen T, Werner S, Wichman R (2009) Comparison of full-duplex and half-duplex modes with a fixed amplify-and-forward relay. In: IEEE 2009 IEEE wireless communications and networking conference. Budapest, Hungary
7. Yang J, Liu X, Yang Q (2014) Power allocation of two-way full-duplex AF relay under residual self-interference. In: IEEE 2014 14th international symposium on communications and information technologies (ISCIT). Incheon, South Korea
8. Zhong C, Suraweera HA, Zheng G, Krikidis I (2014) Relay control for full-duplex relaying with wireless information and energy transfer. IEEE Trans Commun 62(10)
9. Zhong C, Suraweera HA, Zheng G, Krikidis I (2014) Wireless information and power transfer with full duplex relaying. IEEE Trans Commun 62(10)
10. Do D-T (2015) Power switching protocol for two-way relaying network under hardware impairments. Radio Eng J 24(3)
11. Kwon T, Lim S, Choi V, Hong D (2010) Optimal duplex mode for DF relay in terms of the outage probability. IEEE Trans Veh Technol 59(7):3628–3634
12. David HA (1970) Order statistics. Wiley, New York

A Multi-channel MAC Protocol with Power Control for Wireless Ad Hoc Networks

Duc Ngoc Minh Dang, Quynh Tu Ngo, Hanh Ngoc Dang and Choong Seon Hong

Abstract The medium access control (MAC) protocol is designed only for single channel in the IEEE 802.11 standard. That means the throughput of the network is limited by the bandwidth of the channel. While multiple channels can be exploited by Multi-channel MAC algorithm to get more concurrent transmissions, the spatial reuse can be achieved by power control. In this paper, we combine the Multi-channel MAC protocol and Power Control together to exploit multiple channels and frequency reuse. The main idea of our proposal is to use IEEE 802.11 Power Saving Scheme (PSM) with different transmission power level used in the ATIM window and the data window. All nodes transmit ATIM/ATIM-ACK/ATIM-RES with maximum power while contending the data channel in the ATIM window, and use minimum required transmission power in the data window on their negotiated channels. The simulation results show that the proposed MMAC-PC can improve the network performance: aggregate throughput, average delay and energy efficiency.

Keywords Multi-channel · MAC protocol · Power control · Ad hoc networks

D.N.M. Dang (✉) · Q.T. Ngo
Faculty of Electrical and Electronics Engineering, Ton Duc Thang University,
No. 19 Nguyen Huu Tho Street, District 7, Ho Chi Minh City, Vietnam
e-mail: dangngocminhduc@tdt.edu.vn

Q.T. Ngo
e-mail: ngotuquynh@tdt.edu.vn

H.N. Dang
Department of Telecommunications Engineering, HCM City University of Technology,
Ho Chi Minh City, Vietnam
e-mail: hanhdn@hcmut.edu.vn

C.S. Hong
Department of Computer Engineering, Kyung Hee University, Seoul 446-701, Korea
e-mail: cshong@khu.ac.kr

V.H. Duy et al. (eds.), *AETA 2015: Recent Advances in Electrical Engineering and Related Sciences*, Lecture Notes in Electrical Engineering 371,
DOI 10.1007/978-3-319-27247-4_6

1 Introduction

In ad hoc network, nodes can transmit data directly to others within their radio transmission range without the need of an infrastructure. The performance of the ad hoc network is affected by the hidden terminal problem as well as the limited bandwidth of single channel. The IEEE 802.11 standard [1] provides a MAC protocol that uses Distributed Coordination Function (DCF) to share the medium between the nodes. To avoid hidden terminal problem, IEEE 802.11 DCF uses channel reservation technique by exchanging "Request to Send" (RTS) and "Clear to Send" (CTS) messages before data packets are sent. In addition, the IEEE 802.11 DCF employs a Carrier Sense Multiple Access with Collision Avoidance (CSMA/CA) technique. Nodes have to sense the channel before transmission and if it is busy, the node goes through a random backoff time before retrying to transmit when channel is idle. The backoff procedure reduces collision probability as well as ensure the fairness among contending transmission.

Although IEEE 802.11 provides multiple channels for wireless communications at Physical Layer, the MAC protocol is designed only for a single channel. It is not easy to design a MAC protocol that exploits multiple channels to improve the network throughput with a single half-duplex transceiver. The transceiver can switch channel radio dynamically, but it cannot sense all channels simultaneously, which may lose the channel reservation messages from its neighbors on other channels. This leads to the multi-channel hidden terminal problem [2].

Besides addressing the multi-channel hidden terminal problem, the MAC protocol design has to solve the energy problem. Wireless nodes are usually powered by battery which are limited in power capacity. The IEEE 802.11 PSM and power control scheme can be used to conserve energy for ad hoc networks. In addition to providing energy conservation, power control can improve the spatial reuse of the wireless channel.

2 Related Work

The major challenge of multi-channel transmission is to negotiate a data channel while decrease the collision and control packet overhead. As the classification from [3] describes, there are four approaches for multi-channel MAC protocol: Dedicated Control Channel, Split Phase, Common Hopping and McMAC.

In Dedicated Control Channel approach [4, 5], each node has two radios: one is tuned to the channel dedicated to control packets and another can switch to any other channels for data transmission. In DCA-PC, sending control packets will use maximum power on the control channel, and DATA/ACK packets use minimum power on the data channel. This approach does not require time synchronization but requires two radios that increases the cost of device.

In Split Phase approach [2, 6], each node only has one radios and time is divided into alternating sequence of control interval (or contention interval) and data transmission interval. In MMAC [2], all nodes are on the control channel while other data channels are free, which is a wastage of bandwidth of data channel in the control interval. To solve this problem, Traffic Aware Multi-channel MAC (TAMMAC) [6] proposes a mechanism to adjust the control interval dynamically according to the network traffic.

In Common Hopping approach [7, 8], nodes have one radio and have to hop frequently. This approach also requires a tight time-synchronization. According to IEEE 802.11, the required time to switch channel is 224 μs, which cannot be neglected. Pipelining Multi-channel MAC (π-Mc) [8] is similar to pipeline technique. The transmission task is divided into many subtasks. All of the subtasks are transmitted on different channel sequentially. The last approach, McMAC [9], each node picks a seed to generate a different pseudo random hopping sequence. Idle node follows it "home" hopping sequence. Each node puts its seed in every packet that it sends, so its neighbors eventually learn its hopping sequence.

Now, we will describe our proposed protocol: *Multi-channel MAC protocol with Power Control* (MMAC-PC) in detail.

3 The Proposed MMAC-PC Protocol

First, we summarize our assumptions as follows:

- There are N non-overlapping channels which can be used. All channels have the same Beacon Interval which is divided into ATIM Window and Data Window. One channel is defined as a default channel (CH1) only in ATIM window for channel negotiation.
- All control packets in the ATIM windows are transmitted with the maximum power while others in the data windows are sent with negotiated power.
- Nodes have prior knowledge of how many channels are available. Each node is equipped with a single half-duplex transceiver.
- All nodes are time-synchronized and follow the IEEE 802.11 DCF.

3.1 The ATIM Windows

The ATIM window has the same role as in IEEE 802.11 PSM. Since node A has data for node B, node A and B use 3-way handshake to select a data channel. The ATIM/ATIM-ACK/ATIM-RES messages are transmitted with maximum power in this ATIM window (The ATIM window in Fig. 2):

1. ATIM: Node A creates a list of candidate data channel called Preferable Channel List (PCL) included in ATIM packet sent to node B.
2. ATIM-ACK: Node B tries to find the "best" channel based on its own PCL and the PCL from node A. The selected channel and the corresponding transmission power are transmitted to node A in ATIM-ACK message.
3. ATIM-RES: Node A confirms the selected channel and attaches its transmission power level to ATIM-RES message that is sent to node B.

Then both nodes A and B will stay awake for the entire beacon interval. If a node has no data packet in its buffer or does not receive any ATIM message, it goes into doze mode after the ATIM window to save energy.

3.2 Power Control

In this section, we will describe the power control model of the proposed protocol. In the ATIM window, the sender and receiver have to estimate the transmission power which is used in the data window and broadcast to the neighbor nodes through ATIM-ACK and ATIM-RES messages. Transmission power control is a technical mechanism to prevent co-channel interference. Optimal power control improves the frequency utilization efficiency as well as saves the energy of mobile device with limited battery. Transmission Range (TR) is defined as the range that the receiver successfully receive packets from the sender. Let P_{ti}, P_{rij} be the transmission power from node I and receiving power of node J, respectively. By using two-ray ground reflection model [10], the receiving power P_{rj} is calculated from the following formula:

$$P_{rj} = P_{ti} G_t G_r \frac{h_t^2 h_r^2}{d^4 L} \tag{1}$$

where

G_t, G_r antenna gains of transmitter and receiver;
h_t, h_r heights of the transmit and receive antennas;
d distance between transmitter and receiver;
L other losses.

Now, we consider the scenario in Fig. 1 with source S and destination D. The relationship between the receiving power P_{rD} and P_{rS} is

$$\frac{P_{rD}}{P_{rS}} = \frac{P_{tS}}{P_{tD}} \tag{2}$$

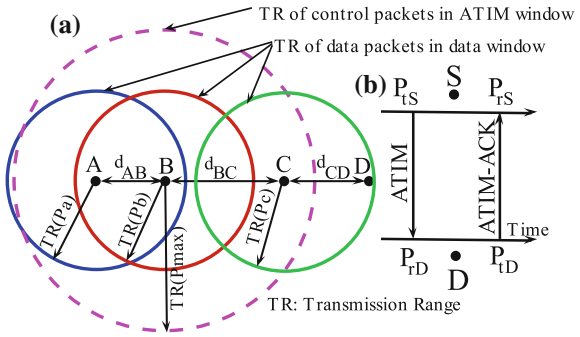

Fig. 1 The power control scheme and the ATIM exchange diagram

Assuming that node S sends a packet (e.g. ATIM packet) to node D with maximum power $P_{tS} = P_{\max}$. Based on the receiving power P_{rD}, node D calculates the minimum transmission power P_{tD} that it can transmit to node S successfully:

$$P_{tD} \geq \frac{P_{thold} P_{\max}}{P_{rD}} \tag{3}$$

3.3 Channel Usage List and Neighbor Information List

Each node maintains its data structures called the Channel Usage List (CUL) and Neighbor Information List (NIL), as shown in Table 1. In CUL, the counter of each channel shows the number of nodes that reserve the channel for data transmission. It is used to balance the channel load as much as possible [2]. Whenever a node overhears any control message from its neighbor node reserving a data channel, the counter will be increased by one.

Each entry in NIL has 4 fields that contain all information about the neighbor nodes: channel, power, status and interference. Channel is the one that neighbor node will switch to after the ATIM window. Power is the required level used to transmit to neighbor node, which is calculated by Eq. 3. Status can be busy or idle. Interference field shows the interference level from the neighbor node.

At the beginning of each beacon, nodes set Status to Idle, Interference to No and Counter to zero. When a node overhears ATIM-ACK or ATIM-RES packet,

Table 1 (a) Node A's CUL (b) Node A's NIL

Channel	Counter	Node	Channel	Power	Status	Interference
CH1	1	B	2	3	Idle	No
CH2	0	C	4	4	Busy	Yes
CH3	1	D	1	7	Busy	No
CH4	2	E	3	1	Idle	No
…	…	…	…	…	…	…

it increases the counter of the corresponding channel, and updates Channel, Status, Power level and Interference information of the corresponding node.

3.4 Rules for Creating Preferable Channel List

When a node A has data for node B, it checks whether node B is Idle or not by using its NIL. If node B is Idle, node A creates Preferable Channel List (PCL) and sends it to node B through ATIM. The PCL is similar to CUL, except that PCL only contains the candidate data channels and their counters. Node A creates the PCL by using Algorithm 1. The channel *CH[i]* is added to PCL that node A sends to node B.

After node B receives ATIM with PCL from node A, it also creates its own PCL. Then, node B compares its own PCL and the received PCL from node A to find the "best" data channel to be used in data window (Algorithm 2). The "best" data channel is a channel that has the minimum total counter in both PCLs of node A and node B.

3.5 The Operation of MMAC-PC Protocol

The operation of MMAC-PC is illustrated in Fig. 2. Now suppose node A has data for node B and node D wants to send data to node C. The MMAC-PC operation is as follow:

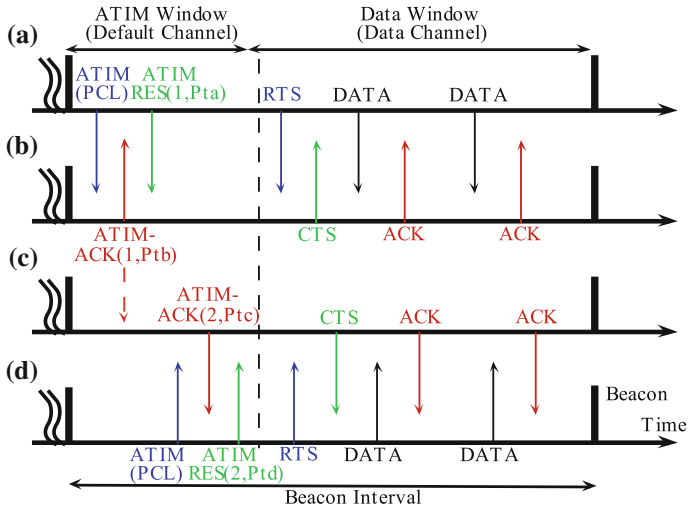

Fig. 2 Negotiation and data exchange in MMAC-PC

Algorithm 1 Create PCL for node A sent to node B

```
for i = 1 to N channels do
  if CH[i].counter = 0 then
    Channel i and its counter are added to PCL
  else
    for j = 1 to M neighbors do
      if Node[j].CHNL = i & Node[j].STAT = Busy & Node[j].INT = No &
      Node[j].PWR > Node[B].PWR then
        Channel i and its counter are added to PCL
      end if
    end for
  end if
end for
```

Algorithm 2 Choose the "best" data channel

```
total_counter ← −1
for i = 1 to N do
  if PCL_B[i].CNTR ≥ 0&PCL_A[i].CNTR ≥ 0 then
    total_counter = PCL_A[i].CNTR + PCL_[i].CNTR
    if total_counter = -1 then
      min_counter = total_counter
      CH ← i
    else {min_counter > total_counter}
      min_counter ← total_counter
      CH ← i
    end if
  end if
end for
```

1. Node A checks node B's status in its NIL. If node B is Busy, node A has to wait for the next beacon. If node B is Idle, node A creates PCL by Algorithm 1 and sends ATIM packet including its PCL to node B.
2. After receiving ATIM(PCL) packet from node A, node B calculates the transmission power P_{tb} and chooses the free common data channel CH[i] by Algorithm 2. Now, node B includes these information into ATIM-ACK(CH[i], P_{tb}), which is sent to node A.
3. Upon receiving ATIM-ACK, node A calculates its transmission power P_{ta} to B and sends ATIM-RES(CH[i], P_{ta}) to confirm the selected channel CH[i].
4. If node D has data for node C, it sends ATIM(PCL) to node C. By overhearing ATIM-ACK from node B, node C may choose another data channel or the same channel with node A and B, but does not interfere with node B.
5. After the ATIM window, nodes A, B and nodes C, D switch to the corresponding data channels. All RTS/CTS/DATA/ACK packets are transmitted at the minimum required power level informed in the ATIM window.

4 Performance Evaluation

In this section, we have simulated IEEE 802.11, DCA, MMAC, DCA-PC and our proposed MMAC-PC protocols.

4.1 Simulation Model

The network consists of n^2 nodes in a n x n square grid. Each node has random location within its square grid. It generates and transmits constant-bit-rate traffic. The destination of each source node is chosen randomly. The transmitter and receiver have 1.5 m height antennas with the gain of 1 dBi. Other simulation parameters in our simulations are listed in Table 2. We use the throughput, average delay and energy-efficiency as the performance metrics.

4.2 Simulation Result

Figure 3 shows the aggregate throughput of different protocol as the network load increases. Under low network load, all protocols perform similarly. The performance of IEEE 802.11, DCA and MMAC protocol do not depend on the network size in our simulation model. When network load nearly approaches saturation, MMAC-PC performs significantly better than IEEE 802.11, DCA, MMAC and DCA-PC. The IEEE 802.11 achieves about 80 % channel data rate because of the overhead of RTS/CTS/ACK and the backoff algorithm. By using 2 channels for data transmission, the throughput of DCA is twice of IEEE 802.11. In MMAC, there is 10 % overhead used in ATIM window and 3 channels are used in data windows. Therefore, the throughput of MMAC is about 90 % × 3 times more than

Table 2 Simulation's parameters

Parameters	Value
Number of channels	3
Number of nodes	36
Beacon interval/ATIM window	50 ms/5 m
Basic rate/data rate	1/2 Mbps
Data packet size	512 byte
Maximum radio power	250 mW
Receiving power threshold	3.25×10^{-10} W
Power control level	8 levels
Transmit/receive power consumption	1.65/1.4 W
Idle/doze power consumption	1.15/0.045 W

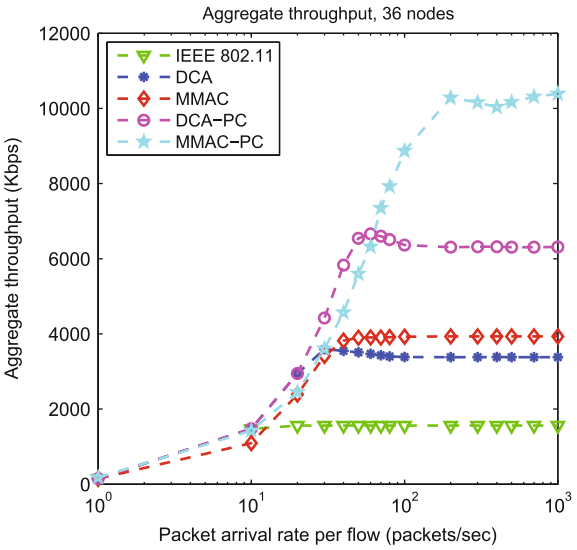

Fig. 3 Aggregate throughput against the packet arrival rate

that of IEEE 802.11. With the power control, DCA-PC and MMAC-PC utilize the spatial reuse to improve throughput.

Figure 4 shows the average delay of different protocols against packet arrival rate. MMAC-PC has one contention phase in the ATIM window to reserve data channel, after that the sender can send multiple packets to receiver without any contention. Other nodes have to wait for the next beacon, therefore the delay of packet is increased. However, when the network nearly approaches saturation, the

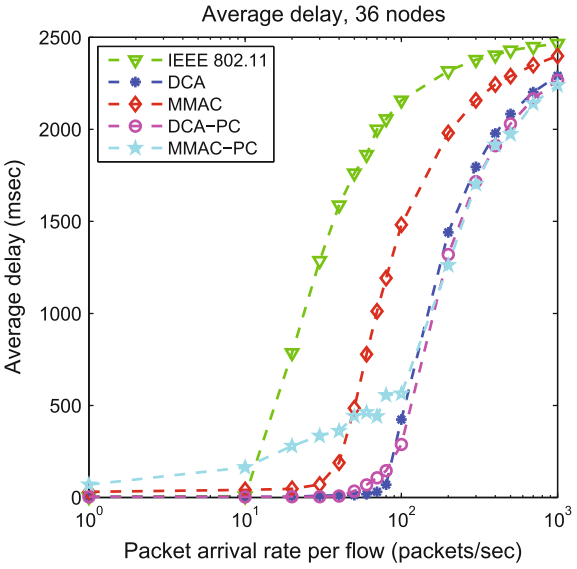

Fig. 4 Average delay against the packet arrival rate

average delay of MMAC-PC is lower than others because it allows more packets to be transmitted. The average delay of IEEE 802.11 is higher than others because of the use of one channel to transmit data packets.

Figure 5 shows the energy efficiency performance of different protocols as the network load increases. When traffic load increases, the energy consumption per data packet decreases for all protocols until saturation. DCA-PC and MMAC-PC have better performance than others because the sender transmits data packets at minimum required power. In IEEE 802.11, all idle nodes consume the idle power of 1.15 W. In DCA, the energy consumption is higher because of 2 transceivers. When the traffic load is low, MMAC consumes more energy per data packet than DCA because of the ATIM/ATIM-ACK/ATIM-RES overhead in ATIM window. When the traffic load is high, MMAC transmits more data packets than DCA meaning its throughput is higher as well as the energy consumption per data packet is lower than DCA. MMAC-PC has lower energy consumption per data packet because of two main reasons. First, MMAC-PC adopts IEEE 802.11 PSM, all nodes which don't have data to exchange or cannot contend the data channel in the ATIM windows enter the doze mode with small power consumption of 0.045 W versus other protocols with idle power of 1.15 W. Second, MMAC-PC's sender-receiver pair use the minimum required power to transmit packets in data channels. MMAC allows many nodes to contend for transmission in data channel so that one sender-receiver pair exchange data packets while other nodes consumes idle power significantly compared to doze power. In MMAC-PC, after nodes contend to negotiate the data channel in the ATIM window, they switch to data channel and transmit multiple packets without any more contention. Other nodes have no data to exchange or cannot win the right to access data channels enter the doze mode to save energy.

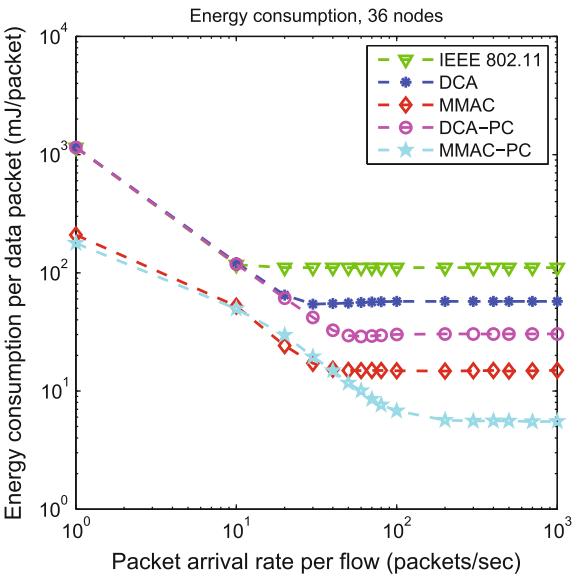

Fig. 5 Energy efficiency against the packet arrival rate

5 Conclusions

In this paper, we propose a new Multi-channel MAC protocol (MMAC-PC) which requires one transceiver for each node resulting in less energy consumption. The power control algorithm helps MMAC-PC exploit the multiple channels and increase the spatial reuse. Simulation results show that MMAC-PC protocol improves the aggregate throughput, average delay and the energy efficiency.

References

1. IEEE 802.11 Working Group (1997) Wireless LAN medium access control (MAC) and physical layer (PHY) specification
2. So J, Vaidya NH (2004) Multi-channel MAC for Ad hoc networks: handling multi-channel hidden terminals using a single transceiver. In ACM international symposium on mobile ad hoc networking and computing (Mobihoc'04)
3. Mo J, So H-SW, Walrand J (2008) Comparison of multichannel MAC protocols. IEEE Trans Mob Comput
4. Wu S-L, Lin C-Y, Tseng Y-C, Sheu J-L (2000) A new multi-channel MAC protocol with on-demand channel assignment for multi-hop mobile ad hoc networks. In Proceedings of the international symposium on parallel architectures, algorithms and networks, I-SPAN 2000
5. Tseng H-C, Wu S-L, Lin C-Y, Sheu J-P (2001) A multi-channel MAC protocol with power control for multi-hop mobile ad hoc networks. In: 2001 International conference on distributed computing systems workshop
6. Chen W-T, Liu J-C, Huang T-K, Chang Y-C (2008) TAMMAC: an adaptive multi-channel MAC protocol for MANETs. IEEE Trans Wireless Commun
7. Tzamaloukas A, Garcia-Luna-Aceves JJ (2000) Channel-hopping multiple access. IEEE Int Conf Commun (ICC 2000)
8. Shih K-P, Chen Y-D, Liu S-S (2010) A collision avoidance multi-channel MAC protocol with physical carrier sensing for mobile ad hoc networks. In: IEEE 24th international conference on advanced information networking and applications workshops (WAINA)
9. Wilson So H-S, Walrand J (2007) McMAC: a multi-channel MAC proposal for ad-hoc wireless networks. In: Proceedings of the IEEE WCNC 2007, Hongkong
10. Rappaport T (1996) Wireless communications: principles and practice. Prentice Hall, New Jersey

A Novel Compressed Sensing Approach to Speech Signal Compression

Tan N. Nguyen, Phuong T. Tran and Miroslav Voznak

Abstract Compressed sensing (CS) is a technique to sample compressible signals below the Nyquist rate, whilst still allowing near optimal reconstruction of the signal. In this paper, we apply the iterative hard thresholding (IHT) algorithm for compressed sensing on the speech signal. The interested speech signal is transformed to the frequency domain using Discrete Fourier Transform (DCT) and then compressed sensing is applied to that signal. The compressed signal can be reconstructed using the recently introduced Iterative Hard Thresholding (IHT) algorithm and also by the tradditional ℓ_1 minimization (basic pursuit) for comparison. It is shown that the compressed sensing can provide better root mean square error (RMSE) than the tradition DCT compression method, given the same compression ratio.

Keywords Compressed sensing · Iterative hard thresholding · Speech signal compression · DCT · ℓ_1 minimization

T.N. Nguyen · P.T. Tran (✉)
Faculty of Electrical and Electronics Engineering, Ton Duc Thang University,
No. 19 Nguyen Huu Tho Street, District 7, Ho Chi Minh City, Vietnam
e-mail: tranthanhphuong@tdt.edu.vn
URL: http://dee.tdt.edu.vn

T.N. Nguyen
e-mail: nguyennhattan@tdt.edu.vn
URL: http://dee.tdt.edu.vn

M. Voznak
VSB-Technical University of Ostrava, 17. Listopadu 15/2172,
708 33 Ostrava-Poruba, Czech Republic
e-mail: miroslav.voznak@vsb.cz
URL: http://www.vsb.cz/en

V.H. Duy et al. (eds.), *AETA 2015: Recent Advances in Electrical Engineering and Related Sciences*, Lecture Notes in Electrical Engineering 371,
DOI 10.1007/978-3-319-27247-4_7

1 Introduction

For more than six decades, the foundation of digital signal processing systems has been based on the Nyquist Shannon sampling theorem [1, 2]. This theorem stated that signals have to be sampled at twice the signal bandwidth so that they can be reconstructed fully later. This increases the demand of high capacity memory devices and high speed processing units to handle large-bandwidth signals. Furthermore, while that theorem holds for general band-limited signals, it does not account for additional signal structures that might be known a priori. Compressed sensing (CS) is a recently emerging field [3–5] that exploits that additional structures. It can provide a new way to reconstruct the original signal with a minimal number of observations. In compressed sensing, signals are assumed to be (approximately) sparse in some transform domain. This sparsity constraint significantly reduces the size of the set of possible signals compared to the signal space dimension.

Instead of taking samples at the Nyquist rate, compressed sensing uses linear sampling operators that map the signal into a small (compared to the Nyquist rate) dimensional space, whilst reconstruction of the signal is highly non-linear. One of the important contributions of the seminal work by Candes et al. [3, 4] and Donoho [5] was to show that linear programming algorithms can be used under certain conditions on the sampling operator to reconstruct the original signal with high accuracy.

For efficient reconstruction of the signals which are compressively sampled, several other algorithms have also been proposed. Most of them use the greedy methods. The tradditional one is Orthogonal Matching Pursuit (OMP), which was presented in [6], and more recently, the Compressive Sampling Matching Pursuit (CoSaMP) [7] and the nearly identical Subspace Pursuit [8] algorithms were introduced and analysed for compressed sensing signal reconstruction. The Iterative Hard Thresholding (IHT) algorithm was proposed and its effectiveness was proven by Blumensath and Davies [9] in 2009. Recently, some advanced recovery techniques have also been proposed toward more efficient reconstruction for compressed sensing [10, 11].

With the support of good recontruction algorithms mentioned above, compressed sensing have proven its important role in many real world applications, especially in audio and image processing [12, 13]. In the preprint [13], the authors have made a comparative study of audio compression using compressed sensing, but only focused on traditional methods such as FFT and OMP. In this paper, we provide a new look to the application of compressed sensing of speech signals. Here, instead of using the traditional reconstruction method, we we focus on using the IHT algorithm to reconstruct the signal to increase the overall data rate of the systems.

The rest of the paper is organized as follows. The theoretical background of compressed sensing is introduced in Sect. 2. Section 3 presents the compressed sensing algorithms that is applied to speech signal compression. Numerical results

to support the proposed algorithm are given in Sect. 4. Finally, Sect. 5 concludes the paper.

2 Compressed Sensing

2.1 Notation

The following notation will be used in this paper:

- $\mathbf{x}$ and $\mathbf{y}$ are the N-dimensional and M-dimensional real or complex vector, respectively.
- $\boldsymbol{\Phi}$ denotes the $M \times N$ sensing matrix, which may be real or complex. $\boldsymbol{\Phi}^{\boldsymbol{H}}$ denotes the Hermitian tranpose of $\boldsymbol{\Phi}$.
- Γ^k and $\mathbf{x}^{(k)}$ denotes the realizations of the set Γ and the vector $\mathbf{x}$ at the kth iteration.
- $\|\cdot\|_2$ is the Euclidean vector norm or, for matrices, the operator norm from L_2 to L_2.
- $\|\cdot\|_1$ is the L_1 vector norm.
- $\|\cdot\|_0$ is the number of non-zero elements in a vector.
- For a general vector $\mathbf{x}$, the vector $\mathbf{x}^s$ is the best s-sparse approximation to vector $\mathbf{x}$. Here, a vector is called s-sparse if no more than s of its elements are non-zero.

2.2 Compressed Sensing Concept

In compressed sensing the signal of interest is an N-dimensional real or complex vector $\mathbf{x}$ assumed to be approximately sparse. Samples are then taken using a linear mapping $\boldsymbol{\Phi}$ into an M-dimensional real or complex observation space to obtain the observed samples

$$\mathbf{y} = \boldsymbol{\Phi}\mathbf{x} + \mathbf{n} \tag{1}$$

Here, $\boldsymbol{\Phi}$ is the sensing matrix and $\mathbf{n}$ are the observation noise added to the systems.

In compressed sensing, there are two main problems to be considered. The first one is to design the sensing matrix $\boldsymbol{\Phi}$ that satisfies certain desirable properties (such as the restricted isometry property), which allow for an efficient estimation of $\mathbf{x}$. The second one is the study of concrete algorithms for the efficient estimation of $\mathbf{x}$ given only $\mathbf{y}$ and $\boldsymbol{\Phi}$.

2.3 The Restricted Isometry Property (RIP)

The analysis of algorithms for compressed sensing relies heavily on the following property of the sensing matrix $\boldsymbol{\Phi}$. A matrix $\boldsymbol{\Phi}$ satisfies the Restricted Isometry Property (RIP) [3] if

$$(1-\delta_s)\|\mathbf{x}\|_2^2 \leq \|\boldsymbol{\Phi}\mathbf{x}\|_2^2 \leq (1+\delta_s)\|\mathbf{x}\|_2^2 \tag{2}$$

for all s-sparse $\mathbf{x}$ and some $\delta_s < 1$. The restricted isometry constant δ_s is defined as the smallest constant for which this property holds for all s-sparse vectors $\mathbf{x}$.

2.4 Signal Reconstruction in Compressed Sensing

Reconstruction of a compressively sensed signal involves trying to recover the sparse vector $\mathbf{x}$, given the sensing matrix $\boldsymbol{\Phi}$ and the observation $\mathbf{y}$. It seems that we cannot reconstruct the signal exactly, because the number of observations (and hence, the number of equations) is less than the number of unknowns (elements of $\mathbf{x}$). However, it has been shown that we can find a s-sparse approximation of $\mathbf{x}$ as long as $\boldsymbol{\Phi}$ satisfies the RIP condition in (2) [5].

There are several reconstruction algorithms used: basis pursuit (BP) [3], orthogonal matching pursuit (OMP) [6], Compressive Sampling Matching Pursuit (CoSaMP) [7], and the recently introduced Iterative Hard Thresholding [9]. The first algorithm, Basic Pursuit, is basically an ℓ_1 minimization problem given by

$$(\mathrm{P1}) : \min\|\mathbf{x}\|_1 = \sum_{i=1}^{n} |x_i| \text{ subject to } : \mathbf{y} = \boldsymbol{\Phi}\mathbf{x} \tag{3}$$

If BP simultaneously decide on elements of $\mathbf{x}$, the second algorithm, OMP, does this on a element-by-element basis. OMP successively approximates $\mathbf{X}^{(k)}$ by finding which basis function would contribute the most to $\mathbf{y}^{(k)} = \boldsymbol{\Phi}^{(k)} \cdot \mathbf{x}^{(k)}$, and then removes the contribution of this component and repeats the process.

The CoSaMP algorithm is also an iterative one. CoSaMP uses an approach inspired by the RIP property. At each iteration, a s-sparse signal can be approximated by a "proxy" signal. The current approximation induces a residual, which is the part of the target signal that has not been approximated. We try to identify the large components in the residual, update the new residual, and repeat the process.

In this paper, we use IHT algorithm for signal reconstruction. This algorithm is introduced in the next sub-section.

2.5 Iterative Hard Thresholding

Let $\mathbf{x}^{(0)} = \mathbf{0}$ and use the iteration

$$\mathbf{x}^{(n+1)} = H_s\left(\mathbf{x}^{(n)} + \mu\boldsymbol{\Phi}^H(\mathbf{y} - \boldsymbol{\Phi}\mathbf{x}^{(n)})\right), \tag{4}$$

where H_s (**a**) is the non-linear operator that sets all but the largest (in magnitude) s elements of a to zero. If there is no unique such set, a set can be selected either randomly or based on a predefined ordering of the elements. The convergence of this algorithm was proven in [9] under the condition that $\|\boldsymbol{\Phi}\|_2 < 1$. In this case, the above algorithm converges to a local minimum of the problem

$$(\text{P2}) : \min_x \|\mathbf{y} - \boldsymbol{\Phi}\mathbf{x}\|_2^2 \text{ subject to : } \|\mathbf{x}\|_0 \leq s. \tag{5}$$

3 Speech Signal Compression Using Compressed Sensing

3.1 Sparsity of Speech Signals

The sampling signal must be sparse, or approximate sparse, to be processed by compressed sensing algorithms. Under normal condition, speech signals in general are not sparse in nature, but through a certain transformation, we can get the approximate sparse signal. We can transform a frame of the speech signal into some transform-domain to make it sparse. Several transforms can sparsify the speech signals sparse, including the ones which are listed as follows.

Discrete Fourier Transform It is the most basic sparsifying method. But it is not suitable for speech because there are a lot of frequency components in speech, that leads to the large amplitude values of the DFT coefficients, which does not allow us to discard spectrum components to increase sparsity. Furthermore, the DFT coefficients are complex numbers in general, that makes the computation more complicated.

Discrete Cosine Transform (DCT) DCT can remove redundancy between neighboring values, which leads to uncorrelated transform coefficients which can be encoded independently. One important characteristic of DCT is that the energy of signals concentrates in lower order coefficients. Hence, we can remove higher order coefficients to make the signal sparse in frequency domain. In addtion, all DCT components are purely real numbers.

Discrete Wavelet Transform (DWT) DWT use wavelets as basis functions. A wavelet typically has finite support, in contrast to Fourier transforms. Hence, it can be used to sparsify signals. However, it's not fully suitable for speech because DWT can't achieve good efficiency at near-transparent compression ratios as compare to DCT and its computational complexity makes it hard to implement.

Linear prediction coefficients (LPC) Speech signal is produced by the convolution of excitation source and time varying vocal tract system components. These excitation and vocal tract components are to be separated from the available speech signal to study these components independently. The redundancy in the speech signal is exploited in the LP analysis. The prediction of current sample as a linear combination of past p samples form the basis of linear prediction analysis where p is the order of prediction. LP residues is the prediction errors, which are sparse and can be used to compute the original signal.

Among those sparsifying methods for speech signals, DCT and LP have been proved to give the best sparse representation of speech. Figure 1 shows the DFT, DCT, DWT, and LP coefficients of a speech signal. It can be observed that DCT and LPC have very few numbers of non-zero elements. Thus we can even increase sparsity of speech by thresholding low value components without considerably affecting speech quality.

3.2 *Compression of Speech Signal Using Compressed Sensing*

The block diagram of our speech compression system is given in Fig. 2. At the input of the system, the speech signal is divided into frames, and then the speech frame signal is transformed to frequency domain or LP residue domain using either sparsifying methods mentioned in previous section. We then use compressed sensing to sample the coefficients obtained from the first step. Here, we may multiply the resulted spectrum with a measurement matrix to get the compressive

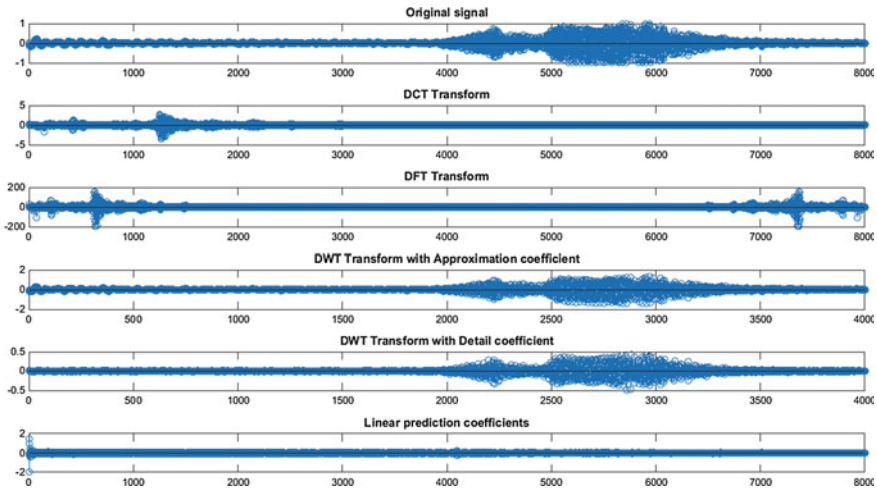

Fig. 1 Original signals and its DCT, DWT, and LPC

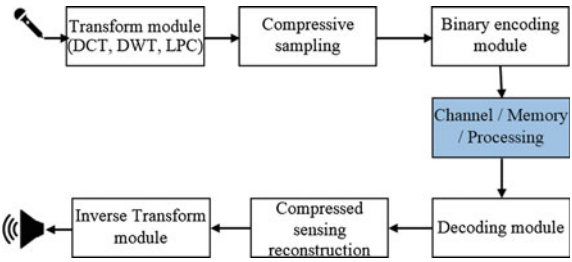

Fig. 2 Speech compression system using compressed sensing

observations. This matrix can be a random ones, which is usually Gaussian random matrix in many CS applications, or can be predefined according to some knowledge about the statistical characteristics of speech signals. The sampled signal is encoded to binary stream to be stored, processed, or transmitted to the destination.

At receiver/output side, the received binary stream is first decoded to obtain the measured values. According to the measured values, the transform coefficients are recovered by using one of the reconstruction algorithms. Here, in this paper, we focus on the IHT algorithm. Finally, the original speech signal can be reconstructed by taking the inverse DCT, DFT, DWT, or LP transform.

3.3 Effect of Measurement Matrix on the Compressed Sensing Algorithms for Speech Signals

As mentioned above, in CS theory, we usually choose Gaussian random matrix for measurement. That means the observation samples are chosen randomly from the original signal. However, for speech signals, certain additional signal structures might be known a priori. In that case, we can choose the sampling position wisely to get more information about the signals. Hence, by intuition, a well-designed measurement matrix can also enhance the performance of the compressed sensing algorithms for speech signals.

4 Simulation Results

4.1 Simulation Setup

In this section, we describe the MATLAB experiments to test our compression algorithms. We try out the algorithms on a set of 3 test speech signals, namely, the words “Hello”, “Goodbye”, and “Tiger” said by one male person. The speech

signals are recorded to .wav at the sampling rate of 8 kHz. The recorded speech signal then goes through the DCT or DWT which transforms a sequence of real data points into frequency domain. Figure 3 shows the "Hello" word recorded using the "wavrecord" function composed of 8000 samples as well as the reconstructed speech signal. Simulation parameters are listed in Table 1.

To make the transformed signal really sparse, we remove the small-value coefficients that have no significant contribution to the signal. The thresholded spectrum is then multiplied by the measurement matrix which in this case is composed of randomly generated numbers. The compressive sampled signals are then reconstructed using two methods: basic pursuit, which is in fact an ℓ_1 optimization problem, and the IHT algorithm, which is the main focus of our paper. Performance of the algorithms is evaluated by calculating the signal-to-noise ratio (SNR) of each signal.

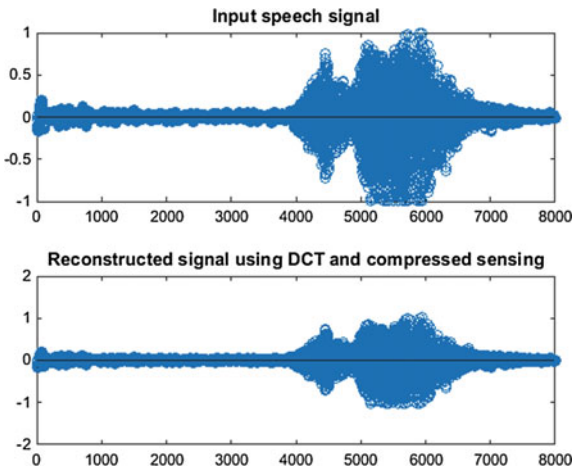

Fig. 3 Signals before and after using compressed sensing

Table 1 Simulation parameters

Symbol	Parameter name	Value
N	Number of samples	8000
L	Signal frame length	2048
M	Number of DCT points	2048
K/L	Sparsity	20–80 %
wname	Wavelet function	Haar
level	Number of DWT levels	5

5 Results

Figure 4 shows the RMSE of the reconstructed speech signals which have been processed using compressed sensing combined with DCT, DWT, and DCT only. We can observed that DCT with compressed sensing outperforms the traditional DCT compression method. Comparing between 2 transform methods, DCT gives better performance than DWT. These results are consistent over different test speech signals. Figure 5 shows the RMSE of the reconstructed speech signals

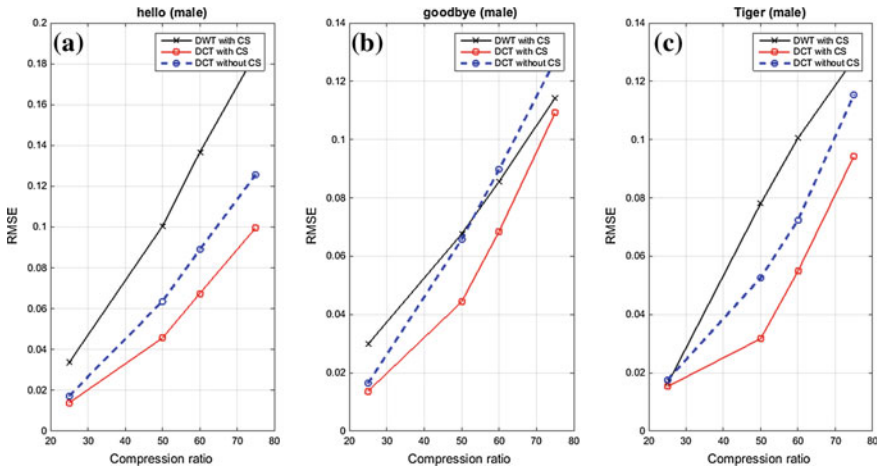

Fig. 4 Comparison of speech signal compression with and without compressed sensing

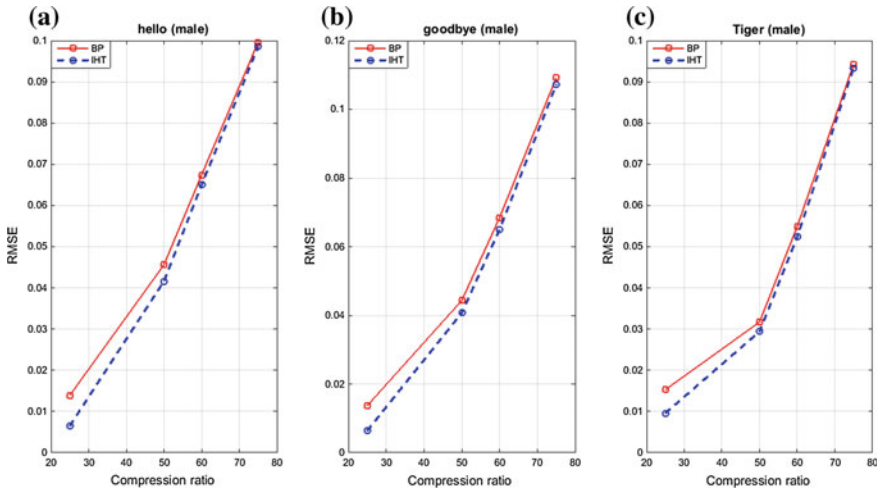

Fig. 5 Comparison of compressed sensing reconstruction algorithms

Table 2 Comparison of different compressed sensing algorithms

Signals	DCT-BP		DCT-IHT	
	RMSE	Execution time (s)	RMSE	Execution time (s)
Hello	0.0456	415.34	0.0416	24.102
Goodbye	0.0443	402.15	0.0407	21.67
Tiger	0.0317	410.63	0.0294	23.12

obtained by using different reconstruction methods. Here, we recommend the IHT algorithm and its performance is compared with the BP algorithm. As we expected, the IHT algorithms can provide a slightly better RMSE performance than BP algorithm, especially at smaller number of compressive samples. However, the most advantage of IHT algorithm is that the execution time has been improved significantly, compared to the BP algorithm. This is confirmed by the data given in Table 2.

6 Conclusion

In this paper, we survey some methods of compressing speech signals using sparse representation theory and suggest a new compressing algorithm based on the IHT algorithm for reconstructing the compressive sampling observations. Simulation results show that this algorithm allows to improve the performance of speech compressing methods using compressed sensing. Among the transforming method applied to speech signal, the DCT is best suitable for compressed sensing methods, because it can sparsify the speech signals significantly. The performance of compression can be improved further by designing the measurement matrix properly, which is the scope of another paper.

References

1. Nyquist H (1928) Certain topics in telegraph transmission theory. Trans AIEE 47:617–644
2. Shannon CE (2001) A mathematical theory of communication. SIGMOBILE Mob Comput Commun Rev 5(1):3–55. http://doi.acm.org/10.1145/584091.584093
3. Candes E, Romberg J, Tao T (2006) Robust uncertainty principles: exact signal reconstruction from highly incomplete frequency information. IEEE Trans Inf Theor 52(2):489–509
4. Candes E, Romberg J, Tao T (2005) Stable signal recovery from incomplete and inaccurate measurements
5. Donoho DL (2006) Compressed sensing. IEEE Trans Inf Theor 52(4):1289–1306. doi:10.1109/TIT.2006.871582
6. Tropp JA, Gilbert AC (2005) Signal recovery from partial information via orthogonal matching pursuit. IEEE Trans Inf Theor

7. Needell D, Tropp J (2009) Cosamp: iterative signal recovery from incomplete and inaccurate samples. Appl Comput Harmonic Anal 26(3):301–321. http://www.sciencedirect.com/science/article/pii/S1063520308000638
8. Dai W, Milenkovic O (2009) Subspace pursuit for compressive sensing signal reconstruction. IEEE Trans Inf Theor 55(5):2230–2249
9. Blumensath T, Davies M (2008) Iterative thresholding for sparse approximations. J Fourier Anal Appl 14(5–6):629–654. doi:10.1007/s00041-008-9035-z
10. Masood M, Al-Naffouri T (2013) Sparse reconstruction using distribution agnostic bayesian matching pursuit. IEEE Trans Sig Process 61(21):5298–5309
11. Kwon S, Wang J, Shim B (2013) Multipath matching pursuit. CoRR abs/1308.4791. http://arxiv.org/abs/1308.4791
12. Griffin A, Hirvonen T, Tzagkarakis C, Mouchtaris A, Tsakalides P (2011) Single-channel and multi-channel sinusoidal audio coding using compressed sensing. IEEE Trans Audio, Speech, Lang Process 19(5):1382–1395
13. Kasem HM, El-Sabrouty M (2014) A comparative study of audio compression based on compressed sensing and sparse fast fourier transform (SFFT): performance and challenges. CoRR abs/1403.3061. http://arxiv.org/abs/1403.3061

Optimization of Mobility Control in Mobile Wireless Networks for Energy Saving

Phuong T. Tran

Abstract In this paper, we consider a multi-hop wireless relay neworks, in which the source node and destination node have fixed location while we can control the positions of the relay nodes. Some strategies to control positions of relay nodes to minimize energy consumption of transmission from sources to sinks is introduced and analyzed. Three different cases were investigated, including networks with single flow, networks with multiple flows, and networks with coverage constraints for the relay nodes. The most contribution of this paper is providing simple localized algorithms for relay nodes, yet optimize the energy consumption problem. The analysis is also confirmed by numerical results.

Keywords Mobility control · Multi-hop relay · Optimization · Wireless sensor network

1 Introduction

Recently wireless sensor networks have emerged as an interesting research topic because of its ability to realize critical missions like in military or wildfire detection, especially, as the capability of mobility becomes more readily available to the wireless nodes. Typical mobile wireless sensor network consists of multiple mobile nodes, such as mobile robots which are equipped with some limited memory and processing capabilities, communication capabilities, and mobility, distributed over some areas that collaboratively form an ad hoc network [1].

Different from static wireless networks, mobility makes the whole mobile wireless network possess the self-configuration ability. If some nodes in network can't work because of some causes, the rest nodes can organize the network again

P.T. Tran (✉)
Faculty of Electrical and Electronics Engineering, Ton Duc Thang University,
No. 19 Nguyen Huu Tho Street, District 7, Ho Chi Minh City, Vietnam
e-mail: tranthanhphuong@tdt.edu.vn
URL: http://dee.tdt.edu.vn/

V.H. Duy et al. (eds.), *AETA 2015: Recent Advances in Electrical Engineering and Related Sciences*, Lecture Notes in Electrical Engineering 371,
DOI 10.1007/978-3-319-27247-4_8

through moving, repair the network topology automatically and complete self-deployment. In addition, mobility can enhance the flexibility of the networks and make the whole network have better node deployment and topology control for completing specific tasks.

Hence, mobility is something that should be adaptively controlled to help network reach requirements posed by specific tasks and limited resources. However, a great deal of current work considering mobility only treats it as an uncontrollable external factor which the communication network has to handle. As a result, the following research is to add one more dimension, i.e. mobility, into network model to be purposefully designed to improve the network performance.

We define the research problem as using mobility to create routing paths between sources and sinks by moving nodes to positions such that the required transmission power for the data flows is minimized so as to maximize the life time of the network. The problems are formulated into optimization problems and use convex optimization methods [2] to develop iterative algorithms to solve.

2 State of the Art

There are several recent studies on using mobility as a control mechanism to improve network systems. Wang et al. [3] added one or a few mobile nodes in a dense network of static nodes and derived the upper bounds of life time in two cases of when add one mobile sink and when add one mobile relay. Then they propose a routing algorithm based on the knowledge of the current position of the mobile relay node to approach the bound. The results of this paper were limited at one mobile sink or one mobile relay.

Dixon et al. [4] used SNR as input into a control system for robotic vehicles to improve and maintain communication performance by using extremum seeking methods, and adaptive model-free ES is presented to control the motion of 2D nonholonomic vehicles without knowledge of the SNR field as communication relays. This paper focused on link performance in terms of SNR but didn't consider the energy consumption of network.

The work most related to this study is using relay node mobility to minimize energy consumption. Goldenberg et al. [5] presented a simple mobility control scheme using neighboring information in which the connections between neighbor nodes do not break. Chen et al. [6] gave two modified versions of this method by using knowledge of optimal positions of each node. However, these paper only studied the constraint that the communications between neighbors were not lost and didn't analyze the optimization problem and proved the convergence of the algorithms mathematically.

The most contribution of this research are in how to develop simple localized algorithms for relay nodes, yet optimize the energy consumption problem and prove the convergence of the proposed algorithm mathematically.

3 Preliminaries

The reason why mobility can reduce transmission power by reducing the transmission distance between nodes lies in the transmission energy model. Power needed for successful wireless data transmission is determined by distance between communication nodes and the noise level of the communication channel. Let $P_T(d)$ be the power needed for data transmission across distance d,

$$P_T(d) = a + bd^{\alpha} \tag{1}$$

where a, b and α are constants dependent on the characteristics of the communication channel. The value of α is greater than or equal to 2. The energy consumption for transmitting L data bits accross distance d is

$$E_T(d, L) = L \cdot P_T(d) \tag{2}$$

For the following research, we assume that a route from the fixed source to the fixed sink consisting of mobile nodes is already discovered and does not change when applying movement control. And, every node has the awareness of its own position and can get location information of its neighboring nodes.

4 Problems and Solutions

4.1 Mobility Control for Network with Single Flow

Label the network nodes as $0, 1, \ldots, n+1$, where nodes $1, \ldots, n$ are relay nodes, and node 0 and node $n + 1$ are source and sink node, respectively.

Optimization of Relay Configuration
First, we assume that the communication channels between any nodes are the same, i.e. $P_T(d)$ are the same for every nodes, then the optimal configuration problem can be formulated as

$$\min_{x_i : i=1,\ldots,n} \sum_{i=1}^{n+1} \|\mathbf{x}_i - \mathbf{x}_{i-1}\|_2^{\alpha}, \tag{3}$$

where $\|x_i - x_{i-1}\|_2$ are Euclidean norms, which are convex with respect to $\mathbf{x} = [x_1, \ldots, x_n]^T$, and $(d)^{\alpha}, (\alpha \geq 2)$ is convex for $d \geq 0$, so this is a convex problem. By first order condition, the optimal configuration is $\mathbf{X}^*$, such that

$$\frac{\partial f(\mathbf{X}^*)}{\partial \mathbf{x}_i^{(k)}} = \alpha(\mathbf{x}_i^{*(k)} - \mathbf{x}_{i-1}^{*(k)})\left\|\mathbf{x}_i^* - \mathbf{x}_{i-1}^*\right\|_2^{\alpha-2} + \alpha(\mathbf{x}_i^{*(k)} - \mathbf{x}_{i+1}^{*(k)})\left\|\mathbf{x}_i^* - \mathbf{x}_{i+1}^*\right\|_2^{\alpha-2}, \quad (4)$$

for $i = 0, \ldots, n; \quad k = 1, 2, 3$. $\mathbf{x}_i^{(k)}$ is the k-th dimension of the position vector $\mathbf{x}_i^{(k)}$. From these systems of equations, we have the solutions

$$\mathbf{x}_i^* = \frac{\mathbf{x}_{i+1}^* + \mathbf{x}_{i-1}^*}{2}, \quad i = 1, \ldots, n. \quad (5)$$

Localized Mobility Control to Reach Optimality
From Eq. (5), every node's optimal position can be directly derived,

$$\mathbf{x}_i^* = \mathbf{x}_0 + \frac{i}{n+1}(\mathbf{x}_{n+1} - \mathbf{x}_0), \quad i = 1, \ldots, n. \quad (6)$$

However, for every node to reach its optimal position, it needs information of source and sink nodes of the flow, which is often not its neighboring nodes. For simplicity and low overhead of the algorithm implemented in network environment, it is desirable to use localized algorithm which only requires information from one's neighbors.

$$\mathbf{x}_i = \frac{\mathbf{x}_{i+1} + \mathbf{x}_{i-1}}{2}, \quad i = 1, \ldots, n. \quad (7)$$

Goldenberg [5] proved that the localized algorithm Eq. (7) can be used to make nodes converge to optimal positions.

4.2 *Mobility Control for Network with Multiple Flows*

Previous section discussed the optimal positions for nodes in a single flow, however, in network a node, such as junction nodes (like node j in Fig. 2), may be included in multiple flows (Figs. 1 and 3).

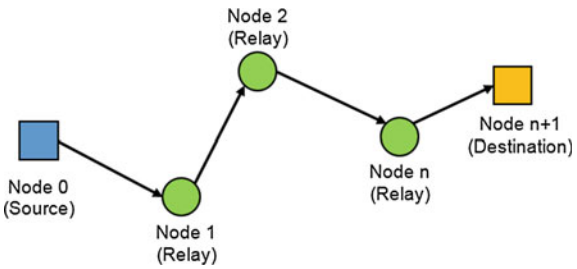

Fig. 1 Single-flow multi-hop relay link

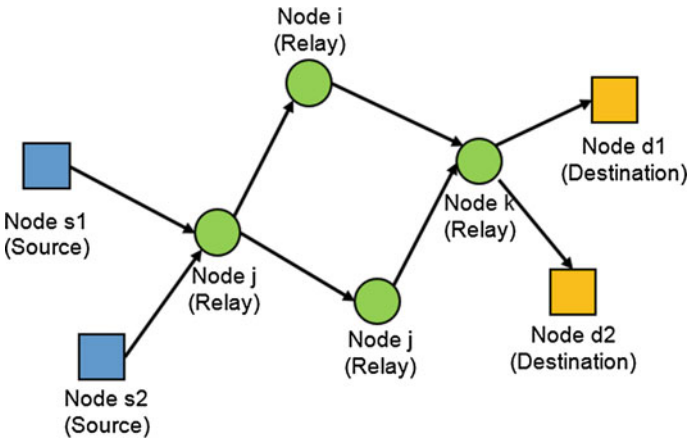

Fig. 2 Single-flow multi-hop relay link

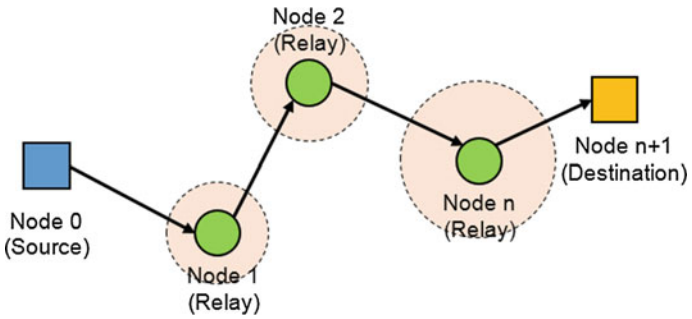

Fig. 3 Network with nodes moving inside coverage areas

Optimization of Relay Configuration

Let t_{ij} be the amount of traffic on link between nodes i and j, L be the set of all pairs of nodes that form a link in the network, $N(i)$ be the set of index of neighboring nodes of the i-th node. Then, the unconstrained optimal configuration problem with multiple flows becomes,

$$\min \sum_{(i,j)\in L} t_{ij} \|\mathbf{x}_i - \mathbf{x}_{i-1}\|_2^{\alpha}, \tag{8}$$

The gradient of the objective function is $\nabla f = \left[\ldots, \frac{\partial f}{\partial x_i^{(k)}}, \ldots\right]^T$, where

$$\frac{\partial f(\mathbf{X}^*)}{\partial x_i^{(k)}} = \alpha \sum_{j \in N(i)} t_{ij} \left\|\mathbf{x}_i - \mathbf{x}_j\right\|_2^{\alpha-2} (x_i^{(k)} - x_j^{(k)}).$$

So, we can derive that the optimal solutions satisfy,

$$\mathbf{x}_i^* = \frac{\sum\limits_{j \in N(i)} t_{ij} \left\|\mathbf{x}_i - \mathbf{x}_j\right\|_2^{\alpha-2} \mathbf{x}_j^*}{\sum\limits_{j \in N(i)} t_{ij} \left\|\mathbf{x}_i - \mathbf{x}_j\right\|_2^{\alpha-2}} \tag{9}$$

Iterative Algorithm

To get analytical solutions from above systems of equations is usually very difficult, but we can use iterative method to approach the optimum.

Algorithm 1 At each step, update the coordinates of the relay nodes using the formula: $\mathbf{x}_i := \mathbf{x}_i + \Delta\mathbf{x}_i$.

Theorem *With the update step*

$$\Delta\mathbf{x}_i = -\frac{1}{\alpha - 1}\mathbf{x}_i + \frac{1}{\alpha - 1} \cdot \frac{\sum\limits_{j \in N(i)} t_{ij} \left\|\mathbf{x}_i - \mathbf{x}_j\right\|_2^{\alpha-2} \mathbf{x}_j}{\sum\limits_{j \in N(i)} t_{ij} \left\|\mathbf{x}_i - \mathbf{x}_j\right\|_2^{\alpha-2}} \tag{10}$$

the Algorithm 1 will converge to the optimal configuration.

Proof First, assume all variables other than $x_i^{(k)}$ are fixed, check the update convergence of $x_i^{(k)}$.

$$\frac{\partial^2 f}{\partial x_i^{(k)2}} = \alpha \sum_{j \in N(i)} t_{ij} \left\|x_i - x_j\right\|_2^{\alpha-2} \left[\frac{\left|x_i^{(k)} - x_j^{(k)}\right|^2}{\left\|x_i - x_j\right\|_2^2}(\alpha - 2) + 1\right] \tag{11}$$

$$\leq \alpha(\alpha - 1) \sum_{j \in N(i)} t_{ij} \left\|x_i - x_j\right\|_2^2 \tag{12}$$

where the inequality comes from the fact that $\frac{\left|x_i^{(k)} - x_j^{(k)}\right|^2}{\left\|x_i - x_j\right\|_2^2} \leq 1$. Since $\frac{\partial^2 f}{\partial x_i^{(k)2}} \geq 0$, the Newtons method [7] works in this case, so it is also convergent for a step size

$\gamma = \left[\alpha(\alpha-1)\sum_{j\in N(i)} t_{ij}\left\|\mathbf{x}_i - \mathbf{x}_j\right\|_2^{\alpha-2}\right]^{-1}$. So, $\mathbf{x}_i$ converges with update step, $\Delta\mathbf{x}_i = -\gamma\frac{\partial f}{\partial \mathbf{x}_i}$, which leads to (10).

4.3 Mobility Control Considering Coverage

Above problems are formulated as unconstrained optimization, however, in many cases, there are some constraints to be included for nodes to make movement decision. One of the examples is the coverage-awareness scenario, which commonly happens in sensor networks. For a node in sensor network, it not only severs as a relay but also takes on surveillance duty to monitor phenomena in certain area. In such a case, when nodes move for communication improvement they are subject to be confined within the area that they are responsible for.

For simplicity, we go back to the single flow case and add coverage constraints, then the problem can be formulated as follows,

$$\min_{x_i: i=1,\ldots,n} \sum_{i=1}^{n+1} \|\mathbf{x}_i - \mathbf{x}_{i-1}\|_2^{\alpha}, \tag{13}$$

$$\text{subject to } \|\mathbf{x}_i - \mathbf{x}_{i0}\|_2^2 \le R_i^2, \quad i = 1,\ldots,n, \tag{14}$$

where x_{i0} is the center of the circle of the coverage area for i-th node, and R_i is its radius. Here, we assume the coverage areas are all circles.

Associate Lagrange multipliers $\boldsymbol{\lambda}$ with the constraints. The Lagrangian is

$$L(\mathbf{x},\boldsymbol{\lambda}) = \sum_{i=1}^{n+1}\|\mathbf{x}_i - \mathbf{x}_{i-1}\|_2^{\alpha} + \sum_{i=1}^{n+1}\lambda_i\left[\|\mathbf{x}_i - \mathbf{x}_{i-1}\|_2^{\alpha} - R_i^2\right]. \tag{15}$$

Since the Slater condition holds, there must exist Lagrange multipliers $\boldsymbol{\lambda}^*$ such that $\mathbf{X}^*$ minimmize $L(\mathbf{X}^*, \boldsymbol{\lambda}^*)$.

$$\frac{\partial f}{\partial \mathbf{x}_i} = \alpha\|\mathbf{x}_i - \mathbf{x}_{i-1}\|_2^{\alpha-2}(\mathbf{x}_i - \mathbf{x}_{i-1}) + \alpha\|\mathbf{x}_i - \mathbf{x}_{i+1}\|_2^{\alpha-2}(\mathbf{x}_i - \mathbf{x}_{i+1}) + 2\lambda_i(\mathbf{x}_i - \mathbf{x}_{i0}). \tag{16}$$

Study the case of $\alpha = 2$, then we have

$$\mathbf{x}_i^* = \frac{1}{\lambda_i + 2}(\mathbf{x}_{i-1}^*) + \frac{\lambda_i}{\lambda_i + 2}\mathbf{x}_{i0}, \quad i = 1,\ldots,n. \tag{17}$$

The update equation for $\boldsymbol{\lambda}$ is

$$\lambda_i^{(new)} = \left[\lambda_i^{(old)} + \gamma(\|\mathbf{x}_i - \mathbf{x}_{i0}\|_2^2 - R_i^2)\right]^+, \quad i = 1, \ldots, n, \tag{18}$$

where γ is the step size.

We can design movement policy as follows,

1. For fixed $\boldsymbol{\lambda}$, move nodes to optimal positions.
2. Update $\boldsymbol{\lambda}$ using Eq. (18), go back to step 1.

5 Simulation Results

In this section, we evaluate the performance of the mobility control algorithm by simulation. Algorithms for three of the above cases will be evaluated. Nodes are distributed in a 150×150 m area. Use the transmission power model $P_T(d) = a + bd^\alpha$, with parameters $a = 10^{-4}$ W/bit, $b = 10^{-7}$ Wm$^{-\alpha}$/bit, and $\alpha = 2$. We assume that the data rate is 1 kbps, hence, the energy consumption to transmit 1 bit is $E_T(d) = (a + bd^\alpha) \times 10^{-3}$ J. The total energy cost to send a bit is the sum of the energy consumption of all links in the path from source to destination.

5.1 Mobility Control for Network with Single Flow

For single flow case, we randomly put 8 relay nodes between a pare of fixed source and sink. Figure 4 shows that using the localized algorithm as Eq. (7), all the nodes converge to the optimal positions, after 269 iterations.

The original energy cost to send a bit is 2.41×10^{-6} J; after position configuration, it requires 1.05×10^{-6} J, which is 56 % of the original cost. After sufficient amount of data transmission, this energy saving will eventually cover the mobility cost and gain more benefit in the long run.

5.2 Mobility Control for Network with Multiple Flows

In this scenario, we consider a network consisting of five nodes, which are two fixed source nodes $S1$ and $S2$, two relay nodes, and two fixed sink nodes D_1 and D_2. In this network there are two flows of data, one is $S1 \rightarrow 1 \rightarrow 2 \rightarrow D1$ and the other is $S2 \rightarrow 1 \rightarrow 2 \rightarrow D2$ with flow rates are both set to 1 Kbps.

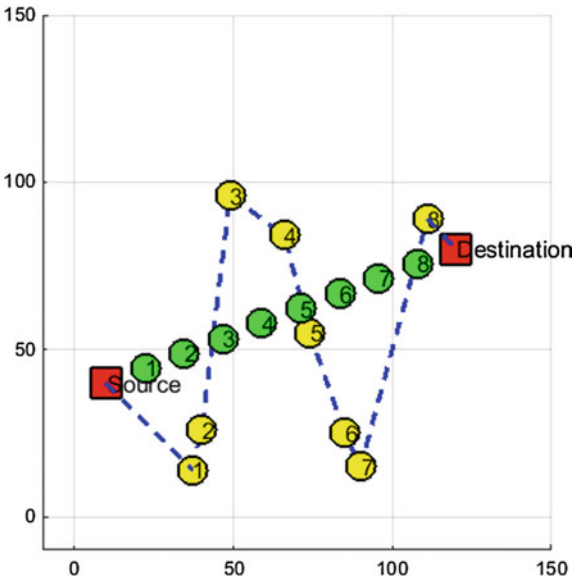

Fig. 4 Nodes before (*yellow*) and after (*green*) moving control

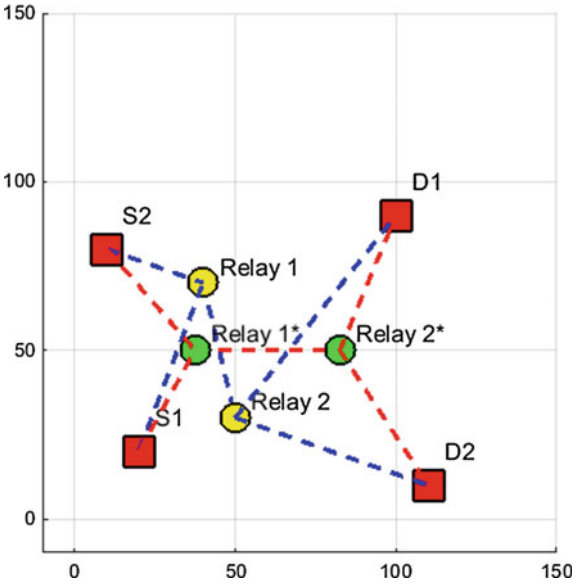

Fig. 5 Multiple-flow relay network before (*yellow*) and after (*green*) moving control

After 19 iterations of localized computation of Eq. (10), we got the results as shown in Fig. 5. This result reduces energy consumption from 2.34×10^{-6} J/bit to 1.72×10^{-6} J/bit, a 27 % saving.

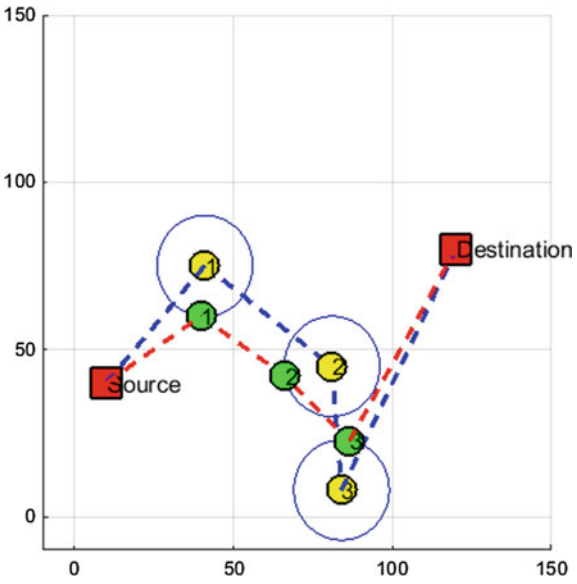

Fig. 6 Single-flow multi-hop relay network considering coverage before (*yellow*) and after (*green*) moving control

5.3 *Mobility Control Considering Coverage*

Single flow with three relay nodes is used for this example. Every node is positioned at the center of the coverage area with radium $R_i = 10$ m. The step size γ is chosen to be 0.01.

After 17 movement iterations, nodes reach their optimum within coverage areas as Fig. 6 illustrates. We can see that nodes 1, 2, and 3 are at edges of the area. Check the final value of $\boldsymbol{\lambda}$, we have $\lambda_{1,2,3} > 0$, which is consistent with the *complementary condition*. Power consumption rate is reduced from 1.65×10^{-6} J/bit to 1.15×10^{-6} J/bit, a 26 % saving.

6 Conclusion and Future Work

This work studies mobility strategies to control positions of relay nodes to minimize energy consumption of transmission from fixed sources to sinks in network. Three different cases were investigated, namely, (1) single flow, (2) multiple flows, and (3) with coverage constraints. The novelty of this work is in formulating problems into optimization whereby simple localized algorithms can be obtained.

In this paper, energy consumption by movement of delay nodes was not considered. This can be justified by the fact that this cost will eventually be paid off by the saving in communication, after sufficient amount of data is transmitted. However, if only limited amount of data is to be sent, then there exists a trade-off

between how much movement to make and how much communication channel to improve, in order to achieve overall energy cost minimization. This opens the door for another optimization study.

References

1. Zeiger F, Kraemer N, Schilling K (2008) Commanding mobile robots via wireless ad-hoc networks—a comparison of four ad-hoc routing protocol implementations. In: IEEE international conference on robotics and automation (ICRA 2008), pp 590–595 (May 2008)
2. Boyd S, Vandenberghe L (2004) Convex optimization, Cambridge University Press
3. Wang W, Srinivasan V, Chua KC (2005) Using mobile relays to prolong the lifetime of wireless sensor networks. In: Proceedings of the 11th annual international conference on mobile computing and networking, MobiCom '05, ACM, New York, NY, USA, pp 270–283. http://doi.acm.org/10.1145/1080829.1080858
4. Dixon C, Frew EW (2007) Maintaining optimal communication chains in robotic sensor networks using mobility control. In: Proceedings of the 1st international conference on robot communication and coordination, RoboComm '07. IEEE Press, Piscataway, NJ, USA, pp 1:1–1:8. http://dl.acm.org/citation.cfm?id=1377868.1377870
5. Goldenberg DK, Lin J, Morse AS, Rosen BE, Yang YR (2004) Towards mobility as a network control primitive. In: Proceedings of the 5th ACM international symposium on mobile Ad Hoc networking and computing, MobiHoc '04, ACM, New York, NY, USA, pp 163–174. http://doi.acm.org/10.1145/989459.989481
6. Chen X, Jiang Z, Wu J (2008) Mobility control schemes with quick convergence in wireless sensor networks. In: IEEE international symposium on parallel and distributed processing, IPDPS 2008, pp 1–7 (April 2008)
7. Chong EK, Zak SH (2011) An introduction to optimization, 3rd edition. Wiley-Interscience (Jul 2011)

Utilizing the Neural Networks for Speech Quality Estimation Based on the Network Characteristics

Jan Rozhon, Miroslav Voznak, Filip Rezac and Jiri Slachta

Abstract The paper deals with an issue of the speech quality estimation in Voice over IP technology under packet loss. Packet loss is a major problem for real-time Internet applications, we applied four-state Markov model for modeling the impact of network impairments on speech quality, afterwards, the resilient back propagation (Rprop) algorithm was used to train a neural network. The general and RFC3611-compliant solution, which allows for quick and precise speech quality estimation without the need to analyze or model the voice signal carried by the RTP (Real-time Transport Protocol) packets, is the contribution of this paper. The proposed solution is tested on G.711 A-law and further generalizes the already presented concepts of the speech quality estimation in the IP environment. The proposed approach of speech quality assessment belongs to non-intrusive methods and is based on the back-propagation neural networks.

Keywords Markov models · Mean opinion score · Neural networks · Speech quality estimation

1 Introduction

For many years the field of VoIP has increased in size and importance paving the way for maintenance and administration costs reduction as well as the increase in the offered services. Together with this trend, the increasing role of service quality

J. Rozhon · M. Voznak (✉) · F. Rezac · J. Slachta
VSB-TU Ostrava 17, Listopadu 15, 70833 Ostrava, Czech Republic
e-mail: miroslav.voznak@vsb.cz

J. Rozhon
e-mail: jan.rozhon@vsb.cz

F. Rezac
e-mail: filip.rezac@vsb.cz

J. Slachta
e-mail: jiri.slachta@vsb.cz

V.H. Duy et al. (eds.), *AETA 2015: Recent Advances in Electrical Engineering and Related Sciences*, Lecture Notes in Electrical Engineering 371,
DOI 10.1007/978-3-319-27247-4_9

monitoring has started to be the topic of high concern for all service providers. To ensure stable and sufficient service quality the service providers employ various network tools meant to measure the quality of speech (or video) in the monitored networks. This creates the high demand for computer power and measuring time and is, therefore, responsible for increasing the overall expenditures related especially to the wireless communication system [1–3]. To counter these excessive expenses, various systems capable of estimating the quality of speech have been developed.

In this paper, the system for estimating the speech quality in VoIP networks is to be presented. This system is built upon the neural networks and takes the generally accessible network parameters as its inputs. The output of the system is the MOS estimation, which is then compared to the output of the ITU-T P.862 PESQ (Perceptual Evaluation of the Speech Quality), which serves as the reference value [4]. The aim of this paper is to present the generally usable system that would allow the user to estimate the speech quality regardless of the signal being carried inside the RTP packets themselves. This system effectively estimates the impact of the packet loss on the speech quality and it can be integrated to any existing environment because it uses general network statistics and the information from the RTP headers. On top of that, the system can further be augmented to employ the playout buffer model and delay model utilizing the information obtained from the external source [5–7]. For the sake of this paper, only the G.711 A-law codec is used to measure the influence of the individual network features and precision of the estimate, but the same system has also been used in conjunction with the SPEEX codec with similar results and accuracies.

2 State of the Art

The survey provided in [8] showed that the PESQ algorithm accommodates the effects of packet loss on speech quality better than the E-model, and is, therefore, better suited for the task making its estimation a sensible way for improving the precision of the estimation. The speech quality estimation system proposed in this paper is an enhancement and generalization of the system proposed in [9]. The author in this paper uses 2-state Gilbert Model to generate the losses and tries to fit the observed packet sequence into the model. This, however, proves problematic for the networks with different packet loss distributions. This gap, as well as the fact that newer version of E-model, PESQ and training algorithms for the neural networks have been devised since the publication of this work are the main motivation for this paper. In [10], the authors use the neural networks to map the cepstrum distance for the frame. This approach leads to a similar error rate as described here and involves the signal analysis of the speech sample, which makes the system much more complex. For this reason, the work has not been used as a basis for this paper. For the synthesized speech the recent research [11] has been performed. The authors use neural networks and genetic algorithms to estimate the quality of speech, but again the model-specific approach for the packet loss determination is used.

3 System Architecture

The speech quality estimation is meant to be used with the basic characteristics of the IP networks—the packet loss, the one-way delay and jitter. Each characteristic impacts the speech quality differently. Moreover, only the packet loss can be acquired by simple packet observation [7]. For jitter effect to be measured, the playout buffer needs to be employed. For the delay measurements the external source, such as RTCP, needs to be harnessed. The entire estimation system is divided into several modules based on the functionality each part implements. These parts are designed to simulate the effect of the above mentioned characteristics and to perform the necessary calculations for the system to work. The complete architecture with closely discussed modules highlighted is depicted in Fig. 1. These modules are:

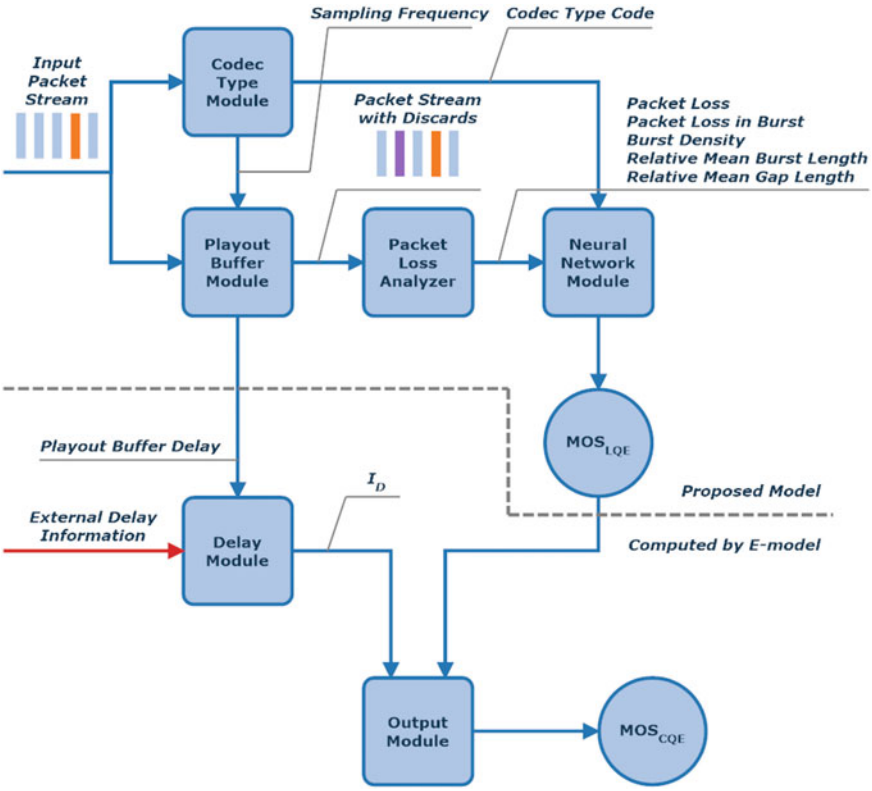

Fig. 1 The architecture of the speech quality estimation system

- Playout Buffer Module simulates the effect of the playout buffer on the receiving side.
- Packet Loss Analyzer takes the output of the playout buffer and searches for the lost and discarded packets using the RTP sequence numbers.
- Codec Type Module detects the codec used (codec type and packetization) and forwards the information in a binary encoded form to the neural network.
- Neural Network Module takes the loss characteristics and codec type and estimates the MOS_{LQO} and R-factor respectively. This module uses the Back-Propagation Algorithm (Rprop) [12] to train the network with the topology of 5–3–1 neurons (plus one bias neuron for each layer) and Elliot activation function [13].

  The architecture of the estimation system is depicted in the Fig. 1.

3.1 Playout Buffer Module

There is a simplistic implementation of the playout (or de-jitter) buffer functionalities in this module. The main purpose of this module is to prove the viability and the accuracy of the original assumption that the delay variations add to both the network loss and network delay impairments. The playout buffer implemented for the testing and measuring purposes is the fixed-length one with an unlimited data space (no early-arriving packets are discarded). It initializes the with the first arriving packet and resynchronizes the time scale after the sequence of five consecutive discards. Let T_0 and T_i be the actual arrival times of first first and *i*th arriving packet (in seconds from unix epoch) and t_0 and t_i be a timestamp in the RTP header of the respective packet (in milliseconds after recalculation using codec sampling frequency), then the ideal packet arrival timetime T'_i can be calculated:

$$T'_i = T_0 + t_i - t_0 \tag{1}$$

By using this ideal arrival time, the packet discard happens under this condition:

$$T_i - T'_i > S \tag{2}$$

where S is the playout buffer size in milliseconds.

By discarding late on arrival packets the playout buffer increases the overall statistics of the network packet loss and their characteristics causing increase in speech quality deterioration [14]. Moreover, the fixed length of the buffer adds to the overall packet delay, which is also used to calculate the effect of the delay.

3.2 Packet Loss Analyzer

The Packet Loss Analyzer converts the information about the network losses and playout buffer discards into 5 RFC 3611 compliant statistics, which are described as follows.

Packet Loss Probability Denoted as P_{PL}, the Packet Loss Probability is the overall percentage of the lost packets in relation to the total number of the packets sent (see Eq. 3).

$$P_{PL} = \frac{N_{LOST}}{N_{SENT}} \; [-] \tag{3}$$

where N_{LOST} is the number of lost packets and N_{SENT} the total number of RTP packets sent.

Packet Loss Probability in Burst Denoted as P_{BPL}, the Packet Loss Probability in Burst is the overall percentage of packets lost in a burst (according the burst definition in RFC 3611) defined as stated in Eq. 4.

$$P_{BPL} = \frac{N_{LOST\_IN\_BURST}}{N_{SENT}} \; [-] \tag{4}$$

where $N_{LOST\_IN\_BURST}$ is the number of packets lost in all bursts in a packet sequence.

Burst Density Denoted as ρ, the Burst Density is the ratio of the number of lost packets in all burst periods and the total length of all bursts in a packet sequence (see Eq. 5).

$$\rho = \frac{N_{LOST\_IN\_BURST}}{N_{BURST}} \; [-] \tag{5}$$

where N_{BURST} is the number of all packets lost in all bursts in a packet sequence.

Relative Mean Burst Length Denoted as E'(B), the Relative Mean Burst Length is derived from the characteristic defined in RFC 3611, but is related to the total length of the captured packet stream (see Eq. 6). This "relativisation" is done for the neural network to be able to categorize similar characteristics of the different-length packet sequences.

$$E'(B) = \frac{N_{BURST}}{N_{SENT} \cdot K_{BURST}} \; [-] \tag{6}$$

where K_{BURST} is the number of bursts in a packet sequence.

Relative Mean Gap Length Denoted as E′(G), the Relative Mean Gap Length is the complement of the E′(B) and is defined in Eq. 7.

$$E'(G) = \frac{N_{GAP}}{N_{SENT} \cdot K_{GAP}} \; [-] \tag{7}$$

where N_{GAP} is the number of packets in all gaps and K_{GAP} is the number of gaps in a packet sequence.

The definition of the burst relies on the G_{min} parameter (RFC 3611), which in this case was set to default of 16 packets as it is recommended in the mentioned RFC.

4 Modeling the Network Characteristics

The network characteristics were, for the purposes of this paper, generated using two models. The first one is the 4-state Markov Model [15, 16] generating the network losses. For this model, the transition probabilities were set to cover the whole range of the MOS_{LQO} scale. The second model is the model simulating the jitter effect. For this purpose, the simple Normal Distribution model has been used. The model was implemented with just one parameter—the jitter threshold, which is the value equal to 2.575 σ of the model. This setting results in 99 % of the observations falling into the interval (–threshold, threshold).

5 Estimating the Effect of Network Impairments on the Speech Quality

There were 10 sound samples encoded in mono-channel linear 16-bit PCM as the simulation inputs, which were taken from the P.862 recommendation. These sound files were transformed into G.711 A-law encoded RTP packets, which were idealized in time (exact 20 ms long packet spacing) and then stored in a PCAP file. These files were then manipulated using the models mentioned above and reconstructed to form the input for the PESQ algorithm.

5.1 Network Losses

First of all, the simulation consisting in pure packet loss manipulations was performed. The 4-state loss model was set with the combinations of transition probabilities stated in Table 1. All unique combinations were used 4 times to smoothen the effect of possible outliers, which resulted in 12,200 observations for training and validation and 3840 observations for testing of neural network.

Table 1 Settings of individual probabilities in a 4-state loss model

Probability	Training values (%)	Testing values (%)
p_{13}	0, 1, 3, 5, 10	1, 3, 7, 15
p_{14}	0, 1, 3, 5, 10	1, 3, 7, 15
p_{32}	0, 1, 3, 5, 10	1, 3, 7, 15
p_{31}	60, 75, 90	50, 80
p_{23}	100	100
p_{41}	100	100

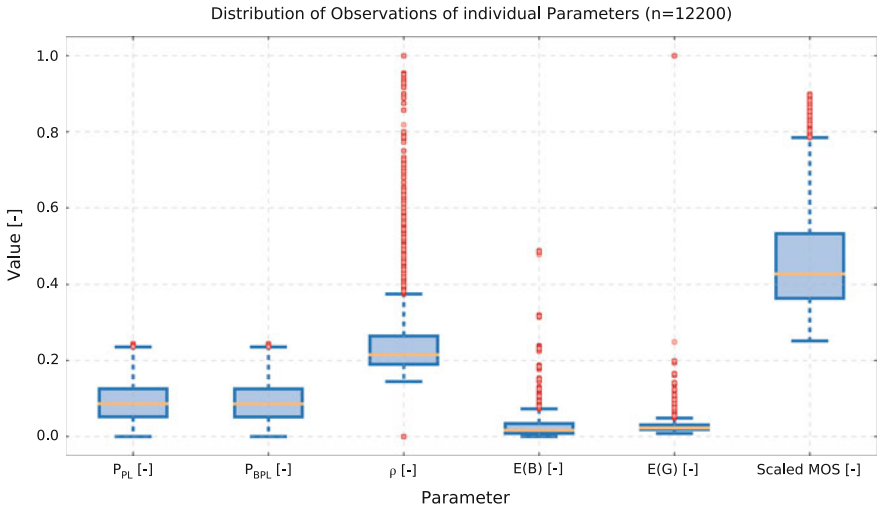

Fig. 2 The statistical features of the observed training set

The given settings produced the network statistics with statistical features of the training set as they are depicted in Fig. 2. For the purposes of readability the MOS is scaled to fit in the range from 0.2 (equals to 1) to 1 (equals to 5).

20 % of randomly chosen observations from the training set then formed a validation set, which was then used to confirm the ability of the neural network to estimate the speech quality of the samples, the features of which resemble those of the training samples. The remaining training set was then preprocessed in a way, so that the groups of same input vectors had the same output. This step is necessary because the neural network is not capable of learning multitude of outputs for the single input. The training and testing was repeated 10 times.

As it is obvious from the Fig. 3 the proposed system achieves high correlation with Pearson's Correlation Coefficient around the 0.95 and RMSE of 0.2 (MOS), which corresponds to an error of approximately 7 % (related to the middle of the MOS Scale). Due to the fact that packet loss has a great impact on speech quality, the most of the observations in all sets are below tolerable value of MOS and can be discarded as unusable. For the threshold of 2.5 (MOS; all observations below this are discarded), the 3819 observations in training set fit this condition and resulting

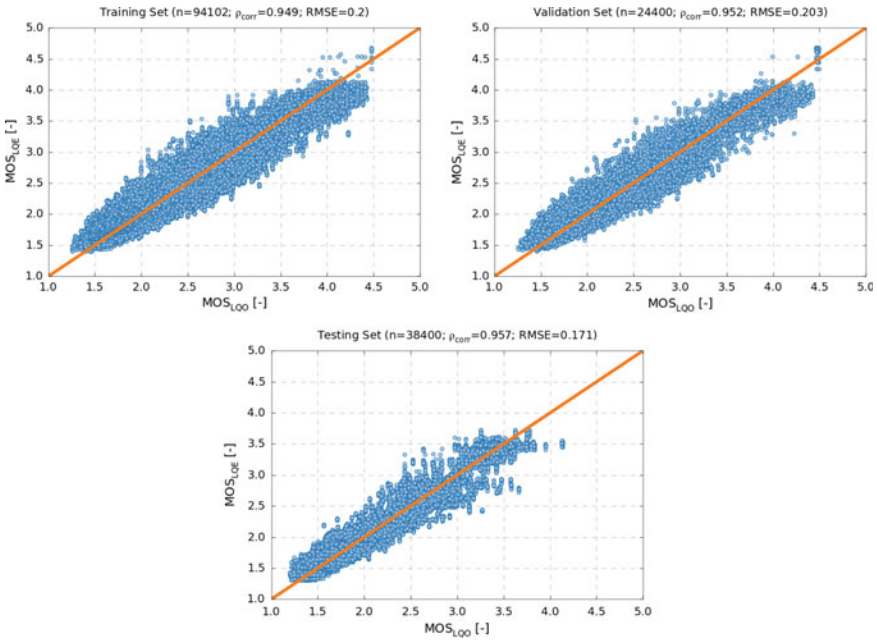

Fig. 3 The correlation diagrams for the estimations training, validation and testing sets. MOS_{LQO} is the reference from PESQ and MOS_{LQE} is the estimation

RMSE gets higher to approximately 0.25. This estimation error is the same as presented in [9], but with the system being able to work with any possible loss model (not just the Gilbert Model). The cumulative distribution function of an error is then depicted in Fig. 4 and shows almost ideal features of the Normal Distribution, which is the desired behavior. In absolute value, around 75 % of the observations lie under 10 % error.

5.2 Jitter

As it was stated in the previous sections, the effect of jitter can be split into the packet loss part and the delay part. Since the delay impact can be calculated using E-model, only the packet loss effect is to be studied. For this purpose the jitter threshold (as it is described above) was set from 0 to 100 ms. The jitter buffer size was set to 30 ms. And each simulation was performed again on 10 unique sound samples and repeated 10 times. This way 10,000 observations were made. For the purposes of estimation, the best performing (in terms of RMSE) neural network from the previous subsection was used to confirm the validity for entirely different loss model. The Fig. 5 shows the appropriate correlation diagram.

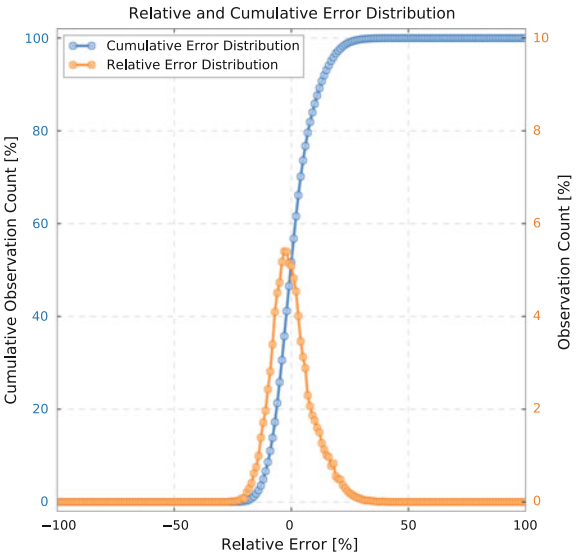

Fig. 4 The relative error distribution and the cumulative error distribution

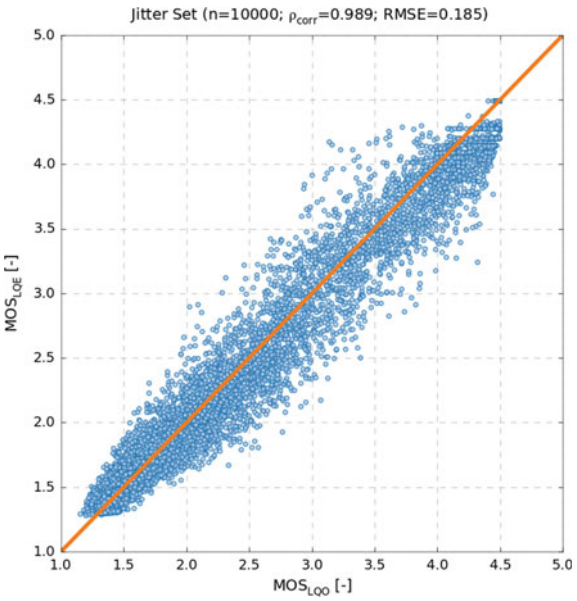

Fig. 5 The correlation diagram for the jitter observations

The performance in this case is 0.989 for Pearson's correlation coefficient and 0.185 for RMSE, which proves the model network is trained well. The error distribution is again very similar to the Normal Distribution.

6 Conclusion

In this paper the speech quality estimation system has been presented. This system takes the observed network loss statistics compliant to those defined in RFC 3611 and perform the MOS_{LQE} estimation using the neural network model. The system has been successfully tested with two codecs—G.711 A-law (no internal PLC) and SPEEX (internal PLC).

The speech quality estimation can be done with RMSE around the 0.25 MOS, which equals to approximately 8 % error, which is the level achieved in similar solutions. The training time for the network has always been below 30 s. Moreower, with more intense data preprocessing the training time can be decreased to approximately 3 s. On the other hand, however, no statistically significant improvement in speech quality estimation has been achieved with any kind of data preprocessing. Due to the general nature of the system, it can be deployed in any existing environment. If there is a need to incorporate the delay effect as well, the E-model calculation can be added to the system seamlessly. This approach, however, requires an external source of the measured one-way delay.

References

1. Pocta P, Kortis P, Vaculik M (2007) Impact of background traffic on speech quality in VoWLAN. In: Advances in multimedia, vol 2007, art no 57423
2. De Rango F, Fazio P, Scarcello F, Conte F (2014) A new distributed application and network layer protocol for voip in mobile ad hoc networks. IEEE Trans Mob Comput 13(10): 2185–2198
3. Chlumsky P, Kocur Z, Vodrazka J (2012) Comparison of different scenarios for path diversity packet wireless networks. Adv Electr Electron Eng 10(4):199–203
4. Partila P, Kohut M, Voznak M, Mikulec M, Safarik J, Tomala K (2013) A methodology for measuring voice quality using PESQ and interactive voice response in the GSM channel designed by openBTS. Adv Electr Electron Eng 11(5):380–386
5. Matousek P, Kmet M, Basel M (2014) On-line monitoring of VoIP quality using IPFIX. Adv Electr Electron Eng 12(4):325–333
6. Kocur Z, Macejko P, Chlumsky P, Vodrazka J, Vondrous O (2014) Adaptable system increasing the transmission speed and reliability in packet network by optimizing delay. Adv Electr Electron Eng 12(1):13–19
7. Kovac A, Halas M, Orgon M, Voznak M (2011) E-model Mos estimate improvement through jitter buffer packet loss modelling. Adv Electr Electron Eng 9(5):233–242
8. Khan HA, Sun L (2008) Assessment of speech quality for VoIP applications using PESQ and E-Model. In: Advances in communications, computing, networks and security, vol 7. University of Plymouth, Plymouth, pp 263–273
9. Sun L, Ifeachor EC (2006) Voice quality prediction models and their application in VoIP networks. IEEE Trans Multimedia 8(4):809–820
10. Meky M, Saadawi T (1997) Prediction of speech quality using radial basis functions neural networks. In: Proceedings of second IEEE symposium on computers and communications. Alexandria, pp 174–178

11. Mrvova M, Pocta P (2013) Quality estimation of synthesized speech transmitted over IP channel using genetic programming approach. In: International conference on digital technologies (DT). Zilina, pp 39–43
12. Igel C, Husken M (2000) Improving the Rprop learning algorithm. In: Proceedings of the second international symposium on neural computation, NC 2000. ICSC Academic Press, pp 115–121
13. Elliot D (1993) A better activation function for artificial neural networks. In: ISR technical report TR 93–8, University of Maryland
14. Burget R, Komosny D, Ganeshan K (2012) Topology aware feedback transmission for real-time control protocol. J Netw Comput Appl 35(2):723–730
15. Clark A (2001) Modeling the effects of burst packet loss and recency on subjective voice quality. IPtel Workshop
16. Raake A (2007) Speech quality of VoIP: assessment and prediction. Wiley, Chichester

Bit Error Rate Performance of Clipped OFDM Signals Over Fading Channel

Dang Le Khoa, Huynh Quoc Anh, Nguyen Huu Phuong and Hiroshi Ochi

Abstract In OFDM systems, the same phase subcarriers add together and create signal peaks. These peaks create nonlinear distortion in the ADC and the amplifier. Clipping method can be used to remove the peaks before putting the OFDM signal into the ADC and the amplifier but the clipping also creates nonlinear noise that degrades the performance of OFDM system. In this paper, we propose a method for determining the bit error rate of clipped OFDM signal over Rayleigh and Rician fading channel. The BER equation is analyzed based on power spectral density function. We build equations and evaluate the analyzed results by simulation. The simulation results fit perfectly with BER equations at any different clipping ratio.

Keywords OFDM · Clipped signal · Bit error rate · Fading

1 Introduction

OFDM technique is more popular because of the spectrum utilization efficiency and simple implementation. The idea of OFDM is the transmission of multiple subcarriers consisting of narrowband orthogonal frequencies overlapping on one another in a wideband. A high speed data stream is split into multiple low speed data streams. Therefore, the OFDM can reduce the influence of multi-path delay and convert the frequency selective fading into flat fading.

D. Le Khoa (✉) · H.Q. Anh · N.H. Phuong
Faculty of Electronics and Telecommunications, HCM City University of Science, HCM City, Vietnam

H. Ochi
Department of Computer Science and Engineering, Kyushu Institute of Technology, Iizuka City, Japan

V.H. Duy et al. (eds.), *AETA 2015: Recent Advances in Electrical Engineering and Related Sciences*, Lecture Notes in Electrical Engineering 371,
DOI 10.1007/978-3-319-27247-4_10

However, a major drawback of OFDM is the high peak-to-average power ratio (PAPR) [1]. OFDM signal is the sum of subcarriers, therefore in some cases, the same phase subcarriers will add together creating signal peaks that decrease the SQNR (Signal to -Quantization Noise Ratio) of the ADC and the efficiency of the power amplifier. Thus we need to reduce the peaks. Several algorithms have been proposed for PAPR reduction such as clipping, PTS, SLM [2, 3]. The clipping is the simplest PAPR reduction and of high commercial value [4]. The method is done by setting a fixed threshold. When the OFDM signal amplitude is higher than the threshold, it will be clipped to the threshold, but this creates nonlinear noise that degrades the BER performance of OFDM system.

The paper [4, 5] have investigated the BER of the clipped OFDM signal over AWGN channels, the paper [6] has investigated the BER of the clipped OFDM signal over the Rayleigh channel but the analyses were weakly fitted with the simulations. The paper [7] has analyzed the bit error ratio of clipped OFDM over Rayleigh but assuming the clipping distortion is much higher than the AWGN. In this paper, we build the BER equation for determining the bit error rate of clipped OFDM signal over Rayleigh and Rician fading. The BER equations were tested by simulation. The rest of this paper is organized as following. Section 2 presents the PAPR problem and clipping methods, Sect. 3 derives the BER equations of the clipped OFDM over Rayleigh and Rician fading, Sect. 4 presents the simulation results, and the last part is the conclusion.

2 Background

2.1 The PAPR Problem

Let d be the input data stream, which is splitted to N parallel lower speed data streams a_k, where k is subcarrier index, and then modulated by a subcarriers $\phi_k(t)$. The subcarriers $\phi_k(t)$ are orthogonal to one another. The baseband OFDM signal with N subcarriers is given by:

$$s(t) = \frac{1}{\sqrt{N}} \sum_{k=0}^{N-1} a_k \phi_k(t) = \frac{1}{\sqrt{N}} \sum_{k=0}^{N-1} a_k e^{j2\pi k \Delta f t}, \quad 0 \le t < T \tag{1}$$

where $k\Delta f$ corresponds to each k th subcarrier at baseband, T is the duration of an OFDM symbol.

From Eq. (1) we see that the OFDM signal comprises many subcarriers. In some situations, the same phase subcarriers will add together and create peaks as Fig. 1. One of the most popular method to limit the peaks is by clipping.

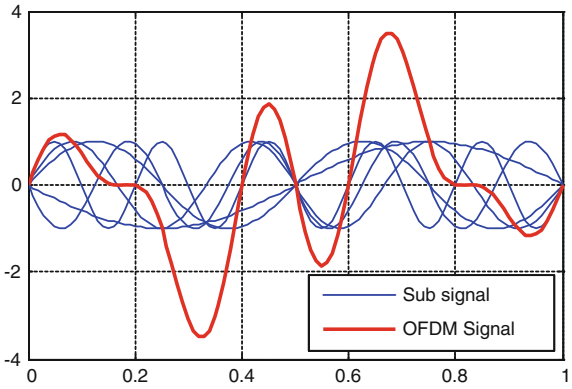

Fig. 1 OFDM signal with high peak value

2.2 *Clipping for PAPR Reduction*

The clipping is done by setting a threshold. When the OFDM signal amplitude is higher than the threshold, it will be clip to the threshold. Let x(n) be the OFDM signal in the time domain, and N is the subcarrier. After clipping, the signal becomes:

$$y(n) = x(n) + c(n) \tag{2}$$

where c(n) is clipped signal.

Based on Bussgang theoretical [8], we can write y(n) as:

$$y(n) = \alpha x(n) + d(n) \tag{3}$$

where $\alpha = \frac{\mathcal{R}_{yx}(0)}{\mathcal{R}_{xx}(0)}$, $\mathcal{R}_{yx}(0)$ is the cross correlation of x(n) and y(n), d(n) and $\mathcal{R}_{xx}(0)$ is the autocorrelation of x(n) at zero time shift.

When N is large, the envelope of OFDM signal is Rayleigh, and the value α becomes:

$$\alpha = 1 - e^{-\frac{A^2}{\mathcal{P}_x}} + \frac{A}{\mathcal{P}_x}\int_A^\infty e^{\frac{-r^2}{\mathcal{P}_x}} dr \tag{4}$$

where A is the clipping threshold, and $\mathcal{P}_x$ the signal power before clipping.

$$\alpha = 1 - e^{-\gamma^2} + \frac{\gamma\sqrt{\pi}}{2} erfc(\gamma) \tag{5}$$

where $\gamma = A/\sqrt{\mathcal{P}_x}$ is the clip factor, and $erfc(.)$ the complementary error function.

$$erfc(x) = \frac{2}{\sqrt{\pi}} \int_{x}^{\infty} e^{-t^2} dt \tag{6}$$

Input Back-Off (IBO) is:

$$IBO = 10 \log\left(\frac{A^2}{\mathcal{P}_x}\right) \tag{7}$$

Signal power after clipping is:

$$\mathcal{P}_y = \left[1 - e^{-\gamma^2}\right] \mathcal{P}_x \tag{8}$$

The nonlinear distortion adds to the clipped signal and $\mathcal{P}_y$ is the total noise and distortion power of the signal with the distortion power D, the power relation is given by:

$$\mathcal{P}_y = \alpha^2 \mathcal{P}_x + D \tag{9}$$

Therefore:

$$D = \mathcal{P}_y - \alpha^2 \mathcal{P}_x = (1 - e^{-\gamma^2} - \alpha^2)\mathcal{P}_x = G\mathcal{P}_x \tag{10}$$

where $G = 1 - e^{-\gamma^2} - \alpha^2$.

3 Clipping Performance Over Fading Channels

3.1 BER Over the Rayleigh Fading Channel

The probability density function of Rayleigh fading is given by [9]:

$$f_p(p) = \frac{1}{P_r} e^{-\frac{p}{P_r}} \tag{11}$$

where P_r is the average fading power, and p is the instant power.

Let s be the simultaneous signal to noise and distortion ratio (SNDR) after transmitting on the fading channel, then s can be written as:

$$s = \frac{\alpha^2 \mathcal{P}_x p}{p\mathcal{D} + \mathcal{N}} = \frac{\alpha^2 p}{p\frac{\mathcal{D}}{\mathcal{P}_x} + \frac{\mathcal{N}}{\mathcal{P}_x}} = h(p) \tag{12}$$

where $\mathcal{N}$ is the noise power of AWGN channel. Also

$$\frac{\mathcal{P}_x}{\mathcal{N}} = \frac{E_s}{N_0} = \log_2(M)\frac{E_b}{N_0} \tag{13}$$

where M is M-level modulation format, E_b/N_0 is the energy per bit (, E_b) to the spectral noise power density before clipping.

Therefore:

$$s = \frac{\alpha^2 p}{pG + \frac{N_0}{E_s}} \tag{14}$$

$$p = \frac{s}{\frac{E_s}{N_0}(\alpha^2 - Gs)} = g(s) \tag{15}$$

where p is the instant power, and $p > 0$. The condition for s is:

$$\frac{s}{\frac{E_s}{N_0}(\alpha^2 - \mathrm{G}s)} > 0 = \ > 0 \le s \le \frac{\alpha^2}{\mathrm{G}} \tag{16}$$

The probability density function of s is given by [9]:

$$f_s(s) = f_p[g(s)]\left[\frac{dg(s)}{ds}\right], \ \ 0 \le s \le \frac{\alpha^2}{\mathrm{G}} \tag{17}$$

Probability density function of s over Rayleigh channel by [11]:

$$f_s(s) = \begin{cases} \frac{\alpha^2}{P_r\frac{E_s}{N_0}(\alpha^2 - Gs)^2} e^{-\frac{s}{P_r\frac{E_s}{N_0}(\alpha^2 - Gs)}}, & 0 \le s \le \frac{\alpha^2}{G} \\ 0, & Otherwise \end{cases} \tag{18}$$

BER over Rayleigh channel can be calculated by [12]:

$$BER = \int_0^{\frac{\alpha^2}{G}} BER_{AWGN}(s) f_s(s) ds \tag{19}$$

In case of QPSK (M = 4), we have:

$$\frac{E_s}{N_0} = \frac{2 \cdot E_b}{N_0} \tag{20}$$

$$BER_{AWGN-QPSK}(s) = \frac{1}{2} erfc\left(\sqrt{s}\sin\left(\frac{\pi}{4}\right)\right) \tag{21}$$

$$BER = \int_0^{\frac{\alpha^2}{G}} \int_{\sqrt{\frac{s}{2}}}^{\infty} \frac{1}{\sqrt{\pi}} \frac{\alpha^2}{P_r \frac{2E_b}{N_0} (\alpha^2 - Gs)^2} e^{-t^2 - \frac{s}{P_r \frac{2E_b}{N_0}(\alpha^2 - Gs)}} dtds \tag{22}$$

3.2 BER Over the Rician Fading Channel

The probability density function of Rician fading is given by [10]:

$$f_p(p) = \frac{(K+1)}{P_r} e^{-\left[\frac{(K+1)p}{P_r} + K\right]} I_0\left(2\sqrt{p}\sqrt{\frac{K(K+1)}{P_r}}\right) \tag{23}$$

where K-factor is the power ratio of LOS and NLOS components. I_0 is the th-zero order Bessel function of first kind. Probability density function of s over Rayleigh channel:

$$f_s(s) = \begin{cases} \left\{ \frac{\alpha^2(K+1)}{P_r \frac{E_S}{N_0}(\alpha^2 - Gs)^2} e^{-\left[\frac{(K+1)s}{P_r \frac{E_S}{N_0}(\alpha^2 - Gs)} + K\right]} \times I_0\left(2\sqrt{\frac{sK(K+1)}{P_r \frac{E_S}{N_0}(\alpha^2 - Gs)}}\right) \right\}, & 0 \le s \le \frac{\alpha^2}{G} \\ 0 & Otherwise \end{cases} \tag{24}$$

BER over Rician channel can be calculated as [12]:

$$BER = \int_0^{\frac{\alpha^2}{G}} BER_{AWGN}(s) f_s(s) ds \tag{25}$$

In case of QPSK ($M = 4$), we have:

$$BER = \int_0^{\frac{\alpha^2}{G}} \frac{1}{2} erfc\left(\sqrt{\frac{s}{2}}\right) \frac{\alpha^2(K+1)}{P_r \frac{2E_b}{N_0}(\alpha^2 - Gs)^2} e^{-\left[\frac{(K+1)s}{P_r \frac{2E_b}{N_0}(\alpha^2 - Gs)} + K\right]} \times I_0\left(2\sqrt{\frac{sK(K+1)}{P_r \frac{2E_b}{N_0}(\alpha^2 - Gs)}}\right) ds \tag{26}$$

To determine BER by using software, we substitute the modified Bessel function [13] into above equation to obtain:

$$BER = \int_0^{\frac{\alpha^2}{G}} \int_{-\pi}^{\pi} \int_{\sqrt{\frac{s}{2}}}^{\infty} \frac{1}{2\pi\sqrt{\pi}} \frac{\alpha^2(K+1)}{P_r \frac{2E_b}{N_0}(\alpha^2 - Gs)^2} \times e^{-\left[t^2 + \frac{(K+1)s}{P_r \frac{2E_b}{N_0}(\alpha^2 - Gs)} + K\right] + 2\sqrt{\frac{sK(K+1)}{P_r \frac{2E_b}{N_0}(\alpha^2 - Gs)}} cosu} dtduds \tag{27}$$

4 Simulation Results

To verify the above equation, we simulated the OFDM system using QPSK with the number of subcarrier of 64, and cyclic prefix of ¼. We assumed that the system was perfectly synchronized, single tap channel, and perfect channel information. The simulation was carried out using data of 10^8 bit. BER equation over Rician channel needs triple integrals, and we use software to numerically calculate those equations [14].

Figure 2 compares the theory with the simulation over Rayleigh channel. The simulation results fit perfectly with BER equations. When the clipping factor is large, the BER approaches the idea case. Figures 3 and 4 present the simulation for K factor of 1 and 10, respectively.

The simulation results fit perfectly with BER equations. For the case of K = 10, the BER performance is degraded when clipping. The BER performance is 10^{-2} when IBO is −5 dB at Eb/No = 20 dB. The BER performances are similar for a small clipping factor (compare Figs. 3 and 4). These results show that clipping factor causes more degrading for larger K factor.

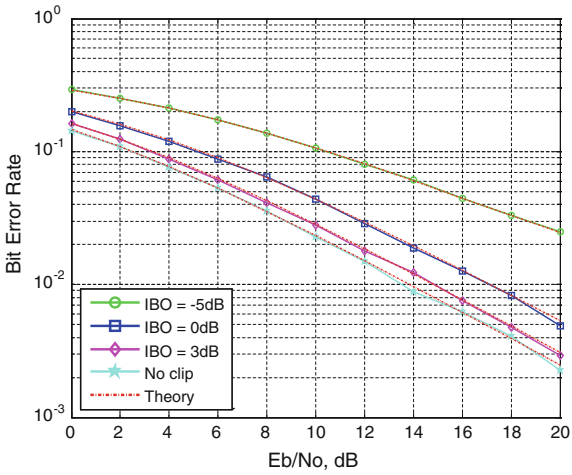

Fig. 2 BER of clipped OFDM over Rayleigh channel

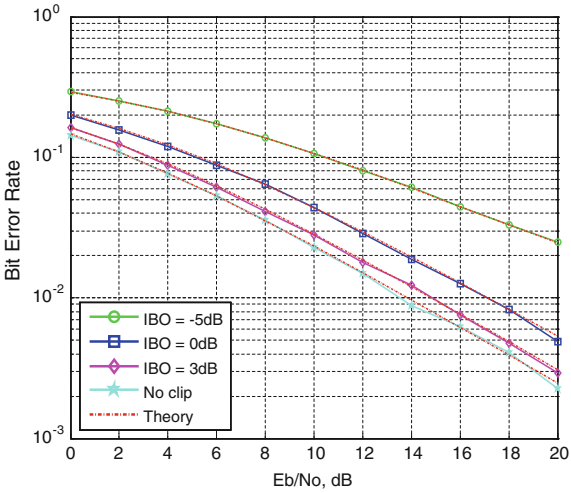

Fig. 3 BER of clipped OFDM over Rician channel (k = 1)

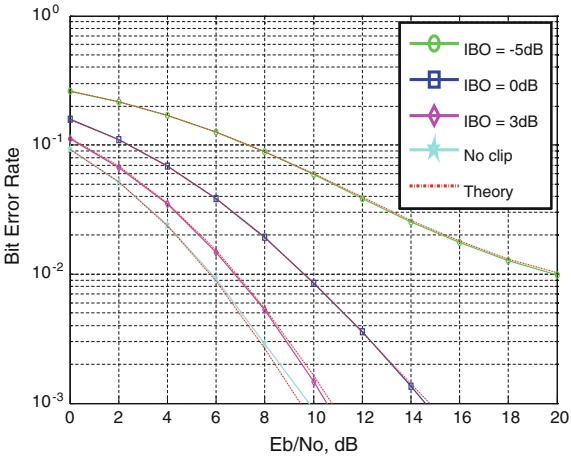

Fig. 4 BER of clipped OFDM over Rician channel (k = 10)

5 Conclusion

In this paper, we build the BER equation for determining the bit error rate of clipped OFDM signal over Rayleigh and Rician fading. The simulation results fit perfectly with BER equations. The results show that when the clipping factor is negligible, the BER performance degrades seriously. BER equation over Rayleigh channel needs double integrals while BER equation over Rician channel needs triple integrals. However, these calculations are easily done by using software. We are currently analyzing more complex channels.

References

1. Wulich D (2005) Definition of efficient PAPR in OFDM. IEEE Commun Lett 9:832–834
2. Tao J, Yiyan W (2008) An overview: peak-to-average power ratio reduction techniques for OFDM signals. IEEE Trans Broadcast 54:257–268
3. Seung Hee H, Jae Hong L (2005) An overview of peak-to-average power ratio reduction techniques for multicarrier transmission. IEEE Wireless Commun 12:56–65
4. Guel D, Palicot J (2009) Clipping formulated as an adding signal technique for OFDM peak power reduction. In: IEEE 69th vehicular technology conference, pp 1–5
5. Ochiai H, Imai H (2002) Performance analysis of deliberately clipped OFDM signals. IEEE Trans Commun 50:89–101
6. Bahai ARS, Singh M, Goldsmith AJ, Saltzberg B (2002) A new approach for evaluating clipping distortion in multicarrier systems. IEEE J Sel Areas Commun 20:1037–1046
7. Lee B, Kim Y, de Figueiredo RP (2010) Performance analysis of the clipping scheme with SLM technique for PAPR reduction of OFDM signals in fading channels. Wireless Pers Commun 63:331–344
8. Bussgang J (1952) Crosscorrelation functions of amplitude-distorted gaussian signals. Research Laboratory of Electronics, Massachusetts Institute of Technology, Technical Report 216
9. Goldsmith A (2005) Wireless communications. Cambridge University Press
10. Leon-Garcia A (2008) Probability, statistics, and random processes for electrical engineering, 3rd edn. Pearson Prentice Hall, USA
11. Zayani R, Shaiek H, Roviras D, Medjahdi Y (2015) Closed-form BER expression for (QAM or OQAM)-based OFDM system with HPA nonlinearity over rayleigh fading channel. IEEE Wireless Commun Lett 4:38–41
12. Proakis JG (2000) Digital communications. McGrawHill
13. Arfken GB, Weber HJ (2005) Mathematical methods for physicists, 6th edn. Elsevier Academic Press, USA
14. http://www.mathworks.com/help/matlab/ref/integral3.html. Accessed 15 May 2015

Part III
Computer Science

Machine Learning Based Phishing Web Sites Detection

Huu Hieu Nguyen and Duc Thai Nguyen

Abstract Phishing is a major problem that involves web sites and fraudulent emails that aim to reveal users important information such as financial data, emails, and other private information. Phishing activities have been in the increasing trend, and many unsuspecting users have fallen victims of these websites and fraudulent emails. This paper has analyzed the evaluation and design of the features used to detect and reduce any false activity. The selected features not only depend on the characteristics of the URL (Uniform Resource Locator), but also on the website content. The TF-IDF algorithm is used to calculate the top keywords of the website content that is used to extract one of the important features. The technique was evaluated on the dataset of 4.420 legitimate URLs and 5.389 phishing URLs. By considering features and evaluating using 5 classification algorithms, the resulting classifiers obtain 98.8 % accuracy on detecting phishing website URLs.

Keywords Phishing · Malicious URL · Phished website · Machine learning

1 Introduction

Phishing is web-based attack that fraudsters use to steal the identity of Internet users such as user id, password, and credit card information [1]. Attackers have a tendency of constructing websites, and use them to fraud users by tricking them into provide their private information. Phishers perform two main activities to make a successful attack. First, they develop a website that is similar in terms of design and functioning to a legitimate website owned by a famous organization. In addition,

H.H. Nguyen (✉) · D.T. Nguyen
Ho Chi Minh City University of Technology, 268 Ly Thuong Kiet Street,
District 10, Ho Chi Minh City, Vietnam
e-mail: huuhieubk@gmail.com

D.T. Nguyen
e-mail: thai@cse.hcmut.edu.vn

V.H. Duy et al. (eds.), *AETA 2015: Recent Advances in Electrical Engineering and Related Sciences*, Lecture Notes in Electrical Engineering 371,
DOI 10.1007/978-3-319-27247-4_11

they urge normal users to visit those websites and trick them to provide sensitive information via online form. The information is then saved to repositories that can be accessed by attackers.

There has been an increasing tendency in phishing sites since 2006 with a 15 % increment per year. The cost of phishing has not been properly documented, but it has been approximated to range from 2 to 3.5 billion dollars per year [2]. Many software companies have introduced several anti-phishing tools that enable them to detect and prevent fraudulent activities. For instance, Google has a free anti-phishing toolbar that enables users to detect suspicious activities [3]. Moreover, eBay has a tool that allows its users to detect sites that are owned by the company. There have been many anti-phishing toolbars that are available online and allow users to download and use them. However, the evaluation of the available anti-phishing tools indicates that very few of these toolbars can detect up to sixty percent of the fraudulent websites and activities without any false positive [4]. The above analysis leads to a need of creating a better model that has the ability to detect these algorithms automatically.

In this paper, the authors proposed a mechanism to detect a phishing web page using the machine learning method. The authors have used techniques to derive properties of an URL, and then predicted whether the target URL is a phishing website using 5 famous classification algorithms. The work made the following contributions:

- Implementation of a system which collected many legit and phishing URLs and extracted effective features for URL classification. The features are extracted from both URL and website content information.
- With the collected dataset, the authors evaluated and compared various classification algorithms such as J48 Decision Tree (DT), Random Forest (RF), Support Vector Machine (SVM), Naive Bayes (NB), and Neural Networks (NN).

The rest of the paper is organized as follows. Section 2 presents related works of anti-phishing methods that are currently used. The details of our approach to URL classification are discussed in Sect. 3. In Sect. 4, the author presents the evaluation results through many of classification algorithms. Section 5 is the conclusion of this paper.

2 Related Works

Although phishing is not a new security problem, internet users are still tricked into typing their private information on malicious web pages. To overcome this kind of attack, many of anti-phishing solutions have been developed to make people aware of this kind of attacks.

The phishing detection techniques, which proposed in [5, 6], is implemented using the blacklist method. A database of phishing website URLs is built using

many reported phising sources. When an URL is submitted, it will be looked up in the database. If the target URL is found in the database, then it is marked as a phishing URL. Unfortunately, this is not a efficient solution because a lot of new phishing websites are created day by day.

Most popular phisihing detection method is using the browser-integrated addon. These addons such as PwdHash [7], SpoofGuard [8] are installed in the browser to protect user's identity and other private information. SpoofGuard determines if the web page is a phishing one by checking for symptoms (e.g. obfuscated URLs).

AntiPhish browser addon [9] helps users to protect their information by warning them whenever their sensitive information is submitted to a site that has different location to the current site. This system has a problem when users want their information to be used in multiple sites, because the system will alert whenever the data is reused.

The machine learning approach [10–12] extracts many features of the URL and the website content, these features are combined using an classification algorithm to detect the phishing URL. In this paper, the author is not only focused on the information in the URL, but also studied the the Google result when querying top keywords derived from website content using the TF-IDF (Term Frequency Inverse Document Frequency).

3 Approach and Implementation

This section has focused on implementation of a crawler, and uses it to analyze the URL and its website content to extract the characteristics.

URLs are separated into 2 classes:

(a) **Legitimate**: URL is safe and the website provides normal services.
(b) **Phishing**: Website performs unintended actions to get sensitive data of its users such as email, password, and credit card details by tricking users to enter their personal information into a form.

3.1 Feature Extraction

The implemented crawler is used to extract features and information of URLs, and categorize them into 3 groups:

(a) **Lexical Features**
IP Address:
Every URL has a numeric address that uniquely identifies it. The numeric value is called the Internet Protocol (IP), and they are a series of numbers used to identify a computer network. Phishing URLs usually contain IP addresses

instead of a domain name. The feature identifies if the domain name of a web page is its IP address [11].

Suspicious URL:

The feature checks if the target URL contains the symbol @ or maybe a dash in its domain name. The symbol @, is responsible for making a string on the left to be disregarded while that on the right is identified as the actual URL for the web page. The limited size of the address bar in the address makes it possible to identify a legitimate URL. Moreover, very limited number of legitimate sites uses dashes on its URL.

Length of hostname:

Legitimate hostname is not long or short. The legitimate sites are also easy to identify through the spelling of the hostname, and any other manipulation used by phishing site. A legitimate site would have a hostname such as www.facebook.com. However, phishing sites would use hostnames such as www.facebooks.com.co. In other instances, the hostname is not spelt correctly or might contain illegitimate extensions that the user can easily identify.

(b) **Page Content Features**

TF-IDF: The significance of the word increases proportionally, but it is set by the number of times it appears in the corpus. The term frequency (TF) refers to the amount of time a word appears in a given document. These terms have to be normalized for long document to prevent any form of biasness in term of its importance. On the other hand, the inverse document frequency (IDF) is the measure of any general significance of a specific term. It measures how common a term is in a given document [13]. Therefore, a word has a high rate of TF-IDF by having a high rate of frequency of the term in a specific document, and having a low rate of frequency in a collection of a specific document.

Many online criminals modify their website to copy a legitimate URL and redirect any user information to their sites. Many companies have fallen victims of such illegal websites including eBay and Google among others. The model detects such modifications and traces the original website that the criminal modified [2].

This feature is calculated by fetching the HTML content of the given URL, deriving 5 terms that mostly occur in the document using the TF-IDF algorithms, then querying them as the keywords in Google search engine. If the domain in the given URL does not appear in top 5 results, then the given URL is more likely to be a phishing site.

Suspicious Links:

This feature checks for any URL links provided in the web page. The testing procedure is the same as the test of suspicious URL described above. If any of the URL link fails the scan, the page is considered as phishing site.

Forms: The Hypertext Markup Language is used to determine the legitimate sites. The HTML for legitimate sites identifies texts that are used by the host to validate the user details. The feature identifies any form of HTML texts that

ask users for their credit card number and any other personal information. Many phishing sites contain these form that ask users for their personal data.

(c) **Domain Features**

Site Popularity (Alexa): Alexa determines the website popularity based on users review and number of users who have ever used the site in the past. However, phishing sites have low popularity, few, or no reviews and lack any standard rating. This feature is used to determine how popular the web site is among users. A low rate in popularity might indicate a phishing site.

Age of Domain: Many phishing sites create a domain name before they send out emails to users. Using WHOIS to implement the given feature is important. As such, this feature examines the number of days from the day of the domain registration [11]. If the domain name has just been registered for a few months, it's more likely a phishing site.

3.2 Dataset

The dataset contains two kinds of samples:

- Legitimate website URLs are collected from [14], the site lists top 5000 websites in the world. People can view the list for free. The authors collected 4.420 website URL from this source by using a crawler.
- 2. Phishing samples are collected from Phish Tank [15], an open project that allows users to submit phishing URLs. 5.389 phishing URLs were collected.

With all the collected URLs, a tool is designed to extract all the needed feature information as described above to create the dataset of 9.809 samples for training and testing process.

3.3 Training

In the training process, the authors used fivefold method to train/test with 5 classifiers in Weka [16]. This software contains a collection of machine learning algorithms, and can be applied to the dataset easily. Below are the classifiers that the authors used to evaluate the dataset.

(a) **Support Vector Machine**:

This is the most effective evaluation method that utilizes decision line to create decision boundaries [4, 17]. A decision plane ensures the approach has a series of objectives in a class membership. This method also classifies objects in two categories: red or green. The red objects fall to the right of the selected line while the green objects to the left of the decision plane.

(b) **Naive Bayes**:
The Naive Bayes classifier [17] originates from the Bayes Theorem, and is effective when the inputs are high. However, the method is complex and requires the user to have extensive knowledge of the model being used. The classifiers used require variable parameters that are highly scaled to output the maximum probability. Moreover, these classifiers are used to evaluate close-form parameters using linear time rather than the iterative estimate.

(c) **J48 decision tree**:
The J48 decision tree allows the user to make a decision by eliminating the irrelevant data [18]. The tree checks for the information gain within a given set of data. Imagine a dataset that has the predictor lists and independent variable. In addition, the dataset contains the required target or the dependent variable. The J48 decision tree would help the user to determine the appropriate target for each new record provided.

(d) **Random forest**:
Random forest works as the random hyperlink in the model [19]. It assumes that an individual knows the formation of a single category. The forest forms other three classifications in the process. The testing and training data process requires the user to record any result from the implementation process. The implementation process also requires the user to take several experiments to validate the importance of the results.

(e) **Neural Networks**:
Neural networks [20] are networks of units (neurons) based on the real neural structure of the brain. Units are arranged in layers. Neural networks "learn" by processing records and comparing their classification of the record with the known actual classification of the record. The errors from current classification step are used to adjust the networks algorithm in the next step, and so on for many iterations.

4 Evaluation

4.1 Feature Group Comparison

The authors separated all the features into 3 groups: Lexical Features, Page Content Features, and Web Page Features to find out how much each feature group affects the classification accuracy. For each feature group, the authors applied 5 learning algorithms: Support Vector Machine, Naive Bayes, J48 Tree Decision, Random Forest and Neural Networks to compare the results. From Fig. 1, the domain features group and the page content feature group have made higher contributions to the classification performance, the yellow columns which show 89.3–97.9 %, the orange columns which show 94.9 % of accuracy while classifying URLs. The

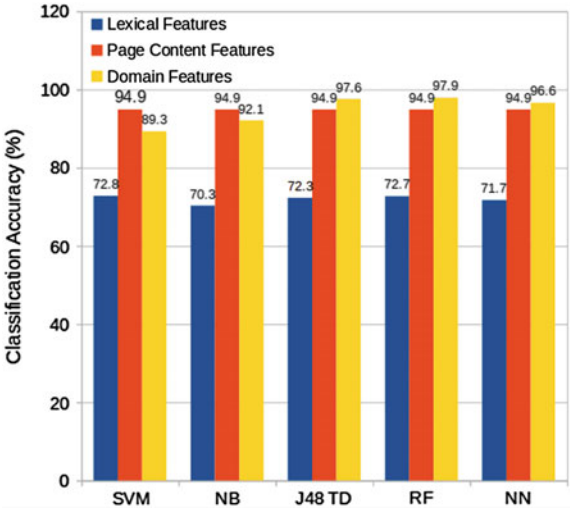

Fig. 1 Classification accuracy for each group of features

lexical features group contributes the least with 70.3–72.8 % of accuracy (the blue columns).

4.2 Classifier Comparison

Given the dataset with 8 features extracted, the authors used 5 classifiers to compare the performance. The results of training/testing the dataset of 9.809 samples using fivefolds method are shown in Table 1. The metadata within the result table is: Runtime Latency (RL), True Positive Rate (TPR), and False Positive Rate (FPR) for each algorithm. Based on the results, the RF algorithm has performed the best classification accuracy with the true positive rate 98.8 %. The NN has nearly the same TPR and FPR with the RF but it's runtime latency is higher (8.47 vs. 1.5 s). The NB has the shortest runtime latency (0.06 s) but the true TPR is not high (96.6 %). The time latency when running SVM algorithm is too high (744.6 s) and the classification accuracy is relatively low. So, the RF learning algorithm gives the best accuracy in acceptable time when working with the dataset.

Table 1 Traing/testing result for 5 algorithms

	SVM	NB	J48 TD	RF	NN
TPR (%)	86.1	96.9	98.5	98.8	98.4
FPR (%)	11.4	2.8	1.5	1.2	1.6
RL (s)	744.6	0.06	0.48	1.5	8.47

5 Conclusion

The paper has proposed the machine learning approach in order to separate web page URLs into 2 classes: legitimate and phishing. A crawler is developed to extract the feature data from 9.809 URLs, which are classified into three groups: Lexical Features, Page Content Features, and Web Page Features. The dataset is trained/tested with 5 classifiers. After selecting features and evaluating with 5 learning algorithms, the system can detect phishing websites with 98.8 % accuracy. It is believed that this approach is complementary to previous approach on detecting phishing website URLs. In future, it is recommended the use of hybrid learning algorithm that could enhance the accuracy of URL classification problem.

References

1. Basnet R, Mukkamala S, Sung AH (2008) Detection of phishing attacks: a machine learning approach. Springer, Berlin, pp 373–383
2. Geng GG, Lee XD, Zhang YM (2015) Combating phishing attacks via brand identity and authorization features. Secur Commun Netw 8(6):888–898
3. Chaudhary S, Berki E, Li L, Valtanen J (2012) Time up for phishing with effective anti-phishing research strategies. Int J Hum Cap Inf Technol Prof (IJHCITP) 49–64 (2015)
4. Ray LL (2015) Countering cross-site scripting in web-based applications. Int J Strateg Inf Technol Appl (IJSITA) 6(1):57–68
5. Sheng S, Wardman B, Warner G, Cranor LF, Hong J, Zhang C (2009) An empirical analysis of phishing blacklists
6. Goodin D (2012) Google bots detect 9,500 new malicious websites every day
7. Joshi Y, Das D, Saha S (2009) Mitigating man in the middle attack over secure sockets layer. In: IEEE international conference on Internet Multimedia Services Architecture and Applications (IMSAA), 2009. IEEE
8. Dudhe MPD, Ramteke PL (2015) A review on phishing detection approaches
9. Kirda E, Kruegel C (2005) Protecting users against phishing attacks with antiphish. In: 29th annual international computer software and applications conference, 2005. COMPSAC 2005, vol 1. IEEE
10. Likarish P, Jung EE, Dunbar D, Hansen TE, Hourcade JP (2008) B-apt: bayesian anti-phishing toolbar. IEEE Int Conf Commun 1745–1749
11. Zhang Y, Hong JI, Cranor LF (2007) Cantina: a content-based approach to detecting phishing web sites. In: The 16th international conference on World Wide Web, p 639648
12. Xiang G, Hong J, Rose CP, Cranor L (2011) Cantina+: a feature-rich machine learning framework for detecting phishing web sites. ACM Trans Inf Syst Secur 14(2):128
13. Salton G, McGill MJ (1986) Introduction to modern information retrieval. Facet Publishing, London
14. 5000 best websites. http://5000best.com/websites
15. PhishTank—Suspected phish submissions. https://www.phishtank.com
16. Hall M, Frank E, Holmes G, Pfahringer B, Reutemann P, Witten IH (2009) The WEKA data mining software: an update. ACM SIGKDD Explor Newsl 11(1):10–18
17. Murph KP (2006) Naive bayes classifiers. University of British Columbia, Vancouver
18. Mohammad RM, Thabtah F, McCluskey L (2014) Predicting phishing websites based on self-structuring neural network. Neural Comput Appl 443–458

19. Pal M (2005) Random forest classifier for remote sensing classification. Int J Remote Sens 217–222
20. Ripley BD (1994) Neural networks and related methods for classification. J Roy Stat Soc 409–456

Simulation and Optimization of a Non-linear Dynamic Process Using Mathematica

Tran Trong Dao, Vo Hoang Duy, Ivan Zelinka, Luu Minh Tung and Pham Nhat Phuong

Abstract Evolutionary algorithms (EAs) have proven to be a powerful and robust optimizing technique even for complex optimization problems. The main aim of this work is to show that such a powerful simulating and optimizing of a non-linear dynamic process. In this paper, the complex reaction sequence used to study various reaction kinetics by optimization the rate constants. Two algorithms from the field of artificial intelligent—Differential evolution (DE), Self-organizing migrating algorithm (SOMA) are used in this investigation. Two optimization techniques were developed using Mathematica for accurately determining the rate constants of the reaction at certain temperature from the experimental data. The results show that EAs are used successfully in the process optimization.

Keywords Simulation · Optimization · Evolutionary algorithms · Differential evolution · Self-organizing migrating algorithms

T.T. Dao (✉)
MERLIN, Ton Duc Thang University, 19 Nguyen Huu Tho Street, District 7, Ho Chi Minh City, Vietnam
e-mail: trantrongdao.@tdt.edu.vn

V.H. Duy · I. Zelinka · L.M. Tung · P.N. Phuong
Faculty of Electrical and Electronics Engineering, Ton Duc Thang University, No. 19 Nguyen Huu Tho Street, District 7, Ho Chi Minh City, Vietnam
e-mail: vohoangduy@tdt.edu.vn

I. Zelinka
e-mail: Ivan.zelinka@vsb.cz

L.M. Tung
e-mail: luuminhtung@tdt.edu.vn

P.N. Phuong
e-mail: phamnhatphuong@tdt.edu.vn

I. Zelinka
Department of Computer Science, VSB-Technical University of Ostrava, 17. listopadu 15/2172, 708 33 Ostrava, Poruba, Czech Republic

V.H. Duy et al. (eds.), *AETA 2015: Recent Advances in Electrical Engineering and Related Sciences*, Lecture Notes in Electrical Engineering 371,
DOI 10.1007/978-3-319-27247-4_12

1 Introduction

The optimization of dynamic process has received growing attention in recent years because it is essential for the process industry to strive for more efficient and agile manufacturing in face of saturated market and global competition [1]. Designing optimal reactor parameters including control constitutes is one of the most complex tasks in process engineering. The situation is particularly complicated by the fact that the precise mechanism of chemical reaction kinetics is very often unknown. For this reason it is necessary to carry out extensive measurements of input and output concentration dependencies of components on time, temperature, etc.

Nowadays, Optimization is one of these words which is used almost every day in different fields of human activities. Everybody wants to maximize profit and minimize cost. This means optimizing in every task of industry, transportation, medicine, everywhere. For these purposes, we need to have suitable tools which are able to solve very difficult and complicated problems. As previous years proved, use of artificial intelligence and soft computing contribute to improvements in a lot of activities. One of such tools of soft computing are evolutionary algorithms [2, 3].

For chemical reactions, the determination of the rate constants is both very difficult and a time consuming process. From the experimental concentration-time data, initial values of rate constants were calculated. Experimental data encountered several types of errors, including temperature variation, impurities in the reactants and human errors. This research was to develop computer programs for determining the rate constants for the general form of any complex reaction. The development of such program can be very helpful in the control of industrial processes as well as in the study of the reaction mechanisms. Determination of the accurate values of the rate constants would help in establishing the optimum conditions of reactor design including pressure, temperature and other parameters of the chemical reaction [4].

In this paper, the modelling of dynamic chemical engineering processes is presented using the unique combination of simplified fundamental theory and direct hands-on computer simulation; then the complex reaction sequence used to study various reaction kinetics by optimization the rate constants by evolutionary algorithms. Two algorithms from the field of artificial intelligent—Differential evolution (DE), Self-organizing migrating algorithm (SOMA) are used in this investigation. The optimized reactor was used in a simulation with optimization by evolutionary algorithms and the results are presented in graphs.

2 Description of a Complex Reaction

This work uses a mathematical model of a complex reaction from the book Chemical Engineering Dynamics: An Introduction to Modelling and Computer Simulation [5].

2.1 System

The complex bath reaction between formaldehyde, A, and sodium p-phenol sulphonate, B, proceeds in accordance with the following complex reaction scheme. All the reactions follows second-order kinetics. Components C, D and F are intermediates, and E is the final product.

Reaction	Rate constants
A + B → C	k1
A + C → D	k2
C + D → E	k3
B + D → F	k4
C + C → F	k5
C + B → G	k6
A + G → F	k7
A + F → E	k8

2.2 Model

For a constant volume batch reaction, the balance equations for each component lead to

$$\frac{dC_A}{dt} = -k_1 C_A C_B - k_2 C_A C_C - k_7 C_A C_G - K_8 C_A C_F$$
$$\frac{dC_B}{dt} = -k_1 C_A C_B - k_4 C_B C_D - k_6 C_C C_B$$
$$\frac{dC_C}{dt} = k_1 C_A C_B - k_2 C_A C_C - k_3 C_C C_D - 2k_5 C_C^2 - k_6 C_C C_B$$
$$\frac{dC_D}{dt} = k_2 C_A C_C - k_3 C_C C_D - k_4 C_B C_D$$
$$\frac{dC_E}{dt} = -k_3 C_C C_D + k_8 C_A C_F$$
$$\frac{dC_F}{dt} = k_4 C_B C_D + k_5 C_C^2 + k_7 C_A C_G - K_8 C_A C_F$$
$$\frac{dC_G}{dt} = k_6 C_C C_B - k_7 C_A C_G$$

where C: Concentration (kmol/m^3); k: Rate constants (m^3/kmol min); R: Rate (kmol/m^3 min) A, B, C, …, G refer to component 1, 2, 3 …, 8 refer to reactions.

3 Simulation of Chemical Process

Many different digital simulation software packages are available on the market. Modern toll are numerically powerful, highly interactive and allow sophisticated types of graphical and numerical output. Many packages also allow optimization and parameter estimation. In this work, we used program Mathematica 7.0 to simulate and present concentration-time profiles using parameters as given in the program, time for simulation is 1000 (Fig. 1).

4 Methods and Optimization

4.1 Select Evolutionary Algorithms

For the experiments described here, stochastic optimisation algorithms, such as Differential Evolution (DE) [6], Self-Organizing Migrating Algorithm (SOMA) [3] were selected. Main reason why DE, SOMA have been seed comes from contemporary state in chemical engineering and EAs use. Since now has been done some research with attention on use of EAs in chemical engineering optimization, including DE. This participation has to show that applicability of relatively new algorithms is also positive and can lead to applicable results, as was shown for example in [7], SOMA is a stochastic optimization algorithm that is modelled on the social behaviour of co-operating individuals [3].

Differential Evolution (DE)
Differential Evolution [1] is a population-based optimization method that works on real-number coded individuals. For each individual xi,G in the current generation G, DE generates a new trial individual x'i,G by adding the weighted difference between two randomly selected individuals xr1,G and xr2,G to a third randomly selected individual xr3,G. The resulting individual x'i,G is crossed-over with the original individual xi,G. The fitness of the resulting individual, referred to as

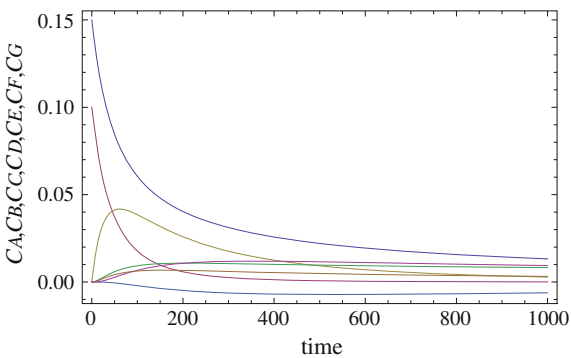

Fig. 1 Concentration-time profiles using parameters as given

$$
\begin{aligned}
&1.\ \text{Input}: D, G_{\max}, NP \geq 4, F \in (0,1+), CR \in [0,1], \text{and initial bounds}: \vec{x}^{(lo)}, \vec{x}^{(hi)}.\\
&2.\ \text{Initialize}: \begin{cases} \forall i \leq NP \wedge \forall j \leq D: x_{i,j,G=0} = x_j^{(lo)} + rand_j[0,1] \bullet \left(x_j^{(hi)} - x_j^{(lo)}\right) \\ i = \{1,2,...,NP\},\ \ j = \{1,2,...,D\}, G = 0, rand_j[0,1] \in [0,1] \end{cases}\\
&\begin{cases} 3.\ \text{While}\ \ G < G_{\max} \\ \quad \forall i \leq NP \begin{cases} 4.\ \text{Mutate and recombine}: \\ \qquad 4.1 \quad r_1, r_2, r_3 \in \{1,2,....,NP\}, \text{randomly selected, except}: r_1 \neq r_2 \neq r_3 \neq i \\ \qquad 4.2 \quad j_{rand} \in \{1,2,...,D\}, \text{randomly selected once each } i \\ \qquad 4.3 \ \ \forall j \leq D, u_{j,i,G+1} = \begin{cases} x_{j,r_3,G} + F \cdot (x_{j,r_1,G} - x_{j,r_2,G}) \\ \qquad\qquad \text{if } (rand_j[0,1] < CR \vee j = j_{rand}) \\ x_{j,i,G} \quad \text{otherwise} \end{cases} \\ 5.\ \text{Select} \\ \vec{x}_{i,G+1} = \begin{cases} \vec{u}_{i,G+1} & \text{if } \ f(\vec{u}_{i,G+1}) \leq f(\vec{x}_{i,G}) \\ \vec{x}_{i,G} & \text{otherwise} \end{cases} \end{cases} \\ G = G + 1 \end{cases}
\end{aligned}
$$

Fig. 2 Pseudocode of DE

perturbated vector ui,G + 1, is then compared with the fitness of xi,G. If the fitness of ui,G + 1 is greater than the fitness of xi,G, xi,G is replaced with ui,G + 1, otherwise xi,G remains in the population as xi,G + 1. Deferential Evolution is robust, fast, and effective with global optimization ability. It does not require that the objective function is differentiable, and it works with noisy, epistatic and time-dependent objective functions. Pseudocode of DE shows (Fig. 2).

Self Organizing Migrating Algorithm (SOMA)

SOMA is a stochastic optimization algorithm that is modelled on the social behaviour of co-operating individuals [3]. It was chosen because it has been proved that the algorithm has the ability to converge towards the global optimum [3]. SOMA works on a population of candidate solutions in loops called migration loops. The population is initialized randomly distributed over the search space at the beginning of the search. In each loop, the population is evaluated and the solution with the highest fitness becomes the leader L. Apart from the leader, in one migration loop, all individuals will traverse the input space in the direction of the leader. Mutation, the random perturbation of individuals, is an important operation for evolutionary strategies (ES). It ensures the diversity amongst the individuals and it also provides the means to restore lost information in a population. Mutation is different in SOMA compared with other ES strategies. SOMA uses a parameter called PRT to achieve perturbation. The PRT Vector defines the final movement of an active individual in search space.

The randomly generated binary perturbation vector controls the allowed dimensions for an individual. If an element of the perturbation vector is set to zero, then the individual is not allowed to change its position in the corresponding dimension. An individual will travel a certain distance (called the path length) towards the leader in n steps of defined length. If the path length is chosen to be

$$
\begin{aligned}
&\text{Input} : N, Migrations\ , PopSize\ \geq 2, PRT\ \in [0,1], Step\ \in (0,1],\ \text{MinDiv}\ \in (0,1],\\
&\quad \text{PathLength}\ \in (0,5],\ Specimen\ \text{with uper and lower bound}\ \ x_j^{(hi)}, x_j^{(lo)}\\
&\text{Inicialization}\ :\ \begin{cases} \forall i \leq PopSize\ \wedge \forall j \leq N : x_{i,j,Migrations\ =0} = x_j^{(lo)} + rand_{\ j}[0,1] \bullet \left(x_j^{(hi)} - x_j^{(lo)}\right) \\ i = \{1,2,...,Migrations\ \},\ j = \{1,2,...,N\},\ \text{Migrations}\ = 0,\ rand_{\ j}[0,1] \in [0,1] \end{cases}\\
&\begin{cases} \text{While}\ \ \text{Migrations}\ < Migrations_{\ \max} \\ \forall i \leq PopSize \begin{cases} \text{While}\ \ t \leq PathLength \\ if\ rnd_{\ j} < PRT\ \ pak\ \ PRTVector_{\ j} = 1\ \ else\ 0\ ,\ \ j = 1,\ldots,N \\ x_{i,j}^{ML\ +1} = x_{i,j,start}^{ML}\ + (x_{L,j}^{ML} - x_{i,j,start}^{ML})\ t\ PRTVector_{\ j} \\ f\left(x_{i,j}^{ML\ +1}\right) = \ \text{if}\ \ f\left(x_{i,j}^{ML}\right) \leq f\left(x_{i,j,start}^{ML}\right)\ \ \text{else}\ \ f\left(x_{i,j,start}^{ML}\right) \\ t = t + Step \end{cases} \\ \text{Migrations}\ = \text{Migrations}\ + 1 \end{cases}
\end{aligned}
$$

Fig. 3 Pseudocode of SOMA

greater than one, then the individual will overshoot the leader. This path is perturbed randomly. For an exact description of use of the algorithms see [3] for SOMA. Pseudocode of SOMA is (Fig. 3).

4.2 Static Optimization of Complex Reaction

Simulation of the kinetic reactions is performed with the aid of a Mathematica computer program. The simulation program reads the initial values of the rate constants, the initial concentration of the reactants and the simulation start, end and interval times.

The simulation results are compared with experimental results at each measured point. All deviations between experimental and calculated values are and summed up to form an objective function F:

$$F = \sum_{t=0}^{t} |\text{exp.conc.} - \text{calc.conc}|$$

where: exp. conc.: experimental concentration; calc. conc.: calculated concentration.

The summation starts from the initial time and ends at the final time. The value of the objective function is stored (Table 1).

Parameter settings for algorithms

The control parameter settings have been found empirically and are given in Table 2 (SOMA) and Table 3 (DE). The main criterion for this setting was to keep the same setting of parameters as much as possible and of course the same number of cost function evaluations as well as population size (parameter PopSize for SOMA and NP for DE).

Table 1 Initial values

Second oder rate constants (m^3/kmol)	Initial concentrations (kmol/m^3)	
$k_1 = 0.16$	A0 = 0.15	INIT A = A0
$k_2 = 0.05$	B0 = 0.1	INIT B = B0
$k_3 = 0.15$	C0 = 0	INIT C = C0
$k_4 = 0.14$	D0 = 0	INIT D = D0
$k_5 = 0.03$	E0 = 0	INIT E = E0
$k_6 = 0.058$	F0 = 0	INIT F = F0
$k_7 = 0.05$	G0 = 0	INIT G = G0
$k_8 = 0.05$		

Table 2 SOMA parameter setting

	A
Path length	3
Step	0.41
PRT	0.1
PopSize	20
Migrations	40
Min div	−1
Individual length	6
CF evaluations	6951

Table 3 DE parameter setting

	A
NP	20
F	0.9
CR	0.2
Generations	200
Individual length	6
CF evaluations	4000

5 Optimization Results

Due to the fact that EAs are partly of stochastic nature, a large set of simulations has to be done in order to get data for statistical data processing. Two algorithms (SOMA, DE) have been applied 50 times in order to find the optimal rate constant reaction parameters. All important data has been visualized directly or/and processed for graphs demonstrating performance of two algorithms. Table 4 present rate constants parameters and their best results which has been optimization done by SOMA and DE. Estimated parameters and their diversity (minimum, maximum and average) are depicted in Figs. 4 and 5. The history of the evolution by SOMA and DE shown in Fig. 6. From those pictures it is visible that results from two algorithms are comparable.

Table 4 Rate constants optimal parameters by SOMA and DE

Rate constants	Optimal parameters by SOMA	Optimal parameters by DE
k_1	0.154071	0.164234
k_2	0.0619295	0.0608726
k_3	0.221181	0.278205
k_4	0.140526	0.18626
k_5	0.0525599	0.0372953
k_6	0.0905671	0.106854
k_7	0.0620407	0.0654213
k_8	0.0509923	0.0534687

Graphics results

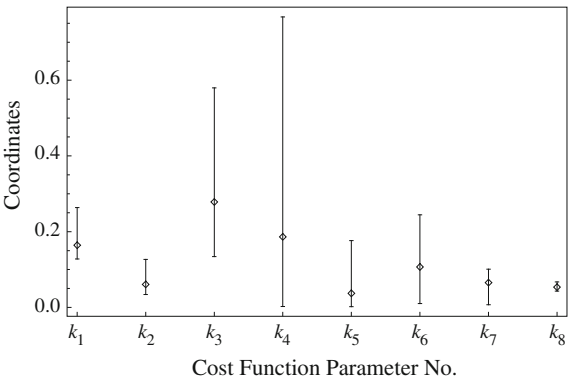

Fig. 4 Parameter variation of DE

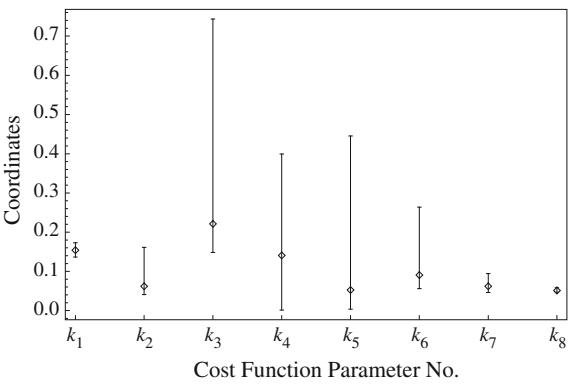

Fig. 5 Parameter variation of SOMA

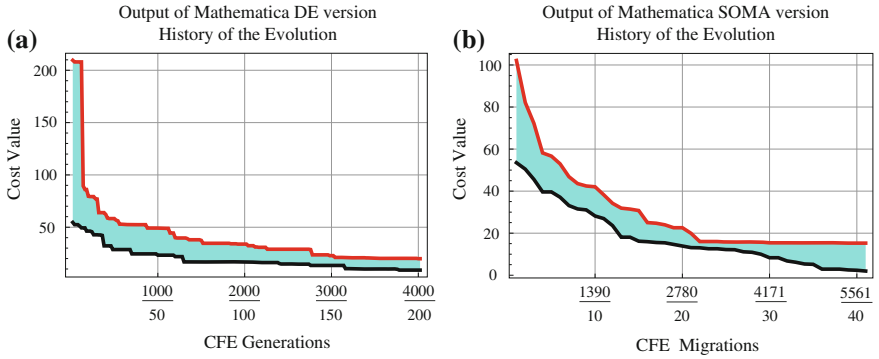

Fig. 6 History of evolution of SOMA and DE. **a** Process evolution by DE. **b** Process evolution by DE

6 Conclusion

Research on this work is concerned with the field of simulation and optimization of chemical engineering through EAs using program Mathematica. From the results, we had successful realized:

- description and analysis of the chosen dynamic system more concretely those in the processes of a complex reaction,
- modelling of dynamic chemical engineering processes is presented using the unique combination of simplified fundamental theory and direct hands-on computer simulation,
- selecting and demonstrating EAs and practical method to optimize the chemical process, especially of complex bath reaction,
- demonstrating the use of designed algorithms for global optimization in oder to determine the rate constants of a complex reaction and comparison between SOMA and DE algorithm.

The results produced by the optimizations depend not only on the problem being solved but also on the way how to define a given function. All simulations were repeated 50 times for each EA with the same initial conditions for each simulation in oder to determine the optimal rate constants parameters.

The proposed procedures could be modified to simulate any kinetic reaction, of any order and nature. Determination of accurate rate constants is very helpful in establishing the optimum conditions of pressure, temperature, feed composition, reactor design and other chemical parameters.

In addition, from this research, we can conclude that EAs have shown great potential and ability to solve complex problems of optimization, not only at the field of chemical engineering process but also in diverse industrial fields.

Acknowledgment This work is part of the Science activities of MERLIN at the Ton Duc Thang University, Ho Chi Minh City, Vietnam.

References

1. Backx T, Bosgra O, Marquardt W (2000) Integration of model predictive control and optimization of processes. Proc ADCHEM 1(2000):249–260
2. Zelinka I (2002) Umělá inteligence v problémech globální optimalizace. BEN, Praha. ISBN 80-7300-069-5
3. Zelinka I (2004) SOMA. In: Babu BV, Onwubolu G (eds) New optimization techniques in engineering. Springer, Berlin, Chapter 7. ISBN 3-540-20167-X
4. Abdel-Latif Aboul S, Abdallah Lamiaa AM (2010) Two optimization methods to determine the rate constants of a complex chemical reaction using FORTRAN and MATLAB. Am J Appl Sci 7(4):509–517. ISSN 1546-9239
5. John I, Irving JD, Elmar H, Jiri EP, Jonathan BS (2007) Chemical engineering dynamics: an introduction to modelling and computer simulation. Completely Revised, 3rd Edn. ISBN 978–3–527–31678–6, VILEY-VCH Verlag GmbH&Co. KGaA
6. Price K (1999) An introduction to differential evolution. In: Corne D, Dorigo M, Glover F (eds) New Ideas in Optimization. McGraw-Hill, London, UK, pp 79–108
7. Zelinka I (2001) Prediction and analysis of dynamical system behavior by means of artificial intelligence and synergetics. Ph.D. thesis, Czech Edition, Univerzita Tomáše Bati ve Zlíně, Fakulta technologická
8. Babu BV, Angira R (2001) Optimization of Non-linear functions using evolutionary computation. In: Proceedings of 12. ISME Conference, India, Jan 10–12, pp 153–157
9. Back T, Fogel DB, Michalewicz Z (1997) Handbook of evolutionary computation. Institute of Physics, London
10. Bruce Nauman E, Chemical reactor design, optimization, and scale up. IBSN 0-07-137753-0
11. Dasgupta D, Michalewicz Z (1997) Evolutionary algorithms in engineering applications. Springer, Berlin
12. Tran TD, Zelinka I (2009) Using method of artificial intelligence to optimise and control chemical reactor. In: Proceedings of the 15th international conference on soft computing (MENDEL '09), Brno, Czech Republic, June 2009
13. Tran TD (2011) Investigation on evolutionary computation techniques of a nonlinear system. Model Simul Eng vol 2011, Article ID 496732, 21 pp. doi:10.1155/2011/496732
14. Tran TD, Zelinka I (2009) Investigation on optimization of process parameters and chemical reactor geometry by evolutionary algorithms. In: 23rd European conference on modelling and simulation—ECMS 2009, Madrid, Spain June 9th–12th, 2009
15. Zelinka I (2004) SOMA—self organizing migrating algorithm. In: Babu BV, Onwubolu G (eds) New optimization techniques in engineering. Springer, New York, pp 167–218

Personality Disorders Identification in Written Texts

Petr Saloun, Adam Ondrejka, Martin Malčík and Ivan Zelinka

Abstract This article describes a method for dealing with the detection of possible personality disorder without the necessary presence of specialists and using the patient's self-essays. Written text is analyzed by using NLP techniques and is categorized into one of the three main groups of personality disorders we chosen—fear, procrastination and intolerance of uncertainty. We customized approach based on features extraction, sentiment analysis and classification by well-known classifiers: Naive Bayes, Multi-Class Support Vector Machine, k-Nearest Neighbors and Decision Tree. The first experiential, based on real data consulted with specialists, have shown promising results. Greater or lesser personality disorders are due to a stressful and time-titch way of life quite frequent nowadays. In the cases of restrictions or complications in the suffering individual's life is early identification and problem solving more than desirable. But some people consider visiting a specialist as a personal failure a and due a shame they do not solve the problem even if it suspects themselves. Psychologists and psychiatrists on the other hand use several methods to detect personality disorders today, either by observation during the interview, a questionnaire and a written self-essay.

Keywords Natural language processing · Web engineering · Personality disorders · Psychology · Psychiatry · Document classification · Features extraction

P. Saloun (✉) · A. Ondrejka · M. Malčík · I. Zelinka
VSB-Technical University of Ostrava, Ostrava, Czech Republic
e-mail: petr.saloun@vsb.cz

A. Ondrejka
e-mail: adam.ondrejka@vsb.cz

M. Malčík
e-mail: martin.malcik@vsb.cz

I. Zelinka
e-mail: ivan.zelinka@vsb.cz

V.H. Duy et al. (eds.), *AETA 2015: Recent Advances in Electrical Engineering and Related Sciences*, Lecture Notes in Electrical Engineering 371,
DOI 10.1007/978-3-319-27247-4_13

1 Introduction

The most widespread and most reliable way to detect personality disorder is, of course, a personal examination by a specialist—psychiatrist. Part of the people who suspect that they might be with something wrong, do not seek professional help, consider it as a kind of personal failure and mental illness deemed inferior physical illness. Such people then worried unnecessarily longer than people who seek help in time. Often they decide to visit only after pushing around. Another way of at least tentatively estimated mental disorder without direct personal contact can be suitably prepared in an advance by answering questions that will lead to at least partial identification or otherwise providing information in written form.

We are focusing on this last possibility of the indirect contact. In our web system user can determine whether his behavior and feelings show signs of one of the three personality disorders, which primarily focuses, namely: *fear and anxiety*, *procrastination* and *tolerance of uncertainty*. The user will be able to choose two ways to ascertain this information. Either by questionnaire or by writing essays himself summed up his feelings and problems. In this article we focus on the problems identified in the self-essay, both approaches are obviously designed and consulted with experts in the field of psychiatric and personality disorders.

This work builds on our previous research [1]. In the first phase of research, we decided to verify that you can recognize personality disorders from text using features extraction, their classification and machine learning. We abandoned the idea of simple comparing the occurrences of words and their frequency in relation to the reference models. Text features are extracted by methods using natural language processing and by estimating polarity, thus analyzing sentiment using our earlier research in this area [2]. The acquired features are then categorized by several well-known classifiers with real data obtained from a medical clinic web site by web engineering method.

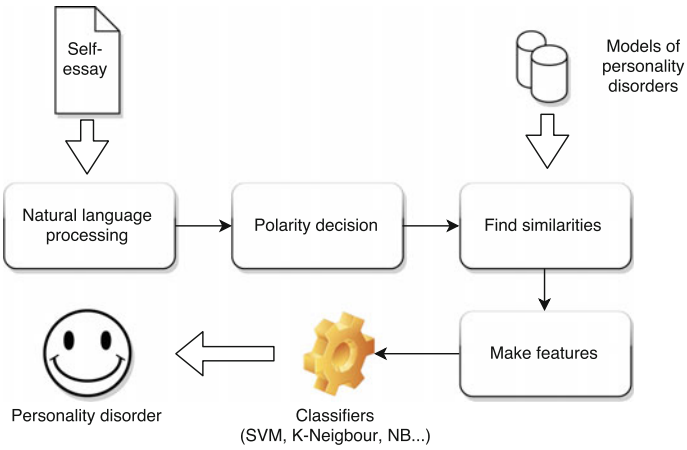

Fig. 1 Identifying personality disorders in user's self-essay

The research described in this article is part of an Internet project dealing with psychology and mental health problems, which is still under development. Web is, except tools to detect personality disorders, also informative in nature and will include a description of mental illness, prevention advice and contacts to specialized units. Our approach is illustrated in Fig. 1.

2 State of the Art

The solving of our problem is offered by documents classification and categorization in which have been already many works, but none of them directly deal with searching for personality disorders or any other mental disorders from the text.

Zang in work [3] to classify web document presents a method based on fuzzy k-Nearest Neighbors (k-NN) network which is modified k-NN. Features extraction is carried out according to the properties used term frequency/inverse document frequency. The experiments indicate that the proposed method is better in comparison with the simple k-NN and SVM.

Quiang in [4] focused on the features extraction from the documents and their following categorization. To obtain the document features he use the Categorical Term Frequency Probability (CTFP), which defines the characteristics of the main terms for each category. Then is used the Mean-Variance-based CTFP to selects key features. Experiments conducted using SVN classifier and data from corpora. The results shown that the chosen method has a better FI-metric for document categorization.

In [5] Li presents learning algorithm using back-propagation neural network for document categorization which, as is shown in article, solve problem with slowness and involving into local minimum in case of common neural network algorithm. The experimental results also shown higher categorization effectiveness.

Work [6] by Polajnar improves Explicit semantic analysis (ESA) method to computing similarities between documents. Article provides two solutions for integration of concept-concept similarities into the ESA model with promising results.

Li use in [7] finds similarity between documents by content analysis. They use a linked-based method based on random walk on graphs. Experimental study shows good accuracy, performance and fast convergent-rate.

Islam presents in [8] a method for measuring the semantic similarity of texts using a corpus-based measure of semantic word similarity. He also describes modified version of Longest Common Subsequence string matching algorithm which uses to support texts similarities. Experiment is although focused on short paragraph, but should be applicable for long texts too. Experiments shown algorithm is better then several competing methods.

Turney in [9] deals with semantic processing of text in Vector space models (VSM). The work summarizes the literature in the field of semantic research in VSM and provides a new perspective. Turney describes methods and approaches

for three main VSMs classes, based on term-document, word-context, and pair-pattern matrices.

Vikas in [10] compares coefficient for finding out the most relevant documents by genetic algorithm. He tries Jaccard, Dice and Cosine coefficient for the given set of keywords retrieved from Google search results. The experiment showed the most relevant results were given by Cosine similarity coefficient followed by Dice and Jaccard.

3 Features Extraction

For above mentioned three basic types of personality disorders we created basic models in cooperation with a specialist. The basic models is consisted of keywords, supporting phrases and reference text. The *keywords* are words which strongly mean analyzed text showing signs of some kind of personality disorder. The words are of negative meaning such as *indecisiveness*, *withdrawal*, *loneliness*. The supporting phrases are more general in nature. They have no power as keywords, according to them, we can determine whether a person has or does not have the problem of psychological nature. They include phrases like: *leave me alone*, *it's somehow turns out*, *I do not want to deal with*. The reference texts are the full texts in sentences, to illustrate how could the description of an individual personality disorder appear.

After the first draft looking for similarities between the words of the text, we decided to use approach based on machine learning algorithms. For this process is necessary to select and extract the correct features of texts that are inputs to the classifiers. Our chosen solution is shown in Table 1.

The features 1–3 means similarity value between compared self-essay and each of three personality disorder models. Similarity is expressed as origin Dice coefficient [11], Eq. 1.

$$d(A,B) = \frac{2\sum_{i=1}^{|A\cap B|} a_i}{|A|\cup|B|} \tag{1}$$

where A and B are sets of compared keywords, a is keyword, $a \in A \cap B$, $d_{y,i}$, is difference between actual year and author's publication of attribute a_i.

Table 1 Model of extracted feature used for classification

Feature no.	Name
1–3	Keywords similarity
4–6	Support phrases similarity
7–9	Reference text similarity
10	Polarity

The features 4–6 are again similarity, but for supporting phrases in reference models, 7–9 means similarity between whole compared text and personality disorders models' reference texts. The last 10th feature represents polarity of text, the sentiment in other words. All available compared texts had negative polarity, so we assume one of the sign of personality disorder is negativity in user self-essay.

To obtain these features is needed to properly adjust the text yet. For this purpose we use the library for Python NLTK [12] and a Czech text parser Morphodita [13]. The text in the first step goes through natural language processing. Firstly, we prepare text for following Morphodita parser to get better results. The excess blank spaces and special characters are removed, possible errors in text, like missing comma accents characters, are corrected. In next step modified text is parsed by Morphodita. We retrieve information about structure of sentences, lemmas, words' part-of-speech, named entities and label whether examining word is negated or not. During our examination we found that the decisive word and phrases are often adjectives, verbs and adverbs, so for these the weight-term is increased. The polarity is estimated by these acquired data. Before finding similarities between reference models are removed stop-words, named entities as *Person*, *Place* which could cause noise in the resulting comparison. Solving similar problem with similar approach, but for Slovak language, is mentioned in work [14].

4 Self-essay Polarity

To determine polarity–sentiment of self-essay we continue are previous research [2]. In the Czech language, we meet with ways to create sentences that complicate the analysis of sentiment. These include the use of double negation, which turns the original idea and gives it the opposite meaning. We use a lexicon approach in combination with sentence analysis. The method is shown in Fig. 2.

Firstly we process text to be more unified, the steps described in previous Chapter are used. We define three sets of words (lexicons): *polarity phrases*, *polarity strengths* and *exceptions*. The polarity phrases contains possible words and phrases occurring in texts that describes the moods and feelings of people written in the first person, so they could be considered as self-essays to identify personality disorders. The second lexicon, polarity strengths, contains phrases with defined strength of polarity. Values are in interval $\langle -2; 2 \rangle$ where -2 is strongly negative and 2 is strongly positive. For each found word or phrases in analyzed self-essay is assigned the right value from lexicon. The last lexicon, exceptions, rules defines exceptions for special cases appearing in Czech language. It is, e.g. double negation, where the rule switch found polarity to the other or shift it to another word.

The step of formula transformation is probably the most important in whole algorithm. A sentence is transformed to formula which is later evaluated for the polarity. In this phase the words and phrases are searched in the all three lexicons and found expressions are evaluated for the final sentiment. The chance of finding match between text and lexicons is increased by performed lemmatization. This

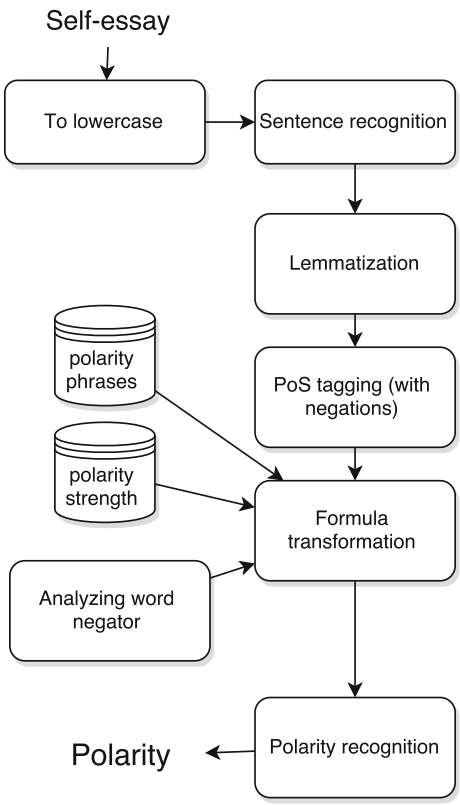

Fig. 2 Polarity analysis in self-essays

step is very important especially for Slavic languages where inflection of words is various. When the formula is evaluated polarity can be recognized. The result is an polarity class which is based on polarity value from interval $\langle -2; 2 \rangle$ and named as *megative2*, *negative1*, *neutral*, *positive1*, *positive2*. There is also a list of all related polarity classes. Unfortunately, from this results it can be difficult sometimes to decide about polarity, so sometimes human intervention could be necessary.

5 Finding Personality Disorders

For finding and identifying the personality disorders in written self-essays we choose a way of learning classifiers by training datasets. For this purpose we use the Python library scikit-learn.[1] The four classifiers were selected: Multi-Class Support Vector Machine, k-Nearest Neighbors classifier, Decision Trees.

[1] http://scikit-learn.org/.

5.1 Multi-class Support Vector Machine

Support Vector Machine (SVM) [15] are supervised learning models with associated learning algorithms. The task classification SVM searches hyperplane in the feature space optimally divides the training data. The optimal hyperplane is such that the points located in the opposite half-space and the value of the minimum distance points from the plane is the greatest. In other words, around hyperplane it is on both sides of the widest streak without points (the maximum distance, maximal margin). On description hyperplane simply the closest points which is usually little—these points are called support vectors. This method is binary by their nature, thus divides the data into two classes. Dividing hyperplane is linear in the feature space.

Since we want to classify more than two classes, a special version Multi-Class SVN [16] is used. In this case is created $n_{class} * (n_{class} - 1)/2$ classifiers, where n_{class} means number of classes.

5.2 K-Nearest Neighbors Classifier

K-Nearest Neighbors classifier (KNN) is a method of supervised learning, which are classified elements represented by multidimensional vectors into two or more classes. In the learning phase is pretreated training set, so that all symptoms had a mean value of 0 and variance 1—This places each element of the training set to some point in N-dimensional space. Classification stage will put the interviewee element into the same space and find the nearest neighbors. The object is then classified into the class where most of those closest neighbors.

5.3 Decision Trees

Decision Trees (DT) [17] are a non-parametric supervised learning method used for classification and regression. are one of the most popular data mining techniques. The reasons for the application of these techniques are several. The main reason lies in its clarity and ease of interpretability, which allows users to quickly and easily evaluate the results and identify key items and retrieve interesting segments of the cases. The aim of the decision tree is to identify the objects described by different attributes to classes. We can imagine them as rows in a table, where each column of attributes (color of eyes, length of the tail). Since it is a tree, the algorithm is very fast. A decision tree must first create a set of given trained dataset.

5.4 Naive Bayes

Naive Bayes (NB) [18] methods are a set of supervised learning algorithms based on applying Bayes' theorem with the naive assumption of independence between every pair of features. NB learners and classifiers can be extremely fast compared to more sophisticated methods. The decoupling of the class conditional feature distributions means that each distribution can be independently estimated as a one dimensional distribution. This in turn helps to alleviate problems stemming from the curse of dimensionality.

6 Experiments

Since we modified algorithm of polarity-sentiment analysis, especially change content of lexicons, we had to verify ability of polarity decision, as well as abilities of each classifiers.

6.1 Verifying Polarity-Sentiment Analysis

To test the polarity analysis, we used 100 real posts similar to self-essays. We examined five levels polarity: *negative2*, *negative1*, *neutral*, *positive1*, *positive2*. Results are in Table 2.

In the first column is retrieved polarity level. Last column is F-Measure result, the popular measurement of a test's accuracy which is defined in Eq. 2.

$$F = 2 \times \frac{precision \times recall}{precision + recall} \tag{2}$$

The experiment showed slightly worse results compared to the results achieved in the original article. This may be caused by using new lexicons, but will also play the role of subjectivity that occurs when evaluating sentiment. Posts can be labeled according to subjective opinion to a different level than it would be evaluated by other person.

Table 2 Verification of polarity analysis

Level	F-measure (%)
Negative2	80
Negative1	73
Neutral	82
Positive1	72
Positive2	80

Table 3 Verification of classifiers to identify types of personality disorders

Classifier	Correct healthy	Correct sick	F-measure (%)
SVN	21/30	34/60	72.4
KNN	20/30	31/60	67.7
NB	20/30	32/60	69.1
DT	17/30	27/60	54.8

6.2 Verifying Classifiers

At this early stage, we tested mentioned classifier to decide if compared self-essay has signs of personality disorders and which type it has. For testing purpose were chosen posts from online advice forum on web site ulekare.cz.[2] We manually selected 90 posts of them. Posts were divided into groups. The first group of 60 posts were texts which have replied by specialists containing possible diagnoses of personality disorder. The second group contained 30 posts of texts which had characteristics of self-essay, but were positive, without signs of personality disorders. The posts were also written as self-essays, samples are very close to real data which will be inputted in preparing web system (Table 3).

The trained dataset consists of 30 retrieved posts and next 10 real self-essays obtained from specialist. The tested dataset contained 30 posts from web site ulekare.cz. The Table 4 describes results of first simple self-essay classification, if it has any kind of personality disorder or was written by mentally healthy user.

In the first column is shown name of classifier method. The second column describes how many of healthy self-essay were correctly detected. The third column summarize number of correctly detected self-essays containing one of three personality disorders. The last column contains F-measure.

As the table shows, the best results reaches the SVN classifier with F-Mesaure 72 %. It correctly identified 21 of 30 healthy posts and 34 of 60 sick posts. The second best result achieved NB with F-Mesaure equals to 69.1 %. The third was K-NN with 67.7 % and last one is DT classifier with F-Measure only 54.8 %.

In the second phase we tested classifiers to verify an ability to deal with categorization of sick self-essay to the right personality disorder category. The same classifiers were chosen. Results are shown in table

The first columns labels used classifier. In the second column is shown number of self-essays which were identified to correct personality disorder category (one of fear, procrastination and intolerance of uncertainty). The third column describes wrongly categorized self-essays and in last column is again the F-measure of classifier. The best results were given by SVN again. It correctly identified 44 from 60 self-essays with F-measure 73 %. Similar results were in cases in KNN and NB.

[2] http://www.ulekare.cz/poradna-lekare.

Table 4 Verification of classifiers to identify healthy self-essays and personality disorders

Classifier	Rightly identified	Wrongly identified	F-measure (%)
SVN	44	16	73
KNN	39	21	64
NB	40	20	65
DT	35	25	61

They returned 39 and 40 correctly identified personality disorders, F-Measure was 64 % for KNN and 65 % for NB. The worst result was returned by DT classifier, but not so significantly as in the previous experiment. F-Measure was 61 %.

7 Conclusion

The main goal of this work was to create method to identify personality disorders in self-essays, the texts summarizing feelings and mood of user. We have chosen a different way of document classification. For features extraction are used similarity with reference models by Dice coefficient and modified polarity-sentiment analysis from our previous research. Identification of personality disorders were decided by well-known classifiers: Multi-Class Support Vector Machine, K-Nearest Neighbors Classifier, Decision Tree and Naive Bayes. In the case of modified sentiment analysis success ratio stay around 72–82 % as in previous research. Slightly worse results were caused by modified lexicons and subjective evaluation polarity of tested posts. The identification of disorders was tested by real dataset of 90 posts from online advice forum. Firstly was verified ability of recognition if tested self-essay is or is not one with personality disorders. The best result achieved the SVM with F-measure 72 %. Secondly, the categorization into individual personality disorders was tested. From previous dataset were selected 60 sick posts and classified with same classifiers. The best one was again the SVM with F-Measure around 71 %.

The next research will aim to increase the training dataset for classifiers and improving and to improve the success rate of identifying the correct personality disorders. We also want to continue in sentiment analysis and add more sophisticated features for sentiment evaluation.

Acknowledgment The following grant are acknowledged for the financial support provided for this research: Technology Agency of the Czech Republic—TACR-TF01000091, partially supported by Grant of SGS No. SP2015/142, VSB—Technical University of Ostrava.

References

1. Saloun P, Ondrejka A, Zelinka I (2014) Similarity of authors' profiles and its usage for reviewers' recommendation. In: 9th international workshop on semantic and social media adaptation and personalization, SMAP 2014, Corfu, Greece, November 6–7, pp 3–8. http://dx.doi.org/10.1109/SMAP.2014.31
2. Saloun P, Hruzik M, Zelinka I (2013) Sentiment analysis—e-bussines and e-learning common issue. In: IEEE 11th international conference on emerging eLearning technologies and applications (ICETA), pp 339–343
3. Zhang J, Niu Y, Nie H (2009) Web document classification based on fuzzy k-nn algorithm. In: International conference on computational intelligence and security, 2009. CIS '09, vol 1, pp 193–196
4. Li Q, He L, Lin X (2013) Categorical term frequency probability based feature selection for document categorization. In: International conference of soft computing and pattern recognition (SoCPaR), pp 66–71
5. Li CH, Song W, Park SC (2009) An automatically constructed thesaurus for neural network based document categorization. Expert Syst Appl 36(8):10 969–10 975. http://dx.doi.org/10.1016/j.eswa.2009.02.006
6. Polajnar T, Aggarwal N, Asooja K, Buitelaar P (2013) Improving ESA with document similarity. In: Serdyukov P, Braslavski P, Kuznetsov S, Kamps J, Rger S, Agichtein E, Segalovich I, Yilmaz E (eds) Advances in information retrieval. Lecture notes in computer science, vol 7814. Springer, Berlin, pp 582–593
7. Li P, Li Z, Liu H, He J, Du X (2009) Using link-based content analysis to measure document similarity effectively. In: Li Q, Feng L, Pei J, Wang S, Zhou X, Zhu Q-M (eds) Advances in data and web management. Lecture notes in computer science, vol 5446. Springer, Berlin, pp 455–467
8. Islam A, Inkpen D (2008) Semantic text similarity using corpus-based word similarity and string similarity. ACM Trans Knowl Disc Data 2(2):10:1–10:25. http://doi.acm.org/10.1145/1376815.1376819
9. Turney PD, Pantel P (2010) From frequency to meaning: Vector space models of semantics. J Artif Int Res 37(1):141–188. http://dl.acm.org/citation.cfm?id=1861751.1861756
10. Thada V, Jaglan DV (2013) Comparison of jaccard, dice, cosine similarity coefficient to find best fitness value for web retrieved documents using genetic algorithm. Int J Innov Eng Technol 2(4):202–205
11. Oco N, Romeritch Syliongka L, Roxas R, Ilao J (2013) Dice's coefficient on trigram profiles as metric for language similarity. In: Oriental COCOSDA held jointly with 2013 conference on Asian spoken language research and evaluation (O-COCOSDA/CASLRE), 2013 international conference, pp 1–4
12. Bird S, Klein E, Loper E (2009) Natural language processing with python, 1st edn. O'Reilly Media, Inc., Sebastopol
13. Straková J, Straka M, Hajič J (2014) Open-source tools for morphology, lemmatization, pos tagging and named entity recognition. In: Proceedings of 52nd annual meeting of the association for computational linguistics: system demonstrations. Baltimore, Maryland: association for computational linguistics, pp 13–18. http://www.aclweb.org/anthology/P/P14/P14-5003.pdf
14. Machova K, Marhefka L (2014) Opinion classification in conversational content using n-grams. In: Badica A, Trawinski B, Nguyen NT (eds) Recent developments in computational collective intelligence. Studies in computational intelligence, vol 513. Springer International Publishing, pp 177–186
15. Cortes C, Vapnik V (1995) Support-vector networks. Mach Learn 20(3):273–297. http://dx.doi.org/10.1023/A:1022627411411

16. Wu T-F, Lin C-J, Weng RC (2004) Probability estimates for multi-class classification by pairwise coupling. J Mach Learn Res 5:975–1005. http://dl.acm.org/citation.cfm?id=1005332.1016791
17. Abdelhalim A, Traore I (2009) A new method for learning decision trees from rules. In: International conference on machine learning and applications, ICMLA'09, pp 693–698
18. Zhang H (2004) The optimality of naive bayes. In: Barr V, Markov Z (eds) Proceedings of the seventeenth international Florida artificial intelligence research society conference (FLAIRS 2004). AAAI Press

Part IV
Power System

Compare Different Recent Methods and Propose Improved Method for Risk Assessment of Damages Due to Lightning

Quyen Huy Anh, Le Quang Trung and Phan Chi Thach

Abstract This paper compares and analyzes the different methods of risk assessment of damages due to lightning in IEC 62305-2 and AS/ANZ 1768 standards. From there, proposes the improved method based on the calculation method recommended by IEC 62305-2 standard, with some additional and more detailed calculation formulas proposed by AS/ANZ 1768 standard and the shielding factors along the distribution line proposed by IEEE 1410 standard. The LIRISAS program for calculating the risk of damages due to lightning is built on the proposed method, has the reliable result, high accuracy and the user utility.

Keywords Risk assessment due to lightning · Damage caused by lightning · Lightning protection

1 Introduction

Vietnam is a country which has monsoon tropical climate, so lightning activity is at a high level and the risk of damage caused by lightning is very serious. Currently, the selection of lightning protection solutions for structures mainly based on experience and preliminary calculation, not based on the results of risk assessment of damage due to lightning. In the world and our country there have currently been a lot of standards and researches on risk assessment of damages caused by lightning, such as: IEC 62305-2 [1, 8–10]; AS/ANZ 1768 [2]; BS EN: 62305 [4];

Q.H. Anh (✉) · L.Q. Trung · P.C. Thach
Faculty of Electrical & Electronics Engineering,
University of Technical Education HCM City, Ho Chi Minh City, Vietnam
e-mail: anhqh@hcmute.edu.vn

L.Q. Trung
e-mail: trungttc276@yahoo.com.vn

P.C. Thach
e-mail: phanchithach12@gmail.com

V.H. Duy et al. (eds.), *AETA 2015: Recent Advances in Electrical Engineering and Related Sciences*, Lecture Notes in Electrical Engineering 371,
DOI 10.1007/978-3-319-27247-4_14

NFPA 780 [5]; ITU-T K.39 [6]; QCVN 32:2011/BTTTT [7];…, each of which has its own advantages, risk assessment approaches and ranges of applications. In particular, the IEC 62305-2 standard and AS/ANZ 1768 standard are the most generic and detailed. For appropriate lightning protection measures adequate to the nature and current status of the structure, and lightning activity in the region. The construction of improved method of risk assessment caused by lightning with the detailed level of the input parameters shall be carried out to bring the accuracy results and the reasonable solutions for lightning protection.

2 Comparison of Risk Components and Proposal for Improvement

2.1 *Risk Components Related to Injury to Living Beings When Lightning Strikes to the Structure*

1. Comparison of risk components related to injury to living beings when lightning strikes to the structure (Table 1):

Where: R_A, R_h are the risk of injury to living beings; N_D, N_d are the number of dangerous events due to flashes to structure; A_D, A_d are the collection area for flashes to structure; C_D, C_d are the location factor; L_A, δ_h are loss of human life; P_A, P_h are the probability of injury to living beings by electric shock due to touch and step voltage; P_{TA} is the probability reducing P_A depending on protection measures against touch and step voltages; p_B is the probability of physical damage to a structure, p_h is the probability that lightning will cause a shock to human being; k_I is the reduction factor for structure lightning protection system; p_s is the probability of a dangerous discharge based on construction materials of the structure.

From the Table 1 above, we can see the difference in the calculation of the probability of shock to living beings due to touch and step voltage ($P_{A,}$ P_h) when lightning strikes to the structure. Whereas, in [2] with the additional probability of a dangerous discharge based on construction materials of the structure (p_s).

2. Proposal for improvement:

To increase the accuracy of the probability P_A for risk component R_A in [1], the probability of dangerous discharge based on structure construction materials (p_s) should be added as follows:

$$P_A = k_1 \times P_h \times p_s \tag{1}$$

Table 1 Risk of injury to living beings when lightning strikes to the structure

IEC 62305-2 [1]	AS/ANZ 1768 [2]
$R_A = N_D \times P_A \times L_A$	$R_h = N_d \times P_h \times \delta_h$
$N_D = N_G \times A_D \times C_D \times 10^{-6}$	$N_D = N_g \times A_d \times C_d$
$P_A = P_{TA} \times p_B$	$P_h = k_1 \times p_h \times p_s$

2.2 Risk Components Related to Physical Damages Due to Lightning Strikes to the Structure

1. Comparison of risk component related to physical damages due to lightning strikes to the structure (Table 2):

Where: R_B, R_s are the risk of physical damage; N_D, N_d are the number of dangerous events due to flashes to structure; P_B is the probability of physical damage to a structure; L_{Bi} (i = 1,4) is the loss in structure related to physical damage; P_s is the probability a direct strike to structure will cause physical damage, δ_f is the damage factor for fire, k_h is the increasing factor for fire and overvoltage; r_p is the factor reducing loss due to provisions against fire; r_f is the reducing loss depending on risk of fire; h_z is the factor increasing the loss when special hazard present; L_F is the loss in the structure due to physical damage; n_z is the number of possible endangered persons; n_t is the expected total number of person, t_z is the time in hours per year that persons are present in a dangerous place; k_f is the reduction factor for fire protection; p_f is the probability that a dangerous discharge will initiate a fire, explosion; k_1 is the reduction factor for structure lightning protection system; p_s is the probability of a dangerous discharge based on construction materials of the structure; P_{ewd} is the probability that external wiring carries a surge from structure that cause physical damage; c_a is the value of animals in the zone; c_b is the value of the building relevant to the zone; c_c is the value of the content in the zone; c_s is the value of internal systems; c_t is the total value of the structure.

From Table 2 above, we can see the level of details when calculating the probability P_s in [2] compared with the probability P_b selected from the table in [1]. However, the reduction factor for fire protection k_f and the probability of lightning discharges cause fire, explosion, mechanical destruction or chemical release p_f in [2] are corresponding to two coefficients r_p and r_f in equations of calculating coefficient L_{Bi} in [1].

2. Proposal for improvement:

To increase the accuracy of the probability P_B for risk component R_B in [1], the probability that external wiring carries a surge from structure that causes physical damage (P_{ewd}) and the probability of dangerous discharge based on structure construction materials (p_s) should be added as follows:

$$P_B = k_1 \cdot p_s + P_{ewd} \tag{2}$$

Table 2 Risk of physical damage due to lightning strikes to the structure

IEC 62305-2 [1]	AS/ANZ 1768 [2]
$R_B = N_D \times P_B \times L_{Bi}, (i = 1, 4)$ $L_{B1} = r_p \times r_f \times h_z \times L_F \times n_z/n_t \times t_z/8760$ $L_{B4} = r_p \times r_f \times L_F \times (c_a + c_b + c_c + c_s)/c_t$	$R_s = N_d \times P_s \times \delta_f \times k_h$ $P_s = k_f \times p_f \times (k_1 \times p_s + P_{ewd})$

2.3 Risk Components Related to Failure of Internal Systems Due to Lightning Strikes to the Structure

1. Comparison of risk components related failure of internal systems due to lightning strikes to the structure (Table 3):

Where: R_C, R_w are the risk of failure of internal systems when lightning strikes directly to the structure risk of physical damage; N_D, N_d are the number of dangerous events due to flashes to structure; P_C, P_w are the probability of failure of internal systems; L_C is the loss related to failure of internal systems; δ_0 is the damage factor for overvoltage, k_h is the increasing factor for fire and overvoltage; P_{SPD} is the probability reducing P_C when coordinated SPD (surge protected devices); C_{LD} is the factor depending on grounding and isolation condition, k_1 is the reduction factor for structure lightning protection system; p_s is the probability of a dangerous discharge based on construction materials of the structure; p_i is the probability of a dangerous discharge based on internal wiring type; k_2 is the reduction factor for isolation equipment on internal equipment; k_3 is the reduction factor for SPD on input of equipment, k_w is the correction factor for impulse level of equipment; P_{ewd0} is the probability that external wiring carries a surge from structure that cause a damaging overvoltage to internal equipment.

According to [1, 2] and from Table 3 above, the probability P_W in [2] is calculated more detail when considering the factors such as: the probability of dangerous discharge based on structure construction materials (p_s); the probability of dangerous discharge based on internal wiring type (p_i); reduction factor for surge protective device on input of equipment (k_3); correction factor for impulse level of equipment (k_w) and probability that external wiring carries a surge from structure that causes a damaging overvoltage to internal equipment (P_{wedo}).

2. *Proposal for improvement:*

When calculating the probability of failure of internal systems due to lightning strikes to the structure P_C in [1], the coefficients such as calculated probability P_w in [2] should be added as follows:

$$P_C = 1 - (1 - k_1 \times p_s \times p_i \times k_2 \times k_3 \times k_w)(1 - P_{ewd0}) \tag{3}$$

Table 3 Risk of internal systems due to lightning strikes to the structure

IEC 62305-2 [1]	AS/ANZ 1768 [2]
$R_C = N_D \times P_C \times L_C$ $P_C = P_{SPD} \times C_{LD}$	$R_w = N_d \times P_w \times \delta_0 \times k_h$ $P_w = 1 - (1 - k_1 \times p_s \times p_i \times k_2 \times k_3 \times k_w)(1 - P_{ewd0})$

2.4 Risk Components Due to Lightning Strikes to and Near Service Lines

1. *Comparison of risk components due to lightning strikes to and near service lines (Table 4):*

Where: P_U, P_V, P_W, P_Z are the probability of injury to living beings, physical damage, failure of internal systems due to lightning strikes to service lines and failure of internal systems due to lightning strikes near service lines; P_{TU} is the probability depending on protection measures against touch voltages; P_{EB} is the probability reducing P_U and P_V depending on line characteristics and withstand voltage of equipment when equipotential bonding is installed, P_{LD} is the probability reducing P_U and P_V depending on line characteristics and withstand voltage of equipment when lightning strikes to service lines; C_{LD} is factor depending on shielding, grounding and isolation conditions of the line for flashes to a line; P_{SPD} is the probability reducing P_C when coordinated SPD; k_5 is the reduction factor for sure protective device on entry point of service line; P_{c1p}, P_{c1} are the probability direct strike to overhead power line and to other overhead line will case a damaging overvoltage to internal equipment; P_{c2p}, P_{2p} are the probability direct strike to underground power line and to other underground line will case a damaging overvoltage to internal equipment; n_{ohp}, n_{oh} are the number of overhead power line and other overhead line; n_{ugp}, n_{ug} are the number of underground power line and other underground line; P_{e0}, P_{e1} are the probability of dangerous discharge based on external wiring type of power line and other line; P_{e2} is the probability of dangerous discharge based on external service type.

From Table 4, we can see that when calculating the probability of lightning strikes directly and indirectly to service lines in [2], the number of overhead lines n_{oh} and the number of underground lines n_{ug} connected to the structure should be considered.

2. Proposal for improvement:

To increase the accuracy when calculating P_U, P_V, P_W, and P_Z, the number of service lines should be added. The equations for calculating P_U, P_V, P_W, and P_Z for overhead lines are defined as follows:

$$P_{U/oh} = P_{TU} \times P_{EB} \times P_{LD} \times C_{LD} \times n_{oh} \tag{4}$$

$$P_{V/oh} = P_{EB} \times P_{LD} \times C_{LD} \times n_{oh} \tag{5}$$

Table 4 The probability for the risk components when lightning strikes to and near service lines

IEC 62305-2 [1]	AS/ANZ 1768 [2]
$P_U = P_{TU} \times P_{EB} \times P_{LD} \times C_{LD}$	$P_{c1p} = n_{ohp} \times k_5 \times P_{e0}$
$P_V = P_{EB} \times P_{LD} \times C_{LD}$	$P_{c1} = n_{oh} \times k_5 \times P_{e1}$
$P_W = P_{SPD} \times P_{LD} \times C_{LD}$	$P_{c2p} = n_{ugp} \times k_5 \times P_{e0}$
$P_Z = P_{SPD} \times P_{LI} \times C_{LI}$	$P_{c2} = n_{ug} \times k_5 \times P_{e2}$

$$P_{W/oh} = P_{SPD} \times P_{LD} \times C_{LD} \times n_{oh} \tag{6}$$

$$P_{Z/oh} = P_{SPD} \times P_{LI} \times C_{LI} \times n_{oh} \tag{7}$$

And the equations for calculating P_U, P_V, P_W and P_Z for underground lines are defined as follows:

$$P_{U/ug} = P_{TU} \times P_{EB} \times P_{LD} \times C_{LD} \times n_{ug} \tag{8}$$

$$P_{V/ug} = P_{EB} \times P_{LD} \times C_{LD} \times n_{ug} \tag{9}$$

$$P_{W/ug} = P_{SPD} \times P_{LD} \times C_{LD} \times n_{ug} \tag{10}$$

$$P_{Z/ug} = P_{SPD} \times P_{LD} \times C_{LI} \times n_{ug} \tag{11}$$

2.5 *Shielding Factor for Calculating the Number of Lightning Strikes to and Near the Overhead Service Lines*

1. Shielding factor in IEEE 1410 [10]:

When calculating the number of lightning strikes to and near the overhead service lines N_L and N_l, in [1]. The coefficients such as: installation factor C_l; environmental factor C_E, and line type factor C_T as in Eqs. (12) and (13) are mentioned.

$$N_L = N_G \times A_L \times C_l \times C_E \times C_T \times 10^{-6} \tag{12}$$

$$N_l = N_G \times A_l \times C_l \times C_E \times C_T \times 10^{-6} \tag{13}$$

Where: N_G is the lightning ground strikes density (strikes/km^2/year); A_L is the collection area for strikes to the service lines (m^2); A_l is the collection area for strikes near the service lines (m^2).

However, environmental factor C_E in Eqs. (12) and (13) without reference to the terrain where the service lines go through as: the pole height h, the horizontal distance between the outer wires b and shielding factor S_f of the object height H, the distance to the service line x (Fig. 1), and in this case, the number of lightning strikes directly to line service follow [3] is determined by equation:

$$N_L = N_G \times C_f \times 10^{-6} \tag{14}$$

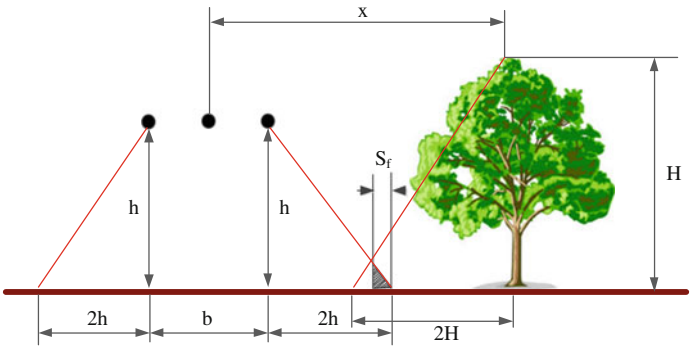

Fig. 1 Shielding power line by nearby object

Where: C_f is the reduction factor due to the shielding of the objects near the line. C_f is defined as follow:

$$C_f = (b + 28h^{0.6})10^{-1}(1 - S_f) \tag{15}$$

2. Proposal for improvement:

To improve accuracy when calculating the number of lightning strikes directly and indirectly on the overhead service lines, coefficient C_E in (12) and (13) should be replaced by the coefficient C_f defined in (15). The number of lightning strikes to and near overhead service lines is defined by the following equations:

$$N_L = N_G \times A_L \times C_l \times C_f \times C_T \times 10^{-6} \tag{16}$$

$$N_l = N_G \times A_l \times C_l \times C_f \times C_T \times 10^{-6} \tag{17}$$

3 Calculate the Risk of Damages Due to Lightning by Improved Method

3.1 The Program Calculates the Risk of Damages Due to Lightning LIRISAS

The program calculating the risk assessment of damages due to lightning LIRISAS is built on the basis of improved method of risk assessment in Sect. 2. Flowchart of the program is shown in Fig. 2.

In LIRISAS program, the user enters the structure dimensions, the lightning ground strikes density, number and length of service lines connected to the structure; and allows users to choose the types of structure risk assessment needed correspond to the types of damage, the elements of environmental conditions,

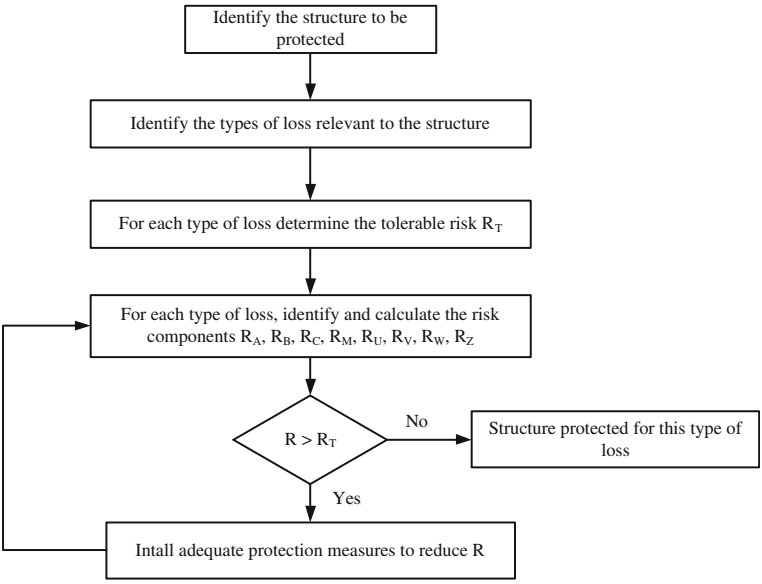

Fig. 2 Flowchart of the program calculates the risk assessment of damage due to lightning. *Note* R_T is the tolerable risk; R_A is the risk of injury to living beings, R_B is the risk of physical damage, R_C is the risk of failure of internal systems when lightning strikes directly to the structure; R_M is the risk of failure of internal systems when lightning strikes near the structure; R_U is the risk of injury to living beings, R_V is the risk of physical damage, R_W is the risk of failure of internal systems when lightning strikes directly to the service lines; R_Z is the risk of failure of internal systems when lightning strikes near the service lines; R is the total value of risk

construction materials, fire prevention and protection measures, the existing lightning protection measures… the program will calculate the results of risk of damage caused by lightning for the structure.

3.2 *Case Study*

- Calculation of risk assessment of damage due to lightning for a commercial building (**Fig. 3**) in Ho Chi Minh City.
- Structure dimensions: 20 × 15 × 35 m
- Lightning density: 12 (strikes/km^2/year) [11], no other buildings nearby.
- Power line has a length of 200 m, overhead; telecommunication cable has a length of 1000 m, underground.

The results of risk of damage caused by lightning for risk of loss of human life in structure R_1 and risk of loss of economic value in structure R_4 are calculated by IEC 62305-2 and LIRISAS program as follow:

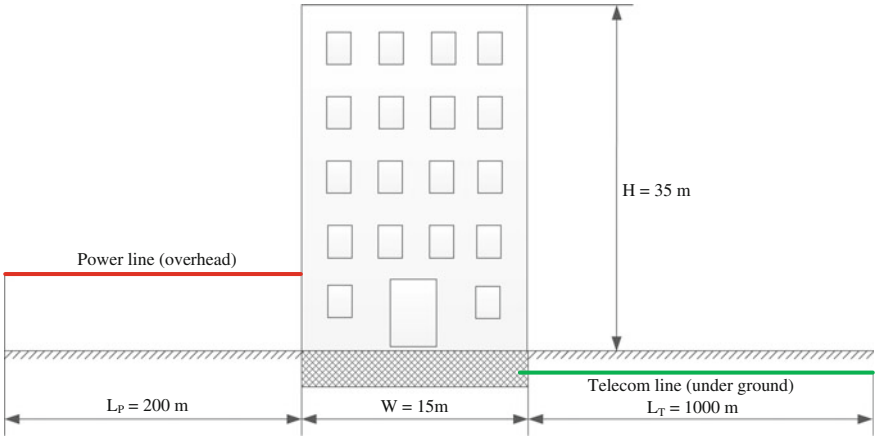

Fig. 3 The structure need to assess the risk of damage due to lightning

Table 5 The risks of value of the building

Type of risk of damage	IEC 62305-2 [1]	LIRISAS	Tolerable risk R_T
R_1	1.24×10^{-4}	3.25×10^{-5}	10^{-5}
R_4	0.255	0.222	10^{-3}

From Table 5, the results of risk assessment are calculated by LIRISAS program are lower than 26.2 % for R_1 and 12.95 % for R_4 compared with the results calculated by IEC 62305-2.

4 Conclusions

The paper compared different calculation methods of risk assessment of damage due to lightning in IEC 62305-2 and AS/ASZ 1768. The proposal for improving the accuracy level of the probability coefficient for risk components in IEC 62305-2 based on additional coefficients such as: the probability of dangerous discharge based on structure construction materials; the probability that external wiring carries a surge from structure that causes physical damage; number of incoming services line; shielding factor according to IEEE 1410 standard has also been added in the calculation of the number of lightning strikes directly and indirectly to the overhead service lines.

The improved calculation method of risk assessment caused by lightning has lower results with greater detail than the previously methods. It appears from this, the investment costs for lightning protection system will be reduced, while ensuring the technical requirements for structures against lightning.

LIRISAS program built to support the risk assessment calculations for damage caused by lightning with intuitive interface helps users easily manipulated, for quick and more accurate results.

Acknowledgments This research was supported by Ho Chi Minh City University of Technology and Education under a research at the Electrical Power System and Renewable Lab.

References

1. A guide to BS EN 62305:2006 (2006) Protection against lightning
2. AFPA 780 (2004) Standard tor the installation of lightning protection systems
3. Australian/New Zealand Standard (2007) Lightning protection
4. IEC 62305-2 (2010) Protection against lightning—part 2: risk management
5. IEEE 1410 (2004) Guide for improving the lightning performance of electric power overhead distribution lines
6. ITU-T Recommendation K.39 (1996) Risk assessment of damages to telecommunication sites due to lightning discharges
7. Kern A, Braun C (2014) Risk management according to IEC 62305-2 edition 2:2010-12. In: Assessment of structures with a risk of explosion. International conference on lightning protection (ICLP). Shanghai, China
8. Lo Piparo GB, Kern A, Mazzetti C (2012) Some masterpoints about risk due to lightning. In: International conference on lightning protection (ICLP). Vienna, Austria
9. Mata CT, Bonilla T (2012) Lightning risk assessment tool, implementation of the IEC 62305-2 standard on lightning protection. In: International conference on lightning protection (ICLP). Vienna, Austria
10. QCVN 32: 2011/BTTTT (2011) National technical regulation on lightning protection for telecommunication stations and outside cable network
11. TCXDVN 9385:2012 (2012) Protection of structures against lightning-Guide for design, inspection and maintenance

An Improvement Forward Floating Search Algorithm for Feature Selection in Power System Transient Stability Classification

Ngoc Au Nguyen, Huy Anh Quyen, Trong Nghia Le and Thi Thanh Binh Phan

Abstract This paper proposed feature selection algorithm in power system transient stability classification. Feature selection is a very important stage aimed at reducing a number of features, retaining distinctive features to reduce memory, increasing identification accuracy. The proven effectiveness of Improvement Forward Floating Search algorithm (IFFS) was compared with Sequential Forward Selection (SFS), Sequential Forward Floating Selection algorithm (SFFS) and Relief algorithm through analysis of results in power system transient stability classification using K-Nearest Neighbour (K-NN) on IEEE 30-bus standard power network. The analytical results showed that the IFFS achieved effective reduction features and recognition accuracy higher than other methods.

Keywords Classification/pattern recognition · Feature selection · Power system · Sequential forward selection

1 Introduction

Large oscillations of power system transient stability state were caused by faults that must be treated quickly so that the power system can be brought back to stability more easily. The problem of transient stability is usually divided into two

N.A. Nguyen (✉) · H.A. Quyen · T.N. Le · T.T.B. Phan
HCM City University of Technology and Education, Ho Chi Minh City, Vietnam
e-mail: ngocau@hcmute.edu.vn

H.A. Quyen
e-mail: anhqh@hcmute.edu.vn

T.N. Le
e-mail: trongnghia@hcmute.edu.vn

T.T.B. Phan
e-mail: thanhbinh055@yahoo.com

V.H. Duy et al. (eds.), *AETA 2015: Recent Advances in Electrical Engineering and Related Sciences*, Lecture Notes in Electrical Engineering 371,
DOI 10.1007/978-3-319-27247-4_15

main categories [1]: assessment [2] and prediction [3]. The key question in transient stability prediction is: the transient swings are finally 'Stable' or 'Unstable' [1, 3, 4]. Pattern recognition or classification method is one of the methods that can meet this requirement and has received great attention of researchers in recent years [1, 3, 5, 6]. However, the recognition system can work quickly, the first thing is to handle features that aim to reduce feature subset size.

Feature selection is actually feature reduction that helps reducing computer memory, improving recognition accuracy and speeding prediction up. In [3] applied ranking method (R) and SFS, sequential backward search (SBS) with distance function Fisher, Divergence and weighting method relief. The Relief algorithm is weight method. Features were ranked in descending order then the top of features was selected. The ranking method has advantages that are simple calculations, but a good subset feature is not guaranteed to be formed by many good single features. In [6] applied SFS for feature selection. Sequential search algorithm includes SFS, SBS, SFFS and sequential backward sequential search algorithm (SBFS). SBS started searching with whole feature set, so SBS has difficulty in calculating the value of covariance matrix or even can not calculate with a large number of features. SBFS is more complex than SBS. SFS is an advantage over SBS because of starting with an empty feature set. During the search, SFFS searches with forward and backward combination, so it can expand more space search than the SFS. In [7], Authors proposed the IFFS algorithm. It was improved from SFFS algorithm. The process backward of searching was extended to finding and replacing a weak feature by a new good feature to improving current subset feature.

The IFFS was presented in this paper as a new algorithm approach to feature selection in power system transient stability prediction. Scatter matrix was chosen as fitness function to driving search algorithm. This paper focused on the stage of feature selection. The K-NN was chosen as the classifier. The K-NN participated in the evaluating recognition accuracy stage. The IFFS was compared with the SFS, SFFS and Relief algorithm. The study was done on IEEE 30-bus power network with the support of simulation software PowerWorld 18.

2 Method

2.1 Scatter Matrix [8, 9]

Let the n data samples be $x_1, x_2, \ldots, x_N$; n = [1, N]. The sample covariance matrix, S_m, is given by (1):

$$S_m = \frac{1}{N}\sum_{n=1}^{N}(x_n - m)(x_n - m)^T \tag{1}$$

S_W, within-class scatter matrix, is:

$$S_w = \frac{1}{N}\sum_{i=1}^{c}\frac{N_i}{N}S_i \tag{2}$$

$$S_i = \frac{1}{N_i}\sum_{x_n \in c}(x_n - m_i)(x_n - m_i)^T \tag{3}$$

Goal is to find a feature subset for which the within-class spread is small and the between-class spread is large. The fitness function is:

$$J = \text{trace}\left\{S_w^{-1}\ S_m\right\} \tag{4}$$

Where: m is the sample mean of all data; m_i is the sample mean of class c_i; c is the number of class; N_i is the number of sample mean of class c_i; N is the number of all samples; S_i is the covariance matrix for class i. The value of J is bigger means that the feature subset is more important. The selected feature subset meets maximum fitness function.

2.2 IFFS Algorithm

Search strategy is divided into a global search and local search. An advantage of global search algorithm is that get an optimal result, but it is not feasible to a large feature set. A sequential search algorithm will spend less time searching because the search process is not through an entire search space.

The SFS begins with an empty set (k = 0), adds one feature at a time to selected subset with (k + 1) features so that the new subset maximizes a fitness function J (k + 1). It stops when the selected subset meets the d desired number of features, k < d.

The SBS method begins with all input features D (k = D), removes one feature at a time to selected subset with (k − 1) features so that the resultant subset maximizes a fitness function J(k − 1). The algorithm stops when the resultant feature set get the d desired number of features, k < d. It stops when the selected subset meets the d desired number of features, k < d.

The SFFS is one of two algorithms of Floating Search Algorithm that are SFFS and SBFS. The SFFS starts with an empty feature set and uses the SFS to add one feature at a time to the selected feature subset. Every time a new feature is added to the current feature set, the algorithm tries to backtrack by using the SBS algorithm to remove one feature at a time to find a better subset. The algorithm terminates when the size of the current feature set is larger than the d desired number of features. It stops when the selected subset meets the d desired number of features, k < d.

That the IFFS improved the SFFS algorithm proposed in [7]. The IFFS starts with an empty feature set and It stops when the selected subset has the d desired number of features, k < d. The SFS was using to add one feature at a time to selected good feature. However, The IFFS is not only applying SBS but also replacing the weak feature in the currently selected feature subset.

This is the following notation in describing the algorithm to select the best subset of d features from the set X of D features.

- X: the set of all D features.
- SET: the current feature subset.
- k: the number of feature in SET.
- X_k: the subset of k features selected by the IFFS algorithm.
- J_k: the value of the fitness function J of X_k.
- d: desired number of features.

The IFFS algorithm follows [7]:
Begin
k = 0, SET = ∅, J_k = 0 for k = 1:D.

Step 1 Adding a feature to the current feature subset: Use the SFS algorithm to add a feature SET and increase k by 1. If k > d, terminate of the algorithm. Otherwise, compute J for new SET. If J(SET) > J_k, set X_k = SET and J_k = J(SET), else set SET = X_k.

Step 2 Checking if backtracking with searching inside current subset: Remove the weak feature x_j in SET i.e. the one such that $J(SET\backslash x_j) = \max_{1 \le i \le k}(SET\backslash x_i)$. That is, removing x_j from SET gives the largest J value of all the resulting subset of (k − 1) features. If $J(SET\backslash x_j) > J_{k-1}$, decrease k by 1 and set $SET = SET\backslash x_j$, then set X_k = SET, J_k = J(SET), and repeat Step 2. Otherwise go to Step 3.

Step 3 Checking if replacing the weak feature with searching outside current subset: Generate k new feature subsets of k features SET^o_i for i = 1:kSET^o_i is found by first removing the ith feature in SET and then using the SFS algorithm to add the best new feature to each resultant feature subsets. Among these SET^o_i, find the one with the largest J value, call it SET^o_s, i.e., $J(SET^o_s) = \max_{1 \le i \le k} J(SET^o_i)$. If $J(SET^o_i) > J_k$, set $J_k = J(SET^o_i)$ and $SET = SET^o_i$ and go to step 2; else go to step 1.

2.3 *Feature Set, Samples*

General Description
The classifier-based power system transient stability can be formulated as a mapping $y_i = f(x_i)$ after learning from a stability database $D = \{x_i, y_i\}_{i=1}^n$. Where: x_i is feature; it is n-dimensional input vector that characterizes the system operating state; and y_i is output vector. The feature subset selection consists of selecting a d dimensional feature vector z, $d < n$; The d selected features represent the original

data in a new knowledge base $D_{new} = \{z_i, y_i\}_{i=1}^{d}$, and the new mapping $y_{newi} = f_{new}(z_i)$.

Initial feature set selection

A large number of samples are generated through off-line simulation and the stable status was evaluated for each fault under study. Data for each bus or line fault occurring in the test systems are recorded in which samples of data are kept in a database.

The input is the vector of system state parameters that characterize the current system state. Fault-on features are variables that characterize at fault-on state of power system occur such as voltage drops in the nodes, changes in nodal powers, in power flows in transmission lines, in powers of generators [4, 10].

Vector output features represent the stable conditions of the power system. The output variables are assigned to label binary variable y{1, 0}. Class 1{1} is stable class and class 2{0} is unstable class.

Simulating observation results, if the angle of the relative rotor generators is larger than 180° then the system is 'Unstable', and less than 180° then the system is 'Stable' [3, 6]. The corresponding data will be put into unstable and stable class. For each considered load samples, the generator sample has been get accordingly by running optimal power flow (OPF) tool in PowerWorld software. The data set is normalized before training.

Classification accuracy

To test the studied methods without loss of generality, the database is randomly partition into k subsets that are D_1, D_2,…, D_i,…, D_k, each equal size. The model is trained on all the subsets except for one that is tested to measuring of validation accuracy. Training and testing is performed k times. The validation accuracy or classification rate is computed for each of the k validation sets, and averaged to get final cross-validation accuracy. Classification rate of training or testing is determined by the formula (5):

$$r(\%) = \frac{n_r}{N} \times 100 \tag{5}$$

Where: n_r is an accurate number of samples for training or testing; N is a total number of samples for training or testing.

3 Results and Discussion

3.1 Feature Set and Samples

The IFFS was tested on the IEEE 30-bus scheme. It includes 30 buses, 21 loads, 6 generators. This is well-known diagram. It can also be downloaded from the website [11]. Off-line simulation was implemented to collection data for training.

Load levels is (20–160) % base load. Setting fault clearing time is 50 ms [12] with three-phase fault at buses and along transmission lines.

Input and output features are x{ΔV_{bus}, ΔP_{load}, ΔQ_{load}, ΔP_{flow}, ΔQ_{flow}, ΔP_{ge}, ΔQ_{ge}} and y{1,0}. Total of input variables is 166(30 + 21 + 21 + 41 + 41 + 6 + 6), and two output features.

From simulated results, there were 463 samples with 305 stable samples and 158 unstable samples. Full feature set was randomly divided into ten feature subsets. Each training subset had 363 samples (230 stable samples, 133 unstable samples). Each testing subset had 100 samples (75 stable samples, 25 unstable samples).

3.2 *Results*

In this paper, IFFS, SFFS, SFS and Relief were four feature selection approaches that were tested to comparing of feature subset selection results. From full feature set, each feature subset selection method had 8 feature subsets that were found. Sizes of each subset were from 8 features to 15 features.

The K-NN was chosen for the experiments. We used k = 1 in K-NN (1-NN) to simplify the evaluation process.

Programs were performed by laptop with CPU Intel CoreTM i3-380 M, 2 GB DDR3 Memory, 500 GB HDD.

Figure 1 showed the average classification rate results obtained by four feature selection methods. Table 1 showed the highest average classification rate of four feature selection methods corresponding feature subset sizes. Table 2 showed the average time calculation of three feature selection methods corresponding feature subset sizes of ten, and 166 features with Relief method. Table 3 showed the average classification rate results of the IFFS method corresponding feature subset sizes of ten and full 166 features of feature set.

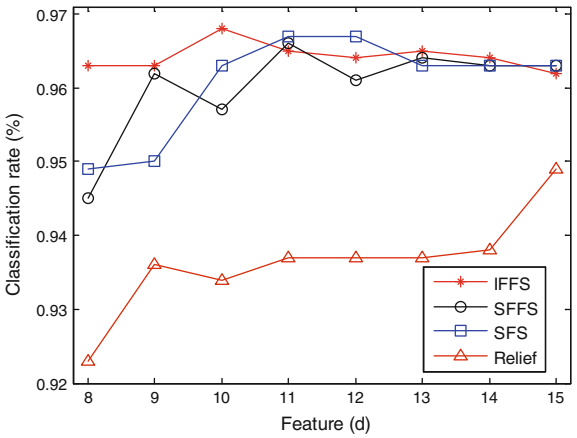

Fig. 1 The average classification rate results of feature selection methods

Table 1 The highest average classification rate of feature selection methods

Algorithm	r (%)	d (Feature)
Relief	94.9	15
SFS	96.7	11
SFFS	96.6	11
IFFS	96.8	10

Table 2 Time calculation of feature subset selection

Algorithm	Time (s)	d (Feature)
Relief	4.16	Ranking, 166
SFS	0.68	10
SFFS	1.17	10
IFFS	14.5	10

Table 3 The average classification rate results

Algorithm	d (Feature)	r (%)
IFFS	10	96.8
All features	166	96.6

3.3 Discussion

Figure 1, in the size range from 8 to 15 features of each subset showed that the IFFS algorithm yielded the highest recognition accuracy with the smallest feature subset size compared with others.

Table 1, the average classification rate was 96.8 % with the 10 selected features of the IFFS, 96.6 % with the 11 selected features of the SFFS, 96.7 % with the selected 11 features of the SFS, 94.9 % with the 15 selected features of the Relief. The Relief method had the lowest classification rate.

Table 2, time calculation of the IFFS was longer than others. Time calculation of SFS was shorter than others.

Table 3, comparing with all features set, the average classification rate of the 10 selected feature subset of the IFFS increased by 0.2 % and the number of features decreased by 16.6 times. This shows that the IFFS algorithm removed the weak and noisy features improving recognition accuracy.

With 10 selected features of the IFFS, the average of classification rate got 96.8 %. This result was also considered acceptable for some studies applying pattern recognition to power system stability. For instance, the expected value in [10] accepted 90 % or more, in [3] 94–97 %, in [1] 95 %.

4 Conclusions

This paper proposed the use of the IFFS algorithm in power system transient stability classification. Feature selection is aimed at reducing the number of features, retaining distinctive features to reduce memory and increasing identification accuracy.

The proven effectiveness of the IFFS was compared with SFS, SFFS and Relief method through analysis of results in power system transient stability classification using K-NN on IEEE 30-bus standard power network. The analytical results showed that the IFFF achieved effective reduction features and recognition accuracy higher than other methods.

The number of features decreased by 16.6 times while the average classification rate increased by 0.2 %. This showed that the IFFS algorithm removed the weak and noisy features, improving recognition accuracy.

Acknowledgement The authors acknowledge the support from the Electrical Power System and Renewable Lab of HCM City University of Technology and Education, Ho Chi Minh City, Vietnam.

References

1. Haidar AMA, Mustafa MW, Ibrahim FAF, Ahmed IA (2011) Transient stability evaluation of electrical power system using generalized regression neural networks. Appl Soft Comput **11** (4):3558–3570
2. Karami A, Esmaili SZ (2013) Transient stability assessment of power systems described with detailed models using neural networks. Int J Electr Power Energy Syst 45(1):279–292
3. Zhang R, Member S, Xu Y, Dong ZY (2012) Feature selection for intelligent stability assessment of power systems. In: IEEE power and energy society general meeting, pp 1–7
4. Abdelaziz AY, El-Dessouki MA (2013) Transient stability assessment using decision trees and fuzzy logic techniques. Int J Intell Syst Appl 5(10):1–10
5. Zhang R, Polytechnic HK, Kong H, Xu Y, Dong ZY, Meng K, Xu Z (2011) Intelligent systems for power system dynamic security assessment : review and classification. In: electric utility DRPT international conference, pp 134–139. Weihai, Shandong
6. Kalyani S, Swarup KS (2013) Pattern analysis and classification for security evaluation in power networks. Int J Electr Power Energy Syst 44(1):547–560
7. Nakariyakul S, Casasent DP (2009) An improvement on floating search algorithms for feature subset selection. Pattern Recognit 42(9):1932–1940
8. Cheriet M, Kharma N, Liu C-L, Suen CY (2007) Character recognition systems—a guide for students and practitioners. Wiley, New York
9. Webb AR, Copsey KD (2011) Statistical pattern recognition, 3rd edn. Wiley, New York
10. Quyen Huy Anh (1994) The application of pattern recognition for fast analysis of the dynamic stability of electrical power system. Electr Technol (Perganon) 2:1–13
11. http://publish.illinois.edu
12. Glover JD, Sarma MS, Overbye T (2008) Power system analysis and design, 5th edn. SI. McGraw Hill, New York

Technical Efficiency and Recommendations for Overcurrent Relay Protection Setting

Tran Hoang Quang Minh

Abstract Among the relay protections, overcurrent relay protections have a large proportion. To study, analyze and develop technical effect criterion for selection of overcurrent relay protection settings (high-voltage lines) and technical efficiency criterion for estimating this setting is main purpose of this paper. The probability statistical algorithms are used to calculate the above criteria. Finally base on these criteria, setting options and recommendations of overcurrent protection are given.

Keywords Technical effect · Technical efficiency · Overcurrent relay protection · Setting · Criterion · Criteria

1 Introduction

In many years, probabilistic approaches, algorithms and methods for designing and setting of relay protection and automation are developed [1, 2]. The latest works of Fedoseyev A.M., Smirnov E.P. are based on the definition of efficiency of relay protection [3–5]. In these materials the concept technical efficiency relay protection is specified as the difference between the potentially possible effect p(A) (the probability of faults on the protected object, which is designed to eliminate the faults) and probability of losses P(Л). Losses of relay protections are formed as: (1) refusals of work p(O) when faults are in the protected object, (2) excessive actions P(И) when faults are in the external elements of the electrical network, (3) false actions P(Л) when there are no faults at all. False actions are possible in the working and abnormal modes. However there are problems of imposing appearance different components of statistical data. Some data, for example, faults are mass enough, but such events as refusals of operation relay protection, false actions at

T.H.Q. Minh (✉)
Faculty of Electrical and Electronics Engineering, Ton Duc Thang University,
No. 19 Nguyen Huu Tho Street, District 7, Ho Chi Minh City, Vietnam
e-mail: tranhoangquangminh@tdt.edu.vn

V.H. Duy et al. (eds.), *AETA 2015: Recent Advances in Electrical Engineering and Related Sciences*, Lecture Notes in Electrical Engineering 371,
DOI 10.1007/978-3-319-27247-4_16

asynchronous modes, etc. are very rare. In this connection it is wrongful to use statistical characteristics with different reliability in interesting criteria functional. Therefore there is an actual problem of support statistical adequacy of all components in considered functional.

The modern technical solutions in the construction equipment of relay protection (differential protection, protection of lines with the information exchange) practical completely eliminate these losses [6, 7]. However large number of these losses has occurred in operating of overcurrent relay protection and distance relay protection. Then the new algorithm for each stages settings of these relay protections is necessary to provide and develop. For distance relay protection, analysis, algorithm and recommendation for their setting are provided in many works [8–12]. In this paper analysis, algorithm and recommendations for setting overcurrent relay protection with using criterion technical efficiency are provided, analyzed, developed and calculated.

2 Main Part

2.1 Analysis Technical Efficiency of Overcurrent Relay Protection

To calculate the technical efficiency of overcurrent relay protection is needed setting values and probabilistic characteristics of regime (current distribution coefficients) for the transfer of electrical quantities at its own coordinates to the neighboring previous and related network elements. For this purpose it is necessary to provide and learn about analysis technical efficiency of overcurrent relay protections in electrical network. Developed a mathematical description of the technical efficiency and algorithms allows to produce mode-switching analysis of technical efficiency of the line overcurrent relay protection in the area of high-voltage network. This analysis (Fig. 1) shows the dependence of the technical efficiency of the overcurrent relay protection on setting time and current setting and their relations with setting overcurrent relay protection on previous lines. The parameter of protected and previous lines in Fig. 1 is displayed in the form of positive sequence resistance. The analysis for setting overcurrent relay protection is illustrated in Fig. 1, which indicated:

S—The structure of the electrical network: (1) A, B, C, D—substation network; (2) protected line №, previous line p and the previous to previous line pp; (3) 1, 2—circuit breakers at the ends of lines; (4) e1, …, e6—electrical sources; (5) z1, …, z4—resistance of other electrical sources; (6) OC1, OC2—bypass shunt connection of the protected and the previous p lines.

T—change of the current (y-axis i) through the protection №1, p1, pp1 for faults along the lines of the network (the x-axis—positive sequence impedance z_1) and temporal characteristics (second ordinate axis t) protection stages along the same

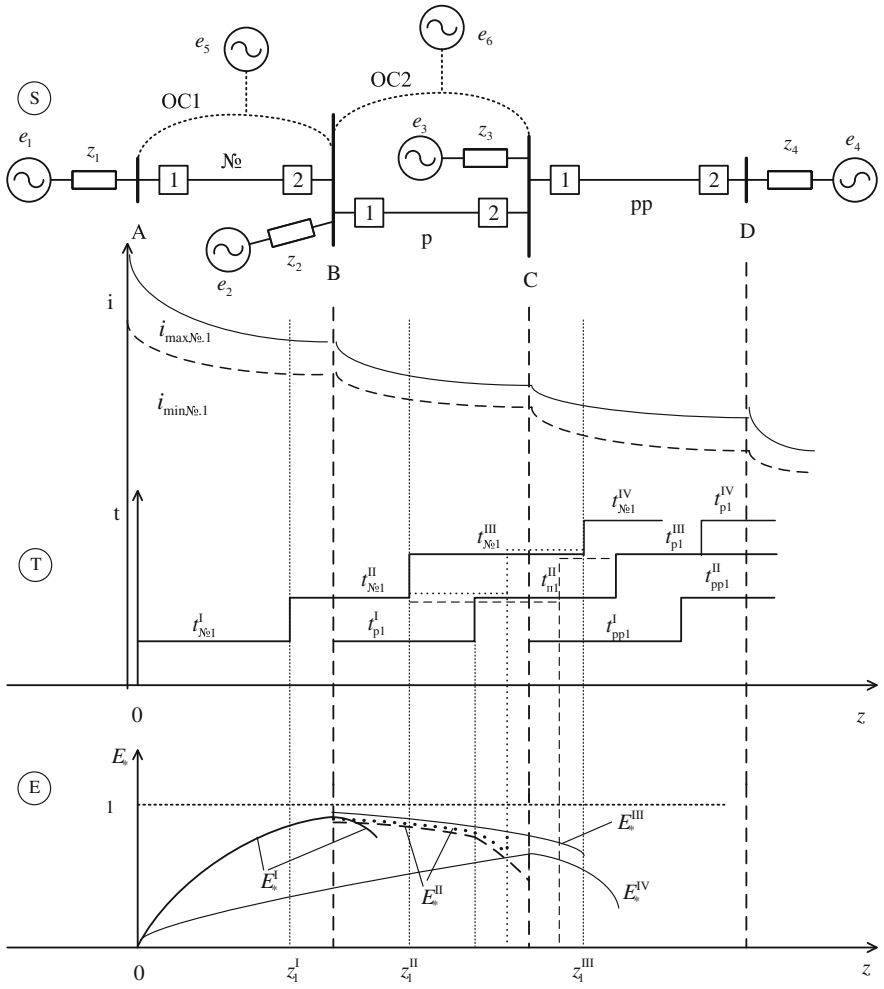

Fig. 1 Scheme of a predetermined network

lines as the weak bypass sources OC1 and OC2. Indicated on the curves and straight lines: (1) letter i—currents with lower indices: max—the maximum, and min—the minimum currents through protection №1, p1, due to regime-switching state on the network; (2) the letter i—current setting with lower indices: №1, p1 and superscripts: I, II, III, IV corresponding stages; (3) the letter t—setting the time with the same subscripts: №1, p1 and superscripts: I, II, III, IV stages; (4) the letters z_i with the same subscripts №1, p1 and superscripts: I, II, III, IV stages—display current settings in the coordinates of the positive sequence impedance z_1 lines.

E—Change in the technical efficiency of I, II, III, IV stages overcurrent relay protection №1.

The solid lines in Fig. 1 shows the curves and straight lines for ordinary cases, setting protection levels, points, dotted line—in the case of ordinary transfer settings setting the second stage protection №1 short of the previous line. The network shows only line, not transformers and auto-transformers because these not fundamentally affect to the discussed setting.

Based on the above, setting the first stage overcurrent relay protection without communication channel and the second stage based on sensitivity is the best option. The second option of setting overcurrent relay protection without communication channel defined by setting of the second stage on the basis of sensitivity, and the first stage by optimizing technical efficiency. Setting back-up stages according to minimizing *excessive* action and technical efficiency.

2.2 Algorithm of Technical Efficiency

Technical effect and its components of overcurrent relay protection are given below:

$$E = p(A) - p(O) - p(Л) - p(И) \tag{1}$$

The letter p designates probabilities of events: A—faults on a protected line, O—operation refusals, *И*—excessive ations; Л—false actions.

1. For main stages of overcurrent relay protection:

$$E^{m}_{№} = p(A^{m}_{№}) - p(O^{m}_{№}) - p(Л^{m}_{№}) - \sum_{i=1}^{n} p(И^{m}_{№pi}) \tag{2}$$

where №—overcurrent relay protection, m—main stages.

Probabilities faults $p(A^{m})$:

$$p(A^{m}_{№}) = \omega_{№} m(T^{m}_{№}) \tag{3}$$

where $\omega_{№}$—the flow parameter of interest fault types on the protected lines, $m(T^{m}_{№})$ average detection fault duration of the main stages (substantially the setting time of main stages).

$$\omega_{№} = \omega^{(1,4)}_{№} = \left[p(1) + p(4)\right].\omega_{0}.\frac{L}{100} \tag{4}$$

where p(1)—the probability of a single-phase faults; p(4)—the probability of the two-phase ground faults; L—length of the line; ω_0—the probability of faults on the 100 km line length.

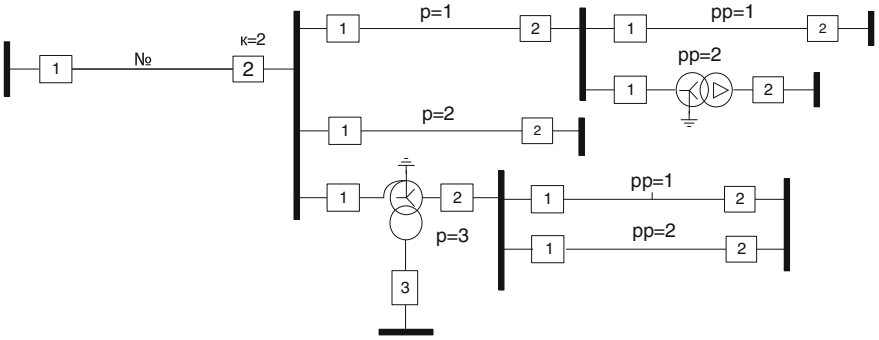

Fig. 2 Scheme of a predetermined network

Probabilities refusals of work

$$p(O^{m}_{№}) = p(O^{m}_{№}/A^{m}_{№}).p(A^{m}_{№}) \tag{5}$$

Probabilities false actions.

$$p(Л^{m}_{№}) = p(Л^{m}_{№}/R^{m}_{№}).p(R^{m}_{№}) \tag{6}$$

where R—type of the false actions

Excessive actions of the first stage

$$\sum_{1pi=1}^{n_p} p(И^{I}_{№1\text{-}1pi}) = \sum_{1pi=1}^{n_p}[\frac{1}{2}p(Д_{№1pi}/ВК_{1pi})p(ВК_{1pi}) + p(O_{№1pi}/ВК_{1\,pi})p(ВК_{1\,pi})] \tag{7}$$

where Д, О—joint action, refusals of protection for the 1pi-th elements, ВК—faults on the 1pi-th elements (Fig. 2).

The definition of conditional probabilities of the joint action, refusals of the previous elements protections (first stage) are show in (7).

$$\begin{aligned} p(Д^{I}_{№1pi}/ВК_{p}) &= [p_{max}(Д^{I}_{№1pi}/ВК_{p}) + p_{min}(Д^{I}_{№1pi}/ВК_{p})]/2, \\ p(O^{I}_{№1pi}/ВК_{p}) &= [p_{max}(O^{I}_{№1pi}/ВК_{p}) + p_{min}(O^{I}_{№1pi}/ВК_{p})]/2 \end{aligned} \tag{8}$$

where maximum (max) and minimum (min) are the maximum and minimum boundaries of the first stage (protection of the protected line) in the space of each the previous elements [13, 14].

The unconditional probability of the external faults at 1pi-th previous elements $p(ВК_{1pi}) = \omega_{1pi}.m(T^{I}_{1pi})$ determined by the product of the flow parameter fault on the previous line ω_{1pi} and the average duration of detection (lock) fault channels of the first stage (protection) of the previous line $m(T^{I}_{1pi})$.

Excessive actions of the second stage

$$\sum_{1pi=1}^{n_p} p(И^{II}_{№1\text{-}1pi}) = \sum_{1pi=1}^{n_p} [\frac{1}{2} p(Д_{№1pi} / ВК_{1pi}) p(ВК_{1pi}) + p(О_{№1pi} / ВК_{1pi}) p(ВК_{1pi})] \quad (9)$$

The definition of conditional probabilities of the joint action, refusals of the previous elements protections (second stage) are show in (9).

$$\begin{aligned} p(Д^{II}_{№1pi} / ВК_p) &= [p_{max}(Д^{II}_{№1pi} / ВК_p) + p_{min}(Д^{II}_{№1pi} / ВК_p)] / 2, \\ p(О^{II}_{№1pi} / ВК_p) &= [p_{max}(О^{II}_{№1pi} / ВК_p) + p_{min}(О^{II}_{№1pi} / ВК_p)] / 2 \end{aligned} \quad (10)$$

where maximum (max) and minimum (min) are the maximum and minimum boundaries of the second stage (protection of the protected line) in the space of each the previous elements (Fig. 2) [13, 14].

The unconditional probability of the external faults at 1pi-th previous elements $p(ВК_{1pi}) = \omega_{1pi}.m(T^{II}_{1pi})$ determined by the product of the flow parameter fault on the previous line ω_{1pi} and the average duration of detection (lock) fault channels of the second stage (protection) of the previous line $m(T^{II}_{1pi})$.

2. For back-up stages of overcurrent relay protection:

$$\begin{aligned} E^b_{№1} = p(A^b_{№}) + \sum_{1pi=1}^{n_{1pi}} p(A^b_{1pk}) - p(O^b_{№1}) - \sum_{1pk=1}^{n_{1pk}} p(O^b_{1pk}) \\ - \sum_{jp=1}^{n_{jp}} \sum_{jpi=1}^{n_{jpi}} \sum_{jpik=1}^{n_{jpik}} p(И^b_{№1\text{-}jpik1}) - p(Л^b_{№}) \end{aligned} \quad (11)$$

where the lower indexes: №—protected line, p—previous lines (elements), pp—previous (elements) of previous lines (elements) (Fig. 1). The letter p designates probabilities of events: A—faults on a protected line, O—operation refusals, И—excessive actions.

Probabilities faults.

$$p(A^b_{№}) + \sum_{1pi=1}^{n_{1p}} p(A^b_{1pk}) = \omega_{№} m(T^b_{№}) + \sum_{1pi=1}^{n_{1p}} \omega_{1pk} m(T^b_{1pk}) \quad (12)$$

where ω_{1pk} the flow parameter of fault types on 1pk-th line, and $m(T^b_{№})$, $m(T^b_{1pk})$ average duration of detection (lock) fault channels of the back-up stages (third and fourth stage time setting).

Probabilities refusals of work.

$$p(O^b_{№1}) + \sum_{1pk=1}^{n_{1pk}} p(O^b_{1pk}) = p(O^b_{№} / A^b_{№}).p(A^b_{№}) + \sum_{1pk=1}^{n_{1pk}} p(O^b_{1pk} / A^b_{1pk}).p(A^b_{1pk}) \quad (13)$$

Probabilities false actions.

$$p(Л^{b}_{№}) = p(Л^{b}_{№}/R^{b}_{№}).p(R^{b}_{№}) \tag{14}$$

where R—type of the false actions.

Mechanism of excessive actions of the back-up stages:

$$\sum_{jп=1}^{n_{jп}} \sum_{jпi=1}^{n_{jпi}} \sum_{jпik=1}^{n_{jпik}} p(И^{b}_{№1\text{-}jпik1}) = \sum_{jп=1}^{n_{jп}} \sum_{jпi=1}^{n_{jпi}} \sum_{jпik=1}^{n_{jпik}} [\frac{1}{2} p(Д^{b}_{№1jпik1} / ВК_{jпik}) p(ВК_{jпik}) + p(О^{b}_{№1jпik1} / ВК_{jпik}) p(ВК_{jпik})] \tag{15}$$

2.3 Numerical Results

A numerical results with using the developed algorithms and packet simulation program ARAM CZA (Russian Version) are shown below on the example of the calculation and analysis of distance relay protection line 220 kV Substation Surgust—Substation Contur (Overcurrent relay protection on side of the substation Surgust) on Russian power system. The topology of the analyzed area is shown in Fig. 3. Line p1, p2 and p3 are previous lines (the first periphery); pp1 and pp2 lines are lines of second peripheral.

The settings of the overcurrent relay protection on the lines p1, p2, p3 are chosen by the guidelines [1, 15, 16]. The maximum technical efficiency of overcurrent relay protection №,1 by varying the settings are presented in the Tables 1 and 2.

Numerical results show that: setting overcurrent relay protection with criterion technical efficiency is closed to and better than setting overcurrent relay protection with [15, 16] (value technical efficiency is nearer to 1). For first and second stage, from the results setting value can choose setting value of overcurrent relay protection from maximum value of technical efficiency.

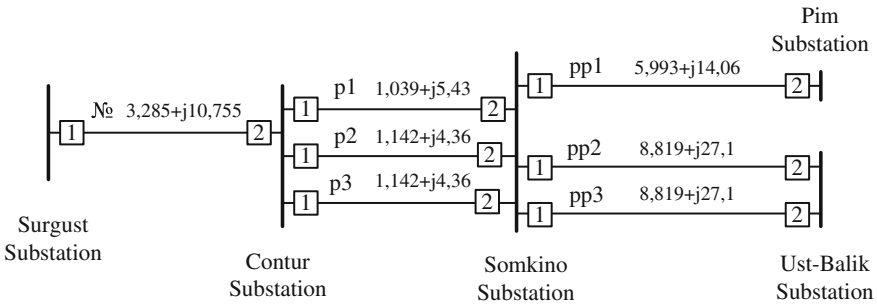

Fig. 3 The topology of the analyzed area

Table 1 Technical efficiency of the main stages overcurrent relay protection №,1

Stage	Setting value (A)	Setting method	Technical efficiency	Sensitivity
I	2292	[15, 16]	99.7881	$\frac{1203}{2292} = 0.52$
I	1830	Criterion technical efficiency	99.8178	$\frac{1203}{2292} = 0.65$
II	1706 (Optimal)	Criterion technical efficiency	99.8254	–
II	1500	Criterion technical efficiency	99.7362	–
II	1000	Criterion technical efficiency	80.7519	–

Table 2 Technical efficiency of the back-up stage distance relay protection №,1

Stage	Setting value (A)	Setting method	Technical efficiency	Sensitivity
III	896	[15, 16]	99.8727	$\frac{1203}{2292} = 1.34$
III	360	Criterion technical efficiency	99.8913	$\frac{1203}{2292} = 3.34$
IV	127	Criterion technical efficiency	99.9439	–

2.4 Recommendations for Setting

On the basis of the analysis and criterion technical efficiency, the method of selecting the settings presented below in the form of customization options. The choice of a particular variant is due to the technical capabilities of its implementation and economic considerations.

Main stages

Option 1 In the previous short lines (short lines of the first periphery) is set relay protection with the information exchange at the ends of these lines (Relay protection with absolute selectivity) [1, 2]. Then, setting the second stages of the protected line may not be consistent with the previous lines, and it is selected on the basis of the conditions of sensitivity

Option 2 On all lines of electrical network set overcurrent relay protection with absolute selectivity [15]. Wherein the second stage are reserved for relay protection with absolute selectivity. Settings such steps clearly and logically selected based on the sensitivity or high technical efficiency

Option 3 The second stage are selected with sensitivity and the first stage with maximum technical efficiency.

Back-up stages
Setting back-up stages of overcurrent relay protection can be carried out both on the basis of the criterion of technical efficiency, and on the basis of its components—the minimum probability of excessive operations.

3 Conclusion

The main results obtained in the paper are as follows:

1. Analysis technical efficiency of overcurrent relay protection in connection with electrical network regime is given.
2. In connection with the criterion of technical efficiency, the mathematical description of the technical efficiency of overcurrent relay protection is designed.
3. Based on regime analysis and mathematical description of the technical efficiency, setting options and recommendations are proposed.
4. Numerical results in the paper is closed to and better than the results from the analysis and the setting guide.
5. For future research, full mathematical algorithm and automatic program for setting and estimating setting of overcurrent relay protection is necessary to propose, develop and apply on electrical network.

References

1. Fedoseev AM (1984) Relay protections power system. Energoatomizdat, Moskva, p 520
2. Schneerson EM (2007) Digital relay protection. Energoatomizdat, Moskva, p 549
3. Smirnov EP (1965) The approach for calculation of the reliability relay protection. Electricity 44–49
4. Shalin AI (2002) Reliability and diagnostic of the relay protection in power system: Novosibirsk, p 384
5. Nudelman GS, Shalin AI (2008) Microprocessor-based relay protection. News of electrical engineering, pp 74–79
6. Gurevich VI (2009) The effectiveness and reliability of microprocessor relay protection. News in the power industry, pp 29–32
7. Gurevich VI (2011) Reliability evaluation of relay protection. Electricity 28–31
8. Minh THQ, Shmoilov AV (2010) Technical efficiency of line distance relay protection. In: The fifth international forum on strategic technology (IFOST 2010), Ulsan University of Technology, Ulsan Korea. pp 335–340
9. Prutik AF, Minh THQ, Shmoilov AV (2010) The selectivity and the technical efficiency of relay protection and automatics. J Energy prob 154–163
10. Shmoilov AV (2002) Probability technologies in electric power industry. In: Proceedings 6-th Russian-Korean international supplement on science and technology KORUS-2002, Novosibirsk, vol 2, pp 421–424

11. Minh THQ, Thang NT (2013) Criterion technical efficiency of line distance relay protection. Int J Adv Sci Technol (Korea) 123–129
12. Minh THQ (2013) Technical efficiency for selection and estimation quality of distance relay protection setting. In: International conference on advanced engineering—theory and applications. Ton Duc Thang University, Vietnam (AETA 2013), pp 243–253
13. Minh THQ (2015) Recommendations for main stages setting-up of line distance relay protection. In: International journal of u- and e-service, science and technology, Korea, pp 45–57
14. Shmoilov AV, Krivova LV, Stoyanov EI, Ignatiev KV (2008) Probabilistic method select of the borders interval data for electro energetic problems. In: Proceedings of the high school, problems of energy–2008, vol 7–8/1, pp 146–157
15. (2005) Guideline for electrical network designing. Moscow, p 320
16. (2002) Electrical engineering handbook: production and distribution of electric power. Moscow, p 964

Enhanced Fault Ride-Through Capability of DFIG Wind Turbine Systems Considering Grid-Side Converter as STATCOM

Tan Luong Van and Van Cuu Ho

Abstract This paper proposes a combined control strategy of energy storage system (ESS) and braking chopper (BC) for fault ride-through (FRT) capability and generated output power smoothening of the doubly-fed induction generator (DFIG) wind power system. At the grid voltage sag, the DC-link voltage is controlled by the energy storage systems (ESS) instead of the grid-side converter (GSC), whereas the GSC is emploited as STATCOM to feed the reactive current into the grid for purpose of the grid voltage recovery. The validity of the proposed system is verified by simulation results for a 2-MW DFIG wind turbine system.

Keywords Braking chopper · DC-link voltage · Doubly-fed induction generator · Energy storage system · Ride-through · Wind turbine

1 Introduction

Among various renewable energy sources, the wind power generation has been concerned as one of the most rapidly growing energy sources. Compared to fixed-speed cage-type induction generator wind turbines, the variable-speed doubly-fed induction generator (DFIG) turbine systems provide the benefits of more power extraction and less mechanical stress, while they give the lower system cost and lower power losses in comparison with the variable-speed PMSG turbine systems [1].

Recently, some countries have issued the dedicated grid codes for connecting the wind turbine system to the electric grid [2, 3]. Also, the micro-grid and the

T.L. Van (✉) · V.C. Ho
Department of Electrical and Electronic Engineering, Sai Gon University,
273 an Duong Vuong District 5, Ho Chi Minh City, Vietnam
e-mail: luonghepc@gmail.com

V.C. Ho
e-mail: cuu_ho_van@yahoo.com

V.H. Duy et al. (eds.), *AETA 2015: Recent Advances in Electrical Engineering and Related Sciences*, Lecture Notes in Electrical Engineering 371,
DOI 10.1007/978-3-319-27247-4_17

smart-grid have been researched for managing the power efficiency [4, 5]. In these systems, however, the grid voltage is much more fluctuated than that in the conventional one. Thus, a ride-through control scheme is needed for the wind power generation system in the grid abnormal conditions. For some national grid codes [3], the wind power systems should stay connected to the grid for the grid fault conditions. In the power system where the wind power generation is of a major portion, the grid will experience the power outage if the wind farms trip off. A diagram of the low-voltage ride-through (LVRT) requirements in which wind turbines should remain connected for voltage sags is shown in Fig. 1 [3].

Several solutions have been proposed for the LVRTs in the variable-speed wind turbine systems. For this purpose, a crowbar system containing an external resistor is connected in the rotor-side of the DFIG to absorb the active power during the grid fault [6, 7]. The wind turbine continues its operation to generate the active power, whereas the reactive power or the voltage at the point of common coupling (PCC) controlled by the GSC for the grid voltage compensation. In the case of a weak grid and during a grid fault, however, the GSC cannot provide enough reactive power or voltage support since the power capacity is small and there is the risk of voltage instability. Also, the ESS added to the wind generation systems can not only suppress the output power smoothening but also offer fault ride-through capability [8]. However, the cost of the ESS is too high to solve this problem practically. Moreover, a braking chopper (BC) with the low cost advantage and the simple control has been employed for the LVRT in the PMSG wind turbine systems [9, 10]. Nevertheless, the power quality at the output of the wind turbine systems is not much improved since the BC can just dissipate the power without capability of returning the power to the grid. Another method using the hybrid system of the ESS and the BC has been introduced in [11, 12], in which the ESS (electric double-layer capacitors (EDLC)) and the BC are connected to the DC-link side of the back-to-back converter in a PMSG wind turbine system. With this method, the power smoothening and fault ride-through can be achieved effectively. The ESS is used to control the power which is absorbed from the system or released to the grid

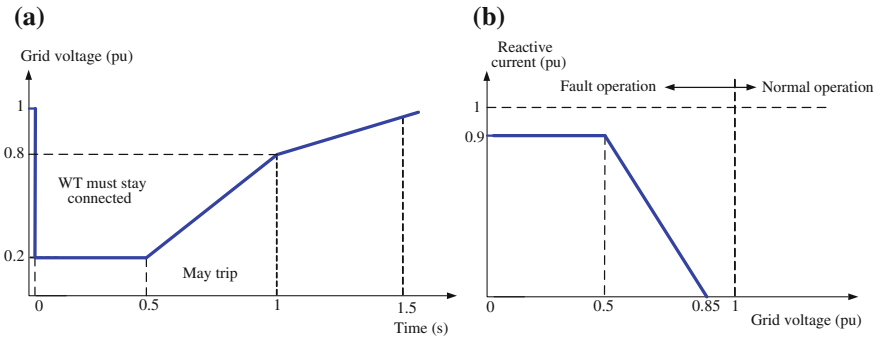

Fig. 1 Spanish grid code [3]. **a** Low-voltage ride-through requirement. **b** Reactive current requirement

for both normal and fault conditions. Meanwhile, the GSC is used to control the DC-link voltage under both normal condition and grid sags and the power mismatched between the turbine and the grid-side are stored in the inertia by increasing the generator speed. However, the amount of energy stored in the turbine inertia is not so large, when the generator operates near the rated speed before the grid sags happen.

In this paper, a novel method combining the BC and ESS is proposed for the LVRT during the grid fault. By switching control mode, the ESS is used to control the DC-link voltage of the back-to-back converters during the grid voltage sags, instead of the GSC. The GSC is used to control the reactive current according to the grid code requirements. Thus, the grid voltage can be recovered rapidly without an external STATCOM after fault clearance. Also, the output power fluctuation of wind turbine system in the steady state is smoothened by the ESS. The validity of the proposed control algorithm is verified by simulation results.

2 Control of DFIG Wind Turbine

2.1 Control of RSC

The control block diagram of the RSC is shown in Fig. 2a. Under unbalanced grid voltage sags, the dual rotor current controllers for positive-sequence dq-axis and

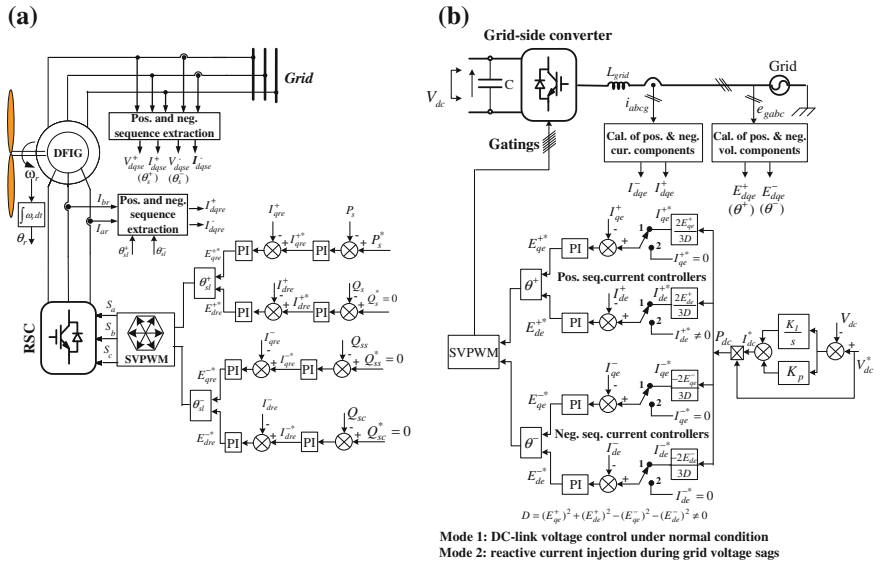

Fig. 2 Control block diagram of DFIG wind turbine system. **a** Rotor-side converter control. **b** Grid-side converter control

negative- sequence dq-axis components are adopted for the RSC. The q-axis rotor current reference of the positive-sequence component and the d-axis rotor current reference of the positive-sequence component are determined by the stator active power controller and stator reactive power controller, respectively. Therefore, the stator active power reference is achieved from the appropriate MPPT method, while the reference of the stator reactive power is set to zero. To eliminate the ripples in the stator reactive power, its oscillating terms (see in [13]) must be nullified ($Q_{ss}^{*} = Q_{sc}^{*} = 0$).

2.2 *Control of GSC*

The GSC controls the DC-link voltage, V_{dc}, to be constant under normal condition. The cascaded control structure consisting of the inner current control loop and the outer DC-link voltage control loop is employed [14, 15]. However, the DC-link voltage is controlled by the ESS when the grid voltage sags happen. Thus, the GSC is exploited as a STATCOM to provide the reactive current to the grid according to the requirement of the grid code. For this reason, the control strategy of the GSC is similar to the control of STATCOM in which the GSC operates as a current source [16, 17].

In the case of unbalanced grid sags, the dual-current controllers for positive- and negative-sequence components are adopted for the GSC. The control block diagram of the GSC is shown in Fig. 2b. At normal operation, the current references for positive- and negative-sequence current controllers are calculated from the output of the DC-link voltage controller as shown in Fig. 2b [15]. At grid sags, this DC-link voltage controller is deactivated and hence the GSC injects the reactive current component to the grid. Thus, the reference of the active current component, I_{qe}^{+*}, is set to zero. In this work, the Spanish grid code as shown in Fig. 1 is referred. The reactive current references, I_{de}^{+*}, depends on the grid voltage drop levels, which are expressed in Fig. 1b. The *dq*-axis current references of the negative-sequence component, I_{dqe}^{-*}, are set to zero to eliminate the unbalanced current component flowing into the grid.

3 Control of ESS and BC

The ESS is used to suppress the generator output power fluctuation under normal condition by absorbing or releasing the pulsated power component from or to the grid, whereas the ESS power reference, P_{ESS}^{*}, is achieved through a high-pass filter [18]. The ESS power is regulated by an outer PI regulator, whereas the supercapacitor current is controlled by an inner PI regulator.

At grid sags, the DC-link voltage of the back-to-back converter is controlled by the ESS instead of the GSC.

3.1 DC-Link Voltage Control

Neglecting the power losses of the converters and considering the active power negligible flowing into the grid, the dynamic equation of the DC-link voltage is expressed as

$$P_r - P_{BC} - P_{ESS} = \frac{1}{2} C \frac{dV_{dc}^2}{dt} \tag{1}$$

where C is the DC-link capacitance, P_r is the rotor power, P_{BC} is the power dissipated by the BC, P_{ESS} is the power of the ESS computed from the ESS voltage, V_{ESS}, and the supercapacitor current, I_{ESS}, as

$$P_{ESS} = V_{ESS} \cdot I_{ESS} \tag{2}$$

From (1), in order to keep the DC-link voltage as constant, the ESS should be able to absorb the generator power fully. For this, selecting the rating of the ESS has been described in detail in [19], in which the rating of the ESS is chosen 30 % of the system power rating for reducing the total system cost.

From the control block diagram shown in Fig. 3, the controller output, I_{ESS}^*, is given as

$$I_{ESS}^* = K_{p2}(V_{dc}^* - V_{dc}) + \frac{K_{I2}}{s}(V_{dc}^* - V_{dc}) + \frac{P_r - P_{BC}}{V_{ESS}} \tag{3}$$

where K_{p2} and K_{I2} are PI controller gains of the DC-link voltage control. By expanding Taylor series of the DC-link voltage at operating point V_{dc0}

$$V_{dc}^2 = V_{dc0}^2 + 2V_{dc0}(V_{dc} - V_{dc0}) \tag{4}$$

From (1)–(4), the equation of the DC-link voltage can be rewritten in "s" domain as

$$CV_{dc0} s V_{dc} = -V_{ESS} K_{p2}(V_{dc}^* - V_{dc}) - V_{ESS} \frac{K_{I2}}{s}(V_{dc}^* - V_{dc}) \tag{5}$$

The transfer function of the voltage controller is obtained as

$$\frac{V_{dc}(s)}{V_{dc}^*(s)} = \frac{V_{ESS} K_{p2}(s + \frac{K_{I2}}{K_{p2}})}{s^2 + \frac{V_{ESS} K_{p2}}{CV_{dc0}} s + \frac{V_{ESS} K_{I2}}{CV_{dc0}}} = \frac{V_{ESS} K_{p2}(s + \frac{K_{I2}}{K_{p2}})}{s^2 + 2\xi\omega_n s + \omega_n^2} \tag{6}$$

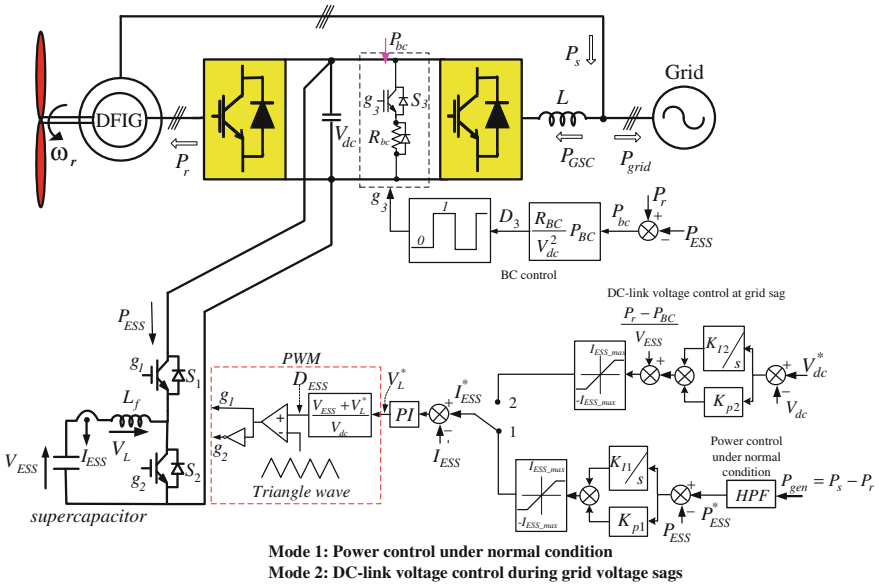

Fig. 3 Control block diagram of ESS and BC

where ξ and ω_n are the damping ratio and natural frequency, respectively.

It is indicated in (6) that the transfer function has a zero and two poles, which they are located in left-half plane. Hence, the control stability is achieved. In this work, the poles of the transfer function are selected as $s_{1,2} = -40 \pm j40$ by a trial-and-error method, from which the PI controller gains are computed as $K_{p2} = 10$ and $K_{I2} = 800$.

3.2 Super-Capacitor Current Control

To set up the current control law for the DC/DC converter, a voltage across the inductance, V_L, is investigated. The dynamic equation of the inductance voltage is described as

$$V_L = L_f \frac{dI_{ESS}}{dt} = D_{ESS} V_{dc} - V_{ESS} \tag{7}$$

where L_f and D_{ESS} are the boost inductance and duty cycle, respectively.

As shown in Fig. 3, the output of the current controller, V_L^*, is given as

$$V_L^* = K_{pc}\left(I_{ESS}^* - I_{ESS}\right) + \frac{K_{ic}}{s}\left(I_{ESS}^* - I_{ESS}\right) \tag{8}$$

where K_{pc} and K_{ic} are the proportional and integral controller gains of the current control, respectively. In this research, the PI controller gains are selected as $K_{pc} = 14.21$ and $K_{ic} = 803.87$.

The error signal between the super-capacitor current and the current reference is processed to produce a voltage across the inductance, V_L [20], which is the output of the super-capacitor current controller as shown in Fig. 3. The duty cycle, D_{ESS}, is calculated by

$$D_{ESS} = \frac{V_{ESS} + V_L^*}{V_{dc}} \tag{9}$$

As shown in Fig. 3, the gating signal for switches S_1 and S_2 are produced by comparing the duty cycle with the carrier waveform of 2 kHz.

3.3 BC Control

During the grid voltage sags, the ESS may not absorb the full generator power, and then the BC will be activated to dissipate the rest of the power, P_{BC} as

$$P_{BC} = P_r - P_{ESS} \tag{10}$$

As shown in Fig. 3, the BC is controlled by the switch S_3. The duty ratio D_3 for the switch depends on P_{BC}, which is expressed as

$$D_3 = \frac{R_{BC}}{V_{dc}^2} P_{BC} \tag{11}$$

where R_{BC} is the braking resistance.

4 Simulation Studies

PSCAD simulations have been carried out for a 2-MW DFIG wind turbine system to verify the feasibility of the proposed method. For WT: R = 44 m; ρ = 1.225 kg/m^3; λ_{opt} = 8. For the DFIG: the grid voltage is 690 V/60 Hz; the rated power is 2 MW; R_s = 0.00488 pu; R_r = 0.00549 pu; L_{ls} = 0.0924 pu; L_{lr} = 0.0995 pu; and J = 200 kg m^2.

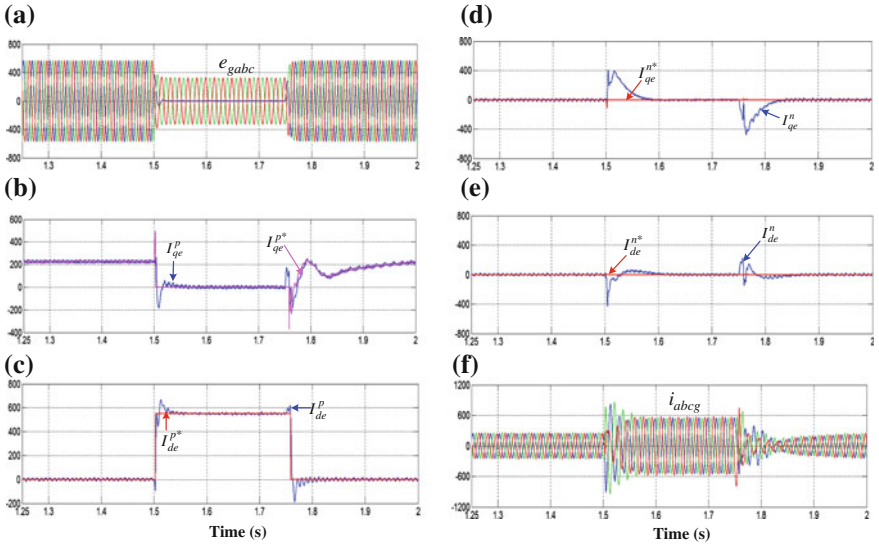

Fig. 4 Performance GSC under unbalanced sag. **a** Grid voltage (V). **b** q-axis positive-sequence grid currents (A). **c** d-axis positive-sequence grid currents (A). **d** q-axis negative-sequence grid currents (A). **e** d-axis negative-sequence grid currents (A). **f** Grid phase currents (A)

Figure 4 shows the performance of the GSC at voltage sags. Figure 4a shows the grid voltage, where three grid-phase voltages drop to 40, 40, and 100 %, respectively during 0.25 s. The q-axis grid current of the positive-sequence component is shown in Fig. 4b, in which it becomes zero during the grid sag since no active power flows into the grid. The reactive current component is injected to the grid as shown in Fig. 4c. The negative-sequence components of q- and d-axis GSC currents are shown in Fig. 4d, e, respectively, in which they are controlled to zero to obtain the balanced GSC current as shown in Fig. 4f.

Figure 5 shows the response of DFIG wind turbine system under unbalanced grid voltage. The stator and rotor power of the DFIG are shown in Fig. 5a, b, respectively. Due to the reduction of generator power reference, the power difference between the turbine and DFIG power accelerates the system. During the grid faults, the rotor speed is increased, as shown in Fig. 5c. The active power produced from the GSC is shown in Fig. 5d. As illustrated in Fig. 5e, the generator torque is also reduced and fluctuated due to the unbalanced grid sags.

Figure 6 shows the performance of the ESS and the BC. The DC-link voltage is controlled well as shown in Fig. 6a, in which its transient value is less than 3.2 %. Figure 6b shows the ESS powers, in which the control performance is good for normal condition. When the grid fault occurs, the power controller is deactivated and the power is absorbed by the ESS as seen in Fig. 6b to keep the DC-link voltage. The current control performance is shown in Fig. 6c. Since the ESS is not able to absorb the full generator power, the rest of the power is dissipated by the

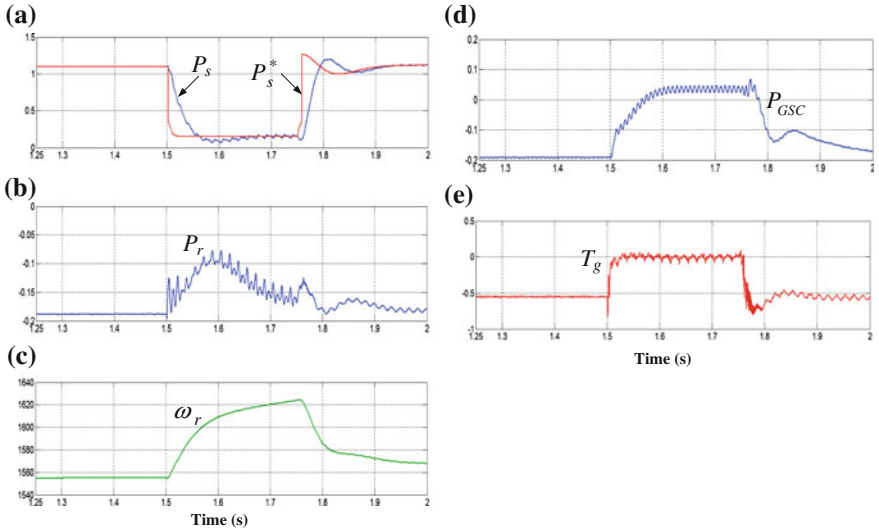

Fig. 5 Generator performance under unbalanced sag. **a** Stator power (MW). **b** Rotor power (MW). **c** Generator speed (rpm). **d** Active power produced from GSC (MW). **e** Generator torque (pu)

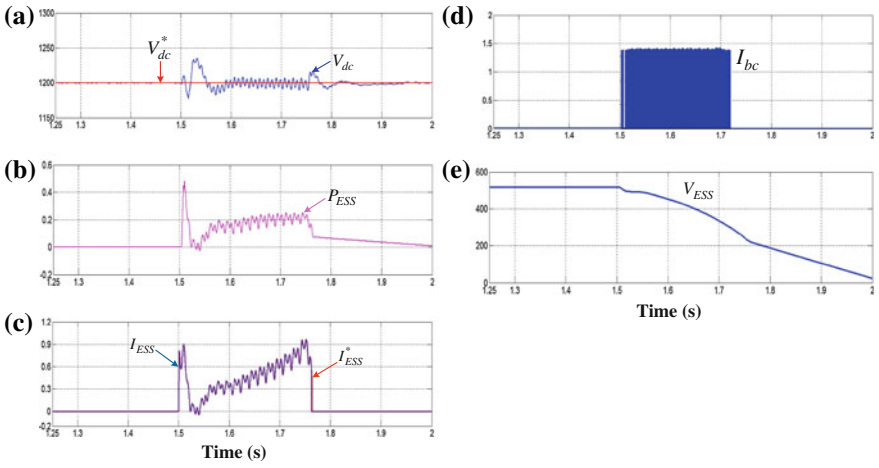

Fig. 6 Performance of the ESS and BC under unbalanced sag. **a** DC-link voltage (V). **b** ESS power (MW). **c** ESS current (KA). **d** Braking chopper current (A). **e** ESS voltage (V)

BC, in which the BC current is shown in Fig. 6d. The super-capacitor voltage is increased as shown in Fig. 6e.

Figure 7 shows the comparison of the DC-link voltage control between the existing method suggested in [18] and the proposed one. The three-phase voltage interruption is considered as shown in Fig. 7a. It can be seen in Fig. 7b that, at this fault, the DC-link voltage can not be controlled well by the grid-side converter.

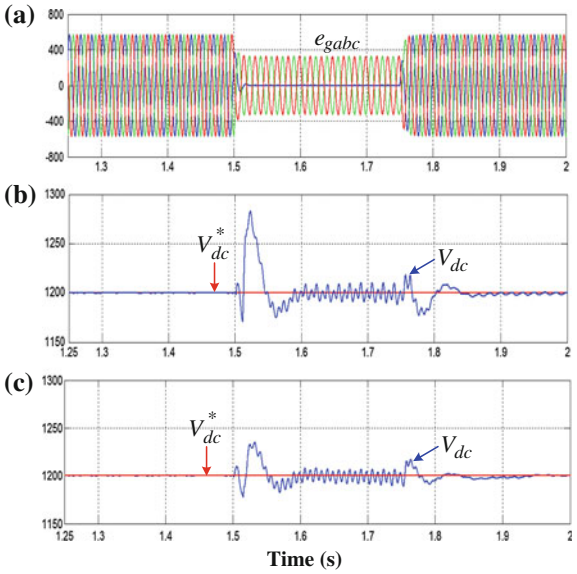

Fig. 7 Comparison of DC-link voltage controls between conventional method in [19] and the proposed one under two-phase interruption. **a** Grid voltages (V). **b** DC-link voltages (V). **c** DC-link voltages (V)

The DC-link voltage is increased by about 5.8 % and includes high ripples during the grid fault. With the suggested method, however, the DC-link voltage is controlled well by the ESS, which is shown in Fig. 7c. The increase of the DC-link voltage is less than 3.2 %.

By switching mode 1, Fig. 8 shows the response of the system when the wind speed varies as shown in Fig. 8a. The super-capacitor will absorb or release the

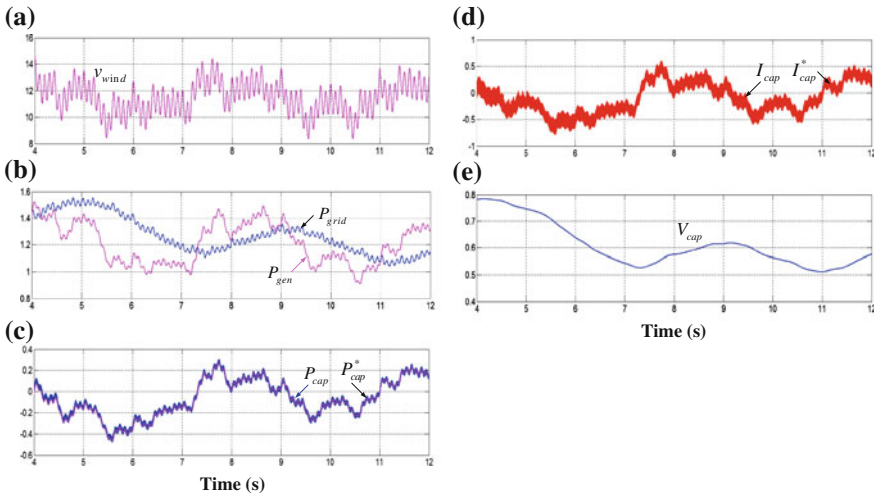

Fig. 8 Responses of system for wind speed variation **a** Wind speed (m/s), **b** Generator power (MW), **c** Super-capacitor power (MW), **d** Super-capacitor currents (KA), **e** Super-capacitor voltage (KV)

high-frequency components of the power, which are obtained through the high-pass filter with the cut-off frequency of 0.628 rad/s. The fluctuated components of the generator power is alleviated before delivering to the grid. Thus, the grid power becomes smoother than the generator power as shown in Fig. 8b. The performance of the super-capacitor is shown in Fig. 8c–e. Figure 8c shows the performance of the power controller and the fluctuated component of the generator power. The performance of current controller is good as shown in Fig. 8d. During the operation, the super-capacitor voltage varies as shown in Fig. 8e.

5 Conclusions

This paper has proposed a method which combines the ESS and the BC for the LVRT in DFIG wind turbine systems. The DC-link voltage is controlled by the ESS, where the GSC is used as STACOM to control the required grid reactive current to able to comply with the grid code. For this, the grid voltage can be recovered rapidly without the added STATCOM after fault clearance. Also, the output power fluctuation of wind turbine system operating in steady state is smoothened by the ESS. The validity of the proposed control algorithm is verified by simulation results.

References

1. Lopez J, Gubia E, Sanchis P, Roboam X, Marroyo L (2008) Wind turbines based on doubly fed induction generator under asymmetrical voltage dips. IEEE Trans Energy Convers 23(1):321–330
2. Tsili M, Papathanassiou S (2009) A review of grid code technical requirements for wind farms. IET Renew Power Gener 3(3):308–332
3. Iov F, Hansen AD, Sørensen P, Cutululis NA (2007) Mapping of grid faults and grid codes, Technical Report Risø-R-1617(EN). Risø National Laboratory, Technical University of Denmark, Roskilde
4. Jeon J-H, Kim S-K, Cho C-H, Ahn J-B, Kim E-S (2006) Development of simulator system for micro-grids with renewable energy sources. J Electr Eng Technol 1(4):409–413
5. Pollin R, Peltier HG, Scharber H (2008) Green recovery: a new program to create good jobs and start building a low-carbon economy. Center for American Progress
6. Lima FKA, Luna A, Rodriguez P, Watanabe EH, Blaabjerg F (2010) Rotor voltage dynamics in the doubly fed induction generator during grid faults. IEEE Trans Power Electron 25(1):118–130
7. Meegahapola LG, Littler T, Flynn D (2010) Decoupled-DFIG fault ride-through strategy for enhanced stability performance during grid faults. IEEE Trans Sustain Energ 1(3):2178–2192
8. Abbey C, Joos G (2007) Supercapacitor energy storage for wind energy applications. IEEE Trans Ind App 43(3):769–776
9. Conroy JF, Watson R (2007) Low-voltage ride-through of a full converter wind turbine with permanent magnet generator. IET Renew Power Gener 1(3):182–189

10. Li W, Abbey C, Joos G (2006) Control and performance of wind turbine generators based on permanent magnet synchronous machines feeding a diode rectifier. In: Proceedings of IEEE PESC, pp 1–6
11. Alepuz S, Calle A, Monge SB, Bordonau J, Kouro S, Wu B (2010) Control scheme for low voltage ride-through compliance in back-to-back NPC converter based wind power systems. In: IEEE International Symposium on Industrial Electronics (ISIE'10), pp 2357–2362
12. Kim KH, Jeung YC, Lee DC, Kim HG (2012) LVRT scheme of PMSG wind power systems based on feedback linearization. IEEE Trans Power Electron 27(5):2376–2384
13. Abo-Khalil AG, Lee D-C, Jang J-I (2007) Control of back-to-back PWM converters for DFIG wind turbine systems under unbalanced grid voltage. In: Proceedings of IEEE International Symposium on Industrial Electronics, pp 2637–2642
14. Jang J-I, Lee D-C (2006) High performance control of three-phase PWM converters under nonideal source voltage. In: Proceedings of IEEE ICIT, pp 2791–2796
15. Song H-S, Nam K (1999) Dual current control scheme for PWM converter under unblanced input voltage conditions. IEEE Trans Ind App 46(5):953–959
16. Li K, Liu J, Wang Z, Wei B (2007) Strategies and operating point optimization of STATCOM control for voltage unbalanced mitigation in three-phase three-wire systems. IEEE Trans Power Delivery 22(1):413–422
17. Slepchenkov MN, Smedley KM, Wen J (2011) Hexagram-converter-based STATCOM for voltage support in fixed-speed wind turbine generation systems. IEEE Trans Ind Electron 58(4):1120–1131
18. Nguyen TH, Lee DC (2011) Improved LVRT capacity and power smoothening of DFIG wind turbine systems. J Power Electron 11(4):568–575
19. Nguyen TH, Lee D-C, Song S-H, Kim E-H (2010) Improvement of power quality for PMSG wind turbine systems. In: Proceedings of IEEE ECCE, pp 2763–2770
20. Camara MB, Gualous H, Gustin F, Berthon A (2008) Design and new control of DC/DC converters to share energy between supercapactiors and batteries in hybrid vehicles. IEEE Trans Veh Technol 57(5):2721–2735

The Solar Collector and Thermal Storage System Using High Temperature Oil

Nguyen Dao, Nguyen Quang Dung and Nguyen Bon

Abstract While solar energy has very large potential in Vietnam, its exploitation and using remain limited. This paper introduces a solar-thermal accumulator using hot oil and proposes theoretical basis to calculate, and design equipment with specific data. This framework could help fabricate a thermal storage system by using solar energy, which provides heat for living and industry. This research also introduces an approach to save energy by building a container with minimum area and a method to calculate the thickness of heat insulation with required accuracy. These methods simultaneously provide safe solutions in design and operation of this solar-thermal accumulator.

Keywords Solar energy · Solar thermal accumulator · Solar storage system · Solar collector · Parabolic trough collector · Solar tracking system

1 Introduction

At present, the increasing demand for energy, the continuous reduction in existing sources of fossil fuels, and the growing concern regarding environment pollution have pushed mankind to explore new technologies for the production of energy using clean, and renewable sources, such as solar energy, wind energy, etc. Among the non-conventional, renewable energy sources, solar energy is the best candidates for massive energy production.

N. Dao (✉) · N.Q. Dung
Faculty of Electrical and Electronics Engineering, Ton Duc Thang University,
No. 19 Nguyen Huu Tho Street, District 7, Ho Chi Minh City, Vietnam
e-mail: nguyendao@tdt.edu.vn

N. Bon
Danang University of Science and Technology—The University of Danang,
54 Nguyen Luong Bang, Da Nang City, Vietnam

V.H. Duy et al. (eds.), *AETA 2015: Recent Advances in Electrical Engineering and Related Sciences*, Lecture Notes in Electrical Engineering 371,
DOI 10.1007/978-3-319-27247-4_18

Solar energy can be directly converted into electricity (by means of photovoltaic cells) or thermal energy (by means of solar thermal collectors). The temperature level achieved when converting solar radiation into thermal energy depends on the type of system which is used for the conversion. Parabolic-trough collectors can produce hot water or air to 400 °C [1]. Though this temperature value is an approximation, it gives a good idea about the typical temperature range for the system mentioned.

Compared to a fixed trough, a parabolic trough driven by a solar tracker is kept under the best possible insolation for all positions of the Sun, as the light falls close to the geometric normal incidence angle. Automatic solar tracking systems (using light intensity sensing) may boost consistently the conversion efficiency of a parabolic trough, thus in this way extract more energy from the sun [2–4]. Among the proposed solar tracking systems for improving the efficiency of solar energy receiving, we can mention single-axis solar tracking [5].

2 A Proposed Solar Thermal Storage System Using Hot Liquid

The sun is a source of immense, and endless renewable energy. However, the instantaneous intensity radiation through the atmosphere to the ground $E_t(\tau) = E_n \sin(\frac{2\pi\tau}{\tau_n})$ is small, and discontinuous, so it is difficult to create high energy, and use in the factory at night [6, 7].

To overcome the disadvantages and expand the range of applications of solar energy, we propose a solar collection and storage system as described in Fig. 1. In that system oil is heated by solar radiation to a temperature of t > 200 °C, by the

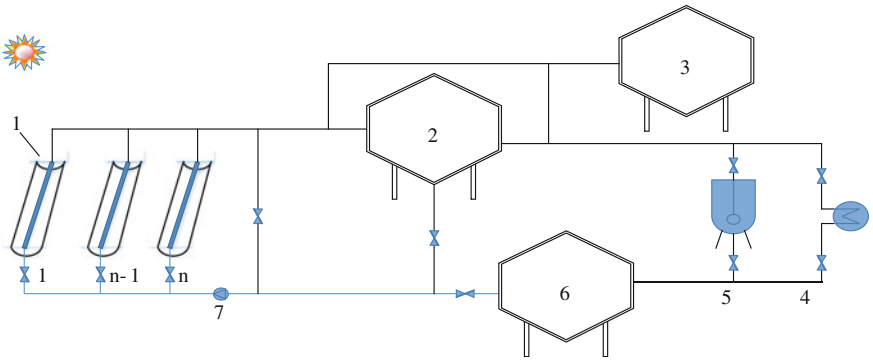

Fig. 1 A proposed design of solar thermal storage system using hot liquid. Where: 1—oil heater; 2—oil hot container; 3—oil boiling container; 4—water boiler; 5—fried equipment; 6—oil cold container; 7—oil pump

Table 1 Input parameters for design [8]

No	Parameter	Symbol	Value
1	Density of oil	ρ	756 kg/m^3
2	Heat capacity of oil	C_p	2482 J/kg K
3	Inlet temperature of oil	t_o	27 °C
4	Boiling temperature of oil	t_s	340 °C
5	Diameter of oil pipeline	d_1	0.03 m
6	Diameter of glass shield pipeline	d_2	0.04 m
7	Radius of parabolic contour	R	0.6 m
8	Length of parabolic semi-cylinder	L	2 m
9	Solar absorption coefficient	ε	0.95
10	Clarity of glass	D	0.95
11	Mirror reflectivity	R	0.94
12	Maximum radiation intensity	E_n	940 W/m^2
13	Day cycle	τ_n	24 h

parabolic trough 1, then heat is stored in the accumulator overnight and provide for life or production (4) and (5) when needed. The input parameters for design of solar thermal collector, and storage system are shown in Table 1.

3 Base Design of Solar Collector Parabolic Trough

3.1 Determining the Temperature Distribution Function

The temperature distribution function over time $t(\tau)$ of oil from the heating pipes in the parabolic collector, with a structure and parameters given in Fig. 2, could be determined according to the heat balance equation for oil during $d\tau \in [\tau \div \tau + d\tau]$ has form [8]:

$$\delta Q_1 = dI_m + dI_G + \delta Q_2, \tag{1}$$

$$\text{or} \quad \varepsilon\left(F_1 D + F_2 D^3 R + F_3 R D\right) E_n \sin(\omega\tau) d\tau / R_e, (\text{J}). \tag{2}$$

After transform $T(\tau) = t(\tau) - t_0$ and set (operator $A \triangleq B$ *means set* $A = B$):

$$a = \frac{\varepsilon E_n (F_1 D + F_2 D^3 R + F_3 R D)}{\rho V C_p} = \frac{p}{C}, (\text{K/s}), \tag{3}$$

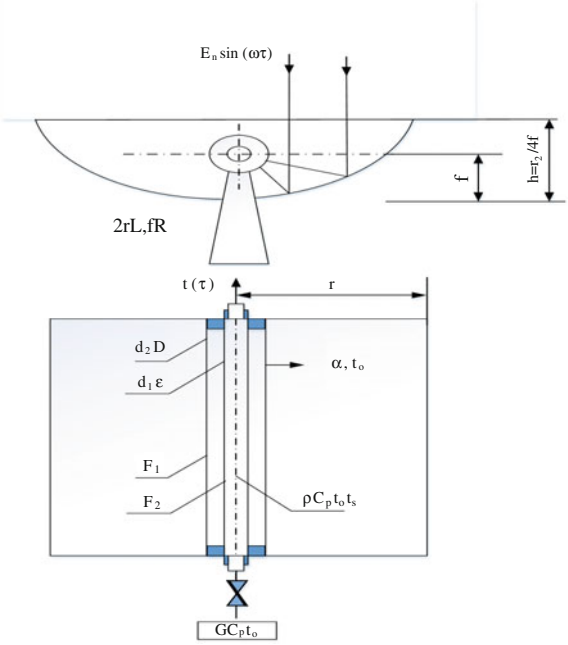

Fig. 2 Dimension of solar collector parabolic trough

$$\text{and} \quad b = \frac{1}{\rho V C_p}\left(GC_p + \frac{L}{R_c}\right) = \frac{W}{C}, (\mathrm{s}^{-1}), \tag{4}$$

then the system of equations for determining T (t) is:

$$\begin{cases} T'(\tau) + bT(\tau) = a\sin(\omega\tau), \ \omega = 2\pi/\tau_n, (\text{rad/s}) \\ T(0) = t(0) - T_0 = 0 \end{cases} \tag{5}$$

Integral equations t will receive the function of oil temperature:

$$T(\tau) = \frac{a}{\sqrt{b^2 + \omega^2}}\sin\left(\omega\tau - artg\frac{\omega}{b}\right) = t(\tau) - t_0, (^{\circ}\mathrm{C}). \tag{6}$$

3.2 Determining Parameters of the Heating Process

We could determine all specific parameters of the heating process of the solar heat collector by investigating the function $T(\tau)$. The main parameters are as follow [8]:

Maximum temperature: $t_m = \frac{a}{\sqrt{b^2+\omega^2}} + t_0$, when $\sin\left(\frac{2\pi\tau}{T_t} - artg\left(\frac{\omega}{b}\right)\right) = 1$, it means when $\tau_m = \tau_n\left(\frac{1}{4} + \frac{1}{2\pi}artg\frac{\omega}{b}\right), \tau_n = 24\,\mathrm{h}$.

The average integral heating degree in a day is:

$$T_n = \frac{2}{\tau_n}\int_0^{\tau_n} T(\tau)d\tau = \frac{a(\omega^2+2b^2)}{\pi b(\omega^2+b^2)} = t_n - t_0, (^oC). \quad (7)$$

The average useful thermal power generated by hot oil is: $Q_n = GC_pT_n, (W)$.

The hot oil production at temperature $t_n = T_n + t_0$ after sunday is: $M = G\tau_n/2, (kg)$.

The hot oil heating efficiency are: $\eta = \frac{Q_n}{E\,2\pi L} = \frac{\pi GC_pT_n}{4E_nrL}, \%$ with $\bar{E}$ denotes the average intensity radiation to the ground, $\bar{E} = \frac{2}{\tau_n}\int_0^{\tau_n/2} E_n \sin\left(\frac{2\pi}{\tau_n}\right)d\tau_n = \frac{2E_n}{\pi}, (W/m^2)$, for example in DaNang city at latitude 16 °N, the maximum intensity radiation is $E_n = 555\,W/m^2$ and the average intensity radiation is $\bar{E} = 598\,W/m^2$.

3.3 Determining the Necessary and Sufficient Conditions of Boiling Process of Hot Oil

Conditions in which liquid could be boiled at temperature $T_m = t_s - t_o$ in the collector is: $T(\tau) \geq T_s$ or $T_m = \frac{a}{\sqrt{\omega^2+b^2}} \geq T_s$. By replacing the above parameters into (3), (4) and solve the inequation, we can find:

- The necessary condition so that liquid could be boiled is that the heat capacity of oil has to be less than critical boiling heat capacity Cs: $C = \sum_{i=1}^{n} \rho_i V_i C_i \leq \frac{\rho}{\omega T_s} = \frac{\varepsilon E_n D(F_1+F_2D^2R+F_3R}{\omega T_s} \triangleq C$, ($C < C_s$ is necessary condition in older to $\sqrt{C_s^2 - C^2}$ is a real number).
- The sufficient condition in which boiling liquid is such as:

$$\begin{cases} W \triangleq GC_p + \frac{L}{R_e} \leq \omega\sqrt{C_s^2 - C^2} \triangleq W, \\ G \leq \frac{W_s - \frac{L}{R_e}}{C_p} \triangleq G_s. \end{cases} \quad (8)$$

3.4 Determining the Boiling Process Parameters

After adjusting parameter G to satisfy the boiling condition $G < G_s$ in which the boiling oil separate to the other container (Fig. 1: Container 3), the parameters of boiling process could be calculated as follows:

Time of beginning boiling process τ_{s1} and time of finishing boiling process s τ_{s2} could be determined by solving equation: $T(\tau) = \frac{a}{\sqrt{\omega^2+b^2}}\sin\left(\frac{2\pi}{\tau_n}\tau - artg\frac{\omega}{b}\right) = T_s$, find τ roots of those equation with sunday condition, $\tau \in [0; \tau_n/2]$, we have:

$$\begin{cases} \tau_{s1} = \frac{\tau_n}{2\pi}\left[artg\frac{\omega}{b} + arsin\frac{T_s\sqrt{\omega^2+b^2}}{a}\right], \\ \tau_{s2} = \frac{\tau_n}{2\pi}\left[\pi + artg\frac{\omega}{b} + arsin\frac{T_s\sqrt{\omega^2+b^2}}{a}\right]. \end{cases} \tag{9}$$

The volume of boiling oil after a sunny day is: $M_s = G_2(T_{s2} - T_{s1}), (\text{kg})$.
The oil boiling efficiency:

$$\eta \triangleq \frac{M_s C_p T_s}{\bar{E}\frac{F\tau_n}{2}} = \frac{\pi G_2 C_p T_s(\tau_{s2} - \tau_{s1})}{2rLE_n\tau_n}, \% \tag{10}$$

In case that is no separation of boiling oil, the boiling oil flows to container and average temperature is computed $t_n = T_n + t_0$, then the other parameters of hot oil are calculated according to the formula as Sect. 3.2.

3.5 Calculating Design Parameter of Solar Collector

The design procedure of the solar thermal storage system using parabolic trough to generate hot oil would be presented in Tables 2 and 3 as follows.

4 Basic Design of Heat Storage Container

Because of heat losing through the cover of thermal storage Q, the cover should be designed with the minimum area, then calculated insulation as required storage system.

4.1 Determining the Size of the Container

Among of the storage with various shapes, the cube one has minimum area of cover, which is equal to: $F_c = \pi d^2 = \pi\left(\frac{6V}{\pi}\right)^{2/3} = 4.836V^{2/3}, \text{m}^2$. But because spherical shape is difficult to make and inconvenient to use, especially in engineering, liquid containers with cylindrical body (diameter d and height h) are often used.

With a given volume V and $h_c = d/4$, we should calculate the optimal ratio $x = \frac{h}{d}$ in so that the area of container is minimum [10] (Fig. 3).

Table 2 Calculating design parameter of solar collector [9]

Type	Parameter	Formula	Value
Intermediate parameter	Direct radiation area	$F_1 = d_1 L$	0.06 m^2
	Glass area	$F_2 = (d_2 - d_1)L$	0.02 m^2
	Reflective area	$F_3 = (2r - d_2)L$	2.32 m^2
	Radiation concentration of parabolic trough	$k \triangleq \frac{E_{tdl}}{E_t} = \frac{2rR + d_1(1-R)}{\pi d_1}$	11.30
	Coefficient	$\propto = \frac{\lambda}{d_2} C(GrPr)^n + \frac{\varepsilon\sigma_o\left(T_w^4 - T_o^4\right)}{T_w - T_o}$	10 W/m^2
	The volume of oil in the pipe	$m = \rho d_1^2 L\pi/4$	1.07 kg
	heat capacity of system oil + pipe	$C = mC_p$	3287 J/kg
	Total thermal resistance of pipe	$R_e = \frac{1}{2\pi\lambda_k}\ln\frac{d_2}{d_1} + \frac{1}{\pi d_2 \alpha}$	2.5 mK/W
	The maximum heating rate	$a \triangleq p/C$	0.34 K/s
	Angular speed of earth rotation	$\omega = 2\pi/\tau_n$	7.27×10^{-5} rad/s
Critical boiling parameters	Critical boiling heat capacity	$C_s \triangleq P/\omega T_s$	53,049 J/K
	Equivalent of water at boiling point	$W_s \triangleq \omega\sqrt{C_s^2 - C^2}$	3.85 W/K
	Flow at boiling point	$G_s \triangleq (W_s - L/R_e)/C_p$	0.00123 kg/s
Designed parameters	Flow of hot oil	$G_1 = 1.2G_s$	0.00147 kg/s
	Flow of boiling oil	$G_2 = 0.8G_s$	0.001 kg/s
Parameters of hot oil and boiling oil	Equivalent of water G1	$W_1 = G_1 C_p + L/R_e$	4.45 W/K
	Equivalent of water G2	$W_2 = G_2 C_p + L/R_e$	3.3 W/K
	Temperature frequency of hot oil	$b_1 = W_1/C$	0.00135 s^{-1}
	Temperature frequency of boiling oil	$b_2 = W_2/C$	0.001 s^{-1}

Table 3 Specific parameter of oil heating (G_1) and boiling process (G_2) [9]

Type	Parameter	Formula	Value	
Parameters of oil heating process	Maximum heating degree	$T_{max} = \frac{a}{\sqrt{b^2+\omega^2}}$	251 °C	340 °C
	Maximum oil temperature	$t_{max} = T_m + t_o$	278 °C	368 °C
	Point time t_m	$\tau_m = \tau_n\left(\frac{1}{4} + \frac{1}{2\pi} artg\frac{\omega}{b}\right)$	6.11 h	6.28 h
	Temperature at the end of the day	$t_c = t_o + \frac{a\omega}{\omega^2+b^2}$	40.5 °C	40.6 °C
	Average integral heating degree	$T_n = \frac{a\left(\omega^2+2b^2\right)}{\pi b(\omega^2+b^2)}$	160 °C	216 °C
	Average temperature of oil	$t_n = T_n + t_o$	187 °C	233 °C
	Effective power of equipment	$Q_n = GC_pT_n$	583.8 W	536 W
	Heat production	$Q = Q_n\tau_n/2$	25.2 MJ	23.15 MJ
	Hot oil production	$M = G\tau_n/2$	104 kg	69 kg
	Heating efficiency via G_1 and G_2	$\eta = \frac{Q_n}{EF_n} = \frac{\pi GC_pT_n}{2E_nE_h}$	63 %	43.2 %
	Ending point time of boiling process	$\tau_{s2} = \frac{\tau_n}{2\pi}\left(artg\frac{\omega}{b} - \arcsin\frac{T_s\sqrt{b^2+\omega^2}}{a}\right)$	0	8.67
	Time of boiling process	$\Delta T_s = T_{s1} - T_{s2}$	0	4.95
	Volume of boiling oil	$M_s = G_2\Delta T_s$	0	28.5
	Boiling efficiency	$\eta_s = \frac{M_sC_pT_s}{\frac{EF\tau_n}{2}} = \frac{\pi G_2G_pT_s\Delta\tau_s}{E_n2rL\tau_n}$	0	35.7 %

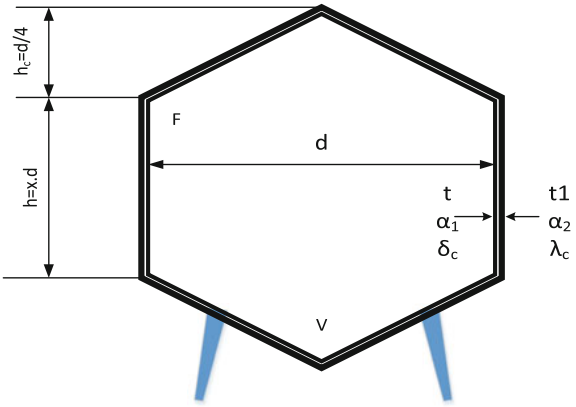

Fig. 3 Dimension of design heat storage container

The relationship $F = F(x, V)$ could be presented as below.
$V = \frac{\pi d^2}{4} xd + 2\frac{\pi d^2}{4}\frac{d}{4\cdot 3} = \frac{\pi}{24} d^3(1+6x)$ leads to $d = \sqrt[3]{\frac{24V}{\pi(6x+1)}}$

$$F = \pi d \cdot xd + 2\pi \frac{d}{2}\sqrt{\left(\frac{d}{2}\right)^2 + \left(\frac{d}{4}\right)^2} = \frac{\pi d^2}{4}\left(4x + \sqrt{5}\right) \tag{11}$$

The area of container when we assigned d = d(V,x) is:

$$F = \left(9\pi V^2\right)^{1/3} \frac{4x+\sqrt{5}}{(6x+1)} \triangleq Af(x). \tag{12}$$

The function $\mathrm{f(x)} = \frac{4x+\sqrt{5}}{(6x+1)}$ reaches minimum when $x = \frac{\sqrt{5}-1}{2} = 0.618$.

The ratio $x = 0.618$ is called optimal ratio, or gold ratio. This ratio helps to choose optimal size for design of container. From gold ration $x = 0.618$ we could calculate sizes of designed container:

Diameter of container $d = \sqrt[3]{\frac{24V}{\pi(6x+1)}} = 1.175V^{\frac{1}{3}}$.

Height of container: $h = x \cdot d = 0.726V^{\frac{1}{3}}$.

Area of container's cover: $F_{\min} = \left(9\pi\left(3\sqrt{5}-2\right)V^2\right)^{1/3} = 5.106V^{2/3}, (\mathrm{m}^2)$. Compared to spherical container, the deviation of area of cover is $\varepsilon = |1 - F_m/F_c| = 5.6\,\%$.

4.2 Design of Insulation for Solar Thermal Storage Container by Hot Oil

Insulation requirements: Input parameters for design of insulation cover have been chosen: material of insulation cover, making of porous vitreous [9]:

- area of container cover, F = 6.69 m^2;
- volume of storage heating oil M = $10M_1$ = 1041 kg;
- the initial temperature of the oil t_n = 187 °C, mounted in air condition with temperature t_o = 27 °C, α = 9.5 W/m^2 K.
- storage time without load: $\Delta\tau = \tau_n/2 = 12\,\text{h}$;
- final temperature of hot oil: $t\left(\frac{\tau_n}{2}\right) \geq t_c = 180\,^{\circ}\text{C}$.

Next step of design of insulation contains: calculating the length δ_c of insulation layer and determining heat transfer coefficient k through insulation layer with condition $t(\frac{\tau_n}{2}) \geq t_c$.

Value k could be exactly determined in differential heat balance equation for oil

$$dl = \delta Q_k \rightarrow MC_p(-dt) = (t - t_f)kFd\tau \rightarrow \int_{t_n}^{t} \frac{dt}{t - t_f} = \int_{0}^{\tau} -\frac{kF}{MC_p}d\tau. \tag{13}$$

Solved differential Eq. (12) gives result: $\ln\left(\frac{t-t_f}{t_n-t_f}\right) = -\frac{kF}{MC_p}\tau$.

From here the distribution $t(\tau)$ in storage process could be calculated by the formula:

$t(\tau) = t_f + (t_n - t_f)\exp\left(-\frac{kF\tau}{MC_p}\right)$, and heat transfer coefficient

$$k = \frac{2MC_p}{F\tau_n}\ln\frac{t_n - t_o}{t_c - t_o}, \left[\frac{\text{W}}{\text{m}^2\,\text{K}}\right].$$

Length δ_c of insulation layer could be determined by k.

$$\delta_c = \lambda_c\left(\frac{1}{k} - \frac{1}{\alpha}\right) = \frac{\lambda_c F\tau_n}{2MC_p\ln\left(\frac{t_n-t_o}{t_c-t_f}\right)} - \frac{\lambda_c}{\alpha}, (\text{m}). \tag{14}$$

Results of calculating numerical value are shown in Table 4.

5 Automatic Solar Tracking System

Solar tracking systems are of several types and can be classified according to several criteria. A first classification can be made based on the number of rotation axes. Thus we can distinguish solar tracking systems by one rotation axis, respectively by two rotation axes. Since solar tracking implies moving parts and control systems that tend to be expensive, single-axis tracking systems seem to be the best solution for small solar heat collector. Automatic solar tracking system contains two parts: mechanic and control system (electric part).

Table 4 Numerical results of design station [10]

Type of parameter	Name of parameter	Formula	Value	Description
Hot oil	Number of parabolic collector		10	Chosen n = 10
	Total volume of hot oil	$M_1 = nG_1\tau_n/2$	1041 kg	At $t_{n1} = 200\,^{\circ}\mathrm{C}$
	Capacity of storage container	$V = 1.1M_1/\rho$	1.509 m^3	V = 110 % V_d
	Diameter of storage container	$d = \sqrt[3]{\frac{24V}{\pi(3\sqrt{5}-2)}}$	1.348 m	
	High of storage container	$h = (\sqrt{5}-1)d/2$	0.833 m	h: optimal high of container
	High of	$h_c = d/4$	0.337 m	
	Area of cover	$F_{min} = \left(9\pi(3\sqrt{5}-2)V^2\right)^{1/3}$		
Heat insulation	Heat coefficient	$\alpha = \frac{\lambda}{d_2}C(GrPr)^n + \frac{\varepsilon\sigma_o\left(T_w^4 - T_o^4\right)}{T_w - T_o}$	9.5 W/m^2 K	
		$k = \frac{2MC_p}{F\tau_n}\ln\frac{t_n - t_o}{t_c - t_o}$	1.094 W/m^2 K	
	Thick of insulation layer	$\delta_c = \lambda_c\left(\frac{1}{k} - \frac{1}{\alpha}\right)$	0.029 m	

5.1 Mechanic Design

The mechanic system is designed to hang the solar collector trough, and rotate them toward the sun. The number of parabolic collectors of design system is 10, so it's large to mount on one chassis. We arrange five collectors on one chassis. The solar collector system needs two chassis in total. System is designed on module basis: easy to mount or unmount. Mechanic system includes: chassis, on which solar parabolic collector troughs is hung on, and the transmission system. The chassis is designed with rectangular shape, and has bearings in order to mount the shaft of solar parabolic trough. Transition mechanism includes gears and chain that allows to rotate all collector trough with same position (Fig. 4).

5.2 Electric Design

Block diagram shows below (Fig. 5).

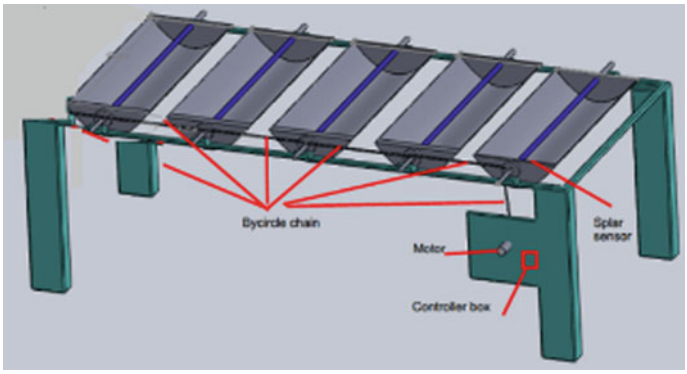

Fig. 4 Installation of solar parabolic trough

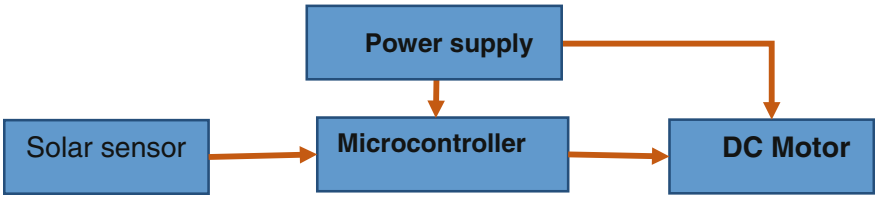

Fig. 5 Block diagram of electronic system

The block electric diagram contains 4 main blocks: power supply, solar sensor, microcontroller and DC motor. After reading signal from solar sensor, microcontroller processes it and generates control signal to DC motor for rotation solar parabolic trough. The power module converts AC with 220 V to DC with 5 V for microcontroller and 24 V for DC motor.

Solar sensor is composed of two photoresistances, as shown in the Fig. 10. The controller reads the voltage value of two photoresistances and compares them. If there is difference between the voltages of two photoresistances, the DC motor is turn on and rotates the solar parabolic trough, directing to the sun. For economical reason, the controller should read the signal from sensor and send control signal to control the motor for rotation solar parabolic trough after each 10 min (Fig. 6).

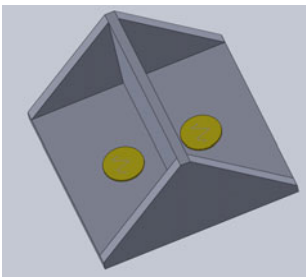

Fig. 6 Design of solar sensor with two photoresistances

DC motor The parameters of the DC motor used as the motion mechanism are: rated voltage is 24 V, rated current is 3 A, maximum speed is 3000 rpm, gear box with a speed reduction ratio of 1:20.

To command the DC motor and read analog signal from 2-wire sensor, we used the microcontroller PIC 16F684. This microcontroller, which has 4 I/O and 8 analog inputs/outputs, satisfies all requirements of task: reading analog signal, generating control signal for DC motor (clockwise, and counterclockwise).

6 Experiment Result

Based on the detail design presented in the previous section, we executed a completely operational small scale experimental model. Starting from this small scale equipment, we can go forward and implement the proposed technology in full scale. The experimental model includes one trough with design parameters given in Table 1 and one container, which is one-half scale of the full-size one mentioned in Table 4.

Experiment procedure was carried out on model and received data (Fig. 7). The dependence of the measurement data t on τ and G is shown in Fig. 8. The error ε between experimental and theoretical data lies in interval $\varepsilon \in (0 \div 10)\,\%$, and the mean error is $\varepsilon_m = 3.5\,\%$.

Some conclusions can be drawn from the research result:

- The calculation formulas derived in Sect. 4 are strongly supported by experimental data, with only insignificant error has been found. Thus the formula could be used in design of thermal storage and solar collector system.
- Using the parabolic trough could provide high energy which is enough for application needs in production.

The test of the solar tracking system was conducted from 12h8′ AM to 1h38′ PM in June, 23 2015, that took about 45 min, and the results are shown in Fig. 9.

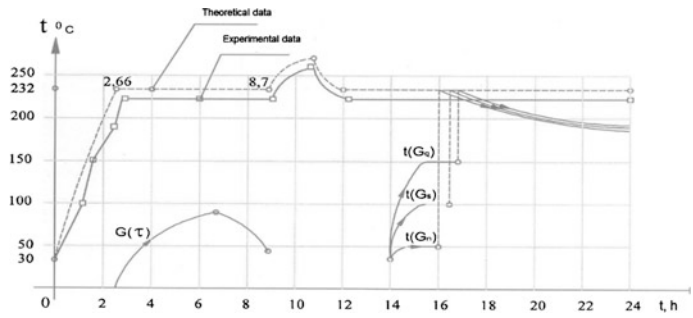

Fig. 7 Graphs t(τ) of liquid and t(τ, G) of hot oil

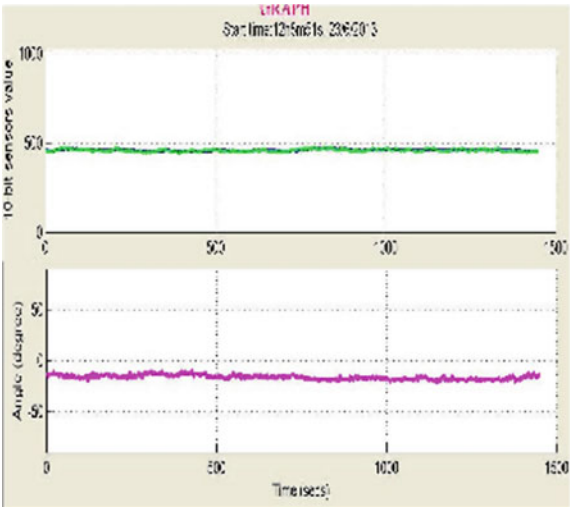

Fig. 8 Experimental data at 12h8′ AM

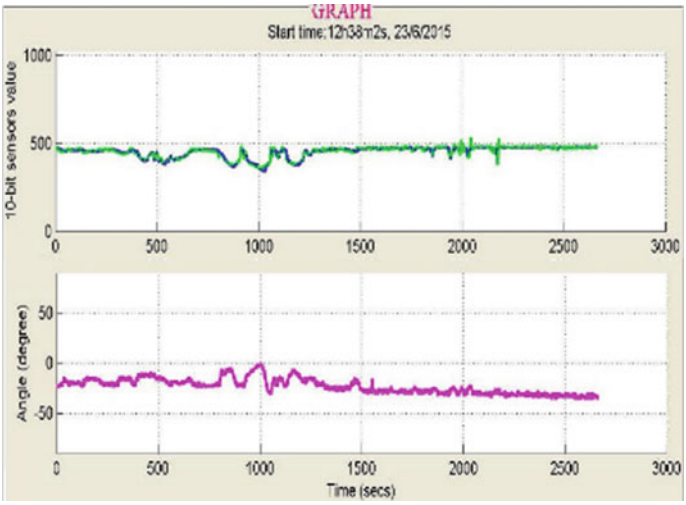

Fig. 9 Experimental data at 12h38′ AM

The experimental data show that the angle of parabolic trough has decreased from around -10° at 12h8′ AM to -45° at 1h38′ PM. The change of angle of solar trough help receive more energy for system.

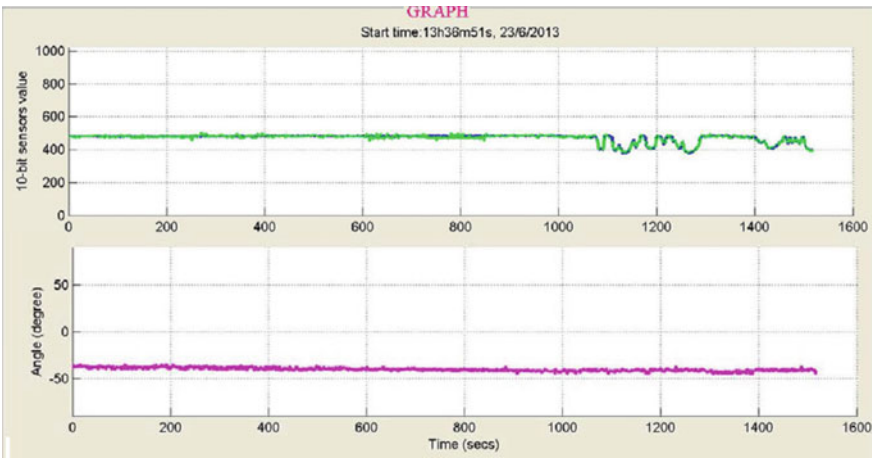

Fig. 10 Experimental data at 1h38′ PM

7 Conclusion

Based on research results we can conclude that the proposed solution for design of solar thermal collector and storage system, including solar thermal collector trough, the storage container system with minimum area, and solar tracking system has the some advantages: low cost; simple design convenient with local condition. With input parameters in Table 1 we designed solar trough with detail parameters in Sect. 3. The storage system is designed in Sect. 4, in which the area of designed storage container is minimum, so that fabricating is simplify. On the other hand this paper proposed solution for the effective using solar tracking system. The solar tracking system is controlled by microcontroller PIC 16F684, which receives signal of solar sensor and generates commands to the DC 24 V motor to rotate the solar trough toward the sun. The design system was verified by model in smaller scale. The experimental data show positive result.

References

1. Zarza E (2008) Medium temperature solar concentrators. Solar Energy Convers Photoenergy (Spain)
2. Beltran JA, Gonzalez Rubio JLS, Garcia-Beltran CD (2007) Design, manufacturing and performance test of a solar tracker made by an embedded control, CERMA 2007. Mexico
3. Panait MA, Tudorache T (2008) A simple neural network solar tracker for optimizing conversion efficiency in off-grid solar generators, ICREPQ. Spain
4. Haryanti M, HaLim A, Yusuf A (2014) Development of two axis solar tracking using five photodiodes. In: Electrical power, electronics, communications, controls and informatics seminar (EECCIS)

5. Abadi I (2014) Design of single axis solar tracking system at photovoltaic panel using fuzzy logic controller. In: 5th Brunei international conference on engineering and technology (BICET 2014)
6. Farahani MES (2006) Case study of design and implementation of a thermal energy storage system. In: Power and energy conference
7. Wirtz R (2004) Thermal and mechanical characteristics of a multi-functional thermal energy storage structure. In: Thermal and thermomechanical phenomena in electronic systems, ITHERM '04
8. Bon N (2001) Temperature distributed function of liquid in solar panel. J Thermal Sci Technol (Vietnam)
9. Bon N (2001) Calculating solar parabolic collector fixed trough. J Thermal Sci Technol (Vietnam)
10. Bon N (2012) Calculating solar thermal accumulator, using hot liquid. J Thermal Sci Technol (Vietnam)
11. Farahani MES, Res N (2006) Case study of design and implementation of a thermal energy storage system. In: IEEE international power and energy conference. PECon '06

Solving Bi-Objective Short-Term Cascaded Hydrothermal Scheduling Problem Using Modified Cuckoo Search Algorithm

Thang Trung Nguyen, Tuan Van Duong, Dieu Ngoc Vo and Bao Quoc Nguyen

Abstract This paper presents a modified cuckoo search algorithm (MCSA) for solving bi-objective short-term cascaded hydrothermal scheduling (BO-STCHTS) problem. The objective of the problem is to determine the optimal operation for thermal plants and a cascaded reservoir system while satisfying all constraints including electrical constraints of both hydro and thermal plants and hydraulic constraints of reservoirs so that the total generation of fuel cost and pollutant emission from thermal power plants are minimized. The MCSA has been developed by modifying the search strategy via Lévy flights to improve the performance of the conventional cuckoo search algorithm for solving the problem. The result comparison from a test system with nonconvex fuel cost function and cascaded reservoir between the proposed MCSA and other methods in the literature has shown that the MCSA is very efficient for the BO-STCHTS problem. Therefore, the proposed NCSA can be a efficient method for solving the nonconvex BO-STCHTS problem.

Keywords Modified cuckoo search algorithm · Cascaded hydropower plants · Lévy flights · Bi-objective cascaded hydrothermal scheduling

T.T. Nguyen (✉) · B.Q. Nguyen
Faculty of Electrical and Electronics Engineering, Ton Duc Thang University,
No. 19 Nguyen Huu Tho Street, District 7, Ho Chi Minh City, Vietnam
e-mail: nguyentrungthang@tdt.edu.vn

B.Q. Nguyen
e-mail: nguyenquocbao@tdt.edu.vn

T. Van Duong
Faculty of Electrical and Electronics Engineering,
University of Technical Education HCM City, 1 Vo Van Ngan Street,
Thu Duc District, Hcm City, Vietnam
e-mail: duongvantuan.cdn@gmail.com

D.N. Vo
Department of Power Systems, HCM City University of Technology,
268 Ly Thuong Kiet Street, 10th District, Hcm City, Vietnam
e-mail: vndieu@gmail.com

V.H. Duy et al. (eds.), *AETA 2015: Recent Advances in Electrical Engineering and Related Sciences*, Lecture Notes in Electrical Engineering 371,
DOI 10.1007/978-3-319-27247-4_19

1 Introduction

Bi-objective short-term cascaded hydrothermal scheduling is to determine the optimal generation of thermal plants and optimal water discharge via hydro turbine so that both fuel cost and the pollutant emission released from the thermal plants are minimized while electrical and hydraulic constraints including power balance, limits on generations, water discharge rate, and as well as reservoir storage limits are exactly met [1].

In recent years, many meta-heuristic algorithms have been employed to solve the bi-objective variable head short-term hydrothermal scheduling problems including evolutionary programming based interactive fuzzy satisfying method (EP-IFS) [2], differential evolution [3, 4], improved quantum-behaved particle swarm optimization (IQPSO) [5], multi-objective differential evolution (MODE) [6] and non-dominated sorting genetic algorithm-II (NSGA-II) [6], improved quantum-behaved particle swarm optimization (IQPSO) [7], Quadratic approximation based differential evolution with valuable trade off approach (QADEVT) [8], and Particle swarm optimization (PSO) [9]. Among the mentioned methods, EP-IFS [2] was the first application for solving the multi-objective variable head short-term hydrothermal scheduling problem and the results obtained by the methods in terms of cost, emission and computational time are worse than those from the other methods. In the study, the bi-objective problem is simplified by converting into single-objective one, a set of nondominated solutions needs to be determined and the interactive fuzzy satisfying method is then employed to determine the best compromise from the nondominated solutions. MODE and NSGA-II have also determined the set of nondominated solutions and then another technique has been employed to choose the best compromise solution. On the contrary, the studies in [3, 4, 7–9] have converted the bi-objective problem into single objective one by using price penalty factor and only the value of price penalty factor needs to be selected in case of finding the best compromise solution in stead of determining a set of nondominated solutions like studies [2, 6].

In this paper, a modified Cuckoo Search Algorithm (MCSA) is first proposed for the BO-STCHTS problem considering cascaded hydropower plants. The MCSA was developed by Walton et al. [10] by improving the search ability of the Conventional Cuckoo search algorithm with several modifications. Namely, in the first new solution generation via Lévy flights all initial eggs are ranked and classified into two groups where top group consists of better eggs and abandoned group contains other eggs, and the updated step size associated with the Lévy flights is adaptive for the two groups at each iteration. The MCSA has ever been successfully applied to short-term fixed hydrothermal scheduling [11] and in the paper, the effectiveness of the proposed MCSA methods has been tested on one system and the obtained results have been compared to those from methods reported in the paper.

2 Problem Formulation

In this section, the mathematical formulation of the BO-STCHTS problem consisting of N_1 thermal units and N_2 hydro units scheduled in M time sub-intervals with t_m hours for each is mathematically formulated.

2.1 Economic Dispatch

The fuel cost function can be accurately modelled in terms of real power output as a non-smooth cost function as follows:

$$F_1 = \sum_{m=1}^{M} \sum_{i=1}^{N_1} t_m \left\{ a_{si} + b_{si} P_{si,m} + c_{si} P_{si,m}^2 \left| e_{si} \times \sin\left(f_{si} \times \left(P_{si}^{\min} - P_{si,m}\right)\right)\right| \right\} \quad (1)$$

where a_{si}, b_{si}, c_{si}, e_{si}, f_{si} are fuel cost coefficients of thermal plant i; $P_{si,m}$ is power output of thermal unit i at subinterval m; t_m is the duration of subinterval m;

2.2 Emission Dispatch

The emission produced can be also expressed in form of a quadratic and exponential function as follows:

$$F_2 = \sum_{m=1}^{M} \sum_{i=1}^{N_1} t_m \left[\alpha_{si} + \beta_{si} P_{si,m} + \gamma_{si} P_{si,m}^2 + \eta_{si} \exp\left(\delta_{si} P_{si,m}\right) \right] \quad (2)$$

where α_{si}, β_{si}, γ_{si}, η_{si}, and δ_{si} are emission coefficients of thermal unit i.

2.3 Combined Economic and Emission Dispatch

In this paper, the bi-objective optimization problem is converted to a single objective one using a price penalty factor based method as follows.

Minimize

$$TC = w_1 \times F_1\left(P_{s,im}\right) + w_2 \times \mathrm{PR_m} \times F_2\left(P_{s,im}\right) \quad (3)$$

where w_1 and w_2 are respectively weight factors associate with fuel cost objective and emission objective; PR_m is the price penalty factor during subinterval m. The way to

determine the price penalty factor PR_m for a particular load over optimal interval is described in [12].

2.4 Considered Constraints

The objective function (3) above must be minimized subject to many following constraints:

(1) *Load Demand Equality Constraint*

The total power generation from thermal and hydro units must satisfy the load demand neglecting power losses in transmission lines.

$$\sum_{i=1}^{N_1} P_{si,m} + \sum_{j=1}^{N_2} P_{hj,m} - P_{L,m} - P_{D,m} = 0 \tag{4}$$

where $P_{L,m}$ and $P_{D,m}$ are load demand and transmission loss at subinterval m; $P_{hj,m}$ is the power output of hydro plant j at subinterval m and is defined as the following function of water discharge and reservoir volume

$$P_{hj,m} = C_{1hj}(V_{j,m})^2 + C_{2hj}(Q_{j,m})^2 + C_{3hj}Q_{j,m}V_{j,m} + C_{4hj}V_{j,m} + C_{5hj}Q_{j,m} + C_{6hj} \tag{5}$$

where C_{1hj}, C_{2hj}, C_{3hj}, C_{4hj}, C_{5hj}, C_{6hj} are the coefficients of the jth hydropower plant

(2) *Hydraulic Continuity Equation*

$$V_{j,m-1} - V_{j,m} + I_{j,m} - Q_{j,m} + \sum_{i=1}^{Nu}\sum_{m=1}^{M}(Q_{i,m-\tau_{i,j}}) = 0 \tag{6}$$

where $V_{j,m,}$ $I_{j,m}$ *and* $S_{j,m}$ are reservoir volume, water inflow and spillage discharge rate of jth hydropower plant in mth interval; $\tau_{i,j}$ is the water delay time between reservoir j and its up-stream i at interval m and Nu is the set of up-stream units directly above hydro-plant j.

(3) *Initial and Final Reservoir Storage*

$$V_{j,0} = V_{j,initial}; \quad V_{j,M} = V_{j,End} \tag{7}$$

(4) *Reservoir Storage and water discharge Limits*

$$V_{j,\min} \le V_{j,m} \le V_{j,\max}; \quad j = 1, 2, \ldots, N_2; \; m = 1, 2, \ldots, M \tag{8}$$

$$Q_{j,\min} \le Q_{j,m} \le Q_{j,\max}; \quad j = 1, 2, \ldots, N_2; \; m = 1, 2, \ldots, M \tag{9}$$

where $V_{j,\max}$ and $V_{j,\min}$ are the maximum and minimum reservoir storage of the hydro plant j, respectively; $Q_{j,\max}$ and $Q_{j,\min}$ are the maximum and minimum water discharge of the hydro plant j.

(5) *Generator Operating Limits*

$$P_{si,\min} \leq P_{si,m} \leq P_{si,\max}; \quad i = 1, 2, \ldots, N_1; \; m = 1, 2, \ldots, M \tag{10}$$

$$P_{hj,\min} \leq P_{hj,m} \leq P_{hj,\max}; \quad j = 1, 2, \ldots, N_2; \; m = 1, 2, \ldots, M \tag{11}$$

where $P_{si,\max}$, $P_{si,\min}$ *and* $P_{hj,\max}$, $P_{hj,\min}$ are maximum, minimum power output of thermal plant i and hydro plant j, respectively.

3 Modified Cuckoo Search Algorithm for BO-STCHTS Problems

3.1 Modified Cuckoo Search Algorithm

In conventional CSA, the new solutions generated via Lévy flights are obtained as below [11]:

$$X_i^{new} = X_i + \alpha.(X_{best} - X_i)\left(v \times \frac{\sigma_x(\beta)}{\sigma_y(\beta)}\right) \tag{12}$$

where X_{best} and X_i are the best egg and the ith egg among the number of eggs; $\alpha > 0$ is an updated step size. The value of α has a significant influence on the final solution because it will lead to different new solutions as it is set to different values. If this parameter is set to a high value, there is a huge difference between the old and new solutions and the optimal solution is either obtained fast or omitted. As the current iteration is high, the new obtained solution should be searched nearby the previous solution. However, the method has to find the optimal solution in a large search zone for this set value which may not reach the best optimal solution. Based on the analyzed drawback of the conventional CSA, it is clearly better to search for the optimal solution in a small zone as the iteration counter is increased to the maximum number of iterations which is predetermined for the iterative process [10].

3.2 Units Calculation of Power Output for Slack Thermal Unit

The slack variables consisting of the water discharge of jth reservoir at subinterval M, $Q_{j,M,d}$ and power output of thermal unit 1 at subinterval m, $P_{s1,m}$ are obtained as follows [11]:

$$Q_{j,M,d} = V_{j,0} - V_{j,M} + \sum_{m=1}^{M} I_{j,m} - \sum_{m=1}^{M-1} Q_{j,m} + \sum_{i=1}^{Nu} \sum_{m=1}^{M} (Q_{i,m-\tau_{i,j}}) = 0 \tag{13}$$

$$P_{s1,m} = P_{D,m} + P_{L,m} - \sum_{i=2}^{N_1} P_{si,m} - \sum_{j=1}^{N_2} P_{hj,m} \tag{14}$$

3.3 *Implementation of the Modified Cuckoo Search Algorithm*

3.3.1 Initialization

Similar to other meta-heuristic algorithms, each nest of Np nests is represented by $X_d = [P_{si,m,d}\ Q_{j,m,d}]$ ($d = 1,\ldots, N_p$). Each nest X_d is randomly initialized where $P_{si,\min} \le P_{si,m,d} \le P_{si,\max}$ ($i = 2,\ldots, N_1$; $m = 1,\ldots, M$) and $Q_{j,\min} \le Q_{j,m,d} \le Q_{j,\max}$ ($j = 1,\ldots, N_2$; $m = 1,\ldots, M - 1$). The reservoir volume at mth subinterval is obtained using Eq. (4), and $Q_{j,M,d}$ and $P_{hj,m,d}$ are then respectively obtained using (13) and (5). The slack thermal unit is obtained using (14).

Based on the initial population of nests, the fitness function to be minimized corresponding to each nest for the considered problem is calculated.

$$FT_d = \left(\begin{array}{l} \sum_{m=1}^{M} \sum_{i=1}^{N1} \left\{ w_1 \times F_1\left(P_{s,im}\right) + w_2 \times \mathrm{PR_m} \times F_2\left(P_{s,im}\right) \right\} + K_s \sum_{m=1}^{M} (P_{s1,m,d} - P_{s1}^{\lim})^2 \\ + K_V \sum_{j=1}^{N2} \sum_{m=1}^{M-1} (V_{j,m,d} - V_j^{\lim})^2 + K_Q \sum_{j=1}^{N2} \left((Q_{j,M,d} - Q_j^{\lim})^2 \right) + K_h \sum_{j=1}^{N2} \sum_{m=1}^{M} (P_{hj,m,d} - P_{hj}^{\lim})^2 \end{array} \right) \tag{15}$$

where K_s and K_h are respectively penalty factors for the slack thermal unit 1 and all hydro units; K_V and K_Q are respectively penalty factors for reservoir volume over $M - 1$ subintervals and water discharge at the subinterval M; The limits of variables in (15) are taken from [13].

In the MCSA all nests are first sorted in the descending order of their fitness function value and then classified into two groups. The nests with high fitness function value $Xabandoned_d$ are put in the abandoned group and the other ones $Xtop_d$ are put in the top group. A nest which is randomly picked among the $Xtop_d$ nests is called $Xtop_r$ and another one with the best quality is named $Xbest_d$. The two new solution generations are respectively described as below.

3.3.2 Generation of New Solution via the Lévy Flights

New Solution Generation for the Abandoned Group

Based on the modification applied to the abandoned eggs ($d = Notop + 1,\ldots, N_p$ where *Notop and Np* are the number of eggs in the top group and in the initial population, respectively), the optimal path for the Lévy flights is calculated using Mantegna's algorithm as follows:

$$Xabandoned_d^{new} = Xabandoned_d + \alpha \times rand \times \Delta X \tag{16}$$

The step size α is determined by $1/\sqrt{G}$ where G is the current iteration number, and ΔX is an increased step [11].

New Solution Generation for the Top Egg Group

The modification is applied to the eggs in the top group ($d = 1,\ldots, Notop$). The new solution for the top group is obtained as follows [11]:

$$Xtop_d^{new} = Xtop_d + \alpha \times rand \times \Delta Xtop_d^{new} \tag{17}$$

3.3.3 The Second New Solution Generation via Discovery of Alien Eggs

In the MCSA, all eggs of the top group and abandoned group are combined into one group first. The new solution due to this action can be found as follows:

$$X_d^{dis} = Xbest_d + K \times \Delta X_d^{dis} \tag{18}$$

where K is the updated coefficient and ΔX_d^{dis} is the increased value [11]. The new solutions can violate their limits and need to be redefined [13].

3.3.4 Stopping Criteria

The above algorithm is stopped when the maximum iteration is reached.

3.3.5 Overall Procedure

The overall procedure of the proposed MCSA for solving the BO-STCHTS problem is described as follows.

Step 1: Select parameters including number of nests N_p, probability of alien eggs to be abandoned P_a, the ratio of the number of eggs in top group to that in abandoned group and maximum number of iterations $N_{\max}$

Step 2: Initialize a population of N_p host nests as in Sect. 3.3.1 and calculate the slack water discharge and slack thermal unit 1 using Eqs. (13) and (14). Set the initial iteration counter $G = 1$

Step 3: Evaluate the fitness function using (15) to evaluate and classify the eggs into two groups including abandoned group, $Xabandoned_d$ ($d = Notop + 1,\ldots, Np$) and top group, $XTop_d$ ($d = 1,\ldots, Notop$). The egg with the lowest fitness function value is set to *Gbest* in the population

Step 4: Generate new solutions via Lévy flights for abandoned group and top group as described in Sects. 'New Solution Generation for the Abandoned Group' and 'New Solution Generation for the Top Egg Group', and calculate the slack water discharge and slack thermal unit 1 using Eqs. (13) and (14)

Step 5: Put the new eggs in top group and abandoned group in the integrated group and evaluate all the eggs to determine the best egg with the lowest fitness function

Step 6: Generate new solutions via the discovery of alien eggs as described in Sect. 3.3.3. Calculate the slack water discharge and slack thermal unit 1 using Eqs. (13) and (14)

Step 7: Evaluate the fitness function using (15) to determine the best egg, *Gbest*

Step 8: If $G < G_{\max}$, $G = G + 1$ and go back to step 3. Otherwise, terminate the iterative procedure

4 Numerical Results

The proposed MCSA has been implemented for solving one hydrothermal system consisting of four cascaded hydropower plants and three thermal plants considering valve-point loading effect and 24 one-hour scheduled subintervals. The data of the system are taken from [6]. The proposed MCSA is coded in Matlab platform and run fifty independent trials on a 1.8 GHz PC with 4 GB of RAM.

For implementation of the proposed MCSA, the number of nests and the maximum number of iterations are respectively set to 100 and 15,000 meanwhile the value of probability of alien egg discovery is from 0.1 to 0.9 with a step of 0.1. The optimal solutions of the bi-objective hydrothermal system scheduling problem are obtained for three dispatch cases including economic dispatch, emission dispatch and economic emission dispatch. Each dispatch is performed depending on values of w_1 and w_2 in Eq. (3). Namely, w_1 and w_2 are respectively fixed at 1 and 0 for economic dispatch, and fixed at 0 and $1/PR_m$ for emission dispatch whereas the values are set to 0 and 1 for economic emission dispatch. After performing the MCSA fifty independent runs for each value of Pa, the best optimal solutions are

Table 1 Comparison of result obtained by the proposed MCSA and other methods

Method	Economic dispatch		Emission dispatch		CEE dispatch		
	Cost ($)	CPU (s)	Emission (ton)	CPU (s)	Cost ($)	Emission (ton)	CPU (s)
RCGA	112,940	3156.5	11.6256	3261.4	–	–	–
NSGA-II	–	–	–	–	127,200	18.9605	4301.1
DE	110,810	2554.1	11.4994	424.4	–	–	–
MODE	–	–	–	–	126,820	17.7019	2957.2
MCSA	94278.4	113	9.5294	124	101,949	13.9674	118

achieved at Pa = 0.8, 0.3 and 0.7 corresponding to economic dispatch, emission dispatch and economic emission dispatch. The obtained cost and emission obtained by the MCSA are compared to those from other methods in [6] including real-coded genetic algorithm (RCGA), non-dominated sorting genetic algorithm-II (NSGA-II), differential evolution (DE), Multi-objective differential evolution (MODE) and reported in Table 1. Clearly, the total fuel cost and emission released into the air for electricity generation by using the proposed MCSA are much less than those from other. Furthermore, the execution time of searching optimal solution by MCSA is also much faster than the others. Note that all methods in [6] have been run on a Pentium-IV, 3.0 GHz computer. Consequently, the MCSA is more effective and robust than the methods and it is deserving of a powerful optimizer for solving the bi-objective short-term cascaded hydrothermal scheduling problem where the valve-point loading effect is taken into account.

5 Conclusion

In this paper, the proposed MCSA method has been applied for finding the optimal solution for the bi-objective short-term cascaded hydrothermal system scheduling where cascaded reservoir with water time delay from the upper reservoir flowing to the lower ones and the valve-point loading effects of thermal plants are considered. In the MCSA, the updated step size is adaptive at each iteration and there is no task for selection of the parameter. This is considered an advantage of the MCSA compared to the conventional CSA. The proposed MCSA has been tested on a four-hydropower plant and three-thermal plant system for three dispatch cases including economic, emission and economic emission dispatches. The results obtained by the proposed method in terms of generation fuel costs, emission and computational time have been compared to those from several other methods available in the paper and the result comparisons have revealed that the MCSA is more effective and robust than these methods. Therefore, the proposed MCSA is one of the promising modern optimizers for searching optimal solution of the bi-objective short-term cascaded hydrothermal scheduling problem.

References

1. Thang TN, Dieu NV (2014) Multi-objective short-term fixed head hydrothermal scheduling using augmented lagrange hopfield network. J Electr Eng Technol 9(6):1882–1890
2. Basu M (2004) An interactive fuzzy satisfying method based on evolutionary programming technique for multi-objective short-term hydrothermal scheduling. Electr Power Syst Res 69(2–3):277–285
3. Lakshminarasimman L, Subramanian S (2006) Short-term scheduling of hydrothermal power system with cascaded reservoirs by using modified differential evolution. IEE Proceedings Generation, Transmission and Distribution 153(6):693–700
4. Mandal KK, Chakraborty N (2008) Short-term combined economic emission scheduling of hydrothermal power systems with cascaded reservoirs using differential evolution. Energy Convers Manag 50:97–104
5. Sun C, Lu S (2010) Short-term combined economic emission hydrothermal scheduling using improved quantum-behaved particle swarm optimization. Expert Syst Appl 37(6):4232–4241
6. Basu M (2010) Economic environmental dispatch of hydrothermal power system. Electrical Power and Energy Systems 32:711–720
7. Lu S, Sun C (2010) Zhengding Lu. An improved quantum-behaved particle swarm optimization method for short-term combined economic emission hydrothermal scheduling. Energy Convers Manag 51:561–571
8. Lu S, Sun C (2011) Quadratic approximation based differential evolution with valuable trade off approach for bi-objective short-term hydrothermal scheduling. Expert Syst Appl 38(11): 13950–13960
9. Mandal KK, Chakraborty N (2011) Short-term combined economic emission scheduling of hydrothermal systems with cascaded reservoirs using particle swarm optimization. Appl Soft Comput 11(1):1295–1302
10. Walton S, Hassan O, Morgan K, Brown MR (2011) Modified cuckoo search: a new gradient free optimisation algorithm. Chaos, Solutions Fractals 44:710–718
11. Thang TN, Dieu NV (2015) "Modified Cuckoo search algorithm for short-term hydrothermal scheduling. Electrical Power and Energy Systems 65:271–281
12. Kulkarni PS, Kothari AG, Kothari DP (2000) Combined economic and emission dispatch using improved back-propagation neural network. Electric Power Comp Syst 28:31–44
13. Thang TN, Dieu NV, Tam TD (2014) Cuckoo search algorithm using different distributions for short-term hydrothermal scheduling with cascaded hydropower plants. In: TENCON 2014–2014 IEEE region 10 conference, pp 1–6

A Backtracking Search Algorithm for Distribution Network Reconfiguration Problem

Thuan Thanh Nguyen, Hiep Ngoc Pham, Anh Viet Truong, Tuan Anh Phung and Thang Trung Nguyen

Abstract This paper proposes a distribution network reconfiguration (DNR) methodology based on a backtracking search algorithm (BSA) for minimizing active power loss and minimizing voltage deviation. The BSA is a new evolutionary algorithm for solving of numerical optimization problems. It uses a single control parameter and two crossovers and mutation strategies for powerful exploration of the problem's search space. The effectiveness of the proposed BSA has been tested on 69-node distribution network system and the obtained test results have been compared to those from other methods in the literature. In addition to BSA, two other algorithms—particle swarm optimization (PSO) and cuckoo search algorithm (CSA)—are implemented for comparisons. The simulation results show that the proposed BSA can be an efficient and promising method for distribution network reconfiguration problems.

Keywords Distribution network reconfiguration · Cuckoo search algorithm · Particle swarm optimization · Backtracking search algorithm · Power loss reduction

T.T. Nguyen · H.N. Pham · A.V. Truong
Faculty of Electrical and Electronics Engineering,
HCMC University of Technology and Education, 1 Vo Van Ngan Street,
Thu Duc District, Ho Chi Minh City, Vietnam

T.T. Nguyen
Dong an Polytechnic, 30/4 Street, Di an Dist, Binh Duong Province, Vietnam

T.A. Phung
Ha Noi University of Technology, 1 Dai Co Viet Street, Ha Noi, Vietnam

T.T. Nguyen (✉)
Faculty of Electrical and Electronics Engineering, Ton Duc Thang University,
No. 19 Nguyen Huu Tho Street, District 7, Ho Chi Minh City, Vietnam
e-mail: nguyentrungthang@tdt.edu.vn

V.H. Duy et al. (eds.), *AETA 2015: Recent Advances in Electrical Engineering and Related Sciences*, Lecture Notes in Electrical Engineering 371,
DOI 10.1007/978-3-319-27247-4_20

1 Introduction

An electric power power distribution network (DN) system carries electricity from the transmission system to individual consumers. Recently, DN systems are becoming large and complex leading to higher system losses and poor voltage regulation. Therefore, loss reduction and voltage profile enhancement in DN systems have constituted one of the most important objectives for researchers. There are many methods available for reducing power loss and improvement of voltage profile at distribution level: capacitor installation, load balancing, reconfiguration and distributed generator installation. Reconfiguration is one of the most economic method among them.

In the last two decades, many researches have been carried out to solve DNR problems using different methods. Merlin and Back [1] were the first to report a method for distribution network reconfiguration to minimize feeder loss. Later on, several intelligent algorithms have been developed for loss minimization and/or voltage profile improvement. The most important algorithms in this category are genetic algorithm (GA) [2, 3] tabu search [4, 5] particle swam optimization (PSO) [6, 7] ant colony optimization (ACO) [8, 9] Recently, several novel methods based on artificial intelligence techniques have been implemented for DNR problems such as shuffled frog leaping algorithm (SFLA) [10], fireworks algorithm (FWA) [11], hybrid big bang-big crunch algorithm (HBB-BC) [12]. In general, most of the above intelligence techniques all inevitably involve a large number of computation requirements and have a lot of control parameters.

The backtracking search optimization algorithm (BSA) developed by Pinar Civicioglu is a new evolutionary algorithm for solving optimization problems [13]. The BSA has a unique mechanism for generating a trial individual which enables it to solve numerical optimization problems successfully and quickly. The BSA uses three basic genetic operators: selection, mutation and crossover to generate trial individuals. In this paper, the BSA is proposed for solving DNR problem considering power losses in transmission systems and voltage profile improvement. The effectiveness of the proposed BSA has been tested on 69-node distribution network system and the obtained results have been compared to those from other methods available in the literature.

This paper is organized as follows: The problem formulation is given in Section ‘Problem formulation’. The implementation of BSA for the problem is presented in Section ‘Backtraking search optimization algorithm for DNR’. The numerical results are provided in Section ‘Numerical results’. Finally, the conclusion is given.

2 Problem Formulation

The reconfiguration is defined as the process of changing the topology of system for a certain objective. The DNR is accomplished by changing open/close state of switches. In this study, the objective is to minimize total system active power loss and voltage deviation. The objective function can be described as follows [11, 14]:

$$minimize\ F = \Delta P_{loss}^{R} + \Delta V_D \tag{1}$$

The net power loss reduced (ΔP_{loss}^{R}) is taken as the ratio of total power loss before and after the reconfiguration of the system:

$$\Delta P_{loss}^{R} = \frac{P_{loss}^{rec.}}{P_{loss}^{0}} \tag{2}$$

The total power loss of the system is determined by the summation of losses in all line sections:

$$P_{loss} = \sum_{i=1}^{Nbr} R_i \times \left(\frac{P_i^2 + Q_i^2}{V_i^2}\right) \tag{3}$$

The voltage deviation index (ΔV_D) can be defined as follows:

$$\Delta V_D = \max\left(\frac{V_1 - V_i}{V_1}\right) \quad \forall i = 1, 2, \ldots, N_{bus} \tag{4}$$

The reconfigured process will try to minimize the ΔV_D closer to zero and thereby improves voltage stability and network performance.

The constraints of objective function are as follows:

(1) For the proposed configuration, the computed voltages and currents should be in their premising range.

$$V_{\min} \le V_i \le V_{\max}; \quad \mathrm{i} = 1, 2, \ldots, \mathrm{N_{bus}} \tag{5}$$

$$0 \le I_i \le I_{\max,i}; \quad \mathrm{i} = 1, 2, \ldots, \mathrm{N_{br}} \tag{6}$$

(2) The radial nature of DN must be maintained and all loads must be served.

3 Backtracking Search Optimization Algorithm for DNR

BSA comprises five processes: initialization, selection-I, mutation, crossover, and selection-II. The BSA method is implemented for DNR problem as follows.

3.1 Initialization

To maintain the radial topology of the network in DNR process, the number of open branches should always be equal to the number of tie-switches (N_{ts}) and could be obtained through Eq. 7:

$$N_{ts} = N_{br} - (N_{bus} - N_{ss}) \tag{7}$$

Therefore, the number of switches which must be open after reconfiguration is specific and must be used as a variable in algorithm. These switches are called tie-switches (SW). Therefore, every member of the initial population is a radial structure of the network. In DNR process using BSA, each radial structure of the network is considered as an individual. A population is represented by $P_i = \left[P^i_1, \ldots, P^i_{Nts-1}, P^i_{Nts}\right]$ *with* $i = 1, 2, \ldots, N$. Where N and N_{ts} are the population size, problem dimension, respectively. In which each P_i represents a solution vector of variables given by:

$$P_i = \left[SW^i_d\right], \quad \text{with } d = 1, 2, \ldots N_{ts} \tag{8}$$

where SW^i_d ($d = 1, 2, \ldots, N_{ts}$) are the tie-switches of corresponding to individuals i to maintain the radial topology of the network.

In order to reduce searching space of each tie-switch, the codification presented in [15] was used for the method proposed in this work. According to [15], the number of tie-switches is also equal the number of fundamental loops. Thus, an individual i is a vector with N_{ts} positions in which each position corresponds to a fundamental loop.

In the BSA, each individual can be regarded as a solution which is randomly generated in the initialization. Therefore, each individual i of the population is randomly initialized as follows:

$$P_i = round\left[SW^i_{\min,d} + rand \times \left(SW^i_{\max,d} - SW^i_{\min,d}\right)\right] \tag{9}$$

where $SW^i_{\min,d}$ and $SW^i_{\max,d}$ are minimum tie-switch and maximum tie-switch which are encoded in fundamental loop d.

Based on the initialized population, the load flow using Newton-Raphson load flow method is run then the fitness of each individual is calculated by the objective function Eq. 1.

In addition, BSA is a dual-population algorithm that uses both current and historical populations. It remembers the population of a randomly selected generation for use in calculating the search direction matrix. The historical population is also initialized by Eq. 10

$$oldP_i = round\left[SW^i_{\min,d} + rand \times (SW^i_{\max,d} - SW^i_{\min,d})\right] \tag{10}$$

3.2 Selection-I

In this stage, BSA generates the historical population *oldP*, used as the search direction. At the beginning of each iteration, BSA redefines *oldP* by comparing between two randomly generated numbers according to Eq. 11:

$$\text{If } rand(0,1) < rand(0,1) \text{ then } oldP = P \tag{11}$$

BSA memory remembers *oldP* as the historical population in each iteration until it is changed. This ensures that BSA designates a population belonging to a randomly selected previous generation. After determining the historical population based on the aforementioned equation, BSA changes the order of the individuals in *oldP* randomly through Eq. 12.

$$oldP = \text{permuting}(oldP) \tag{12}$$

where permuting function is a random shuffling function.

3.3 Mutation

The mutation process of BSA generates *Mutant* as the initial form of the trial population through Eq. 13.

$$Mutant = P + round\left[F \times (oldP - P)\right] \tag{13}$$

where F is a function that controls the amplitude of the search direction matrix, which is the difference between the population and the historical population. In this paper, the standard Brownian movement with $F = 3 \times rand\ (0,1)$ is used.

3.4 Crossover

This operation generates the final form of the trial population. In this process, the initial trial population *Mutant* is changed to the final trial population T through a crossover operator. Trial individuals with better fitness values for the optimization problem are used to evolve the target population individuals. The crossover process has two steps. The first step set the value of T to *Mutant*, then a binary integer-valued matrix (*map*) with N rows and d columns is generated to select the individuals that have to be manipulated. If $map\ (i,j) = 1$, where $i = \{1, 2,\ldots, N\}$ and $j = \{1, 2, 3,\ldots, d\}$, the individual $T(i,j)$ is updated with $T(i,j) = P(i,j)$. The second step applies a procedure related to a mix-rate parameter (*mixrate*) which is the only

control parameter during optimization that controls the number of elements of individuals that will modify in a trial.

Some individuals of T may violate the boundary condition of the optimization problem, so they are redefined at the end of the crossover process, as follows:

If $T(i,j) < SW_{\min j}$ or $T(i,j) > SW_{\max j}$ then:

$$T_i = round\left[SW^i_{\min,d} + rand \times (SW^i_{\max,d} - SW^i_{\min,d})\right] \tag{14}$$

3.5 Selection-II

In Selection-II stage, the individuals of population T with better fitness values than the corresponding particles of population P are used to update P based on a greedy selection. The global minimum among all the individuals is also updated according to the fitness values for T and P.

3.6 Stopping Criteria

In the proposed BSA method, the stopping criterion for the algorithm is based on the maximum number of iterations ($Iter_{\max}$). The algorithm is terminated when the number of iterations ($Iter$) reaches the maximum number of iterations (Fig. 1). The flowchart of the proposed BSA for DNR problem is given in Fig. 2.

4 Numerical Results

To demonstrate the performance and effectiveness of the proposed method using BSA, it is applied to 69-node test system and compared the results with those of PSO which has been applied for many optimal problems related to power system [16] as well as cuckoo search algorithm (CSA), which is a recently developed optimization algorithm [17] and has been applied successfully applied for DNR problem [18]. The BSA based methodology was developed by Matlab R2014a in 2 GHz, i3, personal computer.

4.1 Selection of Parameters

In the proposed BSA method, there are three control parameters to be handled including population size, maximum number of iterations ($Iter_{\max}$) and mix rate

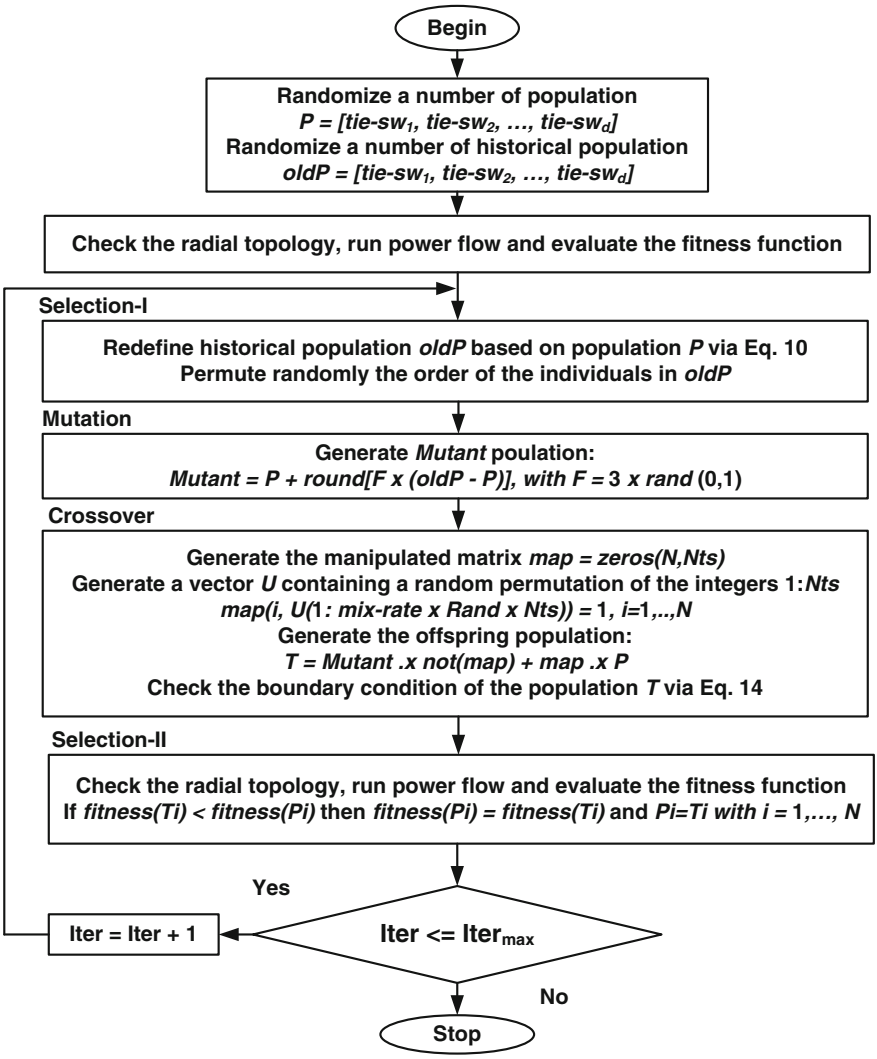

Fig. 1 Flowchart of proposed algorithm based on BSA

parameter (*mixrate*). In the BSA, *mixrate* controls the number of elements of individuals to be engaged in the crossover process and it ranges from 0 to 100 % of population size. To analyze the performance of BSA in DNR problem, the value of *mixrate* will be also adjusted in the range from 0 to 100 % with a step 10 % with the same initial population set. For comparisons, the parameters of PSO algorithm used in the simulation of network are weighting factors C1 = 2, C2 = 1.5, and CSA are probability of an alien egg to be discovered *pa* = 0.25 [18] and the mixrate of proposed BSA is 100 % [19].

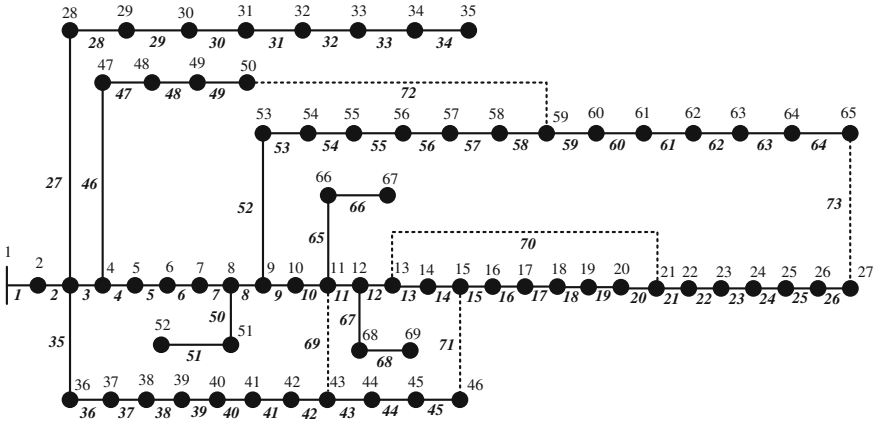

Fig. 2 IEEE 69-bus test system [20]

4.2 69-Node System

The 69-node distribution system, which is a medium-scale system, includes 69 nodes, 73 branches. There are 68 sectionalizing switches and 5 tie switches and total loads are 3.802 MW and 2.696 MVAr [20]. The schematic diagram of the test system is shown in Fig. 3. In a normal operation, switches {69, 70, 71, 72 and 73} are opened.

After performing the proposed reconfiguration problem based on BSA, switches {14, 57, 61, 69, 70} are opened and the network losses are reduced from 224.95 to 98.5875 kW. It is observed that nearly 56.17 % of total power loss has been reduced in the optimum case. Figure 3 shows the voltage profile improvement achieved by the proposed BSA algorithm. As shown, most of the bus voltages have been

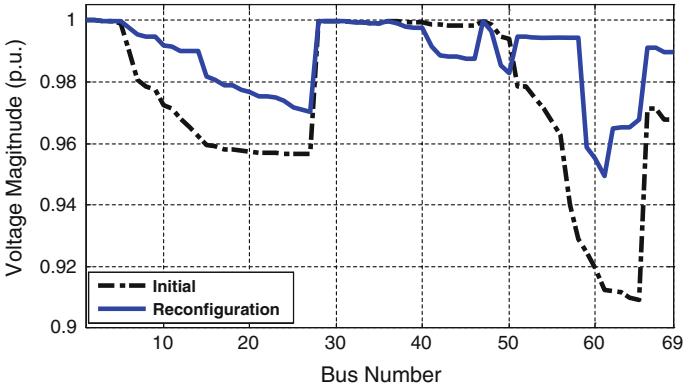

Fig. 3 Voltage profile for the 69-node system before and after reconfiguration

improved after reconfiguration. The minimum bus voltage before reconfiguration was equal to 0.9092 p.u. and after reconfiguration; it is raised to 0.9494 p.u.

The performance of BSA on 69-node system is also compared with the results of GA, Harmony Search Algorithm (HSA) and FWA methods available in the literature and presented in Table 1. From Table 1, it is observed that the results of the proposed method is encouraging and better than all other methods compared in terms of power loss minimization and voltage profile enhancement. The minimum power loss obtained by proposed algorithm is 4.70 and 0.76 kW lower than GA and HSA respectively. Also the minimum bus voltage is 0.0083 and 0.0066 p.u. higher than GA and HSA respectively. This demonstrates well the applicability of proposed method in a medium-scale radial distribution system. In addition, the best and the worst values among the best solutions as well as the average value and STD for the best solutions of PSO, CSA and the proposed algorithm in 200 times are also compared and presented in Table 1. From Table 1, although all three algorithms find the optimal configuration in 200 independent runs, the average power losses of BSA is 98.9055 kW which is 2.8465 kW lower than the PSO and this value is 0.318 kW higher than the CSA but BSA takes only 16.75 s to solve the problem while CSA has calculated the problem in 34.82 s while PSO has calculated in 17.01 s.

To demonstrate the performance of BSA in DNR problem, the value of *mixrate* will be adjusted in the range from 0 to 100 % of population size with a step of 10 % with the same initial population set. For each *mixrate* value, the DNR problem is

Table 1 Performance analysis of BSA for the 69-bus test system

Item	Base case	Optimum case					
		GA [21]	HSA [21]	FWA [14]	PSO	CSA	BSA
Tie-switches	69, 70, 71, 72, 73	14, 53, 61, 69, 70	13, 18, 56, 61, 69	14, 56, 61, 69, 70	14, 57, 61, 69, 70	14, 57, 61, 69, 70	14, 57, 61, 69, 70
$P_{lossBest}$ (kW)	**224.95**	**103.29**	**99.35**	**98.59**	**98.5875**	**98.5875**	**98.5875**
$P_{lossWorst}$ (kW)	–	–	–	–	109.0315	98.5875	104.9106
$P_{lossAverage}$ (kW)	**–**	**–**	**–**	**–**	**101.752**	**98.5875**	**98.9055**
STD of Ploss	**–**	**–**	**–**	**–**	**0.0743**	**0**	**0.0318**
Average % loss reduced	–	–	–	–	54.77	56.17	56.03
Best % loss reduced	–	54.08	55.85	56.17	56.17	56.17	56.17
V_{worts} (p.u.)	**0. 9092**	**0.9411**	**0.9428**	**0.9495**	**0.9494**	**0.9494**	**0.9494**
ΔV_D	0.0908	0.0589	0.0572	0.0505	0.0506	0.0506	0.0506
Average iterations	–	–	–	–	27.06	56.63	63.98
Average CPU time (s)	–	–	–	–	17.01	34.82	16.75

Table 2 The performance of BSA with different values of *mixrate* over 100 runs

Mixrate (%)	Fitness				DeltaP (kW)				ΔV_D
	Max	Min	Average	STD	Max	Min	Average	STD	0.0506
0	0.5367	0.4888	0.4965	8e-4	109.03	98.5875	100.29	17e-2	0.0506
10	0.5367	0.4888	0.4941	5e-4	109.03	98.5875	99.77	12e-2	0.0506
20	0.5169	0.4888	0.4939	13e-4	104.91	98.5875	99.70	28e-2	0.0506
30	0.5169	0.4888	0.4938	23e-4	104.91	98.5875	99.71	52e-2	0.0506
40	0.5169	0.4888	0.4924	4e-4	104.91	98.5875	99.41	8e-2	0.0506
50	0.5169	0.4888	0.4920	3e-4	104.91	98.5875	99.31	7e-2	0.0506
60	0.5169	0.4888	0.4923	25e-4	109.03	98.5875	99.36	56e-2	0.0506
70	**0.5169**	**0.4888**	**0.4916**	**25e-4**	**104.91**	**98.5875**	**99.22**	**57e-2**	**0.0506**
80	0.5169	0.4888	0.4922	3e-4	104.91	98.5875	99.35	8e-2	0.0506
90	0.5169	0.4888	0.4930	4e-4	104.91	98.5875	99.54	10e-2	0.0506
100	0.5169	0.4888	0.4919	25e-4	104.91	98.5875	99.26	56e-2	0.0506

solved 100 times repeatedly. The effect of the *mixrate* on the optimal solution by BSA method for 69-node system is analyzed and obtained results which are given in Table 2. From Table 2, it is observed that, the proposed BSA method can obtain the optimal solution for the values of *mixrate* from 0.0 to 100 % of population size with the average values are very close to the minimum values in all cases and the best value of *mixrate* for this system is 70 % with the minimum fitness and the average fitness are 0.4888 and 0.4916, respectively. Also from Table 2, it is very clear that the STD's value of power losses are very small from 0.07 to 0.57 in all cases, which shows that most of the best solutions are close to the average value. This demonstrates well the applicability of proposed method in DNR problem.

5 Conclusion

In this paper, the recent BSA method has been successfully applied for DNR problem. The objective is to minimize the active power loss and voltage profile enhancement of power distribution systems. The effectiveness of proposed method is demonstrated on 69-node distribution network. The numerical results verify that the proposed algorithm can converge to optimum solution quickly with better accuracy compared to other methods mentioned. The numerical results also show that the proposed method can solve distribution network reconfiguration problem more effectively and stably with less iteration and fewer time. In addition, the BSA based technique needs very little effort in turning the algorithm parameters, which is an advantageous for implementation perspective. Therefore, the proposed method based on BSA can be applied to practical distribution networks.

References

1. Merlin A, Back H (1975) Search for a minimal loss operating spanning tree configuration in an urban power distribution system. In: Proceeding 5th power system computation conference (PSCC), vol 1–18. Cambridge, UK
2. Duan D-L, Ling X-D, Wu X-Y, Zhong B (2015) Reconfiguration of distribution network for loss reduction and reliability improvement based on an enhanced genetic algorithm. Int J Electr Power Energy Syst 64:88–95
3. Gupta N, Swarnkar A, Niazi KR (2014) Distribution network reconfiguration for power quality and reliability improvement using genetic algorithms. Int J Electr Power Energy Syst 54:664–671
4. Zhang D, Fu Z, Zhang L (2006) An improved TS algorithm for loss-minimum reconfiguration in large-scale distribution systems. Electr Power Syst Res 77(7):685–694
5. Abdelaziz AY, Mohamed FM, Mekhamer SF, Badr MAL (2010) Distribution system reconfiguration using a modified Tabu Search algorithm. Electr Power Syst Res 80(8): 943–953
6. Tehzeeb-ul-hassan H, Zafar R, Ali S, Lateef O (2012) Reduction in power transmission loss using fully informed particle swarm optimization. Int J Electr Power Energy Syst 43(1): 364–368
7. Abdelaziz AY, Mohammed FM, Mekhamer SF, Badr MaL (2009) Distribution systems reconfiguration using a modified particle swarm optimization algorithm. Electr Power Syst Res 79(11):1521–1530
8. Swarnkar A, Gupta N, Niazi KR (2011) Adapted ant colony optimization for efficient reconfiguration of balanced and unbalanced distribution systems for loss minimization. Swarm Evol Comput 1(3):129–137
9. Saffar A, Hooshmand R, Khodabakhshian A (2011) A new fuzzy optimal reconfiguration of distribution systems for loss reduction and load balancing using ant colony search-based algorithm. Appl. Soft Comput. J. 11(5):4021–4028
10. Arandian B, Hooshmand R, Gholipour E (2014) Decreasing activity cost of a distribution system company by reconfiguration and power generation control of DGs based on shuffled frog leaping algorithm. Int J Electr Power Energy Syst 61:48–55
11. Mohamed Imran A, Kowsalya M, Kothari DP (2014) A new power system reconfiguration scheme for power loss minimization and voltage profile enhancement using Fireworks Algorithm. Int J Electr Power Energy Syst 62:312–322
12. Sedighizadeh M, Esmaili M, Esmaeili M (2014) Application of the hybrid Big Bang-Big Crunch algorithm to optimal reconfiguration and distributed generation power allocation in distribution systems. Energy
13. Civicioglu P (2013) Backtracking search optimization algorithm for numerical optimization problems. Appl Math Comput 219(15):8121–8144
14. Mohamed Imran A, Kowsalya M, Kothari DP (2014) A novel integration technique for optimal network reconfiguration and distributed generation placement in power distribution networks. Int J Electr Power Energy Syst 63:461–472
15. Mendoza J, López R, Morales D, López E, Dessante P, Moraga R (2006) Minimal loss reconfiguration using genetic algorithms with restricted population and addressed operators: real application. IEEE Trans Power Syst 21(2):948–954
16. Singh SP, Rao AR (2012) Optimal allocation of capacitors in distribution systems using particle swarm optimization. Int J Electr Power Energy Syst 43(1):1267–1275
17. Yang X-S, Deb S (2009) Cuckoo search via Lévy flights In: Proceedings of world congress on nature and biologically inspired computing (NaBIC), India, pp 210–214
18. Nguyen TT, Truong AV (2015) Distribution network reconfiguration for power loss minimization and voltage profile improvement using cuckoo search algorithm. Int J Electr Power Energy Syst 68:233–242

19. Modiri-Delshad M, Rahim NA (2014) Solving non-convex economic dispatch problem via backtracking search algorithm. Energy 77:372–381
20. Chiang HD, Jean-Jumeau R (1990) Optimal network reconfigurations in distribution systems: part 2: solution algorithms and numerical results. IEEE Trans Power Deliv 5(3):1568–1574
21. Rao RS, Ravindra K, Satish K, Narasimham SVL (2013) Power loss minimization in distribution system using network reconfiguration in the presence of distributed generation. IEEE Trans Power Syst 28(1):317–325

Part V
Power Electronics

A Study on the Firing Angle at the Mode Conversion to Improve the Output Characteristics of the Double Converter for Urban Rail DC Power Supply

Sung Woo Han, Seung Sam Seo, Jin Han Lee, SeongGyu Kim, Min Kim and Gi Sig Byun

Abstract This paper proposes a thyrister rectification type of double converter rectification equipment to simplify trolley line equipment and return the regenerative power into AC motion without storage equipment by converting the double converter into Converter(Forward) or Inverter(Reverse) based on voltages supplied for the trolley lines using high current thyristers and keeping voltages supplied for the trolley lines constant and an optimal thyrister firing angle to improve output characteristics in mode conversion of Converter(Forward) or Inverter(Reverse) by the simulation and experiments for operation and output characteristics of the double converter rectification equipment.

Keywords Double converter · Regenerative power · Urban rail DC substation equipment · Railway technology

1 Introduction

To fill transportation demands of big cities and reduce air pollution by the exhaust gas from vehicles in South Korea, some metropolitan cities are constructing urban railways and running for them by national support. In urban rail DC substation equipment, diode rectification and thyrister rectification methods are used. Only in Busan city railways of South Korea, the thyrister rectification method is used. Other

S.W. Han (✉) · S.S. Seo · J.H. Lee · S. Kim
R & D Center, Busan Transportation Corporation, HopoSaedongne-Gil 5, Yangsan, Gyeongsangnam-Do 626-821, Korea
e-mail: h111641@humetro.busan.kr

M. Kim · G.S. Byun
Department of Control and Instrumentation Engineering, Pukyong National University, Busan 608-737, Korea

V.H. Duy et al. (eds.), *AETA 2015: Recent Advances in Electrical Engineering and Related Sciences*, Lecture Notes in Electrical Engineering 371,
DOI 10.1007/978-3-319-27247-4_21

cities except for Busan city in South Korea are using the diode rectification method. The diode rectification method has simple equipment and easy maintenance, but it cannot make the DC output track load change of the trolley line and must install rectifier separation devices (insulated sections) on lines of trolley lines in preparation for unbalance of DC voltage during rectification time in a substation. Moreover, in rising line voltages of trolley lines by regenerative power generated in deceleration of an electrical train, its electrical equipments must be protected for the insulation protection of the interior electrical equipments of the electrical train by installing resistors on the electrical train and dissipating the rising voltage with heat.

Recently, researches recovering the regenerative power generated in deceleration of the electrical train for the urban rail management efficiency through the electrical energy reduction have been actively reported. However, urban rail management organizations are avoiding installing IGBT regenerative inverter or energy storage equipments to the diode rectification type of the substation equipment or IGBT regenerative inverter or energy storage equipments due to low power regeneration rate, the excessive installation area, the increase of the number of member for maintenance, etc. [1–3]. Because a thyrister rectification type of double converter rectification equipments keeps constant voltages of the trolley lines by the mode conversion into Converter(Forward)/Inverter(Reverse) based on line voltage of the trolley lines, its equipment can be simplified, the regenerative power in deceleration of the electrical train can returned be into AC motion without storage equipment.

This paper proposes a thyrister rectification type of double converter rectification equipment with high current and an optimal thyrister firing angle to improve operation and output characteristics of the double converter rectification equipment by simulation and experiment.

2 Thyrister Rectification Type of Double Converter System

2.1 Configuration and Operation of Double Converter

A thyrister rectification type of double converter system is operated with both converter (forward) mode and inverter (reverse) mode and supplies power needed for an electrical train. It is operated in bi-direction and can return the regenerative power into AC motion in braking the electrical train. It can keep constant trolley line voltages of the electric train by adjusting its power supply depending on load. Figure 1 shows the double converter to be operated with 6 phases and 12 pulses by connecting Y type of thyrister converter with 3 phases and 6 pulses and Δ type of thyrister converter with 3 phases and 6 pulses in parallel.

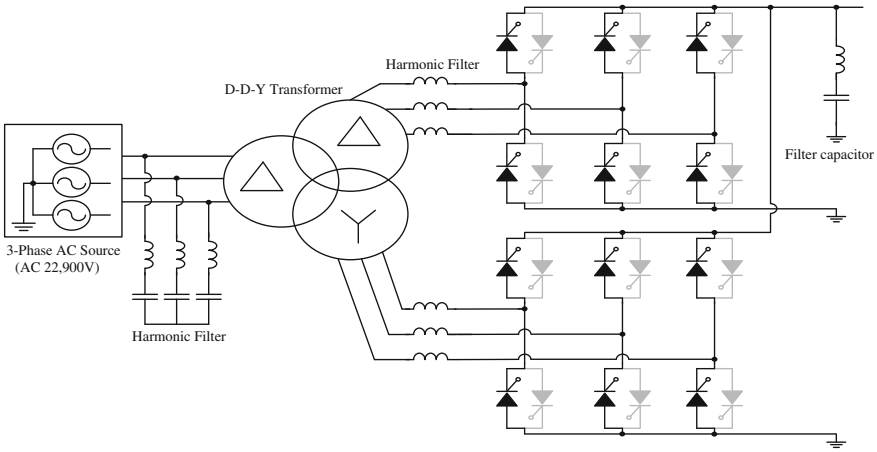

Fig. 1 Structure of the double converter system

2.2 *Phase Control of the Double Converter*

Figure 2 shows the 12-pulse phase controlled rectifier that two 3-phase 6-pulse phase controlled rectifiers connected with the $\Delta - \Delta - Y$ transformer have parallel structure as shown in Fig. 2.

Average output voltage of the two 3-phase 6-pulse phase controlled rectifier can be represented as

$$V_0 = \frac{1}{T}\int_{T+\alpha}^{2T+\alpha} V_{m,l-l}\sin(\omega t)d\omega t \tag{1}$$

where T is a period of the voltage wave, α is a firing angle of SCR, and $V_{m,l-l}$ is an effective value of line voltage.

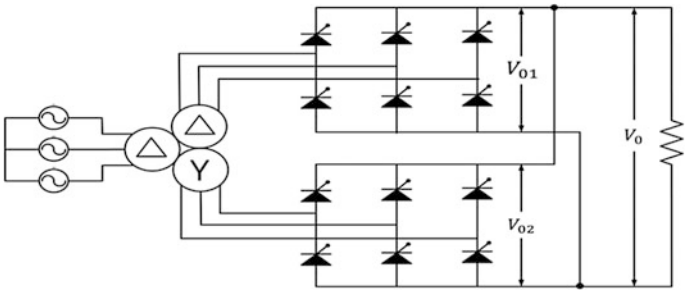

Fig. 2 12-pulse phase controlled rectifier

Input voltage of the phase controlled rectifier is supplied from the $\Delta-\Delta-Y$ transformer. Because the phase difference between line voltages of $\Delta-\Delta$ and $\Delta-\Delta$ is 30°, the output voltage supplied to the phase controlled rectifier is supplied with a 6 phase 12 pulse type with the period of 30°. That is, since the period of the voltage wave T is $\frac{\pi}{6}$, Eq. (2) can be expressed as follows:

$$V_0 = \frac{1}{\pi/6}\int_{\frac{\pi}{6}+\alpha}^{\frac{2\pi}{6}+\alpha} V_{m,l-l}\sin(\omega t)\,d\omega t = \frac{6V_{m,l-l}}{\pi}\int_{\frac{\pi}{6}+\alpha}^{\frac{2\pi}{6}+\alpha} V_{m,l-l}\sin(\omega t)\,d\omega t \tag{2}$$

Taking integral of Eq. (2) yields

$$\begin{aligned} V_0 &= \frac{6V_{m,l-l}}{\pi}[-\cos\omega t]_{\frac{\pi}{6}+\alpha}^{\frac{2\pi}{6}+\alpha} = \frac{6V_{m,l-l}}{\pi}\left[-\cos(\frac{2\pi}{6}+\alpha)-\left\{-\cos(\frac{\pi}{6}+\alpha)\right\}\right] \\ &= \frac{6V_{m,l-l}}{\pi}\left[-\cos(\frac{2\pi}{6}+\alpha)+\cos(\frac{\pi}{6}+\alpha)\right] \end{aligned} \tag{3}$$

By applying cosine theorem and sine theorem in Eq. (3), the following is obtained:

$$\begin{aligned} V_0 &= \frac{6V_{m,l-l}}{\pi}\left[(-\cos\frac{2\pi}{6}\cos\alpha+\sin\frac{2\pi}{6}\sin\alpha)+(\cos\frac{\pi}{6}\cos\alpha-\sin\frac{\pi}{6}\sin\alpha)\right] \\ &= \frac{6V_{m,l-l}}{\pi}\left[(\frac{\sqrt{3}-1}{2}\cos\alpha+\frac{\sqrt{3}-1}{2}\sin\alpha)\right] \\ &= \frac{3(\sqrt{3}-1)V_{m,l-l}}{\pi}(\cos\alpha+\sin\alpha) = \frac{6(\sqrt{3}-1)V_{l-l}}{\pi}\cos(\alpha-\frac{\pi}{4}) \end{aligned} \tag{4}$$

In the 6-phase 12-pulse phase controlled rectifier, the average output voltage is not influenced in the range of the firing angle of 0°–15°. Therefore, by applying the phase difference of $\frac{\pi}{6}$ to Eq. (4), Eq. (4) can be represented as follows:

$$V_0 = \frac{6(\sqrt{3}-1)V_{l-l}}{\pi}\cos(\alpha-\frac{\pi}{4}+\frac{\pi}{6}) = \frac{6(\sqrt{3}-1)V_{l-l}}{\pi}\cos(\alpha-\frac{\pi}{12}) \tag{5}$$

To verify the effectiveness of Eq. (5), PSIM simulation as shown in Fig. 3 is done. The effective value of output line voltage of the $\Delta-\Delta-Y$ transformer is 87.5 V and only resistance load is connected without a harmonic wave filter.

To show the effectiveness of Fig. 3, calculated results by Eq. (5) and simulation results with respect to firing angles are given in Table 1.

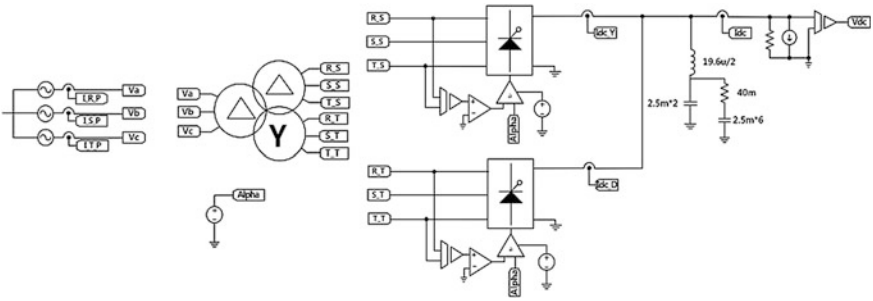

Fig. 3 Double converter phase control simulation configuration

Table 1 Calculated and simulation results of DC voltage output V_0 with respect to the firing angle

Firing angle	Calculated results	Simulation results (V)
0°	122.33	123.35
15°	122.33	123.35
45°	105.945 V	105.53
64.1605246°	80 V	79.2

2.3 Analysis of Control Algorithm for Double Converter

2.3.1 Control Algorithm of the Double Converter

Figure 4 shows the control configuration for the double converter system. By detecting 0 voltage of 3-phase voltage, triggering time of the firing angle ∝ is determined. Moreover, by detecting DC voltage V_{dc} and DC current I_{dc}, DC voltage

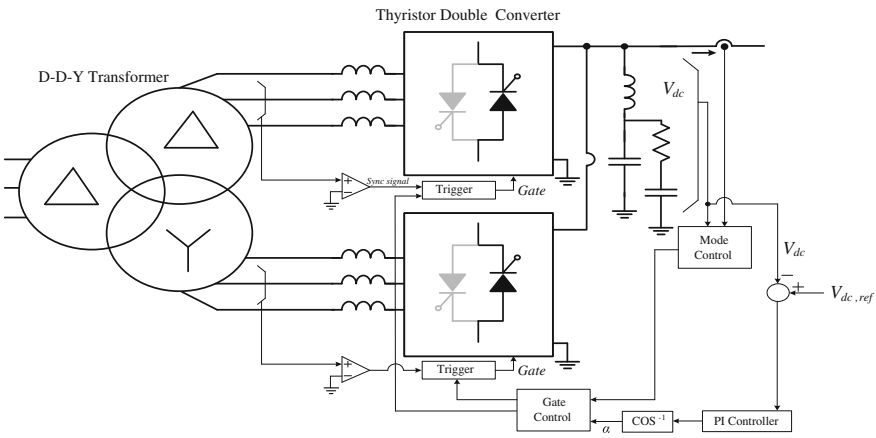

Fig. 4 Control configuration of the double converter system

V_{dc} and DC current I_{dc} are input to PI controller for determination of the double converter mode and calculation of the firing angle α.

The controller makes the thyrister triggered with the firing angle α suitable to the operation condition of converter mode and inverter mode by the signals generated from the control algorithm.

The control objective of the double converter is to keep the voltages supplied to the trolley lines constant based on control conditions. Figure 5 shows a flowchart of the basic control algorithm for this task.

Mode conversion of converter mode and inverter mode must be satisfied with mode conversion conditions and must be complemented to prevent short to each other. When DC voltage V_{dc} is decreased to less than $V_{ref} - V_{\min}$, the double converter is operated as the converter mode and controls the DC voltage V_{dc} to track the referencevoltage V_{ref}. When DC voltage V_{dc} is increased to more than $V_{ref} - V_{\min}$, the double converter is operated as the inverter mode and controls the DC voltage V_{dc} to track the reference voltage V_{ref}. A voltage hysteresis band is used not to generate the sudden mode conversion [3].

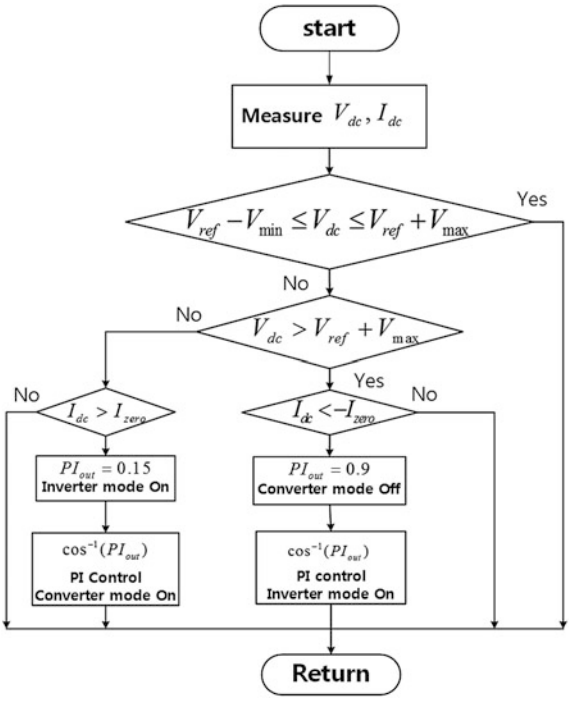

Fig. 5 Flowchart of the double converter control algorithm

2.3.2 Control Algorithm of the Conventional Double Converter System

Figure 6 shows configuration for the PSIM simulation. The fire angle α of the conventional double converter system used for the substation of Busan city railway is verified by PSIM of Fig. 6. The specification of Table 2 is used for the PSIM simulation. The 3-phase 22.9 kV input voltage received from AC motion is transformed into 3-phase 1,750 V voltage by the $\Delta - \Delta - Y$ transformer and this 3-phase 1,750 V voltage is input to the double converter.

For the double converter, converter mode and inverter mode are used alternately based on line voltage and current conditions supplied for the trolley lines. Table 3 shows control conditions for the double converter.

Figure 7 shows simulation results for the double converter. When the trolley line voltage V_{dc} is over 1,700 V, the double converter is operated with inverter mode. When the trolley line voltage V_{dc} is greater than or equal to 1,600 V, the double converter is operated with converter mode. Therefore, V_{dc} keeps constant independently of load change. When the double converter is converted to converter/inverter, it is shown that undershoots/overshoots occurred by the accumulation of errors within the hysteresis band of PI controller.

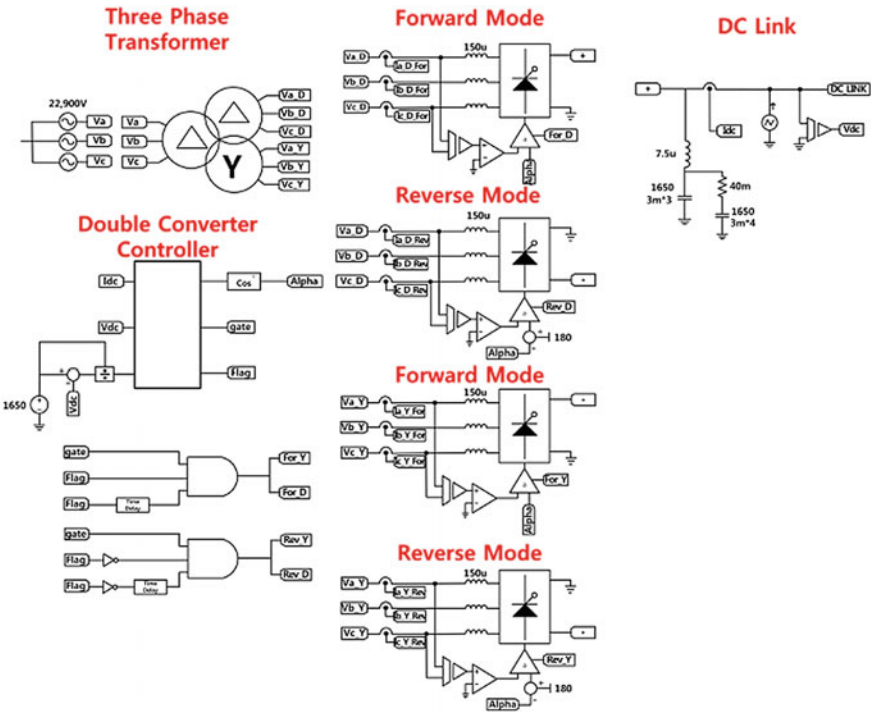

Fig. 6 Configuration of the PSIM simulation

Table 2 Specifications of the double converter used for simulation

Transformers	Input voltage	3Φ 22.9 kV
	Connection	$\Delta - \Delta - Y$
	Transformer turns ratio	$22{,}900: 1{,}750: 1{,}750/\sqrt{3}$
	Output voltage	3Φ 1,750 V
Double converter	Rated output voltage	DC 1,650 V
	capacity	8.25 MW
DC load current	Maximum current	2,500 A
	Minimum current	−2,500 A

Table 3 Control conditions for the double converter

Converter mode	DC voltage	$V_{dc} < 1600$ V
	DC current	$I_{dc} > 20$ A
	Firing angle range	$0° < \alpha < 90°$
Inverter mode	DC voltage	$V_{dc} > 1700$ V
	DC current	$I_{dc} < -20$ A
	Firing angle range	$90° < \alpha < 180°$

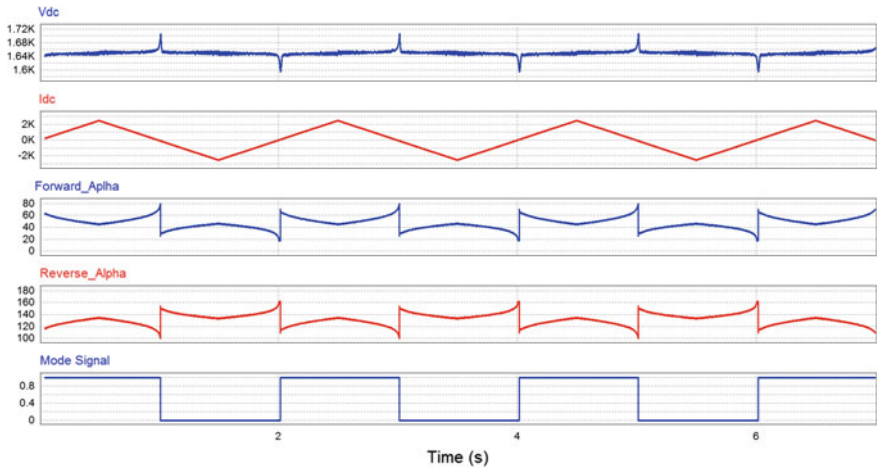

Fig. 7 Simulation results for the double converter

When the mode conversion of the double converter is done, the mode conversion of the double converter is performed based on the control conditions of Table 3. The mode of the double converter can be shown in mode signals of Fig. 7. In case that the mode signal is "1", the double converter is operated with converter mode. On the other hand, in case that the mode signal is "0", the double converter is operated with inverter mode. The fire angle α in converter mode is shown in Forward Alpha of Fig. 7 and is in the range of $0° < \alpha_{For} < 90°$. In conversion from

inverter mode to the converter mode, $\alpha_{For} = 70.4°$. The fire angle α in inverter mode is shown in Reverse_Alpha of Fig. 7 and is in the range of $90° < \alpha_{Rev} < 180°$. In conversion from the converter mode to the inverter mode, $\alpha_{Rev} = 154.7°$.

3 Optimal Firing Angle in Mode Conversion of Double Converter

3.1 Analysis of Optimal Firing Angle for the Double Converter

When the mode conversion of the double converter is done, converted to converter/inverter, it is important to choose the initial firing angle to prevent undershoots/overshoots generated by the accumulation of errors within the hysteresis band of PI controller and to make DC voltage V_{dc} track reference voltage V_{ref} fast as possible. Therefore, simulation is done to verify the output characteristics in conversion of the mode of the double converter due to the choice of the initial firing angle as shown in Fig. 6 showing configuration for the PSIM simulation of the conventional double converter system used for the substation equipment of Busan city railway. Table 4 shows the specification used for simulation in analyzing the initial fire angle. Table 4 applies 1/20 time of the real model in output voltage and current and 1/400 time of the real model in capacity for verification by experiment and manufacture of prototype in future. PI gain values are limited as the minimum value of 0.5 and the maximum value of 0.9 to prevent short between the double converter.

Table 4 Specification used for simulation

Division	Items	Settings
Transformers	Connection	$\Delta - \Delta - Y$
	Input and output frequency	60 Hz
	Primary input voltage	3Φ 380 V
	Secondary Δ connection side output voltage	3Φ 87.5 V
	Secondary Y connection side output voltage	$3\Phi\ 87.5/\sqrt{3}$V
	Transformer turns ratio	$380 : 87.5 : 87.5/\sqrt{3}$V
Double converter	Capacity	5 kVA
	Output voltage	DC 80 V
Double converter controller	DC voltage reference	80 V
	Forward mode	$V_{dc} < 75$ V and $I_{dc} > 2$ A
	Reverse mode	$V_{dc} > 85$ V and $I_{dc} < -2$ A
	Zero current hysteresis band	-1 A $< I_{dc} < 1$ A

3.1.1 Control Algorithm of the Conventional Double Converter System

Table 5 shows relation between the initial firing angle and PI value when the double converter is converted to converter mode.

Figure 8 shows conversion characteristic graph with respect to the initial firing angle when the double converter is converted to converter mode. In the initial fire angle of $\alpha(0) = 70°$, Fig. 8 shows the fast response, the smallest voltage fluctuation rate and the best tracking performance voltage to the reference voltage of the DC voltage.

3.1.2 Response Characteristics with Respect to the Initial Firing Angle in Inverter Mode

Table 6 shows the relation between the initial firing angle and PI value when the double converter is converted to inverter mode. Figure 9 shows conversion characteristic graph with respect to the initial firing angle when the double converter is converted to inverter mode.

Table 5 Relation between initial firing angle and PI value in the converter mode for simulation

No.	Initial firing angle	PI value
1	58°	0.5299
2	62°	0.4694
3	68°	0.4067
4	70°	0.3420
5	74°	0.2756
6	78°	0.2079
7	82°	0.1391

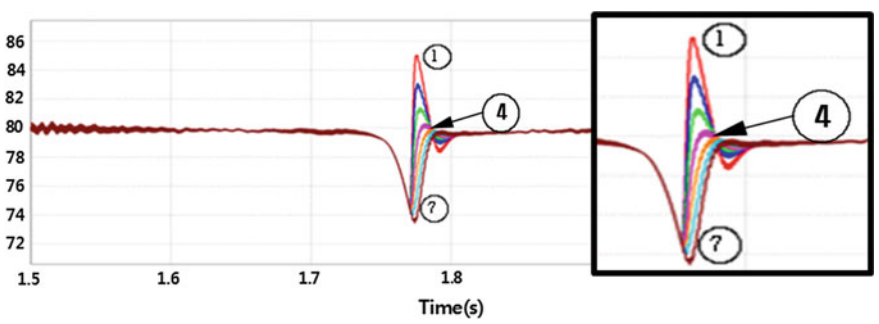

Fig. 8 Conversion characteristics in converter mode with respect to with the initial firing angle

Table 6 Relation between the initial firing angle and PI value in invert mode for simulation

No.	Initial firing angle	PI value
1	130°	0.6427
2	134°	0.6946
3	138°	0.7431
4	142°	07880
5	146°	0.8290
6	150°	0.8660
7	154°	0.8987

In the initial fire angle of $\alpha(0) = 154°$, Fig. 9 shows the fast response, the smallest voltage fluctuation rate and the best tracking performance voltage to the reference voltage of the DC voltage.

Because the initial firing angle is influenced by high pass filter and current reference in mode conversion, the real value of the firing angle used for Busan city railways and the value of the optimal firing angle in simulation were different a little as shown in Table 7.

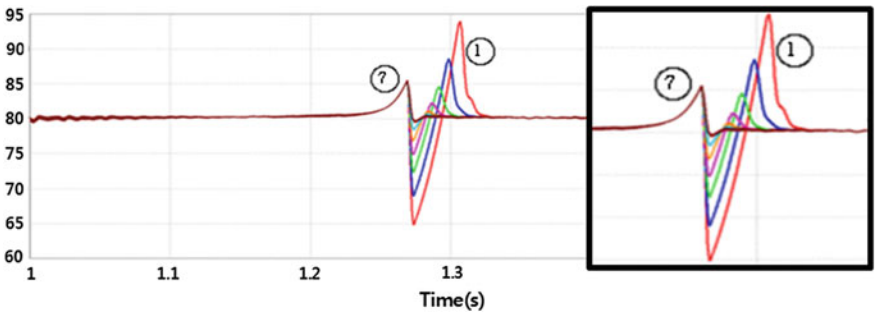

Fig. 9 Conversion characteristics in inverter mode with respect to the initial firing angle

Table 7 Measured and simulated values of the firing angle of Busan city railway

Division	Converter mode conversion from the inverter	Inverter mode conversion from the converter
Busan city railway firing angle	70.4°	154.7°
Simulating firing angle	70°	154°

4 Conclusions

This paper proposed the control of a double converter to be able to reuse the regenerative energy. When the mode conversion of the double converter was done, the simulation results were shown to minimize the undershoot and the overshoot by the optimal initial firing angle. The simulation results showed that the optimal firing angle was $\alpha = 70^\circ$ in the converter mode and $\alpha = 154^\circ$ in the inverter mode.

Acknowledgement This study is a study carried out with the support of the South Korea Agency for Infrastructure Technology Advancement (14RTRP-B091404-01).

References

1. Sekijima Y, Inui M, Monden Y, Nishikawa H (2004) Application study of electric double layer capacitor on regenerative braking for DC railway system. IEE Japan, p 195–19
2. Kim JG, Kim JH, Cho KH, Won CY, Kim YK (2007) Regenerative inverter system for DC traction substation with voltage drop compensation mode. Trans Korean Inst Power Elestron, p 213–220
3. Han SW (2014) Development of algorithm for improving efficiency of dual converter power supply system of city railway, Master Thesis, Donga University
4. Perreaul DJ, Kassakian JG (1995) Effects of firing angle imbalance on 12-pulse, IEEE Trans Power Electron, 10(3):257–262
5. Bae CH, Han MS, Kim YG, Kwon SY (2005) Simulation study of a regenerative inverter for absorption of regenerative energy in a DC traction substatio. In: Proceedings of the 2005 Autumn Conference for Railway, J Korea Soc Railw, p 69–75
6. Visintini R (2004) Rectifier. Intermediate Accelerator Physics, CAS CERN Accelerator School, Warrington, United Kingdom, p 12–18

A Synchronization Method for Three-Phase Grid-Connected Inverters Using Levenberg-Marquardt Technique

Tran Quang Tho, Pham Huu Ly, Truong Viet Anh and Le Minh Phuong

Abstract The controllers of three-phase grid-connected inverters usually need improvements to allow distributed generations to meet the stringent grid codes with high power quality and the fault ride through ability. Therefore, the performance of the grid-connected inverter depends on the response of the selected synchronization method. This paper proposes a method with high accuracy and good dynamics under the unbalanced and highly distorted voltage. The proposed method bases on the least squares technique using the Levenberg-Marquardt algorithm to rapidly converge the solution, thus requiring less hardware and associated cost for real-time implementation. The technique does not base on interdependent loops offering stability and easy estimating process. The robustness and accuracy of the proposed technique are better than the techniques basing on the dual second-order generalized integrator (DSOGI) and the conventional PLL. The simulation results in MATLAB/Simulink under the unbalanced and harmonic voltage conditions validated the performance of the proposed method.

Keywords Grid-connected inverters · Synchronous reference frame based phase-locked loop (SRF-PLL) · Second-order generalized integrator (SOGI) · Synchronization method · Newton-type algorithm (NTA)

T.Q. Tho · T.V. Anh
Hochiminh City University of Technology, Hochiminh City, Vietnam
e-mail: thotq@hcmute.edu.vn

P.H. Ly (✉)
Faculty of Electrical and Electronics Engineering, Ton Duc Thang University,
No. 19 Nguyen Huu Tho Street, District 7, Ho Chi Minh City, Vietnam
e-mail: phamhuuly@tdt.edu.vn

L.M. Phuong
Hochiminh City University of Technology (VNU-HCM), Hochiminh City, Vietnam

V.H. Duy et al. (eds.), *AETA 2015: Recent Advances in Electrical Engineering and Related Sciences*, Lecture Notes in Electrical Engineering 371,
DOI 10.1007/978-3-319-27247-4_22

1 Introduction

The requirement of quick and accurate estimation of grid voltage parameters is one of the priority duties of grid-connected inverters. The estimation of fundamental parameters of grid voltage from a clean sinusoidal waveform is a relatively easy task [1]. However, the parameters of the actual input grid voltage in the grid-connected inverters are often changed such as voltage and frequency fluctuations, unbalance, high harmonics, and dc offset typically introduced by the measurements and data conversion processes. Therefore, the estimation of the distorted grid voltage parameters becomes a relatively difficult duty to meet stringent grid codes [2–9]. Many digital signal processing (DSP) techniques for estimation of the fundamental frequency of grid voltage have been presented in the technical literature. Phase locked loop (PLL) is one of the efficient DSP techniques for estimating the parameters of the fundamental grid voltage [10–15]. However, the estimated parameters of PLL usually contain ripples due to the presence of the harmonic, dc offset, and unbalance voltage [2, 3, 16–18]. In order to reject the ripples from the estimated parameters at the expense of lower bandwidth, the in-loop filters are usually used. But these lead to a slower dynamic response [19]. In addition, the presence of the interdependent loops makes the tuning of PLL controller parameters more complicated. The technique of tuning adaptive frequency [20] uses differentiation and moving average filters in order to avoid the interdependent loops. Thus, it also leads to a slower dynamic response. The significantly high overshoot of estimated parameters of the PLLs is also an obstacle during phase jumps and thus causes delay in the synchronization process [21].

The techniques of quadrature signal generator basing on a second-order generalized integrator (QSG-SOGI) [22–24] can be used to reject high order harmonics and lock the frequency by frequency-locked loop (FLL) methods, but they cannot reject the lower order harmonics and dc offset. They also therefore introduce significant ripples into the estimated fundamental parameters. The technique that combines Multi-Sequence/Harmonic Decoupling Cell (MSHDC) with the conventional PLL [25] offers good dynamics. However, this is computational burden and low accuracy. The technique using DSOGI of [26] rejects the effects of unbalance and slow dynamics and the enhanced PLL (EPLL) combines with the DSOGI to detect the positive consequence (but not completely) are also computational burden, thus requiring the strong and expensive hardware.

The Newton-type algorithm (NTA) [27, 28] is a nonlinear technique that can identify the parameters of grid voltage [29]. However, this can be unstable under the large voltage transient. To increase the stability, a technique combining Notch filters and low-pass filters (LPF) with the NTA least-square method (NTA-LS) is proposed in [30]. But this also makes the dynamic response poor. In order to improve the dynamic response, a technique combining the NTA with a second-order IIR band-pass filter (BPF) at the input to reject the dc offset component is also introduced in [31]. In this technique, a LPF is cascaded with a recursive differentiation filter (DF) for better attenuation of ripple from the

estimated frequency at the expense of a slower dynamic response (NTA-DF). However, the response is also very low.

Levenberg-Marquardt algorithm (L-M) [32, 33] is a standard technique usually applied for solving problems of nonlinear least squares. Least squares problems arise when estimating a function of parameters to a set of measured data points by minimizing the sum of the error squares between the data points and the estimated parameters [34]. The L-M behaves like the gradient-descent technique when the parameters are far away from their optimal values, and behaves like the Gauss-Newton technique when the parameters are near to their optimal values. Therefore, the L-M leads to the faster convergence and the smaller number of iterations and does not require the expensive and strong DSP.

In the conventional PLLs, the voltages v_α and v_β must be used to detect the phase angle θ. When the unbalance of the three-phase voltage happens, the amplitudes of v_α and v_β are not equal. These amplitudes can be equally adjusted by the voltages v_α^+ and v_β^+ in the SOGI PLL but not completely. This paper proposes a PLL using the method of least squares that relies on the L-M to rapidly converge to the solution and decrease the number of iterations. In the proposed PLL, the only voltage v_α is used to define the phase angle θ. This completely rejects the negative effects of the unbalanced voltage. The simulation results of the proposed method validated the performance in the quick and accurate estimation of the frequency under the unbalanced and harmonic conditions compared to the DSOGI and the conventional PLL. The higher accuracy and quick of the estimated frequency result in the higher quality of the estimated phase angle.

2 PLL Basing on the Synchronization Reference Frame

The structure of a three-phase grid-connected inverter system [35] is shown in Fig. 1. The duty of PLL is to quickly and accurately estimate the phase angle θ of fundamental grid voltage. Then, the PLL must produce clean unit amplitude sine and cosine signals, which are called the unit vectors. The clean unit vectors are adopted to synchronize with the grid voltage through the generation of the reference in the closed-loop control of the inverters.

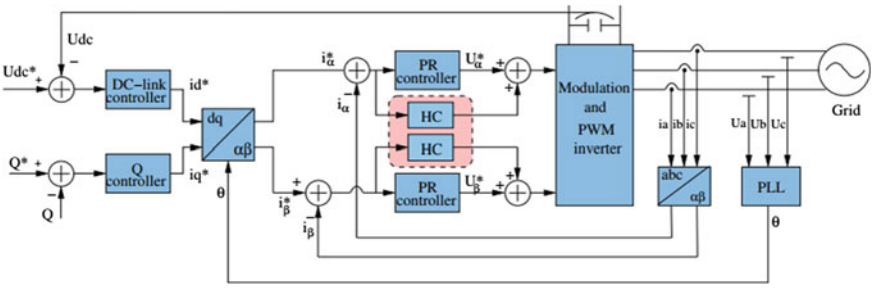

Fig. 1 The structure of a three-phase grid-connected inverter system [35] using PLL

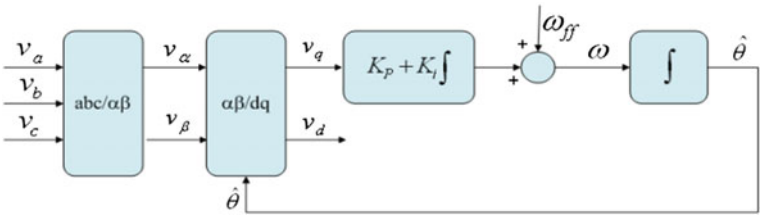

Fig. 2 The general structure of conventional SRF-PLL

2.1 The Conventional PLL

An SRF-PLL is also shown in Fig. 2. The voltages v_α and v_β are defined as (1). The response of SRF-PLL is not good under the unbalanced grid voltage [26].

$$\begin{bmatrix} v_\alpha \\ v_\beta \end{bmatrix} = \frac{2}{3} \begin{bmatrix} 1 & -1/2 & -1/2 \\ 0 & -\sqrt{3}/2 & \sqrt{3}/2 \end{bmatrix} \begin{bmatrix} v_a \\ v_b \\ v_c \end{bmatrix} \tag{1}$$

2.2 The Dual SOGI-PLL

Two SOGIs are used in the quadrature-signals generator to yield two couples of clean orthogonal signals. These four signals are entered in the positive sequence detector. This technique has frequency-adaptive response under the harmonic conditions. Actually, the harmonics are filtered before entering in the PLL [36]. However, the accuracy and dynamics are not good under the unbalanced conditions (Fig. 3).

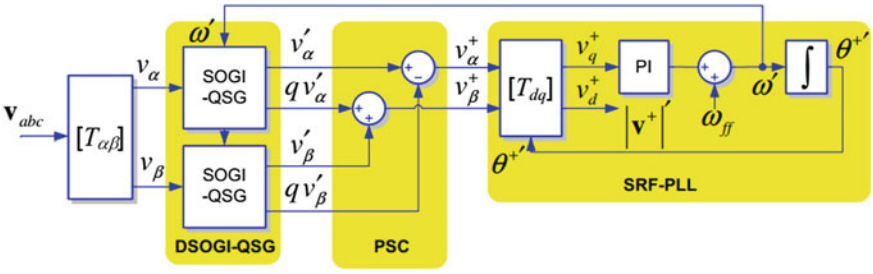

Fig. 3 The block diagram of DSOGI based PLL

3 The PLL Using the Levenberg-Marquardt Technique

Since the transformation from abc to αβ in (1) can reject harmonics and offset dc, the three-parameter model using the L-M technique is shown in Fig. 4 with respect to m samples of input grid voltage. Then, the output μ of the L-M technique consists of three estimated parameters V_{mag}, f, and ϕ. These parameters are also filtered by a discrete second-order filter in order to reject harmonic ripples.

Assume that the data column vector contains the sequence of measurement samples $y = [y_1 \ldots y_m]^T$ taken at time instants $\{t_1, \ldots, t_m\}$. It is also assumed that data of voltage can be modeled by (2).

$$y(t) = V_{mag} \sin(2\pi ft + \phi) \tag{2}$$

where V_{mag} is the voltage amplitude, f is the frequency, and ϕ is the initial phase angle. Then, (2) can also be rewritten as

$$y(t) = V_{mag} \sin(\theta) \tag{3}$$

Thus, a vector μ of three parameters can be expressed as

$$\mu = [\, V_{mag} \quad f \quad \phi \,]^T \tag{4}$$

Then, the sum of the weighted squares of errors $\chi^2(\mu)$ with respect to the unknown parameters μ as

$$\chi^2(\mu) = \frac{1}{m} \sum_{i=1}^{m} \left[\frac{\left(y(t_i) - \hat{y}(t_i; \mu) \right)}{w_i} \right]^2 \tag{5}$$

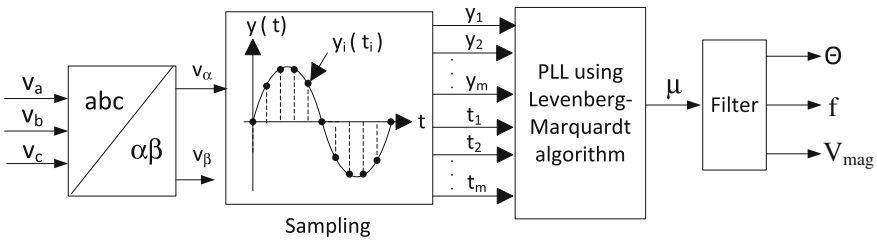

Fig. 4 The PLL structure using the Levenberg-Marquardt technique

where w_i is a value of measure of the error in measurement $y(t_i)$, $\hat{y}(t_i;\mu)$ is the fundamental sine wave described by the estimated parameters μ. Then, (5) can be rewritten as

$$\chi^2(\mu) = (y - \hat{y}(\mu))^T W (y - \hat{y}(\mu)) \tag{6}$$

$$\chi^2(\mu) = y^T W y - 2y^T W \hat{y}(\mu) + \hat{y}(\mu)^T W \hat{y}(\mu) \tag{7}$$

where the weighting matrix W is diagonal with $W_{ii} = 1/w_i^2$. The parameters are estimated by minimizing $\chi^2(\mu)$ with respect to the parameters through an iterative method. The objective of each step of iteration is to find a perturbation value Hessian (H) respect to the parameters that reduce the estimated errors. Then, the gradient of the objective function with respect to the parameters is as follows:

$$\frac{\partial \chi^2}{\partial \mu} = -(y - \hat{y}(\mu)))^T WJ \tag{8}$$

where the matrix J is a Jacobian as (9). It represents the local sensitivity of the function $\hat{y}$ with respect to the variation of the parameters μ. Then, the perturbation H that moves the parameters in the direction of steepest descent is given by (10). Where the positive value α defines the length of the step in the steepest-descent direction.

$$J_{m\times 4} = \left[\frac{\partial \hat{y}(\mu)}{\partial \mu}\right] = \begin{bmatrix} \frac{\partial \hat{y}(t_1;\mu)}{\partial V_{mag}} & \frac{\partial \hat{y}(t_1;\mu)}{\partial f} & \frac{\partial \hat{y}(t_1;\mu)}{\partial \phi} \\ \vdots & \vdots & \vdots \\ \frac{\partial \hat{y}(t_m;\mu)}{\partial V_{mag}} & \frac{\partial \hat{y}(t_m;\mu)}{\partial f} & \frac{\partial \hat{y}(t_m;\mu)}{\partial \phi} \end{bmatrix} \tag{9}$$

$$H = \alpha J^T W (y - \hat{y}(\mu)) \tag{10}$$

In the Gauss-Newton technique, the perturbation H is defined as:

$$H_g = J^T W (y - \hat{y}(\mu)) \left[J^T W J\right]^{-1} \tag{11}$$

While the Levenberg-Marquardt adaptively varies the updates of parameter between the Gauss-Newton update and the gradient descent update as

$$H_{LM} = J^T W (y - \hat{y}(\mu)) \left[J^T W J + \lambda I\right]^{-1} \tag{12}$$

where small values of λ result in a Gauss-Newton update. On the contrary, large values of λ result in a gradient descent update. The value λ is initialized to be large. If the iteration happens to result in a worse approximation, λ is increased. When the solution approaches the minimum, λ is decreased, the L-M behaves

like the Gauss-Newton, and the typical solution rapidly converges to the local minimum.

$$\left[J^T WJ + \lambda diag\left(J^T WJ\right)\right] H_{LM} = J^T W(y - \hat{y}(\mu)) \tag{13}$$

In each iteration ith, the step H is evaluated by comparing $\chi^2(\mu)$ to $\chi^2(\mu + H)$. The step will be accepted if the metric $\gamma_i(H)$ is greater than a user-defined value, ε.

$$\gamma_i(H) = \frac{\chi^2(\mu) - \chi^2(\mu + H)}{2H^T(\lambda_i H + J^T W(y - \hat{y}(\mu)))} \tag{14}$$

If $\gamma_i(H) > \varepsilon$ in each iteration, then μ is substituted by μ + H and λ is decreased by a factor. On the other hand, λ is increased by a factor, and the technique goes to the next iteration.

$$\left.\begin{array}{l} \lambda_0 = \lambda_{initial}; \\ [J^T WJ + \lambda_i diag(J^T WJ)]H = J^T W(y - \hat{y}(\mu)); \\ f\,\gamma_i(H) > \varepsilon : \mu + H \rightarrow \mu; \lambda_{i+1} = \max\left(\frac{\lambda_i}{L_D}, 1e-8\right); \\ otherwise\,\lambda_{i+1} = \lambda_i L_I; \end{array}\right\} \tag{15}$$

4 The Simulation Results

The simulation performance of the proposed technique in MATLAB/Simulink is implemented in this section to compare to the techniques of the DSOGI and the conventional PLL. The input voltages v_a, v_b, and v_c in Fig. 5 are distorted by 7 % of the 5th, 7 % of the 7th, 5 % of the 11th, and 5 % of the 13th harmonics (total harmonic distortion 12.17 %). The amplitudes of v_a and v_b are jumped from 311 V (normal) to 217.7 V (70 % of normal) at the time t = 0.1 s. The fundamental frequency reference is jumped from 50 to 47 Hz at the time t = 0.2 s.

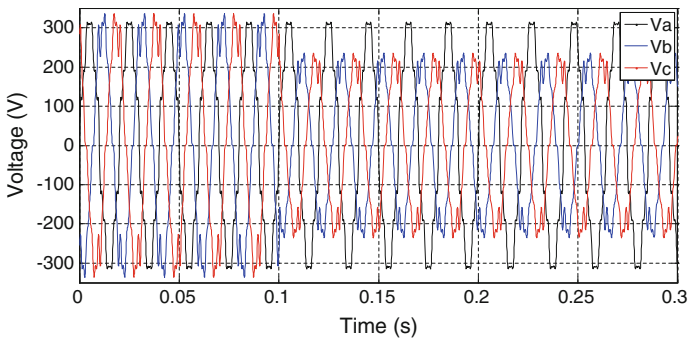

Fig. 5 The input voltage v_a, v_b, and v_c

The factors of the DSOGI and the conventional PLL are chosen K as $\sqrt{2}$, K_p as 0.2958, and K_i as 0.0136 [8]. The window size of the proposed technique has m as 22 and the sampling frequency of input voltage is chosen as 1 kHz. The initial parameter vector is $\beta = [300\ 45\ 0]^T$, $L_D = 9$, $L_I = 11$, and $\lambda_{initial} = 0.01$. The simulation results are shown in Figs. 6, 7, 8 and 9.

The voltages v_α and v_β in stationary reference frame in Fig. 6 show that harmonics and dc offset are rejected by the transformation in (1). The estimated phase angles of three case studies are also shown in Fig. 7.

In the interval 0–0.1 s, the estimated frequencies in Fig. 8 under the balanced voltage showed that the dynamic response of the proposed and the conventional are the same with the settling time of 0.03 s (1.5 fundamental periods). Whereas that of the DSOGI is the worst and the settling one is 0.1 s (five fundamental periods). The steady-state error of the three cases is very good and lower than 0.05 Hz. This means that the steady-state error of the three cases is lower than the standard limit of

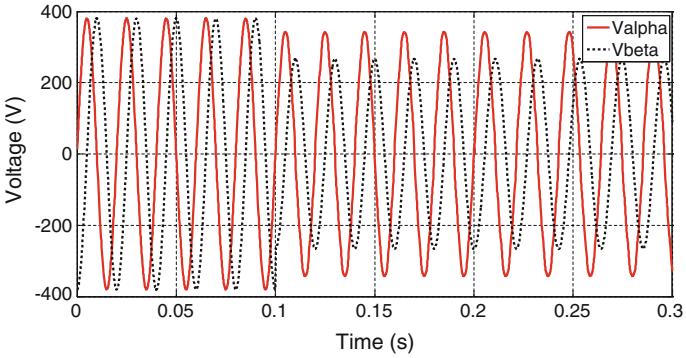

Fig. 6 The voltages v_α and v_β in stationary reference frame

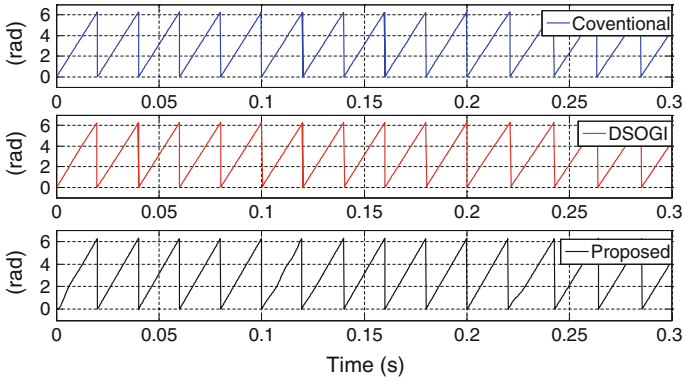

Fig. 7 The estimated phase angles

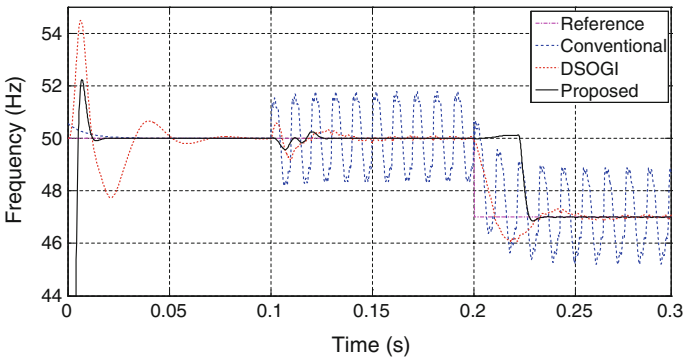

Fig. 8 The response of the estimated frequencies

0.1 % of IEEE-1547 [7] according to the calculation method of total vector error (TVE) described in [37].

In the interval 0.1–0.2 s, the estimated frequencies in Fig. 8 under the unbalanced voltage showed that the error of the conventional (up to 1.5 Hz) is the worst and much higher than the limit. Because the negative sequence components are still in the voltages v_α and v_β. The response of estimated frequencies zoomed in Fig. 9 also shows that the settling time of the DSOGI is 0.1 s, whilst that of the proposed is 0.03 s (1.5 fundamental periods). The error of the DSOGI is 0.1 Hz and also higher than the limit, whereas that of the proposed technique in Fig. 9 is lower than 0.01 Hz and lower than the limit. The frequency undershoot of the DSOGI is similar to the proposed.

In the interval 0.2–0.3 s, the estimated frequencies in Fig. 8 under the unbalanced voltage and frequency jump also yield the similar results as those in the interval 0.1–0.2 s. Thus, the simulation results show that the conventional cannot well operate under the unbalanced voltage due to the effects of the negative sequence components. The DSOGI yields the better results by the capability of

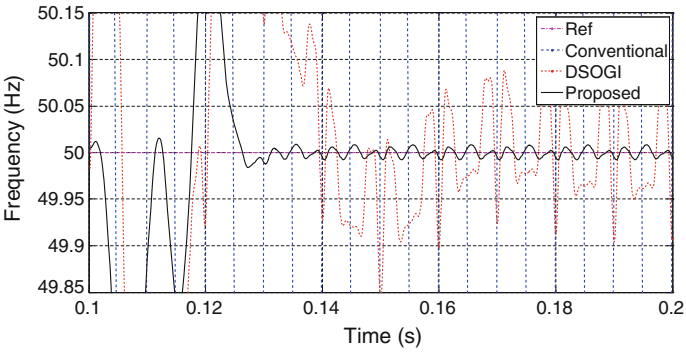

Fig. 9 The zoomed response of the estimated frequencies in the interval 0.1–0.2 s

detecting the positive sequence components but the steady-state error of the estimated frequency is still higher than the limit [7], whereas the proposed offers the best both the dynamics and the steady-state error of the estimated frequency. Thus, the best phase angle is also.

Therefore, the simulation results have validated the performance and the robustness of the proposed PLL under the severe conditions of input grid voltage. The only voltage v_α is used in the proposed PLL to reject the negative effects of the unbalanced voltage. This is an outstanding advantage.

5 Conclusions

The paper proposed a PLL technique for synchronization of grid-connected inverters. The proposed basing on the L-M technique is used to quickly and accurately estimate the parameters of input grid voltage. The simulation results showed the performance and the robustness of this technique compared to the conventional and the DSOGI. The proposed PLL is also immune from the negative effects of input voltage such as dc offset, harmonics, unbalanced voltage, frequency fluctuation. The simulation results also showed that the proposed PLL can meet the stringent standards of IEEE.

Acknowledgment The authors acknowledge the support from the Power System & Renewable Energy Lab C201 and the Power Electronics Lab D406 of Hochiminh city-University of Technology and Education for this research project.

References

1. Grath BP Mc, Holmes DG, Galloway JH (2005) Galloway, power converter line synchronization using a discrete Fourier transform (DFT) based on a variable sample rate. IEEE Trans Power Elect, 20(4):877–884
2. Ciobotaru M, Teodorescu R, Agelidis VG (2008) Offset rejection for PLL based synchronization in grid-connected converters. In: 23rd Annual IEEE Applied Power Electronics Conference and Exposition (APEC), pp 1611–1617
3. Karimi-Ghartemani M, Khajehoddin SA, Jain PK, Bakhshai A, Mojiri M (2012) Addressing DC component in PLL and notch filter algorithms. IEEE Trans. Power Electron, 27(1):78–86
4. Asiminoaei L, Blaabjerg F, Hansen S (2007) Detection is key—Harmonic detection methods for active power filter applications. IEEE Ind Appl Mag 13(2):22–33
5. Gonzalez SA, Garcia-Retegui R, Benedetti M (2007) Harmonic computation technique suitable for active power filters. IEEE Trans. Ind. Electron, 54(5):2791–2796
6. IEEE Recommended Practice for Utility Interface of Photovoltaic (PV) Systems (2000), IEEE Standard 929
7. IEEE Application Guide for IEEE Std 1547™ (2009). IEEE Standard for Interconnecting Distributed Resources with Electric Power Systems

8. Teodorescu R, Liserre M, Rodriguez P (2011) Grid Converters for Photovoltaic and Wind Power Systems. John Wiley & Sons
9. Kobayashi H (2012) Fault ride through requirements and measures of distributed PV systems in Japan. In: Proceedings of the IEEE-PES General Meeting, pp 1–6, 22–26
10. Karimi-Ghartemani M, Karimi H, Iravani MR (2004) A magnitude/phase-locked loop system based on estimation of frequency and in-phase/quadrature-phase amplitudes. IEEE Trans Ind Electron, 51(2):511–517
11. Karimi-Ghartemani M, Iravani MR (2004) Robust and frequency adaptive measurement of peak value. IEEE Trans Power Del, 19(2):481–489
12. Ciobotaru M, Agelidis VG, Teodorescu R, Blaabjerg F (2010) Accurate and less-disturbing active anti-islanding method based on PLL for grid-connected converters. IEEE Trans Power Electron, 25(6):1576–1584
13. Santos Filho RM, Seixa PF, Cortizo PC, Torres LAB, Souza AF (2008) Comparison of three single-phase PLL algorithms for UPS application. IEEE Trans Ind Electron, 55(8): 2923–2932
14. Nicastri A, Nagliero A (2010) Comparison and evaluation of the PLL techniques for the design of the grid-connected inverter system. In: Proceedings of the IEEE International Symposium on Industrial Electronics, 3865–3870
15. Golestan S, Monfared M, Freijedo FD, Guerrero JM (2012) Design and tuning of a modified power-based PLL for single-phase grid-connected power conditioning systems. IEEE Trans Power Electron, 27(8):3639–3650
16. Chung S-K (2000) Phase-locked loop for grid-connected three-phase power conversion systems. In: IEE Proc Electr Power Appl, 147(3):213–219
17. Karimi-Ghartemani M, Iravani MR (2005) Measurement of harmonics/inter-harmonics of time-varying frequencies. IEEE Trans Power Del, 20(2):23–31
18. Carvalho JR, Duque CA, Ribeiro MV, Cerqueira AS, Baldwin TL, Ribeiro PF (2009) A PLL-based multirate structure for timevarying power systems harmonic/interharmonic estimation. IEEE Trans Power Del, 24(4):1789–1800
19. Karimi-Ghartemani M, Khajehoddin SA, Jain PK, Bakhshai A (2012) Derivation and design of in-loop filters in phase-locked loop systems. IEEE Trans Instrum Meas, 61(4):930–940
20. Reza MS, Ciobotaru M, Agelidis VG (2013) Estimation of Single-Phase Grid Voltage Fundamental Parameters Using Fixed Frequency Tuned Second Order Generalized Integrator Based Technique. In: Proceedings of the 4th International Symposium. IEEE on Power Electron (PDEG), 1–8
21. Ghartemani MK, Khajehoddin SA, Jain PK, Bakhshai A (2012) Problems of startup and phase jumps in PLL systems. IEEE Trans Power Electron, 27(4):1830–1838
22. Rodriguez P, Luna A, Ciobotaru M, Teodorescu R, Blaabjerg F (2006) Advanced grid synchronization system for power converters under unbalanced and distorted operating conditions. In: Proceedings of the 32nd Annual Conference IEEE Industrial Electronics (IECON), p 5173–5178
23. Rodriguez P, Luna A, Munoz-Aguilar RS, Etxeberria-Otadui I, Teodorescu R, Blaabjerg F (2012) A stationary reference frame grid synchronization system for three-phase grid-connected power converters under adverse grid conditions. IEEE Trans Power Elect, 27(1):99–112
24. Rodriguez P, Luna A, Candela I, Mujal R, Teodorescu R, Blaabjerg F (2011) Multiresonant frequency-locked loop for grid synchronization of power converters under distorted grid conditions. IEEE Trans Ind Electron, 58(1):127–138
25. Hadjidemetriou L, Kyriakides E, Blaabjerg F(2013) Synchronization of grid-connected renewable energy sources under highly distorted voltage and unbalanced grid fault. In: Proceedings of the IEEE IECON, p. 1887–1892
26. Nicastri A, Nagliero A (2010) Comparison and evaluation of the PLL techniques for the design of the grid-connected inverter systems. In: Proceedings of the IEEE ISIE, pp 3865–3870
27. Ljung L (1987) System Identification—theory for the user. Prentice Hall
28. Johansson R (1993) System modeling and Identification. Prentice Hall

29. Terzija VV, Djuric MB, Kovacevic BD (1994) Voltage phasor and local system frequency estimation using Newton type algorithm. IEEE Trans Power Deliv, 9(3):1368–1374
30. Sadinezhad I, Agelidis VG (2011) Slow Sampling Online Optimization Approach to Estimate Power System Frequency. IEEE Trans Smart Grid, 2(2):265–277
31. Reza MS, Ciobotaru M, Agelidis VG (2015) Power system frequency estimation by using a Newton-type technique for smart meters. IEEE Trans Instrum Meas, doi:10.1109/TIM.2014.2347671
32. Levenberg K (1944) A Method for the Solution of Certain Non-Linear Problems in Least Squares. Q Appl Math 2:164–168
33. Marquardt DW (1963) An algorithm for least-squares estimation of nonlinear parameters. J Soc Ind Appl Math 11(2):431–441
34. Andersson T (2005) Parameter estimation and waveform Fitting for narrowband signals. Ph.D. dissertation, KTH Electrical Engineering., Stockholm, Sweden
35. Blaabjerg F, Teodorescu R, Liserre M, Timbus AV (2006) Overview of control and grid synchronization for distributed power generation systems. IEEE Trans Indu Electron 53(5)
36. Rodríguez P, Teodorescu R, Candela I, Timbus AV, Blaabjerg F (2006) New positive-sequence voltage detector for grid synchronization of power converters under faulty grid conditions. In: Proceeding of PESC, 06:129–135
37. IEEE Standard for Synchrophasors for Power Systems (2006). IEEE Standard C37, 118–2005

Improved Control Strategy of Three-Phase Four-Wire Inverters Using Sliding Mode Input-Ouput Feedback Linearization Under Unbalanced and Nonlinear Load Conditions

Tan Luong Van, Le Minh Thien Huynh, Tran Thanh Trang and Duc Chi Nguyen

Abstract In this paper, a novel nonlinear control scheme is proposed to regulate the three-phase output line-to-neutral voltages of a three-phase split-capacitor inverter as an AC power supplies. First, the nonlinear model of the system consisting of LC filter is obtained in the d-q-0 synchronous reference frame. Then, the input-output feedback linearization is applied through the sliding mode approach which avoids the complex calculations and simplifies further the controller structure. Also, a low-pass filter is employed for the sliding mode control to reduce the chattering of the load variations to acceptable levels without affecting the performance of the controller. The validity of the control method has been verified by simulation results.

T.L. Van (✉) · L.M.T. Huynh
Department of Electrical and Electronic Engineering, Sai Gon University,
273 an Duong Vuong, Ho Chi Minh City, Vietnam
e-mail: luongees2@yahoo.com

L.M.T. Huynh
e-mail: hlmthien@gmail.com

T.T. Trang
Department of Engineering and Technology, Van Hien University,
665-667-669 Dien Bien Phu, Ho Chi Minh City, Vietnam
e-mail: trangtt@vhu.edu.vn; trangtranthanh1979@gmail.com

T.T. Trang
National Key Lab of Digital Control and System Engineering,
University of Technology, Vietnam National University Ho Chi Minh City,
268 Ly Thuong Kiet Ho Chi Minh City, Vietnam

D.C. Nguyen
Department of Electrical and Electronic Engineering, Thu Duc College of Technology,
53 Vo van Ngan, Ho Chi Minh City, Vietnam
e-mail: ducchi.nguyen@mail.tdc.edu.vn

V.H. Duy et al. (eds.), *AETA 2015: Recent Advances in Electrical Engineering and Related Sciences*, Lecture Notes in Electrical Engineering 371,
DOI 10.1007/978-3-319-27247-4_23

Keywords Nonlinear load · Three-phase split-capacitor inverter · Sliding mode · Unbalanced load

1 Introduction

Recently, three-phase inverter for standalone applications has been rapidly increased. The applications could be the vehicles, trucks, or the photovoltaic power systems, and so on [1–3]. These loads could be the three-phase loads and/or single-phase loads which can cause a three-phase unbalanced load, an irregularly distributed single-phase load or a balanced three-phase load running at a fault condition. If the phases are unequally loaded, they produce undesired negative and zero sequence currents. The negative sequence component will cause excessive heating in machines, saturation of transformers and ripple in rectifiers. The zero sequence currents cause both excessive power losses in neutral lines and affect protection.

The three-phase inverter can be interfaced with load which is typically a four-wire system, where the neutral is grounded. There are several methods to provide the neutral point of the source side. The Δ/Y transformer has been used, in which the Δ windings are connected to the inverter and the Y windings are connected to the load [4]. Thus, the zero-sequence current is trapped in the Δ windings. However, the use of this transformer causes a bulky, heavy and costly topology. Also, the three-phase split-capacitor inverters and the four-leg inverters which are formed by eight switches consisting of 16 switch combinations have been employed. Nevertheless, the two switches should be added to the four-leg inverters and the complex three-dimension space vector modulation is required [5]. Fortunately, a three-phase three-leg inverter with split DC bus is one topology which can implement the three-phase four-wire system with a neutral point, as seen in the connection point of the load in Fig. 1. Compared to a three-phase three-wire system, this topology can face with the zero-sequence to regulate the output voltages in balance and the zero-sequence current can flow in the connection between the neutral point and the mid-point of the capacitive divider.

Several researches focusing on regulating the output voltages of the three-phase split-capacitor inverters in the unbalanced load conditions have been proposed. In [6], a control strategy applying the symmetrical sequence decomposition technique to extract the unbalanced three-phase signals as sum of positive, negative and zero-sequence have been developed. The PI controllers for the current and voltage are used to regulate the output voltages of the inverter. However, the using of twelve PI controllers and the processes of the sequence decomposition and composition could increase the calculation time. Also, this control strategy is suitable for only the case of unbalanced linear loads. Another control method using the sliding mode control scheme have been applied to improve the operation of the wind turbine system under grid fault conditions [7]. The discrete sliding mode

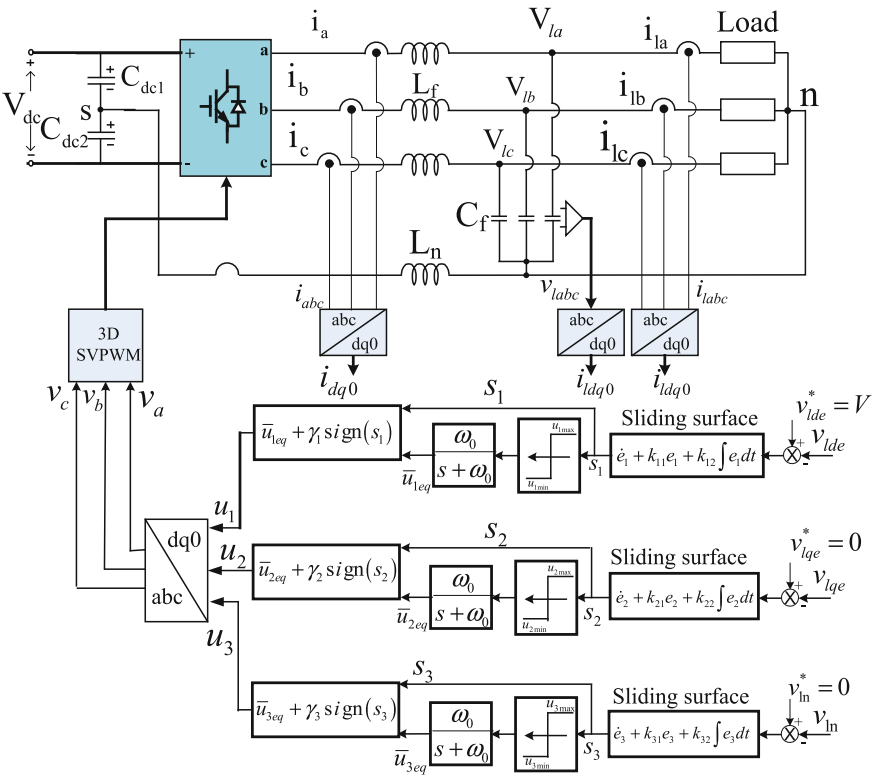

Fig. 1 Block diagram of the simplified sliding mode (SM) controller

controller achieved relatively good control performance such as the fast dynamic response, and insensitiveness to parameter and load variations.

This paper proposed a nonlinear control of three-phase split-capacitor inverters using sliding mode (SM) input-output feedback linearization approach in the case of unbalanced linear/nonlinear loads. The feedback linearization theory via a sliding mode approach is applied to avoid the complex calculations and simplifies further the controller structure. Also, the sliding mode control employing a low-pass filter is to reduce the chattering effects of the types of loads affecting the performance of the controller. The simulation results show the validity of the proposed control method.

2 System Modeling

The three-phase split-capacitor inverter in Fig. 1 can be represented in synchronous d-q-0 reference frame. Due to unbalanced load condition, the zero-sequence components are taken into account as

$$\dot{i}_{dq} = \frac{1}{L_f} v_{dq} - \frac{1}{L_f} v_{ldq} - j\omega i_{dq} \tag{1}$$

$$\dot{i}_0 = \frac{1}{(L_f + 3L_n)} v_0 - \frac{1}{(L_f + 3L_n)} v_{l0} \tag{2}$$

$$\dot{v}_{ldq} = \frac{1}{C_f} i_{dq} - \frac{1}{C_f} i_{ldq} - j\omega v_{ldq} \tag{3}$$

$$\dot{v}_{l0} = \frac{1}{C_f} i_0 - \frac{1}{C_f} i_{l0} \tag{4}$$

where L_f is the filter inductance, L_n is the neutral filter inductance, C_f is the filter capacitance, v_{dq} and v_0 are the d-q-0 axis inverter output voltages, v_{ldq} and v_{l0} are the d-q-0 axis phase load voltages, i_{dq} and i_0 are the d-q-0 axis inverter output currents, i_{ldq} and i_{l0} are the d-q-0 axis load currents, and ω is the source angle frequency.

From (1) to (3), a state-space modeling of the system is derived as follows:

$$\begin{bmatrix} \dot{i}_d \\ \dot{i}_q \\ \dot{i}_0 \\ \dot{v}_{ld} \\ \dot{v}_{lq} \\ \dot{v}_{ln} \end{bmatrix} = \begin{bmatrix} 0 & \omega & 0 & -1/L_f & 0 & 0 \\ -\omega & 0 & 0 & 0 & -1/L_f & 0 \\ 0 & 0 & 0 & 0 & 0 & -\frac{1}{L_f + 3L_n} \\ 1/C_f & 0 & 0 & 0 & \omega & 0 \\ 0 & 1/C_f & 0 & -\omega & 0 & 0 \\ 0 & 0 & 1/C_f & 0 & 0 & 0 \end{bmatrix} \begin{bmatrix} i_d \\ i_q \\ i_0 \\ v_{ld} \\ v_{lq} \\ v_{ln} \end{bmatrix} + \begin{bmatrix} 1/L_f & 0 & 0 \\ 0 & 1/L_f & 0 \\ 0 & 0 & \frac{1}{L_f + 3L_n} \\ 0 & 0 & 0 \\ 0 & 0 & 0 \\ 0 & 0 & 0 \end{bmatrix} \begin{bmatrix} v_d \\ v_q \\ v_n \end{bmatrix} + \begin{bmatrix} 0 \\ 0 \\ 0 \\ -i_{ld}/C_f \\ -i_{lq}/C_f \\ -i_{ln}/C_f \end{bmatrix} \tag{5}$$

3 Sliding Mode Input-Output Feedback Linearization Controller

3.1 Input-Output Feedback Linearization Control

An MIMO feedback linearization approach is proposed for the purpose of eliminating the nonlinearity in the modeled system [8]. Consider a multi-input multi-output (MIMO) system as follows:

$$\dot{x} = f(x) + g \cdot u \tag{6}$$

$$y = h(x) \tag{7}$$

where x is state vector, u is control input, y is output, f and g are smooth vector fields, h is smooth scalar function.

The dynamic model of the inverter in (5) is expressed in (6) and (7) as

$$x = \begin{bmatrix} i_d & i_q & i_0 & v_{ld} & v_{lq} & v_{ln} \end{bmatrix}^T; u = \begin{bmatrix} v_d & v_q & v_n \end{bmatrix}^T; y = \begin{bmatrix} v_{ld} & v_{lq} & v_{ln} \end{bmatrix}^T$$

To generate an explicit relationship between the outputs $y_{i=1,2,3}$ and the inputs $u_{i=1,2,3}$, each output is differentiated until a control input appears.

$$\begin{bmatrix} \ddot{y}_1 \\ \ddot{y}_2 \\ \ddot{y}_3 \end{bmatrix} = A(x) + E(x) \begin{bmatrix} u_1 \\ u_2 \\ u_3 \end{bmatrix} \tag{8}$$

Then, the control law is given as

$$\begin{bmatrix} v_d^* \\ v_q^* \\ v_0^* \end{bmatrix} = \begin{bmatrix} u_1 \\ u_2 \\ u_3 \end{bmatrix} = E^{-1}(x) \left[-A(x) + \begin{bmatrix} v_1 \\ v_2 \\ v_3 \end{bmatrix} \right] \tag{9}$$

where

$$A(x) = \begin{bmatrix} \frac{2}{C_f}\omega i_q - \left(\frac{1}{L_f C_f} + \omega^2\right) v_{ld} - \frac{1}{C_f}\dot{i}_{ld} - \frac{1}{C_f}\omega i_{lq} \\ -\frac{2}{C_{f\,d}} - \left(\frac{1}{L_f C_f} + \omega^2\right) v_{lq} - \frac{1}{C_f}\dot{i}_{lq} + \frac{1}{C_f}\omega i_{ld} \\ -\frac{1}{(L_f + 3L_n)C_f} v_{ln} - \frac{1}{C_f}\dot{i}_{ln} \end{bmatrix};$$

v_1, v_2, and v_3

$$E^{-1}(x) = \begin{bmatrix} L_f C_f & 0 & 0 \\ 0 & L_f C_f & 0 \\ 0 & 0 & (L_f + 3L_n)C_f \end{bmatrix}$$

are new control inputs.

A desired dynamic response can be imposed to the system by selecting

$$\begin{bmatrix} v_1 \\ v_2 \\ v_3 \end{bmatrix} = \begin{bmatrix} \ddot{y}_1^* + k_{11}\dot{e}_1 + k_{12}e_1 \\ \ddot{y}_2^* + k_{21}\dot{e}_2 + k_{22}e_2 \\ \ddot{y}_3^* + k_{31}\dot{e}_2 + k_{32}e_2 \end{bmatrix} \tag{10}$$

where $e_1 = y_1^* - y_1$, $e_2 = y_2^* - y_2$ and $e_3 = y_3^* - y_3$. y_1^*, y_2^*, and y_3^* are the reference values of the y_1, y_2, and y_3, respectively.

The following error dynamics can be formulated from (8) to (10) as

$$\begin{aligned} \ddot{e}_1 + k_{11}\dot{e}_1 + k_{12}e_1 &= 0 \\ \ddot{e}_2 + k_{21}\dot{e}_2 + k_{22}e_2 &= 0 \\ \ddot{e}_3 + k_{31}\dot{e}_3 + k_{32}e_3 &= 0 \end{aligned} \tag{11}$$

which are stable if the gains k_{11}, k_{12}, k_{21}, k_{22}, k_{31}, and k_{32} are positive [9].

In order to have an exact idea of the controller complexity, the control inputs of (8) can be formulated separately as

$$\begin{bmatrix} u_1 \\ u_2 \\ u_3 \end{bmatrix} = \begin{bmatrix} L_f C_f \left[v_1 - \frac{2}{C_f}\omega i_q + \left(\frac{1}{L_f C_f} + \omega^2 \right) v_{ld} + \frac{1}{C_f}\dot{i}_{ld} + \frac{1}{C_f}\omega i_{lq} \right] \\ L_f C_f \left[v_2 + \frac{2}{C_f}\omega i_d + \left(\frac{1}{L_f C_f} + \omega^2 \right) v_{lq} + \frac{1}{C_f}\dot{i}_{lq} - \frac{1}{C_f}\omega i_{ld} \right] \\ \left(L_f + 3L_n \right) C_f \left[v_3 + \frac{1}{\left(L_f + 3L_n \right) C_f} v_{ln} + \frac{1}{C_f}\dot{i}_{ln} \right] \end{bmatrix} \tag{12}$$

As can be seen from (12), even though the voltages (v_{ld}, v_{lq}, v_{ln}) are already linearized, it is not so easy to implement even for the most advanced digital signal processors since it contains many complex operations such as quadratic terms and divisions, and still appears the time derivative of currents (i_{ld}, i_{lq}, i_{ln}). To overcome this drawback, a simple alternative controller based on sliding mode control is proposed, in which the controller input–output linearizes the system and can be easily implemented with a digital or an analog approach.

3.2 *Sliding Mode Input-Output Feedback Linearization Controller*

The sliding surfaces with the errors of the indirect component voltages are expressed as:

$$\begin{aligned} s_1 &= \dot{e}_1 + k_{11}e_1 + k_{12}\int e_1 dt \\ s_2 &= \dot{e}_2 + k_{21}e_2 + k_{22}\int e_2 dt \\ s_3 &= \dot{e}_3 + k_{31}e_3 + k_{32}\int e_3 dt \end{aligned} \tag{13}$$

If the system states operate on the sliding surface, then $s_1 = s_2 = s_3 = 0$ and $\dot{s}_1 = \dot{s}_2 = \dot{s}_3 = 0$. Substituting (13) into $\dot{s}_1 = \dot{s}_2 = \dot{s}_3 = 0$ yields

$$\ddot{e}_1 = -k_{11}\dot{e}_1 - k_{12}e_1; \quad \ddot{e}_2 = -k_{21}\dot{e}_2 - k_{22}e_2; \quad \ddot{e}_3 = -k_{31}\dot{e}_3 - k_{32}e_3 \tag{14}$$

It is guaranteed in (14) that the system states (v_{ld}, v_{lq}, v_{ln}) will exponentially converge towards the reference values when they are kept the sliding surface to be equal to 0. The equivalent control concept of a sliding surface is the continuous control that allows for the maintenance of the state trajectory on the sliding surface $s = \dot{s} = 0$. The equivalent control is obtained from (13) as

$$\begin{aligned}
\dot{s}_1 &= \ddot{e}_1 + k_{11}\dot{e}_1 + k_{12}e_1 = \left[v_1 - \frac{2}{C_f}\omega i_q + \left(\frac{1}{L_f C_f} + \omega^2\right)v_{ld} + \frac{1}{C_f}\dot{i}_{ld} + \frac{1}{C_f}\omega i_{lq}\right] \\
\dot{s}_2 &= \ddot{e}_2 + k_{21}\dot{e}_2 + k_{22}e_2 = \left[v_2 + \frac{2}{C_f}\omega i_d + \left(\frac{1}{L_f C_f} + \omega^2\right)v_{lq} + \frac{1}{C_f}\dot{i}_{lq} - \frac{1}{C_f}\omega i_{ld}\right] \\
\dot{s}_3 &= \ddot{e}_3 + k_{31}\dot{e}_3 + k_{32}e_3 = \left[v_3 + \frac{1}{(L_f + 3L_n)C_f}v_{ln} + \frac{1}{C_f}\dot{i}_{ln}\right]
\end{aligned} \tag{15}$$

where v_1, v_2 and v_3 coincide with the new inputs of the system, whose expressions are

$$\begin{aligned}
v_1 &= \ddot{v}^*_{ld} + k_{11}\dot{e}_1 + k_{12}e_1 \\
v_2 &= \ddot{v}^*_{lq} + k_{21}\dot{e}_2 + k_{22}e_2 \\
v_3 &= \ddot{v}^*_{lo} + k_{31}\dot{e}_3 + k_{32}e_3
\end{aligned} \tag{16}$$

The equivalent control is obtained by making $\dot{s}_1 = \dot{s}_2 = \dot{s}_3 = 0$ as follows:

$$\begin{aligned}
u_{1eq} &= L_f C_f\left[v_1 - \frac{2}{C_f}\omega i_q + \left(\frac{1}{L_f C_f} + \omega^2\right)v_{ld} + \frac{1}{C_f}\dot{i}_{ld} + \frac{1}{C_f}\omega i_{lq}\right] \\
u_{2eq} &= L_f C_f\left[v_2 + \frac{2}{C_f}\omega i_d + \left(\frac{1}{L_f C_f} + \omega^2\right)v_{lq} + \frac{1}{C_f}\dot{i}_{lq} - \frac{1}{C_f}\omega i_{ld}\right] \\
u_{3eq} &= (L_f + 3L_n)C_f\left[v_3 + \frac{1}{(L_f + 3L_n)C_f}v_{ln} + \frac{1}{C_f}\dot{i}_{ln}\right]
\end{aligned} \tag{17}$$

It is noted that the obtained equivalent control is the same as the ones achieved in (12). To drive the state variables to the sliding surface $s_1 = s_2 = s_3 = 0$, in the case of $s_1, s_2, s_3 \neq 0$, the control laws are defined as

$$u_1 = u_{1eq} + \gamma_1 \text{sign}(s_1);\quad u_2 = u_{2eq} + \gamma_2 \text{sign}(s_2);\quad u_3 = u_{3eq} + \gamma_3 \text{sign}(s_3) \tag{18}$$

where $\gamma_1 > 0$, $\gamma_2 > 0$, $\gamma_3 > 0$.

The reaching law can be derived by substituting (18) into (15), which gives

$$\dot{s}_1 = -\gamma_1 \text{sign}(s_1); \quad \dot{s}_2 = -\gamma_2 \text{sign}(s_2); \quad \dot{s}_3 = -\gamma_3 \text{sign}(s_3) \tag{19}$$

The stability and robustness can be tested using Lyapunov's function which are presented in [8]. The idea is to overcome the controller's complexity by assigning a switching function, u_{sw}, to each sliding surface and then just averaging the fast discontinuous switching by a simple low-pass filter as

$$\bar{u}_{ieq} = \frac{\omega_0}{s+\omega_0} u_{iSW} = \begin{cases} \frac{\omega_0}{s+\omega_0} u^+_{i\max} & if \ s_i > 0 \\ \frac{\omega_0}{s+\omega_0} u^-_{i\min} & if \ s_i \le 0 \end{cases} \tag{20}$$

where $\omega_0 = 2\pi f_0$ is the cut-off frequency of the filter. The selection of the cut-off frequency should be neither too low to avoid the delay effect on the system dynamics, nor too high in order to avoid excessive chattering in the system states. In this research, f_0 is selected as to be 2000 Hz. Also, the chattering of the system can be reduced even more if the switching gains such as $u^+_{1\max}$, $u^+_{1\min}$, $u^+_{2\max}$, $u^+_{2\min}$, $u^+_{3\max}$, $u^+_{3\min}$, are chosen around the stationary state of the control inputs (u_{1st}, u_{2st}, u_{3st}) of the system. The steady state of and can be derived from (2) and (3) as

$$\begin{aligned} u_{1st} &= \frac{1}{\left(\frac{1}{L_f C_f} + \omega^2\right)} \left[\frac{2}{C_f}\omega i_q - \frac{1}{C_f}\omega i_{lq}\right]; \\ u_{2st} &= \frac{1}{\left(\frac{1}{L_f C_f} + \omega^2\right)} \left[-\frac{2}{C_f}\omega i_d + \frac{1}{C_f}\omega i_{ld}\right]; \\ u_{3st} &= 0 \end{aligned} \tag{21}$$

The values $u^+_{1\max}$ and $u^+_{1\min}$ can be simply chosen as $u^+_{i\max} = u_{ist} + \Delta_i$ and $u^+_{1\min} = u_{ist} - \Delta_i$ in which Δ_i is a constant value designed to assure the system stabilization around the operating point. Also, the system chattering is related to the magnitude of Δ_i.

Finally, the same input functions (18) have been replaced as

$$u_1 = \bar{u}_{1eq} + \gamma_1 \text{sign}(s_1); \quad u_2 = \bar{u}_{2eq} + \gamma_2 \text{sign}(s_2); \quad u_3 = \bar{u}_{3eq} + \gamma_3 \text{sign}(s_3) \tag{22}$$

where the terms γ_1, γ_2, and γ_3 guarantee the existence of the sliding mode in the surface.

Figure 1 shows the block diagram of the simplified sliding mode input-output feedback linearization controller, in which the reference value of the d-axis voltage (V^*_{ld}) is considered. The other reference values are set to zero since the inverter must supply the balanced three-phase voltage.

4 Simulation Results

To verify the feasibility of the proposed method, PSIM simulations have been carried out for the unbalanced and nonlinear loads. An DC-link voltage at the input of inverter from a three-phase ac source is 500 V, the switching frequency of inverter is 10 kHz. The filter inductor L_f is 3 mH and the filter capacitor C_f is 100 µF which correspond to a cut-off frequency at 450 Hz. The parameters of loads and controllers are shown in the Tables 1 and 2, respectively.

The simulation results for the proposed control and PI control under the different types of the loads are shown from Figs. 2, 3 and 4. Each of figures illustrates the

Table 1 Parameters of loads

Type of load	Parameters
Unbalanced resistor load	$R_a = R_b = 20\ \Omega$, $R_c = 1\ k\Omega$
Unbalanced nonlinear load	$L_s = 1$ mH, $C = 4.7$ mF, $R_{dca} = 50\ \Omega$, $R_{dcb} = R_{dcc} = 1\ k\Omega$

Table 2 Parameters of controllers

Controller Type		Gain of controller	
		Unbalanced resistor load	Unbalanced nonlinear load
PI control	Current controller	$k_p = 5.4$ $k_i = 4000$	$k_p = 17.5$ $k_i = 13{,}100$
	Voltage controller	$k_{pv} = 0.21$ $k_{iv} = 682$	$k_{pv} = 0.32$ $k_{iv} = 896$
SM control		$k_{11} = k_{21} = k_{31} = 5 \times 10^3$, $k_{12} = k_{22} = k_{32} = 8.4 \times 10^6$	

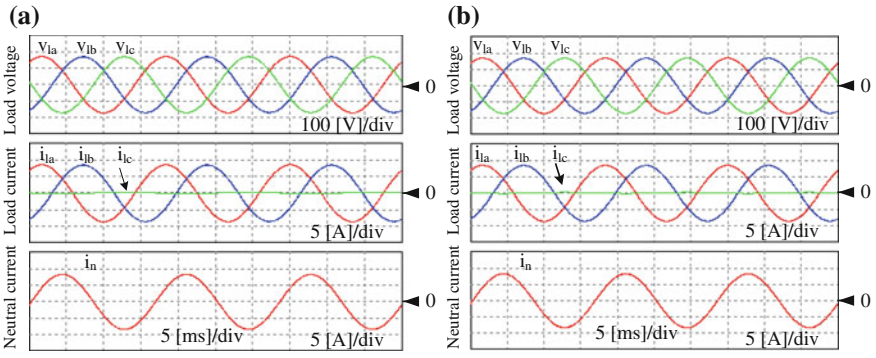

Fig. 2 Dynamic response of **a** PI controller and **b** proposed SM controller under unbalanced load

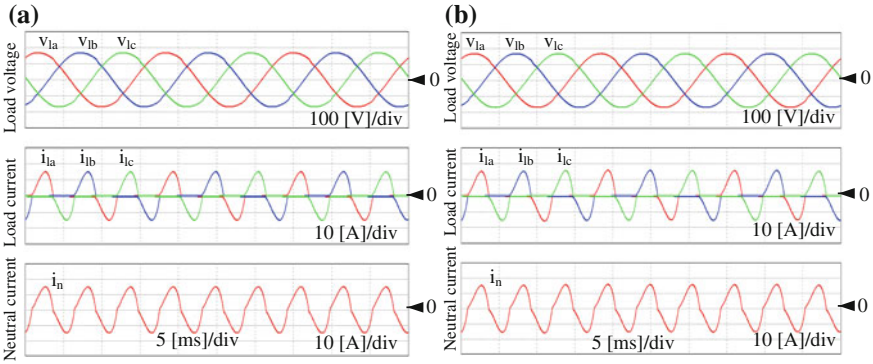

Fig. 3 Dynamic response of **a** PI controller and **b** proposed SM controller under unbalanced load

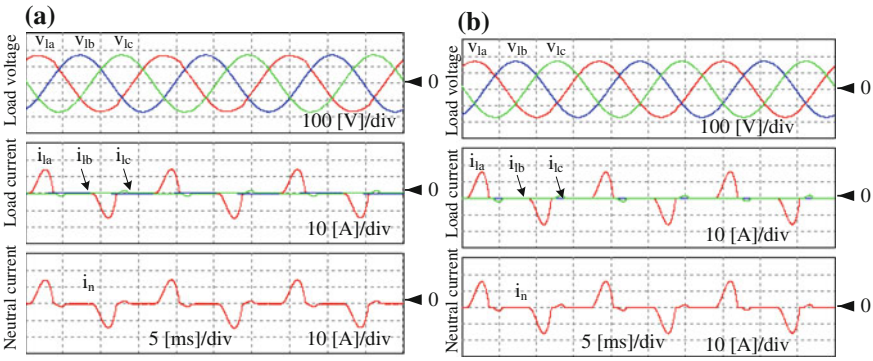

Fig. 4 Dynamic response of **a** PI controller and **b** proposed SM controller under unbalanced nonlinear load

three-phase output line-to-neutral voltages, three-phase load currents, and neutral line current. As can be seen, the phase load voltages always maintain in balanced conditions and the total harmonic distortion (THD) of the phase load voltages is recorded in the Table 3. As can be clearly seen, the THD of two controllers are not much different in the case of unbalanced linear loads. However, the THDs of phase-A load voltage of PI control are significantly increased by 2.14 and 2.5 % in the case of nonlinear load and unbalanced nonlinear load, respectively, in which those of SM control are 0.95 and 1.05 %. The SM control method achieves better control performance than PI control in the cases of nonlinear load and unbalanced nonlinear load.

Table 3 THD of load voltages in simulation

Load type	Controller type	THD (%)		
		THD (phase A)	THD (phase B)	THD (phase C)
Unbalanced resistor load	PI	0.45	0.45	0.44
	SM	0.39	0.38	0.39
Nonlinear load	PI	2.14	0.58	0.45
	SM	0.94	0.45	0.35
Unbalanced nonlinear load	PI	2.5	0.6	0.5
	SM	1.05	0.38	0.39

5 Conclusions

The paper proposed a novel output voltage control of three-phase split-capacitor inverter using sliding mode input-output feedback linearization approach. This control method can regulate the load voltages in balanced condition in the case of unbalanced linear and/or nonlinear load. The application of a feedback linearization controller has been studied to overcome the limitations of the linear controller. However, due to complex calculations, a sliding mode is proposed, which simplifies the controller structure. Also, to reduce the chattering of the load variations affecting the performance of the controller, a low-pass filter is employed for the sliding mode. The feasibility of the proposed control of three-phase split-capacitor inverter is verified by simulation results, which show the better performance than conventional PI method.

References

1. Jeung Y-C, Lee D-C (2012) AC power supply system using vehicle engine—generator set with battery. In: Proceedings of IPEMC (ECCE-Asia), pp 1724–1728
2. Zhang R, Boroyevich D, Prasad VH, Mao H, Lee FC, Dubovsky S (1997) A three-phase inverter with a neutral leg with space vector modulation. In: Proceedings of IEEE APEC, vol. 2, pp 857-863
3. El-Barbari S, Hofmann W (2000) Digital control of a four leg inverter for standalone photovoltaic systems with unbalanced load. In: Proceedings of IEEE IECON, pp 729–734
4. Marwali MN, Dai M, Keyhani A (2006) Robust stability analysis of voltage and current control for distributed generation systems. IEEE Trans Energy Convers 21(2):516–526
5. Zhang R, Prasad H, Boroyevich D, Lee FC (2002) Three-dimensional space vector modulation for four-leg voltage-source converters. IEEE Trans Power Electron 17(3):314–326
6. Mohd A, Ortjohann E, Hamsic N, Sinsukthavorn W, Lingemann M, Schmelter A, Morton D (2010) Control strategy and space vector modulation for three-leg four-wire voltage source inverters under unbalanced load conditions. IET Power Electron 3(3):323–333

7. Itsaso Martinez M, Tapia G, Susperregui A, Camblong H (2012) Sliding-mode control for dfig rotor- and grid-side converters under unbalanced and harmonically distorted grid voltage. IEEE Trans Energy Convers 27(2):328–339
8. Slotine J-JE, Li W (1991) Applied Nonlinear Control. Prentice-Hall, Englewood Cliffs, NJ, pp 207–271
9. Kim D-E, Lee D-C (2010) Feedback linearization control of three-phase ups inverter systems. IEEE Trans Ind Electron 57(3):963–968

Part VI
Materials

The Structural Characteristics of ZnO Nanorods for Flexible Gas Sensor Grown by Hydrothermal Method

JaeHeon Ock, JaeHyeon Oh, HyunMin Lee, SangHyun Kim and Nakwon Jang

Abstract We study the characterization of ZnO nanorods for the fabrication of new types of flexible gas sensors. However, the crystal structure of the amorphous as well as the surface morphology of polyestersulfone (PES) substrate is poor. Therefore, we introduced a ZnO buffer layer to facilitate ZnO nanorods growth. Furthermore, in order to control characteristic on the growth of ZnO nanorods, we grew ZnO nanorods on PES in various growth conditions. Additionally, we analyzed the structural characteristics using XRD, FE-SEM for the fabrication of flexible gas sensors.

Keywords ZnO · Nanorod · Hydrothermal method · Flexible · Gas sensor

1 Introduction

Recently, lightweight, flexible, and easy-to-carry electronic devices have been widely studied because of their potential applications, such as gas sensors, displays, solar cells, and large sensor arrays [1].

Among these, demand for solid-state gas sensors is dramatically growing for a wide range of applications, including the detection of hazardous gases, toxic gases, environmental gas monitoring, humidity and air quality control, and chemical process control [2–4].

Semiconductor gas sensors have the merits of low cost, small size, and high selectivity. In the field of solid-state gas sensors, widespread applications for gas sensors based on semiconducting metal oxides have been found in the past few decades [5].

J. Ock · J. Oh · H. Lee · S. Kim · N. Jang (✉)
Division of Electrical and Electronics Engineering, Korea Maritime and Ocean University, Busan 606-791, Korea
e-mail: nwjang@kmou.ac.kr

V.H. Duy et al. (eds.), *AETA 2015: Recent Advances in Electrical Engineering and Related Sciences*, Lecture Notes in Electrical Engineering 371,
DOI 10.1007/978-3-319-27247-4_24

Zinc oxide (ZnO) is a key electronic material and is particularly promising in nano device applications because of its wide direct band gap of 3.37 eV and large exciton binding energy of 60 meV, and it can be grown on selected patterned substrates, as demonstrated in an earlier publication [6].

However, the sensitivity of the ZnO bulk material is not sufficiently high. The sensitivity can be improved by increasing the surface area of the thin film by growing nanorods.

Recently, several groups applied ZnO nanoparticles as seeds for the growth of large-scale and well-oriented ZnO nanorods on silica substrates. However, it is more significant to synthesize one-dimensional (1D) nanoscale materials on flexible substrates, such as polyestersulfone (PES), polycarbonate (PC), and thermoplastic polyurethane (TPU), for flexible applications [7, 8].

In nanorod synthesis methods, physical vapor deposition (PVD), chemical vapor deposition (CVD), and pulsed laser deposition (PLD) have been used to obtain 1D well-aligned ZnO nanorods arrays. However, these vapor-phase processing fabrication techniques require vacuum conditions, high energy consumption, sophisticated equipment, and rigid experimental conditions.

In order to fabricate a good sensitivity of the flexible gas sensor, it is necessary to increase the surface area. So, we grew the ZnO nanorods on a flexible substrate to increasing the surface area for sensitiveness of gas sensor.

However in order to use flexible substrates, a high temperature process is difficult to use, because the flexible substrate has a low softening point.

Therefore, we grew the ZnO nanorods on a flexible substrate using hydrothermal methods. Hydrothermal methods do not require a high temperature process or vacuum conditions.

Additionally, polyestersulfone (PES), the crystal structure of the amorphous as well as the surface morphology, is poor. Therefore, we introduced a ZnO buffer layer for the growth of ZnO nanorods.

In this study, we research to find the best conditions for fabricate of the flexible gas sensor. The ZnO nanorods were grown on PES substrate with a ZnO buffer layer using hydrothermal methods. Additionally, the structural properties of the ZnO nanorods were investigated in various growth conditions.

2 Experimental Details

2.1 The Deposition of ZnO Buffer Layer

In this experiment, we used an RF magnetron sputter system for the deposition of the ZnO buffer layer. Before deposition, the substrate, which was PES, was 1×1 cm. In addition, the PES substrate was cleaned with an ultra-sonic cleaner using methanol and DI water. The base pressure of the chamber was maintained at 6.0×10^{-6} Torr.

We also supplied the Ar gas at 20 sccm to create plasma. After that, the deposition pressure of the chamber was maintained at 5 mTorr. However, the crystal structure as well as the surface morphology is not good in PES substrate.

2.2 Growth of ZnO Nanorods

For the growth of the ZnO nanorods, the ZnO solution was produced using zinc nitrate hexahydrate, hexamethylenediamine (HMT), and deionized (DI) water. The amount of zinc nitrate hexahydrate and HMT was changed according to the concentrations of the ZnO solutions.

Additionally, we stirred two solutions in each beaker for 15 min. We then placed the flat-bottom flask in a large beaker and warmed it up in a double boiler system using Si oil on the hot plate. The PES substrate was placed upside-down in the flask, because we chose the bottom-up growth method.

The mechanism for the growing of the ZnO nanorods using HMT can be summarized in the following equations:

$$(CH_2)_6N_4 + 6H_2O \rightarrow 6COH_2 + 4NH_3 \quad (1)$$

$$NH_3 + H_2O \rightarrow NH_4^+ + OH^- \quad (2)$$

$$Zn(NO_3)_2 \cdot 6H_2O \rightarrow Zn^{2+} + 2NO_3^- + 6H_2O \quad (3)$$

$$Zn^{2+} + 2OH^- \rightarrow Zn(OH)2 \rightarrow ZnO + H2O \quad (4)$$

Zn^{2+} is known to react readily with OH^- to form more soluble $Zn(OH)_2$ complexes, which act as the growth units of ZnO nanorods. Finally, ZnO nanorods are obtained through the decomposition of $Zn(OH)_2$. Therefore, the key parameter for the growth of ZnO nanorods is controlling the supersaturation of the reactants as Eq. (4).

An Energy-Dispersive X-ray Spectrometer (EDS) was used for analyzing the surface and structural properties of the PES substrate-deposited ZnO buffer layer. Additionally, a Field Effect-Scanning Electron Microscope (FE-SEM) was used for analyzing the structural properties of the ZnO nanorods grown through hydrothermal methods.

3 Results and Discussion

PES substrate has an amorphous structure. Therefore, for obtaining uniform ZnO nanorods, a buffer layer is needed. We deposited the ZnO buffer layer on the PES substrate using the RF magnetron sputter system.

First, we analyzed the ZnO buffer layer. The deposition conditions of the ZnO buffer layer are shown in Table 1.

The structural properties of the ZnO buffer layer are analyzed using XRD. The XRD results are shown in Fig. 1. The peak of the ZnO buffer layer is located near 34.50, the intensity of the ZnO buffer layer is a high value, and the Full Width at Half Maximum (FWHM) is 0.3509. Therefore, the structural properties of the ZnO buffer layer had great structural properties in this deposition condition. Thus, the ZnO nanorods were grown using this ZnO buffer layer on PES substrate.

We then grew the ZnO nanorods on PES substrate with a ZnO buffer layer. The ZnO growth conditions are shown in Table 2.

Table 1 Deposition conditions of ZnO buffer layer on PES

Property	Settings
Target	ZnO
Substrate	PES
Power	100 W
Deposition time	20 min
Thickness	100 nm
Deposition temperature	Room temperature

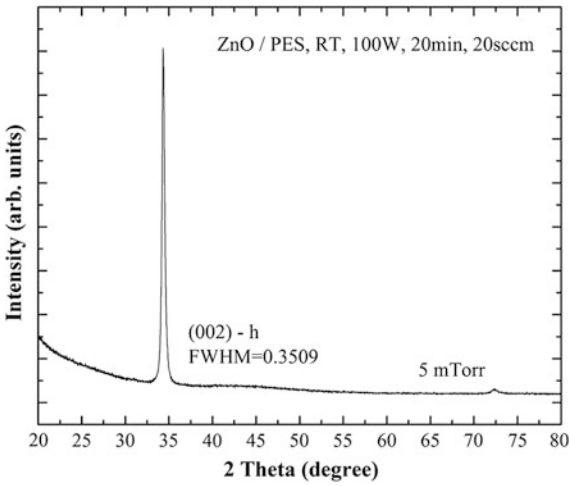

Fig. 1 XRD results of ZnO buffer layer

Table 2 Growth conditions of ZnO nanorods position conditions of ZnO buffer layer on PES

Property	Settings
Concentration	0.05, 0.1, 0.3, 0.5 M%
Growth time	1 h
Growth system	Bottom up
Growth temperature	90 °C

We analyzed the components of the ZnO nanorods using EDS. EDS is equipment that measures the thin-film components or other materials of semiconductors using the X-ray emission spectrum. Before the analysis, we coated the ZnO nanorods on PES substrate to enhance conductivity. This is because that the PES substrate is a transparent and flexible plastic substrate. We used Pt (Platinum) when coating the ZnO nanorods on PES substrate. The thickness of Pt was approximately 20 nm. The EDS results are shown in Fig. 2.

According to the EDS results, the ZnO nanorods had ions, such as Zn, O, C, and Pt. C is carbon tape, and it was attached to enhance conductivity.

In general, the amounts of Zn were increased to 1.2 from 1.05 k according to the increasing concentrations of the Zn solutions. However, the C and Pt were maintained at fixed values.

Furthermore, We analyzed the structural properties of the ZnO nanorods using FE-SEM. FE-SEM images were used to observe the fine ZnO nanorods according to the concentration of growth, and the size of each nanorod is shown in a graph in Fig. 4. And Fig. 3. is Schematic describing the operation of the SEM.

As the result of the FE-SEM images, the diameters and lengths of the ZnO nanorods were increased according to the concentration of zinc nitrate solution.

Additionally, the density of the ZnO nanorods was increased by increasing the concentration of the aqueous solution.

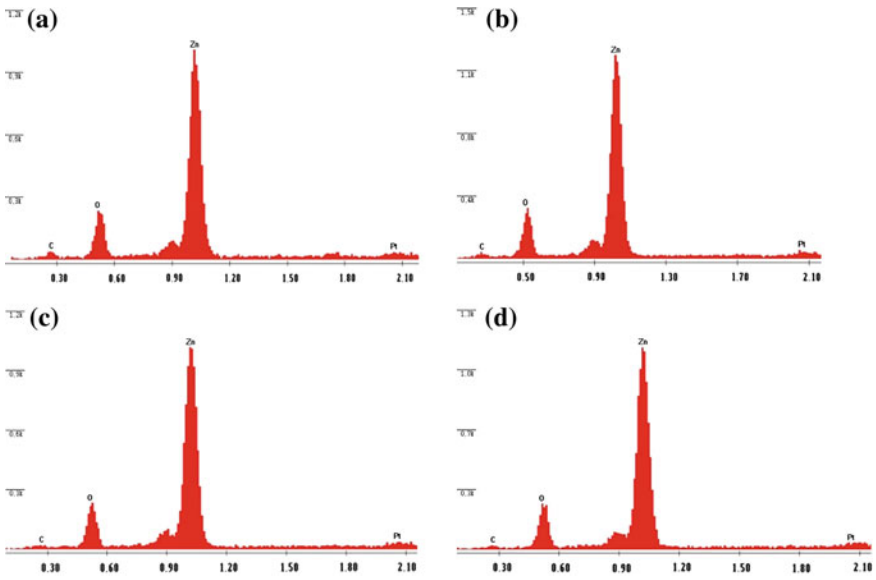

Fig. 2 EDS results: **a** 0.05 M%, **b** 0.1 M%, **c** 0.3 M%, and **d** 0.5 M%

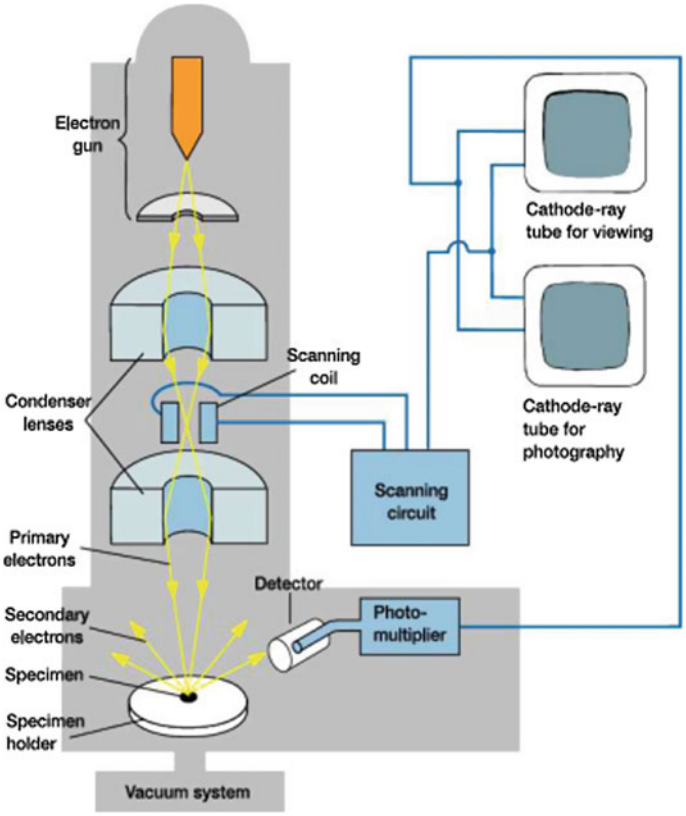

Fig. 3 Schematic describing the operation of the SEM

However, in 0.5 M%, it can be seen that the growth was in several directions in the polycrystalline structure.

The ZnO nanorods were also analyzed to obtain the diameters and the lengths of the ZnO nanorods. The diameters and the lengths are shown in Fig. 5.

In the results of Fig. 5, the diameter is increased linearly. However, in the case of a concentration of 0.5 M%, the diameter of the ZnO nanorods is increased rapidly compared to that of a concentration of less than 0.5 M%.

Additionally, the diameter of the ZnO nanorods is approximately 140 nm at a concentration of 0.5 M%. The length of the ZnO nanorods was increased to a certain size, which was approximately 145 nm.

At the concentration of 0.05 %, the size of the ZnO nanorods was very small, because the Zn source was not enough for sufficient growth.

However, the lengths of the ZnO nanorods at the concentration had any value. This is the reason for the length of the ZnO buffer layer and the small growth of the ZnO nanorods.

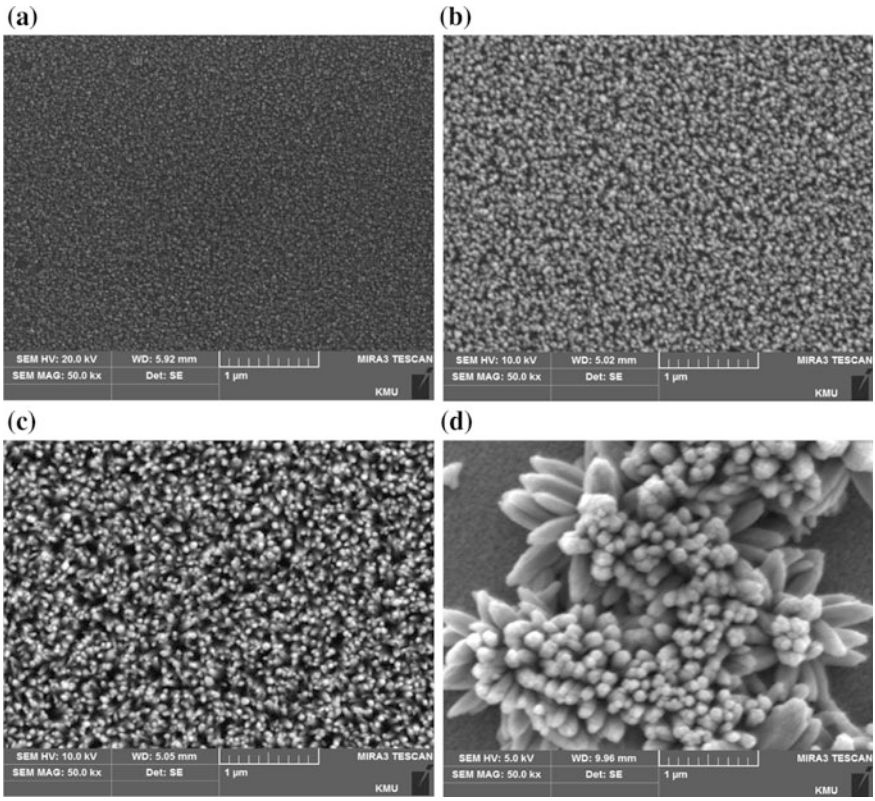

Fig. 4 FE-SEM images of ZnO nanorods grown at different concentrations of Zn^{2+} for 1 h. Experiments were conducted in Zn^{2+} concentrations of **a** 0.05 M%, **b** 0.1 M%, **c** 0.3 M%, and **d** 0.5 M%

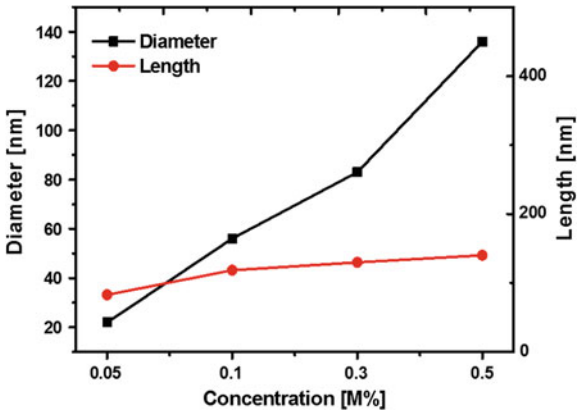

Fig. 5 Diameters and lengths of ZnO nanorods at various concentrations of solutions

4 Conclusion

In this study, we studied the structural properties of ZnO nanorods at various concentrations based on the PES substrate. A ZnO buffer layer was produced using the RF magnetron sputter system. Additionally, the ZnO nanorods were grown by changing the concentration of the Zn solution. The results obtained in our study on the ZnO nanorods growth are as follows.

1. By introducing the ZnO buffer layer, we can grow well-aligned ZnO nanorods on a flexible substrate with the hydrothermal method.
2. As a result of the structural properties of the ZnO nanorods, the ZnO nanorods with direction were grown at a concentration of less than 0.3 M%.
3. Various peaks have been observed in several directions of the polycrystalline structure because of the supersaturated solution at the concentration of 0.5 M%.
4. The optimum solution concentration is 0.3 M% for the growth ZnO nanorods. At this concentration of Zn source, the ZnO nanorods grown having a directional.

References

1. Jin M.Y, Kim J.H (2008) Flexible Display Technology and Market. Displaybank, Physics and high-tech, pp 33–39
2. Simon I, Bârsan N, Bauer M, Weimar U (2001) Micromachined metal oxide gas sensors: opportunities to improve sensor performance. Sens Actuators, B 73:1–26
3. Kolmakov A, Zhang Y, Cheng G, Moskovits M (2003) Detection of CO and O_2 using tin oxide nanowire sensors. Adv Mater 15:997–1000
4. Wan Q, Li QH, Chen YJ, Wang TH, He XL, Li JP, Lin CL (2004) Fabrication and ethanol sensing characteristics of ZnO nanowire gas sensors. Appl Phys Lett 84:3654–3656
5. Solid State Gas Sensing (2009). In: Comini E, Faglia G, Sberveglieri GG (eds) (Springer, New York)
6. Xiong L, Shi J, Gu J, Li L, Shen W (2004) Hua, Z. Solid State Sci 6:1341
7. Tina AR, Voigt JA, Liu J, Mckenzie B, Mcdermott MJ, Rodriguez MA, Konishi H (2003) Xu, H. Nat Mater 2:821
8. Choy JH, Jang ES, Won JH, Chung JH, Kim YW (1911) Adv Mater 15:2003

SiO_2 Powder: A Novel Solution for Improving Spatial Color Uniformity of White LED Lamps

Nguyen Doan Quoc Anh, Yu-Nan Liu, Hsin-Yi Ma and Hsiao-Yi Lee

Abstract This study proposes the addition of SiO_2 scattering-particles into the phosphor layer of a multi-chip white light LED (MCW-LED) for enhancing its performances. It is demonstrated by computer simulations that SiO_2 particles can bring significant effects on the correlated color temperature (CCT) uniformity and luminous flux. Through the simulation experiments, it is found that the MCW-LED with hybrid SiO_2 structure with SiO_2 particle size around 1 μm can achieve higher color uniformity than other package structures. We investigate the influence of SiO_2 (quartz) concentration on the CCT and the output flux of the MCW-LED with CCTs 7000, 7700 and 8500 K, respectively. Comparing with the LED package without SiO_2, SiO_2 packages can shrink the CCT deviation about 48 %. In the study, it is demonstrated that the participation of about 5–10 % SiO_2 can accomplish the MCW-LED with higher spatial color uniformity and optimal lumen output.

Keywords LED · Spatial color uniformity · SiO_2

N.D.Q. Anh (✉)
Faculty of Electrical and Electronics Engineering, Ton Duc Thang University,
No. 19 Nguyen Huu Tho Street, District 7, Ho Chi Minh City, Vietnam
e-mail: nguyendoanquocanh@tdt.edu.vn

Y.-N. Liu · H.-Y. Lee
Department of Electrical Engineering, National Kaohsiung University
of Applied Sciences, Kaohsiung 80778, Taiwan
e-mail: yunan@hotmail.com

H.-Y. Lee
e-mail: leehy@mail.ee.kuas.edu.tw

H.-Y. Ma
Department of Industrial Engineering and Management, Minghsin University of Science
and Technology, Hsinchu 30401, Taiwan
e-mail: hsma@must.edu.tw

V.H. Duy et al. (eds.), *AETA 2015: Recent Advances in Electrical Engineering and Related Sciences*, Lecture Notes in Electrical Engineering 371,
DOI 10.1007/978-3-319-27247-4_25

1 Introduction

MCW-LED, because of its advantages in the cost, the efficiency, the stability as well as the lifetime, are considered as the best candidate to compete with traditional lights. Recently, there are several methods proposed for improving the MCW-LED performances, relating to the Fresnel lens, the chip arrays and the patterned reflectors, [1, 2]. However, the color uniformity and the luminous flux still need to be further improved for the MCW-LED to stand in the current lighting market [3]. With increasing applications, the performances of MCW-LEDs in luminous flux and white light uniformity become more and more important. Therefore, how to optimize the lumen output and the angular color uniformity of MCW-LED is essential for LED lighting development [4, 5].

The phosphor silicone layer (PSL), the mixture of the phosphor particles and the silicone glue, is deposited on the chip surfaces of white light LEDs generally. The phosphor particles can scatter incident light and incur the blue light absorption to make the yellow emission. The PSL absorbs the exciting blue light from the chips to stimulate the yellow light so as to result in the white light [6]. However, there are differences between the phosphor-scattered blue light and the phosphor-emitted yellow light in the radiant intensity distributions. In consequence, a yellow ring phenomenon appears in the illuminating plane, causing worse angular color uniformity (ACU).

In the white light LED packages, the size, the thickness and the concentration as well as the refractive index of the phosphor are the factors in deciding the color temperature, but not beneficial for controlling the CCT distribution [7–9]. There are methods proposed before to solve the ACU problem, but which are demonstrated only for a single-chip LED.

Because of the necessary applications in super high power LED light, MCW-LEDs are considered as the best candidate to serve for the LED lighting market. An MCW-LED consists of multiple blue chips inside, so the interaction process between the light and the LED structures is more complicated than that of the conventional LED with a single chip.

In this study, we apply SiO_2 particles in the phosphor layer or the silicone layer of an MCW-LED to optimize its CCT uniformity and output flux. Through various LED structures involving SiO_2 particles, we will show that the particles can dominate the light scattering process in the MCW-LED, so that the LED light distribution can be independent of its wavelength to achieve the CCT uniformity. The influences on the output efficiency and the spatial color distribution for each proposed LED package with SiO_2 are investigated to find the optimized solution.

2 Theory

In order to investigate the light scattering effect incurred by SiO_2 and phosphor particles in the proposed MCW-LED structures, we use MATLAB software to compute the scattering intensity functions $|S_1|^2$ and $|S_2|^2$, which is based on Mie-scattering theory [7, 10]. Mie-scattering intensities $|S_1|^2$ and $|S_2|^2$ are plotted as a function of cosθ. The results are displayed as the polar diagram of θ with $|S_1|^2$ in the upper half circle ($0 < \theta < \Pi$) and $|S_2|^2$ in the lower half circle ($\Pi < \theta < 2\Pi$). The angular scattering amplitudes, S_1 and S_2 can be calculated by the following equation:

$$S_1 = \sum_{n=1}^{\infty} \frac{2n+1}{n(n+1)} [a_n(x,m)\pi_n(\cos\theta) + b_n(x,m)\tau_n(\cos\theta)] \quad (1)$$

$$S_2 = \sum_{n=1}^{\infty} \frac{2n+1}{n(n+1)} [a_n(x,m)\tau_n(\cos\theta) + b_n(x,m)\pi_n(\cos\theta)] \quad (2)$$

Here $x = 2\pi\alpha/\lambda$ is the particle size parameter, α is the spherical particle radius, λ is the relative scattering wavelength, m is the relative refractive index of the particle. The Mie-scattering depends on x and m values significantly. The scattering functions S1 and S2 are symmetric with respect to both half circles. In the Eqs. (1) and (2), the angular functions πn(cosθ) and τn(cosθ) describe the angular scattering patterns of the spherical harmonics. The parameters an and bn are the expansion coefficients with even symmetry and odd symmetry in turn. If the involved SiO_2 particle is with radius 0.1 μm, then its size parameters are 2.08 for 453 nm and 1.7 for 555 nm. As for the phosphor particle, the size parameters are set as 150.76 and 123.05 for 453 and 555 nm based on the data of commercial MCW-LED samples, respectively.

In this work, our study focuses on MCW-LEDs with CCTs 7000, 7700 and 8500 K, respectively. We use commercial MCW-LEDs of the Siliconware Precision Industries Co., Ltd., MPBGA (Multi-Package Ball Grid Array) as our simulation experimental models. In the simulation processes, the blue light with wavelength 453 nm and the yellow light with wavelength 555 nm are utilized. The computed results show that the light scattering angular distribution angle increases as the SiO_2 particle size decreases, as shown in Fig. 1. And it can be observed that the angular distributions at 453 and 555 nm wavelengths for SiO_2 particles are both broader than those of the phosphor particle, if the SiO_2 particle's radius is set as 0.1 μm. In other words, it is shown that the SiO_2 particles can dominate the phosphor layer scattering process and make the intensity of the scattered blue light stronger. The yellow ring phenomenon usually accompanied with PC-LEDs illumination can thus be balanced to yield better ACU. With optimized package structures, it has been presented that MCW-LEDs can own uniform angular CCT distribution as well as high output lumens at the same time [11].

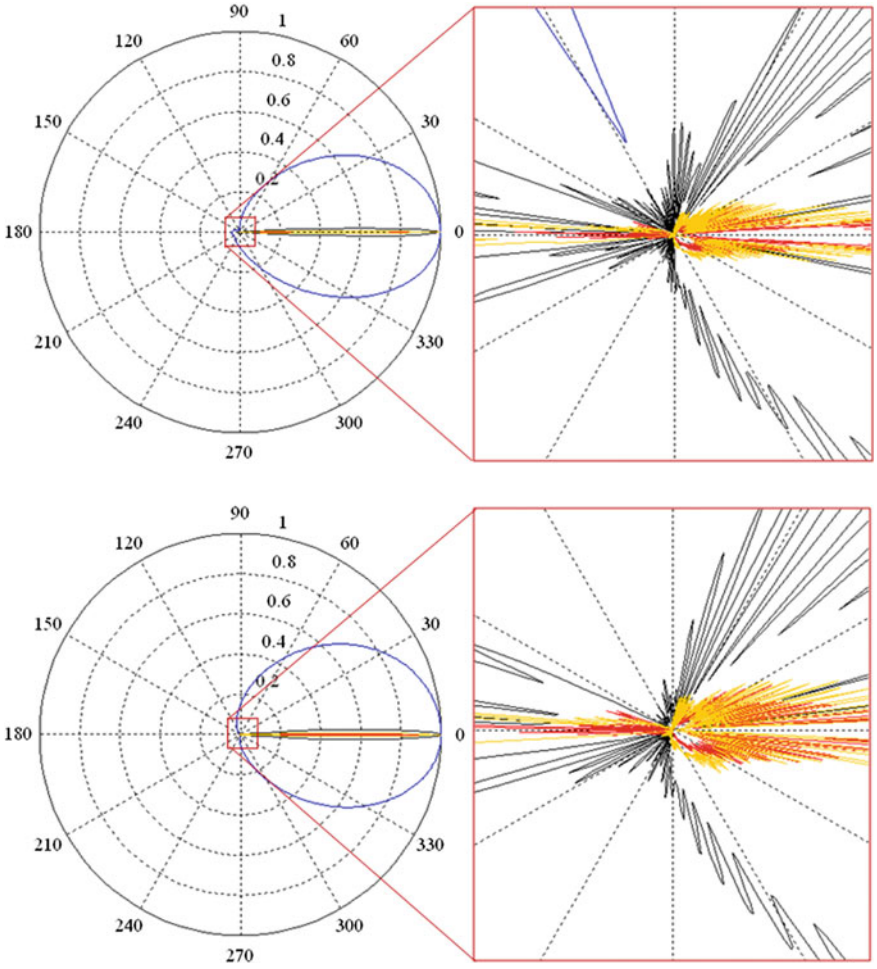

Fig. 1 The Mie-scattering diagrams of the various SiO_2 particle radii, including 0.1 μm (*blue*), 2 μm (*black*), 10 μm (*red*) and that in the phosphor particle size of 7.25 μm (*yellow*) for 453 nm (*top*) and 555 nm (*bottom*)

3 Optical Simulation Experiments and Simulation Results

In order to enhance the angular CCT uniformity and keep high lumen output, we propose four kinds of SiO_2 structures for MCW-LEDs. The conformal structure and the dispense structure are shown in Fig. 2a, b, and SiO_2 particles are involved in the phosphor layer deposited on chips and the silicone layer respectively. The hybrid SiO_2 structure is the combination of the conformal structure and the dispense structure, as shown in Fig. 2c. In the in-cup structure, phosphor and SiO_2 are mixed together in the silicone layer, as shown in Fig. 2d. Based on the commercial

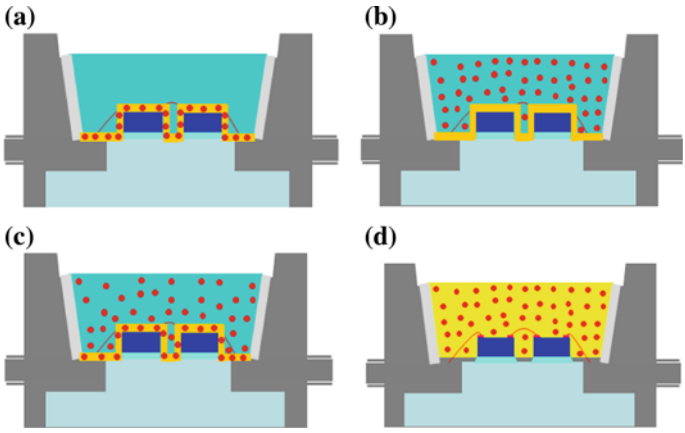

Fig. 2 Schematic diagrams of SiO_2 structure packages: **a** the conformal SiO_2 structure; **b** the dispense SiO_2 structure; **c** the hybrid SiO_2 structure; **d** the in-cup SiO_2 structure

MCW-LED samples, the model structure consists of a reflector cup, a phosphor layer and a silicone layer. The reflector has a bottom length of 8 mm, a height of 2.07 mm and a length of 9.85 mm at its top surface. The phosphor layer depositing on the nine LED chips has the fixed thickness 0.08 mm. Each LED chip with a square base of 1.14 mm and a height of 0.15 mm is bonded in the cavity of the reflector. The radiant flux of each blue chip is 1.16 W, which peak wavelength is 453 nm.

LightTools 8.1.0 optical software is used for the model building and optical analysis in the optical simulation experiments. The refractive index and the density of the quartz particles are 1.54 and 2.65 g/cm^3, respectively. In the proposed MCW-LEDs, the phosphor layer consists of SiO_2 particles, phosphor particles as well as silicone glues. The average radius of the phosphor particles is 7.25 μm and the SiO_2 particle size is varied for optimizing illumination CCT uniformity and output efficiency. Phosphor particles are assumed to be spherical and have a refractive index of 1.83 at all wavelengths of light. The refractive index of the silicone layer and the silicone glue is 1.47 and 1.5, respectively.

The angular CCT uniformity is characterized by CCT P-V deviation, and which is calculated by the subtraction of maximum CCT and minimum CCT. The total weight percentage of the phosphor layer is the sum of the silicone glue's, the phosphor's and the SiO_2's in the MCW-LED. In order to evaluate the performances of the MCW-LEDs with the original structure (0 % SiO_2), the conformal, the dispense and the in-cup SiO_2 structures, their CCT P-V deviation and luminous output are investigated by Monte Carlo ray-tracing methods [12].

In the four proposed SiO_2 structures, there are two locations of the phosphor layer. The first one is the conformal phosphor packages including conformal, dispense and hybrid SiO_2 structures, with the CCT P-V deviation of 2770 K and the luminous flux of 702 lm (without SiO_2 case). The rest is in-cup phosphor package

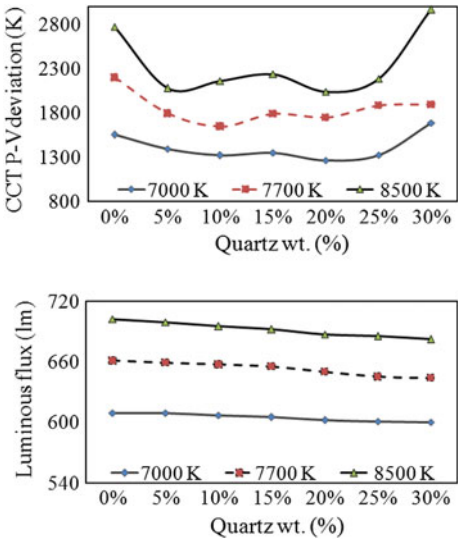

Fig. 3 (*top*) CCT P-V deviation and (*bottom*) luminous flux corresponding to various SiO_2 concentrations for the conformal SiO_2 structure in MCW-LEDs

with the CCT P-V deviation of 9065 K and the luminous flux of 943 lm (without SiO_2 case). Through the Monte Carlo ray-tracing analysis, the lower CCT deviation can be obtained with about 5–10 % SiO_2 concentration in the conformal SiO_2 structure, see Fig. 3 (top). As to the dispense SiO_2 structure, the CCT P-V deviation decays harshly with the increase of the SiO_2 concentration when the SiO_2 weight percentage rises more than 5 %, see Fig. 4a. The CCT deviation of the MCW-LED with SiO_2 can drop 48 % with respect to the package without SiO_2.

The simulation data in Fig. 3 (bottom) and Fig. 4b suggest that the SiO_2 concentration has influences on the lumen output. When the SiO_2 weight percentage increases, the lumen output depresses due to the excessive backward scattering

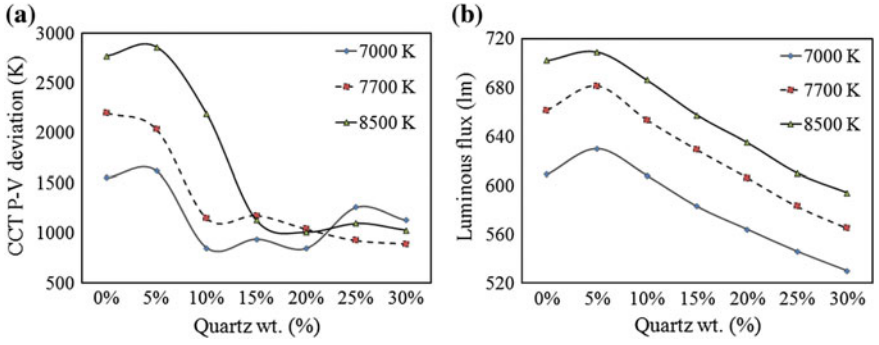

Fig. 4 **a** CCT P-V deviation and (**b**) luminous flux corresponding to various SiO_2 concentrations for the dispense SiO_2 structure in MCW-LEDs

accordingly. With the increase of SiO_2 concentration, the differences of the luminous output between the proposed SiO_2 structures become larger, and the conformal SiO_2 structure has the higher luminous flux than the dispense SiO_2 structure. The reason should be that the conformal SiO_2 structure has thinner SiO_2 layer to absorb less light.

If the SiO_2 concentration is increased over 5 %, the dispense SiO_2 structure performs better than the conformal SiO_2 structure in the CCT P-V deviation. The more scattering events and the larger viewing angle generated by SiO_2 particles in the dispense SiO_2 structure should be the cause.

The MCW-LEDs optimization can be resulted by finding the way to decrease the CCT deviation and the loss of the output lumen at the same time. Through the analysis of the simulation experimental results, the most suitable SiO_2 weight percentages for each SiO_2 structure can be found.

In order to more understand the effect that the SiO_2 particle radius change can bring, the SiO_2 particle radius is varied between 0.1–10 μm and SiO_2 concentration is fixed for proceeding optical simulations. The effect of SiO_2 particle sizes on the luminous flux and the CCT P-V deviation of the proposed SiO_2 structures are presented in Fig. 5 (top) and (bottom) respectively. The phosphor concentration needs to be adjusted for maintaining MCW-LEDs with a certain CCT as the SiO_2 particle size is varied for experiments. The phosphor concentration needs to grow with the SiO_2 particle size to maintain the CCT. In the size range from 0.1 μm to

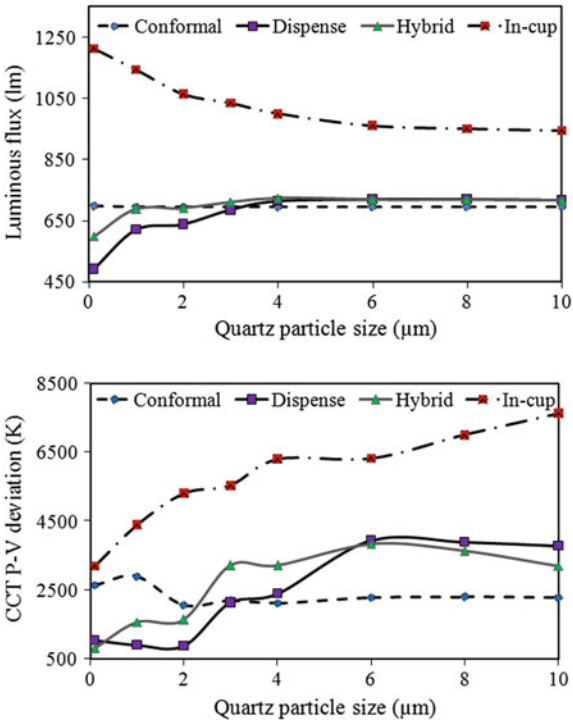

Fig. 5 (*top*) The luminous flux and (*bottom*) the CCT P-V deviation corresponding to various SiO_2 particle sizes in the proposed MCW-LEDs structures with average CCT 8500 K

3 μm, the scattered light has more probabilities to propagate along the large angle direction. And the spatial color distribution gets broader and more backward scattered light are incurred. The energy reflected backward to the MCW-LED package within the encapsulant layer and is trapped inside. Therefore, the lower lumen output is shown in this range. As to 4–10 μm SiO_2 particles, most of the scattered light forwards within a small angle of direction, thus causing worse angular color uniformity But, the absorbed blue light by the chips becomes less, and which results in the higher output luminous flux.

The conformal phosphor package has a better overall CCT uniformity (lower CCT P-V deviation) than the in-cup one, as shown in Fig. 5. However, the conformal phosphor package provides a lower luminous flux, and the more backscattering light absorbed by the chips is mainly the cause.

In summary, the higher angular color uniformity occurs at SiO_2 particle size around 1 μm with the hybrid structure. If we have to use the conformal or dispense structures, it is better to select 2 μm SiO_2 particles for accomplishing the MCW-LED with optimal performance. In the in-cup SiO_2 structure case, 0.1–3 μm SiO_2 particles are more suitable to be used than the larger ones.

4 Conclusions

The lumen output and the angular color uniformity of the MCW-LED packages with the four proposed SiO_2 geometry structures are dependent on the SiO_2 particle size. Under the same conditions, the hybrid SiO_2 structure has the advantageous tendency to the spatial color distribution and the better performance obtained by SiO_2 particle with size around 1 μm. In addition, for each structure or each average CCT of the proposed MCW-LED in the study, applying 5–10 % SiO_2 concentration seems a better choice for achieving the lowest CCT P-V deviation under the least loss of lumens. Moreover, it is found the CCT P-V deviations rise with respect to the increase of the average CCTs of MCW-LED generally, no matter what SiO_2 is added or not. Therefore, it is more difficult to optimize an MCW-LED with high CCTs.

Acknowledgement This work was supported by the Ministry of Science and Technology of the Republic of China; Project: MOST 103-2119-M-151-001.

References

1. Kim B, Choi M, Kim H, Lim J, Kang S (2009) Elimination of flux loss by optimizing the groove angle in modified Fresnel lens to increase illuminance uniformity, color uniformity and flux efficiency in LED illumination. Opt Express 17(20):17916–17927

2. Qin Z, Wang K, Chen F, Luo XB, Liu S (2010) Analysis of condition for uniform lighting generated by array of light emitting diodes with large view angle. Opt Express 18(16):17460–17476
3. Zheng H, Luo XB, Hu R, Cao B, Fu X, Wang YM, Liu S (2012) Conformal phosphor coating using capillary microchannel for controlling color deviation of phosphor-converted white light-emitting diodes. Opt Express 20(5):5092–5098
4. Hu R, Luo XB, Liu S (2011) Effect of the amount of phosphor silicone gel on optical property of white light-emitting diodes packaging. In: Proceedings of the 12th ICEPT-HDP, Shanghai, China, pp 8–11
5. Liu ZY, Liu S, Wang K, Luo XB (2008) Optical analysis of color distribution in white leds with various packaging methods. IEEE Photonics Technol Lett 20(24):2027–2029
6. Liu ZY, Liu S, Wang K, Luo XB (2008b) Analysis of factors affecting color distribution of white LEDs. In: International conference on electronic packaging technology and high density packaging, Shanghai, pp 28–31
7. Liu S, Luo XB (2011) LED packaging for lighting applications: design, manufacturing and testing. Chemical Industry Press, Wiley, Beijing
8. Shuai Y, He YZ, Tran NT, Shi FG (2011) Angular CCT uniformity of phosphor converted white LEDs: effects of phosphor materials and packaging structures. IEEE Photonics Technol Lett 23(3):137–139
9. Sommer C, Reil F, Krenn JR, Hartmann P, Pachler P, Hoschopf H, Wenzl FP (2011) The impact of light scattering on the radiant flux of phosphor-converted high power white light-emitting diodes. J Lightwave Technol 29(15):5145–5150
10. Zhong JJ, Xie MY, Ou ZG, Zhang R, Huang M, Zhao F (2011) Mie theory simulation of the effect on light extraction by 2-D nanostructure fabrication. In: Symposium on photonics and optoelectronics (SOPO), Wuhan, pp 16–18
11. Quoc Anh ND, Lai MF, Ma HY, Lee HY (2014) Enhancing of correlated color temperature uniformity for multi-chip white-light LEDs by adding SiO_2 to phosphor layer. J Chin Inst Eng 38:1–7
12. Fournier F (2013) Freeform reflector design with extended sources. Available from: http://etd.fcla.edu/CF/CFE0003311/Fournier_Florian_R_201008_PhD.pdf

Optical Fiber-Coupled Compact Terahertz Transceiver Module

Hyeon Sang Bark, Young Bin Ji, Dong Woo Park, Sam Kyu Noh, Seung Jae Oh and Tae-In Jeon

Abstract We developed an optical fiber-coupled compact terahertz (THz) transceiver module which uses photoconductive generator and detector driven by a mode-locked Ti:Sapphire laser. The cross section of the module has a diameter of 10 mm and a length of 18 mm, making it small enough to be used as an endoscope system. For a feasibility test, the transceiver module was used to measure the reflective THz signals from glandular stomach (GS) and fore stomach (FS) samples of rats. The THz reflection from the GS samples was 6 % greater than that of the FS sample, indicating that the adipose content of FS in the tissue is greater than that of GS in the tissue.

Keywords Transceiver · Fiber · Module · THz

1 Introduction

The sensitivity of Terahertz (THz) electromagnetic waves is useful for measuring biomedical samples. Because the low energy of the THz frequency does not harm the human body, many studies in the biomedical field have investigated the different properties of the THz frequency [1]. Recently, one study reported the possibility of diagnosing colon, oral, and brain cancer using THz time-domain

H.S. Bark · T.-I. Jeon (✉)
Korea Maritime and Ocean University, Busan 606-791, Korea
e-mail: jeon@kmou.ac.kr

Y.B. Ji · S.J. Oh
Yonsei Institute of Convergence Technology, Yonsei University, Seoul 120-752, South Korea

D.W. Park · S.K. Noh
Nano Materials Evaluation Center, Korea Research Institute of Standards and Science, Aejeon 305-340, South Korea

V.H. Duy et al. (eds.), *AETA 2015: Recent Advances in Electrical Engineering and Related Sciences*, Lecture Notes in Electrical Engineering 371,
DOI 10.1007/978-3-319-27247-4_26

spectroscopy (THz-TDS) [2]. The THz system for in vivo measurements should be small enough to detect cancers organs.

The fiber-coupled THz system [3] is a relatively small THz system [4]. In addition, THz transceiver chips can be used to create smaller modules because the transceiver chip requires only one chip to generate and detect THz beams. Recently, Zhang et al. suggested a single transceiver chip which uses only one antenna to generate and detect THz beams [5]. Because the antenna, however, requires DC bias to generate the THz beam, the THz signal contains offset and noise from the DC bias. Koch et al. added a bias filter to the antenna to reduce noise and offset problems when the transceiver serves as a receiver [6, 7]. More recently, Sakai's group designed a twin antenna which is used as a transmitter and receiver at one chip to avoid the DV bias problem [8]. The separated twin antennas have a higher signal-to-noise ratio (SNR) than a single transceiver antenna because the receiver antenna is less affected by bias noise. Because the THz antenna module is relatively large and cannot freely moves in any direction, it is not feasible for use in biomedical applications.

The THz transceiver module developed here is very small. Moreover, it can be moved in any direction by means of optical fiber. We demonstrate how a THz pulse from the transceiver module can be distinguished between two types of rat stomachs, in this case a GS and a FS.

2 Optical Fiber-Coupled THz Transceiver System Setup

Due to the dispersion of laser pulses in optical fiber, optical fiber-coupled THz transceiver systems usually have a relatively narrow THz band spectrum compared to THz-TDS systems which have independent transmitter and receiver modules delivered by femtosecond laser pulses which travel through air. We measured a frequency bandwidth up to 1.5 THz using a 6 × 6 mm optical fiber-coupled THz transceiver chip.

The laser excitation beam delivered by polarization maintaining (PM) optical fiber was focused onto a dipole antenna gap biased at 12 V. A Ti:Sapphire laser provides 790 nm, 60 fs laser pulses at a repetition rate of 80 MHz with an average power of 12 mW at both antennas. The end of the PM optical fiber is located approximately 5 μm from the dipole antenna to expose the laser beam without an optical lens. The generated THz pulses are emitted to air through a crystalline silicon lens with a diameter of 10 mm and a height of 6.5 mm which was attached to the back side of the transceiver chip, as shown in Fig. 1a. The size of the transceiver module is 10 mm diameter and the length is 18 mm. The module includes an 18-mm-long optical fiber tube, a 6 × 6 mm transceiver chip, and the crystalline silicon lens.

The transceiver chip has two dipole antennas which generate and detect THz pulses. The dipole antenna used as a transmitter in this research consists of two 20-μm-wide stubs separated by a 5-μm gap in a coplanar transmission line

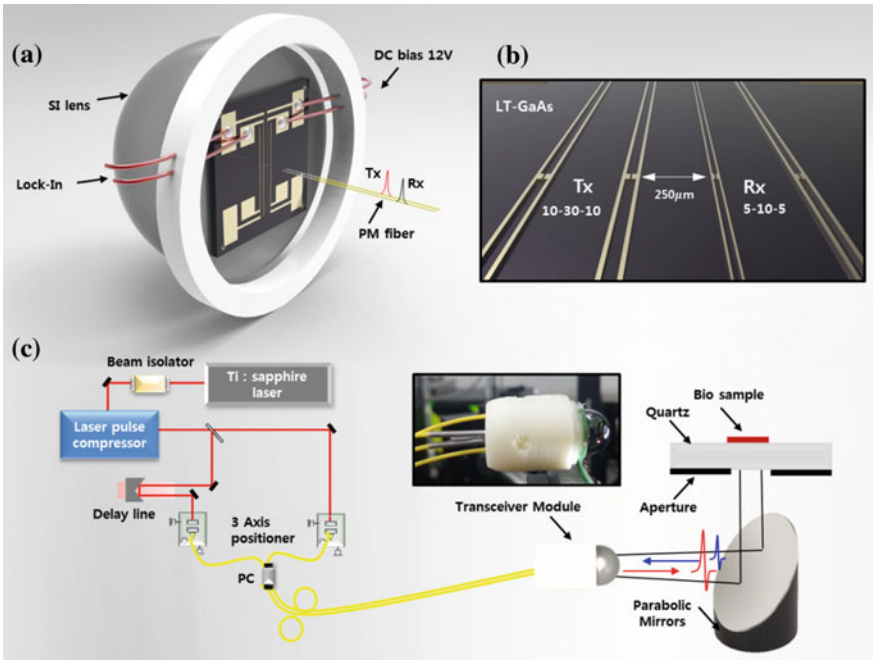

Fig. 1 (**a**) THz transceiver module. (**b**) The antenna structure used at the transceiver chip. (**c**) Schematic diagram of the experimental setup of the THz transceiver system

consisting of two parallel 10-μm-wide metal lines separated from each other by 30 μm. The receiver antenna consists of the same dipole antenna structure expect with two parallel 5-μm-wide metal lines separated from each other by 10 μm as shown in Fig. 1b. The two dipole antennas are separated by 250 μm. These antenna structures are fabricated on a low-temperature grown GaAs wafer.

The THz pulses generated by the dipole antenna of the transceiver chip, biased at 12 V, are emitted to air by the silicon lens. The emitted THz pulses are reflected by a parabolic mirror, where the THz beam is re-collimated into a highly directional beam as shown in Fig. 1c. The sample on a quartz window is positioned in the THz beam path. Finally, the THz beam is reflected in a backward direction by the quartz and the sample interface. The reflected THz beam travels to the receiver antenna of the transceiver chip through the parabolic mirror and the silicon lens. Because only one silicon lens is used, the focal point of the silicon is positioned between the two dipole antenna gaps to ensure the maximum THz signal.

The transceiver chip has two dipole antennas which generate and detect THz pulses. The dipole antenna used as a transmitter in this research consists of two 20-μm-wide stubs separated by a 5-μm gap in a coplanar transmission line consisting of two parallel 10-μm-wide metal lines separated from each other by 30 μm. The receiver antenna consists of the same dipole antenna structure expect with two parallel 5-μm-wide metal lines separated from each other by 10 μm as shown in

Fig. 1b. The two dipole antennas are separated by 250 μm. These antenna structures are fabricated on a low-temperature grown GaAs wafer.

The THz pulses generated by the dipole antenna of the transceiver chip, biased at 12 V, are emitted to air by the silicon lens. The emitted THz pulses are reflected by a parabolic mirror, where the THz beam is re-collimated into a highly directional beam as shown in Fig. 1c. The sample on a quartz window is positioned in the THz beam path. Finally, the THz beam is reflected in a backward direction by the quartz and the sample interface. The reflected THz beam travels to the receiver antenna of the transceiver chip through the parabolic mirror and the silicon lens. Because only one silicon lens is used, the focal point of the silicon is positioned between the two dipole antenna gaps to ensure the maximum THz signal.

3 Measurement and Analysis

Figure 2a shows the measured THz pulse which is reflected by the interface between the quartz and aluminum metal surfaces. Because metal is a nearly perfect conducting material in the THz region, it is useful for carrying the reference THz pulse of the system. To determine the THz beam profile, the THz beam is measured at open apertures of 16, 12, and 8 mm which are located below the quartz plate. When the diameter of the aperture is reduced from 16–12 mm and to 8 mm, the peak-to-peak pulse amplitudes are reduced to 790, 570, and 430 pA, respectively. When the diameter of the aperture is 12 mm, the SNR is approximately 1000:1, which is five times higher than the earlier measurement [5]. Moreover, the bandwidth and the peak amplitude of the spectrum are 1.5 and 0.4 THz, respectively. These THz beam profiles are much better than earlier measurements [8]. Because the dipole length of the receiver antenna of the transceiver chip is only 10 μm including a 5-μm gap, the bandwidth is likely at a high frequency. The frequency at the peak amplitude of the spectrum is typically given as [9]

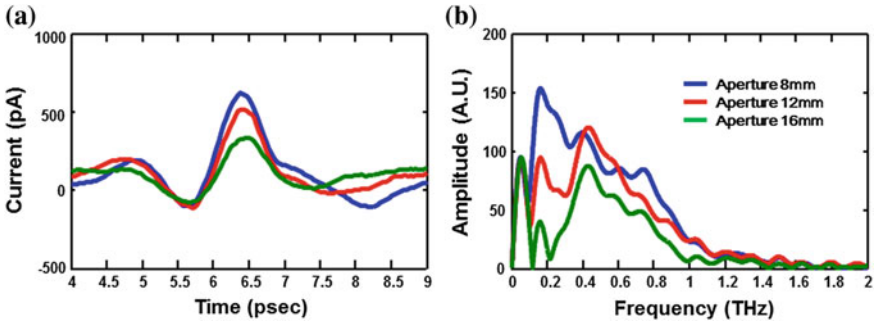

Fig. 2 **a** Measured time-domain THz pulses as reflected from a metal surface with different open apertures, **b** the corresponding amplitude spectra of (**a**)

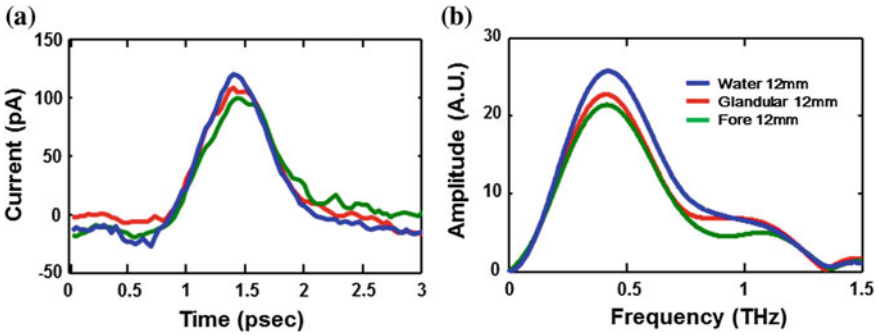

Fig. 3 **a** Measured time-domain THz pulses as reflected from water, GS, and FS, **b** the corresponding amplitude spectra of (**a**)

$$f_o = \frac{c}{2d\sqrt{\varepsilon_{eff}}},$$

where c is the speed of light, d is the antenna length, and ε_{eff} is the effective dielectric constant, i.e. $(\varepsilon_d + 1)/2$. Because the substrate of the transceiver chip is LT-GaAs, the dielectric constant is 13. The measured frequency at the peak amplitude of the spectrum is 10 times lower compared to the theoretical calculation, as the THz beam is not focused on the receiver dipole antenna gap by the Si lens.

In order to apply the THz transceiver module, we measured two different rat stomach samples, termed here the GS and FS samples. Figure 3 shows the measured THz pulses and associated spectra when the aperture is 12 mm and with the samples located on 3-mm-thick quartz plate to create the plate surface. The reference THz pulse is measured using water on a quartz plate, as most biomedical tissues are composed mainly of water. The peak-to-peak amplitude of the THz pulses reflected from the water is reduced by approximately 80 % compared to that of the THz pulses reflected from metal due to the smaller refractive index. The THz bandwidth of the samples is reduced to 1.4 THz due to the high absorption of the high frequency range. The peak-to-peak amplitude of the THz pulse reflected by the GS sample is 6 % greater than that of FS sample, which is in good agreement with the finding of previous research. [10] The water spectrum has the largest amplitude at all measured bandwidths. The amplitude of the GS spectrum is between that of the water and the FS spectra. The different adipose contents of the two sample tissues may have caused the relatively high amplitude of the GS spectrum as compared to that of the FS spectrum. Because adipose tissue has a lower refractive index [10], the FS spectrum has a smaller amplitude than the GS spectrum.

4 Summary and Conclusions

We developed an optical fiber coupled THz transceiver module with a diameter of 10 mm and a length of 12 mm. The THz transceiver chip in the module has two dipole antennas which are independently aligned by a femtosecond laser beam guided by optical fiber. In order to determine the THz beam profile, the THz beam is measured with an open aperture of 16, 12, and 8 mm. Using the THz transceiver module, we measured two different GS and FS stomach rat samples. The THz reflection from the GS sample was found to be 6 % greater than that of the FS sample because the adipose content of FS in the tissue is greater than that of GS in the tissue. We hope that the proposed module can be used for in situ biomedical measurements in the future.

References

1. Ji YB, Lee ES, Kim SH, Son JH, Jeon TI (2009) A miniaturized fiber-coupled terahertz endoscope system. Opt Express 17: 17082–17087
2. Dragomana D, Dragomanb M (2004) Review terahertz fields and applications. Prog Quantum Electron 28:1–66
3. Crooker SA (2002) Fiber-coupled antennas for ultrafast coherent terahertz spectroscopy in low temperatures and high magnetic fields. Rev Sci Instrum 73:3258–3264
4. Krumbholza N, Joerdensa C, Probsta T, Haseka T, Kochb M (2009) Fiber-coupled terahertz transceiver heads for reflection measurements. In: Proceedings of the 34th international conference on infrared, Millimeter, and Terahertz Waves, pp 1–2
5. Tani M, Jiang Z, Zhang XC (2000) Photoconductive terahertz transceiver, Electron Lett, 36:804–805
6. Jördens C, Krumbholz N, Hasek T, Vieweg N, Scherger B, Bähr L, Koch M (2008) Fiber-coupled terahertz transceiver head, Electron Lett 44, pp 1473–1475
7. Krumbholza N, Joerdensa C, Probsta T, Haseka T, Kochb M (2009) Fiber-coupled terahertz transceiver heads for reflection measurements. In Proceedings of the 34th international conference on infrared, Millimeter, and Terahertz Waves, pp 1–2
8. Tani M, Watanabe M, Sakai K (2002) Photoconductive twin dipole antennas for THz transceiver. Electron Lett. 38:5–6
9. Rebeiz GM (1992) Millimeter-wave and terahertz integrated circuit antennas. Proc IEEE 80:1748–1770
10. Ji YB, Lee ES, Kim SH, Son JH, Jeon TI (2009) A miniaturized fiber-coupled terahertz endoscope system, Opt Express 17:17082–17087

Study of a Novel Secondary Lens for LED Fishing Lamps

Thieu Quang Tri and Nguyen Doan Quoc Anh

Abstract A novel LED fishing/working light is proposed for enhancing the lighting efficiency of a fishing boat. The study is focused on the freeform secondary lens design for creating a lamp to attract fishes and shine light on the deck for fishing work. The experimental results show that the proposed multi-segmented freeform lens (MSFL) can accomplish the proposed light three times illuminance more than that of the traditional HID fishing lamp under the same input electrical power.

Keywords Light-emitting diodes · Optical engineering · Illumination design · Optical design and fabrication · Non-imaging optics

1 Introduction

The conventional lights used for fishing ships are incandescent lamps or high intensity discharge (HID) lamps. However, the lamps emit a large amount of infrared energy or ultraviolet rays, so that they are not only inefficient to absorb fishes, but also get fisherman with skins or eyes terrible illness. Furthermore, the light from these lamps is omnidirectional, so most of it does not reach to the target areas, such as the deck and the attracting fish water area, so as to incur much electrical power wasting [1, 2]. LEDs have many advantages such as high efficiency, long lifetime, and fast response as well as climate impact resistance [3–5]. Thus, an LED has been considered as the most promising lighting solution for future. However, an LED usually cannot provide the required intensity distribution for its applications alone. A LED usually needs to be equipped with an additional optical device, called the secondary lens, to tailor its intensity distribution to

T.Q. Tri · N.D.Q. Anh (✉)
Faculty of Electrical and Electronics Engineering, Ton Duc Thang University,
No. 19 Nguyen Huu Tho Street, District 7, Ho Chi Minh City, Vietnam
e-mail: nguyendoanquocanh@tdt.edu.vn

V.H. Duy et al. (eds.), *AETA 2015: Recent Advances in Electrical Engineering and Related Sciences*, Lecture Notes in Electrical Engineering 371,
DOI 10.1007/978-3-319-27247-4_27

achieve the targeted illumination with a high light efficiency [6–9]. According to our investigation to thousands of fishermen, we get their essential and common requirement for the fishing lamp—the ideal lamp of a fishing boat needs to be efficient and can be competent for their fishing work on deck and fishes attracting. In consequence, instead of using conventional fishing lamps or area-focused LED fish lighting attractors, we propose a novel LED lamp, which is not simply used for attracting fishes, and can shine light on the deck for fishing work at darkness. Our study is mainly focused on the freeform secondary lens design of the proposed light. The experimental results will show that the multi-segmented freeform lens (MSFL) can accomplish the proposed light three times illuminance more than that of the traditional HID fishing lamp, no matter which light is on the fish attracting water area or the fishing work region of the deck.

2 Principles

The MSFL design is mainly based on Snell's law, the Monte Carlo ray-tracing method and optimization algorithms. Through optical software simulations, we understand that the conventional conic surface is not competent for implementing the proposed lamp. We find that the proposed MSFL needs to be segmented into at least three sections to accomplish the LED rays as area focused beam for attracting fishes and the large angled beams to light up the whole deck surface for fishing work at darkness. The relations among the incoming light direction vector I, the optical surface normal vector N, and the outgoing light direction vector O are precisely governed by snell's law. The normal vector N can be calculated by Eq. (1) [10–15]:

$$N = \frac{I - O}{|I - O|} \tag{1}$$

Assuming that the center of LED source is located at the origin of a Cartesian coordinate system, one incident ray I_i from a source point is aimed at the corresponding point Q_i to generate the refracted ray O_i. The Q_i is set in the middle position between P_{i-1} and P_i and the surface segment is expressed as $f_i(x)$ ($i = 1, 2$). The f'(x) is the derivation of f(x) and can be calculated to get Ni, which is the surface normal of $f_i(x)$ at Q_i. The end points of each generatrix are preset as P_i which are the boundary conditions of the ordinary differential Eq. (1) involving f'(x). Thus, the line shape of the generatrix f(x) can be obtained by solving the ordinary differential equation.

In the MSFL optimization process, making use of the non-sequential ray tracing mode and the global searching methods of ZEMAX software, $f_i(x)$ is set free to vary, so that N_i is changed until O_1 and O_2 are directed to the target angle of 70° and 0° with respect to y axis respectively, as shown in Fig. 1.

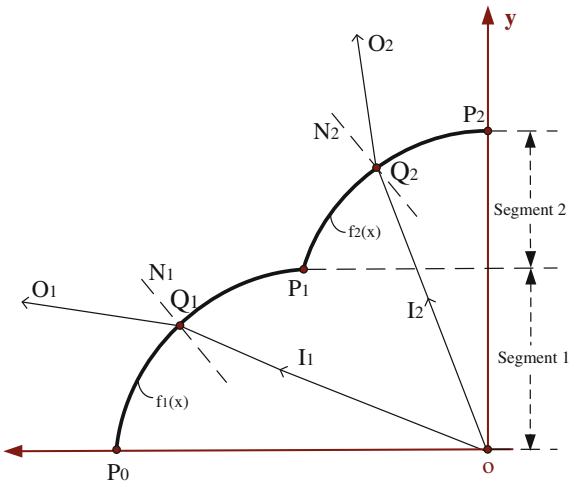

Fig. 1 The two-dimensional ray tracing plot of the MSFL

The design process of the LED fishing/working light is presented by the flow chart shown in Fig. 2. In order for optimizing MSFL efficiently, spherical surface functions are served as $f_i(x)$. The center position and the radius of the spherical surfaces are set as variables for searching the optimized MSFL solution. Once the optimization process is finished, O_1 and O_2 will be in the target angles 70° and 0° with respect to y axis respectively, then the fi(x) can thus be decided to construct the MSFL structure.

3 Experiments and Experimental Results

In order to find out the best MSFL solution, we used the Solidworks software and the optical design software ZEMAX to optimize the MSFL surfaces. The optimized MSFL is shown in Fig. 3. A 5000 K 1 W CREE XPE white Lambertian LED with 110 lumens is used as the light engine and mounts on the optimized MSF to serve as the fishing/working lamp model for experiments. By means of the optical ray tracing functions of TracePro software, the 3D and the 2D intensity distributions of the fishing/working lamp model are resulted and shown in Figs. 4 and 5, respectively. As the Fig. 5 showing, the distributed light within 0°–40° is used for attracting fishes and that within 50°–80°, like a pair of bird wings, is for on deck lighting.

The prototype of the proposed LED fishing/working lamp is produced according to the structures of Fig. 3, as shown in Fig. 6a, and its 3D optical intensity distribution measured by a Goniophotometer is shown in Fig. 6b. In order to evaluate the similarity between the LED fishing/working lamp model and the real LED

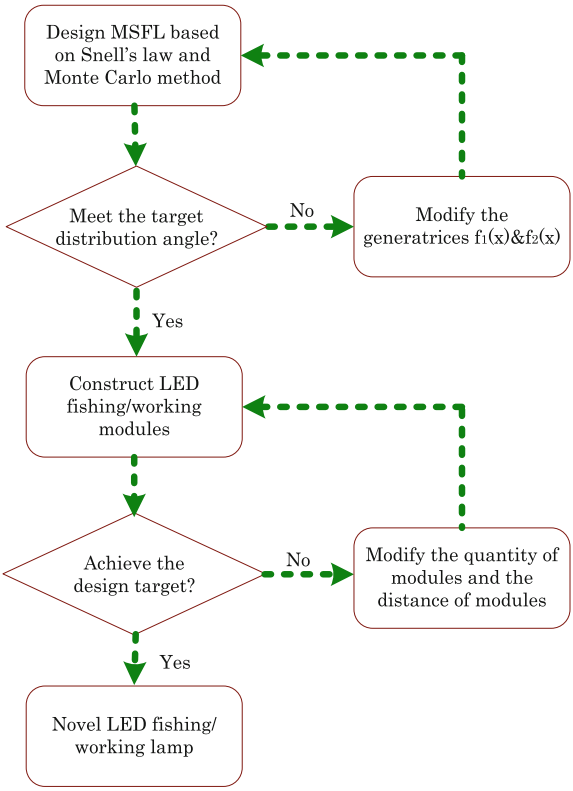

Fig. 2 The flow chart of constructing the proposed LED fishing/working light

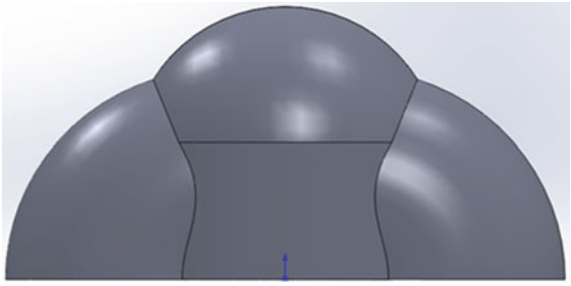

Fig. 3 The MSFL solid body plot

fishing/working lamp sample, we compare them by using the normalized cross correlation (NCC) in intensity angular distribution by Eq. (2).

$$NCC = \frac{\sum_n \left[I(\theta_n)_e \overline{I_e}\right]\left[I(\theta_n)_s \overline{I_s}\right]}{\sqrt{\sum_n \left[I(\theta_n)_e \overline{I_e}\right]^2 \sum_n \left[I(\theta_n)_s \overline{I_s}\right]^2}} \tag{2}$$

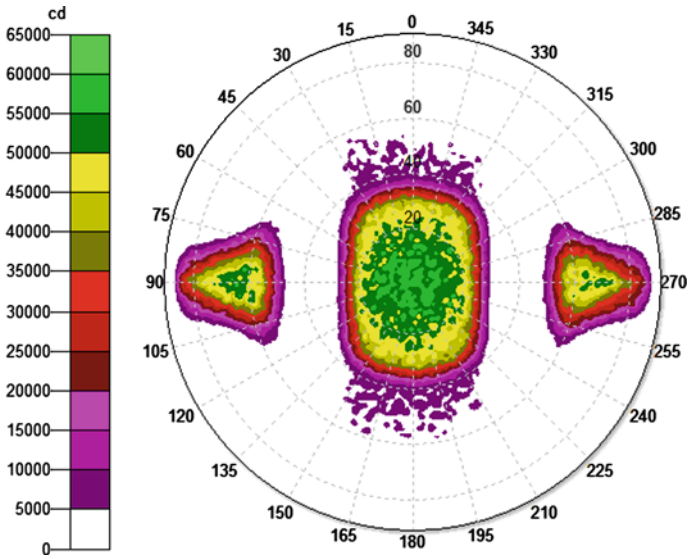

Fig. 4 The simulated 3D optical intensity distribution map of the proposed fishing/working lamp

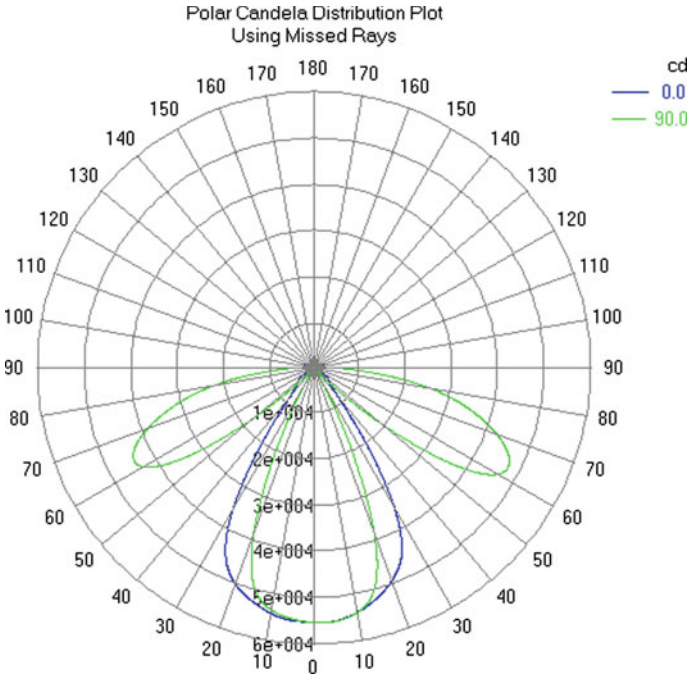

Fig. 5 The simulated 2D optical intensity distribution curves of the proposed fishing/working lamp

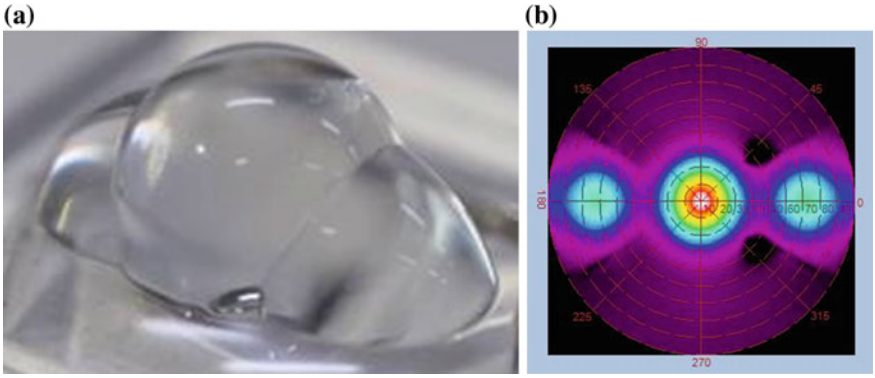

Fig. 6 (**a**) The prototype of the proposed LED fishing/working lamp sample, (**b**) The measured 3D optical intensity distribution map of the LED fishing/working lamp sample by a goniophotometer

Here Is and Ie are the simulated and real experimental values of the relative light intensity, respectively. θ_n is the n-th angular displacement, $\overline{I_s}$ and $\overline{I_e}$ are the average values of simulations and optical measuring experiments accomplished by a goniophotometer. While comparing the data of Fig. 6b with that of Fig. 4, it is found that the NCC value is higher than 97.5 %, so the proposed LED fishing/working lamp model is encouraged to be used in the following experiments.

In order to demonstrate the advantages of the proposed fishing/working lamp, we build a 72,000 lumens/675 W LED light composed of the arrays of the proposed fishing/working lamps to compare the 2,25,000 lumens/2000 W philips HID conventional fishing lamp in their fishing lighting performances. The measured light distribution curve of the HID fishing lamp is shown in Fig. 7. Two 12 m(L) × 3 m (W) fishing boats with a deck 2 m higher than the water surface are utilized for our simulation experiments. One boat is with 20 sets of the 675 W new LED fishing/working lights, shown in Fig. 8 (top). The other one is with 20 sets of the 2000 W HID fishing lamps, as shown in Fig. 8 (bottom). The fishing lights are hang on the poles located on both sides of the fishing boats equally, and 2 m higher than the deck.

Making use of Dialux lighting softwares, we import the intensity distribution file (IES file) of the lights for illumination simulation. The accomplished illuminance distribution on the deck and the water surface around the fishing boat are shown in Figs. 9 and 10, respectively. From the experimental data shown in Figs. 9 and 10, it can be understood that the illumination performances of the proposed LED fishing/working lights are better than the traditional HID lamp, no matter which use is for on deck lighting or attracting fishes. Furthermore the proposed light consumed only 1/3 of electrical power the traditional HID lamp does. In order to study

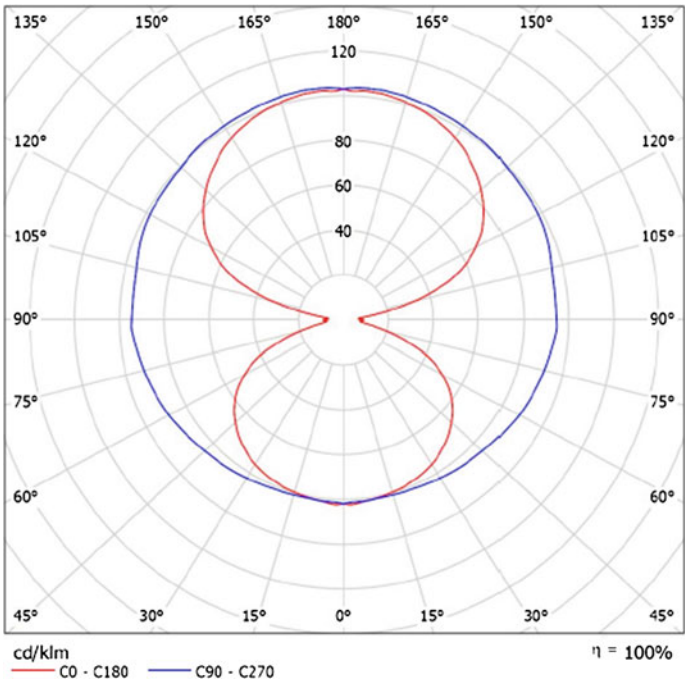

Fig. 7 The measured light intensity distribution of the HID fishing lamp

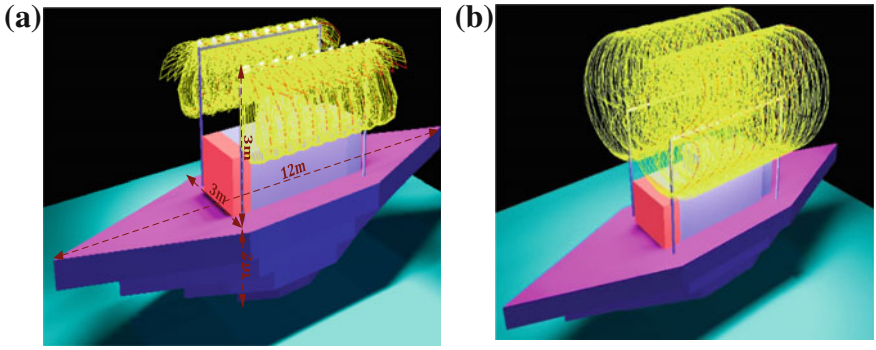

Fig. 8 (**a**) The simulation of the fishing boat equipped with 20 sets of the new LED fishing/working lamp, (**b**) The simulation of the fishing boat equipped with 20 sets of the 2,000 W HID fishing lamp

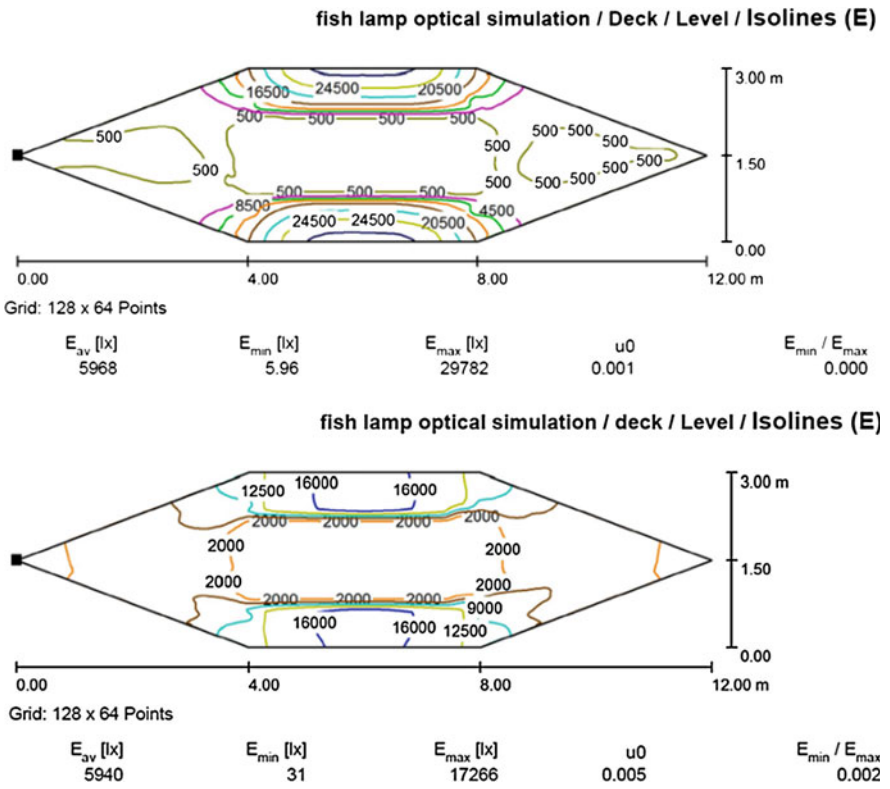

Fig. 9 (*top*) The simulated illuminance distribution map on the deck of a fishing boat, equipped with 20 sets of the 675 W new LED fishing/working lights; (*bottom*) The illuminance distribution map on the deck of a fishing boat, equipped with 20 sets of the 2000 W HID lamps

the underwater light intensity distribution, which is essential for attracting fishes, ZEMAX optical design software is used to investigate the illumination distribution under water. While considering the seawater absorption, the seawater surface reflectivity and the light spectrum, the illumination distribution at 1 m deep underwater is computed and shown in Fig. 11. According to the simulation results, we found that the seawater transmission efficiency of the new fishing/working light is 93 %, and that of the traditional HID fishing lamp is 84 %. Therefore, it is not difficult to understand that the proposed fishing light performs better than the traditional ones even under the water surface.

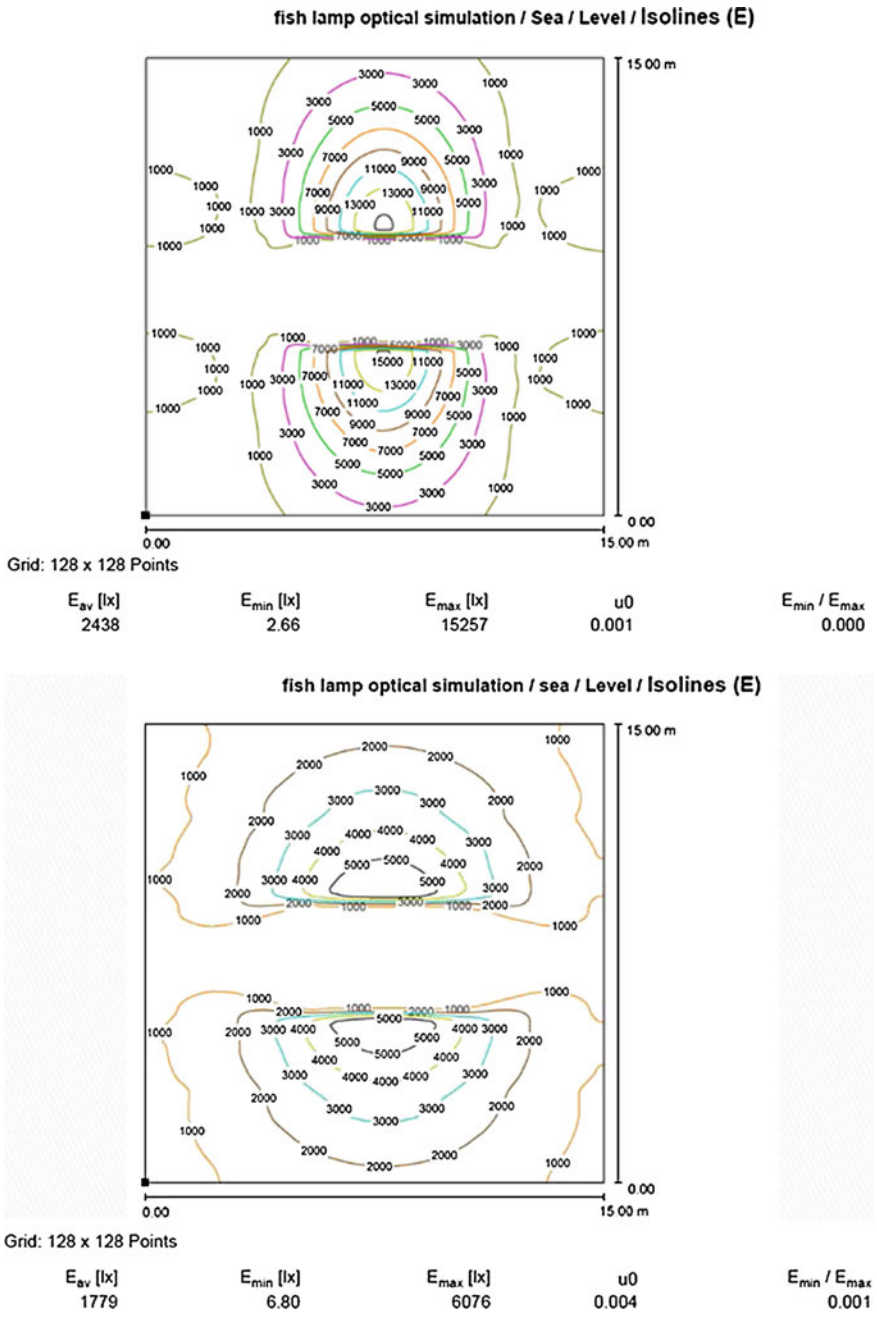

Fig. 10 (*top*) The simulated illuminance distribution map on the water surface around a fishing boat, equipped with 20 sets of the 675 W new LED fishing/working lights, (*bottom*) The simulated illuminance distribution map on the water surface around a fishing boat, equipped with 20 sets of the 2000 W HID lamps

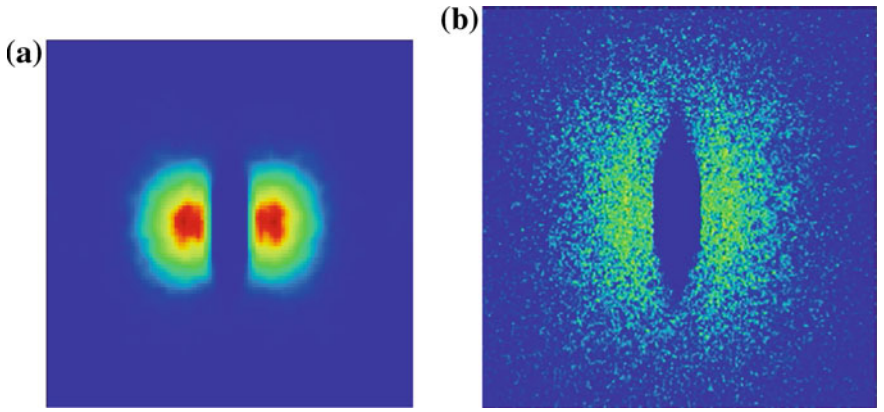

Fig. 11 (**a**)The Illumination at 1 m deep underwater, achieved by the fishing boat equipped with 20 sets of the 675 W new LED fishing/working lamps; (**b**) The Illumination at 1 m deep underwater, achieved by the fishing boat equipped with 20 sets of the 2000 W Philips HID fishing lamps

Table 1 The lighting performances of the new LED fishing/working light and the traditional HID fishing light for the fishing boat

Lamps		20 sets of new LED fishing/working lights/boat	20 sets of HID fishing lights/boat
Total consuming electrical power (w)		13500	40000
Output total lumens (lm)		72000	225000
E_{av} (averaged illuminance) (lx)	On deck surface area	5968	5940
	On seawater surface area (15 m^2) around the fishing boat	2438	1779
E_{min} (minimum illuminance) (lx)	On deck surface area	5.96	31
	On seawater surface	2.66	6.80
$U_0 \equiv E_{min}/E_{ave}$	On deck surface area	0.001	0.005
	On seawater surface	0.001	0.004
Total Lumens (lm)	On seawater surface area (15 m^2) around the fishing boat	944060	1212100
	1 m deep underwater (15 m^2) around the fishing boat	886030	1022100
Optical transmission efficiency through seawater surface (%)		93.853	84.324

4 Conclusion and Discussion

We design and optimize an multi-segmented freeform lens for a high power white light LED to construct a new fishing/working lamp. The fishing/working lamp is used for replacing the traditional HID fishing lamp to serve for attracting fishes and work lighting on the deck of a fishing boat. In order to promise the accuracy of our simulation experiments, it is demonstrated that the proposed LED fishing/working lamp model is largely consistent with the real produced lamp sample through the NCC analysis of the light intensity angular distributions.

450 pieces of the proposed fishing/working lamp are used to build a new 72,000 lumens/675 W fishing light, and 20 sets of the light are set up in a fishing boat. According to the simulation experimental results, it is found that the proposed light can accomplish better illuminance performance and 3 times efficiency than the traditional HID lamp. The performances data are listed and presented in Table 1.

Acknowledgments This work was supported by professor Hsiao-Yi Lee, National Kaohsiung University of Applied Sciences, Taiwan.

References

1. Shen SC, Huang HJ (2012) Design of LED fish lighting attractors using horizontal/vertical LIDC mapping method. Opt Express 20:26135–26146
2. Shen SC, Li JS, Huang MC (2014) Design a light pattern of multiple concentric circles for LED fishing lamps using Fourier series and an energy mapping method. Opt Express 22:13460–13471
3. Liang CW, Koshel J, Sasian J, Breault R, Wang YT, Fang YC (2014) Optical design and testing: introduction. Appl Opt, 53: ODT1-ODT4
4. Derstine MW, Walker AC, Yatagai T (1998) Optics in computing: introduction to the feature issue. Appl Opt 37:2809–2810
5. Camacho RG, Phua SF, Lin ZX, Lo YC, Sun CC, Liang CW (2013) Beam-shaping system with high-uniformity illumination using power LEDs. In: Proceedings of Optics and Photonics of Taiwan International Conference (OPTIC, 2013), pp 45
6. Seassal C, Koshel J (2013) Focus issue introduction: renewable energy and the environment. Opt Express 21:A430–A432
7. Fang YC, Tsai CM, Chung CL (2011) A study of optical design and optimization of zoom optics with liquid lenses through modified genetic algorithm. Opt Express 19:16291–16302
8. Albuquerque BFCD, Sasian J, Sousa FLD, Montes AS (2012) Method of glass selection for color correction in optical system design. Opt Express 20:13592–13611
9. Lieb MA, Zavisian JM, Novotny L (2004) Single-molecule orientations determined by direct emission pattern imaging. JOSA B 21:1210–1215
10. Liu S, Luo XB (2011) LED Packaging for lighting applications: design, manufacturing and testing (Wiley, 2011)
11. Anh NDQ, Lai MF, Ma HY, Lee HY (2014) Design of a free-form lens for LED light with high efficiency and uniform illumination. Appl Opt 53:H140–H145

Part VII
Motor Control

Sliding Mode Observer for Induction Motor Control

Chau Dong, Pavel Brandstetter, Huu Hau Vo and Vo Hoang Duy

Abstract The control of induction motor drives constitutes a vast subject, and the technology has further advanced in recent years. In control algorithms, continuous rotor position is mandatory. But the presence of encoder increases cost, reduces reliability. Therefore, elimination of this sensor is desirable. A sensorless of the vector controlled induction motor means the vector control without using any speed sensor. In the paper, a sliding mode observer and its applications in the sensorless control of the induction motor drive are proposed. The mathematical equations of induction motor, sliding mode observer and vector control are described in the paper. The stability of observer is proved base on Lyapunov theory. Simulation results are also presented in the paper.

Keywords Sliding mode observer · Induction motor · AC drive · Lyapunov · Vector control · Sensorless control

1 Introduction

Induction machines, a type of AC drives, are used widely in practice for variable speed applications in wide power ranges. These machines are very economical, rugged and reliable [8]. However, the control and estimation of important quantities

C. Dong (✉) · H.H. Vo · V.H. Duy
Faculty of Electrical and Electronics Engineering, Ton Duc Thang University,
No. 19 Nguyen Huu Tho Street, District 7, Ho Chi Minh City, Vietnam
e-mail: dongsithienchau@tdt.edu.vn

H.H. Vo
e-mail: vohuuhau@tdt.edu.vn

V.H. Duy
e-mail: vohoangduy@tdt.edu.vn

P. Brandstetter
VSB - Technical University of Ostrava, Ostrava, Czech Republic
e-mail: pavel.brandstetter@vsb.cz

V.H. Duy et al. (eds.), *AETA 2015: Recent Advances in Electrical Engineering and Related Sciences*, Lecture Notes in Electrical Engineering 371,
DOI 10.1007/978-3-319-27247-4_28

of AC drives with induction motors is difficult because of variable frequency of a supply stator phase voltages realized by frequency converters, complex dynamics of AC machines, machine parameters variations, and signal processing of feedback signals [6]. In many decades, induction motor control methods are developed. The control methods of induction machines can be listed as scalar controlling, field oriented control (FOC) and direct torque and flux control (DTC) [4, 6]. Scalar control is simple, easy to implement in practice but it disregards the coupling effect. So it has inferior performance, especially in low speed applications and now scalar control diminished in real world. The DTC, an advanced scalar control method, is introduced in the mid-1980s. The torque and stator flux are controlled by inverter voltage space vector through look-up table [4]. The disadvantage of DTC is that DTC is not stable at low speed. The field-oriented control or vector control was introduced firstly in 1970s. The vector control has been used in industry for high performance, especially in low speed [7]. This method is complicated. However, with developing of semiconductor technology, powerful microcontroller or DSP are used so that FOC overcome its disadvantages and become an industry standard control for AC drives.

In FOC, a flux control loop has been added for precision control of flux. The torque component is generated from the speed control loop. So induction motor control requires accurate flux and motor rotor speed. The flux and rotor speed can be achieved by using Hall sensor and encoder. However, in recent researches, sensors are eliminated because of complexity, higher cost and lower reliability [3, 8, 9, 13]. The observers are used instead. Many kinds of observers are proposed, such as Extended Kalmanm Filter (EKF), Luenberger Observer (LO) and Sliding Mode Observer (SMO) [3–6, 8–10, 12, 13]. Among the observers, the EKF observers get high accuracy at medium and high speed range [9, 13]. They can operate well at the rotor speed above 60 rpm while the SMO and LO observers can work well at very low speed, about 15 rpm [8, 9, 13]. In case of parameters of induction motor not known exactly and noise, the SMOs and LOs have superior performance over to the EKF observers [9, 13]. Among these observers, sliding mode observers have strong robustness to parameter variations such as stator resistance, mutual inductance, etc. [13]. They also have superior performance when the noise increases and they can handle nonlinear systems like IM very well [4, 13]. Moreover, LO and SMO are more applicable in practical than EKF [13].

Because of their outstanding characteristics in nonlinear systems and parameter variations, sliding mode observers are focused in this paper. The mathematical model of induction machines is introduced in Sect. 2. Sliding mode observer and the current model are used to estimate the rotor flux and speed are presented in Sect. 3. In this section, the stability of the method based on Lyapunov's theory is also analyzed. Next, Sect. 4 introduces vector control of induction motor. Some simulation results are presented in Sect. 4. At last, the conclusions are in Sect. 5.

2 Mathematical Model of Induction Machines

Dynamic model of an induction motor in two-phase stationary frame are described as follows [5, 6, 14]:

$$\begin{aligned}
\frac{di_{S\alpha}}{dt} &= -\frac{\left(L_h^2 R_R + L_R^2 R_S\right)}{\sigma L_S L_R^2} i_{S\alpha} + \frac{L_h R_R}{\sigma L_S L_R^2}\psi_{R\alpha} + \frac{L_h \omega_r}{\sigma L_S L_R}\psi_{R\beta} + \frac{1}{\sigma L_S} v_{S\alpha} \\
\frac{di_{S\beta}}{dt} &= -\frac{\left(L_h^2 R_R + L_R^2 R_S\right)}{\sigma L_S L_R^2} i_{S\beta} - \frac{L_h \omega_r}{\sigma L_S L_R}\psi_{R\alpha} + \frac{L_h R_R}{\sigma L_S L_R^2}\psi_{R\beta} + \frac{1}{\sigma L_S} v_{S\beta} \\
\frac{d\psi_{R\alpha}}{dt} &= \frac{L_h R_R}{L_R} i_{S\alpha} - \frac{R_R}{L_R}\psi_{R\alpha} - \omega_r \psi_{R\beta} \\
\frac{d\psi_{R\beta}}{dt} &= \frac{L_h R_R}{L_R} i_{S\beta} + \omega_r \psi_{R\alpha} - \frac{R_R}{L_R}\psi_{R\beta}
\end{aligned} \tag{1}$$

where $i_{S\alpha}$, $i_{S\beta}$—stator current vector components in $[\alpha, \beta]$ stator coordinate system; $v_{S\alpha}$, $v_{S\beta}$—stator voltage vector components in $[\alpha, \beta]$ stator coordinate system; $\psi_{R\alpha}$, $\psi_{R\beta}$—rotor magnetic flux in $[\alpha, \beta]$ stator coordinate system; L_h—magnetizing inductance; L_R—rotor inductance; L_S—stator inductance; R_R—rotor phase resistance; R_S—stator phase resistance; ω_r—rotor angular speed; σ—total leakage factor $\left(\sigma = 1 - \frac{L_m^2}{L_R L_S}\right)$; p—the number of poles.

The electrical torque produced by induction motor is:

$$T_e = \frac{3}{2}\frac{p}{2}\frac{L_h}{L_R}\left(\psi_{R\alpha} i_{S\beta} - \psi_{R\beta} i_{S\alpha}\right) \tag{2}$$

3 Sliding Mode Observer

3.1 Sliding Mode Observer for Speed Estimation

Depending on field oriented control of induction motor, the stator currents, rotor fluxes and rotor speed need to be estimated. The stator currents $i_{S\alpha}$, $i_{S\beta}$, rotor speed ω_r are estimated by using sliding mode observer.

According to Eq. (1), the dynamic model of induction motor is rewritten under state space as follows:

$$\begin{aligned}
\dot{x} &= A \cdot x + B \cdot v \\
y &= C \cdot x
\end{aligned} \tag{3}$$

$$x = \begin{bmatrix} i_{S\alpha} & i_{S\beta} & \psi_{R\alpha} & \psi_{R\beta} \end{bmatrix}^T; \quad v = \begin{bmatrix} v_{S\alpha} & v_{S\beta} \end{bmatrix}^T \tag{4}$$

$$A = \begin{bmatrix} a_{11} & a_{12} & a_{13} & a_{14} \\ a_{21} & a_{22} & a_{23} & a_{24} \\ a_{31} & a_{32} & a_{33} & a_{34} \\ a_{41} & a_{42} & a_{43} & a_{44} \end{bmatrix}, \quad B = \frac{1}{\sigma L_S} \begin{bmatrix} 1 & 0 \\ 0 & 1 \\ 0 & 0 \\ 0 & 0 \end{bmatrix}, \quad C = \begin{bmatrix} 1 & 0 & 0 & 0 \\ 0 & 1 & 0 & 0 \end{bmatrix} \tag{5}$$

$$\begin{aligned} &a_{11} = a_{22} = -\frac{\left(L_h^2 R_R + L_R^2 R_S\right)}{\sigma L_S L_R^2}, \quad a_{12} = a_{21} = 0, \quad a_{13} = a_{24} = \frac{L_h R_R}{\sigma L_S L_R^2}, \quad a_{14} = -a_{23} = \frac{L_h \omega_r}{\sigma L_S L_R} \\ &a_{31} = a_{42} = \frac{L_h R_R}{L_R}, \quad a_{32} = a_{41} = 0, \quad a_{33} = a_{44} = -\frac{R_R}{L_R}, \quad a_{34} = -a_{43} = -\omega_r \end{aligned} \tag{6}$$

The sliding mode observer can be given as:

$$\begin{aligned} &\frac{d}{dt}\hat{x} = \hat{A} \cdot \hat{x} + B \cdot v + G \cdot sign[y - \hat{y}] \\ &y = C \cdot \hat{x} \end{aligned} \tag{7}$$

$$\hat{A} = A_{(\omega_r = \hat{\omega}_r)}; \quad G = \begin{bmatrix} g_1 & -g_2 \\ g_2 & g_1 \\ g_3 & -g_4 \\ g_4 & g_3 \end{bmatrix} \tag{8}$$

Sliding surface is chosen:

$$S = y - \hat{y} \tag{9}$$

The time derivation of sliding mode observer is:

$$\dot{S} = \dot{y} - \dot{\hat{y}} = C\dot{x} - C\dot{\hat{x}} \tag{10}$$

$$\begin{aligned} \dot{S} &= C \cdot \left(A \cdot x + B \cdot v - \hat{A} \cdot \hat{x} - B \cdot v - G \cdot sign[y - \hat{y}]\right) \\ &= C \cdot \left(\left(A - \hat{A}\right) \cdot x + \hat{A} \cdot \tilde{x} - G \cdot sign[y - \hat{y}]\right) \end{aligned} \tag{11}$$

where $\tilde{x} = x - \hat{x}$—the error between the real value and estimated value.

$$A - \hat{A} = \begin{bmatrix} 0 & 0 & 0 & \frac{L_h}{\sigma L_S L_R} \\ 0 & 0 & -\frac{L_h}{\sigma L_S L_R} & 0 \\ 0 & 0 & 0 & -1 \\ 0 & 0 & 1 & 0 \end{bmatrix} \tilde{\omega}_r = W\tilde{\omega}_r \tag{12}$$

where $\tilde{\omega}_r = \omega_r - \hat{\omega}_r$—speed difference between actual rotor speed and estimated rotor speed.

Choosing the positive definite Lyapunov function as follows [7]:

$$V = \frac{1}{2}\left(S^2 + \frac{\tilde{\omega}_r^2}{a}\right) \tag{13}$$

The time derivation of Lyapunov function is derived:

$$\begin{aligned}\dot{V} &= S^T \cdot \dot{S} - \frac{1}{\alpha}\dot{\hat{\omega}}_r\tilde{\omega}_r = S^T \cdot C \cdot \left(\hat{A} \cdot \tilde{x} + W \cdot \tilde{\omega}_r \cdot x - G \cdot sign[y - \hat{y}]\right) - \frac{1}{a}\dot{\hat{\omega}}_r\tilde{\omega}_r \\ &= S^T \cdot C \cdot \hat{A} \cdot \tilde{x} - S^T \cdot C \cdot G \cdot sign[y - \hat{y}] \\ &\quad + \tilde{\omega}_r\left(-\frac{\dot{\hat{\omega}}_r}{a} + \frac{L_h}{\sigma L_R L_S}\left(i_{S\alpha} - \hat{i}_{S\alpha}\right)\psi_{R\beta} - \frac{L_h}{\sigma L_R L_S}\left(i_{S\beta} - \hat{i}_{S\beta}\right)\psi_{R\alpha}\right)\end{aligned} \tag{14}$$

For global asymptotic stability, the time derivation of Lyapunov function $\dot{V}$ must be negative definite function. We obtain:

$$\begin{cases} S^T \cdot C \cdot \hat{A} \cdot \tilde{x} - S^T \cdot C \cdot G \cdot sign[y - \hat{y}] < 0 \\ \tilde{\omega}_r\left(-\frac{\dot{\hat{\omega}}_r}{a} + \frac{L_h}{\sigma L_R L_S}\left(i_{S\alpha} - \hat{i}_{S\alpha}\right)\psi_{R\beta} - \frac{L_h}{\sigma L_R L_S}\left(i_{S\beta} - \hat{i}_{S\beta}\right)\psi_{R\alpha}\right) = 0 \end{cases} \tag{15}$$

We can derive the following equations for the calculation of G matrix elements [17]:

$$\begin{aligned} &g_1 = \lambda(k-1)(R_S L_R + R_R L_S); \quad g_2 = -(k-1)\hat{\omega}_r \\ &g_3 = -\frac{(k-1)(R_R L_S - k R_S L_R)}{L_h}; \quad g_4 = \frac{(k-1)}{\lambda L_h}\hat{\omega}_r \\ &\lambda = \frac{1}{L_R L_S - L_h^2} \end{aligned} \tag{16}$$

Moreover, the rotor speed of induction motor satisfies:

$$-\frac{\dot{\hat{\omega}}_r}{a} + \frac{L_h}{\sigma L_R L_S}\left(i_{S\alpha} - \hat{i}_{S\alpha}\right)\psi_{R\beta} - \frac{L_h}{\sigma L_R L_S}\left(i_{S\beta} - \hat{i}_{S\beta}\right)\psi_{R\alpha} = 0 \tag{17}$$

$$\hat{\omega}_r = K_R \int z dt \tag{18}$$

where $z = \left(i_{S\alpha} - \hat{i}_{S\alpha}\right) \cdot \psi_{R\beta} - \left(i_{S\beta} - \hat{i}_{S\beta}\right) \cdot \psi_{R\alpha}$

According to the (18), the rotor speed of induction motor can be estimated depending on the following update law:

$$\hat{\omega}_r = K_P \cdot z + K_I \int z \cdot dt \tag{19}$$

3.2 Flux Estimator

After estimating the stator currents $i_{S\alpha}$, $i_{S\beta}$, the rotor fluxes $\psi_{R\alpha}$, $\psi_{R\beta}$ are observed by using current model.

The current model is as follows:

$$\begin{aligned} \frac{d\psi_{R\alpha}}{dt} &= \frac{L_h}{T_R} i_{S\alpha} - \frac{1}{T_R}\psi_{R\alpha} - \omega_r \psi_{R\beta} \\ \frac{d\psi_{R\beta}}{dt} &= \frac{L_h}{T_R} i_{S\beta} + \omega_r \psi_{R\alpha} - \frac{1}{T_R}\psi_{R\beta} \end{aligned} \tag{20}$$

where $T_R = \frac{L_R}{R_R}$ is the rotor circuit time constant. The stator currents $i_{S\alpha}$, $i_{S\beta}$, and rotor speed ω_r are the output of sliding mode observer mentioned above.

4 Simulations

The vector control with sliding mode observer diagram is shown in Fig. 1.

All simulations were carried out in MATLAB—SIMULINK, on the three phase two pole machine. The motor parameters used are listed as follows.

- $P_n = 2.7$ kW, $T_n =$ 19 Nm, $\omega_{mn} = 1360$ rpm, $p = 2$
- $I_{Sn} = 7.51$ A, $I_{Rn} =$ 17 A, $I_{Sxn} = 6.8$ A, $I_{Syn} = 8.16$
- $U_{Sn} = 400/230$ V, $\psi_{Sn} = 0.877$ Wb
- $R_S = 1.83\,\Omega$, $R_R = 2.19\,\Omega$, $L_S =$ 0.137 H, $L_R =$ 0.137 H, $L_m =$ 0.129H, $T_R =$ 0.0546 s

In controlling induction machine, the flux is needed to get the reference flux as fast as possible. In this application, the time response of flux is chosen 10 ms so in flux loop control, PI parameters are chosen $T\_R\_Im = 10\,\text{ms}$, $K\_Rm = 10$. In torque loop control, the time respone is chosen about 50 ms, so PI parameters of this loop are $T\_R\_omega = 50\,\text{ms}, K\_Romega = 2$ The simulation results are shown in following figures.

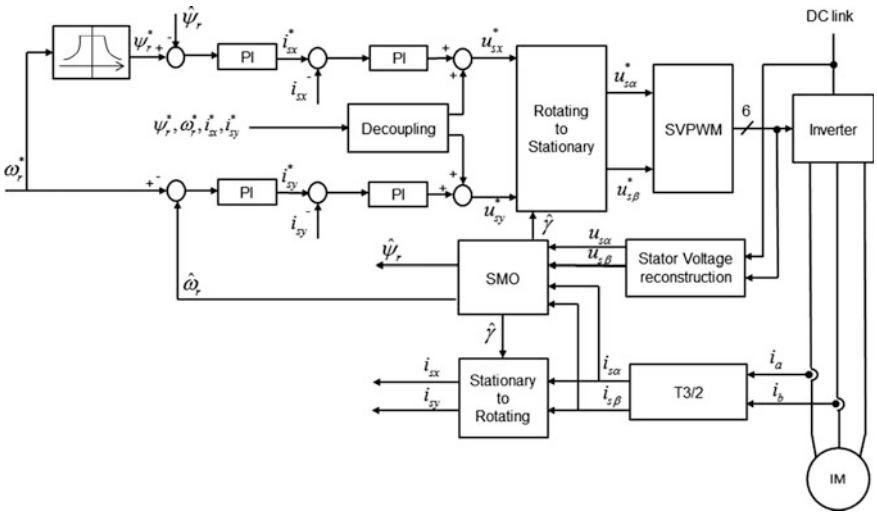

Fig. 1 Schematic of induction motor control

The estimated stator current vector components $i_{S\alpha\_est}$, $i_{S\beta\_est}$ are shown in Fig. 2. Figure 3 shows the error between the real and the estimated of stator current vector $i_{S\alpha\_est}$, $i_{S\beta\_est}$. The error between the real stator current vector components and the estimated stator current vector components is small, the maximum is just only 0.04 and oscilations are around −0.02 and 0.02 in average.

In Fig. 4, firstly, the reference speed is zero, the magnetizing current component i_{Sx} is maximum (8A) so that the flux goes to the reference flux. The rising time of magnetizing current component is about 10 ms. After that, the flux reach to reference flux so the magnetizing current component i_{Sx} is unchanged, the torque current component changes depending on the reference torque. The time response of torque current component is about 50 ms. Figure 5 is the estimated rotor flux vector components $\psi_{R\alpha\_est}$, $\psi_{R\beta\_est}$.

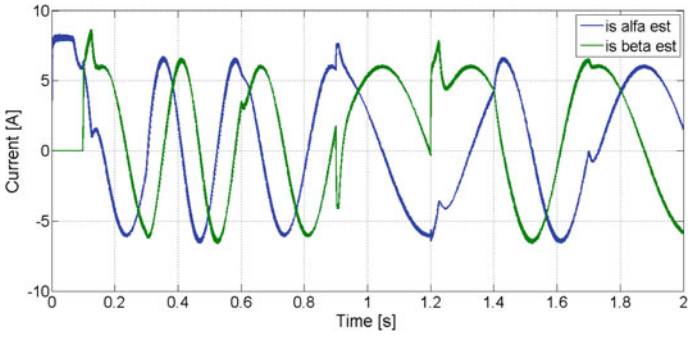

Fig. 2 Estimated stator current vector components $i_{S\alpha\_est}$, $i_{S\beta\_est}$

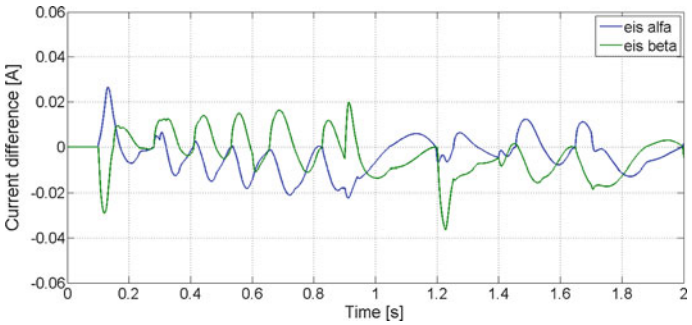

Fig. 3 Current differences $e_{S\alpha}$, $e_{S\beta}$

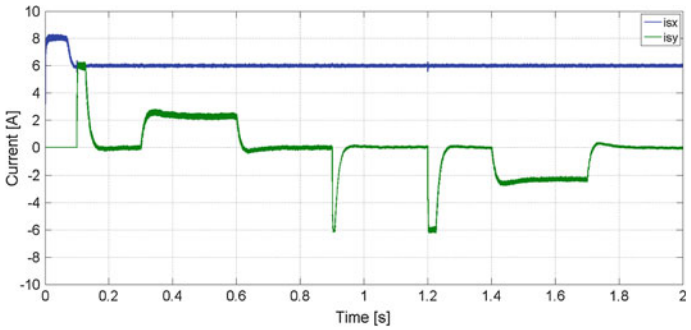

Fig. 4 Magnetizing current component i_{Sx} and torque current component i_{Sy}

Figures 6 and 7 show estimated speed compared to reference speed and the speed difference between the actual speed and the estimated speed. The characteristics of speed are very good. The time response is about 0.1 s, the overshoot is about 10 %, the static error between the actual speed and reference speed is zero.

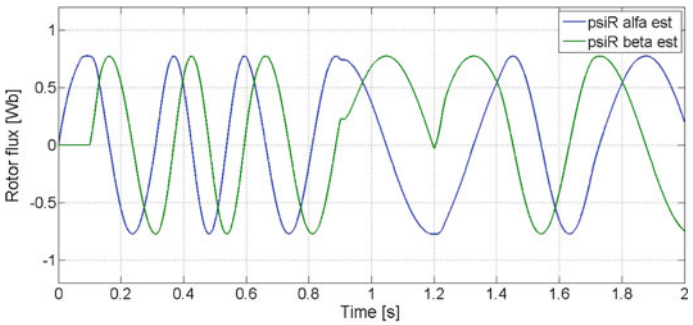

Fig. 5 Estimated rotor flux vector components $\psi_{R\alpha\_est}$, $\psi_{R\beta\_est}$

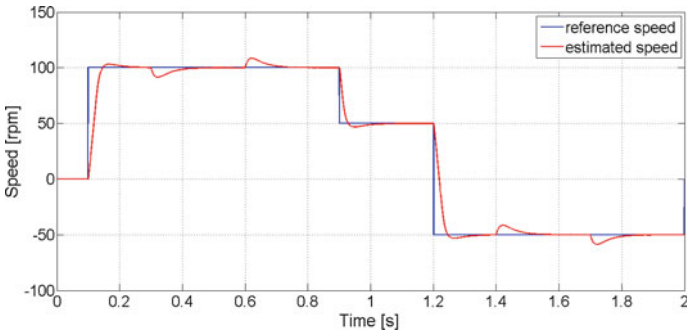

Fig. 6 Reference rotor speed ω_{m_ref} and estimated rotor speed ω_{m_est}

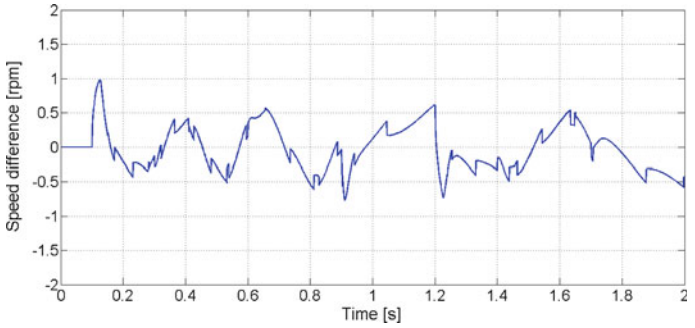

Fig. 7 Speed difference between actual rotor speed ω_m and estimated rotor speed ω_{m_est}

The maximum speed difference between the actual speed and the estimated speed is 1 rpm (1 %) in Fig. 7.

5 Conclusions

The estimation technique for sensorless induction motor drive with vector control was presented in the paper. The sliding mode observer was used to estimate the speed of induction motor. The induction motor drive with the presented speed estimator gives good dynamic responses and the estimation of the mechanical speed is good in steady state and also in transient state, even with the presence of torque load. The disadvantage of this paper is that the speed estimator does not work well when the errors between the real parameters of the induction motor and the nominal parameters occur. In the next research, a sliding mode controller will be proposed together with the sliding mode observer to improve the control characteristics, even with the noise and parameter variations.

Acknowledgments The paper was supported by the projects: IT4Innovations Centre of Excellence project, reg. no. CZ.1.05/1.1.00/02.0070 funded by the European Regional Development Fund and the national budget of the Czech Republic, and project reg.no. SP2015/81 funded by the Student Grant Competition of VSB-Technical University of Ostrava.

References

1. Cao X, Fan L (2009) New DTC scheme based on SVM with sliding mode observer for induction motors. In: IEEE International Conference on Automation and Logistics, 2009, ICAL '09, pp 1484–1488, Aug 2009
2. Chen H-C, Wu C-I, Chang Y-H, Lin H-W (2010) Integral sliding mode flux observer for sensorless vector controlled induction motors. In: International Conference on System Science and Engineering (ICSSE), 2010, pp 298–303, July 2010
3. Foo G, Rahman MF (2009) Sensorless adaptive sliding mode control of an IPM synchronous motor drive using a sliding mode observer and HF signal injection. In: EPE '09, 13th European Conference on Power Electronics and Applications, pp 1–11, Sept 2009
4. Foo G, Rahman MF (2009) Wide speed direc torque and flux controlled interior permanent-magnet synchronous motor drive using a combined adaptive sliding mode observer and high frequency signal injection. In: 8th International Symposium on Advanced Electromechanical Motion Systems Electric Drives Joint Symposium, 2009. ELECTROMOTION 2009, pp 1–7, July 2009
5. Foo GHB, Rahman MF (2010) Direct torque control of an IPM synchronous motor drive at very low speed using a sliding-mode stator flux observer. IEEE Trans Power Electron 25 (4):933–942
6. Galicia MI, Alexander GL, Sanchez EN (2009) Second order sliding mode sensorless torque control of induction motor. In: 6th International Conference on Electrical Engineering, Computing Science and Automatic Control, CCE, 2009, pp 1–6, Jan 2009
7. Jan V, Stephen JD, Peter B (2008) Experimental verification of chattering free sliding mode control of drive position employing PMSM. Electr Eng 59(3):139–145
8. Lascu C, Boldea I, Blaabjerg F (2009) A class of speed-sensorless sliding-mode observers for high-performance induction motor drives. IEEE Trans Ind Electron 56(9):3394–3403
9. Stoicuta O, Campian H, Pana T (2006) The comparative study of the stability of the vector control systems that contain in the loop Luenberger and Kalman type estimators. In: IEEE International Conference on Automation, Quality and Testing, Robotics, vol 1, pp 113–117, May 2006
10. Sutnar Z, Peroutka Z, Rodic M (2009) Sliding mode flux observer and rotor speed estimation for DTC-controlled induction motor drive. In: 13th European Conference on Power Electronics and Applications, EPE '09, pp 1–10, Sept 2009
11. Utkin VI (1993) Sliding mode control design principles and applications to electric drives. IEEE Trans Ind Electron 40(1):23–36
12. Xiao D, Foo G, Rahman MF (2009) Sensorless direct torque and flux control for matrix converter ipm synchronous motor drives using adaptive sliding mode observer combined with high frequency signal injection. In: ECCE Energy Conversion Congress and Exposition, IEEE, pp 4000–4007, Sept 2009
13. Zhang Y, Zhao Z, Lu T, Yuan L, Xu W, Zhu J (2009) A comparative study of luenberger observer, sliding mode observer and extended kalman filter for sensorless vector control of induction motor drives. In: ECCE Energy Conversion Congress and Exposition, IEEE, pp 2466–2473, Sept 2009

14. Zhang Y, Zhu J, Xu W, Hu J, Dorrell DG, Zhao Z (2010) Speed sensorless stator flux oriented control of three-level inverter-fed induction motor drive based on fuzzy logic and sliding mode control. In: IECON 2010 - 36th Annual Conference on IEEE Industrial Electronics Society, pp 2932–2937, Nov 2010

MRAS Observers for Speed Estimation of Induction Motor with Direct Torque and Flux Control

Hau Huu Vo, Pavel Brandstetter and Chau Si Thien Dong

Abstract The paper describes Model Reference Adaptive System (MRAS) observers for the speed estimation of an induction motor with direct torque and flux control. The first estimator is a reference frame MRAS (RF-MRAS) and the second estimator is a current based MRAS (CB-MRAS). At first, direct torque controlled induction motor drive with two estimators are implemented on Matlab-Simulink environment. Then, comparison of two observers is done by evaluation of the rotor speed difference. The simulation results confirm that both MRAS estimators are simple to simulate and experiment. By comparison of both observers, the CB-MRAS observer gives higher accuracy of the rotor speed estimation.

Keywords RF-MRAS · CB-MRAS · Speed control · Direct torque control · Induction motor · AC drive

1 Introduction

The control and estimation of induction motor drives is almost unbounded subject, and the technology has been developing very strong in last few decades. The induction motor drive with a cage type of machine has many applications in industry such as pumps and fans, paper and textile mills, subway and locomotive

H.H. Vo (✉) · C.S.T. Dong
Faculty of Electrical and Electronics Engineering, Ton Duc Thang University,
No. 19 Nguyen Huu Tho Street, District 7, Ho Chi Minh City, Vietnam
e-mail: vohuuhau@tdt.edu.vn

C.S.T. Dong
e-mail: dongsithienchau@tdt.edu.vn

P. Brandstetter
Faculty of Electrical Engineering and Computer Science,
VSB-Technical University of Ostrava, Ostrava, Czech Republic
e-mail: pavel.brandstetter@vsb.cz

V.H. Duy et al. (eds.), *AETA 2015: Recent Advances in Electrical Engineering and Related Sciences*, Lecture Notes in Electrical Engineering 371,
DOI 10.1007/978-3-319-27247-4_29

propulsions, electric and hybrid vehicles, machine tools and robotics, home appliances, heat pumps and air conditioners, rolling mills, wind generation systems. These applications often require adjustable speed and wide power range [1, 2].

The control methods without speed encoder can be classified as follows:

- Methods with machine model [3–9]: open loop estimators, MRAS and observers (such as extended Kalman filter, Luenberger observer, sliding mode observer).
- Methods without machine model [10–14]: estimators with injection methods and estimators using artificial intelligence.

2 Modelling an Induction Motor

State-space equations of induction motor in [α, β] coordinate system can be expressed into [9] (Table 1):

Table 1 Induction motor quantities and parameters

Quantities/parameters	Value/unit	Definition
$u_{s\alpha}$, $u_{s\beta}$		Stator voltages in [α, β] coordinate system
$i_{s\alpha}$, $i_{s\beta}$		Stator currents in [α, β] coordinate system
$\hat{i}_{s\alpha}, \hat{i}_{s\beta}$		Estimated stator currents in [α, β] coordinate system
$\psi_{R\alpha}$, $\psi_{R\beta}$		Rotor fluxes in [α, β] coordinate system
$\hat{\psi}_{R\alpha}, \hat{\psi}_{R\beta}$		Estimated rotor fluxes in [α, β] coordinate system
p	2	Number of pole pairs
R_s	1.115 Ω	Stator resistance
L_m	0.2037 H	Magnetizing inductance
L_s	0.2097 H	Stator inductance
R_r	1.083 Ω	Rotor resistance
L_r	0.2097 H	Rotor inductance
T_r	0.1936 s	Rotor time constant
J	0.02 kg m^2	Moment of inertia
σ	0.0562	Total leakage constant
ω_r	rad s^{-1}	Rotor speed
T_e	Nm	Motor torque
T_L	Nm	Load torque
ξ		Adaptive signal of adaptive mechanism in MRAS structures
K_P	2000	Proportional coefficient of adaptive mechanism in MRAS structures
K_I	1,000,000	Integral coefficient of adaptive mechanism in MRAS structures

$$\frac{dX}{dt} = AX + BU_s \tag{1}$$

$$Y = X \tag{2}$$

where X, U_s, Y are the state variable vector, the input vector and the output vector, respectively as follows:

$$\begin{aligned} X &= \begin{bmatrix} i_{s\alpha} & i_{s\beta} & \psi_{R\alpha} & \psi_{R\beta} \end{bmatrix}^T \\ U_s &= \begin{bmatrix} u_{s\alpha} & u_{s\beta} \end{bmatrix}^T \end{aligned} \tag{3}$$

$$A = \begin{bmatrix} -\left(\frac{L_m^2 R_r + L_r^2 R_s}{\sigma L_s L_r^2}\right) & 0 & \frac{L_m R_r}{\sigma L_s L_r^2} & \frac{L_m \omega_r}{\sigma L_s L_r} \\ 0 & -\left(\frac{L_m^2 R_r + L_r^2 R_s}{\sigma L_s L_r^2}\right) & -\frac{L_m \omega_r}{\sigma L_s L_r} & \frac{L_m R_r}{\sigma L_s L_r^2} \\ \frac{L_m R_r}{L_r} & 0 & -\frac{R_r}{L_r} & -\omega_r \\ 0 & \frac{L_m L_r}{L_r} & \omega_r & -\frac{R_r}{L_r} \end{bmatrix} \tag{4}$$

$$B = \begin{bmatrix} \frac{1}{\sigma L_s} & 0 \\ 0 & \frac{1}{\sigma L_s} \\ 0 & 0 \\ 0 & 0 \end{bmatrix} \tag{5}$$

$$\sigma = 1 - \frac{L_m^2}{L_r L_s} \tag{6}$$

The rotor speed ω_r has relation with the torques as following equation:

$$\begin{aligned} T_e &= \frac{3}{2}\frac{L_m}{L_r} p\left(\psi_{R\alpha} i_{s\beta} - \psi_{R\beta} i_{s\alpha}\right) \\ T_e &= T_L + J\frac{d\omega_m}{dt} = T_L + \frac{J}{p}\frac{d\omega_r}{dt} \end{aligned} \tag{7}$$

3 MRAS Observers

The rotor speed can be estimated by the MRAS. First, difference between the output general quantity X_{RM} of reference model and the output general quantity X_{AM} of an adaptive or adjustable model is evaluated by adaptation mechanism. Then, this mechanism uses a controller (PI controller) for tuning the rotor speed so that the difference between X_{RM} and X_{AM} reach to zero (Fig. 1).

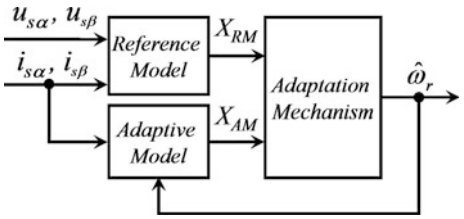

Fig. 1 MRAS structure

3.1 RF-MRAS

The structure of a reference frame model reference adaptive system (RF-MRAS) for the rotor speed estimation is shown in Fig. 2. The stator voltage and current signals are measured and used for calculating the rotor flux vector in this figure. In this model, we can get fluxes from the inputs (stator currents) only if we know the rotor speed exactly. In ideal condition, the fluxes from two models (reference and adaptive) will match. An adaptation algorithm with PI controller can be used to tune the rotor angular speed so that the adaptive signal ξ reach to zero.

The reference model is described with the following equations:

$$\psi_{R\alpha} = \frac{L_r}{L_m}\int (u_{s\alpha} - R_s i_{s\alpha})dt - \sigma L_s i_{s\alpha} \tag{8}$$

$$\psi_{R\beta} = \frac{L_r}{L_m}\int \left(u_{s\beta} - R_s i_{s\beta}\right)dt - \sigma L_s i_{s\beta} \tag{9}$$

The adaptive model is described with the following equations:

$$\hat{\psi}_{R\alpha} = \int \left(\frac{L_m}{T_r} i_{s\alpha} - \frac{1}{T_r}\hat{\psi}_{R\alpha} - \hat{\omega}_r \hat{\psi}_{R\beta}\right)dt \tag{10}$$

$$\hat{\psi}_{R\beta} = \int \left(\frac{L_m}{T_r} i_{s\beta} - \frac{1}{T_r}\hat{\psi}_{R\beta} + \hat{\omega}_r \hat{\psi}_{R\alpha}\right)dt \tag{11}$$

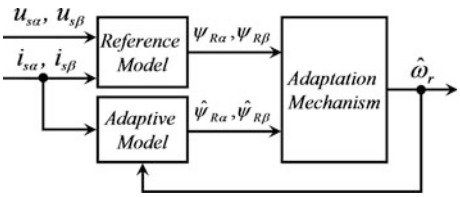

Fig. 2 Structure of RF-MRAS

Using the Popov's criterion for hyperstability for a globally asymptotically stable system, we obtain the adaptation algorithm as following equations:

$$\xi = \hat{\psi}_{R\alpha}\psi_{R\beta} - \hat{\psi}_{R\beta}\psi_{R\alpha} \tag{12}$$

$$\hat{\omega}_r = K_p\xi + K_I \int_0^t \xi dt \tag{13}$$

where $K_P > 0$, $K_I > 0$.

In practice, this method is difficult to implement, particularly at low speeds because of the pure integration of the voltage signals. The integration, however, would be subject to long-term drift in practice and special techniques should be taken to correct this drift. For example, the I-controller with the limitation can be used. Besides that, the estimation accuracy can be good if parameters of motor are constants. However, accuracy is decreased because of parameter variation.

3.2 CB-MRAS

This MRAS estimator uses output stator currents of the induction motor as output quantities of the reference model [15]. The Fig. 3 shows the structure of the CB-MRAS speed observer.

In the RF-MRAS speed observer, the voltage model is used as a reference model, and the current model is an adaptive model. In the CB-MRAS observer, the induction motor is used as a reference system, and the current model together with the current estimator are adaptive models [15].

The current estimator of CB-MRAS is described with the following equations:

$$\hat{i}_{s\alpha} = \frac{1}{T_i}\int \left(K_1 u_{s\alpha} + K_2\hat{\psi}_{R\alpha} + K_3\hat{\omega}_R\hat{\psi}_{R\beta} - \hat{i}_{s\alpha}\right)dt \tag{14}$$

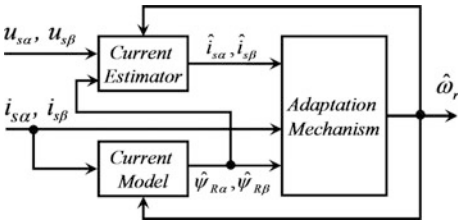

Fig. 3 Structure of CB-MRAS

$$\hat{i}_{s\beta} = \frac{1}{T_i}\int \left(K_1 u_{s\beta} + K_2\hat{\psi}_{R\beta} - K_3\hat{\omega}_R\hat{\psi}_{R\alpha} - \hat{i}_{s\beta}\right)dt \tag{15}$$

$$K_1 = \frac{\frac{L_r}{L_m}}{\frac{L_r R_s}{L_m} + \frac{L_m}{T_r}}; \quad K_2 = \frac{L_m}{L_r R_s T_r + L_m^2}; \quad K_3 = \frac{1}{\frac{L_r R_s}{L_m} + \frac{L_m}{T_r}}; \quad T_i = \frac{\frac{L_s L_r - L_m^2}{L_m}}{\frac{L_r R_s}{L_m} + \frac{L_m}{T_r}} \tag{16}$$

The current model of CB-MRAS is also described with the Eqs. (9)–(10). In the CB-MRAS estimator, the adaptation algorithm is different from the RF-MRAS method and is based on the error between estimated and measured stator current, according to the formula used in the full-order flux observer with speed adaptation, developed in [16, 17] (basing on the minimization of the Lyapunov function). The PI controller is also used to tune the speed as Eq. (12) with the adaption signal as the following equation:

$$\xi = \left(i_{s\alpha} - \hat{i}_{s\alpha}\right)\hat{\psi}_{R\beta} - \left(i_{s\beta} - \hat{i}_{s\beta}\right)\hat{\psi}_{R\alpha} \tag{17}$$

4 Direct Torque Control

The direct torque control (DTC) has comparable performance with the vector control. In this scheme, the torque and the stator flux are controlled directly by selecting voltage space vector of the inverter through a look up table. The block diagram of DTC is shown in Fig. 4. Firstly, this techniques compare the command torque and stator flux with estimated values. Then, the errors will be processed by hysteresis-band controllers.

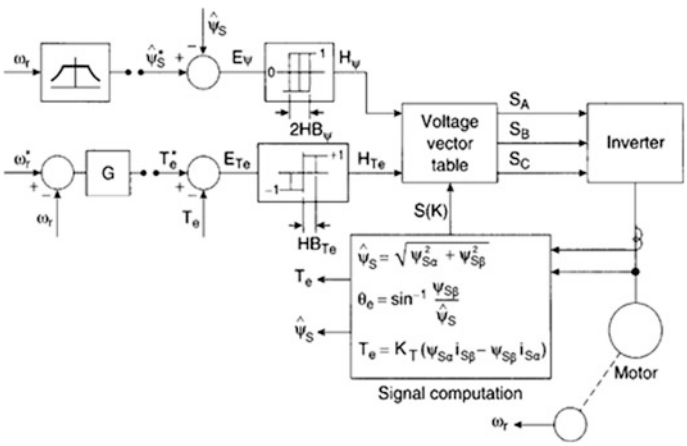

Fig. 4 Block scheme of the direct torque control

High performance control, such as vector control or direct torque control, is based on a dynamic model of the induction motor expressed in a stationary coordinate system or rotating coordinate system which is oriented on the rotor magnetic flux vector.

The flux controller has two levels:

$$\begin{aligned} H_\psi &= 1 \text{ for } E_\psi > +HB_\psi \\ H_\psi &= -1 \text{ for } E_\psi < -HB_\psi \end{aligned} \tag{18}$$

The torque controller has three levels:

$$\begin{aligned} H_{Te} &= 1 \text{ for } E_{Te} > +HB_{Te} \\ H_{Te} &= -1 \text{ for } E_{Te} < -HB_{Te} \\ H_{Te} &= 0 \text{ for } -HB_{Te} < E_{Te} < +HB_{Te} \end{aligned} \tag{19}$$

The signal computation block (see Fig. 4) calculates signals from the voltage model of the induction motor. This block also seeks where stator flux vector lies (see Fig. 5).

DTC technique has some special features:

- no feedback current control,
- no traditional PWM algorithm,
- no vector transformation,

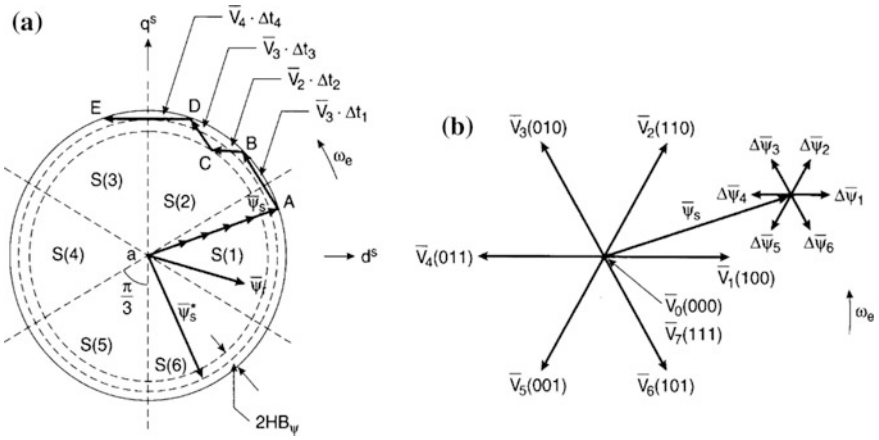

Fig. 5 **a** Trajectory of the stator flux vector in DTC control. **b** Inverter voltage vectors and corresponding flux variation in time Δt

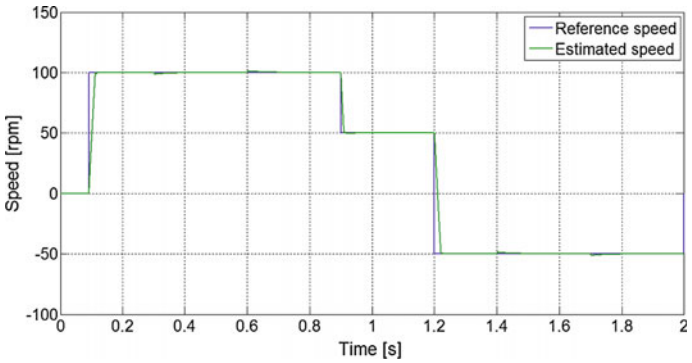

Fig. 6 RF-MRAS, reference speed (*blue*) and estimated speed (*green*)

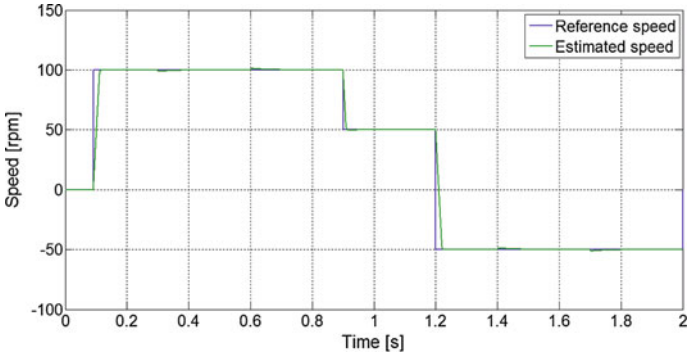

Fig. 7 CB-MRAS, reference speed (*blue*) and estimated speed (*green*)

- feedback signal processing is similar to stator flux-oriented vector control,
- hysteresis-band controller generates flux and torque ripple and switching frequency is not fixed (like hysteresis-band current control) (Figs. 6 and 7).

5 Simulation Results

The described induction motor drive was simulated using Matlab-Simulink. The time courses of important quantities were obtained from the control structure with two observers at the jump of the load torque $T_L = 2$ Nm (see Figs. 10 and 11). The simulation results showed that the speed difference (see Figs. 8 and 9) and torque ripple (see Figs. 10 and 11) of the CB-MRAS were smaller than those of the RF-MRAS.

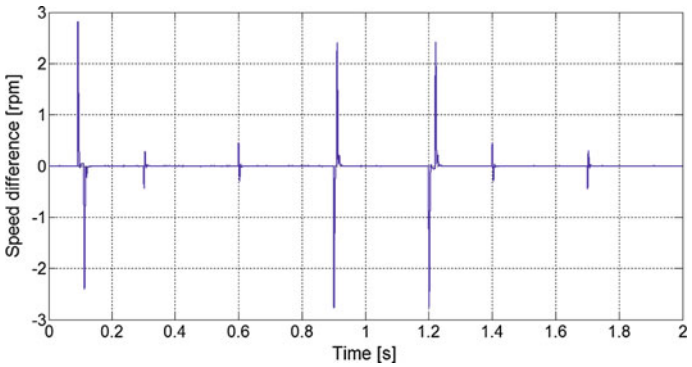

Fig. 8 RF-MRAS, difference between real speed and estimated speed

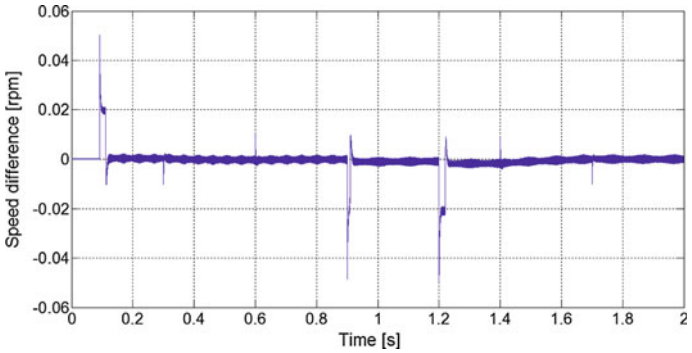

Fig. 9 CB-MRAS, difference between real speed and estimated speed

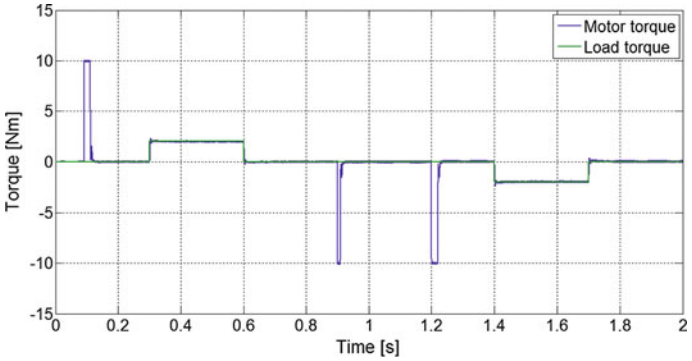

Fig. 10 RF-MRAS, motor torque (*blue*) and load torque (*green*)

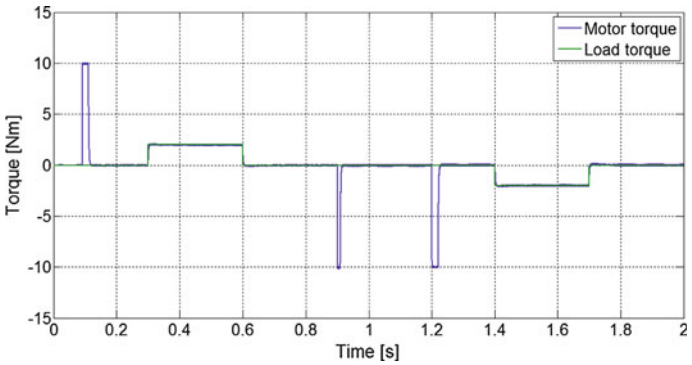

Fig. 11 CB-MRAS, motor torque (*blue*) and load torque (*green*)

6 Conclusion

The estimation technique for sensorless induction motor drive with the direct torque control was presented in the paper. The speed estimator was based on application of the MRAS observers. The induction motor drive with two MRAS estimators gave good dynamic responses and the estimation of the mechanical speed was good in steady state and also in transient state. The CB-MRAS observer gave higher accuracy of the rotor speed estimation than the RF-MRAS observer. This MRAS estimator could be used for rotor speed estimation without speed encoder in the control system with digital signal processor.

Acknowledgments The paper was supported by the projects: IT4Innovations Centre of Excellence project, reg. no. CZ.1.05/1.1.00/02.0070 funded by the European Regional Development Fund and the national budget of the Czech Republic, and project reg. no. SP2015/81 funded by the Student Grant Competition of VSB-Technical University of Ostrava.

References

1. Holtz J (2002) Sensorless control of induction motor drives. Proc IEEE 90(8):1359–1394
2. Vas P (1998) Sensorless vector and direct torque control. Oxford University Press, Oxford
3. Gacho J, Zalman M (2010) IM Based speed servodrive with luenberger observer. J Electr Eng 61(3):149–156
4. Salvatore N, Caponio A, Neri F, Stasi S, Cascella GL (2010) Optimization of delayed-state Kalman-Filter-Based Algorithm via differential evolution for sensorless control of induction motors. IEEE Trans Industr Electron 57(1):385–394
5. Sutnar Z, Peroutka Z, Rodic M (2010) Comparison of sliding mode observer and extended Kalman filter for sensorless DTC controlled induction motor drive. In: Conference Proceedings, 14th International Power Electronics and Motion Control Conference (EPE/PEMC), pp T7-55–T7-62

6. Haron AR, Idris NR (2006) Simulation of MRAS-based speed sensor-less estimation of induction motor drives using MATLAB-SIMULINK. In: The First International Power and Energy Conference PECon, Putrajaya, Malaysia, pp 411–415
7. Lascu CH, Boldea I, Blaabjerg F (2006) Comparative study of adaptive and inherently sensorless observers for variable-speed induction-motor drives. IEEE Trans Ind Electron 53 (1):57–65
8. Consoli A, Scarcella G, Bottiglieri TA (2006) Harmonic analysis of voltage zero-sequence-based encoderless techniques. IEEE Trans Ind Appl 42(6):1548–1557
9. Sbita L, Ben Hamed M (2007) An MRAS – based full Order Luenberger observer for sensorless DRFOC of induction motors. ICGST ACSE J 7(1):11–20
10. Partal S, Senol I, Bakan AF, Bekiroglu KN (2011) Online speed control of a brushless AC servomotor based on artificial neural networks. Turk J Electr Eng Comput Sci 19(3):373–383
11. Gadoue SM, Giaouris D, Finch JW (2009) Sensorless control of induction motor drives at very low and zero speeds using neural network flux observers. IEEE Trans Ind Electron 56 (8):3029–3039
12. Kouzi K, Nait-Said MS, Hilairet M, Berthlot E (2009) Fuzzy MRAS speed estimator for vector control of an induction motor. Int Rev Electr Eng (IREE) 4(2):278–283
13. Perdukova D, Fedor P (2007) Fuzzy model based control of dynamic system. JEE-J Electr Eng 7(3):5–11, ISSN 1582-4594
14. Ma T-T (2010) Adaptive inverse control schemes based on fuzzy neural networks for induction motor drives. Int Rev Electr Eng (IREE) 5(4):1563–1570
15. Orlowska-Kowalska T, Dybkowski M (2010) Stator-current-based MRAS estimator for a wide range speed-sensorless induction-motor drive. IEEE Trans Ind Electron 57(4):1296–1308
16. Kubota H, Matsuse K, Nakano T (1993) DSP-based speed adaptive flux observer of induction motor. IEEE Trans Ind Appl 29(2):344–348
17. Kubota H, Matsuse K, Nakano T (1990) New adaptive flux observer for wide speed range motor drives. In: Proceedings of IEEE-IECON, pp 921–926

Application of Servo Controller Design for Speed Control of AC Induction Motors Using Polynomial Differential Operator

Dae Hwan Kim, Pandu Sandi Pratama, Phuc Thinh Doan, Sea June Oh, Van Tu Duong, Jung Hu Min, Young Seok Jung and Sang Bong Kim

Abstract This paper proposes a servo controller design method for speed control of AC induction motors using polynomial differential operator. To do this task, the followings are done. First, nonlinear modeling for an induction motor is introduced and is linearized at equilibrium points using Taylor's series. Second, an observer is designed to estimate flux, and an extended system incorporating the internal model principle to construct the extended system is shown using polynomial differential operator in case that the types of reference inputs are differential polynomials. Third, a state feedback control law for the extended system to track the given reference input is designed by a regulator design method. A control system is constructed for speed control of the 1.5 KW AC induction motor. The simulation and experimental results are shown to verify the applicability of the proposed controller compared to conventional PI controller for the AC induction motor with a step type of disturbance to track its speed of 3 types of the references such as step, ramp and parabola.

Keywords AC induction motor · Internal model principle · Servo controller · Speed control · State feedback control law

D.H. Kim · P.S. Pratama · P.T. Doan · V.T. Duong · Y.S. Jung · S.B. Kim (✉)
Department of Mechanical Design Engineering, Pukyong National University, Busan 608-739, South Korea
e-mail: kimsb@pknu.ac.kr

S.J. Oh
Korea Maritime and Ocean University, Busan 606-791, South Korea

J.H. Min
Kaltec, Incheon 404-170, South Korea

V.H. Duy et al. (eds.), *AETA 2015: Recent Advances in Electrical Engineering and Related Sciences*, Lecture Notes in Electrical Engineering 371,
DOI 10.1007/978-3-319-27247-4_30

1 Introduction

AC Induction motors are the most popular motor used in industrial fields due to their simple construction, reliability, robustness and low cost. The robust servomechanism problem of AC motors is one of the most basic problems in control engineering.

Naouar [1] proposed FPGA-based speed control of a synchronous machine using P-PI controller with a speed estimator using an absolute encoder. Verghese et al. [2] proposed observers for flux estimation in induction machines. Khalil et al. [3] proposed sensorless field–oriented speed control of induction motors without rotor position sensors using flux and speed observers with PI controllers via linearization to regulate the q-axis current to the reference. They augmented the traditional approach with flux and speed observers and derived a sixth-order nonlinear model in field oriented coordinates. The nonlinear model was linearized to the third order linear model at the desired equilibrium point, and the well known PI controller was adopted for sensorless speed control. They showed that PI-approach based controller has some serious limitation for the robust property and stabilization. The PI controller was not adequate for more high order types of reference signals with disturbances. Davison [4] proposed the output control of linear time-invariant multivariable systems with immeasurable arbitrary disturbances. To solve robust servomechanism problem for SISO system, Kim et al. [5] proposed a bilinear transformation method using internal model principle and pole assignment method in a specific region.

In this paper, a different concept based servo controller design method is proposed for sensorless (or sensor) speed control by adopting polynomial differential operator method. To do this task, the followings are done. First, nonlinear modeling for an induction motor is introduced and is linearized. Second, an observer is designed to estimate flux, and an extended system incorporating the internal model principle to construct the extended system is shown using polynomial differential operator. Third, a state feedback control law for the extended system to track the given reference input is proposed. A control system is constructed for speed control of the 1.5 KW AC induction motor. The simulation and experimental results are shown the applicability of the proposed controller compared to conventional PI controller.

2 System Description and Modeling

The induction motor can be represented in the state frame of reference by [3]

$$\dot{\lambda}_r = (-\alpha_r I + p\omega H)\lambda_r + \alpha_r L_m i_s \tag{1}$$

$$\dot{i}_s = -\beta(-\alpha_r I + p\omega H)\lambda_r - (\beta\alpha_s + \beta\alpha_r L_m)i_s + \gamma\upsilon_s \tag{2}$$

$$\dot{\omega} = -\mu\lambda_r^T H i_s - b\omega - \frac{T_L}{J} \tag{3}$$

where $\lambda_r = [\,\lambda_{rd} \quad \lambda_{rq}\,]^T \in R^2$ is the rotor flux vector, $i_s = [\,i_{sd} \quad i_{sq}\,]^T \in R^2$ is the stator current vector, $\upsilon_s = [\,\upsilon_{sd} \quad \upsilon_{sq}\,]^T \in R^2$ is the stator voltage vector, ω is the rotor speed, L_s, L_r, L_m denote rotor, stator and mutual inductances, R_r, R_s are rotor and stator resistances, p is the number of pole pairs, J is rotor's moment of inertia, b_1 is a friction coefficient, T_L is load torque,

$$I = \begin{bmatrix} 1 & 0 \\ 0 & 1 \end{bmatrix}, \quad H = \begin{bmatrix} 0 & -1 \\ 1 & 0 \end{bmatrix}, \quad \sigma = 1 - \frac{L_m^2}{L_s L_r}, \quad \alpha_r = \frac{R_r}{L_r}, \quad \alpha_s = \frac{R_s}{L_s},$$
$$b = \frac{b_1}{J}, \quad \mu = \frac{3pL_m}{2JL_r}, \quad \beta = \frac{1-\sigma}{\sigma L_m} = \frac{L_m}{\sigma L_s L_r}, \quad \text{and } \eta = \frac{1}{\sigma}.$$

Under the conditions of estimates $\hat{R}_s, \hat{R}_r, \hat{J}, \hat{b}_1$ of uncertain parameters R_s, R_r, J, b_1, Eqs. (1)–(3) can be represented based on the direct-axis components $\lambda_{rd}, i_{sd}, \upsilon_{sd}, e_d$ and on the quadrature-axis components λ_q (= 0:flux of rotor in $q-axis$), $i_{sq}, \upsilon_{sq}, e_q, e_d$ as follows:

$$\dot{\lambda}_{rd} = -\hat{\alpha}_r\lambda_{rd} + \hat{\alpha}_r L_m i_{sd} \tag{4}$$

$$\dot{i}_{sd} = \beta\alpha_r\lambda_{rd} - (\beta\alpha_s + \beta\alpha_r L_m)i_{sd} + \gamma\upsilon_{sd} + p\omega_{ref} i_{sq} + \hat{\alpha}_r L_m \frac{i_{sq}^2}{\lambda_{rd}} - \alpha_r\beta e_d - \beta p\omega e_q \tag{5}$$

$$\dot{i}_{sq} = -\beta p\omega\lambda_{rd} - p\omega_{ref} i_{sd} - (\beta\alpha_s + \beta\alpha_r L_m)i_{sq} + \gamma\upsilon_{sq} - \hat{\alpha}_r L_m \frac{i_{sd} i_{sq}}{\lambda_{rd}} + \beta p\omega e_d - \alpha_r\beta e_q \tag{6}$$

$$\dot{\omega} = \mu[i_{sq}(\lambda_{rd} - e_d) + i_{sd} e_d] - b\omega - \frac{T_L}{J} \tag{7}$$

where $\hat{\alpha}_s = \frac{\hat{R}_s}{L_s}, \hat{\alpha}_r = \frac{\hat{R}_r}{L_r}, \hat{b} = \frac{\hat{b}_1}{J}$, and $\hat{\mu} = \frac{3pL_m}{2JL_r}$.

Error dynamics and rotor flux estimator error vector are presented as follows:

$$\dot{e}_d = \dot{\hat{\lambda}}_{rd} - \dot{\lambda}_{rd} = -\alpha_r e_d + (p\omega_{ref} - p\omega + \frac{\hat{\alpha}_r L_m i_{sq}}{\lambda_{rd}})e_q + (\hat{\alpha}_r - \alpha_r)(L_m i_{sd} - \lambda_{rd}) \tag{8}$$

$$\begin{aligned}\dot{e}_q &= \dot{\hat{\lambda}}_{rq} - \dot{\lambda}_{rq} \\ &= -(p\omega_{ref} - p\omega + \frac{\hat{\alpha}_r L_m i_{sq}}{\lambda_{rd}})e_d - \alpha_r e_q + (\hat{\alpha}_r - \alpha_r)L_m i_{sq} + p(\omega_{ref} - \omega)\lambda_{rd} \quad (9)\end{aligned}$$

$$e_\lambda = \hat{\lambda}_r - \lambda_r \quad (10)$$

where $e_\lambda = [\, e_d \quad e_q \,]^T$ is the rotor flux estimation error vector, $\hat{\lambda}_r = [\, \hat{\lambda}_d \quad \hat{\lambda}_q \,]^T$ is the estimated vector of λ_r which can be estimated by an observer and also regulated by the well known PI controller, and ω_{ref} is the reference rotor speed.

An observer to estimate the rotor flux vector is adopted as follows:

$$\dot{\hat{\lambda}}_r = \left(-\hat{\alpha}_r I + p\omega_{ref} H\right)\hat{\lambda}_r + \hat{\alpha}_r L_m i_s \quad (11)$$

In this paper, the sensorless speed controller design on the state space is the main goal. So how to simplify the model of Eqs. (4)–(11) is important to accomplish the target goal. It is assumed that the speed is estimated by an observer shown in [3] and the flux regulator acts fast enough to regulate the reference rotor flux of λ_{rd} to the reference rotor flux in $d-axis$ of $\lambda_{ref}(\lambda_{rd} = \lambda_{ref})$, and the stator current in $d-axis$ of $i_{sd} = \lambda_{ref}/L_m$, then the speed controller can be designed as the third-order nonlinear model as

$$\dot{e}_d = -\alpha_r e_d + \left(p\omega_{ref} - p\omega + \hat{\alpha}_r L_m i_{sq}/\lambda_{ref}\right)e_q \quad (12)$$

$$\dot{e}_q = -\left(p\omega_{ref} - p\omega + \hat{\alpha}_r L_m i_{sq}/\lambda_{ref}\right)e_d - \alpha_r e_q + (\hat{\alpha}_r - \alpha_r)L_m i_{sq} + p(\omega_{ref} - \omega)\lambda_{ref} \quad (13)$$

$$\dot{\omega} = \mu\left[i_{sq}(\lambda_{ref} - e_d) + \lambda_{ref}/L_m\, e_q\right] - b\omega - \frac{T_L}{J} \quad (14)$$

$$\Omega = \left(\frac{\lambda_{ref} - e_d}{\lambda_{ref}}\right)\omega + \frac{\alpha_r e_q}{p\lambda_{ref}} - a i_{sq} \quad (15)$$

$$a = [(\hat{\alpha}_s - \alpha_s)]\eta + (\hat{\alpha}_r - \alpha_r)\beta L_m]/(\beta p \lambda_{ref})$$

where Ω is viewed as the measured output under the equilibrium point with $\Omega = \omega_{ref}$ as the followings:

$$\bar{e}_d = \bar{e}_q = 0, \quad \bar{\omega} = \omega_{ref} + \frac{(\hat{\alpha}_s - \alpha_s)L_m \bar{i}_{sq}}{p\lambda_{ref}}, \quad \bar{i}_{sq} = \frac{b\omega_{ref} + T_L/J}{\mu\lambda_{ref} - \frac{b(\hat{\alpha}_r - \alpha_r)L_m}{p\lambda_{ref}}} \quad (16)$$

with $\hat{\alpha}_s = \alpha_s$.

The nonlinear model of Eqs. (12)–(15) under the above equilibrium point with $\hat{\alpha}_s = \alpha_s$ can be linearized as the following linear model:

$$\dot{\mathbf{x}} = A\mathbf{x} + Bu \tag{17}$$

$$y = C\mathbf{x}(t) + du(t) \tag{18}$$

$$A = A(t)|_{\bar{\mathbf{x}},\bar{i}_{sq}} = \begin{bmatrix} -\alpha_r & \frac{\alpha_r L_m}{\lambda_{ref}}\bar{i}_{sq} & 0 \\ -\frac{\alpha_r L_m}{\lambda_{ref}}\bar{i}_{sq} & -\alpha_r & -p\lambda_{ref} \\ -\mu\bar{i}_{sq} & \mu\frac{\lambda_{ref}}{L_m} & -b \end{bmatrix}, \quad B = B(t)|_{\bar{\mathbf{x}},\bar{i}_{sq}} = \begin{bmatrix} 0 \\ (\hat{\alpha}_s - \alpha_s)L_m \\ \mu\lambda_{ref} \end{bmatrix},$$

$$C = C(t)|_{\bar{\mathbf{x}},\bar{i}_{sq}} = \begin{bmatrix} \frac{-\bar{\omega}}{\lambda_{ref}} & \frac{\alpha_r}{p\lambda_{ref}} & 1 \end{bmatrix}, \quad d = d(t)|_{\bar{\mathbf{x}},\bar{i}_{sq}} = -\frac{(\hat{\alpha}_r - \alpha_r)L_m}{p\lambda_{ref}},$$

$$\mathbf{x}(t) = [\, e_d \quad e_q \quad \omega \,]^T = [\, x_1 \quad x_2 \quad x_3 \,]^T, \quad u = i_{sq}, \quad y = \Omega, \quad \bar{x} = [\, \bar{e}_d \quad \bar{e}_q \quad \bar{\omega} \,]^T$$

where the speed can be estimated by an observer [3] or measured by sensor, and $\mathbf{x}, y, u$ are state variable vector, output variable and input variable.

At the equilibrium points with $\hat{\alpha}_s = \alpha_s$ and $\hat{\alpha}_r = \alpha_r$, the followings are obtained.

$$A = \begin{bmatrix} -\alpha_r & \frac{\alpha_r L_m}{\lambda_{ref}}\bar{i}_{sq} & 0 \\ -\frac{\alpha_r L_m}{\lambda_{ref}}\bar{i}_{sq} & -\alpha_r & -p\lambda_{ref} \\ -\mu\bar{i}_{sq} & \mu\frac{\lambda_{ref}}{L_m} & -b \end{bmatrix}, \quad B = \begin{bmatrix} 0 \\ 0 \\ \mu\lambda_{ref} \end{bmatrix}, \quad C = \begin{bmatrix} \frac{-\bar{\omega}}{\lambda_{ref}} & \frac{\alpha_r}{p\lambda_{ref}} & 1 \end{bmatrix},$$
$$d = 0,$$

$$\mathbf{x}(t) = [\, e_d \quad e_q \quad \omega \,]^T = [\, x_1 \quad x_2 \quad x_3 \,]^T, \quad u = i_{sq}, y = \Omega, \quad \tilde{\omega} = \bar{\omega} - \omega_{ref} = 0,$$

$$\bar{\mathbf{x}} = [\, \bar{e}_d \quad \bar{e}_q \quad \bar{\omega} \,]^T = [\, 0 \quad 0 \quad \omega_{ref} \,]^T, \quad \bar{u} = \bar{i}_{sq} = \frac{b\omega_{ref} + T_L/J}{\mu\lambda_{ref}},$$
$$\bar{y} = \Omega|_{\bar{\mathbf{x}},\bar{i}_{sq}} = \omega_{ref} = \bar{\omega} = y_r.$$

where $\bar{\mathbf{x}}, \bar{y}, \bar{u}$ are state variable vector, output variable and input variable at the equilibrium point respectively, and y_{ref} is the reference output.

3 Speed Controller Design

3.1 Servo Controller Design Using Polynomial Differential Operator

The plant to be controlled is assumed to be described by the following SISO linear invariant model with a disturbance from Eqs. (17) and (18) as

$$\dot{\mathbf{x}}(t) = A\mathbf{x}(t) + Bu(t) + \boldsymbol{\varepsilon} \tag{19}$$

$$y(t) = Cx(t) \tag{20}$$

where $\mathbf{x} \in R^n$ is the state vector, $y \in R^p$ is the output vector $(p = 1)$, $u \in R^m$ is the input vector $(m = 1)$, $\boldsymbol{\varepsilon} \in R^n$ is an unmeasurable disturbance vector, $A \in R^{n\times n}$ is the system matrix, $B \in R^{n\times 1}$ is the input matrix, $C \in R^{p\times n}$ is the output matrix $(p = 1)$. It is assumed that (A, B) is controllable, and (A, C) is observable. The output error is defined by

$$e = y - y_r \tag{21}$$

where y_r is the reference output and e is the output error.

It is assumed that the following homogeneous differential equation forms for reference and disturbance using linear polynomial differential operators of $L_r(D)$ and $L_\varepsilon(D)$ are satisfied, respectively:

$$L_r(D)y_r = 0 \text{ and } L_\varepsilon(D)\boldsymbol{\varepsilon} = 0 \tag{22}$$

where $L_r(D)$ and $L_\varepsilon(D)$ are assumed as the following differential polynomial operators with constant coefficients.

$$L_r(D) = D^\sigma + \rho_{\sigma-1}D^{\sigma-1} + \cdots + \rho_0 \text{ and } L_\varepsilon(D) = D^l + \mu_{l-1}D^{l-1} + \cdots + \mu_0 \tag{23}$$

where $D = d/dt$ is the differential operator, ρ_i, μ_i are constant coefficients, σ, l are orders of differential polynomials.

This includes the case of most common type of disturbance and reference signals occurring in practice such as polynomial, sinusoidal type signals, etc. $R(D)$ is the greatest common divisor of $L_r(D)$ and $L_\varepsilon(D)$ as follows:

$$L_r(D) = R(D)U(D) \text{ and } L_\varepsilon(D) = R(D)V(D) \tag{24}$$

where $R(D), U(D), V(D)$ are factors of $L_r(D)$ and $L_\varepsilon(D)$, respectively.

If the greatest common divisor $R(D)$ of the differential polynomial operators $L_r(D)$ and $L_\varepsilon(D)$ is equal to a constant, $L_r(D)$ and $L_\varepsilon(D)$ are coprime. Furthermore, finding the least common multiple of the two differential polynomial operators involves finding their common multiple with the smallest order polynomial.

$L(D)$ is defined as the least common multiple of $L_r(D)$ and $L_\varepsilon(D)$ and can be obtained from Eq. (24) as the polynomial differential operator as follows:

$$\begin{aligned} L(D) &= \frac{L_\varepsilon(D)L_r(D)}{R(D)} = U(D)R(D)V(D) = V(D)L_r(D) \text{ or } U(D)L_\varepsilon(D) \\ &= D^q + \alpha_{q-1}D^{q-1} + \cdots + \alpha_0 \end{aligned} \tag{25}$$

where $\dim\{V(D)\} = q - \sigma$ and $\dim\{U(D)\} = q - l$, $\dim\{R(D)\} = l + \sigma - q$ and $\dim\{L(D)\} = q \geq \dim\{L_r(D)\}$ or $\dim\{L_\varepsilon(D)\}$.

To adopt the internal model principle (IMP) to the tracking control system, we will introduce the polynomial differential operator stated and get an extended system.

Operating $L(D)$ for ε_i and y_r of Eq. (22) the following are obtained

$$\begin{cases} L(D)y_r = U(D)R(D)V(D)y_r = V(D)L_r(D)y_r = 0 \\ L(D)\varepsilon_i = U(D)R(D)V(D)\varepsilon_i = U(D)L_w(D)\varepsilon_i = 0 \end{cases} \tag{26}$$

where the dimension of q holds $q \geq l$ or $q \geq \sigma$.

Firstly, eliminate the effect of disturbance in Eq. (22), by operating the polynomial differential operator $L(D)$ to both sides of Eq. (19) under the conditions Eq. (22), as

$$\frac{d}{dt}\{L(D)x\} = AL(D)x + BL(D)u \tag{27}$$

Secondly, by operating $L(D)$ to Eq. (21) and using the property of Eq. (26), the followings can be obtained.

$$\begin{aligned} L(D)e(t) &= D^q e + \alpha_{q-1}D^{q-1}e + \cdots + \alpha_1 De + \alpha_0 e \;\; = L(D)y - L(D)y_r \\ &= CL(D)x \end{aligned} \tag{28}$$

Equation (28) can be described into the matrix form as follows:

$$\dot{z} = ML(D)x + Nz \;=\; \begin{bmatrix} \mathbf{0} \\ \mathbf{0} \\ \vdots \\ \mathbf{c}_1^T \end{bmatrix} L(D)x + Nz_i \tag{29}$$

where

$$N = \begin{bmatrix} 0 & 1 & 0 & 0 & \cdots & 0 \\ 0 & 0 & 1 & 0 & \cdots & 0 \\ 0 & 0 & 0 & 1 & \cdots & 0 \\ \vdots & \vdots & \vdots & \vdots & \ddots & \vdots \\ 0 & 0 & 0 & 0 & \cdots & 1 \\ -\alpha_0 & -\alpha_1 & -\alpha_2 & -\alpha_3 & \cdots & -\alpha_{q-1} \end{bmatrix} \in R^{q\times q},$$

$$M = \begin{bmatrix} \mathbf{0} \\ \cdots \\ \mathbf{c}_1^T \end{bmatrix} = \begin{bmatrix} 0 \\ 0 \\ \vdots \\ 1 \end{bmatrix} \mathbf{c}_1^T \in R^{q\times n},\; C^T = \mathbf{c}_1 \in R^{n\times 1} \text{ and}$$

$$z = \begin{bmatrix} e & e^{(1)} & \cdots & e^{(q-1)} \end{bmatrix}^T \in R^q.$$

By combining the operated system, Eqs. (27) and (29), an extended system can be obtained as follows:

$$\dot{x}_e = A_e x_e + B_e v \tag{30}$$

where $A_e = \begin{bmatrix} A & \mathbf{0} \\ \begin{bmatrix} \mathbf{0} \\ \mathbf{c}_1^T \end{bmatrix} & N \end{bmatrix} \in R^{(n+q)\times(n+q)}$, $B_e = \begin{bmatrix} B \\ \mathbf{0} \end{bmatrix} \in R^{(n+q)\times 1}$, $x_e = \begin{bmatrix} L(D)x \\ z \end{bmatrix} = \begin{bmatrix} L(D)x \\ z_1 \\ z_2 \\ \vdots \\ z_q \end{bmatrix} \in R^{n+q} x_e$ is an extended system state variable vector, $v = L(D)u \in R^m$ is a new control law for the extended system $(m = 1)$, and $z = [z_1 \quad z_2 \quad \cdots \quad z_q]^T \in R^q$ is an error variable vector for the extended system.

A new control law for the extended system is defined by the following form:

$$v = L(D)u = -Fx_e \in R^m \tag{31}$$

where $F = [F_x \quad F_z] \in R^{1\times(n+q)}$ is a feedback control gain matrix, and $F_x \in R^{1\times n}$ and $F_z \in R^{1\times q}$ are feedback control gain matrices for $L(D)x$ and z, respectively.

A new error variable vector for the extende system can be defined as

$$\zeta = L^{-1}(D)z \tag{32}$$

where $\zeta = [\zeta_1 \quad \zeta_2 \quad \cdots \quad \zeta_q]^T \in R^q$, and $\zeta_i \in R^q$ for $i = 1, \ldots, q$.

Using Eqs. (31) and (32), the control law of Eq. (19) can be obtained as follows:

$$u = -Fx_\zeta = -[F_x \quad F_z] \begin{bmatrix} x \\ \zeta \end{bmatrix} \tag{33}$$

where $x_\zeta \in R^{n+q}$ is a new extended system variable vector.

From Eqs. (30) and (31), the closed loop system of the extended system is obtained as

$$\dot{x}_e = (A_e - B_e F)x_e \tag{34}$$

shows that the servo controller problem for Eq. (19) becomes a regulator design problem for the extended system Eq. (30). That is, the closed loop system of Eq. (34) is asymptotically stabilized by designing the feedback control law of Eq. (31) with a feedback control matrix F so as to be $\mathrm{Re}\{\lambda_i(A_e - B_e F\} < 0$. Controllability checking is proved in [8].

According to [8], there exists gain matrix $F = [F_x \quad F_z]$ so that the closed loop control system obtained by applying the feedback control law of Eq. (31) to the

extended system of Eq. (30) is asymptotically stable, i.e. There exists a gain matrix $F = [F_x \quad F_z]$ so that the following matrix is asymptotically stable [6, 7].

$$A_F = A_e - B_e F = A_e - B_e [F_x \quad F_z] \tag{35}$$

When the feedback control law of the extended system of Eq. (30) is designed based on the above regulator design problem [5–7], the output error of Eq. (21) becomes $e(t) \to 0$ as $t \to \infty$.

Since $x_e \to 0$ by regulator design result, that is, $x_e \to 0$ means $[Lx^T \quad z^T]^T \to 0$ as follows:

$$x_e = [L(D)x^T \quad z_1 \quad z_2 \quad \cdots \quad z_q]^T = [L(D)x^T \quad e \quad e^{(1)} \quad \cdots \quad e^{(q-1)}]^T \tag{36}$$

As the result, the error $e(t) \to 0$ *as* $t \to \infty$.

Using the new input v, the extended system of Eq. (30) can be written by

$$\frac{d}{dt}\{L(D)x\} = [A - BF_x]L(D)x - BF_z z + L(D)\varepsilon \tag{37}$$

$$\frac{d}{dt}z = Nz + I_\zeta L(D)e \tag{38}$$

where $L(D)\varepsilon = 0$ from Eq. (26), and $I_\xi = [0 \quad 0 \quad \cdots \quad 1]^T \in R^q$.

The 2nd term for the polynomial differential operator of $L(D)$ in Eq. (38) due to Eq. (26) has the following relation:

$$L(D)e = L(D)(y - y_r) = CL(D)x \tag{39}$$

By operating the inverse polynomial differential operator $L^{-1}(D)$ for Eqs. (37) and (38), the following equations can be obtained due to $L^{-1}(D)(L(D)\varepsilon) = \varepsilon$ by $L(D)\varepsilon = 0$:

$$\frac{d}{dt}x = [A - BF_x]x - BF_z\zeta + \varepsilon \tag{40}$$

$$\frac{d}{dt}\zeta = N\zeta + I_\zeta e \tag{41}$$

The servo compensator of Eq. (41) includes the model of reference and disturbance signals since the matrix N is composed of the least common multiple model of two signals. The configuration of the proposed servo control system can be described as shown in Fig. 1.

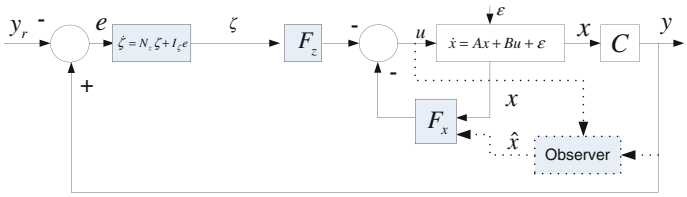

Fig. 1 Configuration of the proposed servo control system

3.2 *Observer Design in the Case of Speed Sensorless (or with Sensor)*

In Eq. (17), e_d, e_q, ω are unknown variables. To get these variables, the following observer is adopted. A full order observer of Eq. (17) and an estimation error vector are defined as

$$\dot{\hat{\mathbf{x}}} = A\hat{\mathbf{x}} + Bu + K(y - C\hat{\mathbf{x}}) \tag{42}$$

$$\sigma = \mathbf{x} - \hat{\mathbf{x}} \tag{43}$$

where $\hat{\mathbf{x}} = [\,\hat{e}_d \quad \hat{e}_q \quad \hat{\omega}\,]^T$ is the estimation vector of $\mathbf{x}$, and K is the observer gain matrix. From Eqs. (17), (42) and (43), the following is obtained.

$$\dot{\sigma} = (A - KC)\sigma \tag{44}$$

To be $\lim_{\delta x \to 0} \sigma = 0$, that is, $\mathbf{x} \to \hat{\mathbf{x}}$, K is designed to make $A - KC$ be a stable matrix by well known regulator design methods.

4 Hardware Configuration

The system used in the experiment is shown in Fig. 2a. AC induction motor for this paper has 3 phase, four poles and 2 Hp/1.5 kW. The powder brake works as a load and it can be controlled by the adjustment of the voltage from DC 0–24 V represent constant load from 0 to 33 Nm. A torque transducer rated at 10 Kgmf and an encoder with 1024 counts/rev. Figure 2b shows the inverter used in experiments. The inverter includes the controller board and the IGBT driver.

Table 1 shows the specification of AC induction motor.

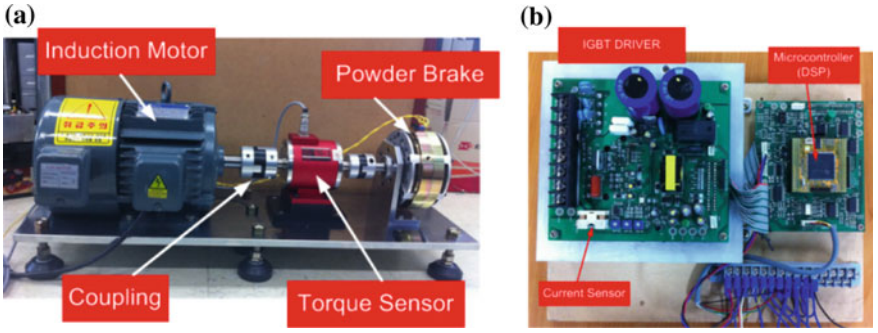

Fig. 2 Experiment equipment **a** Motor testing system. **b** Inverter

Table 1 Rated value of AC induction motor

Descriptions	Values	Descriptions	Values	Descriptions	Values
Rated voltage	220 V	Rated speed	1750 rpm	Rated current	6 A
Rated flux	0.49 Wb	Rated torque	10 Nm	Rated frequency	60 Hz

5 Simulation and Experimental Result

In this section, simulation and experiment has been done to verify the effectiveness and applicability of the proposed servo system and controller. Table 2 shows the parameters of 1.5 Kw AC induction motor for this paper.

Including the parameter value from Table 2 to the induction motor mathematical model of Eqs. (17) and (18) with $\hat{\alpha}_s = \alpha_s$ and $\hat{\alpha}_r = \alpha_r$, the following can be obtained:

$$A = \begin{bmatrix} -701.33 & 25151.9 & 0 \\ -25151.9 & -701.33 & -0.98 \\ -2.2931 & 0.0639 & -0 \end{bmatrix}, \; B = \begin{bmatrix} 0 \\ 0 \\ 0.0239 \end{bmatrix},$$

$$C = \begin{bmatrix} -2040.8 & 715.6514 & 1 \end{bmatrix}$$

Table 2 Parameter and initial values of 1.5 kW induction motor

Parameter	Values	Parameter	Values
Number of pole pairs (p)	2	Stator self-inductance (L_s)	0.387117 H
Moment of inertia (m)	0.089 Kg m^2	Rotor self-inductance (L_r)	0.387117 H
Stator resistance (R_s)	3.285 Ω	Mutual inductance (L_m)	0.374 H
Rotor resistance (R_r)	2.715 Ω	Friction coefficient (b_1)	0.01 Nms
Initial state vector ($x(0)$)	$[0 \quad 0 \quad 0]^T$	Initaial state estimation ($\hat{x}(0)$)	$[0 \quad 0 \quad 0]^T$
Initial compensator ($\zeta(0)$)	[0]		

Table 3 Parameters and gains for the proposed method

Design parameter	Reference types		
	Step	Ramp	Parabolic
Reference model	$\dot{y}_r = 0$ $y_r(0) = 1000$	$\ddot{y}_r = 0, \dot{y}_r(0) = 100$ $y_r(0) = 0$	$\dddot{y}_r = 0, \ddot{y}_r(0) = 10$ $\dot{y}_r(0) = 0, y_r(0) = 0$
Matrix N	$N = [0]$	$N = \begin{bmatrix} 0 & 1 \\ 0 & 0 \end{bmatrix}$	$N = \begin{bmatrix} 0 & 1 & 0 \\ 0 & 0 & 1 \\ 0 & 0 & 0 \end{bmatrix}$
Assigned poles	$\{-60, -61, -62, -63\}$	$\{-19, -20, -21, -22, -23\}$	$\{-18, -19, -20, -21, -22, -23\}$
Gain matrix F_x	$\begin{bmatrix} 2.75 \times 10^7 \\ 1.49 \times 10^9 \\ 471.1 \end{bmatrix}^T$	$\begin{bmatrix} 6.9724 \times 10^6 \\ 4.5207 \times 10^8 \\ 224.1418 \end{bmatrix}^T$	$\begin{bmatrix} 6.2852 \times 10^7 \\ 4.5207 \times 10^9 \\ 203.4504 \end{bmatrix}^T$
Gain matrix F_z	$[0.1672]$	$\begin{bmatrix} 0.0209 \\ 0.0294 \end{bmatrix}^T$	$\begin{bmatrix} 0.0201 \\ 0.0374 \\ 0.0270 \end{bmatrix}^T$
Compensator	$\dot{\zeta} = e$	$\dot{\zeta} = \begin{bmatrix} 0 & 1 \\ 0 & 0 \end{bmatrix} \zeta + \begin{bmatrix} 0 \\ 1 \end{bmatrix} e$	$\dot{\zeta} = \begin{bmatrix} 0 & 1 & 0 \\ 0 & 0 & 1 \\ 0 & 0 & 0 \end{bmatrix} \zeta + \begin{bmatrix} 0 \\ 0 \\ 1 \end{bmatrix} e$

The full order observer is design based on pole assignment. The pole positions are chosen as $[-100, -101, -102]$, and the observer gain is obtained as $K = [-0.0246 \quad 1.2076 \quad 0.2307]^T$. It is assumed that the disturbance is given as step type model. The parameters for simulations and experiments are shown in Table 3.

5.1 Step Input

Figures 3, 4, 5 and 6 show simulation and experimental results for reference of step type of $y_r(t) = 1000$ rpm. Figure 3 shows the control laws of the proposed method and PID method as current in *q-axis* converge to 0.8 A after about 2 s. Figure 4 shows the outputs motor speed for both methods in *q-axis* converge to the step reference. The output for PID shows overshoot and converges to the reference after 2 s, while the output for the proposed method converges to the reference smoothly without overshoot after 0.3 s. Figure 5 shows the output errors for PID

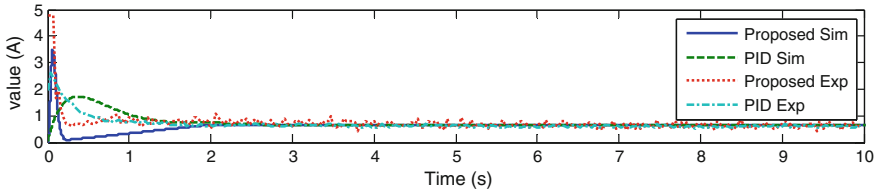

Fig. 3 Control law $u = i_{sq}$ for reference step input

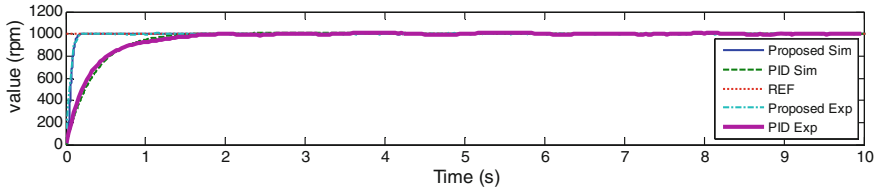

Fig. 4 Output y for step reference input

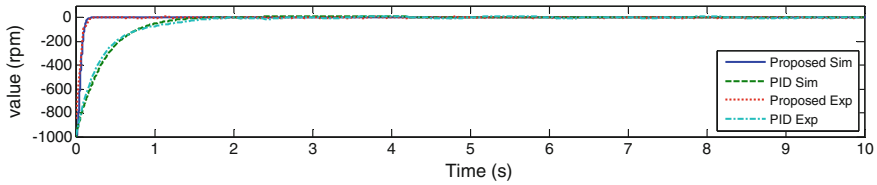

Fig. 5 Output error $\tilde{\omega}$ for step reference input

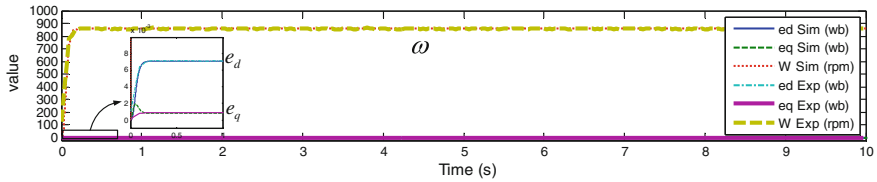

Fig. 6 Estimated state variables for step reference input

converges to zero after 2 s, while the output error for the proposed method converges to zero smoothly after 0.3 s. Figure 6 shows the estimated state variables for the proposed method. $\hat{e}_d, \hat{e}_q, \hat{\omega}$ converge to about 0.014 Wb about 0.001 Wb and 1000 rpm after 2 s.

5.2 *Ramp Input*

Figures 7, 8, 9 and 10 show simulation and experimental results for the ramp reference of $y_r(t) = 100t$. Figure 7 shows the control laws as current in *q-axis* are changed to ramp type after about 2 s. Figure 8 shows the outputs for PID do not converge to the reference input and has steady state errors, while the outputs for the proposed method converge to the reference input smoothly without overshoot after about 1.2 s. Figure 9 shows the output errors for PID converge about −40 rpm after about 4 s, while the output errors for the proposed method converge to zero smoothly after about 1.2 s. Figure 10 shows the estimated state variables for ramp reference using the proposed method.

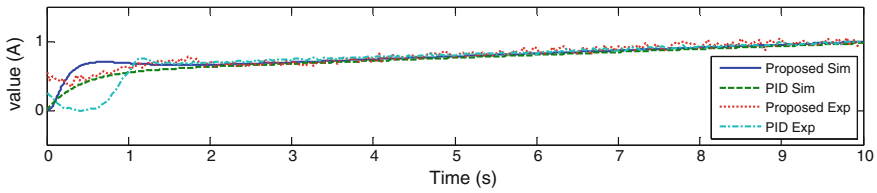

Fig. 7 Control law $u = i_{sq}$ for ramp reference input

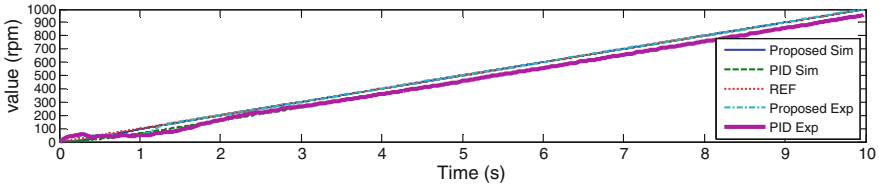

Fig. 8 Output y for ramp reference input

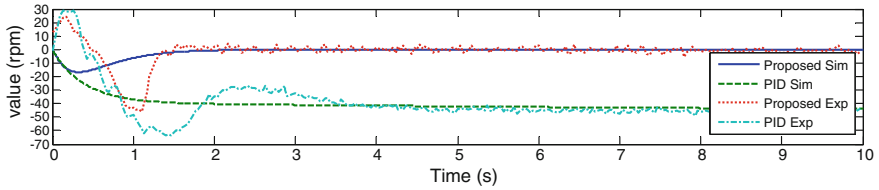

Fig. 9 Output error $\tilde{\omega}$ for ramp reference input

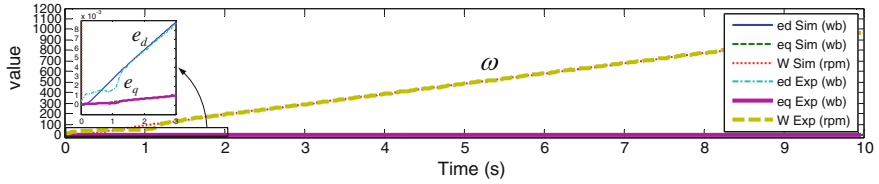

Fig. 10 Estimated state variables for ramp reference input

5.3 *Parabola Input*

Figures 11, 12, 13 and 14 show simulation and experimental results for parabola reference of $y_r(t) = 10t^2$. Figure 11 shows control laws for the proposed method and PID method as current in *q-axis* are changed to parabola type and increase to 0.5 A after about 10 s. Figure 12 shows the outputs for PID have steady state errors without converging to the reference input and then have bigger and bigger steady state error as time goes, while the outputs for the proposed method converge to the

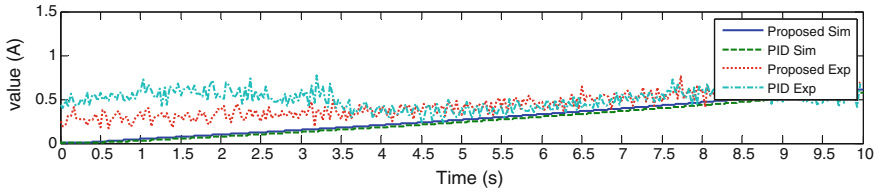

Fig. 11 Control law $u = i_{sq}$ for parabolic reference input

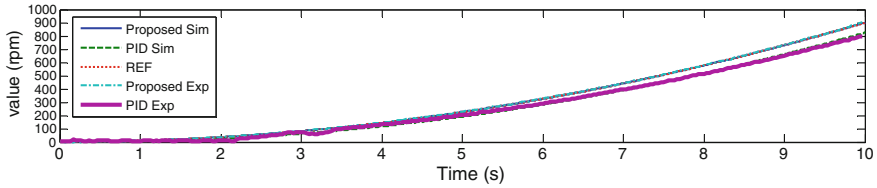

Fig. 12 Output y for parabolic reference input

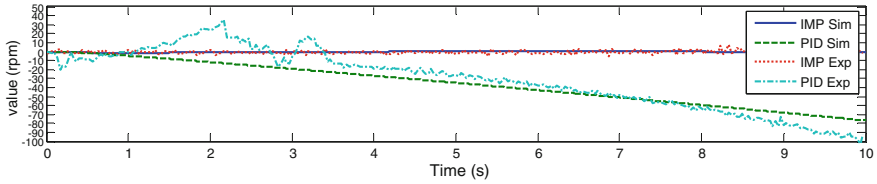

Fig. 13 Output error $\tilde{\omega}$ for parabolic reference input

reference input smoothly without overshoot after about 0.1 s. Figure 13 shows the output errors for both methods. The output errors for PID are always increasing and never converging to zero, while the output errors for the proposed method converge to zero smoothly after about 0.1 s. Figure 14 shows the estimated state variables for the proposed method.

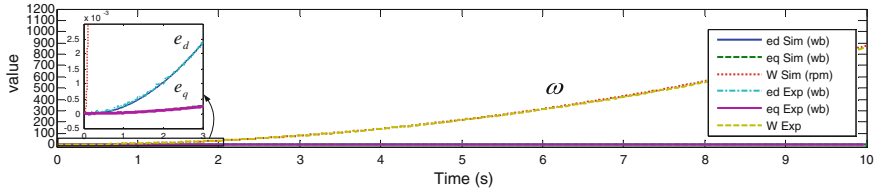

Fig. 14 State variables for parabolic reference input

6 Conclusion

This paper proposed a servo system design for speed control of AC induction motor using polynomial differential operator. The simulation and experimental results were shown to verify the effectiveness and the applicability of the proposed controller compared to PI controller. It shows that the proposed method can overcome the problem for higher order types of reference signals under disturbance.

Acknowledgments This research was supported by a grant (code 15LRP-B079281-02) from Transportation & Logistics Research Program funded by Ministry of Land, Infrastructure and Transport of Korean government.

References

1. Naouar M-W, Naassani A, Monmasson E, Slama-Belkhodja I (2006) FPGA-based speed control of synchronous machine using a P-PI controller. In: IEEE International Symposium on Industrial Electronics on 2. pp 1527–1532 (2006)
2. Verghese G, Sanders S (1988) Observers for flux estimation in induction machines. IEEE Trans Ind Electron 35:85–94
3. Khalil HK, Strangas EG, Jurkovic S (2009) Speed observer and reduced nonlinear model for sensorless control of induction motors. IEEE Trans Control Syst Technol 17:327–339
4. Davison, E.: A generalization of the output control of linear multivariable systems with unmeasurable arbitrary disturbances. IEEE Trans. Automat. Contr. 20, (1975)
5. Kim SB, Oh SJ, Jung YG, Kim HS (1991) Application of bilinear transformation method to servo system design and position control cart system. Trans KIEE 40:290–298
6. Furuta K, Kim SB (1987) Pole assignment in a specified disk. IEEE Trans Autom Control 32:423–427
7. Kim SB, Furuta K (1988) Regulator design with poles in a specified region. Int J Control 47:143–160
8. Kim DH (2015) Servo controller design using polynomial differential operator method and its applications, Doctor Thesis, Mechanical Design Engineering Department, Pukyong National University

Servo Controller Design for Speed Control of BLDC Motors Using Polynomial Differential Operator Method

Trong Hai Nguyen, Jin Woo Lee, Hak Kyeong Kim, Thien Phuc Tran, Yeon Wook Choe, Viet Tuan Dinh and Sang Bong Kim

Abstract This paper proposes a servo controller design method for speed control of Brushless DC (BLDC) motors using polynomial differential operator method. To do this task, the followings are done. Firstly, modeling for a BLDC motor is introduced and an extended system incorporating the internal model principle to construct the servo system is shown using polynomial differential operator in case that the types of reference inputs are differential polynomials. Secondly, a state feedback control law for the servo system to track the given reference input is designed by a well known regulator design method. The implementation of the proposed servo controller for a BLDC motor are completely carried out using a dSPACE DS1104 digital signal processor (DSP). The simulation and experimental results are shown to verify the effectiveness and the applicability of the proposed controller compared to the conventional PI controller for speed control of the BLDC motor with a step type of disturbance and 3 types of the references such as step, ramp and parabola.

Keywords Brushless DC motor · Internal model principle · Servo system · Speed control · State feedback control

T.H. Nguyen · H.K. Kim · S.B. Kim (✉)
Department of Mechanical Design Engineering, Pukyong National University, Busan 608-739, South Korea
e-mail: kimsb@pknu.ac.kr

J.W. Lee
The Korean Occupational Safety and Health Agency, Ulsan 681-230, South Korea

T.P. Tran
Department of Mechanical Engineering, Ho Chi Minh City University of Technology, Ho Chi Minh, Vietnam

Y.W. Choe
Department of Control & Instrumentation Engineering, Pukyong National University, Busan 608-737, South Korea

V.T. Dinh
Information Technology Faculty, Dalat University, Da Lat, Vietnam

V.H. Duy et al. (eds.), *AETA 2015: Recent Advances in Electrical Engineering and Related Sciences*, Lecture Notes in Electrical Engineering 371,
DOI 10.1007/978-3-319-27247-4_31

1 Introduction

BLDC motor has been used extensively in industrial automation, aerospace, instrumentation and automotive industry since 1970's. BLDC motor has the following advantages over brushed DC motors and induction motor such as high torque to inertia ratio, high efficiency, better speed versus torque characteristics, compact size, less maintenance [1]. However, the disadvantages of the BLDC motor have high cost and the necessity of a more complex controller because of its nonlinear characteristics [2].

For controlling the speed of BLDC motor, several controllers are used. The most widely used controller of them is a conventional PI controller because it is facile and easy to understand [3]. The PI controller is simple to realize but difficult for applying to obtain sufficiently high performance in the tracking application. It is, however, well known that the tracking controller problem can be simply solved by using state variable feedback with the extension of the state variables using the output error [4]. For the unknown and inaccessible inputs, the observer technique was studied by [5]. To solve robust servomechanism problem for SISO system, Kim et al. [6] introduced a servo control method with disturbance rejection and reference signal tracking by adopting the internal model principle and bilinear transformation method. In [6], there was not show for the explicit condition and its proof for the controller existence to achieve the robust control objectives. Kim [7] proposed a new concept of MIMO servo design method by extending the results of [6] and introducing a polynomial differential operator.

In this paper, a robust servo controller proposed by [7] is applied for speed control of BLDC motors. To do this task, the followings are done. Firstly, modeling for a BLDC motor is introduced and an extended system incorporating the internal model principle to construct the servo system is shown using polynomial differential operator in case that the types of reference inputs are differential polynomials. Secondly, a state feedback control law for the extended system to track the given reference input is designed by a well known regulator design method. The implementations of the proposed servo controller for a BLDC motor are completely carried out using a dSPACE DS1104 DSP. The simulation and experimental results are shown to verify the effectiveness and the applicability of the proposed controller compared to the conventional PI controller for speed control of the BLDC motor with a step type of disturbance and 3 types of the references such as step, ramp and parabola.

2 Modeling of BLDC Motors

Figure 1 shows the circuit diagram of a BLDC motor. Assuming that the stator resistances R_s of all of the windings stators, self inductances L_s and mutual inductances M are equal and constant, $L = L_s - M$, the voltage equation of the BLDC motor with three phases can be expressed as

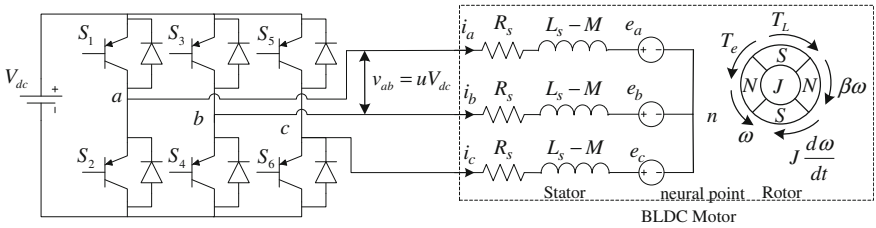

Fig. 1 Circuit diagram of a BLDC motor drive

$$\mathbf{v} = \mathbf{L}\frac{d}{dt}\mathbf{i} + \mathbf{R}\mathbf{i} + \mathbf{e} \tag{1}$$

where $\mathbf{v} = [\, v_a \quad v_b \quad v_c \,]^T$, $\mathbf{i} = [\, i_a \quad i_b \quad i_c \,]^T$, $\mathbf{e} = [\, e_a \quad e_b \quad e_c \,]^T$,

$$\mathbf{L} = \begin{bmatrix} L & 0 & 0 \\ 0 & L & 0 \\ 0 & 0 & L \end{bmatrix}, \ \mathbf{R} = \begin{bmatrix} R_s & 0 & 0 \\ 0 & R_s & 0 \\ 0 & 0 & R_s \end{bmatrix}$$

$\mathbf{v}$, $\mathbf{i}$, $\mathbf{e}$, $\mathbf{L}$, $\mathbf{R}$ are the stator phase voltage matrix, the stator phase current matrix, the stator phase back-electromagnetic forces (back-emfs) matrix, the phase stator inductance matrix and stator phase resistance matrix, respectively.

The electromagnetic torque is given by

$$T_e = \frac{1}{\omega_m}\mathbf{e}^T\mathbf{i} \tag{2}$$

where ω_m is the mechanical angular velocity of the rotor.

The equation of motion for the rotor of BLDC motor is

$$J\frac{d\omega_m}{dt} = T_e - T_L - \beta\omega_m \tag{3}$$

where J, T_L and β are the moment of inertia, load torque and the viscous damping coefficient of the rotor, respectively.

For the estimation of the rotor position, the motor is equipped with three hall sensors H_1, H_2, H_3. With these sensors, 6 different commutations are possible. Figure 2 shows the waveforms of back-emfs, phase currents and electromagnetic torque of BLDC depending on hall sensor values. With right synchronized commutations, the torque remains nearly constant.

The trapezoidal back-emfs vector is modeled as a function of rotor position as

$$\mathbf{e} = E\left[\, F(\theta_e) \quad F\left(\theta_e - \tfrac{2\pi}{3}\right) \quad F\left(\theta_e - \tfrac{4\pi}{3}\right) \,\right]^T \tag{4}$$

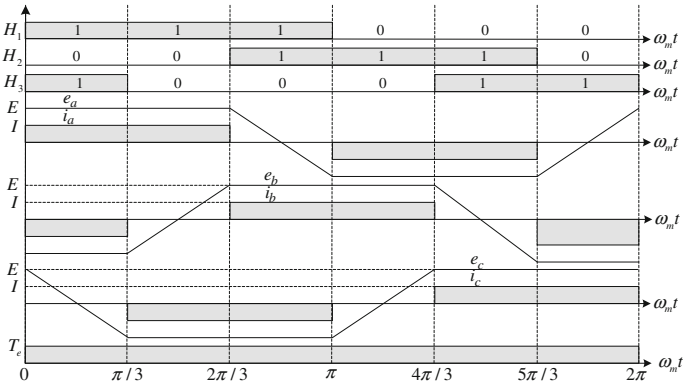

Fig. 2 Waveforms of a back-emfs, a phase current and a torque of BLDC

$$E = K_e \omega_m \tag{5}$$

where

E is the amplitude of the phase back-emfs and proportional to the rotor speed

K_e is back-emfs constant

θ_e is the electrical rotational angle related to the rotor rotational angle θ_m and the number of pole pairs p by $\theta_e = \frac{p}{2}\theta_m$.

The function $F(\cdot)$ gives the trapezoidal waveform of the back-emfs as shown in Fig. 2.

The function for one period $F(\cdot)$ can be written as

$$F(\theta_e) = \begin{cases} 1 & \left(0 < \theta_e \le \frac{2\pi}{3}\right) \\ 1 - \frac{6}{\pi}\left(\theta_e - \frac{2\pi}{3}\right) & \left(\frac{2\pi}{3} < \theta_e \le \pi\right) \\ -1 & \left(\pi < \theta_e \le \frac{5\pi}{3}\right) \\ -1 + \frac{6}{\pi}\left(\theta_e - \frac{5\pi}{3}\right) & \left(\frac{5\pi}{3} < \theta \le 2\pi\right) \end{cases} \tag{6}$$

The electromagnetic torque can be expressed from Eqs. (2) and (4)–(6) as:

$$T_e = K_T \left\{ F(\theta_e) i_a + F\left(\theta_e - \frac{2\pi}{3}\right) i_b + F\left(\theta_e - \frac{4\pi}{3}\right) i_c \right\} \tag{7}$$

where K_T is torque constant and it is assumed that $K_T = K_e = K$ for this paper.

The rotor rotational angle is obtained by integrating the mechanical angular velocity of the rotor:

$$\theta_m = \int \omega_m dt + \theta(0) \tag{8}$$

where $\theta(0)$ is the initial angle of rotor.

There are six commutation steps for one complete cycle. To simplify the problem, one of the six steps will be modeled. The remaining steps are considered to be similar. The voltage relation in each step following line-to-line equation in Figs. 1 and 2 and Eqs. (4) and (5) gives

$$2L\frac{di}{dt} = uV_{dc} - 2K\omega_m - 2R_s i \tag{9}$$

where V_{dc} is a DC bus voltage, u is a duty cycle value and $i = i_a = -i_b$.

During each interval of $\pi/3$ in Fig. 2, the electromagnetic torque can be expressed from Eqs. (6) and (7) and i_a, i_b, i_c in Fig. 2 as:

$$T_e = 2Ki \tag{10}$$

By substituting current obtained from Eqs. (9) and (10) in Eq. (3), a second order differential equation is derived with ω_m as state variable

$$\ddot{\omega_m} + a_1\dot{\omega}_m + a_2\omega_m = b_1 u + b_2 T_L \tag{11}$$

where constants a_1, a_2, b_1 and b_2 are defined as

$$a_1 = \left(\frac{\beta L + JR_s}{JL}\right),\ a_2 = \left(\frac{2K^2 + \beta R_s}{JL}\right),\ b_1 = \frac{KV_{dc}}{JL},\ b_2 = \frac{R_s}{JL}$$

An inaccessible T_L can be considered as disturbance term to be unknown and assumed to be a constant.

The state dynamic equation of a given system Eq. (11) with disturbance ε can be expressed as follows:

$$\dot{x} = Ax + Bu + \varepsilon \tag{12}$$

$$y = \omega_m = Cx \tag{13}$$

where

$$A = \begin{bmatrix} 0 & 1 \\ -a_2 & -a_1 \end{bmatrix},\ B = \begin{bmatrix} 0 \\ b_1 \end{bmatrix},\ C = [\,1 \quad 0\,],\ \varepsilon = \begin{bmatrix} 0 \\ b_2 T_L \end{bmatrix},\ x = \begin{bmatrix} x_1 \\ x_2 \end{bmatrix} = \begin{bmatrix} \omega_m \\ \dot{\omega}_m \end{bmatrix}$$

$\mathbf{x} \in R^n$ is the state vector ($n = 2$), $y \in R^p$ is the output vector ($p = 1$), $u \in R^m$ is the input vector ($m = 1$), $\boldsymbol{\varepsilon} \in R^n$ is an un-measurable disturbance vector, $A \in R^{n\times n}$ is the system matrix,$B \in R^{n\times m}$ is the input matrix, $C \in R^{p\times n}$ is the output matrix. It is assumed that (A, B) is controllable and (A, C) is observable.

3 Servo Controller Design Using Polynomial Differential Operator

The output error for a SISO system ($m = 1, p = 1$) is defined by

$$e = y - y_r \tag{14}$$

where y_r is the reference output and e is the output error.

It is assumed that the following homogeneous differential equation forms for reference and disturbance using linear polynomial differential operators of $L_r(D)$ and $L_\varepsilon(D)$ are satisfied, respectively:

$$L_r(D)y_r = 0 \text{ and } L_\varepsilon(D)\boldsymbol{\varepsilon} = 0 \tag{15}$$

$$L_r(D) = D^\sigma + \rho_{\sigma-1}D^{\sigma-1} + \cdots + \rho_0 \text{ and } L_\varepsilon(D) = D^l + \mu_{l-1}D^{l-1} + \cdots + \mu_0 \tag{16}$$

where $D = d/dt$ is the differential operator, ρ_i, μ_i are constant coefficients and σ, l are orders of differential polynomials.

$R(D)$ is defined as the greatest common divisor of $L_r(D)$ and $L_\varepsilon(D)$ as follows:

$$L_r(D) = R(D)U(D) \text{ and } L_\varepsilon(D) = R(D)V(D) \tag{17}$$

where $U(D), V(D)$ are factors of $L_r(D)$ and $L_\varepsilon(D)$, respectively.

$L(D)$ is defined as the least common multiple of $L_r(D)$ and $L_\varepsilon(D)$ and can be obtained from (17) as the following polynomial differential operator:

$$L(D) = \frac{L_\varepsilon(D)L_r(D)}{R(D)} = U(D)R(D)V(D) = D^q - \alpha_{q-1}D^{q-1} + \cdots + \alpha_0 \tag{18}$$

where $\dim\{V(D)\} = q - \sigma$ and $\dim\{U(D)\} = q - l$, $\dim\{R(D)\} = l + \sigma - q$ and $\dim\{L(D)\} = q \geq \dim\{L_r(D)\}$ or $\dim\{L_\varepsilon(D)\}$.

By operating $L(D)$ of Eq. (18) for ε_i and y_r, the following are obtained:

$$\begin{cases} L(D)y_r = U(D)R(D)V(D)y_r = V(D)L_r(D)y_r = 0 \\ L(D)\varepsilon_i = U(D)R(D)V(D)\varepsilon_i = U(D)L_\varepsilon(D)\varepsilon_i = 0 \end{cases} \tag{19}$$

where the dimension of q holds $q \geq l$ *or* $q \geq \sigma$.

The adaptation of the internal model principle (IMP) to the servo control system design is attempted by 3 steps [7]:

[Step 1] by operating the polynomial differential operator to the given system of Eq. (12) and also the output error of Eq. (14).
[Step 2] an extended system is obtained by using the operated system and output errors obtained through the step 1

[Step 3] for the extended system, a regulator problem is solved based on the well known design method such as pole assignment or optimal control.

Firstly, to eliminate the effect of disturbance in Eq. (12), by operating the polynomial differential operator of $L(D)$ to both sides of Eq. (12) using Eq. (19) as follows:

$$\frac{d}{dt}\{L(D)x\} = AL(D)x + BL(D)u \tag{20}$$

Secondly, by operating $L(D)$ to Eq. (14) and using the property of Eq. (18), the followings can be obtained.

$$L(D)e(t) = D^q e + \alpha_{q-1}D^{q-1}e + \cdots + \alpha_1 De + \alpha_0 e = L(D)y = CL(D)x \tag{21}$$

$$D^q e = -\alpha_{q-1}D^{q-1}e \cdots - \alpha_1 De - \alpha_0 e + CL(D)x \tag{22}$$

Equation (22) can be described into the matrix form as follows:

$$\dot{z} = ML(D)x + Nz \tag{23}$$

where

$$N = \begin{bmatrix} 0 & 1 & 0 & \cdots & 0 \\ 0 & 0 & 1 & \cdots & 0 \\ \vdots & \vdots & \vdots & \ddots & \vdots \\ 0 & 0 & 0 & \cdots & 1 \\ -\alpha_0 & -\alpha_1 & -\alpha_2 & \cdots & -\alpha_{q-1} \end{bmatrix} \in R^{q\times q},\ M = \begin{bmatrix} \mathbf{0} \\ \mathbf{0} \\ \vdots \\ \mathbf{c}_1^T \end{bmatrix} = \begin{bmatrix} 0 \\ 0 \\ \vdots \\ 1 \end{bmatrix} \mathbf{c}_1^T = \begin{bmatrix} \mathbf{0} \\ \mathbf{c}_1^T \end{bmatrix}$$
$$\in R^{q\times n}$$

$$C^T = \mathbf{c}_1 \in R^{n\times 1},\quad \text{and } z = \begin{bmatrix} e & e^{(1)} & \cdots & e^{(q-1)} \end{bmatrix}^T \in R^q$$

By combining Eqs. (20) and (23), an extended system can be obtained as follows:

$$\dot{x}_e = A_e x_e + B_e v \tag{24}$$

where

$$A_e = \begin{bmatrix} A & \mathbf{0} \\ M & N \end{bmatrix} \in R^{(n+q)\times(n+q)},\ B_e = \begin{bmatrix} B \\ \mathbf{0} \end{bmatrix} \in R^{(n+q)\times 1},\ x_e = \begin{bmatrix} L(D)x \\ z \end{bmatrix} \in R^{n+q}$$

x_e is an extended system state variable vector, $v = L(D)u \in R^1$ is a new control law for the extended system and z is an error variable vector for the extended system.

A new control law for the extended system is defined by the following form:

$$v = L(D)u = -Fx_e \in R^1 \tag{25}$$

where $F = [F_x \quad F_z] \in R^{1\times(n+q)}$ is a feedback control gain matrix, and $F_x \in R^{1\times n}$ and $F_z \in R^{1\times q}$ are feedback control gain matrices for $L(D)x$ and z, respectively.

A new error variable vector for the extended system can be defined as

$$\zeta = L^{-1}(D)z \tag{26}$$

where $\zeta = [\zeta_1 \quad \zeta_2 \quad \cdots \quad \zeta_q]^T \in R^q$, and $\zeta_i \in R^q$ for $i = 1, \ldots, q$.

Using Eqs. (25) and (26), the control law of Eq. (12) can be obtained as follows:

$$u = -Fx_\zeta = -[F_x \quad F_z]\begin{bmatrix} x \\ \zeta \end{bmatrix} \tag{27}$$

where $x_\zeta \in R^{n+q}$ is a new extended system variable vector.

Controllability of the extended system Eq. (24) can be easily checked [7].

The closed loop system of the extended system Eqs. (24) using (25) is obtained as

$$\dot{x}_e = (A_e - B_eF)x_e \tag{28}$$

The closed loop system of Eq. (28) is asymptotically stabilized by designing the feedback control law of Eq. (27) with a feedback control matrix F so as to be $\mathrm{Re}\{\lambda_i(A_e - B_eF\} < 0$.

There exists a gain matrix $F = [F_x \quad F_z]$ so that the following matrix is asymptotically stable [8, 9].

$$A_F = A_e - B_eF = A_e - B_e[F_x \quad F_z] \tag{29}$$

When the feedback control law of the extended system of Eq. (24) is designed based on the above regulator design problem [4, 6], the output error of (14) becomes $e(t) \to 0$ as $t \to \infty$.

Since $x_e \to 0$ by regulator design result, that is $x_e \to 0$ means $[Lx^T \quad z^T]^T \to 0$ as follows:

$$x_e = [L(D)x^T \quad z^T]^T = [L(D)x^T \quad e \quad e^{(1)} \quad \cdots \quad e^{(q-1)}]^T \tag{30}$$

As the result, the error $e(t) \to 0$ *as* $t \to \infty$.

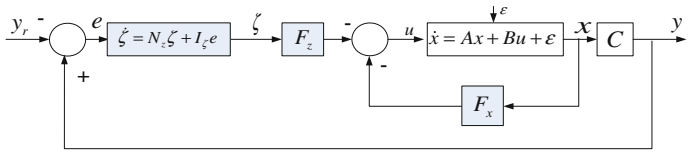

Fig. 3 Configuration of the proposed servo control system

Using the new control input v, the extended system of Eq. (24) can be written by

$$\begin{cases} \dfrac{d}{dt}\{L(D)x\} = [A - BF_x]L(D)x - BF_z z + L(D)\varepsilon \\ \dfrac{d}{dt}z = Nz + I_\zeta L(D)e \end{cases} \tag{31}$$

where $L(D)\varepsilon = 0$ from Eq. (19) and $I_\xi = [\,0 \quad 0 \quad \cdots \quad 1\,]^T \in R^q$.

By operating the inverse polynomial differential operator $L^{-1}(D)$ for Eq. (31), the following equations can be obtained due to $L^{-1}(D)(L(D)\varepsilon) = \varepsilon$ by $L(D)\varepsilon = 0$:

$$\begin{cases} \dfrac{d}{dt}x = [A - BF_x]x - BF_z\zeta + \varepsilon = Ax + Bu + \varepsilon \\ \dfrac{d}{dt}\zeta = N\zeta + I_\zeta e \end{cases} \tag{32}$$

The servo compensator $\dot{\zeta} = \frac{d}{dt}\zeta$ of Eq. (32) includes the model of reference and disturbance signals since the matrix N is composed of the least common multiple model of two signals. It proposes the internal model principle based on the polynomial differential operator.

The configuration of the proposed servo control system can be described as shown in Fig. 3.

4 Simulation and Experimental Results

In this section, and implementation for a BLDC motor are completely carried out using a dSPACE DS1104 digital DSP and MATLAB/Simulink environment to verify the effectiveness and applicability of the proposed servo system and controller as show in Fig. 4. Table 1 shows the parameters values of BLDC motor for this paper.

Three reference inputs are chosen: reference of step type $y_r = 1000$ rpm, reference of ramp type $y_r(t) = 200t$, and reference of parabola type $y_r(t) = 10t^2$. It is assumed that the disturbance is given as step type model of the following:

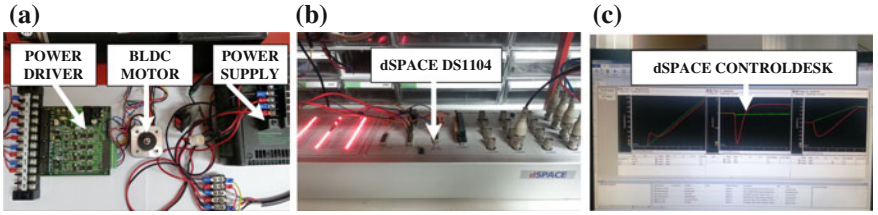

Fig. 4 Experimental apparatus. **a** Power driver. **b** Controller board. **c** Software

Table 1 Parameter values of BLDC motor

Symbols	Descriptions	Values	Units
V_{dc}	Rated voltage	24	V
p	Number of pole pairs	2	Pole pairs
J	Moment of inertia	0.0036	Kgm^2
R_s	Stator resistance	7.3	Ω
L_s	Stator self-inductance	0.0303	H
M	Mutual inductance	0.01	H
K_e	Back-EMF constant	0.25	V/rad/sec
β	Friction coefficient	0.0001	Nms

$$\dot{\varepsilon} \equiv \frac{d\varepsilon}{dt} = 0 \tag{33}$$

Using the parameter values from Table 1 to the BLDC motor mathematical model of Eqs. (12) and (13), the following can be obtained:

$$A = \begin{bmatrix} 0 & 1 \\ -1720.4 & -359.6337 \end{bmatrix},\ B = \begin{bmatrix} 0 \\ 8.2102.10^4 \end{bmatrix},\ C = [1 \quad 0]$$

Table 2 shows the initial state variable values of BLDC motor for this paper Typical PI tuning method is used by Ziegler-Nicholas tuning method.

The parameters, controller gains and servo compensators for 3 types of reference signals are obtained by using the proposed servo controller design method as shown in Table 3.

Table 2 Initial state values of BLDC motor

Symbols	$x(0)$	$\theta(0)$	Step reference $\zeta(0)$	Ramp reference $\zeta(0)$	Parabola reference $\zeta(0)$
Values	$[0 \quad 0]^T$	[0]	[0]	$[0 \quad 0]^T$	$[0 \quad 0 \quad 0]^T$

Table 3 Parameters, controller gains and servo compensators for the proposed method

Design parameter	Reference types		
	Step	Ramp	Parabolic
Reference model and initial value	$\dot{y}_r = 0$ $y_r(0) = 1000$	$\ddot{y}_r(t) = 0,\ \dot{y}_r(0) = 200$ $y_r(0) = 0$	$\dddot{y}_r(t) = 0,\ \ddot{y}_r(0) = 20$ $\dot{y}_r(0) = 0,\ y_r(0) = 0$
Matrix N	$[0]$	$\begin{bmatrix} 0 & 1 \\ 0 & 0 \end{bmatrix}$	$\begin{bmatrix} 0 & 1 & 0 \\ 0 & 0 & 1 \\ 0 & 0 & 0 \end{bmatrix}$
Assigned poles	$\{-10, -11, -12\}$	$\{-10, -11, -12, -13\}$	$\{-5, -6, -7, -8, -9\}$
F_x	$[-0.0165 \quad -0.004]$	$[-0.0113 \quad -0.0038]$	$[-0.015 \quad -0.004]$
F_z	$[0.0161]$	$[0.2090 \quad 0.0734]$	$[0.1842 \quad 0.1373 \quad 0.0405]$
Servo compensator	$\dot{\zeta} = e$	$\dot{\zeta} = \begin{bmatrix} 0 & 1 \\ 0 & 0 \end{bmatrix}\zeta + \begin{bmatrix} 0 \\ 1 \end{bmatrix} e$	$\dot{\zeta} = \begin{bmatrix} 0 & 1 & 0 \\ 0 & 0 & 1 \\ 0 & 0 & 0 \end{bmatrix}\zeta + \begin{bmatrix} 0 \\ 0 \\ 1 \end{bmatrix} e$

4.1 Step Input

Figure 5 shows simulation and experimental results for the reference step input of $y_r(t) = 1000$ rpm using both the proposed control method and the conventional PI control method.

Figure 5a shows the control laws of both control methods. It shows that both control laws converge to 0.816 after about 1.5 s. Figure 5b shows the outputs for both control methods. It shows that both outputs of motor speed converge to the reference step input of 1000 rpm. The outputs for PI converges to the reference step input after about 1.5 s, while the outputs for the proposed method converges to the reference step input smoothly after about 0.7 s. Figure 5c shows the output errors for both methods. The output error for PI converges to zero after about 1.5 s, while the output error for the proposed method converges to zero smoothly after about 0.7 s.

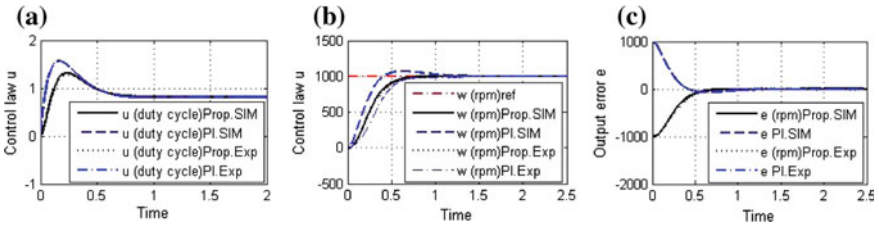

Fig. 5 Control law u, output y and output error for reference step input

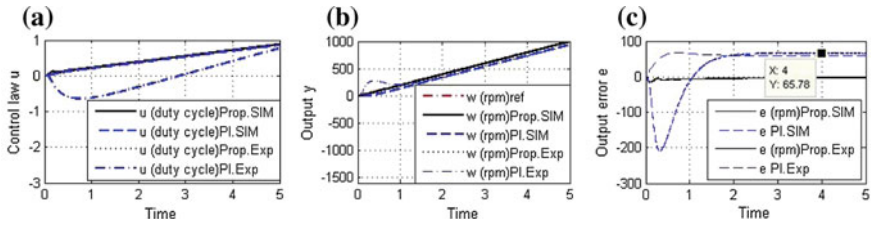

Fig. 6 Control law u, output y and output error for reference ramp input

4.2 Ramp Input

Simulation and experimental results using reference ramp input for the proposed method and the PI controller are shown in Fig. 6. Figure 6a shows the control laws using both methods. Figure 6b shows that only the outputs of the controller using the proposed method can track the reference ramp signals and stabilize the plant after finite time. The outputs of the controller using the PI controller cannot track the reference ramp signal. Furthermore, Fig. 6c shows that the output errors of the controller using the proposed method converge to zero and stabilize the plant after finite time. On the other hand, in the controller using the PI, the steady state errors of 65.78 rpm exists.

4.3 Parabolic Input

Simulation and experimental results using reference parabolic input for the proposed method and the PI controller are shown in Fig. 7. Figure 7a shows the control inputs using both methods. Figure 7b, c shows the same results as shown in the case of ramp for the parabolic type of reference signal, that is, PI controller has steady error for the given parabolic signals is increasing

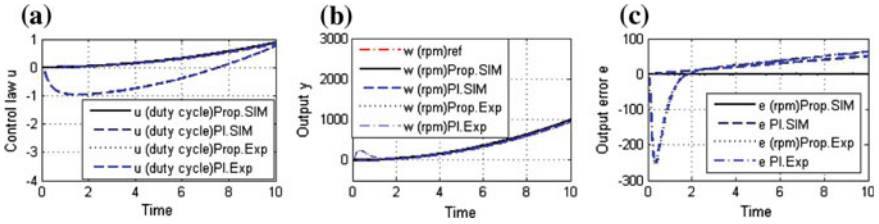

Fig. 7 Control law u, output y and output error for reference parabolic input

5 Conclusion

This paper proposed a servo controller design for speed control of BLDC motors using polynomial differential operator method. Firstly, modeling for an BLDC motor was introduced and extended system incorporating the internal model principle to construct the servo system was shown using polynomial differential operator in case that the types of reference inputs were polynomials. Secondly, a state feedback control law for the servo system to track the given reference input was designed. The implementations of the proposed controller were completely carried out using a dSPACE DS1104 DSP. The simulation and experimental results were shown to verify the effectiveness and the applicability of the proposed controller compared to conventional PI controller. It showed that the proposed method could overcome the problem for more high order types of reference signals under disturbance.

Acknowledgments This research was supported by a grant (code 15LRP-B079281-02) from Transportation & Logistics Research Program funded by Ministry of Land, Infrastructure and Transport of Korean government.

References

1. Tibor B, Fedak V, Durovsky F (2011) Modeling and simulation of the BLDC motor in MATLAB GUI. In: 2011 IEEE International Symposium on Industrial Electronics (ISIE), Gdansk, pp 1403–1407
2. Pearson WR, Sen PC (1984) Brushless DC motor propulsion using synchronous motor for transit system. IEEE Trans Ind Electron 31(4):326–351
3. Lin CT, Hung CW, Liu CW (2007) Fuzzy PI controller for BLDC motors considering variable sampling effect. In: 33rd Annual Conference of the IEEE industrial electronics society (IECON 2007), Taipei, pp 5–8
4. Davison EJ (1972) The output control of linear time-invariant multivariable systems with unmeasurable arbitrary disturbances. IEEE Trans Autom Control 17(5):621–630
5. Meditch JS, Hostetter GH (1973) Observer for systems with unknown and inaccessible inputs. In: 1973 IEEE Conference on decision and control including the 12th symposium on adaptive processes, San Diego, CA, USA, pp 120–124
6. Kim SB, Oh SJ, Jung YG, Kim HS (1991) Application of bilinear transformation method to servo system design and position control for a cart system. Trans KIEE 40(3):290–298
7. Kim DH (2015) Servo controller design using polynomial differential operator method and its applications. PhD thesis, Pukyong National University
8. Furuta K, Kim SB (1987) Pole assignment in a specified disk. IEEE Trans Autom Control 32 (5):423–427
9. Kim SB, Furuta K (1988) Regulator design with poles on a specified region. Int J Control 47 (1):143–160

Optimal Tuning of PI Controller for Vector Control System Using Hybrid System Composed of GA and BA

Dong Hwa Kim, Chau Dong, Cong Thinh Tran and Vo Hoang Duy

Abstract This paper focuses on optimal tuning of PI controller in motor vector control system by using hybrid system composed of GA (Genetic Algorithm) and BA (Bacterial Foraging). Generally, vector control of motor has three PI controllers to control speed and current. In this case, engineer has to tune 6-parameters simultaneously on site. Therefore, it is difficult to tune in high speed motor control system. Also, they cannot sometimes obtain optimal parameters of PI controller using only manually or traditional approaches or conventional artificial intelligence such as GA (Genetic Algorithm), FZ (Fuzzy), NN (Neural Network), and etc. because of local solution and low speed computing characteristics. To obtain optimal gain for vector control and good computing characteristics in high speed, this paper deals with applying hybrid system by GA and BA.

1 Introduction

The Proportional-Integral-Derivative (PID) controller has been widely used owing to its simplicity and robustness in nuclear power plant, thermal power plant, and electrical systems. Its popularity is also due to easy implementation in hardware and software, and friendly to engineer for a long history. However, with only the P, I, D

D.H. Kim (✉)
Korea Hucare, Daejeon, South Korea
e-mail: koreahucare@gmail.com

D.H. Kim · C. Dong · C.T. Tran · V.H. Duy
Faculty of Electrical and Electronics Engineering, Ton Duc Thang University,
No. 19 Nguyen Huu Tho Street, District 7, Ho Chi Minh City, Vietnam
e-mail: dongsithienchau@tdt.edu.vn

C.T. Tran
e-mail: trancongthinh@tdt.edu.vn

V.H. Duy
e-mail: vohoangduy@tdt.edu.vn

V.H. Duy et al. (eds.), *AETA 2015: Recent Advances in Electrical Engineering and Related Sciences*, Lecture Notes in Electrical Engineering 371,
DOI 10.1007/978-3-319-27247-4_32

parameters, it is very difficult to control a plant with complex dynamics, such as large dead time, high speed response, and a highly nonlinear characteristics. That is, since the PID controller is usually poorly tuned in high speed control system, a higher of degree of experience and technology are required for the tuning in the actual plant [1, 2].

The processes with large dead time in the industrial area exist widely in many types of systems such as the chemical rector, biomedical processes, and steam process of power plant. Traditionally, PID controllers applied to these plants are tuned with a reduction of gain so that overall stability can be obtained in vector control. This results in poor performance of control. That is, the process with large dead time or high speed control is usually difficult to be controlled.

Up to the present time, many tuning problems of a PID controller have been studied for these process control systems. However, it cannot effectively provide requirements of both the set-point-following and disturbance rejection as well as industrial experience is required for a higher experience [3, 15, 16]. Especially, since its tuning method and performance in control system depend on the characteristics of system to be controlled, it is necessary to study the tuning on each system through case by case.

To get over these problems, in recent years, there has been growing interest in using intelligent approaches such as fuzzy, neural network, evolutionary method, and their combined technologies for the tuning of a PID controller [4–12]. Also, a number of approaches have been proposed to implement mixed control structures that combine a PID controller with artificial intelligence.

On the other hand, since the immune system possesses a self organizing and distributed memory, it is thus adaptive to its external environment and allows a PDP (Parallel Distributed Processing) network to complete patterns against the environmental situation. That is, it can play an important role to maintain own system dynamically changing environments in motor control. Therefore, immune system would be expected to provide a new paradigm suitable for dynamic problem including control problem dealing with unknown high speed environments than static system [17–21].

In this paper feasibility study for auto-tuning scheme of the PI controller for vector motor control using reference model and foraging bacteria network has been suggested [9–12].

2 Bacteria Foraging Based Optimization

2.1 Behavior Characteristics and Modeling of Bacteria Foraging

As natural selection tends to eliminate animals with poor foraging strategies through locating, handling, and ingesting food and favor the propagation of genes of those animals that have successful foraging strategies, they are more likely to

apply reproductive success to have an optimal solution. After many generations, poor foraging strategies are either eliminated or shaped into good ones. Logically, such evolutionary principles have led scientists and engineers to hypothesize that it is appropriate to model the activity of foraging as an optimization process. That is, a foraging strategy takes actions to maximize the energy obtained per unit time spent foraging, in the face of constraints presented by its own physiology such as, sensing, cognitive capabilities, and environmental changing. It has also valid for social foraging characteristics where groups of animals or fish communicate to cooperatively forage. This paper suggests on how their characteristics can be expressed and applied by a relevant optimization such as self-organization, organisms, and synchronization for engineering areas [7–14].

Generally, each forager with more capabilities helps them succeed in foraging, both as an individual and as a group in modeling. From an engineering perspective, both ends of such a spectrum can be used effectively for optimal tuning.

2.2 Chemotactic Behavior of E. Coli in Bacteria Fragging

This paper represents the foraging behavior of E. coli to move. Its ability to move comes from a set of up to six rigid 100–200 rps spinning flagella, each driven by a biological motor. When the flagella rotate clockwise (counterclockwise), they operate as propellers and hence an E. coli may run or tumble (Chemotactic Actions). If in neutral medium, alternate tumbles and runs. If swimming up a nutrient gradient (or out of noxious substances), swim longer (climb up nutrient gradient or down noxious gradient). If swimming down a nutrient gradient (or up noxious substance gradient), then search avoid unfavorable environments.

In this way, it can climb up nutrient hills and at the same time avoid noxious substances. The sensors it uses are receptor proteins which are very sensitive, and overall there is a high gain (i.e., a small change in the concentration of nutrients can cause a significant change in behavior). The sensor (feedback) averages sensed concentrations and computes a time derivative. This is probably the best-understood sensory and decision-making system in biology. Bacteria are often killed and dispersed and this can be viewed as part of their motility. Mutations in E. coli affect the reproductive efficiency (robustness) at different temperatures, and occur at a rate of gene and generation changing. E. coli occasionally engages in a type of sex called conjugation that affects the characteristics of a population of bacteria (delicate). Some bacteria can change their shape and number of flagella based on the medium to reconfigure so as to ensure efficient foraging in a variety of media (against environment). Moreover, under certain conditions, they will secrete cell-to-cell attractant signals so that they will group and protect each other. These bacteria can swarm.

2.3 Dynamic Equation of Bacteria Foraging for Optimization

Here, the basic goal is to find the minimum of $J_{cc}(\theta)$, $\theta \in R^p$, when we do not have the gradient $\nabla J(\theta)$. Suppose that θ is the position of a bacterium, and $J_{cc}(\theta)$ represents an attractant-repellant profile for optimal gain. That is, it represents where nutrients and noxious substances are located, so J < 0, J = 0, J > 0 represent the presence of nutrients, a neutral medium, and the presence of noxious substances, respectively.

Let

$$P(j,k,l) = \left\{\theta^i(j,k,l)\middle| i = 1,2,\ldots,S\right\} \tag{1}$$

represents the positions of each member in the population of the S bacteria at the jth chemotactic step, kth reproduction step, and lth elimination-dispersal event. Let $J(i, j, k, l)$ denote the cost at the location of the ith bacterium $\theta^i(j,k,l) \in R^p$. Let Nc be the length of the lifetime of the bacteria as measured by the number of chemotactic steps. To represent a tumble, a unit length random direction, we let

$$\theta^i = (j+1,k,l) = \theta^i(j,k,l) + C((i)\phi(j), \tag{2}$$

so that $C(i) > 0$ is the size of the step taken in the random direction specified by the tumble. If at $\theta^i(j+1,k,l)$ the cost $J(i, j + 1, k, l)$ is better (lower) than at $\theta^i(j,k,l)$, then another chemotactic step of size $C(i)$ in this same direction will be taken and repeated up to a maximum number of steps Ns.

Let d_{attract} : the depth of the attractant released by the cell, $w_{attract}$: a measure of the width of the attractant signal, $h_{repellan}$: the height of the repellant effect (magnitude). Then, we may use function $J^i_{cc}(\theta)$, $i = 1, 2, \ldots, S$, to model the cell-to-cell signaling via an attractant and a repellant. That is,

$$\begin{aligned} J_{cc}(\theta) = \sum_{i=1}^{S} J^i_{cc} = \sum_{i=1}^{S} \left[-d_{attract} \exp\left(-w_{attract} \sum_{j=1}^{p} (\theta_j - \theta^i_j)^2 \right) \right] \\ + \sum_{i=1}^{S} \left[-h_{repellant} \exp\left(-w_{attract} \sum_{j=1}^{p} (\theta_j - \theta^i_j)^2 \right) \right], \end{aligned} \tag{3}$$

where $\theta = [\theta_1, \ldots, \theta_p]^T$ is a point on the optimization domain. The expression of $J_{cc}(\theta)$ implies that its value does not depend on the nutrient concentration at position θ. Actually, it is reasonable to assume that the depth of the chemical secreted by a bacterium is affected by environment.

After Nc chemotactic steps (gain size in case of P, I, and D), a reproduction step (re-tuning because there is no optimal gain in PID controller) is taken. Suppose there are Nre reproduction steps (candidate gain in PID controller). For

reproduction, the healthiest bacteria (the ones that have the lowest accumulated cost over their lifetime: useful gain) split, and then we kill the same number of unhealthy ones (hence, we get a constant population size: gain). If let *Ned* be the number of elimination-dispersal events for each elimination-dispersal event (useless gain in PID), each bacterium in the population is subjected to elimination-dispersal (death, then random placement of a new bacterium at a random location on the optimization domain; new parameters in PID) with probability. This paper's objective is simply and fast to obtain optimal gain by the gross characteristics of chemotactic hill climbing and swarming as normal bacterial foraging mthod.

3 Simulation Results

Figure 1 shows for vector control to tune PI. From this block diagram, there are 3-PI controllers to tune and control motor. Usually, motor speed has 3600 rpm in high speed system or generally at least 1800 rpm. In this case, tuning speed should have over these speeds. It means that a higher computing speed should be needed than motor speed or machine.

However, as engineer, it is impossible to obtain 6-optimal gains simultaneously. Herein, we have to develop optimal obtaining approach against dynamically changing environment (speed, load change, etc.). Therefore, in this paper, we introduce BA based tuning method as feasibility study as the above Fig. 1. Figure 2 represents simulation results of BA based tuning for motor vector control system. To obtain an optimal parameter PI controller, this paper candidate low boundary value and upper boundary value for P and I parameter in GA and BA loop and simulates. By simulation of GA and BA loop, these parameters can be selected automatically depends on situation such as load changing or disturbance or so and controlled. This paper uses general GA algorithm to simply.

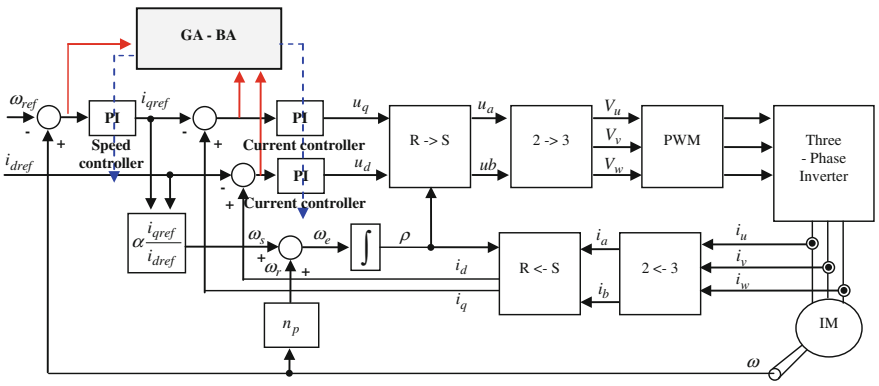

Fig. 1 Block diagram of indirect vector PI controller using GA-BA

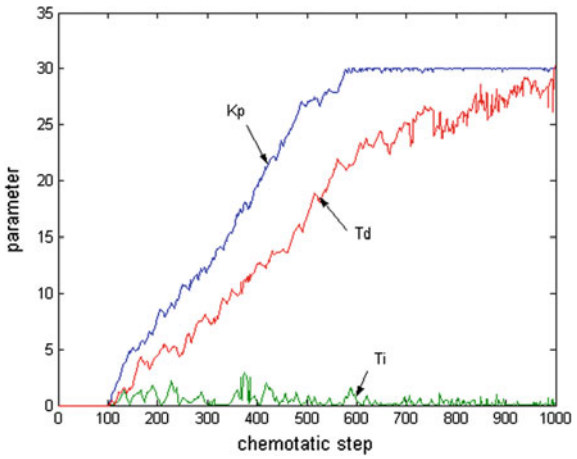

Fig. 2 Search process of optimal PID parameters in GA and BA loop

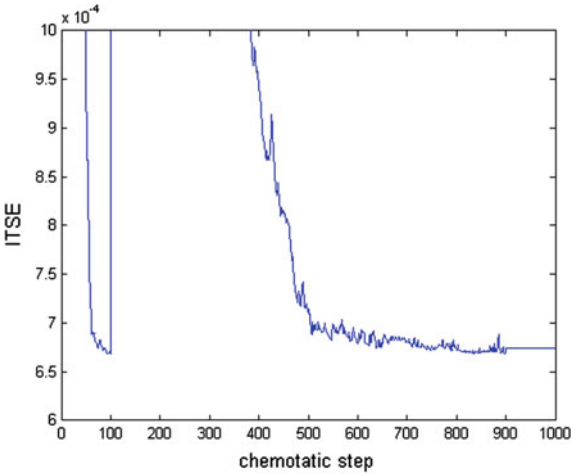

Fig. 3 Search process of performance index (ITSE) depend on load changing in GA and BA loop

4 Conclusion

This paper suggests GA and BA based optimal tuning of PI controller for motor vector control system. BA characteristic has useful approach to survive through reproductive and elimination-dispersal event fast and robust against environment. This function is the best approach ways that engineer want to obtain optimal gain. This paper has the possibility results through simulation. GA and BA loop can automatically select parameter of PI controller depends on load changing or disturbance because GA and BA loop including these characteristics when computing loop. Therefore, this approach can have robust control against disturbance or noise (Fig. 3).

Acknowledgments This research work was supported by the Basic Science Research Program through the National Research Foundation of Korea (NRF) funded by the Ministry of Education, Science and Technology (D00046: Bio based Intelligent Computing Technology) and (2012042098: 2012R1A1A2042098). This research was also supported by the research fund of Hanbat National University for supporting of research professor in 2012 (Research in Hungary), combining department (Bio based intelligent emotion pattern recognition) in 2013, and the research fund of Hanbat National University in 2013.

References

1. Stephens DW, Krebs JR (1986) Foraging theory. Princeton University Press, Princeton
2. Astrom KJ, Hagglund T (1995) PID controllers, theory, design, and tuning. Research Triangle Park, USA
3. Ho MJ, Datta A, Bhattacharyya SP (2000) Structure and synthesis of PID controllers. Springer, London
4. Alcock J (1998) Animal behavior: an evolutionary approach. Sinauer Associates, Sunderland
5. Bell WJ (1991) Searching behavior: the behavioral ecology of finding resources. Chapman and Hall, London
6. Grunbaum D (1998) Schooling as a strategy for taxis in a noisy environment. Evol Ecol 12:503–522
7. Bonabeau E, Dorigo M, Theraulaz G (1999) Swarm intelligence, from natural to artificial systems. Oxford University Press, New York
8. Adami C (1998) Introduction to artificial life. Springer, New York
9. Resnick M (1994) Turtles, termites, and traffic jams.: explorations in massively parallel microworlds. MIT Press, Cambridge
10. Levy S (1992) Artificial life. a report from the frontier where computers meet biology. Vintage Books, New York
11. Arin S, Deneubourg JL, Goss S, Pasteels JM (2002) Functional self-organization illustrated by interest traffic in ants: the case of the argentine ant, biological motion. Lect Notes Biomathematics 115:3
12. Parrish JK, Hamner WM (1997) Animal groups in three dimensions. Cambridge University Press, Cambridge
13. Camazine S et al (2001) Self-organization in biological systems. Princeton University Press, Princeton
14. Passino KM (2001) Biomimicry of bacterial foraging for distributed optimization. University Press, Princeton
15. Lindsley D (1991) Boiler control systems. McGrawill, New York
16. Matsummura S (1998) Adaptive control for the steam temperature of thermal power plants. In: Proceedings the 1993 IEEE on control applications, pp 1105–1109
17. Farmer JD, Packard NH, Perelson AS (1986) The immune system, adaptation, and machine learning. Physica 22:187–204
18. Mori K, Tsukiyama M (1993) Immune algorithm with searching diversity and its application to resource allocation problem. Trans JIEE 113:C-10
19. Kim DH (2002) Intelligent tuning of a PID controller using a immune algorithm. Trans KIEE 51-D(1)
20. Kim DH (2002) Auto-tuning of reference model based PID controller using immune algorithm. In: IEEE international conference on evolutionary computation, Hawaii, 12–17 May 2002
21. Kim DH (2001) Speed control of 2 inertia system using optimal pole allocation. Trans KIEE 49D(1)

Part VIII
Control System

Vehicle Side-Slip Angle and Lateral Force Estimator Based on Extended Kalman Filtering Algorithm

Chih-Keng Chen and Anh-Tuan Le

Abstract This paper describes a vehicle state variable estimator for an electronic stability program control system that operates using an extended Kalman filtering (EKF) algorithm. The proposed estimator uses the steering angle and vertical forces on the tires as inputs. Subsequently, according to a seven-degree-of-freedom vehicle model and the measured sensor signals regarding longitudinal and lateral accelerations, the steering angle, the yaw rate, and the wheel speed, the EKF algorithm is used to identify unmeasurable state variables such as lateral velocity, the vehicle side-slip angle, and lateral tire forces. The estimation results of the proposed control system exhibited high performance.

Keywords 7-DOF vehicle model · Extended kalman filtering (EKF) · Lateral force · Side-slip angle · State variable estimation

1 Introduction

Modern intelligent automotive systems are equipped with an electronic stability program (ESP), which is intended to enhance the active safety and handling predictability of drivers. ESPs increase driver control on curves and slippery roads, substantially reducing the risk of fatal crashes. The operating principle of an ESP system is using differential braking mainly according to the exact steering angle, longitudinal velocity, yaw rate, vehicle side-slip angle, and tire slip angle to generate stabilizing yaw moment. In reality, longitudinal velocity can be measured according to wheel speed. The steering angle, yaw rate, and wheel speed can be

C.-K. Chen (✉) · A.-T. Le
Department of Mechanical and Automation Engineering, Dayeh University,
168 University Rd, Changhua 515, Taiwan
e-mail: ckchen@mail.dyu.edu.tw

A.-T. Le
e-mail: tuanleanh83@gmail.com

V.H. Duy et al. (eds.), *AETA 2015: Recent Advances in Electrical Engineering and Related Sciences*, Lecture Notes in Electrical Engineering 371,
DOI 10.1007/978-3-319-27247-4_33

determined using widely available and inexpensive sensors. The vehicle side-slip angle and tire slip angle can be derived if lateral tire forces and velocity, respectively, are known. However, the sensors typically used to measure these variables are expensive. Therefore, different estimation methods have been proposed for identifying these variables by using available low-cost sensors [1–5]. Some methods involve using kinematic integration to directly estimate the side-slip angle [6, 7]. However, these methods cannot provide reliable estimation because of integration error. Some methods involve using two states of the bicycle model, including lateral velocity and the yaw rate, to design the observer identifying the lateral velocity [7–9]. The bicycle model is based on assumptions such as a constant vehicle longitudinal velocity and small tire slip angle. These methods do not ensure exact estimation over all driving conditions because of the high nonlinearity of overall vehicle motion. For overcoming this problem by using a seven-degree-of-freedom (7-DOF) four-wheel nonlinear vehicle model, an extended Kalman filtering (EKF) algorithm is applied to identify the difficult-to-measure vehicle variables. By using the proposed method, the vehicle side-slip angle and lateral forces of each tire can be estimated reliably.

This paper comprises five parts: The motivation of the study is presented in Sect. 1. In Sect. 2, the 7-DOF vehicle and tire models for the estimator design are described. The method for estimating unmeasurable vehicle state variables is proposed in Sect. 3. Section 4 presents the simulation results. Finally, conclusions are presented in Sect. 5, summarizing the main points of the paper and recommending future research directions.

2 Vehicle System

2.1 7-DOF Vehicle Model

A mathematical model of the 7-DOF vehicle depicted in Fig. 1 is considered. The roll dynamics are ignored and the nomenclature is defined in Table 1.

The governing equations of motion, including longitudinal, lateral, and yaw dynamics, and the rotational dynamics of the four wheels, are

$$\dot{V}_x = \frac{1}{m}\left(m\dot{\theta}V_y + F_{x1}\cos\delta_l + F_{x2}\cos\delta_r + F_{x3} + F_{x4} - F_{y1}\sin\delta_l - F_{y2}\sin\delta_r\right), \tag{1}$$

$$\dot{V}_y = \frac{1}{m}\left(-m\dot{\theta}V_x + F_{x1}\sin\delta_l + F_{x2}\sin\delta_r + F_{y3} + F_{y4} + F_{y1}\cos\delta_l + F_{y2}\cos\delta_r\right), \tag{2}$$

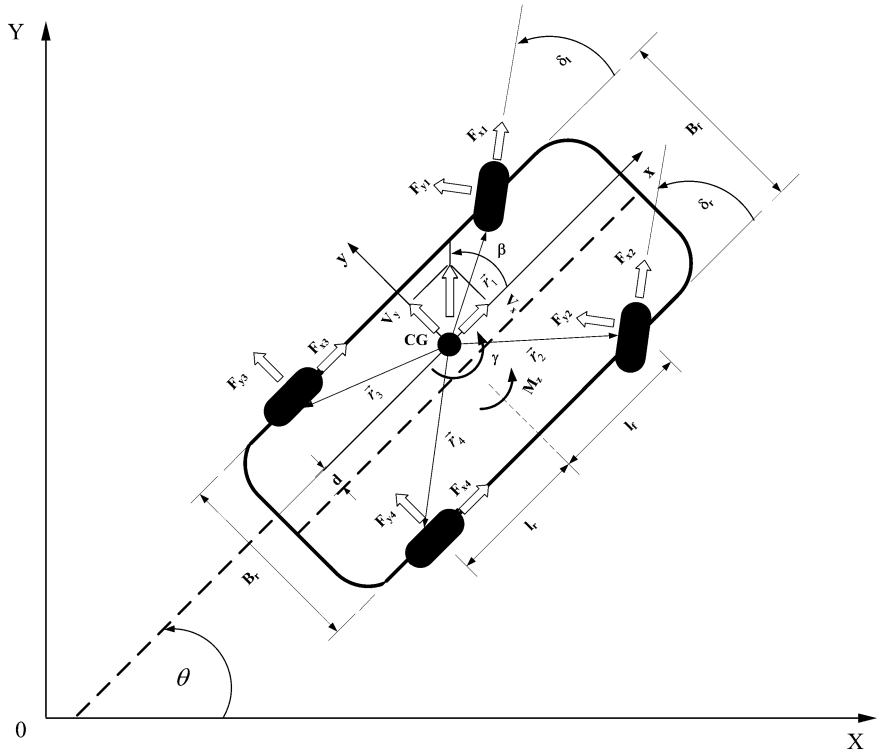

Fig. 1 7-DOF vehicle model

$$\dot{\gamma} = \frac{1}{I_z}\left(F_{y1}\left(l_f \cos\delta_l + A_{af}\sin\delta_l\right) - \left(F_{y3}+F_{y4}\right)l_r + F_{y2}\left(l_f\cos\delta_r - B_{bf}\sin\delta_r\right)\right)$$
$$+ F_{x1}\left(-A_{af}\cos\delta_l + l_f\sin\delta_l\right) + F_{x2}\left(l_f\sin\delta_r + B_{bf}\cos\delta_r\right) - F_{x3}A_{ar} + F_{x4}B_{br}\Big), \tag{3}$$

$$\dot{\omega}_n = \frac{1}{I_w}\left(rF_{xn} - T_{bn}\right), \quad (n = 1,4), \tag{4}$$

where

$$A_{af} = 0.5B_f - d, \qquad A_{ar} = 0.5B_r - d, \tag{5}$$

$$B_{bf} = 0.5B_f + d, \qquad B_{br} = 0.5B_r + d, \tag{6}$$

$$\gamma = \dot{\theta}. \tag{7}$$

Table 1 Nomenclature

Symbol	Description	Unit
F_{xn}, F_{yn}	Longitudinal and lagged lateral tire forces	N
F_{zn}	Vertical force on each tire	N
B_f, B_r	Front and rear track widths	m
m	Vehicle mass	kg
d	Offset from CG	m
I_z	Mass moment of inertia about the z axis	kg m^2
l	Wheelbase	m
r	Wheel radius	m
l_f, l_r	Distances from CG to front and rear axles	m
T_{bn}	Braking torque of each wheel	Nm
δ	Steering angle	rad
V_x, V_y	Vehicle longitudinal and lateral velocities	m/s
a_x, a_y	Longitudinal and lateral accelerations	m/s^2
θ	Vehicle heading angle measured from x axis	rad
α_n	Slip angle of each tire	rad
γ	Yaw rate	rad/s
β	Side-slip angle	rad
i_{dn}	Longitudinal skid ratio of each tire	none
C_{dn}	Longitudinal tire stiffness during braking	N/rad
C_n	Cornering stiffness of each tire	N/rad
μ	Tire-road frictional coefficient	none

2.2 Tire Model

The Dugoff tire model [10] is used to represent nonlinear tire behavior because of its small number of parameters, which are sufficient for evaluating the tire-road forces. Both the longitudinal and lateral forces of each tire can be expressed as

$$F_{xn} = C_{dn}\frac{i_{dn}}{1+i_{dn}}f(\lambda_n), \tag{8}$$

$$\bar{F}_{yn} = -C_n\frac{\tan\alpha_n}{1+i_{dn}}f(\lambda_n), \tag{9}$$

where

$$\lambda_n = \frac{\mu F_{zn}(1+i_{dn})}{2\left((C_{dn}i_{dn})^2+(C_n\tan\alpha_n)^2\right)^{1/2}}, \qquad (n=1,4). \tag{10}$$

The slip angles of the front and rear tires can be obtained using

$$\alpha_1 = \delta - \arctan\left(\frac{V_y + l_f\gamma}{V_x - (0.5B_f - d)\gamma}\right), \quad \alpha_2 = \delta - \arctan\left(\frac{V_y + l_f\gamma}{V_x + (0.5B_f + d)\gamma}\right), \tag{11}$$

$$\alpha_3 = -\arctan\left(\frac{V_y - l_r\gamma}{V_x - (0.5B_r - d)\gamma}\right), \quad \alpha_4 = -\arctan\left(\frac{V_y - l_r\gamma}{V_x + (0.5B_r + d)\gamma}\right). \tag{12}$$

Following [10], lag exists between a sudden change in the slip angle of each tire and the buildup of a corresponding lateral force. This lag can be modeled as

$$\dot{F}_{yn} = \frac{V_x}{\varepsilon}\left(-F_{yn} + \bar{F}_{yn}\right), \tag{13}$$

where F_{yn} is the lagged lateral force of each tire and ε is the relaxation length.

3 Extended Kalman Filtering Algorithm

3.1 Nonlinear State-Space Model

For simplicity in implementing the algorithm, the vehicle system must be simplified by employing the following suppositions: $d = 0$, $\delta_l = \delta_r = \delta$, $F_{x3} = F_{x4} = 0$, $F_{x1} + F_{x2} = F_{x11}$, and $F_{x2} - F_{x1} = F_{x12}$. Consequently, after (5)–(7) are used, (1)–(3), (11) and (12) become

$$\dot{V}_x = \frac{1}{m}\left(m\gamma V_y + F_{x11}\cos\delta - \left(F_{y1} + F_{y2}\right)\sin\delta\right), \tag{14}$$

$$\dot{V}_y = \frac{1}{m}\left(-m\gamma V_x + F_{x11}\sin\delta + \left(F_{y1} + F_{y2}\right)\cos\delta + F_{y3} + F_{y4}\right), \tag{15}$$

$$\begin{aligned}\dot{\gamma} = \frac{1}{I_z}\big(&l_f F_{x11}\sin\delta + l_f\left(F_{y1} + F_{y2}\right)\cos\delta - l_r\left(F_{y3} + F_{y4}\right)\\ &+ 0.5B_f F_{x12}\cos\delta + 0.5B_f\left(F_{y1} - F_{y2}\right)\sin\delta\big),\end{aligned} \tag{16}$$

$$\alpha_1 = \delta - \arctan\left(\frac{V_y + l_f\gamma}{V_x - 0.5B_f\gamma}\right), \quad \alpha_2 = \delta - \arctan\left(\frac{V_y + l_f\gamma}{V_x + 0.5B_f\gamma}\right), \tag{17}$$

$$\alpha_3 = -\arctan\left(\frac{V_y - l_r\gamma}{V_x - 0.5B_r\gamma}\right), \quad \alpha_4 = -\arctan\left(\frac{V_y - l_r\gamma}{V_x + 0.5B_r\gamma}\right). \tag{18}$$

From (14) and (15), the longitudinal and lateral accelerations are derived as follows:

$$a_x = \dot{V}_x - \gamma V_y = \frac{1}{m}\left(F_{x11}\cos\delta - \left(F_{y1} + F_{y2}\right)\sin\delta\right), \tag{19}$$

$$a_y = \dot{V}_y + \gamma V_x = \frac{1}{m}\left(F_{x11}\sin\delta + \left(F_{y1} + F_{y2}\right)\cos\delta + F_{y3} + F_{y4}\right). \tag{20}$$

Following (20), the lateral dynamics (15) can be obtained in an alternative manner, namely by using

$$\dot{V}_y = -\gamma V_x + a_y. \tag{21}$$

During EKF calculation, (21) should be prioritized over (15) because the yaw rate γ, longitudinal speed V_x, and lateral acceleration a_y can be measured using the available sensors, yielding an accurate lateral velocity estimate.

Subsequently, according to the supposition that the longitudinal skid ratio of each tire is zero (i_{dn} = 0), (8)–(10) are similar to

$$F_{xn} = 0, \tag{22}$$

$$\bar{F}_{yn} = -(C_n \tan\alpha_n) f(\lambda_n), \tag{23}$$

where

$$f(\lambda_n) = \begin{cases} (2-\lambda_n)\lambda_n & if\ \lambda_n < 1, \\ 1 & if\ \lambda_n \geq 1, \end{cases} \tag{24}$$

and

$$\lambda_n = \frac{\mu F_{zn}}{2C_n \tan\alpha_n}. \tag{25}$$

Therefore, the dynamic tire model (13) becomes

$$\dot{F}_{yn} = \frac{V_x}{\varepsilon}\left(-F_{yn} - (C_n \tan\alpha_n) f(\lambda_n)\right), \tag{26}$$

where $f(\lambda_n)$ is obtained from (24) and (25), and $\tan\alpha_n$ (n = 1, 4) is calculated by changing (17) and (18) as follows:

$$\begin{aligned} \tan\alpha_1 &= \frac{\left(V_x - 0.5B_f\gamma\right)\tan\delta - V_y - l_f\gamma}{V_x - 0.5B_f\gamma + \left(V_y + l_f\gamma\right)\tan\delta}, \\ \tan\alpha_2 &= \frac{\left(V_x + 0.5B_f\gamma\right)\tan\delta - V_y - l_f\gamma}{V_x + 0.5B_f\gamma + \left(V_y + l_f\gamma\right)\tan\delta}, \end{aligned} \tag{27}$$

$$\tan\alpha_3 = \frac{l_r\gamma - V_y}{V_x - 0.5B_r\gamma}, \quad \tan\alpha_4 = \frac{l_r\gamma - V_y}{V_x + 0.5B_r\gamma}. \tag{28}$$

Converting the state differential equation $\dot{x}(t) = f[x(t), u(t), t]$ by using Euler discretization [11] yields

$$\hat{x}_{k|k-1} = \hat{x}_{k-1|k-1} + \hat{\dot{x}}_{k-1|k-1} T_s, \tag{29}$$

where T_s is the sampling time and the derivative is obtained from

$$\hat{\dot{x}}_{k-1|k-1} = f\left(\hat{x}_{k-1|k-1}, u_k, t_k, t_{k-1}\right). \tag{30}$$

The nonlinear discrete-time process of the whole vehicle system can then be rewritten in the following standard state-space form:

$$\begin{cases} \hat{x}_{k|k-1} = f\left(\hat{x}_{k-1|k-1}, u_k, t_k, t_{k-1}\right) + w_{k-1}, \\ \tilde{y}_k = \hat{y}_k + v_k, \end{cases} \tag{31}$$

where

$$\hat{y}_k = h\left(\hat{x}_{k|k-1}, u_k, t_k\right). \tag{32}$$

and the states of the process are expressed as

$$\hat{x}_{k|k-1} = \Big[\hat{V}_{x,k|k-1}\ \hat{V}_{y,k|k-1}\ \hat{\gamma}_{k|k-1}\ \hat{F}_{y1,k|k-1}\ \hat{F}_{y2,k|k-1}\ \hat{F}_{y3,k|k-1}\ \hat{F}_{y4,k|k-1}\ \hat{F}_{x11,k|k-1}\ \hat{F}_{x12,k|k-1}\ \hat{\dot{V}}_{y,k|k-1}\ \hat{\dot{a}}_{y,k|k-1}\Big].$$

Vector of inputs

$$u_k = [\,\delta_k \quad F_{z1,k} \quad F_{z2,k} \quad F_{z3,k} \quad F_{z4,k}\,]. \tag{33}$$

Vector of the measured process outputs

$$\tilde{y}_k = \left[\,\tilde{V}_{x,k} \quad \tilde{\gamma}_k \quad \tilde{a}_{x,k} \quad \tilde{a}_{y,k}\,\right]. \tag{34}$$

3.2 EKF Algorithm Description

To implement the EKF, the process and measurement noise autocovariance matrices of w_{k-1} and v_k must be specified as follows:

$$Q_{k,k-1} = E\left\{w_{k-1} \cdot w_{k-1}^T\right\}, \tag{35}$$

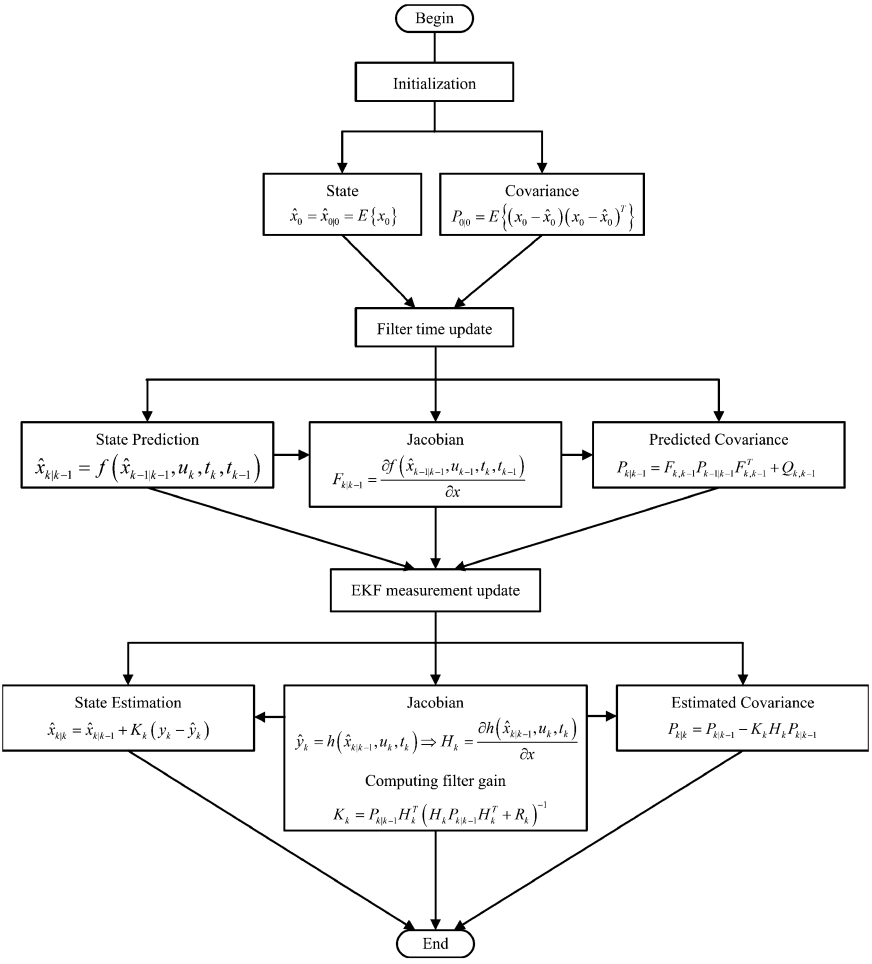

Fig. 2 Flow chart for implementing the EKF algorithm

$$R_k = E\{v_k \,.\, v_k^T\}. \tag{36}$$

The EKF algorithm is described using a flow chart (Fig. 2). The input vector in the algorithm comprises the steering angle and vertical forces on the tires. These forces can be calculated approximately [5] by

$$\begin{aligned} F_{z1} &= \frac{m}{l}\left(\frac{gl_r}{2} - \frac{h_c a_x}{2} - \frac{h_c l_r a_y}{B_f} + \frac{h_c^2 a_x a_y}{B_f g}\right), \\ F_{z2} &= \frac{m}{l}\left(\frac{gl_r}{2} - \frac{h_c a_x}{2} + \frac{h_c l_r a_y}{B_f} - \frac{h_c^2 a_x a_y}{B_f g}\right), \end{aligned} \tag{37}$$

$$F_{z3} = \frac{m}{l}\left(\frac{gl_f}{2} + \frac{h_c a_x}{2} - \frac{h_c l_f a_y}{B_r} - \frac{h_c^2 a_x a_y}{B_r g}\right),$$
$$F_{z4} = \frac{m}{l}\left(\frac{gl_f}{2} + \frac{h_c a_x}{2} + \frac{h_c l_f a_y}{B_r} + \frac{h_c^2 a_x a_y}{B_r g}\right), \tag{38}$$

where h_c is the height of the center of gravity (CG). The vertical forces (37) and (38) can be measured using the information from the longitudinal and lateral acceleration sensors.

4 Simulation Results

Simulations were conducted in the MATLAB and Simulink environment and linked to the CarSim software. The CarSim vehicle model was a full sedan; the parameters of its tires and aerodynamics, such as sprung mass, powertrain, and suspension, are shown in [12]. The vehicle was assumed to be driven on a road with a steering input that changes according to the steering wheel angle, similar to that shown in Fig. 3.

For comparison, each estimate (Figs. 4, 5 and 6) respectively contains the output responses of lateral forces, lateral velocity, and the side-slip angle from the CarSim vehicle model as the standard signals for the estimator performance evaluation, lateral forces, lateral velocity, and the side-slip angle from the estimator if its vertical-force inputs are directly obtained from CarSim vehicle model, and lateral forces, lateral velocity, and the side-slip angle from the estimator if its vertical-force inputs are calculated using (37) and (38). Figures 4, 5 and 6 present the results of the simulation with road and driving conditions for which the tire-road frictional coefficient was 0.85 and vehicle longitudinal velocity was 100 km/h. In all the

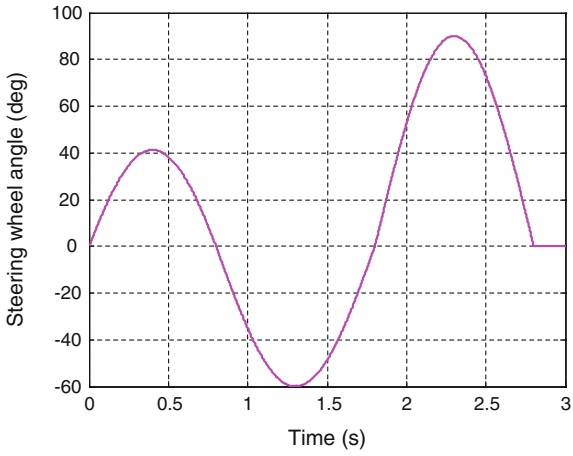

Fig. 3 Steering wheel angle input

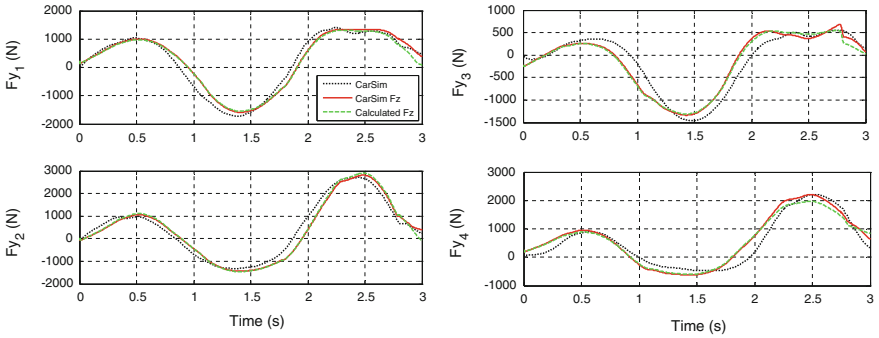

Fig. 4 Estimation of the four-wheel-lateral-tire forces

simulations, using the estimator whose vertical-force inputs are directly obtained from CarSim vehicle model always yielded the optimal estimation results.

The first lateral force estimates (Fig. 4) are relatively favorable and exhibit acceptable errors. The EKF linearized the state and measurement equations neighboring the predicted state as an operating point. This may be one reason for the errors in the lateral force estimation. Other reasons may be that the rear longitudinal tire forces are assumed to be zero in estimator design but are not zero in practice. The lateral tire forces are affected by the camber angle, which is neglected in the vehicle model. In addition, errors exist in (37) and (38), namely in the calculation of the vertical forces, which are part of the estimator input. The lateral velocity can be obtained using the estimation algorithm in the simulation (Fig. 5).

Fig. 5 Estimation of the lateral velocity

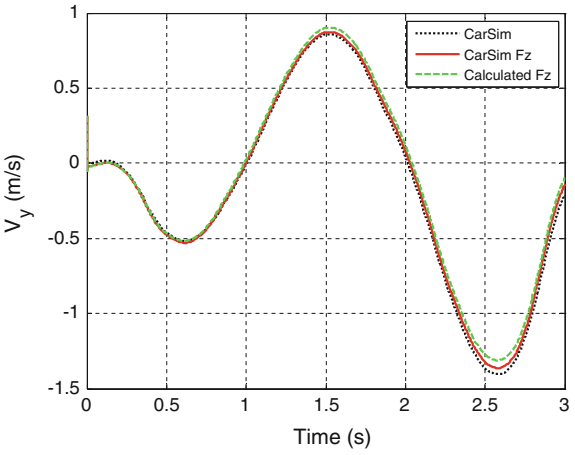

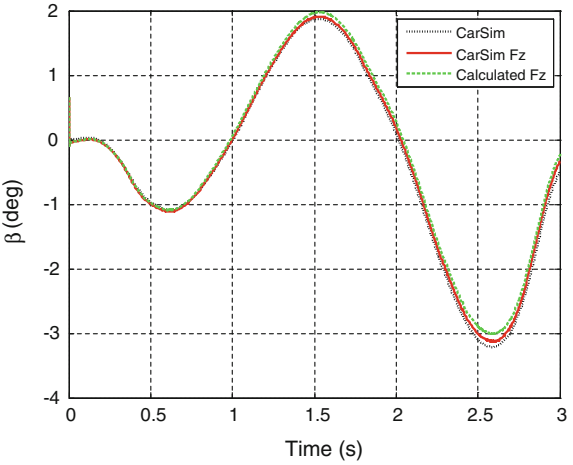

Fig. 6 Estimation of the vehicle side-slip angle

In addition, the lateral velocity is also the basis for estimating the vehicle side-slip angle by using:

$$\hat{\beta} = \arctan\left(\frac{\hat{V}_y}{\hat{V}_x}\right). \tag{39}$$

The second estimate of the lateral velocity (Fig. 5) matches the CarSim standard value almost exactly. The reason for this is the prior consideration of the usage between lateral dynamics (15) and (21) while implementing the EKF algorithm.

The final side-slip angle estimate derived from (39) is favorable, being highly similar to its real value in CarSim (Fig. 6).

5 Conclusions

This study involved applying the EKF algorithm for designing a vehicle side-slip angle and lateral force estimator, and smoothing the sensor measurement noise of an ESP control system. The estimator was derived using a 7-DOF vehicle model that considers nonlinear tire characteristics. Some assumptions in the vehicle and tire models, and the linearization of the state and measurement equations characterized by EKF algorithm were intended to reduce the estimation performance. In future studies, complete nonlinear vehicle and tire models, and methods such as the iterated EKF, adaptive iterated EKF, and unscented Kalman filtering algorithms, can be examined to determine whether they yield improved estimation results. Furthermore, future research can consider estimation algorithms for the vertical forces on each tire and hardware-in-the-loop simulations.

References

1. Leung KT, Whidborne JF, Purby D, Dunoyer A (2011) A review of ground vehicle dynamic state estimations utilizing GPS/INS. Veh Syst Dyn 49(1–2):29–58
2. Wei L, Wenying L, Haitao D, Konghui G (2012) Side-slip angle estimation for vehicle electronic stability control based on sliding mode observer. In: 2012 international conference on measurement, information and control
3. Chen BC, Hsieh FC (2008) Side-slip angle estimation using extended Kalman filter. Veh Syst Dyn 46:353–364
4. Wang W, Yuan L, Tao S, Zhang W, Su T (2010) Estimation of vehicle side-slip angle in nonlinear condition based on the state feedback observer. In: Proceedings of the 2010 IEEE international conference on automation and logistics, 16–20 Aug 2010
5. Doumiati M, Charara A, Victorino A, Lechner D (2013) Vehicle dynamics estimation using Kalman filtering, ISTE Ltd and John Wiley & Sons, Inc
6. Mingli S, Liang C, Jianhua G, Yong F (20100 Estimation of vehicle side-slip angle using hybrid observer. In: Proceedings of the 29th Chinese control conference, 29–31 July 2010
7. Limroth J (2009) Real-time parameter estimation and adaptive stability control. A Dissertation, Presented to the Graduate School of Clemson University
8. Ungoren AY, Peng H (2004) A study on lateral speed estimation methods. Int J Veh Auton Syst 2(1–2)
9. Deng W, Zhang H (2006) RLS-based online estimation on vehicle linear sideslip. In: Proceedings of the 2006 american control conference, 14–16 June 2006
10. Rajamani R (2006) Vehicle dynamics and control. Springer Science and Business Media, Inc., New York
11. Franklin GF, Powell JD (1998) Digital control of dynamic systems, 3rd edn. Addison Wesley Longman, Inc., Menlo Park
12. Chen CK, Dao TK, Lin HP (2010) A compensated yaw-moment-based vehicle stability controller. Int J Veh Des 53(3):220–238

Motion Control System Design for a Barge Type Vessel Moored by Ropes

Anh-Minh D. Tran, Jung-In Yoon and Young-Bok Kim

Abstract These days, the important resources powering industrial societies are oil and natural gas. Because many shallow-water fields already drained, oil companies are turning their attention to resources at ever greater depths. Semi-submersible rigs and drilling ships are used in deep oceans. Station keeping of these types of drilling equipment is the most important task. Therefore, this paper focuses on designing a Position Mooring (PM) system for a barge type surface vessel. We derive a mathematical model of a system including a barge ship and mooring system. In addition, we identify the hydrodynamic coefficients of the low speed model for PM vessel via experiments and simulation and design a proportional-derivative controller (PD controller) based on identified vessel model. The experiments show the performance of the proposed control system.

Keywords Barge ship · Experimental result · Position mooring system · Station keeping · 1/50 scale model ship

1 Introduction

Safety is a primary concern when Floating Production Storage and Offloading (FPSO) units move towards deep water locations because small movements above the water's surface can severely have an impact on the drilling equipment on the

A.-M.D. Tran
Department of Control and Mechanical Engineering, the Graduate School, Pukyong National University, Busan, South Korea

J.-I. Yoon
Department of Refrigeration and Air-Conditioning Engineering, Pukyong National University, Busan, South Korea

Y.-B. Kim (✉)
Department of Mechanical System Engineering, Pukyong National University, Busan, South Korea
e-mail: kpjiwoo@pknu.ac.kr

V.H. Duy et al. (eds.), *AETA 2015: Recent Advances in Electrical Engineering and Related Sciences*, Lecture Notes in Electrical Engineering 371,
DOI 10.1007/978-3-319-27247-4_34

deep ocean floor. Hence offshore vessels should be stable although wind, waves and currents change during drilling operation, production development, etc.

In the 1960s, Dynamic Positioning (DP) systems were developed. These systems simultaneously control of surge, sway and yaw motions. Vessels integrated DP systems are used in station keeping, drilling and offloading, etc. Azimuth thrusters and tunnel thrusters in addition to main propeller equipped on the vessel produce thrust in different directions [1–3]. Balchen et al. [1] introduced a computer-based, dynamic positioning system for floating vessels with Kalman filter for optimal estimation of vessel motions and environmental forces from wind, waves and current. Strand and Fossen [2] presented passive nonlinear observer with adaptive wave filtering for moored and free-floating ships. Pettersen and Fossen [3] solved the problem of under-actuated dynamic positioning of vessel. They developed a time-varying feedback control law including integral action and proved that the control law exponentially stabilizes both the position and orientation of the vessel.

Recently Position Mooring (PM) systems have been designed for ships and floating structures [4, 5]. In these systems, a deployed anchor system with the assistance of thrusters maintains vessel at desired position or predefined trajectory. The PM system is more efficient than DP system because it decreases the level of thrust needed, reduces the operational cost as well as risk. Sorensen et al. [4] outlined a thruster assisted position mooring system that can reduce possible large oscillatory motions, keep the vessel at a fixed position and heading and move vessel along position and heading set-points specified by the operator. Verification tests were done on turret-anchored Varg FPSO equipped with 3 identical azimuth thrusters and 10 anchor lines, spread out in a symmetrical pattern. Strand et al. [5] developed a new model-based multivariable control strategy accounting for both horizontal and vertical motions, with the exception of heave. A 45,000t dynamically positioned semi-submersible equipped with four azimuth thrusters and a spread mooring system is used to simulate and demonstrate the effect of proposed method. The results showed that the new controller saved more energy than the conventional design.

Our study is different with existing PM designs. There is no thruster and the mooring ropes work as the only actuator for controlling vessel motion. The tensions of mooring ropes are controlled by linear motion actuators equipped on the vessel and measured by load cells. As well known, the more hydrodynamic coefficients are precisely identified, the more maneuvering or station keeping ability of vessel is increased. Thus parameters of model ship are identified from experiments and simulations. Finally, the proposed system is applied and evaluated on the 1/50 scale barge ship model with proportional-derivative controller (PD controller).

2 Mathematical Model

The 3 DOF low frequency equations of motion in surge, sway and yaw of the floating vessel are generally formulated as follows [6]:

$$\begin{aligned} \dot{\boldsymbol{\eta}} &= \mathbf{T}(\psi)\mathbf{v}, \\ \mathbf{M}\underline{\mathbf{v}} + \mathbf{D}\mathbf{v} &= \boldsymbol{\tau} \end{aligned} \tag{1}$$

where $\boldsymbol{\eta} = [x, y, \psi]^{\mathrm{T}} \in \mathbf{R}^3$ represents inertial position (x, y) and heading angle ψ in the earth fixed coordinate frame, and $\mathbf{v} = [u, v, r]^{\mathrm{T}} \in \mathbf{R}^3$ describes the surge, sway and yaw rate of ship motion in the body fixed coordinate frame. The rotation matrix in heading direction $\mathbf{T}(\psi) \in \mathbf{R}^{3\times3}$ describes the kinematic equation of motion; that is

$$\mathbf{T}(\varphi) = \begin{bmatrix} \cos\psi & -\sin\psi & 0 \\ \sin\psi & \cos\psi & 0 \\ 0 & 0 & 1 \end{bmatrix}. \tag{2}$$

$\mathbf{M} \in \mathbf{R}^{3\times3}$ is the system inertia matrix including added mass, $\mathbf{D} \in \mathbf{R}^{3\times3}$ is the damping matrix, $\boldsymbol{\tau} \in \mathbf{R}^3$ is the vector of control inputs.

Our vessel is equipped with 4 rope mooring systems. The rope is attached at one end to the vessel via a spindle axes's slide and a pulley system and the other end is fixed to the wall of the model basin.

The vector of control inputs can be given by the following expression:

$$\boldsymbol{\tau} = \mathbf{B}(\alpha)\mathbf{f} \tag{3}$$

where $\mathbf{f} \in \mathbf{R}^4$ presents tension of mooring ropes and $\mathbf{B}(\alpha) \in \mathbf{R}^{3\times4}$ is the mooring rope configuration matrix. Then, this matrix can be defined as

$$\mathbf{B}(\alpha) = \begin{bmatrix} \cos\alpha_1 & \ldots & \cos\alpha_4 \\ \sin\alpha_1 & \ldots & \sin\alpha_N \\ x_1\sin\alpha_1 - y_1\cos\alpha_1 & \ldots & x_4\sin\alpha_4 - y_4\cos\alpha_4 \end{bmatrix} \tag{4}$$

where x_i, y_i and α_i are moment arms and angle, between mooring rope and X axis of vessel as shown in Fig. 1.

3 Hydrodynamic Coefficients Estimation

For simplicity, it is assumed that the vessel has homogeneous mass distribution, xz and yz plane symmetry as well as the center of gravity coincides with center of geometry. This allows for the following reduction of the inertia and damping matrix:

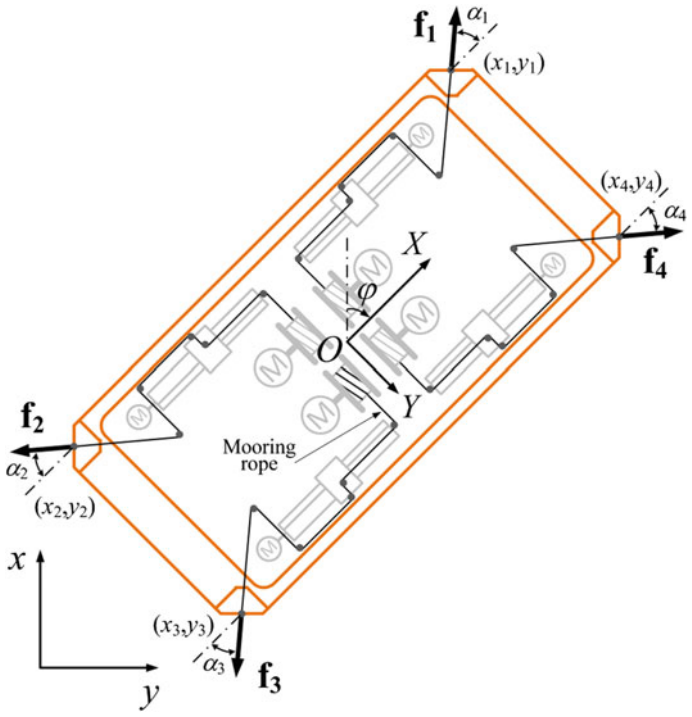

Fig. 1 Mooring rope configuration in vessel motion control system

$$\mathbf{M} = \begin{bmatrix} m - X_{\dot{u}} & 0 & 0 \\ 0 & m - Y_{\dot{v}} & 0 \\ 0 & 0 & I_z - N_{\dot{r}} \end{bmatrix}, \quad \mathbf{D} = \begin{bmatrix} -X_u & 0 & 0 \\ 0 & -Y_v & 0 \\ 0 & 0 & -N_r \end{bmatrix} \tag{5}$$

Motions of the vessel in surge, sway and yaw direction are decoupled based on this assumption. Substituting (5) into (1) gives the mathematical equations for system parameter identification:

$$\begin{cases} (m - X_{\dot{u}})\dot{u} - X_u u = \tau_x \\ (m - Y_{\dot{v}})\dot{v} - Y_v v = \tau_y \\ (I_z - N_{\dot{r}})\dot{r} - N_r r = \tau_\varphi \end{cases} \tag{6}$$

where $\tau_x, \tau_y, \tau_\varphi$ are pulling forces in surge, sway and yaw direction, respectively.

In order to estimate the hydrodynamic coefficients of **M** and **D** matrix, the vessel is tested in the model basin. The vessel has a mass m: 215 kg, length L: 2 m and breath B: 1 m. Vessel motion data are obtained by pulling the vessel in surge, sway and yaw direction. To obtain objective and accurate data, 10 times more experiments have been performed.

Once the load cell measures the amplitude of the pulling force, the load cell amplifier is then used for signal conditioning such that the signal can be amplified and converted into an output value. The analog input module and real-time controller takes and saves these values. Host computer collects these pulling force data via wireless router. Motions in the x, y direction and rotation about z axis are obtained by using camera system.

For instance, considering the surge motion, then the 1st equation of (6) is used to estimate parameters $m - X_{\dot{u}}$ of system inertia matrix and X_u of damping matrix. Measured pulling force data is fed into τ_x. Then $m - X_{\dot{u}}$ and X_u are found by tuning and matching numerical simulation data with experimental data.

Based on above method, all data about surge, sway and yaw motions are obtained. Using the experiment results, the unknown parameters appeared in hydrodynamic matrix **M** and **D** are calculated by simulation. In the results, the partially unknown hydrodynamic matrix **M** and **D** are obtained as follows:

$$\mathbf{M} = \begin{bmatrix} 351.2 & 0 & 0 \\ 0 & 332.4 & 0 \\ 0 & 0 & 113.2 \end{bmatrix}, \quad \mathbf{D} = \begin{bmatrix} 11.44 & 0 & 0 \\ 0 & 12.17 & 0 \\ 0 & 0 & 7.36 \end{bmatrix} \tag{7}$$

4 Controller Design and Experiment Results

With small angle $\delta\psi$ the expression (2) simplifies to

$$\mathbf{T}(\varphi) \approx \begin{bmatrix} 1 & -\delta\psi & 0 \\ \delta\psi & 1 & 0 \\ 0 & 0 & 1 \end{bmatrix} \approx \mathbf{I}_{3\times 3} \tag{8}$$

Under this assumption, the model of vessel (1) becomes

$$\begin{aligned} \dot{\boldsymbol{\eta}} &= \mathbf{v}, \\ \mathbf{M}\ddot{\boldsymbol{\eta}} + \mathbf{D}\dot{\boldsymbol{\eta}} &= \boldsymbol{\tau} \end{aligned} \tag{9}$$

Substituting identified hydrodynamic matrix **M** and **D** into Eq. (9) yields

$$\begin{bmatrix} 351.2 & 0 & 0 \\ 0 & 332.4 & 0 \\ 0 & 0 & 113.2 \end{bmatrix} \begin{bmatrix} \ddot{x} \\ \ddot{y} \\ \ddot{\psi} \end{bmatrix} + \begin{bmatrix} 11.44 & 0 & 0 \\ 0 & 12.17 & 0 \\ 0 & 0 & 7.36 \end{bmatrix} \begin{bmatrix} \dot{x} \\ \dot{y} \\ \dot{\psi} \end{bmatrix} = \begin{bmatrix} \tau_x \\ \tau_y \\ \tau_\psi \end{bmatrix} \tag{10}$$

The next step is to design controller for each motion direction. For instance, considering the surge motion

$$351.2\ddot{x} + 11.44\dot{x} = \tau_x \tag{11}$$

Let PD controller be written as:

$$\tau_{PD\_x} = K_{p\_x}\tilde{x} + K_{d\_x}\dot{\tilde{x}} \tag{12}$$

where $\tilde{x} = x_d - x$, x: actual motion vector, and x_d: desired motion vector for surge position.

Suppose the criteria for the controller are settling time <10 s and overshoot <5 %. Then relative damping ratio is $\zeta = 0.6901$ and natural frequency is $\omega_n = 0.4341$. Using pole placement algorithm with poles defined above, proportional and derivative gains of controller are obtained:

$$\begin{aligned} K_{p\_x} &= 351.2\left(\omega_n^2\right) = 66.1802 \\ K_{d\_x} &= 351.2(2\zeta\omega_n) - 11.44 = 198.9802 \end{aligned} \tag{13}$$

Similarly, gains of controllers in sway and yaw motions are calculated. The resulting PD control gains $\mathbf{K}_p$ and $\mathbf{K}_d$ are:

$$\begin{aligned} \mathbf{K}_p &= \begin{bmatrix} 66.1802 & 0 & 0 \\ 0 & 62.6375 & 0 \\ 0 & 0 & 21.3314 \end{bmatrix}, \\ \mathbf{K}_d &= \begin{bmatrix} 198.9802 & 0 & 0 \\ 0 & 186.9863 & 0 \\ 0 & 0 & 60.4634 \end{bmatrix} \end{aligned} \tag{14}$$

The next step is to apply the designed controller to control the vessel motion. Figure 2 shows the experimental setup. As illustrated in this figure, the control system (NI CompactRIO) is placed on the vessel and the CCD camera attached on the celling to capture the vessel motions.

The information including vessel motions and all sensing signals are transferred to the monitoring system (Host Computer) by the wireless network. Using the vector code correlation technique, vessel motions (surge, sway motions and yaw angle) are calculated in real time [7]. Then the calculated positions and yaw angle are sent to the control system (NI CompactRIO) placed on the vessel.

The controlled vessel is a barge type in which the mooring system is installed with 4 mooring ropes. And they are properly interconnected between the vessel through four sail winches and the wall of the basin. In addition, on the keel of the vessel, there are four linear motion actuators.

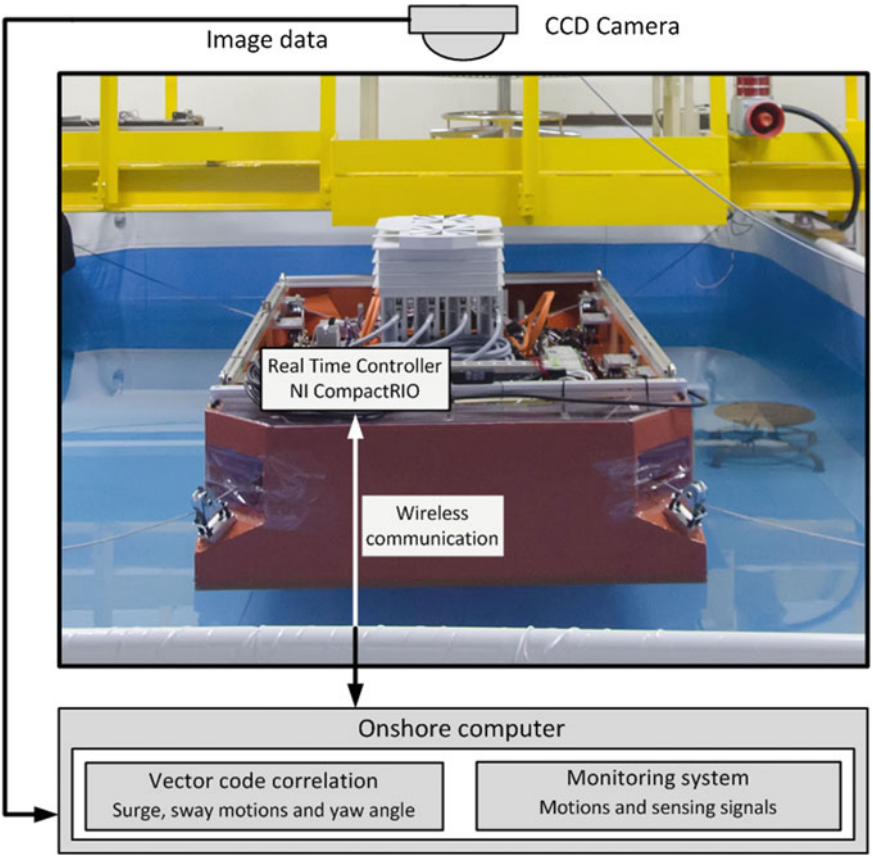

Fig. 2 Photo of the experimental setup

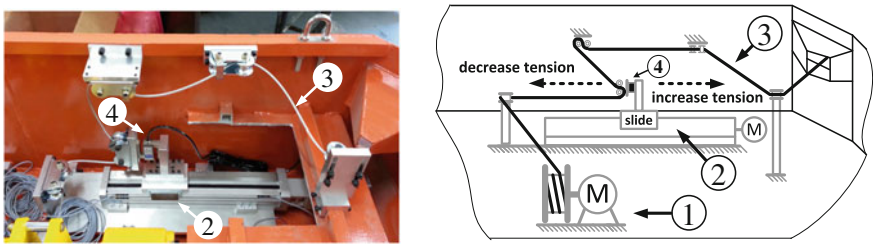

Fig. 3 Operation of linear motion actuator to control rope tension. (① winch, ② linear motion actuator, ③ rope and ④ load cell)

Figure 3 describes how the linear motion actuators work to control rope tensions. In this figure, rope is connected between winch and the wall of the model basin. The linear actuator is installed on the keel controls tension by pulling or releasing the

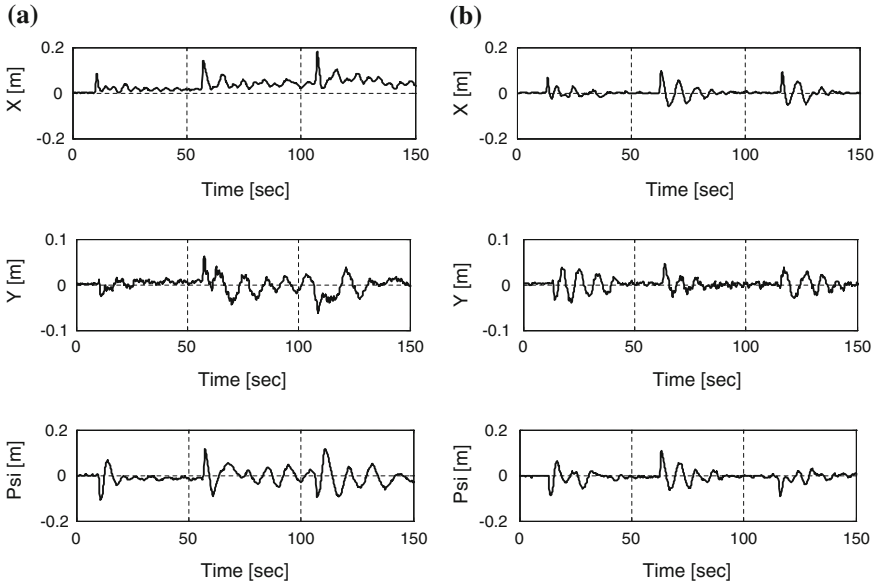

Fig. 4 **a** Vessel motions in wave disturbance without control and **b** Station keeping experiment result in wave disturbance by using PD control

rope. The rope tension increases when the linear actuator moves to the right side. On the other hand, we can decrease the rope tension by moving the actuator to the left side.

Firstly, Fig. 4a shows the vessel motions (surge, sway positions and yaw angle, respectively) of the uncontrolled case. Even though the vessel is slightly restricted by the ropes, we can see that the influence of the wave attack remains for long time. On the other hand, Fig. 4b shows the controlled case, PD controller operates and the environmental condition is same as the uncontrolled case. The vessel is affected by wave disturbance, but the surge, sway positions and yaw heading angle return to the initial state after a short time. The result explains that the proposed vessel motion control strategy can cope with disturbance.

5 Concluding Remarks

In this paper, we proposed new motion control system design for a barge type vessel moored by ropes. For this purpose, we presented a tension control method only using the linear actuator system without any propelling system. Hydrodynamic coefficients were estimated through experiments and simulations. After that, we designed controller to keep vessel position. The experiment results with PD controller proved that the proposed control strategy can work well. However in real

operating condition weight and center of gravity of vessel may change. Next we will extend this research and apply robust or adaptive control method to solve these problems.

Acknowledgments This research was supported by the Basic Science Research Program through the National Research Foundation of Korea (NRF) funded by the Ministry of Education, Science and Technology (2012R1A1A2039012).

References

1. Balchen JG, Jenssen NA, Mathisen E, Sælid S (1980) A dynamic positioning system based on Kalman filtering and optimal control. Model Ident Control 1(3):135–163
2. Strand JP, Fossen TI (1999) Nonlinear passive observer for ships with adaptive wave filtering. In: Nijmeijer H, Fossen TI (eds) New directions in nonlinear observer design, pp 113–134
3. Pettersen KY, Fossen TI (2000) Underactuated dynamic positioning of a ship—experimental results. IEEE Trans Control Syst Technol 8(5):856–863
4. Strand JP, Sørensen AJ, Fossen TI (1998) Design of automatic thruster assisted position mooring systems for ships. Model Ident Control 19(2):61–75
5. Sørensen A, Strand JP, Fossen TI (1999) Thruster assisted position mooring system for turret anchored FPSOs. In: Proceedings of the IEEE international conference on control applications (CCA'99), Hawaii
6. Fossen TI (2002) Marine control system guidance, navigation, rigs and underwater vehicle. Norwegian University of Science and Technology, Trondheim
7. Kawai H, Kim YB, Choi Y (2012) Measurement of a container crane spreader under bad weather conditions by image restoration. IEEE Trans Instrum Meas 61(1):35–42

A Novel Advanced Controller for Robust Stability of High Order Plants with Time-Delay and Uncertainty

Ho Pham Huy Anh and Nguyen Ngoc Son

Abstract This paper introduces a new graphical design method for obtaining the full range of advanced PID control gains that robustly stabilize a system in the presence of time delays and additive uncertainty. This proposed design method primarily depends on the frequency response of the system, which proves effective to reduce the complexities involved in plant modelling and identification. The fact that time-delays and parametric uncertainties are almost always present in real time processes makes this proposed controller design method very promising for process control. For testing, this new design method was applied to control a DC motor system with a communication delay. The simulation results were satisfactory and the robust stability was achieved for this perturbed plant.

Keywords Robust PID controller · Graphical design method · High-order plants · DC motor with communication delay · Modeling and identification · Robust stability

1 Introduction

Up to now, there were lots of works which have done in concentrated in finding advanced PID controllers that stabilize an industrial plant model. Bhattacharyya et al. introduced a mathematical generalization of the Hermite theorem to determine all stabilizing PID controllers available for systems with time-delay [1, 2]. In [3, 4] an innovative controller design method, not required complex mathematical derivation, was proposed. The authors of [3, 4] improved their research by fixing the full range of PID controllers that satisfied the gain and phase margin requirements. Techniques for determining all achievable PID controllers robust stabilized an arbitrary order system and satisfied weighted and complementary sensitivity,

H.P.H. Anh (✉) · N.N. Son
FEEE, DCSELAB, Ho Chi Minh City University of Technology, Vnu-Hcm, Vietnam
e-mail: hphanh@hcmut.edu.vn

V.H. Duy et al. (eds.), *AETA 2015: Recent Advances in Electrical Engineering and Related Sciences*, Lecture Notes in Electrical Engineering 371,
DOI 10.1007/978-3-319-27247-4_35

robust stability and performance constraints were introduced in [4–8]. New PID control approaches were proposed for reducing Area Control Error (ACE), and the stability of a power operation system in [9–14]. In [11], a PI controller was designed for AGC control of a two-area reheat thermal system where a new ACE method was applied. An offline genetic algorithm (GA) method was introduced in [12] to optimize PI controller gains for a single power system with multi-source power generation. In [13], a hybrid neuro-fuzzy controller was implemented for AGC control of two interconnected power systems. The authors in [14] proposed an H∞ robust controller for a single-input multiple-output (SIMO) nonlinear hydro-turbine generation model.

In this paper, a graphical design method to get the optimal PI/PID controller gains to achieve robust stability for arbitrary order plants with time-delay and parametric uncertainty is investigated. Additive uncertainty modelling is applied as to model the entire uncertainty set. The controller design methodology is initiatively proposed to determine if the uncertain plant remains stable for the entire uncertainty set. The frequency domain application of this new design method helps to reduce the complexities of plant identification. This control design method is then implemented to a DC motor model with time-delay. In such test, advanced PID controller gains are demonstrated that they will guarantee the robust and closed loop stability.

The rest of this paper is organized as follows. In Sect. 2, the mathematical formulation of the novel proposed controller design method is presented. Application system with time-delay of this new control design method is investigated in Sect. 3. Finally, Sect. 4 summarizes the results obtained in this research.

2 Design Methodology

In this section, the mathematical formulations will be discussed that are most vital in order to obtain the set of advanced PID controller gains that will enable us to fix the nominal stability boundary and robust stability range for an arbitrary perturbed plant with additive uncertainty, while ensuring closed loop stability.

In Fig. 1, a SISO and linear time invariant (LTI) system with additive uncertainty is considered. Here $G_p(s)$ is the investigated plant, K(s) is the PID controller, and WA(s) is the additive weight. R(s) and Z(s) are the referential input signal and the weighted output signal, respectively [4].

From Fig. 1, it represents the perturbed plant which includes $\Delta_A(s)$, which is any stable transfer function with $|\Delta_A(j\omega)| \leq 1 \; for \; \forall\omega$. The transfer functions of principal blocks in Fig. 1 can be represented in the frequency domain as follows,

$$G_p(j\omega) = \mathrm{Re}(\omega) + \mathrm{jIm}(\omega) \tag{1a}$$

$$K(j\omega) = K_p + \frac{K_i}{j\omega} + K_d j\omega \tag{1b}$$

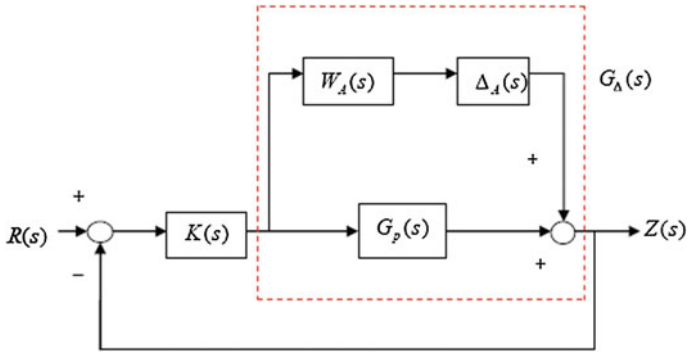

Fig. 1 Block diagram of system with additive uncertainty weight

$$W_A(j\omega) = A_A(\omega) + jB_A(\omega) \tag{1c}$$

In order to achieve robust stability for the perturbed system, it is necessary to find all PID controller gains that stabilize the closed loop system for the full range of uncertainties. This purpose can be accomplished if the investigated plant is stable and the following robust stability constraint is satisfied,

$$\|W_A(j\omega)K(j\omega)S(j\omega)\|_\infty \leq \gamma \tag{2}$$

where $S(j\omega)$ is the sensitivity function and $\gamma = 1$.

$$S(j\omega) = \frac{1}{1 + G_p(j\omega)K(j\omega)} \tag{3}$$

The weighted sensitivity constraint of the investigated system can be expressed as;

$$W_A(j\omega)K(j\omega)S(j\omega) = |W_A(j\omega)K(j\omega)S(j\omega)|e^{j\angle W_A(j\omega)K(j\omega)S(j\omega)} \tag{4}$$

Then the robust stability constraint can be rewritten as,

$$W_A(j\omega)K(j\omega)S(j\omega)e^{j\theta_A} \leq \gamma \text{ for } \forall\omega \tag{5}$$

$$\frac{W_A(j\omega)K(j\omega)}{1 + G_p(j\omega)K(j\omega)}e^{j\theta_A} \leq \gamma \text{ for } \forall\omega \tag{6}$$

where $\theta_A = \angle W_A(j\omega)K(j\omega)S(j\omega)$.

Hence Eq. (6) should be satisfied with some values of $\theta_A \in [0, 2\pi]$. As known, all PID controllers, satisfying Eq. (2), have to lie at the intersection of all controllers that meet Eq. (5) for all $\theta_A \in [0, 2\pi]$.

For each value of $\theta_A \in [0, 2\pi]$, it is necessary to find all PID controllers on the boundary of Eq. (6). It can reduce from Eq. (6), that all the PID controllers on the boundary must satisfy

$$P(\omega, \theta_A, \gamma) = 0 \tag{7}$$

where the characteristic polynomial $P(\omega, \theta_A, \gamma)$ can be represented as,

$$P(\omega, \theta_A, \gamma) = 1 + \mathrm{G}_p(j\omega)K(j\omega) - \frac{1}{\gamma}\left\{W_A(j\omega)K(j\omega)e^{j\theta_A}\right\} \tag{8}$$

Now, by substituting the frequency responses represented by Eq. (1a–1c), and replace $e^{j\theta_A} = \cos\theta_A + j\sin\theta_A$ into (8), we have,

$$\begin{aligned} P(\omega, \theta_A, \gamma) = 1 &+ \left((\mathrm{Re}\omega + j\,\mathrm{Im}(\omega))\left(K_p + \frac{K_i}{j\omega} + K_{d^{j\omega}}\right)\right) \\ &- \left(\frac{1}{\gamma}(A_A(\omega) + jB_A(\omega))\left(K_p + \frac{K_i}{j\omega} + K_d j\omega\right)(\cos\theta_A + j\sin\theta_A\right) \end{aligned} \tag{9}$$

Let $\gamma \to \infty$, (9) reduces to the general characteristic polynomial. Thus, the nominal stability boundary can be obtained for $\gamma \to \infty$. Expanding (7) into real and imaginary parts yields

$$\begin{aligned} X_{R_p}K_P + X_{R_i}K_i + X_{R_d}K_d &= 0 \\ X_{I_p}K_P + X_{I_i}K_i + X_{I_d}K_d &= -\omega \end{aligned} \tag{10}$$

where the real components are given by

$$\begin{aligned} X_{R_p} &= -\omega\left(\mathrm{Im}(\omega) + \frac{1}{\gamma}(A_A\sin\theta_A + B_A\cos\theta_A)\right) \\ X_{R_i} &= \left(\mathrm{Re}(\omega) + \frac{1}{\gamma}(A_A\cos\theta_A + B_A\sin\theta_A)\right) \\ X_{R_d} &= -\omega^2\left(\mathrm{Re}(\omega) + \frac{1}{\gamma}(A_A\cos\theta_A + B_A\sin\theta_A)\right) \end{aligned} \tag{11}$$

And the imaginary components are given by

$$\begin{aligned} X_{I_p} &= \omega\left(\mathrm{Re}(\omega) + \frac{1}{\gamma}(A_A\cos\theta_A + B_A\sin\theta_A)\right) \\ X_{I_i} &= \left(\mathrm{Im}(\omega) + \frac{1}{\gamma}(A_A\sin\theta_A + B_A\cos\theta_A)\right) \\ X_{I_d} &= -\omega^2\left(\mathrm{Im}(\omega) + \frac{1}{\gamma}(A_A\sin\theta_A + B_A\cos\theta_A)\right) \end{aligned} \tag{12}$$

The boundary of $P(\omega, \theta_A, \gamma) = 0$ for the (K_p, K_i) plane for a constant K_d value is determined using Eq. (10), which can be rewritten as

$$\begin{bmatrix} X_{R_p} & X_{R_i} \\ X_{I_p} & X_{I_i} \end{bmatrix} \begin{bmatrix} K_P \\ K_i \end{bmatrix} = \begin{bmatrix} 0 - X_{R_d}\bar{K}_d \\ -\omega - X_{I_d}\bar{K}_d \end{bmatrix} \tag{13}$$

Solving (13) for all $\omega \neq 0$ and $\theta_A \in [0, 2\pi]$, the controller gains are obtained as follows,

$$K_p(\omega, \theta_A, \gamma) = \frac{-\mathrm{Re}(\omega) - \frac{1}{\gamma}(A_A \cos\theta_A - B_A \sin\theta_A)}{X(\omega)} \tag{14}$$

$$K_I(\omega, \theta_A, \gamma) = \omega^2 \bar{K}_d + \frac{-\omega\left(\mathrm{Im}(\omega) - \frac{1}{\gamma}(A_A \sin\theta_A - B_A \cos\theta_A)\right)}{X(\omega)} \tag{15}$$

with

$$\begin{aligned} X(\omega) &= \left|G_p(j\omega)\right|^2 + \frac{1}{\gamma^2}|W_A(j\omega)|^2 + \frac{2}{\gamma}\begin{pmatrix} \mathrm{Re}(\omega)(\mathrm{A}_A cos\theta_A - \mathrm{B}_A sin\theta_A) \\ +\mathrm{Im}(\omega)(\mathrm{A}_A \sin\theta_A - \mathrm{B}_A \cos\theta_A) \end{pmatrix} \\ \left|G_p(j\omega)\right|^2 &= \mathrm{Re}^2(\omega) + \mathrm{Im}^2(\omega) \\ |W_A(j\omega)|^2 &= A_A^2(\omega) + B_A^2(\omega) \end{aligned} \tag{16}$$

By setting $\omega = 0$ from Eqs. (11)–(13) yields

$$\begin{bmatrix} 0 & X_{R_i}(0) \\ 0 & X_{I_i}(0) \end{bmatrix} \begin{bmatrix} K_p \\ K_i \end{bmatrix} = \begin{bmatrix} 0 \\ 0 \end{bmatrix} \tag{17}$$

It concludes that $K_p(0, \theta_A, \gamma)$ is arbitrary and $K_i(0, \theta_A, \gamma) = 0$ unless Im(0) = Re (0) = 0which holds only when $G_p(s)$ has a zero at the origin.

3 Advanced PID Control Applied on DC Motor System with Communication Time-Delay

In this section, the novel control method is applied to control a DC motor model with a communication time-delay, as shown in Fig. 2 where G(s) is the transfer function of the DC motor, K(s) is the PID controller, and $e^{-\tau s}$ represents the τ second communication time-delay, R(s) and Y(s) are reference input and output, respectively.

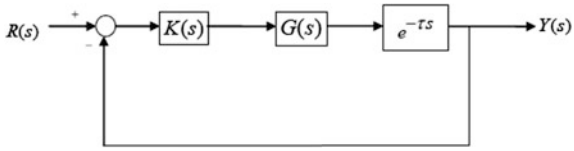

Fig. 2 DC motor model with time delay

3.1 Design Goal

The design goal is to find a set of PID controllers ensured robust stability constraint

$$\|W_A(j\omega)K(j\omega)S(j\omega)\|_\infty \leq \gamma \tag{18}$$

is satisfied for $\gamma = 1$, hence ensuring nominal and robust stability for the perturbed plant. Here W_A $(j\omega)$, K $(j\omega)$, *and* S $(j\omega)$ are the additive uncertainty weight, PID controller, and sensitivity function given in Eq. (3), respectively.

3.2 Plant Model

The transfer function model of the investigated DC motor can be represented as

$$G(s) = \frac{65.5}{s(s+34.6)} \tag{19}$$

In this paper, the range of the unknown communication time-delay is

$$\tau \in [0.05, 0.15] \tag{20}$$

The nominal model of the DC motor for controller design is chosen to be

$$G_p(s) = \frac{65.5}{s(s+34.6)} e^{-\bar{\tau}s} \tag{21}$$

where $\bar{\tau}$ is selected to be the mean value of the time delay range, i.e., $\bar{\tau} = 0.1$.

3.3 Designing Additive Uncertainty Weight

As known, the parametric and un-modelled dynamics uncertainty can be combined into a single lumped perturbation of a chosen structure. Here, an additive uncertainty structure is considered in order to overrun the range of uncertainties implied in the plant.

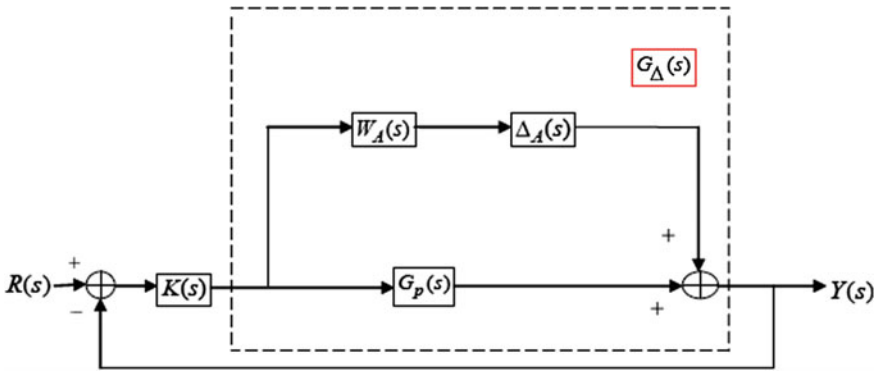

Fig. 3 Additive uncertainty representation for DC motor with time delay

Figure 3 represents an additive uncertainty structure used for the uncertain model.

The uncertain DC motor model is represented as,

$$G_\Delta(s) = G_p(s) + W_A(s)\Delta_A(s) \tag{22}$$

where $\Delta_A(s)$ is any stable transfer function for $\forall\omega$ [4],

$$\|\Delta_A(j\omega)\| \leq 1 \tag{23}$$

In which,

$$|\triangle_A(\mathrm{j}\omega)| = \left|\frac{G_\triangle(j\omega) - G(j\omega)}{W_A(j\omega)}\right| \tag{24}$$

Combining Eq. (23) and (24) we obtain,

$$\left|\frac{G_\triangle(\mathrm{j}\omega) - G_p(\mathrm{j}\omega)}{W_A(\mathrm{j}\omega)}\right| \leq 1, \forall\omega \tag{25}$$

Therefore in order to cover the entire uncertainty set, it is required to find an additive uncertainty weight $W_A(s)$ such that

$$|W_A(\mathrm{j}\omega)| \geq \left|G_\triangle(\mathrm{j}\omega) - G_p(\mathrm{j}\omega)\right| \tag{26}$$

where

$$\left|G_\triangle(\mathrm{j}\omega) - G_p(\mathrm{j}\omega)\right| = \left|\frac{65.5}{\mathrm{j}\omega(\mathrm{j}\omega + 34.6)}\right|\left|e^{-\tau\mathrm{j}\omega} - e^{-\bar{\tau}\mathrm{j}\omega}\right|$$

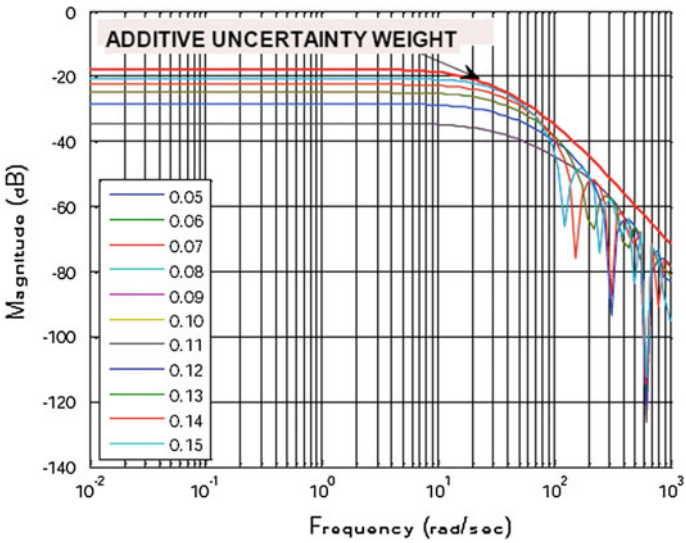

Fig. 4 The additive uncertainty weight

i.e., the additive uncertainty weight is designed such that,

$$|W_A(\mathrm{j}\omega)| \geq \left|\frac{65.5}{\mathrm{j}\omega(\mathrm{j}\omega + 34.6)}\right| \left|e^{-\mathrm{j}\tau\omega} - e^{-\mathrm{j}\bar{\tau}\omega}\right| \tag{27}$$

We choose the following form for the weight,

$$W_A(s) = \frac{M_h}{(\mathrm{s}/\omega_{c_1} + 1)(\mathrm{s}/\omega_{c_2} + 1)} \tag{28}$$

The additive weight transfer function obtained was,

$$W_A(s) = \frac{0.13}{(\mathrm{s}/20.67 + 1)(\mathrm{s}/100 + 1)} \tag{29}$$

Figure 4 shows the additive uncertainty weight that bounds entire uncertainty set.

3.4 *Finding Robust PID Controllers in* ($\mathbf{K_p}$, $\mathbf{K_i}$) *Plane with Constant Value of* $\mathbf{K_d}$

In this section, using the design methodology explained in Sect. 2, the set of PID controllers that will ensure robust stability in the (K_p, K_i) plane for a constant value

of K_d. The DC motor model $G(s)$ is as presented in Eq. (33). As explained in Sect. 2, with K_d constant, it is possible to obtain the entire set of PID controllers at the boundary of $P(\omega, \theta_A, \gamma) = 0$ in the (K_p, K_i) plane. In this paper, $\bar{K}_d = 0.2$.

Using Eqs. (14) and (15), the nominal stability boundary and robust stability region are obtained in the (K_p, K_i) plane. As discussed in Sect. 2, the PID nominal stability boundary of the plant can be obtained by setting $\gamma \to \infty$. PID controllers that satisfy the robust stability constraint in Eq. (32) are found by setting $\gamma = 1$ and then finding the intersection of all regions for $\theta_A \in (0, 2\pi)$.

The region that satisfies the robust stability constraint and the nominal stability boundary in the (K_p, K_i) plane for K_d = 0.2 is shown in Fig. 5.

The intersection of all regions inside the nominal stability boundary of the (K_p, K_i) is the robust stability region.

To verify the results, a PID controller, $K_1(s)$ is selected from the robust stability region and another PID controller, $K_2(s)$ is selected from outside this region.

$$K_1(s) = 3.6763 + \frac{3.0994}{s} + 0.2s \tag{30}$$

$$K_2(s) = 4.8675 + \frac{2.9825}{s} + 0.2s \tag{31}$$

Substituting (30) and (29) into (18) give,

$$\|W_A(j\omega)K_1(j\omega)S(j\omega)\|_\infty = 0.8289$$

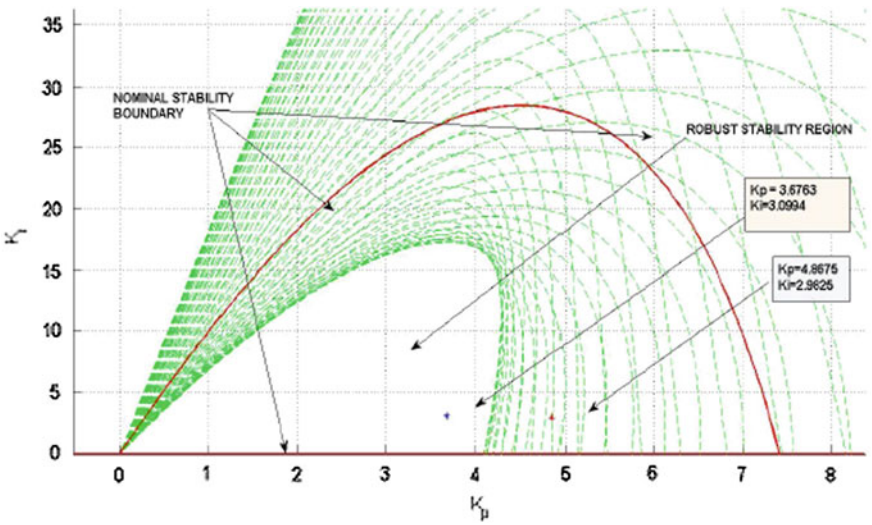

Fig. 5 Nominal stability boundary and robust stability region for K_p and K_i values

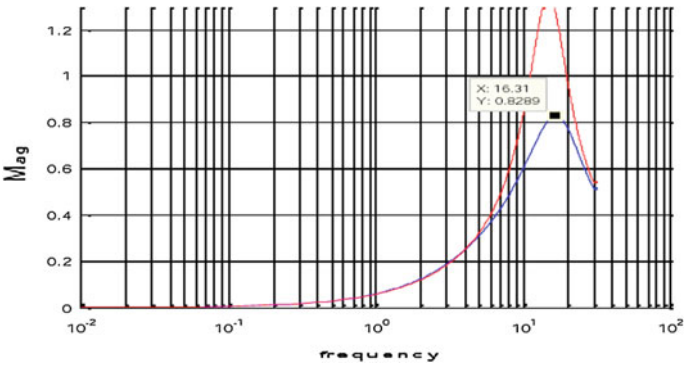

Fig. 6 Bode plot for PID controller, $K_1(s)$ and $K_2(s)$ selected from the (K_p, K_i) plane

Repeating this process for Eqs. (29) and (31) results in

$$\|W_A(j\omega)K_2(j\omega)S(j\omega)\|_\infty > 1$$

Figure 6 shows the Bode plot for PID controller, $K_1(s)$ and $K_2(s)$ selected from the (K_p, K_i) plane.

Thus, the PID controller selected from the robust stability region clearly satisfies the robust stability constraint while the other does not. After repeated simulations done in MATLAB it can be concluded that any controller selected from inside the robust stability region will enable robust stability for the perturbed system. Thus, the design goal is met in this plane.

In summary, a graphical design method for obtaining all PID controllers that will satisfy a robust stability constraint for a DC motor with time delay was discussed. Observing the results in Sects. 3.4 it can be concluded that the PID controllers selected from the robust stability regions in the (K_p, K_i) planes satisfy the robust stability constraint for the time-delay DC motor model.

4 Conclusion

In this paper, a graphical design method was introduced for finding all achievable PI/PID compensators that ensured nominal stability and robust stability for any arbitrary order nonlinear plant with additive uncertainty. This compensator design method may reduce the complexities involved in plant modelling as it was based on the frequency response of the plant rather than the plant transfer function coefficients. A cascade DC motor model with time delay was studied to demonstrate the application of this design method. AGC and its role in power generation control were also discussed. The results were satisfactory as the weighted sensitivity constraints were satisfied for our selected PID/PI compensators.

Acknowledgments This research is funded by Vietnam National Foundation for Science and Technology Development (NAFOSTED) and the DCSELAB, VNU-HCM, Vietnam.

References

1. Ho KW, Datta A, Bhattacharya SP (2003) PID stabilization of LTI plants with time-delay. In: Proceedings of the 42nd IEEE conference on decision and control, Maui, Hawaii
2. Bhattacharyya SP, Keel LH (2005) PID controller synthesis free of analytical methods. In: Proceedings of the IFAC 16th triennial world congress, Prague, Czech Republic
3. Sujoldzic S, Watkins JM (2006) Stabilization of an arbitrary order transfer function with time delay using PI and PD controllers. Proceedings of the american control conference, pp 2427–2432
4. Sujoldzic S, Watkins JM (2005) Stabilization of an arbitrary order transfer function with time delay using PID controller. Proceedings of the IEEE conference on decision and control, vol 45, Dec 2005
5. Emami T, Watkins JM (2008) Weighted sensitivity design of PID controllers for arbitrary-order transfer functions with time-delay. Proceedings of the IASTED international conference on intelligent systems and control, pp 20–25
6. Emami T, Watkins JM (2009) Robust stability design of PID controllers for arbitrary-order transfer functions with uncertain time delay. In: South-eastern symposium on system theory. University of Tennessee Space Institute, pp 184–189
7. Emami T, Watkins JM(2008) Complementary sensitivity design of PID controllers for arbitrary-order transfer functions with time delay. Proceedings of the 2008 ASME dynamic systems and control conference, Oct 2008
8. Emami T, Watkins JM (2009) Robust performance characterization of PID controllers in the frequency domain. WSEAS Trans J Syst Control 4(5):232–242
9. Jaleeli N, Vansiyck L, Ewart D, Fink L, Hoffmann AG (1992) Understanding automatic generation control. Trans Power Syst 7(3):1106–1111
10. Athay TM (1987) Generation scheduling and control. Proc IEEE 75(12):1592–1605
11. Kothari NL, Nanda J, Kothari DP, Das D (1989) Discrete-mode automatic generation control of a two-area reheat thermal system with new area control error. IEEE Trans Power Syst 4(9):730–736
12. Ramakrishna KSS, Bhatti TS (2007) Automatic generation control of single area power system with multi-source power generation. Proc IMechE Power Energy 222(A):1–11
13. Panda G, Panda S, Ardil C (2009) Automatic generation control of interconnected power system with generation rate constraints by hybrid neuro fuzzy approach. World Acad Sci Eng Technol 52:543–548
14. Eker I (2004) Governors for hydro-turbine speed control in power generation: a SIMO robust design approach. Energy Convers Manag 45:2207–2221

A Stable Lyapunov Approach of Advanced Sliding Mode Control for Swing up and Robust Balancing Implementation for the Pendubot System

Cao Van Kien, Nguyen Ngoc Son and Ho Pham Huy Anh

Abstract This paper investigates the two-link Pendubot with one active joint at shoulder. The modified sliding mode controller for swinging up the Pendubot to the upright position and for robust balancing it at upright position. As to improve the performance, a novel advanced sliding mode controller is developed for robust balancing the Pendubot system at upright position. Simulation results have proved that the proposed sliding mode swinging up and balancing controller are successful techniques for robust balancing the Pendubot system at the upright position. They are strongly robust and tolerate noise and external disturbance. The proposed advanced sliding mode controller improves the robustness, reduces the chattering and the hitting time of sliding surface as well.

Keywords Pendubot system · Lyapunov stability · Swing-up and balancing control · Robust control · Advanced sliding mode control (ASMC)

1 Introduction

Pendubot mechanical system has fewer actuators than the degrees of freedom to be controlled [1]. The Pendubot system is underactuated since the angular acceleration of the second link cannot be controlled directly. The control problem of the Pendubot relates to the task of swing up both links nearly to the equilibrium position with

C. Van Kien (✉) · H.P.H. Anh
FEEE DCSELAB, HCM City University of Technology, Ho Chi Minh City, Vietnam
e-mail: kien_cv@yahoo.com

H.P.H. Anh
e-mail: hphanh@hcmut.edu.vn

N.N. Son
Faculty of Electronics Engineering, IUHYRA Member,
Industrial University of HCM City, Ho Chi Minh City, Vietnam
e-mail: nguyenngocson@hui.edu.vn

V.H. Duy et al. (eds.), *AETA 2015: Recent Advances in Electrical Engineering and Related Sciences*, Lecture Notes in Electrical Engineering 371,
DOI 10.1007/978-3-319-27247-4_36

highest potential energy followed by stabilization [2]. In [2], a feedback linearization based linear quadratic regulator (LQR) was proposed to stabilize the Pendubot system. Authors in [3] utilized an energy approach and applied the passivity properties of Pendubot in order to swing the first link to a small neighbourhood of the unstable equilibrium point while the second link oscillates and converges to the upright position. Authors in [4] introduced a non-trivial class of global feedback transformations for passivity based swing-up control of the Pendubot system. Zhang and Tarn in [5] proposed a hybrid controller for feedback stabilization of the Pendubot. Li et al. in [6] introduced a fuzzy controller as to keep the first link swinging periodically while the second link maintains standing vertically. Freidovich et al. in [7] applied the new virtual holonomic constraint technique, in order to generate periodic motions of the passive link of the Pendubot. Based on an impulse momentum approach, a new method for swing-up the Pendubot was developed in [8]. However, the main concern remains from such papers above related to the Pendubot stability and control performance when Pendubot system is subjected to external disturbances.

As to overcome this drawback, the sliding mode control (SMC) has been recognized as an effective robust control strategy in the control of complex systems with external disturbances [9]. The main purpose of the SMC is first to design a sliding surface with desired performance characteristics. Then, a discontinuous control input is implemented to put the state trajectory to the sliding surface and to remain on this surface afterward. The dynamic feature of the Pendubot closed-loop control system will be implemented based on the sliding surface design for driving the Pendubot to a desired zero dynamics position regardless of external disturbances [10]. Qian et al. in [11] introduced a hierarchical sliding mode controller for a Pendubot system in which the Pendubot was divided into two subsystems in terms of its structural features. Authors in [12] proposed an advanced sliding mode controller for a Pendubot system. Unfortunately, it appears that the problem of robust sliding mode control of the Pendubot system with external disturbances has not yet been fully solved.

This paper considers the robust stabilization problem of Pendubot systems in the presence of external disturbances. Concretely, by using the Lyapunov method, a sufficient condition is derived in terms of linear matrix inequality to ensure that the sliding mode dynamics is bounded within a ball whose radius can be minimized. A sliding mode controller is then designed to drive the Pendubot system towards the sliding surface which is bounded in finite time and maintain it on the surface afterwards. The main contribution in this paper can be summarized by the development of the robust sliding mode swinging up and balancing controllers for the Pendubot system and improving it with novel proposed robust balancing controllers.

The rest of this paper is organized as follows. Section 2 we present the dynamics of the Pendubot. Section 3 verifies the controllability of the Pendubot. In Sect. 4, the proposed control strategy for swinging up the Pendubot to the upright position is presented. In Sect. 4, the proposed control strategy for robust balancing the

Pendubot at the upright position is introduced. Section 5 analyses the simulation and experimental results of proposed control strategy. Finally, in Sect. 6, we summarize and conclude the results of the proposed control strategy.

2 Dynamics of the Pendubot System

A two link Pendubot is considered as shown in Fig. 1. This system represents an underactuated manipulator with one active joint at the shoulder. In this Section, the dynamics of Pendubot is presented. From Pendubot kinematics, Pendubot dynamics is derived as follows: Consider v_{c1} and v_{c2} to be the linear velocity of the Pendubot centre of link one and link two, respectively. These linear velocities are related to joint velocities $\dot{\theta} = \begin{bmatrix} \dot{\theta}_1 \\ \dot{\theta}_2 \end{bmatrix}$ by the following equations:

$$v_{c1} = J_{vc1} \cdot \dot{\theta} \tag{1}$$

$$v_{c2} = J_{vc2} \cdot \dot{\theta} \tag{2}$$

In which, J_{vc1} and J_{vc2} are the Jacobian matrices determined by:

$$J_{vc1} = \begin{bmatrix} -l_{c1}\sin(\theta_1) & 1 \\ l_{c1}\cos(\theta_1) & 0 \\ 0 & 0 \end{bmatrix} \tag{3}$$

$$J_{vc2} = \begin{bmatrix} -l_1\sin(\theta_1) - l_{c2}\sin(\theta_1+\theta_2) & -l_{c2}\sin(\theta_1+\theta_2) \\ -l_1\cos(\theta_1) - l_{c2}\cos(\theta_1+\theta_2) & -l_{c2}\cos(\theta_1+\theta_2) \\ 0 & 0 \end{bmatrix} \tag{4}$$

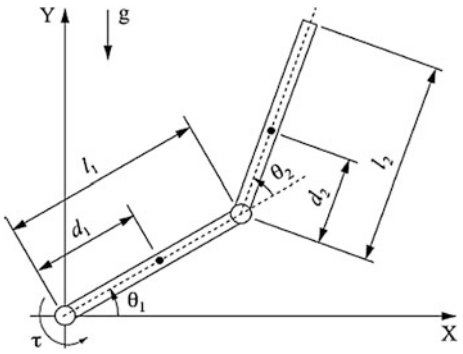

Fig. 1 Pendubot system

Then the total kinetic energy of the Pendubot is:

$$K = \frac{1}{2}\dot{\theta}\left\{m_1 J_{vc1}^T J_{vc1} + m_2 J_{vc2}^T J_{vc2}\right\}\dot{\theta} \tag{5}$$

Continually, the potential energy of link one and link two equal,

$$V_1 = m_1 g l_{c1} \sin(\theta_1) \tag{6}$$

$$V_2 = m_2 g(l_1 \sin\theta_1 + l_{c2} \sin(\theta_1 + \theta_2)) \tag{7}$$

Then the total potential energy of Pendubot system equals

$$V = V_1 + V_2 = m_1 l_{c1} g \sin\theta_1 + m_2 g(l_1 \sin\theta_1 + l_{c2} \sin(\theta_1 + \theta_2)) \tag{8}$$

$$\text{Apply the Lagrange function : } \mathrm{L} = \mathrm{K} - \mathrm{V} \tag{9}$$

The equations of motion for link one and link two are determined as follows,

$$\tau_1 = \frac{d}{dt}\frac{\partial L}{\partial \dot{\theta}_1} - \frac{\partial L}{\partial \theta_1} \tag{10}$$

$$\tau_2 = \frac{d}{dt}\frac{\partial L}{\partial \dot{\theta}_2} - \frac{\partial L}{\partial \theta_2} \tag{11}$$

where τ_1 and τ_2 are the torques supplied to the joint 1 and joint 2, respectively. By carrying out the above differentiation, using the geometric identities and definition of link moment of inertia, making the necessary modification and noticing joint 2 is passive joint, i.e. $\tau_2 = 0$. Then, (10) and (11) can be reduced to,

$$\begin{aligned}(\alpha_1 + \alpha_2 + 2\alpha_3 \cos\theta_2)\ddot{\theta}_1 + (\alpha_2 + \alpha_3 \cos\theta_2)\ddot{\theta}_2 - \alpha_3 \sin(\theta_2)\dot{\theta}_2^2 \\ - 2\alpha_3 \sin(\theta_2)\dot{\theta}_1\dot{\theta}_2 + \alpha_4 g \cos\theta_1 + \alpha_5 g \cos(\theta_1 + \theta_2) = \tau_1\end{aligned} \tag{12}$$

$$\alpha_2\ddot{\theta}_2 + (\alpha_2 + \alpha_3 \cos\theta_2)\ddot{\theta}_1 - \alpha_3 \sin(\theta_2)\dot{\theta}_1^2 + \alpha_5 g \cos(\theta_1 + \theta_2) = 0 \tag{13}$$

In which

$$\alpha_1 = m_1 l_{c1}^2 + m_2 l_1^2 + I_1, \quad \alpha_2 = m_2 l_{c2}^2 + I_2, \quad \alpha_3 = m_2 l_1 l_{c2}$$

$$\alpha_4 = m_2 l_{c1} + m_2 l_1, \quad \alpha_5 = m_2 l_{c2}$$

In matrices form, the equations of motion of the two link Pendubot can be described as follows:

$$D(\theta)\ddot{\theta} + C(\theta, \dot{\theta})\dot{\theta} + G = \tau \tag{14}$$

with $\tau = \begin{bmatrix} \tau_1 \\ 0 \end{bmatrix}$ $D = \begin{bmatrix} \alpha_1 + \alpha_2 + 2\alpha_3 \cos\theta_2 & \alpha_2 + \alpha_3 \cos\theta_2 \\ \alpha_2 + \alpha_3 \cos\theta_2 & \alpha_2 \end{bmatrix}$

$$C = \begin{bmatrix} -\alpha_3 \sin(\theta_2)\dot{\theta}_2 & -\alpha_3 \sin(\theta_2)\dot{\theta}_2 - \alpha_3 \sin(\theta_2)\dot{\theta}_1 \\ -\alpha_3 \sin(\theta_2)\dot{\theta}_1 & 0 \end{bmatrix}$$

$$G = \begin{bmatrix} \alpha_4 g\cos\theta_1 + \alpha_5 g\cos(\theta_1 + \theta_2) \\ \alpha_5 g\cos(\theta_1 + \theta_2) \end{bmatrix}$$

Figures 2 and 3 illustrate the 3D simulation of Pendubot with Solid-works in unstable balancing position (Fig. 2) and in stable balancing position (Fig. 3).

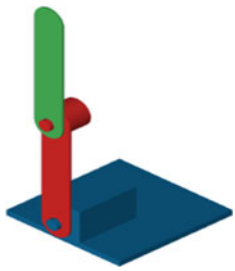

Fig. 2 3D simulation of Pendubot system with solid-works

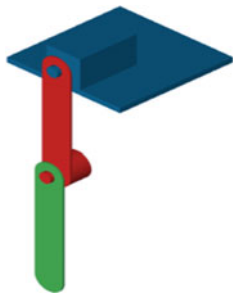

Fig. 3 Matlab/Simulink

3 Swing-up Pendubot Using Advanced Sliding Mode Control

The sliding mode controller is derived using the state dynamics described by equation,

$$\bar{d}_{11}\ddot{\theta}_1 + \bar{h}_1 + \ddot{\varphi}_1 = \tau_1 \tag{15}$$

In which

$$\bar{d}_{11} = \left(d_{11} - \frac{d_{12}}{d_{22}}\right), \quad \bar{h}_{11} = \left(h_1 - \frac{d_{12}}{d_{22}}h_2\right), \quad \bar{\varphi}_1\left(\varphi_1 - \frac{d_{12}}{d_{22}}\varphi_2\right)$$

Consider a state space form of Pendubot system as $\tilde{x}_1 = \theta_1$ and $\dot{\theta}_1 = \dot{x}_1 = \tilde{x}_2$. We have, $\dot{\tilde{x}}_1 = \tilde{x}_2$ and $\dot{\tilde{x}}_2 = f_1(\tilde{x}) + b_1\tau_1$ with

$$f_1(\bar{x}) = \frac{(\bar{x}_{11}\dot{\theta}_1 + \bar{c}_{12}\dot{\theta}_2 + \bar{\varphi}_1)}{\bar{d}_{11}}, \quad b_1 = \frac{1}{\bar{d}_{11}}, \quad \bar{d}_{11} = \left(d_{11} - \frac{d_{12}d_{21}}{d_{22}}\right)$$

$$\bar{\varphi}_1 = \left(\varphi_1 - \frac{d_{12}}{d_{22}}\varphi_2\right), \quad \bar{c}_{11}\left(c_{11} - \frac{d_{12}d_{21}}{d_{22}}\right), \quad \bar{c}_{12} = c_{12}$$

Forwardly, consider a sliding surface as follows:

$$S = \lambda\left(\theta_1 - \theta_1^d\right) + \left(\dot{\theta}_1 - \dot{\theta}_1^d\right) = \lambda\tilde{x}_1 + \tilde{x}_2 \tag{16}$$

The goal is to choose the scalar λ value such that the system restricted on the surface (16) is of the stable characteristics. Consider the followed Lyapunov function:

$$V_1 = \frac{1}{2}S^2 \tag{17}$$

The sliding mode controller can be chosen by the way that the velocity vectors are aimed to the sliding surface. This is accomplished by satisfying,

$$\dot{V}_1 \leq 0 \tag{18}$$

$$\dot{V}_1 = S \cdot \dot{S} = S(\lambda\tilde{x}_2 + f_1(\tilde{x}) + b_1\tau_1) \tag{19}$$

In order to satisfy (18), the input torque can be chosen as follows:

$$\tau_1 = \tilde{\tau}_1 - \frac{(u\,\mathrm{sgn}(S) + kS_1)}{b_1} \tag{20}$$

$$\tilde{\tau} = \frac{(\lambda x_2 + f_1(\tilde{x}))}{b_1} \tag{21}$$

In which, λ, k, μ are constants to be designed for the sliding surface. To design these constants we first need to find their limits. The maximum value of μ is computed from the maximum torque produced by servo motor as follows:

$$\mu_{\max} = \tau_{\max} = 0.5\,\mathrm{N\,m} \tag{22}$$

where τ_{max} is the maximum torque produced by servo motor. The maximum value of λ is computed as follows:

$$\lambda_{\max} = \frac{(\tau_{\max} - \bar{d}_{11} \cdot f_{1\max})}{\bar{d}_{11} \cdot \dot{\theta}_{1\max}} \tag{23}$$

In which f_{1max} is defined as:

$$f_{1\max} = \frac{(\bar{c}_{11\max}\dot{\theta}_{1\max} + \bar{c}_{12\max} \cdot \dot{\theta}_{2\max} + \bar{\varphi}_{1\max})}{\bar{d}_{11}} \tag{24}$$

The maximum velocity of joint one is the maximum speed of the servo motor. However, it is practically difficult to obtain this high velocity. Consequently it is available to apply the maximum velocity and acceleration during the simulation of classical feedback linearization technique simulation.

$$\dot{\theta}_{1\max} = 40\,\mathrm{rad/s},\ \dot{\theta}_{2\max} = 15\,\mathrm{rad/s},\ \ddot{\theta}_{1\max} = 1400\,\mathrm{rad/s^2}$$

$$\bar{\varphi}_{1\max} = 0.0886\,\mathrm{N},\ |\bar{c}_{11\max}| = 0.0091\,\mathrm{rad/s},\ |\bar{c}_{12\max}| = 0.0077\,\mathrm{rad/s}$$

Replace to (23–24), the values f_{1max} and λ_{max} now are calculated to be:

$$f_{1\max} = 266.7 \text{ and } \lambda_{\max} = 14.7$$

Continually, the value of k is selected by the way that the poles of the following equation must be located in the left side plane,

$$(\ddot{\theta}_1 - \ddot{\theta}_1^d) + k|S| = 0 \tag{25}$$

Three parameters were chosen as follows, $\lambda = 8, \quad k = 24, \quad \mu = 0.3.$

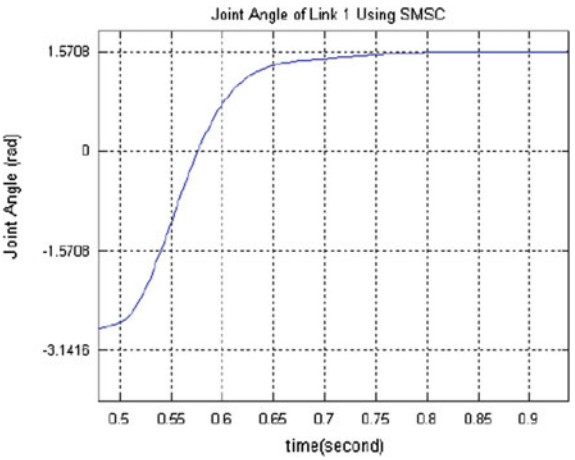

Fig. 4 Joint angle of link one using sliding mode swinging up controller

Then Lyapunov function got stable and satisfied requirements as joint angle of link 1 using sliding mode swinging up controller which is shown in followed Fig. 4:

4 Balancing Pendubot Using Advanced Sliding Mode Control

The required orbit at which the controller should be switched to the balancing controller where the second link of the manipulator moves toward the equilibrium point $(\theta_1 = \frac{\pi}{2}, \theta_2 = 0)$ is formulated as,

$$\frac{1}{2} = \alpha_2 \dot{\theta}_2^2 = \alpha_5 g(1 - \cos\theta_2) \tag{26}$$

The control algorithm is switched from swinging to balancing controller when

$$\left|\theta_1 - \frac{\pi}{2}\right| < 0.2\,\text{rad} \quad \text{and}\, |\theta_2| < 0.3 \tag{27}$$

Since the system under study is underactuated, i.e. we have one control input for two degrees of freedom manipulator, we used hierarchical sliding mode controller. The equation of motion of two link Pendubot (23) can be expressed as:

$$\begin{bmatrix} \ddot{\theta}_1 \\ \ddot{\theta}_2 \end{bmatrix} = D^{-1}\left(\tau - C\begin{bmatrix} \dot{\theta}_1 \\ \dot{\theta}_2 \end{bmatrix} + G\right) = D^{-1}\tau - D^{-1}\left(C\begin{bmatrix} \dot{\theta}_1 \\ \dot{\theta}_2 \end{bmatrix} + G\right) \tag{28}$$

Given,

$$\tilde{x}_1 = \theta_1^d - \theta_1,\ \tilde{x}_2 = \dot{\theta}_1^d - \dot{\theta}_1,\ \tilde{x}_3 = \theta_2^d - \theta_2,\ \tilde{x}_4 = \dot{\theta}_2^d - \dot{\theta}_2$$

Equation (28) can be expressed as follows:

$$\begin{cases} \dot{\tilde{x}}_1 = \tilde{x}_2 \\ \dot{\tilde{x}}_2 = f_1(\tilde{x}) + b_1\tau_1 \\ \dot{\tilde{x}}_3 = \tilde{x}_4 \\ \dot{\tilde{x}}_4 = f_2(\tilde{x}) + b_2\tau_2 \end{cases} \tag{29}$$

with $t_2 = 0\,(\textit{underactuated})$, *and* $\tilde{x} = [\tilde{x}_1 \quad \tilde{x}_2 \quad \tilde{x}_3 \quad \tilde{x}_4]^T$

$$f_1(x) = \frac{1}{\alpha_1\alpha_2 - \alpha_3^2\cos^2(\theta_2)} \begin{bmatrix} \alpha_2\alpha_3\sin(\theta_2)(\dot{\theta}_1 + \dot{\theta}_2)^2 + \alpha_3^2\cos\theta_2\ \sin(\theta_2)\dot{\theta}_1^2 \\ -\ \alpha_2\alpha_4 g\cos\theta_1 + \alpha_3\alpha_5 g\cos\theta_2\ \cos(\theta_1 + \theta_2) \end{bmatrix} \tag{30}$$

$$b_1 = \alpha_2(\alpha_2\alpha_1 - (\alpha_3\cos\theta_2)^2) \tag{31}$$

$$f_1(x) = \frac{1}{\alpha_1\alpha_2 - \alpha_3^2\cos^2(\theta_2)} \begin{bmatrix} -\alpha_3(\alpha_2 + \alpha_3\cos\theta_2\ \sin\theta_2(\dot{\theta}_1 + \dot{\theta}_2)^2 \\ -(\alpha_1 + \alpha_3\cos\theta_2)\ \sin(\theta_2)\dot{\theta}_1^2 \\ +(\alpha_2 + \alpha_3\cos\theta_2)\,\alpha_4 g\cos\theta_1 \\ -(\alpha_1 + \alpha_3\cos\theta_2)\,\alpha_5 g\cos(\theta_1 + \theta_2) \end{bmatrix} \tag{32}$$

$$b_2 = -\left(\frac{\alpha_2 + \alpha_3\cos\theta_2}{\alpha_2\alpha_1 - (\alpha_3\cos\theta_2)^2}\right) \tag{33}$$

Then the sliding surfaces of the first joint and second joint are defined as follows:

$$S_1 = \lambda_1\tilde{x}_1 + \tilde{x}_2, \quad \lambda_1 > 0 \tag{34}$$

$$S_2 = \lambda_2\tilde{x}_2 + \tilde{x}_4, \quad \lambda_2 > 0 \tag{35}$$

Since Pendubot is an underactuated system, we need to define a second level sliding surface that simultaneously stabilizes the above surfaces. The second level sliding surface can be defined as follows:

$$S = \beta S_1 + \delta S_2 \tag{36}$$

In addition, the input control torque applied on joint one will be defined as:

$$\tau_1 = \tau_{equiv1} + \tau_{equiv2} + \tau_{sw} \tag{37}$$

with

$$\tau_{equiv1} = -\frac{f_1(x) + \lambda_1 \tilde{x}_2}{b_1} \tag{38}$$

$$b_1 = \alpha_2(\alpha_2\alpha_1 - (\alpha_3 \cos\theta_2)^2) \neq 0, \text{ since} \frac{\sqrt{\alpha_2\alpha_1}}{\alpha_3} = 2.4228 > 1$$

$$\tau_{equiv2} = -\frac{f_2(x) + \lambda_2 \tilde{x}_4}{b_2}, \quad b_2 \neq 0 \tag{39}$$

Then Lyapunov function can be chosen as,

$$V_1 = \frac{1}{2}S^2 \tag{40}$$

The sliding mode controller can be chosen by the way that the velocity vectors are aimed to the sliding surface. This is accomplished by satisfying,

$$\dot{V}_1 \leq 0 \tag{41}$$

$$\begin{aligned} \dot{V}_1 &= S\dot{S} = S(\beta \dot{s}_1 + \delta \dot{s}_2) \\ &= S\big(\beta b_1 \tau_{equi2} + \delta b_2 \tau_{equi1} + \tau_{sw}(\beta b_1 + \delta b_2)\big) \end{aligned} \tag{42}$$

As to conform (41), torque τ_{sw} value can be defined as follows,

$$\tau_{sw} = \frac{\delta b_2 \tau_{equiv1} + \beta b_1 \tau_{equiv2} - \mu \text{sgn}(S) - kS}{\delta b_2 + \beta b_1} \tag{43}$$

with $\mu > 0$, $k > 0$

From (37–39) and (43), the total input torque equals,

$$\tau_1 = \frac{\beta b_1}{\beta b_1 + \delta b_2}\tau_{equiv1} + \frac{\delta b_2}{\beta b_1 + \delta b_2}\tau_{equiv2} - \hat{\mu}\,\text{sgn}(S) - \hat{k}S \tag{44}$$

with $\hat{\mu} = \frac{\mu}{\beta b_1 + \delta b_2}$, $\quad \hat{k} = \frac{k}{\beta b_1 + \delta b_2}$

Substitute (43) into (42), we have,

$$\dot{V}_1 = -kS^2 - u|s| < 0 \tag{45}$$

with $\mu > 0$, $k > 0$

Hence the second level sliding surface is proved to be stable.

To choose the parameters δ, β, λ_1, λ_2, it needs to vary the parameters δ, β, λ_1, λ_2 within specific ranges and calculate the summation of sliding surfaces S for a period of time z. Value β is selected relative to δ and similarly, value λ_1 is chosen relative to λ_2. The set of parameters δ, β, λ_1, λ_2 that reaches the minimum summation of sliding surface which are the final chosen values. Especially, the parameters μ, k must be ensured greater than zero. The detailed of experimental and simulation results and the way for selection of parameters will be carefully introduced in the next section.

5 Simulation Results

In this section, the simulation results using sliding mode controller to swing up the Pendubot system at the upright position will be investigated. Also we compare the results of sliding mode swinging up controller with the classic feedback linearization technique. For comparison study, the LQR method is still adopted for comparison.

The swinging up torque of sliding mode controller is shown in Fig. 5. The comparison of swinging up control actions produced by the LQR technique and the sliding mode controller are shown in Fig. 5. From Fig. 5, one can observe that the pumping torque remains unchanged, and the swinging up torque produced by sliding mode control methodology slightly differs from LQR technique. However, as shown in Fig. 6a, b, the sliding mode control methodology is successful in swinging the both links of Pendubot to the upright position.

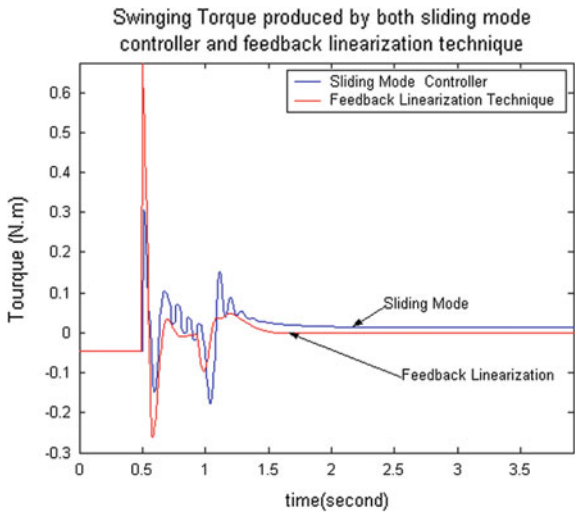

Fig. 5 Comparison of swing torques produced by sliding mode and LQR controllers

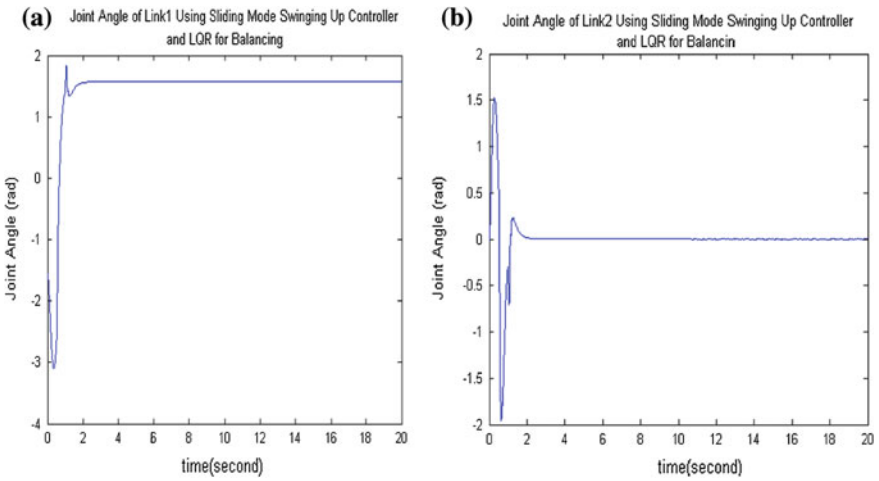

Fig. 6 Joint angle of two links of Pendubot using sliding mode swinging up controller

Forwardly, the simulation results of the sliding mode balancing controller and compare these results with LQR technique. In order to select the best combination of parameters δ, β, λ_1, λ_2, the summation of sliding surfaces for a period of time is determined for a range of parameter values. Based on the summation of sliding surfaces against the ratio of δ, β and λ_1, λ_2, the minimum value of the sum of sliding surface is fixed on the following ratios: $\beta/\delta = 0.738$ and $\lambda_1/\lambda_2 = 0.74$

Let λ_2 = 8.5, δ = 0.62, then λ_1 = 6.29, β = 0.458.

Continually, the parameters μ, k are selected to be as: μ = 0.02, k = 13.

The balancing torque produced by the sliding mode controller is shown in Fig. 7.

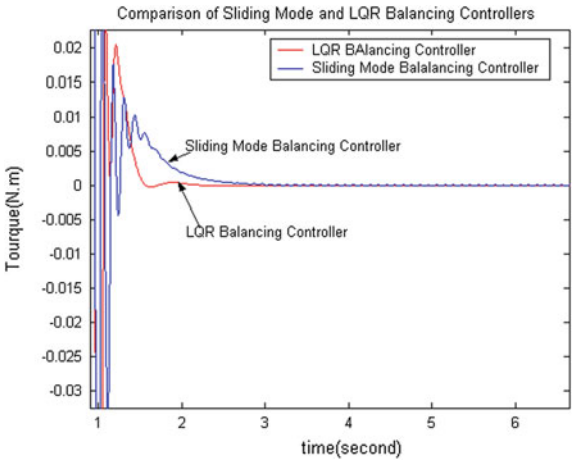

Fig. 7 Comparison between proposed sliding mode and LQR balancing controllers

The joint angle of link one and link two are shown in Fig. 8a, b.

Finally, we consider the effect of external disturbance on stability performance of swinging up and balancing sliding mode controllers.

From Fig. 9, the sliding mode controllers were able to stabilize the Pendubot system at the upright position after the interference of external disturbance. Under external disturbance interfering at the 4th second, Fig. 9a shows the joint angle response of Pendubot stabilized by the proposed sliding mode controllers. On the contrary, Fig. 9b shows the oscillating joint angle response of Pendubot using LQR technique.

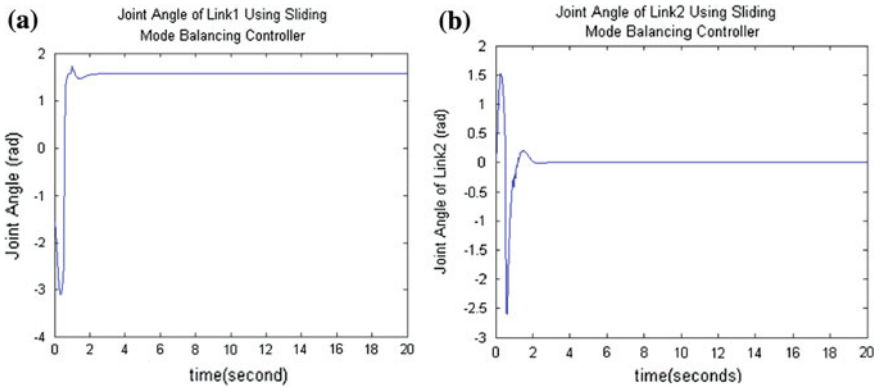

Fig. 8 Joint angle of both links of Pendubot using sliding mode balancing controller

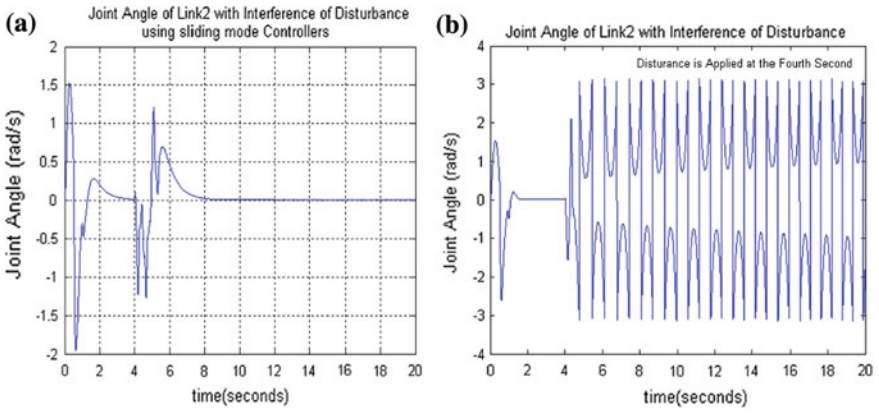

Fig. 9 Joint angle of link 2 with interference of external disturbance using sliding mode controller (**a**) and using LQR technique (**b**)

Table 1 Pendubot parameters

l_1	0.15	d_1	0.1125
l_2	0.25	d_2	0.1250
m_1	0.15	b_1	0.01
m_2	0.25	b_2	0.001
g	9.81	ε	2

6 Conclusions

In this paper the proposed advanced sliding mode control for swinging up and balancing the Pendubot system has successful applied for balancing the Pendubot at the upright position. They are robust and tolerate to a certain levels of noise and external disturbance. However the sliding mode balancing controller have minor chattering problem around the sliding surface. To overcome the chattering and reduce the hitting time of sliding surface, the stable Lyapunov method is integrated with sliding mode controller. The novel proposed robust sliding mode controller improves the robustness, reduce the chattering and the hitting time of sliding surface as well (Table 1).

Acknowledgments This paper was fully supported by the HCM City University of Technology, VNU-HCM, under Project TSĐH-2015-ĐĐT-04.

References

1. Raja Ismail RMT, That ND, Ha QP (2012) Observer-based trajectory tracking for a class of underactuated lagrangian systems using higher order sliding modes. In: The 8th IEEE international conference on automation science and engineering, Seoul, Korea, pp 1200–1205
2. Spong MW, Block DJ (1995) The Pendubot: a mechatronic system for control research and education. In: Proceedings of the 34th IEEE conference on decision and control, New Orleans, pp 555–556
3. Fantoni I, Lozano R, Spong MW (2000) Energy based control of the Pendubot. IEEE Trans Autom Control 45(4):725–729
4. Kolesnichenko O, Shiriaev AS (2002) Partial stabilization of underactuated EulerLagrange systems via a class of feedback transformations. Syst Control Lett 45:121–132
5. Zhang M, Tarn TJ (2002) Hybrid control of the Pendubot. IEEE/ASME Trans Mechatronics 7(1):79–86
6. Li W, Tanaka K, Wang HO (2004) Acrobatic control of a Pendubot. IEEE Trans Fuzzy Syst 12(4):549–552
7. Freidovich L, Robertsson A, Shiriaev A, Johansson R (2008) Periodic motions of the Pendubot via virtual holonomic constraints: theory and experiments. Automatica 44:785–791
8. Albahkali T, Mukherjee R, Das T (2009) Swing-up control of the Pendubot: an impulse momentum approach. IEEE Trans Rob 25(4):975–982
9. Utkin VI (1977) Variable structure control systems with sliding modes. IEEE Trans Autom Control 22(2):212–222

10. Orlov Y, Aguilar LT, Acho L (2005) Model orbit robust stabilization (MORS) of Pendubot with application to swing up control. In: Proceedings of the 44th conference on decision and control, Seville, Spain, pp 6164–6169
11. Qian D, Yi J, Zhao D (2007) Hierarchical sliding mode control to swing up a Pendubot. In: Proceedings of the 2007 American control conference, New York, pp 5254–5259
12. Kien CV, Son NN, Anh HPH (2015) Swing up and balancing implementation for the Pendubot using advanced sliding mode control. In: 2015 international conference on electrical, automation and mechanical engineering (EAME-2015), Phuket, ThaiLand, pp 389–392

Tuning PID Controllers for Unstable Systems with Dead Time Based on Dual-Input Describing Function Method

Yeon Wook Choe

Abstract Though various techniques have been studied as a way of adjusting PID parameters, no perfect method of determining parameters is available to date. Especially the design of PID controller for unstable processes with dead time (UPWDT) is even more difficult when the normalized dead time is quite large. In this paper, the Dual-Input Describing Function (DIDF) method is proposed, by which the performance and robustness of the closed-loop system can be improved. The method is based on moving the critical point $(-1 + j0)$ of Nyquist's stability to a new position arbitrarily selected on the complex plane. This can be done by determining appropriate coefficients of the DIDF. As a result, we can easily determine parameters of PID-type controller by using existing conventional tuning methods for stable or unstable systems. Simulation results are included to show the effectiveness of the proposed method.

Keywords PID controller tuning · Dual-Input describing functions · Unstable systems with dead time

1 Introduction

Though PID control, which was established more than a half century ago, is one of classical control algorithms, but 80 % of control methods in the industry is currently known as PID. This is because PID is easily applicable to systems if we can obtain outputs and their derivatives. Well-known methods for determining coefficients of PID are as follows: Ziegler-Nichols, Chien-Hrones-Reswick [1], and constrained optimization method by Astrom etc. [2–5]. However most methods need a premise that the stable plant can be approximated as '1st-order delay with dead time'. That

Y.W. Choe (✉)
Department of Control and Measurement Engineering, Pukyong National University, Busan 608-739, South Korea
e-mail: wook@pknu.ac.kr

V.H. Duy et al. (eds.), *AETA 2015: Recent Advances in Electrical Engineering and Related Sciences*, Lecture Notes in Electrical Engineering 371,
DOI 10.1007/978-3-319-27247-4_37

is, PID parameters are determined by dead time, time constant, and DC gain of its approximated system.

As to unstable systems, there are several methods, for example, one of which was using the approximation process of gain and phase margin formula [6–8]. It is, however, known that there exists a problem when applying to real systems [9]. Besides, many new methods have been tried, for example, inner-loop method [10] and iterative algorithm [11–13]. Although lots of methods have been proposed, but still some disadvantages such as excessive overshoot and poor closed-loop characteristics have been reported as practical problems.

Xiang et al. [14] has introduced a mathematical device which they call a dual-input describing function. It is an extension of the conventional describing function, which linearizes nonlinearity forced by two sinusoids. This method especially helps to understand input-output responses of the system which is in the state of limit cycle due to the presence of non-linear elements. If the application of DIDF is limited to the structure of feedback system tracking reference signals with non-linearity, the two inputs of the nonlinear element would be composed of two signals, that is, the error signal of steady-state and the sinusoid due to the limit cycle of the closed loop. Recently a new results, which shows that periodic disturbance is effective removed by using DIDF, is reported [15].

As mentioned above, conventional design methods for unstable plants with dead time not only limit the type of plant but require lots of computation for approximation. As a result, the applicability may not be so high. In this paper, we propose a new PID controller designing method for unstable systems with dead time by using DIDF compensator. In other words, if nonlinear elements with two inputs (DIDF) are connected in series to the plant, the critical point $(-1 + j0)$ can be moved to a position arbitrarily selected on the complex plane by selecting necessary coefficients of the DIDF appropriately. This makes the application of the conventional PID tuning methods a lot easier, and stability and robustness of the system are improved simultaneously. We propose a suitable DIDF structure and ways of determining its coefficients for this purpose, and verify its effectiveness through simulation.

2 Dual-Input Describing Function

2.1 Dual-Input Describing Function

In case a signal having non-linearity of a high level such as a non-sinusoidal wave is input to a nonlinear element, it is difficult to analyze it with describing functions alone. It is thought that a signal having non-linearity of a high level is composed of the sum of two sine functions in most of the cases. Therefore, for the purpose of utilizing calculations of describing functions, an input to nonlinear element could be expressed as follows:

$$x(t) = x_1(t) + x_2(t) = h\sin(\omega_1 t + \theta_1) + l\sin(\omega_2 t + \theta_2) \tag{1}$$

Since the amplitudes h, l and frequencies ω_1, ω_2 of two sine waves are determined by the state of the system and the external input, it seems reasonable that a harmonic relation is not thought to be existent between the frequencies of the two sine waves. As an example, we take the system which is in the state of limit cycle corresponding to a sinusoidal input. In this case, the frequencies of two inputs of nonlinear system are composed of ω_1 due to the limit cycle of the system (inner frequency) and ω_2 of an external sinusoidal input to nonlinear element.

On the other hand, let's think of a case where if signal x_1 in Eq. (1) 'varies slowly,' against the amplitude l of x_2, namely.

$$T\left|\frac{dx_1(t)}{dt}\right| \ll l \tag{2}$$

is satisfied, where T is the period of $x_2(t)$. If it is assumed that input and output of nonlinear elements are, for example

$$x(t) = B + A\sin(\omega t + \theta), y(t) = B' + \sin(\omega t + \theta) \tag{3}$$

then, describing functions representing nonlinear elements could be expressed as two DIDF's as follows, and as a result of this, it is confirmed that N, the nonlinear elements of Fig. 1, is composed of 'real part + imaginary part,' that is, let $N = N_o + jN_s$, then (refer to Fig. 1).

$$N_o = \frac{A'}{A}e^{-j\theta} : \text{DIDF for limit cycle}, N_s = \frac{B'}{B} : \text{DIDF for error signal} \tag{4}$$

2.2 Establishment of Proposition

Intervention of nonlinear elements makes it possible to move Nyquist's critical point on a complex plane, thereby indicating that tuning of PID parameters is made simple and the whole performance could be enhanced.

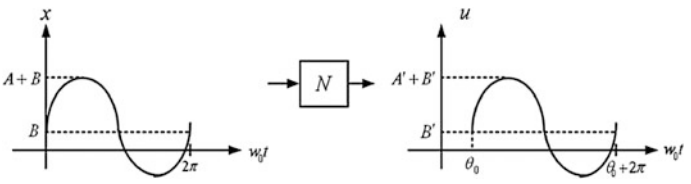

Fig. 1 Linearization of nonlinearity in the presence of a sinusoid and DC term

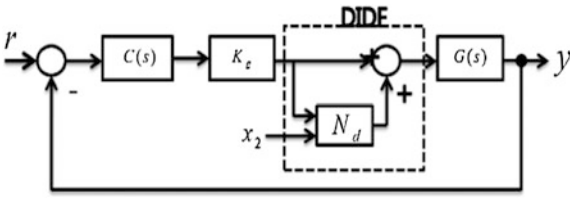

Fig. 2 PID control with DIDF compensator

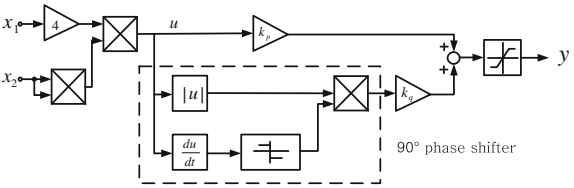

Fig. 3 The construction of the complex DIDF

The characteristic equation of Fig. 2 is given as follows:

$$1 + K_g(1 + N_d)G(s)C(s) = 0 \tag{5}$$

where K_g is a parameter used to adjust the gains of the DIDF compensator, $C(s)$ the transfer function of PID controller, is generally given in the form as follows:

$$C(s) = K_P\left(1 + \frac{1}{T_I s} + T_D s\right) = K_P + \frac{K_I}{s} + K_D s \tag{6}$$

where K_p, T_I and T_D refer to the PID controller's proportional gain, integral time and derivative time, respectively. In Fig. 3, N_d represents a describing function of nonlinear element used for the purpose of performance improvement.

The performance of the overall system of Fig. 3 including stability is determined by the roots of Eq. (6) which contains the nonlinear part N_d. Accordingly, the establishment of the structure of N_d with two inputs and determination of its coefficients play an important role to improve its performance, that is, to change its existing characteristics.

3 The Structure of DIDF and Determinant of Parameters

3.1 Complex DIDF and Its Composition

Here is how N_d, the describing function of nonlinear elements intended to enhance performance of a PID control system, is composed [10].

As a way of realizing the complex DIDF given as a function of l, the equation

$$N_d(l) = N_p(l) + jN_q(l),\ (l > 0) \tag{7}$$

$$N_p(l) = k_p l^2,\ N_q(l) = k_q l^2 \tag{8}$$

is used [11], where k_p and k_q are constants. Here it is known that, the rate of the frequencies of two inputs of N_d, that is, $\gamma = \omega_2/\omega_1$ being an irrational number has led to Eqs. (7) and (8).

3.2 Realization of N_d

Under the assumptions that ($\omega_2 \gg \omega_1$) is met and γ is an irrational number, the method set forth in literature [11] is used as a way of constructing N_d. Since it is assumable that x_1 stays almost constant, compared with x_2 under the assumption of the relation with Eq. (8) and the condition ($\omega_2 \gg \omega_1$), the real part, N_p, becomes the function of l. By using such a fact, it is easily derived that the input and output relationships (of the real part) of nonlinear $N_d(l)$ having two inputs are given as follows:

$$y(x_1, x_2) = 2k_p x_1 x_2^2,\ x_1 \in (-h, h), x_2 \in (-l, l) \tag{9}$$

By using similar techniques of the real part, the same type of Eq. (9)

$$y(x_1, x_2) = 2k_q x_1 x_2^2 \tag{10}$$

is acquired with regard to the imaginary part of N_d. A '90°' phase shift, however, is required for the realization of 'j', the imaginary number. A block diagram is shown in Fig. 3, designed to realize N_d, a nonlinear element, as a complex DIDF, based on the foregoing description.

3.3 Coefficients Determination for Complex DIDF

The problem here is how to set up k_p and k_q, the DIDF variables, which facilitates the setup of the parameters tuning for PID controller. The paper proposes a way of securing stability of the closed loop system composed of plant $G(s)$ and the nonlinear part N_d of Eq. (7) by choosing coefficients N_d of Eq. (8). In other words, the study uses, and is based on, the fact that stability of Fig. 3 (where $C(s) = 1$), namely, the roots of the characteristic equation of the closed loop

$$1 + K_g(1 + N_d)G(s) = 0 \tag{11}$$

are determined by $G(s)$-locus and $\{-1/K_g(1 + N_d), j0\}$, a point on the complex plane.

(1) By using step response of the closed-loop system

A conventional method using step response is not applicable to all ordinary (of course, unstable) plants. In such cases, if the DIDF compensator is inserted into the loop, the transfer function of the closed loop becomes as follows:

$$1 + K_g[1 + N_d(l)]G(j\omega) = 0 \;\rightarrow\; G(j\omega) = -\frac{1}{K_g[1 + N_d(l)]} \tag{12}$$

Using (12), the critical point is given as

$$p_e = -\frac{N_p + 1}{(N_p + 1)^2 + N_q^2} + j\frac{N_q}{(N_p + 1)^2 + N_q^2} \tag{13}$$

It is noted that N_p and N_q of Eq. (13a) depend on k_p, k_q as well as l, the amplitude of the input $x_2(t)$. Because the position of p_e is closely related with the amplitude of sensitivity function and the step response of the closed-loop system, it is desirable to determine using iteration of simulation.

(2) By using the plant's step-response:

First, find out the conditions of DIDF compensator in order to stabilize Eq. (12). That is, in Eq. (13), let $K_1 = K_g[1 + N_d(l)]$, we confirm the range of K_1 by which the following plant can be stabilized.

$$G(s) = \frac{K}{Ts - 1}e^{-Ls} \tag{14}$$

For this, we apply Taylor series of dead time, $e^{-Ls} \fallingdotseq 1\text{-}Ls + 0.5L^2s^2$, to Eq. (14). Then the characteristic equation of the closed-loop becomes:

$$0.5K_1KL^2s^2 + (T - K_1KL)s + (K_1K - 1) = 0 \tag{15}$$

By using Routh-Hurwitz Table, Eq. (15) is stable polynomial when K_1 is

$$\frac{1}{K} < K_1 < \frac{T}{LK} \tag{16}$$

Therefore, in order to stabilize Eq. (12) by DIDF compensator, two conditions are required: (1) $T/L > 1$, (2) K, which is dependent on k_p, k_q as well as K_g, must satisfy Eq. (16). If the value that satisfies above conditions does not exist, it is necessary to stabilize the plant with inner loop (P or PD) before using DIDF compensator [14–16]. In this paper we adopt the structure of Fig. 4.

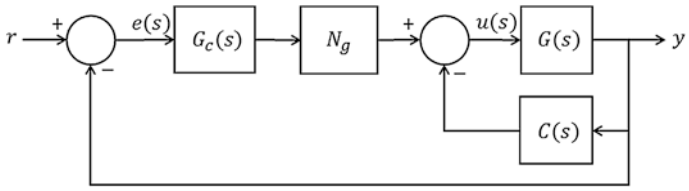

Fig. 4 PID-DIDF structure with an inner loop

In Fig. 4, $G(s)$, $G_c(s)$, and $C(s)$ represent unstable plant with dead time, PID controller of Eq. (6), and compensator for inner loop stabilization, respectively. And N_g is DIDF compensator give as follows:

$$N_g = K_g\left[(1+N_p)+jN_q\right] \tag{17}$$

After securing stabilization of inner loop with $C(s)$, we, then, determine the three parameters of PID by applying conventional methods. It is not generally so simple to obtain a diamond-shaped response curve with an unstable plant with dead time. However, it is confirmed that, if parameters of DIDF are appropriately chosen, it is possible to obtain desirable step (S-shaped) response.[1]

We show that the structure of Fig. 4 consequently becomes 2-degree-of-freedom (2-DOF) with DIDF compensator. That is, from Fig. 4, the control signal u(s) is

$$\begin{aligned} u(s) &= \mathrm{Ng} - \left(K_P + \frac{K_I}{s} + K_D s\right)(r-y) - (K_1 + K_2 s)y \\ &= K_P^*(b_n r - y) + \frac{K_I^*}{s} + K_D^*(c_n s r - s y) \end{aligned} \tag{18}$$

$$\begin{aligned} K_I^* &= N_g K_P + K_1 \\ K_D^* &= N_g K_D + K_2, \quad K_I^* = N_g K_I, \quad b_n = \frac{N_g K_P}{N_g K_P + K_1}, \quad c_n = \frac{N_g K_D}{N_g K_P + K_2} \end{aligned} \tag{19}$$

Since Eq. (18) is a well-known 2-DOF format, we can change Fig. 4 into 2-DOF structure by applying set-point filter $F(s)$ given by

$$F(s) = \frac{c_n\left(K_I^* K_D^*\right)s^2 + b_n\left(K_I^* K_P^*\right)s + \left(K_P^*\right)^2}{\left(K_I^* K_D^*\right)s^2 + \left(K_I^* K_P^*\right)s + \left(K_P^*\right)^2} \tag{20}$$

[1]When DIDF variables k_p, k_q and K_g are adjusted, a reaction curve is readily found.

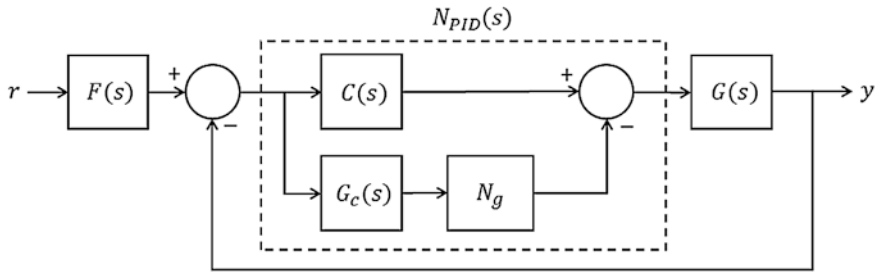

Fig. 5 Controller structure using 2-DOF

Referring to Eqs. (18)–(20), PID controller with DIDF $N_{\mathrm{PID}}(s)$ is given as follows:

$$\begin{aligned} N_{PID}(s) &= K_P^* + \frac{K_I^*}{s} + K_D^* s \\ &= (K_1 + K_2 s) + N_g\left(K_P + \frac{K_I}{s} + K_D s\right) \end{aligned} \tag{21}$$

The structure of Eq. (21) is shown in Fig. 5, which is the same type as Fig. 2 except pre-filter $F(s)$.

If we, however, realize the structure of Fig. 5, complex value N_{g} of filter $F(s)$ should be handled properly. Coefficients of Numerical polynomial $F(s)$ are real since

$$\begin{aligned} c_n\left(K_I^* K_D^*\right) &= \frac{N_g K_D}{K_D^*} \cdot \frac{K_P^*}{K_I^*} \cdot \frac{K_D^*}{K_P^*} = \frac{K_D}{K_I} \\ b_n\left(K_I^*\right) &= \frac{N_g K_P}{K_P^*} \cdot \frac{K_P^*}{K_I^*} = \frac{K_P}{K_I} \end{aligned} \tag{22}$$

But coefficients of denominator are complex because they include complex number N_{g}. Since $\left|1 + N_p\right| \gg \left|N_q\right|$ is satisfied in most cases, if we let $N_g \approx K_g\left(1 + N_p\right)$, then Eq. (22) becomes real.

$$\begin{aligned} K_I^* K_D^* &\approx \frac{K_D}{K_I} + \frac{K_2}{K_I} \cdot \frac{1}{K_g\left(1 + N_p\right)} \\ K_I^* &\approx \frac{K_P}{K_I} + \frac{K_1}{K_I} \cdot \frac{1}{K_g\left(1 + N_p\right)} \end{aligned} \tag{23}$$

Based on the above-mentioned procedures, determination of k_p and k_q of DIDF can be summarized as follows:

1. Check stabilization of closed-loop by DIDF and K_g, then determine a new critical point p_e in case of stabilization.
2. If stabilization is not possible, use the inner loop with $C(s)$. Then return to step 1.
3. Determine k_p and k_q of DIDF using the relationship of Eqs. (9) and (14).

4 Examples

In this paper, the performances of proposed controllers are evaluated based on three categories:

(I) 3 indexes related to Integral of error

$$\text{IAE} = \int_0^\infty |e(t)|dt,\ \text{ISE} = \int_0^\infty e^2(t)dt,\ \text{ITAE} = \int_0^\infty t|e(t)|dt \tag{24}$$

(II) Size of overshoot, (III) Plant parameter variations.

4.1 Stabilization Is Possible Without Using C(S)

[Case 1]: Normalized dead time is small, that is τ = 1/6 ([9, 12, 15])

$$G(s) = \frac{1}{s-1}e^{-0.2s} \tag{25}$$

The results of simulation is shown in Fig. 6, where parameters of DIDF compensator are chosen as k_p = 0.4, k_q = 0.3, l = 0.2, and K_g = 1.The results clearly show the differences according to controller design methods.

Figure 7 shows results when the pole of plant is moved from 1 to 1.5.

[Case 2]: Normalized dead time is medium, that is, τ = 1/3 ([12, 14])

$$G(s) = \frac{4}{4s-1}e^{-2s} \tag{26}$$

The simulation results are shown in Fig. 8. In this case, parameters of DIDF are given as k_p = 0.7, k_q = 0.3, l = 0.2 and K_g = 0.3. And Fig. 9 shows the results when we changed dead time L more than 10 %, which represents quite strong robustness of DIDF compensator.

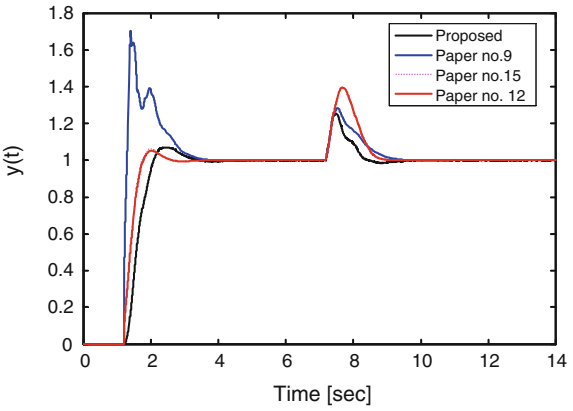

Fig. 6 Simulation results of [Case 1]

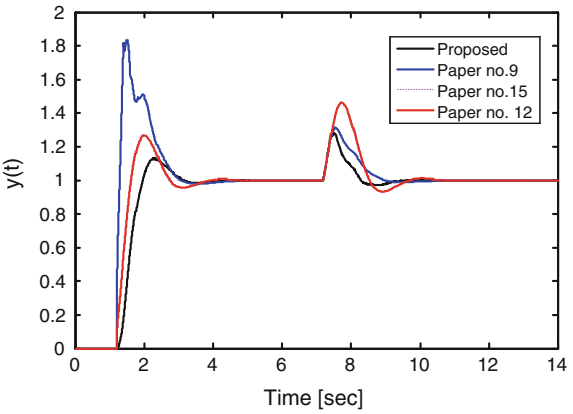

Fig. 7 A pole is moved from 1 to 1.5

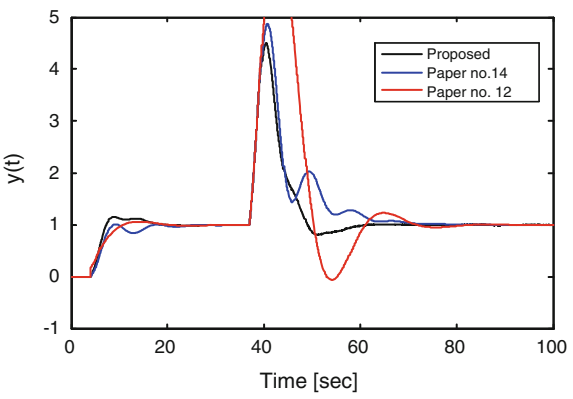

Fig. 8 Simulation results of [Case 2]

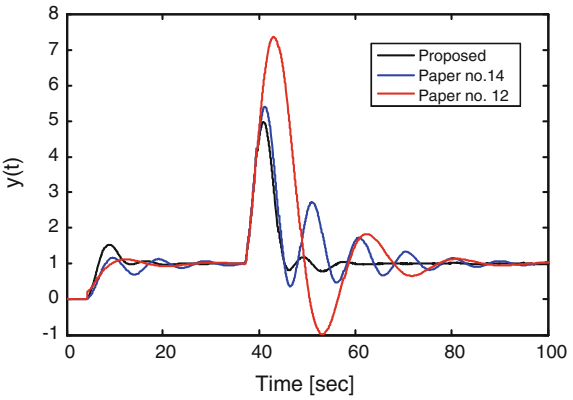

Fig. 9 Results of [Case 2] (when dead time $L = 2.2$)

4.2 *Inner Loop Is Needed for Stabilization*

[Case 3]: As mentioned above, we first stabilized plant with $C(s)$ and apply DIDF compensator, then compares it with the results of [14].

$$G(s) = \frac{1}{s-1} e^{-1.5s} \tag{27}$$

Since plant (30) has high normalized dead time, it is impossible to stabilize without inner loop. Simulation results are shown in Fig. 10.

(3) Plant is unstable 2nd-order system with dead time:

[Case 4]: Plant is given in [9].

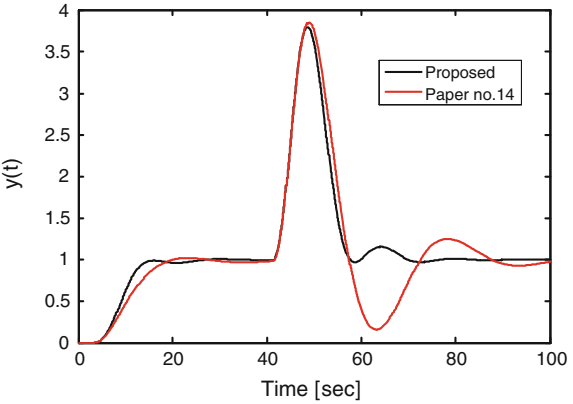

Fig. 10 Simulation results of [Case 3]

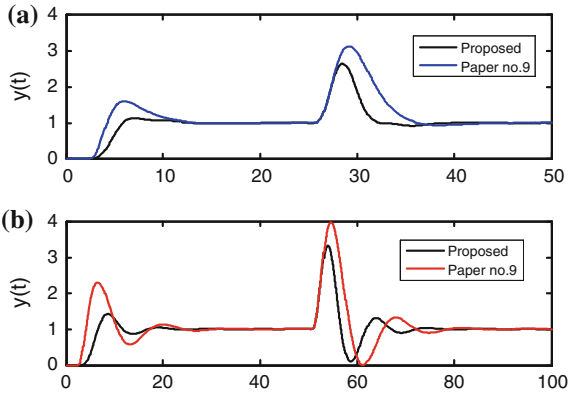

Fig. 11 Simulation results of [Case 4]

$$G(s) = \frac{27}{(s-0.1)(s+2.8)} e^{-0.5s} \tag{28}$$

Equation (28) can be stabilized without inner loop, and DIDF parameters are given as $k_p = 0.3$, $k_q = 0.3$, $l = 0.6$ and $K_g = 0.2$. The simulation results are shown in Fig. 11.

5 Conclusion

It is generally known that unstable plant with dead time is quite difficult to design control systems. This paper proposed a new method for determining PID parameters by using DIDF compensator, by which we improve performance of the conventional controller design method. That is, by inserting DIDF compensator, the critical point $(-1 + j0)$ of Nyquist's theory could be moved to an appropriate location, that is, we can overcome the difficulties of the conventional PID tuning methods, and be easily applicable. Two kinds of techniques of determining proper coefficients k_p, k_q and l for DIDF are suggested. To sum up:

(1) It is possible to set up parameters of PID controllers through simple calculations by applying properly designed DIDF, thereby improving input and disturbance responses.
(2) It is possible to enhance robustness of the closed loop due to nonlinear element inserted

References

1. Hidenobu S (1992) PID Control (in Japanese), Asakura-shoten, in Japan, pp 17–18
2. Astrom K, Hagglund T (2001) The future of PID control. Control Eng Pract 9:1163–1175
3. Panagopoulos H, Astrom K, Hagglund T (2002) Design of PID controllers based on constrained optimization. IEEE Proc Control Theor Appl 149(1):32–40
4. Silva GJ, Datta A, Battacharyya SP (2002) New results on the synthesis of PID controllers IEEE Trans Auto Contr 47(2):241–252
5. Skogestad S (2003) Simple analytic rules for model reduction and PID controller tuning. J Process Control (13):291–209
6. Ho WK, Hang CC, Cao LS (1995) Tuning of PID controllers based on gain and phase margin specifications. Automatica 31(3):497–502
7. Ho WK, Hang CC, Zhou J (1997) Self-tuning PID control of a plant with under-damped response with specifications on gain and phase margins. IEEE Trans Control Syst Technol 5:446–452
8. Astrom K, Hagglund T (2004) Revisiting the Ziegler-Nichols step response method for PID control. J Process Control 14:635–650
9. Malwatkar GM, Bhosale PT, Nikam SD (2009) PID controllers tuning for improved performance of unstable processes. In: International. conference on advances in computing, control, and telecommunication technologies, pp 624–628
10. Shafiei Z, Shento AT (1994) Tuning of PID-type controllers for stable and unstable systems with time delay. Automatica 30:1609–1615
11. Lee Ching-Hung, Teng Ching-Cheng (2002) Tuning of PID controllers for unstable processes based on gain and phase margin specifications: a fuzzy neural approach. Fuzzy Sets Syst 128:95–106
12. Wang Y-G, Xu X-M (2009) PID tuning for unstable processes with sensitivity specification. In: Proceedings of the 2009 Chinese control and decision conference(CCDC 2009), pp 3460–3464
13. Paraskevopoulos PN, Pasgianos GD, Arvanitis KG (2006) PID-type controller tuning for unstable first order plus dead time processes based on gain and phase margin specification. IEEE Trans Control Syst Technol 14(5):926–936
14. Xiang C, Nguyen, LA (2005) Control of unstable processes with dead time by PID controllers, ICCA2005
15. Wang Y-G, Cai W-J (2002) Advanced PID tuning for integrating and unstable processes with gain and phase margin specifications. Ind Eng Chem Res 41:2910–2914
16. Shamsuzzoha M, Lee M (2002) IMC-PID controller design for improved rejection of time-delayed processes. Ind Eng Chem Res 46:2077–2091
17. Gibson JE (1963) Nonlinear Automatic Control. McGraw-Hill Book Co., New York
18. West C, Douce JL, Livesley RK (1955) The dual-input describing function and its use in the analysis of nonlinear feedback systems. Proc IEEE 103B:463–474
19. Choe YW, Lee HY (2009) Periodic disturbance cancellation by DIDF method, ICCA2009
20. Choe, YW (2013) A method for performance improvement of PID control by DIDF method. In: proceeding of the 9th Asian control conference

Cross-Coupling Synchronous Velocity Control for an Uncertain Model of Transformer Winding System Using Model Reference Adaptive Control Method

Van Tu Duong, Jae Hoon Jeong, Nam Soo Jeong, Min Saeng Shin, Tan Tien Nguyen, Gi Sig Byun and Sang Bong Kim

Abstract This paper proposes cross-coupling synchronous velocity control based on model reference adaptive control (MRAC) method for an uncertain model of transformer winding system with two non-symmetrical axial systems such as a winding spindle system and a nozzle feed drive system. Since it is difficult to achieve the physical parameters in modeling of the transformer winding system, MRAC is used to ensure the stability of the transformer winding system. In order to minimize the synchronous velocity error between two axial systems, a cross-coupling synchronous control is employed. Accordingly, the velocity error of the winding spindle system is reflected to the nozzle feed drive system and vice versa. Simulation and experimental results show that the proposed controller which is applied to the transformer winding system with uncertain parameters can reduce the synchronous velocity error between two axial systems.

Keywords Model reference adaptive control · Cross-coupling · Synchronous speed control · Winding system

V. Tu Duong · J.H. Jeong · S.B. Kim (✉)
Department of Mechanical Design Engineering, College of Engineering,
Pukyong National University, Busan 608-739, South Korea
e-mail: kimsb@pknu.ac.kr

N.S. Jeong · M.S. Shin
Department of Shipbuilding and Ocean Engineering,
Dongwon Institute of Science and Technology, Yangsan 626-740, South Korea

G.S. Byun
Department of Control and Instrumentation Engineering, College of Engineering,
Pukyong National University, Busan 608-737, South Korea

T.T. Nguyen
Faculty of Mechanical Engineering, Ho Chi Minh City University of Technology,
Ho Chi Minh, Vietnam

V.H. Duy et al. (eds.), *AETA 2015: Recent Advances in Electrical Engineering and Related Sciences*, Lecture Notes in Electrical Engineering 371,
DOI 10.1007/978-3-319-27247-4_38

1 Introduction

In industrial manufacturing, the increasing demand to improve dimensional accuracy for high precision machine has become more challenge. There are tremendous researchers who have attracted to achieve minimizing the contour error of CNC machine, electric wire discharge machine [1–6]. These machines consist of two or more symmetrical axes to drive a cutting tool and work piece for the processing of design part. For a winding system, there are two non-symmetrical axes such as a winding spindle axis and a nozzle feed drive axis incorporated to produce an apparatus with transformer bobbin, filament mandrel, speaker coil, relay wire coil, etc. To construct a coil, the wire which is sent from the nozzle feed drive wraps around a bobbin which is inserted to the winding spindle by a rotation of bobbin about its axis. The velocity error of each axis is minimized by a closed loop controller while the incorporating motion between two axes have to be controlled by a synchronous controller to meet the requirement of neither overlap nor gap generation among wire coils. There are two typical synchronous motion control schemes for controlling multi-axes of machine. The first control scheme is described as a master-slave configuration. The reference command input is only fed to one axis defined as master while the other axis defined as slave is tracking the output of master. This typical control has the advantage as using a simple algorithm, however the velocity error of the master is reflected to the slave while the velocity error of the slave is not be thrown back to the master. Therefore, the synchronous velocity error cannot be controlled to converge to zero. The second control scheme known as cross-coupling control (CCC) was proposed firstly by [1]. Some modification of CCC presented in [2, 3] showed that the good contour tracking error was achieved. Dam and Ouyang [4] took advantage of both CCC and a type of feedback controller called event-driven to form a novel control method in which the CCC was turned into position domain instead of time domain as traditional CCC. A combination of CCC and friction compensation was proposed by [5]. The CCC can reduce the contour error of two axial systems while friction compensation can be used to reduce positioning errors in machining systems. Sun in [6] developed an adaptive cross-coupling control algorithm for position synchronization of multiple axes. The CCC was incorporated to adaptive control through feedback of position error, synchronous error and control parameter estimator. These above researches either only give a theory control without experiment test or take account into the experiment model with unknown parameters. In practical application, in order to diminish the synchronous error between two axial systems, a model with known parameters is needed to obtain for developing a synchronous controller. However, some physical parameters are difficult to be computed or identified for constructing a model system. To overcome this drawback, a control method called as model references adaptive control (MRAC) was developed for various unknown model system [7–13]. The advantage of MRAC is to control an unknown model system with its real output tracking the output of the reference model.

This paper proposes a cross-coupling synchronous velocity controller for an uncertain model of a transformer winding system with non-symmetrical two axial systems such as a winding spindle system and a nozzle feed drive system by combination of CCC algorithm and MRAC. Since the parameters of dynamic model of each axial system of the transformer winding system are difficult to obtain fully for developing a controller, the real output of the transformer winding system is controlled to track the output of reference model due to updating controller parameters. To do this task properly, two axial systems modeling with uncertain parameters of the transformer winding system is achieved firstly. Then, based on two axial systems modeling, references models with parameters chosen such that the outputs of the reference models track the reference inputs of the axial systems are defined. Meanwhile, the synchronous velocity error between two axial systems are controlled to converge to zero by using CCC. Accordingly, the velocity error of the winding spindle system is reflected to the nozzle feed drive system and vice versa. The simulation and experimental results show that the proposed controller can diminish the synchronous velocity error between two non-symmetrical axial systems of the transformer winding system.

2 System Modeling

The prototype of a transformer winding system shown in Fig. 1 consists of a winding spindle system, a nozzle feed drive system, wire tensioner and wire spool. The winding spindle and the nozzle feed drive are described in Fig. 2. For the winding spindle system, DC motor drives a transformer bobbin inserted in a spindle

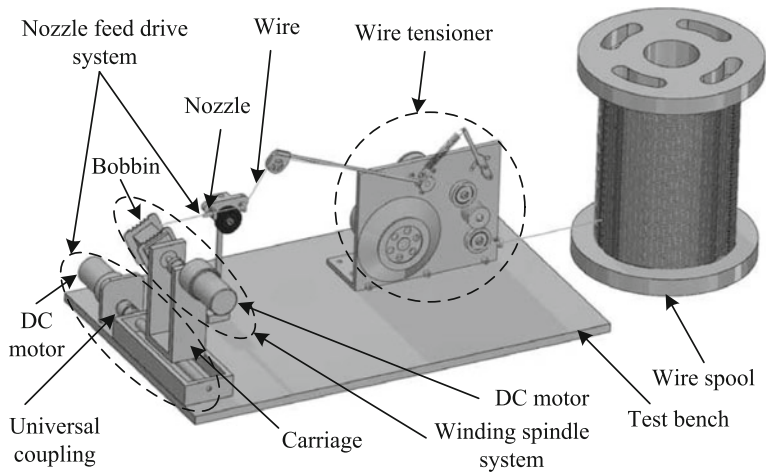

Fig. 1 Transformer winding system

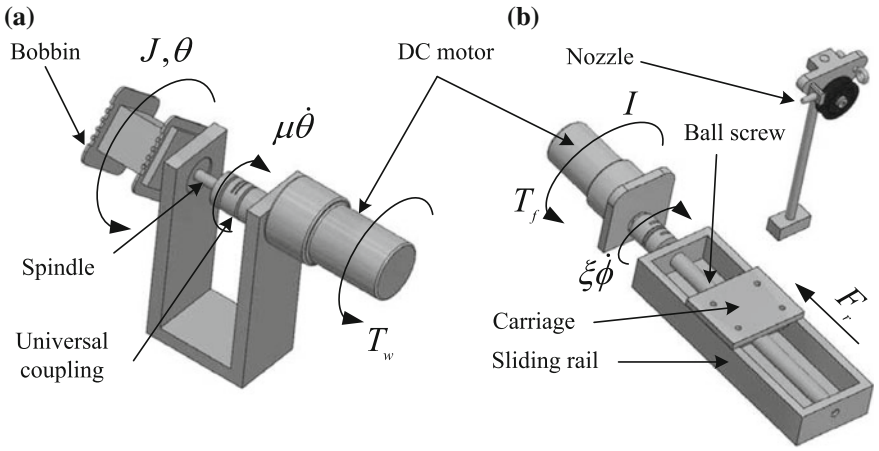

Fig. 2 Description of the winding spindle system and the nozzle feed drive system. **a** Winding spindle system. **b** Nozzle feed drive system

spinning through a universal coupling. The nozzle feed drive system is composed of a ball screw coupled to a DC motor for driving a carriage sliding laterally along a sliding rail and a nozzle for delivering a wire to the bobbin. All mechanisms of the winding spindle system are mounted onto the carriage. By the rotation of the winding spindle, a wire from the wire spool kept in sufficient tension force by the wire tensioner is fed through passing the nozzle and wrapped around the transformer bobbin to form a wire coil. Since the nozzle is fixed on a test bench perpendicularly to the sliding rail while the bobbin moves along with the carriage, the wire is distributed over the area of bobbin. Accordingly, a layer of the wire coil is constructed by a synchronous motion of the winding spindle system and the nozzle feed drive system. To develop a synchronous controller for two axial systems of the transformer winding system, the modeling of each axial system is achieved. For the winding spindle system of Fig. 2a, the rotational behavior is represented by:

$$J\ddot{\theta} + \mu\dot{\theta} + d_w\theta = T_w \tag{1}$$

where J is the combined moment inertia of the DC motor and the universal coupling with the subscript "w" standing for winding spindle, θ is the angular displacement of the winding spindle system, μ is the rotational viscous coefficient of motor rotor, spindle and bearing, the term $d_w\theta$ is the lumped disturbance caused by wire tension and un-modeled dynamics, d_w is the torsional disturbance coefficient, and T_w is the motor torque driving the winding spindle.

For the nozzle feed drive system of Fig. 2b, the rotational motion of the DC motor coupled to the ball screw is represented by:

$$I\ddot{\phi} + \xi\dot{\phi} + T_r = T_f \tag{2}$$

where I is the combined moment inertia of the DC motor, the universal coupling and the ball screw, ϕ is the angular displacement of motor shaft, ξ is the rotational viscous coefficient of motor rotor, ball screw and bearing, T_r is the reaction torque applied by the carriage of the ball screw, and T_f is the motor torque driving the ball screw.

The linear behavior of the nozzle feed drive system can be represented by:

$$M\ddot{\delta} + v\dot{\delta} + d_f\delta = F_r \tag{3}$$

where M is the mass which is composed of the winding spindle system and the carriage on the ball screw, δ is the linear displacement of the carriage, v is the linear viscous coefficient between the carriage and the sliding rail of the ball screw, $d_f\delta$ is the lumped disturbance caused by un-modeled dynamics, d_f is the translational disturbance coefficient, and F_r is the reaction force generating the reaction torque by $T_r = F_r r$ where r is the radius of the ball screw.

The relation of the linear displacement of the carriage and the angular displacement of the DC motor ϕ is determined by:

$$\delta = \frac{\phi l}{2\pi} \tag{4}$$

where l is the lead of the ball screw.

From Eqs. (2), (3) and (4) can be combined as follows:

$$\left(M + \frac{2\pi l}{lr}\right)\ddot{\delta} + \left(v + \frac{2\pi\xi}{lr}\right)\dot{\delta} + d_f\delta = \frac{T_f}{r} \tag{5}$$

By defining a state vector as $X = \left[\Theta^T \ \ \Delta^T\right]^T$ with $\Theta = \left[\theta \ \ \dot{\theta}\right]^T$ and $\Delta = \left[\delta \ \ \dot{\delta}\right]^T$, an extended system combined with Eq. (1) of a real winding spindle system (WSS) and Eq. (5) of a real nozzle feed drive system (NFDS) can be rewritten as follows:

$$\begin{cases} \dot{X} = AX + BU \\ Y = CX \end{cases} \tag{6}$$

where $A = \begin{bmatrix} A_\theta & \mathbf{0} \\ \mathbf{0} & A_\delta \end{bmatrix}, A_\theta = \begin{bmatrix} 0 & 1 \\ -a_0 & -a_1 \end{bmatrix}, A_\theta = \begin{bmatrix} 0 & 1 \\ -\alpha_0 & -\alpha_1 \end{bmatrix}, B = \begin{bmatrix} b\bar{B} & \mathbf{0} \\ \mathbf{0} & \beta\bar{B} \end{bmatrix}$, $\bar{B} = \begin{bmatrix} 0 \\ 1 \end{bmatrix}$, $C = \begin{bmatrix} \bar{C} & \mathbf{0} \\ \mathbf{0} & \bar{C} \end{bmatrix}$, $\bar{C} = [0 \quad 1]$, the control input vector is defined as $U = \begin{bmatrix} T_w \\ T_f \end{bmatrix}$, the output vector is defined as $Y = \begin{bmatrix} \varphi \\ v \end{bmatrix} = \begin{bmatrix} \dot{\theta} \\ \dot{\delta} \end{bmatrix}$, $a_1 = \frac{\mu}{J}$, $a_0 = \frac{d_w}{J}$, $b = \frac{1}{J}$, $\alpha_1 = \frac{vlr + 2\pi\xi}{Mlr + 2\pi\xi}$, $\alpha_0 = \frac{d_f lr}{Mlr + 2\pi\xi}$, $\beta = \frac{l}{Mlr + 2\pi\xi}$, and φ, v are the rotational velocity and the linear velocity of the WSS and NFDS, respectively.

Commonly, a feedback controller is designed readily for a known or certain system. However, in this case, since none of all physical parameters of the real system of Eq. (6) are measurable, a model reference adaptive control (MRAC) is appropriate for controlling a such system. Accordingly, the output of the real system is controlled to track the output of a stable reference system. The reference model of Eq. (6) is defined respectively as:

$$\begin{cases} \dot{X}_m = A_m X_m + B_m R \\ Y_m = C X_m \end{cases} \tag{7}$$

where $X_m = \left[\Theta_m^T \ \Delta_m^T\right]^T$ with $\Theta_m = \left[\theta_m \ \dot{\theta}_m\right]^T$ and $\Delta_m = \left[\delta_m \ \dot{\delta}_m\right]^T$ is the state vector of the reference model system for the system of Eq. (6), $R = [\varphi_r \ v_r]^T$ is defined as the velocity reference vector consisting of the angular velocity reference and the linear velocity reference of the system of Eq. (6) with $v_r = \lambda\varphi_r$, $Y_m = [\varphi_m \ v_m]^T$ is the output vector of the reference model consisting of its angular velocity and its linear velocity, $A_m = \begin{bmatrix} A_{\theta m} & \mathbf{0} \\ \mathbf{0} & A_{\delta m} \end{bmatrix}$, $A_{\theta m} = \begin{bmatrix} 0 & 1 \\ -a_{m0} & -a_{m1} \end{bmatrix}$, $A_{\delta m} = \begin{bmatrix} 0 & 1 \\ -\alpha_{m0} & -\alpha_{m1} \end{bmatrix}$, $B_m = \begin{bmatrix} b_m\bar{B} & \mathbf{0} \\ \mathbf{0} & \beta_m\bar{B} \end{bmatrix}$ are the matrices with constant parameters which are chosen such that

$$\lim_{t\to\infty} \|Y_m - R\| = 0 \tag{8}$$

3 Controller Design

A tracking error vector E is defined as the difference between the velocity output vector Y in Eq. (6) and its the velocity reference vector R as follows:

$$E = Y - R = \begin{bmatrix} e_w \\ e_f \end{bmatrix} = \begin{bmatrix} \varphi - \varphi_r \\ v - v_r \end{bmatrix} = \begin{bmatrix} \dot{\theta} - \varphi_r \\ \dot{\delta} - \lambda\varphi_r \end{bmatrix} \tag{9}$$

where e_w, e_f are the velocity tracking error of WSS and NFDS, respectively and λ is the positive-synchronous scale factor which indicates a step of the nozzle feed drive system followed by each turn of the winding spindle.

A synchronous velocity error is defined as the difference linear velocities between WSS and NFDS as follows:

$$e_{syn} = \lambda e_w - e_f = GE \tag{10}$$

where the vector G is defined by $G = [\lambda - 1]$.

A modeling error vector is defined as the state vector difference between the real winding system and the reference model system are defined by:

$$\tilde{X} = \left[\tilde{\Theta}^T \;\; \tilde{\Delta}^T\right]^T = X - X_m \tag{11}$$

where $\tilde{\Theta} = \left[\tilde{\theta} \;\; \dot{\tilde{\theta}}\right]^T$ and $\tilde{\Delta} = \left[\tilde{\delta} \;\; \dot{\tilde{\delta}}\right]^T$.

From Eqs. (6), (7) and (11), a modeling error dynamics can be obtained as follows:

$$\dot{\tilde{X}} = A_m \tilde{X} + BU + \Psi \tag{12}$$

where $\Psi = \bar{A}X - B_m R = [\bar{B}^T\psi_\theta \;\; \bar{B}^T\psi_\delta]^T$, $\psi_\theta = -(a_1 - a_{m1})\dot{\theta} - (a_0 - a_{m0})\theta - b_m\varphi_r$, $\psi_\delta = -(\alpha_1 - \alpha_{m1})\dot{\delta} - (\alpha_0 - \alpha_{m0})\delta - \beta_m\lambda\varphi_r$.

For any symmetric positive-definite matrix Q, there exists the unique symmetric positive-definite matrix P such that satisfying the linear equations as

$$A_m^T P + PA_m = -Q \tag{13}$$

where $P = diag[P_\theta \;\; P_\delta]$, $Q = diag[Q_\theta \;\; Q_\delta]$.

In additional, a cross-coupling MRAC synchronous velocity controller vector for the system of Eq. (6) is given by:

$$U = \begin{bmatrix} T_w \\ T_f \end{bmatrix} = K_1 X + K_2 R + \varepsilon \begin{bmatrix} -1 \\ 1 \end{bmatrix} e_{syn} \tag{14}$$

where $K_1 = \left[K_{1\theta}^T \;\; K_{1\delta}^T\right]^T$, $K_2 = \left[K_{2\theta}^T \;\; K_{2\delta}^T\right]^T$ with $K_{1\theta} = [k_1(t) \;\; k_0(t) \;\; 0 \;\; k_3(t)]$, $K_{1\delta} = [0 \;\; k_7(t) \;\; k_5(t) \;\; k_4(t)]$, $K_{2\theta} = [k_2(t) \;\; 0]$ and $K_{2\delta} = [0 \;\; k_6(t)]$ are the controller gain matrices which have unknown control parameters updated by an adaptation law, and ε is the synchronous controller gain.

To determine an update law for the unknown control parameters $k_i(t)(i = 0 - 7)$ the candidate Lyapunov function is defined with the tracking error terms in Eq. (11) as follows:

$$V = V_1 + V_\theta + V_\delta \tag{15}$$

where

$$\begin{aligned}
V_1 =& \frac{1}{2}\tilde{X}^T P\tilde{X},\\
V_\theta =& \frac{1}{2b\eta_0}(bk_0(t) + b\varepsilon\lambda - a_1 + a_{m1})^2 + \frac{1}{2b\eta_1}(bk_1(t) - a_0 + a_{m0})^2\\
&+ \frac{1}{2b\eta_2}(bk_2(t) - b_m)^2 + \frac{b}{2\eta_3}(k_3(t) + \varepsilon)^2,\\
V_\delta =& \frac{1}{2\beta\eta_4}(\beta k_4(t) - \beta\varepsilon - \alpha_1 + \alpha_{m1})^2 + \frac{1}{2\beta\eta_5}(\beta k_5(t) - \alpha_0 + \alpha_{m0})^2\\
&+ \frac{\lambda}{2\beta\eta_6}(\beta k_6(t) - \beta_m)^2 + \frac{\beta}{2\eta_7}(k_7(t) + \varepsilon\lambda)^2
\end{aligned}$$

Using Eqs. (6), (9), (10) and (12)–(14), the time derivative of the first term of Lyapunov function V is given by:

$$\begin{aligned}
\dot{V}_1 =& \frac{1}{2}\left(\dot{\tilde{X}}^T P\tilde{X} + \tilde{X}^T P\dot{\tilde{X}}\right)\\
=& \frac{1}{2}\left(\tilde{X}^T A_m^T P\tilde{X} + \tilde{X}^T PA_m\tilde{X}\right) + \tilde{X}^T PBU + \tilde{X}^T P\Psi\\
=& -\frac{1}{2}\tilde{X}^T Q\tilde{X} + \tilde{\Theta}^T P_\theta\bar{B}(bT_w + \psi_\theta) + \tilde{\Delta}^T P_\delta\bar{B}\left(\beta T_f + \psi_\delta\right)\\
=& -\frac{1}{2}\tilde{X}^T Q\tilde{X} + \tilde{\Theta}^T P_\theta\bar{B}\Big[(bk_0(t) - b\varepsilon\lambda - a_1 + a_{m1})\dot{\theta} + (bk_1(t) - a_0 + a_{m0})\theta\\
&+ (bk_2(t) - b_m)\varphi_r + b(k_3(t) + \varepsilon)\dot{\delta}\Big]\\
&+ \tilde{\Delta}^T P_\delta\bar{B}\Big[(\beta k_4(t) - \beta\varepsilon - \alpha_1 + \alpha_{m1})\dot{\delta} + (\beta k_5(t) - \alpha_0 + \alpha_{m0})\delta\\
&+ \lambda(\beta k_6(t) - \beta_m)\varphi_r + (k_7(t) + \varepsilon\lambda)\dot{\theta}\Big]
\end{aligned} \tag{16}$$

The time derivative of V_θ and V_δ are obtained as follows:

$$\begin{aligned}
\dot{V}_\theta =& \frac{\dot{k}_0}{\eta_0}(bk_0(t) - b\varepsilon\lambda - a_1 + a_{m1}) + \frac{\dot{k}_1}{\eta_1}(bk_1(t) - a_0 + a_{m0})\\
&+ \frac{\dot{k}_2}{\eta_2}(bk_2(t) - b_m) + \frac{\dot{k}_3}{\eta_3}b(k_3(t) + \varepsilon)
\end{aligned} \tag{17}$$

$$\dot{V}_\delta = \frac{\dot{k}_4}{\eta_4}(\beta k_4(t) - \beta\varepsilon - \alpha_1 + \alpha_{m1}) + \frac{\dot{k}_5}{\eta_5}(\beta k_5(t) - \alpha_0 + \alpha_{m0}) + \frac{\dot{k}_6}{\eta_6}\lambda(\beta k_6(t) - \beta_m) + \frac{\dot{k}_7}{\eta_7}\beta(k_7(t) + \varepsilon\lambda) \tag{18}$$

The time derivative of Lyapunov function is achieved

$$\dot{V} = \dot{V}_1 + \dot{V}_\theta + \dot{V}_\delta \tag{19}$$

Parameter update laws of WSS and NFDS can be chosen as

$$\begin{cases} \dot{k}_0 = -\eta_0 \tilde{\Theta}^T P_\theta \bar{B}\dot{\theta}, \quad \dot{k}_1 = -\eta_1 \tilde{\Theta}^T P_\theta \bar{B}\theta, \\ \dot{k}_2 = -\eta_2 \tilde{\Theta}^T P_\theta \bar{B}\varphi_r, \quad \dot{k}_3 = -\eta_3 \tilde{\Theta}^T P_\theta \bar{B}\dot{\delta} \end{cases} \tag{20}$$

$$\begin{cases} \dot{k}_4 = -\eta_4 \tilde{\Delta}^T P_\delta \bar{B}\dot{\delta}, \ \dot{k}_5 = -\eta_5 \tilde{\Delta}^T P_\delta \bar{B}\delta, \\ \dot{k}_6 = -\eta_6 \tilde{\Delta}^T P_\delta \bar{B}\varphi_r, \ \dot{k}_7 = -\eta_7 \tilde{\Delta}^T P_\delta \bar{B}\dot{\theta} \end{cases} \tag{21}$$

From Eq. (16)–(21), the time derivative of the Lyapunov function can be satisfied as

$$\dot{V} = -\frac{1}{2}\tilde{X}^T Q \tilde{X} < 0 \tag{22}$$

Using the controller of Eq. (14), the control parameter update laws of Eqs. (20)–(21), (15) and (22) and Barbalat's lemma, $\lim_{t\to\infty} \tilde{X} \to 0$. In the other words, the following equation is obtained at steady state:

$$Y - Y_m = \mathbf{0} \tag{23}$$

Recalling the previous condition of Eq. (8) as $\lim_{t\to\infty} \|Y_m - R\| = 0$ and using Eq. (23), the tracking error vector E defined in Eq. (9) and the synchronous velocity error e_{syn} defined in Eq. (10) can achieved at steady state as follows:

$$\begin{cases} E = Y - R = Y_m - R = \mathbf{0} \\ e_{syn} = GE = 0 \end{cases} \tag{24}$$

The block diagram of MRAC for the proposed cross-coupling synchronous velocity controller of the transformer winding system is shown in Fig. 3.

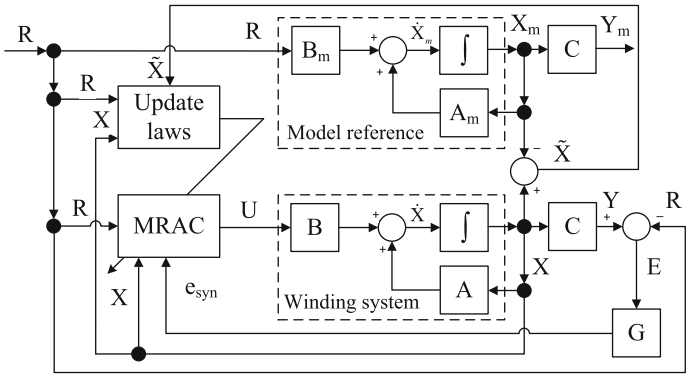

Fig. 3 Block diagram of the proposed cross coupling synchronous velocity controller

4 Simulation and Experimental Results

In coil winding manufacturing, the transformer bobbin is wound to form many layers of wire coil. Therefore, the winding spindle is driven to spin the bobbin for winding wire and stopped when the setting number of wire turn is reached. Hence, the nozzle feed drive system handles the bobbin sliding laterally along the nozzle in several cycle to form multi-layer of wire coil.

However, for evaluating the synchronous velocity error between WSS and NFDS, simulation is taken in the condition of making only one layer of wire turn. Therefore, the reference rotational velocity of WSS is given as a step function known as a desired winding speed. Accordingly, the reference linear velocity of NFDS is converted from the reference rotational velocity through the synchronous scale factor. Actually, the system modeling parameters of the transformer winding system are unknown or difficult to calculate. For simulation purpose, these parameters are shown in Table 1. The control parameters are defined as $\eta_0 = \eta_1 = \eta_2 = \eta_3 = \eta_4 = \eta_5 = \eta_6 = \eta_7 = 5$, $P_\theta = P_\delta = diag[1\ 1]$. The initial

Table 1 System modeling parameters

Parameters	Value	Unit	Parameter	Value	Unit
a_1	5.72	s^{-1}	a_{m1}	10	s^{-1}
a_0	2.56	s^{-2}	a_{m0}	0	s^{-2}
b	6.84	rad/(Nms^2)	b_m	10	s^{-1}
α_1	2.16	s^{-1}	α_{m1}	2	s^{-1}
α_0	3.25	s^{-2}	α_0	0	s^{-2}
β	5.79	1/(Ns^{-2})	β_m	2	s^{-1}
φ_r	2π	rad/s	ε	5	Ns
λ	0.095×10^{-3}	m/rad	l	0.6	mm

values of control inputs T_w, T_f, the state vector X and X_m, the tracking error vector $\tilde{X}$ and the updated control parameters $k_i (i = 0 - 7)$ are set to zero.

The simulation results of angular velocity of WSS and linear velocity of NFDS are shown in Fig. 4. The angular velocity of the real WSS is almost tracking the angular velocity output of the reference model $(\varphi_r = 2\pi)$ after 1 s as shown in Fig. 4a, while the linear velocity of the real NFDS is more vibrated than the linear velocity output of the reference model within 0.5 s early as shown in Fig. 4b due to a irrelevant value of the update control parameters. However, the linear velocity of NFDS tracks its reference $(v_r = \varphi_r l/2\pi)$ after 3 s.

The modeling errors and the synchronous velocity error in simulation are shown in Fig. 5. Both of $\dot{\tilde{\theta}}$ and $\dot{\tilde{\delta}}$ converge to zero after 2 s as shown in Fig. 5a, while it takes 3 s until the synchronous velocity error in Fig. 5b reaches zero.

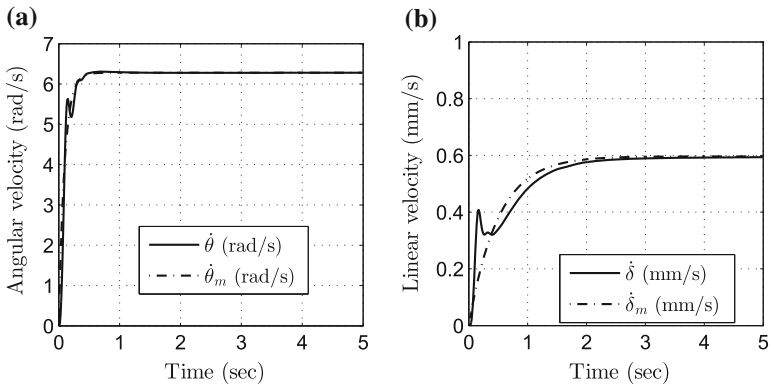

Fig. 4 Simulation results of angular and linear velocity. **a** Angular velocity of WSS. **b** Linear velocity of NFDS

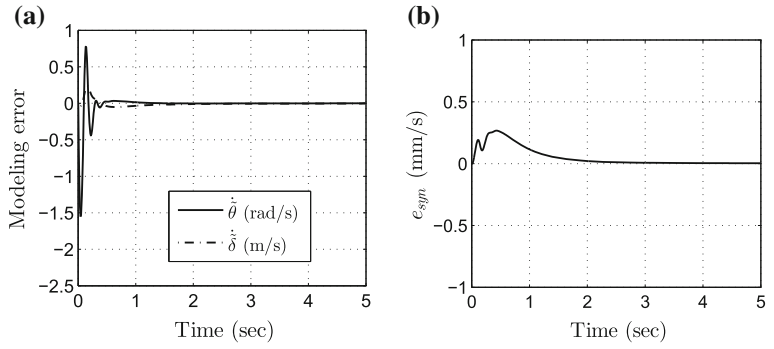

Fig. 5 Simulation results of modeling errors and synchronous velocity error. **a** Modeling errors. **b** Synchronous velocity error between

The updated control parameters and control inputs of the proposed controller in simulation are shown in Fig. 6. The control parameters are updated by the update laws in Eqs. (20)–(21) and obtain the steady state value when the output of the real axial system reaches the output of the reference system. In Fig. 6a, the control parameters $(k_0 \sim k_3)$ for WSS have small vibration and reach the steady state after 3 s. Meanwhile, the control parameters $(k_4 \sim k_7)$ for NFDS are proportional to time due to the nozzle's trajectory increased by time.

Additionally, the proposed controller is also tested on the prototype of the transformer winding system as shown in Fig. 7. By the controlling of DSP TMS320F28069 chip with the sampling time at 1 ms, the experimental results of angular velocity of WSS and the linear velocity of NFDS are shown in Fig. 8. In comparison to the output of the reference model, the angular and linear velocities

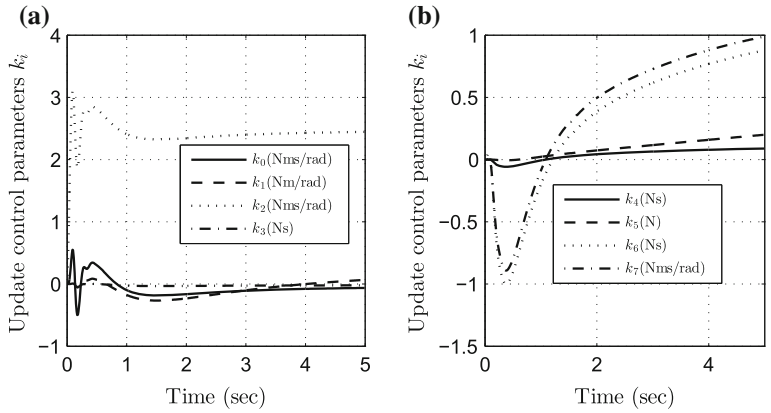

Fig. 6 Updated control parameters and control inputs. **a** Updated control parameters of WSS. **b** Updated control parameters of NFDS

Fig. 7 Experimental setup

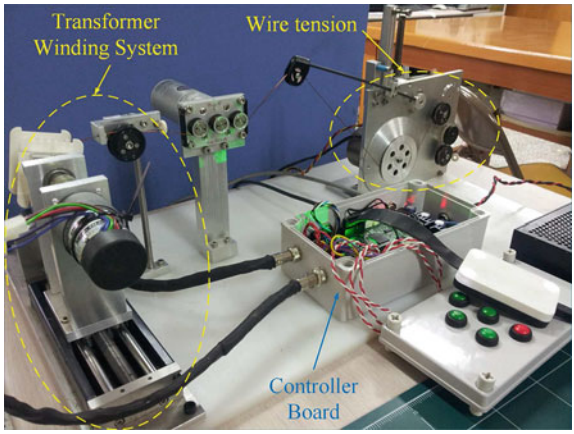

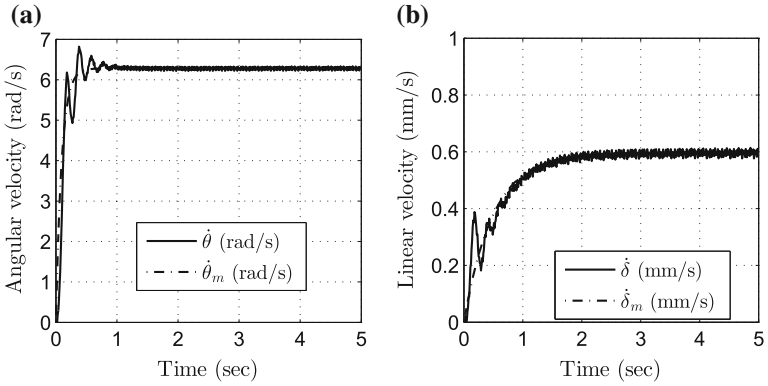

Fig. 8 Experimental results of tracking errors. **a** Angular velocity of WSS. **b** Linear velocity of NFDS

have more vibration due to the low resolution of hall sensors equipped in DC motors. The angular velocity of WSS tracks its reference within ±0.05 (rad/s) after 1 s while the linear velocity of NFDS tracks its reference within ±0.015 (mm/s) after 1.5 s. The modeling errors and synchronous velocity error in experimental results are shown in Fig. 9a, b, respectively. Both of $\dot{\tilde{\theta}}$ and $\dot{\tilde{\delta}}$ converge to zero after 1 s as shown in Fig. 9a. The modeling error of WSS is bounded within ±0.05 (rad/s) after 1 s while the modeling error of NFDS is bounded within ±0.015 (mm/s) after 1 s. The synchronous velocity error between the angular velocity of WSS transferred to a linear velocity and the linear velocity of NFDS is shown in Fig. 9. The synchronous velocity error converges to zero after 2 s and is bounded within ±0.01 (mm).

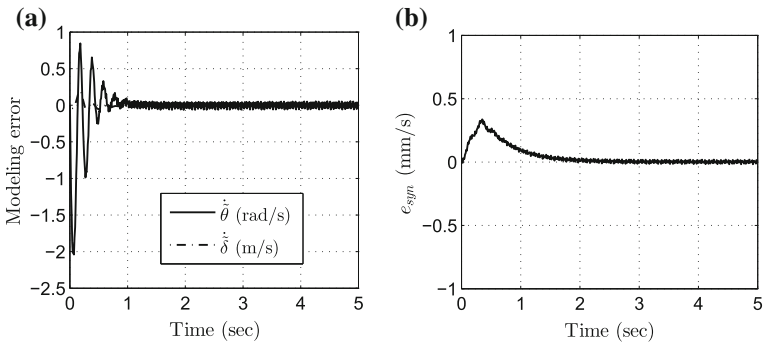

Fig. 9 Experimental results of modeling errors and synchronous velocity error. **a** Modeling errors. **b** Synchronous velocity error

5 Conclusion

In this paper, a cross-coupling synchronous velocity control based on a model reference adaptive control (MRAC) method for an uncertain model of transformer winding system with two non-symmetrical axial systems such as a winding spindle system and a nozzle feed drive system was proposed. MRAC was used to stabilize the system with unmeasurable physical parameters while the cross-coupling synchronous velocity error was adopted to eliminate the difference of linear velocities between two axial systems. The proposed controller was built in a DSP based microcontroller chip equipped to a prototype of transformer winding system. The simulation results showed that the proposed controller could control WSS and NFDS to obtain the desired objective. Even though the experimental results had some vibration in the measured values due to the low resolution of hall sensors, the effectiveness of the proposed controller was acceptable. This means that the synchronous velocity error could be reduced to ensure the wire coil of transformer wound with a limited gap/overlapping among wire turns.

References

1. Koren Y (1980) Cross-coupled biaxial computer control for manufacturing systems. J Dyn Syst Meas Contr 102:265–271
2. Koren Y, Lo CC (1991) Variable-gain cross-coupling controller for contouring. CIRP Annals Manuf Technol 40:371–374
3. Koren Y, Lo CC (1992) Advanced controllers for feed drives. CIRP Annals Manuf Technol 41:689–698
4. Dam T, Ouyang PR (2012) Position domain contour tracking with cross-coupled control. In: 2012 IEEE international symposium on industrial electronics (ISIE), Hangzhou, pp 1303–1308
5. Chen BC, Tilbury DM, Ulsoy AG (1998) Modular control for machine tools: cross-coupling control with friction compensation. In: Proceedings of the 1998 ASME international mechanical engineering congress and exposition, Anaheim, pp 455–462
6. Sun D (2003) Position synchronization of multiple motion axes with adaptive coupling control. Automatica 39:997–1005
7. Canigur E, Ozkan M (2012) Model reference adaptive control of a nonholonomic wheeled mobile robot for trajectory tracking. In: 2012 international symposium on innovations in intelligent systems and applications (INISTA), Trabzon, pp 1–5
8. Hua CC, Leng J, Guan XP (2012) Decentralized MRAC for large-scale interconnected systems with time-varying delays and applications to chemical reactor systems. J Process Control 10:1985–1996
9. Montanaro U, Gaeta A, Giglio V (2014) Robust discrete-time MRAC with minimal controller synthesis of an electronic throttle body. IEEE/ASME Trans Mechatronics 19:524–537
10. Das A, Lewis FL (2010) Cooperative adaptive control for synchronization of second-order systems with unknown nonlinearities. Int J Robust Nonlinear Control 21:1509–1524
11. Prakash R, Anita R (2012) Modeling and simulation of fuzzy logic controller-based model reference adaptive controller. Int J Innovative Comput Inf Control 8:2533–2550

12. Xu Q, Jia M (2014) Model reference adaptive control with perturbation estimation for a micropositioning system. IEEE Trans Control Syst Technol 22:352–359
13. Salvi A, Santini S, Biel D, Olm JM, Bernado, M (2013) Model reference adaptive control of a full-bridge buck inverter with minimal controller synthesis. In: 52nd IEEE conference on decision and control, Florence, pp 3469–3474

Comparing Convergence of PSO and SFLA Optimization Algorithms in Tuning Parameters of Fuzzy Logic Controller

Duc-Hoang Nguyen and Manh-Dung Ngo

Abstract The paper presents using the Particle Swarm Optimization (PSO) and Shuffled Frog Leaping Algorithm (SFLA) to optimally tune parameters of a fuzzy logic controller stabilizing a rotary inverted pendulum system at its upright equilibrium position. Both the PSO and SFLA are meta-heuristic search methods. PSO is inspired by bird flocking behavior searching for food while SFLA is inspired from the memetic evolution of a group of frogs when seeking for food. In this study, the rule base of the Fuzzy Logic Controller (FLC) is brought by expert experience, and the parameters of the controller, i.e. the membership function parameters and scaling gains, are optimally tuned by the PSO and SFLA such that a predefined criterion is minimized. Simulation results show that the designed fuzzy controller is able to balance the rotary inverted pendulum system around its equilibrium state. Besides, convergent rate of SFLA is faster than that of PSO.

Keywords PSO · SFLA · Optimization · Fuzzy logic controller · Rotary inverted pendulum system

1 Introduction

A fuzzy logic controller can be considered as a control expert system which simulates the human thinking. It consists of input and output variables with membership functions, a set of (IF…THEN) rules and an inference system. Designing fuzzy controllers involves choosing input and output variables of the controller,

D.-H. Nguyen (✉) · M.-D. Ngo
Faculty of Electrical and Electronics Engineering, HCMUT, Vietnam
e-mail: ndhoang@hcmut.edu.vn

M.-D. Ngo
e-mail: dung.nhattinh@gmail.com

V.H. Duy et al. (eds.), *AETA 2015: Recent Advances in Electrical Engineering and Related Sciences*, Lecture Notes in Electrical Engineering 371,
DOI 10.1007/978-3-319-27247-4_39

defining membership functions for each input and output variables, constructing the rule base reflecting the linguistic relationship between the inputs and outputs, and tuning the parameters of the membership functions and values of the scaling gains in order to achieve the required performance. Usually, when designing fuzzy controllers these parameters are chosen by trial and error. This manual design method is time-consuming and the control results are not optimal. In order to overcome this problem, optimization techniques are used to tune parameters of fuzzy controller to obtain the best possible solution according to a given criterion or fitness function [1].

Many optimization techniques have been proposed to tune parameters of fuzzy logic controller. In [2], authors used Genetic Algorithm to tune fuzzy control rules. The results showed that the fuzzy control rules obtained greatly improve the behavior of the FLC systems. In [3], authors showed that the PSO can simultaneously tune the premise and consequent parameters of the fuzzy rules for the appropriate design of fuzzy systems. In [4], the Bees Algorithm has been proved to be a useful tool for tuning fuzzy logic controllers to achieve better performance. In [5], Ant Colony Optimization (ACO) was applied to design a fuzzy controller, called ACO-FC. The proposed ACO-FC performance was shown to be better than other evolutionary design methods on one simulation example. In [6], Shuffled Frog Leaping Algorithm was used to optimally tune parameters of a fuzzy logic controller stabilizing a ball and beam system at its equilibrium position. Simulation results show that the designed fuzzy controller is able to balance the ball and beam system around its equilibrium state and the performance of the fuzzy controller is better than that of the well-known LQR controller.

In this paper, the authors introduce an application of the Particle Swarm Optimization and Shuffled Frog Leaping Algorithm in tuning parameters of a fuzzy logic controller for balancing a rotary inverted pendulum system in the upright position and compare convergent rate of two these optimization algorithms. This paper is organized as follows. Section 2 introduces the rotary inverted pendulum system and dynamics. Section 3 presents overview of the Particle Swarm Optimization and Shuffled Frog Leaping Algorithm. The description how to design and tune parameters of the fuzzy controller is given in Sect. 4. Section 5 shows obtained results and Sect. 6 concludes this paper.

2 Dynamics of the Rotary Inverted Pendulum System

The rotary inverted pendulum is an ideal experiment when introducing important control concepts such as non-linear systems. It's a natural unstable nonlinear system and a powerful tool to check the control theory and control algorithm. Figure 1 depicts the rotary inverted pendulum system.

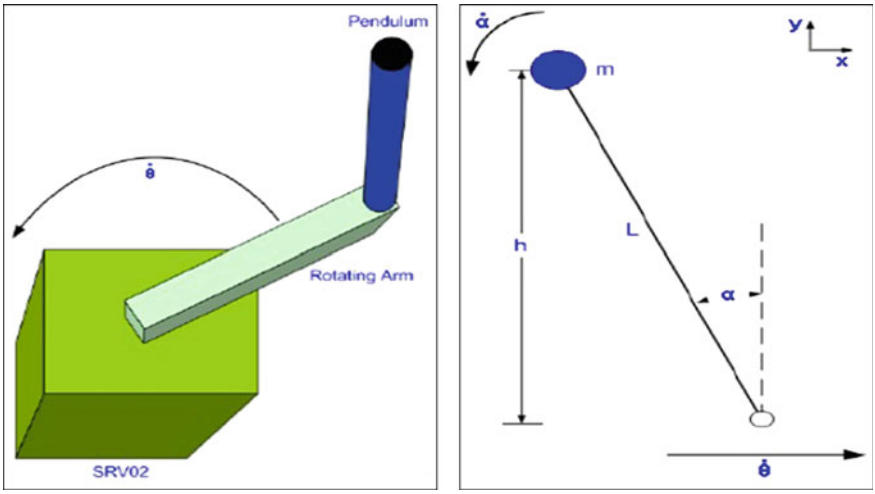

Fig. 1 Top view (*Left*) and side view (*Right*) of rotary inverted pendulum

System dynamic equations:

$$a\ddot{\theta} - b\cos(\alpha)\ddot{\alpha} + b\sin(\alpha)\dot{\alpha}^2 + G\dot{\theta} = \frac{\eta_m \eta_g K_t K_g}{R_m} V_m \tag{1}$$

$$c\ddot{\alpha} - b\cos(\alpha)\ddot{\theta} - d\sin(\alpha) = 0 \tag{2}$$

where:

$$a = J_{eq} + mr^2, \quad b = mLr, \quad c = \frac{4}{3}mL^2, \quad d = mgL,$$

$$E = ac - b^2, \quad G = \frac{\eta_m \eta_g K_t K_m K_g^2 + B_{eq} R_m}{R_m}$$

The parameters of the rotary inverted pendulum system are given in Table 1. Further information about this system, refer to [7].

The purpose of the paper is to design a FLC that will balance the inverted pendulum at the upright position when the initial condition is not zero. Parameters of FLC will be tuned by SFLA and PSO methods. Besides, convergent rate of PSO and SFLA will be also compared.

Table 1 Rotary inverted pendulum system model parameters used in simulation

Symbol	Description	Value	Unit
L	Length to pendulum's center of mass	0.335/2	m
M	Mass of pendulum	0.125	kg
R	Length of arm that attaches to SRV02	0.158	m
G	Gravitational constant	9.81	m/s^2
R_m	Motor armature resistance	2.6	Ohm
K_t	Motor torque constant	0.00767	N m/A
K_m	Motor back-EMF constant	0.00767	V s/rd
K_g	Total gear ratio	70	
η_m	Motor efficiency	0.69	
η_g	Gearbox efficiency	0.90	
B_{eq}	Equivalent viscous damping coefficient as seen at the load	4e-3	Nms/rd
J_{eq}	Equivalent inertia as seen at the load	0.0036	kg m^2
V_m	Control signal	0 ÷ 24	V

3 Overview of PSO and SFLA Optimization Techniques

3.1 Particle Swarm Optimization (PSO)

PSO is a global optimization technique that has been developed by Eberhart and Kennedy in 1995 [8]. PSO is a population based search algorithm where each individual is referred to as particle and represents a candidate solution. Each particle in PSO flies through the search space with an adaptable velocity that is dynamically modified according to its own flying experience and also the flying experience of the other particles. In PSO each particles strive to improve themselves by imitating traits from their successful peers. Further, each particle has a memory and hence it is capable of remembering the best position in the search space ever visited by it.

Velocity and position of individual particles updated as follows:

$$V_i^{k+1} = \omega V_i^k + c_1 rand_1\left(X_{pi} - X_i^k\right) + c_2 rand_2\left(X_g - X_i^k\right) \tag{3}$$

$$X_i^{k+1} = X_i^k + V_i^{k+1} \tag{4}$$

where:

V_i^{k+1}	velocity of particle i at loop k + 1
X_i^{k+1}	position of particle i at loop k + 1
ω	inertia weight
c_1, c_2	cognitive and social parameters
$rand_1, rand_2$	random numbers between 0 and 1

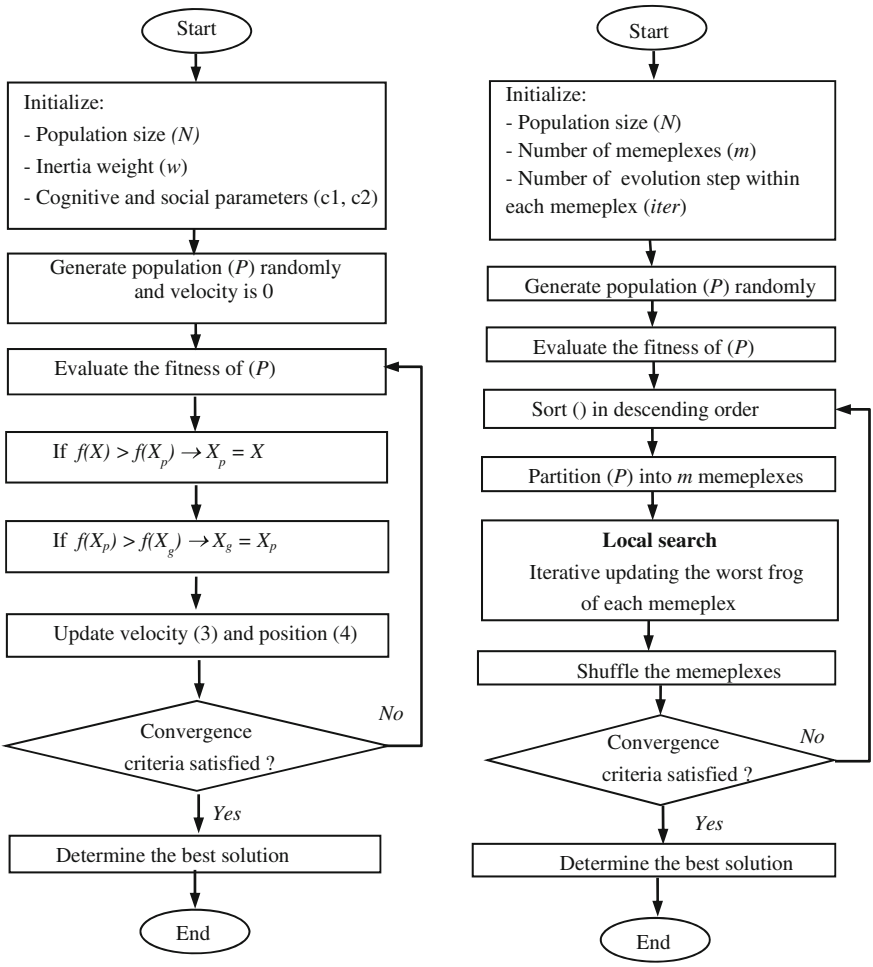

Fig. 2 Flowcharts of the PSO (*left*) and SFLA (*right*)

X_{pi} best "remembered" individual particle i position
X_g best "remembered" swarm position

Flowchart of particle swarm optimization algorithm as in Fig. 2.

3.2 Shuffled Frog Leaping Algorithm (SFLA)

The SFLA is a meta-heuristic optimization method that mimics the memetic evolution of a group of frogs when seeking for the location that has the maximum

amount of available food. The algorithm contains elements of local search and global information exchange. The SFLA involves a population of possible solutions defined by a set of virtual frogs that is partitioned into subsets referred to as memeplexes. Within each memeplex, the individual frog holds ideas that can be influenced by the ideas of other frogs, and the ideas can evolve through a process of memetic evolution. The SFLA performs simultaneously an independent local search in each memeplex using a particle swarm optimization-like method. To ensure global exploration, after a defined number of memeplex evolution steps (i.e. local search iterations), the virtual frogs are shuffled and reorganized into new memeplexes in a technique similar to that used in the shuffled complex evolution algorithm. The flowchart of the SFLA is illustrated in Fig. 2 [6].

4 Design of Fuzzy Logic Controller

This section discusses the design of a fuzzy logic controller for balancing the rotary inverted pendulum in the upright position presented in Sect. 2. The block diagram of the control system is shown in Fig. 3.

The PSO and SFLA methods are used to optimize the fuzzy logic controller obtained from expert knowledge. The controller's inputs and output are chosen to be the 4 states of the process (position and velocity of servo load gear, position and velocity of pendulum arm) and the control moment respectively. Defining 3 linguistic values denoted as NE (Negative), ZE (Zero), and PO (Positive) for each input variables. The linguistic values are qualified by piece-wise membership functions defined in the universe of discourse of [−1, 1] as shown in Fig. 4. The output variable has 9 linguistic values denoted as ZE, Nj (Negative j), Pj (Positive j) (j = 1 ÷ 4). The index j represents the strength of the linguistic values such that the higher the index, the stronger the linguistic value. These output's linguistic values are qualified by singleton membership functions in the universe of discourse of [−1, 1] as illustrated in Fig. 4. Notice that the input's membership functions NE and PO are symmetric about 0. Similarly, the output's membership functions Nj and Pj are symmetric also. By defining symmetric membership functions, the number of

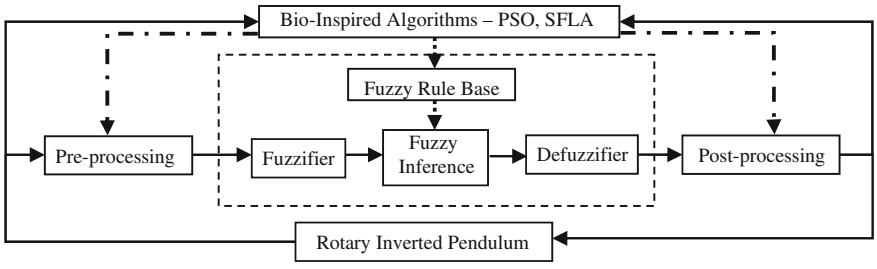

Fig. 3 Ideas tune parameters of fuzzy logic controller

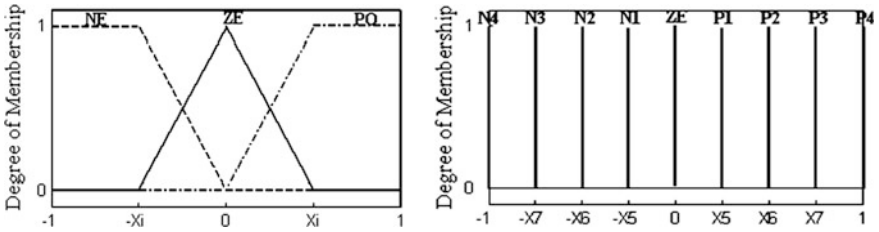

Fig. 4 Input membership functions (i = 1 ÷ 4) (*left*) and output membership functions (*right*)

adjustable parameters is reduced. As a result, the optimization problem to be solved later is easier.

The Sugeno model is used as the basis of the proposed fuzzy logic controller. The rule base consists of 81 (IF…THEN) rules derived from human knowledge. The complete rule base presented in Table 2. Ideas of rule base system like Section IV in [6].

Table 2 Rule base system

#	θ	α	$\dot{\theta}$	$\dot{\alpha}$	u	#	θ	α	$\dot{\theta}$	$\dot{\alpha}$	u
1	NE	NE	NE	NE	P1	42	ZE	ZE	ZE	PO	P1
2	NE	NE	NE	ZE	P2	43	ZE	ZE	PO	NE	N2
3	NE	NE	NE	PO	P3	44	ZE	ZE	PO	ZE	N1
4	NE	NE	ZE	NE	ZE	45	ZE	ZE	PO	PO	ZE
5	NE	NE	ZE	ZE	P1	46	ZE	PO	NE	NE	P1
6	NE	NE	ZE	PO	P2	47	ZE	PO	NE	ZE	P2
7	NE	NE	PO	NE	ZE	48	ZE	PO	NE	PO	P3
8	NE	NE	PO	ZE	P1	49	ZE	PO	ZE	NE	ZE
9	NE	NE	PO	PO	P2	50	ZE	PO	ZE	ZE	P1
10	NE	ZE	NE	NE	P2	51	ZE	PO	ZE	PO	P2
11	NE	ZE	NE	ZE	P3	52	ZE	PO	PO	NE	N1
12	NE	ZE	NE	PO	P4	53	ZE	PO	PO	ZE	ZE
13	NE	ZE	ZE	NE	P1	54	ZE	PO	PO	PO	P1
14	NE	ZE	ZE	ZE	P2	55	PO	NE	NE	NE	N4
15	NE	ZE	ZE	PO	P3	56	PO	NE	NE	ZE	N3
16	NE	ZE	PO	NE	ZE	57	PO	NE	NE	PO	N2
17	NE	ZE	PO	ZE	P1	58	PO	NE	ZE	NE	N4
18	NE	ZE	PO	PO	P2	59	PO	NE	ZE	ZE	N3
19	NE	PO	NE	NE	P2	60	PO	NE	ZE	PO	N2
20	NE	PO	NE	ZE	P3	61	PO	NE	PO	NE	N4
21	NE	PO	NE	PO	P4	62	PO	NE	PO	ZE	N3
22	NE	PO	ZE	NE	P2	63	PO	NE	PO	PO	N2

(continued)

Table 2 (continued)

#	θ	α	$\dot{\theta}$	$\dot{\alpha}$	u	#	θ	α	$\dot{\theta}$	$\dot{\alpha}$	u
23	NE	PO	ZE	ZE	P3	64	PO	ZE	NE	NE	N2
24	NE	PO	ZE	PO	P4	65	PO	ZE	NE	ZE	N1
25	NE	PO	PO	NE	P2	66	PO	ZE	NE	PO	ZE
26	NE	PO	PO	ZE	P3	67	PO	ZE	ZE	NE	N3
27	NE	PO	PO	PO	P4	68	PO	ZE	ZE	ZE	N2
28	ZE	NE	NE	NE	N1	69	PO	ZE	ZE	PO	N1
29	ZE	NE	NE	ZE	ZE	70	PO	ZE	PO	NE	N4
30	ZE	NE	NE	PO	P1	71	PO	ZE	PO	ZE	N3
31	ZE	NE	ZE	NE	N2	72	PO	ZE	PO	PO	N2
32	ZE	NE	ZE	ZE	N1	73	PO	PO	NE	NE	N2
33	ZE	NE	ZE	PO	ZE	74	PO	PO	NE	ZE	N1
34	ZE	NE	PO	NE	N3	75	PO	PO	NE	PO	ZE
35	ZE	NE	PO	ZE	N2	76	PO	PO	ZE	NE	N2
36	ZE	NE	PO	PO	N1	77	PO	PO	ZE	ZE	N1
37	ZE	ZE	NE	NE	ZE	78	PO	PO	ZE	PO	ZE
38	ZE	ZE	NE	ZE	P1	79	PO	PO	PO	NE	N3
39	ZE	ZE	NE	PO	P2	80	PO	PO	PO	ZE	N2
40	ZE	ZE	ZE	NE	N1	81	PO	PO	PO	PO	N1
41	ZE	ZE	ZE	ZE	ZE						

After constructing the structure of the fuzzy controller based on human knowledge, the next step is to optimize its parameters. The parameters to be optimized consist of the input membership function parameters X1, X2, X3, X4 (see Fig. 4), the output membership function parameters X5, X6, X7 (see Fig. 4), and the scaling gains X8, X9, X10, X11, X12 (see Fig. 5). The parameters of the

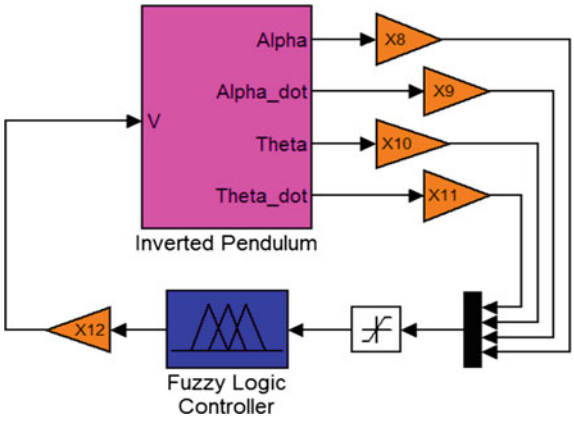

Fig. 5 Simulation schematic of the rotary inverted pendulum

fuzzy controller are optimized according to the quadratic criterion (5), in which the weighting matrices Q and R are positive definite.

$$J_{LQR} = \int_0^{\infty} \left(x^T Q x + u^T R u\right) dt \tag{5}$$

The PSO and SFLA methods discussed in Sect. 3 are employed to solve this optimization problem.

5 Results and Discussions

Matlab and Simulink are used to implement the PSO or SFLA based fuzzy controller. Simulation schematic of the rotary inverted pendulum as in Fig. 5.

The parameters of FLC that need to be tuned are divided into 2 groups. Group 1 consist of 5 variables from X8 to X12 need to be tuned (remaining parameters have fixed value: X1 = X2 = X3 = X4 = 0.5; X5 = 0.25, X6 = 0.50, X7 = 0.75). Group 2 consist of 12 variables from X1 to X12 are tuned simultaneously. Parameters of PSO and SFLA is given in Table 3. These parameters are chosen based on many simulations having best results. The weighting matrices in (5) reflecting the desired control performance are chosen to be Q = diag[10, 1, 20, 1] and R = 0.1 through a "trial and error" process.

Evolution of quadratic performance index in case of tuning 5 and 12 parameters are presented in Fig. 6. Closed responses of system in case of tuning 5 (typically chosen as using PSO) and 12 (typically chosen as using SFLA) parameters as in Fig. 7.

Table 3 The PSO and SFLA parameters

	N	G	c_1	c_2	w	m	iter	D_{max}
PSO	50	500	2.5	1.8	0.6			
SFLA	50	500	2			10	10	∞

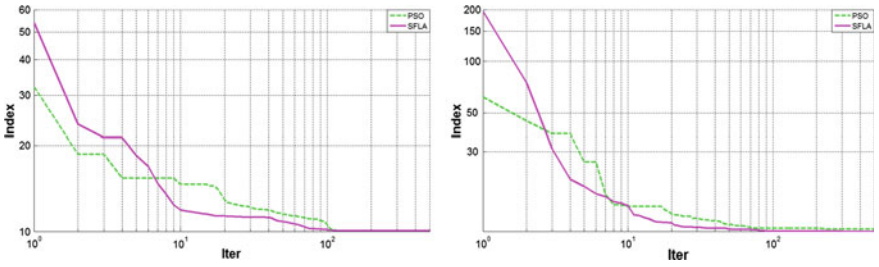

Fig. 6 Evolution of index in case of tuning 5 (*left*) and 12 parameters (*right*)

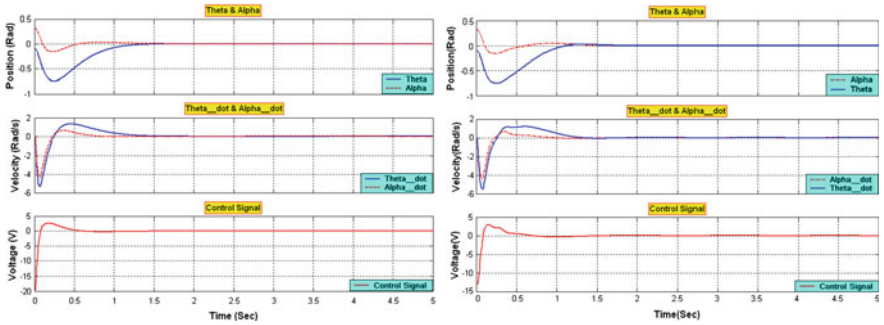

Fig. 7 Closed response of system in case of tuning 5 (*left*) and 12 (*right*) parameters

Remarks:

- In both cases, it can be observed that SFLA has convergent rate is faster than PSO despite that PSO has value of objective function is smaller than SFLA in several of first generations.
- In the case of tuning 12 parameters, SFLA has value of objective function is smaller than PSO.

Above remarks show that SFLA is better than PSO in terms of convergent rate and an ability to find global optimal solution. These remarks can be explained as follows: SFLA is able to exchange information to find global solution better than PSO does. Agents in SFLA exchange information not only among small groups (local search) but also entire agents in generation through a process of shuffle (global search). Besides, the worst agents will be replaced by random agents in order to escape local optima and increase an ability to find global search. That is reason why SFLA has faster convergent rate and ability to escape local optima to find global solutions.

6 Conclusions

PSO and SFLA are techniques that inspired by swarm intelligence, and have proved to be effective solutions to optimization problems. The objective of this paper is to compare the convergent rate of these two optimization techniques for a fuzzy logic controller design. Both PSO and SFLA are employed for tuning the parameters of FLC in 2 cases: 5 and 12 parameters of FLC are tuned. Overall, the results indicate that both PSO and SFLA algorithms can be used in the optimizing the parameters of a fuzzy logic controller to stabilize a rotary inverted pendulum system at its upright equilibrium position. It can be observed that, in terms of convergent rate, SFLA approach is faster than PSO in both cases. Besides, SFLA technique has smaller value of objective function, especially in the case of tuning 12 parameters.

References

1. Passino KM, Yurkovich S (1998) Fuzzy logic. Addison-Wesley Longman, Menlo Park
2. Herrera F, Lozano M, Verdegay JL (1995) Tuning fuzzy logic controllers by genetic algorithms. Int J Approximate Reasoning 12:299–315
3. Feng M (2005) Particle swarm optimisation learning fuzzy systems design. In: Proceedings of the Third International Conference on Information Technology and Applications (ICITA'05), vol 2
4. Pham DT, Dqrwish AH, Eldukhri EE, Otri S (2007) Using the bees algorithm to tune a fuzzy logic controller for a robot gymnast. In: Proceedings of the 3rd Virtual International Conference on Intelligent Production Machines and Systems
5. Juang C-F, Huang H-J, Lu C-M (2007) Fuzzy controller design by ant colony optimization. In: IEEE International Conference on Fuzzy Systems (FUZZ-IEEE 2007), pp 1–5
6. Nguyen D-H, Huynh T-H (2008) A SFLA-based fuzzy controller for balancing a ball and beam system. In: Tenth IEEE International Conference on Control, Automation, Robotics and Vision (ICARCV 2008), Hanoi, Vietnam, pp 17–20
7. Quanser SRV02-Series Rotary Experiment # 7, Rotary Inverted Pendulum
8. Kennedy J, Eberhart RC (1995) Particle swarm optimization. In: Proceedings of IEEE International Conference on Neural Networks (Perth, Australia), IEEE Service Center, Piscataway, NJ, 5(3), 1942–1948
9. Sidhartha P, Padhy NP (2007) Comparison of particle swarm optimization and genetic algorithm for TCSC-based controller design. Int J Comput Sci Eng 1(1)

MIMO Robust Servo Controller Design Based on Internal Model Principle Using Polynomial Differential Operator

Sang Bong Kim, Dae Hwan Kim, Pandu Sandi Pratama, Jin Wook Kim, Hak Kyeong Kim, Sea June Oh and Young Seok Jung

Abstract This paper proposes a controller design method for the multi-input multi-output robust servo system based on the internal model principle using polynomial differential operator. To do this task, the followings are done. Firstly, the basic idea of internal model principle is described. Secondly, the extended system by operating the polynomial differential operator to a given system with disturbance under the given conditions of reference and disturbance expressed into polynomial differential equation form and an output error is introduced. Thirdly, the controllability checking of the extended systems is done. Fourthly, a state feedback law is obtained by solving the pole assignment problem with all the poles of the extended system. Fifthly, a full observer is designed to estimate unknown states. Sixthly, the proposed control method is applied to a four steering wheel vehicle. Simulation results show that the proposed method can successfully make the system with a step and ramp type of disturbance track three references such as step, ramp and parabola types.

Keywords Internal model principle · Multi-input multi-output · Polynomial differential equation · Robust servo controller

1 Introduction

The multivariable robust servo system controller design problem is one of the most interested problems in control engineering field. The servo controller design problem is usually desired to find a controller for a plant to solve the robust

S.B. Kim (✉) · D.H. Kim · P.S. Pratama · J.W. Kim · H.K. Kim · Y.S. Jung
Department of Mechanical Design Engineering, Pukyong National University, Busan 608739, South Korea
e-mail: kimsb@pknu.ac.kr

S.J. Oh
Division of Mechatronics Engineering, Korea Maritime University, Busan, South Korea

V.H. Duy et al. (eds.), *AETA 2015: Recent Advances in Electrical Engineering and Related Sciences*, Lecture Notes in Electrical Engineering 371,
DOI 10.1007/978-3-319-27247-4_40

servomechanism problem such that the stability of the closed loop system and asymptotic regulation occur, and also other desirable properties of the controlled system are satisfied under existences of disturbance and system parameter perturbation.

To solve the servomechanism problem, several researchers have studied several design concepts. Davison and Smith [1] considered the servo controller design problem for the special case that disturbance term is a constant un-measurable case. Davison [2] considered the output control problem of multivariable systems as being a multivariable generalization of the classical single-input, single-output servomechanism problem. The method taken to develop the result relies extensively on properties of the asymptotic solution of a stable linear constant system subject to a specified class of forcing function inputs. It was initially shown that the closed loop system with the proposed controller is controllable if and only if the original system is controllable. Kim et al. [3] introduced a servo control method with disturbance rejection and reference signal tracking by adopting the uses of the internal model principle and bilinear transformation method. However, there was not shown for the explicit condition and its proof for the controller existence of the extended system to achieve the robust servo control object.

In this paper, the main result on robust controller is obtained by modifying the well known concept of the internal model principle shown in Kim et al. [3], introducing a polynomial differential operator for the state space model and error signal, and getting its extended system. The servo controller can be easily designed by using several kinds of regulator design methods. In order to get the robust controller for the extended system, an existence condition is shown in the view how to get the controllability for the design of the time-invariant feedback control system.

2 Preliminaries

A real plant can be expressed by the linear time invariant model as follows:

$$\frac{dx}{dt} = Ax + Bu + \omega \tag{1}$$

$$y = Cx \tag{2}$$

where $A \in R^{n\times n}$ is the system matrix, $B \in R^{n\times m}$ is the input matrix, $C \in R^{p\times n}$ is the out matrix, $x = [x_1 \quad x_2 \quad \cdots \quad x_n]^T \in R^n$ is the system state vector, $u = [u_1 \quad u_2 \quad \cdots \quad u_m] \in R^m$ is the control input vector, $y = [y_1 \quad y_2 \quad \cdots \quad y_p]^T \in R^p$ is the system output vector, $\omega = [\omega_1 \quad \omega_2 \quad \cdots \quad \omega_n]^T \in R^n$ is the unmeasurable disturbance vector, and $m \geq p$.

The output error vector is defined by

$$e = y_r - y \tag{3}$$

where $y_r = [\, y_{r1} \quad y_{r2} \quad \cdots \quad y_{rp} \,]^T \in R^p$ is the reference output vector, and $e = [\, e_1 \quad e_2 \quad \cdots \quad e_p \,]^T \in R^p$ is the output error vector.

The following homogeneous differential equations for the ith disturbance $\omega_i(t)$ and the ith reference output vector y_{ri} are assumed to be described respectively as:

$$L_r(D)y_{ri}(t) = 0 \quad for\ i = 1 - p \text{ and } L_\omega(D)\omega_i(t) = 0 \quad for\ i = 1 - n \tag{4}$$

where $L_\omega(D)$ and $L_r(D)$ are assumed to be described as the following differential polynomial operators with constant coefficients.

$$L_r(D) = D^\sigma + \rho_{\sigma-1}D^{\sigma-1} + \cdots + \rho_0 \text{ and } L_\omega(D) = D^l + \mu_{l-1}D^{l-1} + \cdots + \mu_0 \tag{5}$$

where $D = d/dt$ is the differential operator, ρ_i, μ_i are constant coefficients, σ, l are orders of differential polynomials. $L_\omega(D)$ and $L_r(D)$ can be expressed as

$$L_r(D) = R(D)U(D) \text{ and } L_\omega(D) = R(D)V(D) \tag{6}$$

where $R(D)$ is the greatest common divisor of $L_r(D)$ and $L_\omega(D)$, and $U(D), V(D)$ are factors of $L_r(D)$ and $L_\omega(D)$, respectively.

$L(D)$ is defined as the least common multiple of $L_r(D)$ and $L_\omega(D)$ and can be obtained from Eqs. (5) and (6) as the polynomial differential operator as follows:

$$\begin{aligned} L(D) &= \frac{L_\omega(D)L_r(D)}{R(D)} = U(D)R(D)V(D) = V(D)L_r(D) \text{ or } U(D)L_\omega(D) \\ &= D^{(q)} + \alpha_{q-1}D^{(q-1)} + \cdots + \alpha_0 \end{aligned} \tag{7}$$

where $\dim\{V(D)\} = q - \sigma$, $\dim\{U(D)\} = q - l$, $\dim\{R(D)\} = l + \sigma - q$, and $\dim\{L(D)\} = q \geq \dim\{L_r(D)\}$ or $\dim\{L_w(D)\}$.

For simplicity, let us consider a single-input single-output (SISO) system case with disturbance in Eq. (1). Then the block diagram of the closed loop control system can be shown in Fig. 1.

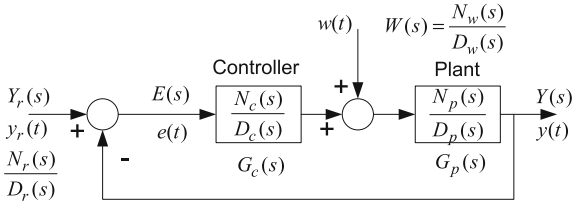

Fig. 1 Block diagram of a closed-loop control system

From Fig. 1, the output error after Laplace transform for the reference signal $Y_r(s)$ with disturbance $W(s)$ is obtained as:

$$E(s) = \frac{1}{1 + G_c(s)G_p(s)} Y_r(s) - \frac{G_p(s)}{1 + G_c(s)G_p(s)} W(s) = E_r(s) - E_w(s) \quad (8)$$

where

$$\begin{cases} E_r(s) = \frac{D_p(s)D_c(s)}{D_p(s)D_c(s) + N_p(s)N_c(s)} \frac{N_r(s)}{D_r(s)} \\ E_w(s) = \frac{D_c(s)N_p(s)}{D_p(s)D_c(s) + N_p(s)N_c(s)} \frac{N_w(s)}{D_w(s)} \end{cases} \quad (9)$$

The following polynomial equation obtained from Eq. (9) is the closed-loop characteristic polynomial equation of the closed-loop system depicted in Fig. 1 consisting of the polynomial poles and polynomial zeros of transfer functions of plant and controller and its roots are the closed-loop poles:

$$D_p(s)D_c(s) + N_p(s)N_c(s) = 0 \quad (10)$$

Theorem 1 (Internal model principle based on least common multiple model) *Let us assume that the given system of Eq. (1) and the controller of $G_c(s)$ has no transmission zeros at the origin point and the closed loop poles of Fig. 1 are located in open left half plane under disturbance condition. Under assumptions of Eq. (4) for the disturbance and reference signals, the output error $e(t)$ of Eq. (3) becomes zero: $\lim_{t\to\infty} e(t) = 0$ if and only if the least common multiple polynomial for disturbance and reference signals is a factor of $D_c(s)$.*

Proof of Theorem 1 By the final value theorem, the error function shown in Fig. 1 can be given as:

$$\lim_{t\to\infty} e(t) = \lim_{s\to 0} sE(s) = \lim_{s\to 0} sE_r(s) - \lim_{s\to 0} sE_w(s) \quad (11)$$

For the sufficient condition, in order to obtain $\lim_{t\to\infty} e(t) = 0$, firstly, the first term in the right side of Eq. (11) becomes $\lim_{s\to 0} sE_r(s) \to 0$.

The denominator $D_r(s)$ of $Y_r(s)$, Laplace transform of the reference y_r, must be included as a factor of the open-loop characteristic polynomial $D_p(s)D_c(s)$. This means that the tracking controller must be designed in such way that the open-loop transfer function, $G_p(s)G_c(s)$, contains a model of the reference signal to be tracked.

For the reference signal of Eq. (8), its Laplace transform can be written by (SISO case)

$$Y_r(s) = \frac{N_r(s)}{D_r(s)} = \frac{N_{r0}(s)}{L_r(s)} y_r(0) \quad \text{for } y_r^{(i)}(0) = 0 \ \ (\ i = 1, \ldots, \sigma) \tag{12}$$

where $N_{r0}(s) = s^{\sigma-1} + \rho_{\sigma-1} s^{\sigma-2} + \cdots + \rho_2 s + \rho_1$,

$$D_r(s) = L_r(s) = s^{\sigma} + \rho_{\sigma-1} s^{\sigma-1} + \cdots + \rho_1 s + \rho_0, \text{ and } N_r(s) = N_{r0}(s) y_r(0)$$

When the open loop characteristic polynomial $D_p(s)D_c(s)$ includes the reference model of $L_r(s)$, $D_p(s)D_c(s)$ yields:

$$D_p(s)D_c(s) = L_r(s)D_{pc}(s) \text{ or } D_r(s)D_{pc}(s) \tag{13}$$

where $D_{pc}(s)$ is a common factor of the denominator $D_p(s)D_c(s)$ of the open-loop transfer function $G_p(s)G_c(s)$.

For the disturbance signal of Eq. (8), its Laplace transform can be expressed by (SISO case) the form:

$$W(s) = \frac{N_w(s)}{D_w(s)} = \frac{N_{w0}(s)}{L_w(s)} \omega(0) \quad \text{for } \omega^{(i)}(0) = 0 \ \ (\ i = 1, \ldots, l) \tag{14}$$

where $N_{w0}(s) = s^{l-1} + \mu_{l-1} s^{l-2} + \cdots + \mu_2 s + \mu_1$,

$$D_w(s) = L_w(s) = s^{l} + \mu_{l-1} s^{l-1} + \cdots + \mu_1 s + \mu_0 \text{ and } N_r(s) = N_{w0}(s)\omega(0).$$

Using the least common multiple of disturbance and reference signals $L(s)$, the denominator of the controller can be expressed as

$$D_c(s) = L(s)D_{wr}(s) = D_r(s)V(s)D_{wr}(s) = D_w(s)U(s)D_{wr}(s) \tag{15}$$

where $D_{wr}(s)$ is a common factor of two signals.

The steady state error with respect to reference signal using Eqs. (11), (12) and (15) can be obtained as

$$\begin{aligned} \lim_{t\to\infty} e_r(t) = \lim_{s\to 0} sE_r(s) &= \lim_{s\to 0} s \frac{[s^{\sigma-1} + \rho_{\sigma-1} s^{\sigma-2} + \cdots + \rho_2 s + \rho_1] D_p(s) D_{wr}(s) y_r(0)}{[s^q + \alpha_{q-1} s^{q-1} + \cdots + \alpha_1 s + \alpha_0] D_p(s) D_{wr}(s) + N_p(s) N_c(s)} \\ &= \lim_{s\to 0} s \frac{\rho_1 D_p(0) D_{wr}(0) y_r(0)}{\alpha_0 D_p(0) D_{wr}(0) + N_p(0) N_c(0)} = 0 \end{aligned} \tag{16}$$

where $N_p(0)$ and $N_c(0)$ are not zero because the transmission zeros are not at the origin that is, $N_p(s) = \det[RSM(s)] = \det[(sI - A)G_p(s)] \neq 0$ at $s = 0$ and $N_c(s)$ is also done similarly.

$$RSM(s) = \begin{bmatrix} sI - A & B \\ -C & 0 \end{bmatrix} : \text{Rosenbrock system matrix} \tag{17}$$

And the steady state error with respect to disturbance signal using Eqs. (11), (14) and (15) can be obtained as

$$\begin{aligned} \lim_{t\to\infty} e_w(t) &= \lim_{s\to 0} sE_w(s) \\ &= \lim_{s\to 0} s\frac{[s^{l-1} + \mu_{\sigma-1}s^{l-2} + \cdots + \mu_2 s + \mu_1]U(s)D_{wr}(s)N_p(s)\omega(0)}{[s^q + \alpha_{q-1}s^{q-1} + \cdots + \alpha_1 s + \alpha_0]D_p(s)D_{wr}(s) + N_p(s)N_c(s)} \\ &= \lim_{s\to 0} s\frac{\mu_1 U(0)D_{wr}(0)N_p(0)\omega(0)}{\alpha_0 D_p(0)D_{wr}(0) + N_p(0)N_c(0)} = 0 \end{aligned} \tag{18}$$

To satisfy $e(t) \to 0$ for $t \to \infty$, the two error conditions of $e_r(t) \to 0$ and $e_w(t) \to 0$ must be satisfied simultaneously. Therefore, the controller $G_c(s)$ must includes the least common multiple $L(s)$ in its denominator $D_c(s)$.

As we can see, from the results of Eqs. (16) and (18), if the controller $G_c(s)$ includes the order of the least common multiple polynomial model for reference and disturbance signals as a factor of $D_c(s)$, the tracking error $e(t)$ becomes zero for $t \to \infty$.

The necessary condition is as follows:

If $\lim_{t\to\infty} e(t) = 0$, the least common multiple polynomial for disturbance and reference signals $L(s)$ is a factor of $D_c(s)$, that is, $L(s)$ is included in $D_c(s)$ of $G_c(s)$. For the proof of the necessary condition, the contradiction of '$L(s)$ is not a factor of $D_c(s)$' is considered.

From $\dim\{L(s)\} \geq \dim\{L_r(s)\}$ *or* $\dim\{L_w(s)\}$, the followings are obtained:

(1) $\dim\{L_r(s)\} = \dim\{L_w(s)\} \to \dim\{L(s)\} \geq \dim\{L_r(s)\}$ *or* $\dim\{L_w(s)\}$
(2) $\dim\{L_r(s)\} \geq \dim\{L_w(s)\}$ or $\dim\{L_r(s)\} \leq \dim\{L_w(s)\}$
$\to \dim\{L(s)\} \geq \dim\{L_r(s)\}$ or $\dim\{L_w(s)\}$

As the results, it contradicts the assumption that $L(s)$ is not a factor of $D_c(s)$. Theorem 1 shows that when the dimension of the controller is equal or larger than the dimension of the reference or the disturbance model as the following, then $e(t) \to 0$ for $t \to \infty$:

$$\dim\{D_c(s)\} \geq \dim\{L_r(s)\} \text{ or } \dim\{L_w(D)\}$$

But, when $D_c(s)$ does not include the least common multiple model of $L(s)$, that is, the controller has the relation as the following dimension, then $e(t)$ does not go to zero:

$$\dim\{D_c(s)\} \leq \dim\{L_r(s)\} \textit{ or } \dim\{L_w(s)\}$$

So, to satisfy $e(t) \to 0$, at least, the least common multiple model should be included in $D_c(s)$.

In Theorem 1, the operator $L(D)$ should become a factor of the open-loop characteristic polynomial $D_p(D)D_c(D)$ such that $D_p(D)D_c(D) = Q(D)L(D)$ which $Q(D)$ is a polynomial. From the above stated result, the IMP can be incorporated into the state equation form based on the polynomial differential operator. In order to satisfy the internal model principle (IMP) for the robust tracking control system, the reference polynomial differential operator of $L(D)$ must be operated on Eqs. (1)–(3).

3 Robust Tracking Controller Design Method for MIMO System

Kim et al. [3] applied the tracking controller concept based on the previous stated Theorem 1 to the single input and single output system (SISO), but in the case of multi-input and multi-output (MIMO) system, it is not directly applicable and also it is very difficult to incorporate the design concept. Therefore, we should consider a different type of the robust tracking controller design concept.

In order to adopt the IMP of Sect. 2 to the robust MIMO tracking control system, we will introduce the polynomial differential operator stated in the previous section and get an extended system.

Operating $L(D)$ for ω_i and y_{ri} of Eq. (4), the following are obtained

$$\begin{cases} L(D)y_{ri} = U(D)R(D)V(D)y_{ri} = V(D)L_r(D)y_{ri} = 0 \\ L(D)\omega_i = U(D)R(D)V(D)\omega_i = U(D)L_w(D)\omega_i = 0 \end{cases} \tag{19}$$

where the dimension of q holds $q \geq l$ or $q \geq \sigma$.

Firstly, to eliminate the effect of disturbance in Eq. (1), operating the polynomial differential operator of $L(D)$ to both sides of Eq. (1) by using Eqs. (6) and (19) can be written as

$$\frac{d}{dt}\{L(D)x\} = AL(D)x + BL(D)u \tag{20}$$

The ith output error of Eq. (3) can be written as

$$e_i(t) = y_i(t) - y_{ri}(t) \text{ for } i = 1 - p \tag{21}$$

Secondly operating $L(D)$ to Eq. (21) and using the property of Eq. (19), the followings can be obtained.

$$\begin{aligned} L(D)e_i(t) &= D^q e_i + \alpha_{q-1}D^{q-1}e_i + \cdots + \alpha_1 De_i + \alpha_0 e_i \\ &= L(D)y_i - L(D)y_{ri} = c_i L(D)x_i \quad \text{for } i = 1, \ldots, p \end{aligned} \tag{22}$$

From Eq. (22), the following can be obtained as the matrix form:

$$\dot{z}_i = M_i L(D)x + Nz_i = \begin{bmatrix} \mathbf{0} \\ \mathbf{0} \\ \vdots \\ \mathbf{c}_i^T \end{bmatrix} L(D)x + Nz_i \tag{23}$$

where

$$N = \begin{bmatrix} 0 & 1 & 0 & 0 & \cdots & 0 \\ 0 & 0 & 1 & 0 & \cdots & 0 \\ 0 & 0 & 0 & 1 & \cdots & 0 \\ \vdots & \vdots & \vdots & \vdots & \ddots & \vdots \\ 0 & 0 & 0 & 0 & \cdots & 1 \\ -\alpha_0 & -\alpha_1 & -\alpha_2 & -\alpha_3 & \cdots & -\alpha_{q-1} \end{bmatrix} \in R^{q\times q},\ M_i = \begin{bmatrix} \mathbf{0} \\ \cdots \\ \mathbf{c}_i^T \end{bmatrix} = \begin{bmatrix} 0 \\ 0 \\ \vdots \\ 1 \end{bmatrix} \mathbf{c}_i^T \in R^{q\times n},\ \mathbf{c}_i \in R^n$$

$$C^T = [\mathbf{c}_1 \quad \mathbf{c}_2 \quad \cdots \quad \mathbf{c}_p] \in R^{n\times p},\ \text{and}\ z_i = [e_i \quad De_i \quad \cdots \quad D^{q-1}e_i]^T \in R^q$$

By combining the operated system, Eqs. (20) and (23), an extended system can be obtained as follows:

$$\dot{x}_e = A_e x_e + B_e v \tag{24}$$

where

$$A_e = \begin{bmatrix} A & \mathbf{0} & \cdots & \mathbf{0} & \mathbf{0} \\ \begin{bmatrix} \mathbf{0} \\ \mathbf{c}_1^T \end{bmatrix} & N & \mathbf{0} & \vdots & \mathbf{0} \\ \begin{bmatrix} \mathbf{0} \\ \mathbf{c}_2^T \end{bmatrix} & \mathbf{0} & N & \mathbf{0} & \vdots \\ \vdots & \vdots & \ddots & \ddots & \mathbf{0} \\ \begin{bmatrix} \mathbf{0} \\ \mathbf{c}_2^T \end{bmatrix} & \mathbf{0} & \cdots & \mathbf{0} & N \end{bmatrix} \in R^{(n+pq)\times(n+pq)},\ B_e = \begin{bmatrix} B \\ \mathbf{0} \\ \vdots \\ \vdots \\ \mathbf{0} \end{bmatrix}^{(n+pq)\times m},$$

$$x_e = \begin{bmatrix} L(D)x \\ z_1 \\ z_2 \\ \vdots \\ z_p \end{bmatrix} \in R^{n+pq}$$

$x_e = \begin{bmatrix} L(D)x^T & z^T \end{bmatrix}^T$ is an extended system state variable vector, $v = L(D)u \in R^m$ is a new control law for the extended system, and $z = \begin{bmatrix} z_1^T & z_2^T & \cdots & z_p^T \end{bmatrix}^T \in R^{pq}$ is an error variable vector for the extended system.

A new control law for the extended system is defined by the following form:

$$v = L(D)u = -Fx_e \in R^m \tag{25}$$

where $F = \begin{bmatrix} F_x & F_z \end{bmatrix} \in R^{m\times(n+pq)}$ is a feedback control gain matrix, and $F_x \in R^{m\times n}$ and $F_z \in R^{m\times pq}$ are feedback control gain matrices for $L(D)x$ and z, respectively.

A new error variable vector for the extended system can be defined as

$$\zeta = L^{-1}(D)z \tag{26}$$

where $\zeta = \begin{bmatrix} \zeta_1^T & \zeta_2^T & \cdots & \zeta_p^T \end{bmatrix}^T \in R^{pq}$, and $\zeta_i \in R^q$ for $i = 1, \ldots, p$

Using Eqs. (25) and (26), the control law of Eq. (1) can be obtained as follows:

$$u = -Fx_\zeta = -\begin{bmatrix} F_x & F_z \end{bmatrix}\begin{bmatrix} x \\ \zeta \end{bmatrix} \tag{27}$$

where $x_\zeta \in R^{n+pq}$ is a new extended system variable vector.

From Eqs. (24) and (25), the closed loop system of the extended system is

$$\dot{x}_e = (A_e - B_eF)x_e \tag{28}$$

Theorem 2 shows that the servo controller problem for Eq. (1) with reference and disturbance of Eq. (4) becomes a regulator design problem for the extended system of Eq. (24) such that the closed loop system of Eq. (28) is asymptotically stabilized by designing the feedback control law of Eq. (25) with a feedback control matrix F so as to be $\mathrm{Re}\{\lambda_i(A_e - B_eF\} < 0$. The controllability checking of extended system can be obtained from [4].

Theorem 3 (Regulator design) *Consider the system of Eq. (1) and assume that Theorem 2 holds; then there exists gain matrix* $F = \begin{bmatrix} F_x & F_z \end{bmatrix}$ *so that the closed loop control system obtained by applying the feedback control law of Eq. (25) to the extended system of Eq. (24) is asymptotically stable, i.e. there exists a gain matrix* $F = \begin{bmatrix} F_x & F_z \end{bmatrix}$ *so that the following matrix is asymptotically stable [5].*

$$A_F = A_e - B_eF = A_e - B_e\begin{bmatrix} F_x & F_z \end{bmatrix} \tag{29}$$

When the feedback control law of the extended system of Eq. (24) is $e(t) \to 0$ *as* $t \to \infty$ *designed based on Theorems 2 and 3, the output error vector of Eq. (21) becomes*

Since $x_e \to 0$ *by regulator design result, that is* $x_e \to 0$ *means* $\begin{bmatrix} Lx^T & z^T \end{bmatrix}^T \to 0$ *as follows:*

$$\begin{aligned} x_e &= \begin{bmatrix} L(D)x^T & z_1^T & z_1^T & \cdots & z_p^T \end{bmatrix}^T \\ &= \left[L(D)x^T \quad \begin{bmatrix} e_1 & e_1^{(1)} & \cdots & e_1^{(q-1)} \end{bmatrix}^T \quad \cdots \quad \cdots \quad \begin{bmatrix} e_p & e_p^{(1)} & \cdots & e_p^{(q-1)} \end{bmatrix}^T \right]^T \end{aligned} \tag{30}$$

As the result, the error $e(t) = \begin{bmatrix} e_1(t) & e_2(t) & \cdots & e_p(t) \end{bmatrix}^T \to 0$ *as* $t \to \infty$.

Theorem 4 (Stabilizing servo compensator) *Let a new control input v in Eq. (25) be given for the extended system of Eq. (24) such that the extended system satisfies Theorem 2 and also based on Theorem 3, the new control input is obtained by well known regulator design methods* [1, 3, 5–7]. *Then, the robust servo compensator is given by the following form:*

$$\frac{d\zeta}{dt} = N_z \zeta + I_\zeta e \tag{31}$$

where ζ *is a new error variable vector defined by*

$$\zeta = L^{-1}(D)z = \begin{bmatrix} \zeta_1^T & \zeta_2^T & \cdots & \zeta_p^T \end{bmatrix}^T \in R^{pq}, \quad \zeta_i \in R^q \quad \text{for } i = 1, \ldots, p$$

The proof of theorem 4 can be obtained from [4].

In Theorem 4, the servo compensator of Eq. (31) includes the model of reference and disturbance signals since the matrix N_z is composed of the least common multiple model of two signals. It proposes the internal model principle based on the polynomial differential operator. The configuration of the proposed servo control system can be described as shown in Fig. 2.

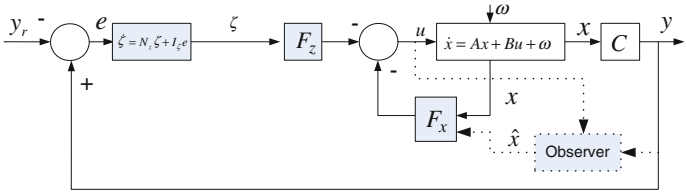

Fig. 2 Configuration of the proposed servo control system

4 Simulation Results

To verify the effectiveness of the proposed controller design method, our controller is compared with PI controller for a four steering wheel vehicle as a MIMO system with two inputs and two outputs as given in [8]. By defining the state vector $x = [\kappa \quad \gamma]^T$, input vector $u = [\delta_f \quad \delta_r]^T$ and output vector $y = [\kappa \quad \gamma]^T$, the system matrices of the four steering wheel vehicle model in [8] can be written in the state-space form as follows (Fig. 3):

$$A = \begin{bmatrix} -\frac{2(C_f + C_r)}{mV} & -\frac{2(l_f C_f - l_r C_r)}{mV^2} - 1 \\ -\frac{2(l_f C_f - l_r C_r)}{J_z} & -\frac{2(l_f^2 C_f - l_r^2 C_r)}{J_z V} \end{bmatrix} = \begin{bmatrix} -3.41 & -0.9045 \\ 46.5451 & 3.173 \end{bmatrix}$$

$$B = \begin{bmatrix} \frac{2C_f}{mV} & \frac{2C_r}{mV} \\ \frac{2C_f}{J_z} & -\frac{2C_r}{J_z} \end{bmatrix} = \begin{bmatrix} 1000 & 2069 \\ 18.046 & -37.3367 \end{bmatrix},$$

$$C = \begin{bmatrix} 1 & 0 \\ 0 & 1 \end{bmatrix}$$

where κ and γ denote the sideslip angle and yaw rate of vehicle at the CG; m is the vehicle mass; J_z is the yaw moment of inertia about its mass centre *z-axis*; V denotes the velocity of vehicle; l_f and l_r are the distances from the CG (centre of gravity) to the front and rear axles; δ_f and δ_r denote the steering angles of front and rear tires; C_f and C_r denote the lateral stiffness of the front and rear tires, respectively.

4.1 PI-MIMO Controller

The tunable gain matrices of K_P and K_I have eight tunable variables. Initial values for the controller are generated as shown in [8]. The gain value for PI-MIMO controller in this simulation was chosen as:

$$K_P = \begin{bmatrix} 0.5 & 2 \\ 2 & 0.5 \end{bmatrix} \quad K_I = \begin{bmatrix} 0.5 & 0.1 \\ 0.1 & 0.5 \end{bmatrix}$$

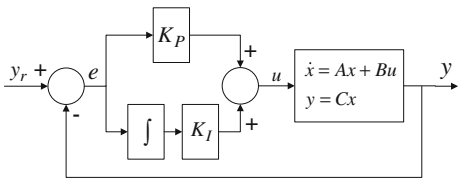

Fig. 3 PI-MIMO controller

4.2 The Proposed Servo Control System

The proposed servo control system is shown in Fig. 2. The parameters, controller gains and servo compensators for 3 types of reference signals are obtained by using the proposed robust servo controller design method as shown in Table 1.

4.3 Step Reference

Simulation results using step reference for the proposed method and the PI-MIMO controller are shown in Figs. 4, 5 and 6. Figure 4 shows the control inputs using for the proposed method and the PI-MIMO. Figure 5 shows that the outputs of the controllers used for both methods track the reference values and stabilize the plant after finite time. As we can see, the outputs of controller using the proposed method can track the reference signal faster than the output of the controller using the PI-MIMO. Figure 6 shows that the output errors of the controllers using both methods converge to zero and stabilize the plant after finite time. However, the output errors of the closed loop system using the proposed method can become zero faster than the output errors of the controller using the PI-MIMO.

4.4 Ramp Input

Simulation results using ramp input for the proposed method and the PI-MIMO controller are shown in Figs. 7, 8 and 9. Figure 7 shows the control inputs using both methods. Figure 8 shows that only the outputs of the controller using the proposed method can track the reference signals and stabilize the plant after finite time. The outputs of the controller using the PI-MIMO cannot track the reference signal. Furthermore, Fig. 9 shows that the output errors of the controller using the proposed method converge to zero and stabilize the plant after finite time. On the other hand, in the controller using the PI-MIMO, the steady state errors exist.

4.5 Parabolic Input

Simulation results using parabolic input for the proposed method and the PI-MIMO controller are shown in Figs. 9, 10 and 11. Figure 9 shows the control inputs using both methods. Figures 10 and 11 show the same results as shown in the case of ramp for the parabolic type of reference signal, that is, PI controller has steady error for the given parabolic signals (Fig. 12).

Table 1 Parameters and gains for proposed method

Design parameter	Reference types		
	Step	Ramp	Parabolic
Reference Model	$y_{r1} = 0.1, y_{r2} = 0.01$	$\dot{y}_{r1} = 0.1, \dot{y}_{r2} = 0.01$	$\dot{y}_{r1} = 0.1, \ddot{y}_{r2} = 0.01$
Matrix N	$N = [0]$	$N = \begin{bmatrix} 0 & 1 \\ 0 & 0 \end{bmatrix}$	$N = \begin{bmatrix} 0 & 1 & 0 \\ 0 & 0 & 1 \\ 0 & 0 & 0 \end{bmatrix}$
Assigned poles	$\{-10, -11, -12, -13\}$	$\{-10, -11, -12, -13, -14, -15\}$	$\{-10, -11, -12, -13, -14, -15, -16, -17\}$
Gain matrix F_x	$\begin{bmatrix} 1.3004 & 0.6693 \\ -0.6181 & -0.3239 \end{bmatrix}$	$\begin{bmatrix} 1.3449 & 1.1334 \\ -0.6337 & -0.5475 \end{bmatrix}$	$\begin{bmatrix} 1.2630 & 1.5923 \\ -0.5862 & -0.7711 \end{bmatrix}$
Gain matrix F_z	$\begin{bmatrix} 0.0780 & 3.0478 \\ 0.0377 & -1.4731 \end{bmatrix}$	$\begin{bmatrix} 6.848 & -2.4031 \\ 1.1859 & -0.3509 \\ 54.1180 & -26.0385 \\ 13.0744 & -6.3002 \end{bmatrix}^T$	$\begin{bmatrix} -100.7003 & 66.9356 \\ -23.1968 & 15.7626 \\ -1.5543 & 1.2687 \\ 899.5088 & -437.1666 \\ 271.1928 & -131.6198 \\ 30.4197 & -14.7434 \end{bmatrix}^T$
Compensator	$\dot{\zeta} = \begin{bmatrix} 0 & 0 \\ 0 & 0 \end{bmatrix} \zeta + \begin{bmatrix} 1 & 0 \\ 0 & 1 \end{bmatrix} e$	$\dot{\zeta} = \begin{bmatrix} 0 & 1 & 0 & 0 \\ 0 & 0 & 0 & 0 \\ 0 & 0 & 0 & 1 \\ 0 & 0 & 0 & 0 \end{bmatrix} \zeta + \begin{bmatrix} 0 & 0 \\ 0 & 1 \\ 0 & 0 \\ 0 & 1 \end{bmatrix} e$	$\dot{\zeta} = \begin{bmatrix} 0 & 1 & 0 & 0 & 0 & 0 \\ 0 & 0 & 1 & 0 & 0 & 0 \\ 0 & 0 & 0 & 0 & 0 & 0 \\ 0 & 0 & 0 & 0 & 1 & 0 \\ 0 & 0 & 0 & 0 & 0 & 1 \\ 0 & 0 & 0 & 0 & 0 & 0 \end{bmatrix} \zeta + \begin{bmatrix} 0 & 0 \\ 0 & 0 \\ 1 & 0 \\ 0 & 0 \\ 0 & 0 \\ 0 & 1 \end{bmatrix} e$

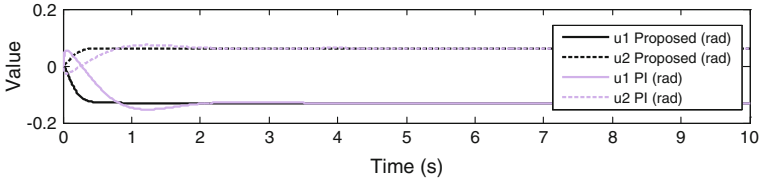

Fig. 4 Control inputs of PI and proposed methods for step reference

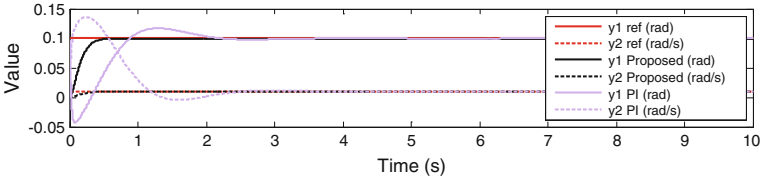

Fig. 5 Outputs of PI and proposed methods for step reference

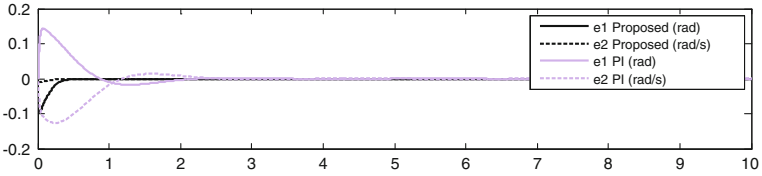

Fig. 6 Output errors of PI and proposed methods for step reference

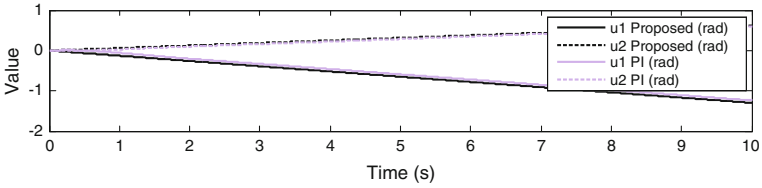

Fig. 7 Control inputs of PI and proposed methods for ramp reference

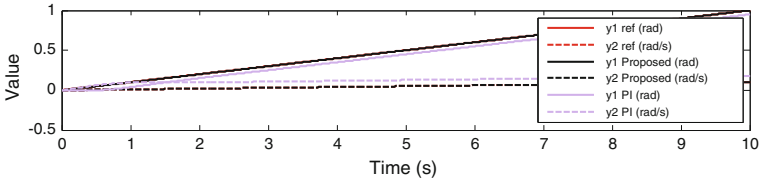

Fig. 8 Outputs of PI and proposed methods for ramp reference

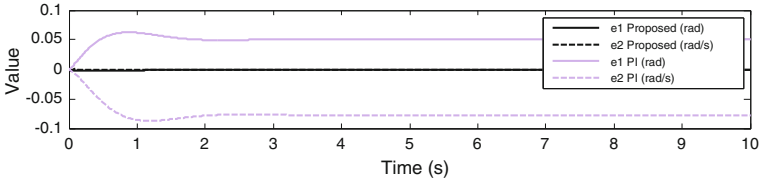

Fig. 9 Output errors of PI and proposed methods for step reference

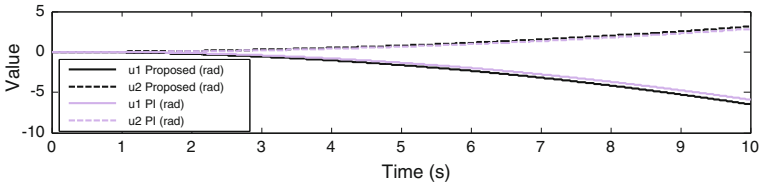

Fig. 10 Control inputs of PI and proposed methods for parabolic reference

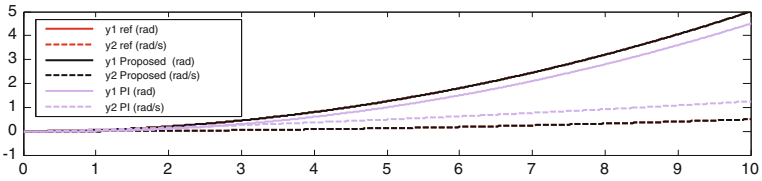

Fig. 11 Outputs of PI and proposed methods for parabolic reference

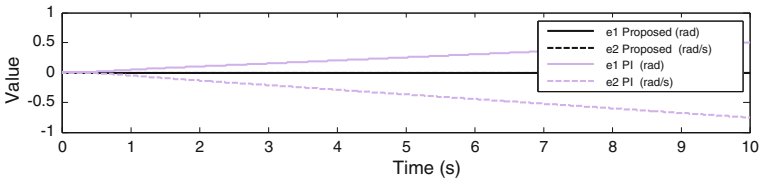

Fig. 12 Outputs of PI and proposed methods for parabolic reference

5 Conclusions

This paper proposed a controller design method for the multi input multi output (MIMO) robust servo systems using polynomial differential operator based on the internal model principle. In this paper, the servo system design was done as follows. Firstly, the basic idea of internal model principle was described. Secondly, the extended system including reference and disturbance in polynomial differential

equation form was introduced. Thirdly, the controllability checking of the extended system was done. Finally, the state feedback law was obtained by solving the pole assignment problem with all the poles of extended system in the specific region. In order to show the effectiveness of proposed method, the simulation was done. Simulation results showed that the proposed method could make the system track the reference.

Acknowledgments This study is a part of the results of the R&D project, Development of a deep-Seabed Mining Technologies, supported by Korea Government, Ministry of Oceans and Fisheries. Authors are indebted to appreciate their full supports of this pioneering work.

References

1. Davison EJ, Smith HW (1971) Pole assignment in linear time-invariant multivariable systems with constant disturbances. Automatics 7:489–498
2. Davison EJ (1972) The output control of linear time-invariant multivariable systems with unmeasureable arbitrary disturbances. IEEE Trans Autom Control AC-17(5)
3. Kim SB, Oh SJ, Jung YG, Kim HS (1991) Application of bilinear transformation method to servo system design and position control for a cart system. Trans KIEE 40(3)
4. Kim DH (2015) Servo controller design using polynomial differential operator method and its applications, Doctor Thesis, Mechanical Design Engineering Department, Pukyong National University
5. Furuta K, Sano A, Atherton D (1988) State variable methods in automatic control. Wiley, Chichester
6. Furuta K, Kim SB (1987) Pole assignment in a specified disk. IEEE Trans Auto Control 32(5):423–427
7. Kim SB, Furuta K (1988) Regulator design with poles on a specified region. Int J Control 47(1):143–160
8. Lv H, Liu S (2013) Closed-loop handling stability of 4WS vehicle with yaw rate control. J Mech Eng 59(10):595–603

Design and Control Automatic Chess-Playing Robot Arm

Nguyen Duy Anh, Luong Thanh Nhat and Tran Van Phan Nhan

Abstract This paper presents a 3DoF robot manipulator system which can play chess physically with human. The system consists of three main parts: a computer vision program written by Visual Studio to recognize chess moves, a chess program to choose the best move to response and a robot arm to perform chess move on a real chessboard. In this paper, the authors focus on analyzing mechanical design, methods to detect chess moves and algorithm applied to control the SCARA robot arm. Based on the design, a robot arm was manufactured and set up. Chess matches between robot and human were held to experiment the operation of robot arm as well as the result of the matches.

Keywords Chess robot · Chess program · SCARA

1 Introduction

Chess is a two-player strategy game played on chessboard. The question is: "What will happened if the opponent is a robot?". Nowadays, super computers can beat chess grand masters, however, there must be one man who reads the result of calculation from the computer, then, execute the move on chessboard [1]. Therefore, an autonomous chess-playing process has been being researched in the world. In Vietnam, there have not been any researches about autonomous chess-playing system, authors decided to manufacture a robot arm which can play chess automatically and physically.

N.D. Anh (✉) · L.T. Nhat · T. Van Phan Nhan
Faculty of Mechanical, HCMC University of Technology, 268 Ly Thuong Kiet Street, Ward 14, District 10, Ho Chi Minh City, Vietnam
e-mail: duyanhnguyen@hcmut.edu.vn

V.H. Duy et al. (eds.), *AETA 2015: Recent Advances in Electrical Engineering and Related Sciences*, Lecture Notes in Electrical Engineering 371,
DOI 10.1007/978-3-319-27247-4_41

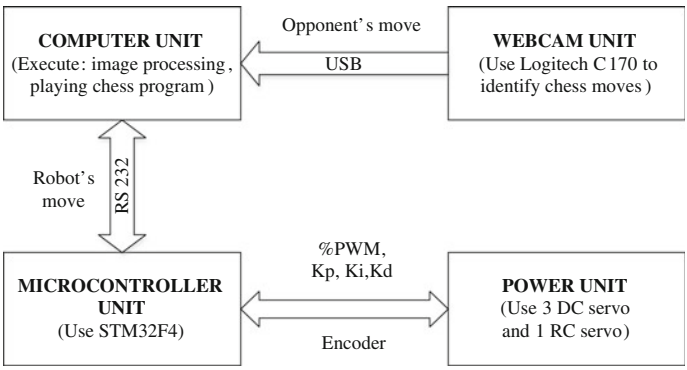

Fig. 1 System diagram

In the first part of project, SolidWorks was used to calculate and design structure, dimension of links, joints of robot arm. In the second part, one camera hung above the chessboard and taking pictures to detect chess moves. A chess-playing program written on Visual Studio will evaluate and find the best move for robot. In the final part, a PID controller was used to control position of robot arm. A whole system is briefly described in Fig. 1.

2 Mechanical Design

2.1 Kinematics

The kinematics model was built by the algorithm of Denavit Hartenberg; the DH parameters are the relationships among the robot's serial links. Base on requirements of the system, the SCARA type was used that has a schematic shown in Fig. 2. The DH parameters according to the configuration of the SCARA are presented in Table 1.

Considering Table 1 and Fig. 2, the forward kinematic equations are obtained as follows:

$$x = l_2 c(\theta_1 + \theta_2) + l_1 c\theta_1 \tag{1}$$

$$y = l_2 s(\theta_1 + \theta_2) + l_1 s\theta_1 \tag{2}$$

$$z = h_1 + h_2 - d_3 \tag{3}$$

where $c(\theta_1 + \theta_2) = \cos(\theta_1 + \theta_2)$; $s(\theta_1 + \theta_2) = \sin(\theta_1 + \theta_2)$; $s(\theta_1) = \sin(\theta_1)$; $c(\theta_1) = \cos(\theta_1)$

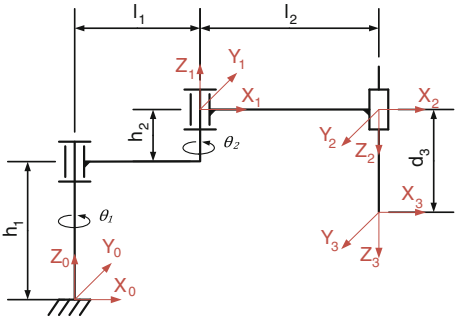

Fig. 2 Kinematic diagram with geometric configuration [2]

Table 1 DH parameters

Link	a_i (mm)	α_i (°)	θ_i (°)	d_i (mm)
1	l_1	0	θ_1	$h_1 + h_2$
2	l_2	180	θ_2	0
3	0	0	0	d_3

And the inverse kinematics is calculated as follow:

$$d_3 = h_1 + h_2 - z \tag{4}$$

$$\theta_2 = \pm \arccos\left(\frac{(x^2 + y^2) - (l_1^2 + l_2^2)}{2 \cdot l_1 \cdot l_2}\right) \tag{5}$$

$$\theta_1 = \arcsin\left(\frac{x^2 + y^2 + l_1^2 - l_2^2}{\sqrt{(2xl_1)^2 + (2yl_1)^2}}\right) \pm \arccos\left(\frac{2 \cdot y \cdot l_1}{\sqrt{(2xl_1)^2 + (2yl_1)^2}}\right) \tag{6}$$

where $-130^\circ \leq \theta_1 \leq 130^\circ, -160^\circ \leq \theta_2 \leq 160^\circ, d_3 : 0 \div 250\,\text{mm}$

2.2 *Robot Arm Design*

Figure 3 describes that link I is driven by motor I through a closed coupling I, link II is driven by motor II which is connected with link I by a closed coupling II. Motor III controls the height position of the end-effector through a mixed transmission between ball screw and timing belt. Figure 4 shows the 3D design of the robot arm and Fig. 5 shows the gripper designed by SolidWorks.

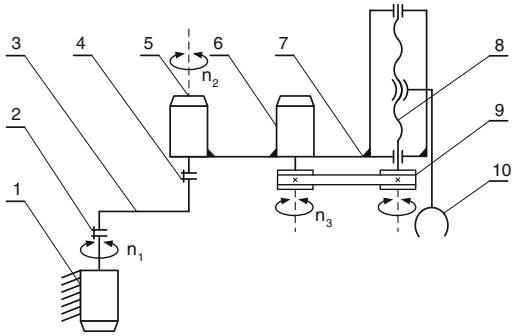

1. Motor I
2. Closed coupling I
3. Link I
4. Closed coupling II
5. Motor II
6. Motor III
7. Link II
8. Ball screw
9. Timing belt transmission
10. End-effector

Fig. 3 Schematic diagram of chess-playing robot arm

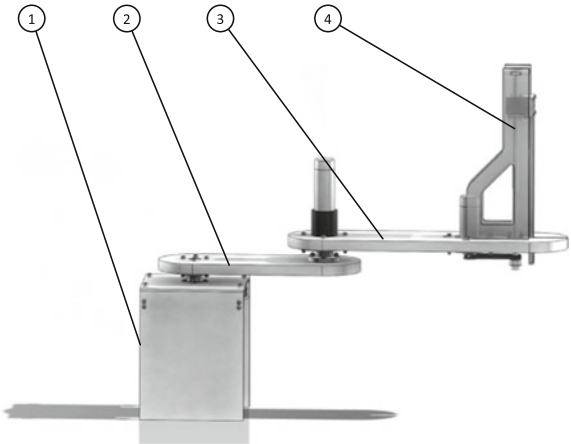

Fig. 4 3D design of the robot arm. *1* Base; *2* Link 1; *3* Link 2; *4* Link 3

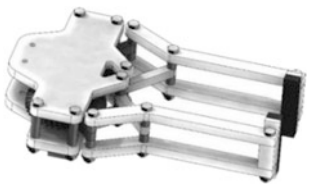

Fig. 5 3D design of the gripper

3 Algorithm for Detecting Chess Moves

Logitech C170 webcam was used to perceive the chess moves (Fig. 6) and connected with the computer via USB port. The process (Fig. 7) began with camera calibration to ensure the precision of capturing pictures, then, a picture of an empty chessboard (chessboard without chess piece) was taken. After every chess move, camera will capture an image and execute image subtraction to determine if the chess piece was presented on each chess cell.

Pre-processing Image:
Two steps of pre-processing: Crop (Fig. 8) and Grayscale (Fig. 9) were executed to improve image's quality. Chess board is a square, but the image taken by camera is in rectangular shape, therefore, unnecessary parts must be cropped to focus on 64 squares of the chessboard. In addition, images taken by camera are in RGB scale so they have three different layers that will complicate the process, so, converting those images into Grayscale which has only one layer is necessary (Fig. 10).

Fig. 6 Webcam C170 used in experiment

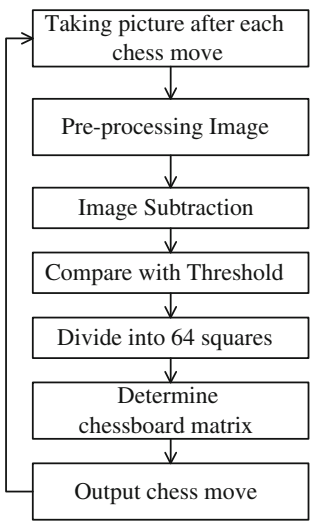

Fig. 7 Detecting chess move diagram

Fig. 8 Cropped image in RGB scale

Fig. 9 Image in gray scale format

Fig. 10 Image taken after opponent's move

3.1 Image Subtraction

This method was applied to find differences between two input pictures. After subtraction, pixel value will be compared with threshold, the position of each chess piece will be shown in a Binary picture (Fig. 11).

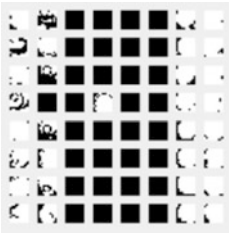

Fig. 11 Binary image after subtraction

3.2 Determine Chessboard Matrix

Based on the results of Binary Image, a 8 × 8 chess board matrix will be created respectively with 8 × 8 chess board, and chess cells that chess piece is standing on will have a value of "1", otherwise, the value is "0" [1] (Figs. 12 and 13).

Information combined from two matrices (before and after opponent's move), the chess move will be determined easily by a "delta matrix" (Fig. 14). In "Delta matrix", "−1" element describes the chess move beginning point, "1" element describes the chess move ending point. Then, we compare the matrix with chess board notation in Fig. 15 to record the move.

After image processing, the chess programming on computer will calculate and compute chess move to response to the opponent. Chess programming uses a library containing: opening moves and sample moves [3]. In addition, the program

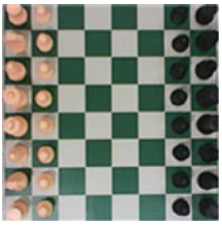

1	1	0	0	0	0	1	1
1	1	0	0	0	0	1	1
1	1	0	0	0	0	1	1
1	1	0	0	0	0	1	1
1	1	0	0	0	0	1	1
1	1	0	0	0	0	1	1
1	1	0	0	0	0	1	1

Fig. 12 Chess board matrix before opponent's move

1	1	0	0	0	0	1	1
1	1	0	0	0	0	1	1
1	1	0	0	0	0	1	1
1	0	0	1	0	0	1	1
1	1	0	0	0	0	1	1
1	1	0	0	0	0	1	1
1	1	0	0	0	0	1	1
1	1	0	0	0	0	1	1

Fig. 13 Chess board matrix after opponent's move

$$\begin{matrix} 0 & 0 & 0 & 0 & 0 & 0 & 0 & 0 \\ 0 & 0 & 0 & 0 & 0 & 0 & 0 & 0 \\ 0 & 0 & 0 & 0 & 0 & 0 & 0 & 0 \\ 0 & -1 & 0 & 1 & 0 & 0 & 0 & 0 \\ 0 & 0 & 0 & 0 & 0 & 0 & 0 & 0 \\ 0 & 0 & 0 & 0 & 0 & 0 & 0 & 0 \\ 0 & 0 & 0 & 0 & 0 & 0 & 0 & 0 \\ 0 & 0 & 0 & 0 & 0 & 0 & 0 & 0 \end{matrix}$$

Fig. 14 Delta matrix after chess move

Fig. 15 Chess board notation

$$\begin{matrix} A1 & A2 & A3 & A4 & A5 & A6 & A7 & A8 \\ B1 & B2 & B3 & B4 & B5 & B6 & B7 & B8 \\ C1 & C2 & C3 & C4 & C5 & C6 & C7 & C8 \\ D1 & D2 & D3 & D4 & D5 & D6 & D7 & D8 \\ E1 & E2 & E3 & E4 & E5 & E6 & E7 & E8 \\ F1 & F2 & F3 & F4 & F5 & F6 & F7 & F8 \\ G1 & G2 & G3 & G4 & G5 & G6 & G7 & G8 \\ H1 & H2 & H3 & H4 & H5 & H6 & H7 & H8 \end{matrix}$$

applied Min-max and Alpha-beta algorithm to choose the best move from all possible moves [4]. The selected move will be sent to the microcontroller to control robot arm grip and drop chess pieces on the real chessboard.

4 Control System

Control system diagram was shown in Fig. 16. Microcontroller receives chess moves sent from PC via RS232, processes and control motors. Positions of motor will response to microcontroller by encoder. Working range of robot arm was limited by limit switches.

When design the control system, it was necessary to select the appropriate actuators. In this case, DC servo motors were chosen because of its high accuracy and easy control. The system needs a position control algorithm in order to help the robot arm reach correct position. Because the motor's parameters are not enough for the simulation, PID algorithm with the Zeigler–Nichols II method using feedback signal from encoder was applied to calculate and create the PWM signal to control the position of the motor's angle. When the system is turned on, it is necessary to initialize PID parameters, enable microcontroller's interrupt and move the robot arm to "HOME" position in order to reset the encoder. Then, the system returns to waiting state, waiting for the process enable bit in RS232 interrupt. When the computer sends a process statement to microcontroller, the process is enabled, the arm reaches each position from start to end in sequence through PID position algorithm subroutine.

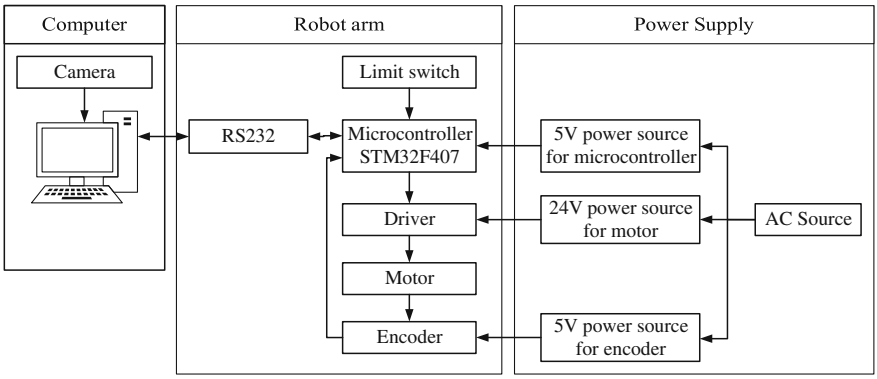

Fig. 16 Control system block diagram

5 Experiment and Results

5.1 Robot Arm

According to the 3D design, authors manufactured entire robot arm and the gripper to test the operating of system in real match. Robot's material is Acrylic plastic PMMA (Figs. 17 and 18).

Fig. 17 Experimental setup

Fig. 18 Gripper of robot arm

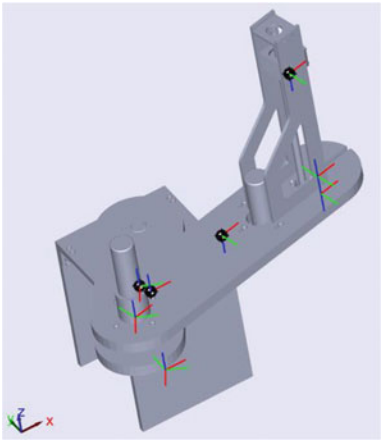

Fig. 19 Robot model in Mathlab

5.2 *Trajectory Simulation Processing*

The Figs. 19 and 20 show the straight trajectory of robot end-effector when processing a move the Knight from B8 (261;−120;0) to C6 (357;−72;0) using MATHLAB simulation. The move started from stand by position (24;185;250).

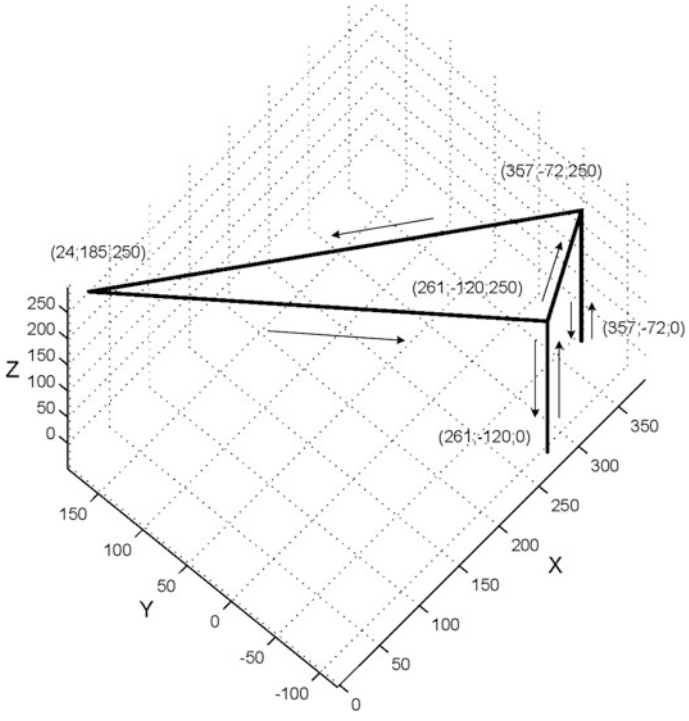

Fig. 20 End-effector's trajectory

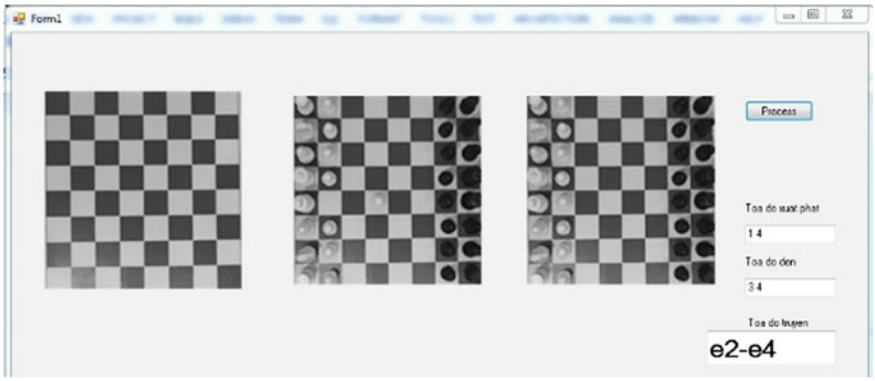

Fig. 21 Image process interface designed by Visual Studio

5.3 *Image Processing*

In Fig. 21, there are three images, the first is empty chess board's image, the next two images are the chess board before and after opponent's move. It can be seen from the picture, white pawn was moved from E2 to E4 and the result of process is written in the textbox. Image processing's accuracy is secured if we provide low noise lighting condition and place chess pieces within square area.

5.4 *Testing System in Real Chess Match*

The system include: standard FIDE chessboard, camera, robot manipulator, programs on computer. To secure lighting condition, an additional lamp was used and placed above the chessboard (Fig. 17). Five chess games versus five different random opponents were held and the results were shown in Table 2.

Gripper's errors include impact between gripper and different chess pieces when moving as well as the opening distance of gripper is not wide enough to release chess piece. The position accuracy of robot arm is based on how it put chessmen right in the square on the chessboard. If the footprint intersects with the borderline,

Table 2 Results of five matches

Match no.	Result	Total moves executed	Total error moves	Causes of error moves		
				Position error of robot arm	Gripper impact chess piece	Gripper do not release chess piece
Sum		159	8	2	5	1
Percentage (%)			5.03	1.26	3.14	0.63

it will be known as error. Otherwise, if the footprint's center and the center of chessboard's square are not coincident, it will be acceptable.

5.5 Assess the Result

After five matches, it can be seen that the working of system is stable, follow the setting sequence: taking picture, image processing, choosing best move and moving chess pieces on physical chessboard. There is no failure when system process images and transmit data, however, the match will stop if the gripper do not release chessman or chess piece was not placed inside chess cell. Accuracy of moving chess pieces decrease after every move because of robot's repeatability error and vibration of the gripper when moving. These make error happened easily when matches last longer than 30 moves.

6 Conclusion

The paper gives an overview of an automatic chess-playing robot which consists of three main modules. The system was experimented with human opponents in real matches and the results were really positive (high accuracy percentage, stable, etc. …). The robot arm can be used for research, educational purpose and entertainment. Module design makes it easy to be developed (both hardware and software) and able to compete in rapid and blitz chess game. The paper also help authors get the basic experience to expand their research on developing an autonomous system in industry combining image processing and artificial intelligence for making decisions. This opens up new opportunities to apply it to industrial applications where the system can be improved to adapt to the changes of the objects that it's currently working on. Making it a highly automated system that is capable of taking the appropriate action in most cases without human intervention.

References

1. Arda M, Kuşçu H, Öztürk E (2013) Obtain chess moves with image processing. In: Proceeding of the Unitech Grabovo international scientific conference
2. Quoc LH (2005) Kỹ thuật người máy Phần 1: Robot công nghiệp. Vietnam National University Publisher, Ho Chi Minh City
3. Tan NN, Quoc NX (2010) Thiết kế chương trình chơi cờ vua. Graduate thesis, Cao Thang College
4. Khac VV, Cuong LBQ (2013) Robot chơi cờ tướng. Gaduate thesis, HCM City University of Technology

Adaptive Controller Design for Mechanical Transmission Systems with Backlash

Nguyen Duy Anh, Tran Ngoc Cong Thuong and Nguyen Tan Tien

Abstract Backlash is one of the nonlinear characteristics which has a huge impact to the precision of mechanical transmission systems. This paper proposes methods and experiments on model of a transmission system using lead screw and nut. The anti-backlash methods are backlash inverse and adaptive control. Firstly, mathematical function of backlash and inverse backlash are presented based on research of Gang Tao. After that, model of mechanical transmission are proposed to design an adaptive controller for the systems which have backlash. Finally, the results of the experiments are shown. In this part, the results of backlash inverse and adaptive control are also presented for comparing and discussing.

Keywords Mechanical transmission systems model · Backlash · Adaptive control

1 Introduction

In mechanical engineering, backlash, sometimes called lash or play, is clearance or lost motion in the mechanism caused by gaps between the parts. Backlash exists in almost any transmission systems of industrial machine and is one of the nonlinear characteristic which has an impact to the accuracy of position and velocity control.

Systems with backlash are not suitable for application that require high accuracy. The motor will lose control with the load when the gap opens. This leads to bad affects to the systems, especially when a disturbance acts on the load, or when motor has to take a corrective action in the opposite direction to where the load is moving or is positioned at the time. Furthermore, the force or moment generated by the motor drives only the motor itself (and the parts of the transmission before the

N.D. Anh (✉) · T.N.C. Thuong · N.T. Tien
Faculty of Mechanical, HCM City University of Technology,
268 Ly Thuong Kiet Street, Ward 14, District 10, Ho Chi Minh City, Vietnam
e-mail: duyanhnguyen@hcmut.edu.vn

V.H. Duy et al. (eds.), *AETA 2015: Recent Advances in Electrical Engineering and Related Sciences*, Lecture Notes in Electrical Engineering 371,
DOI 10.1007/978-3-319-27247-4_42

backlash) and not the load. One might claim that in those instances the load is "uncontrollable".

The control of transmission systems with backlash has been researched since 1940s [1], both linear and nonlinear controllers are applied. Some linear controllers can be listed such as: PI, PID and state feedback control. The main analytical tool to describe the backlash has been the describing function technique. Besides, backlash inverse approximating method, non adaptive and adaptive controllers are also used to control the systems. These researches was presented in the survey about controlling with backlash of Mattias Nordian and Per-Olof Gutman [1]. However, most of the researches only propose methods and simulation, experiments are still limited.

In this paper, authors utilize two anti-backlash methods to experiment and take the results, including: backlash inverse, and adaptive control. Based on the results, efficiency of the controllers are evaluated and discussed.

The paper has six sections: Sect. 1 is introduction about backlash, impaction and researches of backlash on mechanical transmission systems as presented. Section 2 proposes the model of backlash and anti-backlash method by backlash inverse based on research of Gang Tao. Section 3 presents the model of mechanical transmission systems, the theory for adaptive control is presented in Sect. 4. Section 5 presents, compares and analysis the results from the experiments of the controllers and final is the conclusion.

2 Backlash and Backlash Inverse

This section presents mathematical model of backlash and inverse backlash. Next is the method to identify backlash parameters in actual transmission systems. This section is theoretical basis to apply backlash inverse controller and backlash inverse combine with linear controller.

2.1 Backlash

According to results of [2], backlash function ($B(\cdot)$) can be expressed by this equation:

$$\dot{u}(t) = \begin{cases} m_b \dot{v}(t) & \begin{array}{l} if\,(\dot{v}(t) > 0\, and\, u(t) = m_b(v(t) - c_r)) \\ or (\dot{v}(t) < 0\ and\ u(t) = m_b(v(t) - c_l)) \end{array} \\ 0 & other \end{cases} \tag{1}$$

With u: output, v: input, c_r: right limitation, c_l: left limitation, m_b: slope of the line, c_r and c_l are constants, $\dot{u}(t) = 0$ means that output was not change with the change of input signal. Figure 1 illustrates mathematical model of backlash.

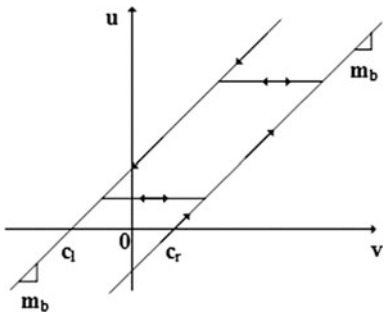

Fig. 1 Backlash model

2.2 Backlash Inverse

Gang Tao and Kokotovic propose a backlash inverse function to remove impaction of backlash [2]. Backlash inverse function ($BI(\cdot)$) which is illustrated by Fig. 2 satisfies the condition $BI(\cdot) \cdot B(\cdot) = I$, and can be expressed by the equations:

$$\dot{v}(t) = \begin{cases} \frac{1}{m}\dot{u}_d(t) \; if \left(\dot{u}_d(t) \cdot 0 \; and \; v(t) = \frac{u_d(t)}{m} + c_r\right) \\ \qquad or \; (\dot{u}_d(t) < 0 \; and \; v(t) = \frac{u_d(t)}{m} + c_l) \\ \qquad 0 \; if \; \dot{u}_d(t) = 0 \\ g(\tau.t) \; if \; (\dot{u}_d(t) > 0 \; and \; v(t) = \frac{u_d(t)}{m} + c_l) \\ -g(\tau.t) \; if \; (\dot{u}_d(t) < 0 \; and \; v(t) = \frac{u_d(t)}{m} + c_r) \end{cases} \tag{2}$$

With: $\delta(\tau - t)$: direct impulse function, u_d: input, v: output, c_r: right limitation, c_l: left limitation, m: slope of line.

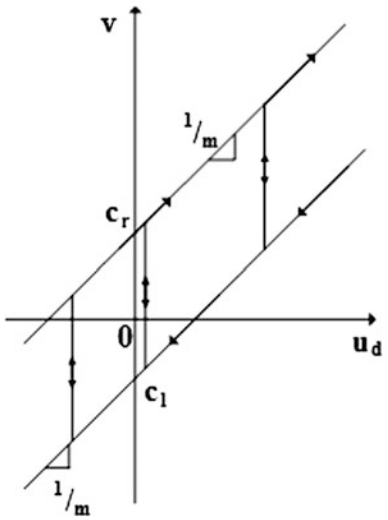

Fig. 2 Backlash inverse model

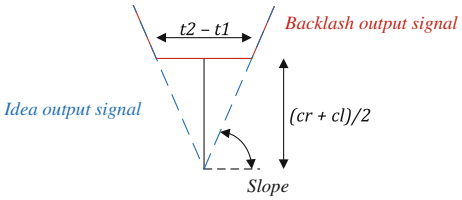

Fig. 3 Identify backlash parameters

2.3 Backlash Identifying Method

$v(t)$ is the input, $u(t)$ is the output; m, c_r, c_l are the parameters of backlash function.

The parameters are identified by geometrical method: the input is a triangle signal with constant amplitude and frequency, the output of the system will be trapezoid (Fig. 3). Position error appears because of backlash when the system reverse direction. Assume that $m = 1; c_l = c_r$, then backlash parameters are calculated at the reversing position by geometric.

Formula:

$$m = \frac{c_r + c_l}{t_2 - t_1} \tag{3}$$

With t_1, t_2 are the moment between two creasing position of the output signal which can be measured. Slope can be identified. Based on relations between m, c_r, c_l which is assumed above, c_r, c_l are calculated.

2.4 Backlash Inverse Controller

With the identified parameters above, backlash inverse is calculated. To reduce backlash in mechanical transmission systems, backlash inverse is applied to the control systems after the control signal u_d as the block diagram in Fig. 4.

If the backlash function $B(\cdot)$ is pure backlash, backlash inverse $BI(\cdot)$ can eliminate error completely. However, error still appears in systems using backlash inverse. This problem will be discussed and solved in next sections.

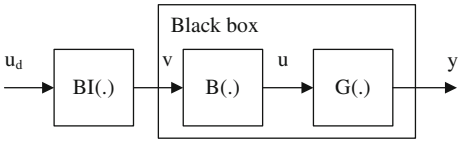

Fig. 4 Backlash inverse controller model

3 Mechanical Transmission Model

A general mechanical transmission system can be modeled to a system which includes: gain k, damper c and spring K. The differential equation which is the relation between the input signal (angular of motor) and the output signal (out position) is:

$$\mathrm{x} = \mathrm{k} \times \varphi + \mathrm{K} \cdot \dot{\varphi} + \mathrm{c} \cdot \ddot{\varphi} \tag{4}$$

With: X—out position, φ—angular of motor, k—gain, K—stiffness of spring, c—damper coefficient.

Laplace Eq. (4), we obtain:

$$\mathrm{X(s)} = \left(\mathrm{k} + \mathrm{Ks} + \mathrm{cs}^2\right)\varphi(S)$$

$$\frac{\varphi(S)}{\mathrm{X(s)}} = \frac{1}{\mathrm{k} + \mathrm{Ks} + \mathrm{cs}^2} \tag{5}$$

Equation (5) is used to design adaptive control in Sect. 4.

4 Adaptive Controller

4.1 Adaptive Law

The gradient method, also named the MIT rule due to fact that it was developed by the Instrumentation laboratory at Massachusetts Institute of Technology (MIT), is the approach for MRAC discussed in this paper.

We choose an adaptive control following MIT rule [3], the evaluation function is:

$$J(\theta) = \frac{e^2}{2} \tag{6}$$

With e being the error between the actual output and model reference output, θ is parameter adjustment.

The parameter θ must be adjusted to minimize the evaluation function to 0. So, parameter θ can have different sign with gradient of J. Equation of MIT rule is:

$$\frac{d\theta}{dt} = -\gamma \frac{\partial J}{\partial \theta} = -\gamma e \frac{\partial e}{\partial \theta} \tag{7}$$

γ—adaptive coefficient; $\frac{\partial e}{\partial \theta}$—sensitive function of system.

4.2 Design Adaptive Controller

Transfer function of mechanical transmission systems has a model as shown in (5). However, in an actual system, it is hard to identify damper and stiffness coefficients. So adaptive controller is applied to adapt with various systems. The gain—damper—spring process is a second order element, the model reference function is:

$$G_m = \frac{Y_m(s)}{R(s)} = \frac{\omega_n^2}{s^2 + 2\zeta\omega_n s + \omega_n^2} \tag{8}$$

Control law is:

$$u(t) = k_1 r(t) - k_2 y(t) - k_3 \dot{y}(t) \tag{9}$$

Laplace (9), we obtain:

$$U(s) = k_1 R(s) - k_2 Y(s) - k_3 s Y(s)$$

Equation (5) can be rewritten as:

$$G(s) = \frac{1}{k + Ks + cs^2} = \frac{\frac{1}{c}}{s^2 + \frac{K}{c}s + \frac{k}{c}} = \frac{\alpha_1}{s^2 + \alpha_2 s + \alpha_3} \tag{10}$$

$$GY(s) = G(s)U(s) = \frac{\alpha_1}{\mathrm{s}^2 + \alpha_2 \mathrm{s} + \alpha_3}[k_1 R(s) - k_2 Y(s) - k_3 s Y(s)] \tag{11}$$

$$Y(s) = \frac{\alpha_1 k_1 R(s)}{\mathrm{s}^2 + (\alpha_2 + \alpha_1 k_3)s + (\alpha_1 k_2 + \alpha_3)}$$

$$y(t) = \frac{\alpha_1 k_1 r(t)}{\mathrm{p}^2 + (\alpha_2 + \alpha_1 k_3)p + (\alpha_1 k_2 + \alpha_3)} \tag{12}$$

As a consequence, the error is:

$$e = \left(\frac{\alpha_1 k_1}{\mathrm{p}^2 + (\alpha_2 + \alpha_1 k_3)p + (\alpha_1 k_2 + \alpha_3)} - \frac{\omega_n^2}{s^2 + 2\zeta\omega_n p + \omega_n^2}\right) r(t) \tag{13}$$

The sensitivity derivatives are obtained by taking the partial derivatives of the error and considering the controller parameters:

$$\frac{\partial e(t)}{\partial k_1} = \frac{a_1 r(t)}{\mathrm{p}^2 + (\alpha_2 + \alpha_1 k_3)p + (\alpha_1 k_2 + \alpha_3)} \tag{14}$$

$$\frac{\partial e(t)}{\partial k_2} = \frac{-\alpha_1^2 k_1 r(t)}{(\mathrm{p}^2 + (\alpha_2 + \alpha_1 k_3)p + (\alpha_1 k_2 + \alpha_3))^2} = \frac{a_1 y(t)}{p^2 + (\alpha_2 + \alpha_1 k_3)p + (\alpha_1 k_2 + \alpha_3)} \tag{15}$$

$$\frac{\partial e(t)}{\partial k_3} = \frac{-\alpha_1^2 p k_1 r(t)}{(\mathrm{p}^2 + (\alpha_2 + \alpha_1 k_3)p + (\alpha_1 k_2 + \alpha_3))^2} = \frac{a_1 \dot{y}(t)}{\mathrm{p}^2 + (\alpha_2 + \alpha_1 k_3)p + (\alpha_1 k_2 + \alpha_3)} \tag{16}$$

Due to the fact that the process parameters are unknown, none of the three equations above can be used. Furthermore, the transfer function of the system are close to the transfer function of the reference model in adaptive control, it means that Eq. (10) will approximate to Eq. (8), so:

$$\mathrm{p}^2 + (\alpha_2 + \alpha_1 k_3)p + (\alpha_1 k_2 + \alpha_3) = p^2 + 2\zeta\omega_n p + \omega_n^2 \tag{17}$$

The adjustment for the controller parameters is:

$$\frac{dk_1(t)}{dt} = -\gamma\left(\frac{1}{p^2 + 2\zeta\omega_n p + \omega_n^2} r(t)\right) e(t) \tag{18}$$

$$\frac{dk_2(t)}{dt} = \gamma\left(\frac{1}{p^2 + 2\zeta\omega_n p + \omega_n^2} y(t)\right) e(t) \tag{19}$$

$$\frac{dk_3(t)}{dt} = \gamma\left(\frac{1}{p^2 + 2\zeta\omega_n p + \omega_n^2} y(t)\right) e(t) \tag{20}$$

With $\gamma = \alpha_1$ is adaptive gain parameters.

4.3 Simulation Results

The closed loop control system was simulated in Matlab/Simulink for the nominal values of the uncertain parameters. The model reference function is $\frac{0.3}{s^2+0.3s+0.6}$ and the transfer function is $\frac{25}{s^2+6s+25}$ (Fig. 5).

Result of simulation the controllers:
Using adaption gain equal to $\gamma = 3.5$ and the desired input is a squared pulse. It takes about 10 s to process the output tracking to input. By analysing the signals it can be concluded that the system's performances are acceptable (Fig. 6).

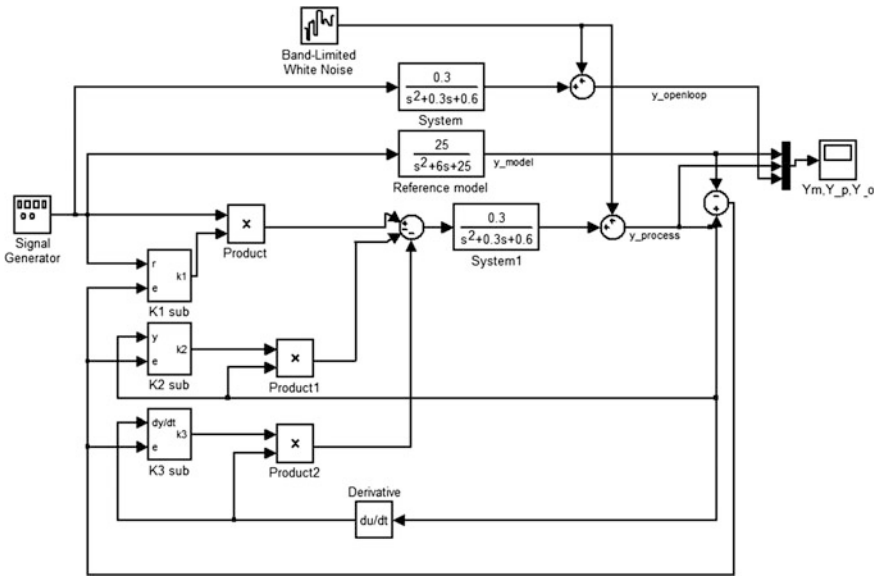

Fig. 5 Simulation of adaptive control on Matlab

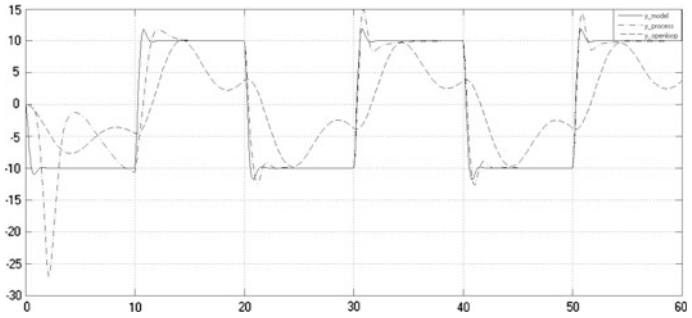

Fig. 6 Result of simulation with square pulse input

5 Experiment and Result

5.1 Experiment System

The transmission system includes: motor, harmonic driving gears, belt, lead screw and nut. The system can change the gap of backlash to experiment, the gap can be changed from 0 to 3 mm.

5.2 Backlash Measurement

The results of backlash measurement based on part 3 of Sect. 2, with 155 samples, we obtain the backlash parameters. The mean of the backlash gap is 1.165 mm and variance of measurement is 0.055 mm.

5.3 Experiment Results

Input is: $x_c = 10\sin(2\pi ft)$ (mm)

Figure 7 expresses error of a mechanical transmission system with backlash. The maximum error is 1.2 mm However, the error is also varies and depends on the moving direction. As Fig. 7, the error in forward direction is approximately around −0.15 mm and reverse direction is around 1.2 mm. This consequence is relevant with actual systems because the error of tracking also depends on the initial location and direction.

Figure 8 expresses error of backlash inverse controller. The error of the system is reduced from 1.165 to ±0.08 mm, but the error is oscillate with the same frequency

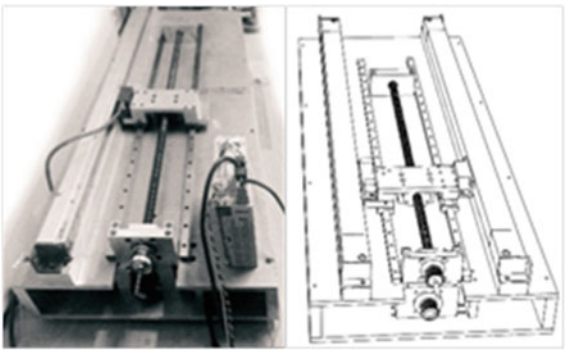

Fig. 7 Mechanical experiment system

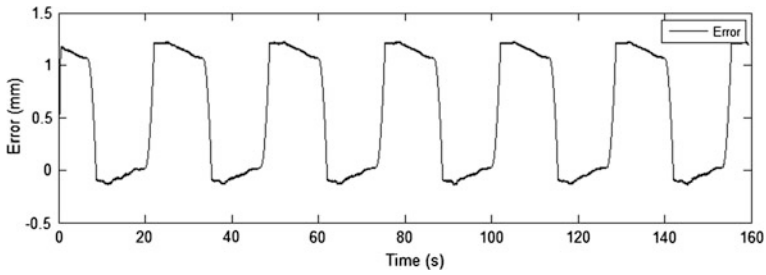

Fig. 8 Error between input desired and output process with backlash

of the input signal. The first reason is the error of data acquisition and measuring backlash, so the gap of backlash includes mean value and variance. The second reason is the disturbance acting on the system. For that reason, the error of the system with backlash inverse is reduced to ± 0.08 mm and larger error of measurement 0.055 mm

Next, we analysis the process of anti-backlash by backlash inverse. The process includes two steps: the system will compensate the gap in reversing direction. In this step, output will not change because the motor will no affect to load. After that, the output is delayed comparing to the desired input. Second step is that the system will run to compensate the delay and track to the input signal, output is a line which has slope equal to velocity max of system.

Backlash inverse compensation is different with pure backlash function of Gang Tao because of the limitation of the control signal. In pure backlash function of Gang Tao, control signal can be infinite and this is unrealistic.

Figure 8 expresses the error of adaptive control in the experimental system. The errors can be separated into two parts: error in reversing direction and error in tracking the desired input. When the system reverses direction, the gap of backlash appears, the controller run to compensate it. After that the adaptive controller run to track input. So the error of reversing direction is larger and around ± 0.1 mm while the error of tracking is around ± 0.05 mm.

Other characteristics of the error is oscillating. The main reason for this is the hysteresis of mechanical transmission system. The error in positive direction is positive because the process output is delayed comparing the input, the input is larger than output. It is similar in the reverse direction with negative error.

There are two things that affect to the hysteresis of the system. The first is the response of the system. It takes a period of time to transfer the motor's motion to the load through the transmission. The second is the digital control system. It takes time to collect data from output, run the controller on the computer, transfer control signal to microcontroller to control the motor. So there are always time delay between input and output in any mechanical transmission system.

This experiment has a time delay around 0.02 ms. If we neglect the hysteresis of the system the error will not oscillate and the error of tracking reach 0.01 mm, the error of reversing direction keeps its value around 0.1 mm (Fig. 9).

The result of adaptive control is better than backlash inverse compensation. The error of tracking input of adaptive control is ± 0.05 mm comparing to ± 0.08 mm of backlash inverse. If we neglect the hysteresis of the system the error of adaptive can reach ± 0.01 mm. This cannot be applied to backlash inverse compensation because of open loop control. However, the error of reversing direction of backlash inverse (± 0.08 mm) is better than adaptive control (± 0.1 mm). The reason of this is that backlash inverse compensation use maximum value of control signal when it reverses direction while adaptive control use control signal from controller, it is less than the maximum control value (Figs. 10 and 11).

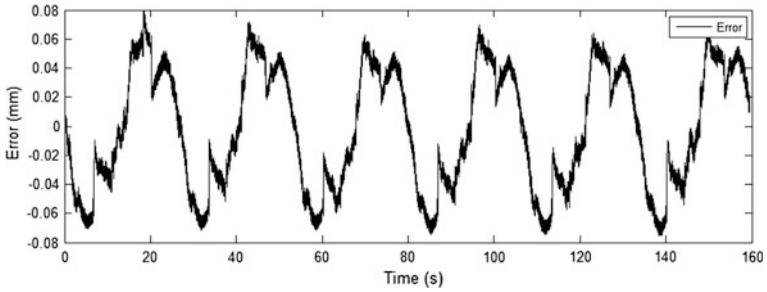

Fig. 9 Error between input desired and output process with backlash inverse

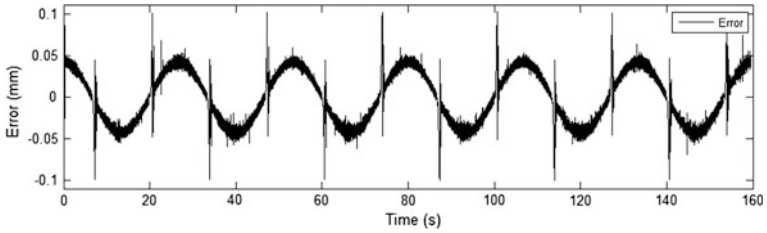

Fig. 10 Error between input desired and output process with adaptive control

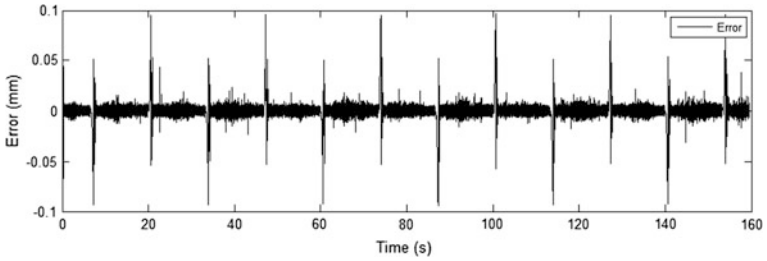

Fig. 11 Error between input desired and output process with adaptive control

6 Conclusion

The paper proposed two methods to eliminate backlash in mechanical transmission system. Each method is suitable for specific system. The backlash inverse compensation is useful for systems using open loop control and adaptive control is suitable for systems which have changing parameters and use close loop control.

With backlash inverse compensation, the experiment proved the efficiency of the theory about backlash function, backlash inverse function and method to identify backlash parameters. The error was reduced from 1.165 mm in a system with

backlash to ± 0.08 mm in backlash inverse method. The adaptive control is also efficient in controlling mechanical transmission system with backlash. This was shown in part 3 of Sect. 5 above. However, adaptive control is only applied in the experimental system and still has not proved the efficiency for different systems.

References

1. Nordin M, Gutman P-O (2002) Controlling mechanical systems with backlash—a survey. Automatica 38(10):1633–1649
2. Tao G, Kokotovic PV (1993) Continuous-time adaptive control of systems with unknown backlash. In: Proceedings of the American control conference, pp 1344–1348
3. Coman S, Boldişor C (2014) Adaptive PI controller design to control a mass-damper-spring process. Bull Transilvania Univ Braşov 7(56):2
4. Boneh R, Yaniv O (1998) Control of an elastic two-mass system with large backlash. J Dyn Syst Measur Control
5. Dean SRH, Surgenor BW, Iordanou HN (1995) Experimental evaluation of a backlash inverter as applied to a servomotor with gear train. In: Proceedings of the 4th IEEE conference on control applications, pp 580–585
6. Vörös J (2012) Parametric identification of systems with general backlash. Informatica 23 (2):283–298

Image Processing for Smoke Detection Based on Embedded System

Thao Phuong Thi Nguyen and Hoanh Nguyen

Abstract In this paper, we propose a new method for smoke detection in both outdoor and indoor video sequences based on embedded system. The proposed method is composed from three main steps to determine the smoke in the field of view of the camera. The first step is to determine the moving area by using background subtraction algorithm. The second step is to find color of every pixel in the moving area by using pixel extraction algorithm. The final step is to find the shape of the moving area by using dispersion and growth rate parameters. Dispersion is based on ratio of perimeter and area of the moving area. Growth rate is calculated from increasing the number of pixel of the moving area. A new contribution of the proposed approach is that all algorithms are executed on embedded system. For embedded system, we chose BeagleBone Black embedded board because of its cost and efficient. Furthermore, a firefighter robot based on this board is built to demonstrate the efficacy of the proposed method.

Keywords Image processing · Smoke detection · Background subtraction · Pixel extraction · Embedded system · BeagleBone black

1 Introduction

Fire is one of the main reasons causing the significant damages to human and environment. In recently there are many serious disasters from fire made us really concern. But this can be totally prevented or reduced with the intelligent fire

T.P.T. Nguyen (✉)
Faculty of Electrical and Electronics Engineering, Ton Duc Thang University,
No. 19 Nguyen Huu Tho Street, District 7, Ho Chi Minh City, Vietnam
e-mail: nguyenthiphuongthao@tdt.edu.vn

H. Nguyen
Department of Electrical and Electronics Engineering,
Ho Chi Minh City University of Technology, Ho Chi Minh City, Vietnam

V.H. Duy et al. (eds.), *AETA 2015: Recent Advances in Electrical Engineering and Related Sciences*, Lecture Notes in Electrical Engineering 371,
DOI 10.1007/978-3-319-27247-4_43

detection systems. To achieve this, it is important to detect the fire as early as possible so that it can be put out before growing too large. Smoke detection is the best way helping us to detect fire early.

There are various kinds of smoke detectors currently being used including optical smoke detectors, ionization smoke detectors and air sampling smoke detectors. It can be noticed that these detectors are quite expensive to set up and is usually only for closed spaces. Another problem is that the response time is too slow, as it requires smoke to heat to dissipate. Due to the rapid developments in digital camera technology and video processing techniques, there is a big advantage to replace conventional smoke detection techniques with computer vision-based systems which have the ability to serve large and open spaces with low cost. Recently algorithms for smoke detection based on vision-based method have had a quick development. The method proposed in [1] used an approximate median method to segment moving regions in a video frame, extracted the features and trained a support vector machine (SVM) classifier. An accumulative motion model based on integral image by fast estimation of smoke motion orientation was proposed in [2]. The model is able to eliminate the disturbances from artificial lights and non-smoke moving objects by using the accumulation of motion. Together with chrominance detection, the model can correctly detect the existence of smoke. In [3], the author extracted smoke regions based on fractal encoding concepts. The property of self-similarity of smoke shape is used to search for smoke regions in the code generated by image fractal encoding. A method proposed in [4] used concatenated histograms of the LBP pyramid and trained a neural network classifier to distinguish smoke and non-smoke objects. It is able to operate at 10 fps. As smoke blurs the texture and edges in the background of an image [5], the wavelet energy of smoke region is decreased. This can be an important clue for smoke detection. This method is efficient in many real cases and it has been commercialized. In [6] the authors introduced an online algorithm that models the ratio between the current input frame energy and the background energy. Nevertheless, this method needs long reaction time and more precise validation of the input data. In [7], the features are generated based on Discrete Cosine Transforms (DCT) and Discrete Wavelet Transform (DWT). After a rigorous analysis of features at different levels, three levels of wavelets decomposition are used. A smoke block is identified by using SVM. The processing speed is slow, only at 3 fps. A statistical pattern based algorithm is proposed in [8, 9]. The color of smoke, DWT energy and shape information is used for smoke identification. The smoke pixels are detected based on HMM (Hidden Markov Models).

However, these above methods are executed on the window operating system with high accuracy and require a high performance computer for the processing speed is fluently. These algorithms cannot be run on low hardware devices such as embedded computers.

In this paper, we present a real-time smoke detection algorithm using texture and color features. This algorithm combines motion, appearance and color of object region to detect smoke. Our method is able to detect white, black, grey smoke and can be executed on the embedded platform where hardware is limited. Further, our

method can be applied directly to the surveillance camera or integrated complete smoke detection systems such as firefighter robot. We use the BeagleBone Black embedded board running Linux to execute algorithms. After implementation, we calculate to ensure the accuracy above 80 %. To evaluate the performance of our method for future development, we calculate the average executed speed (frame per second) on embedded system and measure the distance from embedded system to smoke detector. The remaining sections of this paper are organized as follows. Our method is explained in details in Sect. 2. Experimental results and discussion are presented in Sect. 3. Finally, the conclusion of this paper is presented in Sect. 4.

2 Proposed Smoke Detection Algorithm

Our algorithm for real-time smoke detection is the combination of motion, appearance and color detect method. The flow chart for the proposed method is show in Fig. 1.

2.1 Movement Detection

Video is a sequence of consecutive frames. Detecting the movement region is essentially comparing consecutive frames in a video so that we can find the difference between frames. This is the basic principle to determine the moving objects, because the differences between consecutive frames can only exist when there are moving objects in the frame. Many methods have been devised to resolve this problem, each of them may be suitable for some specific conditions circumstances. In general, it can be classified into the following group of methods:

- Background Subtraction
- Statistical Methods
- Temporal differencing

In this paper, we use background subtraction algorithm to detect moving objects. The reason for choosing this algorithm is the output frames are easy for noise filtering and fast calculation. This advantage increases execution speed on embedded system where hardware is limited.

Background subtraction algorithm
Background subtraction algorithm is based on a comparison between two frames, the one in considered frame sequences and a reference in image sequences with a reference image called background. Background image is the image obtained without any moving object. Denote B as the collected background, we have the difference between the background image and image the kth image in image sequences.

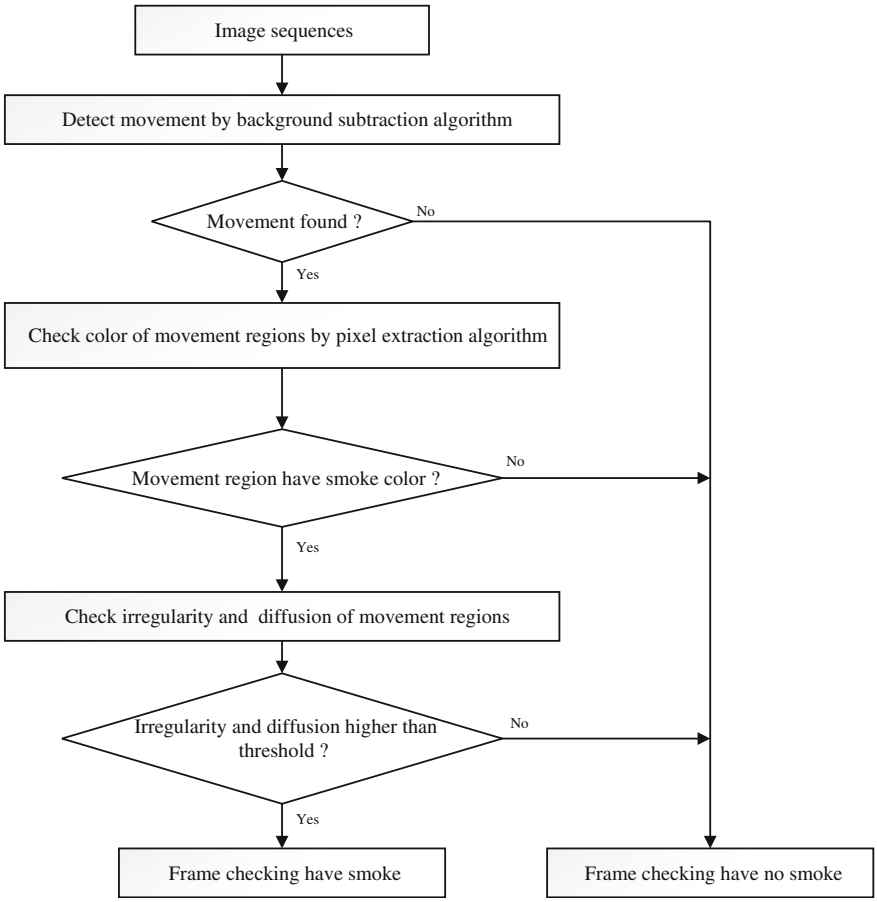

Fig. 1 Flow chart of our proposed method

$$D_k = F_k - B \tag{1}$$

where: D_k is the parameter characterizing the difference between the two frames, F_k is the kth frame obtained from the camera, B denotes the background image.

In practice, noise always exists in the system so we must set up a threshold to limit the noise

$$M_k(\mathrm{x,y}) = \begin{cases} 1 \ where\, D_k(\mathrm{x,y}) \geq \mathrm{T} \\ 0 \ where\, D_k(\mathrm{x,y}) < \mathrm{T} \end{cases} \tag{2}$$

where: M_k is a motion mask, i.e., the point (x, y) is considered to be moving when $M_k(\mathrm{x,y}) = 1$ and stationary when $M_k(\mathrm{x,y}) = 0$, and T is the threshold to limit the noise.

In fact, the background image always changes due to changes in brightness caused by the wind, the clouds flying past, etc. So we need to update the background continuously. Denote B_k as the background at the time k. The background at the time k + 1 is updated as follows

$$B_{k+1}(\mathrm{x,y}) = \begin{cases} \alpha * B_k(\mathrm{x,y}) + (1-\alpha)\mathrm{F}_k(\mathrm{x,y}) \ where\, M_k(\mathrm{x,y}) = 0 \\ B_k(\mathrm{x,y}) \ where\, M_k(\mathrm{x,y}) = 1 \end{cases} \tag{3}$$

where: α is a constant called the learning rate, which reflects the background update speed (fast or slow) and B_{k+1} is the updated background of the background image B_k.

2.2 Color Checking

It can be observed that smoke is usually in white, black or gray color. Every pixel within the movement region from the first step is checked to determine the smoke color. If the following conditions are met, pixel p(x) will be judged as a smoke color pixel:

Let $C_{\max} = \max(\mathrm{R,G,B}) \quad C_{\min} = \min(\mathrm{R,G,B})$

Condition 1:

$$|C_{\max} - C_{\min}| \leq T_{gray} \tag{4}$$

Condition 2:

$$(I_{fg} - I_{bg}) > T_{white} \tag{5}$$

Condition 3:

$$T_{black1} > (I_{bg} - I_{fg}) > \mathrm{T}_{black2} \tag{6}$$

Condition 1 check for gray or black smoke. Because of the R, G, B values of the gray or black pixels are not different too much. Therefore T_{gray} is a preset threshold for gray and black pixels, choose T_{gray} = 0.15. Condition 2 and condition 3 check for black and white smoke. I_{fg} and I_{bg} denote the gray value of that pixel in the background image and current frame respectively. Condition 2 base on the fact that, pixel of white color have intensity greater than background and black color will be within a certain range of gray. These values T_{white}, T_{black1}, T_{black2} are the threshold for white color and the upper and lower thresholds for black color, respectively. In this paper, we choose the corresponding values for T_{white}, T_{black1}, T_{black2} as 0.1, 0.3 and 0.1.

Combining 3 conditions, we can determine smoke colors by checking which condition is met:

$$(\text{Condition 1}) \text{ OR } (\text{Condition 2}) \text{ OR } (\text{Condition 3}) \tag{7}$$

To increase the accuracy, we checked all the pixels in the movement region, and if there are more than 25 % of the pixels satisfying the above conditions, we conclude that the movement region have color the same color of smoke.

2.3 Irregularity and Diffusion Checking

After the previous stage, we can remove the things which do not have smoke color and moving in the background. But if there are some things which might be confused with the smoke, such as shadows, people who are moving and so on, then we can proceed to the following step to clarify these things. In this step we will focus on two dynamic characteristics of smoke, namely, irregularity and diffusion.

Irregularity of smoke
Because of air flowing, smoke is constantly changing shape. Hence determining the shape of the smoke is indeed a difficult task. To resolve this problem, we use two geometric parameters which are the perimeter and the smoke area. We calculate the ratio between the perimeter and the smoke area. Then, we compare this ratio with a certain threshold. If the ratio is greater than this threshold, this area could be the smoke area. Otherwise, it is discarded. The equation is shown below:

$$\frac{\textit{the perimeter of smoke area}^2}{\textit{smoke area}} \geq \textit{threshold} \tag{8}$$

where: perimeter of smoke area is total pixel on the perimeter boundary of smoke, smoke area is total pixel in the whole of the smoke, threshold is a threshold to distinguish between smoke clear shapes. In this paper, we choose the threshold as 40.

Diffusion of smoke
Due to the diffusion of smoke, the size of smoke will continue to increase. Therefore, we calculate the period of time for the growth rate of the extracted area in order to determine the diffusion of the smoke. In digital images, the area of the smoke can be represented by the number of pixels. The time interval can be expressed as the number of frames. So we have the equation:

$$\nabla A_{di} = \frac{d_p}{d_t} = \frac{p_{i+k} - p_i}{(i+k) - i} \tag{9}$$

where: ∇A_{di} represents the rate of change in number of pixel extracted from the smoke area, from the i th frame to (i + k)th frame, p_i: total pixels in the smoke region of the ith frame.

To reduce errors caused by wind effects, we calculated the rate of change during cycle of 10 frames

$$\overline{\nabla A_{di}} = \frac{1}{n}\sum \nabla A_{di} \tag{10}$$

By comparing $\overline{\nabla A_{di}}$ with threshold values, we can conclude whether the movement region in the frame is smoke or not. In this paper, we choose the threshold values as 0.02.

3 Experimental Results and Discussion

The proposed algorithm was programmed in C++ with the support of the open source libraries OPEN CV. The method is implemented on embedded systems specifically the embedded board BeagleBone Black. Some technical characteristics of this board: 1 GHz ARM® Cortex-A8 processor, 512 MB DDR3 RAM, Linux operating system. Video inputs was obtained from Logitech C520 Webcam and be scaled to 320 × 240 resolution for fast processing speed. Algorithm is compiled using g++ compiler. With this embedded board, we can execute the proposed algorithm at the speed of 3–11 fps and with the maximum distance of 100 m in open environment.

The output of this algorithm will be result frames, in which red square is drew around the smoke to indicate the location of smoke in the frame. In case that the moving region is not smoke, blue squares will be drawn. Each square will be accompanied by the text “smoke” and “no smoke” correspondingly.

There are five different video segments to be tested to check the accuracy of our method. Each video has around 20–1500 frames. The videos a, b, d in Fig. 2 following were recorded in different environments with dedicated camera or surveillance camera and videos c, d is used from data set publicly available at web address http://signal.ee.bilkent.edu.tr/VisiFire/. The first video is about smoke in a garden, the second video is about a white car on the road (no smoke), the third video is about smoke emitting toward white wall, the fourth video is about a tunnel light on (no smoke) and the fifth video is about a red car on the road.

To evaluate the accuracy of the algorithm, two conclusions of the methods are given: correct result and wrong result.

Correct result: smoke correctly detected as smoke and no smoke correctly identified as no smoke in frame.

Wrong result: conclude smoke when there is no smoke and conclude no smoke when there is smoke in frame.

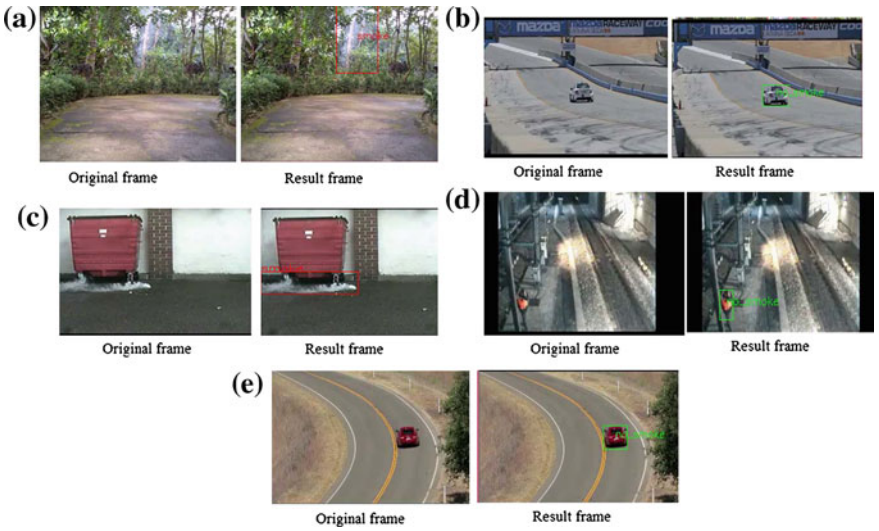

Fig. 2 Result frame of each video

The accuracy of each video is calculated using the equation:

$$accuracy = \frac{number\ of\ correct\ result}{number\ of\ wrong\ result} \cdot 100\% \tag{11}$$

Figure 2 shows the results frame of a representative of each video. Table 1 shows the statistical results of all videos.

As we can see from Table 1, this method can detect smoke with high accuracy, especially in an environment where everything is either smoke or no smoke. Video 1 shows smoke in a garden where the effect of winds make smoke changes quickly. Therefore, the accuracy becomes wrong when the smoke disappeared or its shape looks like natural objects. Video 2 shows a white car run on a road. This car is moving, have the same color as smoke but its shape is very different from the shape

Table 1 Statistical results of all videos

Video	Number of frame	Number of smoke frame	Processing speed	Result of method		
				Correct result	Wrong result	Accuracy (%)
Video 1	247	247	3 fps–4 fps	197	50	80
Video 2	58	0	8 fps–10 fps	57	1	99
Video 3	282	282	4 fps–5 fps	227	55	80
Video 4	171	0	4 fps–5 fps	170	1	99
Video 5	16	0	11 fps	16	0	100

of the smoke. So the accuracy for this case is nearly 100 %. Video 3 shows smoke emitting forward white wall. Wind effects and white wall make color and shape of smoke region sometime like natural objects therefore accuracy has decreased. Video 4 and Video 5 show moving objects with shape and color different from the smoke so accuracy for this case is nearly 100 %.

4 Conclusion

This research proposes a smoke detection method based on image processing. We use the combination of motion, color and appearance method. Our method is able to detect white, black and grey smoke. We use embedded system to implement the method to reduce costs and create maneuverability so that can be integrated into the surveillance camera.

The system can detect smoke in a open environment, such as a forest, tunnel, highway, not like the smoke sensor dedicated, can only detect smoke in small space.

However, because the smoke detection system is based on collected images so it can not detect smoke when smoke is masked by other objects or when the wind is too strong. The system will not detect smoke when environment is too bright or too dark, because it is not possible to detect moving objects should not be able to handle the next step in program.

References

1. Tung TX, Kim J-M (2011) An effective four-stage smoke detection algorithm using video images for early fire alarm systems. Fire Saf J 46:276–282
2. Yuan F (2008) A fast accumulative motion orientation model based on integral image for video smoke detection. Pattern Recogn Lett 29:925–932
3. Fujiwara N, Terada K (2004) Extraction of a smoke region using fractal coding. In: IEEE International Symposium on Communications and Information Technology, ISCIT 2004, vol 2, pp 659–662
4. Yuan F (2011) Video-based smoke detection with histogram sequence of LBP and LBPV pyramids. Fire Saf J 46:132–139
5. Toreyin BU, Dedeoglu Y, Cetin AE (2005) Wavelet based real-time smoke detection in video. In: EUSIPCO
6. Piccinini P, Calderara S, Cucchiara R (2008) Reliable smoke detection in the domains of image energy and color. In: ICIP, pp 1376–1379
7. Gubbi J, Marusic S, Palaniswami M (2009) Smoke detection in video using wavelets and support vector machines. Fire Saf J 44:1110–1115
8. Kim C, Han Y, Seo Y, Kang H (2011) Statistical pattern based real-time smoke detection using dwt energy. In: International Conference on Information Science and Applications (ICISA), pp 1–7
9. Lee C, Lin C, Hong C (2009) Spatio-temporal analysis in smoke detection. In: IEEE International Conference on Signal and Image Processing Application, pp 80–83

Second Order Sliding Mode Control Design for Active Magnetic Bearing System

Van Van Huynh and Bach Dinh Hoang

Abstract This paper presents a new second order sliding mode control to stabilze a five-degree-of-freedom (DOF) active magnetic bearing (AMB) system. The new single phase sliding surface is introduced first. Then, the continous sliding mode controller is designed to relax the chattering problems in the control input. Furthermore, since the control characteristics of the five-DOF AMB are highly non-linear and time varying, the continous sliding mode controller is proposed to further improve the control performance and increase the robustness of the five-DOF AMB system. Finally, the performance of the controller applied to the five-DOF AMB model is demonstrated through simulation works under various rotational speeds and system conditions.

Keywords Active magnetic bearing system · Continuous sliding mode controller · Chattering problems · Sliding mode control

1 Introduction

The theory of sliding mode control (SMC) is known to be an effective robust control technique, and has been successfully and widely applied for both linear and nonlinear systems such as robot manipulators, aircrafts, underwater vehicles, spacecrafts, flexible space structures, electrical motors, power systems, and automotive engines [1]. The main advantages of SMC are fast response and strong robustness with respect to uncertainties and external disturbances [2–4]. Generally speaking, the traditional SMC design can be divided into two phases: the reaching

V.V. Huynh · B.D. Hoang (✉)
Faculty of Electrical and Electronics Engineering, Ton Duc Thang University,
No. 19 Nguyen Huu Tho Street, District 7, Ho Chi Minh City, Vietnam
e-mail: dinhhoangbach@tdt.edu.vn

V.V. Huynh
e-mail: huynhvanvan@tdt.edu.vn

V.H. Duy et al. (eds.), *AETA 2015: Recent Advances in Electrical Engineering and Related Sciences*, Lecture Notes in Electrical Engineering 371,
DOI 10.1007/978-3-319-27247-4_44

phase and the sliding phase. Firstly, in the reaching phase, the feature of SMC is to use a switching control law to drive system state trajectories onto a switching surface and remain on it thereafter. Secondly, in the sliding phase, the essence of SMC is to keep the state trajectories moving along the surface towards the origin with desired performance [5, 6].

Although the sliding mode controller guarantees robustness, chattering is its main drawback. the chattering phenomenon is is caused by the switching function of hitting control which leads to premature wear and tear or even breakdown of the system being applied to. This disadvantage of chattering could be reduced by techniques such as nonlinear gains, dynamic extensions or by using more recent strategies such as second order sliding mode control.

Magnetic bearings are electromechanical devices that use magnetic forces to completely levitate a rotor or suspend it in an air gap without physical contact. Based on the noncontact and frictionless characteristics, active magnetic bearing (AMB) offers many practical and promising advantages over conventional bearings such as longer life, lower rotating frictional losses, higher rotational speed, and elimination of the lubrication.

In recent years, many control techniques, such as sliding mode control, fuzzy control, adaptive PID control, neural networks control, adaptive fuzzy control, and other control methods, have been developed and applied to the position control for AMB system [7–10]. The authors of [9] developed a new fuzzy sliding mode controller to stablize the axial channel of magnetically suspended rotor. In [10], the decentralised intelligent double integral sliding-mode control was proposed for the control of a high performance fully suspended five (DOF) AMB system. However, these control schemes given in [7–10] suffered the drawback of severe chattering in the control input that can increase power consumption, make the controlled plant vibrate and reduce control precision.

The goal of this research is to ensure the system's robustness to uncertainties and disturbances and to relax the chattering problems in the control input by utilizing the second order sliding mode control technique. A new adaptive is proposed to deal with the unknown gravitational force periodic disturbances caused by rotor mass imbalance and other disturbances and ensure good transients.

2 Modeling of an Active Magnetic Bearing System

In order to synthesize the proposed sliding surface with the controller, a horizontal shaft AMB system model for the 5-DOF AMB system is re-derived based on the work done in [9, 10]. A 5-DOF AMB system consists of two radial bearings and one axial bearing as shown in Fig. 1. To achieve a stable levitation every DOF requires a position sensor. In this paper the radial and axial bearings are separated for control design. Assuming that the rotor is rigid floating body, the principle of flight dynamics is used to derive the equation.

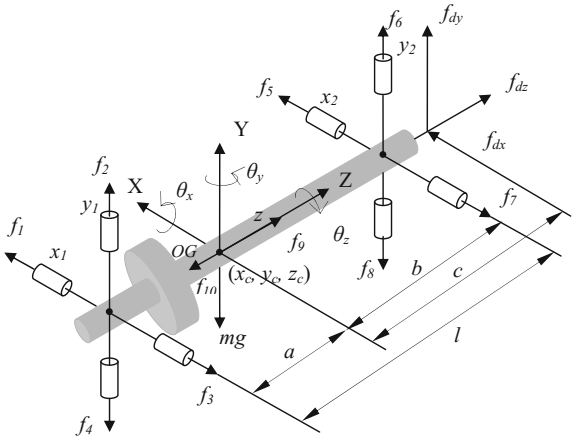

Fig. 1 Geometry relationships of rotor and AMB systems

Based on the work in [9] and [10], the rotor's equations of motion for five DOF are

$$\begin{aligned} m\ddot{x}_c &= F_{x_1} + F_{x_2} + f_{dx} \\ m\ddot{y}_c &= F_{y_1} + F_{y_2} + f_{dy} \\ m\ddot{z}_c &= F_z + f_{dz} \\ J\ddot{\theta}_y - J_z\omega\dot{\theta}_x &= -aF_{x_1} + bF_{x_2} + cf_{dx} \\ J\ddot{\theta}_x - J_z\omega\dot{\theta}_y &= -aF_{y_1} - bF_{y_2} + cf_{dy} \end{aligned} \tag{1}$$

where J is the transverse moment of inertia of the rotor about $X-Y$ axes and J_z is the polar moment of inertia of the rotor about Z-axis; $-J_z\omega\dot{\theta}_x$ and $-J_z\omega\dot{\theta}_y$ are the gyroscopic effects; F_{x_1}, F_{x_2}, F_{y_1}, F_{y_2} and F_z are the electromagnetic forces in respective axes; f_{dx}, f_{dy} and f_{dz} are the external disturbance forces; θ_x, θ_y and θ_z denote the pitch, yaw and spin angles displacements around the X–Y–Z axes of the rotor; a, b and c represent the distances from the CG to the left AMB, right AMB and external disturbances, respectively, in which $l = a + b$. The rotational speed of the rotor can be denoted by ω.

This is possible under a few assumption which are described in [10]. The mathematical model of a rigid rotor, which is supported by a 5-DOF AMB system used COG coordinates is:

$$M\ddot{X} = AX + BU(t) + MH \tag{2}$$

where $X = [x_1\, x_2\, y_1\, y_2\, z]$ is the state vector, $U = \left[i_{x_1}\, i_{x_2}\, i_{y_1}\, i_{y_2}\, i_z\right]$ is the control current vector, $H = \left[h_{x_1}\, h_{x_2}\, h_{y_1}\, h_{y_2}\, h_z\right]$, M, A and B are the mass, stiffness and control

gain matrices, respectively, and defined as follows: $M = \begin{bmatrix} 1 & 0 & 0 & 0 & 0 \\ 0 & 1 & 0 & 0 & 0 \\ 0 & 0 & 1 & 0 & 0 \\ 0 & 0 & 0 & 1 & 0 \\ 0 & 0 & 0 & 0 & 1 \end{bmatrix}$, $A = \begin{bmatrix} k_{rp}\beta_1 & 0 & 0 & 0 & 0 \\ 0 & k_{rp}\beta_3 & 0 & 0 & 0 \\ 0 & 0 & k_{rp}\beta_1 & 0 & 0 \\ 0 & 0 & 0 & k_{rp}\beta_3 & 0 \\ 0 & 0 & 0 & 0 & k_{ap}\beta_4 \end{bmatrix}$, $B = \begin{bmatrix} k_{ri}\beta_1 & 0 & 0 & 0 & 0 \\ 0 & k_{ri}\beta_3 & 0 & 0 & 0 \\ 0 & 0 & k_{ri}\beta_1 & 0 & 0 \\ 0 & 0 & 0 & k_{ri}\beta_3 & 0 \\ 0 & 0 & 0 & 0 & k_{ai}\beta_4 \end{bmatrix}$, where k_{rp}, k_{ap} and k_{ri}, k_{ai} are the position and current stiffness parameters, $\beta_1 = (1/m) + (a^2/J)$, $\beta_2 = (1/m) + (ab/J)$, $\beta_3 = (1/m) + (b^2/J)$, $\beta_4 = (1/m)$.In order to synthesize a type of robust controller for this class of system, the AMB model derived in Eq. (2) will be treated as uncertain system in which deterministic approach to classify the system will be used. By using this approach, the AMB model can be decomposed into its nominal and uncertain parts as shown below

$$\ddot{x}(t) = Ax(t) + Bu(t) + L(x,t) \tag{3}$$

where A and B are the nominal constant matrices; $L(x,t)$ is called the lumped uncertainty and defined as

$$L(x,t) = \Delta Ax(t) + \Delta Bu(t) + h(x,t) \tag{4}$$

Lemma 1 [12] *Let X and Y are real matrices of suitable dimension then, for any scalar $\mu > 0$, the following matrix inequality holds:*

$$X^T Y + Y^T X \leq \mu X^T X + \mu^{-1} Y^T Y.$$

3 Define a New Sliding as the Following

$$s(t) = \dot{x}(t) + \dot{x}(0) - \int_0^t [(A - BK)x + Ps(t)]dt \tag{5}$$

where $K \in R^{n\times n}$ and $P \in R^{n\times n}$ are the parameter matrices to be designed. The sliding mode $s(t)$ is expected to be converging to zero, i.e. $s(t) = 0$. Furthermore, the system behavior is restricted to the sliding mode, which can be described by Eq. (5) and $\dot{s}(t) = 0$ as follows

$$\begin{aligned} \ddot{x}(t) &= Ax(t) + Bu_{eq}(t) + L(x,t) \\ 0 &= Bu_{eq}(t) + L(x,t) + BKx \end{aligned} \tag{6}$$

where $u_{eq}(t)$ is the equivalent control input of the corresponding SMC when $s(t) = \dot{s}(t) = 0$. Combined with Eq. (6), it can be further derived that

$$u_{eq}(t) = -B^{-1}L(x,t) - Kx \tag{7}$$

Using Eq. (7), Eq. (3) becomes

$$\ddot{x}(t) = (A - BK)x(t) \tag{8}$$

By setting $z_1 = x$, $z_2 = \dot{x}$, the Eq. (8) can be rewritten as

$$\begin{bmatrix} \dot{z}_1 \\ \dot{z}_2 \end{bmatrix} = \begin{bmatrix} 0 & I \\ (A - BK) & 0 \end{bmatrix} \begin{bmatrix} z_1 \\ z_2 \end{bmatrix} \tag{9}$$

The first result of designing a new sliding surface is given as follows.

Theorem 1 *The state of the system (3) restricted to the single phase sliding surface s(t) = 0 (the Eq. (5)) is robust assymptotically stable if there exist matrix $K \in R^{n\times n}$, symmetric positive definite matrices $Q_1 \in R^{n\times n}$ and $Q_2 \in R^{n\times n}$satisfy the following LMI,*

$$\begin{bmatrix} -\hat{\varepsilon}^{-1}K^T B^T Q_2 Q_2 BK & Q_1 + A^T Q_2 \\ Q_1 + Q_2 A & -\hat{\varepsilon} I \end{bmatrix} \tag{10}$$

for some scalar $\hat{\varepsilon} > 0$.
The proof of theorem 1
Let us consider the following positive definition function:

$$V = \begin{bmatrix} z_1 \\ z_2 \end{bmatrix}^T \begin{bmatrix} Q_1 & 0 \\ 0 & Q_2 \end{bmatrix} \begin{bmatrix} z_1 \\ z_2 \end{bmatrix} \tag{11}$$

Then, taking the time derivative of V along the state trajectory of system (9), we can obtain that

$$\dot{V} = z_2^T Q_2 A z_1 - z_2^T Q_2 BK z_1 + z_1^T Q_1 z_2 + z_2^T Q_1 z_1 + z_1^T A^T Q_2 z_2 - z_1^T K^T B^T Q_2 z_2 \quad (12)$$

Applying Lemma 1 to Eq. (12), we can obtain

$$\dot{V} < \begin{bmatrix} z_1 \\ z_2 \end{bmatrix}^T \begin{bmatrix} -\hat{\varepsilon}^{-1} K^T B^T Q_2 Q_2 BK & Q_1 + A^T Q_2 \\ Q_1 + Q_2 A & -\hat{\varepsilon} I \end{bmatrix} \begin{bmatrix} z_1 \\ z_2 \end{bmatrix} \quad (13)$$

From Eqs. (10) and (13), we have

$$\dot{V} < 0 \quad (14)$$

Inequality (14) implies that if LMI (10) holds, then sliding motion (8) is asymptotically stable. □

4 A Continous Sliding Mode Controller Design

From the sliding manifold (5) it is easily to obtain that

$$r(t) = \dot{s}(t) = \ddot{x}(t) - (A - BK)x - Ps(t) \quad (15)$$

Then continuously differentiate of Eq. (15) with respect to time t,

$$\dot{r}(t) = \ddot{s}(t) = B\dot{u}(t) + \dot{L}(x,t) + BK\dot{x} - P\dot{s}(t) \quad (16)$$

Assumption 1 The disturbance $\dot{L}(x,t)$ in (16) is assumed to be bounded and satisfy the following condition:

$$\dot{L}(x,t) \leq \beta + \lambda \|x\| \quad (17)$$

where β and λ are unknown bounds which are not easily obtained due to the complicated structure of the uncertainties in the AMB control systems.

Theorem 2 *Let us consider the system* (3) *with the sliding surface given by Eq.* (5)*. The trajectory of the closed loop system* (3) *can be driven onto the sliding manifold* $r(t)$ *in finite time by using the controller given by* (18).

$$\begin{aligned} \dot{u}(t) &= -B^{-1}[BK\dot{x} - P\dot{s}(t) + (\hat{a}(t) + \hat{b}(t)\|x(t)\|)sign(r(t)) \\ &\quad + \mu r(t) + \eta sign(r(t))], \qquad if\ r(t) \neq 0 \\ &= 0 \qquad otherwise \end{aligned} \tag{18}$$

where $\dot{\hat{\beta}}(t) = q(-\hat{q}\hat{\beta}(t) + \|r(t)\|)$ *and* $\dot{\hat{\lambda}}(t) = \bar{q}(-\tilde{q}\hat{\lambda}(t) + \|r(t)\|\|x(t)\|)$.
The proof of the theorem 2
Let us define a Lyapunov function V_0 as follows

$$V_0(t) = \frac{1}{2}r^T(t)r(t) + \frac{\tilde{\beta}^2}{2q} + \frac{\tilde{\lambda}^2}{2\bar{q}} \tag{19}$$

where $\hat{\beta}(t) = \beta - \tilde{\beta}(t)$ and $\hat{\lambda}(t) = \lambda - \tilde{\lambda}(t)$ are the estimation errors of the adaptive gains. The time derivative of $V_0(t)$ is obtained as

$$\dot{V}_0(t) = r^T(t)\{B\dot{u}(t) + \dot{L}(x,t) + BK\dot{x} - P\dot{s}(t)\} - \frac{\tilde{\beta}\dot{\hat{\beta}}(t)}{q} - \frac{\tilde{\lambda}\dot{\hat{\lambda}}(t)}{\bar{q}} \tag{20}$$

According to Eqs. (18) and (20), we achieve

$$\dot{V}_0(t) \leq -\alpha\|r(t)\|^2 - \eta\|r(t)\| - \hat{q}(\frac{\beta}{2} - \hat{\beta}(t))^2 - \tilde{q}(\frac{\lambda}{2} - \hat{\lambda}(t))^2 + \hat{q}\frac{\beta^2}{4} + \tilde{q}\frac{\lambda^2}{4} \tag{21}$$

Then, from (21), it is easy to see that the uniform ultimate boundedness can be obtained by using the result and terminology in [11, 12].

5 Simulation Results

To prove the feasibility of the proposed second order sliding mode tecchniques, simulation models have been applied to test our method. The model of the 5 DOF AMB system is from paper [10] (Table 1).

In order to view the performance of the controller, the system is run at speed 2400 rpm as stated in [10]. By using the proposed continuous control scheme (18) to control the AMB system (1), the simulation results are shown by Figs. 2 and 6, respectively, where Fig. 1 shows rotor trajectories and Figs. 2, 3, 4, 5 and 6 express the displacements of the AMB system. Figures 2, 3, 4, 5 and 6 show that the rotor position of the AMB system is in the center and all the displacements appoach zero.

From Figs. 2, 3, 4, 5 and 6, comparing the performance of system given in [10], the proposed second order sliding mode control achieve good performance and can be applied to control the highly nonlinear and time-varying AMB system effectively.

Table 1 System parameters of five-DOF AMB system

Parameter	Description	Value	Unit
m	Mass of rotor	2.56478	kg
L	Length of rotor	0.505	m
τ	Diameter of rotor	0.0166	m
J	Transverse mass moments of inertia of rotor about X–Y axes	4.004×10^{-2}	kg m^2
J_z	Polar mass moment of inertia of rotor about Z-axis	6.565×10^{-4}	kg m^2
k_{ri}	Current stiffness of electromagnetic force of RAMB	80	N/A
k_{rp}	Position stiffness of electromagnetic force of RAMB	2.2×10^5	N/m
k_{ai}	Current stiffness of electromagnetic force of TAMB	40	N/A
k_{ap}	Position stiffness of electromagnetic force of TAMB	$3.6 \times s10^4$	N/m
a	Distance between CG and left RAMB	0.16	m
b	Distance between CG and right RAMB	0.19	m
c	Distance between CG and external disturbances	0.263	m
x_d, y_d	Nominal air gaps in X–Y axes of RAMB	0.4	mm
z_0	Nominal air gap in Z-axis of TAMB	0.5	mm

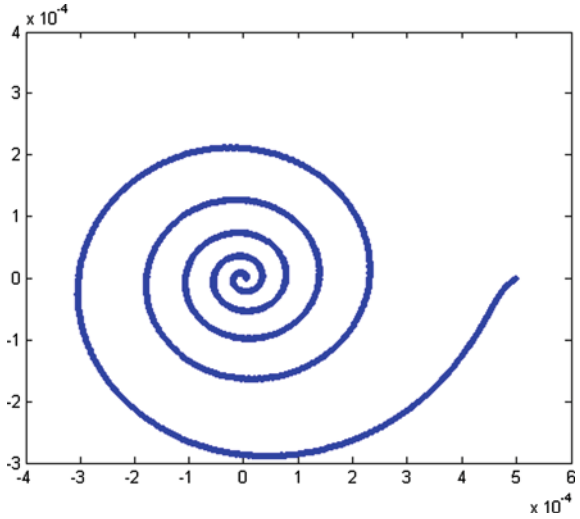

Fig. 2 Simulation results: rotor trajectories

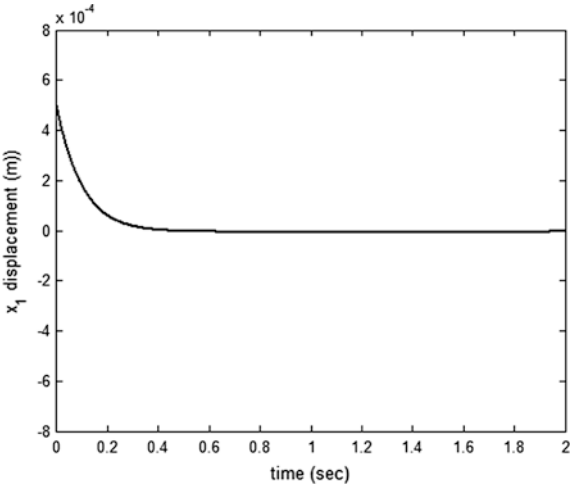

Fig. 3 Simulation results: displacement responses

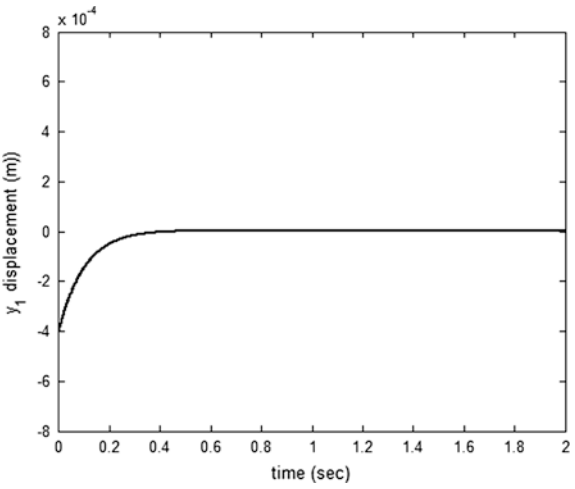

Fig. 4 Simulation results: displacement responses

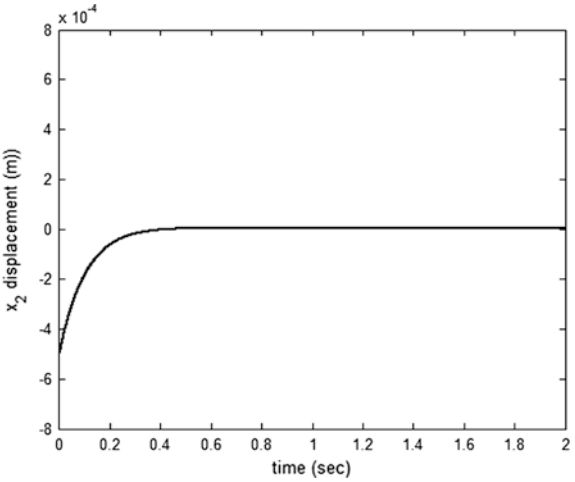

Fig. 5 Simulation results: displacement responses

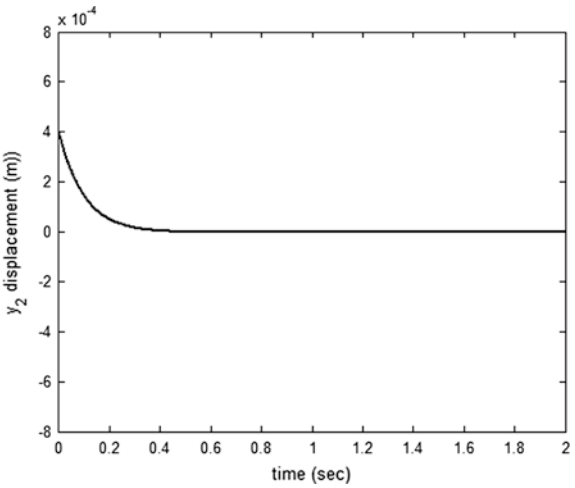

Fig. 6 Simulation results: displacement responses

6 Conclusion

For the five-DOF AMB system, a new second order sliding mode control strategy is developed in this paper. There is no need of the knowledge of upper bound on disturbances cuased by rotor mass imbalance and other disturbances. Besides the continous sliding mode control scheme is robust with respect to disturbances without chattering problems. The stability of the five-DOF AMB system is proved via Lyapunov method, which is also demonstrated by simulation results.

References

1. Choi HH (2007) LMI-based sliding surface design for integral sliding mode control of mismatched uncertain systems. IEEE Trans Autom Control 52(4):736–742
2. Choi HH (1998) An explicit formula of linear sliding surfaces for a class of uncertain dynamic systems with mismatched uncertainties. Automatica 34(8):1015–1020
3. Zak SH, Hui S (1993) On variable structure output feedback controllers for uncertain dynamic systems. IEEE Trans Autom Control 38(10):1509–1512
4. Kwan CM (1996) On variable structure output feedback controllers. IEEE Trans Autom Control 41(11):1691–1693
5. Tsai YW, Mai KH, Shyu KK (2006) Sliding mode control for unmatched uncertain systems with totally invariant property and exponential stability. J Chin Inst Eng 29(1):179–183
6. Mantz RJ, Battista HD, Puleston P (2001) A new approach to reaching mode of VSS using trajectory planning. Automatica 37(5):763–767
7. Chen H-C (2008) Optimal fuzzy pid controller design of an active magnetic bearing system based on adaptive genetic algorithms. In: Proceedings of the International Conference on Machine Learning and Cybernetics (ICMLC 08), vol 4, pp 2054–2060, Kunming, China, July 2008
8. Chen S-Y, Lin F-J (2011) Robust nonsingular terminal sliding-mode control for nonlinear magnetic bearing system. IEEE Trans Control Syst Technol 19(3):636–643
9. Xu S, Su D (2013) Research of magnetically suspended rotor control in control moment gyroscope based on fuzzy integral sliding mode method. In: International Conference on Electrical Machines and Systems (ICEMS), 2013, pp 1901–1906, 26–29 Oct 2013
10. Lin F-J, Chen S-Y, Huang M-S (2011) Intelligent double integral sliding-mode control for five-degree-of-freedom active magnetic bearing system. Control Theory Appl IET 5(11): 1287–1303
11. Corless MJ, Leitmann G (1981) Continuous state feedback guaranteeing uniform ultimate boundedness for uncertain dynamic systems. IEEE Trans Autom Control 26(5):1139–1144
12. Khargonekar PP, Petersen IR, Zhou K (1990) Robust stabilization of uncertain linear systems: quadratic stabilizability and H_∞ control theory. IEEE Trans Autom Control 35(2):356–361

Optimizing the CRI Method by Improving the Implication Step in MISO Fuzzy Expert Systems

Thoai Phu Vo

Abstract In conventional MISO fuzzy expert systems, the implication step requires the excessive operations and spatial complexity using compositional rule based inference (CRI). This paper proposes a novel method, sort compositional rule-based inference (SCRI) aimed at reducing both temporal and spatial complexity by changing the implication step. It shows the advanced SCRI in MISO fuzzy systems. We also propose a divide-and-conquer technique, called Quicksort, to verify the accuracy of SCRI deployment to easily outperform the CRI method.

Keywords CRI · SCRI · Quicksort · Temporal complexity · Spatial complexity

1 Introduction

The inference compositional rule (CRI) was first proposed by Zadeh [1] to solve the Fuzzy Modus Ponens (FMP) and Fuzzy Modus Tollens (FMT) models. Later Dubois and Prade [2] introduced two approaches to present the inference of a set of parallel rules for solving the local inference approach, known as IRI and the global inference approach, which is known as CRI. Many researches have been conducted on CRI. The first topic, "aggregation operator", [3] introducing two methods to deal with aggregation operator issues. The first infer-then aggregate (FITA), is known as IRI, and the first aggregate-then infer (FATI), is known as CRI. They attempted to find an operator for CRI and IRI aggregation. Assilian [4] used the max-min method. A "min" operator is selected as a conjunction in the rule premise and the

T.P. Vo (✉)
Faculty of Electrical and Electronics Engineering, Ton Duc Thang University,
No. 19 Nguyen Huu Tho Street, District 7, Ho Chi Minh City, Vietnam
e-mail: vophuthoai@tdt.edu.vn

V.H. Duy et al. (eds.), *AETA 2015: Recent Advances in Electrical Engineering and Related Sciences*, Lecture Notes in Electrical Engineering 371,
DOI 10.1007/978-3-319-27247-4_45

implication function while a "max" operator is used for aggregation. Dubois and Prade [5] used a "min" operator for aggregation in decision making. To reduce the computational time the authors [6, 7] replaced a MISO fuzzy rule with an equivalent collection of SISO rules with two kinds of aggregation operators.

The second topic involves fuzzy logic application in many fields using the CRI method. Mamdani [8] applied fuzzy logic in designing controllers for industrial plants. Reference [9] applied an adaptive fuzzy inference scheme to stock data and showed that the adaptive fuzzy rule based schemes provide clean decision to buy, hold and sale. Reference [10] proposed a fuzzy interval reasoning (FIR) and [11] introduced a fuzzy logic controller to serve web shopping. The third topic is new algorithms based on the CRI context. Reference [12] presented a new feedback method based on CRI (FBCRI) to improve the robustness of CRI fuzzy reasoning methods. Reference [13] introduced a CMI (compatibility modification inference), which is reduced by CRI. References [14–21] developed the Triple I method, based on CRI imperfections. Accordingly, [14] proposed the full implication Triple I method (a hybrid method based on implication and composition), designed as a supplement for the CRI method. Reference [15] proposed the triple I FMP and FMT for generalized α-triple I method. An investigation into a formalized Triple I method is reported in [16] where the authors tried to set a sound logical foundation for the unified TI algorithms.

We have shown three research topics to view that the improvement of CRI implication step has never done. SCRI is used to reduce the computational time and spatial complexity of CRI in this research.

The main contributions of this paper are as follows:

- This paper proposes a new method, sort compositional rule-based inference (SCRI) aimed at reducing the operation and spatial complexity of the implication step.
- This paper clearly showed the advantages of SCRI comparing to CRI in MISO fuzzy system.

2 Quicksort

This study adopted a method referred to as Quicksort, a divide-and-conquer method, which proceeds through four steps: (1) Arbitrarily select an element in the array (the pivot), (2) Divide the array into two sub-arrays of uneven size (the partition phase), (3) Sort the sub-arrays recursively, and (4) Position the pivot between the two sorted sub-arrays to obtain the final sorted array. The Quicksort performance depends on the pivot elements in the array, as outlined below.

2.1 The Worst Case

The worst case scenario occurs when the pivot element is the largest or smallest element in the array. In Fig. 1, the pivot element is the smallest element in the array. The total number $C(l)$ of comparisons performed by Quicksort in sorting an array of size l is calculated as

$$C(l) \approx l^2/2 \in O(l^2) \tag{1}$$

As shown in Fig. 2, the best case has the pivot element with the middle element in the array. The total number $C(l)$ can be approximately examined as

$$C(l) = l \cdot \log_2 l \tag{2}$$

2.2 The Average Case

The average case occurs when the pivot element is near the middle element in the array (random pivot). As shown in Fig. 3, random pivots are used to generate the average case in the recursion tree for Quicksort.

In summary, three cases are used to understand the calculation complexity for the Quicksort algorithm. Currently, there is an axiom could be decided.

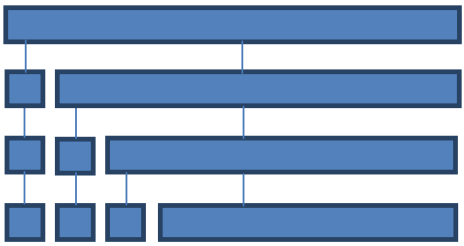

Fig. 1 The worst recursion tree case for Quicksort

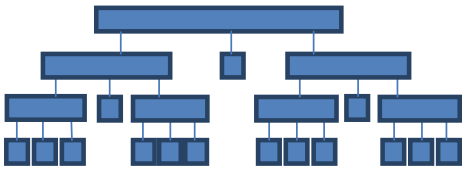

Fig. 2 The best recursion tree case for Quicksort

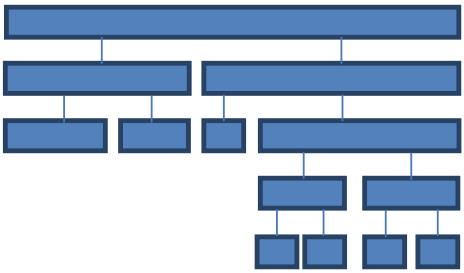

Fig. 3 The average recursion tree case for Quicksort

Theorem 1 *The average case in Quicksort has the expected run time of O (l·log$_2$l), with l as the number of elements in the array.*

3 MISO Single-Rule System

Suppose that one rule exist in the fuzzy expert system rule base as follows

$$\text{If } x_1 \text{ is } A_1 \text{ and } x_2 \text{ is } A_2 \ldots \text{ and } x_N \text{ is } A_N, \text{ then } y \text{ is } B \tag{3}$$

where N is the number of inputs,A_I is the I th input, B is the output. Assume that n_I is the number of elements in the input A_I with $I = 1, 2,\ldots, N$, and m indicates the number of elements in the output. A_I and B, are fuzzy sets defined in the universe of discourses V_I and W, respectively.

3.1 The Comparison of CRI and SCRI

- **CRI**

In order to achieve a meaningful inference result based on Zadeh's Compositional Rule of Inference (CRI) [2], for a given system observation A_I', there is a basic method adopted as important illustrations. This one is called CRI or FATI (First Aggregate Then Infer) [3]. In this method, for the given observation of A_I' with $I = 1, 2,\ldots, N$, the first CRI method step is the implication step, which includes two sub-steps. The first sub-step is defined as $(N + 1)$Dim cylindrical extension. Every input and output are extended to the size of $n_1 \times n_2 \times \cdots \times n_N \times m$. Calculating relation matrix is the second sub-step to be defined and it is written as

$$\underset{(v_1,v_2,\ldots,v_N,w)}{R} = \min\left(\underset{(v_1,v_2,\ldots,v_N,w)}{A_1\_ex}, \underset{(v_1,v_2,\ldots,v_N,w)}{A_2\_ex}, \ldots, \underset{(v_1,v_2,\ldots,v_N,w)}{A_N\_ex}, \underset{(v_1,v_2,\ldots,v_N,w)}{B\_ex}\right) \tag{4}$$

where $R : (n_1 \times n_2 \times \cdots \times n_N \times m) \in (v_1, v_2, \ldots, v_N, w) \rightarrow \{0, 1\}$ is the relation matrix, $A_1\_ex : (n_1 \times n_2 \times \cdots \times n_N \times m) \in (v_1, v_2, \ldots, v_N, w) \rightarrow \{0, 1\}$ is extended by $A_1 : n_1 \in v_1 \rightarrow \{0, 1\}$, $A_2\_ex : (n_1 \times n_2 \times \cdots \times n_N \times m) \in (v_1, v_2, \ldots, v_N, w) \rightarrow \{0, 1\}$ is extended by $A_2 : n_2 \in v_2 \rightarrow \{0, 1\}$,..., $A_N\_ex : n_1 \times n_2 \times \cdots \times n_N \times m \in (v_1, v_2, \ldots, v_N, w) \rightarrow \{0, 1\}$ is extended by $A_N : n_N \in v_N \rightarrow \{0, 1\}$ and $B\_ex : (n_1 \times n_2 \times \cdots \times n_N \times m) \in (v_1, v_2, \ldots, v_N, w) \rightarrow \{0, 1\}$ is extended by $B : m \in w \rightarrow \{0, 1\}$. Mamdani proposed to use min implication. Composition is the final CRI step and it is defined as

$$\begin{aligned} \underset{w \in W}{B'} &= \left(\min_{I=1}^{N} (A'_I\_ex) \right) \circ R \\ &= \sup_{v_1, v_2, \ldots, v_N} \left(\min \left(\min_{I=1}^{N} (\underset{(v_1, v_2, \ldots, v_N, w)}{A'_I\_ex}), \underset{(v_1, v_2, \ldots, v_N, w)}{R} \right) \right) \\ &= [b'_1 \, b'_2 \ldots b'_m] \end{aligned} \tag{5}$$

where $A'_I\_ex : (v_1, v_2, \ldots, v_N, w)$ is extended by $A'_I : v_I$ with $I = 1, 2, \ldots, N$, B' is the inference result which is calculated by compositing the min of all extended observation A'_I_ex and the relational matrix R, and $\circ$ represents the composition method. Zadeh proposed to use sup-min composition.

- **SCRI (Sort CRI)**

In this subsection, the SCRI method for a MISO single rule fuzzy system is introduced. It includes two steps. The first step is Implication which has two sub-steps. The first sub-step is Sorting program and the second sub-step is Getting relational matrix. Composition is the final step which is calculated as follows:

$$\begin{aligned} \underset{w \in W}{B'} &= \left(\min_{I=1}^{N} (A'_I\_ex) \right) \circ R \\ &= \sup_{v_1, v_2, \ldots, v_N} \left(\min \left(\min_{I=1}^{N} (\underset{(v_1, v_2, \ldots, v_N, w)}{A'_I\_ex}), \underset{(v_1, v_2, \ldots, v_N, w)}{R} \right) \right) \\ &= [b'_1 \, b'_2 \ldots b'_m] \end{aligned} \tag{6}$$

where $B' : w \in W$ is the inference result, which is induced by the composition of min all extended observations $A'_I\_ex : (v_1, v_2, \ldots, v_N, w)$ and the relational matrix $R : (v_1, v_2, \ldots, v_N, w)$. Moreover, let's discuss the SCRI method implication step for MISO single rule fuzzy system in detail. The SCRI implication has two sub steps. The matrix C is necessary for processing the first sorting program step, which can be expressed as

$$C = \begin{bmatrix} a_{1.1} & a_{1.2} & \ldots & a_{1.n_1} & a_{2.1} & a_{2.2} & \ldots & a_{2.n_2} & \ldots \\ 1.1 & 1.2 & \ldots & 1.n_1 & 2.1 & 2.2 & \ldots & 2.n_2 & \ldots \\ a_{N.1} & a_{N.2} & \ldots & a_{N.n_N} & b_1 & & b_2 & \ldots & b_m \\ N.1 & N.2 & \ldots & N.n_N & (N+1).1 & & (N+1).2 & \ldots & (N+1).m \end{bmatrix}_{2\times(n_1+n_2+\ldots+n_N+m)} \tag{7}$$

where the elements in the first row of Eq. (7) are a combination of $A_I, I = 1, 2, \ldots, N$ and B with $A_I = [a_{I.1}, a_{I.2}, \ldots, a_{I.n_I}]$, $B = [b_1, b_2, \ldots, b_m]$. In addition, the second row of Eq. (7) has two arguments for every cell in the first row. The first argument could be "1", "2",… "N" or "$N + 1$" depending on if the cell in the first row belongs to $A_1, A_2, \ldots, A_N$ or B. Moreover, the second argument for the second row in Eq. (7) could be $a_{I.1} = 1, a_{I.2} = 2, \ldots, a_{I.n_I} = n_I$ with I = 1, 2,…,N or $b_1 = 1, b_2 = 2, \ldots, b_m = m$, where $a_{I.1} \ldots a_{I.n_I}$ and $b_1 \ldots b_m$ belong to A_I and B, respectively.

Sort the matrix C based on the 1st row is the second step which is obtained as

$$C = \text{quicksort}(C, 1st\ row) \tag{8}$$

The Quick sort algorithm then sorts the C as

$$C = \begin{bmatrix} c_1 & c_2 & \ldots & c_{n_1+\ldots+n_N+m} \\ \ldots & \ldots & \ldots & x_{n_1+\ldots+n_N+m} y_{n_1+\ldots+n_N+m} \end{bmatrix}_{2\times(n_1+\ldots+n_N+m)} \tag{9}$$

where c_1 is min of the 1st row, $c_{n_1+\cdots+n_N+m}$ is max of the 1st row, $x_{n_1+\cdots+n_N+m}$ is 1, 2,…,N or $N + 1$ to indicate the value $c_{n_1+\cdots+n_N+m}$ belongs to $A_1, A_2, \ldots, A_N$ or B, respectively. $y_{n_1+\cdots+n_N+m}$ in Eq. (9) is used to specify the position of the value $c_{n_1+\cdots+n_N+m}$ in A_1, A_2, …, A_N or B depending if $x_{n_1+\cdots+n_N+m}$ is 1, 2, …, N or $N + 1$, respectively. The second sub-step is Getting relational matrix, which has $n_1 + \ldots + n_N + m$ steps. In the first step, with $R : n_1 \times n_2 \times \cdots \times n_N \times m \rightarrow \{0, 1\}$, consider the condition of $x_{n_1+\cdots+n_N+m}$ as

- If $x_{n_1+\cdots+n_N+m}$ = 1 then all values in the $y_{n_1+\cdots+n_N+m}$th plane of the dimension n_2,…,n_N, m in R are equal to $c_{n_1+\cdots+n_N+m}$
- If $x_{n_1+\cdots+n_N+m}$ = 2 then all values in the $y_{n_1+\cdots+n_N+m}$th plane of the dimension n_1, n_3,…, n_N, m in R are equal to $c_{n_1+\cdots+n_N+m}$
- If $x_{n_1+\cdots+n_N+m} = N$ then all values in the $y_{n_1+\cdots+n_N+m}$th plane of the dimension n_1, n_2,…, $n_{N\text{-}1}$, m in R are equal to $c_{n_1+\cdots+n_N+m}$
- If $x_{n_1+\cdots+n_N+m}$ = N + 1 then all values in the $y_{n_1+\cdots+n_N+m}$th plane of the dimension n_1, n_2, …, n_N in R are equal to $c_{n_1+\cdots+n_N+m}$

In the second step, consider the condition of $x_{n_1+\cdots+n_N+m-1}$, and keep on continuing until x_1.

3.2 CRI and SCRI Schemes

In the implication step the main CRI operation is "Calculating relational matrix" and the main SCRI operation is "Sorting program".

Time complexity
SCRI is an improvement method from correcting the CRI implication step. Following Theorem 1, the time complexity of an array with $(n_1 + n_2 + \cdots + n_N + m)$ elements is $O((n_1 + n_2 + \cdots + n_N + m)\log_2(n_1 + n_2 + \cdots + n_N + m))$. With MISO single rule fuzzy system, basing on Eq. (8), the time complexity of the implication step of SCRI method is denoted as

$$O((n_1 + n_2 + \cdots + n_N + m)\log_2(n_1 + n_2 + \cdots + n_N + m)) \tag{10}$$

Based on Eq. (4), the time complexity of the implication step for CRI method can be determined as

$$O(N \times n_1 \times n_2 \times \cdots \times n_N \times m) \tag{11}$$

All input dimensions and the output dimension are equal in Fig. 4. The Red line (solid line for CRI) shows the relation of x (dimension of inputs and output) and y (operations), and the Blue line (dash line for SCRI) shows the relation of x (dimension of inputs and output) and y (operations), respectively. Moreover, the Green line (vertical solid line) shows a reference line with the input dimension as 40 and the output dimension as 40. The red point (the point on the solid line) with input dimensions = 40, output dimension = 40, number of inputs = 2, shows $CRI = 128,000$ operations. The blue point (the point on the dash line) with input

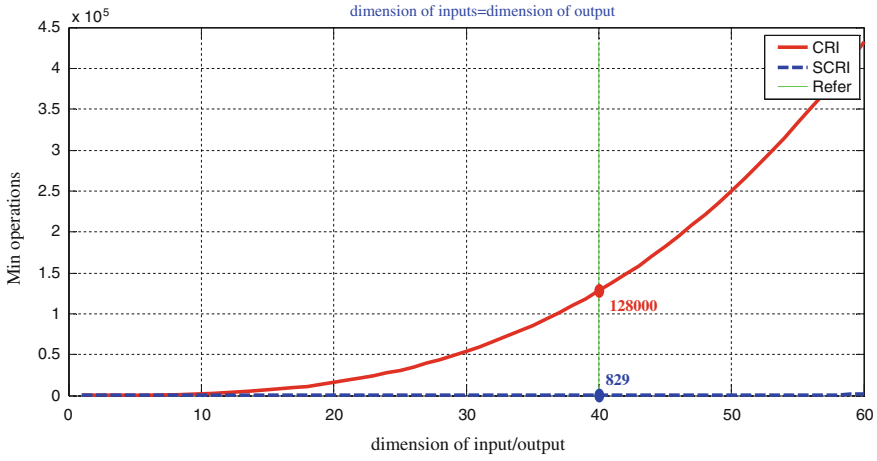

Fig. 4 CRI and SCRI implication step time complexity for MISO single rule systems

dimensions = 40, output dimension = 40, number of input = 2, shows $SCRI = 829$ operations. It is clear to see that the CRI method time complexity is greater than the SCRI method time complexity.

Space complexity
With MISO single rule fuzzy system, basing on Eq. (8), the space complexity of the implication step of SCRI method is denoted as

$$O(n_1 \times n_2 \times \cdots \times n_N \times m) \tag{12}$$

Based on Eq. (4), the space complexity of the implication step for CRI method can be determined as

$$O((N+1) \times n_1 \times n_2 \times \cdots \times n_N \times m) \tag{13}$$

4 Conclusion

The SCRI schemes for improving CRI operation performance in the fuzzy control theoretical approach are proposed in this article. The previous method was proven to reduce the time and space complexity for fuzzy expert systems by improving the most important step (implication). It was shown that the time consuming, e.g. the MISO N-input (n_I-element of the Ith input with $I = 1, 2,\ldots,N$, m-element output) implication step needs an operation of $O(N \times n_1 \times n_2 \times \cdots \times n_N \times m)$, in the traditional method with Compositional Rule based Inference (CRI) will be significantly decreased as $O((n_1 + n_2 + \cdots + n_N + m)\log_2(n_1 + n_2 + \cdots + n_N + m))$. This paper generated better SCRI (Sort CRI) performance in which it can replace the traditional CRI.

References

1. Zadeh LA (1973) Outline of a new approach to the analysis of complex systems and decision Processes. IEEE Trans Syst Man Cybern, SMC-3
2. Dubois D, Prade H (1991) Fuzzy sets in approximate reasoning, part1: inference with possibility distributions. Fuzzy Sets Syst 40
3. Türken IB, Tian Y (1992) How to select combination operators for fuzzy expert systems using CRI. In: NAFIP'92, Puerto Vallarta, Mexico, I, pp 29–38
4. Assilian S (1974) Aritificial intelligence in the control of real dynamic systems. PhD Thesis, Queen Mary College, University of London
5. Dubois D (2010) The role of fuzzy sets in decision sciences: old techniques and new directions. In: EUROFUSE Workshop Preference Modelling and Decision Analysis, Pamplona
6. Lazzerini B, Marcelloni F (2000) Reducing computation overhead in MISO fuzzy systems. Fuzzy Sets Syst 113:485–496
7. Demirli K, Turksen IB (1992) Rule break up with compositional rule of inference. IEEE

8. Mamdani EH (1977) Application of fuzzy logic to approximate reasoning using linguistic synthesis. IEEE Trans Comput C-26(12)
9. Shahjalal M, Sultana A, Mitra NK, Khodadad Khan AFM (2013) Compositional rule of inference and adaptive fuzzy rule based scheme with applications. Ann Pure Appl Math 3(2):155–168
10. Liu F, Geng H, Zhang Y (2005) Interactive fuzzy interval reasoning for smart web shopping. Appl Soft Comput 5:433–439
11. Iancu I (2012) A Mamdani type fuzzy logic controller. In: Fuzzy Logic - Controls, Concepts, Theories and Applications, ISBN: 978–953-51-0396-7, InTech
12. Zheng Z, Wu S, Liu W, Cai KY (2011) A feedback based CRI approach to fuzzy reasoning. Appl Soft Comput 11(1):1241–1255
13. Villar J (1996) Conditions for equivalence betwen the Compositional rule of infernce and compatibility modification inference. Fuzzy Syst 1:444–449
14. Wang G (1999) On the logic foundation of fuzzy reasoning. Inf Sci 117:47–88
15. Song S, Feng C, Lee ES (2002) Triple I method of fuzzy reasoning. Comput Math Appl 44:1567–1579
16. Pei D (2012) Formalization of implication based fuzzy reasoning method. Int J Approximate Reasoning 53:837–846
17. Wang G (2014) On robustness of the full implication triple I inference method with respect to finer measurements. Int J Approximate Reasoning 55(3)
18. Tang Y, Yang X (2013) Symetric implicational method of fuzzy reasoning. Int J Approximate Reasoning 54:1034–1048
19. Luo M, Yao N (2013) Triple I algorithms based on Schweizer-Sklar operators in fuzzy reasoning. Int J Approximate Reasoning 54:640–652
20. Pei D (2008) Unified full implication algorithms of fuzzy reasoning. Inf Sci 178:520–530
21. Yan L, Mucong Z (2014) The dual Triple I method of FMT and IFMT. Math Prob Eng 2014 (507401)

Model Predictive Control Nonlinear System of Active Magnetic Bearings for a Flywheel Energy Storage System

Yao-Wen Tsai, Phan Van Duc, Viet Anh Duong, Nguyen Cong Trang and Trung Dung Chu

Abstract This paper proposes the model predictive control (MPC) approach in order to control the nonlinear multiple-input-multiple-output (MIMO) system. A nonlinear model of a five degree of freedom (DOF) flywheel energy storage system (FESS) obtained using Lagrange's equation is proposed. The so-called MPC technique is proposed not only to out-perform the proportional integral differential (PID) control but also to show some advantages. Firstly, the MPC technique optimally solves the energy control problem in the FESS systems. Secondly, in order to cope with hard constraints on controls and states, its ability is showed explicitly in this study. A numerical example has been obtained and compared with the conventional PID control.

Keywords Flywheel energy storage system (FESS) · Active magnetic bearing (AMB) · Model predictive control (MPC) · Nonlinear system

Y.-W. Tsai (✉) · P. Van Duc · V.A. Duong · N.C. Trang · T.D. Chu
Department of Mechanical and Automation Engineering, Da-Yeh University,
No. 168, University Road, Changhua 51591, Taiwan, Republic of China
e-mail: ywtsai@mail.dyu.edu.tw; ywtsai.tw@gmail.com

P. Van Duc
e-mail: chuduc095@yahoo.com

V.A. Duong
e-mail: anhdv.ihere@gmail.com

N.C. Trang
e-mail: congtrang0810@gmail.com

T.D. Chu
e-mail: d0311801@mail.dyu.edu.tw

V.H. Duy et al. (eds.), *AETA 2015: Recent Advances in Electrical Engineering and Related Sciences*, Lecture Notes in Electrical Engineering 371,
DOI 10.1007/978-3-319-27247-4_46

1 Introduction

In recent decades, many conventional power backup or energy storage systems have been developed due to their cost-effectiveness, long life cycle, high efficiency, absence of lubrication and mechanical maintenance, wider range of work temperature and environment friendly energy storage system. The flywheel energy storage system has emerged as a viable option, as it encompasses these aforementioned properties [1–5].

Generally speaking, active magnetic bearings (AMB) [2, 3] are a viable part of the FESS because they enable noncontact operation and can guarantee a good performance of the system at high speed without lubrication. However, modeling and control of AMBs are challenging as AMBs have unstable behavior and are nonlinear mechatronic systems. Most of the control design approaches for AMBs are based on the linearized model about a nominal operating point. The behavior of the linear model is acceptable when the operating point is close enough to the linearized point. In order to ensure the system's performance in a wide range of working conditions, a nonlinear model should be considered in controller design.

In modern industrial engineering, model predictive control is probably the most popular strategy within the past two decades. MPC is an advanced control technique that uses a dynamic model of the system to make predictions of what the control trajectory of a system will be in order to reach a set-point value. The performance of the controller is also improved by using a cost function to reduce the error of the system, and updating the states of the system during operation by using an estimator in the design of the controller. Also, as MPC was developed in the industry process where slower processes with larger time constants are usually encountered, another challenge will be to implement real-time control with MPC on the FESS where fast time-constants are required for optimal control [7–9].

As mentioned previously, in this paper, a five mechanical degree of freedom (DOF) is introduced [1]. A nonlinear electromechanical model of FESS was derived from Lagrange's equation by using symbolic computation package such as Maple®. The MPC method is presented and an optimal control strategy is applied to regulate the nonlinear multi-input-multi-output system. Main contributions of this paper are given as follows.

- The non-linear model structure machine functions as a FESS, which can replace the conventional battery without maintenance and environment degradation.
- In order to save the energy of AMBs of FESS, it is better to use the low-bias current in the non-linear control system.
- It can cope with hard constraints under controls and states.
- Finally, numerical simulation results are presented to demonstrate the dynamic behavior of the system, and the performance of MPC for this machine is compared with classical PID control. Obtained results point out the validity and potentials of the MPC in the control of real-time, high-performance, and complex systems such as flywheel energy storage system.

2 The Proposed Flywheel System

The FESS is also illustrated in Fig. 1 the layout of the axial and radial AMBs. This figure shows the axial AMBs controlling the position of the rotor in the z-axis, and the upper and lower radial AMBs controlling the position and force generated of the rotor in the x- and y-axes. The permanent magnet synchronous machine is used to rotate the flywheel rotor about the z-axis, which may cause a complex rotor dynamic problem in the x- and y-axes as a disturbance, e.g. a rotor unbalance, may lead to limit cycles, the amplification of external excitations, or even the instability of the system [11].

Each radial bearing consists of four electromagnets (of the same parameters) controlled separately which is constructed around the circumference of hollow center. Radial position sensors are integrated into the bearings (collocated). The radial and axial motions can be controlled independently, or decoupled. Because of the translations and rotations about the x and y-axes, there exists a cross coupling between the control of the radial bearings, a and b. However, this coupling is low for slow rotation because of small gyroscopic coupling [10, 11].

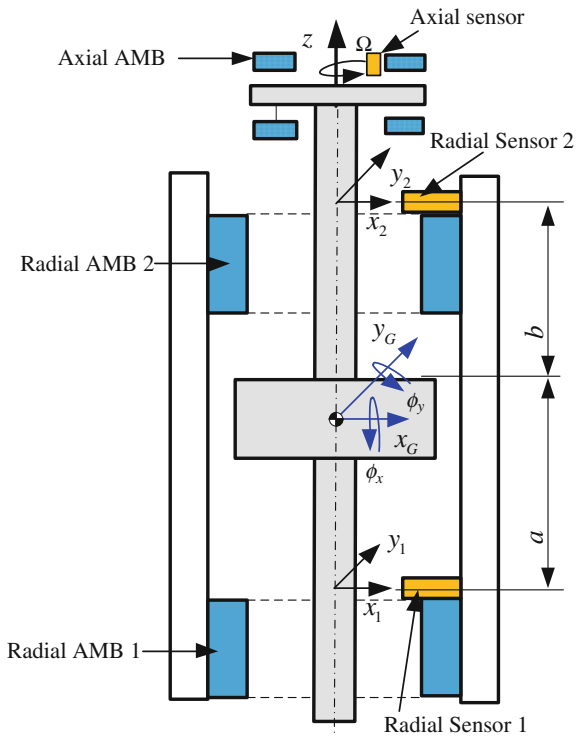

Fig. 1 Flywheel energy storage system

3 Mathematical Analysis

3.1 Electromechanical Model

In this section, a model of AMB with a single mechanical degree of freedom (Fig. 2) is introduced to illustrate the Lagrange's equation approach for an electromechanical system.

$$Ke_M = \frac{1}{2}m\dot{x}^2, \quad Ke_E = \frac{1}{2}L_{x+}\dot{q}_{x+}^2 + \frac{1}{2}L_{x-}\dot{q}_{x-}^2, \quad V_M = 0, \quad V_E = 0. \tag{1}$$

Energy contributions of this system are showed in Eq. (1), where Ke_M, V_M are the kinetic and potential energy of mechanical part. Ke_E and V_E are the kinetic and potential energy of electrical part. The electrical charge in each coil, q_{x+}, q_{x-} is generalized coordinates of electrical part. x is the displacement of the rotor. L_{x+}, L_{x-} are coil inductances.

The relation of coil inductance with air gap T_R and the coil characterizing parameters is described in Eq. (2).

$$L_{x+} = \mu_0 \frac{N_R^2 A_R}{2(T_R - x)}, \quad L_{x-} = \mu_0 \frac{N_R^2 A_R}{2(T_R + x)}. \tag{2}$$

The dissipation of copper losses in the coils is ($i = \dot{q}$)

$$P = \frac{1}{2}R_R\dot{q}_{x+}^2 + \frac{1}{2}R_R\dot{q}_{x-}^2 \tag{3}$$

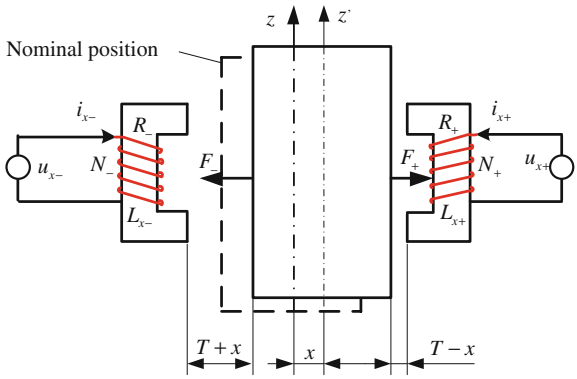

Fig. 2 Single DOF AMB model

The dynamic equation of single DOF AMB model can be derived from Lagrange's equation

$$\frac{d}{dt}\left(\frac{\partial L}{\partial \dot{\mathbf{s}}}\right) - \frac{\partial L}{\partial \mathbf{s}} + \frac{\partial P}{\partial \dot{\mathbf{s}}} = \mathbf{Q} \tag{4}$$

where $\mathbf{s}$ is the generalized coordinate vector

$$\mathbf{s} = [q_{x+}, q_{x-}, x]^T, \tag{5}$$

$\mathbf{Q}$ is a vector of generalized external forces (control input voltage and mechanical force)

$$\mathbf{Q} = [u_{x+}, u_{x-}, F_x]^T, \tag{6}$$

and L is the Lagrangian function

$$L = Ke_M + Ke_E - V_M - V_E \tag{7}$$

3.2 Rotor Dynamics

Consider a rigid rotor depicted in Fig. 1 with assumptions, there is no axial flexural and rotation angle should be small (except for spinning rotation Ω).

The displacements at radial AMB1 and AMB2 are described in the mechanical generalized coordinates $\mathbf{s}_{MA}$

$$\mathbf{s}_{MA} = [x_1, x_2, y_1, y_2, z]^T \tag{8}$$

However, for more convenient when investigating the influence of gyroscopic effect and unbalance effect on the rotating rotor, another generalized coordinates ($\mathbf{s}_{MG}$) fix on the rotor's center of gravity is used. The relationship between $\mathbf{s}_{MA}$ (the point of AMB1 and AMB2) and $\mathbf{s}_{MG}$ (the point of center) can be written as

$$\mathbf{s}_{MA} = \mathbf{C}\mathbf{s}_{MG} = \begin{bmatrix} 1 & -a & 0 & 0 & 0 \\ 1 & b & 0 & 0 & 0 \\ 0 & 0 & 1 & a & 0 \\ 0 & 0 & 1 & -b & 0 \\ 0 & 0 & 0 & 0 & 1 \end{bmatrix} \begin{bmatrix} x_G \\ \phi_y \\ y_G \\ \phi_x \\ z_G \end{bmatrix} \tag{9}$$

The equations of motion are obtained by the introduced approach. The generalized coordinates for electromechanical model are

$$\mathbf{s}_{state} = \begin{bmatrix} \mathbf{s}_E \\ \mathbf{s}_{MA} \end{bmatrix} \tag{10}$$

where $\mathbf{s}_E$ is the vector of electrical charges in the coils, this leads to fully couple radial and axial state-space model with ten coils inputs (eight coils of radial AMBs and two coils of axial AMB). $\mathbf{s}_E$ can be written as

$$\mathbf{s}_E = \left[q_{x_1+}, q_{x_1-}, q_{x_2+}, q_{x_2-}, q_{y_1+}, q_{y_1-}, q_{y_2+}, q_{y_2-}, q_{z+}, q_{z-}\right]^T \tag{11}$$

$$\mathbf{s}_{state} = \left[q_{x_1+}, q_{x_1-}, q_{x_2+}, q_{x_2-}, q_{y_1+}, q_{y_1-}, q_{y_2+}, q_{y_2-}, q_{z+}, q_{z-}, x_1, x_2, y_1, y_2, z\right]^T \tag{12}$$

Assume that the rotor is rotating at an initial angular velocity Ω. When the influence of gyroscopic effect and unbalance mass effect are taken into account, the translational and rotational kinetic energy of the rotor in $\mathbf{s}_{MG}$ are [10, 11]:

$$\begin{aligned} Ke_{M\_Trans} &= \frac{1}{2}m\left\{\left(\dot{x}_G^2 + \dot{y}_G^2 + \dot{z}_G^2 + \varepsilon^2\Omega^2\right) + 2\varepsilon\Omega[-\dot{x}_G\sin(\Omega t+\alpha) + \dot{y}_G\cos(\Omega t+\alpha)]\right\}, \\ Ke_{M\_Rot} &= \frac{1}{2}\left\{J_t\left(\dot{\phi}_x^2 + \dot{\phi}_y^2 + \chi^2\Omega^2\right) + J_p\left(\Omega^2 + 2\Omega\dot{\phi}_x\phi_y\right) + 2\Omega\chi(J_p - J_t)\left[\dot{\phi}_x\cos\theta + \dot{\phi}_y\sin\theta\right]\right\}, \end{aligned} \tag{13}$$

where unbalance of a phase angle α, the center of gravity owing to the eccentricity angular error χ, displacement of eccentricity ε and $m\varepsilon$ is the eccentric mass. The kinetic energy of mechanical part Ke_M can be transformed to $\mathbf{s}_{MA}$ by using Eq. (9). The other terms of energy contribution in the system can be derived by the approach proposed in single DOF model and can be described as (L_i *and* R_i *are the same for 10 coils*)

$$Ke_E = \sum_{i=1}^{10}\frac{1}{2}L_i\dot{q}_i^2,\ V_M = mgz,\ V_E = 0,\ P = \sum_{i=1}^{10}\frac{1}{2}R_i\dot{q}_i^2, \tag{14}$$

where i is the ith row of vector $\mathbf{s}_E$. The generalized nonconservative forces are

$$\mathbf{u} = [u_{x_1+}, u_{x_1-}-, u_{x_2+}, u_{x_2-}, u_{y_1+}, u_{y_1-}, u_{y_2+}, u_{y_2-}, u_{z+}, u_{z-}, F_{x1}, 0, F_{x2}, 0, F_{y1}, 0, F_{y2}, 0, F_z, 0]^T \tag{15}$$

Applied the Eqs. (4) and (7),

$$\frac{d}{dt}\left(\frac{\partial L}{\partial \dot{\mathbf{s}}}\right) - \frac{\partial L}{\partial \mathbf{s}} + \frac{\partial P}{\partial \dot{\mathbf{s}}} = \mathbf{u} \tag{16}$$

$$\begin{aligned} L &= Ke_M + Ke_E - V_M - V_E \\ &= \frac{1}{2}m\left(\dot{x}_G^2 + \dot{y}_G^2 + \dot{z}_G^2 + \varepsilon^2\Omega^2\right) + m\varepsilon\Omega[-\dot{x}_G \sin(\Omega t) + \dot{y}_G \cos(\Omega t)], \\ &\quad + \frac{1}{2}J_t\left(\dot{\phi}_x^2 + \dot{\phi}_y^2\right) + \frac{1}{2}J_p\left(\Omega^2 + 2\Omega\dot{\phi}_x\phi_y\right) + \sum_{i=1}^{10}\frac{1}{2}L_i\dot{q}_i^2 - mgz - 0 \end{aligned} \tag{17}$$

The equations of motion of the system can be derived in a standard form of differential equation

$$\mathbf{M}\dot{\mathbf{s}}_{state} = \mathbf{u}, \text{ with } \dot{\mathbf{s}}_{state} = \frac{d(\mathbf{s}_{state})}{dt} \tag{18}$$

where $\mathbf{M} \in R^{20\times 20}$ is the inertial matrix and $\mathbf{u} \in R^{20\times 1}$ is the vector of nonlinear function. The Eq. (18) have nonlinear relationships with the control currents and displacements of rotor. These equations are solved in MATLAB/Simulink by C MEX S-function block and computation package Maple®.

4 Controller Design

In this study, a five mechanical degree of freedom of the FESS is controlled via MPC approach. As MPC is a model-base scheme, it requires an integrated model to predict system's behavior (as showed in Fig. 1). In the previous section, a dynamic model of FESS has already obtained. This model can describe the nonlinear relationships of force-current and force-distance more accurate. However, this model is too complicated to use as a prediction model. That leads to the demand of a simpler linear model, which will be discussed in the foregoing section.

Model predictive control

MPC uses a horizontal receding strategy, which can be explained using Fig. 3. An internal model is used to predict how the plant will react, starting at the current time k, over a discretized prediction interval. The letter N_p is used to denote the number of discrete steps in the interval. The control history solved for by MPC is a sequence of vector values: the number of vectors in this sequence is represented by N_u. Once the optimal control has been chosen, the first N time steps of the solution are applied to the plant and the other are discarded. After these N time steps have passed, the cycle of forming predicted behaviors and computing the control history is repeated.

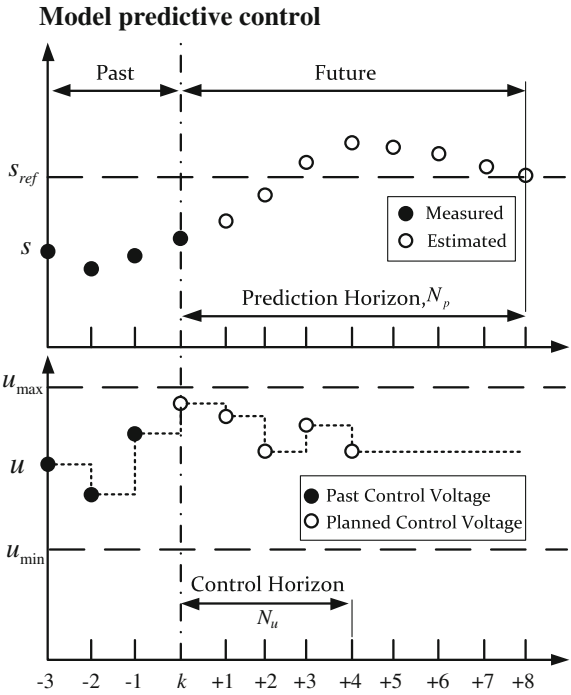

Fig. 3 Interpretation of MPC

MPC uses a model of the plant to predict future behaviors. The type of model being considered in this section is discrete and linear time-invariant (LTI) with the state-space form given by

$$\begin{aligned} \mathbf{s}_{state}(k+1) &= \mathbf{A}\boldsymbol{s}_{state}(k) + \mathbf{B}\mathbf{u}(k) \\ \mathbf{y}(k) &= \mathbf{C}\mathbf{s}_{state}(k) \end{aligned} \tag{19}$$

Equation (19), used to generate a predicted output trajectory of the plant as a function of known parameters and a control history.

Equation (19) is a discrete and linear time-invariant with state space form. This model is obtained from Eq. (18) with MATLAB command "c2d".

The considering of constrained MPC computes leads to an optimal control sequence with respect to the following cost function.

$$J(k) = \sum_{i=1}^{N_p} \left\| \mathbf{s}_{ref}(k+i) - \hat{\mathbf{s}}_{state}(k+i) \right\|^2_{\mathbf{Q}(i)} + \sum_{i=0}^{N_u-1} \left\| \hat{\mathbf{u}}(k+i) \right\|^2_{\mathbf{R}(i)} \tag{20}$$

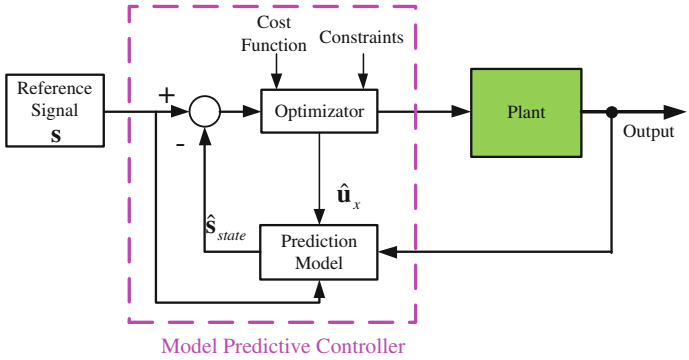

Fig. 4 Structure diagram of MPC

and subject to

$$\mathbf{u}_{\min} \leq \hat{\mathbf{u}}(k+i) \leq \mathbf{u}_{\max} \tag{21}$$

where $\mathbf{s}_{ref}$ is the reference signal, $\mathbf{u}_{\min}, \mathbf{u}_{\max}$ is the lower and upper limitation of input torque and $\hat{\mathbf{u}}(k+i)$ is the predicted control input vector, N_p is the prediction, N_u control horizon, and $Q(i)$ and $R(i)$ are the weighting matrices for tracking errors and control inputs respectively ($N_u \leq N_p$). The numerical results are given in this study, $Q(i)$ and $R(i)$ are assumed to be constant.

The general structure of MPC is show in Fig. 3. This figure indicates the two main parts of the MPC strategy, such as the prediction model and the optimization. The optimization is used to determine the optimal control trajectory by minimising the objective function.

Figure 4 shows an attractive feature of MPC is that it can handle general constrained nonlinear systems with multiple inputs and outputs in a unified and clear manner, however, the PID control can not.

5 Simulation

The physical parameters of this FESS model for simulation are given follow tables (Table 1).

In this section, dynamic behaviors of the system and control performance are discussed in simulation results. Initial conditions with $\Omega = 1500(\text{rpm})$, $[x_1(0), x_2(0), y_1(0), y_2(0), z(0)]^T = \left[1e^{-5}, 0, 0, 0, 5e^{-4}\right]^T(\text{m})$

To demonstrate the rotor dynamics clearly, a low bias current $i_0 = 0.1$ A is used. The rotor is rotating at an initial speed $\Omega = 15000$ rpm, the controller's parameters, $N_p = 50$, $N_u = 20$, Q(i) = eye(15), R(i) = $1e^{-6} * eye(15)$, $T_s = 0.001$ s and the

Table 1 Axial and radial magnetic bearing parameters

Parameters	Symbol	Value	Unit
Mass	m	98	Kg
Polar moment of inertial	J_p	1.25	Kgm^2
Transversal moment of inertial	J_t	1.38	Kgm^2
Distance from COG to radial bearing 1	a	0.138	m
Distance from COG to radial bearing 2	b	0.138	m

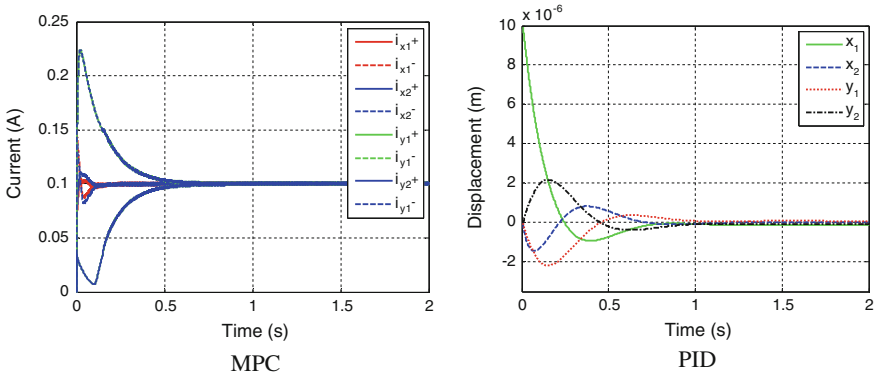

Fig. 5 Displacements of the rotor

initial displacement $x_1(0) = 0.01$ mm. Under the influence of gyroscopic effect, the control force in x_1 direction will effect to the others. After about 1 s, the rotor's displacements will be kept at the nominal value (Fig. 5).

6 Conclusion

In this study, the multiple-input-multiple-output nonlinear system model, the so-called are active magnetic bearings for a five DOF of FESS, is obtained. The simulation results demonstrated that MPC technique is a very strong and suitable for designing controllers with modern high-performance, complex and drive systems. The stability, sensitivity and robustness problem of the MPC approach are superior to PID control. Particularly, at the very high speed of the flywheel, MPC technique has shown that the addition of the contractive constraint to the optimal control problem can guarantee the rotor stays close to the desired displacement even when disturbance and dynamic effect of rotating are taken into considering.

Acknowledgments The authors would like to thank the financial support provided by the National Science Council in Taiwan (NSC 102-2632-E-212-001-MY3).

We would like to acknowledge professor Chih-Keng Chen at Dayeh University for his consultant of dynamic modeling.

References

1. Chen CK, Chu TD (2014) Nonlinear modeling and control of active magnetic bearings for a flywheel energy storage system. IEEE Int Conf Intell Hum Mach Syst Cybern 1(6):284–287
2. Mystkowski A (2012) Energy saving robust control of active magnetic bearing in flywheel. ACTA mechanica et automatica 6(3):72–76
3. Mystkowski A, Rowinski A (2011) Contruction and control of AMBs high speed flywheel. Arch Mech Eng 8(1):79–89
4. Zhu KY, Xiao Y, Rajendra AU (2009) Optimal control of the magnetic bearings for a flywheel energy storage system. Mechatronics 19:1221–1235
5. Sivrioglu S, Nonami K (2000) Active permanent magnet support for a superconducting magnetic-bearing flywheel rotor. IEEE Trans Appl Supercond 10(4):1673–1677
6. Cortés P, Kazmierkowski MP, Kennel RM, Quevedo DE, Rodríguez J (2008) Predictive control in power electronics and drives. IEEE Trans Industr Electron 55(12):4312–4324
7. Model-based predictive control for a compact and efficient flywheel energy storage system with magnetically assisted bearings. In: 35th Annual IEEE Power Electronics Specialists Conference, pp. 3573–3579 (2004)
8. Maciejowski JM (2002) Predictive control with constraints. Pearson Education Limited, Essex
9. Wang L (2009) Model predictive control system design and implementation using MATLAB, Melbourne. Springer, London
10. Genta G (2004) Dynamics of rotating systems. Springer, New York
11. Schweitzer G, Maslen EH (2009) Magnetic bearings, theory, design, and application to rotating machinery. Springer, Berlin

Observer-Based Output Feedback Control Design for Mismatched Uncertain Systems

Van Van Huynh and Minh Hoang Quang Tran

Abstract In this paper, the observer-based output feedback control is developed for a class of mismatched uncertain systems with both mismatched in the state matrix and in the input matrix. The objective is to reduce the conservatism and enhance the robustness of the control systems by using only the estimation error of output variables. The control and observer gains are given from linear matrix inequalities feasible solution. A numerical example is used to demonstrate the efficacy of the proposed method.

Keywords Linear matrix inequalities (LMI) · Mismatched uncertain systems · Observer-based output feedback control · Output feedback control

1 Introduction

General speaking, the aim of the observer is to estimate the unmeasurment state variables of a system, which has important applications in many aspects such as realization of feedback control, system supervision, gas-fired furnace system, and fault diagnosis. The significant advantages of the observer-based control is its insensitivity to parameter variations, fast dynamic response and the output observer error to converge to zero in finite time, while the observer states converge asymptotically to the system states.

Based on these advantages, the observer-based control is considered by many researchers in the recent years. In [1], the linear matrix inequalitty (LMI) approach is used to find the control and observer gains for the observer-based control of

V.V. Huynh · M.H.Q. Tran (✉)
Faculty of Electrical and Electronics Engineering, Ton Duc Thang University,
No. 19 Nguyen Huu Tho Street, District 7, Ho Chi Minh City, Vietnam
e-mail: tranhoangquangminh@tdt.edu.vn

V.V. Huynh
e-mail: huynhvanvan@tdt.edu.vn

V.H. Duy et al. (eds.), *AETA 2015: Recent Advances in Electrical Engineering and Related Sciences*, Lecture Notes in Electrical Engineering 371,
DOI 10.1007/978-3-319-27247-4_47

uncertain system. Designing the observer based feedback control was designed using the LMI optimization approach for a class of uncertain systems [2]. Additionally, the robust analysis of observer without disturbance input and the H_∞ control including disturbance inputs were used to determine the control and observer gains. In [3], adopted the Lyapunov stability theory to prove that the observer is exponentially stabilizabled. Moreover, the LMI approach is used in the design of the robust observer based control for a class of uncertain systems. In [4], used a constrained Lyapunov function to estimate the system state variables of the asymptotic observer for the matched and mismatched uncertainties system. In [5], in their research, designed the sliding mode observer using LMI approach to find the gains of the observer for a class of uncertain systems. The purpose of this paper is to exploit the degrees of freedom available in this design. In [6], used the LMI approach to design and find the gain matrices of the sliding mode observer for a class of multivariable uncertain systems. In addition to this, they adopted the necessary and sufficient condition of the LMI for the existence of the observer to ensure a stable sliding motion. In [7], using the necessary and sufficient conditions on the stability matrix, replaced the eigenvalues and eigenvectors approach of linear stability matrix, ensuring asymptotic stability of the observer for the class of Lipschitz nonlinear systems. The author also constructed the systematic computational algorithm, to find the gain matrices of the observer. In [8], utilizing the LMI approach to the LMI approach was utilized to design a linear full-order non-fragile observer based control for continuous-timelinear systems, and to guarantee the observer is exponentially stabilizable. Moreover, the LMI was also used to find the control and observer gains. In [9], the authors used a separation principle for the observer based dynamic surface controller (ODSC) of the nonlinear systems, and proved the quadratic stability of ODSC by using a convex optimization problem. In [10], dealt with the designing problem of the observer-based controllers using the famous Young relation for uncertain linear system. Besides this, the authors also proved that the Young relation was less restrictive than the LMI condition. In [11], observer-based output feedback control and minimizing the driving energy of the controller was designed by using linear quadratic performance (LQP) optimality for uncertain system with external disturbance. Furthermore, the authors used the separation principle to separate design of the feedback control law and observer. However, these approaches given in [1–11] only considered the estimation error of the observer based full state feedback control, which increases the computation of burden due to theassociated closed-loop system, possessing a dynamical order double that of the actual systems. This motivate us to design observer based output feedback control for a class of uncertain systems.

In this paper, the proposed observer based output feedback control is designed using LMI approach. A numerical example is given to illustrate the performance of the proposed observer based output feedback control approach.

2 Statement of the Problem

Consider the following mismatched uncertain systems:

$$\dot{x}(t) = [A + \Delta A]x(t) + [B + \Delta B]u(t) \tag{1}$$

$$y(t) = Cx(t) \tag{2}$$

where $x(t) \in R^n$ is the state vector, $u(t) \in R^m$ is the control input, $y(t) \in R^p$ is the output. The matrices A, B and C are constant matrices with appropriate dimensions. The term ΔA represents the mismatched uncertainty of the plant, which the matching condition is not satisfied. The term ΔB represents the input matrix uncertainty.

The following assumptions are useful for the development of our work.

Assumption 1 The matrix pair (A, C) is observable.

Assumption 2 The mismatched uncertainty of the plant and the input matrix uncertainty satisfy

$$[\,\Delta A(x(t), t) \quad \Delta B(x(t), t)\,] = MF(x(t), t)[\,N_1 \quad N_2\,] \tag{3}$$

where $F(x(t), t)$ is unknown but bounded as $\|F(x(t), t)\| \leq 1$ for all $(x(t), t) \in R^n \times R$, and M, N_1 and N_2 are known matrices of appropriate dimensions.

Lemma 1 [12]: Let X, Y and F are real matrices of suitable dimension with $F^T F \leq I$ then, for any scalar $\varphi > 0$, the following matrix inequality holds:

$$XFY + Y^T F^T X^T \leq \varphi^{-1} XX^T + \varphi Y^T Y.$$

For system (1) and (2), construct the following dynamical system

$$\dot{\hat{x}}(t) = A_c \hat{x}(t) + Bu(t) + L[y(t) - \hat{y}(t)] \tag{4}$$

$$\hat{y}(t) = C\hat{x}(t) \tag{5}$$

$$u(t) = -KC\hat{x}(t) = -K\hat{y}(t) \tag{6}$$

where $\hat{x}(t) \in R^n$ is the estimation of $x(t)$, $\hat{y}(t) \in R^p$ is the observer output, $K \in R^{m \times p}$ is the controller gain, $L \in R^{n \times p}$ is the observer gain and A_c is the constant matrix to be determined.

Let $e(t) = x(t) - \hat{x}(t)$, from the systems (1), (2), (4) and (5) we have

$$\begin{aligned}\dot{e}(t) &= (A - A_c)\hat{x}(t)) + Ae(t) - LCe(t) \\ &\quad + MF(t)[N_1 e(t) + (N_1 - N_2 KC)\hat{x}(t)]\end{aligned} \tag{7}$$

According to Eqs. (4) and (7) we achieve

$$\begin{bmatrix}\dot{\hat{x}}(t) \\ \dot{e}(t)\end{bmatrix} = \begin{bmatrix}A_c - BKC\, LC \\ A - A_c\, A - LC\end{bmatrix}\begin{bmatrix}\hat{x}(t)) \\ e(t)\end{bmatrix} + \begin{bmatrix}0 \\ M\end{bmatrix}F(t)[(N_1 - N_2 KC)\, N_1]\begin{bmatrix}\hat{x}(t)) \\ e(t)\end{bmatrix} \tag{8}$$

3 Main Results

Now we are in position to derive sufficient conditions in terms of linear matrix inequalities (LMI) such that the system (8) is robustly stabilizable. Let us begin with considering the following LMI:

$$\begin{bmatrix}\phi_1 + \phi_1^T - B\hat{K}C - C^T K^T B^T & \phi_3 & 0 & (N_1 Q_1 - N_2 \hat{K}C)^T \\ \phi_3^T & \Xi & M & 0 \\ 0 & M^T & -\varepsilon^{-1} I & 0 \\ (N_1 Q_1 - N_2 \hat{K}C) & 0 & 0 & -\varepsilon I\end{bmatrix} < 0 \tag{9}$$

where $\phi_1 = A_c Q_1$, $\phi_2 = KQ_1$, $\phi_3 = Q_1(A - A_c)^T + \hat{L}C + \varepsilon^{-1}(N_1 Q_1 - N_2 \hat{K}C)^T N_1 Q_2$, $\Xi = AQ_2 - \hat{L}C + Q_2 A^T - C^T \hat{L}^T + Q_2\, \varepsilon^{-1} N_1^T N_1 Q_2$, $Q_1 \in R^{n\times n} > 0$, $Q_1 \in R^{n\times n} > 0$ and $Q_2 \in R^{n\times n} > 0$ and the scalar $\varepsilon > 0$. Then, we can establish the following theorem.

Theorem 1 Suppose that the LMI (9) has a solution for the positive matrices $Q_1 \in R^{n\times n}$, $Q_2 \in R^{n\times n}$ and $\hat{K} \in R^{m\times p}$, $\hat{L} \in R^{n\times p}$, the scalar $\varepsilon > 0$. Consider the system (1) and (2) with assumptions 1–2 and the observer-based output feedbach control (4) and (6). Then the system (1) and (2) is robustly stabilizable by the observer-based output feedbach control (4) and (6) with $L = \hat{L}\hat{Q}_2^{-1}$ and $K = \hat{K}\hat{Q}_1^{-1}$.

Proof Let us first consider the following positive definition function

$$V(\hat{x}(t), e(t)) = \begin{bmatrix}\hat{x}(t) \\ e(t)\end{bmatrix}^T \begin{bmatrix}P_1 & 0 \\ 0 & P_2\end{bmatrix}\begin{bmatrix}\hat{x}(t) \\ e(t)\end{bmatrix} \tag{10}$$

where $P_1 \in R^{n\times n} > 0$ and $P_2 \in R^{n\times n} > 0$. Then, the time derivative of V along the state trajectories of system (8) is given by

$$\begin{aligned}\dot{V}(\hat{x}(t), e(t)) = &\begin{bmatrix}\hat{x}(t)\\ e(t)\end{bmatrix}^T \left\{ \begin{bmatrix} P_1 & 0\\ 0 & P_2\end{bmatrix}\begin{bmatrix} A_c - BKC & LC\\ A - A_c & A - LC\end{bmatrix}\right.\\ &\left. + \begin{bmatrix} A_c - BKC & LC\\ A - A_c & A - LC\end{bmatrix}^T \begin{bmatrix} P_1 & 0\\ 0 & P_2\end{bmatrix}\begin{bmatrix}\hat{x}(t)\\ e(t)\end{bmatrix}\right\}\\ &+ 2\begin{bmatrix}\hat{x}(t)\\ e(t)\end{bmatrix}^T \begin{bmatrix} P_1 & 0\\ 0 & P_2\end{bmatrix}\begin{bmatrix} 0\\ M\end{bmatrix} F(t)[(N_1 - N_2KC) \;\; N_1]\begin{bmatrix}\hat{x}(t)\\ e(t)\end{bmatrix}\end{aligned} \tag{11}$$

Applying Lemma 1 to Eq. (11) yields

$$\begin{aligned}\dot{V}(\hat{x}(t), e(t)) \le &\begin{bmatrix}\hat{x}(t)\\ e(t)\end{bmatrix}^T \begin{bmatrix} P_1 & 0\\ 0 & P_2\end{bmatrix}\begin{bmatrix} A_c - BKC & LC\\ A - A_c & A - LC\end{bmatrix} + \begin{bmatrix} A_c - BKC & LC\\ A - A_c & A - LC\end{bmatrix}^T\\ &\times \left.\begin{bmatrix} P_1 & 0\\ 0 & P_2\end{bmatrix}\begin{bmatrix}\hat{x}(t)\\ e(t)\end{bmatrix}\right\} + \varepsilon \begin{bmatrix}\hat{x}(t)\\ e(t)\end{bmatrix}^T \begin{bmatrix} P_1 & 0\\ 0 & P_2\end{bmatrix}\begin{bmatrix} 0\\ M\end{bmatrix}\begin{bmatrix} 0\\ M\end{bmatrix}^T \begin{bmatrix} P_1 & 0\\ 0 & P_2\end{bmatrix}^T \begin{bmatrix}\hat{x}(t)\\ e(t)\end{bmatrix}\\ &+ \varepsilon^{-1}\begin{bmatrix}\hat{x}(t)\\ e(t)\end{bmatrix}^T [\,(N_1 - N_2KC) \;\; N_1\,]^T [\,(N_1 - N_2KC) \;\; N_1\,]\begin{bmatrix}\hat{x}(t)\\ e(t)\end{bmatrix}\\ = &\begin{bmatrix}\hat{x}(t)\\ e(t)\end{bmatrix}^T \left\{\begin{bmatrix} P_1 & 0\\ 0 & P_2\end{bmatrix}\begin{bmatrix} A_c - BKC & LC\\ A - A_c & A - LC\end{bmatrix} + \begin{bmatrix} A_c - BKC & LC\\ A - A_c & A - LC\end{bmatrix}^T \begin{bmatrix} P_1 & 0\\ 0 & P_2\end{bmatrix}\right\}\begin{bmatrix}\hat{x}(t)\\ e(t)\end{bmatrix}\\ &+ \varepsilon^{-1}\begin{bmatrix}\hat{x}(t)\\ e(t)\end{bmatrix}^T \begin{bmatrix} (N_1 - N_2KC)^T(N_1 - N_2KC) & (N_1 - N_2KC)^T N_1\\ N_1^T(N_1 - N_2KC) & N_1^T N_1\end{bmatrix}\begin{bmatrix}\hat{x}(t)\\ e(t)\end{bmatrix}\\ &+ \varepsilon \begin{bmatrix}\hat{x}(t)\\ e(t)\end{bmatrix}^T \begin{bmatrix} 0 & 0 & \\ 0 & P_2MM^T & P_2\end{bmatrix}\begin{bmatrix}\hat{x}(t)\\ e(t)\end{bmatrix}\\ = &\begin{bmatrix}\hat{x}(t)\\ e(t)\end{bmatrix}^T \left\{\begin{bmatrix} P_1(A_c - BKC) + (A_c - BKC)^T P_1 & (A - A_c)^T P_2 + P_1 LC\\ P_2(A - A_c) + (LC)^T P_1 & P_2(A - LC) + (A - LC)^T P_2\end{bmatrix}\right.\\ &\left. + \varepsilon^{-1}\begin{bmatrix} (N_1 - N_2KC)^T(N_1 - N_2KC) & (N_1 - N_2KC)^T N_1\\ N_1^T(N_1 - N_2KC) & N_1^T N_1\end{bmatrix}\right\}\begin{bmatrix}\hat{x}(t)\\ e(t)\end{bmatrix}\\ &+ \varepsilon \begin{bmatrix}\hat{x}(t)\\ e(t)\end{bmatrix}^T \begin{bmatrix} 0 & 0 & \\ 0 & P_2MM^T & P_2\end{bmatrix}\begin{bmatrix}\hat{x}(t)\\ e(t)\end{bmatrix}\end{aligned} \tag{12}$$

In addition, pre- and post-multiplying the LMI (9) by X and X^T, where

$$X = \begin{bmatrix} P_1 & 0 & 0 & 0\\ 0 & P_2 & 0 & 0\\ 0 & 0 & I & 0\\ 0 & 0 & 0 & I\end{bmatrix} = \begin{bmatrix} Q_1^{-1} & 0 & 0 & 0\\ 0 & Q_2^{-1} & 0 & 0\\ 0 & 0 & I & \\ 0 & 0 & & I\end{bmatrix} \tag{13}$$

Then, we have

$$\begin{bmatrix} P_1(A_c - BKC) + (A_c - BKC)^T P_1 & W_1 & 0 & (N_1 - N_2KC)^T \\ P_2(A - A_c) + (LC)^T P_1 + \varepsilon^{-1} N_1^T (N_1 - N_2KC) & W_2 & P_2M & 0 \\ 0 & M^T P_2 & -\varepsilon^{-1} I & 0 \\ (N_1 - N_2KC) & 0 & 0 & -\varepsilon I \end{bmatrix} < 0 \tag{14}$$

where $W_1 = (A - A_c)^T P_2 + P_1 LC + \varepsilon^{-1}(N_1 - N_2KC)^T N_1$, $W_2 = P_2(A - LC) + (A - LC)^T P_2 + \varepsilon^{-1} N_1^T N_1$.

By the Schur complement of [13], the LMI condition (14) is equivalent to

$$\begin{bmatrix} P_1(A_c - BKC) + (A_c - BKC)^T P_1 & (A - A_c)^T P_2 + P_1 LC \\ P_2(A - A_c) + (LC)^T P_1 & P_2(A - LC) + (A - LC)^T P_2 \end{bmatrix} + \varepsilon \begin{bmatrix} 0 & 0 \\ 0 & P_2 M M^T P \end{bmatrix} + \varepsilon^{-1} \begin{bmatrix} (N_1 - N_2KC)^T (N_1 - N_2KC) & (N_1 - N_2KC)^T N_1 \\ N_1^T (N_1 - N_2KC) & N_1^T N_1 \end{bmatrix} < 0 \tag{15}$$

According to Eqs. (12) and (15), we cac obtain that

$$\dot{V}(\hat{x}(t), e(t)) < 0 \tag{16}$$

The inequality (16) show that if LMI (9) holds, which further implies that Then the system (1) and (2) is robustly stabilizable by the observer-based control (4) and (6).

4 Numerical Example

In order to demonstrate the validity and effectiveness of the proposed observer based output feedbach control, in this section, we are going to apply the proposed method given in previous sections for the mismatched uncertain system, which is modified from [1] as the following

$$\begin{aligned} \dot{x} &= \left(\begin{bmatrix} 1 & 1 & 1 \\ 0 & -2 & 1 \\ 1 & -2 & -5 \end{bmatrix} + \Delta A \right) x + \begin{bmatrix} 1 & 0 \\ 0 & 1 \\ 0 & 0 \end{bmatrix} u \\ y &= \begin{bmatrix} 1 & 0 & 1 \end{bmatrix} x \end{aligned} \tag{17}$$

The mismatched uncertainties are given as $\Delta A = MFN$ with $M = I$, $N_1 = \begin{bmatrix} \beta & 0 & 0 \\ 0 & \alpha & 0 \\ 0 & 0 & \gamma \end{bmatrix}$ and

$$F(t) = \begin{bmatrix} \frac{a(t)}{\alpha} & 0 & 0 \\ 0 & \frac{b(t)}{\beta} & 0 \\ 0 & 0 & \frac{c(t)}{\gamma} \end{bmatrix} = \begin{bmatrix} \frac{\cos(3t)}{\alpha} & 0 & 0 \\ 0 & \frac{1-0.3\sin(2t)}{\beta} & 0 \\ 0 & 0 & \frac{1.3\sin(4t)}{\gamma} \end{bmatrix} \tag{18}$$

For this work, the following parameters are given as follows: $\hat{K} = [10.8 \quad 0.135]^T$, $\hat{L} = [22 \quad 0.4 \quad 12]^T$, the scalar $\varepsilon = 2$. By solving LMI (9), it is easy to verify that conditions in Theorem 1 are satisfied with positive matrices $Q_1 \begin{bmatrix} 0.1051 & -0.0216 & -0.0075 \\ -0.0216 & 0.0208 & 0.0081 \\ -0.0075 & 0.0081 & 0.1364 \end{bmatrix}$, $Q_2 = \begin{bmatrix} 3.1471 & -0.3948 & 0.9715 \\ -0.3948 & 1.5653 & -0.3104 \\ 0.9715 & -0.3104 & 4.4855 \end{bmatrix}$, $K = [95.3642 \quad 1.1921]^T$ and $L = [4.5950 \quad 0.0835 \quad 2.5064]^T$.

The initial conditions for the system (17) are selected to be $x(0) = [2 \quad 3 \quad -4]^T$. The system states, using the proposed observer, are plotted in Fig. 2. From Fig. 2, it is obvious that the system has a good performance and is effective in dealing with matched and mismatched uncertainties (Fig. 1).

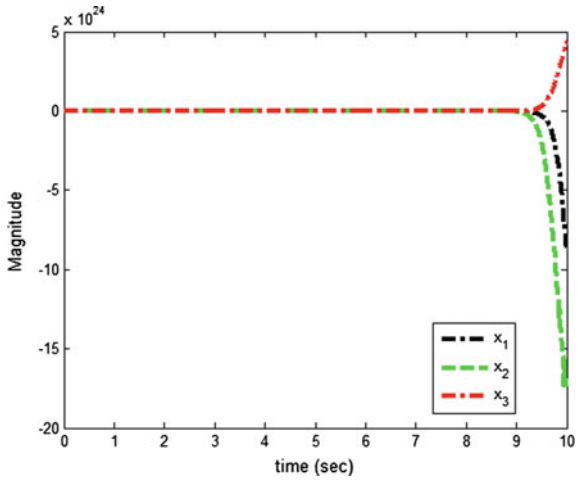

Fig. 1 Trajectories of the uncontrolled system

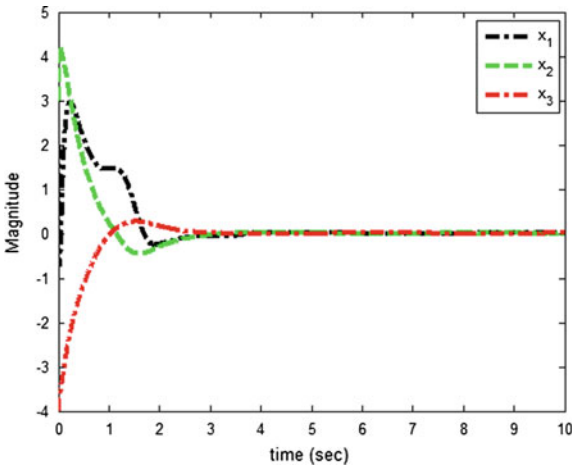

Fig. 2 Trajectories of the feedback-controlled system

5 Conclusion

An observer-based output feedback control is developed to stabilize a class of mismatched uncertain systems. The control scheme is designed to be dependent on only the observer output. Therefore, the conservatism is reduced and the roboustness is enhanced. The proposed approach does not need the availability of the state variables so that our method is very useful and more realistic since it can be easily implemented in practice. Finally, a numerical example has been given to demonstrate the use of our results.

References

1. Lien C-H (2004) Robust observer-based control of systems with state perturbations via LMI approach. IEEE Trans Autom Control 49(8):365–1370
2. Lien C-H, Yu K-W (2008) LMI optimization approach on robustness and H∞ control analysis for observer-based control of uncertain systems. Chaos, Solitons Fractals 36(3):617–627
3. Lien C-H (2004) An efficient method to design robust observer-based control of uncer-tain linear systems. Appl Math Comput 158(1):29–44
4. Yan X-G, Spurgeon SK, Edwards C (2005) Dynamic sliding mode Con-trol for a class of systems with mismatched uncertainty. Eur J Control 11(1):1–10
5. Tan CP, Edwards C (2000) An LMI approach for designing sliding mode observers. In: Proceedings of the 39th IEEE Conference on Decision and Control, 3:2587–2592
6. Choi HH, Ro KS (2005) LMI-based sliding-mode observer design method In: IEE proceedings of control theory and applications, 152(1):113–115
7. Rajamani R (1998) Observers for Lipschitz nonlinear systems. IEEE Trans Autom Control 43(3):397–401
8. Lien C-H, Cheng W-C, Tsai C-H, Yu K-W (2007) Non-fragile observer-based controls of linear system via LMI approach. Chaos, Solitons Fractals 32(4):1530–1537

9. Song B, Hedrick JK (2004) Observer-based dynamic surface control for a class of non-linear systems: an LMI approach. IEEE Trans Autom Controlon 49(11):1995–2001
10. Kheloufi H, Zemouche A, Bedouhene F, Boutayeb M (2013) On LMI condi-tions to design observer-based controllers for linear systems with parameter uncertain-ties. Automatica 49(12):3700–3704
11. Kamarudin MN, Rozali SM, Husain AR (2013) Observer-based output feedback control with linear quadratic performance. Procedia Eng 53:233–240
12. Pai M-C (2009) Observer-based adaptive sliding mode control for nonlinear uncertain state-delayed systems. Int J Control Autom Syst 7(4):536–544
13. Boyd S, Ghaoui EL, Feron E, Balakrishna V (1998) Linear Matrix Inequalities in System and Control theory. SIAM, Philadelphia

Single and Multi Chaos Enhanced Differential Evolution on the Selected PID Tuning Problem

Roman Senkerik, Michal Pluhacek and Ivan Zelinka

Abstract This paper presents results of the utilization of single and multi chaos enhanced differential evolution (DE) algorithm in the task of PID controller design for the selected 4th order dynamical system. The aim of the paper is to highlight the advantages and disadvantages of utilizing such complex chaos enhanced heuristics for simple real life and fast optimization process. The results of four versions of chaos driven DE are compared with canonical DE versions, which do not utilize the chaos in the place of pseudo-random number generator.

Keywords Differential evolution · Deterministic chaos · Optimization · PID tuning

1 Introduction

This research is focused on the interconnection of the two different softcomputing fields, which are theory of chaos and evolutionary computation. Currently the methods based on softcomputing such as evolutionary algorithms are known as powerful tool for solving many difficult and complex optimization problem.

In the past decades, simple PID controllers became a fundamental part of many automatic control systems. The successful design (tuning of parameters) of PID

R. Senkerik (✉) · M. Pluhacek
Faculty of Applied Informatics, Tomas Bata University in Zlin,
Nam T.G. Masaryka 5555, 760 01, Zlin, Czech Republic
e-mail: senkerik@fai.utb.cz

M. Pluhacek
e-mail: pluhacek@fai.utb.cz

I. Zelinka
Faculty of Electrical Engineering and Computer Science, Technical University
of Ostrava, 17. Listopadu 15, 708 33, Ostrava-Poruba, Czech Republic
e-mail: ivan.zelinka@vsb.cz

V.H. Duy et al. (eds.), *AETA 2015: Recent Advances in Electrical Engineering and Related Sciences*, Lecture Notes in Electrical Engineering 371,
DOI 10.1007/978-3-319-27247-4_48

controller was mostly based on deterministic methods involving complex mathematics [1, 2].

Recently, many different softcomputing techniques were successfully utilized for solving the complex task of PID controller parameter setup [3]. These techniques [4–7] use random operations and typically use various kinds of pseudo-random number generators (PRNGs) that depend on the operation system platform, where the algorithm is implemented. More recently it was shown that chaotic systems could be used as PRNGs for various stochastic methods with great results with the predisposition that unlike stochastic approaches, a chaotic approach is able to bypass local optima stagnation, which is very important for the utilization of evolutionary algorithms. Some of these chaos driven stochastic methods were tested on the task of PID controller design in [8]. In [3] it was shown that Particle Swarm optimization (PSO) algorithm is able to deal with the task of PID controller design with very good results. Following that in [9–13] the performance of chaos driven PSO algorithm was tested on this task with great results.

This paper presents the results of the utilization of single and multi chaos enhanced differential evolution (DE) algorithm in the task of PID controller design for the selected 4th order dynamical system. The aim of the paper is to highlight the advantages and disadvantages of utilizing such complex chaos enhanced heuristics for simple real life and fast optimization process.

2 Motivation

Till now the chaos was observed in many of various systems (mechanical, physical electronic) and in the last few years, it is also used to replace the pseudo-number generators (PRGNs) in evolutionary algorithms (EAs).

This research is a continuation and extension of the previous successful initial application based experiments with chaos driven PSO and DE in PID tuning task [9–13]. In this paper the DE/rand/1/bin strategy driven either by one (single ChaosDE) or two different chaotic systems (Multi-ChaosDE) were utilized to solve the issue of evolutionary optimization of PID controller settings. Thus the idea was to utilize the hidden chaotic dynamics in pseudo random sequences given by chaotic system to help Differential evolution algorithm in searching for the best controller settings.

Moreover the idea was to utilize the results and knowledge with alternating of different chaotic systems within one run of chaos embedded heuristics. The focus of this research is to experimentally analyze and highlight the advantages and disadvantages of utilizing simple canonical, complex chaos enhanced heuristics and even more complex heuristic with two alternating driving chaotic systems in the task of simple real life and fast optimization process.

3 Differential Evolution

DE is a population-based optimization method that works on real-number-coded individuals [7]. For each individual $\vec{x}_{i,G}$ in the current generation G, DE generates a new trial individual $\vec{x}'_{i,G}$ by adding the weighted difference between two randomly selected individuals $\vec{x}_{r1,G}$ and $\vec{x}_{r2,G}$ to a randomly selected third individual $\vec{x}_{r3,G}$. The resulting individual $\vec{x}'_{i,G}$ is crossed-over with the original individual $\vec{x}_{i,G}$. The fitness of the resulting individual, referred to as a perturbed vector $\vec{u}_{i,G+1}$, is then compared with the fitness of $\vec{x}_{i,G}$. If the fitness of $\vec{u}_{i,G+1}$ is greater than the fitness of $\vec{x}_{i,G}$, then $\vec{x}_{i,G}$ is replaced with $\vec{u}_{i,G+1}$; otherwise, $\vec{x}_{i,G}$ remains in the population as $\vec{x}_{i,G+1}$. DE is quite robust, fast, and effective, with global optimization ability. It does not require the objective function to be differentiable, and it works well even with noisy and time-dependent objective functions. Description of used DERand1Bin strategy is presented in (1). See [7, 14] and [15] for the description of all other strategies.

$$u_{i,G+1} = x_{r1,G} + F \cdot \left(x_{r2,G} - x_{r3,G}\right) \tag{1}$$

4 The Concept of CPRNG

The general idea of CPRNG is to replace the default PRNG with the chaotic system [16]. As the chaotic system is a set of equations with a static start position, we created a random start position of the system, in order to have different start position for different experiments. This random position is initialized with the default PRNG, as a one-off randomizer. Once the start position of the chaotic system has been obtained, the system generates the next sequence using its current position.

Generally there exist many other approaches as to how to deal with the negative numbers as well as with the scaling of the wide range of the numbers given by the chaotic systems into the typical range 0–1:

- Finding of the maximum value of the pre-generated long discrete sequence and dividing of all the values in the sequence with such a maxval number.
- Shifting of all values to the positive numbers (avoiding of ABS command) and scaling.

4.1 Chaotic Systems for CPRNG

This section contains the description of two discrete chaotic maps, which were used as the CPRNG. The direct output iterations of the chaotic map were used for the generation of the both integer numbers and real numbers scaled into the typical range for random function: $\langle 0\text{–}1 \rangle$.

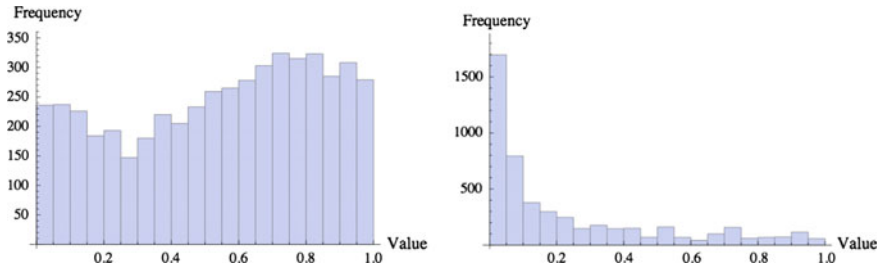

Fig. 1 Histogram of the distribution of real numbers transferred into the range ⟨0–1⟩ generated by means of the chaotic Dissipative standard map (*left*) and Burgers map (*right*)—5000 samples

The Dissipative Standard map is a two-dimensional chaotic map. The parameters used in this work are $b = 0.6$ and $k = 8.8$ as suggested in [17]. The map equations are given in (2).

$$\begin{aligned} X_{n+1} &= X_n + Y_{n+1} (\mathrm{mod} 2\pi) \\ Y_{n+1} &= bY_n + k \sin X_n (\mathrm{mod} 2\pi) \end{aligned} \tag{2}$$

The Burgers mapping is a discretization of a pair of coupled differential equations which were used by Burgers [18] to illustrate the relevance of the concept of bifurcation to the study of hydrodynamics flows. The map equations are given in (3) with control parameters $a = 0.75$ and $b = 1.75$ as suggested in [17].

$$\begin{aligned} X_{n+1} &= aX_n - Y_n^2 \\ Y_{n+1} &= bY_n + X_n Y_n \end{aligned} \tag{3}$$

The illustrative histograms of the distribution of real numbers transferred into the range ⟨0–1⟩ generated by means of studied chaotic maps are in Fig. 1.

5 Problem Design

5.1 PID Controller

The PID controller contains three unique parts; proportional, integral and derivative controller [1–3, 8]. A simplified form in Laplace domain is given in (4)

$$G(s) = K\left(1 + \frac{1}{sT_i} + sT_d\right) \tag{4}$$

The PID form most suitable for analytical calculations is given in (5).

$$G(s) = k_p + \frac{k_i}{s} + k_d s \tag{5}$$

The parameters are related to the standard form through: $k_p = K$, $k_i = K/T_i$ and $k_d = KT_d$. Acquisition of the combination of these three parameters that gives the lowest value of the test criterions was the objective of this research. Selected controlled system was the 4th order system that is given by Eq. 6.

$$G(s) = \frac{1}{s^4 + 6s^3 + 11s^2 + 6s} \tag{6}$$

5.2 Cost Function

Test criterion measures properties of output transfer function and can indicate quality of regulation [1–3, 8]. Following one different integral criterion was used for the test and comparison purposes: ITAE (Integral Time Absolute Error) (7). This test criterion was minimized within the cost function for the enhanced DE algorithm.

Integral of Time multiplied by Absolute Error (ITAE)

$$I_{ITAE} = \int_0^T t|e(t)|dt \tag{7}$$

6 Results

In this section, the results obtained within experiments with single-ChaosDE and Multi-ChaosDE algorithms are compared with each other and with canonical DE. Previously published works and comparisons can be found in [3, 8–12].

Table 1 shows the typical used settings for the both Single/Multi ChaosDE and Canonical DE.

Following versions of adaptive Single/Multi-ChaosDE were studied:

- *ChaosDE Disi:* Single-chaos driven DE with Dissipative map as the CPRNG.
- *ChaosDE Bur:* Single-chaos driven DE with Burgers map as the CPRNG.
- *ChaosDE Disi-Bur*: Start with Dissipative standard map CPRNG, and then switch to the Burgers map CPRNG when the switching rule will be fulfilled (half of the max. generations interval).
- *ChaosDE Bur-Disi*: Start with Burgers map CPRNG, then switch to the Dissipative standard map CPRNG when the switching rule will be fulfilled (half of the max. generations interval).

Table 1 DE settings

DE Parameter	Value
Popsize	25
F (for ChaosDE)	0.5
CR (for ChaosDE)	0.9
F (for Canonical DE)	0.5
CR (for Canonical DE)	0.9
Dim	3
Max. Generations	100
Max Cost Function Evaluations (CFE)	2500

Table 2 Simple results statistics for the Canonical DE and Single/Multi-ChaosDE—4th order system PID controller design

	Avg CF	Median CF	Max CF	Min CF	StdDev
Canonical DE	15.20054	15.19068	15.28961	**15.19041**	0.031294
ChaosDE Disi	**15.19065**	**15.19067**	**15.19068**	**15.19041**	**8.34E-05**
ChaosDE Bur	15.24547	15.19173	15.50558	15.19067	0.108157
ChaosDE DisiBur	15.21419	**15.19067**	15.42609	**15.19041**	0.074454
ChaosDE BurDisi	15.25067	**15.19067**	15.65032	**15.19041**	0.146789

Statistical results of the selected experiments are shown in comprehensive Table 2 which represents the simple statistics for cost function (CF) values, e.g. average, median, maximum values, standard deviations and minimum values representing the best individual solution for all 50 repeated runs of DE.

Table 3 compares the progress of all versions of Single/Multi-ChaosDE and Canonical DE. This table contains the average CF values for the generation No. 25, 50, 75 and 100 from all 50 runs. The bold values within the both Tables 2 and 3 depict the best obtained results.

Table 3 Comparison of progress towards the minimum

DE Version	25	50	75	100
Canonical DE	15.97809	15.33126	15.243	15.20054
ChaosDE Disi	15.66296	**15.19221**	**15.1907**	**15.19065**
ChaosDE Bur	15.98638	15.2609	15.24888	15.24547
ChaosDE DisiBur	15.64624	15.23651	15.21615	15.21419
ChaosDE BurDisi	**15.64487**	15.29743	15.26091	15.25067

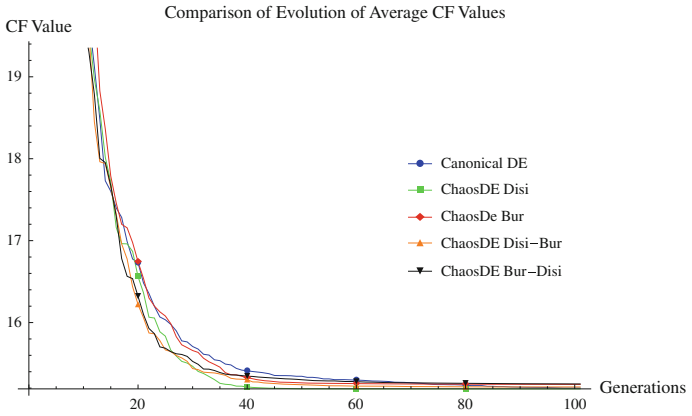

Fig. 2 Comparison of the time evolution of avg. CF values for the all 50 runs of Canonical DE, and four versions of Single/Multi-ChaosDE

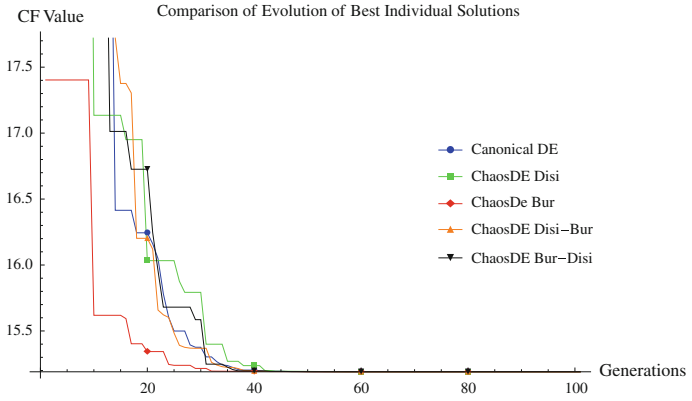

Fig. 3 Comparison of the time evolution of the best individual solutions (with minimal final CF values) for the all 50 runs of Canonical DE, and four versions of Single/Multi-ChaosDE

Furthermore, examples of time evolutions of CF values for average, the best individual and the most progressive solutions are depicted in Figs. 2, 3 and 4.

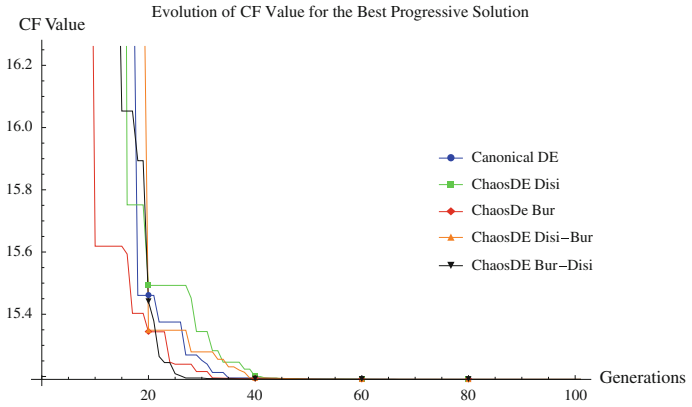

Fig. 4 Comparison of the time evolution of the most progressive solutions (with minimal sum of CF values in 20 generations steps) for the all 50 runs of Canonical DE, and four versions of Single/Multi-ChaosDE

7 Conclusion

In this paper the single/multi chaotic approach combining dissipative standard map and burgers map was presented and investigated over its capability of enhancing the performance of DE in the task of PID controller design. This approach is suitable for the system of any order; moreover due to the limited amount of iterations and very fast convergence of DE towards optimal solution, it can be used also in real time applications.

From the comparisons, it follows that through the utilization of chaotic systems; the best overall results were obtained and entirely different statistical characteristics for different single/multi-chaos CPRNGs-based heuristic can be achieved. Thus the different influence to the system, which utilizes the selected CPRNG, can be chosen through the implementation of particular inner chaotic dynamics given by the particular chaotic system.

When comparing both single/multi chaos approaches, it seems that for the very fast optimization process, which is the PID tuning issue, it is very advantageous to keep the heuristic simple without any adaptation and alternation of driving complex dynamical chaotic systems. Initial strong progress towards global CF extreme of Burgers map based ChaosDE and persistent searching abilities with satisfactory statistical results of Dissipative standard map based driven heuristics were not possible to combine in the Mutli-Chaos approach to ensure even better results. We assume, that in requires many generations for the positive influence of adaptation/alternation of driving chaotic dynamics for the DE to its performance. Multi-chaotic approach proved itself to be very advantageous in higher dimensional optimization tasks with high number of generations required.

Promising results were presented, discussed and compared with other methods of PID controller design. More detail experiments are needed to prove or disprove these claims and explain the effect of the chaotic systems on the optimization and controller design.

Acknowledgements This work was supported by Grant Agency of the Czech Republic—GACR P103/15/06700S, further by financial support This work was supported by the Ministry of Education, Youth and Sports of the Czech Republic within the National Sustainability Programme project No. LO1303 (MSMT-7778/2014) and also by the European Regional Development Fund under the project CEBIA-Tech No. CZ.1.05/2.1.00/03.0089, partially supported by Grant of SGS No. SP2015/142 of VSB—Technical University of Ostrava, Czech Republic and by Internal Grant Agency of Tomas Bata University under the projects No. IGA/FAI/2015/057.

References

1. Åström KJ (2002) Control system design—lecture notes for ME 155A. http://www.cds.caltech.edu/~murray/courses/cds101/fa02/caltech/astrom.html
2. Landau ID, Gianluca Z (2006) Digital control systems. Communications and control engineering. Springer, London
3. Nagaraj B, Subha S, Rampriya B (2008) Tuning algorithms for PID controller using soft computing techniques. Int J Comput Sci Netw Secur 8(4):278–281
4. Kennedy J, Eberhart R (1995) Particle swarm optimization. In: IEEE international conference on neural networks, pp 1942–1948
5. Dorigo M, Di Caro G (1999) Ant colony optimization: a new meta-heuristic. In: CEC 99. Proceedings of the 1999 congress on evolutionary computation
6. Goldberg DE (1989) Genetic algorithms in search, optimization, and machine learning. Addison-Wesley, Boston
7. Storn R, Price K (1997) Differential evolution—a simple and efficient heuristic for global optimization over continuous spaces. J Global Optim 11(4):341–359
8. Davendra D, Zelinka I, Senkerik R (2010) Chaos driven evolutionary algorithms for the task of PID control. Comput Math Appl 60(4):1088–1104
9. Pluhacek M, Senkerik R, Davendra D, Zelinka I (2012) Designing PID controller for DC motor system by means of enhanced PSO algorithm with discrete chaotic Lozi map. In: 26th European conference on modelling and simulation, ECMS 2012, pp 405–409
10. Pluhacek M, Senkerik R, Davendra D, Zelinka I (2012) PID controller design for 4th order system by means of enhanced PSO algorithm with lozi chaotic map. In: Paper presented at the 18th international conference on soft computing MENDEL 2012, pp 35–39
11. Pluhacek M, Senkerik R, Davendra D, Zelinka I (2013) Designing PID controller for DC motor by means of enhanced PSO algorithm with dissipative chaotic map. In: Snášel V, Abraham A, Corchado ES (eds) Soft computing models in industrial and environmental applications, vol 188., Advances in intelligent systems and computingSpringer, Berlin, pp 475–483
12. Pluhacek M, Senkerik R, Davendra D, Zelinka I (2012) Designing PID controller for 4th order system by means of enhanced PSO algorithm with discrete chaotic dissipative standard map. In: EMSS 2012 24th European modeling and simulation symposium, pp 396–401
13. Senkerik R, Pluhacek M, Zelinka I, Davendra D, Kominkova Oplatkova Z (2014) Comparison of chaos driven PSO and differential evolution on the selected PID tuning problem. In: Saeed K, Snášel V (eds) Computer Information Systems and Industrial Management, vol 8838. Lecture Notes in Computer Science. Springer, Heidelberg, pp 67–76. doi:10.1007/978-3-662-45237-0_8

14. Price KV (1999) An introduction to differential evolution. In: Corne D, Dorigo M, Glover F (eds) New ideas in optimization. McGraw-Hill Ltd, pp 79–108
15. Price KV, Storn RM, Lampinen JA (2005) Differential evolution—a practical approach to global optimization. Natural computing series. Springer, Berlin
16. Caponetto R, Fortuna L, Fazzino S, Xibilia MG (2003) Chaotic sequences to improve the performance of evolutionary algorithms. IEEE Trans Evol Comput 7(3):289–304
17. Sprott JC (2003) Chaos and time-series analysis. Oxford University Press, Oxford
18. ELabbasy E, Agiza H, EL-Metwally H, Elsadany A (2007) Bifurcation analysis, chaos and control in the burgers mapping. Int J Nonlinear Sci 4(3):171–185

Part IX
Robotics

A Study on the Dynamics of Marine Umbilical Cable for Underwater Vehicle

The-Vu Mai, Hyeung-Sik Choi, Joon-Young Kim, Dae-Hyeung Ji, Hyun-Joong Son and Ngoc-Huy Tran

Abstract The dynamics of underwater umbilical cable (UC) for underwater vehicle (UV) are an important in ocean engineering. These UC are widely used in the ocean environment for signal and power transmission application. To apply the cable to power and data transmission for small UV, the dynamics of the UC are studied in the paper. The nonlinear and coupled UC dynamics are complicated, but need to be analyzed in real time for application. In the study, the governing equations of cables are established based on the catenary equation method. The shooting method is applied to solve a two-point boundary value problem. This paper presents the formulation and solution of governing equations that can be used to estimate the three dimensions (3-D) position and forces of the cable end point under the action of concentrated and distributed forces due to underwater currents in 3-D. The validity of the proposed method is shown by simulation results.

Keywords Underwater vehicle · Umbilical cable · Shooting method · Dynamic system

1 Introduction

Generally, the deep-sea-operated vehicle systems typically consist of a large supported vessel, a winch, UC and UV. UC is used for both power supply and communication to UV. The UC that connects the UV to the vessel can be affected by

T.-V. Mai · H.-S. Choi (✉) · D.-H. Ji · H.-J. Son · N.-H. Tran
Division of Mechanical and Energy Systems Engineering,
Korea Maritime University, Pusan, Korea
e-mail: hchoi@hhu.ac.kr

T.-V. Mai
e-mail: maithevu90@gmail.com

J.-Y. Kim
Division of Marine Equipment Engineering, Korea Maritime University, Pusan, Korea

V.H. Duy et al. (eds.), *AETA 2015: Recent Advances in Electrical Engineering and Related Sciences*, Lecture Notes in Electrical Engineering 371,
DOI 10.1007/978-3-319-27247-4_49

many parameters, including the motions of either the UV or the vessel, the current along the cable and the total length of the cable itself. The UC configuration can be optimized by numerical simulations. However, most of researches on the numerical model of predicting the motion of the UV neglect the UC effect. The main reason is that including the UC effect will cause the numerical model to be very complicated and difficult to solve. Therefore, only a few authors dealt with such kind of problem. Ablow and Schechter [1] proposed an implicit finite difference method to simulate an UC that has been frequently referenced in the relevant literatures. However, their algorithm will become singular if the tension in the cable is lost. Burgess [2] indicated the internal forces generated by the cable curvature could avoid the singular behavior of the implicit finite difference scheme, which was made by implementing three additional rotational equations of motion. Buckham et al. [3] applied the finite-element method to calculate the tension and bending force on the slack tether attached to the ROV. Recently Feng and Allen [4] extended the numerical scheme developed by Milinazzo et al. [5] and presented a finite difference method to evaluate the effects of the UC on an underwater flight vehicle, which showed that the numerical scheme was effective and provided a means for developing a feed-forward controller to compensate for the cable effects. It means that the proposed numerical scheme can handle the dynamics of an underwater flight vehicle with cables of non-fixed length.

2 General Structure of Umbilical Cable and Assumptions for Simulation

2.1 Basic Assumptions

In the present study, for simplifying the problem, the following assumptions are made to solve the corresponding configuration and tension of the UC attached to the UV:

- The UC can only resist tension force, not for bending moment and compression force.
- The hydrodynamic force on the UC can be resolved into tangential component and normal component.

2.2 General Structure of UC

In the present study, a cable is adopted as the numerical model for calculations. The UC is divided into 100 equal length elements and the result from one element is propagated into next till it reaches the final end point at the UV. The global coordinates of initial position of the connected point to the UV and the other end

point at the free surface near supported vessel are assumed to be (−85.36, 0, 47.51 m) and (0, 0, 0) m, respectively. The initial length of the UC is set to be 100 m. The initial cable tension, T = 10 N and the constant current speed U = 0.1 m/s is considered in the study. Cable's weight is W_c = −0.5 N/m, diameter d_c = 0.025 m, modulus of elasticity E_c = 200 × 10^9 N/m^2, axial stiffness $EA = 3 \times 10^4$ N and density $\rho_c = 662.2$ kg/m^3. The inertial reference frame (X, Y, Z) is defined at surface of waterline and the first cable's element is attached to the supported vessel. The 3-D of the UC is computed by the method in Sagatun [6] that uses catenary equations with end forces estimates.

3 Forces Acting on the Cable

3.1 Weight and Buoyancy Forces

Consider Fig. 1 which shows a cable segment. The cable's weight per unit length in air is denoted w_a = mg, where g is the earth's gravity, m is the mass per length unit, respectively. When the cable is submerged a hydrostatic force will appear according to:

$$B = \rho_w g A \tag{1}$$

where ρ_w is the density of water and A is the cross-sectional area. This leads to the following definition of the stretched cable's weight in water w_1:

$$w_1 = w_a - B \tag{2}$$

3.2 Hydrodynamic Forces

Consider the current acting on a small cable element dp in Fig. 2. The drag force has two components, namely, the tangential drag force (R_n) and the normal drag force (R_s), respectively.

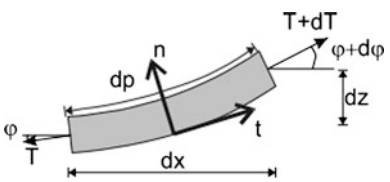

Fig. 1 An infinite cable segment

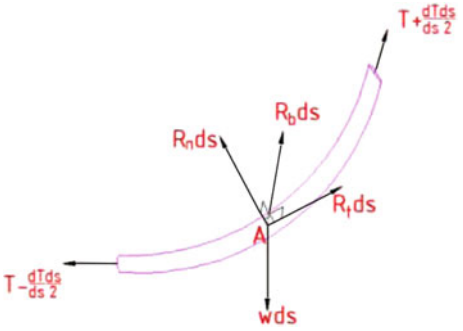

Fig. 2 Forces acting on a segment of a cable

$$R_n = \frac{1}{2}\rho t C_n V^2 \sin\psi|\sin\psi|, \quad R_s = \frac{1}{2}\rho t C_f V^2 \cos\psi|\cos\psi| \tag{3}$$

where ρ is the water density, t is the diameter of the cable, C_n is the normal drag coefficient, C_f is the tangential drag coefficient, V is current velocity relative to the cable, ψ is the angle between current and cable. R_s, R_θ and R_φ are the fluid force per unit length along i_s, i_θ and i_φ directions, respectively, and the formulas can be stated as below:

$$R_s = \frac{1}{2}\rho t\pi C_f V^2 \cos\overline{\psi}|\cos\overline{\psi}|, \quad R_\theta = R_{nx}\cos(\overline{\theta}+\frac{\pi}{2}) + R_{ny}\sin(\overline{\theta}+\frac{\pi}{2}) \tag{4}$$

$$R_\varphi = R_{nx}\cos\overline{\theta}\cos(\overline{\varphi}+\frac{\pi}{2}) + R_{ny}\sin\overline{\theta}\sin(\overline{\varphi}+\frac{\pi}{2}) + R_{nz}\sin(\overline{\varphi}+\frac{\pi}{2}) \tag{5}$$

in which

$$R_{nx} = R_n\cos(\psi-\frac{\pi}{2}), \quad R_{ny} = R_n\sin(\psi-\frac{\pi}{2})\cos\gamma, \quad R_{nz} = R_n\sin(\psi-\frac{\pi}{2})\sin\gamma \tag{6}$$

where γ is the angle between xoy plane and the plane composed of is direction and current direction. The direction of the current is assumed to be coincident with the x-axis. The relationship between all angles of cable system frame can be expressed:

$$\cos\psi = \cos\varphi \times \cos\theta, \quad \tan\gamma = \frac{\tan\varphi}{\sin\theta} \tag{7}$$

3.3 Tension Force

The tension T_e acts along the tangent of the average cable configuration, where the average cable configuration is defined as the smoothest possible profile of the cable. The force on an element with un-stretched length can be written as:

$$\frac{d}{ds}(T_e \vec{t})ds = \left[\frac{\partial T_e}{\partial s}\vec{t} + \frac{T_e}{\rho}\vec{n}\right]ds \tag{8}$$

Given a cable tension, T_c Triantafyllou [7] shows that the effective tension, T_e may be written as:

$$T_e = T_c + p_e A \tag{9}$$

where p_e is the hydrostatic pressure at the specific point of the cable.

4 Dynamic Equations of Cable

4.1 Three Coordinate Systems

To analyse the motion of the cable as well as its effect on the vehicle, it is convenient to define three coordinate systems, i.e. the earth-fixed frame (i, j, k) and the local frames along the cable (t, n, b) and the vehicle-fixed frame (x, y, z).

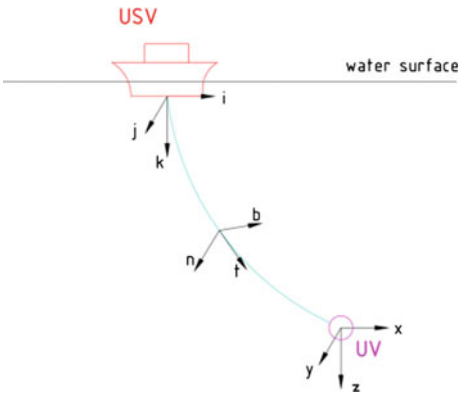

Fig. 3 Three coordinates of the system

As shown in Fig. 3 the earth-fixed frame is selected with k pointing vertically downwards. The vehicle-fixed frame (x, y, z) is located at the centre of the hull, with x coinciding with the longitudinal axis, and y pointing to starboard.

The relationship between the vehicle-fixed frame and the earth-fixed frame can be expressed in terms of Euler angles, i.e.:

$$[x \quad y \quad z] = [i \quad j \quad k]R(\phi, \theta, \psi) \tag{10}$$

with

$$R(\phi, \theta, \psi) = \begin{bmatrix} c\theta c\psi & s\phi s\theta c\psi - c\phi s\psi & c\phi s\theta c\psi + s\phi s\psi \\ c\theta s\psi & s\phi s\theta s\psi + c\phi c\psi & c\phi s\theta s\psi - s\phi c\psi \\ -s\theta & s\phi c\theta & c\phi c\theta \end{bmatrix} \tag{11}$$

where *c.* = *cos*, *s.* = *sin* and φ, θ, ψ are the roll, pitch and yaw angle of the vehicle, respectively.

The local frames (t, n, b) are located at points along the cable with t tangent to the cable in the direction of increasing arc length from the tow-point, and b in the plane of (i, j). They are obtained by three rotations of the earth-fixed frame in the following order: (1) a counter-clockwise rotation through angle about the k axis to bring the i axis into the plane of t and n; (2) a counter-clockwise rotation about the new the i axis through π/2 to bring the k axis into coincidence with b; and (3) a clockwise rotation about b through to bring i and j into coincidence with t and n. Thus, the relationship between the local frames and the earth-fixed frame can be expressed as follows [1]:

$$[t \quad n \quad b] = [i \quad j \quad k]W(\vartheta, \varphi) \tag{12}$$

where

$$W(\vartheta, \varphi) = \begin{bmatrix} \cos\vartheta\cos\varphi & -\cos\vartheta\sin\varphi & \sin\vartheta \\ -\sin\vartheta\cos\varphi & \sin\vartheta\sin\varphi & \cos\vartheta \\ -\sin\varphi & -\cos\varphi & 0 \end{bmatrix} \tag{13}$$

In terms of Eqs. (10)–(13), the relationship between the local frames and the vehicle-fixed frame can be written as:

$$[t \quad n \quad b] = [x \quad y \quad z]R^T(\phi, \theta, \psi)W(\vartheta, \varphi) \tag{14}$$

where the orthogonal property of R has been used.

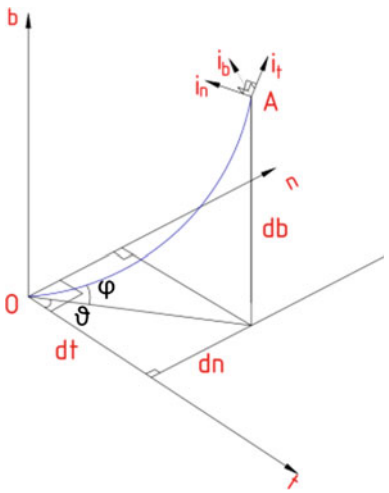

Fig. 4 Coordinate for the UC

4.2 Static Catenary Analysis

The coordinate system for analyzing the UC is shown in Fig. 4. The origin 0 coincides with the end point of the UC. ϑ is the angle between tnb plane and the plane which includes the tangential line passing through the point A and perpendicular to t0n plane. φ is the angle between the tangential line passing through the point A and t0n plane. i_t, i_b and i_n are the unit vector along the cable length s, ϑ and φ, respectively, and perpendicular to each other. Both i_t and i_n are located on the vertical plane.

Considering the configuration of the UC as shown in Fig. 4 and the equilibrium state of the external force on the cable as shown in Fig. 2, we can obtain the full linear differential equations of cable as follows:

$$\frac{dt}{ds} = \cos\varphi \times \cos\vartheta, \quad \frac{dn}{ds} = \cos\varphi \times \sin\vartheta, \quad \frac{db}{ds} = \sin\varphi \tag{15}$$

And

$$\frac{dT}{ds} = w\sin\varphi - R_t, \quad \frac{d\vartheta}{ds} = -\frac{R_\vartheta}{T\cos\varphi}, \quad \frac{d\varphi}{ds} = \frac{(-R_\varphi + w\cos\varphi)}{T} \tag{16}$$

where s is the arc length from the origin to the point A on the cable. T is the tension force along the cable. w is the cable weight per unit length in the water. R_t, R_ϑ and R_φ are the forces per unit length due to the current in i_t, i_b and i_n directions, respectively.

4.3 Solution of the Catenary Equation in the 3-D Case

In this section, a detailed procedure for finding the general elastic catenary equations in 3-D is presented. The UC forces in 3-D are computed by the method reported by Sagatun [6] which uses catenary equations with end forces estimates. Consider a cable of length L with one end fixed in space and the other end free. The cable may have varying axial stiffness EA along its length. And UC is divided into n equal length elements and result of one element is propagated into the next till it reaches the end point of the UV. The force vector f_0 represents the reaction forces from the cable on its termination point. The force vector $\bar{f}_i$ represents a concentrated force acting on an arbitrary point i along the cable, and the distributed load vector p_i force per unit length acts on the cable segment between points i and i-1. The result of the proposed method is an analytical piecewise continuous static solution of the form $F(s) = [F_x \quad F_y \quad F_z]^T$, where the symbol s represents the Lagrangian coordinate along the unstrained cable and F_c is the local forces in X, Y, Z within the cable's element. Considering the cable with one-dimensional strain along the Lagrangian variables, Hooke's law is:

$$T = EA\left(\frac{dp}{ds} - 1\right) \tag{17}$$

Seeking a solution in Cartesian coordinates of the cable as a function of s, the identity $\frac{dF}{ds} = \frac{dF}{dp}\frac{dp}{ds}$ will be useful. This leads to the relation:

$$\frac{dF}{ds} = \frac{dF}{dp}\left(\frac{T}{EA} + 1\right) \tag{18}$$

Assume that the cable is terminated in point 0, the concentrated forces $\bar{f}_i$ may act discrete points (cable nodes) and axial tension T in the end point. We have the following equation for the forces acting in the cable's terminating point:

$$f_o = T\frac{dr}{dp}\bigg|_{s=L} + \sum_{i=1}^{n}\bar{f}_i + wL \tag{19}$$

Where $\{s \in [0, L] \to \mathbb{R}, k \in [1, n] \to \mathbb{N} | s \in [s_{k-1}, s_k]\}$. n is the number of cable segments and L is the cable's unstretched length. $w = [w_x \quad w_y \quad w_z]^T$ indicates the constant distributed force along the cable.

We want to find the tension vector as a function of s. And the following relation must hold

$$T\frac{dF}{dp}(s) = f_o - \sum_{i=1}^{k} \overline{f}_i - ws \tag{20}$$

where $\{s \in [0, L] \rightarrow \mathbb{R}, k \in [1, n] \rightarrow \mathbb{N} | s \in [s_{k-1}, s_k]\}$. We define:

$$T(p) = T\frac{dF}{dp} \tag{21}$$

where $T \in \mathbb{R}^3$, $F = [F_x \quad F_y \quad F_z]^T$. The substitution:

$$f_k = f_0 - \sum_{i=1}^{k} \overline{f_i} \tag{22}$$

where $\{k \in [0, n] \rightarrow \mathbb{N}, s \in [1, L] \rightarrow \mathbb{R} | s \in [s_{k-1}, s_k]\}$ gives:

$$T_s = \sqrt{(f_k - ws)^T (f_k - ws)} \tag{23}$$

Use of (18) we have:

$$T\frac{dF}{dp}(s) = \left(\frac{1}{EA} + \frac{1}{T}\right)^{-1} \frac{dF}{ds} = f_k - ws \tag{24}$$

Reordering and substituting (23) gives the final differential equation:

$$\frac{dF}{ds} = (f_n - ps)\left(\frac{1}{\sqrt{(f_k - ps)^T (f_k - ps)}} + \frac{1}{EA}\right) \tag{25}$$

where k is the actual cable segment. By integration of (25), the resulting force F_k which is an expression for the local solution within segment k of end point of the cable can be obtained.

4.4 Boundary Conditions

Boundary conditions must be given at both ends of the cable (upper end and lower end). As we assume that the vessel motion is fixed by using dynamic position control, the first boundary condition is given by fixing the position of the surface vessel. At the lower end, cable is connected to the vehicle. So, the second boundary

condition of lower end of the cable $X_0 = X_0(t)$ is given as a function of time. These two conditions can be expressed as follows:

$$x_0(0,t) = 0, \quad y_0(0,t) = 0, \quad z_0(0,t) = 0$$

And

$$x_L(L,t) = x_L, \quad y_L(L,t) = y_L, \quad z_L(L,t) = z_L$$

Where x_L, y_L and z_L are position of UV during its motion.

4.5 Cable Effects

The tension of the cable at the two-point, i.e. $F = (F_x, F_y, F_z)$, results in the additional forces and moments that affect the motion of the vehicle. The additional forces can be obtained by expressing the cable tension in the vehicle-fixed frame:

$$F_c(t) := \begin{bmatrix} F_{cX} \\ F_{cY} \\ F_{cZ} \end{bmatrix} = -R^T(\phi, \theta, \psi) W(\vartheta, \varphi) \begin{bmatrix} F_x \\ F_y \\ F_z \end{bmatrix} \tag{26}$$

In terms of the position of the tow-point in the vehicle-fixed frame, the cable induced moments are:

$$M_c(t) := \begin{bmatrix} M_{cX} \\ M_{cY} \\ M_{cZ} \end{bmatrix} = r_c \times F_c(t) = \begin{bmatrix} x_c \\ y_c \\ z_c \end{bmatrix} \times \begin{bmatrix} F_{cX} \\ F_{cY} \\ F_{cZ} \end{bmatrix} = \begin{bmatrix} y_c F_{cZ} - z_c F_{cY} \\ z_c F_{cX} - x_c F_{cZ} \\ x_c F_{cY} - y_c F_{cX} \end{bmatrix} \tag{27}$$

where $\overrightarrow{r_c} = (x_c, y_c, z_c)$ is vector from the center of the gravity of UV to the connected point between the cable and UV.

5 Simulation and Discussion

A shooting method based on the accurate analytical solution might be applied. Shooting method is used to compute the static equilibrium configuration of a composite single cable with boundary conditions specified at both ends. The inertial reference frame (X, Y, Z) is defined at surface of waterline and the first cable's

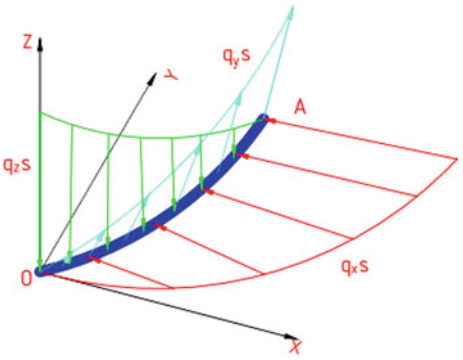

Fig. 5 The forces acting on the UC

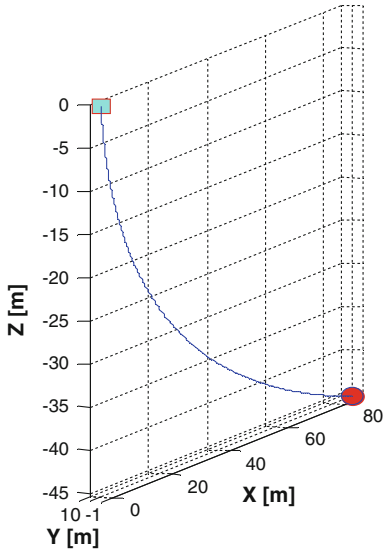

Fig. 6 Static configuration of UC

element is attached to the supported vessel. MATLAB's routine bvp4c was applied to these parameters, and an estimate of the end force was found. The results were dependent on the numerical option and the mesh in the variables. Figure 5 shows profile of 3-D forces acting on the UC.

Figure 6 shows a cable of length L attached to a blue point and a red point. These points are defined as the cable supports and they are fixed in space. Here, as in the simulation, the top end or blue point is assumed to be fixed to the support ship, the bottom or red point is attached to the UV. When the current is turned on, the cable is pushed to the left and during this motion, under the influence of the side current, and provided there is slack in the cable, the UC will form a curve. The position of the red point is calculated equal E_p = [86.40 −45.42] m. The Eq. 25 gives the end force equal f_{end} = [230.5 −117.9 −27.97]′ N.

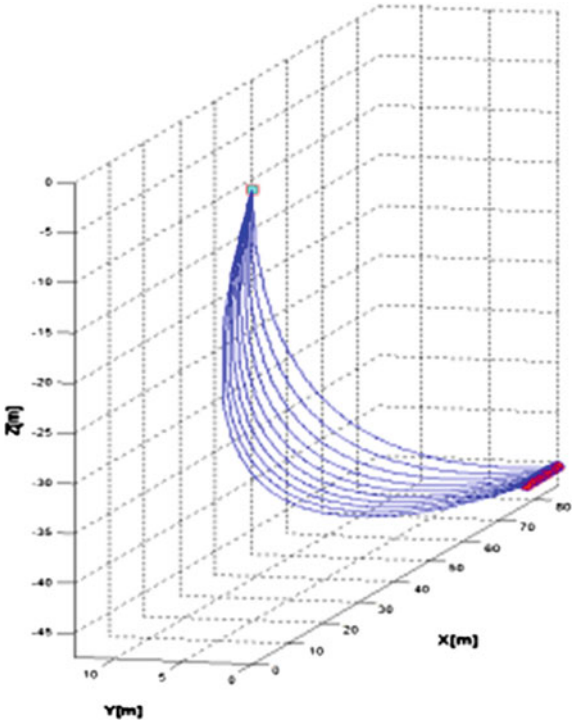

Fig. 7 Dynamic configuration of UC

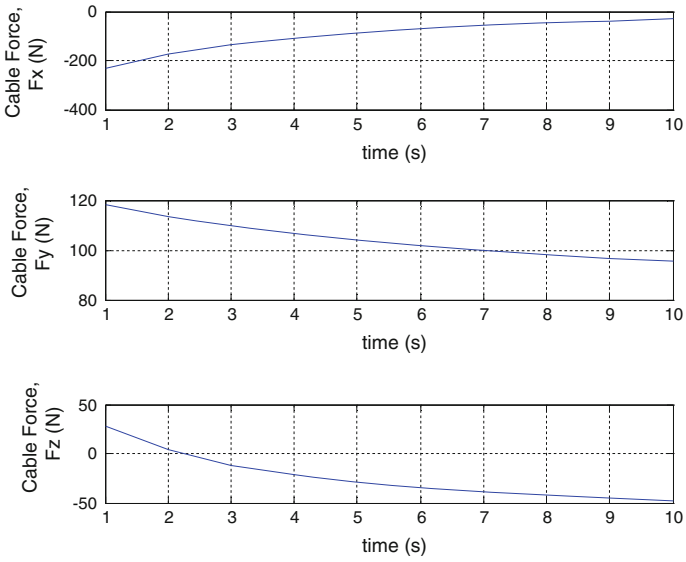

Fig. 8 The end point forces of UC

The dynamic configuration of UC and the end point forces of cable are shown in Figs. 7 and 8, respectively. It is observed from Fig. 7 that the trajectory of the red point move backward for about 10 m in 10 s because the speed of red point is 1 m/s. The end point forces in 3 dimensions of UC when the red point moves backward is shown in Fig. 8. As we can see from this figure that the end point forces increases gradually with increasing in time in three components F_x, F_y, F_z.

6 Conclusion

In this paper, a study on the dynamics of the UC for UV has been conducted. The modeling of the cable dynamics using catenary equations was presented. The catenary equations were used for representation of the forces acting on the UV where the cable is attached.

This paper presented the formulation and solution of governing equations to estimate the 3-D position and forces of the UC end point by the action of concentrated or distributed forces due to underwater currents. To numerically estimate the position and forces of the cable end, the dynamics equation was formulated as a two-point boundary value problem and the shooting method was applied. A simplified and fast estimation of the position and forces of the UC under the action of distributed and concentrated loads was presented. The validity of the proposed method was shown through simulation results.

The presented results for the two case studies show that the numerical scheme is good to estimate the position and forces of the cable end point under the action of concentrated and distributed forces which may vary along the cable. It is believed that the modeling, simulation results shown here can offer some important information about the interaction effects between the UV and UC for the designers of the related field.

Acknowledgements This research was a part of the project titled 'R&D center for underwater construction robotics', funded by the Ministry of Oceans and Fisheries (MOF) and Korea Institute of Marine Science & Technology Promotion (KIMST), Korea (PJT200539). Also, it was supported by the development of a multi-legged underwater walking robot project under the Ministry of land, infrastructure, and transport.

References

1. Albow CM, Schechter S (1983) Numerical simulation of undersea cable dynamics. Ocean Eng 10(6):443–457
2. Burgess JJ (1992) Equations of motion of a submerged cable with bending stiffness. Offshore Mar Arct Eng 1-A:283–289
3. Buckham B, Nahon M, Cote G (2000) Validation of a finite element model for slack ROV tethers. IEEE J Oceanic Eng 1129–1136

4. Feng Z, Allen R (2004) Evaluation of the effects of the communication cable on the dynamics of an underwater flight vehicle. Ocean Eng 31:1019–1035
5. Milinazzo F, Wilkie M, Latchman SA (1987) An efficient algorithm for the dynamics of towed cable systems. Ocean Eng 14(6):513–526
6. Sagatun Svein I (2001) The elastic cable under the action of concentrated and distributed forces. J Offshore Mech Arct Eng 123:43–45
7. Triantafyllou MS (1990) Cable mechanics with marine applications. Department of Ocean Engineering, Massachusetts Institute of Technology, Cambridge
8. Hooke R, Jeeves TA (1961) Direct search solution of numerical and statistical problems. J Assoc Comput Mach 8:212–229

Adaptive Backstepping Control Design for Trajectory Tracking of Automatic Guided Vehicles

Pandu Sandi Pratama, Jae Hoon Jeong, Sang Kwun Jeong, Hak Kyeong Kim, Hwan Seong Kim, Tae Kyeong Yeu, Sup Hong and Sang Bong Kim

Abstract This paper is to design an adaptive trajectory tracking controller for an Automatic Guided Vehicle (AGV) to track the desired reference trajectory with unknown slip. To do this task, the followings are done. Firstly, system description and mathematical modelings of a differential drive AGV system are presented. Kinematic model of AGV is derived based on the wheel configuration and the nonholonomic constraint. Dynamic model of AGV is obtained from the Lagrangian formula. Secondly, an adaptive backstepping trajectory tracking controller is designed. By choosing appropriate Lyapunov function based on its kinematic modeling of AGV system with unknown slip parameter stability is guaranteed, a control law and an update law to estimate the unknown slip parameter can be obtained. The simulation and experimental results show that the proposed controller successfully estimates the unknown parameters and tracks a reference trajectory.

Keywords Automatic guided vehicle · Tracking · Adaptive · Backstepping

1 Introduction

To track the generated trajectory, a trajectory tracking control is needed. In conventional AGV system, there were several kinds of navigation methods to track the generated trajectory such as a vision based line tracking algorithm [1], inductive

P.S. Pratama · J.H. Jeong · H.K. Kim · S.B. Kim (✉)
Pukyong National University, Busan 608-739, Korea
e-mail: kimsb@pknu.ac.kr

S.K. Jeong
Department of Automation System, Korea Polytechnics, Jinju 660-996, Korea

H.S. Kim
Korea Maritime and Ocean University, Busan 606-791, South Korea

T.K. Yeu · S. Hong
Technology Center for Offshore Plant Industries, KRISO Daejeon, Korea

V.H. Duy et al. (eds.), *AETA 2015: Recent Advances in Electrical Engineering and Related Sciences*, Lecture Notes in Electrical Engineering 371,
DOI 10.1007/978-3-319-27247-4_50

guidance using electrical wire buried under the floor [2], semi-guided navigation methodology by using magnetic tapes [3], navigation method based on wall following algorithm [4] and laser navigation system [5].

To track the given trajectory, several control algorithms has been proposed. A PID controller for trajectory tracking was proposed by [6]. The navigation of AGV using fuzzy control was proposed in [7]. Those controllers are easy to be applied to AGV system but not robust. A parameter-based controller design method has been proposed using sliding mode control theory in [8] and using Lyapunov stability in [5]. In those controllers, the stability of the system was guaranteed, but to find an appropriate controller law was not an easy task. Therefore, a backstepping control method was proposed in [9]. In parameter-based controller design, all parameters of the system should be known. However, in real AGV application, some parameters such as slip, wheel diameter, wheel distance and mass are changed during the operation caused by uneven load distribution or manufacturing imperfection, and loading the goods. Therefore, the controller should be adaptive to the changing of parameters.

To solve this task, this paper proposed an adaptive trajectory tracking controller for Automatic Guided Vehicle (AGV) to track the desired reference trajectory with unknown slip. Firstly, system description and mathematical modelings of a differential drive AGV system are presented. Secondly, an adaptive backstepping trajectory tracking controller is designed. By choosing appropriate Lyapunov function based on its kinematic modeling of AGV system with unknown slip parameter stability is guaranteed, a control law and an update law to estimate the unknown slip parameter can be obtained. The simulation and experimental results show that the proposed controller successfully estimates the unknown parameters and tracks a reference trajectory.

2 System Modeling

The AGV system used in this paper are shown in Fig. 1 as follows:

The slip ratio i of two wheels is defined as follows:

$$i = \frac{(r\dot{\phi}_L - v_L)}{r\dot{\phi}_L} = \frac{(r\dot{\phi}_R - v_R)}{r\dot{\phi}_R} \quad \text{and} \quad 0 \leq i < 1 \tag{1}$$

where r is the radius of the wheel, $\dot{\phi}_L$ and $\dot{\phi}_R$ are the angular velocities of the left and the right wheels, respectively. v_L and v_R are the linear velocities of the left and right wheels with slip.

A slip parameter is defined as:

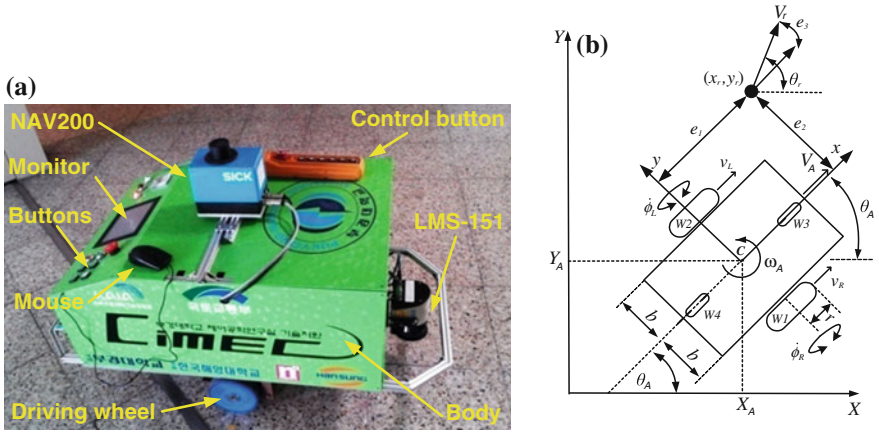

Fig. 1 Automatic guided vehicles (AGV) system. **a** System design. **b** System model

$$c = \frac{1}{(1-i)} \quad \text{and} \quad 0 \le i < 1 \tag{2}$$

2.1 Kinematic Model

The kinematic modeling of a AGV including the slip parameter can be written as

$$\begin{bmatrix} \dot{X}_A \\ \dot{Y}_A \\ \dot{\theta}_A \end{bmatrix} = \begin{bmatrix} \frac{r}{2c}\cos\theta_A & \frac{r}{2c}\cos\theta_A \\ \frac{r}{2c}\sin\theta_A & \frac{r}{2c}\sin\theta_A \\ \frac{r}{bc} & \frac{-r}{bc} \end{bmatrix} \begin{bmatrix} \dot{\phi}_R \\ \dot{\phi}_L \end{bmatrix} \Leftrightarrow \dot{\boldsymbol{\xi}}_1 = \mathbf{S}(\boldsymbol{\xi}_1)\dot{\boldsymbol{\Phi}} \tag{3}$$

If the velocity vector of the AGV in local coordinate is defined as $\boldsymbol{\eta}_A = [V_A \quad \omega_A]^T$, the relations between $\boldsymbol{\Phi}$ and $\boldsymbol{\eta}_A$ including the slip can be described as follows:

$$\begin{bmatrix} V_A \\ \omega_A \end{bmatrix} = \begin{bmatrix} \frac{r}{2c} & \frac{r}{2c} \\ \frac{r}{bc} & -\frac{r}{bc} \end{bmatrix} \begin{bmatrix} \dot{\phi}_R \\ \dot{\phi}_L \end{bmatrix} \quad \text{or} \quad \begin{bmatrix} \dot{\phi}_R \\ \dot{\phi}_L \end{bmatrix} = \frac{1}{r} \begin{bmatrix} c & \frac{bc}{2} \\ c & -\frac{bc}{2} \end{bmatrix} \begin{bmatrix} V_A \\ \omega_A \end{bmatrix} \tag{4}$$

$$\boldsymbol{\eta}_A = \mathbf{T}\dot{\boldsymbol{\Phi}} \qquad \dot{\boldsymbol{\Phi}} = \mathbf{T}^{-1}\boldsymbol{\eta}_A$$

Substituting Eq. (4) into Eq. (3) yields

$$\dot{\xi}_1 = \begin{bmatrix} \dot{X}_A \\ \dot{Y}_A \\ \dot{\theta}_A \end{bmatrix} = \begin{bmatrix} \cos\theta_A & 0 \\ \sin\theta_A & 0 \\ 0 & 1 \end{bmatrix} \begin{bmatrix} V_A \\ \omega_A \end{bmatrix} \Leftrightarrow \begin{array}{l} \dot{\xi}_1 = \mathbf{J}(\xi_1)\boldsymbol{\eta}_A \\ \quad = \mathbf{S}(\xi_1)\mathbf{T}^{-1}\boldsymbol{\eta}_A \end{array} \tag{5}$$

2.2 Dynamic Modeling

The system dynamics of a nonholonomic AGV is as follows:

$$\mathbf{M}(\xi_1)\,\ddot{\xi}_1 + \mathbf{V}(\xi_1, \dot{\xi}_1)\dot{\xi}_1 = \mathbf{B}(\xi_1)\boldsymbol{\tau} - \mathbf{A}^T(\xi_1)\boldsymbol{\lambda} \tag{6}$$

where $\mathbf{M}(\xi_1) \in \mathbf{R}^{n\times n}$ is a symmetric positive definite inertia matrix; $\mathbf{V}(\xi_1, \dot{\xi}_1) \in \mathbf{R}^{n\times n}$ is a centripetal and Coriolis matrix; $\mathbf{B}(\xi_1) \in \mathbf{R}^{n\times r}$ is an input transformation matrix; $\mathbf{A}(\xi_1) \in \mathbf{R}^{n\times m}$ is a matrix of nonholonomic constraints; $\boldsymbol{\tau} = [\,\tau_R \quad \tau_L\,]^T$ is an input torque vector consisting of torques exerted on right and left wheels; and $\boldsymbol{\lambda} \in \mathbf{R}^m$ a constraint force vector.

Differentiating Eq. (3), substituting this result in Eq. (6) and multiplying by $\mathbf{S}^T$, the constraint term $\mathbf{A}^T(\xi_1)\boldsymbol{\lambda}$ of Eq. (6) is eliminated. Dynamic model in platform system of the nonholonomic AGV with the constraint is as follows:

$$\mathbf{S^T M S}\,\ddot{\boldsymbol{\Phi}} + \mathbf{S^T}(\mathbf{M\dot{S}} + \mathbf{VS})\dot{\boldsymbol{\Phi}} = S^{\mathbf{T}}\mathbf{B}\tau \tag{7}$$

Multiplying by $(\mathbf{S}^T\mathbf{B})^{-1}$ in both sides Eq. (7) yields:

$$\bar{\mathbf{M}}(\xi_1)\,\ddot{\boldsymbol{\Phi}} + \bar{\mathbf{V}}(\xi_1, \dot{\xi}_1)\dot{\boldsymbol{\Phi}} = \tau \tag{8}$$

where

$$\bar{\mathbf{M}}(\xi_1) = (\mathbf{S}^T\mathbf{B})^{-1}\mathbf{S}^T\mathbf{MS} \in \mathbf{R}^{r\times(n-m)}, \quad \bar{\mathbf{V}}(\xi_1) = (\mathbf{S}^T\mathbf{B})^{-1}\mathbf{S}^T(\mathbf{MS} + \mathbf{VS}) \in \mathbf{R}^{r\times(n-m)}$$

$$\bar{\mathbf{M}} = \begin{bmatrix} \frac{r^2}{4b^2}(mb^2 + I) + I_w & \frac{r^2}{4b^2}(mb^2 - I) \\ \frac{r^2}{4b^2}(mb^2 - I) & \frac{r^2}{4b^2}(mb^2 + I) + I_w \end{bmatrix},$$

$$\bar{\mathbf{V}} = \begin{bmatrix} 0 & \frac{r^2}{2b} m_c d\dot{\theta}_A \\ -\frac{r^2}{2b} m_c d\dot{\theta}_A & 0 \end{bmatrix}$$

$$I = m_c d^2 + 2m_w b^2 + I_c + 2I_m$$

where $m = m_c + 2m_w$ is total mass of the AGV, m_c is mass of the body without driving wheels, m_w is mass of each wheel, I_m is moment of inertia of each motor, I_w

is moment of inertia of each wheel, I_c is moment of inertia of the body, and d is distance between geometric center and mass center. Using Lagrange formula, $\bar{\mathbf{M}}$ and $\bar{\mathbf{V}}$ can be obtained [10].

3 Controller Design

The purpose of this section is to design an adaptive trajectory tracking controller for AGV to track the desired reference trajectory $\boldsymbol{\xi}_\mathbf{r} = [x_r(t), y_r(t), \theta_r(t)]^T$ with reference velocities $\boldsymbol{\eta}_r = [\, V_r(t) \quad \omega_r(t) \,]^T$. $(x_r(t), y_r(t))$ is reference position of AGV in global coordinate, θ_r is AGV reference orientation, $V_r(t)$ is reference linear velocity and $\omega_r(t)$ is reference angular velocity. The following procedure is to design a control law that minimizes the tracking errors.

3.1 Non-adaptive Kinematic Controller Design

The first procedure is to determine a desired velocity control law that drives the tracking error between the current posture vector $\boldsymbol{\xi}_1$ and the reference posture vector $\boldsymbol{\xi}_\mathbf{r}$.

A kinematic tracking error vector $\mathbf{e}_c$ and its time derivative $\dot{\mathbf{e}}_c$ are defined as:

$$\mathbf{e}_c = \begin{bmatrix} e_1 \\ e_2 \\ e_3 \end{bmatrix} = \begin{bmatrix} \cos\theta_A & \sin\theta_A & 0 \\ -\sin\theta_A & \cos\theta_A & 0 \\ 0 & 0 & 1 \end{bmatrix} \begin{bmatrix} X_r - X_A \\ Y_r - X_A \\ \theta_r - \theta_A \end{bmatrix} \tag{9}$$

$$\dot{\mathbf{e}}_c = \begin{bmatrix} \dot{e}_1 \\ \dot{e}_2 \\ \dot{e}_3 \end{bmatrix} = \begin{bmatrix} \cos e_3 & 0 \\ \sin e_3 & 0 \\ 0 & 1 \end{bmatrix} \begin{bmatrix} V_r \\ \omega_r \end{bmatrix} + \begin{bmatrix} -1 & e_2 \\ 0 & -e_1 \\ 0 & -1 \end{bmatrix} \begin{bmatrix} V_A \\ \omega_A \end{bmatrix} \tag{10}$$

To guarantee the stability of the system, Lyapunov function is chosen as:

$$V_0 = \frac{1}{2}\left(e_1^2 + e_2^2\right) + \frac{(1 - \cos e_3)}{k_2} > 0 \tag{11}$$

and the kinematic derivatives becomes

$$\begin{aligned} \dot{V}_0 &= e_1\dot{e}_1 + e_2\dot{e}_2 + \dot{e}_3 \frac{\sin e_3}{k_2} \\ &= e_1(-V_A + V_r \cos e_3) + \frac{1}{k_2}(\sin e_3)(\omega_r - \omega_A + k_2 e_2 V_r) \end{aligned} \tag{12}$$

To achieve $\dot{V}_0 \leq 0$, a desired kinematic control law vector is chosen as follows:

$$\boldsymbol{\eta}_{\mathbf{d}} \equiv \boldsymbol{\eta}_A = \begin{bmatrix} V_A \\ \omega_A \end{bmatrix} = \begin{bmatrix} V_r \cos e_3 + k_1 e_1 \\ \omega_r + k_2 V_r e_2 + k_3 \sin e_3 \end{bmatrix} \tag{13}$$

Substituting Eq. (13) into Eq. (12) yields

$$\dot{V}_0 = -k_1 e_1^2 - \frac{k_3}{k_2} \sin e_3 \leq 0 \tag{14}$$

The conditions $V_0 > 0$ and $\dot{V}_0 \leq 0$ show the boundness of $\mathbf{e}_c$, and by Barbalat's Lemma, Eqs. (10), (13) and (14), the error $\mathbf{e}_c$ converge to zero.

The desired kinematic control law vector $\boldsymbol{\eta}_A = [\, V_A \quad \omega_A \,]$ of (13) can be used directly as the reference of dynamic controller $\boldsymbol{\eta}_{\mathbf{d}} = [\, V_{Ad} \quad \omega_{Ad} \,]$. Therefore, since $(\boldsymbol{\eta}_{\mathbf{d}} = \boldsymbol{\eta}_A)$, a desired wheel angular velocity vector $\boldsymbol{\Phi}_{\mathbf{d}}$ is given by

$$\begin{bmatrix} \dot{\phi}_{Rd} \\ \dot{\phi}_{Ld} \end{bmatrix} = \frac{1}{r} \begin{bmatrix} c & \frac{bc}{2} \\ c & -\frac{cb}{2} \end{bmatrix} \begin{bmatrix} V_A \\ \omega_A \end{bmatrix} \Leftrightarrow \boldsymbol{\Phi}_{\mathbf{d}} = \mathbf{T}^{-1} \boldsymbol{\eta}_{\mathbf{d}} \tag{15}$$

3.2 Dynamic Controller Design

By a feedback linearization of the system, a input torque vector τ is defined by computed torque method as follows:

$$\boldsymbol{\tau} = \bar{\mathbf{M}}(\mathbf{q}) \mathbf{u}_{\mathbf{D}} + \bar{\mathbf{V}}(\xi_1, \dot{\xi}_1) \boldsymbol{\Phi} \tag{16}$$

where $\mathbf{u}_{\mathbf{D}}$ is the dynamic control input.

From Eqs. (3), (8) and (16), dynamic control problem can be converted into the kinematic control problem as follows:

$$\begin{cases} \dot{\xi}_1 = \mathbf{S}(\xi_1) \dot{\boldsymbol{\Phi}} \\ \ddot{\boldsymbol{\Phi}} = \mathbf{u}_{\mathbf{D}} \end{cases} \tag{17}$$

To convert the kinematic desired wheel angular velocity control law $\dot{\Phi}_{\mathbf{d}}$ into the input torque vector $\boldsymbol{\tau}$ that will be applied to the system, a dynamic tracking wheel angular velocity error vector is defined by

$$\mathbf{e}_{\mathbf{d}} = \begin{bmatrix} e_4 \\ e_5 \end{bmatrix} = \dot{\boldsymbol{\Phi}} - \dot{\boldsymbol{\Phi}}_{\mathbf{d}} \tag{18}$$

where $\dot{\boldsymbol{\Phi}} - \dot{\boldsymbol{\Phi}}_{\mathbf{d}}$ represents the error between the real wheel angular velocity vector $\dot{\boldsymbol{\Phi}}$ and the desired wheel angular velocity vector $\dot{\boldsymbol{\Phi}}_{\mathbf{d}}$ of the AGV.

The dynamic control input $\mathbf{u_D} = [\,u_1 \quad u_2\,]^T$, which assures that $\mathbf{e_d}$ converges to zero, is given by the following expression:

$$\mathbf{u_D} = \ddot{\mathbf{\Phi}}_\mathbf{d} - \mathbf{K_4 e_d} \quad \text{and} \quad \mathbf{K_4} = \begin{bmatrix} k_4 & 0 \\ 0 & k_4 \end{bmatrix} \tag{19}$$

where k_4 is a positive constant.

From Eqs. (18) and (19), the derivative of the error $\mathbf{e_d}$ is given by

$$\dot{\mathbf{e}}_\mathbf{d} = \begin{bmatrix} \dot{e}_4 \\ \dot{e}_5 \end{bmatrix} = \ddot{\mathbf{\Phi}} - \ddot{\mathbf{\Phi}}_d = \mathbf{u_D} - \ddot{\mathbf{\Phi}}_d = -\mathbf{K_4 e_d} = -\begin{bmatrix} k_4 & 0 \\ 0 & k_4 \end{bmatrix} \begin{bmatrix} e_4 \\ e_5 \end{bmatrix} \tag{20}$$

To show that an entire tracking error vector $\mathbf{e} = [\,\mathbf{e_c} \quad \mathbf{e_d}\,]^T$ goes to zero at $t \to \infty$, the following Lyapunov function candidate is chosen:

$$V_1 = V_0 + \frac{1}{2k_4}\left(e_4^2 + e_5^2\right) = \frac{1}{2}\left(e_1^2 + e_2^2\right) + \frac{(1 - \cos e_3)}{k_2} + \frac{1}{2k_4}\left(e_4^2 + e_5^2\right) > 0 \tag{21}$$

and its derivatives becomes

$$\dot{V}_1 = e_1\dot{e}_1 + e_2\dot{e}_2 + \dot{e}_3\frac{\sin e_3}{k_2} + \frac{e_4}{k_4}\dot{e}_4 + \frac{e_5}{k_4}\dot{e}_5 = -k_1 e_1^2 - \frac{k_3}{k_2}\sin^2 e_3 - e_4^2 - e_5^2 \leq 0 \tag{22}$$

The conditions $V_1 > 0$ and $\dot{V}_1 \leq 0$ shows the boundness of $\mathbf{e} = [\,e_1 \quad e_2 \quad e_3 \quad e_4 \quad e_5\,]^T$, and by Barbalat's Lemma, Eqs. (10), (13), (19), (20) and (22), it can be proved that the entire tracking error vector $\mathbf{e}$ converges to zero.

3.3 *Adaptive Backstepping Control Design*

If the parameter i in Eq. (1) is unknown, c is unknown and the desired wheel angular velocity vector of Eq. (15) is invalid. Therefore, an update law to estimate the parameter $c = 1/(1 - i)$ is needed.

Replacing $\mathbf{\Phi}$ with the desired wheel angular velocity vector $\mathbf{\Phi_d}$, Eq. (4) can be written into

$$\begin{bmatrix} V_A \\ \omega_A \end{bmatrix} = \begin{bmatrix} \frac{r}{2c} & \frac{r}{2c} \\ \frac{r}{bc} & -\frac{r}{bc} \end{bmatrix} \begin{bmatrix} \dot{\phi}_{Rd} \\ \dot{\phi}_{Ld} \end{bmatrix} \tag{23}$$

Substituting Eq. (23) into Eq. (10), the derivative errors can be written as follows:

$$\begin{bmatrix} \dot{e}_1 \\ \dot{e}_2 \\ \dot{e}_3 \end{bmatrix} = \begin{bmatrix} V_r \cos e_3 \\ V_r \sin e_3 \\ \omega_r \end{bmatrix} + \begin{bmatrix} -1 & e_2 \\ 0 & -e_1 \\ 0 & -1 \end{bmatrix} \begin{bmatrix} \frac{r}{2c} & \frac{r}{2c} \\ \frac{r}{bc} & -\frac{r}{bc} \end{bmatrix} \begin{bmatrix} \dot{\phi}_{Rd} \\ \dot{\phi}_{Ld} \end{bmatrix} \tag{24}$$

For unknown constant slip parameter, Eq. (23) can't be applied. To solve this problem, the estimation $\hat{c}$ of c is needed. By introducing the estimation $\hat{c}$ for c, Eq. (4) can be written as:

$$\mathbf{\Phi_d} = \begin{bmatrix} \dot{\phi}_{Rd} \\ \dot{\phi}_{Ld} \end{bmatrix} = \frac{1}{r} \begin{bmatrix} \hat{c} & \frac{b}{2}\hat{c} \\ \hat{c} & -\frac{b}{2}\hat{c} \end{bmatrix} \begin{bmatrix} V_{As} \\ \omega_{As} \end{bmatrix} = \frac{1}{r} \hat{\mathbf{T}}^{-1} \mathbf{\eta_{ds}} \tag{25}$$

where $\mathbf{\Phi_d}$ is the desired wheel angular velocity vector, and $\mathbf{\eta_{ds}}$ are the estimated desired velocity vector of the AGV, V_{As} and ω_{As} are the estimated desired linear velocity and the estimated desired angular velocity of AGV to satisfy $\mathbf{\Phi_d}$.

Replacing c with $\hat{c}$ in Eq. (24), the kinematic modeling of a AGV can be written as

$$\begin{bmatrix} \dot{e}_1 \\ \dot{e}_2 \\ \dot{e}_3 \end{bmatrix} = \begin{bmatrix} V_r \cos e_3 \\ V_r \sin e_3 \\ \omega_r \end{bmatrix} + \begin{bmatrix} -1 & e_2 \\ 0 & -e_1 \\ 0 & -1 \end{bmatrix} \begin{bmatrix} \frac{r}{2\hat{c}} & \frac{r}{2\hat{c}} \\ \frac{r}{b\hat{c}} & -\frac{r}{b\hat{c}} \end{bmatrix} \begin{bmatrix} \dot{\phi}_{Rd} \\ \dot{\phi}_{Ld} \end{bmatrix} \tag{26}$$

Substituting Eq. (4) into Eq. (26) becomes:

$$\begin{bmatrix} \dot{e}_1 \\ \dot{e}_2 \\ \dot{e}_3 \end{bmatrix} = \begin{bmatrix} V_r \cos e_3 \\ V_r \sin e_3 \\ \omega_r \end{bmatrix} + \begin{bmatrix} -1 & e_2 \\ 0 & -e_1 \\ 0 & -1 \end{bmatrix} \begin{bmatrix} \frac{\hat{c}}{c} & 0 \\ 0 & \frac{\hat{c}}{c} \end{bmatrix} \begin{bmatrix} V_{As} \\ \omega_{As} \end{bmatrix} \tag{27}$$

The estimation error is defined as follows:

$$\tilde{c} = c - \hat{c} \tag{28}$$

where the c is the true value of the slip parameter, and $\tilde{c}$ is the estimation error of slip parameter.

Using Eqs. (28), and (27) can be rewritten as follows:

$$\dot{\mathbf{e}}_c = \begin{bmatrix} \dot{e}_1 \\ \dot{e}_2 \\ \dot{e}_3 \end{bmatrix} = \begin{bmatrix} V_r \cos e_3 \\ V_r \sin e_3 \\ \omega_r \end{bmatrix} + \begin{bmatrix} -1 & e_2 \\ 0 & -e_1 \\ 0 & -1 \end{bmatrix} \begin{bmatrix} (1 - \frac{\tilde{c}}{c}) V_{As} \\ (1 - \frac{\tilde{c}}{c}) \omega_{As} \end{bmatrix} \tag{29}$$

To obtain an update law for obtaining the estimation $\hat{c}$, the following Lyapunov function is considered.

$$V_3 = V_1 + \frac{\tilde{c}^2}{2\gamma c} > 0 \tag{30}$$

with $c \geq 1$ and $\gamma > 0$,

The derivatives of Eq. (30) becomes

$$\dot{V}_3 = e_1\dot{e}_1 + e_2\dot{e}_2 + \dot{e}_3\frac{\sin e_3}{k_2} + \frac{e_4}{k_4}\dot{e}_4 + \frac{e_5}{k_4}\dot{e}_5 + \frac{\tilde{c}\dot{\tilde{c}}}{\gamma c} \tag{31}$$

Substituting Eqs. (20) and (29) into Eq. (31) yields:

$$\begin{aligned}\dot{V}_3 = {} & e_1(-V_{As} + V_r\cos e_3) + \frac{\sin e_3}{k_2}(\omega_r - \omega_{As} + k_2 e_2 V_r) - e_4^2 - e_5^2 \\ & - \frac{\tilde{c}}{c}\left[\frac{\dot{\tilde{c}}}{\gamma} - \left(V_{As}e_1 + \frac{\omega_A \sin e_3}{2k_2}\right)\right]\end{aligned} \tag{32}$$

To achieve $\dot{V}_3 \leq 0$, an estimated desired kinematic control law vector is chosen as follows:

$$\boldsymbol{\eta}_{\mathbf{ds}} = \begin{bmatrix} V_{As} \\ \omega_{As} \end{bmatrix} = \begin{bmatrix} V_r\cos e_3 + k_1 e_1 \\ \omega_r + k_2 V_r e_2 + k_3 \sin e_3 \end{bmatrix} \tag{33}$$

Therefore, the estimated desired kinematic control law vector for the system with unknown slip parameter in Eq. (33) is equal to the kinematic control law vector for the system without unknown slip parameter in Eq. (13).

The update law for obtaining the estimation $\hat{c}$ can be chosen as

$$\dot{\tilde{c}} = \gamma\left(V_{As}e_1 + \frac{\omega_{As}\sin e_3}{2k_2}\right) \tag{34}$$

Substituting Eqs. (33) and (34) into Eq. (32), $\dot{V}_3$ becomes

$$\dot{V}_3 = \dot{V}_1 = -k_1 e_1^2 - \frac{k_3}{k_2}\sin^2 e_3 - e_4^2 - e_5^2 \leq 0 \tag{35}$$

To guarantees the closed-loop stability, it must be shown that the equilibrium point of $\mathbf{e} = [\,e_1 \quad e_2 \quad e_3 \quad e_4 \quad e_5\,]^T = \mathbf{0}$ is asymptotically stable.

The e_3 is bounded in the domain D as $D = \{e \in R^3 | -\pi < e_3 < \pi\}$. The Lyapunov function given in Eq. (30) is positive definite in D with its derivative vector $\dot{V}_3 \leq 0$ in D. This implies that V_3 is a nonincreasing function that converges to some constant value and the entire tracking error vector $\mathbf{e}$ and the estimation parameter $\tilde{c}$ are bounded. Since the reference velocity vector $\boldsymbol{\eta}_{\mathbf{r}} = [\,V_r \quad \omega_r\,]^T$ is assumed to be bounded, the desired kinematic velocity $\boldsymbol{\eta}_{\mathbf{ds}}$ of the AGV is also

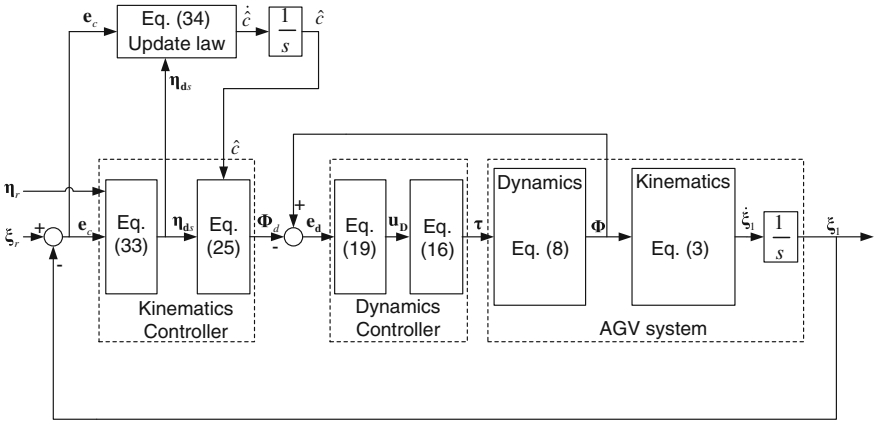

Fig. 2 Block diagram of the proposed adaptive backstepping control

bounded from Eq. (33). Thus, $\dot{\mathbf{e}}$ is bounded by Eqs. (20) and (29). After all, $\ddot{V}_3(\mathbf{e}, \dot{\mathbf{e}})$ given by

$$\ddot{V}_3 = -2k_1 e_1 \dot{e}_1 - \frac{2k_3}{k_2} \sin e_3 \cos e_3 \dot{e}_3 - 2e_4 \dot{e}_4 - 2e_5 \dot{e}_5 \tag{36}$$

is also bounded.

Since V_3 is a nonincreasing function that converges to some constant value, Barbalat's Lemma shows that $\dot{V}_3 \to 0$ as $t \to \infty$ from the boundness of $\ddot{V}_3$. Thus, e_1, e_3, e_4 and e_5 tend to zero as $t \to \infty$. From Eq. (34), $\hat{c}$ is constant. e_2 must also converge to zero.

Since $e_3 \to 0$, $\dot{e}_3 = 0$. If $V_r \neq 0$ and $\tilde{c} = 0$ as $t \to \infty$, then $e_2 \to 0$ as $t \to \infty$. Thus, the equilibrium point $\mathbf{e} = 0$ is asymptotically stable. e_2 is constant for $\tilde{c} \neq 0$. Figure 2 shows the block diagram of proposed controller.

4 Simulation and Experimental Result

To clarify the effectiveness of the proposed controllers, simulation and experiment are done. The physical parameter and initial values for the model are given by Table 1.

The reference trajectory is shown as in Fig. 3a. To verify the effectiveness of the proposed adaptive backstepping controller, the slip parameter $c = 1.25$ is added every time the AGV turning as shown in Fig. 3b. In straight condition, slip parameter is $c = 1$. In this simulation and experiment, slip parameters are 1.25 at the time intervals $t = 35 - 49$ s, $t = 61 - 68$ s, $t = 100 - 114$ s, $t = 126 - 140$ s,$t = 152 - 166$ s, $t = 195 - 209$ s, $t = 241 - 248$ s, $t = 281 - 288$ s,$t = 320 - 334$ s, $t = 363 - 377$ s,$t = 389 - 403$ s, $t = 414 - 428$ s, and $t = 461 - 468$ s.

Table 1 Parameter and initial value

Parameter	Value	Parameter	Value	Parameter	Value
b	0.3 m	$X_A(0)$	1.5 m	$\omega_A(0)$	0 rad/s
r	0.075 m	$Y_A(0)$	2.5 m	$\hat{a}(0)$	1
m_w	1 kg	$\theta_A(0)$	$\pi/2$ rad	$\hat{c}(0)$	1
k_1	3 s^{-1}	$V_A(0)$	0 m/s	γ	100 m^{-2}
k_2	3 m^{-2}	I_w	1.08 kg m^2	m_c	80 kg
k_3	2 rad/s	I_c	9.5 kg m^2	d	0 m
k_4	10 s^{-2}	I_w	0.187 kg m^2		

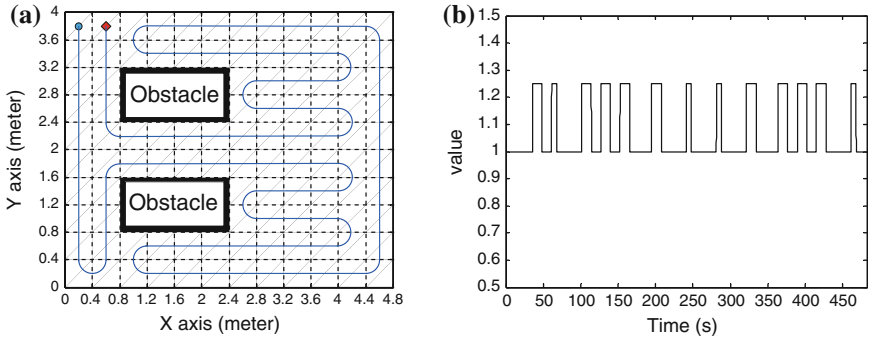

Fig. 3 Reference trajectory and slip parameter c

The simulation and experiment results are shown in Figs. 4, 5, 6 and 7. Figure 4a shows the desired kinematic control law vector $\boldsymbol{\eta}_\mathbf{d}$. The linear velocity V_A is 0.1 m/s in straight path, and V_A is 0.05 m/s in turning path. The angular velocity ω_A is 0 rad/s in straight path and 0.25 rad/s in turning path. The kinematic control law makes AGV be adaptive to the changing of slip parameter. Figure 4b shows the input torque vector $\boldsymbol{\tau}$. At the starting points and the end points of turning, the torque

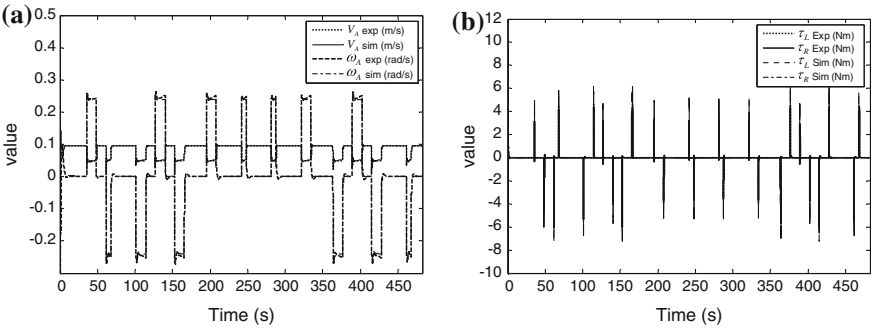

Fig. 4 Desired kinematic control law vector $\boldsymbol{\eta}_\mathbf{d}$ and Input torque vector $\boldsymbol{\tau}$

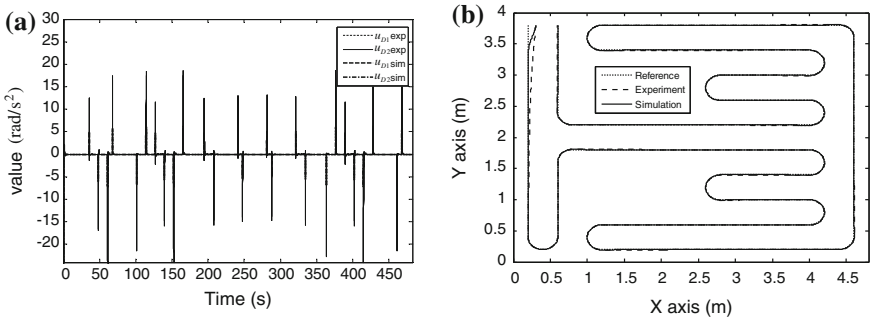

Fig. 5 Dynamic control input vector $\mathbf{u_D}$ and trajectory tracking output

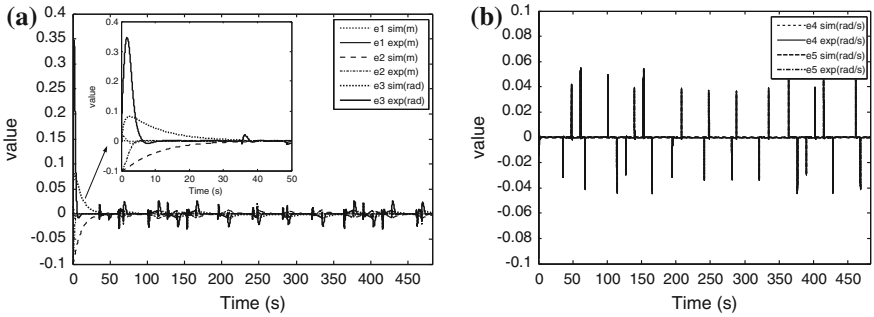

Fig. 6 Kinematic and dynamic tracking error vectors. **a** Kinematic tracking error vector $\mathbf{e_c}$. **b** Dynamic tracking velocity error vector $\mathbf{e_d}$

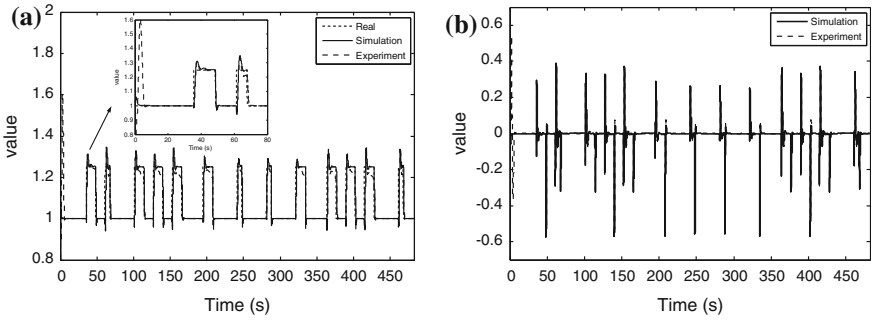

Fig. 7 Estimation $\hat{c}$ of the slip parameter and update law

vector $\boldsymbol{\tau}$ is changed roughly since the desired wheel angular velocities are changed and slip parameters is changed.

Figure 5a shows the dynamic control input vector $\mathbf{u_D}$ of the proposed adaptive backstepping controller. The controller values are bounded around ± 20 rad/s^2.

Figure 5b shows the trajectory tracking result obtained from simulation and experiment. At the beginning, the AGV adjusts its posture quickly to reduce the initial error and tracks the reference trajectory successfully.

Figure 6a shows the kinematic tracking error vector $\mathbf{e}_c$. It shows the kinematic tracking errors converge to zero after 5 s and at the times $t = 35$ s and $t = 50$ s, the kinematic tracking errors increase due to the step change in the slip parameter. At the starting points and the end points of turning, the kinematic tracking error vector $\mathbf{e}_c$ is changed roughly since the reference velocities are changed. The e_1 is bounded around ± 0.01 m, the e_2 is bounded around ± 0.015 m, and the e_3 is bounded around ± 0.03 rad. Figure 6b shows the dynamic tracking wheel angular velocity error vector $\mathbf{e_d}$. It can be seen that the tracking wheel angular velocity error vector also converges to zero. The dynamic tracking wheel angular velocity error vector $\mathbf{e_d}$ converges to zero faster than the kinematic tracking wheel angular error vector $\mathbf{e}_c$. At the starting points and the end points of turning, the dynamic tracking wheel angular velocity error vector $\mathbf{e_d}$ is changed roughly since the reference wheel angular velocities are changed. The error vector $\mathbf{e_d}$ is bounded around ± 0.06 rad/s.

Figure 7a shows the estimation $\hat{c}$ of the slip parameter. From $t = 0$ s to $t = 35$ s, the value of c is 1. This represents the condition without slip $(i = 0)$. From $t = 35$ s to $t = 50$ s, the value of c is 1.25. This represents the condition with slip $(i = 0.2)$. The simulation and experiment result shows that estimation $\hat{c}$ follows the real value c. At $t = 0$ s, the errors e_c, e_d are not equal to zero. Therefore, the value of estimation $\hat{c}$ is changed. At $t = 5$ s, the value of estimation $\hat{c}$ converges to the real value c. At $t = 35$ s and $t = 50$ s, the value of estimation $\hat{c}$ successfully converges to the real value. At the starting points and the end points of turning, the estimation $\hat{c}$ of the slip parameter is changed roughly since the reference velocities are changed. Figure 7b shows the update law $\dot{\hat{c}}$ for estimating of the slip parameter. The value of update law is changed since the value of slip parameter is increased. The update law is bounded around $0.48\ \mathrm{s}^{-1}$.

5 Conclusion

An adaptive trajectory tracking controller for Automatic Guided Vehicle (AGV) was proposed to track the desired reference trajectory with unknown slip. Firstly, system description and mathematical modelings of a differential drive AGV system were presented. Secondly, an adaptive backstepping trajectory tracking controller is designed. The simulation and experimental results show that the proposed controller successfully estimates the unknown parameters and tracks the reference trajectory. The linear velocity of AGV V_A is 0.1 m/s in straight path, and V_A is 0.05 m/s in turning path. The angular velocity of AGV ω_A is 0 rad/s in straight line, and 0.25 rad/s in turning line. The e_1 is bounded around ± 0.01 m, the e_2 is bounded around ± 0.015 m, and the e_3 is bounded around ± 0.03 rad. The error vector $\mathbf{e_d}$ is bounded around ± 0.06 rad/s. The update law is bounded around $0.48\ \mathrm{s}^{-1}$.

Acknowledgement This study is a part of the results of the R&D project, Development of a deep-Seabed Mining Technologies, supported by Korea Government, Ministry of Oceans and Fisheries. Authors are indebted to appreciate their full supports of this pioneering work.

References

1. Armesto L, Tornero J (2009) Automation of industrial vehicles: a vision-based line tracking application. In: ETFA 2009—2009 IEEE conference on emerging technologies and factory automation
2. Chen C, Wang B, Ye QT (2004) Application of automated guided vehicle (AGV) based on inductive guidance for newsprint rolls transportation system. J Donghua Univ 21:88–92
3. Fujimoto T, Ota J, Arai T, Ueyama T, Nishiyama T (2001) Semi-guided navigation of AGV through iterative learning. In: International conference on intelligent robots and systems. Expanding the societal role of Robotics in the the next millennium, pp 968–973
4. Chen YS, Yao L (2009) Robust type-2 fuzzy control of an automatic guided vehicle for wall-following. In: 2009 International conference of soft computing and pattern recognition, pp 172–177
5. Bui TL, Doan PT, Park SS, Kim HK, Kim SB (2013) AGV trajectory control based on laser sensor navigation. Int J Sci Eng 4:16–20
6. Turki YA, Abdulkareem AA (2012) PSO-based optimum design of PID controller for mobile robot trajectory tracking. Int J Comput Appl 47:30–35
7. Lin H-H, Tsai C-C (2008) Laser pose estimation and tracking using fuzzy extended information filtering for an autonomous mobile robot. J Intell Robot Syst 53:119–143
8. Solea R, Filipescu A, Nunes U (2009) Sliding-mode control for trajectory-tracking of a wheeled mobile robot in presence of uncertainties. In: 2009 7th Asian control conference, pp 1701–1706
9. Jiang ZP, Nijmeijer H (1997) Tracking control of mobile robots: a case study in backstepping. Automatica 33:1393–1399
10. Chung TL, Bui TH, Kim SB (2004) Sliding mode control of two-wheeled welding mobile Robot for tracking smooth curved welding path. KSME Int J 18:1094–1106

Obstacle Avoidance Control for Four Wheels Independent Steering Automatic Guided Vehicles

Pandu Sandi Pratama, Amruta Vinod Gulalkari, Jin Wook Kim, Chung Hwan Lee, Tae-Kyeong Yeu, Sup Hong, Hak Kyeong Kim and Sang Bong Kim

Abstract This paper proposes an obstacle avoidance algorithm for translational and rotational motions of four wheels independent steering (4WIS) automatic guided vehicles (AGV) based on fuzzy potential method (FPM) and backstepping control method. Firstly, the system is described and mathematical modeling is introduced. The AGV consists of 4 wheels driving system, laser measurement system, laser navigation system and industrial PC. Secondly, the Fuzzy Potential Field (FPM) is proposed to obtain an optimal path for an AGV. The shape and the size of the vehicle are considered when the FPM generates the optimal path from the current position to the goal position. This method allows the rectangular shape AGV to avoid unknown obstacles safely and efficiently. Backstepping controller is proposed to track the optimal path generated by FPM. Finally, the simulations are conducted to verify the effectiveness of the proposed algorithm. The simulation results show that the proposed algorithm can make the 4WIS-AGV avoid the obstacles in cluttered environment.

Keywords Automatic guided vehicle (AGV) · Fuzzy potential method (FPM) · Obstacle avoidance

P.S. Pratama · A.V. Gulalkari · J.W. Kim · H.K. Kim · S.B. Kim (✉)
Department of Mechanical and Automotive Engineering,
Pukyong National University, Busan 608-739, South Korea
e-mail: kimsb@pknu.ac.kr

C.H. Lee
Department of Shipbuilding and Ocean Engineering,
Dongwon Institute of Science and Technology, Yangsan 626-740, South Korea

T.-K. Yeu · S. Hong
Technology Center for Offshore Plant Industries, Kriso, Daejon, South Korea

V.H. Duy et al. (eds.), *AETA 2015: Recent Advances in Electrical Engineering and Related Sciences*, Lecture Notes in Electrical Engineering 371,
DOI 10.1007/978-3-319-27247-4_51

1 Introduction

Automatic Guided Vehicles (AGVs) have been used in many industries due to their high efficiency for material handling [1]. Several kinds of wheel configurations for AGVs have been developed such as differential drive [2], tricycle [3], and car-like wheeled configuration [4]. However, non-holonomic constrains of these wheel configurations limit the performance of the AGV. The AGVs performance can be improved by developing AGVs maneuverability and flexibility since the higher these characteristics are, the better the AGVs performance is. To get higher maneuverability and flexibility, four wheel independent steering configuration is proposed for the development of AGVs, hereafter referred to as 4WIS-AGVs. Four wheels independent steering configuration is a wheel configuration that each wheel orientation is adjusted separately. As a result, 4WIS-AGVs can move in any direction in their work environment.

Since the AGV works automatically, safety is crucial in AGVs operation. Therefore, obstacle avoidance algorithms were proposed to increase the safety and prevent serious damage to the system. There have been several approaches to realize obstacle avoidance of mobile robot. Choi et al. [5], Borenstein and Koren [6] only considered translational motion and the shape of the robot was assumed as a circle, while the orientation of AGV was not considered. Fox et al. [7], Wang and Chirikjian[8] considered the orientation of the robot but worked only in known environment where the obstacle position is known. Suzuki and Takahashi [9], Nagata et al. [10], Tsuzaki and Yoshida [11] proposed an obstacle avoidance control based on fuzzy potential field method (FPM). This method computed control input for the translational and rotational motion considering the shape of the robot and obstacle. The information was obtained from the external sensor. Therefore, this algorithm could work in unknown environment. However, it wasn't applied to the real system.

Controlling four wheels configuration to make the 4WIS-AGVs is an interesting topic in the practical field applications. This is because the orientation of each wheel has to be adjusted with particular formation such that the vehicle can move in the expected direction. Thus, appropriate controllers are necessary for 4WIS-AGVs. There have been many researches developing controllers for four wheel steering vehicles, such as optimal control [12], nonlinear decoupling control with an observer [13], unknown disturbance observer [14] and multi-mode control strategy based on fuzzy selector [15]. However, these controllers are not sufficient for 4WIS-AGVs, because 4WIS-AGVs need a path tracking controller that can make them follow reference path and consequently handle material. In [16], a path tracking control for four wheels independently steered ground robotic vehicles was proposed. In the controller, they implemented velocity control and wheel steering angle control to track a reference path. Simulation results showed that the controller could adjust wheel velocity and steering angles. However, this controller was considered still not suitable to be applied to 4WIS-AGVs because the vehicle position and orientation were not adjusted properly in this controller.

To solve the above problem, this paper proposes an obstacle avoidance algorithm for translational and rotational motions of four wheels independent steering (4WIS) automatic guided vehicles (AGV) based on fuzzy potential method (FPM) and backstepping control method. Firstly, the system is described and mathematic modeling is introduced. Secondly, the Fuzzy Potential Field (FPM) is proposed. The shape and the size of the vehicle are considered when the FPM generates the optimal path from current position to goal position. This method allows the rectangular shape AGV to avoid unknown obstacles safely and efficiently. A backstepping controller is proposed to track the optimal path generated by FPM. Finally, the simulations s are conducted to verify the effectiveness of proposed algorithm. The simulation results show that the proposed algorithm can make the 4WIS-AGV avoid the obstacles in cluttered environment.

2 System Description and Modeling

The 4WIS-AGV system of this paper is shown in Fig. 1 and was developed in [17]. It consists of body platform, 4 wheel driving systems, laser measurement system LMS151 and laser navigation system NAV200. The 4WIS-AGV has dimension of 0.50 (h) × 0.70 (w) × 1.00 (*l*) m.

The electrical configuration of the 4WIS-AGV is shown in Fig. 2. The controller consists of an industrial PC with RS-232 communication. Users give commands to the 4WIS-AGV through Graphic User Interface (GUI) on monitor. The control signals generated from the controller are sent to 8 motor drivers. Subsequently, these signals are converted to Pulse Width Modulation (PWM) signals which are then converted to voltage signals to control 4 DC motor for steering and 4 DC motor for driving. Laser navigation system NAV200 is used to obtain the vehicle position data. The position data is then sent to the trajectory tracking controller in industrial PC. Laser measurement system LMS151 is used to measure the distance between AGV and the obstacles.

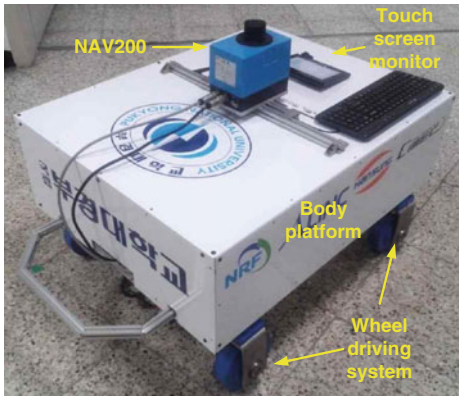

Fig. 1 4WIS-AGV system

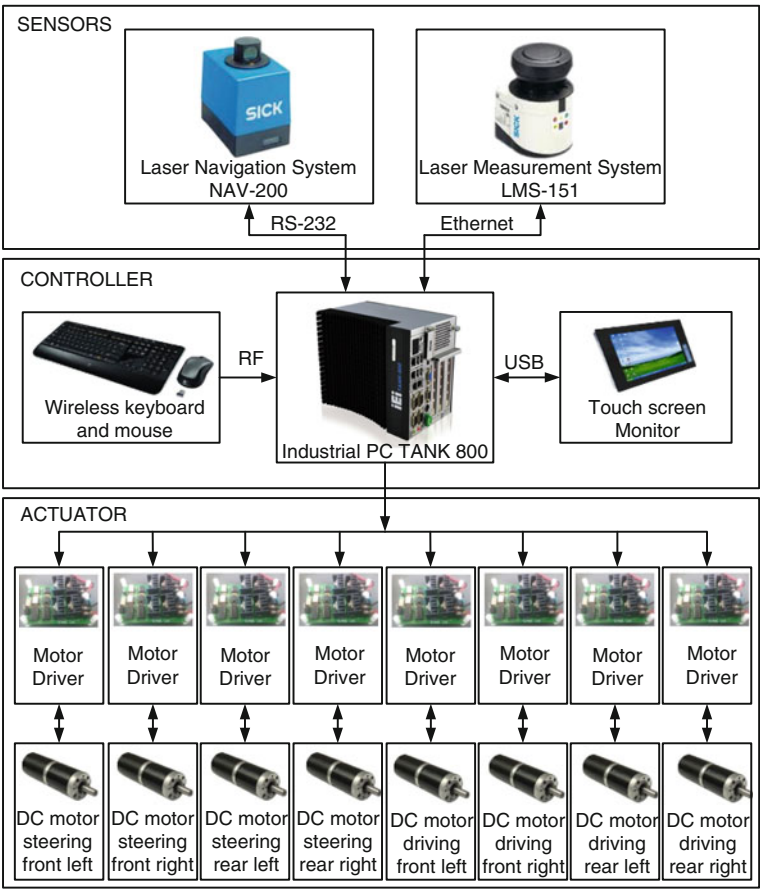

Fig. 2 Electrical configuration of 4WIS-AGV

A configuration of the 4WIS-AGV for the system modeling is shown in Fig. 3. The *XOY* coordinate is a global coordinate whereas the *xAy* coordinate is a local coordinate. In this paper, it is assumed that the mass and inertia of the robot is small. Therefore, the changes in speed is nearly instantaneous. Furthermore, it is assumed that in the wheel there is no sliding and the wheel is pure rolling. The kinematic modeling of 4WIS AGV is given as follows:

$$\dot{\mathbf{q}} = \begin{bmatrix} \dot{X} \\ \dot{Y} \\ \dot{\theta} \end{bmatrix} = \begin{bmatrix} \cos\theta & -\sin\theta & 0 \\ \sin\theta & \cos\theta & 0 \\ 0 & 0 & 1 \end{bmatrix} \begin{bmatrix} v_x \\ v_y \\ \omega \end{bmatrix} \equiv \mathbf{S}\xi \tag{1}$$

where $\dot{X}$ is the vehicle linear velocity in X axis of global coordinate, $\dot{Y}$ is the vehicle linear velocity in Y axis of global coordinate, and $\dot{\theta}$ is the vehicle angular velocity

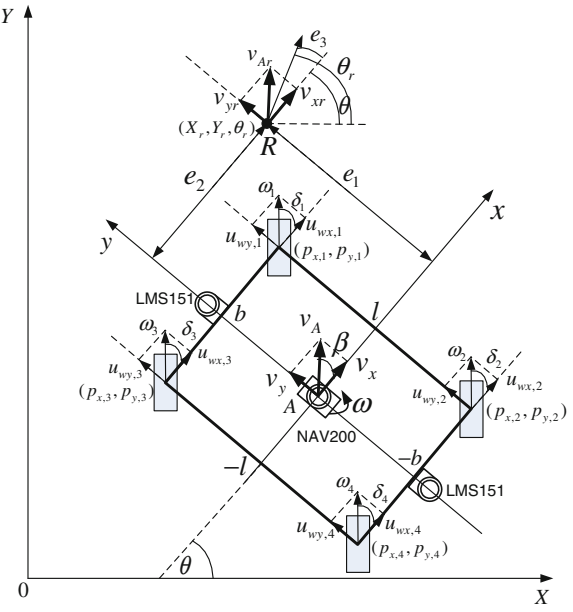

Fig. 3 Configuration for system modeling

in global coordinate. v_x is the vehicle linear velocity in x axis of local coordinate, v_y is the vehicle linear velocity in y axis of local coordinate, and ω is the vehicle angular velocity in local coordinate. (X_r, Y_r) is reference position and θ_r is reference orientation. δ_i and ω_i $(i = 1, 2, 3, 4)$ are the ith wheel steering angle and the ith wheel angular velocity, respectively.

Given the total linear velocity of AGV in local coordinate v_A and vehicle sideslip angle β, the vehicle linear velocities v_x and v_y in local coordinate can be obtain as follows:

$$\begin{cases} v_x = v_A \cos\beta \\ v_y = v_A \sin\beta \end{cases} \tag{2}$$

The vehicle sideslip angle β is defined as angle between the movement directions of AGV and x axis of AGV as follows:

$$\beta = \text{atan2}(v_y, v_x) \tag{3}$$

Target velocities in x and y direction $u_{wx,i}$ and $u_{wy,i}$ of the ith wheel in local coordinate of AGV can be obtained as follows:

$$\begin{cases} u_{wx,i} = v_x - p_{y,i}\omega \\ u_{wy,i} = v_y + p_{x,i}\omega \end{cases} \tag{4}$$

where $(p_{x,i}, p_{y,i})$ is the position of the ith wheel in local coordinate of AGV as shown in Fig. 3.

The ith wheel steering angle δ_i and the ith wheel angular velocity ω_i are given as follows:

$$\delta_i = \tan^{-1}\left(\frac{u_{wy,i}}{u_{wx,i}}\right) \tag{5}$$

$$\omega_i = \frac{u_{wx,i}\cos\delta_i + u_{wy,i}\sin\delta_i}{R_w} \tag{6}$$

where R_w is a radius of a wheel.

3 Fuzzy Potential Method

In this section, the outline of fuzzy potential method (FPM) as in [13], which is an obstacle avoidance method based on fuzzy logic, is explained. The purpose of FPM is to generate references position (X_r, Y_r), reference orientation θ_r, reference linear velocity (v_{xr}, v_{yr}) and reference angular velocity ω_r for the AGV. Figure 4 depicts the protection area of vehicle and obstacle. The FPM is based on the membership function of translational and rotational motions. For FPM in order to simplify the membership functions considering the shape and size of the vehicle, the rectangular shape of the vehicle is considered as a capsule shape which contains the vehicle as depicted in Fig. 4, where c_a, c_L, c_R are design parameters. FPM sets safe distance d_s around obstacles as shown in Fig. 4 to avoid obstacles and it computes the control input for avoiding the regions.

This method has three steps. The first step is generating potential method membership function (PMF). The second step is to decide the command velocity

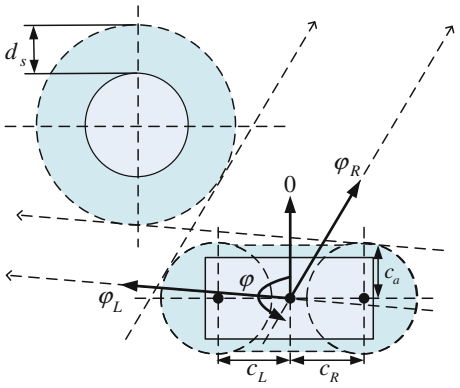

Fig. 4 Parameters of FPM

vector using fuzzy inference to integrate the PMFs. The design method of PMF for translational and rotational movements that takes into consideration the width of the vehicle is described in the following sections.

3.1 FPM for Translational Movement

Firstly, PMF μ_d^t is specified by depth and width, which are calculated based on the geometrical relation between an obstacle and the AGV as in [13]. a is defined as the depth of the concave PMF and can be described as follows:

$$a = \frac{\alpha - \|do\|}{c_a + d_s} \quad if \ \|do\| < \alpha \tag{7}$$

where do is distance between AGV and object, and α is design parameter. PMF μ_d^t can be obtained by scanning the passable direction by scanning angle direction φ as shown in Fig. 4. φ_L is minimum passable direction on the left side of vehicle, and φ_R is minimum passable direction on the right side of vehicle. If the obstacle dimension is known, the value of φ_R and φ_L can be obtained from calculation as in [13]. Figure 5 shows the scanning result of passable direction.

Secondly, to represent the direction to the goal, PMF μ_g^t is generated as shown in Fig. 6. The maximum value g_a can be obtained at an angle toward the goal θ_g and

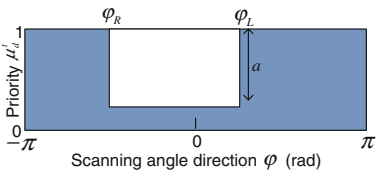

Fig. 5 Example of FPM for object

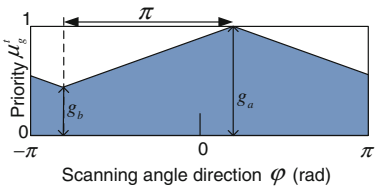

Fig. 6 Example of FPM for a goal

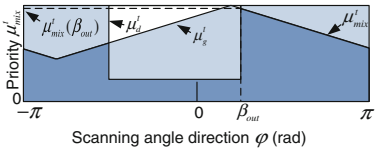

Fig. 7 Example of mixed PMF for translational movement

the minimum value g_b can be obtained at an angle opposite to the goal. The values of g_a and g_b is defined as follows:

$$g_a = \begin{cases} \frac{\|d_g\|}{Th} & if \ \|d_g\| \le Th \\ 1.0 & if \ \|d_g\| \le Th \end{cases} \qquad (8)$$
$$g_b = \eta g_a \quad (0 \le \eta < 1)$$

where d_g is distance from the current position of AGV to the goal, and η is design parameter. Th is threshold value that chosen to make the AGV decelerate and stop smoothly when it closes to the goal.

Thirdly, the PMF μ^t_d and PMF μ^t_g are integrated by fuzzy operation into μ^t_{mix} using logical product ($\wedge$) as shown in Eq. (9). Figure 7 shows the example of mixed PMF for translational movement.

$$\mu^t_{mix} = \mu^t_g \wedge \mu^t_d \qquad (9)$$

Finally, by defuzzification, the translational reference velocity vector is calculated as a reference sideslip angle β_r and the reference total linear velocity v_{Ar} based on the mixed PMF $\mu^t_{mix}(\beta_r)$ as follows:

$$v_{Ar} = \mu^t_{mix}(\beta_r)(v_{\max} - v_{\min}) + v_{\min} \qquad (10)$$

where $v_{\max}$ and $v_{\min}$ are maximum and minimum linear velocities of the vehicle, respectively.

3.2 FPM for Rotational Movement

Firstly, to enable a wide vehicle to decide the appropriate AGV orientation θ for real time obstacle avoidance, PMF μ^r_o as shown in Fig. 8 is generated as follows:

$$\mu^r_o = \mu^r_e - \mu^r_c \qquad (11)$$

where PMF μ^r_e is generated based on the distances from the center of the vehicle to obstacles corresponding to all directions obtained from laser scanner LMS151, and

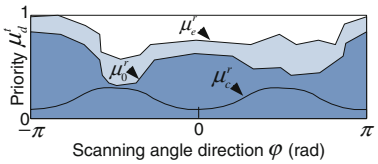

Fig. 8 Example of PMF for obstacle

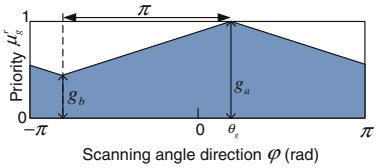

Fig. 9 Example of FPM for a goal

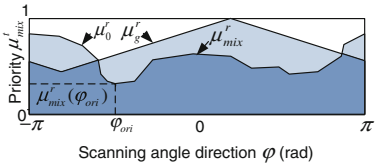

Fig. 10 Example of mixed PMF for rotational movement

PMF μ_c^r is generated based on the capsule case represented as the dimension of the protecting area of the AGV.

Secondly, to represent the direction from current position to the goal, PMF μ_g^t is generated as shown in Fig. 9. This PMF is similar with the PMF for translational movement in Fig. 6.

Thirdly, the PMF μ_o^r and PMF μ_g^r are integrated by fuzzy operation into μ_{mix}^r using logical product ($\wedge$) as shown in Eq. (12). Figure 10 shows the example of mixed PMF for rotational movement.

$$\mu_{mix}^r = \mu_g^r \wedge \mu_o^r \tag{12}$$

Finally, by defuzzification, the rotational reference direction φ_{ori} is calculated based on μ_{mix}. The rotational reference direction φ_{ori} is decided as the direction that minimizes the μ_{mix}. Based on φ_{ori}, reference angular velocity ω_r is calculated as follows:

$$\omega_r = \mu_{mix}^r(\varphi_{ori})(\omega_{\max} - \omega_{\min}) + \omega_{\min} \tag{13}$$

where $\omega_{\max}$ and $\omega_{\min}$ are maximum and minimum angular velocity of the vehicle.

3.3 Planning Reference Path

The purpose of this subsection is generate the reference position (X_r, Y_r) and orientation θ_r with given total reference linear velocity of AGV in local coordinate v_{Ar} and reference sideslip angle β_r obtained from FPM for translational movement and ω_r obtained from FPM for rotational movement. Substituting v_{Ar} and β_r instead of v_A and β into (2) and (3), v_{xr}, v_{yr} and ω_r can be obtained. Furthermore, since the path is generated in real time, the references position (X_r, Y_r) and reference orientation θ_r can be obtained as follows:

$$\begin{bmatrix} X_{r(k+1)} \\ Y_{r(k+1)} \\ \theta_{r(k+1)} \end{bmatrix} = \begin{bmatrix} X_{r(k)} \\ Y_{r(k)} \\ \theta_{r(k)} \end{bmatrix} + \begin{bmatrix} \cos(\theta+\omega_r) & -\sin(\theta+\omega_r) & 0 \\ \sin(\theta+\omega_r) & \cos(\theta+\omega_r) & 0 \\ 0 & 0 & 1 \end{bmatrix} \begin{bmatrix} v_{xr} \\ v_{yr} \\ \omega_r \end{bmatrix} \Delta T \quad (14)$$

where ΔT is the sampling time, and subscripts k and $k + 1$ are the discrete time steps.

4 Controller Design

The purpose of this section is to design a controller for the 4WIS-AGV to track references position (X_r, Y_r) and orientation θ_r with vehicle linear velocities (v_{xr}, v_{yr}) and vehicle angular velocity ω_r generated by the fuzzy potential method (FPM) based on backstepping method.

Firstly, when the vehicle is controlled to track a given reference trajectory, a tracking error vector can be expressed as follows:

$$\mathbf{e} = \begin{bmatrix} e_1 \\ e_2 \\ e_3 \end{bmatrix} = \begin{bmatrix} \cos\theta & \sin\theta & 0 \\ -\sin\theta & \cos\theta & 0 \\ 0 & 0 & 1 \end{bmatrix} \begin{bmatrix} X - X_r \\ Y - Y_r \\ \theta - \theta_r \end{bmatrix} \Leftrightarrow \mathbf{e} = \mathbf{S}\mathbf{e}_\mathbf{q} \quad (15)$$

Time derivative of the tracking error vector can be obtained as follows:

$$\dot{\mathbf{e}} = \begin{bmatrix} \dot{e}_1 \\ \dot{e}_2 \\ \dot{e}_3 \end{bmatrix} = \begin{bmatrix} 1 & 0 & e_2 \\ 0 & 1 & -e_1 \\ 0 & 0 & 1 \end{bmatrix} \begin{bmatrix} v_x \\ v_y \\ \omega \end{bmatrix} - \begin{bmatrix} \cos\theta & \sin\theta & 0 \\ -\sin\theta & \cos\theta & 0 \\ 0 & 0 & 1 \end{bmatrix} \begin{bmatrix} v_{xr} \\ v_{yr} \\ \omega_r \end{bmatrix} \quad (16)$$

Subsequently, the stability of the system is checked by Lyapunov stability theory. A Lyapunov function candidate is chosen as follows:

$$V = \frac{1}{2}e_1^2 + \frac{1}{2}e_2^2 + \frac{1}{2}e_3^2 \quad (17)$$

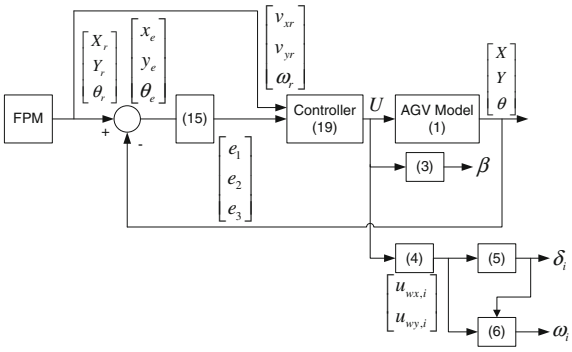

Fig. 11 Block diagram of the proposed controller

Stability checking is used to find a control law U that can make the system stable and track the given reference trajectory. From the error dynamic in (16), the time derivative of the Lyapunov function equation $\dot{V}$ is obtained as follows:

$$\begin{aligned}\dot{V} &= e_1\dot{e}_1 + e_2\dot{e}_2 + e_2\dot{e}_2 \\ &= e_1(v_x - v_{xr}\cos e_3 - v_{yr}\sin e_3) \\ &\quad + e_2(v_y - v_{xr}\cos e_3 - v_{yr}\sin e_3) \\ &\quad + e_3(\dot{\theta} - \dot{\theta}_r)\end{aligned} \tag{18}$$

Lyapunov stability criterion states that system is stable when $\dot{V} \leq 0$. Therefore, to meet this condition, a control law U is chosen as follows:

$$U = \begin{bmatrix} v_x \\ v_y \\ \omega \end{bmatrix} = \begin{bmatrix} -k_1 e_1 + v_{xr}\cos e_3 + v_{yr}\sin e_3 \\ -k_2 e_2 - v_{xr}\sin e_3 + v_{yr}\cos e_3 \\ -k_3 e_3 + \omega_r \end{bmatrix} \tag{19}$$

where k_1, k_2 and k_3 are positive constants.

Substituting (19) into (18) yields

$$\dot{V} = -k_1 e_1^2 - k_2 e_2^2 - k_3 e_3^2 \tag{20}$$

The proposed controller for is summarized in the block diagram in Fig. 11.

5 Simulation Results

The effectiveness of the proposed method was verified by simulation. The parameters for simulation are shown in Table 1. The simulation results of proposed method are shown in Figs. 12, 13, 14, 15 and 16. Figure 12 shows that the vehicle moves from start position to goal position and performed translational and

Table 1 Parameter and initial values

Parameter	Value	Parameter	Value
c_a	0.5 m	k_1	1
c_L	0.5 m	k_2	1
c_R	0.5 m	k_3	0.5
d_s	0.1 m	α	0.1 π rad
l	0.35 m	b	0.5 m
Th	0.5 m	(X_0, Y_0, θ_0)	(−2, 0, 0)
(v_{A0}, β_0)	(0, 0)	(X_g, Y_g, θ_g)	(2, 11, 0)

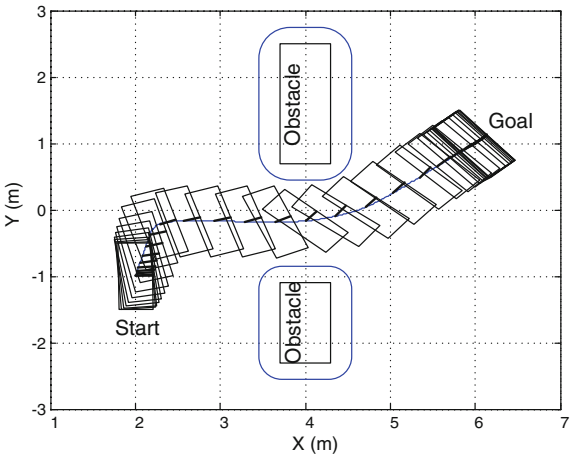

Fig. 12 Simulation result

rotational movements simultaneously and succeeded in going between two divided objects. Finally, the vehicle reaches the goal position.

Figure 13 shows the linear velocity and angular velocity of the vehicle. In the beginning, the vehicle moves and increases the linear velocity gradually. The linear velocity of the vehicle decreases smoothly when the vehicle approaches goal position. The angular velocity increases at 25 s to avoid the collision with the obstacle, and decreases at 30 s after passing the obstacle. Figure 14 shows the error vector obtained from the backstepping controller. It can be observed that all the errors have very small values and finally converged to zero. The result shows that the controller successfully tracks the generated path obtained from the FPM. Figures 15 and 16 show the *i*th wheel angular velocity and the *i*th wheel steering angle, respectively.

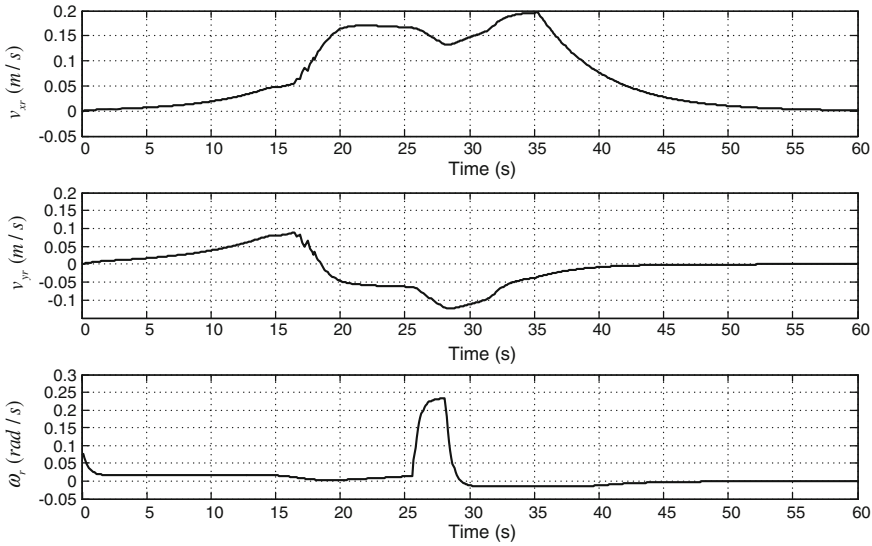

Fig. 13 Simulation result for v_{xr}, v_{yr}, and ω_r

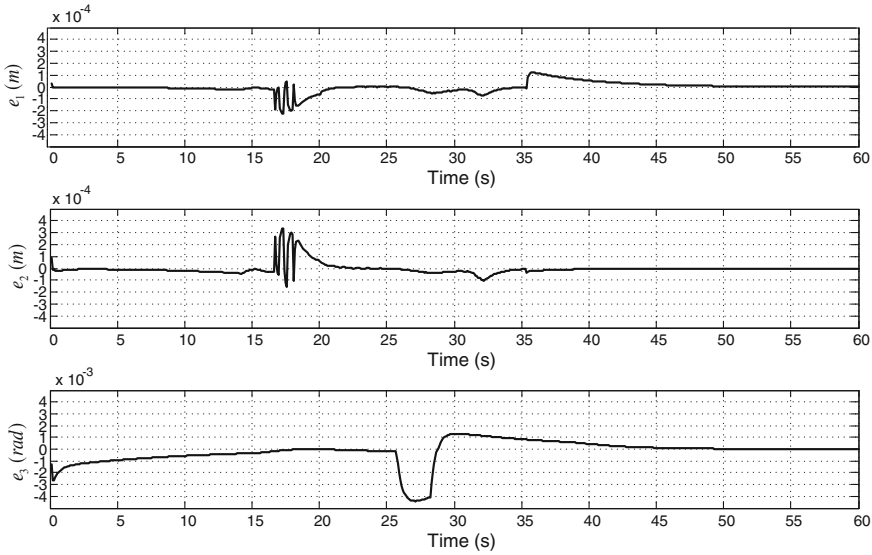

Fig. 14 Error vector

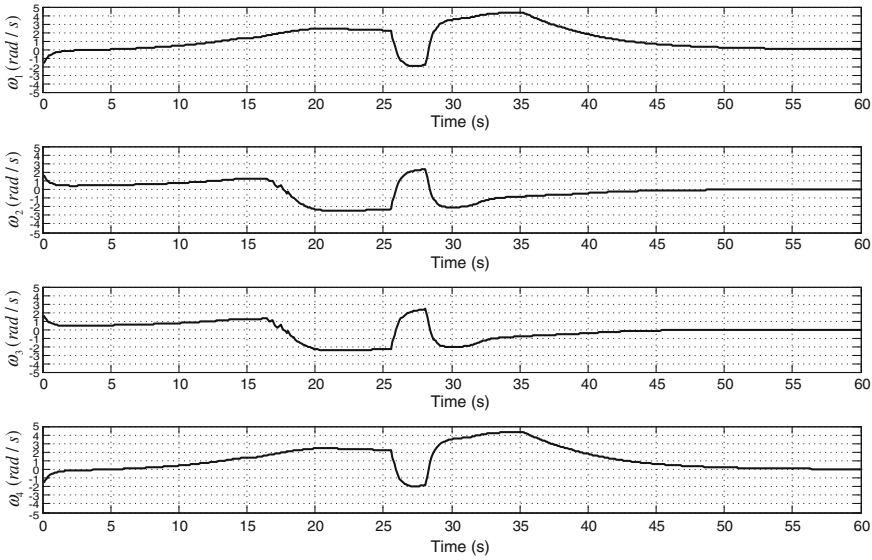

Fig. 15 *i*th wheel angular velocity ω_i

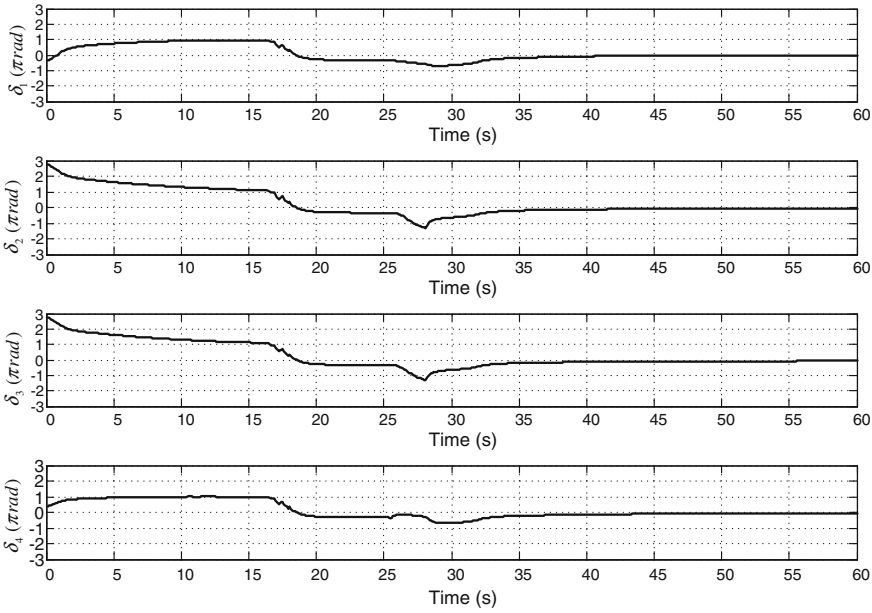

Fig. 16 *i*th wheel steering angle δ_i

6 Conclusion

In this paper, an obstacle avoidance algorithm for translational and rotational motion of a four wheel independent steering automatic guided vehicle (4WIS-AGV) was proposed based on fuzzy potential method (FPM) and backstepping control method. The FPM algorithm generated the optimal path from the current position to the goal position considering the size of the vehicle. The generated trajectory was tracked successfully using backstepping controller. The effectiveness of the proposed algorithm was verified by simulations. It was shown that the proposed algorithm could make the 4WIS-AGV avoid the obstacles in cluttered environment safely and efficiently.

Acknowledgments This study is a part of the results of the R&D project, Development of a deep-seabed Mining Technologies, supported by Korea Government, Ministry of Oceans and Fisheries. Authors are indebted to appreciate their full supports of this pioneering work.

References

1. Cheng X, Tao R (2011) Design of automatic guided vehicles and dunking robot system. In: The 3rd international conference on intelligent human-machine systems and cybernetics, pp 3–6
2. Pratama PS, Jeong SK, Park SS, Kim SB (2013) Moving object tracking and avoidance algorithm for differential driving AGV based on laser measurement technology. Int J Sci Eng 4 (1):11–15
3. Doan PT, Nguyen TT, Dinh VT, Kim HK, Kim SB (2011) Path tracking control of automatic guided vehicle using camera sensor. In: The 1st International symposium on automotive and convergence engineering
4. Tamba TA, Hong BH, Hong KS (2009) A path following control of an unmanned autonomous forklift. Int J Control Autom Syst 7(1):113–122
5. Choi J, Curry RE, Elkaim GH (2009) Obstacle avoiding real-time trajectory generation and control of omnidirectional vehicles. Am Control Conf 2009:5510–5515
6. Borenstein J, Koren Y (1991) The vector field histogram-fast obstacle avoidance for mobile robots. IEEE Tran Robot Autom 7(3):278–288
7. Fox D, Burgard W, Thrun S (1997) The dynamic window approach to collision avoidance. IEEE Trans Robot Autom 4(1):23–33
8. Wang Y, Chirikjian GS (2000) A new potential field method for robot path planning. In: The 2000 IEEE international conference on robotics and automation, pp 977–982
9. Suzuki T, Takahashi M (2009) Translational and rotational movement control considering width for autonomous mobile robot by using fuzzy inference. In: The 2009 international conference on robotics and biomimetics, pp 257–262
10. Nagata A, Nonaka K, Sekiguchi K (2014) Model predictive obstacle avoidance control for omni-directional mobile robots based on fuzzy potential method. In: European control conference, pp 352–357
11. Tsuzaki R, Yoshida K (2003) Motion control based on fuzzy potential method for autonomous mobile robot with omnidirectional vision. J Robot Soc Jpn 21(6):656–662
12. Amdouni I, Jeddi N, Amraoui LE (2013) Optimal control approach developed to four-wheel active steering vehicles. In: The 5th international conference on modeling, simulation and applied optimization (ICMSAO), pp 1–6

13. Chen C, Jia Y (2012) Nonlinear decoupling control of four-wheel-steering vehicles with an observer. Int J Control Autom Syst 10(4):697–702
14. Kim HS, You SS (2001) Estimation of vehicle sideslip angle for four-wheel steering passenger cars. Trans Control Autom Syst Eng 3(2):71–76
15. Yang Z, Wang Z, Su W, Zhang J (2010) Multi-mode control method based on fuzzy selector in the four wheel steering control system. In: The 8th IEEE international conference on control and automation, pp 1221–1226
16. Selekwa MF, Nistler JR (2011) Path tracking control of four wheel independently steered ground robotic vehicles. In: The 50th IEEE conference on decision and control and european control conference, pp 6355–6360
17. Setiawan YD (2015) Development and controller design of four wheel independent steering automatic guided vehicles, Master thesis, Mechanical Design Engineering Department, Pukyong National University, Busan, Korea

Steering and Diving Control of a Small-Sized AUV

Ngoc-Huy Tran, Hyeung-Sik Choi, Ngoc-Duc Nguyen, Sung-Won Jo and Joon-Young Kim

Abstract This paper presents a steering and diving control of an autonomous underwater vehicle (AUV) platform named KAUV, which is designed as a torpedo with light weight and small size. Through a unique ducted propeller and rudder located at the aft, the KAUV can perform horizontal motion. It also control pitch angle and depth motion with an inside mass shifter mechanism which changes the vehicle center of gravity. Because the system to be controlled is highly nonlinear, a sliding mode control (SMC) is constructed to compensate the effects of modeling nonlinearity, parameter uncertainty, and disturbance. This proposed control algorithm is derived from the linearized vehicle dynamics for steering and diving planes. To check the response of the vehicle system with the developed controllers, a series of simulation results are also simulated and presented.

Keywords AUV · Steering control · Diving control · Sliding mode control

1 Introduction

Nowadays, AUVs have become a main tool for surveying below the sea in scientific, military, and commercial applications because of the significant improvement in their performance. Despite the considerable improvement in AUV performance, however, AUV technologies are still attractive to scientists and engineers as a challenging field. The challenges in design such as the torpedo-AUVs are designed with a fixed propeller at the aft and use pairs of fins for

N.-H. Tran · H.-S. Choi (✉) · N.-D. Nguyen · S.-W. Jo
Department of Mechanical Engineering, Korea Maritime and Ocean University, Pusan, Korea
e-mail: hchoi@hhu.ac.kr

J.-Y. Kim
Division of Marine Equipment Engineering, Korea Maritime and Ocean University, Pusan, Korea

V.H. Duy et al. (eds.), *AETA 2015: Recent Advances in Electrical Engineering and Related Sciences*, Lecture Notes in Electrical Engineering 371,
DOI 10.1007/978-3-319-27247-4_52

steering and diving [1]. However, the drawback of these designs is that they could not work effectively at low speeds. A more advanced architecture of AUV without any fins was devised for Bluefin [2], whose propeller that is in a double gimbal arrangement could be actuated in the horizontal and vertical directions, worked as both a rudder and an elevator. In this configuration, the vehicle is more clean-lembed, and the control system is smaller. However, both rudder and elevator of this vehicle are tied with the single propeller, so interoperability between them may be pretty much limited, for example, in case of a sharp turn with nonzero roll which results in an undesired change in depth. This issue needs a coupled control system to mix rudder and elevator commands to minimize disturbances in depth as mentioned in [3]. From the challenges mentioned above, a model for the KAUV was designed. The main design concept is that of a small vehicle small enough to cruise in the basin, to be handled easily by one or two people, and overcome the mentioned drawbacks. It has a fixed propeller and rudder located at the aft of AUV to perform horizontal motion. For elevator, the KAUV uses a mass shifter mechanism, similar to the one often used in underwater gliders, e.g., Seaglider, Spray and Slocum [4], which changes the vehicle center of gravity to control pitch angle and then depth of the vehicle.

The KAUV's dynamics is very complex, highly nonlinear and depend on several parameters like added-mass, hydrodynamics damping coefficients. For these reasons, the designed controller must be robust against the uncertainties and environmental distributions. According to sliding mode approach, the depth and heading control of the KAUV are proposed in order to maintain the desired depth and heading angle with sufficient accuracy.

2 Structure and Control System of the AUV

2.1 Structure of the AUV

The AUV has an approximative length of 1.6 m, a maximum diameter of 0.18 m, and weight of 21.5 kg as shown in Fig. 1. It is composed of a pressure hull, propulsion system, rudder, mass shifter mechanism, and electronic control system, etc. The vehicle is designed with a buoyancy is slightly greater than its weigh, so that the AUV will eventually float to the surface in the event of a computer or power failure. To promote the stability of the vehicle, three fixed fins are mounted on the perimeter of the circular aft with intervals of 120°.

With a unique ducted propeller and rudder located at the aft, as shown in Fig. 2, the AUV can perform horizontal motion. It also control pitch angle and depth motion with an inside mass shifter mechanism which changes the center of gravity of the AUV. This mechanism is designed with a linear motor (LM) guide actuator, and a movable mass (2.5 kg) fixed onto the LM block, as shown in Fig. 3. When the movable mass goes forwards or backwards, the center of gravity of the whole

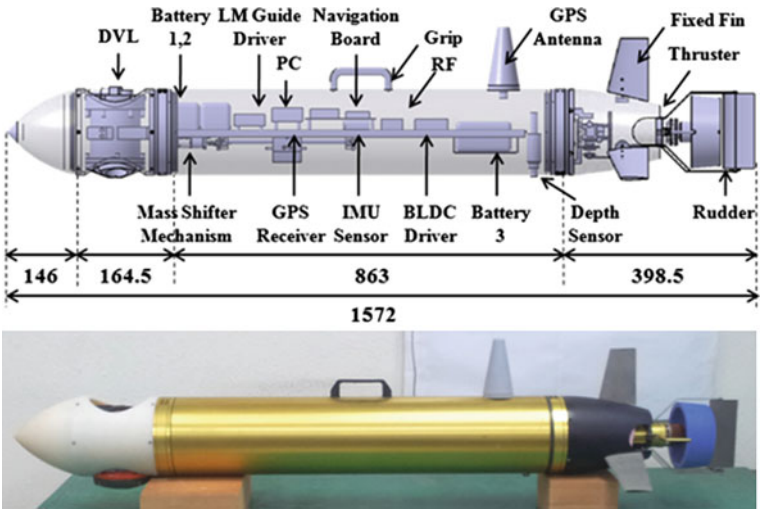

Fig. 1 The virtual design and developed AUV

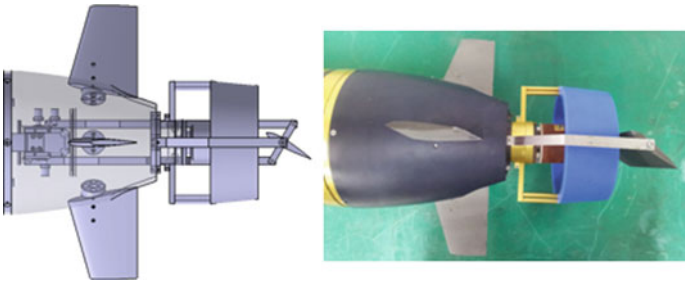

Fig. 2 Propeller and rudder of the AUV

vehicle also shifts forwards or backwards, respectively. These shifts make the vehicle pitch down or up; and under propulsion, the vehicle will be propelled downward or upward, respectively. The length of stroke [−10 cm, 10 cm], the movable mass, and the installation location of the LM guide are designed in the limited space inside the vehicle such that the pitch angle can promptly change within an appropriate range for control purposes.

2.2 Hardware Architecture

The control system shown in Fig. 4 includes one main board using IEC-667 embedded system and two sub-boards using digital signal processors

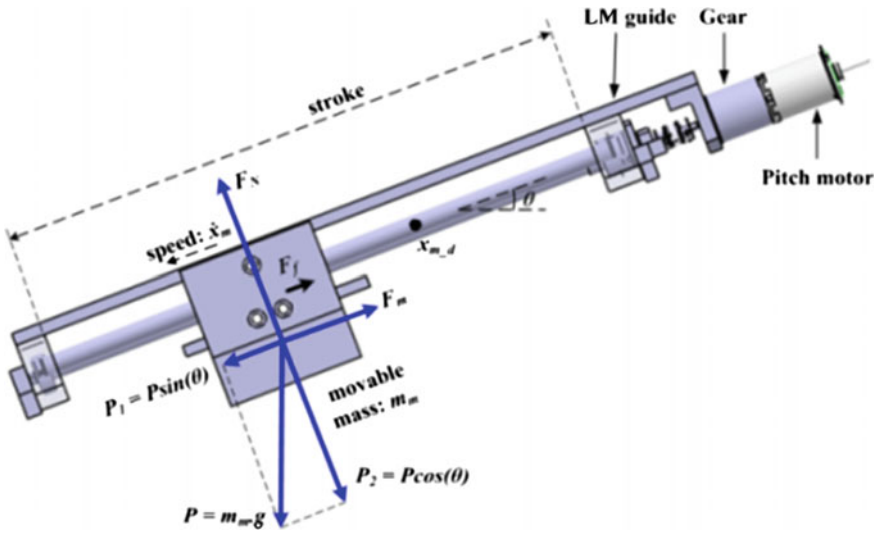

Fig. 3 Mass shifter mechanism of the AUV

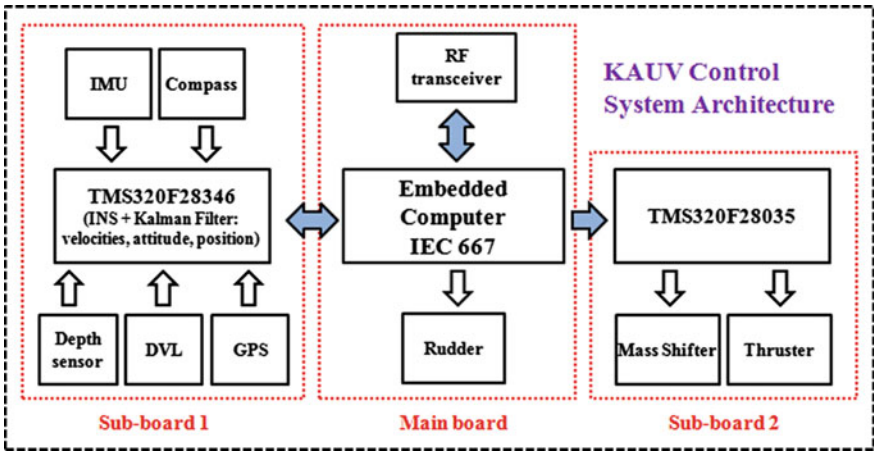

Fig. 4 Control system architecture block diagram

(DSP) TMS320F28346 and TMS320F28035. The DSP TMS320F28346 (sub-board 1) is connected to sensors including IMU, compass, depth sensor, DVL and GPS receiver. After receiving data from sensors, the sub-board 1 will run the algorithm programs of the INS and the Kalman filter to estimate the velocities, attitude and position of the vehicle and then transfers these calculation results to the main board [5]. The DSP TMS320F28035 (sub-board 2) receives instructions from the main board to control the mass shifter actuator and thruster. The main board can

communicate with the sub-boards 1 and 2, the RF transceiver, and the driver of the rudder. When the vehicle is on the surface, the RF transceiver receives commands from the surface station and transfers them to the main board. Using the data obtained from the sub-board 1 and RF transceiver, the embedded computer directly controls the rudder and gives out instructions to the sub-board 2 to control the mass shifter equipment or thruster.

3 Dynamics Equations of Motion

3.1 Mass Shifter Mechanism

Figure 3 shows all the forces acting on the movable mass, they are the weight of the movable mass P, normal force F_N, total frictional force F_f, and force of the pitch motor F_M. In this figure, it is assumed that the movable mass is moving towards the stern of the vehicle with speed $\dot{x}_m$ and the vehicle pitches up from horizontal at a pitch angle θ. Because friction always acts in a direction opposite the speed, the direction of total frictional force F_f is towards the bow of the vehicle. The weight of the movable mass could be resolved into two components at right angles to each other, P_1 and P_2. P_1 is parallel to the screw shaft and P_2 is perpendicular to P_1. P_2 is balanced by the normal force F_N which is exerted on the movable mass by the screw shaft.

The differential equation describing the dynamics of the mass shifter mechanism is as follows:

$$m_m \ddot{x}_m = P_1 + F_f + F_M \tag{1}$$

where $\ddot{x}_m$ denotes the acceleration of the movable mass.

From Eq. (1), with assumption F_f small compared to the other forces, we can simply to:

$$\ddot{x}_m = f + u_m \tag{2}$$

where $u_m = F_M/m_m$ and $f = g \sin\theta$.

With Eq. (2), to drive the movable mass to the desired position x_{m_d}, the appropriate force um need to be calculated by a position controller. In control strategies section, a MSM position controller will be presented by using sliding mode control.

3.2 Underwater Vehicle Dynamics

Given that the origin of the body-fixed coordinate system is located at the center of buoyancy as noted previously, the following represents the equations of motion for a rigid body in six degrees of freedom, defined in terms of body-fixed coordinates [6]:

$$\begin{aligned}
m[\dot{u} - vr + wq - x_g(q^2 + r^2) + y_g(pq - \dot{r}) + z_g(pr + \dot{q})] &= \sum X \\
m[\dot{v} - wp + ur - y_g(r^2 + p^2) + z_g(qr - \dot{p}) + x_g(qp + \dot{r})] &= \sum Y \\
m[\dot{w} - uq + vp - z_g(p^2 + q^2) + x_g(rp - \dot{q}) + y_g(rq + \dot{p})] &= \sum Z \\
I_{xx}\dot{p} + (I_{zz} - I_{yy})qr - (\dot{r} + pq)I_{xz} + (r^2 - q^2)I_{yz} + (pr - \dot{q})I_{xy} & \\
+ m[y_g(\dot{w} - uq + vp) - z_g(\dot{v} - wp + ur)] &= \sum K \\
I_{yy}\dot{q} + (I_{xx} - I_{zz})rp - (\dot{p} + qr)I_{xy} + (p^2 - r^2)I_{xz} + (qp - \dot{r})I_{yz} & \\
+ m[z_g(\dot{u} - vr + wq) - x_g(\dot{w} - uq + vp)] &= \sum M \\
I_{zz}\dot{r} + (I_{yy} - I_{xx})pq - (\dot{q} + rp)I_{yz} + (q^2 - p^2)I_{xy} + (rq - \dot{p})I_{xz} & \\
+ m[x_g(\dot{v} - wp + ur) - y_g(\dot{u} - vr + wq)] &= \sum N
\end{aligned} \tag{3}$$

where

- u, v, w: surge, sway, heave velocities respectively
- p, q, r: roll, pitch, yaw rates
- X, Y, Z: external forces
- K, M, N: external moments
- x_g, y_g, z_g: vehicle center of gravity
- Ia_b: moments of inertia (a and b symbolize x or y or z). Because the movable mass just moves within a small range, Ia_b change very little. So, we assume they are constant.
- m: total mass of the vehicle.

Linearized diving system dynamics

The control system is decoupled in the vertical and horizontal directions, meaning that the diving motion is controlled independently with the steering motion. So, to design a diving controller, only the equations of vertical-plane motion need to be considered. The following assumptions can be made:

- $v = p = r = \dot{v} = \dot{p} = \dot{q} = 0$
- Surge velocity u is constant
- Heave velocity w is small compared to the other terms.
- Moments of inertia are affected very little by the position change of the movable mass.

From Eq. (3), the lineared diving dynamics equations of motion are therefore [7]:

$$\begin{cases} I_y\dot{q} + z_g W\theta = M_q q + M_{\dot{q}}\dot{q} - Wx_g \\ \dot{\theta} = q \\ \dot{z} = -U\theta \end{cases} \tag{4}$$

where

- W denotes the weight of the vehicle
- I_y moment of inertia about y-axis
- x_g vehicle center of gravity.

The remaining factors are other nonlinear maneuvering coefficient of forces and moments. From theory of solid mechanics, it is easy to get the formula for calculating the vehicle center of gravity as:

$$x_g = \frac{m_m \cdot x_m + m_o \cdot x_o}{m} = \frac{m_m \cdot x_m}{m} \tag{5}$$

where x_m denotes the position of the movable mass, x_0 is the position of the center of gravity of the vehicle excluding the movable mass (assuming that is zero). m_0 is the vehicle mass excluding m_m.

Finally, substituting Eq. (5) into Eq. (4), the lineared diving dynamics equations of motion are expressed as follows:

$$\begin{bmatrix} \dot{q} \\ \dot{\theta} \\ \dot{z} \end{bmatrix} = \begin{bmatrix} M_q/(I_y - M_{\dot{q}}) & -Wz_g/(I_y - M_{\dot{q}}) & 0 \\ 1 & 0 & 0 \\ 0 & -U & 0 \end{bmatrix} \begin{bmatrix} q \\ \theta \\ z \end{bmatrix} + \begin{bmatrix} M_{x_m}/(I_y - M_{\dot{q}}) \\ 0 \\ 0 \end{bmatrix} [x_m] \tag{6}$$

where $M_{x_m} = -W.m_m/m$ which we simply expressed as:

$$\dot{x}_1 = A_1 x_1 + B_1 u_1 \tag{7}$$

Linearized steering system dynamics

Similarly, some state vectors related the diving-plane are considered as null for design a steering controller. The following assumptions can be made:

- $w = p = q = z = \phi = \theta = 0$
- Surge velocity u is constant $u = U = 1.543$ m/s
- The vehicle is symmetric in its inertial properties.

From Eq. (3), the lineared steering dynamics equations of motion have been formed as follows [7]:

$$\begin{bmatrix} m - Y_{\dot{v}} & -Y_{\dot{r}} & 0 \\ -N_{\dot{v}} & I_z - N_{\dot{r}} & 0 \\ 0 & 0 & 1 \end{bmatrix} \begin{bmatrix} \dot{v} \\ \dot{r} \\ \dot{\psi} \end{bmatrix} = \begin{bmatrix} Y_v & Y_r - mU & 0 \\ N_v & N_r & 0 \\ 0 & 1 & 0 \end{bmatrix} \begin{bmatrix} v \\ r \\ \psi \end{bmatrix} + \begin{bmatrix} Y_\delta \\ N_\delta \\ 0 \end{bmatrix} \delta_r(t) \quad (8)$$

where $\delta_r(t)$ is the rudder angle of the AUV which we is simply expressed as:

$$\dot{x}_2 = A_2 x_2 + B_2 u_2 \quad (9)$$

4 Controller Design

4.1 Sliding Mode Controller Design

As a nonlinear control technique, the sliding mode control (SMC) has provided an effective means of designing robust state feedback controllers for uncertain dynamic systems. The SMC makes system states stay in a switching surface on which the system remains insensitive to internal parameter variations and extraneous disturbances.

Generally, the lineared model of AUV for diving-plane and steering-plane can be written as single-input multi-output model as:

$$\dot{x} = Ax + Bu + d \quad (10)$$

Now, sliding surface can be defined in the error state space form as follows

$$S_s = S^T \tilde{x} = [s_1 \ldots s_n]\tilde{x} = 0 \quad (11)$$

where $\tilde{x} = x - x_d$ are state errors, x_d is desired tracking state.

The positive definite Lyapunov function candidate is

$$V(S_s) = \frac{1}{2} S_s^T S_s = \frac{1}{2} \tilde{x}^T S S^T \tilde{x} \quad (12)$$

$V(S_s)$ guarantees that the error state converges to sliding surface exists if following condition is satisfied

$$\dot{V}(S_s) = S_s \dot{S}_s < 0 \quad (13)$$

If we select

$$\dot{S}_s = -\eta sign(S_s) \quad \eta > 0 \tag{14}$$

Differentiating the sliding surface (11)

$$\dot{S}_s = S^T \dot{\tilde{x}} = S^T (Ax + Bu + d - \dot{x}_d) = -\eta sign(S_s) \tag{15}$$

The control input u from (20) can be extracted as

$$u = -K^T x + (S^T B)^{-1} [S^T \dot{x}_d - S^T \hat{d} - \eta sign(S_s)] \tag{16}$$

with $K^T = (S^T B)^{-1} S^T A$.

From Eq. (15), it can be rewritten as follows

$$\dot{S}_s = S^T A_c x - \eta sign(S_s) + S^T (\hat{d} - d) \tag{17}$$

where $A_c = A - BK^T$.

Choosing S as the eigenvector of A_c^T for eigenvalue $\lambda = 0$ that is

$$\dot{S}_s = -\eta sign(S_s) + S^T (\hat{d} - d) \tag{18}$$

Differentiation of Lyapunov function candidate is

$$\begin{aligned} \dot{V}(S_s) &= -\eta S_s sign(S_s) + S_s S^T (\hat{d} - d) \\ &= -\eta |S_s| + S_s S^T (\hat{d} - d) \end{aligned} \tag{19}$$

Error state converging to sliding surface exists if η is chosen as follows

$$\eta > \left\| S^T \right\| \left\| \hat{d} - d \right\| \tag{20}$$

To prevent chattering because of the discontinuity in control law with switching function $sign(S_s)$, the sign function could be replaced by the continuous function $\tanh(S_s/\phi)$, where ϕ is the sliding surface boundary layer thickness.

4.2 Steering Controller Design

In Fig. 5, a block diagram of heading controller is described. With the input value of ψ_d and feedback values of the AUV states $x = [v\ r\ \psi]$, the steering controller will estimate a rudder angle δ_{rudder} that is input into AUV nonlinear dynamics to maneuver the AUV. Substituting the hydrodynamic coefficients [8] of the AUV into

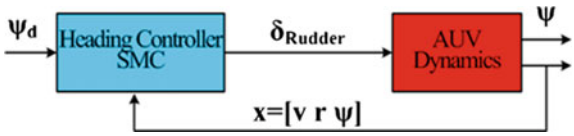

Fig. 5 Block diagram of steering control system

Eq. (9), the sliding poles of the steering control system selected arbitrarily at (−1.4, −1.55, 0), and then using Eqs. (16) and (20), we get the steering control law as:

$$\begin{cases} S_{s2} = [\,0.056 \quad 0.477 \quad 0.877\,]\tilde{x}_2 \\ u_2 = \delta_R = -0.8v + 0.682r + 1.868\eta_2 \tanh(S_{s2}/\phi_2) \\ -\pi/6 \le u_2 \le \pi/6 \\ \eta_2 = 0.5, \quad \phi_2 = 0.1 \end{cases} \tag{21}$$

4.3 Diving Controller Design

A diving control law is proposed for the AUV as in Fig. 6. All the controllers are designed by sliding mode control. First, the state errors calculated from desired set-points and feedback values of the vehicle states $x = [q\ \theta\ z]$ are the input of the diving controller block whose output is the desired movable mass position x_{m_d}. Then, the movable mass position error is calculated from the desired and feedback values of the movable mass position and becomes the input of the position controller block. The output of the position controller block is the appropriate force u_m used to drive the movable mass from position x_m to x_{m_d}. And finally, with this diving control law, the vehicle constructed by nonlinear equations will be controlled to the desired depth.

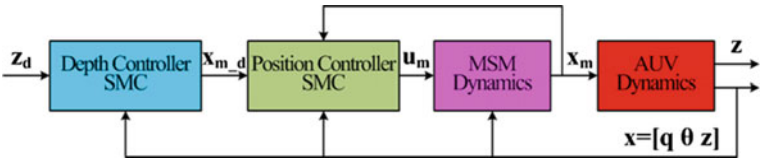

Fig. 6 Block diagram of diving control system

Substituting the coefficients [8] into Eq. (7) and the sliding poles of the diving control system selected arbitrarily at (−0.6, −0.5, 0), we get the depth controller as

$$\begin{cases} S_{s1} = [0.667 \quad 0.7337 \quad -0.1297]\tilde{x}_1 \\ u_1 = x_{m\_d} = 0.067q - 0.098\theta + 0.3637\eta_1 \tanh(S_{s1}/\phi_1) \\ -0.1 \le u_1 \le 0.1 \\ \eta_1 = 0.3, \quad \phi_1 = 0.1 \end{cases} \tag{22}$$

As expressed in SMC theory [9], the position controller for movable mass is designed from Eq. (2) as follows

$$\begin{cases} S_{sm} = \dot{\tilde{x}}_m + \lambda\tilde{x}_m \\ u_m = -f - \lambda\dot{\tilde{x}}_m - \eta_m \tanh(S_{sm}/\phi_m) \\ \lambda = 4.3, \quad \eta_m = 0.7, \quad \phi_m = 0.1 \end{cases} \tag{23}$$

5 Simulation Results

Under effects of modeling nonlinearity and parameter uncertainty, a numerical simulation has been performed in order to show the effectiveness of the proposed control system. The simulation program, which is developed using Matlab/Simulink, is shown in Fig. 7. The 6 DOF nonlinear vehicle model in Eq. (3) is simulated and nonlinear coefficients are referred in [8]. The controller blocks are composed of the steering and diving controllers designed in previous sections.

Figure 8 shows the desired heading, tracking trajectory, and rudder angle variable for the steering control simulation. This simulation is performed together with zero diving control in order to prevent the vertical motion occurring from the coupling. The initial heading angle of 0° was kept static in 5 s. After that, the AUV

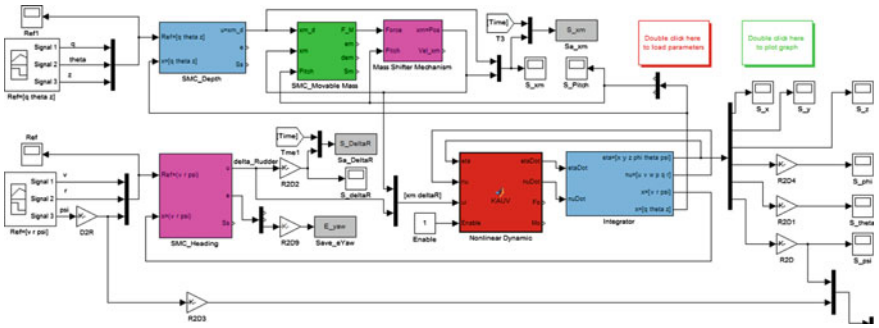

Fig. 7 Simulink diagram of steering and diving control system

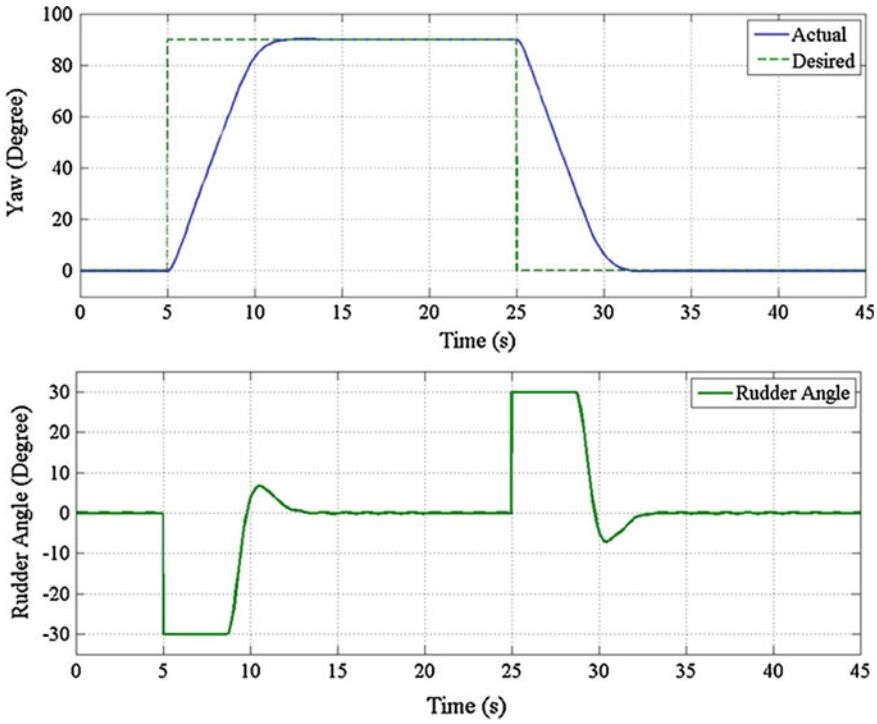

Fig. 8 Simulation result of steering control

was commanded to track two desired heading angles of 90° and 0° in 20 s for each turn. From these figures, the proposed control system has accurate tracking performance with rudder angle limited in ±30°. Also, sliding mode control show the robustness on the presence of modeling nonlinearity and parameter uncertainty.

Figure 9 shows the response of the diving control. The initial depth of 0 m is kept in 5 s. The desired depth is given 3 m down from the initial depth during 65 s, and then returning back to the initial depth. The mass shifter mechanism is controlled in bound of stroke's length [−10 cm, 10 cm] to shift the center gravity of the whole vehicle for diving and floating. The simulated results show good convergence with the desired depth. The proposed control system makes the nonlinear AUV model robust and controllable.

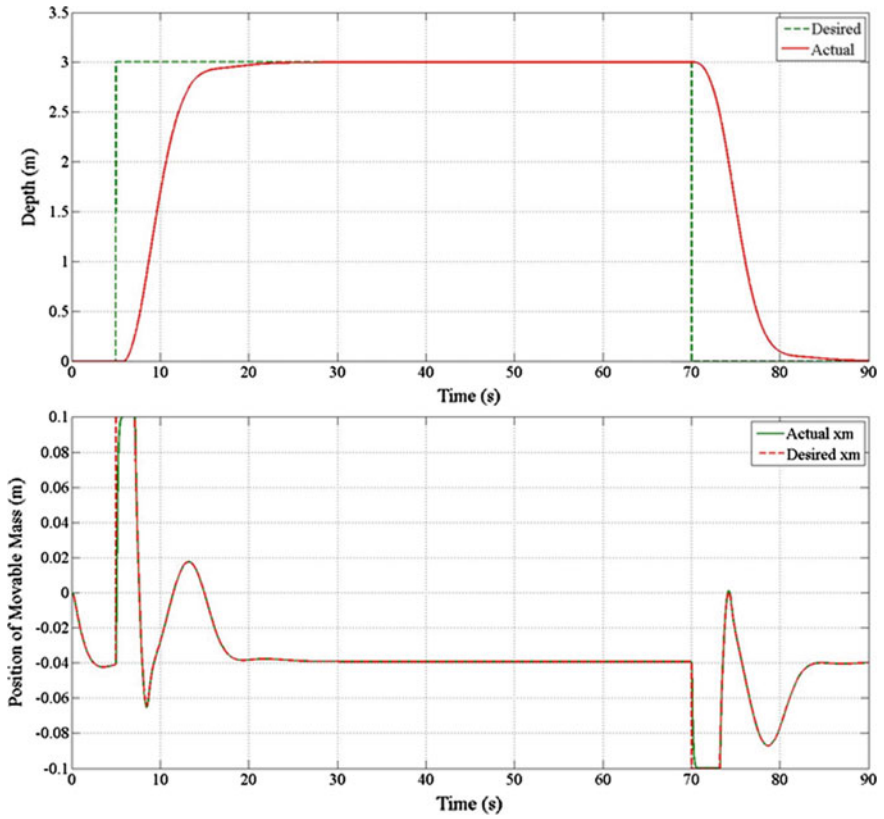

Fig. 9 Simulation result of diving control

6 Conclusion

In this paper, the use of sliding mode methods has been shown to provide robust performance of the KAUV's autopilots when designed separately for steering and diving control. This method is generally suitable for a wide variety of nonlinear control problems such as modeling nonlinearity, parameter uncertainty, and disturbance. The designed controllers using the sliding surface coefficients were derived from the linearized vehicle model for steering and diving planes. Finally, the simulation results show that the proposed controllers can maneuver the KAUV nonlinear model to be robust and maintain the desired depth and heading angle with sufficient accuracy.

Acknowledgements This research was a part of the project titled 'Base Research for Building Wide Integrated Surveillance System of Marine Territory', funded by the Ministry of Oceans and Fisheries and Basic Science Research Program through the National Research Foundation of Korea(NRF) funded by the Ministry of Education (2015R1D1A3A01015804).

References

1. Kukuly A et al (2010) Under-ice operations with a REMUS-100 AUV in the Arctic. In: Proceeding of AUV 2010 IEEE conference, Monterey, CA, USA, pp 1–8
2. McEwen R (2006) Modeling and control of a variable-length AUV. Technical report
3. Panish R (2006) Dynamic control capabilities and developments of the Bluefin robotics AUV fleet. In: Proceedings of 16th international symposium on unmanned untethered submersible technology, Durham, NH, USA
4. Jenkins SA Humphreys DE, Sherman J et al (2003) Underwater glider system study. Technical report, Office of Naval Research
5. Tran NH, Choi HS et al (2014) Navigation and depth control of a small-sized AUV with mass shifter mechanism. In: Proceeding of the 24th international ocean and polar engineering conference (ISOPE), Busan, Korea, 15–20 June 2014
6. Fossen TI (1994) Guidance and control of ocean vehicles. Wiley, New York
7. Healey AJ, Lienard D (1993) Multivariable sliding mode control for autonomous diving and steering of unmanned underwater vehicles. IEEE J Oceanic Eng 18(3):327–339
8. Prestero T (2001) Verification of a six-degree of freedom simulation model for the REMUS autonomous underwater vehicle. M.S. thesis, Massachusetts Institute of Technology, USA
9. Slotine JJ, Li W (1991) Applied nonlinear control. Prentice Hall, Upper Saddle River

Design and Implementation of Dynamic Positioning Control System for USV

Ngoc-Huy Tran, Hyeung-Sik Choi, Ji-Youn Oh and Sang-Ki Jeong

Abstract Nowadays, the dynamic positioning (DP) performance of an unmanned surface vehicle (USV) is receiving special attention for marine research and surveying exploration in coastal areas. So, this paper describes a structure design of a USV disposed with three thrusters. With this disposition, by means of active thrust, the USV can be controlled at a fixed position with fixed heading. Also, hardware and software architectures of the control system are addressed and the functions of all parts are clarified. A strategy for DP control is presented to compensate the deviations due to disturbances from waves, wind, sea current, or sensor inaccuracy. Finally, according to this developed strategy, a number of experiments were performed through sea trials and the results will be shown.

Keywords Unmanned surface vehicle · Dynamic positioning · Kalman filter

1 Introduction

The ocean is the cradle of life, a precious resource, and transportation artery. In the 21st century, we will face three challenges: the contradictions between the population explosion and limited living space, between exhausted land resource and the growing requirement of social production, and between eco-environmental degradation and human development. In addition, there exist sea regions with dangerous mines that should be eradicated for military affairs, humanitarian reasons, and marine safety. So, it is necessary to use unmanned vehicles for ocean survey in coastal areas, supporting the work of underwater vehicles by aiding in communication and localization, with no risks for human as a priority, as shown in Fig. 1.

N.-H. Tran · H.-S. Choi (✉) · J.-Y. Oh · S.-K. Jeong
Department of Mechanical Engineering, Korea Maritime and Ocean University, Pusan, South Korea
e-mail: hchoi@hhu.ac.kr

V.H. Duy et al. (eds.), *AETA 2015: Recent Advances in Electrical Engineering and Related Sciences*, Lecture Notes in Electrical Engineering 371,
DOI 10.1007/978-3-319-27247-4_53

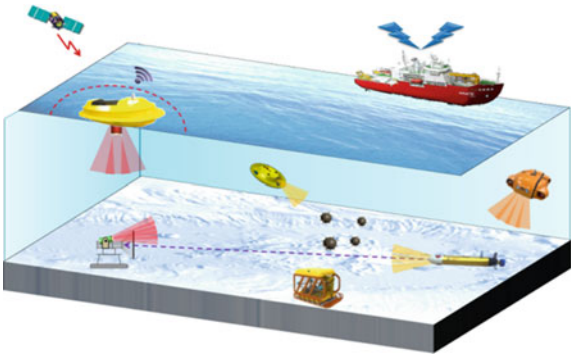

Fig. 1 The USV application

The unmanned surface vehicle (USV) is an intelligent motion platform, which can be relied on for remote control, or autonomous and safe navigation in the real marine environment, and for the completion of various tasks. The USV has many merits, such as a variety of functions, flexibility of operations, little injury, and a flexible network information center [1]. Despite these merits, few researches have been performed about the USV [2]. It has only had 15–20 years of development, and there are a small number of USVs on the market or in use so far, especially compared to autonomous underwater vehicles (AUV). One of the application cases of the USV is the Italian catamaran USV, called SESAMO, which is used in oceanographic research [3]. The stability, payload capacity and ease for manufacturing make catamarans a compelling choice for researching USVs. The ROAZ vehicles from Portugal, like SESAMO, exemplify the general arrangements [4]. Also, there was a research on a mine disposal system using an autonomous marine surface vehicle (AMSV) [5], which supported surveys and networked operations with AUVs. In general, more attention to USV research and development will be paid in the future.

For the purpose of supporting communication, reference localization, or docking for the underwater vehicles, a USV using three thrusters is designed. With this structure design and developed control system, the USV can perform dynamic positioning control to keep a desired position and heading. Moreover a dynamic positioning control algorithm to eliminate the disturbance errors is suggested and performed in experiments.

2 Structure and Control System of the USV

2.1 Structure of the USV

The hull structure of the USV is designed with a closed cover for waterproofing. The body is made of FRP (Fiber Reinforced Plastic), which has high corrosion resistance, is of light weight, and has high durability. To control surge, sway, and

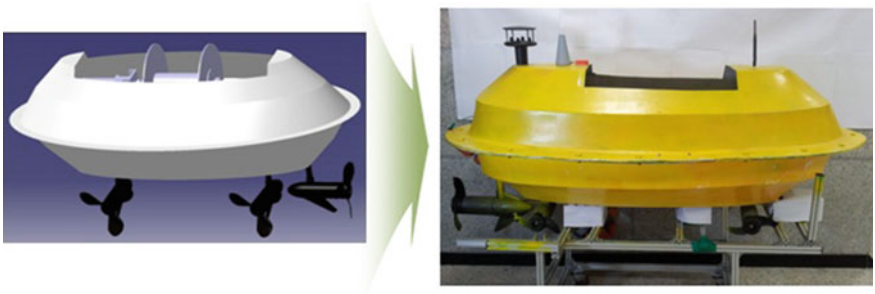

Fig. 2 The virtual design and developed USV

Table 1 Specifications of the USV system structure

Hull structure specifications	1.9 m × 0.9 m × 0.7 m Max. speed: 3 knots
Propulsion module	One Endura50 thruster and Two Endura30 thrusters
Control system module	Embedded computer: IEC667 Processors: DSP28335, DSP2812 RF module: 24XStream
Navigation sensors	GPS_AsteRx1, IMU_MTi DVL_NavQuest 600, WindSonic sensor

yaw motion fully, three thrusters for the USV are required and disposed as in Fig. 2. The main thruster disposed at the USV's stern is an Endura50 with 50 lbs (22.68 kgf) thrust force, and two Endura30 lateral thrusters provide 30 lbs (13.61 kgf) thrust force for each one. The weight of the USV is 150 kg, and the center point (CP) of the USV is at 0.75 m forward from the USV's stern. The main thruster is 0.7 m away along the X axis, and the lateral thrusters are at 0.5 m forward and afterward from the CP point. With this structure enclosed with a navigation system and control algorithm, the USV can flexibly move in multiple directions and automatically maintain at a desired position and heading. The specifications of the USV are described in Table 1.

2.2 Hardware Architecture

As shown in Fig. 3, the USV control system is composed of six modular parts, which are the ground monitoring station, onboard control system, navigation system, battery, actuators, and communication system.

The ground monitoring station is composed of computer, joystick, and wireless communication equipment. Its mission is to collect and process signals received from the USV. With the multifunctional operating interface programmed by Visual

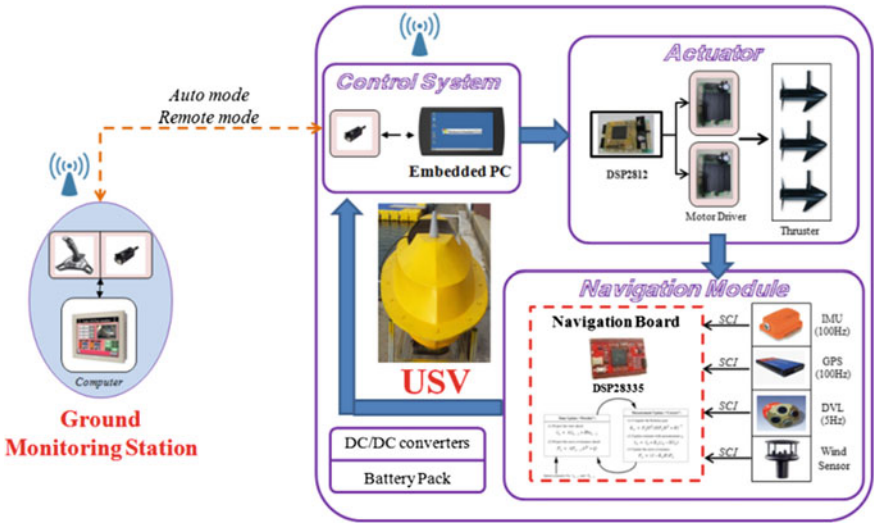

Fig. 3 Hardware architecture of the USV motion control system

Studio 2008, the USV can be controlled by two modes that are auto mode and remote mode. Furthermore, the ground monitoring station can also be extended to build on a host ship, and carry on multi-USV operations, by setting an ID account for each vehicle.

The navigation module is composed of IMU, doppler velocity log (DVL), GPS, and wind sensor. They are used to determine the position, velocity, acceleration, course, and distance traveled of the vehicle. The USV is equipped with an inertial navigation system (INS), which can calculate the position, velocity, and attitude of the vehicle from the data given by the IMU sensor. Since the INS accumulates errors, due to the inherent drift of dead-reckoning velocities and integration of acceleration, a Kalman Filter algorithm should be implemented, which utilizes a wide range of navigation sensors, to compensate for the accumulation in position error [6]. The collection of sensor signals and estimation of the Kalman Filter algorithm are accurately performed in the developed navigation board, using the powerful DSP28335 [7] (150 MHz), as shown in Fig. 3.

Finally, the onboard control system module contains an embedded IEC667 computer connected with two microprocessors TMS320F28335 (Digital Signal Processors) and TMS320F2812, which cooperate to perform all the control tasks of the USV, as shown in Fig. 3. The TMS320F28335 processor, programmed in the navigation module, calculates the attitude, velocity, and position of the USV, by using a developed Kalman Filter algorithm, and transfers the results to the embedded computer used for guidance and control of the USV. After receiving the data from the navigation module, as well as the requirements from the ground monitoring station, the IEC667 will automatically compute an optimal trajectory or path for the USV by Visual Studio 2008, and deliver control commands to

TMS320F2812, for driving the actuator modules. At the same time, the IEC667 will inform about the states of the USV, and can directly receive commands from the control center on the ground, via the RF communication module.

2.3 Control Software Architecture

The control software architecture of the USV system is composed of two elements: monitoring system software programmed for the ground station, and control system software used in the onboard USV module. The programming language used in both of them is Visual Studio 2008.

(a) **Ground monitoring system software**

To monitor the states and to communicate with the USV, the GUI (Graphic User Interface) control software of the ground system is programmed. This interface is not only prompt and flexible to set control modes and parameters for the USV's operation, but also quite accurate to transmit a pre-scheduled or real time trajectory following commands, and receive state feedback from the vehicle. The algorithm diagram of the ground monitoring system is shown in Fig. 4. After starting the GUI

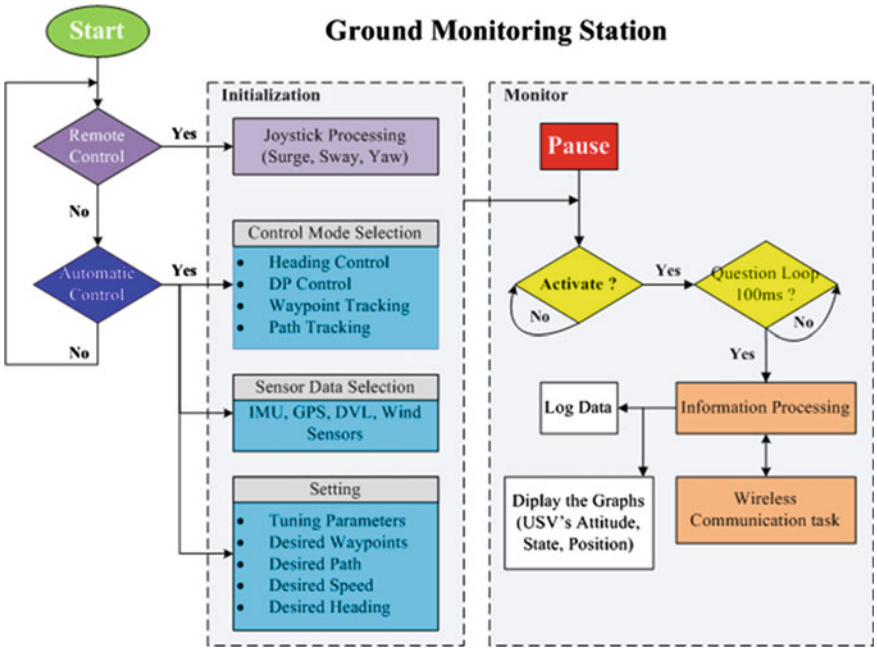

Fig. 4 An algorithm diagram of the ground monitoring system

program, the user will be asked to select control modes of remote control or automatic control. For each control mode, there will be a different parameter initialization. In remote control mode, the axis and buttons on the joystick should be declared to correspond with the axes (surge, sway and yaw) of the body-fixed co-ordinate put on the USV, maximum and minimum speeds of the vehicle when adjusting the joystick potentiometer, and sensitivity (loop time) for reading signal from the joystick, etc. With automatic control mode, first, the user should select control algorithms, such as heading control, dynamic positioning (DP) control, waypoint tracking, and path tracking, etc. Next, sensors selection (IMU, GPS, DVL, wind sensor) used in the navigation system, desired trajectory, and control gains should be chosen, to complete declaration for the parameter initialization. After that, the monitor of the GUI program starts operating. With a question loop every 100 ms (10 Hz), the ground monitoring system can quickly update, exactly log, and intuitively display the states of the USV through real-time visual graphs. Moreover, a special feature of this ground monitoring program is its synchronous nature. If errors, such as tracking error, navigation error, out of battery, and damaged equipment (sensors, thrusters, control boards), are detected from the processing of feedback signals, the user can immediately interfere in the onboard control system software, to solve these problems.

(b) **Onboard control system software**

The software architecture of the onboard control system is presented in Fig. 5. In this, the mission of the information processing block is to receive commands from the ground monitoring station, and to sort them according to separated missions already shown in the ground monitoring system software, such as control modes, control algorithms, and processing errors, etc. Then, these delivered missions will be completely performed by the next control blocks. The control task decomposition block is used to initialize control parameters for each different control. These parameters will be sent to the navigation and motion control algorithm block that is the main control block, to process the control missions, such as remote control, heading control, waypoint tracking, etc. Besides, navigation values (attitude, position, velocity) are also estimated in this block, through data received from the sensors. The navigation algorithm will be particularly described in the strategy design section. According to situations of the control tasks and navigation estimation, control instructions are processed by the embedded computer, and sent to the actuator modules to operate the USV. In addition, the states of the USV, as well as onboard equipment and sensor information, will be summarized to save in logbook memory, and also to answer the question loop (10 Hz), received from the ground monitoring station.

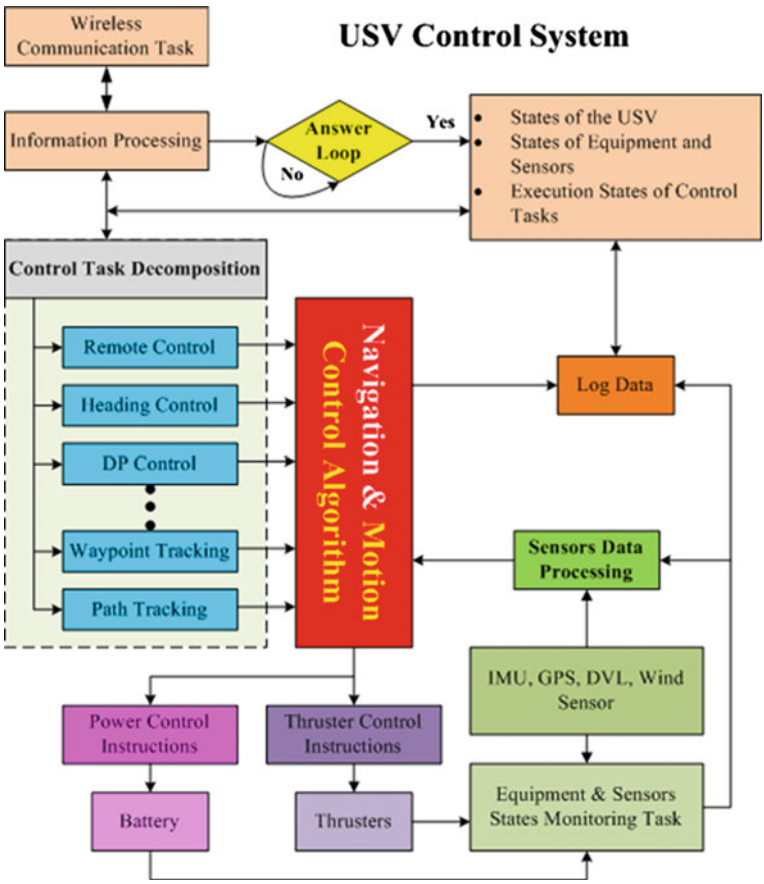

Fig. 5 An algorithm diagram of the onboard control system

3 Control Strategy for Dynamic Positioning

3.1 The Fusion Control Algorithm

Figure 6 shows the control algorithm diagram describing the main functions of the USV control system influenced by environment (wave, current, wind). There are three objectives for motion control: position, heading, and speed. They are measured by using the GPS, IMU, DVL sensors, and their data are feedback to the filter module. A Kalman Filter algorithm is applied to filter noises out, and to estimate the actual states of the USV. The PID controller generates force instructions for thrusters, to compensate for position, yaw angle, and velocity errors of the USV. The allocation algorithm is developed to map the generalized force instructions into appropriate force instructions for the various actuators of the USV.

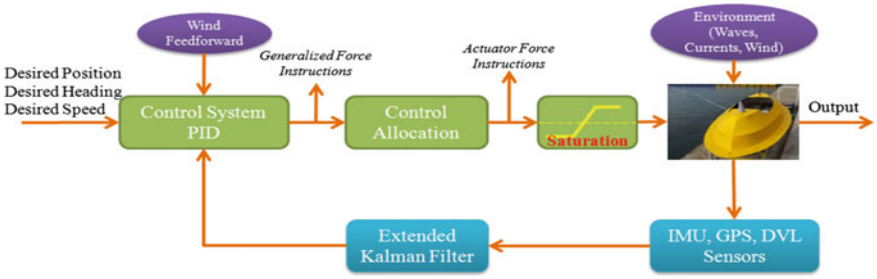

Fig. 6 The fusion control system of the USV

3.2 *Dynamic Positioning (DP) Control Algorithm*

DP control is used to keep the position and heading of the vehicle by using its own thrusters and sensors. For a vehicle to perform position-keeping and/or heading-keeping operations in a seaway, some deviations always occur due to disturbances from waves, wind, sea current, or sensor inaccuracy. Hence, to facilitate DP control of the USV, three deviation levels are defined in heading-keeping and position-keeping controls: the inner level (L1) represents the minimum deviation zone, the mid level (L2) represents the allowable operation zone, and the outer level (L3) represents the maximum operation bound, as shown in Fig. 7, which is referred from [8]:

In level 1 (inner level):

$$\text{Surge L1} = \max\left(\text{North}-\text{South sensor error},\ \text{East}-\text{West sensor error}\right) + \text{offset surge}$$
$$\text{Sway L1} = \max\left(\text{North}-\text{South sensor error},\ \text{East}-\text{West sensor error}\right) + \text{offset sway}$$
$$\text{Yaw L1} = \text{maximum sensor error} + \text{offset yaw}$$

The offsets for surge, sway, and yaw are function of the vessel operational conditions (VOC) and are defined as the minimum obtainable deviation for the VOC.

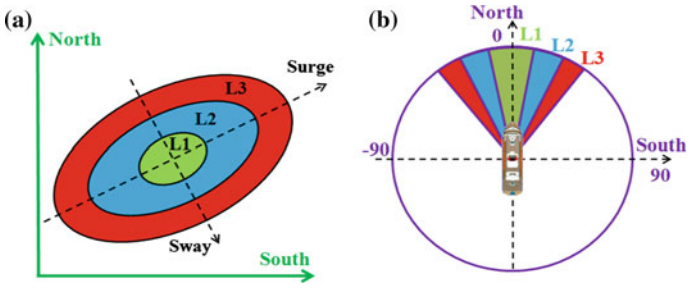

Fig. 7 The position levels (**a**) and heading levels (**b**)

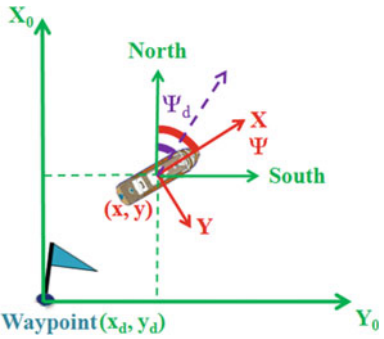

Fig. 8 Dynamic positioning control of the USV

In level 2 (mid level):

$$\begin{aligned}\text{Surge L2} &= \text{surge L1} + \gamma(\text{surge L3} - \text{surge L1})\\ \text{Sway L2} &= \text{sway L1} + \gamma(\text{sway L3} - \text{sway L1})\\ \text{Yaw L2} &= \text{yaw L1} + \gamma(\text{yaw L3} - \text{yaw L1})\end{aligned}$$

where $\gamma \in \langle 0, 1 \rangle$

In level 3 (outer level):

Surge L3 = max operation area in surge—max (North-South sensor error, East-West sensor error)
Sway L3 = max operation area in sway—max (North-South sensor error, East-West sensor error)
Yaw L3 = max heading deviation—maximum sensor error

With desired attitude $[x_d, y_d, \psi_d]$ and vehicle current attitude $[x, y, \psi]$ shown in Fig. 8, the errors of the USV in the earth-fixed coordinate can be written as:

$$e = [e_{X_0}, e_{Y_0}, e_\psi] \tag{1}$$

From Eq. (1), the propulsion vector in the earth-fixed can be set as

$$PID = [X_{X_0}, Y_{Y_0}, N_{Z_0}] \tag{2}$$

where X_{X_0}, Y_{Y_0} are forces, N_{Z_0} is moment [8]

$$X_{X_0} = K_{Px} e_{X_0} + K_{Ix} \int e_{X_0} dt + K_{Dx} \frac{de_{X_0}}{dt} \tag{3}$$

$$Y_{Y_0} = K_{Py} e_{Y_0} + K_{Iy} \int e_{Y_0} dt + K_{Dy} \frac{de_{Y_0}}{dt} \tag{4}$$

$$N_{Z_0} = K_{P\psi} e_\psi + K_{I\psi} \int e_\psi dt + K_{D\psi} \frac{de_\psi}{dt} \tag{5}$$

The propulsion vector can be converted from the earth-fixed coordinate to the body-fixed coordinate as

$$\begin{bmatrix} X \\ Y \\ N \end{bmatrix} = \begin{bmatrix} \cos\psi & \sin\psi & 0 \\ -\sin\psi & \cos\psi & 0 \\ 0 & 0 & 1 \end{bmatrix} \begin{bmatrix} X_{X_0} \\ Y_{Y_0} \\ N_{Z_0} \end{bmatrix} \tag{6}$$

The propulsion vector $[X, Y, N]^T$ in the body-fixed coordinate can be applied to control thrusters of the vehicle to keep the USV to the desired position and angle.

4 Experiments

For application of the DP control algorithm to experiments, the deviation levels are empirically selected as:

Surge L1 = sway L1 = 0.5 m
Surge L2 = sway L2 = 1 m
Surge L3 = sway L3 = 1.5 m
Yaw L1 = ±2°, Yaw L2 = ±4°, Yaw L3 = ±8°

Figures 9 and 10 show results of the dynamic positioning control performance. The DP experiment was performed for 40 s. The USV received instructions to maintain the yaw angle at −90°, and kept the position at zero. According to the data, the USV was controlled well to keep itself in the inner level (radius = 0.5 m) and heading angle in the mid level (bound is ±4°) regardless of the wave and wind disturbances.

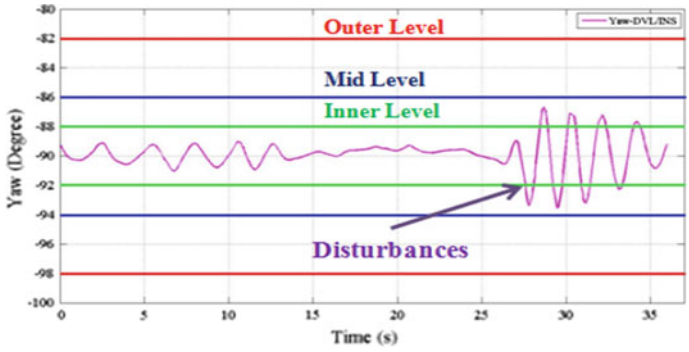

Fig. 9 Heading performance of dynamic positioning control

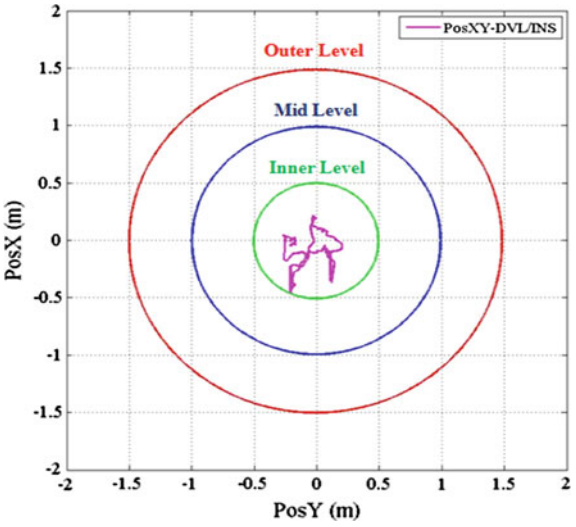

Fig. 10 Position performance of dynamic positioning control

5 Conclusion

In this paper, the structure design and control system of the three degree of freedom USV were presented. The USV using three thrusters was designed for dynamic positioning and navigation controls. Also, the control system for DP control was developed, including the power microcontrollers, GPS, IMU and DVL sensors. With these sensors, the USV can apply Kalman Filter algorithm to accurately estimate the position, velocity, acceleration, and traveled distance of the vehicle. For easy management of the control process, the control software architecture composed of the ground monitoring system software and onboard control system software were developed.

The strategy for DP control was presented to compensate the deviations due to disturbances from waves, wind, sea current, or sensor inaccuracy. Based on the values received from the estimation of Kalman Filter, the USV's PID controller can estimate the needed forces and moments to keep the vehicle in desired position and heading with three deviation levels L1, L2, and L3. To validate the designed control system and the developed algorithm, a sea-trial experiment was performed. According to the experimental results, the USV was well controlled to stay in position deviation of 0.5 m radius, and to keep its heading within ±4° bound under effect of wave, current, and wind disturbances.

Acknowledgements This research was a part of the project titled 'R&D center for underwater construction robotics, funded by the Ministry of Oceans and Fisheries (MOF) and Korea Institute of Marine Science and Technology Promotion (KIMST), Korea (PJT200539). Also, it was supported by the development of a multi-legged underwater walking robot project under the Ministry of land, infrastructure, and transport.

References

1. Roberts G, Sutton R (2006) Advances in unmanned marine vehicle. Institution of Engineering and Technology
2. Manley JE (2008) Unmanned surface vehicles, 15 Years of development. In: Proceedings of oceans 2008 MTSIIEEE Quebec conference and exhibition (Ocean'08), IEEE Press, pp 1–4
3. Caccia M, Bono R, Bruzzone GA, Bruzzone GI, Spirandelli E, Veruggio G, Stortini AM, Capodaglio G (2005) Sampling sea surfaces with SESAMO. Robot Autom Mag 12(3):95–105
4. Ferreira H, Martins R, Marques E, Pinto J, Martins AO, Almeida JM, Sousa JB, Silva EP (2007) Swordfish: an autonomous surface vehicle for network centric operations. In: Proceedings of the oceans Europe '07 conference, IEEE OES, Aberdeen, Scotland
5. Pereda FJ, de Marina HG, Jiménez JF, Giron-Sierra JM (2010) A development project of autonomous marine surface vehicles for sea demining. In: Control, automation, robotics and vision conference, IEEE, Singapore, 7–10th December 2010
6. Titterton DH, Weston JL (2004) Strapdown inertial navigation technology. American Institute of Aeronautics and Astronautics
7. Tran NH, Choi HS, Kim JY, Lee MH (2012) Development of rotational motion estimation system for a UUV/USV based on TMS320F28335 microprocessor. Int J Ocean Syst Eng 2(4):223–232
8. Alme J (2008) Autotuned dynamic positioning for marine surface vessels. Master thesis of Science in Engineering Cybernetics

Study on Mechanical Structure Design for Innovative Multi-function Assistive Mobile Robot

Vo Hoang Duy, Tran Trong Dao, Nguyen Thanh Quang and Ngoc-Bich Le

Abstract It is of great significance to develop devices which can support the elderly, disabled lower limbs persons and mobility degraded patients in their daily activities such as transferring from bed to wheelchair or from wheelchair to toilet and so forth. It is evident that the assistant of human in these activities especially in toilet activity cause uncomfortable for both of them in term of physical and psychological health. This paper presents the concept design and the experimental results of a full-sized prototype assistive mobile robot with lift, transfer and locomotion functions, which confirms the design effectiveness. The experiment results indicated that the robot with flexible dynamic giving excellent moving ability in narrow space. Furthermore, self-locking mechanism in all operations as well as tilt angle alert sensor give absolutely safety ability.

Keywords Self-transfer · Assistive robotic · Multi-function

V.H. Duy (✉) · N.T. Quang
Faculty of Electrical and Electronics Engineering, Ton Duc Thang University,
No. 19 Nguyen Huu Tho Street, District 7, Ho Chi Minh City, Vietnam
e-mail: vohoangduy@tdt.edu.vn

N.T. Quang
e-mail: nguyenthanhquang@tdt.edu.vn

T.T. Dao
MERLIN, Ton Duc Thang University, No. 19 Nguyen Huu Tho Street, District 7,
Ho Chi Minh City, Vietnam
e-mail: trantrongdao@tdt.edu.vn

N.-B. Le
School of Enginering, Eastern International University, Binh Duong New City, Vietnam
e-mail: bich.le@eiu.edu.vn

V.H. Duy et al. (eds.), *AETA 2015: Recent Advances in Electrical Engineering and Related Sciences*, Lecture Notes in Electrical Engineering 371,
DOI 10.1007/978-3-319-27247-4_54

1 Introduction

In Vietnam, there are more than 30 % of cerebrovascular patients with and subsequently lost their movement ability. Furthermore, according to survey data [1], in 2013, Vietnam has 29,385 traffic accidents caused 39,000 deaths and 25,000 disabilities. In addition, elderly people and other disabilities take a significant number. By 2050, the current youth population in developed countries will become "older population", which comprises 27 % of total world population. This will affect the socio-economic development of these countries [2].

Consequently, various devices and robots have been developed. The first candidate for these devices is Dependent lift devices [3–5]. As the name implies, the wheel chair user needs to depend on care givers for transferring to another surface.

The second type is self-transfer systems. S-transfer systems assist an elderly or disabled to lift up and transfer to another surface without the assistance of caregiver. A simple device known as Trapeze lift, which can be connected to the bed or on a free-standing base, assists patients and elderly with some upper body strength to lift themselves to facilitate the provision of bedpan or to reposition [6].

The third candidate of assistive devices is wheel chairs with transfer modules. Mori et al. [7] had proposed a wheel chair with lifting function that could assist a caregiver in transferring a wheel chair dependent. However, the dimensions of the device are large may cause difficulties for the chair to approach the commode. Moreover, the device has to be moved towards the commode in reverse direction, which would be difficult for an elderly to perform independently.

Yoshihiko Takahashi et al. proposed a novel design to facilitate self-transfer from a wheel chair to a toilet commode [8, 9]. However, this proposed device is quite simple in term of operation functions. That is, it just has lifting ability why complete devices require multi-function including lift, transfer and locomotion.

All the assistive devices discussed above are either to serve a single specific purpose or need multiple sub-devices to achieve locomotion and transfer task. Consequently, this study proposed a novel self-transfer robot with compact design and multi-function including lift, transfer and locomotion. Receiving very high demands, however, the proposed design requires simple structure and operation.

2 Robot Structure Design

Y. Takahashi's proposed device is shown in Fig. 1 and its corresponding structure mechanism is indicated in Fig. 2. It is evident that the design consists of a robotic arm with a saddle on the top which can be elongated and a motorized horizontal rotation mechanism.

With the proposed mechanism, Y. Takahashi's robot operations were shown in Fig. 2, specifically, (1) The user positions the wheelchair in front of the toilet seat. The user takes a near-sitting posture and places his or her abdomen or chest on the

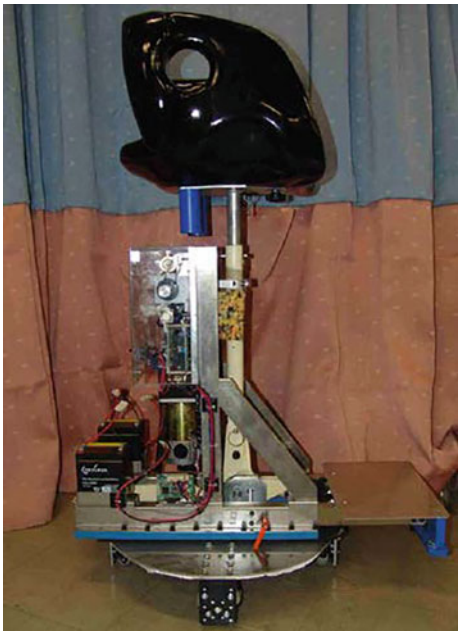

Fig. 1 Self-transfer aid robot with moving wheels of Y. Takahashi [8]

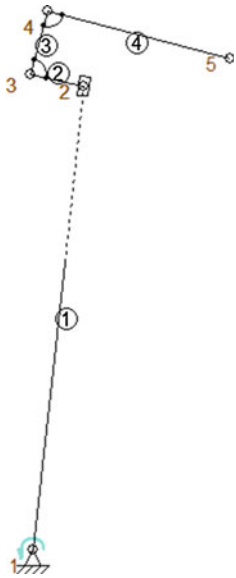

Fig. 2 Y. Takahashi's design

saddle. (2) A motor drive system rotates and lifts the robotic arm to straighten up the user. The motor stops when the user is ready to place weight on the saddle. (3) The transfer aid system is rotated horizontally and is stopped when the user is

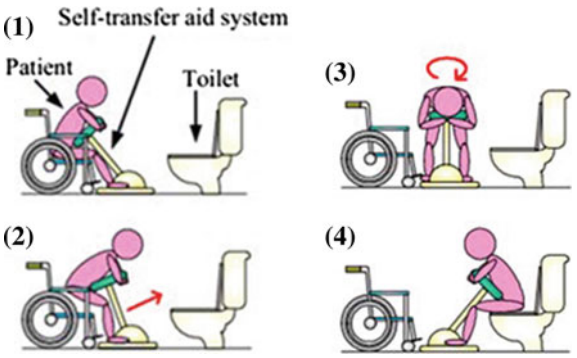

Fig. 3 Self-transfer aid robot of Y. Takahashi [8]

positioned toward the toilet seat. (4) The user's pants are pulled down, assuming a pair of pants that can be easily removed by hand. The user is seated, he or she uses the toilet, and moves back from the toilet seat to the wheelchair reversing these procedures (Fig. 3).

Y.Takahashi proposed design was a novel design for self-transfer robot, however, according to its structure and operation; it is evident that the following drawbacks have not yet comprehensively solved. That is, the operation function is still simple and the patient needs to perform holding all the operation time. As a result, this study proposed a new design with supporting seat mechanism was proposed to overcome Y.Takahashi's design drawbacks. The supporting seat helps lifting the patient comfortably when picking them up and vice versa. In addition, the seat also help patient seat firmly and conveniently during transferring process (Fig. 4).

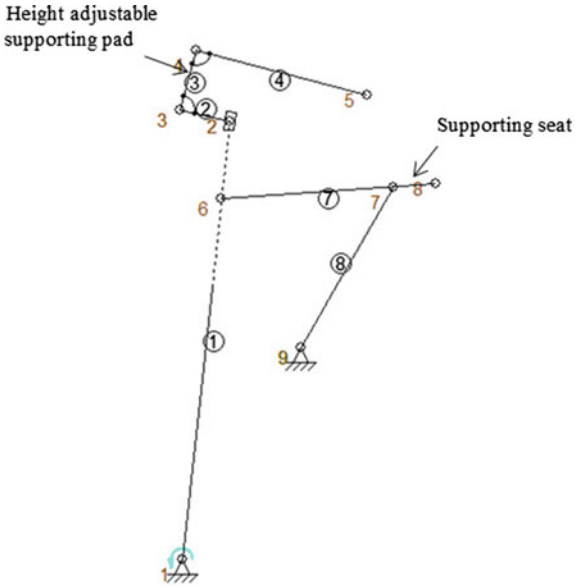

Fig. 4 Proposed design with supporting seat

In order to acquire suitable moving trajectory for supporting seat, SAM 6.1 commercial package was utilized to analyze the mechanism. Figure 5a, b indicated the supporting seat analysis results including moving trajectory and hodograph at initial and lower position, respectively. Figure 5c presented the graphed parameters including velocity, position of Node 3. After getting the suitable analysis results, the resulted structure parameters such as linkages' length, relative joints' coordinate were used to build the 3D structure.

The proposed novel mechanism shows the following advantages: Multi-function: Lift, transfer, locomotion; flexible dynamic giving excellent moving ability in narrow space; safety design with self-locking mechanism in all operations and tilt angle alert sensor; small size and simple structure.

Figure 6 demonstrates the robot design with boundary dimension. Specifically, Fig. 6a is four projection views and Fig. 6b is robot 3D design perspective view.

Robot structure was validated utilizing Solidworks Commercial Pakage with corresponding results were presented in Fig. 7. Figure 7a, c are analyzed model setting with external load is 700 N for main robot hand and supporting seat, respectively. Figure 7b, d are their corresponding von Mise stress graph. It is evident that the maximum von Mise stress in both structures is much lower than the material Yeild Strength. In other words, the proposed structures are strong enough.

The proposed structure gives robot the following merits: Take patient from/to wheel chair, take patient from/to bed, transfer patient from wheel chair or bed to toilet tube and reverse, supporting seat help patient seat firmly and comfortably during transferring process, holding pad height can be adjudged to fit different user sizes, self-lock mechanism.

3 Experiment

This project uses a dsPIC33FJ128MC506 microcontroller to automatically control the robot turn left, right, forward, and backward by using 02 DC motors which are 24 VDC with a rated moment of 100 kgf-cm and gear reduction ratio of 1/546.

Experiment was conducted with the operation steps shown in Fig. 8. That is,

1. To initiate the process, using remote control to control robot to intended position.
2. Press the control button to low the robot arm toward the user. The angle is depending on the user's most comfortable.
3. When the robot arm is in suitable position, release the button to stop.
4. Press the Auto-button to let the robot perform the lifting and 180° rotating automatically. There are two options for this operation including clockwise or counter clockwise.

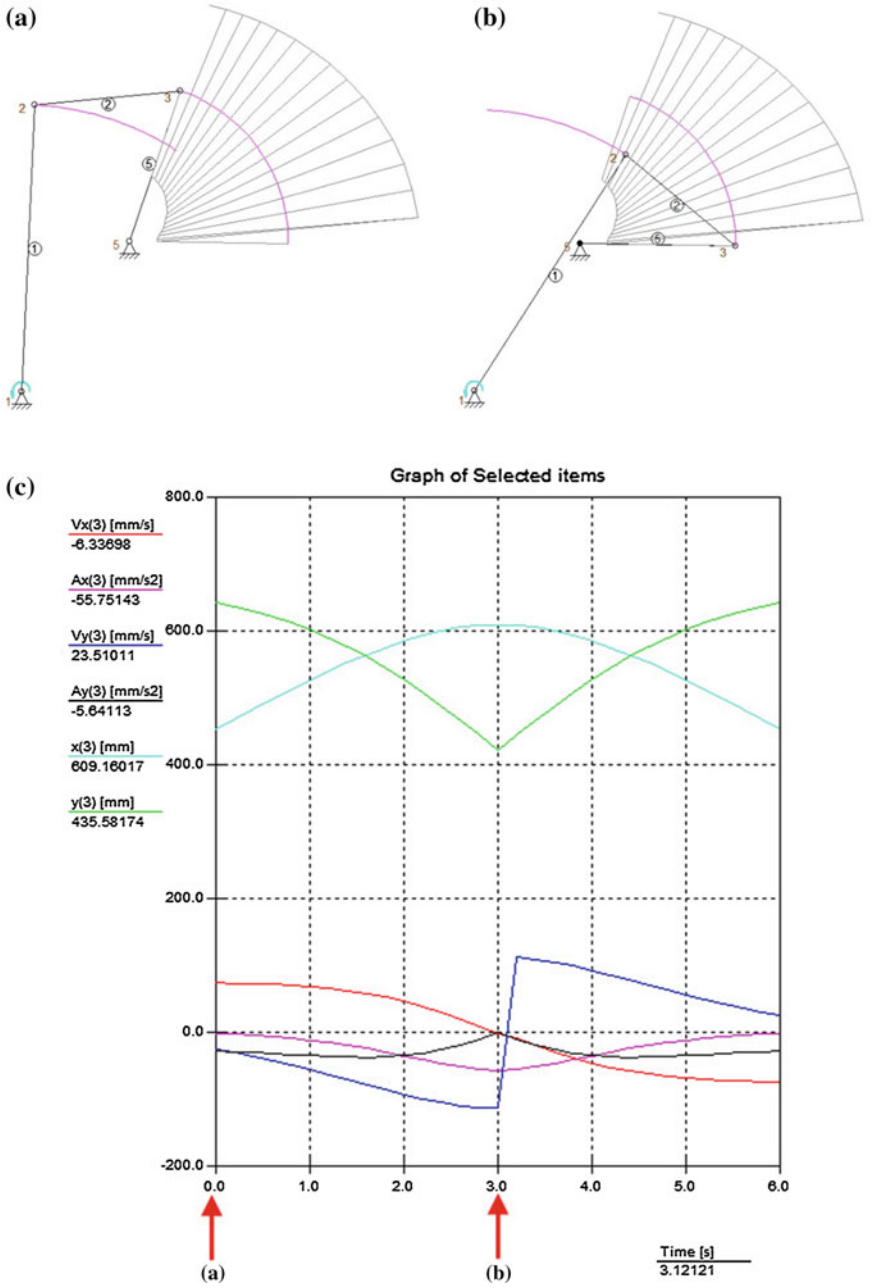

Fig. 5 **a** Supporting seat trajectory and hodograph at initial position; **b** Supporting seat trajectory and hodograph at low position; **c** Graph parameters of Node 3

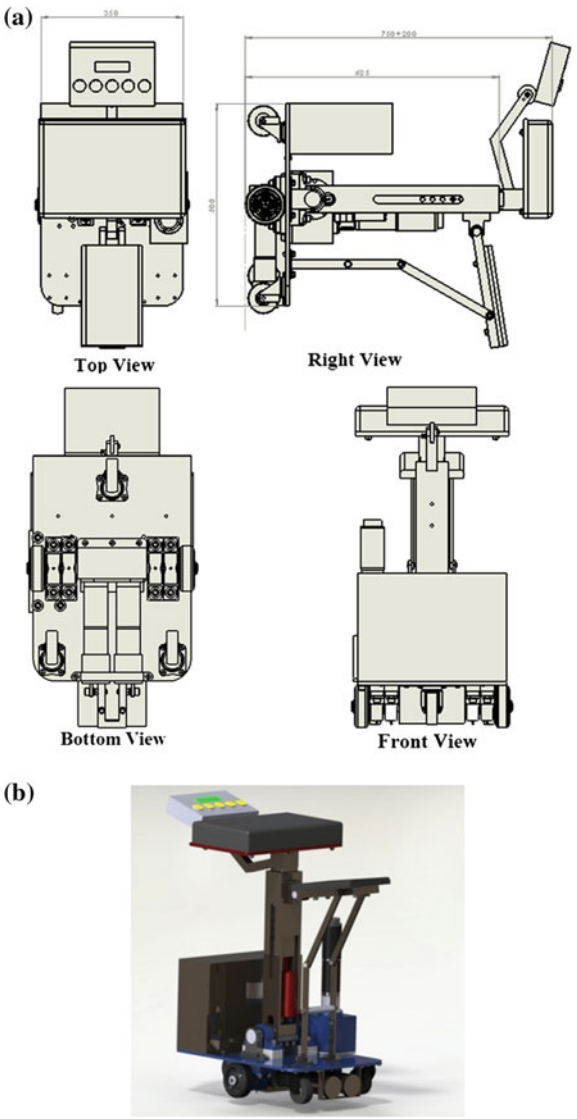

Fig. 6 **a** Robot design projection views with boundary dimension, **b** Perspective view

5. The user hold the top paddle, lifting process is performed within 3 s automatically.
6. After lifting process, the user can seat comfortably on the supporting seat.
7. Robot then rotate 180° automatically.
8. There are two options to perform the positioning action. That is, the user can manually control the robot arm to low down to suitable angle or using automatic option to let robot do it by itself with predefined angle.

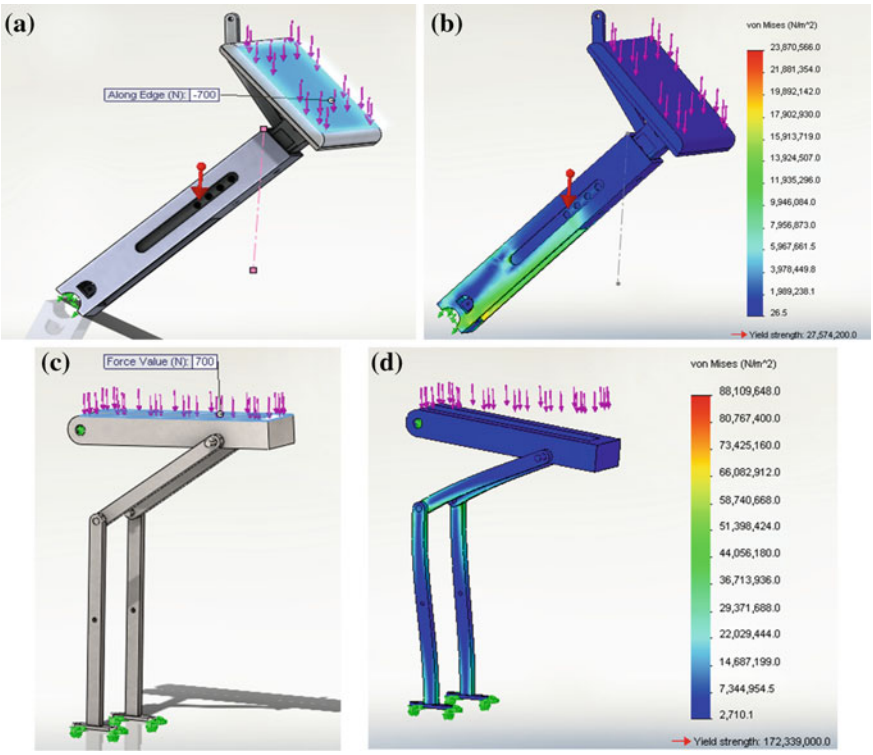

Fig. 7 FME analyzed results of supporting seat structure

9. Now, the supporting seat is right next to the toilet seat, the user just need to slightly slide to the toilet.
10. End of transferring process from wheel chair to toilet seat.

The transferring process from toilet seat back to wheelchair is performed similarly. Furthermore, robot can be controlled to move flexibly for locomotion purposed, that is, moving from bed to toilet, from bed to chair and vice versa.

Experimental results showed that, operations were performed correctly and smoothly as expected. Attended patients showed highly satisfaction. Additionally, the experimental results indicated that the robot with flexible dynamic giving excellent moving ability in narrow space; self-locking mechanism in all operations as well as tilt angle alert sensor give absolutely safety ability.

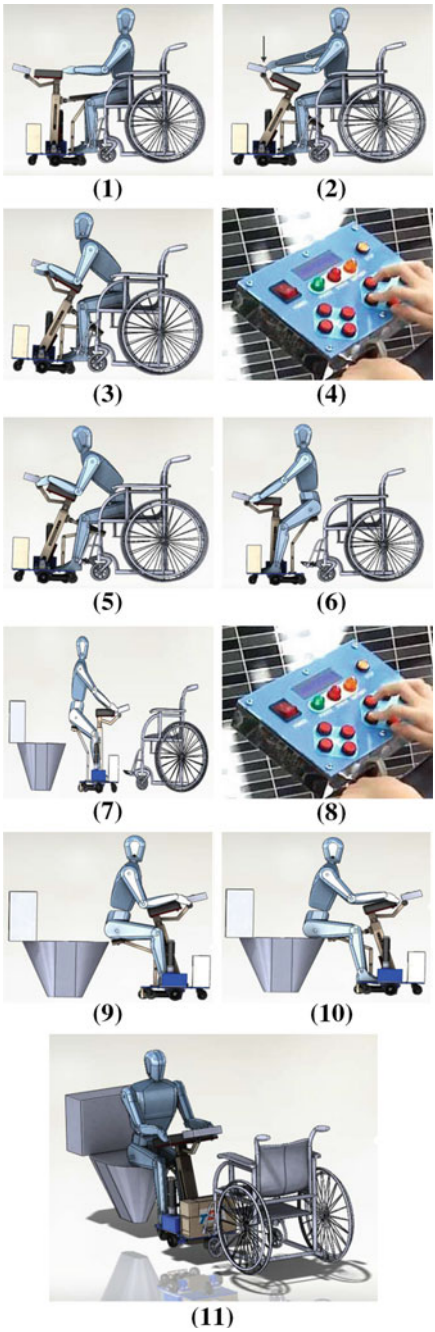

Fig. 8 Operation steps

4 Conclusion

In this study, we proposed a novel assistive robot with the following merits: lift-transfer-locomotion functions, simple structure, simple operation, flexible moving. Especially, safety was highly considered and taken into account with self-locking mechanism and tilt angle alert sensor. The results showed that, operations were performed correctly and smoothly as expected. Additionally, the experimental results indicated that the robot with flexible dynamic giving excellent moving ability in narrow space; self-locking mechanism in all operations as well as tilt angle alert sensor give absolutely safety ability.

References

1. Vietnam Traffice Safety Commity. http://antoangiaothong.gov.vn/
2. Hari Krishnan R, Pugazhenthi S (2014) Mobility assistive devices and self-transfer robotic systems for elderly, a review. Intel Serv Robot 7:37–49
3. Alamgir H, Li OW et al (2009) Evaluation of ceiling lifts: transfer time, patient comfort and staff perceptions. Injury 40(9):987–992
4. Bostelman R, Albus J (2006) Survey of patient mobility and lift technologies: toward a advancements and standards. Internal report no: 7384, Intelligent systems division. National Institute of Standards and Technology
5. Stein J (2009) Stroke and the family: a new guide. Harvard University Press, Harvard
6. Bell F (1984) Patient-lifting devices in hospitals. CUP Archive
7. Mori Y, Sakai N, Kaoru K (2012) Development of a wheelchair with a lifting function. Adv Mech Eng, 1–9
8. Takahashi Y, Manabe G, Takahashi K, Hatakeyama T (2003) Simple self-transfer aid robotic system. In: Proceedings of the IEEE international conference on robotics and automation. Taipei, Taiwan, September, pp 2305–2309
9. Takahashi Y, Manabe G et al (2006) Basic study on self-transfer aid robotics. J Robot Mech 18(1):4–10

Object Following Controller Design for Four Wheel Independent Steering Automatic Guided Vehicle

Amruta Vinod Gulalkari, Pandu Sandi Pratama, Jae Hoon Jeong, Hak Kyeong Kim and Sang Bong Kim

Abstract This paper presents a vision-based object following four wheel independent steering automatic guided vehicle (4WIS-AGV) system using Kinect camera sensor. To do this task, the following steps are executed. Firstly, an image processing is done for object detection using Kinect camera sensor. A candidate colored object is detected using color-based object detection method and its position in local coordinates is obtained. NAV200 navigation sensor is used to obtain global position of the detected object and the 4WIS-AGV. Secondly, the position of the detected moving object is estimated using Kalman filter algorithm. Kalman filter is used to estimate the global position of the detected moving object. Thirdly, a backstepping controller based on Lyapunov stability is proposed to achieve object following task. Finally, the effectiveness of the proposed system is verified by using simulation and experimental results. The results show that the proposed controller makes the 4WIS-AGV follow the detected moving object well with an acceptable error.

Keywords 4WIS-AGV · Kinect camera · Kalman filter · Backstepping method

1 Introduction

In the recent years, object following is one of the interesting topics of research in the field of robotic vision. In the autonomous robotics, a mobile robot equipped with camera sensor can analyze its ambience well to follow the object. There are numerous researches carrying out object following using camera sensors. In some research works, cameras were installed on different kinds of wheeled robotic platforms to achieve object following task [1, 2]. The difficulty with such wheeled

A.V. Gulalkari · P.S. Pratama · J.H. Jeong · H.K. Kim · S.B. Kim (✉)
Department of Mechanical and Automotive Engineering, Pukyong National University, Busan 608-739, Republic of Korea
e-mail: kimsb@pknu.ac.kr

V.H. Duy et al. (eds.), *AETA 2015: Recent Advances in Electrical Engineering and Related Sciences*, Lecture Notes in Electrical Engineering 371,
DOI 10.1007/978-3-319-27247-4_55

configurations is their less flexibility and limited maneuverability. Selection of appropriate controller is also an important issue in such kind of systems. There are several control algorithms available such as optimal control [3], multi-mode control method based on Fuzzy selector [4], etc. In these controllers, although the stability of the system is guaranteed, it is not an easy task to find an appropriate control law.

To solve the above problems, this paper proposes an object following system for the four wheel independent steering automatic guided vehicle (4WIS-AGV) system using Kinect camera sensor based on a Kalman filter and backstepping control method. The object following task is executed by the 4WIS-AGV using Kinect camera sensor as follows. First, the Kinect camera is installed on four wheel independent steering configuration of AGV. In this wheeled configuration, each wheel is adjusted separately. As a result, it can move in any direction in its work environment. A candidate color object is detected by the Kinect camera sensor based on color-based object detection method. In this step, the local position of detected object is obtained using Kinect camera sensor. Then, NAV200 navigation system is used to get the position of the detected object and the 4WIS-AGV in the global coordinate system. Second, global position of the detected moving object is tracked using Kalman filter algorithm. Third, a backstepping control method using Lyapunov function is adopted for the 4WIS-AGV to perform a moving object following task. Among several controller methods, a backstepping control method is adopted since the system stability is guaranteed for the 4WIS-AGV based on Lyapunov stability theory. Finally, simulation and experimental results are presented to verify the effectiveness of the proposed system. The results show that the 4WIS-AGV with Kinect camera sensor can follow the moving object successfully using designed controller with an acceptable small error.

2 System Description

Figure 1 shows object following 4WIS-AGV system used in this paper. The 4WIS-AGV has dimension of 1.00 m (l) × 0.70 m (w) × 0.50 m (h). This system consists of body platform and wheel driving configuration where each wheel uses two high power DC motors: one for driving and other for steering as shown in Fig. 2. This 4WIS-AGV is controlled by Industrial PC (Tank 800) with RS232 communication and eight ATmega128 microcontrollers (one for each motor). Two 12 V batteries are used for the power supply to the system. A monitor and wireless keyboard–mouse are used as an input device for the 4WIS-AGVsystem.

The sensors used for the proposed system are Kinect camera sensor, laser navigation sensor: NAV200 and eight encoders, one for each motor. A Kinect camera sensor is mounted on the top-front side of the 4WIS-AGV, whereas NAV-200 laser navigation sensor is mounted on the top-center of the 4WIS-AGV.

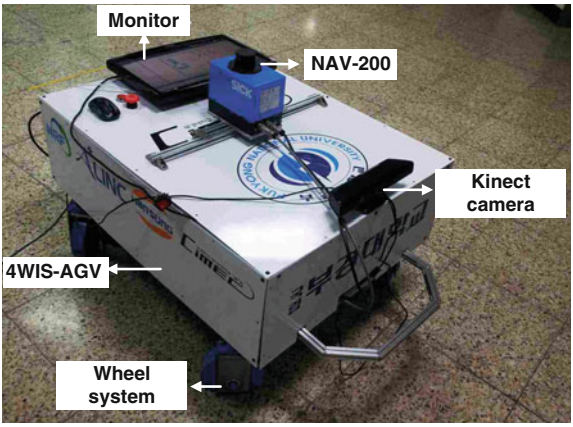

Fig. 1 Kinect camera sensor-based object tracking and following 4WIS-AGV system

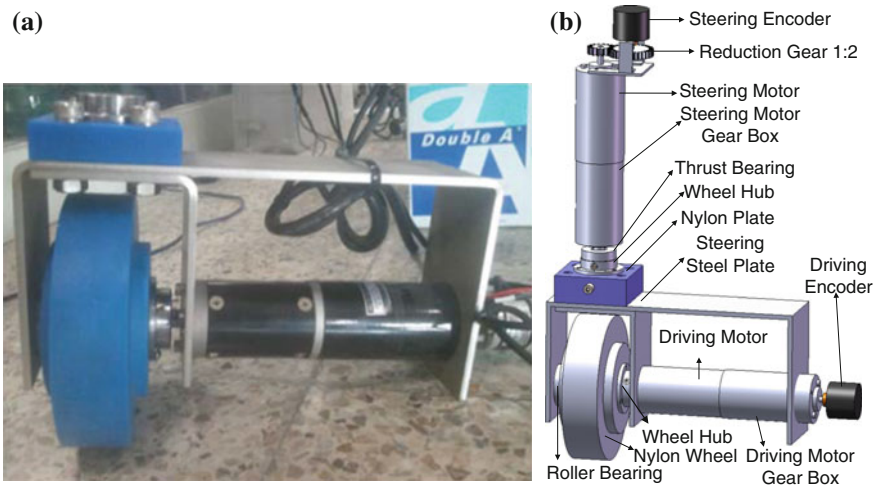

Fig. 2 Wheel configuration of 4WIS-AGV system. **a** Real wheel configuration. **b** Designed wheel configuration

The Kinect camera sensor captures both color and depth images at the speed of 30 frames per second with the sensing range from 0.8 to 4 m. NAV-200 sensor with an accuracy ±25 mm is used to obtain the positions for both object and 4WIS-AGV in the global coordinate system. Out of eight encoders, four encoders are used to measure wheel steering angles of the steering motors and other four are used to measure angular velocities of the driving motors.

3 Kinematic Modeling of 4WIS-AGV System

Figure 3 shows the configuration of the 4WIS-AGV for the system kinematic modeling. The coordinate *Axy* represents local coordinate, whereas the coordinate *OXY* represents global coordinate.

The kinematic equation for the proposed 4WIS-AGV is given as follows:

$$\begin{bmatrix} \dot{X}_A \\ \dot{Y}_A \\ \dot{\theta}_A \end{bmatrix} = \begin{bmatrix} \cos\theta_A & -\sin\theta_A & 0 \\ \sin\theta_A & \cos\theta_A & 0 \\ 0 & 0 & 1 \end{bmatrix} \begin{bmatrix} v_x \\ v_y \\ \omega \end{bmatrix} \tag{1}$$

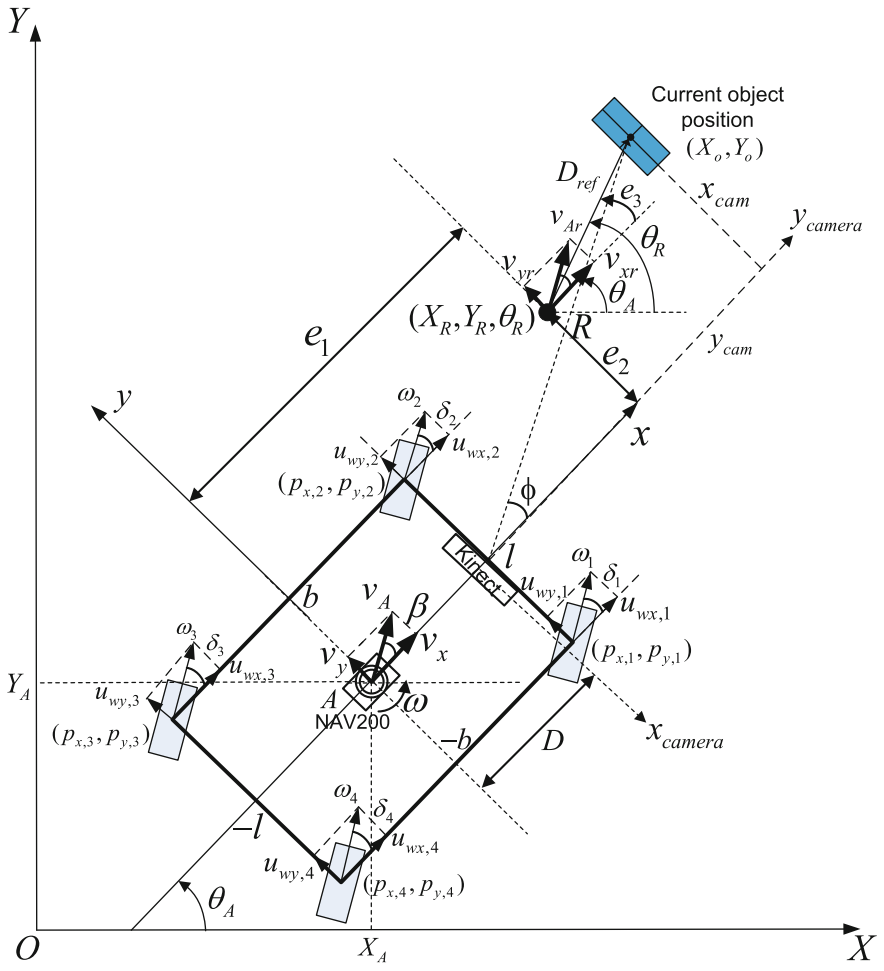

Fig. 3 Configuration of the 4WIS-AGV system

where $\dot{X}_A$ is the vehicle linear velocity in X axis of global coordinate, $\dot{Y}_A$ is the vehicle linear velocity in Y axis of global coordinate, and $\dot{\theta}_A$ is the vehicle angular velocity in global coordinate. v_x is the vehicle linear velocity in x axis of local coordinate, v_y is the vehicle linear velocity in y axis of local coordinate, and ω is the vehicle angular velocity in local coordinate. (X_A, Y_A) is the current position of the 4WIS-AGV. (X_R, Y_R) is reference position and θ_R is reference orientation. δ_i and ω_i $(i = 1, 2, 3, 4)$ are the ith wheel steering angle and the ith wheel angular velocity, respectively.

For the given total linear velocity of 4WIS-AGV in local coordinate v_A and vehicle sideslip angle β, the vehicle linear velocities v_x and v_y in the local coordinate can be obtained as follows:

$$\begin{cases} v_x = v_A \cos\beta \\ v_y = v_A \sin\beta \end{cases} \tag{2}$$

The vehicle sideslip angle β is defined as angle between the movement directions of 4WIS-AGV and x axis of 4WIS-AGV as follows:

$$\beta = \mathrm{a}\tan2(v_y, v_x) = \tan^{-1}\left(v_y/v_x\right) \tag{3}$$

Target velocities in x and y directions: $u_{wx,i}$ and $u_{wy,i}$ of the ith wheel in local coordinate of 4WIS-AGV can be obtained by as follows:

$$\begin{cases} u_{wx,i} = v_x - p_{y,i}\omega \\ u_{wy,i} = v_y + p_{x,i}\omega \end{cases} \tag{4}$$

where $\left(p_{x,i}, p_{y,i}\right)$ is the position of the ith wheel in the local coordinate of 4WIS-AGV as shown in Fig. 3.

The ith wheel steering angle δ_i and the ith wheel angular velocity ω_i are given as follows:

$$\delta_i = \tan^{-1}\left(\frac{u_{wy,i}}{u_{wx,i}}\right) \tag{5}$$

$$\omega_i = \frac{u_{wx,i}\cos\delta_i + u_{wy,i}\sin\delta_i}{R_w} \tag{6}$$

where R_w is the radius of a wheel.

4 Object Position Measurement

This section explains the procedure for getting the candidate object position in the global coordinate frame and then tracking it by using Kalman filter algorithm.

4.1 Object Detection

In this paper, a color-based object detection algorithm [5] using Aforge.NET C# framework is used to obtain the position of candidate blue colored object in the local coordinate frame (i.e., in Kinect RGB image frame).

Figure 4 shows an extended view of the real candidate object and the detected candidate object in a Kinect RGB image frame. According to the image principle [5], an angle ϕ between the center of the detected object and the center of the RGB image is given as follows:

$$\phi = \arctan\left(\frac{x_m \alpha}{f}\right) \tag{7}$$

where x_m is the object position in x direction from the center of the Kinect RGB image, α is the coefficient of transformation from pixel to length and f is the focal length of the Kinect camera. Since the value of x_m is in pixels, it is necessary to convert this value into meter value as x_{cam} as follows:

$$x_{cam} = y_{cam} \tan\phi \tag{8}$$

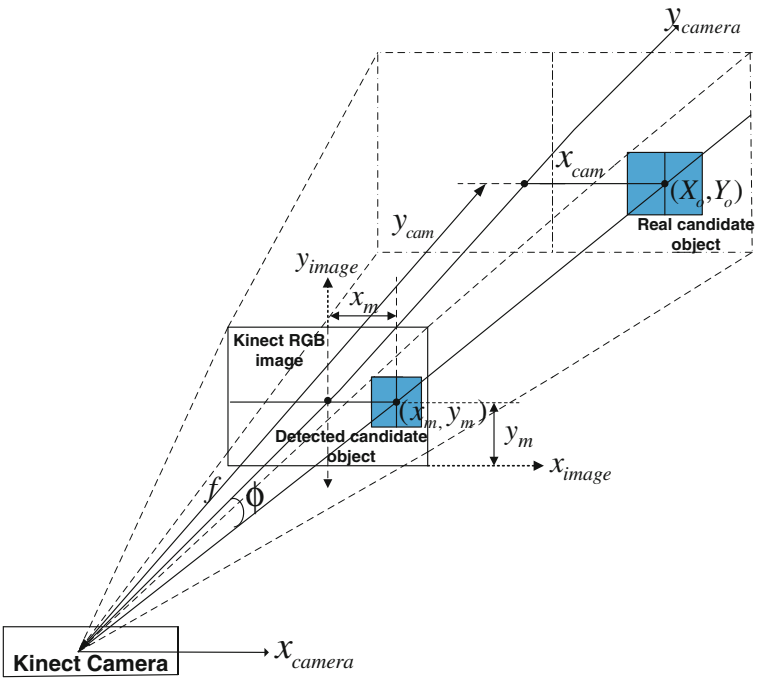

Fig. 4 Extended view of the real candidate object and the detected candidate object in a Kinect RGB image frame

where y_{cam} represents the depth of the object from the Kinect camera sensor in meter and is obtained directly from the Kinect depth data.

The position (x_{cam}, y_{cam}) of the detected object in local coordinate frame can be transformed into the global coordinate frame as shown in Fig. 3 as follows:

$$\begin{bmatrix} X_o \\ Y_o \end{bmatrix} = \begin{bmatrix} X_A \\ Y_A \end{bmatrix} + \begin{bmatrix} \cos\theta_A & -\sin\theta_A \\ \sin\theta_A & \cos\theta_A \end{bmatrix} \begin{bmatrix} x_{cam} \\ y_{cam} \end{bmatrix} + \begin{bmatrix} \cos\theta_A \\ \sin\theta_A \end{bmatrix} D \tag{9}$$

where (X_o, Y_o) is the current position of detected object in global coordinate frame and $D = 0.45$ m is the distance between the Kinect camera sensor and the NAV200 sensor placed on the 4WIS-AGV.

4.2 Object Tracking Using Kalman Filter

To follow the moving object well, it is essential to track its position. However, because it is difficult to get clear images of objects and due to the variations in the ambient light conditions and noise of the Kinect camera sensor, exact tracking is difficult. Therefore, to deal with these problems, Kalman filter is adopted in this paper [6].

The positions and velocities of the moving object are described in global coordinate frame OXY by the linear state space as follows:

$$\mathbf{x}_k = \begin{bmatrix} X_o & Y_o & \dot{X}_o & \dot{Y}_o \end{bmatrix}^T \tag{10}$$

where $\dot{X}_o$ is the object velocity in X direction i.e., derivative of position X_o with respect to time and $\dot{Y}_o$ is the object velocity in Y direction i.e., derivative of position Y_o with respect to time.

Between $(k-1)$ and k time step, object undergoes a constant acceleration of a_k that is normally distributed (Gaussian) with mean 0 and standard deviation σ_a. The dynamic behavior of the moving object at time step k is given by the state matrix $\mathbf{x}_k$ as follows:

$$\mathbf{x}_k = \mathbf{F}\mathbf{x}_{k-1} + \mathbf{w}_k \tag{11}$$

where $\mathbf{F}$ is the transition matrix and $\mathbf{w}_k$ is the Gaussian process noise at time step k with covariance matrix $\mathbf{Q}$ such that $\mathbf{w}_k \sim N(0, \mathbf{Q})$ and are obtained as follows:

$$\mathbf{F} = \begin{bmatrix} 1 & 0 & T & 0 \\ 0 & 1 & 0 & T \\ 0 & 0 & 1 & 0 \\ 0 & 0 & 0 & 1 \end{bmatrix} \text{ and } \mathbf{Q} = \begin{bmatrix} T^4/4 & 0 & 0 & 0 \\ 0 & T^4/4 & 0 & 0 \\ 0 & 0 & T^2 & 0 \\ 0 & 0 & 0 & T^2 \end{bmatrix} \sigma_a^2$$

where T is the sampling time.

The measurement $\mathbf{z}_k$ of the true position of an object at time step k obtained from the Kinect camera sensor is expressed as follows:

$$\mathbf{z}_k = \mathbf{H}\mathbf{x}_k + \mathbf{v}_k \tag{12}$$

where $\mathbf{H}$ is the measurement matrix and $\mathbf{v}_k$ is the Gaussian measurement noise at time step k with covariance matrix $\mathbf{R}$ such that $\mathbf{v}_k \sim N(0, \mathbf{R})$ and are obtained as follows:

$$\mathbf{H} = \begin{bmatrix} 1 & 0 & 0 & 0 \\ 0 & 1 & 0 & 0 \\ 0 & 0 & 1 & 0 \\ 0 & 0 & 0 & 1 \end{bmatrix} \text{ and } \mathbf{R} = \begin{bmatrix} \sigma_p^2 & 0 & 0 & 0 \\ 0 & \sigma_p^2 & 0 & 0 \\ 0 & 0 & \sigma_v^2 & 0 \\ 0 & 0 & 0 & \sigma_v^2 \end{bmatrix}$$

The Kalman filter exhibit two steps: prediction step and update step as follows:
Prediction step:

$$\begin{cases} \hat{\mathbf{x}}_k^- = \mathbf{F}\hat{\mathbf{x}}_{k-1} + \mathbf{w}_k \\ \mathbf{P}_k^- = \mathbf{F}\mathbf{P}_{k-1}\mathbf{F}^T + \mathbf{Q} \end{cases} \tag{13}$$

where $\hat{\mathbf{x}}_k^-$ is the predicted state estimation at time step k and $\mathbf{P}_k^-$ is the predicted covariance matrix estimation at time step k.
Update step:

$$\begin{cases} \mathbf{K}_k = \mathbf{P}_k^-\mathbf{H}^T(\mathbf{H}\mathbf{P}_k^-\mathbf{H}^T + \mathbf{R})^{-1} \\ \hat{\mathbf{x}}_k = \hat{\mathbf{x}}_k^- + \mathbf{K}_k(\mathbf{z}_k - \mathbf{H}\hat{\mathbf{x}}_k^-) \\ \mathbf{P}_k = (\mathbf{I} - \mathbf{K}_k\mathbf{H})\mathbf{P}_k^- \end{cases} \tag{14}$$

where $\mathbf{K}_k$ is the Kalman gain at time step k, $\hat{\mathbf{x}}_k$ is the updated state estimation at time step k and $\mathbf{P}_k$ is the updated covariance matrix estimation at time step k.

5 Controller Design

The objective of this section is to design a controller that can follow the reference position (X_R, Y_R) and reference orientation θ_R with vehicle reference linear velocities (v_{xr}, v_{yr}) and vehicle reference angular velocity ω_R keeping a given safe distance $D_{ref} = 1.25$ m between 4WIS-AGV and a moving object.

The reference position coordinates (X_R, Y_R) in Fig. 3 can be obtained as follows:

$$\begin{bmatrix} X_R \\ Y_R \end{bmatrix} = \begin{bmatrix} \hat{X}_o \\ \hat{Y}_o \end{bmatrix} - \begin{bmatrix} \cos\theta_R \\ \sin\theta_R \end{bmatrix} D_{ref} \tag{15}$$

where $(\hat{X}_o, \hat{Y}_o)$ is the estimated positions of the moving object by Kalman filter.

From Fig. 3, the reference orientation angle θ_R is calculated as follows:

$$\theta_R = \arctan\left(\frac{\hat{X}_o - X_R}{\hat{Y}_o - Y_R}\right) \tag{16}$$

The reference vehicle linear velocity in global coordinate v_{Ar} can be expressed as follows:

$$v_{Ar} = \dot{\hat{X}}_R \cos\theta_R + \dot{\hat{Y}}_R \sin\theta_R = \dot{\hat{X}}_o \cos\theta_R + \dot{\hat{Y}}_o \sin\theta_R \tag{17}$$

The reference vehicle velocities in local coordinate in Fig. 4 can be expressed as

$$\begin{cases} v_{xr} = v_{Ar}\cos e_3 \\ v_{yr} = v_{Ar}\sin e_3 \end{cases} \tag{18}$$

The reference angular velocity ω_R can be obtained as follows:

$$\omega_R = \dot{\theta}_R \tag{19}$$

Referring Fig. 3, a tracking error vector $\mathbf{e}$ can be defined as follows:

$$\mathbf{e} = \begin{bmatrix} e_1 \\ e_2 \\ e_3 \end{bmatrix} = \begin{bmatrix} \cos\theta_A & \sin\theta_A & 0 \\ -\sin\theta_A & \cos\theta_A & 0 \\ 0 & 0 & 1 \end{bmatrix} \begin{bmatrix} X_A - X_R \\ Y_A - Y_R \\ \theta_A - \theta_R \end{bmatrix} \tag{20}$$

where e_1 is the error in local coordinate x-axis, e_2 is the error in local coordinate y-axis and e_3 is the vehicle orientation error.

To minimize these errors i.e., to make the 4WIS-AGV follow the moving object, a backstepping controller is designed for 4WIS-AGV.

Using backstepping control method [5], a candidate Lyapunov function (clf) is chosen as follows:

$$V = \frac{1}{2}e_1^2 + \frac{1}{2}e_2^2 + \frac{1}{2}e_3^2 \tag{21}$$

The time derivative of clf $\dot{V}$ is obtained as follows:

$$\dot{V} = e_1\dot{e}_1 + e_2\dot{e}_2 + e_3\dot{e}_3 \tag{22}$$

Time derivative of the tracking error vector can be obtained as follows:

$$\dot{\mathbf{e}} = \begin{bmatrix} \dot{e}_1 \\ \dot{e}_2 \\ \dot{e}_3 \end{bmatrix} = \begin{bmatrix} 1 & 0 & e_2 \\ 0 & 1 & -e_1 \\ 0 & 0 & 1 \end{bmatrix} \begin{bmatrix} v_x \\ v_y \\ \omega \end{bmatrix} - \begin{bmatrix} \cos\theta_A & \sin\theta_A & 0 \\ -\sin\theta_A & \cos\theta_A & 0 \\ 0 & 0 & 1 \end{bmatrix} \begin{bmatrix} v_{xr} \\ v_{yr} \\ \omega_R \end{bmatrix} \tag{23}$$

Substituting Eq. (23) in (22) yields

$$\begin{aligned} \dot{V} \; &= e_1(v_x - v_{xr}\cos e_3 - v_{yr}\sin e_3) \\ &\quad + e_2(v_y - v_{xr}\cos e_3 - v_{yr}\sin e_3) \\ &\quad + e_3(\omega - \omega_R) \end{aligned} \tag{24}$$

Lyapunov stability criterion states that system is stable if $\dot{V} \leq 0$. Therefore, to meet this condition, a control law U can be chosen as follows:

$$U = \begin{bmatrix} v_x \\ v_y \\ \omega \end{bmatrix} = \begin{bmatrix} -k_1 e_1 + v_{xr}\cos e_3 + v_{yr}\sin e_3 \\ -k_2 e_2 - v_{xr}\sin e_3 + v_{yr}\cos e_3 \\ -k_3 e_3 + \omega_R \end{bmatrix} \tag{25}$$

where k_1, k_2 and k_3 are positive constants.

Substituting Eq. (25) to (24) yields

$$\dot{V} = -k_1 e_1^2 - k_2 e_2^2 - k_3 e_3^2 \tag{26}$$

which shows that the $\dot{V} \leq 0$ by using the chosen control law U. In other words, the system becomes stable because $e_1, e_2, e_3 \to 0$ as $t \to \infty$ by using Eqs. (21), (23), (25), (26) and Barbalat's lemma.

The reference vehicle linear velocity v_{xr} in x axis of local coordinate with $\beta = 0$ and $e_3 = 0$ can be expressed as

$$v_y = v_{yr} = 0 \tag{27}$$

$$v_{xy} = v_{Ar} = \dot{\hat{X}}_0 \cos\theta_R + \dot{\hat{Y}}_0 \sin\theta_R \tag{28}$$

Figure 5 shows the block diagram of the proposed system.

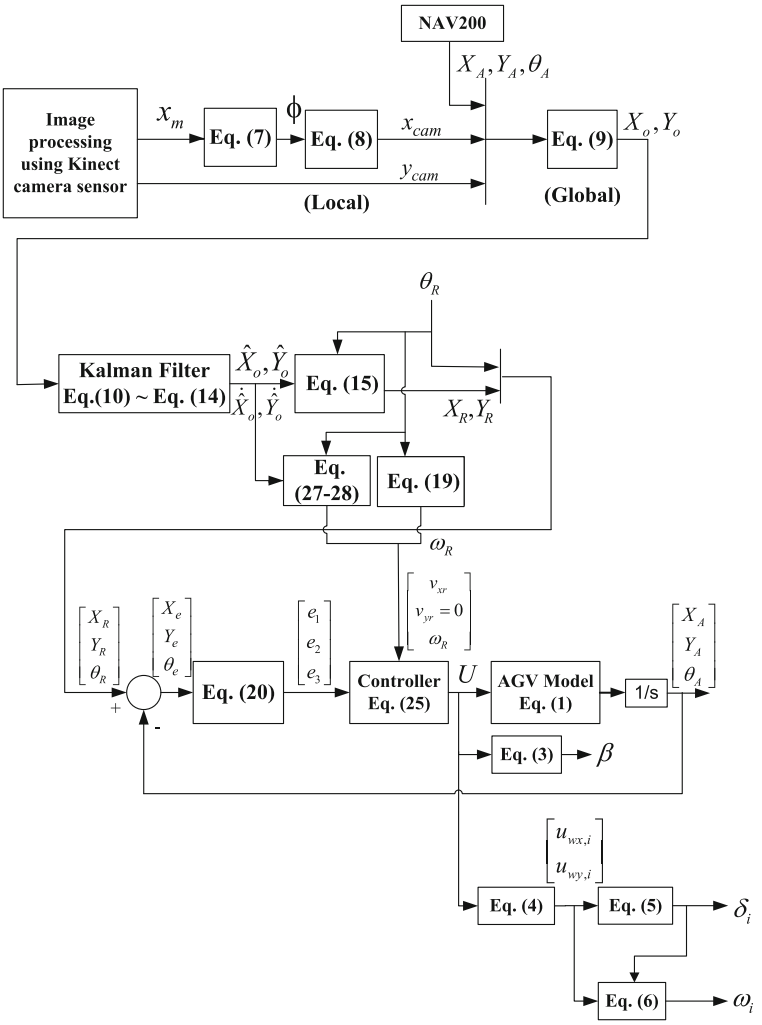

Fig. 5 Block diagram of the proposed system

6 Simulation and Experimental Results

The performance and the effectiveness of the proposed system were verified by simulation and experiment. The parameter and initial values for the simulation and experiment are shown in Table 1.

Table 1 Parameter and initial values

Description	Symbol	Value
Initial position of the 4WIS-AGV	(X_A, Y_A)	(0, 0) m
Initial values of 4WIS-AGV orientation and sideslip angle	(θ_A, β_A)	(0, 0) rad
Initial position of the candidate object	(X_o, Y_o)	(1, 2.5) m
Initial velocity of the candidate object	$(\dot{X}_o, \dot{Y}_o)$	(0.1, 0.1) m/s
Controller gain 1	k_1	1
Controller gain 2	k_2	1
Controller gain 3	k_3	1

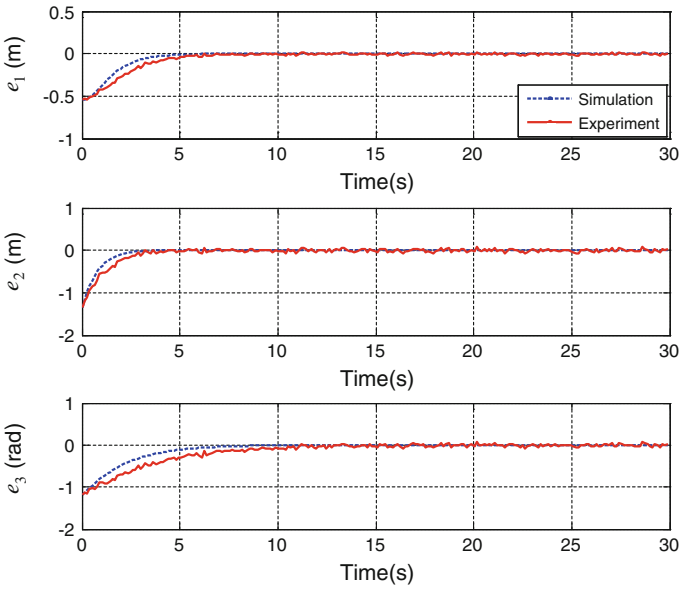

Fig. 6 Tracking error vector

Based on the initial positions of the 4WIS-AGV and the candidate object, the simulation and experimental results of the proposed system are shown in Figs. 6, 7 and 8. Figure 6 shows the tracking error vector. The maximum values of the tracking errors e_1, e_2, e_3 are −0.5, −1.2, −1.1, respectively. In the simulation case, the errors e_1, e_2, $e_3 \rightarrow 0$ at 5, 2.5, 8 s, respectively. In the experimental case, error e_1 is bounded between ±0.05 m after 7 s, error e_2 is bounded between ±0.01 m after 5 s, and error e_3 is bounded between ±0.1 rad after 12 s. Figure 7 shows the results for the control law U. Figure 7a shows the results for the vehicle linear velocity in

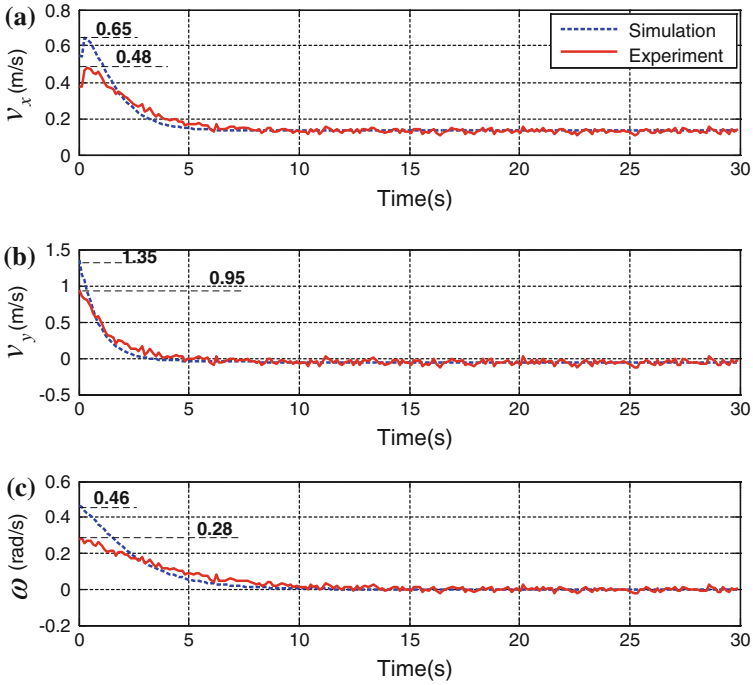

Fig. 7 Control law U. **a** Linear velocity of 4WIS-AGV in x direction. **b** Linear velocity of 4WIS-AGV in y direction. **c** Angular velocity of 4WIS-AGV

x direction. In the simulation, the maximum linear velocity is 0.65 m/s and then it decreased and keeps constant to 0.17 m/s at 5 s. In the experiment, the maximum velocity is 0.48 m/s and then it is bounded between 0.16 and 0.18 m/s after 7 s. Figure 7b shows the results for the vehicle linear velocity in y direction. It can be observed that in the simulation result, the maximum velocity 1.35 m/s and then it decreased and keeps constant to −0.05 m/s at 2.5 s, whereas in the experiment, the maximum velocity is 0.95 m/s and then it is bounded between −0.05 and 0 m/s after 7 s. The simulation and experimental results for the vehicle angular velocity is shown in Fig. 7c. In the simulation, the maximum angular velocity is 0.46 rad/s and then it converged to 0 at 8 s, whereas in the experimental case, the maximum angular velocity is 0.28 rad/s and then it is decreased and bounded between ±0.02 rad/s after 10 s. Figure 8 shows the simulation and experimental results of the estimated values of the candidate object movement such as $\hat{X}_o$, $\hat{Y}_o$, $\dot{\hat{X}}_o$ and $\dot{\hat{Y}}_o$ obtained using Kalman filter.

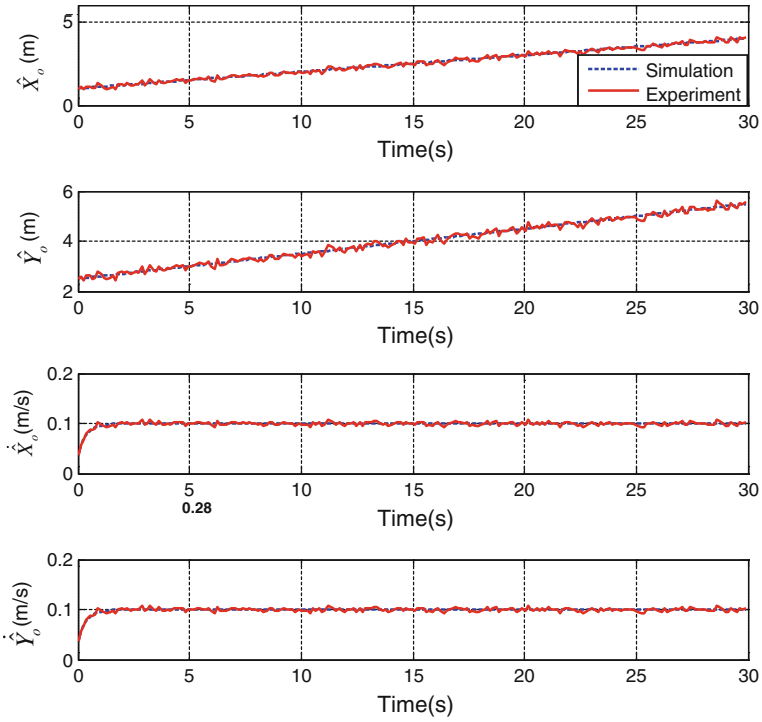

Fig. 8 Estimated values of candidate object movement obtained using Kalman filter

7 Conclusion

In this paper, an object following algorithm for four wheel independent steering automatic guided vehicle (4WIS-AGV) using Kinect camera sensor was proposed based on Kalman filter and backstepping control method. The Kinect camera sensor was installed on the 4WIS-AGV to obtain color and depth images. A candidate object was detected using color-based object detection method. The global position coordinate of the candidate object was tracked efficiently using Kalman filter algorithm. The effectiveness of the proposed controller was verified by the simulation and experiment. The results showed that the proposed algorithm made the 4WIS-AGV follow the candidate object successfully with minimum errors.

Acknowledgments This study is a part of the results of the R&D project supported by the preparatory association of Pukyong National University. Authors are debt to appreciate Pukyong National University for their full supports to this pioneering work.

References

1. Mir-Nasiri N (2006) Camera-based 3D object tracking and following mobile robot. In: The 2006 IEEE conference on robotics, automation and mechatronics, pp 1–6
2. Kao ST, Chung YY, Ming TH (2010) Design and implementation of a stereo vision—guided omnidirectional mobile robot for real-time object tracking. SICE Ann Conf 2010:2968–2974
3. Amdouni I, Jeddi N, Amraoui LE (2008) Optimal control approach developed to four-wheel active steering vehicles. In: The 5th international conference on robotics and biometrics, pp 536–541
4. Yang Z, Wang Z, Su W, Zhang J (2010) Multi-mode control method based on fuzzy selector in the four wheel steering control system. In: The 8th IEEE international conference on control and automation, pp. 1221–1226
5. Gulalkari AV, Hoang G, Pratama PS, Kim HK, Kim SB, Jun BH (2014) Object following control of six-legged robot using kinect camera. In: The 3rd international conference on advances in computing, communications and informatics, pp. 758–764
6. Chen SY (2012) Kalman filter for robot vision: a survey. IEEE Trans Industr Electron 59(11):4409–4420

Walking Gait Planning Using Central Pattern Generators for Hexapod Walking Robot

Dong Bo Sheng, Hung Nguyen Huy, Pandu Sandi Pratama, Hak Kyeong Kim, Vo Hoang Duy and Sang Bong Kim

Abstract This paper presents walking gait planning using a Central Pattern Generator (CPG) for a hexapod walking robot. Our CPG network model is introduced based on the Matsuoka's neural oscillators, which is known as a neural network that generates rhythmic movements. Different output waveform can be obtained by setting the parameters of the model differently. To do this task, the followings are done. First, a CPGs network based on six Matsuoka oscillators to control the hip joint angle of the hexapod walking robot is built. Second, a mapping function to establish the relation between knee joint angle, ankle joint and hip joint is designed. Third, three kinds of gaits such as walking gait with five leg support, quadruped support gait and tripod support gait are generated by simulation. Finally, gait transition is presented by replacing the connection weight matrix of the model. Simulation results show that CPG can transition different gaits smoothly.

Keywords Central pattern generator (CPG) · Matsuoka oscillators · Hexapod robot · Gait transition

1 Introduction

In recent years, applying the mechanism in animal's central neural system to control robot's locomotion is becoming more and more popular. Central Pattern Generator (CPG) is a biological neural network, which can produce rhythmic movement of

D.B. Sheng · H.N. Huy · P.S. Pratama · H.K. Kim · S.B. Kim (✉)
Department of Mechanical Design Engineering, Pukyong National University, Busan 608-739, South Korea
e-mail: kimsb@pknu.ac.kr

V.H. Duy
Faculty of Electrical and Electronics Engineering, Ton Duc Thang University, No. 19 Nguyen Huu Tho Street, District 7, Ho Chi Minh City, Vietnam

V.H. Duy et al. (eds.), *AETA 2015: Recent Advances in Electrical Engineering and Related Sciences*, Lecture Notes in Electrical Engineering 371,
DOI 10.1007/978-3-319-27247-4_56

animals such as walking, running, chewing, respiration, heartbeat, etc. The earliest CPG model was proposed by Cohen et al. [1] in 1980s through the research on the dissection of a lamprey spinal cord. In Matsuoka [2], a necessary and sufficient condition for the oscillator to sustain stable oscillations was shown. In Matsuoka [3], the frequency and pattern control that could be realized by the model was described. Kimura et al. used the Matsuoka neuron models with two neurons mutually inhibited to generate the oscillation and to control the walking of a quadruped robot [4–6]. Taga et al. [7] changed the constant input continuously to realize the transition from walking to running in a biped robot model. Manoonpong et al. [8] achieved some high level behaviors in his robot such as reflex and escape through the sensor-driven neural control. There are few researches for a hexapod robot using a CPG-based control method. Xu et al. [9] designed a CPGs network using six Matsuoka oscillators to control the hip joint angle of a hexapod robot. They also made a mapping function to control the knee joints and ankle joints. However, the mapping function was not perfect.

This paper presents walking gait planning using a Central Pattern Generator (CPG) for a hexapod walking robot. Our CPG network model is introduced based on the Matsuoka's neural oscillators, which is known as a neural network that generates rhythmic movements. Different output waveform can be obtained by setting the parameters of the model differently. To do this task, the following are done. First, a CPGs network based on six Matsuoka oscillators to control the hip joint angle of the hexapod walking robot is built. Second, a mapping function to establish the relation between knee joint, ankle joint and hip joint is designed. Third, three kinds of gaits such as walking gait with five leg support, quadruped support gait and tripod support gait are generated by simulation. Finally, gait transition is presented by changing the connection weight matrix of the model. Simulation results show that CPG can transition different gaits smoothly.

2 System Description and CPG Model

2.1 System Description

Figure 1 show configuration of the proposed hexapod walking gait. Figure 1a shows that the six-legged robot consists of body and legs. Each leg has four joints which are operated by 4 servo motors as shown in Fig. 1b. The mySen-M sensor is used to measure the robot angles. The host computer sends command to the micro-controller by Bluetooth through RS232 interface.

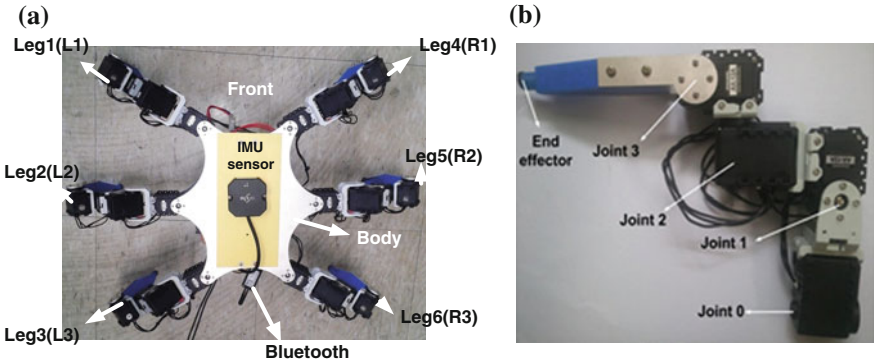

Fig. 1 Configuration of the proposed hexapod walking robot. **a** Overall configuration, **b** configuration of one leg

2.2 Gait Description of Hexapod

A leg cycle is composed of two phases called swing phase and support phase. As shown in Fig. 2, the swing phase is the period while the leg moves from Posterior Extreme Position (PEP) to the Anterior Extreme Position (AEP) which is the position at the end of the swing phase. The support phase is the period while the leg moves from Anterior Extreme Position to the Posterior Extreme Position which is the position at the end of the support phase.

A method of walking forward with legs is called a gait. There are many gaits used by animals. For instance, a cat can easily vary its gait from walk to trot, also from trot to gallop, etc. Different gaits have different speeds. A gait can be described by the concepts of cycle time (T), duty factors (δ), and relative phase in [10]. The cycle time is the sum of swing phase time and support phase time.

$$T = T_{sw} + T_{sp} \tag{1}$$

Fig. 2 Leg cycle of one leg

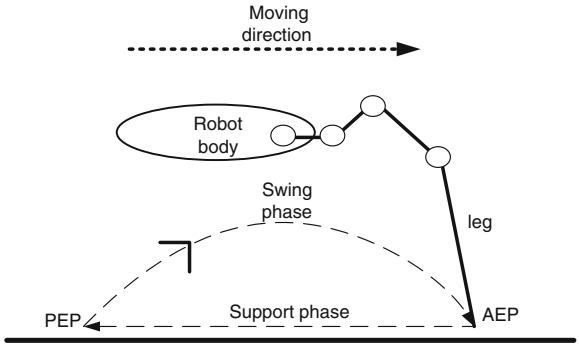

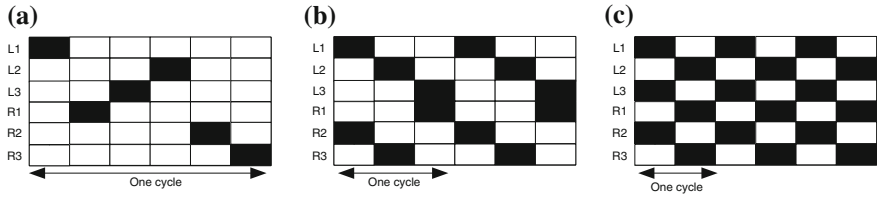

Fig. 3 Periodic gait patterns of hexapod robot. **a** Walking gait with five leg support, **b** quadruped support gait, **c** tripod support gait

where T_{sw} is the swing phase time and T_{sp} is the support phase time. The duty factor $\delta = T_{sp}/T$ of a leg is the time ratio of support phase per cycle time.

In this paper, three kinds of gaits are introduced as shown in Fig. 3. The walking gait with five leg support (Fig. 3a) is adopted when moving slowly, usually with a duty factor of $\delta = 5/6$. Only one leg is in swing phase every time.

The quadruped support gait (Fig. 3b) is used to move at a medium speed and the duty factor of the gait is $\delta = 2/3$. L1 and R2, L2 and R3, L3 and R1 move together in swing phase and others are in support phase.

The tripod support gait (Fig. 3c) is used to move at a rapidly speed and the duty factor of the gait is $\delta = 1/2$. Legs are divided into two parts. L1, L3 and R2 are in same phase and R1, R3 and L2 are in same phase.

2.3 Neuron Oscillator in CPG Model

CPG model is used to generate rhythmic signal to control rhythmic locomotion for hexapod walking robot. In this paper, the CPG model is described as Kimura's oscillator based on Matsuoka's neuron model [2, 3]. A single NO consists of two mutually inhibiting neurons as shown in Fig. 4. The dynamics of each neuron is given by the following second-order system of differential equations so that the total system is a fourth-order one:

$$\begin{cases} \tau \dot{u}_{\{e,f\}i} = -u_{\{e,f\}i} + w_{fe} y_{\{f,e\}i} - \beta v_{\{e,f\}i} + \sum_{j=1}^{n} w_{ij} y_{\{e,f\}j} + u_0 + feed_{\{e,f\}i}, \\ \tau' \dot{v}_{\{e,f\}i} = -v_{\{e,f\}i} + y_{\{e,f\}i}, \\ y_{\{e,f\}i} = \max(u_{\{e,f\}i}, 0). \\ (i,j = 1,\ldots,n) \end{cases} \tag{2}$$

where the subscripts e, f, i and j denote an extensor neuron, a flexor neuron, the ith NO and the jth NO, respectively. $u_{\{e,f\}i}$ is u_{ei} or u_{fi},that is, the inner state of an extensor neuron or a flexor neuron of the ith NO; $v_{\{e,f\}i}$ is a variable representing the degree of the self-inhibition effect of the neuron; y_{ei} and y_{fi} are the outputs of

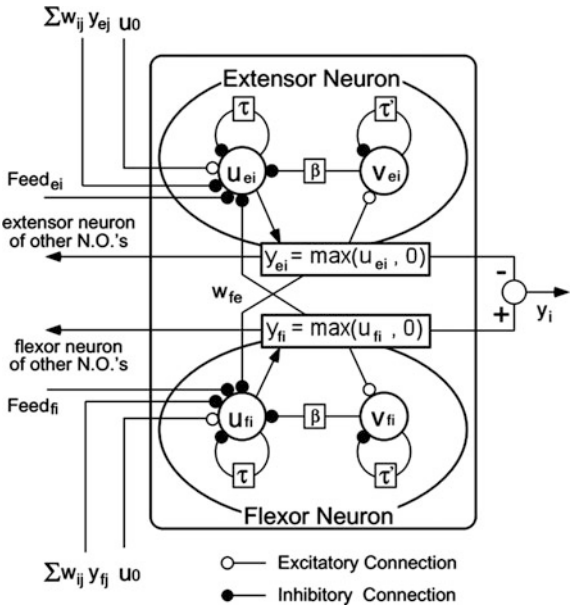

Fig. 4 Neural oscillator as a model of CPG [4]

extensor and flexor neurons; u_0 is an external input with a constant rate; $feed_{\{e,f\}i}$ is a feedback signal from the robot, that is, a joint angle, angular velocity and so on; and β is a constant representing the degree of the self-inhibition influence on the inner state. The quantities τ and τ' are time constants of $u_{\{e,f\}i}$ and $v_{\{e,f\}i}$; w_{fe} is a connection weight between flexor and extensor neurons; w_{ij} is a connection weight between neurons of the ith and jth NO. In Fig. 4, the output of a CPG is a phase signal y_i as follows:

$$y_i = -y_{ei} + y_{fi} \tag{3}$$

2.4 CPG Network and Parameter Analysis

For a hexapod robot, it is necessary to control six hip joints, so a CPG network is designed based on six neuron oscillators, each of which drives a hip joint of a leg. The six oscillators are vertexes of digraph. All vertexes are connected each other as shown in Fig. 5. L1, L2, L3 represents the left three legs, and R1, R2, R3 represents the right three legs. The adjacency matrix of the digraph, $\mathrm{W} = [w_{ij}]_{6\times 6}$ is used as the connection weight matrix of CPG network. Its element w_{ij} is defined as the connection weight from oscillator j to i. Three principles to set W are proposed as follows:

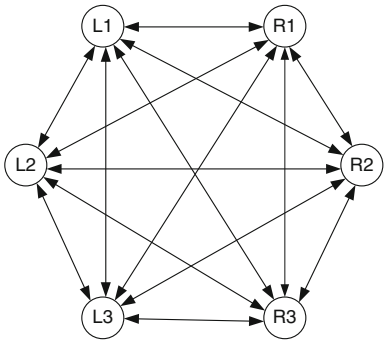

Fig. 5 CPG network of the hexapod walking robot

- There is no self-inhibition in CPG network. So self-connecting weight of each leg is zero, and all elements in the leading diagonal of W are zero.
- Inhibition between any two legs is reciprocal and coequal. So W is a symmetric matrix.
- If two legs are in phase, exciting connections are adopted between the two oscillators and their corresponding elements are set to positive number. If two legs are out of phase, inhibiting connections are adopted and their corresponding elements are set to negative number.

Although the CPG model contains two nonlinear elements, a stable oscillation can be produced by deriving an exact condition for system [2] as follows:

$$1 + \frac{\tau}{\tau'} < w_{fe} < 1 + \beta \tag{4}$$

In Eq. (2), there are many tunable parameters. It's important to find the relationship between parameters and the qualities of the output signals such as frequency, amplitude and phase. In this paper, a numerical analysis method is used to analyze the effect of the parameters on the waveform of the output signals. Then the parameters are adjusted according to the desired patterns. The parameters of the oscillator must be modulated according to the controlled robot, like the walking cycle, walking pattern, etc. The parameter effects on the CPG model are shown as follows:

Parameter u_0: the value must be positive to oscillate the interconnected neurons. Figure 6 shows that this value can be used to adjust the amplitude of the output rhythm signal.
Parameter β: From Fig. 7, the period and amplitude of CPG decreases as the value of β is increased.

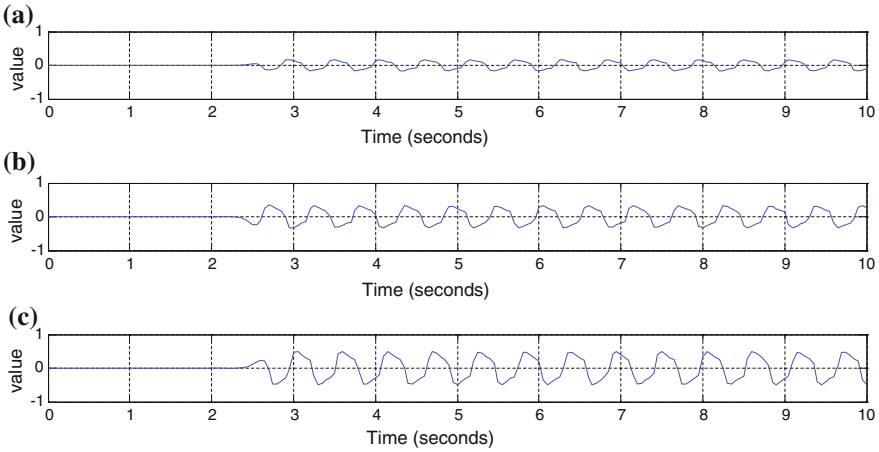

Fig. 6 Output of CPG according to u_0 values. **a** Output of CPG at $u_0 = 0.5$, **b** output of CPG at $u_0 = 1$, **c** output of CPG at $u_0 = 1.5$

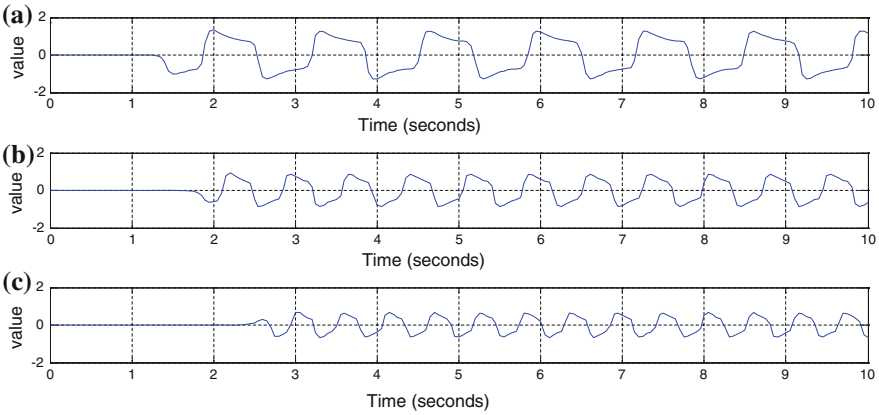

Fig. 7 Output of CPG according to β values. **a** Output of CPG at $\beta = 2$, **b** output of CPG at $\beta = 4$, **c** output of CPG at $\beta = 6$

Parameter w_{fe}: this is the gain of mutual inhibition between two neurons. Figure 8 shows that the value of w_{fe} is related to output amplitude and oscillation period. Parameters τ and τ': Frequency is negatively correlated to the rise time τ and adaptation time τ'. With an increase in rise time, the neuron output rises to the same amplitude within the increase time. Similarly, output drops within increased adaptation. Both of these changes reduce the frequency of oscillations (Fig. 9).

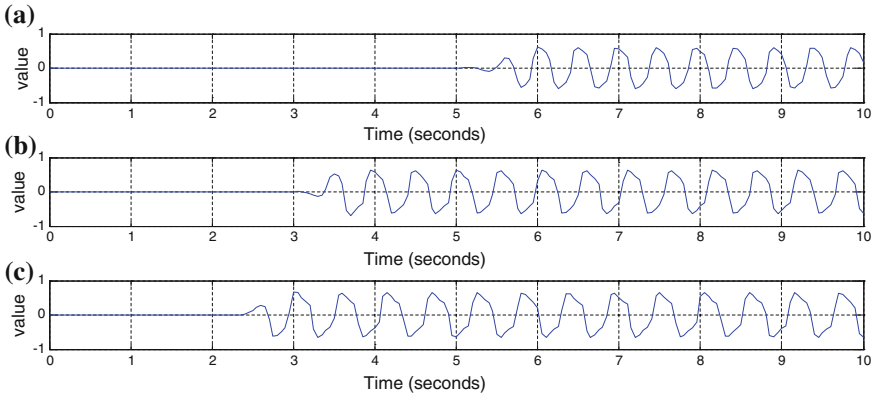

Fig. 8 Output of CPG according to w_{fe} values. **a** Output of CPG at w_{fe} = 1.5, **b** output of CPG at w_{fe} = 1.8, **c** output of CPG at w_{fe} = 2

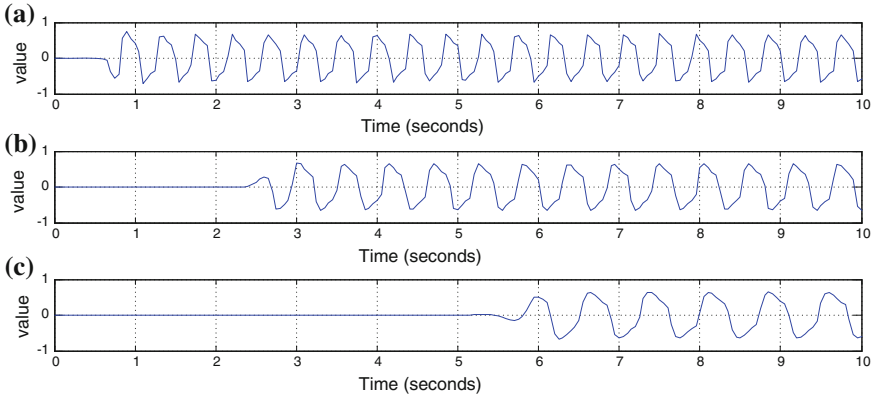

Fig. 9 Output of CPG according to τ and τ' values. **a** Output of CPG at τ = = 0.02 and τ' = 0.6, **b** output of CPG at τ = 0.04 and τ' = 0.6, **c** output of CPG at τ = 0.08 and τ' = 0.6

3 Mapping Function

The adjusted signal can be used to control the hip joint angle. The adjusted signal, which is a periodic signal, represents the periodic swing of the hexapod robot legs. There are few researches focused on how to convert the CPG signal to the angle value of joint. Chen et al. [11] applied a threshold to decide the transfer phase. Suppose the wave of CPG exceeds a threshold, this leg enters a swing phase. When the wave value falls down the threshold, the leg begins its support phase again. This paper only focuses on gait planning, so the value of joint 2 is always made constant.

Figure 10 shows the mapping functions between CPG signal and joint angles. When the value of CPG signal exceeds the threshold, this leg enters a swing phase

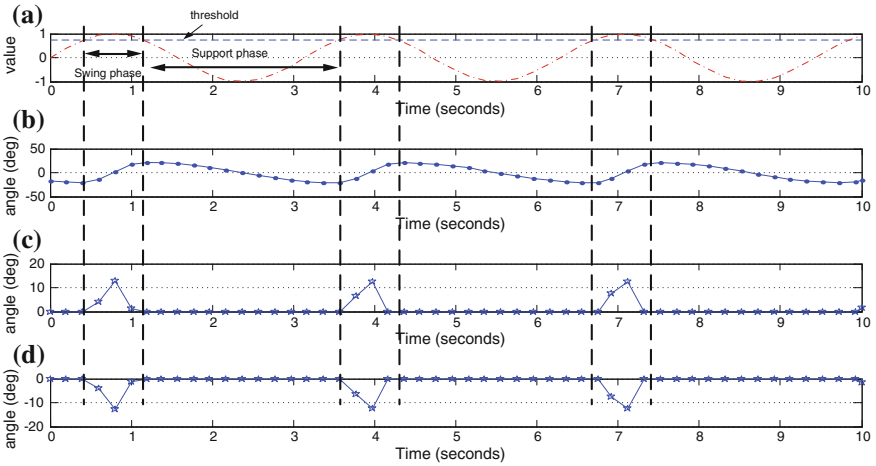

Fig. 10 Mapping functions between CPG signal and joint angles. **a** CPG signal, **b** the angle of hip joint, **c** the angle of knee joint, **d** the angle of ankle joint

in Fig. 10a. The angle of hip joint is from −20° to 20° in Fig. 10b. At the same time, the angles of knee joint and ankle joint turn to maximum angle in Fig. 10c, d. When the swing phase is finished, the angles of knee joint and ankle joint should be back to the initial position. When the value of CPG falls down the threshold, the angle of hip joint will back to the initial position, and the angles of knee joint and ankle joint must be constant.

4 Simulations Results

Simulation is done to generate different waveforms to control the locomotion of each leg. For walking gait with five leg support, the CPG must generate six output waveforms to achieve the desired locomotion. For quadruped support gait, three kinds of waveforms must be generated. For tripod support gait, two kinds of waveforms must be generated. Table 1 shows the parameters values of Neural Oscillator used in this paper.

Table 1. Parameter values of neural oscillator

Parameters	Values
Rising time constant τ	0.04
Adaptability time constant τ'	0.6
Self-inhibition β	6
External input u_0	2
Connecting weight w_{fe}	2
Feedback signal $feed_{\{e,f\}i}$	0
Initial value $u_{\{e,f\}i}$ and $v_{\{e,f\}i}$	0

From Eq. (4) and Table 1, $1.7 < w_{fe} < 7$ can be obtained. Because $w_{fe} = 2$ in Table 1, a stable oscillation can be produced.

A duty factor δ is defined as the fraction of the cycle time that each leg is on the ground. For walking gait with five leg support, quadruped support gait and tripod support gait, the duty factors δ satisfy $\delta = 5/6$, $\delta = 2/3$ and $\delta = 1/2$, respectively. The connection weight matrices in this paper are defined by

$$W_{walking} = \begin{bmatrix} 0 & -1 & -1 & -1 & -1 & -1 \\ -1 & 0 & -1 & -1 & -1 & -1 \\ -1 & -1 & 0 & -1 & -1 & -1 \\ -1 & -1 & -1 & 0 & -1 & -1 \\ -1 & -1 & -1 & -1 & 0 & -1 \\ -1 & -1 & -1 & -1 & -1 & 0 \end{bmatrix},$$

$$W_{quadruped} = \begin{bmatrix} 0 & -0.4 & -0.4 & -0.4 & 0.4 & -0.4 \\ -0.4 & 0 & -0.4 & -0.4 & -0.4 & 0.4 \\ -0.4 & -0.4 & 0 & 0.4 & -0.4 & -0.4 \\ -0.4 & -0.4 & 0.4 & 0 & -0.4 & -0.4 \\ 0.4 & -0.4 & -0.4 & -0.4 & 0 & -0.4 \\ -0.4 & 0.4 & -0.4 & -0.4 & -0.4 & 0 \end{bmatrix},$$

$$W_{tripod} = \begin{bmatrix} 0 & -0.4 & 0.4 & -0.4 & 0.4 & -0.4 \\ -0.4 & 0 & -0.4 & 0.4 & -0.4 & 0.4 \\ 0.4 & -0.4 & 0 & -0.4 & 0.4 & -0.4 \\ -0.4 & 0.4 & -0.4 & 0 & -0.4 & 0.4 \\ 0.4 & -0.4 & 0.4 & -0.4 & 0 & -0.4 \\ -0.4 & 0.4 & -0.4 & 0.4 & -0.4 & 0 \end{bmatrix}$$

4.1 Walking Gait with Five Leg Support

For walking gait with five leg support, only one leg is on the swing phase, and five legs are on the ground. Figure 11 shows that every leg has different phase positions, also they have same phase difference one leg by one leg. The sequence of leg in the swing phase is as follows: L1 → R1 → L3 → L2 → R2 → R3. The duty factor of the proposed walking gait is $\delta = 5/6$.

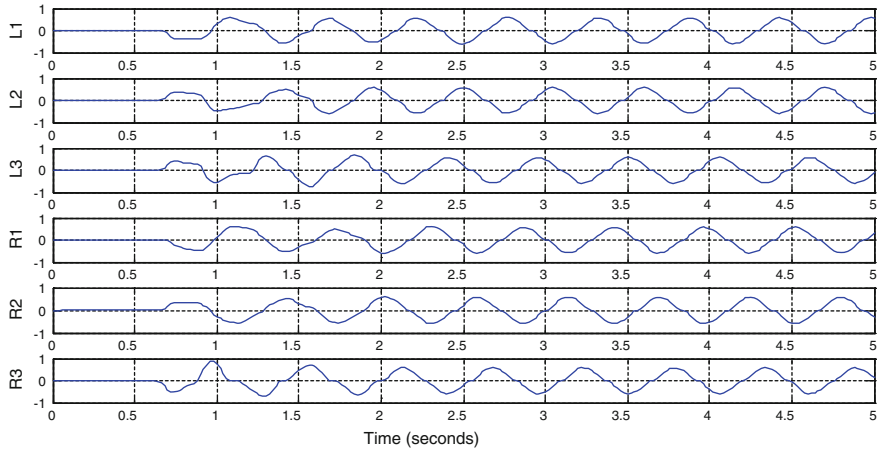

Fig. 11 CPG outputs of walking gait with five leg support

4.2 Quadruped Support Gait

For quadruped support gait, there are two legs at same swing phase, and other four legs are on support phase. Figure 12 shows that L1 and R2, L2 and R3, L3 and R1 are in same phase each other. The duty factor of the proposed quadruped gait is $\delta = 2/3$.

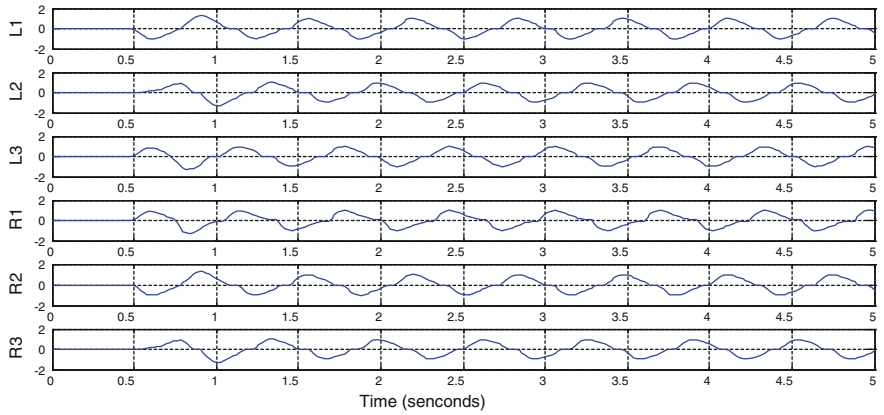

Fig. 12 CPG outputs of quadruped support gait

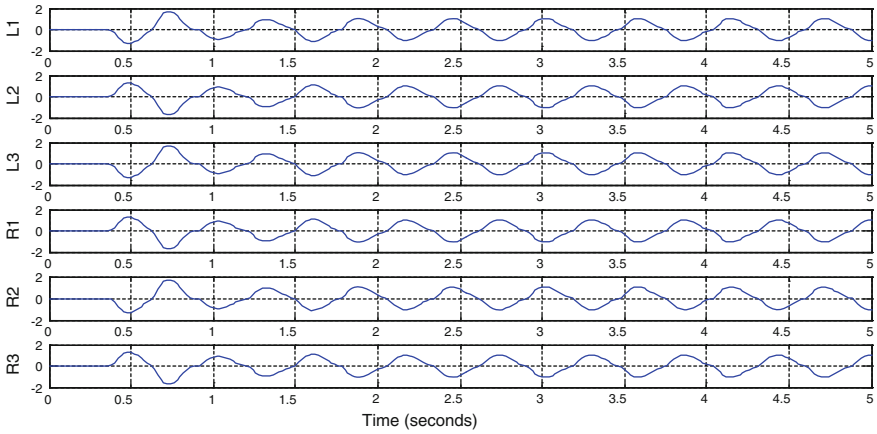

Fig. 13 CPG outputs of tripod support gait

4.3 Tripod Support Gait

For tripod support gait, six legs are divided into two sets, each set consists three legs. Figure 13 shows that L1, L3 and R2 are in same phase, and L2, R1 and R3 are in same phase. The duty factor of the proposed tripod gait is $\delta = 1/2$.

4.4 Gait Transition

Multi-legged robot should work in various environments and can finish different tasks. Gait transitions among walking gait with five leg support, quadruped support

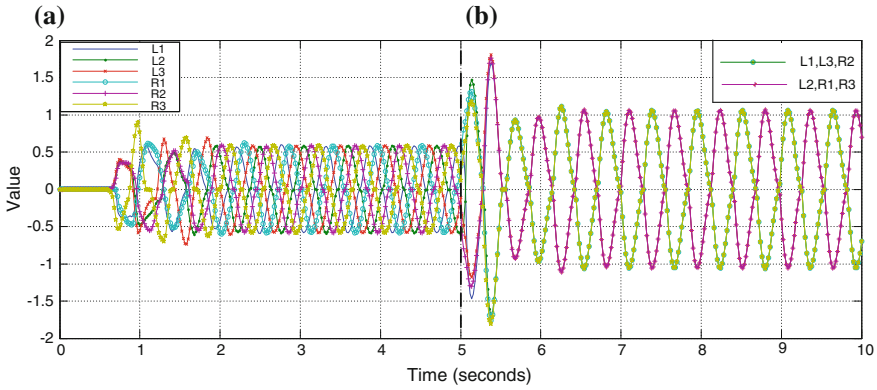

Fig. 14 Gait transition from **a** walking gait with five leg support to **b** tripod support gait

gait and tripod support gait are required. The transition between different rhythmic patterns is proposed by changing the connection weight matrix. Figure 14 shows transition from walking gait with five leg support in Fig. 14a to tripod support gait in Fig. 14b at 5 s.

5 Conclusion

This paper presented walking gait planning using a Central Pattern Generator (CPG) for a hexapod walking robot. Our CPG network model was introduced based on the Matsuoka's neural oscillators, which was known as a neural network that generates rhythmic movements. Different output waveform could be obtained by setting the parameters of the model differently. To do this task, the following were done. First, a CPGs network based on six Matsuoka oscillators to control the hip joint angle of the hexapod walking robot was built. Second, a mapping function to establish the relation between knee joint, ankle joint and hip joint was designed. Third, three kinds of gaits such as walking gait with five leg support, quadruped support gait and tripod support gait were generated by simulation. Finally, gait transition was presented by changing the connection weight matrix of the model. Simulation results showed that CPG can transition different gaits smoothly.

Acknowledgments This study is a part of the results of the R&D project. Development of multi-legged underwater walking-flying robot supported by Korea Government. Authors are debt to appreciate Ministry of Oceans and Fisheries for the full support to this work.

References

1. Cohen AH, Holmes PJ, Rand RH (1982) The nature of the coupling between segmental oscillators of the lamprey spinal generator for locomotion: a mathematical model
2. Matsuoka K (1985) Sustained oscillations generated by mutually inhibiting neurons with adaptation. Biol Cybern 52:367–376
3. Matsuoka K (1987) Mechanisms of frequency and pattern control in the neural rhythm generators. Biol Cybern 56:345–353
4. Kimura H, Fukuoka Y, Cohen AH (2007) Adaptive dynamic walking of a quadruped robot on natural ground based on biological concepts. Int J Rob Res 26;475–490
5. Kimura H, Akiyama S, Sakurama K (1999) Realization of dynamic walking and running of the quadruped using neural osciallator. Auton Robots 72:247–258
6. Kimura H, Fukuoka Y, Konaga K, Hada Y, Takase K (2001) Towards 3D adaptive dynamic walking of a quadruped robot on irregular terrain by using neural system model. Proceedings of the 2001 IEEE/RSJ intelligent robots and systems expand. Societal role of robotics. Next Millenn. (Cat. No.01CH37180), vol 4, pp 2312–2317
7. Taga G, Yamaguchi Y, Shimizu H (1991) Self-organized control of bipedal locomotion by neural oscillators in unpredictable environment. Biol Cybern 65:147–159
8. Manoonpong P, Pasemann F, Wörgötter F (2008) Sensor-driven neural control for omnidirectional locomotion and versatile reactive behaviors of walking machines. Rob Auton Syst 56:265–288

9. Xu L, Liu W, Wang Z, Xu W (2013) Gait planning method of a hexapod robot based on the central pattern generators: simulation and experiment, pp 0–5
10. Frasca Mattia, Arena Paolo, Fortuna Luigi (2006) Bio-inspired emergent control of locomotion systems. World Acad Sci Eng Technol 15:2006
11. Chen W, Ren G, Zhang J, Wang J (2012) Smooth transition between different gaits of a hexapod robot via a central pattern generators algorithm. J Intell Robot Syst Theory Appl 67:255–270

Diameter-Adjustable Controller Design of Wheel Type Pipe Inspection Robot Using Fuzzy Logic Control Method

Husam Hasan Aldulaimi, Trong Hai Nguyeni, Pandu Sandi Pratama, Hui-Ryong Yoo, Dong Kyu Kim, Vo Hoang Duy and Sang Bong Kim

Abstract To make the pipe-inspection robot move inside the specific dimension pipeline, the crucial problem is to adjust the diameter of the robot inside the pipeline. This paper proposes a fuzzy logic controller design method for diameter control of a wheeled-type pipe inspection robot. To do this task, the following steps are executed. Firstly, a wheeled-type pipe inspection robot that can work in 150–250 mm radius pipeline is developed. The robot is developed with two modules: active module and passive module such that each module has three wheel configurations with different mechanism to expand the wheels. Secondly, kinematic models of 4 bar linkage of the robot and dc motor are presented. Thirdly, the PI controller and the fuzzy logic controller are presented for the robot to track the given robot diameter. Finally, simulation is performed to verify the performance of two proposed control methods. The results show that the proposed fuzzy logic controller can track the reference diameter better than using PI controller.

Keywords Pipe inspection robot · Kinematic modeling · Fuzzy

1 Introduction

Pipelines are widely used to carry natural gas and oil to destinations. They range from high-pressure transmission lines to low-pressure distribution lines. In order to prevent a failure/leakage in a pipeline due to corrosion and/or high pressure, the

H.H. Aldulaimi · T.H. Nguyeni · P.S. Pratama · S.B. Kim (✉)
Department of Mechanical Design Engineering, Pukyong National University, Busan, Korea
e-mail: kimsb@pknu.ac.kr

H.-R. Yoo · D.K. Kim
Korea Gas Corporation, Incheon, Korea

V.H. Duy
Faculty of Electrical and Electronics Engineering, Ton Duc Thang University, No. 19 Nguyen Huu Tho Street, District 7, Ho Chi Minh City, Vietnam

V.H. Duy et al. (eds.), *AETA 2015: Recent Advances in Electrical Engineering and Related Sciences*, Lecture Notes in Electrical Engineering 371,
DOI 10.1007/978-3-319-27247-4_57

interiors of the pipes need to be routinely monitored and inspected to evaluate the need to maintain or repair the pipeline, and to decide the most effective means to do so. Although cutting one or more samples of the pipe is one of the most common methods used for diagnosing a pipeline, this method needs high cost and a long time. Moreover, this method also does not provide comprehensive information about the status of the whole pipe because of the variations in corrosion rate found in different sections of a pipe.

Since space availability is one of the challenges that face in-pipe robots, many concepts have been adopted to solve this challenge and resulted in developing different kinds of in-pipe robots such as pig type [1], caterpillar type [2, 3], walking type [4], inchworm type [5, 6], screw types [7, 8], and wheel type [9, 10].

In this paper, the wheel type pipe inspection robot is used. Wheel type pipe inspection robot has ability to navigate inside a pipe of changing diameter such as a pipe with segments of different diameters. In these scenarios, when the robot passes from a large pipe to a small pipe diameter, it has to be able to find the location at the cross-section where the pipes diameter is changed, has to be able to change its radial dimension to negotiate with the pipe diameter, and move autonomously forward and backward in a limited and constrained space. Therefore, a diameter-adjustable controller for a wheel type pipe inspection robot is needed.

This paper proposes a controller design method for diameter control of a wheeled-type pipe inspection robot. To do this task, the following steps are executed. Firstly, a wheeled-type pipe inspection robot that can work in 150–250 mm radius pipeline is developed. The robot is developed with two modules: active module and passive module such that each module has three wheel configurations with different mechanism to expand the wheels. Secondly, kinematic models of 4 bar linkage of the robot and dc motor are presented. Thirdly, the PI controller and the fuzzy logic controller are designed for the robot to track the given robot diameter. Finally, simulation is performed to verify the performance of two proposed control methods. The results show that the fuzzy logic controller can track the reference diameter better than using PI controller.

2 System Description and Modeling

2.1 System Description

A wheel type pipe inspection robot used in this paper is shown in Fig. 1. The inspection robot consists of two modules, namely active module and passive module. The active module uses a motor to expand and contract the three wheels, whereas the passive module uses spring to expand and contract the three wheels. The active module is used for giving pressure to the pipe wall so that the pipe inspection robot can grip the pipe wall especially when it moves in pipes.

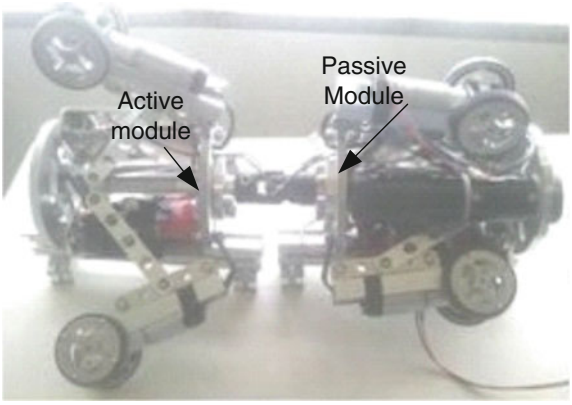

Fig. 1 The design of pipe inspection robot

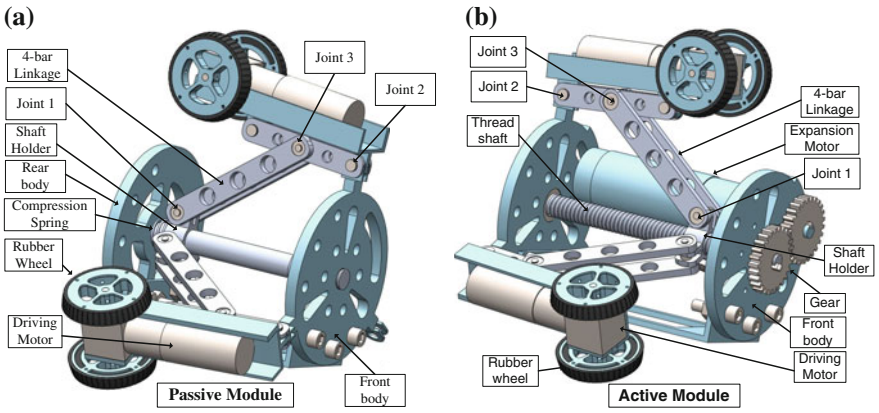

Fig. 2 Design of passive module and active module. **a** Design of passive module, **b** design of active module

Figure 2a depicts the structure design of the passive module. This module consists of three wheel configurations. Passive module uses compression spring for expansion and contraction of 4-bar linkage. Figure 2b shows the structure design of active module. Active module has similar structure with the passive module. Instead of using compression spring, in active module, thread shaft, gear and high power 33.5 W expansion motor are used to expand and contract the wheels.

The detailed design of the active module is shown in Fig. 3.

The specification of the pipe inspection robot is shown in Table 1.

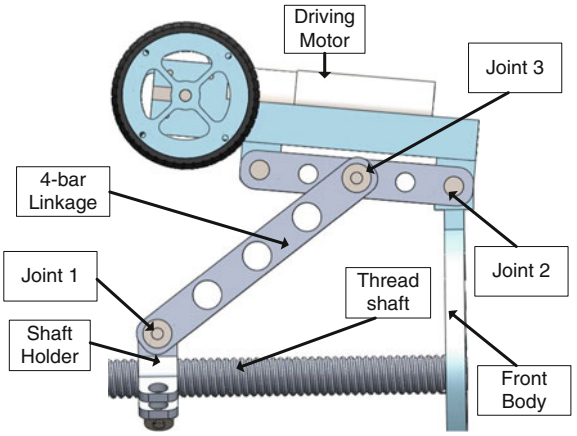

Fig. 3 Side view of 4 bar linkage of active module

Table 1 The specification of the robot

Specification	Value	Specification	Value
Total weight	11 kg	Total length of the robot	685 mm
Length of active module	255 mm	Exterior diameter	300–500 mm
Weight of active module	5.5 kg	Nominal speed	9 cm/s
Length of passive module	220 mm	Maximum speed	21 cm/s
Weight of passive module	4.5 kg	Camera module length	135 mm

2.2 System Modeling

In this section, firstly, kinematic modeling of 4 bar linkage of the pipe inspection robot is used to adjust the diameter of the robot. Secondly, modeling of dc motor to move the shaft holder of the active module using screw mechanism is introduced. The nomenclature of symbols used in the modeling are shown in Table 2.

The mechanism system of active module in Fig. 3 is shown in Fig. 4.

To determine h_t of the pipe inspection robot in the pipe, using trigonometry rules, the followings are obtained as:

$$\Delta x = \frac{p}{2\pi}\theta_m \tag{1}$$

$$l_0 = l - \Delta x \tag{2}$$

$$l_4 = \sqrt{l_0^2 + (d_2 - d_1)^2} \tag{3}$$

$$\theta_3 = \tan^{-1}\left(\frac{d_2 - d_1}{l_0}\right) = \sin^{-1}\left(\frac{d_2 - d_1}{l_4}\right) = \cos^{-1}\left(\frac{l_0}{l_4}\right) \tag{4}$$

Table 2 Nomenclature of linkage and DC motor

Symbol	Parameters
h	Distance from the center of the wheel to joint 1
θ_1	Angle between link 1 and thread shaft
θ_2	Angle between link 2 and thread shaft
θ_3	Angle between virtual link and thread shaft
θ_4	Angle between link 3 and virtual link
θ_5	Outside angle between link 2 and link 3
h_t	Distance from thread shaft to wall
d_1	Radius from joint 1 to the center of thread shaft
d_2	Radius from joint 2 to the center of thread shaft
Δx	Moving displacement of shaft holder
l_0	Distance between front body to shaft holder
l_1	Length of link 1
l_2	Length of link 2
l_3	Length of link 3
l_4	Length of virtual link from joint 1 to joint 2
l	Distance from the rear body to the front body
θ_m	Rotation angle of DC motor
r	Radius of a driving wheel
p	Lead of screw
J	Moment of inertia of the motor
K_{emf}	Emf constant
L	DC motor inductance
u	DC motor voltage
b	Viscous friction
R	DC motor resistance
i_m	DC motor current

$$\theta_4 = \cos^{-1}\left(\frac{l_2^2 + l_4^2 - l_1^2}{2l_2 l_4}\right) \tag{5}$$

$$\theta_2 = \theta_4 - \theta_3 \tag{6}$$

$$h_t = d_2 + l_2 \sin\theta_2 + l_3 \sin(\theta_5 - \theta_2) + r \tag{7}$$

The moving displacement of shaft holder Δx is controlled by changing the rotation angle of DC motor θ_m. The DC motor system is shown in Fig. 5.

The system equation of DC motor is expressed by

$$\dot{\mathbf{x}} = \mathbf{A}\mathbf{x} + \mathbf{B}u \tag{8}$$

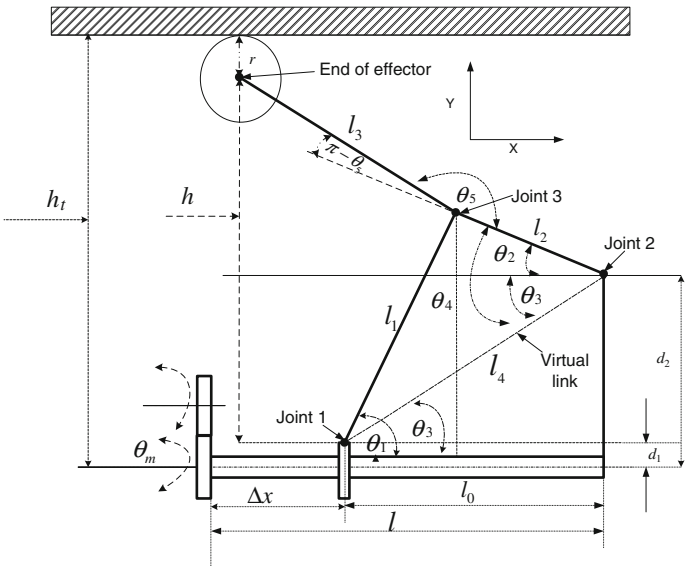

Fig. 4 Linkage of the proposed pipe inspection robot

Fig. 5 DC system motor

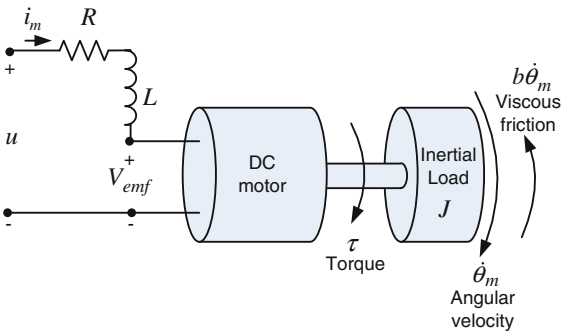

where

$$\mathbf{A} = \begin{bmatrix} -\frac{R}{L} & -\frac{K_{emf}}{L} \\ \frac{K_{emf}}{J} & -\frac{b}{J} \end{bmatrix} \quad \mathbf{B} = \begin{bmatrix} \frac{1}{L} \\ 0 \end{bmatrix} \quad \mathbf{x} = \begin{bmatrix} i_m & \dot{\theta}_m \end{bmatrix}^T$$

where **x** is the system state variable vector, u is the motor voltage as an control input.

The rotation angle of DC motor for Eq. (1) can be obtained as follows:

$$\theta_m = \int \dot{\theta}_m dt + \theta_m(0) \tag{9}$$

The tracking error of radius for the pipe inspection robot is defined as follows:

$$e_h = h_{ref} - h_t \tag{10}$$

where h_{ref} is reference radius of the pipe inspection robot.

3 Controller Design

To track the reference radius of the pipe inspection robot, PI controller and fuzzy logic controller are proposed. The controllers are designed so that the tracking error e_h goes to zero. The controller u in Eq. (8) can be obtained using PI controller u_{PI} and fuzzy logic controller u_{FLC}.

3.1 PI Controller

PI controller is used for controlling diameter of the pipe inspection robot as follows:

$$u_{PI} = K_P e_h + K_I \int e_h dt \tag{11}$$

where K_P and K_I are the PI controller gains.

Block diagram of the proposed PI controller is shown in Fig. 6.

3.2 Fuzzy Logic Controller

The fuzzy rules are constructed by expert experience or knowledge database. First, set the error e_h and the error variation $\dot{e}_h$ are used as the input variables of the fuzzy

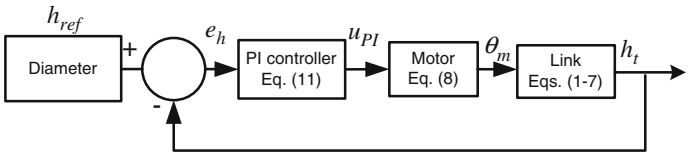

Fig. 6 Block diagram of PID controller

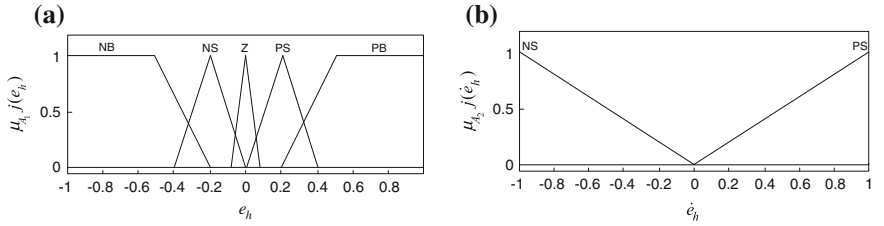

Fig. 7 Inputs membership functions. **a** Membership function for input e_h, **b** membership function for input $\dot{e}_h$

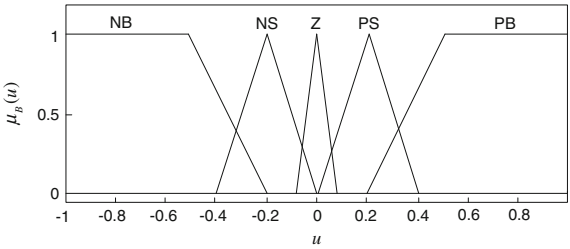

Fig. 8 Membership function for output u

logic controller. The control voltage u is chosen as the output variable of the fuzzy logic controller. The linguistic variables are defined as {NB, NS, Z, PS, PB}, where NB means negative big, NS means negative small, Z means zero, PS means positive small and PB means positive big. The input and output membership functions are shown in Figs. 7 and 8.

The fuzzy rules are summarized in Table 3.

The type of fuzzy inference engine used in this paper is Mamdani's method. In this paper, max-min type decomposition is used and the final output for system is calculated by using center of area gravity method.

$$\mu_B(u) = \max\left[\mu_{A_1} j(e_h), \mu_{A_2} j(\dot{e}_h), \mu_B j(u)\right] \tag{12}$$

Table 3 Fuzzy rules

$\dot{e}_h$	e_h	
	NS	PS
NB	NB	NB
NS	NS	NS
Z	NS	PS
PS	PS	PS
PB	PB	PB

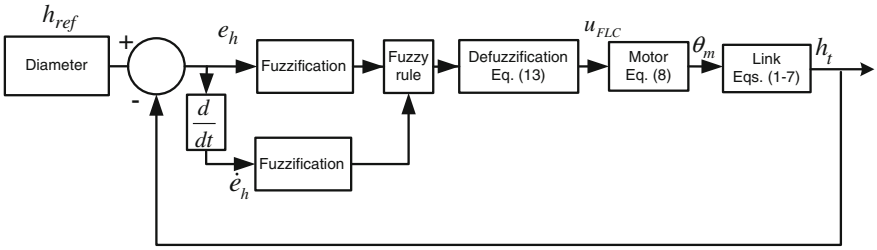

Fig. 9 Block diagram of the proposed fuzzy logic controller

where

$\mu_{A_1}j(e_h)$ the membership of e_h

$\mu_{A_2}j(\dot{e}_h)$ the membership function $\dot{e}_h$

$\mu_B j(u)$ the membership function of u

j is an index of every membership function of fuzzy set. Fuzzy logic outputn

u can be calculated by the center of gravity defuzzification as:

$$u_{FLC} = \frac{\sum_{i=1}^{m} \mu_B(u_i) \cdot u_i}{\sum_{i=1}^{m} \mu_B(u_i)} \tag{13}$$

where m is the number of rules and is the inference result.

Block diagram of the proposed fuzzy logic controller is shown in Fig. 9.

4 Simulation Results

Simulations are performed to verify the proposed controllers performances. The parameter and initial values used in the simulation are listed in Table 4.

By using DC motor parameter in Table 4, matrix **A** and **B** in Eq. (8) can be calculated

$$\mathbf{A} = \begin{bmatrix} -20 & -3 \\ 3 & -0.1 \end{bmatrix} \quad \mathbf{B} = \begin{bmatrix} 10 \\ 0 \end{bmatrix}$$

Figure 10 shows the simulation results of the radius of the pipe inspection robot by using two controllers such as PI controller and Fuzzy logic controller. The results show that the proposed controllers enable the robot to follow the reference radius very well. Figure 11 shows that input control for various walls using PC controller and fuzzy logic controller. Figure 12 shows that the radius error for two

Table 4 Parameters and inital values of DC motor

Parameter	Value	Parameter	Value (cm)
J	0.1 kg m^2	l	15
K_{emf}	0.3 J/A	l_1	13
b	0.01 J s/rad	l_2	5
R	2 Ω	l_3	10
L	0.1 H	r	3.5
$i(0)$	0 A	p	2
$\dot{\theta}_m(0)$	0 rad/s	d_2	9.5
θ_5	5°	d_1	0.75
$\theta_m(0)$	0 rad		

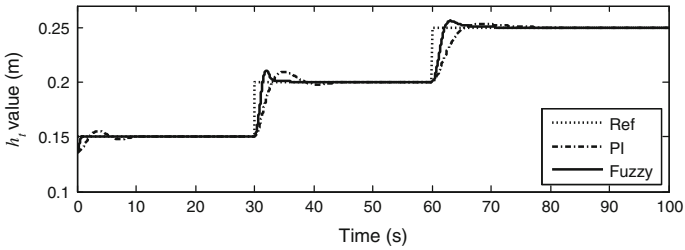

Fig. 10 Output radius h_t of pipe inspection robot using PI and fuzzy logic controllers

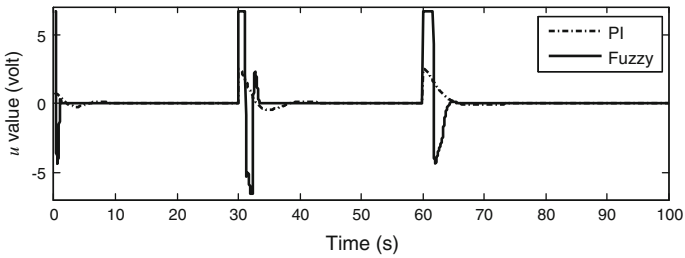

Fig. 11 Input control u using PI and fuzzy logic controllers

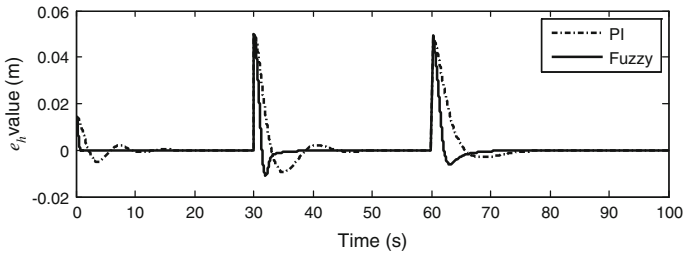

Fig. 12 Radius error diameter e_h using PI and fuzzy logic controllers

controllers in this paper go to zero. The simulation results indicate that the fuzzy logic controller is better than the PI controller since the output obtained from fuzzy logic controller converges to the reference faster with smaller overshot compared to PI controller.

5 Conclusion

A diameter-adjustable pipe inspection robot that works in 150–250 mm radius pipe was developed. The pipe inspection robot consisted of two modules, namely active module and passive module. The PI controller and Fuzzy logic controller was proposed to control diameter of the pipe inspection robot. Simulations were conducted to verify performances of the designed robot and the proposed controller. The results showed that fuzzy logic controller and PI controller could work very well to adjust the size of the pipe inspection robot according to the reference radius of the pipe. According to the simulation results, it is found that the proposed fuzzy logic controller is better in the raising time and overshoot of the pipe inspection robot output than the conventional PI controller.

Acknowledgements This research was financially supported by the Ministry of Trade, Industry and Energy (MOTIV), Korea Institute for Advancement of Technology (KIAT) and Dongnam Institute for Regional Program Evaluation through the Leading Industry Development for Economic Region.

References

1. Okamoto J, Adamowski JC, Tsuzuki MSG, Buiochi F, Camerini CS (1999) Autonomous system for oil pipelines inspection. Mechatronics 9:731–743
2. Park J, Kim T, Yang H (2009) Development of an actively adaptable in-pipe robot. In: IEEE 2009 international conference on mechatronics, ICM 2009, pp. 1–5
3. Moghaddam MM, Tafti MRA (2005) Design, modeling and prototyping of a pipe inspection robot. In: International symposium on automation and robotics in construction, pp 1–6
4. Neubauer W (1994) A spider-like robot that climbs vertically in ducts or pipes. In: Proceedings of IEEE/RSJ international conference on intelligent robots and systems (IROS'94), pp 1178–1185
5. Saga N, Nakamura T (2004) Development of a peristaltic crawling robot using magnetic fluid on the basis of the locomotion mechanism of the earthworm. Smart Mater Struct 13:566–569
6. Fukuda T, Hosokai H, Uemura M (1989) Rubber gas actuator driven by hydrogen storage alloy for in-pipe inspection mobile robot with flexible structure. In: Proceedings, 1989 international conference on robotics and automation, pp 1–6
7. Hayashi I, Iwatsuki N, Morikawa K, Ogata M (1997) An in-pipe operation microrobot driven based on the principle of screw. In: 1997 international symposium on micromechatronics and human science, pp 125–129
8. Horodinca M, Doroftei I, Mignon E, Preumont A (2002) A simple architecture for in-pipe inspection robots. In: Proceedings of the international colloquium on autonomous and mobile systems. Magdeburg, Germany, pp 61–64

9. Roh SG, Choi HR (2005) Differential-drive in-pipe robot for moving inside urban gas pipelines. IEEE Trans Robot 21:1–17
10. Min J, Setiawan YD, Pratama PS, Kim SB, Kim HK (2014) Development and controller design of wheeled-type pipe inspection robot. In: 2014 international conference on advances in computing, communications and informatics (ICACCI), IEEE, pp 789–795

Development of RFECT System for In-line Inspection Robot for Unpiggable Natural Gas Pipeline

Jae-Ha Park, Hui-Ryong Yoo, Dae-Kwang Kim, Dong-kyu Kim, Sung-Ho Cho, Hak-Joon Kim and Sung-Jin Song

Abstract This paper focuses on the RFECT (Remote Field Eddy Current Testing) technology for use on the ILI (In-Line inspection) robot platform to inspect unpiggable natural gas pipeline. An effective design for RFECT system is proposed to minimize the system architecture modification that is required in implementing large diameter of RFECT system of which sensor channel must be increased according to the increase in diameter of pipeline to be inspected. The parallel digital LIA (Lock-In Amplifier) is designed considering the increase in sensor channel. The performance of proposed RFECT system is verified through the pull-rig experiment including a set of artificial defects simulating metal loss on the pipeline.

Keywords Remote-field eddy current · In-line inspection · NDE · In-pipe robot

1 Introduction

Pipeline have been typically inspected for metal loss using a tool called "smart pig" that is inserted into the pipeline at special launching trap and carried along by the gas flow. The most common type of smart pigs usually adapt MFL (Magnetic Flux Leakage), where strong magnets magnetically saturate pipe wall and hall sensor system measure the change of magnetic flux density caused by the metal loss.

J.-H. Park (✉) · H.-J. Kim · S.-J. Song
Department of Mechanical Engineering, Sungkyunkwan University,
Suwon 440-746, Korea
e-mail: jaehapark@skku.edu

H.-R. Yoo (✉) · D.-K. Kim · D. Kim · S.-H. Cho
Gas Facility Technology Center, R&D Division, Korea Gas Corporation,
Incheon 406-130, Korea
e-mail: yoohr@kogas.or.kr

V.H. Duy et al. (eds.), *AETA 2015: Recent Advances in Electrical Engineering and Related Sciences*, Lecture Notes in Electrical Engineering 371,
DOI 10.1007/978-3-319-27247-4_58

Pipelines that can not be inspected by the conventional smart pig are generally deemed “unpiggable”. The main reason that make pipeline unpiggable are the presence of obstacles that prohibit passage of conventional smart pigs and insufficient pressure and flow rate to propel smart pigs such as MFL pigs which need large drag force to carry it. And many unpiggable pipelines are also under the condition that launching and receiving trap cannot be installed. Therefore, deployment of the conventional smart pigs into the unpiggable pipeline is nearly impossible. Thus, pipeline operators aspire to develop ILI robot which can negotiate short radius and mitered bends, tees, back to back bends, vertical sections, valves, etc. and self-propel without tether line in the pressurized pipeline as well as provide NDE data, camera image data and digital mapping data.

RFECT system can be considered as the most suitable among NDE systems which can be coupled with traction robot system because it doesn’t cause large drag force and has many advantages as the follows. Exciter coil doesn’t need to be close to the pipe wall so that it can be smaller than half of pipeline diameter. Since receiving sensor coil also doesn’t need contact with pie wall and it can be very small and simple, the diameter of the array type receiver module can be easily adjusted to match the internal diameter of pipeline reduced by pipeline features such as dents, valves, buckles, wall thickness changes, etc. As long as sensor coil is close to the pipe wall, the sensitivity and accuracy of RFECT system is compatible with MFL system. And it is possible to compensate lift-off though sensitivity and accuracy would be compromised.

The larger the diameter of pipeline to be inspected gets, the more sensor channels of RFECT system should be necessary to cover fully circumference of the pipe. Even the latest editions of RFECT system as well as conventional types have the same system architecture where the only one DSP (Digital Signal Processor) proceed to calculate phase and magnitude difference between reference wave and the measured wave by the receiving coil sensor for each sensor channel. For detecting phase difference related closely to depth of defect, DSP should include digital LIA (Lock-in Amplifier) that usually have time constant which is mainly due to filter delay and processing time. Therefore, this architecture of RFECT may not be applied in case that demand for many receiving sensors is high to cover full circumference of pipeline having large diameter.

Thus, in this paper an effective system architecture for RFECT considering extendibility of receiving sensor channel is proposed by introducing parallel type of digital LIA. Also, to optimize the exciter coil and receiving sensor coils of the RFECT system to 8 inch pipe, exciter coil is designed so that it can have higher magnetic moment and minimize lower power consumption at same time. Also receiving coil is designed to maximize the induced electromotive force within restricted volume. The signal pattern and sensitivity according to the measurement direction of receiving coil are analyzed by pull-rig test. The performance of proposed RFECT system is verified through the pull-rig experiment including a set of artificial defects simulating metal loss on the pipeline.

2 RFECT System for In-line Inspection Robot

2.1 Overall Design of ILI Robot

The RFECT system is preferred as NDE system adapted for ILI robot. Because it cause small drag force comparing other NDE tools such as MFL and EMAT. Usually, tetherless type ILI robot for long distance inspection consist of two traction system and 1NDE system. They are used to be symmetrically linked with NDE system as a center. Since, traction robot system has restricted power, it is important for NDE system to minimize the drag force. As above mention, RFECT technology is best way to reduce drag force accouring from friction with pipe wall during inspection. Because it dosen't need to contact strongly with pipe wall.

Typically RFECT system should be equipped with exciter module, DAS module and receiver module. Receiver module should be kept position away from exciter coil in order not to be aspected by direct field based on RFECT phenomenon. Figure 1 shows a ILI robot named PIBOT (Pipeline Inspection roBOT) and developed to provide ILI service commercially. PIBOT consist of 15 element. Each modules connected by active joint which function yawing and pitching. Overall body design articulating 15-elements provides camera module, driving module, support module, battery module and NDE system. PIBOT system can move forward and backward using TRS (Traction robot system) 1 and 2. And each end of the both side of PIBOT has camera system to inspect the inside of pipe in real-time.

2.2 Phenomenon of Remote Field Eddy Current

RFECT is based on a phenomenon that take place in the vicinity of solenoidal transmission coil in a conductive material. When the alternating current is induced to the transmission coil, the magnetic field is generated around the coil and induced current is generated in surface of the pipe. The circulating eddies of current is called

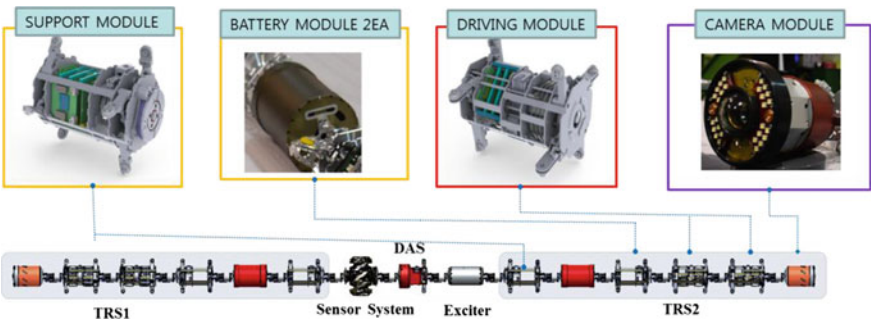

Fig. 1 Configuration of the PIBOT system integrated RFECT tool

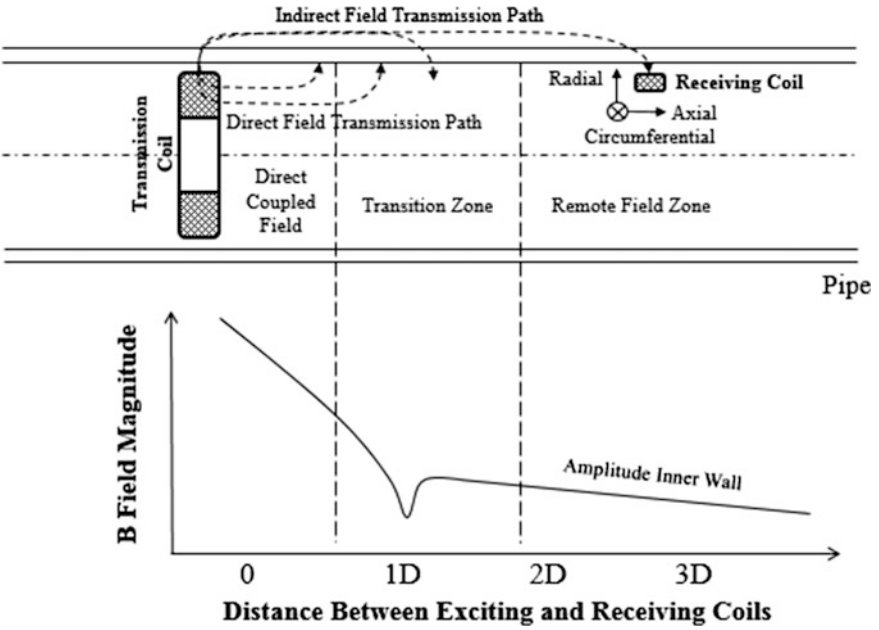

Fig. 2 Principle of RFECT

eddy current. In the pipeline, the electromagnetic waves of near transmission coil traveling inside the pipe by eddy current are rapidly attenuated. This section is called the direct coupled field. Outside of the pipe, indirect electromagnetic waves flow from backward to inside of the pipe. These two direct and indirect waves are coupled, then transition zone occurs and then indirect electromagnetic waves is more stronger than direct waves. This section is called the remote eddy current field. In the remote field zone, electromagnetic waves are gradually attenuated according as the distance increase from the transmission coil. The distance between transmission and receiving coil have to be kept because of RFECT phenomenon. Generally, in pipeline, the distance between the transmission and receiving coils should be kept two times of pipe diameter or more from the transmission coil. The principle of RFECT is depicted in Fig. 2.

2.3 Design of RFECT System

To develop the applicable RFECT system for inspection of ILI robot, it is important to design of optimal transmission and receiving coil suitable to use in measurement target. In this work, 8 inch urban-gas pipeline has targeted to inspection. RFECT using the electromagnetic wave with solenoidal coils could be estimated the sensitivity of coils. So, to increase the receiving sensitivity, we has considered

configuration of high resolution typed array receiving coils. And transmission coil has designed to maximize the dipole magnetic moment. Operational frequency for transmission in 8 inch pipe is 50 Hz that can be applied with skin depth. The skin depth effect is dominant to the thickness and frequency. RFECT phenomenon takes two-wall through inspection. So operational frequency should be applied in two pipe thickness or more. To evaluate the receiving coil sensitivity and transmission efficiency, we carry out a pull-rig test from typical defect of 8 inch pipeline.

To optimize the exciting coil in 8 inch pipe, we has considered the performance of coil which can have higher magnetic moment contrast with lower power consumption. So calculation model has been applied in performance evaluation considering the coil parameters. And dissipating transient current has been set to 1 A per h. Maximum outer diameter of exciting coil is 92 mm approximately 50 % of pipe inner diameter and input voltage is 12 V_{pp}. Also space factor of winding coil has considered 75 %. So some cases are selected by considering the mechanical design. Parameters and equations for calculation are presented in Eqs. 1–7. Where R is resistance and L is inductance. I and J are current and current density. Also P and M are power consumption and magnetic moment.

$$\text{Turns (N)} = \frac{D \times l_{coil} \times S_f}{0.25 \times d_{wire}^2 \times \pi} \tag{1}$$

$$\text{Resistance (R)} = \frac{l_{wire}}{\sigma_{copper} \times S_{wire}} \ [\Omega] \tag{2}$$

$$\text{Inductance (L)} = \mu_r \frac{0.9 r_{coil}^2 \times turn^2}{6 r_{coil} + 9 l_{coil} + 10 D} \ [\text{H}] \tag{3}$$

$$\text{Current (I)} = \frac{V}{R + \omega L} \ [\text{A}] \tag{4}$$

$$\text{Current density (J)} = \frac{I}{S_{wire}} \ \left[\text{A}/\text{m}^2\right] \tag{5}$$

$$\text{Power (P)} = I^2 R \ [\text{W}] \tag{6}$$

$$\text{Magnetic moment (M)} = \mu N I S_{coil} \ \left[\text{A m}^2\right] \tag{7}$$

Increasing the transmission efficiency, an impedance dominated by resistance and inductance could be key parameter to determine the performance of the coil. Allowable current with coil diameter is different from cross-sectional area of each coils. So Increased allowable power consumption for system will compensate for the decrease in coil diameter. So, we choose the one considering size and current limit. Transmission coil is fabricated of 715 turns of #17 copper wire wound 80 mm wide on a 92 mm diameter spool similar to calculation model. The selected model has a high dipole magnetic moment contrast with low power consumption near to

Table 1 Comparison with calculation and measurement model

	Coil diameter (mm)	Turns (Times)		I (A)		P (W)	M (A m)^2
		Calculation	Measurement	Calculation	Measurement		
Transmitter	1.1	726	715	0.995	0.994	3.299	3.677

1 A as shown Table 1. More high input current than 1 A is applied to the coil, the larger magnetic moment can be generated. However we always consider a compromise between geometrical design and system capacity.

To increase the receiving efficiency, we has consider coil turns and size and orientation of sensor on the pipe. Performance of receiving coil is proportional to magnetic flux through unit area and number of turns of coil. This representation is Maxwell-Faraday' law as with Eq. 8. So, to increase the induced electromotive force of receiving coil, it is good to wind the coil as much as possible. However sensor size of high resolution type for full coverage of pipe is limited by number of sensors.

In this study, arrangement of receiving coils is 36 channel for 8 inch pipeline. We wound the coil to 40,000 turns with 0.02 mm copper wire and maximum diameter is 16∅.

$$\varepsilon = -\mathrm{N}\frac{d\emptyset}{dt} \tag{8}$$

To investigate the effect of orientation of receiving coil on the pipe, experiment with 2 configuration of receiving coil by radial and axial direction has performed. Amplitude and phase angle are measured by pull-out test and imperfection sensitivity has evaluated for same defect. Signal pattern and sensitivity are different by orientation of receiving coil. Assuming that the pattern of signal with B_r and B_z component of magnetic field leaking in the vicinity of flaw, signal pattern has a mono-peak by axial direction and bipole-peak by radial peak. As shown Fig. 3, the variation of peak magnitude with radial direction is larger than axial direction. Amplitude variation is greater 4.7 times and phase angle variation is greater 2.6

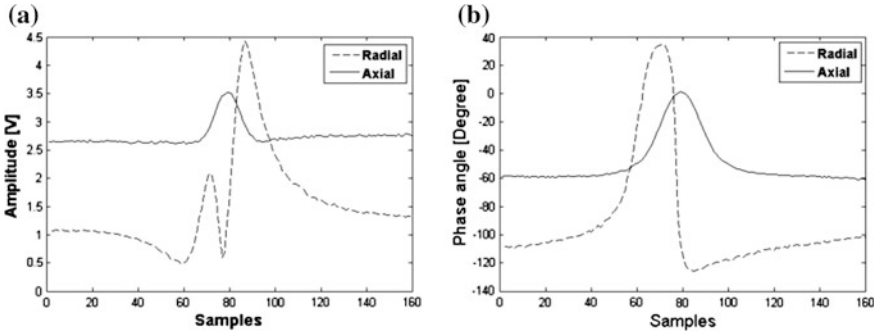

Fig. 3 Acquired signals depending on the orientation of pick-up coil; **a** amplitude and **b** phase

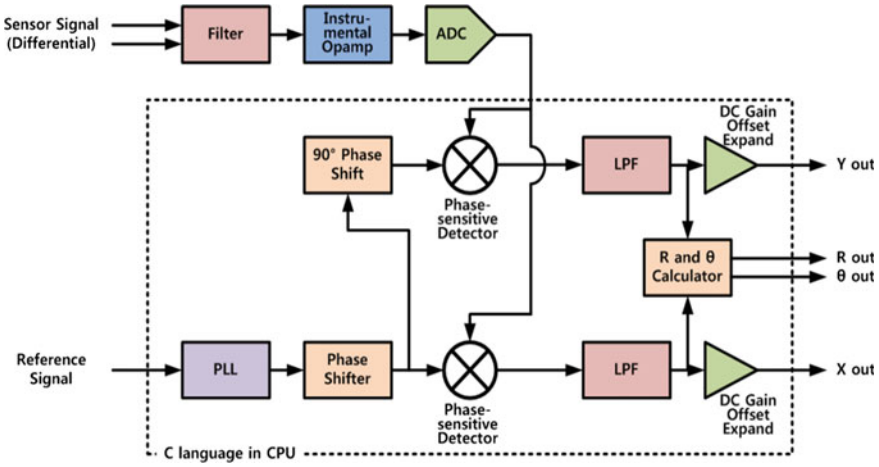

Fig. 4 Structure of parallel type of digital LIA

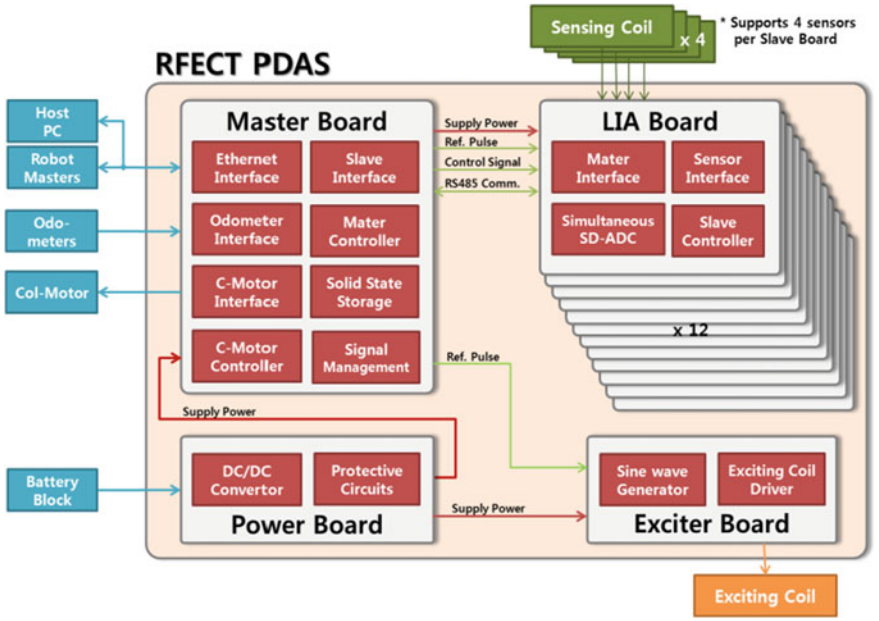

Fig. 5 Block diagram of electronics of RFECT system with parallel LIA

times in radial direction. Radial amplitude has presented as positive bipole-peak because the amplitude is represented square root of in-phase and quadrature component. So orientation of receiving coil with radial direction is good for sensitivity.

Figure 4 shows structure of the developed digital LIA which consist of amplifier, several types of filter, phase sensitive detector, PLL (Phase Loop Lock). It output

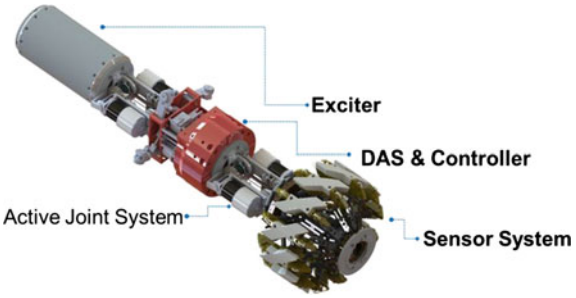

Fig. 6 Developed RFECT system for ILI robot

in-phase and quadrature component by RS485 communication. Therefore, master controller can access many LIAs within the limit that capacity of serial communication allows. DAS for RFECT was designed using parallel type of digital LIA as Fig. 5.

From the design above mentioned, optimal design of RFECT system is resulted as Fig. 6. Each LIA cover 4 sensor coils. And twelve LIAs was accommodated for 8 inch pipe.

3 Flaw Detection and Evaluation

The main purpose of in-line inspection is the characterization of external flaws. For this work, data analysis method is important. The available data using lock-in amplifier are in-phase (X) and quadrature (Y) component. The relation of this two components is represented the amplitude and phase angle. The variation of magnetic field leaking in the vicinity of flaw present variation of amplitude and phase. So we can estimate the size of flaw using variation of amplitude and phase. Equations 9 and 10 are calculation of amplitude and phase.

$$\text{Amplitude (R)} = \sqrt{X_2 + Y_2} \tag{9}$$

$$\text{Phase } (\theta) = \tan^{-1}\frac{Y}{X} \tag{10}$$

To verify the detectability of flaw, we has machined the artificial flaws which has various typed artificial defects on the 8 inch pipe. Sizes of defects are 2t × 2t, 2t × 4t, 4t × 4t, 6t × 2t, 6t × 6t (length × width) with depth of 20–80 % thickness of 8 inch pipe. Thickness(t) of 8 inch pipe wall is 5.85 mm. The pull-rig test has performed in test pipe. Figure 7 shows the configuration of test pipeline and strip chart of scan data. And image scan by sections 1, 2 shown Fig. 8. All defects are detected using RFECT system.

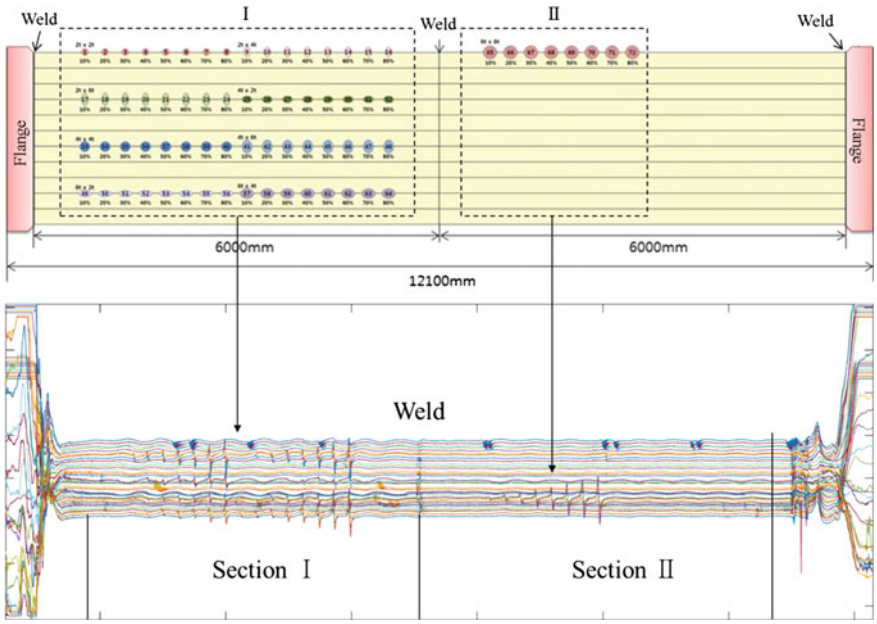

Fig. 7 Configuration of test pipeline and strip chart of scan data

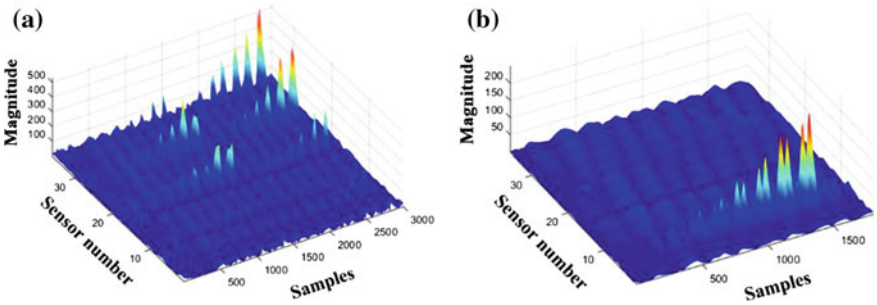

Fig. 8 Image scan; **a** section 1 and **b** section 2

The phase angle have decreased depending on increasing wall thickness. Phase angle represents depth because time delay in passing speed of wall differs depending on the wall thickness. So phase variation has important information of depth of defect. Figure 9 shows the relation of phase angle depending on depth variation. The relations have a tendency with linearly decreasing depending on increasing wall thickness. The 20 and 80 % depth of flaw has evaluated in each of 52.86° and −8.0°. The phase angle is a difference of 9° when the wall thickness is increased 10 %. And magnitude variation is also effected to depth variation.

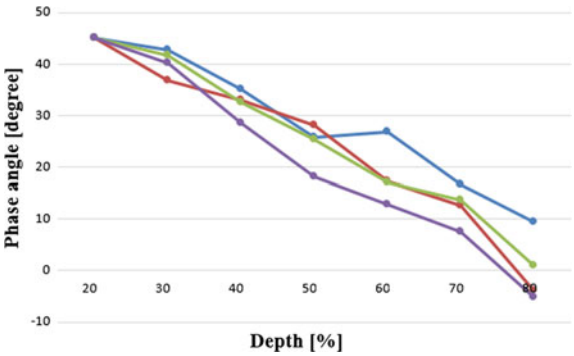

Fig. 9 Phase variation depending on the depth

However phase is more dominant than magnitude. As you can see in the experimental results, the performance of RFECT system was verified.

4 Conclusions

In this paper an effective system architecture for RFECT considering extendibility of receiving sensor channel is proposed by introducing parallel type of digital LIA. Also, to optimize the exciter coil and receiving sensor coils of the RFECT system to 8 inch pipe, exciter coil is designed so that it can have higher magnetic moment and minimize lower power consumption at same time. Also receiving coil is designed to maximize the induced electromotive force within restricted volume. The signal pattern and sensitivity according to the measurement direction of receiving coil are analyzed by pull-rig test. The performance of proposed RFECT system is verified through the pull-rig experiment including a set of artificial defects simulating metal loss on the pipeline.

Acknowledgments This research was supported by Korea evaluation institute of industrial technology in 2015 as South Korea's economic resources.

References

1. D'Zurko D (2008) Completion of development of robotics systems for inspecting unpiggable transmission pipelines.
2. Gomez P, Lee R (2013) Robotic ILI of unpiggable natural gas pipelines with Explorer
3. Schempf H, Mutschler E, Goltsberg V, Skoptsov G, Gavaert A, Vradis G (2013) Explorer: untethered real-time gas main assessment robot system
4. Choi HR, Ryew SM (2002) Robotic system with active steering capability for internal inspection of urban gas pipelines. Mechartronics 12:713–736
5. Schempf H (2006) Explorer-ii: wireless self-powered visual and NDE robotic inspection system for live gas distribution. Technical Report, Carnegie Mellon University

6. Cho SH, Kim YK, Yoo HR (2001) Development of intelligent pig for detecting corrosion on pipeline using MFL technology. J KSME 1(2):235–240
7. Kim HM, Park GS, Rho YW et al (2012) A study on the measurement of axial cracks in the magnetic flux leakage NDT system. Korean Magn Soc 22(2):49–57
8. Lord W, Sun S, Udpa SS, Nath S (1988) A finite element study of the remote field eddy current phenomenon. IEEE Trans Magn 24(1):435–438

Research on Design and Simulation of an Automatic Car Painting System in Thaco-Kia Company

Tri Cong Phung and Duy Anh Nguyen

Abstract An automatic car painting system is so popular in the world, especially in car manufacture factories. However, this system is still rarely used in Vietnam. Thaco-Kia Company is the first company concentrating on manufacturing cars in Vietnam. This paper proposes an automatic system for painting cars in the company. A system is designed in the painting room using industrial robots. An algorithm for painting all the surface of the car is considered. Finally, the idea is verified by simulation using MATLAB software.

Keywords Painting robot · Forward kinematic · Inverse kinematic · Path planning · Automatic system

1 Introduction

Nowadays industrial robots are used popularly in many factories, especially in car manufactures. They can be used in welding systems, assemble systems, loading systems, etc. A painting system plays an important role in manufacturing cars. There are many researches about programming robots for painting cars automatically. However, to get the good painting surface is a challenge.

There are several researches on using industrial robots for painting cars. Li et al. [1] present a paint deposition simulation method developed for the automotive painting line. Asakawa and Takeuchi [2] deal with the automatic spray-painting by a 6-DOF industrial robot equipped with an air spray gun to generate the robot control commands without any special knowledge on spray-painting. Tang and Chen [3]

T.C. Phung (✉) · D.A. Nguyen
Faculty of Mechanical Engineering, Ho Chi Minh City University of Technology, Ho Chi Minh City, Vietnam
e-mail: ptcong@hcmut.edu.vn

D.A. Nguyen
e-mail: duyanhnguyen@hcmut.edu.vn

V.H. Duy et al. (eds.), *AETA 2015: Recent Advances in Electrical Engineering and Related Sciences*, Lecture Notes in Electrical Engineering 371,
DOI 10.1007/978-3-319-27247-4_59

describe an efficient and flexible tool trajectory optimization scheme using T-Bezier curves calculated in a new way from trigono-metrical bases. Kamani et al. [4, 5] propose a new computer vision system for automatic painted car body inspection in the context of quality control in industrial manufacturing. Pichler et al. [6] present an approach that uses range image data to obtain the geometry of an unknown part and to automatically generate the robot spray painting trajectories. Chen et al. [7] present a review of automated tool path planning methods to investigate the advantages and disadvantages of the current techniques. From et al. [8] present the experiment results of a new spray paint algorithm implementing on an ABB robot.

In Vietnam, an application of industrial robots for painting objects is still a challenge. In Thaco-Kia Company the car painting chain still used human resource. To improve the quality and increase the productivity, we should apply industrial robots for car painting works. Another requirement is that the company needs to apply for many different cars. So a simulation program is needed to check the working of robots before buying them.

This paper suggests one automatic car painting system for Thaco-Kia Company. This mechanical system uses two industrial robots and two tracks to paint all the surface of the car. The robots that we chose are the industrial robots from ABB Company. So the controller of the system is IRC5, a modern controller of ABB Company. We also suggest an algorithm to assure that the robots can paint all the surface of the car.

The paper includes 6 sections. Section 1 proposes the problem of the paper. Mechanical system is described in Sect. 2. Section 3 talks about the controller of the system. An algorithm for painting all the surface of the car is proposed in Sect. 4. Simulation to verifying the above algorithm is done in Sect. 5. Section 6 is conclusion.

2 Mechanical Design

In this section, we propose a solution for designing an automatic car painting system that can paint all the surface of the car.

2.1 Condition of the Painting Room

The dimension of the painting room is 15 m × 6 m × 6 m. In the room, we already have Flex Track to carry the car. The parameters of the Flex Track are as follows: name Flex Track IRT 501-90R, error 0.1 mm, acceleration 1 m/s^2, velocity 1.2 m/s, mass 559 kg, capacity 2950 kg. Figure 1 shows the Flex Track used in the company.

Fig. 1 Flex Track

The car that the paper concentrates on is Kia New Carens whose dimension is 4545 mm × 1820 mm × 1650 mm.

2.2 *Proposed Design*

The problem is that we need to design a system that can paint all the surface of the car. To do this, we have three choices.

The first one is that the car and the robot are standing. In this choice, we need a large robot so that it can reach all the surface of the car. Or we need more than one robot. Thus this method is not economic.

The second one is that the robot is standing and the car is moving. It is more difficult to make painting because the moving of the car. So the quality of the painting surface is not good.

The third one is that the robot is moving and the car is standing. This method combines the advantages of both these above methods. We need two more tracks to move robots. This is the design that we choose.

2.3 *Painting Robot*

Basing on the dimension of the painting room, the car, and the Flex Track, we choose industrial robots IRB2600ID of the ABB Company for our solution. Figure 2 shows the robot and its workspace. The painting tool is Robobell 925 shown in Fig. 3.

To paint entire the inside surface of the car, we need a lifter to lift the car. We choose a Flex Lifter 600 of ABB Company.

Finally a perfect automatic car painting system can be shown in Fig. 4.

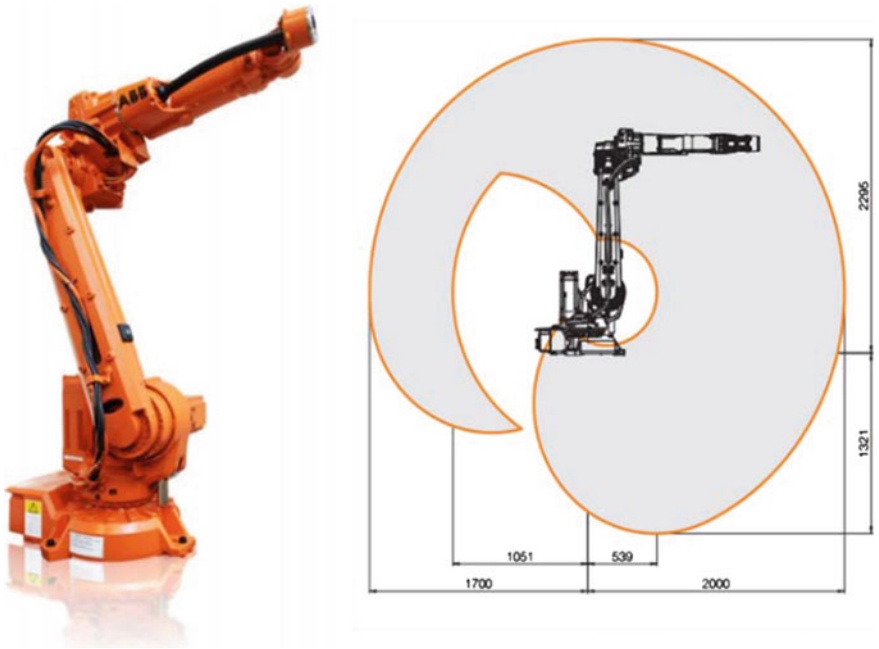

Fig. 2 Robot IRB2600ID

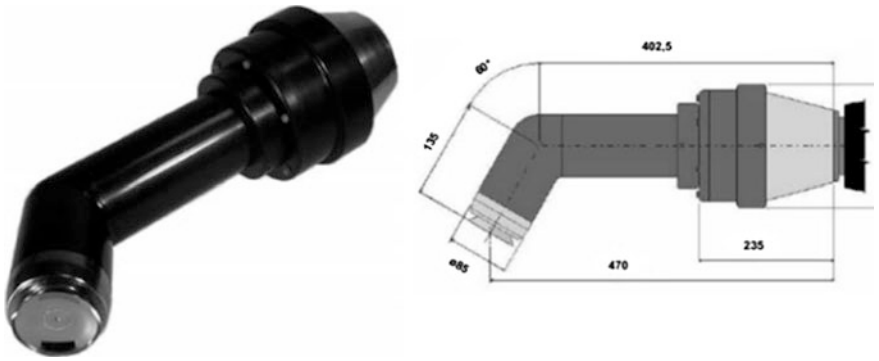

Fig. 3 Spray painting gun: Robobell 925

2.4 Kinematic Analysis of Robot

To control the robot to follow a desired trajectory, we need to solve the kinematic problem of the robot. In this part, we will solve the forward kinematic problem of the robot IRB2600ID. The global and local frames were added to the robot shown in Fig. 5. DH parameters table is show below in Table 1.

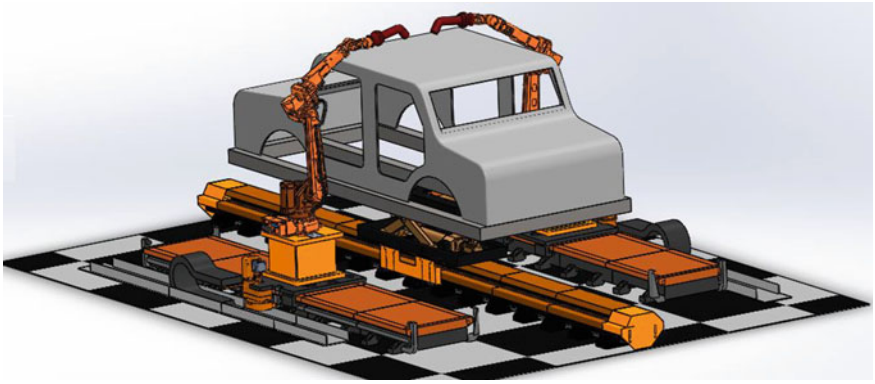

Fig. 4 An automatic car painting system

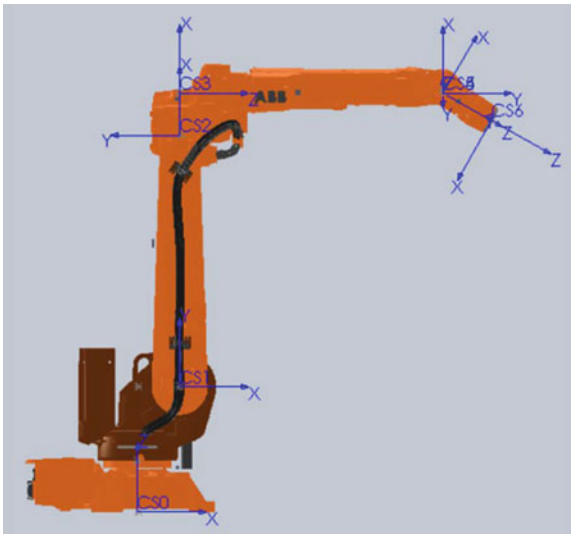

Fig. 5 Frames attached to the robot

Table 1 DH parameters table

i	α_i	a_i (mm)	θ_i	d_i (mm)
1	90°	150	θ_1	445
2	0°	900	θ_2	0
3	90°	150	θ_3	0
4	90°	0	θ_4	938
5	−90°	0	θ_5	0
6	0°	0	θ_6	200

The transformation matrix ${}^0T_6$ describes the related position between the frame of the painting tool and the frame of the ground.

$$ {}^0T_6 = {}^0T_1\,{}^1T_2\,{}^2T_3\,{}^3T_4\,{}^4T_5\,{}^5T_6 = \begin{bmatrix} n_x & s_x & a_x & p_x \\ n_y & s_y & a_y & p_y \\ n_z & s_z & a_z & p_z \\ 0 & 0 & 0 & 1 \end{bmatrix} \tag{1} $$

where $n_x, n_y, n_z, s_x, s_y, s_z, a_x, a_y, a_z$ are orientation components of the painting tool compared to the ground frame. They depend on the values of robot joints and link lengths.

$$ n_x = c_1 s_5 c_6 s_{23} + c_5(s_1 s_4 + c_1 c_4 c_{23}) + s_6(s_1 c_4 - c_1 s_4 c_{23}) \tag{2} $$

$$ n_y = s_1 s_5 c_6 s_{23} - c_5(c_1 s_4 - s_1 c_4 c_{23}) - s_6(c_1 c_4 + s_1 s_4 c_{23}) \tag{3} $$

$$ n_z = -s_5 c_6 c_{23} - s_{23}(c_4 c_5 + s_4 s_6) \tag{4} $$

$$ s_x = c_1(c_4 c_5 c_{23} - s_5 s_6 s_{23}) + c_6(s_1 c_4 - c_1 s_4 c_{23}) + s_1 s_4 c_5 \tag{5} $$

$$ s_y = s_1(c_4 c_5 c_{23} - s_5 s_6 s_{23}) - c_6(c_1 c_4 + s_1 s_4 c_{23}) - c_1 s_4 c_5 \tag{6} $$

$$ s_z = s_5 s_6 c_{23} - s_{23}(c_4 c_5 + s_4 c_6) \tag{7} $$

$$ a_x = c_1 c_5 s_{23} - s_5(s_1 s_4 + c_1 c_4 c_{23}) \tag{8} $$

$$ a_y = s_1 c_5 s_{23} + s_5(c_1 s_4 - s_1 c_4 c_{23}) \tag{9} $$

$$ a_z = -c_5 c_{23} - c_4 s_5 s_{23} \tag{10} $$

The position of the painting tool can be described by these following equations:

$$ p_x = c_1(a_1 + a_2 c_2 + a_3 c_{23} + d_4 s_{23}) + d_6 c_1 c_5 s_{23} - s_5(s_1 s_4 + c_1 c_4 c_{23}) \tag{11} $$

$$ p_y = s_1(a_1 + a_2 c_2 + a_3 c_{23} + d_4 s_{23}) + d_6 s_1 c_5 s_{23} + s_5(c_1 s_4 - s_1 c_4 c_{23}) \tag{12} $$

$$ p_z = s_{23}(a_3 + c_4 s_5) - c_{23}(d_4 + d_6 c_5) + a_2 s_2 + d_1 \tag{13} $$

The inverse kinematic problem of the robot can be solved when giving the values of position and orientation of the painting tool. We may receive many solutions for the inverse kinematic problem. We choose the solution that satisfy the working condition of robots. When the robot moves along the track or the flex lifter lifts the car, the new values of position and orientation of the car can be received from a translation from previous ones.

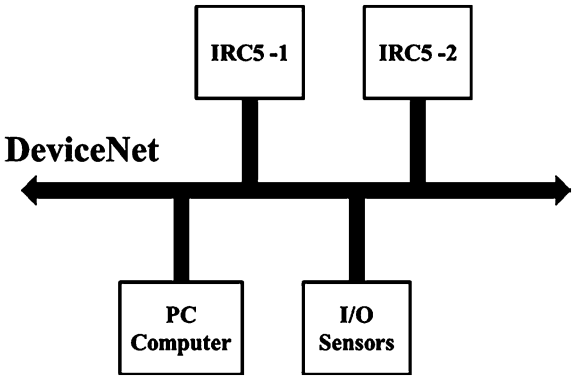

Fig. 6 The system controller

3 Electronic Design

In our design, we use IRC5 controllers of ABB Company to control all the system. Based on more than four decades of robotic experiences, the IRC5 is the robotic industry's benchmark in robot controller technology. In addition to ABB's unique motion control it brings flexibility, safety, modularity, application interfaces, multi-robot control and PC tool support. The IRC5 controller includes two modules: driver module and control module. Each IRC5 controller can control maximum 4 different robots. The communication between IRC5 controllers is based on industrial communication network in which DeviceNet is most popular.

We need to control the system that includes two robots IRB2600ID, two robot tracks, one car track, and one flex lifter. The total number of controlled robots is 6. So we need total two IRC5 controllers. One controls two robots and two robot tracks. The other controls the car track and the flex lifter. Figure 6 shows the electronic connection of the system.

4 Control Algorithm

In the automatic car painting system, we use linear interpolation paths to control the painting tool. From the 3D CAD design of the car, we can determine the position and orientation of the painting tool of robot. A robot trajectory includes linear lines passing designed points. Because the car surface is curved and the robot trajectory is lines, we need to divide the trajectory into many points.

When the velocity of the painting tool is constant, the quality of the thickness of painting on the surface is good. So the movement of the robot follows the parabola

trajectory. To get the good painting surface, we need to determine the velocity of the painting tool and the distance between painting lines. The velocity can be calculated as follow in Eq. 14.

$$v = \frac{Q}{a \times L \times (1 - x)} \tag{14}$$

where v is painting velocity (mm/s), Q is painting flow ($mm^3/2$), a is the painting thickness (mm), L is painting radius (mm), x is painting performance (%).

Figure 7 shows our control algorithm. First the PC checks if the car reaches the robot position or not. If there is the car, the robot starts to paint the car. After painting the outside surface of the car, the flex lifter lift the car and the robots continue to paint the inside surface of the car. When robots finishing painting the inside surface of the car, the system can continue painting or stopping depending on the decision of system control engineer.

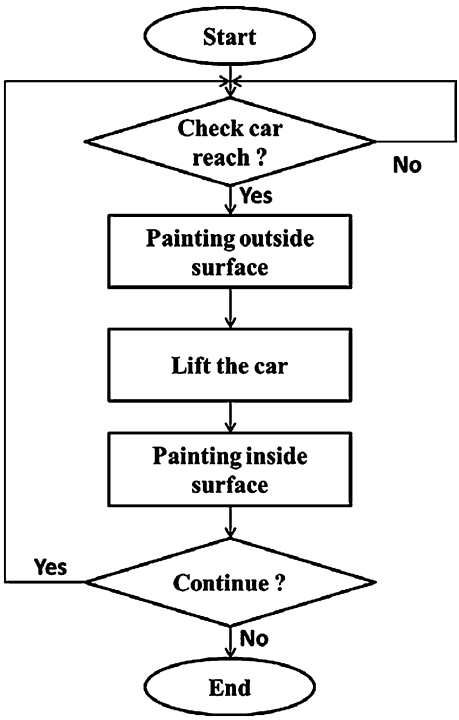

Fig. 7 Algorithm flow chart

5 Simulation

In this paper, the robot is designed in SolidWorks software. After that, we save the robot model as STL file so that we can import it to MATLAB software for simulation. STL file is a format that is supported by much software to numeric the surface of the 3D object. The object is divided into many triangle parts. Each part includes three surfaces and each surface includes three points. The values of these points are saved in STL file.

In the simulation, we simulate the robot to move along X-axis, Y-axis, and Z-axis. Next we simulate the car painting system using robots. Figure 8 shows the working of robot in linear axis. Figure 9 shows several positions of the robots when painting the outside surface of the car. Figure 10 shows the working of painting the inside surface.

The simulation results verify that our proposed system and algorithm can paint the car automatically. This increase the productivity and the quality of the product comparing with existing system.

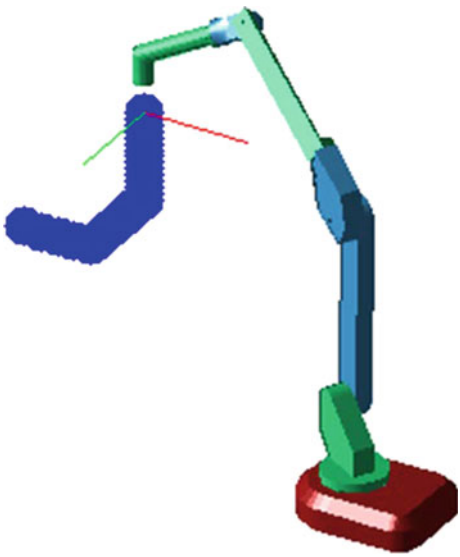

Fig. 8 Robot moves along X, Y, and Z-axis

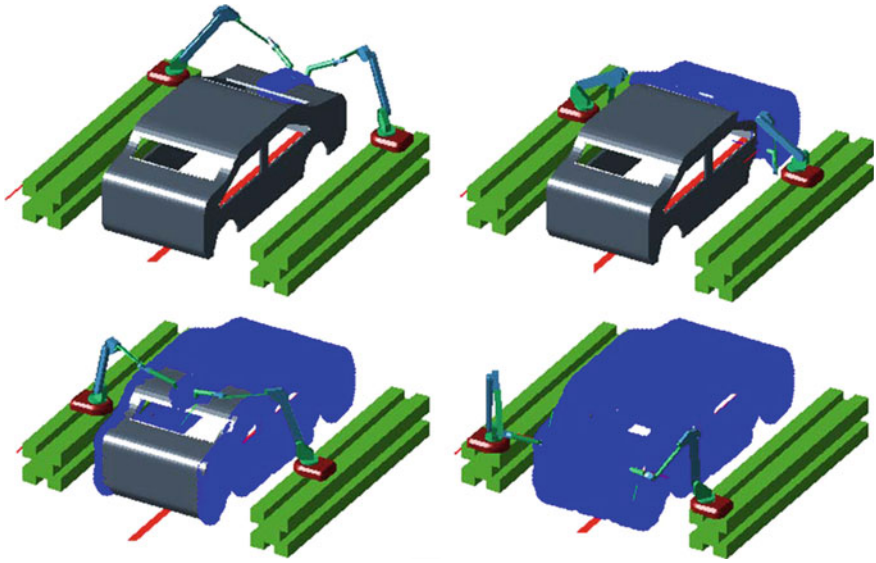

Fig. 9 Robots paint the outside surface of the car

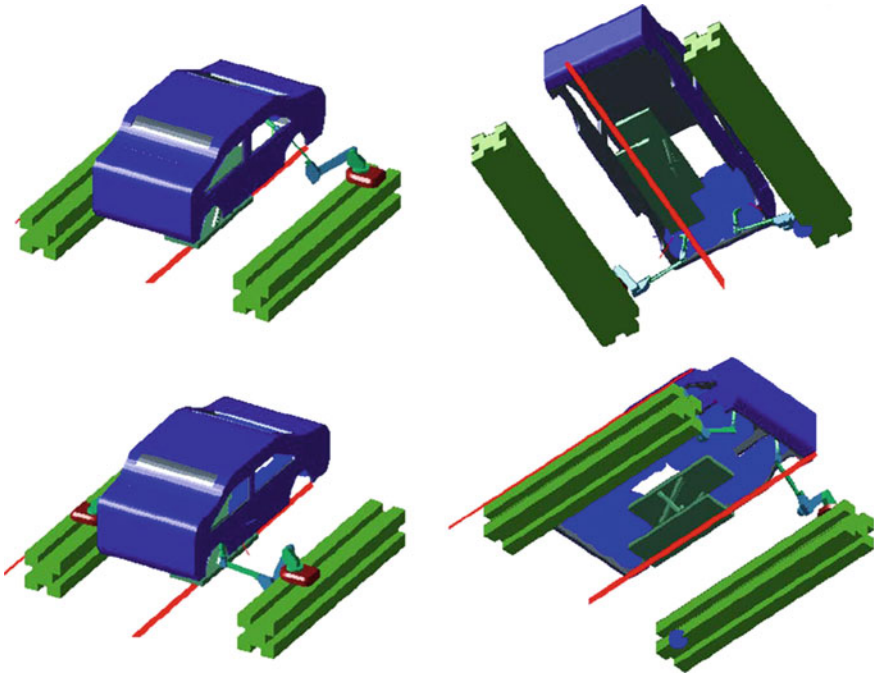

Fig. 10 Robots paint the inside surface of the car

6 Conclusion

In this paper, we have already suggested a solution for designing an automatic car painting system in Thaco-Kia Company. This system includes two industrial robots, two robot tracks, one car track, and one flex lifter. An algorithm to assure that robots can paint all the surface of the car has been proposed. The algorithm is verified by simulation using MATLAB. The simulation results show that the design can get the goal. However we need an experimental system to verify our solution because there are some differences between simulation results and real results.

References

1. Li X, Zhang B, Fuhlbrigge TA, Landsnes O, Riveland S (2014) Paint deposition simulation for robotics automotive painting line. In: 2014 IEEE 4th annual international conference on cyber technology in automation, control and intelligent systems, Hong Kong, 4–7 June 2014, pp 349–354
2. Asakawa N, Takeuchi Y (1997) Teachingless spray-painting of sculptured surfaces by an industrial robot. In: 1997 IEEE international conference on robotics and automation, vol 3, Albuquerque, NM, 20–25 Apr 1997, pp 1875–1879
3. Tang Y, Chen W (2015) Surface modeling of workpiece and tool trajectory planning for spray painting tool. Public Library of Science, published online 18 May 2015
4. Kamani P, Noursadeghi E, Afshar A, Towhidkhah F (2011) Automatic paint defect detection and classification of car body. In: 2011 7th Iranian machine vision and image processing, Tehran, 16–17 Nov 2011, pp 1–6
5. Kamani P, Afshar A, Towhidkhah F, Roghani E (2011) Car body paint defect inspection using rotation invariant measure of the local variance and one-against-all support vector machine. In: 2011 1st international conference on informatics and computational intelligence, Bandung, 12–14 Dec 2011, pp 244–249
6. Pichler A, Vincze M, Andersen H, Madsen O (2002) A method for automatic spray painting of unknown parts. In: Proceedings ICRA2002 IEEE international conference on robotics and automation, vol 1, pp 444–449
7. Chen H, Fuhlbrigge T, Li X (2008) Automated industrial robot path planning for spray painting process: a review. In: IEEE international conference on automation science and engineering, Arlington, VA, 23–26 Aug 2008, pp 522–527
8. From PJ, Gunnar J, Gravdahl JT (2011) Optimal paint gun orientation in spray paint applications—experimental results. IEEE Trans Autom Sci Eng 8:438–442

On-line Training Solution to Modify the Inverse Kinematic Approximation of a Robot Manipulator

Bach H. Dinh

Abstract This paper describes a new practical approach for approximating the inverse kinematics of a manipulator using an RBFN (Radial Basis Function Network). In fact, sometimes a well-trained network cannot work effectively in the operational phase because the initial network training occurs in an environment that is not exactly the same as the environment where the system is actually deployed. In this paper, an online retraining solution using a "free interference rule" is presented for systems whose characteristics change due to environmental variations. It helps the learning process avoiding the interference where a new training point may upset some of the weights which were trained with previous points. The simulation results prove that the proposed approach is effective.

Keywords Radial basis function networks · Regularly-spaced position centres · Constrained training data

1 Introduction

In robot kinematics there are two important problems, forward and inverse kinematics. Forward kinematics can be regarded as a one-to-one mapping from the joint variable space to the Cartesian coordinate space (world space). From a set of joint angles, forward kinematics determines the corresponding location (position and orientation) of the end-effector. This problem can be easily solved by the 4×4 homogenous transformation matrices using the Denavit and Hartenbergh representation [1]. Inverse kinematics is used to compute the corresponding joint angles from location of the end-effector in space. Obviously, inverse kinematics is a more

B.H. Dinh (✉)
Faculty of Electrical and Electronics Engineering, Ton Duc Thang University,
No. 19 Nguyen Huu Tho Street, District 7, Ho Chi Minh City, Vietnam
e-mail: dinhhoangbach@tdt.edu.vn

V.H. Duy et al. (eds.), *AETA 2015: Recent Advances in Electrical Engineering and Related Sciences*, Lecture Notes in Electrical Engineering 371,
DOI 10.1007/978-3-319-27247-4_60

difficult problem than forward kinematics because of its multi-mapping characteristic. There are many solutions to solve the inverse kinematics problem, such as the geometric, algebraic, and numerical iterative methods. In particular, some of the most popular methods are mainly based on inversion of the mapping established between the joint space and the task space using the Jacobian matrix [2]. But, this solution does not always guarantee to produce all the possible inverse kinematic solutions and involves significant computation. In cases where the manipulator geometry cannot be exactly specified, the traditional methods become too difficult, for example the robot-vision systems.

The artificial neural network which has significant flexibility and learning abilities has been used in many robot control problems. In fact, for the inverse kinematics problem several neural network architectures have been used, such as MLP (Multi-Layer Perceptron), Kohonen self-organizing map and RBFN [3–8]. All the mentioned approaches tried to produce an inverse solution of the forward kinematic transformation to build the mapping from world coordinate space to joint angle space, but their results were not likely to satisfy in practice due to the complexity of the inverse kinematics problem. Indeed, the performance of an approximation function based neural networks depends on three main factors: the network's structure, training method, and training patterns as well. To improve the performance of RBFNs in inverse kinematics problem, a new approach has been presented in [9] where centres of the hidden-layer units are regularly distributed in the workspace and training phase is implemented with constrained training data whose inputs are collected around the centre positions. Using this approach an appropriate approximation of the inverse kinematic function of a robotic manipulator can be produced. However, sometimes a well-trained network cannot work effectively in the operational phase because the initial network training occurs in an environment that is not exactly the same as the environment where the system is actually deployed. An example of this is a robot-vision system whose structure changes due to environment alterations between the initial training phase and practical deployment, e.g., different type of camera or variation in distance and view angle between the camera and robot. Therefore, an effective retraining solution is proposed to modify the RBFN performance through on-line training by using the Delta rule. This solution can be effectively applied for systems whose characteristics change due to environmental variations.

2 Approximate the Inverse Kinematics of a Robot-Vision System Using RBFNs

The basic architecture of an RBFN is the three layer network consisting of an input layer, a hidden layer and a linear output layer [10–12]. The unique feature of the RBFN compared to the MLP and other networks is the process performed at the hidden layer. In this hidden layer, the radial basis function works as a local selector

in which the corresponding output depends on the distance between its centre and input. It can be presented as:

$$\Phi_i(x) = \exp\left(-\frac{\|x - c_i\|}{\sigma^2}\right) = \exp\left(-\frac{r_i^2}{\sigma^2}\right) \tag{1}$$

$$r_i = \sqrt{\sum_{k=1}^{K} (x_k - c_{ki})^2} \tag{2}$$

where

Φ_i Radial basis function (Gaussian function)
c_i centre of the i-th hidden unit (i = 1, 2,…, I)
σ width (or spread) of the Gaussian function
r_i distance between input and centre of the i-th hidden unit
x input of the RBFN—image coordinates (k = 1, 2)

then, the outputs of the RBFN are expressed as:

$$y_i(x) = \sum_{i=1}^{M} W_{ji}\Phi_i(x) \tag{3}$$

where

W_{ji} synaptic weight between the i-th hidden unit and the j-th output,
y_j the j-th output of the RBFN- joint angles (j = 1, 2)

Because of the distinctive structure of an RBFN, the training process can be separated into two phases, building a hidden layer structure where centres and widths of the hidden units are firstly determined, and then training the linear weights based on input-output patterns [10]. In our approach, the hidden layer was simply pre-defined as regularly spaced positions (squares or cubics) in the workspace of the manipulator by an intuitive method (involving trial and error). These hidden-layer parameters were simply adjusted by varying centre's distances in a heuristic trial and error manner. The number of hidden units (neurons of the hidden layer) is depended on the workspace area and the distance between hidden units. Thus, the smaller the distance between centres, the better the performance of the RBFN. In practice, due to the limited computer memory capacity and the computational complexity, the number of hidden units must be limited to a sensible value so that a feasible training process can be implemented. Moreover, as the centres of the hidden layer units (Gaussian functions) are regularly distributed in the workspace, these functions should have the same spread. The spread value affects

the smoothness of the network by varying the local-filter feature of the hidden units. Thus, it was experimentally selected so that the RBFN can produce an appropriate inverse kinematics approximation.

After the hidden layer structure has been selected, training process of the linear layer can be implemented to build up an approximation of the inverse kinematics function of manipulators in any working environment.

3 On-Line Learning Method and Free Interference Rule to Modify the Performance of RBFNs

The Delta rule is a popular training method for both MLPNs and RBFNs. In our approach the linear weights of the RBFN are incrementally updated whenever there is a training pattern presenting to the network. As described in [10], the linear weights can be modified by the Delta rule as:

$$\Delta W_{ji} = \eta \cdot e_j \cdot \Phi_i \tag{4}$$

$$e_j = T_j - y_j \tag{5}$$

where
e_j error between target and actual output j
η learning rate ($0 \leq \eta \leq 1$)

The Delta rule is simple and only related to the learning rate and how large the training data is used. Based on this on-line process the inverse kinematics approximation is modified through an effectively training phase. It can be used to deal with the sensitive structure of the robot-vision system, which can occur due to variation in the set-up of the visual measurement or in case the set-up and actual application environments are different. However, one drawback of this on-line training process is the occurence of learning interference where a current training point may upset some of the weights which were trained with previous points if they are close enough [11]. Consequently, the RBFN at a retraining step can converge to the desired function in one area but diverge in other areas. This learning interference is more serious if the spread and/or the learning rate are large. Based on the characteristics of Gaussian functions, a simple rule is proposed to select appropriate pattern points in order to avoid learning interference as below.

From Eq. (1), the relationship between the ratio of the distance D to the spread value and the output of the Gaussian function can be determined as

$$\frac{D}{\sigma} = \sqrt{\frac{\ln \Phi}{-0.693}}, \tag{6}$$

where
$D = \|x - c\|$ distance between an input and a centre, and
σ the spread of Gaussian functions

Thus, the effect of a training point on the output of a hidden unit is dependent on the distance between this training point and the centre of the hidden unit in proportion to the spread. If the ratio between the distance and the spread is high enough, the point almost has no effect to the network. It can be formulated as follows:

$$\Phi \leq 0.05 \Leftrightarrow D \geq 2.079\sigma. \tag{7}$$

The principle of "***free interference rule***" is that if the position of a new training point is further than twice the spread value from the position of the previous training point used to train the network, then the training process (with this new point) will not interfere in the weights of hidden units whose centres are close to the previous point. Therefore, following the free interference rule, the RBFN may be modified gradually and smoothly in this online retraining process.

4 Simulation

A MATLAB simulation was developed to demonstrate the proposed approach. This simulation used a two-link manipulator. This simulation focused on *how an approximation function can be improved by an online training process* and *which factors affect this retraining process*. Thus, we need to build an inaccurate approximation function then using online training process with "free interference rule" to modify the trained function step-by-step. The simulation procedure can be described as below:

Step 1 Select the hidden layer parameters where:

i/ centres of the hidden layer are predefined as regularly spaced positions in the workspace,
ii/ the spread of the Gaussian functions is heuristically selected as a proportion of the centre distance.

In this simulation, a set of regularly-spaced position centres were selected as 10 mm × 10 mm grids in the workspace.

Step 2 Generate a constrained training set where its inputs are coincident with the centre positions in the workspace using the mathematical inverse kinematics functions. A constant error (offset value) is then added to the target outputs (10° in this simulation). Training the RBFN with this training set produces an inappropriate inverse kinematics approximation.

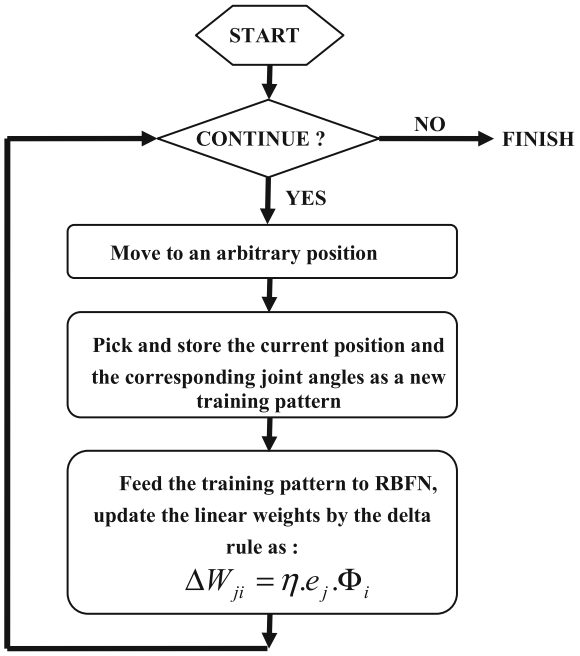

Fig. 1 Online retraining flowchart

Step 3 Update the linear weights of the RBFN through the online training process with a learning rate from 0.1 to 0.5. The inverse kinematics function gets beter and better performance after each training point applied. The flowchart in Fig. 1 describes step 3.

To examine the network's performance, a range of test data distributed as 5 mm × 5 mm grids in the square area {x = 22–52 mm; y = 22–52 mm} were sent to the RBFN. Figure 2 presents the outputs (joint angles) of the desired inverse kinematics function and the incorrect approximation (the RBFN) in this test area. It shows that the surface of the approximation functions ($\theta_1 = f_1(x, y)$ and $\theta_2 = f_2(x, y)$) are parallel to the surface of the desired functions but differ by a 10° offset. To present the network performance the root mean square error between the approximation function and the desired function (**RMSE**), the mean absolute errors in Y direction between the actual positions and the desired positions (**MAE_X**), and the mean absolute errors in Y direction between the actual positions and the desired positions (**MAE_Y**) are defined as belows:

$$RMSE = \frac{\sqrt{\sum_{i=1}^{N}\left(\left(\theta_{1Di} - \theta_{1Ai}\right)^2 + \left(\theta_{2Di} - \theta_{2Ai}\right)^2\right.}}{N} \tag{8}$$

$$MAE\_X = \frac{\sum_{i=1}^{N} |X_{Di} - X_{Ai}|}{N} \tag{9}$$

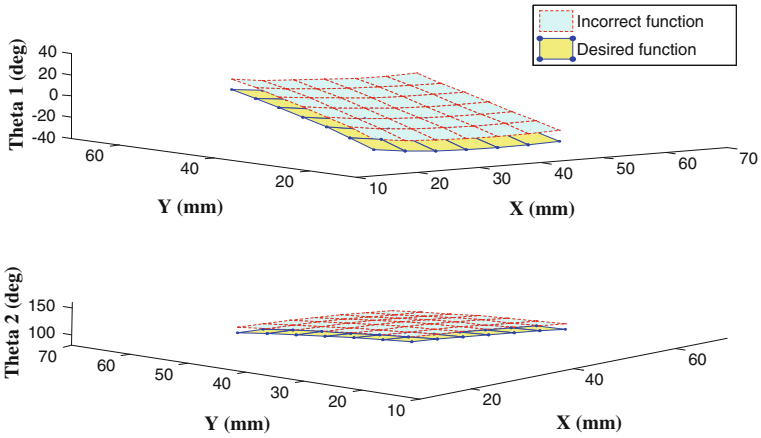

Fig. 2 Surfaces of desired (mathematical expression) and approximation functions (RBFN) in the test area

$$MAE\_Y = \frac{\sum_{i=1}^{N} |Y_{Di} - Y_{Ai}|}{N} \tag{10}$$

where

$(\theta_{1Di}, \theta_{2Di})$ and $(\theta_{1Ai}, \theta_{2Ai})$ desire and actual joint angles, respectively

(X_{Di}, Y_{Di}) and (X_{Ai}, Y_{Ai}) desire and actual position, respectively

In Fig. 2 the values of RMSE, MAE_X, and MAE_X are 9.91°, 14.39 mm, and 3.21 mm, respectively.

To clarify the effect of online retraining in modifying the inverse kinematics approximation, a series of the network's performances through 5 training points, collected using the free interference rule, are shown in Figs. 3, 4, 5 6 and 7. The retraining process was performed with a spread of 10 mm and a learning rate of 0.4. To illustrate how the inverse kinematics approximation is modified through retraining, three functions are shown on the same figure: the incorrect function (before retraining phase), modified function and the desired function.

The improvement of the RBFN is dependent on the learning rate, the spread and the position of training points in the workspace. A large learning rate and/or a large spread can improve the RBFN approximation in the area around the current training point whilst other areas become poorer due to learning inference. In this research, it is preferred to adopt a small learning rate and an average spread value for the retraining process.

The results show that the online retraining has modified the inverse kinematics approximation gradually and smoothly. After 5 online training epochs, the RBFN is close to the desired function. By selecting the training patterns following the free

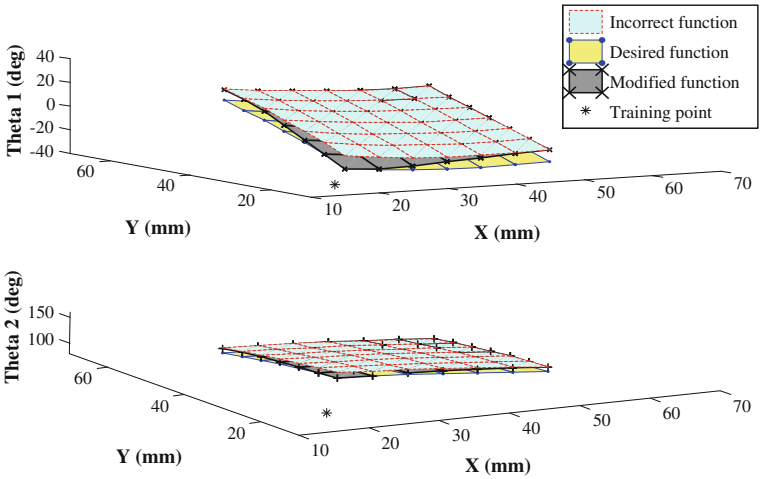

Fig. 3 The network's performance after retraining by the first point (20 mm; 21 mm)

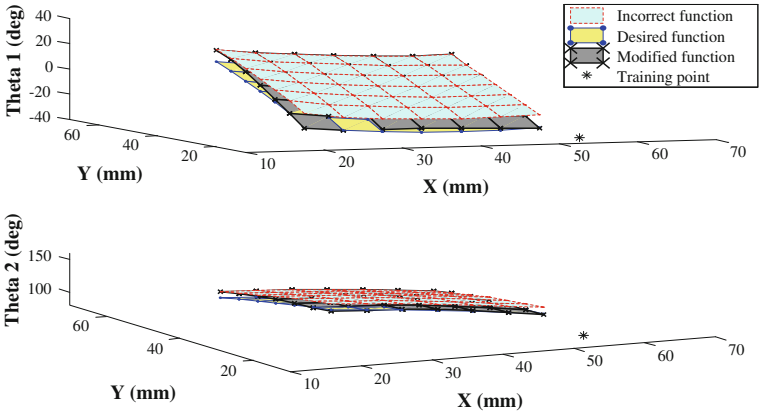

Fig. 4 The network's performance after retraining by the second point (56 mm; 19 mm)

interference rule, the current modified function at each epoch approaches the desired function in the area surrounding the training point whilst not affecting other areas.

The retraining process can be continued with new training points. The performance results of the RBFN after retraining with 5 more points (10 training points in total). These were: {(20 mm; 21 mm), (56 mm; 19 mm), (53 mm; 56 mm), (20 mm; 54 mm), (40 mm; 40 mm), (24 mm; 25 mm), (50 mm; 24 mm), (51 mm; 49 mm), (25 mm; 50 mm), (38 mm; 37 mm)}. A better performance is obtained as: **RMSE = 0.73°, MAE_X = 0.74 mm, and MEA_Y = 0.33 mm**.

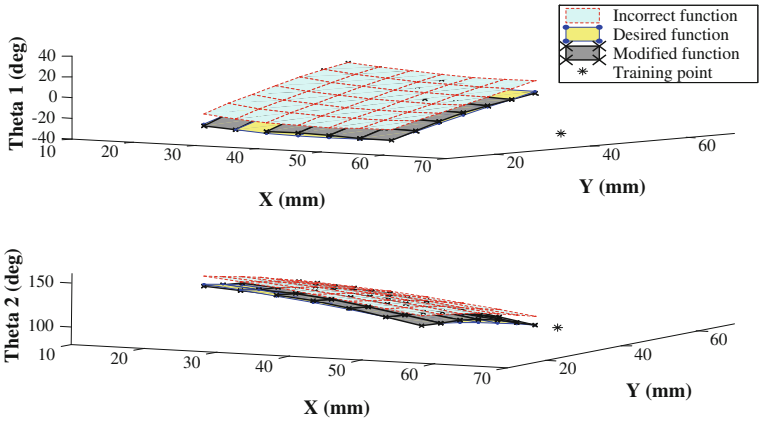

Fig. 5 The network's performance after retraining by the third point (63 mm; 56 mm)

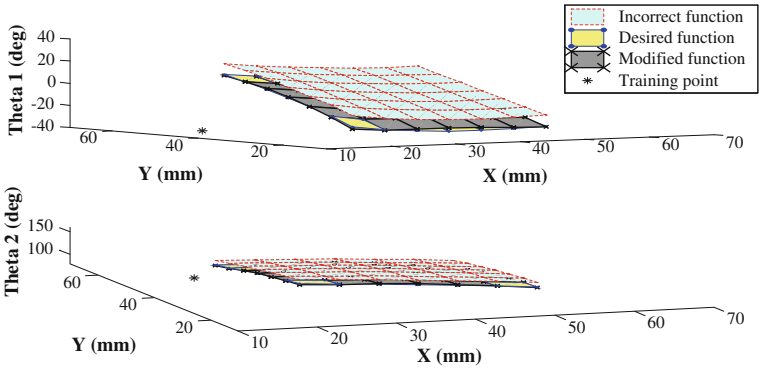

Fig. 6 The network's performance after retraining by the fourth point (20 mm; 54 mm)

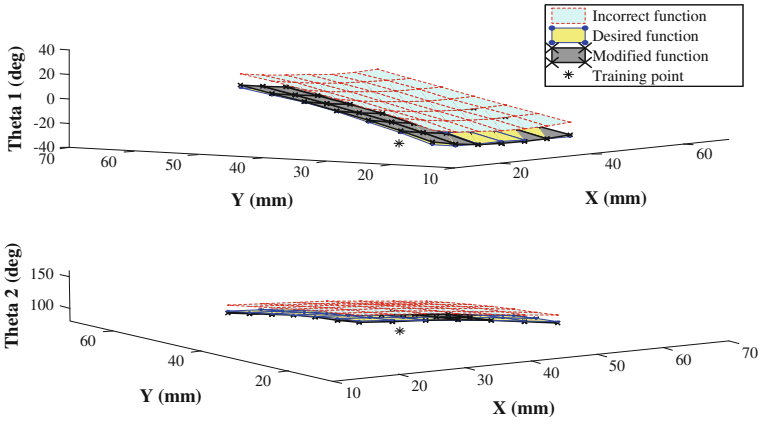

Fig. 7 The network's performance after retraining by the fifth point (40 mm; 40 mm)

Thus, we can see that the online retraining process tends to continuously improve the inverse kinematics approximation with further training points.

5 Conclusion

This paper has presented a novel approach where the inverse kinematics approximation is modified through an online retraining process. The simulations demonstrate that the RBFN performance after online retraining noticeably improves. There are three factors: the learning rate, the spread value and the position of the training points that can affect the online retraining phase. Thus, the choice of learning rate and the spread value must be carefully considered. The selection of training points following the "free learning interference rule" can produce better results. This online retraining approach can be effectively applied when the structure of the practical robotic system alters due to environmental variations.

References

1. Fu KS, Gonzalez RC, Lee CSG (1987) Robotics: control, sensing, vision, and intelligence. McGraw-Hill, New York
2. Khalil W, Dombre E (2002) Modeling, identification, and control of robots. Hermes Penton
3. Choi BB, Lawrence C (1992) Inverse kinematics problem in robotics using neural networks. NASA Technical Memorandum, 105869
4. Watanabe E, Shimizu H (1991) A study on generalization ability of neural network for manipulator inverse kinematics. In: Proceedings of the seventeenth international conference on industrial electronics, control and instrumentation, vol 2, Kobe, Japan. 28 Oct–1 Nov 1991, pp 957–962
5. Morris AS, Mansor A (1997) Finding the inverse kinematics of manipulator arm using artificial neural network with lookup table. Robotica 15:617–625
6. Alsina PJ, Gehlot NS (1995) Robot inverse kinematics: a modular neural network approach. In: Proceedings of 38th Midwest symposium on circuits and systems, vol 2. Rio de Janeiro, Brazil. 13–16 Aug 1995, pp 631–634
7. Zhang PY, Lu TS, Song LB (2004) RBF networks-based inverse kinematics of 6r manipulator. Int J Adv Manuf Technol 26:144–147
8. Yang SS, Moghavvemi M, Tolman JD (2000) Modelling of robot inverse kinematics using two ANN paradigms. In: Proceedings of TENCON2000-intelligent system and technologies for the new millennium, vol 3. Kuala Lumpur, Malaysia. 24–27 Sept 2000, pp 173–177
9. Dinh BH, Dunnigan MW, Reay DS (2008) A Practical approach for position control of a robotic manipulator using a rbfn and a simple vision system. WSEAS Trans Syst Control 3 (4):289–298
10. Haykin S (1999) Neural networks—a comprehensive foundation. Prentice Hall Inc., Englewood Cliffs
11. Irwin GW, Warwick K, Hunt KJ (1995) Neural network applications in control. IEE control engineering series, vol 53
12. Orr MJL (1996) Introduction to radial basis function networks. Available: http://www.anc.ed.ac.uk/rbf/rbf.html

A Research on Designing, Manufacturing and Controlling of a Motion Simulation System for Containers

Nguyen Duy Anh, Tran Ngoc Hoang and Kim Hwan Seong

Abstract Cargo transportation by container trucks is a popular way of transport in our country, but the risk that the cargoes may get damaged due to collisions and crashes inside the container is an unsolved problem. For that reason, the paper decided to research and design a system that can simulate the movement of a container to test the safety of the cargo securing process inside the container. This paper will present the design, structural analysis, simulation and testing operation of the experimental model. The obtained results will be the basis for future experiments about durability and safety testing of secured cargoes on a container.

Keywords Delta robot · Forward kinematic · Inverse kinematic · Simulation · Container · Fixed cargo

1 Introduction

As our country's economy grows, the amount of cargo transportation increases in both quantity and quality. Therefore, the freight traffic is like the backbone of our country's economy. In particular, this mode of transport is being used more and more in transportation business. Although it has the advantages of large cargo quantity, short shipping time and reasonable cost, there still exists risks that can lead to losses in cargo's quality and quantity. Among such risks, collisions and the impact of forces from multiple directions during the shipping process as well as the delivery process are the main causes. To protect and increase the safety of cargoes, the cargo securing process plays a vital role. From these practical requirements,

N.D. Anh (✉) · T.N. Hoang
Faculty of Mechanical Engineering, HCMC University of Technology,
268 Ly Thuong Kiet Street, Ward 14, District 10, Ho Chi Minh City, Vietnam
e-mail: duyanhkmu@hcmut.edu.vn

K.H. Seong
Korea Maritime and Ocean University, 727, Taejong-ro, Yeongdo-gu, Busan, Korean

V.H. Duy et al. (eds.), *AETA 2015: Recent Advances in Electrical Engineering and Related Sciences*, Lecture Notes in Electrical Engineering 371,
DOI 10.1007/978-3-319-27247-4_61

a motion simulation system is researched and designed in this paper with the aim to help the safety inspection of the cargo securing process.

Base on the oscillation of the container when the truck moves or when the cranes are active, the research's target is to design a model that can recreate all of these oscillations. To achieve that requirement, the paper has used the Delta Robot structure to create motion in all three axes xyz including forward and backward, left and right, up and down. In addition to a position control of the Delta structure in order to keep it in a desired orbit, a speed control with different speed settings is also an important factor to help simulate the movement of cargoes inside the container.

2 Design Model

The model was designed based on the requirements that it can carry cargoes with the maximum weight of 300 kg and fluctuate in three xyz axes. The stroke's maximum length is 300 mm in each direction. Since the weight of the cargoes is relatively large, the structures design must ensure that the system is stable when it oscillates with different frequencies. The model includes the following main components:

- I: Delta transmission components.
- II: Sliding support components.
- II: Holding components.
- IV: Rotating support components (Fig. 1).

2.1 Model Design Analysis

Cargoes are fixed on the holding plate and oscillate in three axes xyz, based on the collaboration movement of the three AC servo motor in the Delta structure. The rotational motion of the motor (1) will turn into translational motion by using leadscrew system (2). With the coupling (3) and shake joint (4), three translational motion of three linear actuators will be combined into a single motion of the moving platform (5). To control the moving platform (5) in three axis xyz, we just need to control the collaboration of the positions and speeds of the three AC servo motor. To link and transmit motion of the moving platform (5) to the holding plate (11), the paper designed "Sliding support components" and "Rotating support components" (Figs. 2 and 3).

Rotating support components uses the cylindrical roller bearing (7) and the support base (8) to convert the translational movement of the moving platform (5) in the horizontal X axis and the vertical Z axis into oscillation of the holding plate (11) rotating around the back sole of the system (Figs. 4 and 5).

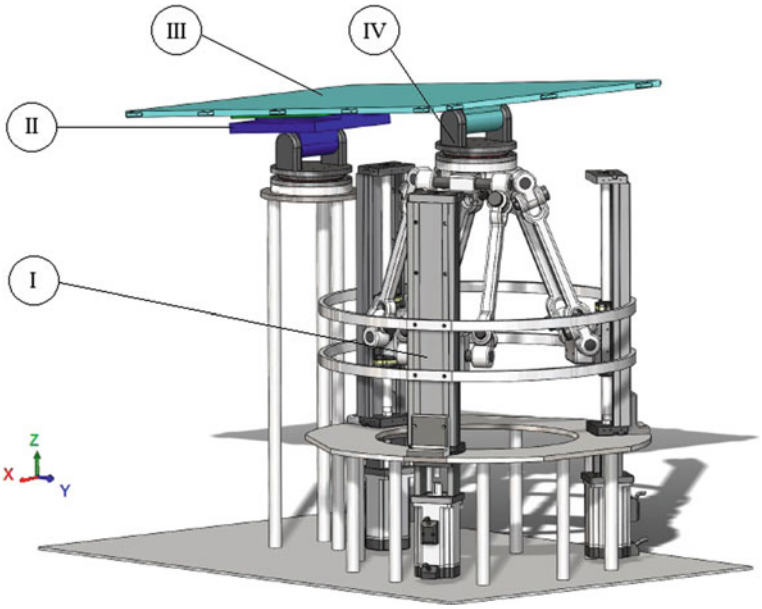

Fig. 1 3D model of the system

Fig. 2 Delta transmission

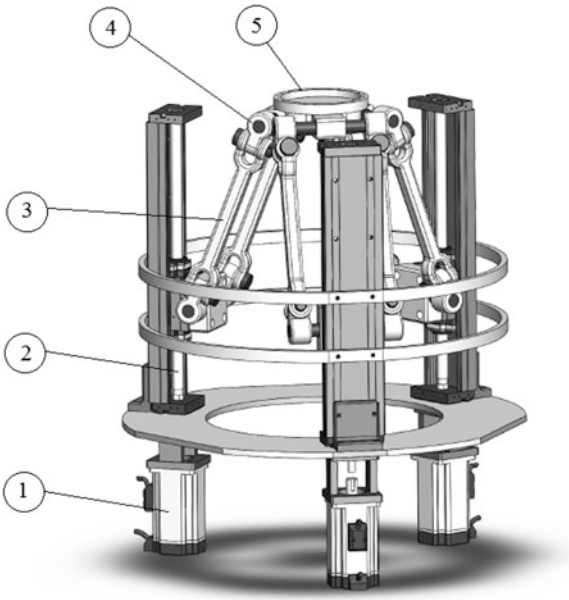

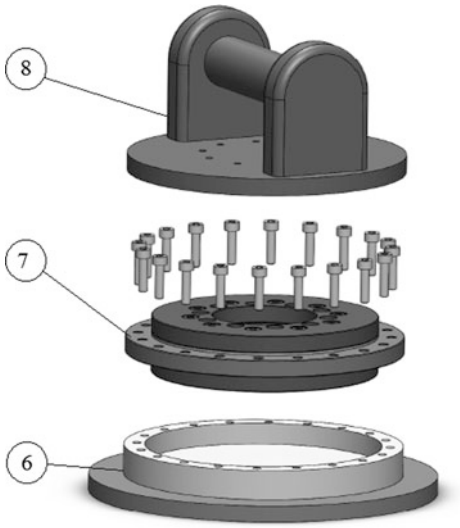

Fig. 3 Rotating support

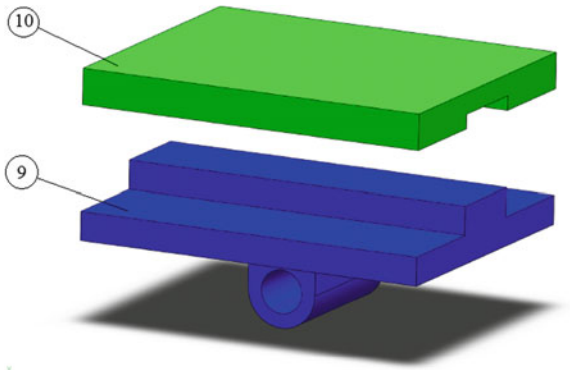

Fig. 4 Sliding support

Fig. 5 Holding plate

Sliding support components is used in the moving platform (5). When the moving platform make a translational movement in the Y axis, the sliding plate (10) connected to the holding plate (11) will slip on the sliding sole (9).

2.2 Stress Simulation

After the design was completed, to test the load applied on the system as well as its safety before manufacturing, a stress analysis was conducted using the Simulation add on in SOLIPWORKS software. The force applied to the system presents the largest mass that can be put on the system (300 kg). Materials that were selected for the system is AISI 1045 Steel, with the limit stress of 5.3e+008 (N/m^2). For every positions that the holding plate oscillates (along xyz axes), the following results were obtained (Figs. 6, 7, 8 and 9):

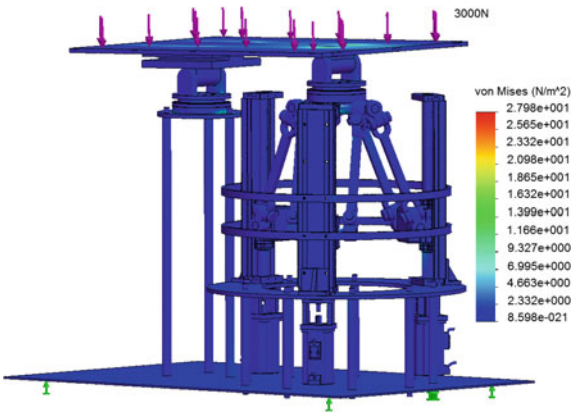

Fig. 6 Stress in initial state

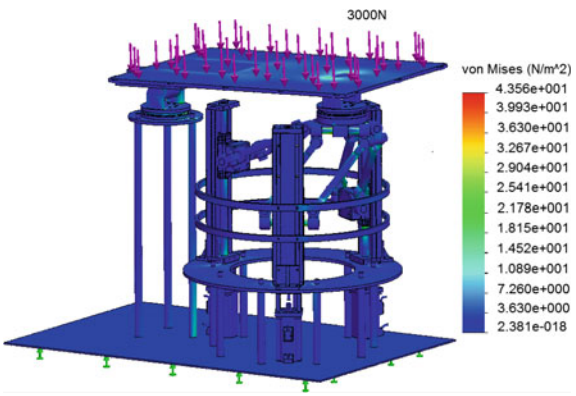

Fig. 7 Stress in forward state

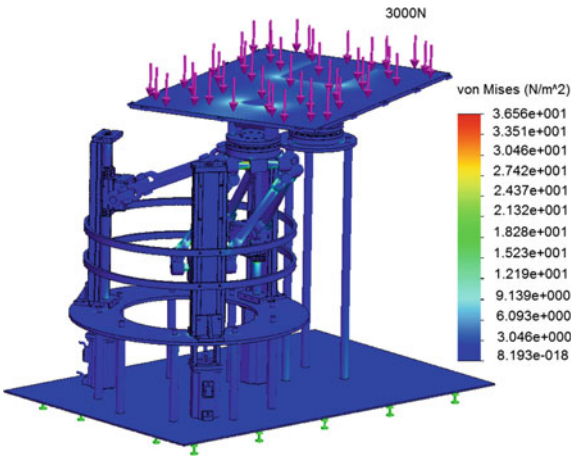

Fig. 8 Stress in right state

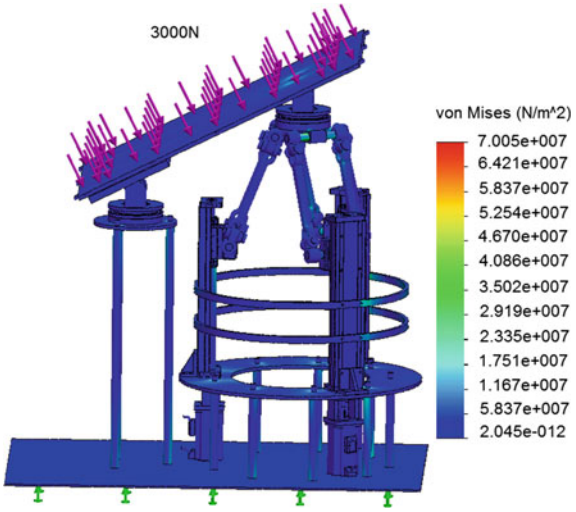

Fig. 9 Stress in up state

With those stress analysis results corresponding to the positions above, the stress when the system oscillates vertically in Z direction at "up" state has the maximum value of 7.005e+007 (N/m^2). Lowest safety factor is calculated using the following formula:

$$\text{MinFOS} = \frac{\sigma_y}{\sigma_w} = \frac{5.3 \times 10^8}{7.005 \times 10^7} = 7.5$$

The calculated safety factor value is reasonable, proving that the design model has fully capable of withstanding forces of cargoes during oscillation.

3 Kinematic Analysis of Delta Structure

3.1 Overview of Delta Structure

Delta Robot is one of the structures developed within the framework of parallel robot based on linear actuators. This configuration features high stiffness in the vertical axis due to the symmetric design of 3 linear actuators. These will transmit motion to the moving platform in its workplace.

In this paper, the actuator that was used is MCM10030H10K00 NSK. With the stroke length of each device is 330 mm and the load capacity is 3380 N, ensuring that the requirements of the subject are met. The motors used in this research is the MSMD08 (750 W) Panasonic motors (Fig. 10).

3.2 Kinematic Analysis

To control the Delta structure to move in an orbit and to make the whole system work, an analysis in inverse kinematic is needed.

The input of inverse kinematics equations is the coordinates of the points in the orbit that we want to keep the moving platform in and the output of the equations will be the transition of three linear actuators (Di mm). Analyzing Fig. 11, the point that we need to control to move in orbit is O′ which is attached to the center of the moving platform. Point O' is in O′-x′-y′-z′ coordinate which is relative to the original coordinate system O-x-y-z located at the center of the Delta structure support. To find the relation of these coordinates, the author used the 3D vector method.

We have:

$$OA = OB = OC = R = 207\,\text{mm}$$

$$O'P_1 = O'P_2 = O'P_3 = r = 77.5\,\text{mm}$$

$$G_1P_1 = G_2P_2 = G_3P_3 = L = 348\,\text{mm}$$

Fig. 10 3D model of linear actuator

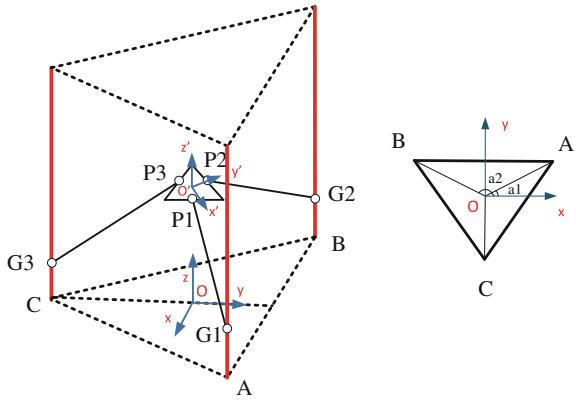

Fig. 11 Delta structure's configuration

The moving distance of three linear motors for each corresponding positions of O′ are: D_1, D_2 and D_3 respectively.

Angle a_i indicates the angle between X axis and OA, OB, OC:

$$a_i = (i-1) \times \left(\frac{2\pi}{3}\right) \text{ with } i = 1, 2, 3 \tag{1}$$

The length L of each link is calculated by vector magnitude formula:

$$L_i = |P_i - G_i| \Rightarrow L^2 = (x - x_i)^2 + (y - y_i)^2 + (z - z_i)^2 \tag{2}$$

In this formula:
x, y, z: the coordinates of point O' in the original coordinate O-x-y-z
with i = 1, 2, 3

$$x_i = (R - r) \cdot \cos(a_i);\ y_i = (R - r) \cdot \sin(a_i);\ z_i = D_i \tag{3}$$

Result of inverse kinematic problem for the Delta structure with the linear actuator system is shown in Fig. 11. It is obtained as follow:

$$D_i = z \pm \sqrt{L^2 - (x - x_i)^2 - (y - y_i)^2} \text{ with } i = 1, 2, 3 \tag{4}$$

4 Simulation

4.1 Simulation with Simulink

The forward kinematic model will be evaluated using MATLAB simulation. The obtained result is a graph of the moving platform's center of the Delta structure in

the desired orbit (with a distance of 300 mm in three xyz axes). Base on that, it will give a clear insight on the kinematic behavior of the Delta structure.

At the start of the simulation process, because all the movements of the system depend on the Delta structure, only the position control process of the delta structure was simulated. The research has built a model of a Delta structure using SolidWorks 3D design software. Simulink function was used to import the robotic arm model to the Simulink environment (Figs. 12 and 13).

After putting the structure in the simulation environment, we built linear control blocks, central control block and applied kinematic equations to test if the desired orbit's parameters was correct in order to reduce errors in the actual control of the system.

4.2 Simulation Results

To make sure that the target will move in the desired orbit with a moving distance of 300 mm in each axis, a desired orbit was created, from the starting point (0, 0, 323)

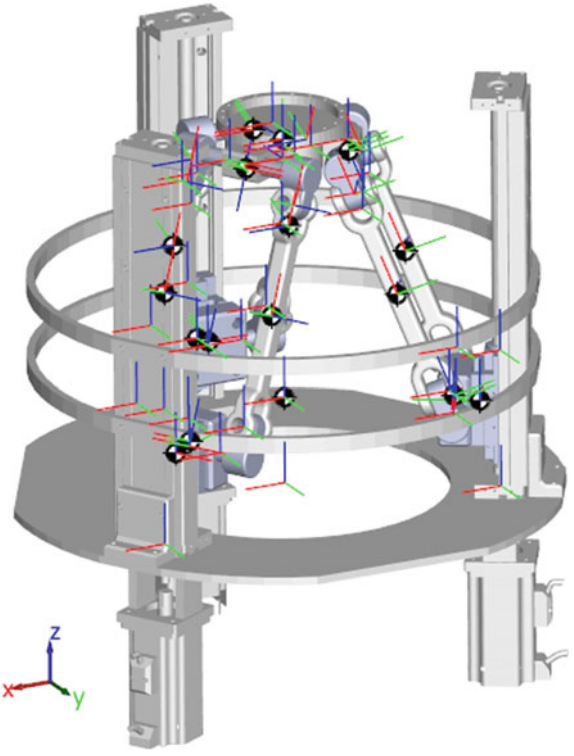

Fig. 12 Delta in Simulink environment

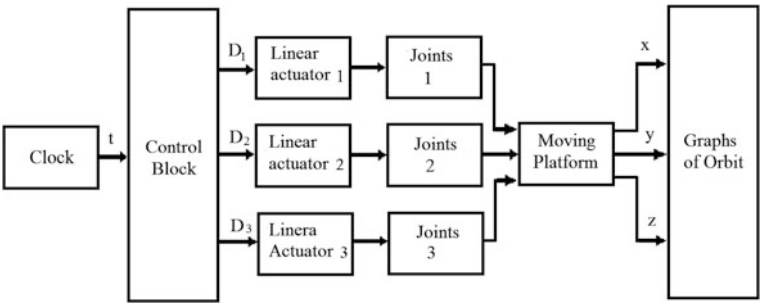

Fig. 13 Flowchart of control system in Simulink environment

when the linear actuators is in its original position, the moving platform moved along the z-axis to the point with coordinate (0, 0, 450). After that, the moving platform moves in the y-axis to coordinate (0, 180, 450) and then moves straight backwards 300 mm to coordinate (0, −120, 450). Similar for the x-axis, the moving platform will move in a straight orbit with the length of 300 mm. The obtain result is the orbit of the moving platform's center (Figs. 14, 15, 16 and 17).

The results matches with the desired trajectory. It demonstrated that the kinematic equations were calculated properly and had the ability to apply to the actual control of the system.

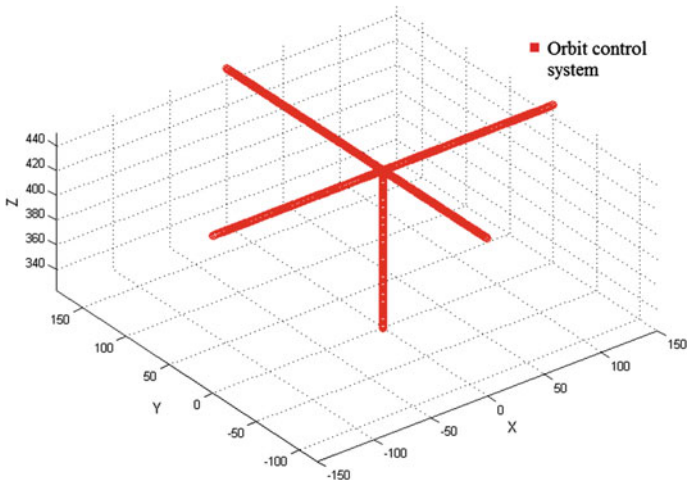

Fig. 14 Orbit of Delta structure is controlled in Simulink environment

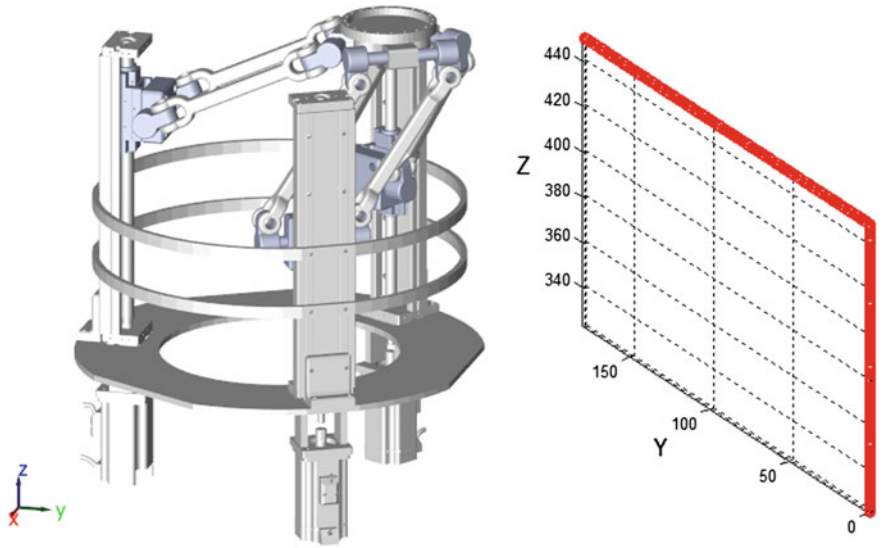

Fig. 15 The moving platform at coordinate (0, 180, 450)

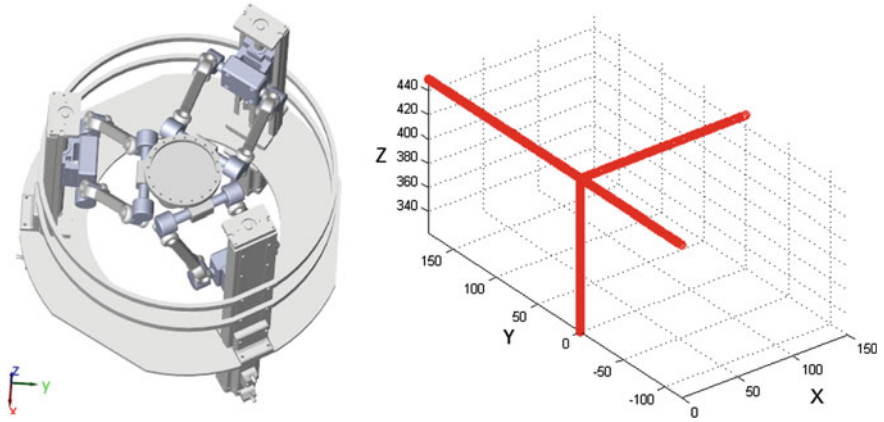

Fig. 16 The moving platform at coordinate (150, 0, 450)

5 Experimental Model

5.1 Control System

The control system was designed to control three linear motors. This research built a program in the computer via Visual Studio 2010 Software. The desired orbit and kinematics equations are inputted to the program, then, the program will use those

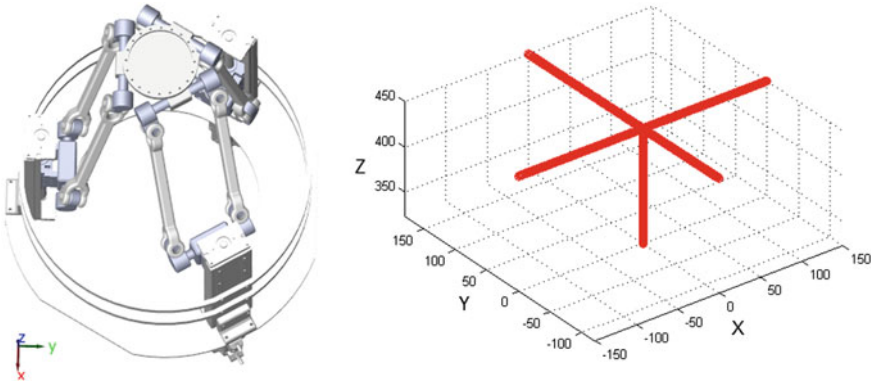

Fig. 17 The moving platform at coordinate (−150, 0, 450)

to calculate kinematics equations to get the output that is used to control the three linear motors. The microcontroller used in the system is the STM32F407VG microcontroller, it receives the analyzed signal from the computer via the RS-232 standard. After receiving the signal, the MCU will generate control pulse to control the motors as desired (Fig. 18).

Figure 19 show the control experiments.

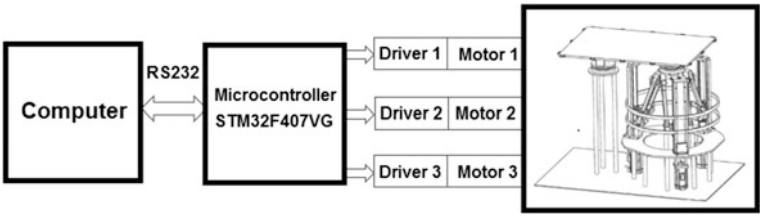

Fig. 18 Control system

Fig. 19 Control experiments

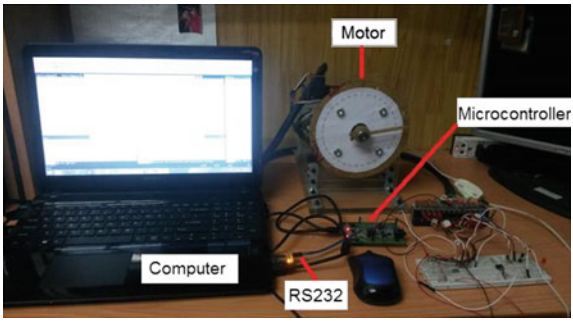

5.2 Manufacturing and Experimental Model

After designing and simulating, the experimental model was built and installed with the control system. Initially, the experimental model operated in accordance with the fluctuation around the x-y-z-axis as required. With the 300 kg containers' mass, the system still had all around good responses (Figs. 20 and 21).

The research used the motion simulation of the containers to inspect the durability of strappings used for secured cargoes. The purpose of this experiment is to choose the suitable strapping materials that can handle the fluctuation of the

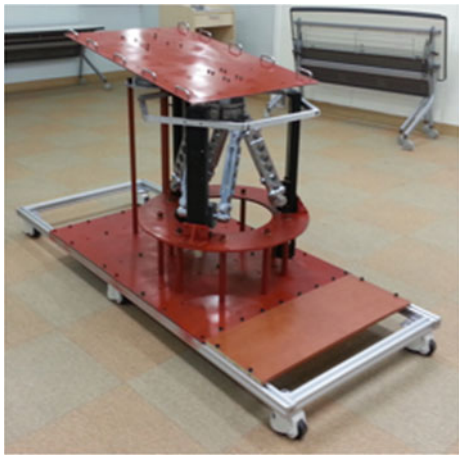

Fig. 20 Actual model

Fig. 21 Inspect the tension of strapping

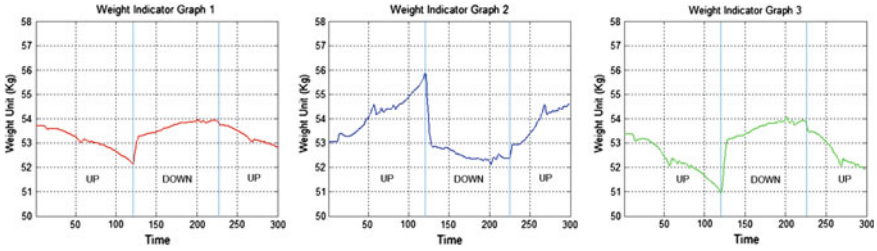

Fig. 22 Tension result of strapping

container, prevent the cargoes from breaking due to poor strapping quality. Figure 21 shows the tension testing experiments which was carried out in three strappings made from fabric. In these experiments, the container's load is 50 kg, the motor speed is 100 rpm and the system is controlled to fluctuate around z-axis. Figure 22 displays tension of three different strappings; UP for lifting status and DOWN for the reverse.

From the chart, we can see that when the system switches from UP to DOWN status, the maximum tension of the middle strapping is approximately 56 kg, while the third strapping has a minimum of 51 kg. From these results, the strappings will be analyzed and tested to choose suitable materials before using them on the cargoes in the containers.

6 Conclusion

A motion simulation system of cargoes in containers was designed, manufactured and controlled successfully in this research. The simulation results about load capacity and motion analysis using kinematics equations are accurate. The results have also been tested using the experimental model carefully. This system helps with cargoes' safety, contributes to the increase in productivity and quality in cargo transportation.

References

1. Yang X, Feng Z, Liu C, Ren X (2014) A geometric method for kinematics of delta robot and its path tracking control. In: Proceedings of the international conference on control, automation and system (ICCAS 2014)
2. Lou Y, Zhang Y, Huang R, Chen X, Li Z (2014) Optimization algorithms for kinematically optimal design of parallel manipulators. IEEE Trans Auto Sci Eng
3. Castaneda LA, Luviano-Juarez A, Chairez I (2015) Robust trajectory tracking of a delta robot through adaptive active disturbance rejection control. IEEE Trans Control Syst Technol 23(4)

Design and Control Humanoid Hand to Implement Hand Shaking Task Applied for Service Robot

Tri Dung Nguyen, Tan Tien Nguyen and Thien Phuc Tran

Abstract The problem of design and control Humanoid is now interested in the world. Humanoid is a complex entity, this object contain many of issues needed to solve. This paper focuses on research in hand shaking task applied for service robot. Solution of using wires of mechanical structure is used, the simulation and experiment results will prove the feasibility of proposed solution.

Keywords Humanoid · Hand shaking task · Service robot

1 Overview

1.1 Introduction to Humanoid Robot

A humanoid robot is a robot that has a human-like shape, the features of humanoid robots can be summarized as follows [1]: (1) Humanoid robots can work in the environment for humans as it is. (2) Humanoid robots can use tools for humans as it is. (3) Humanoid robots has a human-like shape. Like a human, humanoid robot contain many parts: head, body, upper and lower limb. This paper focuses on the

T.D. Nguyen (✉) · T.T. Nguyen
Department of Mechatronics, Faculty of Mechanical Engineering, HCM University of Technology, 268 Ly Thuong Kiet, District 10, Ho Chi Minh City, Vietnam
e-mail: nguyentridung_92@yahoo.com.vn

T.T. Nguyen
e-mail: nntien@hcmut.edu.vn

T.P. Tran
Department of Machine Design, Faculty of Mechanical Engineering, HCM University of Technology, 268 Ly Thuong Kiet, District 10, Ho Chi Minh City, Vietnam
e-mail: ttphuc.rectie@hcmut.edu.vn

V.H. Duy et al. (eds.), *AETA 2015: Recent Advances in Electrical Engineering and Related Sciences*, Lecture Notes in Electrical Engineering 371,
DOI 10.1007/978-3-319-27247-4_62

hand shaking task of service robot, so that the hand with wrist is researched and developed with following objectives: (1) Realization hand shaking task. (2) Having a human-like shape.

2 Structure Characteristics of Human Hand

Human hand is constituted by bones, bones are connected together through ligaments at joint, movement of each joint is caused by the contraction of muscles, tendon attach a muscle to a bone. *Joint*: All the bones on a hand are connected through revolute joints or fixed joint. There are only three types of joint: condyloid joint, hinge joint and saddle joint. In which, condyloid joint and saddle joint has 2 DOFs each, hinge joint has 1 DOF only. These joints and their equivalents as follow (Fig. 1):

Bone: The bone's length on the hand (measure at the center of rotation of the joints) comply with Fibonacci factor [2].

From these analyzes, we can replace the biological joints with mechanical joints.

2.1 Existing Robot Hand

Over the last decades, several multi-fingered dexterous robotic hands have been developed. The Center for Engineering Design at the University of Utah, and the Artificial Intelligence Laboratory at the Massachusetts Institute of Technology researched and developed UTAH/M.I.T. Dextrous Hand model with four fingers [3]. Nasa designed Robonaut hand model [4]. This model are being used in Robonaut 2 which can be able to do a select set of astronaut tasks. Robonaut hand is a human sized five-fingered, the hand itself has 12 DOF and two additional DOF in the wrist. It is logically divided into three groups: Grasping fingers (ring and little finger), Dexterous fingers (index and middle finger) and Thumb, fingers in each groups has the same structure. Custom Entertainment Solutions developed the MechaTE hand with five fingers, number of joint on the hand is completely like human hand. However, joints are coupled and actuator is transmitted in one direction only.

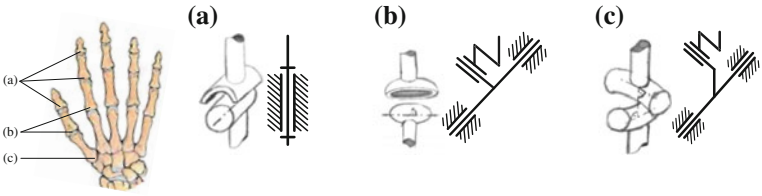

Fig. 1 Three types of hand joint. **a** Hinge joint, **b** condyloid joint, **c** saddle joint

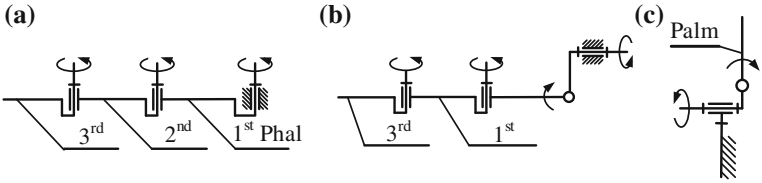

Fig. 2 Principle diagram of finger, thumb and wrist. **a** Finger principle diagram, **b** thumb principle diagram, **c** robot wrist principle diagram

Table 1 Dimensions used to design

	Thumb	Index	Middle	Ring	Little
1st phalanges	37	45	50	47.5	37.5
2nd phalanges	–	28	31	29.5	23
3rd phalanges	23	17	19	18	14.5
Total length (mm)	60	90	100	95	75

3 Mechanical Design

When take the hand shaking task, all fingers (except thumb) always nearly side by side, so that adduction and abduction movement of the Metacarpophalangeal joint isn't necessary. To guarantee human-like shape, we propose a finger structure with three joints. Thumb with 4 DOFs is designed, adduction and abduction movement Metacarpophalangeal joint are skipped. Dimensions are based on human hand sizes (Table 1).

Based on human wrist, proposing 2 DOFs principle diagram for robot wrist as Fig. 4. Assembling parts together, we have overall principle diagram of robot hand (Figs. 2 and 3).

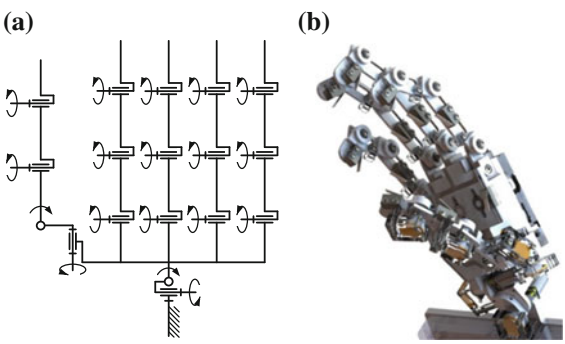

Fig. 3 Principle diagram of robot hand. **a** Robot hand principle diagram, **b** 3D model of robot hand

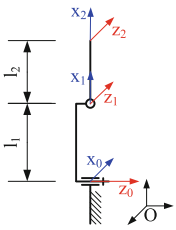

	a	α	d	θ
1	l_1	$\frac{\pi}{2}$	0	θ_1
2	l_2	0	0	θ_2

$$ {}^0T_1 = \begin{bmatrix} cos(\theta_1) & 0 & sin(\theta_1) & l_1 cos(\theta_1) \\ sin(\theta_1) & 0 & -cos(\theta_1) & l_1 sin(\theta_1) \\ 0 & 1 & 0 & 0 \\ 0 & 0 & 0 & 1 \end{bmatrix} $$

$$ {}^1T_2 = \begin{bmatrix} cos(\theta_2) & -sin(\theta_2) & 0 & l_2 cos(\theta_2) \\ sin(\theta_2) & cos(\theta_2) & 0 & l_2 sin(\theta_2) \\ 0 & 0 & 1 & 0 \\ 0 & 0 & 0 & 1 \end{bmatrix} $$

$$ {}^0T_2 = {}^0T_1 \, {}^1T_2 $$

Fig. 4 Wrist's modeling

4 System Modeling

4.1 Wrist $(-30° \leq \theta_1 \leq 30°, -45° \leq \theta_2 \leq 45°)$

Wrist is a first component of this system, it has a significant to regulate the direction of the palm. Position of the second coordinate origin in zero coordinate: ${}^0X_2 = l_1 \cos(\theta_1) + l_2 \cos(\theta_1)\cos(\theta_2), {}^0Y_2 = l_1 \sin(\theta_1) + l_2 \cos(\theta_2)\sin(\theta_1), {}^0Z_2 = l_2 \sin(\theta_2)$

Then, we can find the rotation angles to reach the expected position:

$$ \theta_1 = \arcsin\left({}^0Y_2/(l_1 + l_2\cos(\theta_2))\right) \textit{ and } \theta_2 = \arcsin\left({}^0Z_2/l_2\right) \tag{1} $$

4.2 Thumb

Thumb has rotation under all three axes, it's responsible for increasing the clamping force to support for grasping something. Position of thumb's fingertip can be specified as follow: $c_x = \cos(\theta_x), s_x = \sin(\theta_x)$

$$ \begin{cases} {}^2X = a_{23} + l_{45}s_4 + l_{56}c_5s_4 + l_{67}c_5c_6s_4 - l_{67}s_4s_5s_6 \\ {}^2Y = l_{67}c_6(c_3s_5 - c_4c_5s_3) + l_{67}s_6(c_3c_5 + c_4s_3s_5) \\ \qquad l_{34}s_3 - l_{45}c_4s_3 + l_{56}(c_3s_5 - c_4c_5s_3) \\ {}^2Z = l_{67}c_6(s_3s_5 + c_3c_4c_5) + l_{67}s_6(c_5s_3 - c_3c_4s_5) \\ \qquad l_{23} - l_{34}c_3 + l_{45}c_3c_4 + l_{56}s_3s_5 + l_{56}c_3c_4c_5 \end{cases} \tag{2} $$

In the mission to take the hand shaking task, thumb has a supporting role and don't need to take the movement to the desired position.

4.3 Other Fingers

These fingers have a significant role to perform the function of hand. All of them can be modelled with the same solution. So, we analyze the index finger as a typical.

$$
{}^2T_6 = {}^2T_3\,{}^3T_4\,{}^4T_5\,{}^5T_6 \Rightarrow \begin{cases} {}^2X = l_{34}\cos(\theta_3) + l_{45}\cos(\theta_3+\theta_4) \\ \qquad + l_{23} + l_{56}\cos(\theta_3+\theta_4+\theta_5) \\ {}^2Y = l_{34}\sin(\theta_3) + l_{45}\sin(\theta_3+\theta_4) \\ \qquad + l_{56}\sin(\theta_3+\theta_4+\theta_5) \\ {}^2Z = a_{23} \end{cases} \tag{3}
$$

is the fingertip's position corresponding to rotation angles θ (Fig. 5).

Solve these equations and define $A = {}^2X - l_{23} - l_{56}\cos(\varphi), B = {}^2Y - l_{56}\sin(\varphi), C = A^2 + B^2$ we can find θ values to reach the predefined position

$$
\begin{cases} \theta_4 = 2\arctan 2\left(\sqrt{\left((l_{34}+l_{45})^2 - C\right)/\left(C - (l_{34}-l_{45})^2\right)}\right) \\ \theta_3 = \arctan 2(B/A) - \arctan 2(l_{45}\sin(\theta_4)/l_{34} + l_{45}\cos(\theta_4)) \\ \theta_5 = \varphi - \theta_3 - \theta_4, \theta_i \in [0°, 90°] \end{cases} \tag{4}
$$

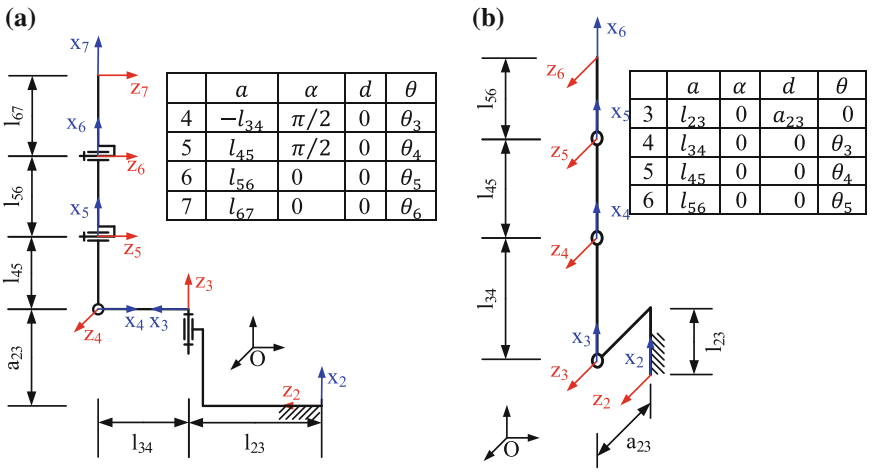

	a	α	d	θ
4	$-l_{34}$	$\pi/2$	0	θ_3
5	l_{45}	$\pi/2$	0	θ_4
6	l_{56}	0	0	θ_5
7	l_{67}	0	0	θ_6

	a	α	d	θ
3	l_{23}	0	a_{23}	0
4	l_{34}	0	0	θ_3
5	l_{45}	0	0	θ_4
6	l_{56}	0	0	θ_5

Fig. 5 Thumb and index finger's modeling. **a** Thumb modeling, **b** index finger modeling

4.4 Cooperating Movement

This section concentrate to propose a solution to move all fingertips to target points. From the result in previous section, we notice that all rotation angles can be found if the second coordinate origin $\begin{bmatrix} {}^2X & {}^2Y & {}^2Z \end{bmatrix}^T$ is defined

$$\begin{bmatrix} {}^2X & {}^2Y & {}^2Z & 1 \end{bmatrix}^T = {}^0T_2^{-1} \begin{bmatrix} {}^0X & {}^0Y & {}^0Z & 1 \end{bmatrix}^T \tag{5}$$

In which $\begin{bmatrix} {}^0X & {}^0Y & {}^0Z & 1 \end{bmatrix}^T$ is destination point, $\begin{bmatrix} {}^0X_2 & {}^0Y_2 & {}^0Z_2 & 1 \end{bmatrix}^T$ is wrist position. All of them are identified in zero coordinate, ${}^0T_2$ is specified as (3). Then using (18) ${}^2Z = a_{23} \Rightarrow {}^0X \sin(\theta_1) - {}^0Y \cos(\theta_1) = a_{23}$

$$\theta_1 = \arcsin\left(a_{23}/\sqrt{{}^0X^2 + {}^0Y^2}\right) + \arcsin\left({}^0Y/\sqrt{{}^0X^2 + {}^0Y^2}\right) \tag{6}$$

If desired position $\begin{bmatrix} {}^2X & {}^2Y & {}^2Z \end{bmatrix}^T$ is in the workspace of the corresponding finger, at least one θ_2 value will be found. Appendix D [19] present the Matlab function calculating the θ_2 value. Then, using (4), we completely determine $\theta_3, \theta_4, \theta_5$ values.

***Condition for all fingertip to reach the desired position**

Since the adduction and abduction movement are denied, fingertips can reach the predefine position only if these positions are content with relationship equation. Objectives of this section is using the result of kinematic analyzing to find this equation.

Using the result of kinematic analyzing: ${}^0X \sin(\theta_1) - {}^0Y \cos(\theta_1) = a_{23}$.

Define $({}^0X_t, {}^0Y_t, {}^0Z_t)$, $({}^0X_g, {}^0Y_g, {}^0Z_g)$, $({}^0X_r, {}^0Y_r, {}^0Z_r)$ and $({}^0X_u, {}^0Y_u, {}^0Z_u)$ corresponding to destination position of index, middle, ring and little finger. Define a_{23t}, a_{23g}, a_{23r}, a_{23u} corresponding to a_{23} value of index, middle, ring and little finger.

$a_{23g} = 0$ (Table 2), inferred that: $\tan(\theta_1) = {}^0Y_g/{}^0X_g$, and:

Table 2 Desired position of fingers

Finger	${}^0X$	${}^0Y$	${}^0Z$	φ
Index	–	100	70	$2\pi/3$
Middle	0	100	70	$3\pi/4$
Ring	–	100	70	$2\pi/3$
Little	–	80	50	$3\pi/4$
Finger	${}^0X$	${}^0Y$	${}^0Z$	φ

$$\begin{cases} {}^0X_t = a_{23t}\sqrt{1+\left({}^0X_g/{}^0Y_g\right)^2} + {}^0Y_t{}^0X_g/{}^0Y_g \\ {}^0X_r = a_{23r}\sqrt{1+\left({}^0X_g/{}^0Y_g\right)^2} + {}^0Y_r{}^0X_g/{}^0Y_g \\ {}^0X_u = a_{23u}\sqrt{1+\left({}^0X_g/{}^0Y_g\right)^2} + {}^0Y_u{}^0X_g/{}^0Y_g \end{cases} \quad (7)$$

Equation (7) are the relationship equations that we need to find.

5 Control Law Design

The major function of control law is ensuring the rotation angle of joint to reach the desired angle. To ensure that, we modeling the movement of joint by the impact of the wire, thence find the relationship between rotation angle of joints with wires's length.

5.1 *Modeling of One Joint*

To use this scheme, we assume that (Fig. 6):

- $\theta = 0$ is origin position where the deformation angle of the torsion spring is φ_0 and the moment at joint is $M_0 = k\varphi_0$, in which k is the spring stiffness.
- Within the range of forces, links are absolutely rigid.
- $\vec{F}$ is caused by actuator, in which $F = M/R$, M is moment of actuator and R is radius's wheel.
- Each joint is pulled by only one wire and the displacement of joint is caused by the force on this wire only.
- At equilibrium position, the pull force is equal to moment of torsion spring:

$$F \cdot OE = k\theta + M_0 \quad (8)$$

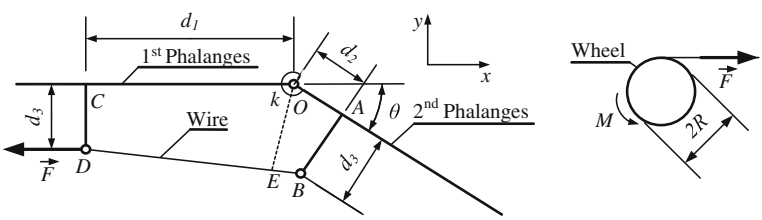

Fig. 6 Scheme for modeling of one joint

In which, OE is lever arm of pull force F.

By set the coordinate system at joint, we can find the moment arm OE, and the wire's length corresponding to rotation θ of joint is: $L(\theta) = L_0 + BD(\theta)$.

L_0: Total constant lengths, $BD(\theta)$: Length of BD corresponding to θ.

$$BD(\theta) = \sqrt{\begin{matrix} d_1^2 + 2d_3^2 + 2d_1 d_2 \cos(\theta) - 2d_1 d_3 \sin(\theta) \\ + d_2^2 - 2d_2 d_3 \sin(\theta) - 2d_3^2 \cos(\theta) \end{matrix}} \tag{9}$$

We define the BD_0 corresponding to origin position is the biggest value of wire's length. So that, the variation of wire's length shown as follow:

$$\Delta L = BD_0 - BD(\theta) = d_1 + d_2 - BD(\theta) \tag{10}$$

5.2 Modelling of One Finger

We define L_1, L_2, L_3 are the length's wire corresponding to 1st joint, 2nd joint and 3rd joint. We assume that the wire isn't stretched, the variations of wire's: $\Delta L_1 = \Delta D_1 D_2 + \Delta L_w, \Delta L_2 = \Delta D_1 D_2 + \Delta D_2 D_3 + \Delta L_w, \Delta L_3 = \Delta D_1 D_2 + \Delta D_2 D_3 + \Delta D_3 D_4 + \Delta L_w$. These expressions show that the wire's length is not only depended on the rotation angle of the corresponding joint but also depended on all other joints before it (Fig. 7).

Using the result in Sect. 4.1, we completely determine the values $D_1 D_2(\theta_3), D_2 D_3(\theta_4), D_3 D_4(\theta_5)$.

ΔL_w is the variation of wire's length at wrist, we can see: $\Delta L_w = \Delta AB$. Set coordinate system as show in Fig. 8, positions of point A and B can calculate as Fig. 8.

The distance between A and B is determined:

$$^0AB(\theta_1, \theta_2) = \sqrt{^0AB_x^2 + {}^0AB_y^2 + {}^0AB_z^2} \tag{11}$$

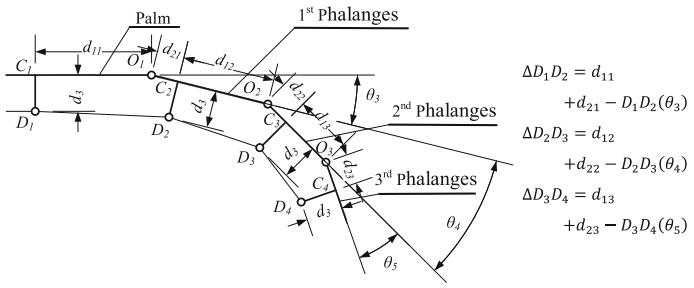

Fig. 7 Scheme for modeling of one finger

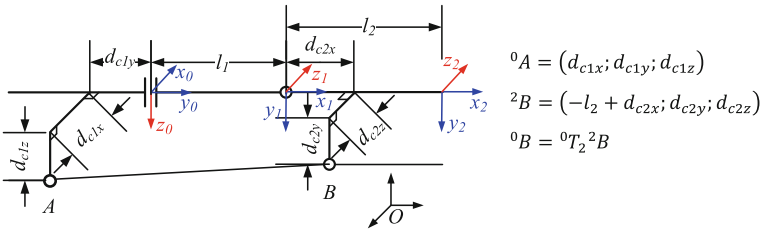

Fig. 8 Scheme for modeling of wrist

Moreover, the variation of wire's length at wrist is:

$$\Delta AB = {}^0AB_{max} - {}^0AB(\theta_1, \theta_2) \tag{12}$$

In which ${}^0AB_{max}$ correspond to $\theta_1 = \pi/4$, $\theta_2 = \pi/6$

6 Hand Shaking Task Analyzing

- Analyzing main stages in hand shaking movement.
- Determining rotation angle's value of joints in each stages.
- Converting the biology joints angles to mechanical joints angles (Fig. 9).

To measure the joints angles of human hand, we use potentiometer. Fixing sensors on the hand, each joint is connected with one sensor and we need total 18 potentiometer for all. Performing hand shaking task with the real hand, recording the values receiving from sensors, we have the datasets for this movement.

From the above chart, we can see the hand shaking task is divided into four stages (Figs. 10 and 11).

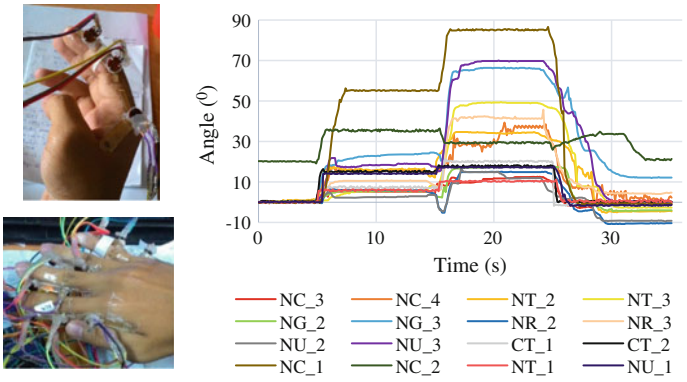

Fig. 9 Rotation angles of real hand

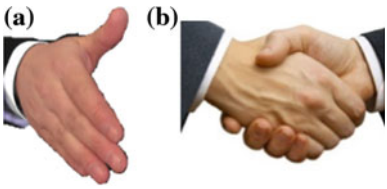

Fig. 10 Hand shaking task of human hand. **a** Human hand is ready for hand shaking task. **b** Human hand in hand shaking task

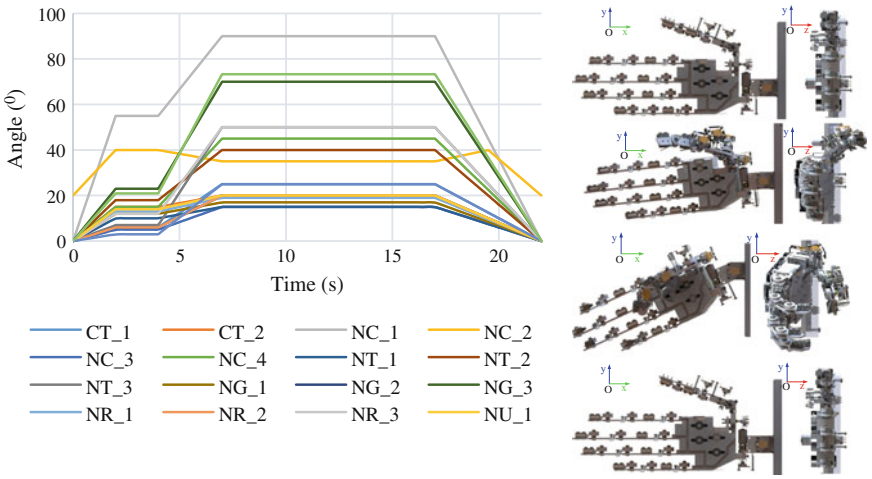

Fig. 11 Rotation angle converted to robot

7 Simulation and Experiment Results

The simulation is made to check the inverse kinematic analyzing result. Simulation process is supported by Simmechanics Environment and the output result is a 3D animation and the value of fingertips position. To check easily, we choose the same desired position for index, middle and ring finger, and the little finger must be different. Checking the simulation result, all fingertips reach the desired position

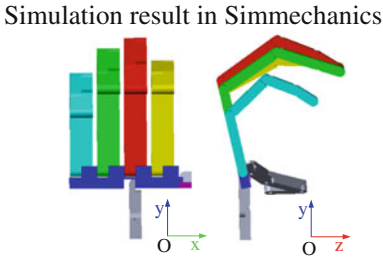

Fig. 12 Inverse kinematic simulation

Fig. 13 Result of realization hand shaking task

and direction, this result verify the correctness of the inverse kinematic analyzing result (Fig. 12).

The main purpose of making experiment is checking feasibility of the control law, here, it is the compensation wire's length law in Sect. 4. The right law must be guarantee the position of one joint while other joints are changed. Firstly, set the second joint rotation angle: $\theta_4 = 45°, \theta_5 = 0°, \theta_3 = 0°$, check the respond. Then, change the value of first joint: $\theta_3 = 45°$, check the respond. We can see the position of second joint is guarantee although the first joint are changed, the control law is verified (Fig. 13).

8 Conclusion

The humanoid hand model is designed, it can take two basic functions: moving the fingertips to desired position and taking the active hand shaking task. To do that, the control law that is the compensation wire's length law is designed. Through simulation and experiment process, the inverse kinematic analyzing result and the control law proposed are suitable. The next research of this paper is fabrication 3D robot hand model, using the experiment results as the basis to improve design.

References

1. Kajita S et al Introduction to humanoid robotics, p 1
2. Park AE et al The Fibonacci sequence—relationship to the human hand, p 160
3. Siciliano B et al Approaching human performance, p 12–32
4. Ambrose RO et al Robonaut: NASA's space humanoid, p 58
5. Floyd RT, EdD, ATC, CSCS Manual of structural, Chap 7: The wrist and hand joints
6. Agur AMR et al Grant's Atlas of anatomy, 10th edn. Lippincott Williams and Wilkins
7. Morecki A et al Cybernetic systems of limb movements in man, animals, and robots. Polish Scientific Publishers, Warsaw, Ellis Horwood Limited Publishers, Chinchester, p 198
8. Hirth J et al Designing arms and hands for the humanoid robot ROMAN, p 3
9. Institute of Robotics and Mechatronics, RMC, DLR German aerospace center—design of the DLR hand arm system, p 15

10. Mouri T et al Anthropomorphic robot hand: Gifu Hand III, p 1288
11. Kajita S et al Introduction to humanoid robotics
12. Cobos S et al Simplified human hand models for manipulation tasks
13. Kawabuchi Mechanical Engineering Laboratory, Inc—A designing of humanoid robot hands in endo skeleton and exoskeleton styles, p 3
14. Oommen A et al A study of the correlation between hand length and foot length in humans, p 56
15. Adewusi S et al Modal parameters of the human hand-arm using finite element and operational modal analysis, p 4
16. Jacobsen SC et al (1984) UTAH/MIT dextrous hand-work in progress. Int J Robot Res 3 (4):21–50
17. Lotti F et al Development of UB hand 3: early results, p 3

Study on an Automatic Solution for Container Transporting at Tan Thuan Port

Minh Doan Vu Hoang, Tan Tung Phan and Tan Tien Nguyen

Abstract The demand for container transporting at Tan Thuan Port raises a problem for automated container transportation from seaside to container yard and vice versa. This paper proposes an automated solution based on the port's available surface using AGV. AGV model includes two coordinated ones, each AGV has two active wheel and two self-aligning wheel. Mathematical model of the system is established, then design the tracking line controller for AGV. Simulation and experiment in laboratories demonstrate the effectiveness of proposed solution.

Keywords AGV · Container · Line tracking

1 Introduction

Nowadays, maritime transportation plays a major role in transporting goods with approximately 80 % of imported ones are transported by sea route. Because the world's terrain is surrounded by oceans, the maritime transportation workspace is extremely wide. Moreover a large load capacity and low cost make maritime transport became a business potential was exploited by many countries.

In the end of the twentieth century, the world has adopted a special transport tool, called containers, on freight. Container not only change themselves transport industry but also transformed other economic sectors in need freighter. Method of carrying goods by container shortens transport time, ensures the safety of objects

M.D.V. Hoang (✉) · T.T. Phan · T.T. Nguyen
The Faculty of Mechanical Engineering, HCM City University of Technology,
268 Ly Thuong Kiet Street District 10, Ho Chi Minh City, Vietnam
e-mail: doanvuhoangminh@gmail.com

T.T. Phan
e-mail: pttung@hcmut.edu.vn

T.T. Nguyen
e-mail: nttien@hcmut.edu.vn

V.H. Duy et al. (eds.), *AETA 2015: Recent Advances in Electrical Engineering and Related Sciences*, Lecture Notes in Electrical Engineering 371,
DOI 10.1007/978-3-319-27247-4_63

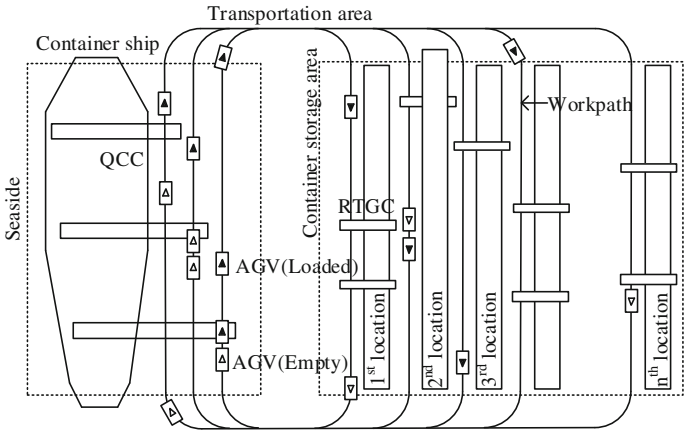

Fig. 1 Model of container port using AGVs [1]

transported and reduces costs to the lowest level. This creates a difference between the transport container transportation by wrapping conventional crude.

The problem that the container transportation industry is facing today is the problem of excess capacity is continuing, and the congestion at the ports remained unresolved. Also, a great reason causing problems is that the management of container storage and goods have not been effective. Most of the processing at the port depends on people and this makes slow response speed, large operating costs. The container terminal is aiming to automate parts of the load/unload processing. Basic architecture of a container terminal includes seaside, storage yard, and landside.

The transportation of containers between the three areas of a container port depends mainly on trucks and container tractors. Speed of container handling in ports is closely related to the arrangement of lanes in port as well as the ability of the driver of trucks and tractors. Accidents between vehicles and other means container occur frequently, causing significant damage to ports. To control this and toward an unused manpower seaside and storage yard, the biggest ports in the world currently has and is continuing to study and use AGVs. For a purpose of automation in container transportation and will automate the entire container terminal in the future (Fig. 1).

Currently in the world, AGV models for port automation problem was boom. Forefront of this industry is Terex Corporation with nearly 30 years of research and development. Some of the highlights of Terex Corporation: Battery AGV [2] reduces to 45 % energy consumption compared with using diesel engines [3], environmentally friendly because of no CO2 emissions and maintenance costs reducing. Additionally, Terex Corporation Lift AGV [2] with automatic loading container design without the aid of quay cranes and RTG. This design saves a lot of time in the yard container handling.

With the geographical location situated at the T junction of important trade in South Asia, Vietnam has favorable conditions for the development of maritime transport business. However, at the moment, ports in Vietnam has not yet used

AGV applications in processing container transport, mainly depends on the people, leading to frequent accidents and low productivity. Tan Thuan Port isn't also exceptional. Port gets also problems like the others. The productivity of Tan Thuan Port is 800 container per day now. From the real status of the ports in Vietnam, namely the current surface of the Tan Thuan Port, proposed an automatic solution to the problem of transporting container at the port of Tan Thuan (Fig. 3).

2 Structure of the System

2.1 Proposal for the Arrangement of Port's Surface

There are two forms of storage yard:

Type 1 is the form of the container perpendicularly to the QC (quay crane) (Fig. 2, left). Characteristics of this type is that the tire gantry cranes and AGV are less on duty so less energy but productivity will be lower.

Type 2 is the form of the container parallel to the port crane (Fig. 2, right). In this form, AGV's mileage is very low, but the RTG must operate much more, consumes more energy but get more productivity.

Tan Thuan Port currently has two QCs, three RTGs, with these numbers, the arrangement of container yard is reasonable (Type 1). Proposing an arrangement plan for the surface of Tan Thuan Port to easily apply AGV system. Moreover, this proposal still doesn't change the port's surface so much (Figs. 4 and 5).

Note for Figs. 3, 4 and 5:

Loaded trucks and AGVs	Gates in, out
Empty trucks and AGVs	Path of RTGs
Collision point	Path of trucks and AGVs
Direction of trucks	Width of work paths is 3.5 m
Direction of AGVs	

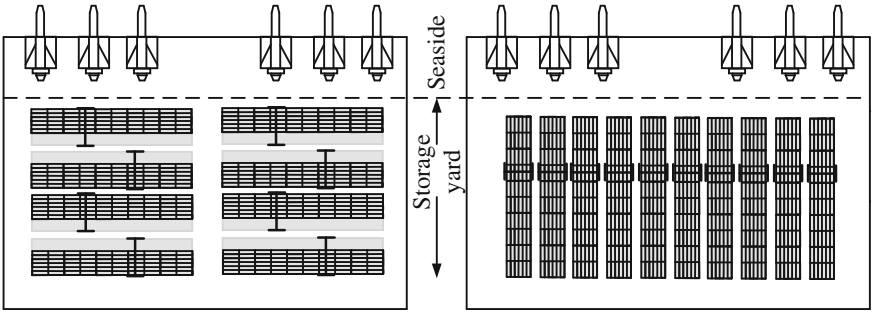

Fig. 2 Models for storage yard arrangement perpendicular or parallel to port cranes [4]

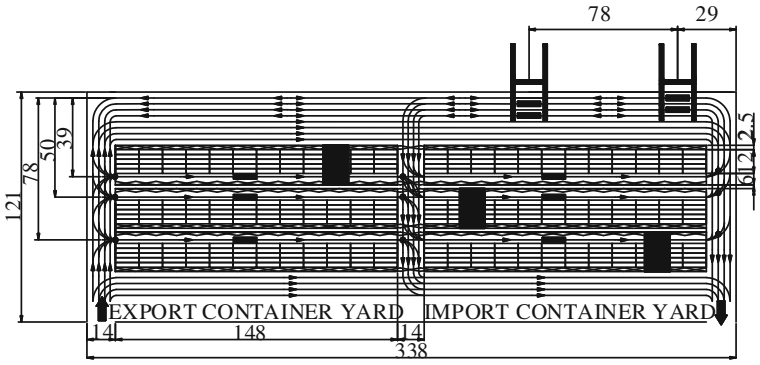

Fig. 3 The container yard of Tan Thuan Port

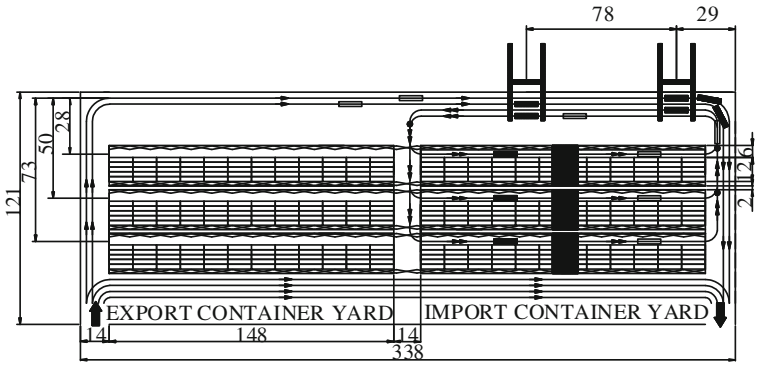

Fig. 4 Proposal of importing container

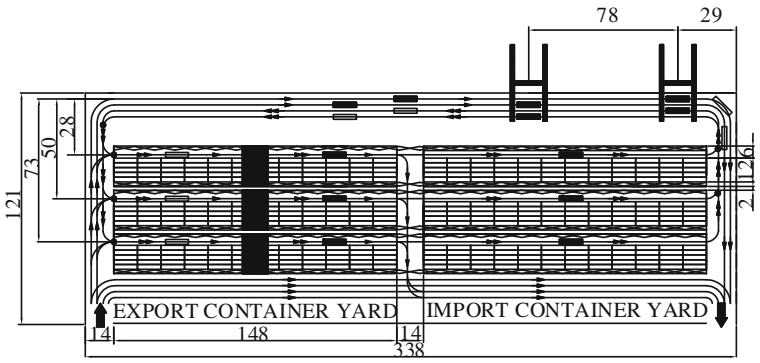

Fig. 5 Proposal of exporting container

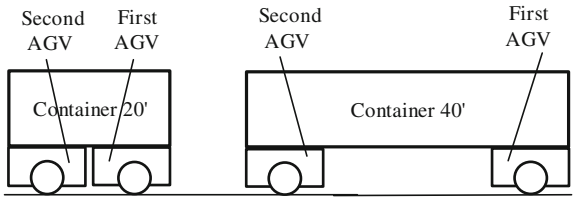

Fig. 6 AGV system loading two types of container

2.2 Proposal of Coordinating Two AGV to Load One Container

The system uses two AGV, every AGV itself tracks line and corporate with each other to ensure a constant distance of container. The downside of this system is that must have a stable controller because the system is disjointed and the load is huge. This proposal has an advantage of saving a huge cost for the production of a long AGV to load a container. In addition, the system also towards a higher goal for a swarm algorithm. It's that loading a very large and heavy object can't be transported by any vehicle alone (Fig. 6).

3 Modeling and Control

3.1 System Modeling

C is the tracking point (center of the line connecting midpoints of two wheels) (Fig. 7)

R is the desired point of C (located on the reference).

r is the radius of the wheel.

b is the distance from the tracking point (C) to the geometry center of wheel.

ρ is the radius of curve at point R.

d is the distance between two AGV's center (d is constant).

Hypotheses: Velocity and the angular velocity of the AGV at point C is v and ω.

The dynamic equations of AGV

$$\begin{bmatrix} \dot{x} \\ \dot{y} \\ \dot{z} \end{bmatrix} = \begin{bmatrix} \cos\emptyset & 0 \\ \sin\emptyset & 0 \\ 0 & 1 \end{bmatrix} \begin{bmatrix} v \\ \omega \end{bmatrix} \tag{1}$$

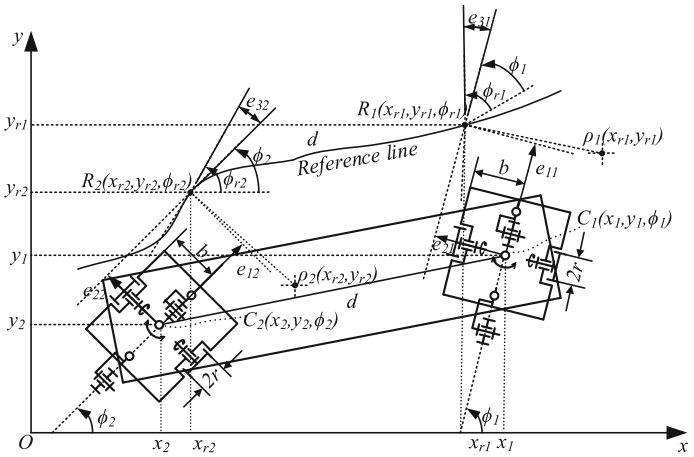

Fig. 7 Modeling AGV system

The relationship between v, ω together with angular velocity of the AGV's wheels:

$$\begin{bmatrix} \omega_r \\ \omega_l \end{bmatrix} = \begin{bmatrix} 1/r & b/r \\ 1/r & -b/r \end{bmatrix} \begin{bmatrix} v \\ \omega \end{bmatrix} \tag{2}$$

Reference point $R\ (x_R, y_R)$ travels with constant velocity v_R follows equations:

$$\dot{x}_r = v_r \cos \emptyset_r, \dot{y}_r = v_r \sin \emptyset_r, \dot{\emptyset_r} = \omega_r \tag{3}$$

Consider error between R and C

$$e = [e_1, e_2, e_3]^T \tag{4}$$

We have

$$\begin{bmatrix} e_1 \\ e_2 \\ e_3 \end{bmatrix} = \begin{bmatrix} \cos \emptyset & \sin \emptyset & 0 \\ -\sin \emptyset & \cos \emptyset & 0 \\ 0 & 0 & 1 \end{bmatrix} \begin{bmatrix} x_r - x \\ y_r - y \\ \emptyset_r - \emptyset \end{bmatrix} \tag{5}$$

Derivate errors, we got

$$\begin{bmatrix} \dot{e}_1 \\ \dot{e}_2 \\ \dot{e}_3 \end{bmatrix} = \begin{bmatrix} v_r \cos\ e_3 \\ v_r \sin\ e_3 \\ \omega_r \end{bmatrix} + \begin{bmatrix} -1 & e_2 \\ 0 & -e_1 \\ 0 & -1 \end{bmatrix} \begin{bmatrix} v \\ \omega \end{bmatrix} \tag{6}$$

Choose positive definite Lyapunov function

$$V = \frac{1}{2}e_1^2 + \frac{1}{2}e_2^2 + (1 - \cos\ e_3)/k_2 \tag{7}$$

Therefore

$$\dot{V} = e_1(v_R \cos e_3 - v) + (k_2 v_R e_2 + \omega_R - \omega)\sin\ e_3/k_2 \tag{8}$$

Select v and ω so that the derivative of V is negatively defined

$$v = v_R \cos e_3 + k_1 e_1, \omega = k_2 v_R e_2 + \omega_R + k_3 \sin e_3 \tag{9}$$

where:k_1, k_2, k_3 are positive constants.

So we calculate the velocity of the wheels to control the AGV to the desired position.

3.2 Coordinated Algorithm Between 2 AGV

Let the first AGV run with a constant velocity v_1, the second one will run at the change speed v_2 to ensure the constant distance d (Fig. 8).

The speed V_2 depends on V_1, α, β according to the following formula:

$$V_2 = V_1 \times \cos\alpha / \cos\beta \tag{10}$$

where V_1, V_2 is the first and second AGV's speeds respectively, $V_1 = v_{R1}$,$V_2 = v_{R2}$

α is the angle between the first AGV and container.

β is the angle between the second AGV and container.

Fig. 8 Container in a curve

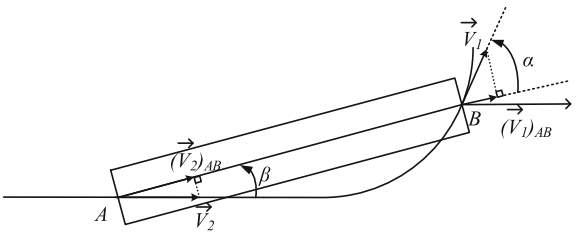

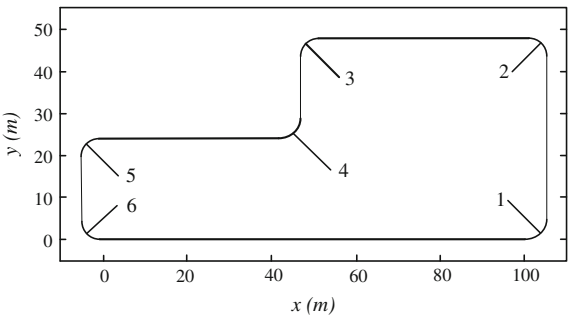

Fig. 9 Reference line

4 Simulation Results

To test the ability of mathematical models and algorithms proposed, let two AGVs load container 40′ and run simulations on the reference lines as shown in Fig. 9.

The constants are selected as follows: $k_{11} = 1$, $k_{21} = 25$, $k_{31} = 1$, $k_{22} = 5$, $k_{32} = 15$, (k_{11}, k_{21}, k_{31}, k_{12}, k_{22}, k_{32} is the control parameters of the two AGVs).

Simulation results:
From the simulation results we see when the first AGV during curve, the second AGV's error does not change significantly. When the second AGV is in curve, to ensure the distance, the second AGV's velocity must change because of the design of algorithm. However, two AGVs in the simulation results still follow the line. Error e_2 of the first AGV is ±12 mm (0.5 %), and error e_2 of the second AGV is ±25 mm (1 %). Error e_3 of two AGVs both are ±2° (Figs. 10 and 11).

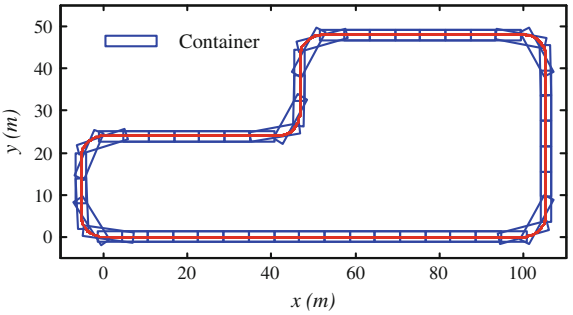

Fig. 10 Simulation of container in line

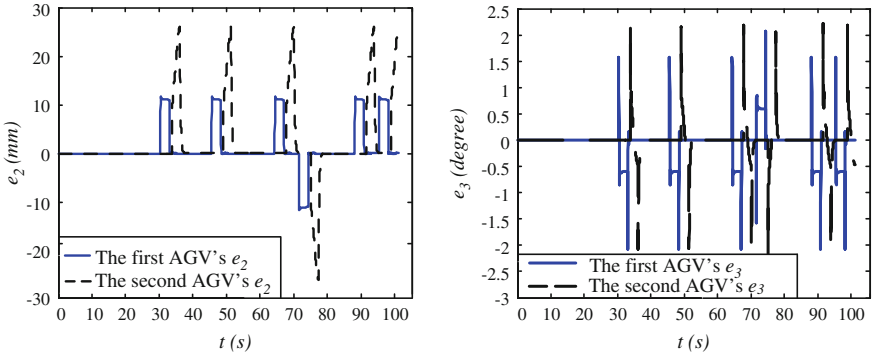

Fig. 11 Errors of two AGVs

5 Experiment

To test the feasibility of the algorithm, experiments on models with the following parameters in Table 1:

We do experiments on two maps: Map 1 (Fig. 12a) is representative of curves 1, 2, 5, 6 (Fig. 9). Map 2 (Fig. 12b) is representative of crabs 3, 4. The real map only has the curves 1, 2, 5 and 6. However, to demonstrate the flexibility, usability of algorithm, two sudden curves 3 and 4 were added.

Table 1 Input parameters of two AGVs [2, 3]

Name	Value	
	Simulation	Experiment
AGV's width	2.8 m	178 mm
AGV's height	1.8 m	120 mm
AGV' length	2.8 m	200 mm
Wheel's diameter	1.6 m	95 mm
Distance between two wheel	2.5 m	162 mm
Curve radius	5.25 m	340 mm
Velocity	3 m/s	0.2 m/s

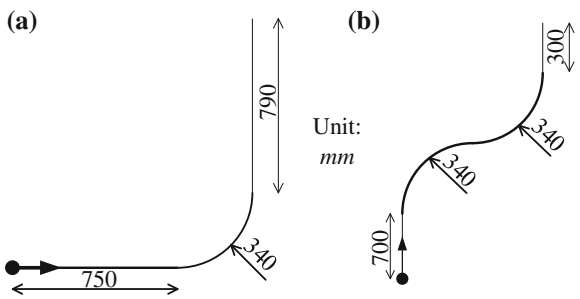

Fig. 12 Experiment maps. **a** Map 1. **b** Map 2

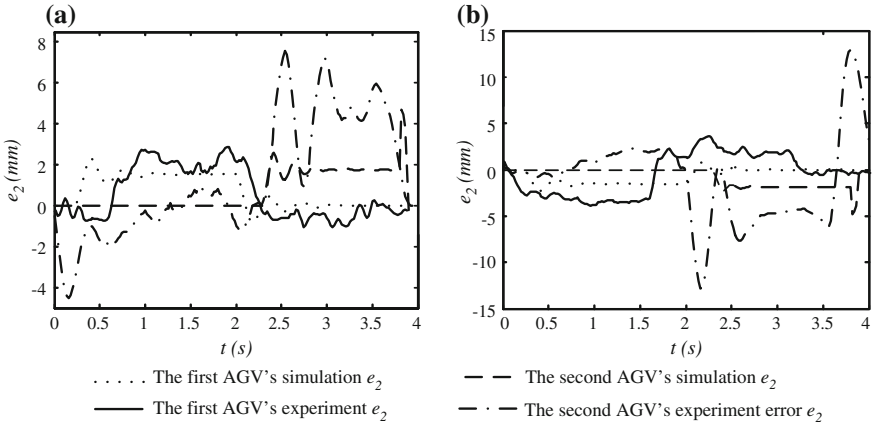

Fig. 13 Error e_2 of two AGVs in two experiment maps. **a** Map 1. **b** Map 2

Experiment results:
The maximum experiment error e_2 of the first AGV is ±3 mm (2 %) and the second AGV is ±12 mm (7 %). In Fig. 13, we can compare the simulation and experiment results. The shape of experiment errors is closely look like the simulation error. When the simulation errors change, the experiment errors also change. The difference between this two rors is the threshold and the speed of convergent. We will ignore the first AGV's errors because this AGV move in a constant velocity so this AGV's errors are so small. We will focus on the second AGV's errors. In map 1, the maximum experiment error e_2 of the second AGV is ±8 mm (5 %), and in map 2 the second AGV's error e_2 is ±12 mm (7 %). In both of two maps, we all see the fluctuation of the errors e_2. when the second AGV approach the curve. It still converges finally but it seem to be needed to improve the control by choosing the control parameter better. It will help increase the speed of convergent and reduce the maximum of errors.

6 Conclusion

This paper proposes a solution for the Tan Thuan Port based on the port's available surface: an arrangement plan for container yard, a transporting plan for import/export activity, an AGV system for transporting container at port. The feasibility of the solution set out by the results of simulation and experiment at HiTech Mechatronics Lab of University of Technology at HCM City.

References

1. Hoshino S, Ota J, Shinozaki A, Hashimoto H (2005) Highly efficient AGV transportation system management using agent cooperation and container storage planning. IEEE Conf Intell Robots Syst 1 (2005)
2. Terex Port Solution (2013) Lift AGV brochure english.pdf, p 3
3. Toyota (2013) Toyota industries' container transport AGV system contributing to evolution of port logistics. Toyota industries report
4. Hoshino S, Ota J, Shinozaki A, Hashimoto H (2006) Design of an AGV transportation system by considering management model in an ACT. Intell Auton Syst (IOS Press) 9:2
5. Liu C-I, Jula H, Vukadinovic K, Ioannou P (2014) Automated guided vehicle system for two container yard layouts. Transport Res Part C 12:351–352
6. Terex Port Solutions (2014) 10 most FAQ's about AGV's. TOC Europe, London
7. Doan PT, Nguyen TT, Dinh VT, Kim HK, Kim SB (2011) Path tracking control of automated guided vehicles using camera sensor. In: Proceedings of the 2011 international symposium on automotive and convergence engineering, pp 89–94, 19–21 Jan 2011
8. Saputra RP, Rijanto E (2012) Automated guided vehicles system and its coordination control for containers terminal logistics application. In: Proceedings of the conference on international logistic seminar and workshop 2012, Jakarta, At Jakarta, Indonesia, p 4

A Study on Moving Direction and Surge Velocity Control of a Carangiform Fish Robot Driven by Flexible Pectoral Fins

Van Anh Pham, Khac Anh Hoang, Tan Tien Nguyen and Tuong Quan Vo

Abstract This paper proposes a hydrodynamic model of a Carangiform fish robot whose motions are driven by two pectoral fins. The fish robot is composed of the main body, a pair of flexible pectoral fins actuated by DC servo motors and a free–tail. The mathematical model of pectoral fins is achieved by the approximation solution of beam vibration in fluid environment. The Rayleigh-Ritz method is used to obtain the eigenvalues and fundamental mode shape of fins. The thrust force model is computed through the Morrison's formulation. Then, the control law based on the Lyapunov's theory is designed to stabilize the moving direction and velocity of robot in the 2 dimensions (2D) space. The Hammerstein-Wiener model is also used to estimate the inverse hydrodynamic model of the two pectoral fins. Finally, the simulation results are conducted to prove the effective of the proposed model of our fish robot.

Keywords Pectoral fins · Vibration · Flexible fins · Mode shape · Surge velocity · Moving direction

1 Introduction

In the recent decades, many studies on the biomimetic robots including fish robot are mostly concerned. To compare to the traditional screw-propeller underwater vehicles such as Remotely Operated Vehicles (ROVs) or Autonomous Underwater Vehicles (AUVs), the bio-inspired aquatic robots would be more high maneuverability, efficiency and silent moving.

For the fish robot, there are several ways to generate the propulsion force using a caudal fin which actuated by motors or different kind of smart materials. In [1], the

V.A. Pham · K.A. Hoang · T.T. Nguyen (✉) · T.Q. Vo
Faculty of Mechanical Engineering, HCM City University of Technology,
VNU-HCM, Ho Chi Minh City, Vietnam
e-mail: vtquan@hcmut.edu.vn

V.H. Duy et al. (eds.), *AETA 2015: Recent Advances in Electrical Engineering and Related Sciences*, Lecture Notes in Electrical Engineering 371,
DOI 10.1007/978-3-319-27247-4_64

model of free locomotion fish robot have been developed propelled by vibrating ionic polymer metal composites (IPMCs). Robot has only one tail fin that enabled it to move in 2D space. In [2], Kopman et al. developed a fish robot with the tail part modeled by using Euler-Bernoulli beam theory and Morison equations. The nonlinear vibrations of the propulsion tail are modeled using modal analysis and the study results of large vibration of slender cylinders in fluid. Jianxin Xu et al. proposed a motion control approach for a multi-joint robotic fish with the pectoral fins assistance in [3]. The fish robot undulates its body and tail to produce the basic swimming patterns that are aimed by a general internal model (GIM), while twists its pectoral fins to assist the body to reach the desired direction. In [4], a novel design of flexible joints for connecting the pectoral fins to the actuators is proposed. This design allows the pectoral fin to sweep back passively in the recovery stroke while maintaining its prescribed motion in the power stroke. In the another research [5], the angle of attack theory based dynamic model of Ostraciiform robotic fish is established that they used the CPG controller to predict mechanical behaviors of the robot and guide the search for CPG parameters and gain optimization of the robot. In [6], a model of the pectoral driven by SMA is developed for Koi Carp. In fin-ray form, this is very flexible and maneuverable, but complicated to control. Based on previous work, this paper proposes modeling a Carangiform robotic fish aimed by a pair of flexible uniform pectoral fin. The undulating tail part is free. We also employed a controller using Lyapunov's theory to track the desired heading angle and surge velocity trajectory and validate the built modeling results.

This paper is organized as follow: In Sect. 2, the hydrodynamic modeling of fish robot actuated the pectoral fins is presented. In Sect. 3, the design of the controller based on Lyapunov's theory is conducted to support for motion in 2D plane. In Sect. 4, the simulations are shown and discussed to validate results. Finally, conclusions are summarized in Sect. 5.

2 Fish Robot Modeling

2.1 Modeling of the Flexible Fin

The Carangiform fish robot model driven by pectoral fins is illustrated in the Fig. 1. Several assumptions are made for modeling such as: the fins vibrate along its

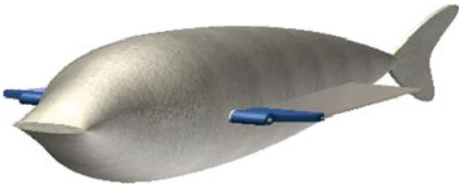

Fig. 1 The model of fish robot with flexible pectorals

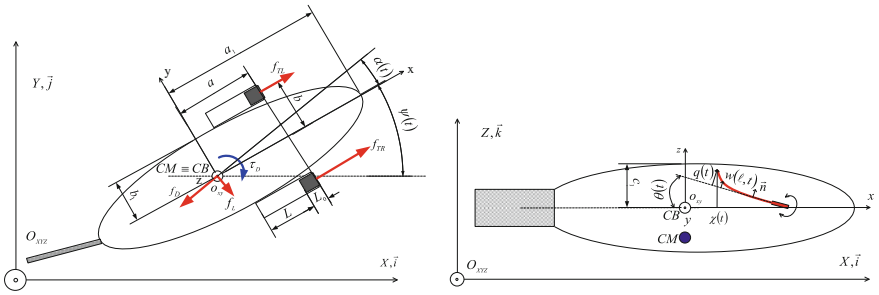

Fig. 2 The schematic of in-plane swimming fish robot with the flexible fins are considered as cantilever beam

fundamental mode shape; the fins are only bended along the longitudinal direction; the bending directions of the fins in other directions are ignored. Therefore, an approximate solution for propulsion' mechanism is proposed by using some first mode shapes (Fig. 2).

By using classical Euler-Bernoulli beam theory, the partial differential equation describing the vibration of the forced underwater uniform fins can be presented as [7]:

$$K_M \frac{\partial^4 w(\ell,t)}{\partial \ell^4} + \rho \frac{\partial^2 w(\ell,t)}{\partial t^2} + c \frac{\partial w(\ell,t)}{\partial t} = F(\ell,t) \tag{1}$$

where $K_M = (1/12)Eh^3 d_0$; $\rho = md_0/A$; $A = d_0 L$; E, d_0, h, A, L are elastic module, thickness, width, area and length of fin respectively; c is a viscous damping coefficient. This force per unit length $F(l,t)$ acting on the fins to the encompassing fluid is expressed by the Morison equation [8]:

$$F(\ell,t) = -\frac{1}{2}\rho_h d_0 C_d v(\ell,t)|v(\ell,t)| - \frac{1}{4}\pi\rho_h d_0^2 C_a \dot{v}(\ell,t) \tag{2}$$

where C_d and C_a describe the damping and added mass effects, ρ_h is the density of water, $v(\ell,t)$ is the flow velocity. To estimate the flow velocity on the points of fin, we consider motions of pectoral fins and their hinge peduncles when robot moves (Fig. 2).

Assume that the fish robot is always at the neutrally buoyant state. And, the center of mass and the center of buoyancy have the same projection on the XY-plane. Some coordinate systems are demonstrated in Fig. 2. The robot can move in the Earth-fixed frame and the body frame is fixed in the central buoyancy of robot. We also assume that the pectoral fins include two parts: the rigid hinge peduncles on one end and flexible beam on the other. The unit vector which is perpendicular to the peduncle

plane, called $\vec{n}(t)$, given as: $\vec{n}(t) = \vec{i}\sin\theta(t)\cos\psi(t) + \vec{j}\sin\theta(t)\sin\psi(t) + \vec{k}\cos\theta(t)$. Using the approaching in [2], the displacement of points on the flexible beam in the body frame is given by:

$$\vec{u}(\ell,t) = \vec{u}_B + \vec{u}_H(\ell,t) + w(\ell,t)\vec{n}(t) \tag{3}$$

where:

$$\vec{u}_B = \vec{i}\Big[a\cos\psi(t) - (-1)^{lr} b\sin\psi(t)\Big] + \vec{j}\Big[a\sin\psi(t) + (-1)^{lr} b\cos\psi(t)\Big] + 0.\vec{k} \tag{4}$$

$$\vec{u}_H(\ell,t) = (L_0+\ell)\Big(-\vec{i}\cos\psi(t)\cos\theta(t) - \vec{j}\sin\psi(t)\cos\theta(t) + \vec{k}\sin\theta(t)\Big) \tag{5}$$

The angle $\theta(t)$ deflected by the servomotor is of form: $\theta(t) = B\sin(2\pi ft + \delta)$; $lr = 0$ for the left fin, $lr = 1$ for the right fin. We employ $\vec{u}_B$ to denote the positon of the original hinge in the Earth-fixed. $\vec{u}_H(\ell,t)$ accounts for the beam position in the hinge-fixed frame and $w(\ell,t)\vec{n}(t)$ for the displacement due to the beam's vibration.

Taking the derivative of (3) with respect to time once and twice, after projecting it onto $\vec{n}(t)$, yields the velocity and acceleration of the flexible beam:

$$\dot{\vec{u}}(\ell,t)\vec{n}(t) = \sum_{m=1}^{\infty} \dot{q}_i(t)\varphi_i(\ell) + (L_0+\ell)\dot{\theta}(t) - (-1)^{lr} b\sin\theta(t)\dot{\psi}(t) \tag{6}$$

$$\begin{aligned}\ddot{\vec{u}}(\ell,t)\vec{n}(t) = &\sum_{m=1}^{\infty} \ddot{q}_i(t)\varphi_i(\ell) + (L_0+\ell)\left[\ddot{\theta}(t) + \frac{1}{2}\sin(2\theta(t))\dot{\psi}^2(t)\right] \\ &- \left(\dot{\psi}^2(t)\sin^2\theta(t) + \dot{\theta}^2(t)\right)\sum_{m=1}^{\infty} q_i(t)\varphi_i(\ell) \\ &- \sin\theta(t)\left[a\dot{\psi}^2(t) + (-1)^{lr} b\sin(2\psi(t))\right]\end{aligned} \tag{7}$$

Combining that: $v(\ell,t) = \dot{\vec{u}}(\ell,t)\vec{n}(t)$, $\dot{v}(\ell,t) = \ddot{\vec{u}}(\ell,t)\vec{n}(t)$ and substitute the Eqs. (6) and (7) into Eq. (2), we can obtain solution of the Morison's force equation. Where, the displacement of the points of the fin, with respect to time, is approximated by the series:

$$w(\ell,t) = \sum_{i=1}^{\infty} q_i(t)\varphi_i(\ell) \tag{8}$$

For robot operation, the pectoral fins vibrate in their first vibrational modes. An approximate solution is obtained by projecting the equation of motion onto the fundamental mode shapes beam vibration in vacuum. By using the Rayleigh-Ritz method [9], the solution of the eigenvalue problem for the fixed-free beam in axial vibration can be obtained.

Solving the algebraic eigenvalue problem, we obtain the natural frequencies and modal vectors. Normalizing $\varphi_i(\ell)$ to a unitary fin-tip displacement, that is, $\varphi_i(L) = 1$. Following the Eigen function superposition method, we assumed that the force loading along fin can be expressed as:

$$F(\ell, t) = \sum_{i=1}^{\infty} p_i(t)\varphi_i(\ell) \tag{9}$$

where φ_i is the eigenfunction of free un-damped vibration of the ith mode of the fins. By multiplying both sides of Eq. (9) by a typical eigenfunction φ_j, integrating over the length of fins and taking advantage of the orthogonality condition, we obtain:

$$p_i(t) = \frac{\int_0^{L_0} F(\ell, t)\varphi_i(\ell)d\ell}{\int_0^{L_0} \varphi_i^2(\ell)d\ell} \tag{10}$$

Substituting Eqs. (8), (10) into Eq. (1), we obtain:

$$K_M \sum_i^{\infty} q_i(t) \frac{\partial^4 \varphi_i(\ell)}{\partial \ell} + \rho \sum_i^{\infty} q_i(t)\, \ddot{\varphi}_i(\ell) + c \sum_i^{\infty} q_i(t)\dot{\varphi}_i(\ell) = \sum_i^{\infty} p_i(t)\varphi_i(\ell) \tag{11}$$

Combining the solution of the free vibration equation $K_M \varphi_i^4(\ell) = \rho\omega_i^2\varphi_i(\ell)$ into Eq. (11), then multiplying both by φ_j, then integrating over the length of the fin and using orthogonality condition, we obtain:

$$\rho\, \ddot{q}_i(t) + c\dot{q}_i(t) + \beta_i^4 \left(\frac{K_M}{L^4}\right) q_i(t) = p_i(t) \tag{12}$$

where: $\beta_i^2 = \omega_i L^2 \sqrt{\rho/K_M}$, ω_i are fundamental frequencies. By solving the differential equations Eq. (12), $q_i(t)$ can archive. In this research, we use the first ten mode shapes of homogenous cantilever beam. The detail of the method can be found in [7].

2.2 Fish Robot Body Hydrodynamics

In order to model motion of the fish robot, we assume the following conditions such as: the robot body is a rigid body, the moving of robot in a fluid, the fish robot is driven by a pair of pectoral fins. The undulating tail part is free. In this paper, we focus on the movement of the robot in XY plane, which has three degree of freedoms, surge (u), sway (v) and yaw (r). The heading angle ψ, satisfying $r = \dot{\psi}$, is

also the angle between the body-fixed frame and the Earth frame system We assume that the XZ-plane is a plane of symmetry for the vehicle body and neglect inertial coupling between sway, surge and yaw motion. According to [10], the motion equation of the rigid body is reduced to:

$$\begin{bmatrix} m_b + m_x & 0 & 0 \\ 0 & m_b + m_y & 0 \\ 0 & 0 & J_{bz} + J_r \end{bmatrix} \begin{bmatrix} \dot{u} \\ \dot{v} \\ \dot{r} \end{bmatrix} + \begin{bmatrix} -(m_b + m_y)vr \\ (m_b + m_x)ur \\ -(m_x - m_y)uv \end{bmatrix} = \begin{bmatrix} F_x \\ F_y \\ M_z \end{bmatrix} \tag{13}$$

where, the mass and the added mass of a fin m_f , $m_{af} = (4/3)\rho_h \pi L(d_0/2)^2$ respectively. The other added mass terms are given by [10]: $m_b = (4/3)\rho_h \pi a_1 b_1^2$; $m_x = k_1 m_f$; $m_y = k_2 m_f$; $J_z = k' J_{fz}$. Where, the positive constants: k_1, k_2 and k' are Lamb's k-factor that depend only on the geometry of the body. Select $m_f = \rho \forall_s$ as the mass of the displaced fluid, where $\forall_s = (4/3)\pi a b^2$ is the volume of the spheroid; $J_{fz} = (1/5)m_f(a^2 + b^2)$ is the moment of inertia of the fluid's spheroidal mass.

The total external forces and moments obtained from the free-body diagram in the Fig. 2 are expressed as:

$$\begin{bmatrix} F_x \\ F_y \\ M_z \end{bmatrix} = \begin{bmatrix} 1 & 1 \\ 0 & 0 \\ -b & b \end{bmatrix} \begin{bmatrix} f_{TL} \\ f_{TR} \end{bmatrix} + \begin{bmatrix} -\cos\alpha & \sin\alpha & 0 \\ -\sin\alpha & -\cos\alpha & 0 \\ 0 & 0 & -1 \end{bmatrix} \begin{bmatrix} f_D \\ f_L \\ f_D \end{bmatrix} \tag{14}$$

The produced robot thrust is primarily due to the surrounding fluid inertia. The instantaneous thrust of the fish robot is approximated as [2]: $f_{Tlr} = 0.5 C_T \rho_h A_t \dot{\chi}_{lr}^2(t)$, where: $\chi_{lr}(t) = w(L,t)\cos\theta_{lr}(t) + L_t \sin\theta_{lr}(t)$, lr is symbol of left or right fin, $L_t = L_0 + L$: the total length of the pectoral fin included fin and peduncle.

The hydrodynamic actions are expressed as [11, 12]: the body drag force $f_D = 0.5\rho_h V^2 S C_D$, the lift force $f_L = 0.5\rho_h V^2 S C_L \alpha$ and the drag moment $\tau_D = 0.5\rho_h V^2 S(2a)(C_{M\alpha} a + (2a/V)C_{Mr} r)$. Where ρ_h is the density of water. The coefficient of drag C_D, coefficient of lift C_L, coefficient of hydrodynamic restoring moment $C_{M\alpha}$, and coefficient of hydrodynamic viscous moment C_{Mr}. These coefficients depend on the Reynolds number and on the attack angle α. The angle of attack is as angle that the linear velocity vector of the vehicle whose the magnitude is $V = \sqrt{u^2 + v^2}$, form with the positive of the x-axis.

3 Controller Design

In our previous research, the stabilization of robot heading angle is done without caring the surge velocity. The moving velocity of robot is not controlled. In this paper, we propose a method of tracking moving direction and surge velocity of robot. This is based on the directive Lyapunov's stabilization method (Fig. 3).

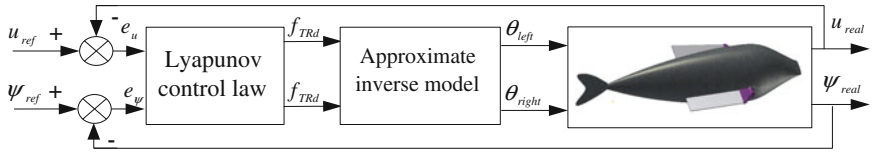

Fig. 3 The structure of the direction and velocity control system

To stabilize the heading angle of robot to referent direction, the control law is chosen to satisfy the condition below:

$$V = \frac{1}{2}\dot{e}_\psi^2 + \frac{1}{2}e_\psi^2 + \frac{1}{2}e_u^2 \tag{15}$$

where: $e_\psi = \psi - \psi_r$, $\dot{e}_\psi = \dot{\psi} - \dot{\psi}_r$, $e_u = u - u_r$ are the error, error differential of heading angle and the error of velocity surge.

$$\dot{V} = \dot{e}_\psi\left(\ddot{e_\psi} + e_\psi\right) + \dot{e}_u e_u \tag{16}$$

In order to $\dot{V} \leq 0$, we choose: $\ddot{e_\psi} = -\lambda_1 \dot{e}_\psi - e_\psi$ and $\dot{e}_u = -\lambda_2 e_u$, rewriting these conditions, we obtain: $\ddot{\psi} = -\lambda_1 \dot{e}_\psi - e_\psi + \ddot{\psi}_r$ and $\dot{u} = -\lambda_2 e_u + \dot{u}_r$. Where, λ_1 and λ_2 are the positive constants. Substituting into Eq. (13) and combining Eq. (14). We obtain:

$$\begin{bmatrix} f_{TLd} \\ f_{TRd} \end{bmatrix} = \begin{bmatrix} 1/2 & -1/2b \\ 1/2 & 1/2b \end{bmatrix} \begin{bmatrix} (m_b + m_x)(\dot{u}_r - \lambda_2 e_u) - vr\left(m_b + m_y\right) + f_D \cos\alpha - f_L \sin\alpha \\ (J_{bz} + J_r)\left(\ddot{u}_r - \lambda_1 \dot{e}_\psi - e_\psi\right) - \left(m_x - m_y\right)uv + \tau_D \end{bmatrix} \tag{17}$$

The Eq. (17) describes the desired force of each fin. Because of the difficulties of the explicitly presenting the inverse hydrodynamic model of pectoral fins, we used black-box modeling approach to reconstruct the mathematical relationships between the produced thrust and the desired pectoral fin angles. To reduce the complexity of the identified model, some constraints are added such as: the fin vibration frequency and the maximum vibration amplitude are constants. The identified system is a single input single output system. The Hammerstein-Wiener estimation model is proposed to simply processing issue and guarantee accuracy of alternative model. This structure is nonlinear estimator model chosen by trial-error method. The structure of Hammerstein-Wiener model includes three blocks: nonlinear input block, linear block described by a linear transfer function and nonlinear output block. Because the thrust force produced by high frequency oscillation of fins, so we approximate the desired thrust force as average force. The chosen input and output nonlinearity estimators are the piecewise linear functions. The number

of zeros, poles and the input delay of linear block are one, two and three, respectively. The fit of the identified model tested independence can reach more than 94 %.

4 Simulation Results

To validate the feasibility and reliability of our fish robot's fins modelling, the fins oscillation and swimming mode simulation are implemented. The geometric parameters of the fish robot are included as follow: a = 0.05 m, a_1 = 0.10 m, b = 0.04 m, b_1 = 0.03 m, c_1 = b_1, $L_0 = 0.010$ m, $L = 0.050$ m, $d_0 = 0.015$ m, $\rho_h = 1000$ kg/m^3. The mass of each fin: $m_f = 0.35.10^{-3}$ kg, the damping coefficient: $c = 500$ Ns/m^2. The Reynolds number $12133 \leq \mathrm{Re}_f \leq 30903$ and the thrust coefficient $C_T = 0.496 \cdot 10^{-3}$; C_D = 2.1, C_L = 16, $C_{M\alpha} = 0.7$, $C_{Mr} = 1$, $C_d = -$ 2.031, $C_a = -0.134$, $Eh^3 = 0.9.10^{-2}$ Nm. The sampling time: dt = 0.001 S. The vibration frequency and initial phase of fins are 35 Hz and 0(rad), respectively. The maximum vibration amplitude of fins: $B_{\max} = \pi/6$. The control parameters include: the parameter of direction and stabilizer and the parameter of controller: $\lambda_1 = 0.5$, $\lambda_2 = 5$, respectively. The reference heading angle and surge velocity trajectory equation are in the form: $\psi_r = (\pi/6)\sin(0.025\pi t)(rad)$, $u_r = 0.025(1 + \sin(0.01\pi t))(\mathrm{m/s})$, respectively.

The Fig. 4 illustrates the heading angle response of the fish robot movement. The moving direction respond quite rapidly converge to the desired trajectory. This motion is quite smooth because there are not the phase difference of fin vibrations. The settling time is about 12 s.

While moving, the surge velocity can be changed by the reference velocity. The settling time is only about 10 s. This surge velocity is fluctuated by the discontinuity of the thrust forces.

The change of thrust force on the fins is demonstrated in the Fig. 5. The real thrust forces have large switch phenomenon. These have the same frequency of pectoral fins.

The responds of fin vibration amplitude are shown in the Fig. 6. These have the same shapes with that the desired thrust forces respond.

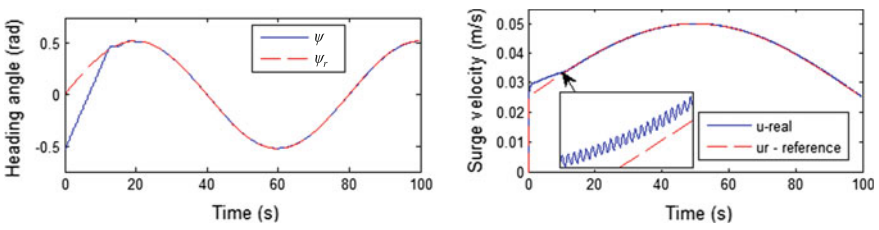

Fig. 4 The real and reference responds of heading angle and surge velocity

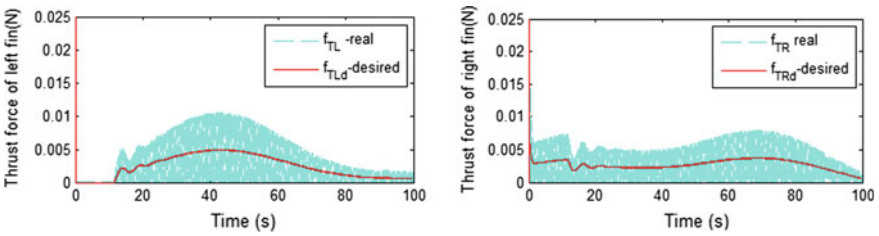

Fig. 5 The desired and produced thrust forces on the pectoral fins

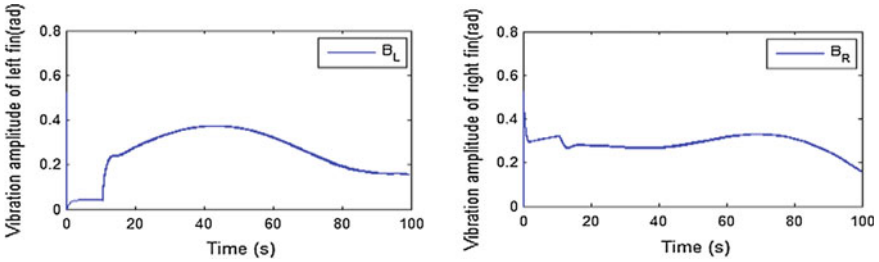

Fig. 6 The real vibration amplitude on the pectoral fins

5 Conclusion

In this paper, we presented a hydrodynamic model for the fish robot actuated by the flexible pectoral fins. The mathematical model of the pectoral fins is based on Euler—Bernoulli beam theory. The Rayleigh-Ritz method is used to approximate the eigenvalue problem and mode shape. The simulations are carried out by numerical approximate method. The dynamic of the fish body are obtained by considering this part is the rigid body and using Kirchhoff's equation. In particular, the important hydrodynamic properties are also considered, such as: the added mass and damping. The control law based Lyapunov's stabilization theory is proposed to track the desired direction and velocity. The Hammerstein-Wiener model is also used to approximate the complex inverse dynamic model of pectoral fins. The simulation results showed the suitability of the proposed modeling and the performance of the control system.

Acknowledgement This research is funded by the Ho Chi Minh City University of Technology, Vietnam under grant number TNCS-CK-2015-13.

References

1. Aureli M, Kopman V, Porfiri M (2010) Free-locomotion of underwater vehicles actuated by ionic polymer metal composites. IEEE/ASME Trans Mechatron 15:603–614
2. Kopman V, Laut J, Acquaviva F, Rizzo A, Porfiri M (2015) Dynamic modeling of a robotic fish propelled by a compliant tail. IEEE J Oceanic Eng 40:209–221
3. Xu J, Ren Q, Guo Z, Niu X (2013) Motion control for a multi-joint robotic fish with the pectoral fins assistance. In: IEEE international symposium on industrial electronics (ISIE), pp 1–6
4. Behbahani SB, Xiaobo T (2014) A flexible passive joint for robotic fish pectoral fins: design, dynamic modeling, and experimental results. In: IEEE/RSJ international conference on intelligent robots and systems, pp 2832–2838
5. Wei W, Guangming X, Hong S (2014) Dynamic modeling of an ostraciiform robotic fish based on angle of attack theory. In: International joint conference on neural networks (IJCNN), pp 3944–3949
6. Shiwu Z, Bo L, Lei W, Qin Y, Kin Huat L, Jie Y (2014) Design and implementation of a lightweight bioinspired pectoral fin driven by SMA. In: IEEE/ASME transactions on mechatronics, 19:1773–1785
7. Arthur MSQ, Leissa W (2011) Vibrations of continuous systems: the McGraw-Hill companies
8. Graham JMR (1980) The forces on sharp-edged cylinders in oscillatory flow at low Keulegan-Carpenter numbers. J Fluid Mech 97:331–346
9. Meirovitch L (2001) Fundamentals of vibrations, Graw Hill
10. Fossen TI (1995) Guidance and control of ocean vehicles, Wiley
11. Petrich J, Neu WL, Stilwell DJ (2007) Identification of a simplified AUV pitch axis model for control design: theory and experiments. In: OCEANS, pp 1–7
12. Stepanyan V, Hovakimyan N, Woolsey C A (2005) Adaptive output feedback control of a spheroidal underactuated underwater vehicle. In: Proceedings of MTS/IEEE OCEANS, 1:278–284

Precise Position Control of Shoes-Upper for Screen Printing Machine Using SCARA Robot

Trong Hieu Bui, Anh Tuan Bui and Thanh Huy Phung

Abstract This paper proposes a new method to enhance precise position control of shoes-upper for screen printing machine. The method is based on control of SCARA robot and image processing. The system has a SCARA robot attached a suction plate on its end-effector, a fixed table and a conveyor system for screen printing machine. The suction plate takes supplied a shoes-upper on fixed table and calibrates its position from the table to conveyor. Position errors are eliminated during robot's motion. The SCARA robot is controlled by a simple PD controller. The effectiveness of the method is verified through a model-based simulation and its results.

Keywords Inverse kinematics · Kinetics · SCARA robot · Image processing

1 Introduction

Recently, various products of leather textile industry have decorations printed by screen printing machines. Especially in sport shoes, many types of printed decorations make shoes become more beautiful and valuable. In Fig. 1, the parallel stripes are used as press-segments.

T.H. Bui (✉) · T.H. Phung
Faculty of Mechanical Engineering, HCMC University of Technology,
Ho Chi Minh City, Vietnam
e-mail: hieutkm@gmail.com

T.H. Phung
e-mail: thanhhuy.phung@gmail.com

A.T. Bui
Faculty Mechanical Engineering, Ly Tu Trong Technical College,
Ho Chi Minh City, Vietnam
e-mail: anhtuanbm88@gmail.com

V.H. Duy et al. (eds.), *AETA 2015: Recent Advances in Electrical Engineering and Related Sciences*, Lecture Notes in Electrical Engineering 371,
DOI 10.1007/978-3-319-27247-4_65

Fig. 1 Shoes with white stripes

These stripes are printed by automatic printing machines through many stages then dried up automatically with drying mechanism inside. These screen printing machines reduce stages and save time, labour, cost of products. However, shoes-upper supplied for printing machine has been executed totally by hand. This work depends on the experience and psychology of workers, so it increases the errors, labour charge and price of products. This affects to next stage, which is sewing contour lines on printed stripes which could make more waste products. So, the problem is how to innovate the technology in order to optimize and automate the feeding stage for the conveyor of screen printing machines.

To solve this problem, some feeder systems for screen printing machines have recently been developed. Bui et al. [1] developed successfully a ball screw feeder system. But this system is pretty bulky and not flexible. It's only suitable for screen printing machines with stations along line.

This research proposes another method that is able to apply many types of screen printing machines using SCARA robot. SCARA robot may be applied to enhance precision of shoes-upper's position on the conveyor of screen printing machines. This can be achieved from SCARA robot's wide flexible operation range. SCARA will eliminate the position errors of shoes-upper when it moves its joints. The objective of this research is to be applied in many fields outside leather and shoes industry as medical service or fuel supplying.

The executive steps to eliminate the errors of shoes-upper by using SCARA robot are as follows

- *Step 1*. A shoes-upper is located on the fixed table.
- *Step 2*. To reduce noise, a CCD camera (put above fixed table) takes an image of current shoes-upper. Apply image processing to calculate the geometric properities of this image as centroid and oriented angle.
- *Step 3*. Use a SCARA robot to move the shoes-upper from fixed table to conveyor of screen printing machine. The SCARA's end-effector moves to the center of the image, then moves to a desired position in the conveyor. The rotation error will be adjusted by end-effector after that (Fig. 2).

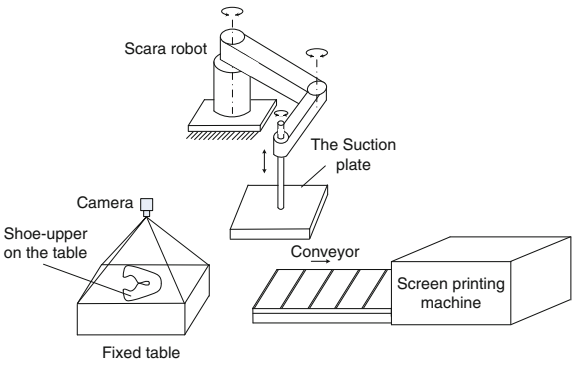

Fig. 2 The process of eliminating errors using a SCARA robot

2 System Modelling

2.1 Systematic Coordinators and Notations

To analyse the system, the coordinate are set as Fig. 3. (Oxy) is the global coordinate system, which has the origin O at the origin of the Scara robot; (Iuv), (Au_1v_1) and (Bu_2v_2) are the coordinate systems attached to the image, the table and the conveyor respectively. For the sake of simplicity, it is assumed that the captured image covers the fixed table. This could be achieved by camera calibration. The coordinates of local origins in the global system are $I(x_I, y_I), A(x_A, y_A), B(x_B, y_B)$. The SCARA robot is described in 2D as Fig. 3b. $(O_1x_1y_1)$ is local coordinate system, θ_I and θ_2 are joints angles, L_I and L_2 are lengths of the arms. In 2D global system, the coordinates of end-effector is (p_x, p_y).

Transformation from the image coordinate to the robot coordinate is as follows:

$$\begin{bmatrix} x \\ y \\ 1 \end{bmatrix} = \begin{bmatrix} 1/k_1 & 0 & x_I \\ 0 & -1/k_2 & y_I \\ 0 & 0 & 1 \end{bmatrix} \begin{bmatrix} u \\ v \\ 1 \end{bmatrix} \tag{1}$$

where k_1, k_2 are the scale factors by u and v directions, respectively.

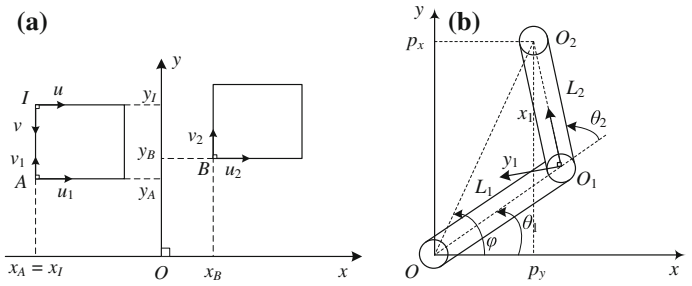

Fig. 3 The relationship of coordinate systems

2.2 Shoes-Upper Image Processing

Similarly to paper [1], the centroid and oriented angle of shoes-upper on image are used to control SCARA robot. The captured images are RGB image while the images used to calculate are binary image. Therefore, the images will be converted to binary image using Otsu's method after image pre-processing, then used to determine the geometric properties. It is also necessary to interest the reliable hardware and stability of light source.

Two geometric properties of area concerned with the image are centroid of area $C(u_C, v_C)$ and oriented angle α [1–3] (Fig. 4).

The centroid of plane area is

$$\begin{cases} u_C = \dfrac{1}{F}\displaystyle\sum_{u=1}^{n} F(u,v) \times u \\ v_C = \dfrac{1}{F}\displaystyle\sum_{v=1}^{m} F(u,v) \times v \end{cases} \tag{2}$$

where $m \times n$ is size of image, $F(u, v)$ is the value at pixel (u, v) and F is sum of all pixel values.

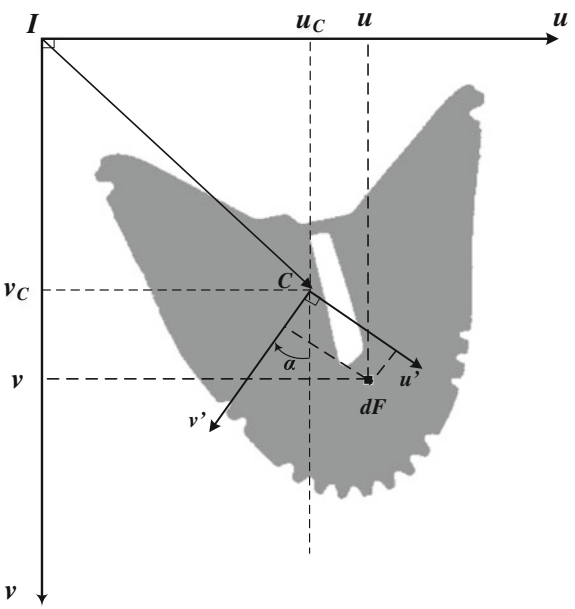

Fig. 4 The centroid and oriented angel of a shoes-upper in image coordinate (*Iuv*)

And the oriented angel α

$$\alpha = \frac{1}{2}\,\text{atan}\left(\frac{-2\left(\sum\limits_{1\le u\le n, 1\le v\le m}(u-u_C)(v-v_C)F(u,v)\right)}{\left(\sum\limits_{1\le v\le m}(v-v_C)^2F(u,v) - \sum\limits_{1\le u\le n}(u-u_C)^2F(u,v)\right)}\right) \tag{3}$$

2.3 Position of End-Effector

With a SCARA as Fig. 3b, the position of end-effector in 2D:

$$\begin{bmatrix} p_x \\ p_y \end{bmatrix} = \begin{bmatrix} L_2\cos(\theta_1+\theta_2)+L_1\cos(\theta_1) \\ L_2\sin(\theta_1+\theta_2)+L_1\sin(\theta_1) \end{bmatrix} \tag{4}$$

Hence,

$$p_x^2+p_y^2 = (L_2\cos(\theta_1+\theta_2)+L_1\cos(\theta_1))^2 + (L_2\sin(\theta_1+\theta_2)+L_1\sin(\theta_1))^2 \tag{5}$$

With configuration as Fig. 3b:

$$\Rightarrow \theta_2 = \arccos\left(\frac{p_x^2+p_y^2-L_1^2-L_2^2}{2L_1L_2}\right) \tag{6}$$

$$\Rightarrow \theta_1 = \arctan\left(\frac{p_y}{p_x}\right) - \arccos\left(\frac{p_x^2+p_y^2+L_1^2-L_2^2}{2L_1\sqrt{p_x^2+p_y^2}}\right) \tag{7}$$

To take the shoes-upper, the end-effector should go to the calculated center of the shoes-upper image. From Eq. (1):

$$\begin{cases} p_x = \frac{u_C}{k_1} + x_I \\ p_y = -\frac{v_C}{k_2} + y_I \end{cases} \tag{8}$$

After taking the shoes-upper, the robot move to get the desired position (p_{xd}, p_{yd}) on the conveyor. When the moving is accomplished, the end-effector rotate an angle Ω:

$$\Omega = \alpha - \alpha_d - \theta_1 - \theta_2 \tag{9}$$

where α_d is desired oriented angle of the reference shoes-upper on the conveyor.

2.4 Dynamics of SCARA Robot

Dynamic equations of SCARA robot is determined using Lagrangian method. Firstly, only two joints (θ_1, θ_2) change to take and move the shoes-upper, after that, the end-effector rotates independently, so it is able to consider the robot as a two link robot. Consider this model of SCARA robot contains 2 rods with masses *M1*, *M2* and length of rods are *L1*, *L2*. The mass of motor attached on the first link is *M3* and the motor and end-effector on second link is *M4* as Fig. 5.

TP1: consider 2 links as 2 homogeneous rods with masses *M1*, *M2* and length *L1*, *L2*.

TP2: 2 links are considered 2 point masses *M3*, *M4* attached on 2 rods without mass and have length *L1*, *L2*.

Lagrangian function is given as [4]:

$$L = K - P \tag{10}$$

where *L*: Lagrangian, *K*: the kinetic energy of body, *P*: the potential energy of body.

Lagrangian equation describes the dynamics of a link robot

$$\tau_i = \frac{d}{dt}\left(\frac{\partial L}{\partial \dot{\theta}_i}\right) - \frac{\partial L}{\partial \theta_i} \tag{11}$$

where τ_i is torque exerted on each joint, $i = 1, 2$.

While two joints moving, assume potential energy equals zero ($P = 0$; $L = K$).

The kinetic energy of each mass of SCARA robot [4]:

$$K_i = \frac{1}{2} M_i v_{Ci}^T v_{Ci} + \frac{1}{2} {}^i\omega_i^T {}^{Ci} I_i {}^i\omega_i, \quad i = 1...4 \tag{12}$$

where, v_{Ci}: the linear velocity at the center of mass *i*.

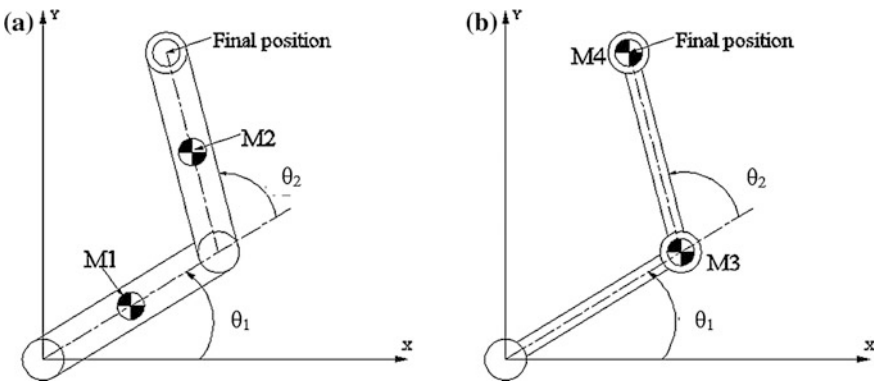

Fig. 5 The parts of SCARA robot

${}^{Ci}I_i$: the inertia tensor with respect to center of mass i.
ω_i: the angular velocity of the mass i.

The model of SCARA robot could be divided into 2 separated parts as follows
System TP1 with 2 homogeneous rods with masses M1, M2:

$$\begin{cases} \tau_{11} = \ddot{\theta}_1\left[M_2L_1^2 + \frac{1}{3}M_2L_2^2 + M_2L_1L_2c_2 + \frac{1}{3}M_1L_1^2\right] \\ \quad -\dot{\theta}_1\dot{\theta}_2M_2L_1L_2s_2 + \ddot{\theta}_2\left(\frac{1}{3}M_2L_2^2 + \frac{1}{2}M_2L_1L_2c_2\right) - \frac{1}{2}\dot{\theta}_2^2M_2L_1L_2s_2 \\ \tau_{21} = \ddot{\theta}_2\left(\frac{1}{3}M_2L_2^2\right) + \ddot{\theta}_1\left(\frac{1}{3}M_2L_2^2 + \frac{1}{2}M_2L_1L_2c_2\right) + \frac{1}{2}\dot{\theta}_1^2M_2L_1L_2s_2 \end{cases} \quad (13)$$

System TP2 contains 2 point masses M3, M4:

$$\begin{cases} \tau_{12} = \ddot{\theta}_1\left[M_3L_1^2 + M_4L_1^2 + 2M_4L_1L_2c_2 + M_4L_2^2\right] - 2\dot{\theta}_1\dot{\theta}_2M_4L_1L_2s_2 \\ \quad + \ddot{\theta}_2\left(M_4L_2^2 + M_4L_1L_2c_2\right) - \dot{\theta}_2^2m_4L_1L_2s_2 \\ \tau_{22} = \ddot{\theta}_1\left(M_4L_2^2 + M_4L_1L_2c_2\right) + \ddot{\theta}_2\left(M_4L_2^2\right) + \dot{\theta}_1^2M_4L_1L_2s_2 \end{cases} \quad (14)$$

The dynamic equations of SCARA robot are obtained as:

$$\begin{cases} \tau_1 = \tau_{11} + \tau_{12} \\ \tau_2 = \tau_{21} + \tau_{22} \end{cases} \quad (15)$$

3 Control Process

Consider the SCARA robot with dynamic equation given by [5] as follows:

$$M(\theta)\ddot{\theta} + V\left(\theta, \dot{\theta}\right) = \tau \quad (16)$$

where $\theta = [\theta_1, \theta_2]^T$.

And the following PD control law is given as shown in Fig. 6:

$$\tau = K_PE + K_D\dot{E} \quad (17)$$

where $E = \theta_d - \theta$; K_P, K_D are diagonal gain matrices and positive definite.

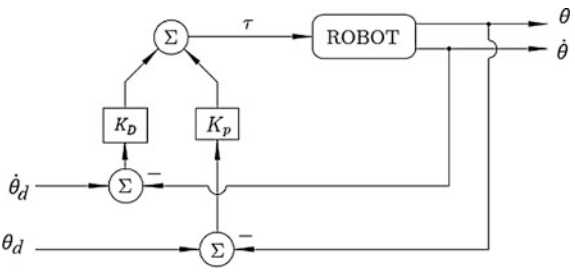

Fig. 6 Scheme of SCARA robot control

Using Lyapunov's method to proof the globally asymptotically stability of robot, a candidate Lyapunov function is chosen as [5]:

$$v = \frac{1}{2}\dot{\theta}^T M(\theta)\dot{\theta} + \frac{1}{2}E^T K_P E \tag{18}$$

The first derivative of Eq. (17) with respect to time is obtained as follows:

$$\begin{aligned} \dot{v} &= \dot{\theta}^T M(\theta)\ddot{\theta} + \frac{1}{2}\dot{\theta}^T \dot{M}(\theta)\dot{\theta} - \dot{\theta}^T K_p E \\ &= \dot{\theta}^T M(\theta)\ddot{\theta} + \frac{1}{2}\dot{\theta}^T \dot{M}(\theta)\dot{\theta} - \dot{\theta}^T \left[M(\theta)\ddot{\theta} + V\left(\theta, \dot{\theta}\right) + K_D\dot{\theta}\right] \end{aligned} \tag{19}$$

Hence

$$\dot{v} = \dot{\theta}^T \left[\frac{1}{2}\dot{M}(\theta) - V_m(\theta, \dot{\theta})\right]\dot{\theta} - \dot{\theta}^T K_D \dot{\theta} \tag{20}$$

where

$$\dot{\theta}^T \left[\frac{1}{2}\dot{M}(\theta) - V_m(\theta, \dot{\theta})\right]\dot{\theta} = 0 \tag{21}$$

From Eq. (21), Eq. (22) leads to:

$$\dot{v} = -\dot{\theta}^T K_D \dot{\theta} = -\dot{\theta}_1^2 K_{D1} - \dot{\theta}_2^2 K_{D2} < 0 (\forall \theta) \tag{22}$$

According to Lyapunov's method from Eqs. (18), (19) and (23), the system is globally stability.

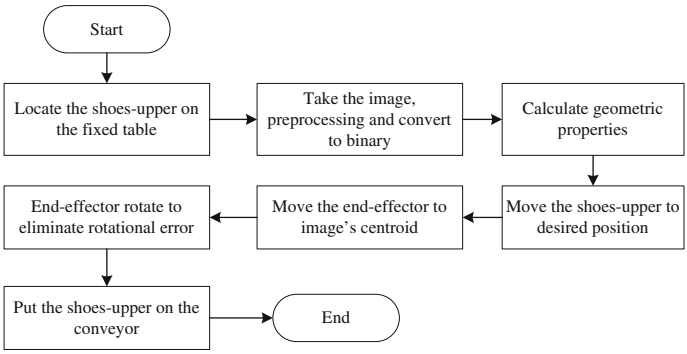

Fig. 7 Algorithm scheme of eliminating errors

The nonlinear differential equations of system are (Fig. 7):

$$\begin{bmatrix} \ddot{\theta}_1 \\ \ddot{\theta}_2 \end{bmatrix} = M(\theta)^{-1} \begin{bmatrix} K_{P1}(\theta_{1d} - \theta_1) - K_{D1}\dot{\theta}_1 \\ K_{P2}(\theta_{2d} - \theta_2) - K_{D2}\dot{\theta}_2 \end{bmatrix} - V\left(\theta, \ddot{\theta}\right) \tag{23}$$

$$\begin{cases} \tau_1 = K_{P1}(\theta_{1d} - \theta_1) - K_{D1}\dot{\theta}_1 \\ \tau_2 = K_{P2}(\theta_{2d} - \theta_2) - K_{D2}\dot{\theta}_2 \end{cases} \tag{24}$$

4 Simulation Results

The robot parameters: L1 = L2 = 0.5 m; M1 = M2 = M3 = M4 = 1 kg.

Images used to simulate: (1115 × 912) pixels.

Systematic parameters: $x_A = x_I = -650$ mm; $y_A = 500$ mm; $x_B = 650$ mm; $y_B = 500$ mm; $k_1 = 7.5$; $k_2 = 6.5$.

Desired centroid and oriented angle of the reference shoes-upper on the conveyor in global frame: $x_{Cr} = 720.7325$ mm; $y_{Cr} = 572.0748$ mm; $\alpha_{Cr} = 32.9706°$ (Figs. 8, 9, 10 and 11)

$$Kp_1 = 20;\ Kd_1 = 10;\ Kp_2 = 15;\ Kd_2 = 10.$$

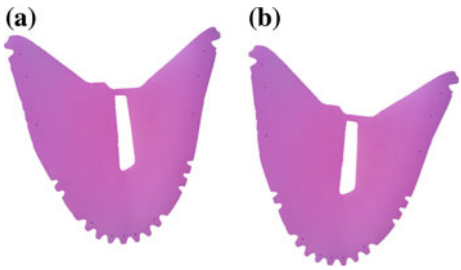

Fig. 8 Supplied image (**a**) and desired image (**b**) of shoes-upper

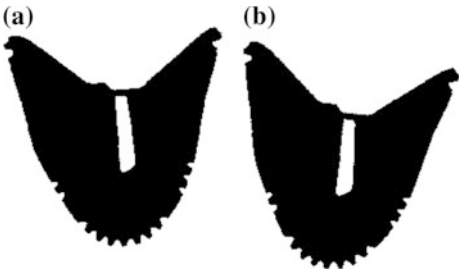

Fig. 9 Binary image of supplied shoes-upper's image before (**a**) and after simulation (**b**)

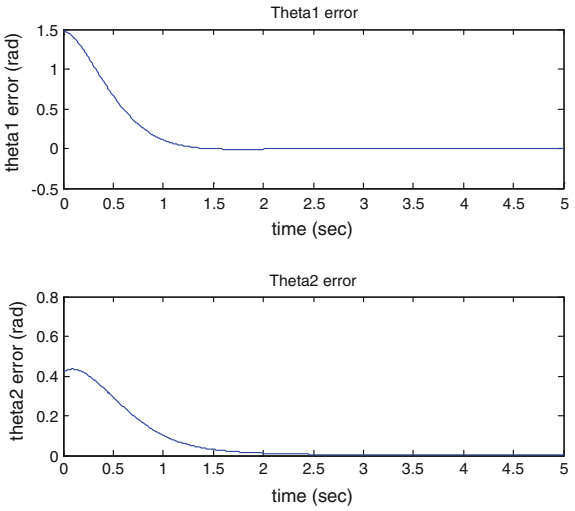

Fig. 10 Joints when end-effector move from original position to supplied image's centroid

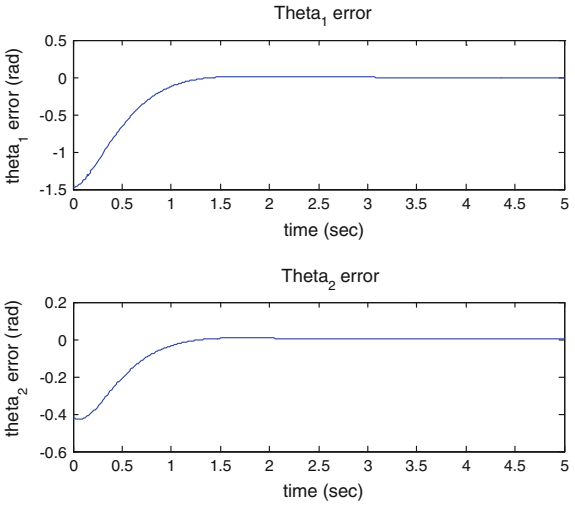

Fig. 11 Joints when end-effector move from supplied image's centroid to desired position

5 Conclusions

This paper introduced a precise position control of shoes-upper using image processing techniques and SCARA robot for the screen printing machine which is used to print the stripes on the shoes-upper. The inverse kinematic model of the SCARA robot was analyzed to control precise position of shoes-upper. And the kinetic model of the SCARA robot was analyzed to simulate the motion of end effector from the conveyor to the fixed table and return. The effectiveness of the proposed controller was proved through simulation results.

References

1. Bui TH, Phung TH (2014) Design and fabrication of precise shoe-upper feeder system for screen printing machine in shoe industry. In: Proceedings of the international conference on engineering mechanics and automation-ICEMA3, pp 213–220
2. Gross D, Hauger W, Schröder J, Wall WA, Rajapakse N (2009) Engineering mechanics 1 (Statics). Springer, Berlin
3. Burger W, Burge MJ (2009) Principles of digital image processing core algorithms. Springer, London
4. McKerrow PJ (1991) Introduction to robotics. Electronic systems engineering series. Addison-Wesley
5. Craig JJ (2005) Introduction to robotics. Prentice Hall
6. Niku SB (2001) Introduction to robotics: analysis, systems, applications. Prentice Hall

A Study on Controllers Design of a 3-Joint Carangiform Fish Robot in 3D Environment

Khac Anh Hoang, Van Anh Pham, Tan Tien Nguyen and Tuong Quan Vo

Abstract This paper proposes a dynamic analysis to control a 3-joint Carangiform fish robot to swim to the 3D environment by using Newton-Euler and Euler-Lagrange concepts. The fish robot is designed into two parts: the head of fish robot and the tail of fish robot. The tail of fish robot will be analyzed which is quite similar to the analysis of the dynamic model of the manipulator. By controlling the tail of fish robot with respect to the desired profiles and controlling the changing central system, the fish robot can be controlled in the 3D environment. To simplify, the motions of fish robot are assumed to consist of two main motions: the movement of fish robot on the horizontal plane and movement of fish robot to the desired depth. The Fuzzy controller is designed to control the centroid displacements system. The Adaptive Back Stepping controller is developed to control the tail of fish robot.

Keywords Fish robot · Dynamic model · Manipulator · Back stepping controller · Fuzzy controller

1 Introduction

Recently, the research directions on robotic fish has strongly developed and achieved many accomplishments. J. Edward Colgate and Kevin M. Lynch presented a review about mechanics and control of swimming for the fish robot [1]. The most of the fish robots are developed based on the Carangiform type because of its flexibility and easiness in control. Normally, the Carangiform fish robot is designed with 2-joint, 3-joint or 4-joint. Motomu Nakashima et al. described a numerical and experimental study of a 2-jointed fish robot and using self-excitation

K.A. Hoang · V.A. Pham · T.T. Nguyen · T.Q. Vo (✉)
Faculty of Mechanical Engineering, HCM City University of Technology,
VNU-HCM, Ho Chi Minh City, Vietnam
e-mail: vtquan@hcmut.edu.vn

V.H. Duy et al. (eds.), *AETA 2015: Recent Advances in Electrical Engineering and Related Sciences*, Lecture Notes in Electrical Engineering 371,
DOI 10.1007/978-3-319-27247-4_66

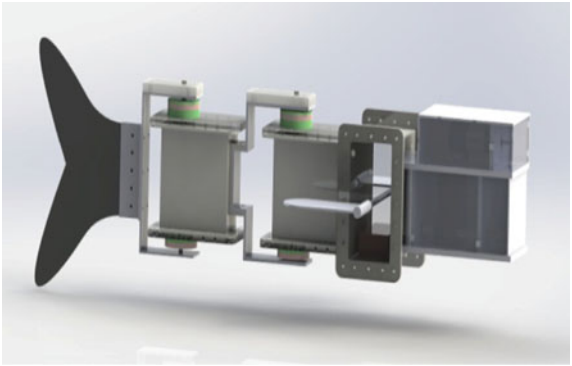

Fig. 1 Structure of 3-Joint carangiform fish robot

[2]. QinYan et al. developed a Carangiform robotic fish with 4-joint of tail, they considered the influences of characteristic parameters including the frequency, the amplitude, the wave length, the phase difference and the coefficient on forward velocity [3]. The design and control of fish robot swim like real fish by using the continuous structures instead of discrete. That is the important contributions of [4]. Feitian Zhang el al. developed the fish robot which was combined by the strengths of both underwater gliders and robotic fish and established a dynamic model of robot [5]. Michail Makrodimitris el al. researched the method depth control for robotic fish. By using small dc pump, the depth system dynamic and controller are developed. Though experiment, they expected the low-cost and energy-efficient small underwater vehicles [6].

In this paper, a new method of modeling the dynamics of this fish robot is presented. The design concept is the combination of dynamic of AUVs (Autonomous Underwater Vehicles) and dynamic of manipulator. Then, the design of the controllers will be discussed. These controllers help the fish robot swim to the desired angles. Because the model system is a nonlinear system, the intelligent controllers or nonlinear controllers are required to control the robot to meet the desired requirements. The Fuzzy controller, which is an intelligent controller, will be controlled the pitch angle. And, the Adaptive Back Stepping controller, which is a nonlinear controller, is developed to control the tail of fish robot. Thereby, the yaw angle will be controlled. Then, some simulation results are introduced to prove the effectiveness and feasibility of our proposed methods (Fig. 1).

2 Fish Robot Modeling

With the simple design, the fish robot has 3-Joint and head part. The tail of fish robot is combined by 2 active joint and 1 passive joint. The structure of our fish robot is described in Fig. 2. The fish robot moves in horizontal plane by the caudal part's oscillations. This caudal part's oscillation will generate the propulsion force

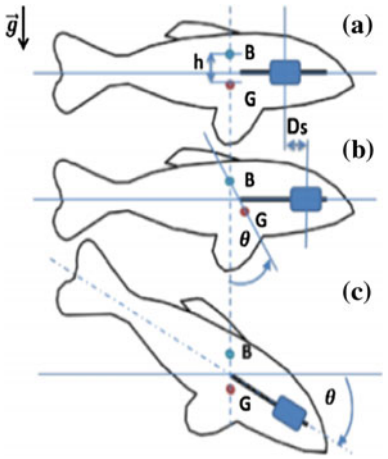

Fig. 2 The method depth control for fish robot [10]

that make fish robot swim forward. The centroid displacements system is a simple system which is combined the mass (m), guide screw DC servo motor (Table 1).

The idea of dynamic is developed by Newton-Euler function and dynamic of robot manipulator. The equations of motion of head robotic fish are nonlinear function and it is described by Eq. (1) [7]:

$$M^{*}n + C(n) + D(n)n + g(\eta) = T \tag{1}$$

where, M^{*}—Inertia matrix; $C(n)$—Coriolis and Centripetal matrix; $D(n)$—Damping matrix; $g(\eta)$—The resultant vector of gravity and buoyancy; T—total forces and moments are acting on the vehicle with respect to the body-fixed coordinates; $n = [u\, v\, w\, p\, q\, r]^{T}$; n—The translational and rotational velocities in body-fixed coordinates.

Equation (1) is the equations of motion of head robotic fish in six degrees of freedom with body-fixed coordinates. The relation of translational velocities between body-fixed and earth-fixed coordinates is show in [7].

Table 1 The control parameters for fish robot

DOFs	Motions & rotation	Linear & angular velocities	Position & euler angles (Earth-fixed coordinates)
1	Surge	u	x
2	Sway	v	y
3	Heave	w	z
4	Roll	p	ϕ
5	Pitch	q	θ
6	Yaw	r	ψ

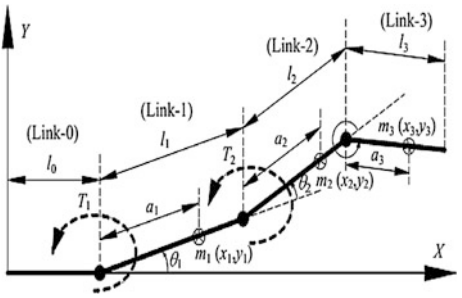

Fig. 3 Fish robot analytical model [8]

The forces exerting on fish robot are created by the tail of fish robot. The value of forces is depended on the frequency and amplitude of tail. They are presented in [8]. F_V is the inertial fluid force and F_J is lift force on the tail fin. F_F is the thrust force component at tail fin, F_C is lateral force component at tail fin and F_D is the drag force. Based on [3, 8] the equations of forces are described in Eqs. (2) and (3).

$$F_v = \pi\rho LC^2\dot{U}\sin\alpha + \pi\rho \mathrm{LC}^2\underline{\alpha}\mathrm{U}\cos\alpha \tag{2}$$

$$F_J = 2\pi\rho LCU^2\sin\alpha\cos\alpha \tag{3}$$

$$F_F = F_{FV} - F_{FJ} = (F_V - F_J)\sin(\theta_1 + \theta_2 - \theta_3) \tag{4}$$

$$F_C = F_{CV} - F_{CJ} = (F_V - F_J)\cos(\theta_1 + \theta_2 - \theta_3) \tag{5}$$

where, L is the span of the tail fin, ρ is the water density, U is relative velocity at the center of the fin, α is the attack angle and $2C$ is the chord length. θ_i (i = 1, 2, 3) is horizontal rotated angle at the joints. The tail of fish robot can be modeled as a three link system. It is shown in Fig. 3. To like the aim robot system, the model must have spring k_1 at the first joint, spring k_2 at the second joint and k_3 at the final joint. The c_1, c_2 and c_3 are the damping coefficients at center of link. The Euler-Lagrange equation is applied for the tail of fish robot. The generalized forces include the moment of actuator and the moment is caused by F_F and F_C, because the tail of fish

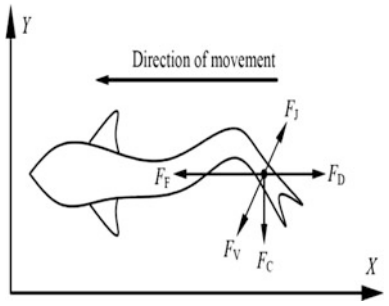

Fig. 4 Forces distribution on fish robot [8]

robot only moves in Oxy plane. The equation of the three links is written as follows (Fig. 4):

$$\begin{bmatrix} M_{11} & M_{12} & M_{13} \\ M_{21} & M_{22} & M_{23} \\ M_{31} & M_{32} & M_{33} \end{bmatrix} \begin{bmatrix} \ddot{\theta}_1 \\ \ddot{\theta}_2 \\ \ddot{\theta}_3 \end{bmatrix} = \begin{bmatrix} N_1 \\ N_2 \\ N_3 \end{bmatrix} + \begin{bmatrix} P_1 \\ P_2 \\ P_3 \end{bmatrix} \tag{6}$$

The details of M_{ij} and N_i are described in [8] ($i, j = 1, 2, 3$). P_i is the moment of actuator at the joint ($i = 1, 2, 3$). By using have the angle variables (θ_i ($i = 1, 2, 3$)), F_F and F_C are calculated. Based on Eq. (1), the motion of equation is presented in Eq. (7):

$$\begin{cases} m\left[\dot{u} - vr + wq - x_g(q^2 + r^2) + y_g(-\dot{r}) + z_g(\dot{q})\right] = \sum X_{ext} \\ m\left[\dot{v} + ur - y_g(r^2) + z_g(qr) + x_g(\dot{r})\right] = \sum Y_{ext} \\ m\left[\dot{w} - uq - z_g q^2 - x_g\dot{q} + y_g rq\right] = \sum Z_{ext} \\ I_{yy}\dot{q} + m\left[z_g(\dot{u} - vr + wq) - x_g(\dot{w} - uq)\right] = \sum M_{ext} \\ I_{zz}\dot{r} + m\left[x_g(\dot{v} + ur) - y_g(\dot{u} - vr + wq)\right] = \sum N_{ext} \end{cases} \tag{7}$$

where, m-the mass of robot; (x_g, y_g, z_g)—The central coordinates of central of fish robot in body-fixed coordinate; I_{zz}, I_{yy} *and* I_{xx}—the moment of inertia according to Oz axis, Oy axis and Ox axis; $\sum X_{ext}$—The sum of forces along the Ox axis; $\sum Y_{ext}$—The sum of forces along the Oy axis; $\sum Z_{ext}$—The sum of forces along the Oz axis; $\sum N_{ext}$—The sum of moments according to the Oz axis; $\sum M_{ext}$—The sum of moments according to the Oy axis.

3 Controllers Design

In this section, the controllers for the fish robot are designed. The centroid displacement system is controlled by the Fuzzy controller and Adaptive Back Stepping controller controls the tail of the fish robot. With the desired profiles, the tail of the fish robot can create forces and moment to control the robot. Because the tail acts as the robot manipulator system, so each joint will have the dedicated controller.

3.1 Fuzzy Controller

In reality, Fuzzy logic controller is used to control many systems including linear and nonlinear ones. This is the intelligent controller which is not depended on the dynamic of the system that it will control. But it is depended by the experience of programmer. The Fuzzy controller has two inputs (the error of pitch angle (e) and

Table 2 Fuzzy rules for L1

L1	ec							
e		NB	NM	NS	ZE	PS	PM	PB
	NB	PB	PB	PM	PS	PS	ZE	ZE
	NM	PB	PB	PM	PS	PS	ZE	NS
	NS	PM	PM	PM	PS	ZE	NS	NS
	ZE	PM	PM	PS	NS	NS	NM	NM
	PS	PS	PS	ZE	NS	NS	NM	NM
	PM	PS	ZE	NS	NM	NM	NM	NB
	PB	PB	PB	PB	NM	NM	NB	NB

the rate of the change of error of pitch angle (ec)) and one output (L1—location of mass). The triangle membership function is used for input and output variables. The defuzzification method chosen is COG. The fuzzy variables and the rule for Fuzzy controller are defined:

e (the error) = {NB (Negative Big), NM (Negative Medium), NS (Negative Small), ZE (Zero), PS (Positive Small), PM (Positive Medium), PB (Positive Big)}.

ec (the change of error) = NB (Negative Big), NM (Negative Medium), NS (Negative Small), ZE (Zero), PS (Positive Small), PM (Positive Medium), PB (Positive Big)}.

L1 (location of mass) = {NB (Negative Big), NM (Negative Medium), NS (Negative Small), ZE (Zero), PS (Positive Small), PM (Positive Medium), PB (Positive Big)} (Table 2).

3.2 Adaptive Back Stepping Controller

Back Stepping controller is one of the nonlinear controllers that is used for the trajectory following control problem. Based on [9], the Adaptive Back Stepping controller is designed to control tail of robot. Equation (6) can be written to Eq. (8):

$$M\ddot{\theta} = N + P \tag{8}$$

where, $M = \begin{bmatrix} M_{11} & M_{12} & M_{13} \\ M_{21} & M_{22} & M_{23} \\ M_{31} & M_{32} & M_{33} \end{bmatrix}; \ddot{\theta} = \begin{bmatrix} \ddot{\theta}_1 \\ \ddot{\theta}_2 \\ \ddot{\theta}_3 \end{bmatrix}; N = \begin{bmatrix} N_1 \\ N_2 \\ N_3 \end{bmatrix}; P = \begin{bmatrix} P_1 \\ P_2 \\ P_3 \end{bmatrix}$

Now, the followings are defined: $H = -M^{-1}N; s_1 = \theta; s_2 = \dot{\theta}$. Then, Eq. (8) becomes:

$$\begin{cases} \dot{s}_1 = s_2 \\ M(\dot{s}_2 + H) = P \end{cases} \tag{9}$$

Define: $e_1 = \theta_{ref} - s_1; e_2 = \omega_{ref} - s_2; \omega_{ref} = \varepsilon_1 e_1 + \dot{\theta}_{ref}$

$$\dot{e}_2 = \left(-\varepsilon_1^2 e_1 + e_2\varepsilon_1 + \ddot{\theta}_{ref}\right) - M^{-1}P + H \tag{10}$$

With ε_1 and ε_2 are the positive constants. θ_{ref} is the reference angle matrix at the joints. Based on Eq. (10) the control input is chosen:

$$P = \hat{M}\left(\left(1-\varepsilon_1^2\right)e_1 + e_2(\varepsilon_1+\varepsilon_2) + \ddot{\theta}_{ref} + \hat{H}\right) \tag{11}$$

In Eq. (11), $\hat{M}$ and $\hat{H}$ are the estimated functions matrix of M and H functions matrix. The errors of the estimate functions are defined as:

$$\bar{M} = M - \hat{M}; \bar{H} = H - \hat{H}$$

By substituting Eq. (11) into Eq. (10):

$$\dot{e}_2 = -e_1 - e_2\varepsilon_2 + M^{-1}\bar{M}\left(\left(1-\varepsilon_1^2\right)e_1 + e_2(\varepsilon_1+\varepsilon_2) + \ddot{\theta}_{ref} + \hat{H}\right) + \bar{H} \tag{12}$$

The estimated functions are found by using the Lyapunov function.

$$V = \frac{1}{2}e_1^T e_1 + \frac{1}{2}e_2^T e_2 + \frac{M^{-1^T}}{2}\bar{M}^T\bar{M} + \frac{1}{2}\bar{H}^T\bar{H} \tag{13}$$

The time derivative of V is presented in Eq. (13):

$$\dot{V} = e_1^T\dot{e}_1 + e_2^T\dot{e}_2 + M^{-1^T}\bar{M}^T\left(-\frac{d}{dt}\hat{M}\right) + \bar{H}^T\left(-\frac{d}{dt}\hat{H}\right) \tag{14}$$

Substituting Eq. (12) into Eq. (14):

$$\begin{aligned}\dot{V} &= -\varepsilon_1 e_1^T e_1 - \varepsilon_2 e_2^T e_2 \\ &+ (M^{-1}\bar{M})^T\left[e_2\left(\left(1-\varepsilon_1^2\right)e_1 + e_2(\varepsilon_1+\varepsilon_2) + \ddot{\theta}_{ref} + \hat{H}\right) - \frac{d}{dt}\hat{M}\right] \\ &+ \bar{H}^T\left[e_2 - \frac{d}{dt}\hat{H}\right]\end{aligned} \tag{15}$$

Our purpose is $\dot{V} < 0$ so the estimated functions can be chosen as:

$$\frac{d\hat{M}}{dt} = e_2\left(\left(1-\varepsilon_1^2\right)e_1 + e_2(\varepsilon_1+\varepsilon_2) + \ddot{\theta}_{ref} + \hat{H}\right); \frac{d\hat{H}}{dt} = e_2$$

Meanwhile: $\dot{V} = -\varepsilon_1 e_1^T e_1 - \varepsilon_2 e_2^T e_2 < 0$. Now, the dynamic of tail system is stable.

Table 3 Parameters of fish robot

$I_{xx} = 0.01304$ (m^4)	$m_1 = 0.354$ (kg)	$a_2 = 0.035$ (m)
$I_{yy} = 0.3722$ (m^4)	$l_1 = 0.167$ (m)	$c_2 = 8 \times 10^{-2}$
$I_{zz} = 0.271$ (m^4)	$a_1 = 0.115$ (m)	$k_2 = 2 \times 10^{-2}$
$m_0 = 1.54$ kg	$c_1 = 12 \times 10^{-2}$	$i_3 = 0.0215$ (m^4)
$\rho = 998$ kg/m^3	$k_1 = 6.9 \times 10^{-2}$	$m_3 = 0.05$ kg
$C_D = 0.5$	$i_2 = 0.195$ (m^4)	$a_3 = 0.1$ (m)
$S_X = 0.021$ (m^2)	$m_2 = 0.06$ kg	$c_3 = 2 \times 10^{-2}$
$i_1 = 0.813$ (m^4)	$l_2 = 0.088$ (m)	$k_3 = 25 \times 10^{-2}$

4 Simulation Results

The simulations are carried out which is based on the equation of fish robot as introduced in Sect. 2. In this section, Fuzzy controller and Adaptive Back Stepping controller, which are showed in Sect. 3, are used to operate the yaw angle and pitch angle of fish robot. The desired yaw angle is 60° and the desired pitch angle is 30°. The sin profiles of tail of the fish robot are as follows:

$$\theta_{1ref} = D + A_1 \sin(2\pi f_1 t + \varphi_1); \theta_{2ref} = D + A_2 \sin(2\pi f_2 t + \varphi_2)$$

where, θ_{1ref} is desired angle of first-joint, θ_{2ref} is desired angle of second-joint, D are the desired yaw angle of robot with $D = -K_p erroryaw$; K_P is the rate factor; *erroryaw* is the error of yaw angle of robotic fish. A_1 and A_2 are the amplitude of sin profiles of tail. f_1 *and* f_2 are the frequency of sin wave; φ_1 *and* φ_2 are the phase angles (Table 3).

Choose: $K_P = 1; A_1 = A_2 = 0.0873 rad, f_1 = f_2 = 0.5\text{Hz}, \varphi_1 = -\pi/12; \varphi_2 = \pi/12$

Parameters of Back Stepping controller: $\varepsilon_1 = \begin{bmatrix} 2 \\ 5 \end{bmatrix}; \varepsilon_2 = \begin{bmatrix} 2 \\ 9 \end{bmatrix}$

The response of yaw angle is introduced in Fig. 5. Base on Fig. 5, the response takes about 40 s to control fish robot to the desired yaw angle. The yaw angle is oscillated quite strong at the beginning time but it gradually stable at about 4 s. When fish robot swims to the desired yaw angle of 60°, the fish robot's yaw angle

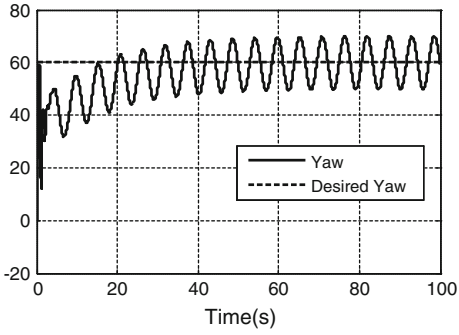

Fig. 5 The yaw angle of robotic fish (Degree)

still has small oscillations with amplitude about ±10°. Whole body still has some light oscillations which are similar to the real fish. The Figs. 6, 7 and 8 show the angle variables of tail of robot in the body-coordinate.

Using Fuzzy controller, the response of pitch angle is showed in the Fig. 9, it takes about 20 s to control fish robot to the desired pitch angle of 30°. The pitch angle is oscillated with decreasing amplitude but it gradually stable at about 18 s. The Fig. 10 shows the location of mass of the centroid displacement system, it has the length about 0.1 m. The position of fish robot is introduced in the Figs. 11 and 12.

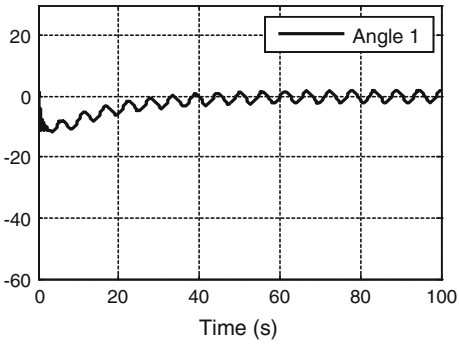

Fig. 6 θ_1 angle (Degree)

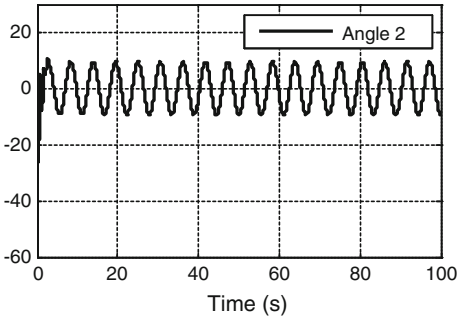

Fig. 7 θ_2 angle (Degree)

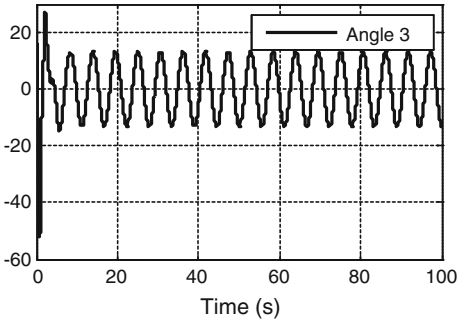

Fig. 8 θ_3 angle (Degree)

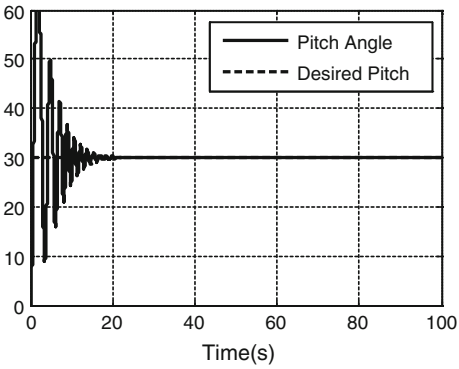

Fig. 9 The pitch angle of robotic fish (Degree)

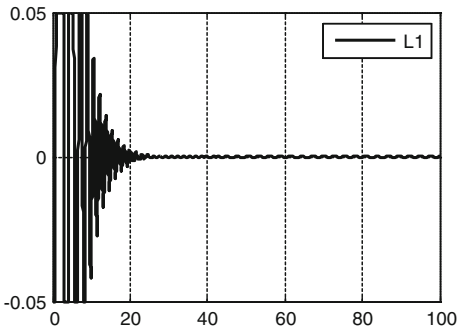

Fig. 10 The L1 distance (m)

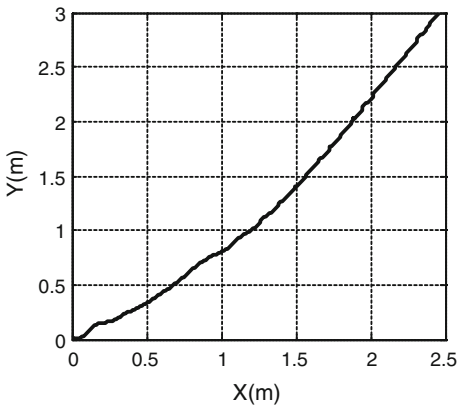

Fig. 11 The trajectory of robotic fish in Oxy

5 Conclusion

In this paper, the dynamic equation of a 3-joint Carangiform fish robot is introduced. Then, based on the dynamic equation of the fish robot, the Fuzzy controller and Adaptive Back Stepping controllers are designed to control fish robot moving

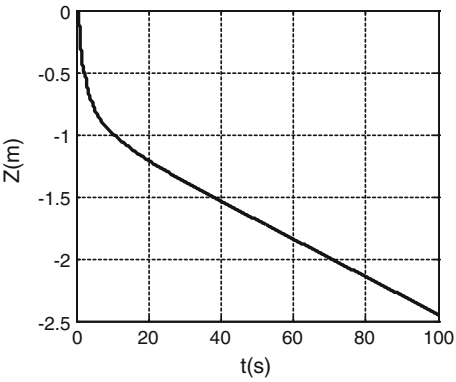

Fig. 12 The depth value of robotic fish

in Oxy and Oxz planes. The simulation results for Fuzzy, Adaptive Back Stepping controllers to following the desired yaw and pitch angles. The fish robot's yaw angle has small oscillations with amplitude about $\pm 10°$. Whole body still has some oscillations which are similar to the real fish.

Acknowledgments This research is funded by the Ho Chi Minh City University of Technology, Vietnam under grant number TNCS-CK-2015-13.

References

1. Colgate JE, Lynch KM (2004) IEEE mechanics and control of swimming: a review. IEEE J Oceanic Eng 29(3)
2. Motomu N, Norifumi O, Kyosuke ONO (2003) A study on the propulsive mechanism of a double joint fish robot utilizing self-excitation control. JSME Int J Series C 46(3)
3. Yan Q, Han Z, Zhang S-W, Yang J (2008) Parametric research of experiments on a carangiform robotic fish. J Bionic Eng 5
4. Daou HEL, Salumäe T, Ristolainen A, Toming G, Listak M, Kruusmaa M (2011) A Bio-mimetic design and control of a fish-like robot using compliant structures. In: The 15th International Conference on Advanced Robotics Tallinn University of Technology Tallinn, Estonia, June 20–23, 2011
5. Zhang F, Thon J, Thon C, Tan X (2012) Miniature underwater glider: design, modeling, and experimental results. In: 2012 IEEE International Conference on Robotics and Automation RiverCentre, Saint Paul, Minnesota, USA, May 14–18, 2012
6. Makrodimitris M, Aliprantis I, Papadopoulos E (2014) Design and implementation of a low cost, pump-based, depth control of a small robotic fish. In: 2014 IEEE/RSJ International Conference on Intelligent Robots and Systems (IROS 2014) September 14–18, 2014, Chicago, IL, USA
7. Fjellstad O-E (1994) Control of unmanned underwater vehicles in six degrees of freedom a quaternion feedback approach. Dr. Ing Thesis, Department of Engineering Cybernetics, The Norwegian Institute of Technology, University of Trondheim, November 1994
8. Vo TQ, Kim HS, Lee BR (2009) Propulsive velocity optimization of 3-Joint fish robot using genetic-hill climbing algorithm. J Bionic Eng 6:415–429

9. Rudra S, Barai RK (2012) Robust adaptive backstepping control of inverted pendulum on cart system. Int J Control Autom 5(1)
10. Alessi A, Sudano A, Accola D, Guglielmelli E (2012) Development of an autonomous robotic fish. In: The Fourth IEEE RAS/EMBS International Conference on Biomedical Robotics and Biomechatronics, Roma, Italy. June24–27, 2012
11. Vo TQ, Kim HS, Lee BR (2012) Smooth gait optimization of a fish robot using the genetic-hill climbing algorithm. Robot J 30:257–278
12. Vo TQ, Nguyen TT, Tran TP, Lee BR (2010) Turning motion control of a 3-Joint carangiform fish robot using sliding mode and fuzzy sliding controllers. In: The 11st Asia Pacific Industrial Engineering and Management Systems Conference, Melaka Malaysia, 7–10 December 2010

Decentralized Motion Control for Omnidirectional Mobile Platform—Tracking a Trajectory Using PD Fuzzy Controller

Thanh Luan Bui

Abstract The development of intelligent mobile robot has become an important and active research topic in the face of emerging markets for autonomous guided vehicle and service mobile robot. In this paper, a new decentralized algorithm for motion control of omnidirectional mobile platform (OMP) with three sets of omnidirectional wheel is introduced. The proposed OMP is a platform with three sets of omnidirectional wheel arranged equally spaced at 120° from one to another. In this decentralized algorithm, the motion of OMP is separated into three independent components of motion expressed in body coordinate frame including rotational moving, horizontal moving and vertical moving. By using omnidirectional wheels, these motion components can be controlled simultaneously as well as separately. The OMP uses a laser-based sensor for recognizing its position and orientation. Based on the proposed decentralized algorithm and OMP's configuration measured by laser sensor, a trajectory tracking control method using fuzzy logic is applied to control the OMP. The use of fuzzy logic for control law makes the proposed system insensitive to parametric uncertainty, load and parameter fluctuations, while guaranteeing stability. The effectiveness of the proposed system is demonstrated by simulation and experimental results.

Keywords Omnidirectional mobile platform · Omnidirectional wheels · 3 wheels · Trajectory tracking · Fuzzy control

1 Introduction

Research interest in mobile robots has been tremendous in the past few years. High mobility of mobile robot in industries is needed when the robot does some special works on the narrow space. Among many types of the mobile robots, the OMP,

T.L. Bui (✉)
Faculty of Mechanical Electrical and Electronic Engineering, Hutech University, Ho Chi Minh City, Vietnam
e-mail: buithanhluan@gmail.com

V.H. Duy et al. (eds.), *AETA 2015: Recent Advances in Electrical Engineering and Related Sciences*, Lecture Notes in Electrical Engineering 371,
DOI 10.1007/978-3-319-27247-4_67

which is considered as holonomic parallel system, has 3 degrees of freedom in the horizontal motion plane. Thus, it can fully use the null space motions in cabined work environment. Generally, it has more advantages than the nonholomic differential-driven platform which is provided with only two independent driving inputs. The OMP is a platform with three or more than three sets of omnidirectional wheel. In this paper, the proposed OMP with three sets of omnidirectional wheel arranged equally spaced at 120° from one to another is considered.

There are many researches on dynamic modeling [1, 2], control method [3, 4] and time-optimal movement [5, 6] of OMP. Han et al. [3] proposed a holonomic and omnidirectional mobile robot platform using active dual-wheel caster assembly mechanisms. In this paper, they used feedback control system based on a resolved velocity control system for the robot. Huang et al. [7] proposed an adaptive robust controller to achieve trajectory tracking and path following for an omnidirectional mobile platform incorporated with two uncertain motors parameters in polar coordinates. In another paper, Huang et al. [8] also proposed a simultaneous point stabilization and trajectory tracking method using backstepping for an omnidirectional mobile platform with parameter variations and the uncertainties from friction and slip. Dinh et al. [9] introduced a tracking control method for OMP with disturbance using differential sliding mode controller. Nguyen et al. [10] proposed the OMP controller for trajectory tracking problem using integral sliding mode controller. With the main advantages of a sliding mode control (SMC) such as fast response and strong robustness against the system with uncertainties and external disturbances, several studies using an SMC have been done for wheeled mobile robots. However, their controller normally is based on dynamic modeling. Kim et al. [11] presented trajectory control method of 3 wheels omnidirectional mobile robot using fuzzy azimuth estimator but they only presented experiment a tracking control move some angle without self-rotation. Liu et al. [12] proposed a nonlinear controller based on trajectory linearization to improve the path following. Watanabe et al. [13] presented a PI feedback control method for an omnidirectional mobile platform which is equipped with three lateral orthogonal-wheel assemblies. Wong et al. [14] proposed to design a fuzzy system to control an omnidirectional mobile robot based on Genetic Algorithms method. Sharbafi et al. [15] proposed controller based on the brain-emotional-learning algorithm, which was inspired from a computational model of limbic system in the mammalian brain. The brain-emotional-learning-based intelligent controller with quadratic reward, comparable to linear-quadratic-regulator control, was used for an omnidirectional robot. However, they presented only simulation results. Xu et al. [16] proposed the robust neural network-based sliding mode method for trajectory tracking control of the omnidirectional mobile manipulator with three castor wheels.

It is said that the OMP has closed-chain mechanism with redundant actuation. The redundant actuation provides an effective means for eliminating singularities and improving the performance. However, a major difficulty, which prevents vast control strategies from applying in redundant actuated system, is the lack of an efficient dynamic model and control method. Most of previous papers mentioned above only considered the OMP's motion control in global coordinate, and their

controllers was too much complicated and difficult to apply to a real system. Furthermore, some of previous controllers were based on dynamic modeling of OMP [3, 7–10, 17]. Therefore, they were sensitive with parameter uncertainty, load and parameter fluctuations.

To overcome these problems, a new decentralized algorithm for motion control of OMP is introduced in this paper. The decentralized algorithm is expressed in body coordinate frame. In this decentralized algorithm, the motion of OMP is separated into three independent components of motion including rotational moving, horizontal moving and vertical moving. Because these components in body coordinate frame are independent, they can be controlled simultaneously as well as separately. The motion of OMP can be controlled in pure horizontal moving mode, pure vertical moving mode, or pure rational moving mode. If horizontal moving and vertical moving are combined, a pure translation moving in any direction can be obtained. If three components of motion are applied simultaneously, translation and rotation can be obtained simultaneously. The new decentralized algorithm makes motion control of OMP become simple, flexible and effective. To apply this algorithm, the position and orientation of OMP should be measured in global coordinate. The OMP is equipped with a laser-based localization sensor, SICK NAV200, to measure the position and orientation of OMP. Based on the proposed decentralized algorithm, a trajectory tracking control method using fuzzy logic is proposed to control the OMP. This fuzzy controller is based on the kinematic modeling of OMP. The use of fuzzy logic for control law makes the proposed system insensitive to parametric uncertainty, load and parameter fluctuations, while guaranteeing stability. In comparison with previous tracking control algorithms, the fuzzy controller is simpler to apply and independent on accurate mathematical model of the controlled object. The effectiveness of the proposed system is demonstrated by experimental results.

This paper is organized as follows: In Sect. 2, modeling and decentralized algorithm for motion control of OMP are presented. In Sect. 3, trajectory tracking controller design is proposed. In this section, the PD fuzzy controller for trajectory tracking of OMP based on the proposed decentralized algorithm is designed. In Sect. 4, the description of the OMP and controller system are shown. Section 5 shows the simulation and experimental results of the trajectory tracking control using PD fuzzy controller based on the proposed decentralized algorithm. Finally, conclusions are presented in Sect. 6.

2 Modeling and Decentralized Algorithm for Motion Control of OMP

2.1 OMP Modeling

Figure 1 shows configuration for geometric model of the OMP. The center of geometry of OMP is denoted by C. *Oxy* represents the global coordinate frame in

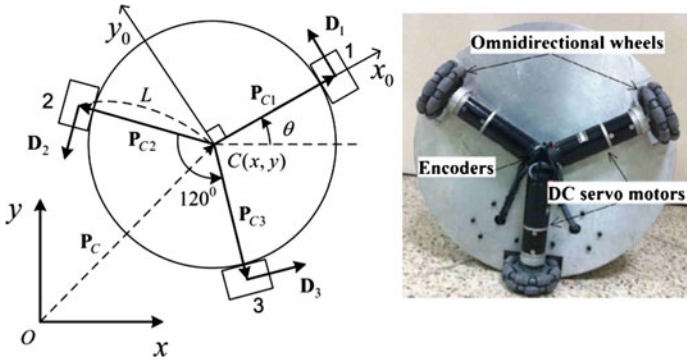

Fig. 1 Configuration of geometric model of the OMP

the workspace and Cx_0y_0 denotes the body coordinate frame attached to the robot body. Cx_0—*axis* is aligned to the wheel 1. θ is angle between the x_0—*axis* and Cx_0—*axis*. The three omnidirectional wheels have the same radius denoted by r and are driven by three DC motors. L is the distance from wheel's center to the center of geometry, C.

Each of the omnidirectional wheel assembly consists of a pair of "orthogonal wheels": one wheel in active direction (the propelling direction of the actuator) and another wheel in passive direction (free-wheeling).

For modeling the OMP, the assumptions are given as follows:

- The omnidirectional wheels move with pure rolling and no slipping.
- Each link is rigid.

The rotation matrix $\mathbf{R}_1(\theta)$ from the body coordinate frame to the global coordinate frame is given by:

$$\mathbf{R}_1(\theta) = \begin{bmatrix} \cos(\theta) & -\sin(\theta) \\ \sin(\theta) & \cos(\theta) \end{bmatrix} \tag{1}$$

The position vector of each wheel with respect to the body coordinate frame, $\mathbf{P}_{Ci}(i = 1,\ 2,\ 3)$, are given with the help of the rotation matrix as follows.

$$\begin{aligned} &\mathbf{P}_{C1} = L\begin{bmatrix} 1 \\ 0 \end{bmatrix}, \quad \mathbf{P}_{C2} = \mathbf{R}_1(\frac{2\pi}{3}) \times \mathbf{P}_{C1} = \frac{L}{2}\begin{bmatrix} -1 \\ \sqrt{3} \end{bmatrix}, \\ &\mathbf{P}_{C3} = \mathbf{R}_1(\frac{4\pi}{3}) \times \mathbf{P}_{C1} = -\frac{L}{2}\begin{bmatrix} 1 \\ \sqrt{3} \end{bmatrix} \end{aligned} \tag{2}$$

Similarly, the unit vectors with respect to the body coordinate frame, $\mathbf{D}_i(i = 1,\ 2,\ 3)$, that specify the drive direction vector of each wheel are given by:

$$\mathbf{D}_i = \frac{1}{L}\mathbf{R}_1\left(\frac{\pi}{2}\right) \times \mathbf{P}_{Ci},\ \mathbf{D}_1 = \begin{bmatrix} 0 \\ 1 \end{bmatrix},\ \mathbf{D}_2 = -\frac{1}{2}\begin{bmatrix} \sqrt{3} \\ 1 \end{bmatrix},\ \mathbf{D}_3 = \frac{1}{2}\begin{bmatrix} \sqrt{3} \\ -1 \end{bmatrix} \tag{3}$$

The configuration of the OMP in the global coordinate frame is specified by the posture vector $\mathbf{q} = [x \quad y \quad \theta]^T$. $\mathbf{P}_C = [x \quad y]^T$ is defined as the position vector of point C with respect to the global coordinate frame.

The positions vector, $\mathbf{P}_i$, and linear velocity vector, $\mathbf{v}_i = \dot{\mathbf{P}}_i$ of OMP's wheels with respect to global coordinate frame are given by:

$$\mathbf{P}_i = \mathbf{P}_C + \mathbf{R}_1(\theta)\mathbf{P}_{Ci} \tag{4}$$

$$\mathbf{v}_i = \dot{\mathbf{P}}_C + \dot{\mathbf{R}}_1(\theta)\mathbf{P}_{Ci} \tag{5}$$

The angular velocity of wheel $i(i = 1,\ 2,\ 3)$ can be expressed as:

$$\omega_i = \frac{1}{r}\mathbf{v}_i^T\mathbf{R}_1(\theta)\mathbf{D}_i \tag{6}$$

Substituting $\mathbf{v}_i$ in Eq. (5) into Eq. (6) yields:

$$\omega_i = \frac{1}{r}\left[\dot{\mathbf{P}}_C^T\mathbf{R}_1(\theta)\mathbf{D}_i + \mathbf{P}_{Ci}^T\dot{\mathbf{R}}_1^T(\theta)\mathbf{R}_1(\theta)\mathbf{D}_i\right] \tag{7}$$

Angular velocity vector for three OMP's wheels is denoted by $\boldsymbol{\omega} = [\omega_1 \quad \omega_2 \quad \omega_3]^T$. From Eq. (7), the kinematic equation of the OMP with respect to global coordinate frame can be expressed as follows:

$$\boldsymbol{\omega} = \frac{1}{r}\begin{bmatrix} -\sin\theta & \cos\theta & L \\ -\sin(\pi/3-\theta) & -\cos(\pi/3-\theta) & L \\ \sin(\pi/3+\theta) & -\cos(\pi/3+\theta) & L \end{bmatrix}\begin{bmatrix} \dot{x} \\ \dot{y} \\ \dot{\theta} \end{bmatrix} = \frac{1}{r}\mathbf{A}(\theta)\dot{\mathbf{q}} \tag{8}$$

$$\dot{\mathbf{q}} = r\mathbf{A}^{-1}(\theta)\boldsymbol{\omega}_C \tag{9}$$

where $\mathbf{A}(\theta) = \begin{bmatrix} -\sin\theta & \cos\theta & L \\ -\sin(\pi/3-\theta) & -\cos(\pi/3-\theta) & L \\ \sin(\pi/3+\theta) & -\cos(\pi/3+\theta) & L \end{bmatrix}$ and $\dot{\mathbf{q}} = [\dot{x} \quad \dot{y} \quad \dot{\theta}]^T$ is velocity vector of OMP in global coordinate frame.

Equation (9) is kinematic equation of the OMP expressed in global coordinate frame. For decentralized algorithm, the motion of OMP should be expressed in body coordinate frame. In Fig. 2, the motion of OMP in body coordinate frame can be separated into three components of motion including rotational moving, ω_C, horizontal moving, H, and vertical moving, V.

Velocity vector of OMP in body coordinate frame is denoted by $\mathbf{u} = [H \quad V \quad \omega_C]^T$ where H is the component of linear velocity of OMP on Cx_0—*axis*,

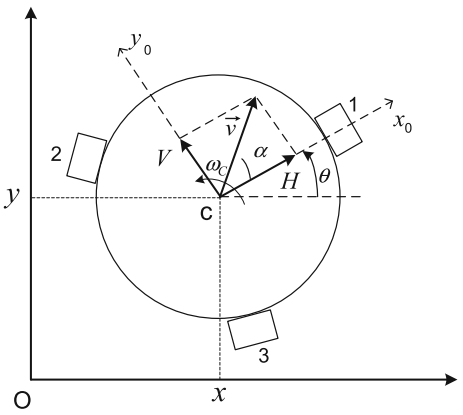

Fig. 2 Configuration of velocity vector of OMP in body coordinate frame

V is the component of linear velocity of OMP on Cy_0—*axis* and ω_C is angular velocity of OMP.

A transformation from global coordinate frame to body coordinate frame can be easy to obtain as follows:

$$\dot{\mathbf{q}} = \mathbf{R}_2(\theta)\mathbf{u} \tag{10}$$

where $\mathbf{R}_2 = \begin{bmatrix} \cos(\theta) & -\sin(\theta) & 0 \\ \sin(\theta) & \cos(\theta) & 0 \\ 0 & 0 & 1 \end{bmatrix}$ is rotation matrix.

By substituting Eq. (10) into Eq. (8), the following can be obtained.

$$\boldsymbol{\omega} = \frac{1}{r}\mathbf{A}(\theta)\mathbf{R}_2(\theta)\mathbf{u} \tag{11}$$

By simplifying $\mathbf{A}(\theta)\mathbf{R}(\theta)$ in Eq. (11), the following can be obtained.

$$\boldsymbol{\omega} = \frac{1}{r}\mathbf{B}\mathbf{u} \tag{12}$$

where $\mathbf{B} = \mathbf{A}(\theta)\mathbf{R}_2(\theta) = \begin{pmatrix} 0 & 1 & L \\ -\sqrt{3}/2 & -1/2 & L \\ \sqrt{3}/2 & -1/2 & L \end{pmatrix}$ is a full rank constant matrix.

2.2 *Decentralized Algorithm for Motion Control of OMP*

An OMP is more powerful to move than a conventional wheeled robot. Using three omnidirectional wheels, the OMP is considered as holonomic parallel system with three degrees of freedom (three DOF) in the horizontal motion plane. Based on the

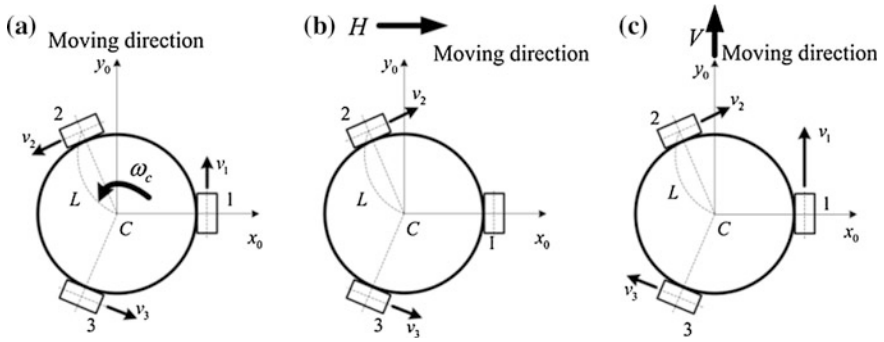

Fig. 3 Three pure-moving modes of OMP. **a** Pure-rotational moving, **b** pure-horizontal moving, **c** pure-vertical moving

characteristic of omnidirectional wheel, the decentralized algorithm for motion control of OMP in body coordinate frame is proposed. In this algorithm, five moving modes of OMP's motion are introduced.

Figure 3 shows three pure-moving modes of OMP: pure-rotational moving (a), pure-horizontal moving (b) and pure-vertical moving (c).

A pure rotational moving is obtained when angular velocity is not zero, $\omega_C \neq 0$, while horizontal moving and vertical moving are zero, $H = V = 0$. Similarly, a pure horizontal moving or a pure vertical moving is obtained by the same way.

From Eq. (12), a pure rotational moving is obtained as $(\omega_C \neq 0,\ H = V = 0)$:

$$\omega_1 = \omega_2 = \omega_3 = \frac{L}{r}\omega_C \tag{13}$$

A pure horizontal moving is obtained as $(H \neq 0,\ V = \omega_C = 0)$:

$$\begin{cases} \omega_1 = 0 \\ \omega_2 = -\sqrt{3}H \Big/ 2r \\ \omega_3 = \sqrt{3}H \Big/ 2r \end{cases} \tag{14}$$

A pure vertical moving is obtained as $(V \neq 0, H = \omega_C = 0)$:

$$\begin{cases} \omega_1 = V/r \\ \omega_2 = -V/2r \\ \omega_3 = -V/2r \end{cases} \tag{15}$$

If horizontal moving and vertical moving are combined, a pure translation moving in any direction can be obtained. In this case, the moving direction of OMP is specified by graphical method for vector sum of V and H as shown in Fig. 4.

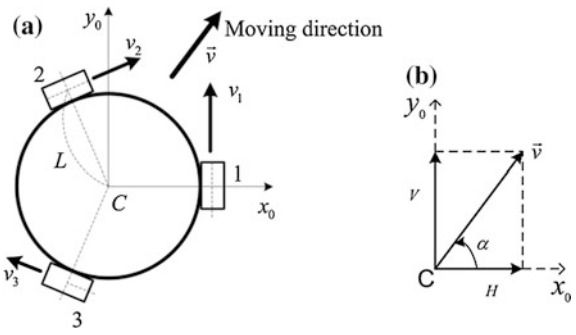

Fig. 4 Pure translation moving in any direction on *xy* plane. **a** Pure-translation moving, **b** vector sum *V* and *H*

Equation 16 shows the formula of pure translation moving ($H \neq 0$, $V \neq 0$ and $\omega_C = 0$).

$$\begin{cases} \omega_1 = V/r \\ \omega_2 = -\sqrt{3}H/2r - V/2r \\ \omega_3 = \sqrt{3}H/2r - V/2r \end{cases} \tag{16}$$

The translation moving angle, α, is obtained by Eq. 17 as follows:

$$\alpha = \text{atan}\left(\frac{V}{H}\right) \tag{17}$$

If all three components of OMP's motion, *H, V* and ω_C, are different from zero, translation and rotation can be obtained simultaneously that is the case shown in Eq. (12) and Fig. 2. This case is named as simultaneous translation-rotation mode.

In new decentralized algorithm, five motion modes of OMP including pure-horizontal moving, pure-vertical moving, pure-rotational moving, pure-translation moving and simultaneous translation and rotation moving have been presented.

The new decentralized algorithm makes motion control of OMP become simple, flexible and effective. Using the proposed decentralized algorithm such as pure-translation mode, pure-vertical mode or pure-horizontal mode, it helps to reduce time consuming for rotational moving when the OMP need to move from point to point. Using pure-rotational moving, it help the OMP changes its direction easily in narrow work environment. Simultaneous translation-rotation mode can be used to apply to trajectory tracking control problem of OMP that will be presented in the next section.

3 Trajectory Tracking Controller Design

3.1 Trajectory Tracking Error

Most of previous papers proposed trajectory tracking controllers considered in global coordinate frame. The previous controllers are normally multi inputs-multi outputs system (MIMO). In this paper, trajectory tracking controller is designed in the body coordinate frame based on the proposed decentralized algorithm. It consists of three sub-PD fuzzy controllers. For developing the proposed controller, a tracking error configuration should be defined in body coordinate frame.

Figure 5 shows the trajectory tracking and tracking error configuration in body coordinate frame of OMP.

From Fig. 5, the tracking error configuration in body coordinate frame is given as follows:

$$\mathbf{e}_b = \mathbf{R_2}(-\theta)\mathbf{e}_g = \mathbf{R_2}(-\theta)\left(\mathbf{q}_{ref} - \mathbf{q}\right) \tag{18}$$

where $\mathbf{e}_b = [e_H \; e_V \; e_\theta]^T$ denotes posture tracking error vector in body coordinate frame, $\mathbf{e}_g = \left[e_x \; e_y \; e_\theta\right]^T$ denotes posture tracking error vector in global coordinate frame, $\mathbf{q}_{ref} = [x_r \; y_r \; \theta_r]^T$ is posture vector of reference point R,$\mathbf{q} = [x \; y \; \theta]^T$ is current posture vector of OMP at point C.

3.2 PD Fuzzy Controller

From the proposed decentralized algorithm, three components of OMP's motion, H, V and ω_C, can be controlled separately or simultaneously. Especially, the OMP can move in pure-horizontal moving mode that is impossible with conventional mobile

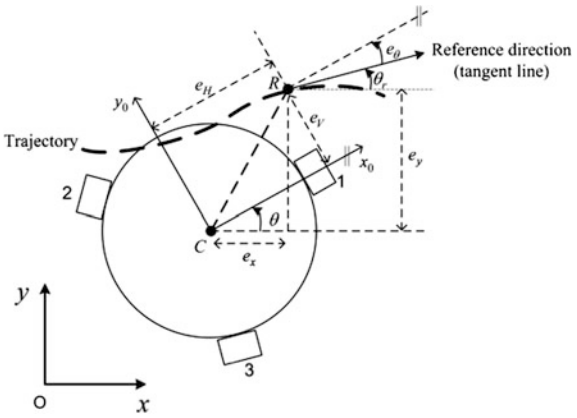

Fig. 5 Trajectory tracking of OMP and tracking error configuration

robot. Based on this characteristic of OMP, instead of a MIMO controller, this paper introduces a controller that consists of three sub-controllers.

It is known that the PID controller is the most widely used in modern industry due to its simple control structure and easy to design. But the conventional PID controllers do not yield reasonable performance over a wide range of operation conditions. Hence, another controller such as PD fuzzy controller is needed. Generally, a fuzzy controller is insensitive to parametric uncertainty, load and parameter fluctuations while it is generating stability of the system.

Three PD fuzzy sub-controllers are combined to form the overall PD fuzzy controller for trajectory tracking of OMP. In the first sub-controller, the inputs are horizontal tracking error e_H and its derivative, and the output is horizontal linear velocity H of OMP. In the second sub-controller, the inputs are vertical tracking error e_V and its derivative, and the output is vertical linear velocity V of OMP. In the third sub-controller, the inputs are rotational tracking error e_θ and its derivative, and the output is angular velocity ω_C of OMP. Figure 6 shows full block control diagram for trajectory tracking of OMP with the PD-fuzzy controller.

From the fuzzy structure, there are two inputs and one output to each sub-controller. The normalized ranges of inputs and outputs are from −1 to 1. The control output is obtained through center-of-gravity (COG) defuzzification.

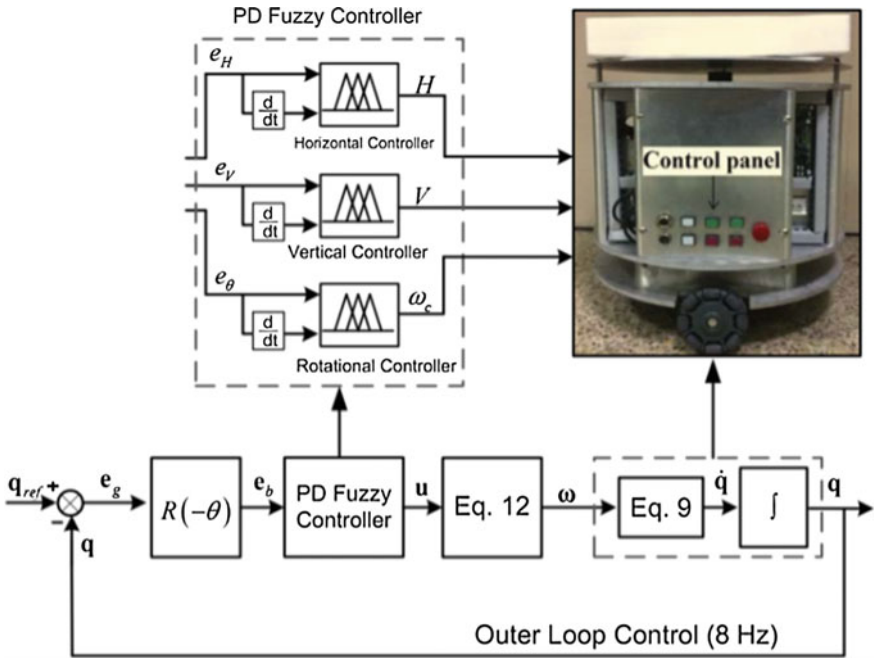

Fig. 6 PD fuzzy controller based on decentralize algorithm

Table 1 Control law rules applied for all three controllers

u		e				
		NB	NS	ZE	PS	PB
ė	N	PB	PS	PS	NS	NB
	Z	PB	PS	ZE	NS	NB
	P	PB	PS	NS	NS	NB

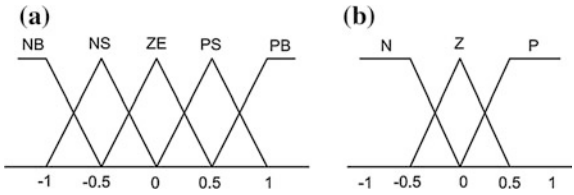

Fig. 7 Membership functions. **a** e_H, e_V, e_θ, H, V, ω_C, **b** $\dot{e}_H$, $\dot{e}_V$, $\dot{e}_\theta$

Membership functions applied for the fuzzy controllers are shown in Fig. 9. The control law rules applied for all three controllers are given in Table 1. The body of the Table 1 shows fuzzy implication in the form:

$$\textit{If } e \textit{ is } M \textit{ and } \dot{e} \textit{ is } N \textit{ Then } u \textit{ is } K.$$

where $\mathbf{e} = \{e_x \; e_y \; e_\theta\}$; $M = K = \{\text{NB NS ZE PS PB}\}; N = \{\text{N Z P}\}$; P—Positive; N—Negative; Z—Zero; ZE—Zero; PB—Positive big; PS—Positive small; NB—Negative big; NS—Negative small (Fig. 7).

4 System Description

Figure 8 depicts the developed OMP composed of a platform and three sets of omnidirectional wheel arranged equally spaced at 120° from one to another. It is equipped with a laser-based localization sensor, SICK NAV200, and an embedded industrial PC. The NAV200 is used to measure the position and orientation of the OMP in the global coordinate frame.

Figure 9 shows a control block diagram of the OMP having two control loops: outer loop and inner loop. The outer loop, programmed in C# on the industrial PC, generates three desired commands: angular velocities for three omnidirectional wheels of OMP $\boldsymbol{\omega} = [\,\omega_1 \quad \omega_2 \quad \omega_3\,]$. These commands are updated upon the errors between the reference posture vector $\mathbf{q}_{ref} = [x_r \; y_r \; \theta_r]^T$ and the current posture vector $\mathbf{q} = [x \; y \; \theta]^T$ measured by NAV200 at a sampling frequency of 8 Hz. The inner loop, using three microcontroller ARM CORTEX-M3 STM32F103, generates three control voltage signals to control three DC motors for driving three omnidirectional wheels in the fashion that the omnidirectional wheels follow the commanded angular velocities from the outer loop. The three control signals are

Fig. 8 The OMP used in experiment

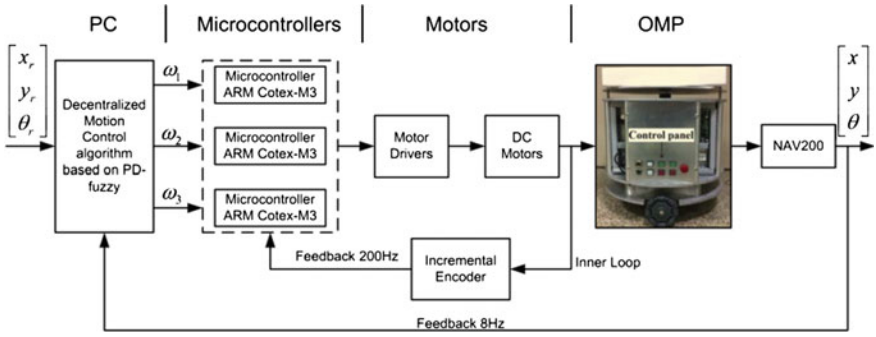

Fig. 9 Control block diagram

calculated using the desired commands and the encoders feedback at the frequency of 200 Hz. Communication between the industrial PC and three microcontrollers is done via RS232.

5 Simulation and Experimental Results

To verify the effectiveness of the proposed system, experiments have been done. The OMP used in experiment has: wheel radius r = 62.5 mm, distance from center of mass to each wheel L = 275 mm, and weight of OMP 45 kg. Three DC motors are used

to drive three omnidirectional wheels. The specification of the motors are given as follows: power 48.6 W, rated speed 3,550 rpm, rated voltage 24 V, rated torque 1,300 $g_f$cm and gear box ratio 1/12. Initial condition at starting point in simulation and experiment: $x(0) = 2,200\,\text{mm}$, $y(0) = 0\,\text{mm}$, $\theta(0) = 85^{\circ}$, $\omega_1 = \omega_2 = \omega_3 = 0$.

Figure 10 shows tracking result the circle trajectory of OMP in the global coordinate frame. The radius of the circle is 2000 mm. In Fig. 10, the dashed line is the reference trajectory. The continuous line is the trajectory of OMP that is measured by laser sensor in experiment.

Figures 11, 12, 13, 14, 15 and 16 shows the tracking errors of OMP and the PD fuzzy controller outputs applied to the OMP in simulation and experiment. In Figs. 11, 12, 13, 14, 15 and 16, the dashed line denotes simulation result and the continuous line denotes the experimental result.

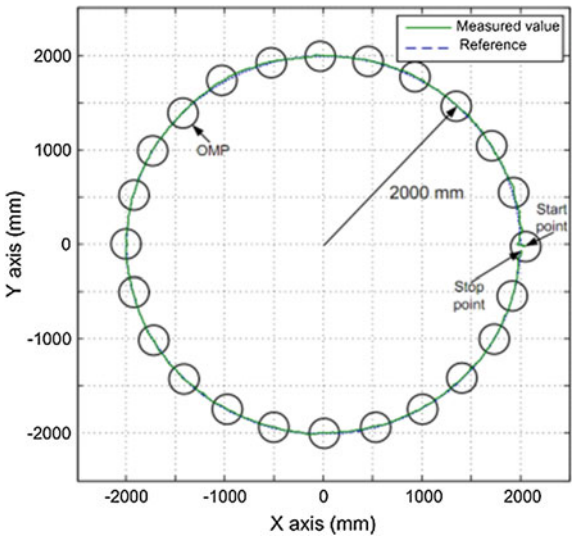

Fig. 10 Tracking a circle trajectory in experiment

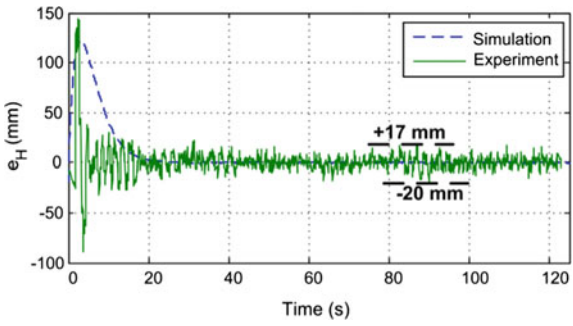

Fig. 11 Horizontal tracking error

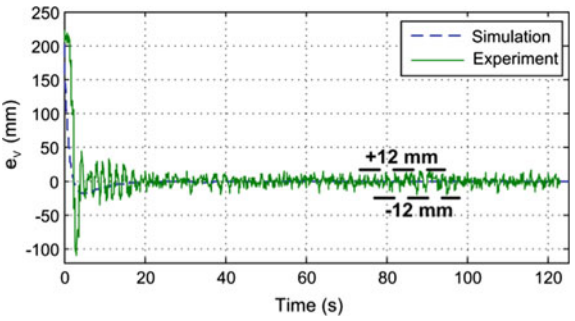

Fig. 12 Vertical tracking error

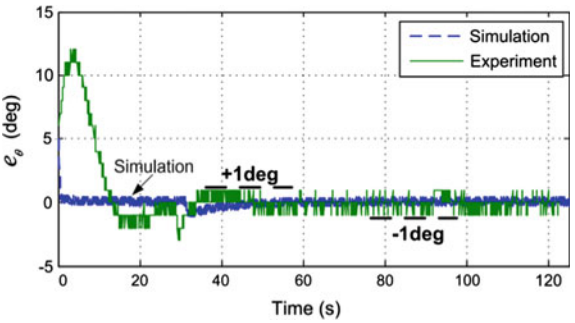

Fig. 13 Rotational tracking error of OMP

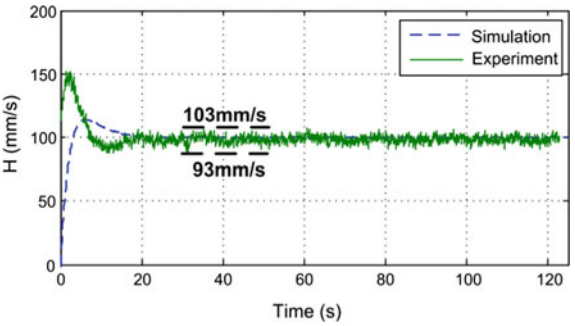

Fig. 14 Horizontal linear velocity of OMP

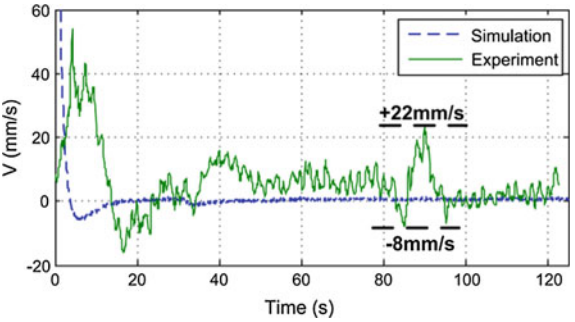

Fig. 15 Vertical linear velocity of OMP

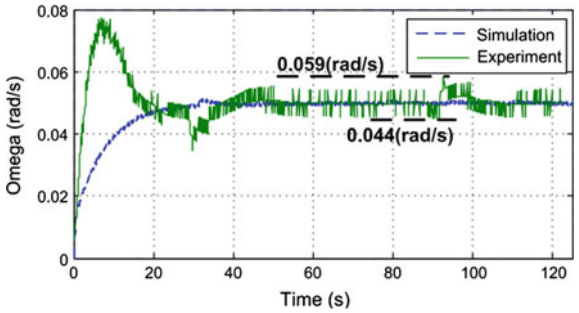

Fig. 16 Angular velocity of OMP

Figure 11 shows the horizontal tracking error of OMP in simulation and experiment. For the first time of 20 s, the horizontal tracking error is big. However, it reduces quickly. After 20 s, the error becomes small and it is bounded from −20 mm to +17 mm around zero.

Figure 12 shows the vertical tracking error of OMP in simulation and experiment. For the first time of 20 s, the vertical tracking error is big. However, it reduces quickly. After 20 s, the error becomes small and it is bounded within ±12 mm around zero.

Figure 13 shows the rotational tracking error in simulation and experiment. The simulation result converges to around zero after 1 s while the experimental result converges to around zero after 35 s. After 35 s, the rotational tracking error is bounded within ±1°.

Figures 14, 15 and 16 show the outputs of three PD-fuzzy controllers, respectively. The horizontal linear velocity H of OMP converges to 100 mm/s after 20 s in simulation and experiment. The vertical linear velocity V of OMP converges to around zero after 20 s in simulation. After 20 s, the vertical linear velocity is bounded from −8 to +22 mm/s in experiment. After 20 s, the angular velocity of OMP converges to 0.05 rad/s in simulation. After 40 s, the angular velocity of OMP is bounded within from 0.044 to 0.059 rad/s in experiment. Simulation results and experimental results are almost same in all three controllers.

Figure 17 shows the angular velocities of three wheels. The angular velocity of wheel 1 converges to 0.22 rad/s after 20 s in simulation and experiment. The

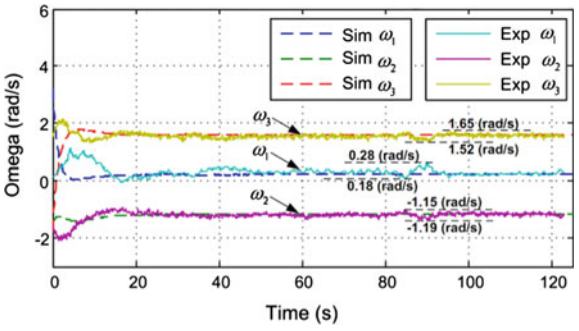

Fig. 17 Wheel angular velocities

angular velocity of wheel 2 converges to −1.17 rad/s after 20 s in simulation and experiment. The angular velocity of wheel 3 is converges to 1.6 rad/s after 20 s in simulation and experiment. Simulation result and experimental result are almost same.

6 Conclusion

First, a new decentralized algorithm for motion control of OMP was introduced. In this decentralized algorithm, the motion of OMP was separated into three independent components of motion expressed in body coordinate frame including rotational moving, horizontal moving and vertical moving. By using omnidirectional wheels, these motion components could be controlled simultaneously as well as separately. There were 5 motion modes including pure-horizontal moving, pure-vertical moving, pure-rotational moving, pure-translation moving and simultaneous translation and rotation moving have been presented. The new decentralized algorithm made motion control of OMP became simple, flexible and effective. Using the proposed decentralized algorithm such as pure-translation mode, pure-vertical mode or pure-horizontal mode, it helped to reduce time consuming for rotational moving when the OMP need to move from point to point. Using pure-rotational moving, it helped the OMP changes its direction easily in narrow work environment. Simultaneous translation-rotation mode could be used to apply to trajectory tracking control problem of OMP.

Experiment has been done using a real OMP. Hardware and controller system was described. The position and orientation of OMP in global coordinate were measured using the laser-based sensor, NAV200. In experiment, the OMP tracked a circle trajectory with 2000 mm radius. The experimental results showed that the OMP could track the trajectory very well. For the first time of 10 s, the horizontal tracking error and vertical tracking error were big. After the first time of 10 s, the horizontal tracking error and vertical tracking error was small. For the first time of 35 s, the rotational tracking error was big. After the first time of 35 s, the rotational error was small.

References

1. Kalmár-Nagy T, D'Andrea R, Ganguly P (2004) Near-optimal dynamic trajectory generation and control of an omnidirectional vehicle. Robot Auton Syst 46(1):47–64
2. Bi ZM, Wang L (2010) Dynamic control model of acobot with three omni-wheels. Original Res Article Robot Comput Integr Manuf 26(6):558–563
3. Han F, Yamada T, Watanabe K (2000) Construction of an omnidirectional mobile robot platform based on active dual-wheel caster mechanisms and development of a control simulator. J Intell Robots Syst 29(3):257–275

4. Villagra J, Herrero-Perez D (2012) A comparison of control techniques for robust docking maneuvers of an AGV. IEEE Trans Control Syst Technol 20(4):1116–1123
5. Kim BK, Kim BK (2011) Minimum-time trajectory for three-wheeled omnidirectional mobile robots following a bounded-curvature path with a referenced heading profile. Robot IEEE Trans 27(4):800–808
6. Wang SM, Lai LC, Wu CJ, Shiue YL (2007) Kinematic control of omni-directional robots for time-optimal movement between two configurations. J Intell Robots Syst 49(4):397–410
7. Huang HC, Tsai CC (2008) Adaptive robust control of an omnidirectional mobile platform for autonomous service robots in polar coordinates. J Intell Robots Syst 51(4):439–460
8. Huang HC, Tsai CC, Lin SC (2011) Adaptive polar-space motion control for embedded omnidirectional mobile robots with parameter variations and uncertainties. J Intell Robots Syst 62(1):81–102
9. Dinh VT, Nguyen H, Shin SM, Kim HK, Kim SB, Byun GS (2012) Tracking control of omnidirectional mobile platform with disturbance using differential sliding mode controller. Int J Precis Eng Manuf 13(1):39–48
10. Ngyen H, Kim DH, Kim HK, Kim SB (2010) Motion control of an omnidirectional mobile for trajectory tracking using an integral sliding mode controller. 8(6):1221–1231
11. Kim S, Hyun C, Cho Y, Kim S (2010) Tracking control of 3 wheeled omnidirectional mobile robot using fuzzy azimuth estimator. In: Proceedings of the 10th WSEAS international conference on robotics control and manufacturing technology, pp 47–51
12. Liu Y, Zhu JJ, Williams RL II, Wu J (2008) Omni-directional mobile robot controller based on trajectory linearization. Robot Auton Syst 56(5):461–479
13. Watanabe K, Shiraishi Y, Tzafestas SG, Tang J, Fukuda T (1998) Feedback control of an omnidirectional autonomous platform for mobile service robots. J Intell Robots Syst 22 (3):315–330
14. Wong CC, Lin YH, Lee SA, Tsai CH (2005) GA-based fuzzy system design in FPGA for an omni-directional mobile robot. J Intell Robots Syst 44(4):327–347
15. Sharbafi MA, Lucas C, Daneshvar R (2010) Motion control of omni-directional three-wheel robots by brain-emotional-learning-based intelligent controller. IEEE Trans Appl Rev 40 (6):630–638
16. Xu D, Zhao D, Jianqiang Y, Tan X, Chen Z (2009) Trajectory tracking control of omnidirecitonal wheeled mobile manipulators: robust neural network based sliding mode approach. IEEE Trans Syst Man Cybern 39(3):788–799
17. Huang HC (2011) SOPC-Based parallel ACO algorithm and its application to optimal motion controller design for intelligent omnidirectional mobile robots. IEEE Trans Ind Inform 9 (4):1828–1835
18. Williams II RL, Carter BE, Gallina P, Rosati G (2002) Dynamic model with slip for wheeled omnidirectional robots. IEEE Trans Robot Autom 18(3):285–293
19. Tang J (1996) Watanabe, K.; Shiraishi, Y.: Design and traveling experiment of an omnidirectional holonomic mobile robot. IEEE/RSJ Int Intell Robots Syst Conf 1:66–73
20. Pin FG, Killough SM (1994) A new family of omnidirectional and holonomic wheeled platforms for mobile robots. IEEE Trans Robot Autom 10(4):489–490
21. Barreto S, Conceicao AGS, Dorea CET, Martinez L, de Pieri ER (2014) Design and implementation of model-predictive control with friction compensation on an omnidirectional mobile robot. IEEE/ASME Trans Mechatron 19(2):467–476
22. Hidaka K (2007) Adaptive control design of an omnidirectional automated guided vehicle in consideration of mass change. In: Proceedings of the 2007 annual conference SICE, pp 2578–2581
23. Hashemia E, Jadidib MG, Jadidib NG (2011) Model-based PI–fuzzy control of four-wheeled omni-directional mobile robots. Robot Auton Syst. 59(11):930–942

Part X
Mechanical Engineering

Data Processing Assessment of the Comfort of Passengers on Board for Small Passenger Boat

Nguyen Anh Tuan and Tat-Hien Le

Abstract The paper is to present an analysis process of a comfort assessment of small passenger boat under 24 m length. The wave energy spectrum for analysing the characteristic of uncoupled roll motion response spectrum will be calculated in order to evaluate a motion sickness incidence.

Keywords Data processing assessment · Roll motion · Yacht · Passenger boat

1 Introduction

Since the late 19th century, several motion-damping devices were developed and applied as anti-rolling for ship stability [1]. In addition, some wave spectra such as Bretschneider wave spectrum (1969) and JONSWAP wave spectrum (1968) were widely recognized and applied in ship motion research field [1]. Up to now, ship motion is still open topic for researchers in academic and international yacht builders. In 18th International Ship and Offshore Structures Congress (2012), ship motion was discussed through the analysis of the comfort of yacht by Yacht Design Committee [2]. Ship motion affects deeply the comfort of passengers and crew on board yachts and cruises. In 1974, O'Hanlon and McCauley suggested Motion Sickness Incidence (MSI) to estimate the percentage of people cope with sea sickness [3].

This paper will introduce the data processing for analysing the comfort of passengers on board yacht based on MSI with a case study of yacht under 24 m length.

N.A. Tuan (✉) · T.-H. Le
Department of Naval Architecture and Marine Engineering,
Faculty of Transportation Engineering, HCMC University of Technology,
HCMC Vietnam National University, Ho Chi Minh City, Vietnam
e-mail: TyVy.net@gmail.com

V.H. Duy et al. (eds.), *AETA 2015: Recent Advances in Electrical Engineering and Related Sciences*, Lecture Notes in Electrical Engineering 371,
DOI 10.1007/978-3-319-27247-4_68

2 Data Processing

Figure 1 represents the data analysis process for the comfort assessment of passengers based on wave energy spectrum and MSI parameter.

First of all, the database of the wave energy spectrum will be accumulated based on the characteristic wave collected in ocean and the circular frequency depending on observation. Next, the encounter wave energy spectrum will be calculated based on the encounter frequency. The course of vessel and the wave direction strongly influence the encounter frequency.

Next step, Response Amplitude Operator (RAO) calculated by Matlab using standard model of ship motion will be used. RAO will be computed based on the chacracteristic of vessel and the assumption of the uncoupled roll motion. After RAO calculation, the motion response spectrum will be estimated. Finally, the characteristic of motion response spectrum will be analyzed, and especially MSI will be assessed by ISO 2631/3-1985.

2.1 Encounter Wave Spectrum

The research is to study in case of two type of common wave energy spectra including Bretschneider spectrum and JONSWAP (Joint North Sea Wave Project) spectrum.

Bretschneider wave spectrum

Bretschneider wave spectrum is also known as International Towing Tank Conference (ITTC) 2 parameters wave spectrum. The spectrum is based on two parameters such as the characteristic wave height $\bar{H}$ (m) and the average period $\bar{T}$ (s) [4]. In open sea areas with long crest, it is acceptable for Bretschneider wave

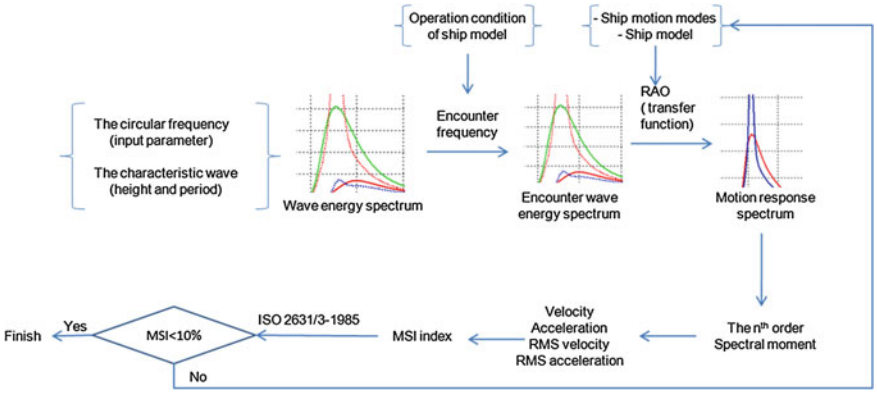

Fig. 1 Analysis process of yacht comfort

spectrum to be applied. The following equation will describe Bretschneider wave spectrum $S_\zeta(\omega)$ (m^2 s) [5]:

$$S_\zeta(\omega) = 172.75\frac{\bar{H}^2}{\bar{T}^2}\omega^{-5}\exp\left(-\frac{691}{\bar{T}^4}\omega^{-4}\right) \tag{1}$$

JONSWAP wave spectrum

Since 1978, JONSWAP wave spectrum was offered by the 15th ITTC [1]. JONSWAP spectrum is generally used in coastal areas because it was researched from Srylt Island to the North Sea [4]. The JONSWAP spectrum with the peakedness factor $\gamma = 3.3$ in the paper will be described as follows [4, 5]:

$$S_{JONSWAP}(\omega) = 0.658 \cdot 172.75\frac{\bar{H}^2}{\bar{T}^4}\omega^{-5}\exp\left(-\frac{691}{\bar{T}^4}\omega^{-4}\right) \cdot C(\omega) \tag{2}$$

$$C(\omega) = \gamma^{\exp\left(-\frac{1}{2\sigma^2}\left(\frac{\omega}{\omega_0}-1\right)\right)^2} \tag{3}$$

where:

ω: the circular wave frequency $\left(\frac{\text{rad}}{\text{S}}\right)$

σ: the step function

$\sigma = 0.07$ for $\omega < \omega_0$

$\sigma = 0.09$ for $\omega > \omega_0$

Circular frequency at spectral peak $\omega_0 = \frac{4.849}{\bar{T}}$

As Eq. (2), JONSWAP spectrum has a part of Brestchneider spectrum. For instance, the difference between Brestchneider and JONSWAP spectrum will be analyzed by MSI_BK program based on statistic data in Aegean Sea [6]. It is easy to recognize the peak of JONSWAP spectrum is taller and narrower than the peak of Bretschneider spectrum at the characteristic wave height of 1.88 m and the average period of 6.25 m in Fig. 2.

The encounter wave energy spectrum

When yacht moves on wave, the direction of yacht and the direction of wave travel will make an angle which is called the encountering angle μ, see Fig. 3. Depending on the direction between yacht and wave travel μ is advised as 0° in following wave condition, 90° in beam wave condition and 180° in heading wave condition [7].

The encounter frequency will be calculated as follows [7]

$$\omega_e = \omega\left(1 - \frac{\omega V}{g}\cos\mu\right) \tag{4}$$

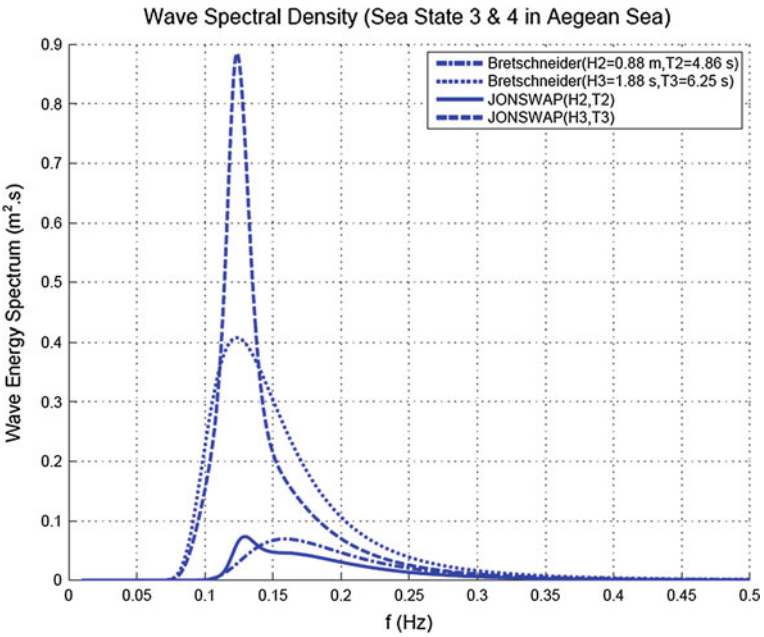

Fig. 2 Wave energy spectrum

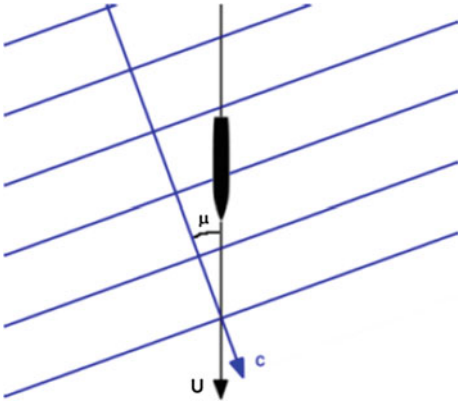

Fig. 3 The encountering angle μ [5]

where:
V ship speed (m/s)
g gravitational acceleration (m/s^2)
ω Wave frequency (rad/s)

The relationship between the wave energy spectrum, $S(\omega)$, and the encounter wave energy spectrum, $S(\omega_e)$, is based on the encounter frequency as follows [7]:

$$S(\omega_e) = \frac{S(\omega)}{\left|1 - \frac{2\omega V}{g}\cos\mu\right|} \tag{5}$$

2.2 Uncoupled Roll Motion in Regular Sea Wave

In our research, the standard model of uncoupled roll motion in regular wave is the second order differential equation is expressed as [2]:

$$(I_4 + A_{44})\ddot{\eta} + B_{44}\dot{\eta} + C_{44}\eta = F_4(\cos\omega_e t + i\sin\omega_e t) \tag{6}$$

where:

η	roll angle (°)
I_4	Mass moment of inertia of roll motion, $I_4 = k_{xx}^2 \nabla\rho$ (kg m^2)
k_{xx}	Gyradius of yacht about the x-axis through the center of gravity CG (m)
∇	Displacement volume of yacht (m^3)
ρ	Density of sea water, 1025 kg/m^3
A_{44}	the added inertia coefficient of roll motion, $A_{44} = 0.3I_4$ [8],
C_{44}	Hydrostastic restoring coefficient of roll motion, $C_{44} = GM_t \cdot \nabla \cdot \rho \cdot g$
GM_t	Transverse metacenter height (m)

Response amplitude operator (RAO) is also known as transfer function. In the roll motion, RAO for the above model of uncoupled roll motion depends on tuning factor $\lambda = \frac{\omega_e}{\omega_0}$ with the natural frequency of uncoupled roll motion $\omega_0 = \sqrt{\frac{C_{44}}{I_4 + A_{44}}}$ (rad/s) and damping factor β_{44}, as follows [5]:

$$RAO_{roll} = \frac{1}{\sqrt{\left(1 - \lambda^2\right)^2 + 4\beta_{44}^2\lambda^2}} \tag{7}$$

As Fig. 4, since damping factor deeply influences RAO, ship will spend long time reducing the motion with small damping factor. RAO will be calculated based on different damping factors in conjunction with different anti-rolling devices.

2.3 Ship Motion Response

The encounter wave energy from wave travel and excitation forces will transform into ship motion through RAO [7]. Depending on RAO factors of different motions, the yacht will create the different motion response spectra $S_z(\omega_e)$. In case of roll

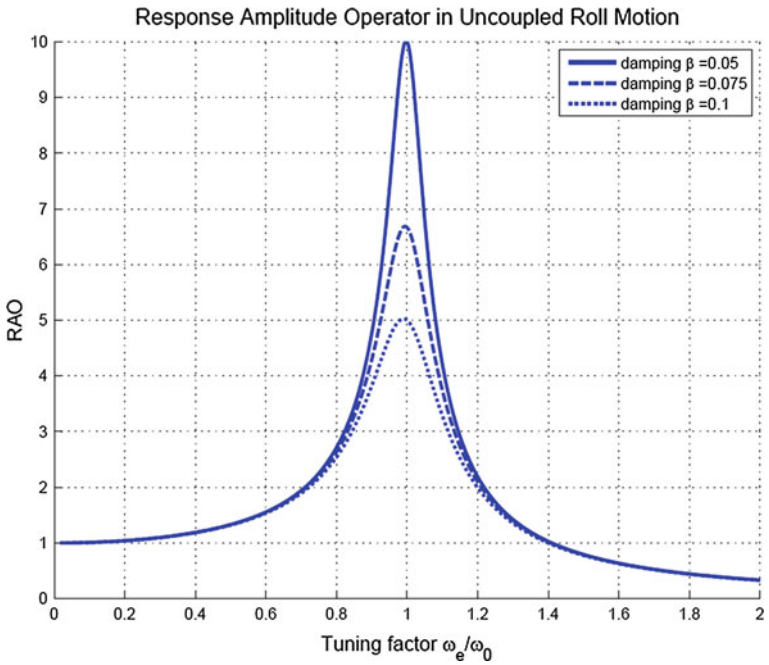

Fig. 4 RAOs with different damping factors

motion, the ship motion response will use RAO of roll motion to damp the motion. The ship motion response of roll motion will be calculated as follows (Fig. 5):

$$S_{zRoll}(\omega_e) = RAO^2_{roll} S_\zeta(\omega_e) \tag{8}$$

2.4 The Criteria of the Yacht Comfort

In our research, the criteria of the yacht comfort will be analysed by Motion Sickness Incidence obeying ISO 2631/3-1985, it will show how many percent of passengers will encounter the vomit incidence.

The root mean square (RMS) of the 2nd order spectral moment of roll motion response spectrum m_2 is the root mean square acceleration v_{zRMS} ($m/s^{0.5}$) [5]:

$$v_{zRMS} = \sqrt{m_2} = \sqrt{\int_{\min(\omega_e)}^{\max(\omega_e)} \omega_e^2 \cdot S_{zRoll}(\omega_e) \cdot d\omega_e} \tag{9}$$

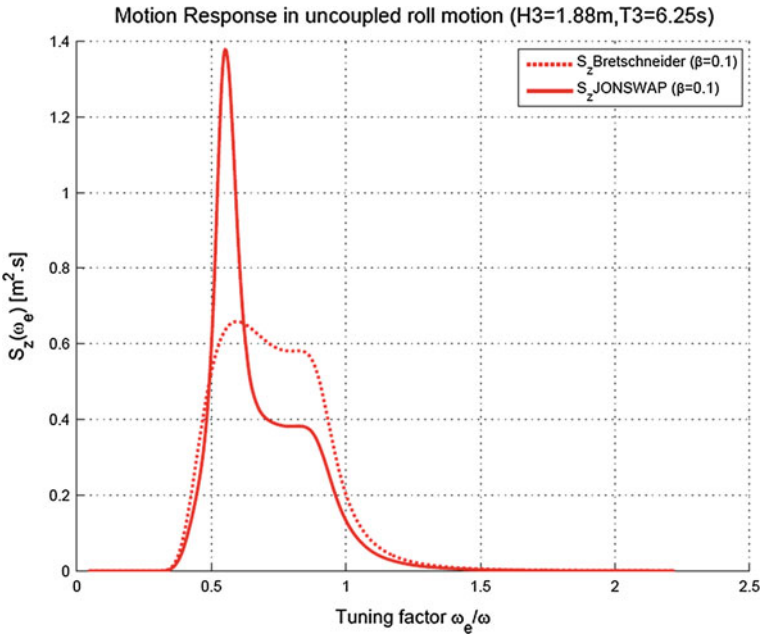

Fig. 5 The result of the motion response spectrum with damping factor $\beta = 0.1$ of uncoupled roll motion

The root mean square (RMS) of the 4th order spectral moment of roll motion response spectrum m_4 is the root mean square acceleration a_{zRMS} (m/s$^{1.5}$) [5]:

$$a_{zRMS} = \sqrt{m_4} = \sqrt{\int_{\min(\omega_e)}^{\max(\omega_e)} \omega_e^4 \cdot S_{zRoll}(\omega_e) \cdot d\omega_e} \tag{10}$$

Motion sickness incidence is also called "Motion Sickness Index". In 1974, it is firstly represented by O'Hanlon and McCauley [2]. MSI can be estimated based on motion response spectrum of vessel. Obeying ISO 2631/3-1985, MSI value has to be smaller than 10 % in 2 h exposure time [9]. Lloyd (1998) offered the following expression to estimate MSI after 2 h exposure based on the heave acceleration ($\ddot{s}_3 = 0.798\sqrt{m_4}$, m/s^2) and the standard normal cumulative distribution function Φ with zero mean and unity standard deviation [8]:

$$MSI(\%) = 100 \cdot \Phi\left\{\frac{\log_{10}\left(\frac{|\ddot{s}_3|}{g}\right) - \mu_{MSI}}{0.4}\right\} < 10\,\% \tag{11}$$

O'Hanlon and McCauley (1974) suggested the factor μ_{MSI} based on the encounter frequency f_e as the below expression [3]:

$$\mu_{MSI} = 0.654 + 3.697 \log_{10} f_e + 2.32(\log_{10} f_e)^2 \quad (12)$$

In 1998, Lloyd offered other expression of the factor μ_{MSI} using encounter frequency $\omega_e = \sqrt{\frac{m_4}{m_2}}$ (rad/s), based on the 2nd spectral moment m_2 and the 4th spectral moment m_4, as follows [8]:

$$\mu_{MSI} = -0.819 + 2.32(\log_{10} \omega_e)^2 \quad (13)$$

In order to analysis the data processing of the comfort assessment, a case study will be carried out.

3 Case Study

The model in Fig. 6 will be applied in case study, the model of vessel built by fibre-reinforced plastic (FRP) composite material with waterline length L_{WL} = 22.5 m, maximum beam B = 6.931 m, draft T = 1.215 m, displacement volume ∇ = 157 m^3, transverse metacenter height GM_t = 1.682 m, radius of gyration of roll motion k_{xx} = 2.782 m. Yacht model will move with velocity of 10 knot in beam sea condition. The characteristics of wave at level 4 of the sea state (Sea State 4) in Aegean Sea include the characteristics wave height 1.88 m and the average period 6.25 s was applied for the comfort assessment in our research [6, 10].

Figure 7 demonstrates the wave energy spectrum at Sea State 4 in Aegean Sea after analysing the average period of wave T = 6.25 s and the characteristics wave height H = 1.88 m. The shape of spectrums is similar to the theory of Bretschneider Spectrum and JONSWAP. JONSWAP spectrum is narrower and higher than Bretschneider spectrum.

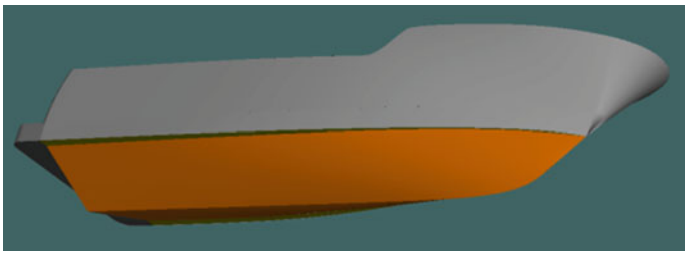

Fig. 6 Yacht model using for analysing the comfort of passenger

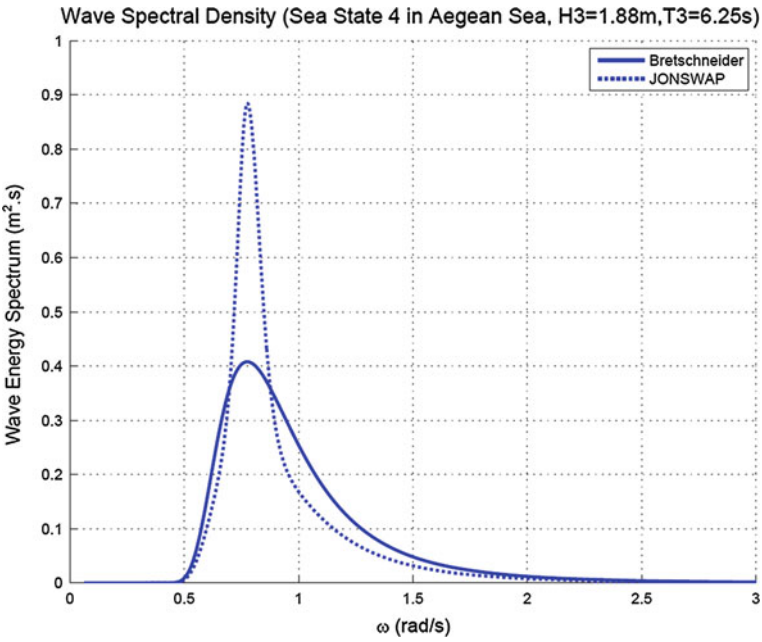

Fig. 7 Wave energy spectrum at Sea State 4 in Aegean Sea

In Fig. 8, the motion response spectrums of JONSWAP are higher than the motion response spectrums of Bretschneider. Moreover, JONSWAP response spectrums are decline faster than Bretschneider response spectrum. On the contrary, the high damping factor will positively affect the motion response. The motion response spectrums with damping factor of 0.1 decline faster than the motion response spectrums with damping factor of 0.05 and 0.075.

The range of damping factor is between 0.05 and 0.1 for most vessels without anti-motion devices [5]. From Table 1, all results of MSI exceed 10 % obeying ISO 2631/3-1985 in 2 h exposure time. It is showed that 10 % more passengers will put up with seasickness and vomit and the boat does not satisfy the criteria of ISO 2631/3-1985. In order to satisfy the criteria of the passenger comfort, yacht owners should use the damping devices on board.

It is recommended that MSI is strongly influenced by radius of gyration of roll motion k_{xx}, transverse metacenter height GM_t, and the ship direction. To reduce MSI, ship designer should reduce radius of gyration of roll motion k_{xx} by redistributing the weights such as ballast tanks and fuel tanks in initial design stage. As a result, Table 1 showed that MSI with small radius k_{xx} = 1 m do not exceed the criteria of ISO 2631/3-1985.

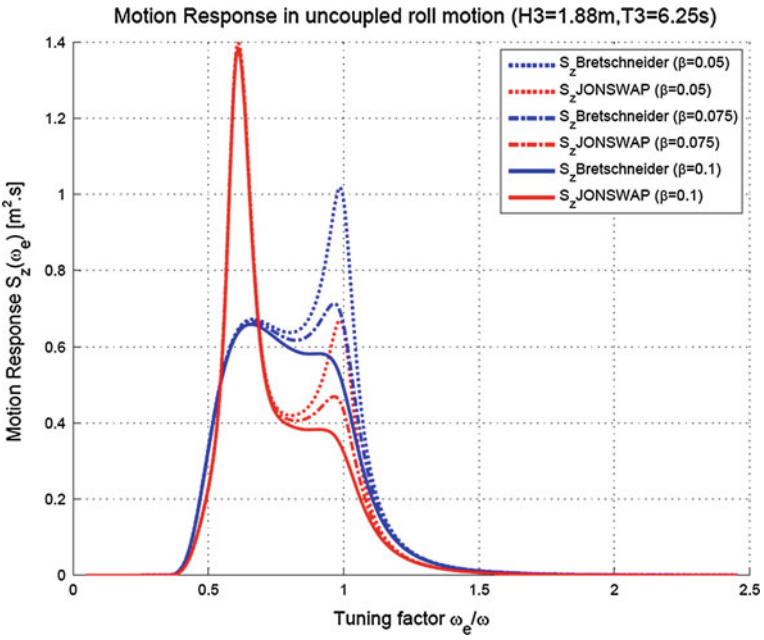

Fig. 8 Motion response with RAO using particular damping factor

Table 1 Results calculated

Frequency, f (Hz)	0.01 ÷ 0.5			
Circular frequency, ω_e (rad/s)	0.0628 ÷ 3.1416			
Motion model	Uncoupled roll motion			
Direction of wave and yacht, μ	90°, beam sea condition			
Damping factor	0.05			
Wave spectrum	JONSWAP		Bretschneider	
Significant wave height (m)	1.88		1.88	
Average period (s)	6.25		6.25	
Radius of gyration k_{xx} (m)	2.785	1	2.785	1
The 2nd order spectral moment (m^2/s)	0.5226	0.2485	0.6768	0.3019
The 4th order spectral moment (m^2/s^3)	0.7245	0.5259	1.0258	0.7513
Heave RMS Acceleration, a_{zRMS} ($m/s^{1.5}$)	0.8512	0.7252	1.0128	0.8668
Heave acceleration (m/s^2)	0.6792	0.5787	0.8082	0.6917
MSI (Lloyd 1998) (%)	13.0123	7.7191	16.9757	9.6076
MSI (O'Hanlon and McCauley 1974) (%)	13.0273	7.7513	17.0018	9.6553

4 Conclusion

Nowadays, many vessels use anti-rolling devices such as bilge keels, controllable fins, anti-rolling tanks and gyro-stabilizers to reduce roll motion [2]. Our study will help yacht owner give decision to choose the suitable anti-rolling solutions at initial design stage or consider the necessary of the damping device installment. Besides that, it helps undergraduate students comprehend the essential issues in ship motion such as wave energy spectrum, RAO and MSI.

References

1. Nghi TC (2006) Tĩnh học tàu và động học tàu (Ship hydrostatic and ship hydrodynamic). HCMC National University, Ho Chi Minh City
2. Nguyen TA, Le HT (2015) Study of the effects of roll motion on transverse stability of a small boat. Transportation engineering technology. Int J Mech Eng Appl 3:24–28
3. O'Hanlon JF, McCauley ME (1974) Motion sickness incidence as a function of the frequency and acceleration of vertical sinusoidal motion. Aerosp Med 45:366–369
4. Journée JMJ, Pinkster J (2002) Introduction in ship hydrodynamics. Delft University of Technology
5. (2013) Maxsurf motions manual. Bentley System Inc
6. Erikson JH (2000) Common procedures for seakeeping in the ship design process. STANAG 4154 2000
7. Bhattacharyya R (1978) Dynamics of marine vehicles. Wiley, New York
8. Lloyd ARJM (1998) Seakeeping: ship behaviour in rough weather. Ellis Horwood Limited
9. Kivimaa S et al (2014) Ship motions, vibration and noise influence on crew performance and well-being studies in FAROS project. In: Transport Research Arena, Paris
10. Alkan AD (2014) Comfort on board analyses and recommendations for yachts. In: Proceedings of the 10th symposium on high speed marine vehicle, Naples, Italy, pp 1–7

Development of a New Clutch Featuring MR Fluid with Two Separated Mutual Coils

Quoc Hung Nguyen, Le Dai Hiep, Bui Quoc Duy and Seung-Bok Choi

Abstract In this paper, a new configuration of clutch featuring MR fluid (MRC) with 2 mutual coils placed separately out of the rotary housing of the clutch is considered. With this proposed configuration, the coils are fixed and brushes are eliminated. Therefore, disadvantages of conventional MRC can be handled. In addition, the proposed clutch is easier to manufacture and assemble than previous developed one, especially the air gap between the winding core and the rotary housing of the clutch can be adjust easily. After an introduction of the proposed configuration, transmitting torque of the MRC is analyzed based on Bingham-plastic rheological model of MR fluid. The optimization of the proposed and conventional MRC is then performed considering maximum transmitting torque and moment of inertia of the clutch housing. Based on the optimal results, a comparison of the proposed MRC and the conventional ones is undertaken and discussions on performance of the proposed MRC are given.

Keywords Magneto-rheological fluid (MRF) · Smart fluid · MR clutch

Q.H. Nguyen (✉)
Faculty of Electrical and Electronics Engineering, Ton Duc Thang University,
No. 19 Nguyen Huu Tho Street, District 7, Ho Chi Minh City, Vietnam
e-mail: nguyenquochung@tdt.edu.vn

Q.H. Nguyen · L.D. Hiep · B.Q. Duy
Mechanical Engineering, Industrial University of Hochiminh City,
Ho Chi Minh City, Vietnam

S.-B. Choi
Smart Structures and Systems Laboratory, Inha University, Incheon 402-751, Korea

V.H. Duy et al. (eds.), *AETA 2015: Recent Advances in Electrical Engineering and Related Sciences*, Lecture Notes in Electrical Engineering 371,
DOI 10.1007/978-3-319-27247-4_69

1 Introduction

Magneto-rheological fluids (MRF) are suspensions of particles, which can be magnetized, and exhibit fast, strong, and reversible changes in their rheological properties when a magnetic field is applied. Therefore, the fluids hold great potential in many applications including clutches, brakes, valves, dampers, haptic systems and robotics [1, 2]. Recently, there have been a number of researches on clutch using MRF [3–6]. In conventional MRC, generally coils are placed on a cylindrical housing of the clutch as shown in Fig. 1. This causes many disadvantages such as difficulties in manufacturing, the "bottle-neck" problem of the clutch magnetic circuit, high friction due to brushes.

Recently, a new configuration of MRC, as shown in Fig. 2, with the coil placed on a stationary housing (stationary winding core) was proposed [7]. With this proposed configuration, the coils are fixed and brushes are eliminated. Therefore, disadvantages of conventional MRC can be handled. In addition, it was shown that the moment of inertia of the output part in case of the proposed MRC was significantly smaller than that in case of the conventional one, which make it convenient to control speed of the output shaft. However, there were still some disadvantages in manufacturing such as; a nonmagnetic cylindrical housing was used and it was difficult to adjust the air gap between the stationary housing (the winding housing) and the rotary housing of the clutch.

In this paper, a new configuration of MRC with two mutual coils placed separately out of the rotary housing of the clutch is proposed. With this proposed configuration, the coils are fixed and brushes are eliminated. Therefore,

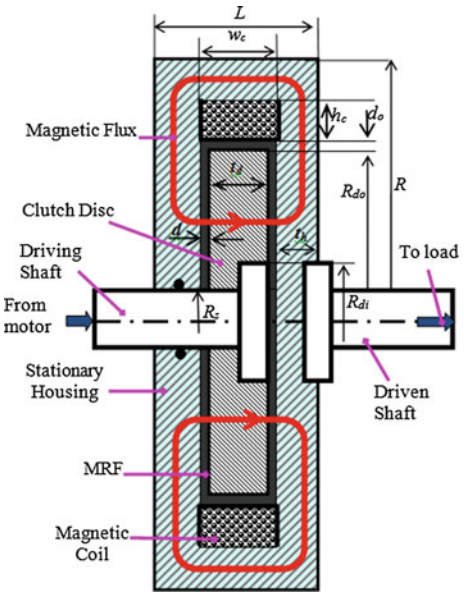

Fig. 1 Configuration of conventional MR clutch

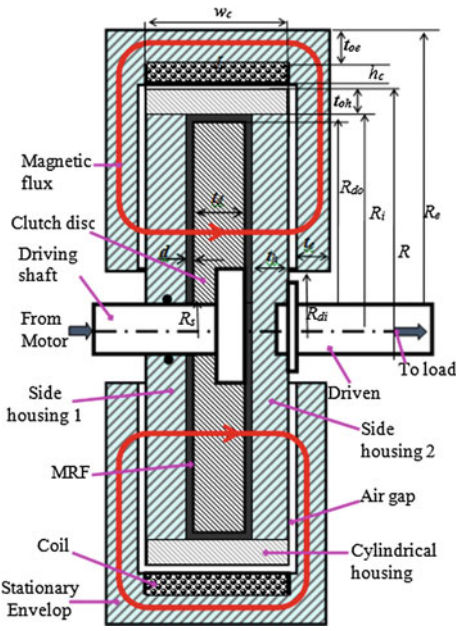

Fig. 2 Configuration of the MR clutch with stationary winding core [7]

disadvantages of conventional MRC can be handled. In addition, the proposed clutch is easier to manufacture and assemble than previous developed one, especially the air gap between the winding core and the rotary housing of the clutch can be adjust easily. After an introduction of the proposed configuration, transmitting torque of the MRC is analyzed and optimization of the proposed MRC is then performed considering maximum transmitting torque and mass of the clutch, together with the moment of inertia of the clutch rotary housing. Based on the optimal results, a comparison of the proposed MRC and the previous developed ones is undertaken and discussions on performance of the proposed MRC are given.

2 The Proposed MR Clutch with a Separated Coil

Figure 3 shows a configuration of the proposed MRC. As shown in the figure, a disc made of magnetic steel is fastened to the driving shaft made of nonmagnetic steel. The disc is embedded inside the clutch rotary housing made of magnetic steel. The space between the disc and the housing is filled with MRF. In order to prevent the leaking of MRF, lip seals are used. The clutch housing is then placed inside a stationary envelop with two mutual coils placed each side. To make sure that the clutch housing can freely rotate inside the envelope, a small air gap (0.3 mm) is left between the housing and the envelope. When counter currents are applied to the coils, a magnetic field is generated as shown in the figure, and the MRF in the gap

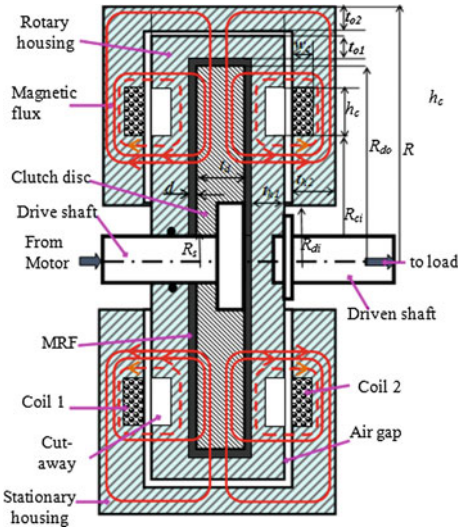

Fig. 3 Configuration of the proposed MR clutch

between the disc and the side housing parts becomes solid-like instantaneously. This results in a controllable torque transferred from the disc (the driving shaft) to the housing (the driven shaft) via the solidified MR fluid. It is noted that a cut-away section is made at each side of the rotary housing to prevent the magnetic flux from going through it (the dashed lines) without going through the MRF duct.

In order to evaluate the transmitted torque of the clutch, it is assumed that the MRF follows Bingham plastic rheological model and velocity profile of the MRF is linearly distributed from the disc to the housing. In this case, the induced transmitted torque and the off-state torque of clutch can be respectively determined by

$$T_c = \frac{\pi\mu_{e1}R_{do}^4}{d}[1-(\frac{R_{co}}{R_{do}})^4]\Omega + \frac{4\pi\tau_{ye1}}{3}(R_{do}^3 - R_{co}^3) + \frac{\pi\mu_{e2}R_{ci}^4}{d}[1-(\frac{R_{di}}{R_{ci}})^4]\Omega + \frac{4\pi\tau_{ye2}}{3}(R_{ci}^3 - R_{di}^3) + 2\pi R_{do}^2 t_d(\tau_{ya} + \mu_a\frac{\Omega R_{do}}{d_o}) + 2T_{sf} \quad (1)$$

$$T_{c0} = \frac{\pi\mu_0 R_{do}^4}{d}[1-(\frac{R_s}{R_{do}})^4]\Omega + \frac{4\pi\tau_{y0}}{3}(R_{do}^3 - R_s^3) + 2\pi R_{do}^2 t_d(\tau_{y0} + \mu_0\frac{\Omega R_{do}}{d_o}) + 2T_{sf} \quad (2)$$

where R_{do} is the outer radius of the disc, R_{di} is the inner radius of the active MRF volume in the end-face duct which is almost equal to the outer radius of the shaft flange, R_s is the shaft radius at the sealing, R_{ci} and R_{co} are the inner radius and outer radius of the coil, d is the gap size of the MRF duct, t_d is the thickness of the disc, Ω is the relative angular velocity between the drive shaft and the driven shaft, μ_{e1} and μ_{e2} are respectively the average post yield viscosities of MRF in the outer and inner end-face ducts, μ_a is the average post yield viscosity of MRF in the annular duct,

τ_{ye1} and τ_{ye2} are respectively the average yield stresses of MRF in the outer and inner end-face ducts, τ_{ya} is the average yield stress of MRF in the annular duct, τ_{y0} and μ_0 are the zero-field yield stress and viscosity of the MRF, and T_{sf} is the friction torque between the shaft of the brake and the sealing. It is noted that the induced yield stresses τ_{ye1}, τ_{ye2}, τ_{ya}, and the average post yield viscosities μ_{e1}, μ_{e2}, μ_a are fluid properties depending on the exerted magnetic flux density across the ducts of MRF and can be estimated by the following equation [8]:

$$Y = Y_\infty + (Y_0 - Y_\infty)(2e^{-B\alpha_{SY}} - e^{-2B\alpha_{SY}}) \tag{3}$$

where Y stands for a rheological parameters of MRF such as the yield stresses (τ_{ye1}, τ_{ye2}, τ_{ya}) and the post yield viscosities (μ_{e1}, μ_{e2}, μ_a). The value of Y tends from the zero-applied field value Y_0 to the saturation value Y_∞. α_{SY} is the saturation moment index of the Y parameter. B is the applied magnetic density.

The lip seal friction torque T_{sf} can be approximately calculated by [9]

$$T_{sf} = 0.65(2R_s)^2\Omega^{1/3} \tag{4}$$

In the above, T_{sf} is the friction torque of a lip seal in ounce-inches, Ω is measured in rounds per minute (RPM), and R_s is measured in inches.

3 Optimal Design of the Proposed MR Clutch

In design of MR clutch, besides the transmission torque, other issues should be taken into account are moment of inertia of the rotating housing and total mass of the clutch. It is obvious that the moment of inertia of the housing and total mass of the clutch should be as small as possible to reduce the clutch size and facilitate the speed and torque control of the driven shaft. The moment of inertia of the rotating housing can be approximately calculated by

$$I_h = \frac{1}{2}\pi\rho_h[t_h(2R_{hi}^4 - R_s^4) + L(R_{ho}^4 - R_{hi}^4) - 2t_c(R_{co}^4 - R_{ci}^4)] \tag{5}$$

where ρ_h is material density of the clutch housing. R_{ho} and R_{hi} are respectively the outer and inner radius of the cylindrical housing part, R_s is the shaft radius, t_h is the thickness of the side housing part, L is the length of the cylindrical housing part, t_c is the thickness of the cut-away section.

The mass of the clutch can be approximately calculated by

$$m_c = V_d\rho_d + V_h\rho_h + V_s\rho_s + V_{MR}\rho_{MR} + V_{wh}\rho_{wh} + V_c\rho_c \tag{6}$$

where V_d, V_h, V_s,V_{MR}, V_{wh} and V_c are respectively the geometric volume of the disc, the housing, the shaft, the MRF, the winding housing and the coil of the brake.

There parameters are functions of geometric dimensions of the MRB structures, which vary during the optimization process. ρ_d, ρ_h, ρ_s, ρ_{MR}, ρ_{wh} and ρ_c are density of the discs, the housing, the shaft, the MRF, the winding housing and the coil material, respectively.

Consequently, the optimization design problem of the MRC can be summarized as follows: *Find optimal value of significant dimensions of the MRC so that the brake mass determined by Eq. (6) is minimized, while its maximum transmitting torque determined by Eq. (1) is constrained to be greater than a required torque. During the optimization, the moment of inertia of the rotating housing, the off-state torque and the outer diameter of the clutch are taken into account as a reference parameter.*

In the optimization, the disc thickness t_d, the inner disc radius R_{di}, the outer disc radius R_{do}, the coil width w_c, the coil height h_c, the coil radius R_{ci}, the clutch outer housing thickness t_o, the winding outer housing thickness t_{o2}, the clutch side housing thickness t_{h1}, the winding side housing thickness t_{h2} are considered as design variables. It is noteworthy that the smaller value of the MRF duct size d is the higher braking torque and the smaller mass of the MR clutches can be obtained. Therefore, in this paper, the MRF gap sizes are not considered as a design variable and empirically set by 1 mm. The thickness of the cut-away section is set by 1.2 mm considering manufacturing convenience of the clutch.

In order to obtain the optimal solution, a FEA code integrated with an optimization tool is employed. In this paper, the first order method with steepest descent algorithm of ANSYS optimization tool is used.

4 Results and Discussions

Figure 4 show the optimal solution the proposed MRC. The transmitting torque is constrained to be greater than 10 Nm and the convergence rate is set by 0.1 %. It is noteworthy that the shaft radius in this case is set by R_s = 6 mm considering the strength of the shaft. As shown in the figure, the optimization is converged after 31 iterations. The optimal results at the 31st iteration are (mm): t_d = 8.1, R_{di} = 11.5, R_{do} = 47.4, w_c = 4.5, h_c = 10.6, R_{ci} = 34.3, t_o = 2, t_{o2} = 2, t_{h1} = 3; t_{h2} = 9.8. At the optimum, the transmission torque can reach up to 10 Nm as constrained, the mass of the MRC is 2.1 kg, the minimum mass inertia moment is 4.8×10^{-4} kg m^4, the off-state torque is 0.34 Nm and the outer diameter is 52.6 mm. The magnetic flux and geometry of the clutch at the optimum is shown in Fig. 4b.

In order to evaluate the proposed MRC, optimal solution of the previous MRC (Fig. 2) is also obtained and presented in Fig. 5. As shown in the figure, the optimization is converged after 31 iterations. The optimal results at the 31st iteration are (mm): t_d = 5, R_{di} = 21.8, R_{do} = 46.6, h_c = 4.6, t_o = 2, t_{o2} = 3.5, t_{h1} = 3; t_{h2} = 4.8. At the optimum, the transmission torque can reach up to 10 Nm as constrained, the mass of the MRC is 1.85 kg, the minimum mass inertia moment is 5.24×10^{-4} kg m^4, the off-state torque is 0.32 Nm and the outer diameter is

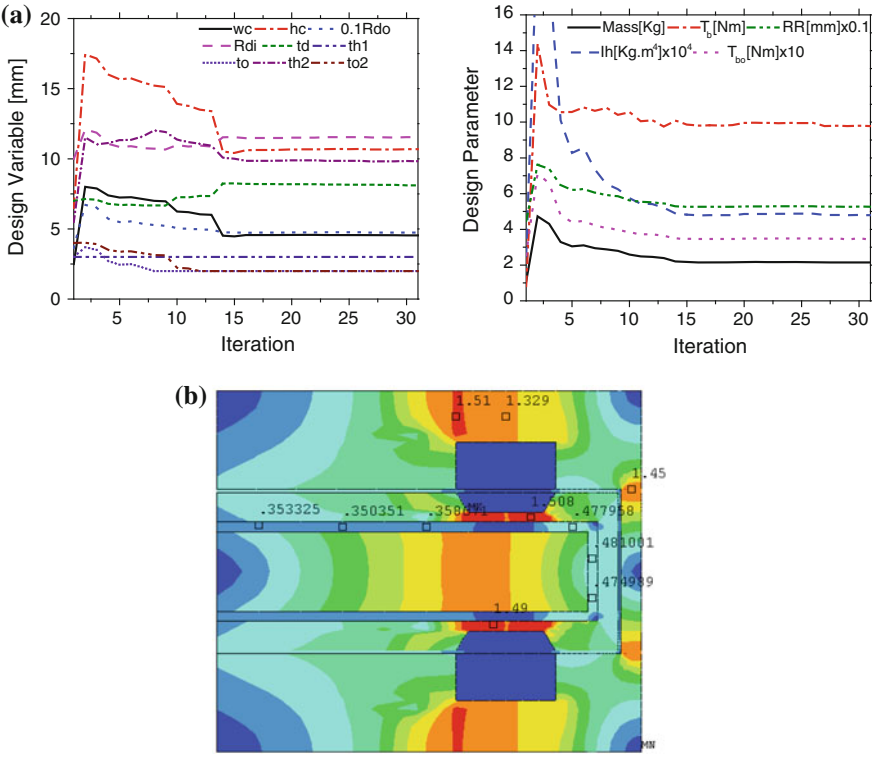

Fig. 4 Optimization solution of the proposed MRC. **a** Design variables, **b** magnetic flux density at the optimum

58.7 mm. The magnetic flux and geometry of the clutch at the optimum is shown in Fig. 5b.

In order to evaluate the proposed MRC at different required transmitting torque, optimal solutions of the proposed MRC and the previous MRC with different constrained transmitting torque are obtained and presented in Fig. 6. From the figure, it is observed that the mass and off-state torque of the proposed MRC are a bit greater than those of the previous MRC, however the moment of inertia and the outer radius of the proposed one are smaller than those of the previous one. Figure 7 shows the percentage difference between parameters of the proposed and the previous ones. It is seen that at high value of the required transmitting torque, the mass and off-state torque of the proposed MRC converge to those of the previous one while the moment of inertia and the outer radius become smaller and smaller.

It is again to note that the proposed MRC is much easier for manufacturing and maintenance compared to the previous one. This is a very important factors should be taken into account in design and application of the MRC.

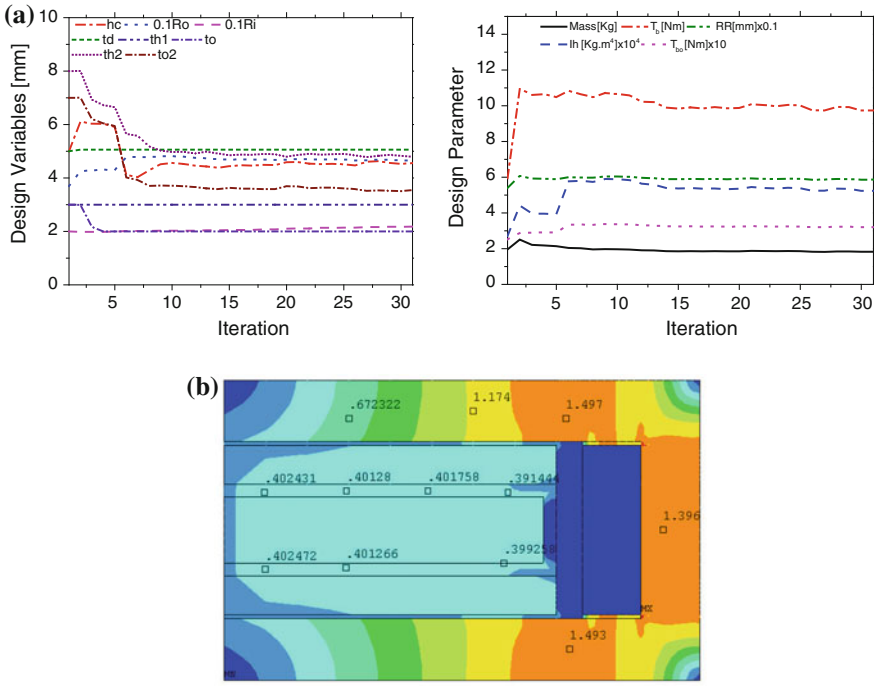

Fig. 5 Optimization solution of the previous MRC [7]. **a** Design variables, **b** magnetic flux density at the optimum

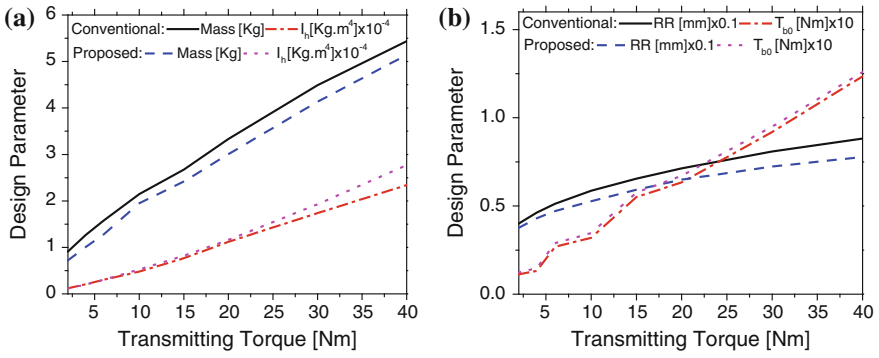

Fig. 6 Dependence of design parameters on transmitting torque. **a** Mass and moment of inertia, **b** off-state torque and outer radius

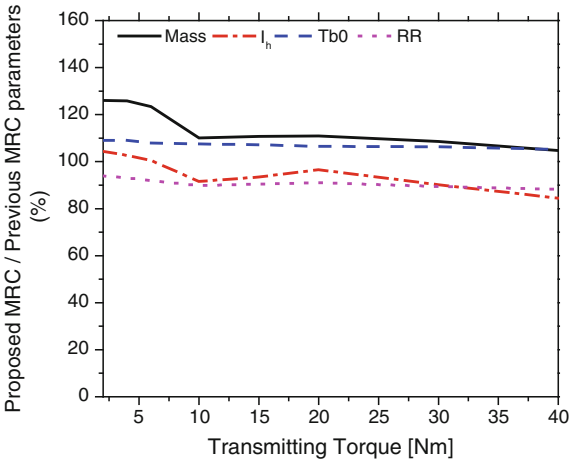

Fig. 7 Percentage of the design parameters

5 Conclusions

In this paper, a new configuration of magneto-rheological clutch (MRC) was proposed. In the new configuration, the clutch is placed inside a stationary envelope (the winding housing) on which the coils are wounded. Two mutual coils are placed on each side of the winding housing. With this configuration, no nonmagnetic cylindrical housing of the clutch is required as previous developed MRC [7]. In addition, a gasket can be employed between the two parts of the winding housing. This make the proposed MRC is much easier for manufacturing, assemble and maintenance because the coil is fixed and no brushes are required. After the introduction of the proposed configuration, transmitting torque of the MRC was analyzed based on Bingham-plastic rheological model of MRF and the optimization of the MRC was performed. The optimal solutions showed that the mass and off-state torque of the proposed MRC are a bit greater than those of the previous MRC, however the moment of inertia and the outer radius of the proposed one are smaller than those of the previous one. It was also showed that at high value of the required transmitting torque, the mass and off-state torque of the proposed MRC converge to those of the previous one while the moment of inertia and the outer radius become smaller and smaller.

Acknowledgments This research was funded by the Vietnam National Foundation for Science and Technology Development (NAFOSTED) under grant no.107.01-2015.32.

References

1. Wang J, Meng G (2001) Magneto-rheological fluid devices: principles, characteristics and applications in mechanical engineering. J Mater Des Appl 215(3):165–174
2. Muhammad A, Yao XL, Deng JC (2006) Review of magnetorheological (MR) fluids and its applications in vibration control. J Mar Sci Appl 5(3):17–29
3. Lampe D (1998) MRF-clutch—design considerations and performance. In: ACTUATOR 98, Bremen
4. Lee U, Kim D, Hur N, Jeon D (1999) Design analysis and experimental evaluation of an MR fluid clutch. J Intell Material Syst Struct 10:701–707
5. Kikuchi T, Ikeda K, Otsuki K, Kakehashi T, Furusho (2009) Compact MR fluid clutch device for human-friendly actuator. J Phys Conf Ser 149:012059
6. Nguyen QH, Choi SB (2014) A new method for speed control of a DC motor using magnetorheological clutch. In: Proceedings of SPIE 9057, San Diego, USA
7. (2014) Development of a new clutch featuring MR fluid with two separated mutual coils. In: Proceedings of the 14th international conference on electro-rheological fluids and magneto-rheological suspensions, Granada, Spain
8. Nguyen QH, Choi SB (2010) Optimal design of an automotive magneto-rheological brake considering geometric dimensions and zero-field friction heat. Smart Mater Struct 19(11):1–10
9. EPS Division (2006) Rotary seal design guide. Parker Hannifin Corporation, Catalog EPS 5350

Estimation of Static Hydrodynamic Coefficient in Waves Using Static Drift Test

M.J. Jeon, D.H. Lee, D.M. Lee, V.M. Nguyen and H.K. Yoon

Abstract This paper describes oblique towing tests for estimating ship maneuverability in waves. PMM test in towing tanks is widely used to estimate the hydrodynamic coefficient in the hydrodynamic force model. In this paper, the static drift test was carried out to derive the static hydrodynamic coefficients in calm water and in waves. The 4600TEU container ship was selected to analyze the difference of hydrodynamic coefficient between in calm water and in waves.

Keywords Maneuverability · Static drift test · Hydrodynamic coefficient · Waves

1 Introduction

When ships turn on the way, many accidents have been occurred at sea due to the environmental effect. As the accidents increase due to the environmental effect, the strict maneuverability is needed for safety at sea. In general, ship maneuverability has been researched in calm water condition through the model test or sea trial, however, the environmental effects such as current, wind, shallow water and waves exist in the real situation. The influence of wind on the external force acting on a ship has been researched by carrying out wind tunnel test [1]. Ship maneuverability in waves can be different from the one in calm sea condition. These days, according to the increase in economic viability of ship operation and safe navigation, ship maneuverability in waves has been considered so much. Commonly free running model test in waves is the effective method to estimate ship maneuverability in waves and some research papers were announced [2]. Recently, ship maneuverability considering ship motion and its nonlinear motion have been researched [3]

M.J. Jeon · D.H. Lee · D.M. Lee · V.M. Nguyen · H.K. Yoon (✉)
Changwon National University, Changwon, Korea
e-mail: hkyoon@changwon.ac.kr

V.H. Duy et al. (eds.), *AETA 2015: Recent Advances in Electrical Engineering and Related Sciences*, Lecture Notes in Electrical Engineering 371,
DOI 10.1007/978-3-319-27247-4_70

(Sung et al. 2012). As the first step to investigate the maneuverability of a ship in waves, we performed the static drift test which is the one of the Planar Motion Mechanism (PMM) test, and it gives us the hydrodynamic force and moment acting on an oblique towing ship. Static hydrodynamic coefficients can be estimated by its results.

2 Model Test

2.1 Test Facility

The model test was conducted in the square towing tank in Changwon National University (CWNU) as shown in Fig. 1. The wave maker is at the end of towing tank. The wave absorber is at the opposite side. The wave maker can make wave with a height of up to 20 cm and a wave length of up to 3 m in regular wave condition. The principal dimensions of the towing tank in CWNU are listed in Table 1.

2.2 A Model Ship

The 4600TEU container ship was selected as the target ship of the model test since the geometry is similar with KCS which is widely known in the field of naval architect. So, the hydrostatic and hydrodynamic characteristics of KCS could be easily acquired. And, the results of static drift test in calm water of 4600TEU container ship can be compared with the same test result of KCS. The principal dimensions of 4600TEU container ship are listed in Table 2. The scale ratio was decided considering the size of the towing tank. The model test was carried out in designed Froude number. A 6-component potentiometer and 3-component load cell are installed on the model ship in order to measure ship's motion caused by waves

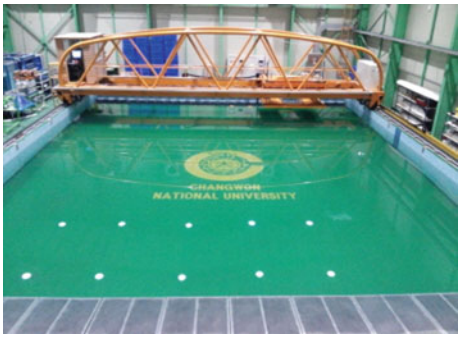

Fig. 1 Square towing tank in Changwon National University

Table 1 Principal dimensions of the CWNU square tank

Item (unit)	Value
Length (m)	20
Breadth (m)	14
Depth (m)	1.8
Max. towing velocity (m/s)	1.0
Max. length of a model ship (m)	1.5

Table 2 Principal dimensions of 4600TEU container ship

Item (unit)	Real	Model
Scale ratio	247	
Fn	0.24	
LBP (m)	237	0.96
Breadth (m)	37	0.15
Depth (m)	22	0.089
Draft (m)	12	0.049
Displacement (m^3)	70,825	0.0047
Wetted Surface Area (m^2)	10,982	0.18
Speed (m/s)	12	0.74

and force and moment. During the model test, surge, sway, roll and yaw are fixed, while heave and pitch are free (Fig. 2).

2.3 Test Condition for Static Drift Test

Test condition for static drift test in calm water and waves are listed in Table 3. The wave length and height were selected in accordance with model ship's length and to satisfy the linear waves which is valid only on the small wave steepness. The oblique towing was carried out in calm water and waves without diagonal towing, so all the waves come to the ship in the front.

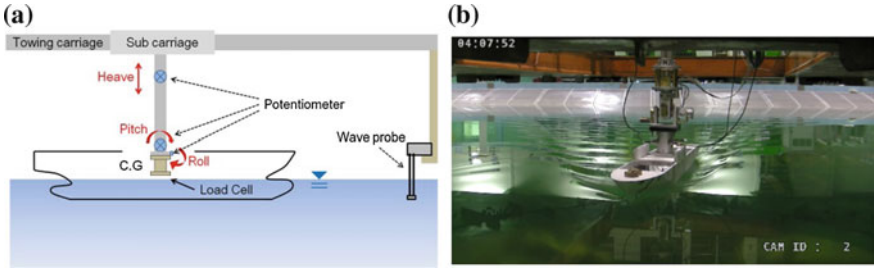

Fig. 2 4600TEU container model ship. **a** Diagram of installed model ship, **b** actual figure of installed model ship

Table 3 Test condition in calm water and waves

Class	Test condition	
	Variable (unit)	Value
Oblique towing	$\beta\,(^{\circ})$	$0, \pm 2, \pm 4, \pm 6, \pm 8, \pm 10, \pm 12, \pm 15$
Wave length	λ/L_{BP}	0.7, 1.0, 1.2
Wave height	A/L_{BP}	0.01
Wave direction	$\mu\,(^{\circ})$	180

3 Hydrodynamic Force and Moment

3.1 Coordinate Systems

The coordinate system to describe hydrodynamic force and moment acting on a ship maneuvering is shown in Fig. 3. The o-$x_o y_o$ is the earth-fixed coordinate fixed at a point in the earth. And the o-xy is body-fixed coordinate fixed at center of gravity of a ship.

3.2 Hydrodynamic Force and Moment Model

The horizontal plane motion consisting of surge, sway and yaw was considered and its equations of motion in calm water with respect to the body-fixed coordinate are described as follows;

$$\begin{aligned} &m(\dot{u} - vr - x_G r^2) = X_H + X_T \\ &m(\dot{v} + ur + x_G \dot{r}) = Y_H + Y_T \\ &I_{zz}\dot{r} + mx_G(\dot{v} + ur) = N_H + N_T \end{aligned} \tag{1}$$

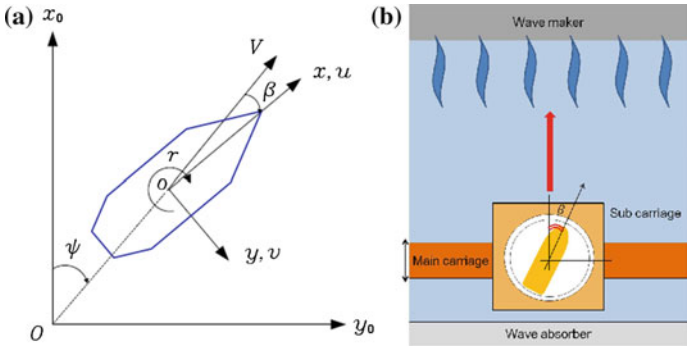

Fig. 3 Coordinate systems. **a** Coordinate systems of a ship, **b** definition of drift angle and wave direction

where:

m	Mass of a ship (kg)
u, v	Surge and sway velocities (m/s)
$\dot{u}$	Surge acceleration (m/s^2)
$\dot{v}$	Sway acceleration (m/s^2)
$\dot{r}$	Yaw acceleration (m/s^2)
I_{zz}	Mass moment of inertia with respect to z-axis ($kg\,m^2$)
X_H, Y_H, N_H	Hydrodynamic force and moment (N, N m)
X_T, Y_T, N_T	Towing (negative measuring) force and moment (N, N m)

Hydrodynamic force and moment in Eq. (1) are modeled as follows, and the towing force and moment measured by load cells installed on the model as shown in Fig. 2.

$$\begin{aligned} X_H &= X_{\dot{u}}\dot{u} + X_{uu}u^2 + X_{v|v|}v^2 + X_{vr}vr + X_{rr}r^2 \\ Y_H &= Y_{\dot{v}}\dot{v} + Y_{\dot{r}}\dot{r} + Y_v v + Y_r r + Y_{vvv}v^3 + Y_{vvr}v^2 r + Y_{vrr}vr^2 + Y_{rrr}r^3 \\ N_H &= N_{\dot{v}}\dot{v} + N_{\dot{r}}\dot{r} + N_v v + N_r r + N_{vvv}v^3 + N_{vvr}v^2 r + N_{vrr}vr^2 + N_{rrr}r^3 \end{aligned} \tag{2}$$

where:

$X_{\dot{u}}, Y_{\dot{v}}, Y_{\dot{r}}, N_{\dot{v}}, N_{\dot{r}}$	Linear added mass coefficients
Y_v, Y_r, N_v, N_r	Linear damping coefficients
$X_{uu}, X_{v\|v\|}, X_{rr}$	Nonlinear hydrodynamic coefficient
$Y_{vvv}, Y_{vvr}, Y_{vrr}, Y_{rrr}$	Nonlinear hydrodynamic coefficient
$N_{vvv}, N_{vvr}, N_{vrr}, N_{rrr}$	Nonlinear hydrodynamic coefficient

Even though prime notation is not represented for convenience, ship related parameters, motion variable, external force, external moment, and hydrodynamic coefficients in Eqs. (1) and (2) are non-dimensional values. Nondimensionalization was performed based on the Society of Naval Architects and Marine Engineers (SNAME) definition, as follows:

$$F' = \frac{F}{\frac{\rho}{2}L_{BP}^2 V^2}, \quad M' = \frac{M}{\frac{\rho}{2}L_{BP}^3 V^2} \tag{3}$$

4 Test Result

4.1 Static Drift Test in Calm Water Condition

The linear damping coefficient Y_v and N_v could be derived from static drift test. And the hydrodynamic coefficients of 4600TEU container ship was compared to the one of KCS carried out in KRISO (Korea Research Institute of Ship and Ocean Engineering). The results of static drift test which was carried out in CWNU are

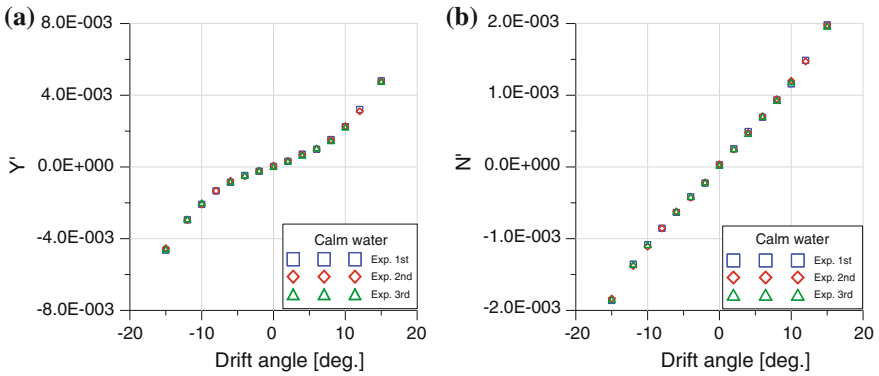

Fig. 4 Measured hydrodynamic force and moment in the static drift test of 4600TEU container ship in calm water. **a** Sway, **b** yaw

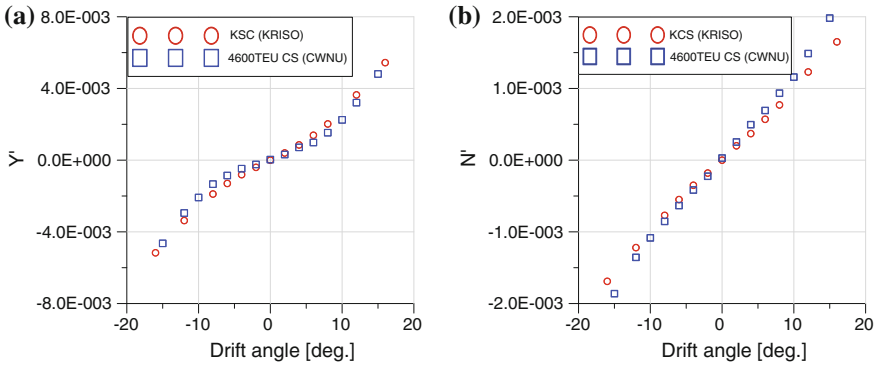

Fig. 5 Comparison of results between 4600TEU container ship and KCS in calm. **a** Sway, **b** yaw

shown in Figs. 4 and 5. All tests were repeatedly conducted more than 3 times. As shown in Fig. 4, the repeatability of the experiment could be guaranteed. The small difference between 4600TEU container ship and KCS appears due to the effect of difference of those shapes near bow and stern.

4.2 Static Drift Test in Waves

Static drift test in waves was carried out in 3 wave parameters. The sway hydrodynamic force and yaw hydrodynamic moment acting on a ship in waves are larger than the one measured in calm water condition. The tests are repeatedly conducted more than 2 times. Figures 6, 7 and 8 show the results of hydrodynamic force and

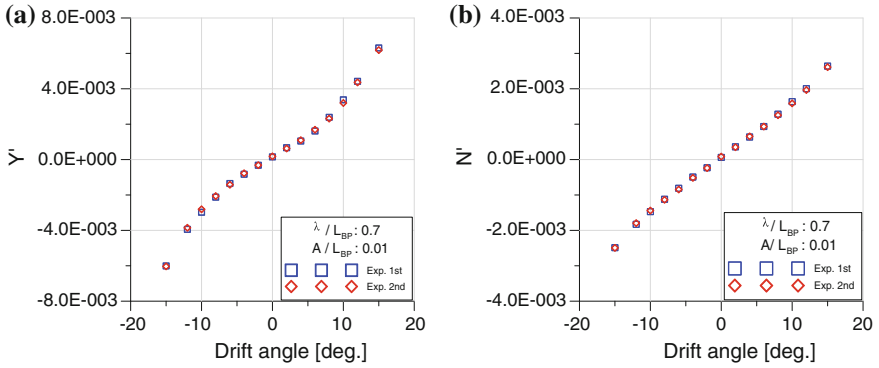

Fig. 6 Measured hydrodynamic force and moment in the static drift test of 4600TEU container ship in the waves ($\lambda/L_{BP} = 0.7$). **a** Sway, **b** yaw

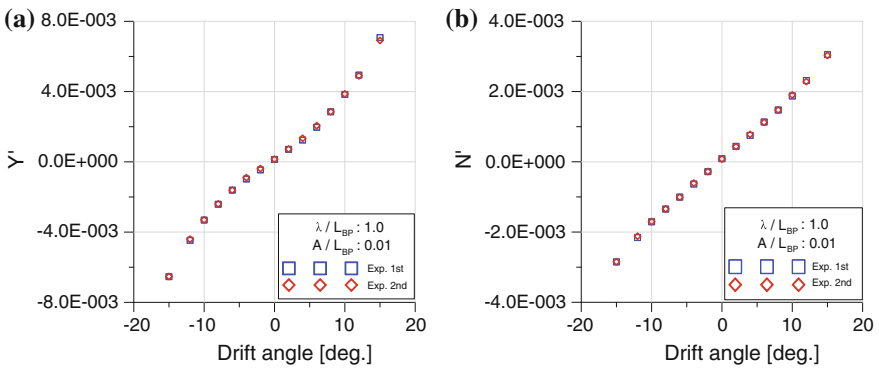

Fig. 7 Measured hydrodynamic force and moment in the static drift test of 4600TEU container ship in the waves ($\lambda/L_{BP} = 1.0$). **a** Sway, **b** yaw

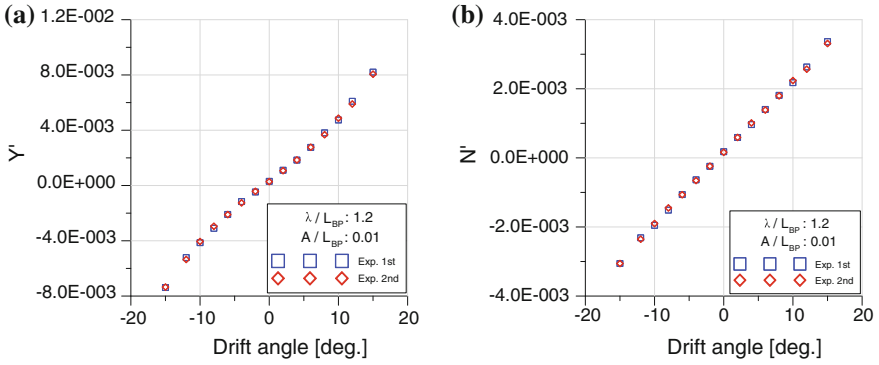

Fig. 8 Measured hydrodynamic force and moment in the static drift test of 4600TEU container ship in the waves ($\lambda/L_{BP} = 1.2$). **a** Sway, **b** yaw

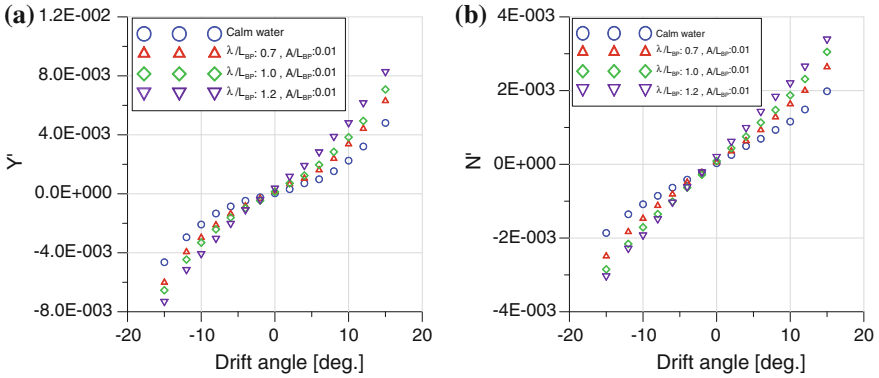

Fig. 9 Comparison of test results in calm water and waves. **a** Sway hydrodynamic force, **b** yaw hydrodynamic force

moment acting on a ship in various wave conditions. The repeatability in wave condition is also guaranteed.

Figure 9 shows the comparison results between in calm water and in waves. As the wave length increases, the motion response in heave and pitch also increased in this experiment. The increase of the radiation component caused by a ship's motion and the diffraction component caused by waves are the reasons why the hydrodynamic force and moment in waves increase.

As shown in Fig. 9, as the wave frequency approaches to the low frequency, the values of hydrodynamic coefficient appear to be large. Since the waves acting on ships generate the ship motion, its radiation components causing the additional resistance can be increased. For this reason, the hydrodynamic force can be different between in calm water and in waves. The hydrodynamic coefficients of 4600TEU container ship derived from static drift test in calm water and in waves are listed in Table 4. As the wave length is larger, sway damping and negative yaw damping due to the drift become larger, too. That means course keeping stability becomes worse in near the same wave length condition as the ship's length.

Table 4 The hydrodynamic coefficient

Hydrodynamic coefficient	Calm water	$\lambda/L_{BP} = 0.7$	$\lambda/L_{BP} = 1.0$	$\lambda/L_{BP} = 1.2$
X'_{vv}	−5.2401E-3	−4.2704E-3	−3.8363E-3	−1.5215E-3
Y'_{v}	−2.5168E-3	−7.9665E-3	−1.1111E-2	−1.8259E-2
$Y'_{v\|v\|}$	−5.9272E-2	−5.9457E-2	−5.6826E-2	−4.4225E-2
N'_{v}	−5.5664E-3	−7.2856E-3	−9.0313E-3	−1.1252E-2
$N'_{v\|v\|}$	−6.6429E-3	−9.6350E-3	−8.5971E-3	−3.8882E-3

5 Conclusion

The 4600TEU container ship was used in the static drift test in calm water and in waves. In this experiment, the hydrodynamic force and moment model in the equations of maneuvering motion were used to estimate hydrodynamic coefficient. From the static drift test in calm water condition, the availability was determinable by comparing with the results of static drift test using KCS and carrying out repetitive tests. From the static drift tests in waves, as the wave length increases, so the hydrodynamic coefficients do.

In the future, the dynamic test will be carried out in various wave directions such as bow quartering sea, stern quartering sea, following sea and beam sea conditions. While the test conditions in this experiment included a single wave height, various wave height and wave length will be included in the next testing conditions. Furthermore, the maneuvering simulation in calm water and in waves will be conducted by using various hydrodynamic coefficients derived from the model test in calm water and in waves.

Acknowledgements This study was supported by the research project "Development of Solution for Safety and Optimal Navigation Path of a Ship Considering the Sea State" supported by Ministry of Trade, Industry and Energy in Korea.

References

1. Fujiwara T, Ueno M, Nimura T (1998) Estimation of wind forces and moments acting on ships. J Soc Naval Architects Jpn (183):77–90
2. Hirano M, Takashina J, Takaishi Y, Saruta T (1980) Ship turning trajectory in regular waves. Trans West-Jpn Soc Naval Architects (40):17–31
3. Seo MG, Kim Y (2011) Numerical analysis on ship maneuvering coupled with ship motion in waves. Ocean Eng 38:1934–1945
4. Kim YG, Yeo DG, Son NS, Kim SY, Yun KH, Oh BI (2011) Prediction of maneuverability of KCS with 4 degrees of freedom. JSNAK 48(3):267–274
5. Jeon MJ, Nyugen VM, Yoon HK (2015) An analysis of added resistance in waves in various heading angles based on model test. ACMSSR
6. Kang SH, Yoon HK (2012) The comparison of hydrodynamic coefficients obtained by diverse method in the square tank. ACMSSR

Part XI
Computational Mechanics

Calibrating a Fracture Criterion for a Numerical Simulation of Warm-Incremental Forming Process

Le Van Sy

Abstract Incremental sheet forming (ISF) is an innovative die-less technique for forming the product from sheet materials. This process has been attracted a considerable interest of the scientific community due to its high formability, flexibility, short lead-time and inexpensive equipment. However, applicability of this process in practices is limited by anticipating mechanical failures during the forming process. This paper presents implementing a developing fracture model into finite element simulation to predict the occurrence of fracture in forming a cone shape. The works were begun by analyzing material properties, choosing fracture criteria, and implementing into ABAQUS environment. Finally, the simulated results were validated by one of practical experiments in aspects of, for instance, geometric accuracy and formability. They showed an excellent agreement between the simulated work and the experiment conducted in this study.

Keywords ISF · Fracture criteria · Incremental forming · ABAQUS · Die-less

1 Introduction

Incremental sheet forming (ISF) has been known as a pre-eminent process which enables strains much higher than one of traditional sheet forming processes like deep drawing, stamping and stretching. Experimental evidence showed that sheet metal is stretched more than once in the conventional stamping operation. A consequence of this is a higher forming limitation of ISF in comparison with the common forming limited curve (FLC). However, ISF is limited by the type of deformation which is close to plane strain for the part deformed in normal forming way of this process (i.e. in ISF process with one stage) [1]. Higher FLC of ISF

L.V. Sy (✉)
PetroVietnam University (PVU), Ba Ria City, Vietnam
e-mail: sylv@pvu.edu.vn

V.H. Duy et al. (eds.), *AETA 2015: Recent Advances in Electrical Engineering and Related Sciences*, Lecture Notes in Electrical Engineering 371,
DOI 10.1007/978-3-319-27247-4_71

process is widely recognized and accepted in many researches but the explanation for this is still a challenging task for scientists in future researches.

The experimental evidence and analysis concluded that the formability of ISF process is mainly influenced by four major parameters: depth step, forming-tool speed, tool diameter, sheet thickness [1]. The forming-tool speed means as both feed-rate and spindle speed. The feed-rate is the displacement velocity of the tool which affects the efficiency of the forming process and also increases mechanical failures (e.g. formability) in the formed part. The spindle speed is known to influence the formability due to its influence on friction between forming tool and sheet surface. The influence of sheet thickness and depth steep is explained through sine law [1]. The last parameter, i.e. tool diameter, is usually explained to be due to the contacted area concentrating the strain. The larger tool diameter expands the distribution of strain over extended zone.

There are efforts to explain the deformation mechanism of ISF process through theoretical analyses and experimental evidence found in the literature. The questions arise from experimental observations such as enhanced forming limit and crack propagation along the circumferential direction. Silva et al. [2] used membrane analysis of a small plastic zone in the rotational symmetry components to explain aspects of formability and damage. The authors concluded that cracks triggered off in ISF process due to meridional tensile stresses. Martins et al. [3] used the Silva's results to study on careful examination of the geometry at the zone of localized deformation. The authors pointed out the evidence in which formability is limited by fracture without previous necking. It means that there is no evidence of an actual neck before the failure occurs in the part. The crack cannot grow because forming tool always moves in the deformation process. When the crack is going to obtain the fracture limit, the tool has already moved in another place. This explanation is not satisfactory because the sheet still stands in deformation tension.

Emmens [4] investigated the continuous bending under tension (BUT) to study aspects of ISF. The author explained that the case of the bending radius is constant, the formability defined that the limit strain in a single operation should become proportional to the sheet thickness assuming the bending under a tension mechanism to operate. Allwood et al. [5] presented that through-thickness shear can affect the formability by modeling ISF process with a finite element method. The authors demonstrated a significant through-thickness shear (TTS) occurring in the direction that is parallel to tool motion. It is explained that the material on the top surface of the sheet metal tends to move in the tool-moving direction due to a friction effect. However, another publication of the author showed that shear band being perpendicular to the forming-tool direction could not be explained directly by the friction effect due to the direction of the toolpath. Jackson [6] continued this work by examining experimentally through deforming the copper sheet with both TPIF (two point incremental forming) and SPIF (Single point incremental forming) approaches. The author presented that the deformation mechanisms are due to stretching and shear for both SPIF and TPIF process. The deformation due to stretching in the plane is perpendicular to the forming-tool direction which was similarly observed in FEM simulations [1]. The deformation due to shear effect is

parallel to the forming-tool direction and increases along the cross-section in the copper sheet which is similar to an experimental investigation of Allwood [5].

Eyckens et al. [7] used Marciniak–Kuczynski (MK) model to predict local necking in ISF process. The authors revealed that TTS occurred in this process. The presence of TTS can influence significantly the limit strain, which depends on the strain mode. The increase of the Forming Limited Diagram (FLD) is only the shear component in the plane perpendicular to the minor strain which is again in the moving direction of the tool has an effect on the FLD. Increasing in the formability of ISF process due to TTS is explained by the delay in a necking process. This delay is similar to the one in the onset of necking under a biaxial stretching mode in conventional forming process.

In general, the deformation mechanism and fracture mechanism in ISF process were explained on the viewpoint of the localized deformation without an explanation. Understanding the deformation and fracture mechanics in this process plays an important role in predicting the mechanical failures in forming the product before the practical manufacturing process is performed, which will emerge the potential performances of this process with the industrial applications. This work has been triggered off two significant impediments which meet the previous research efforts: (i) no agreement among the above-mentioned hypotheses of deformation mechanisms; (ii) what fracture criteria can apply for this process. Thus, this study uses a recently developing fracture model combined with finite element analyses to predict the occurrence of fracture in forming a cone shape. It was begun by analyzing material properties, choosing fracture criteria, and implementing into ABAQUS environment. Finally, the simulated results were validated by one of practical experiments in aspects of, for instance, geometric accuracy and formability. The works are organized concisely into three sections. The first section presents the reasons to select a valid fracture criteria for ISF process and role of stress triaxiality on mechanical fracture. The practical mechanical experiments are performed to calibrate the selected fracture criteria and the calibrated result are demonstrated in the second section. The final section is archived results and discussion.

2 Fracture Criteria and Calibaration

2.1 The Fracture Criteria for Sheet Metal

In the past decades, various fracture criteria to predict a ductile fracture of sheet metal have been proposed and developed. They are based on different mechanical models with different assumptions. Three main mechanisms can cause the fracture in a ductile metal sheet: ductile fracture due to the nucleation, growth, and coalescence of voids; shear fracture due to shear band localization; and instability due to local necking (Fig. 1). Based on phenomenological observations, these three mechanisms called for different forms of the damage criteria. The damage criteria

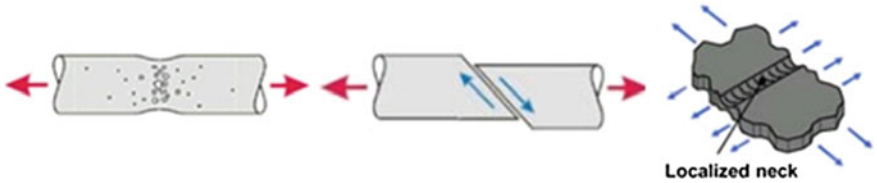

Fig. 1 Three mechanisms of damage in ductile metal

can be categorized into two groups: damage initiation criteria for fracture and damage initiation criteria for necking instability. This division is a convenience for using fracture criteria to predict mechanical failure in ISF process. The first group (Johnson-Cook, Wilkins, Gurson, FFLD, shear criteria) does not directly reflect the physical mechanism of ductile fracture, but it predicts the initiation of damage in deforming part. It is based on a macroscopic definition of a damage accumulation function. The second group (forming limit diagrams and Marciniak-Kuczynski) is the damage initiation criteria for the necking instability of sheet metal.

Generally, those criteria only consider solely the phenomenological observations (or fracture mechanisms) and give relative accuracy in prediction of damage. They have not carried out in a situation in general which the fracture mechanics of the forming process has not been clarified. Fortunately, Gese and Hooputra [8] proposed a fracture criteria named CrachFEM for thin sheets and extrusions (plane stress), which distinguishes among three mechanisms (i.e. ductile fracture, shear fracture and sheet instability) that are described by three different expressions. However, all three failure modes are uncoupled from each other due to avoiding a localization of the strains as a result of the softening of the material prior to fracture.

Ductile fracture model: For plane stress condition, the equivalent strain to fracture is assumed to depend only on the stress triaxiality. The equivalent plastic strain is given by

$$\bar{\varepsilon}_d(\eta, \dot{\bar{\varepsilon}}) = \frac{\varepsilon_T^+ \sinh[k_d(\eta^- - \eta)] + \varepsilon_T^- \sinh[k_d(\eta - \eta^+)]}{\sinh[k_d(\eta^- - \eta^+)]} \tag{1}$$

where ε_T^+ and ε_T^-: the equivalent plastic strain at ductile damage initiation for equi-biaxial tensile and equi-biaxial compressive deformation, respectively. η^- and η^+ : the stress triaxiality in equi-biaxial tensile deformation state and in equi-biaxial compressive deformation state, respectively.

For 3D-stress condition, the stress triaxiality η is no longer unique. Thus, the equivalent plastic strain is given by (2) (where d_0, d_1, and c are material dependent parameters)

$$\bar{\varepsilon}_f^d = d_0 e^{-3c\eta} + d_1 e^{3c\eta} \tag{2}$$

Shear fracture model: In the shear dominated zone, the fracture strain is postulated to depend both on the hydrostatic and deviatoric state.

$$\bar{\varepsilon}_f^s = d_2 e^{-f_s \theta_S} + d_3 e^{f_s \theta_S} \tag{3}$$

$$\begin{cases} \theta_S = \dfrac{\sqrt{24}(3k_s\eta - 1)\left(2 - 3\eta - \sqrt{3}\eta\sqrt{4 - 9\eta^2}\right)}{9\eta - 2 - \sqrt{3}\eta\sqrt{4 - 9\eta^2}} & \text{with } 0 \le \eta \le 0.33 \\ \theta_S = \dfrac{\sqrt{24}(3k_s\eta - 1)\left(2 - 3\eta - \sqrt{3}\eta\sqrt{4 - 9\eta^2}\right)}{9\eta - 4 + \sqrt{3}\eta\sqrt{4 - 9\eta^2}} & \text{with } 0.33 \le \eta \le 0.67 \end{cases} \tag{4}$$

where d_2, d_3, f_s, and k_s are three material constants; θ_s is shear fracture parameter.

Instability: The basic concept of sheet instability in CrachFEM algorithm is based on Marciniak–Kuczynski model (M-K). In CrachFEM model, the thickness ratio of imperfection and sheet is defined approximately at the neck cross section as following:

$$\frac{h}{h_0} = \left(1 - d_C \cos\left(\frac{\pi x'}{l}\right)\right) \tag{5}$$

where h and h_0 are the thickness of imperfection and initial sheet, respectively; d_C is the inhomogeneity; x'/l is the changing level of necking.

The CrachFEM model is implemented into ABAQUS coupled with the modular elasto-plastic material model under an explicit-dynamic integration scheme through VUMAT subroutine (user-defined material model) by [8]. CrachFEM can be used to predict the damage driven to three mechanisms for both shell and solid elements. However, the prediction of localized necking is only suited for shell elements. Thereby, there are two models for ductile fracture with the shell element and solid element.

2.2 Calibrating the Fracture Criteria

The CrachFEM model was clearly developed with a view of industrial application but involves totally in seven free parameters. The shear fracture model acknowledges the jointed effect of both stress triaxiality and the deviatory state through the definition of the parameter θ_S. Both fracture models are based on a fracture locus of the equivalent plastic $\bar{\varepsilon}$ strain and stress triaxiality η. The previous research [9] showed that the range of stress triaxialities in general deformation is from −1/3 to 2/3. The diagram presented a large range of the stress triaxiality as Fig. 2. To construct the locus of the stress triaxiality, many mechanical experiments need to be performed with different kinds of specimen such as normal tensile testing,

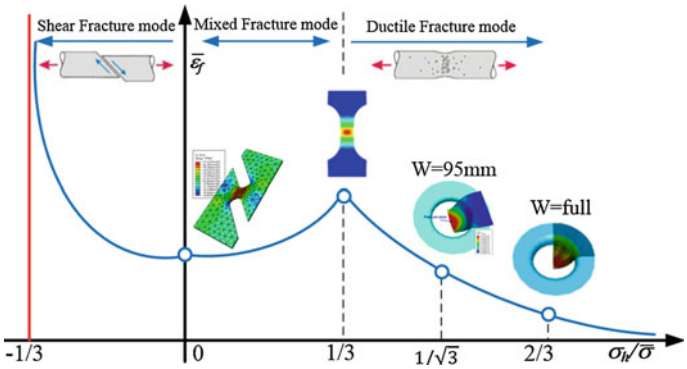

Fig. 2 Full range of stress triaxiality versus equivalent strain

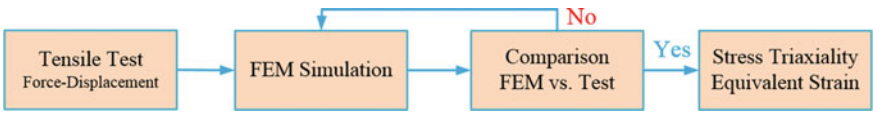

Fig. 3 Procedure to calibrate the fracture criteria

Nakazima testing, and shear testing with a special specimen, namely butterfly specimen.

The procedure to calibrate the fracture locus of the equivalent plastic strain and stress triaxiality η is shown in Fig. 3. Firstly, the practical experiments (Tensile, Nakazima, shear testing) were performed with different specimens (Fig. 4). The experimental results were input into a FEM simulation of the mechanical testing. Then, simulated results were compared to the practical results to evaluate the accuracy of a FEM model. If there is excellent agreement in stress-strain relation between practical and simulated results, the values of the equivalent plastic strain $\bar{\varepsilon}$ and stress triaxiality η were extracted from the simulated results. The calibrated fracture locus is shown in Fig. 5a, b, and c with different ranges of stress triaxility.

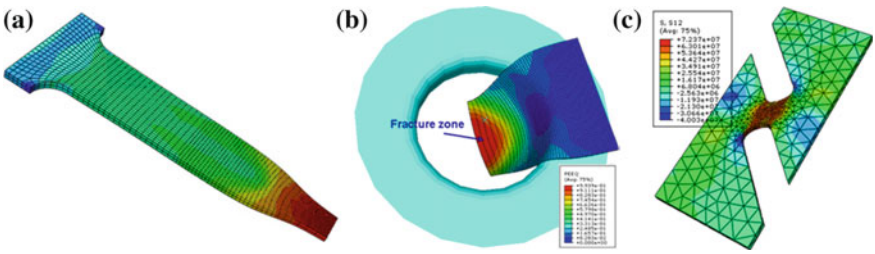

Fig. 4 Simulated results of **a** Tensile testing, **b** Nakazima testing, **c** Shear testing

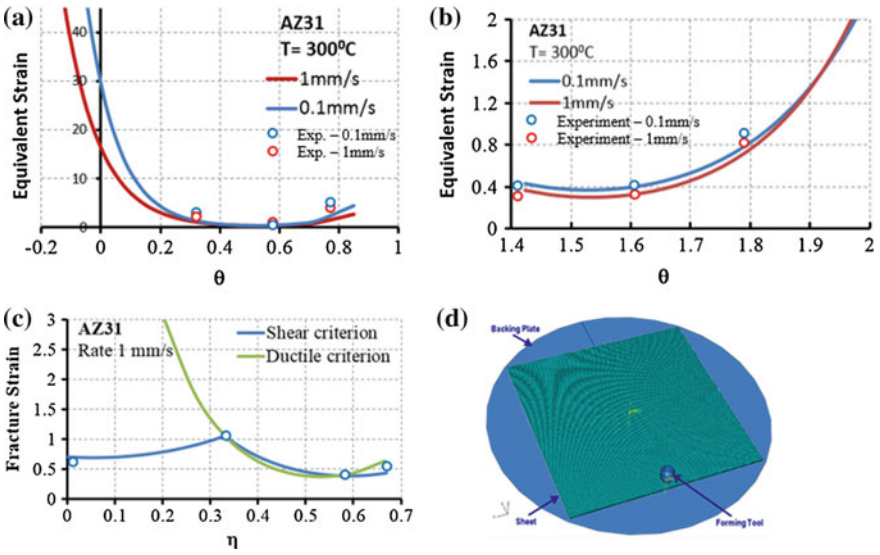

Fig. 5 Calibrated results in different ranges of stress triaxiality and simulating models

3 FEM Simulation of ISF Process

FEM simulation of ISF process is a very complicated task due to large and complex models and long movement of forming tool. A full model should be used for simulation of ISF process because this process is not symmetrical even for producing symmetric parts. The full model of cone shape with curvature generatrix should be used in FEM simulation to predict mechanical failures in ISF process due to two reasons: (i) the fracture position occurred on a deformed part cannot be foreknown; (ii) a partial model gives inaccuracy results because of incomplete boundary conditions. However, several previous studies performed the simulation with great efforts to simplify the calculation by modeling only one sector of symmetric part [3, 4]; sequentially, considerable errors occur in the analyses.

The results of mechanical testing showed that magnesium alloy sheet has a high sensitivity with temperature and strain rate. The linear thermal expansion of magnesium alloy sheet is higher than aluminum and steel alloy at both room and elevated temperature [3]. Thus, 3D-fully coupled thermal simulation is needed to take into account of thermal effects and strain rate. In addition, the heat conducted between surfaces of forming tool and sheet due to local deformation in ISF process should be obtained simultaneously rather than sequentially. In FEM simulation of ISF process, the previous researchers claimed that implicit solver met the difficult convergent problems and large computational time consuming. They are due to large model and many nonlinear problems contributed in this process. To overcome these, the explicit solver is a first choice for FEM simulation in which the mass-scale and time-scale approach are used to speed up the computational time.

Because of using full model and large deformation in ISF process, the distortion of elements in simulation is difficult to avoid. To overcome this problem, meshing adaptive approach should be used in an FEM simulation. It can trigger off a slight increase of computational time. However, reasonable setting of the parameters in adaptive meshing brings the computational efficiency in correspondence with the acceptable accuracy of the simulated results. The configuration for FEM simulation of ISF process includes:

- Forming tool and backing plate are modeled as isothermal rigid bodies.
- Sheet is modeled as a deformable body with a dimension of 200 × 200 × 1.5 mm. It is meshed with an eight-node brick element (C3D8RT) with reduction integration used in the fully coupled thermal analysis for saving computational time.
- Sheet is meshed in three layers to take into account of bending stiffness.

The element type used in FEM simulation has a significant influence on the obtained result. In previous research, it is reported that the best results can be achieved with the four-node shell element (S4R) which has assumed in a plane-stress state [7]. The computational time of this element is shorter than the brick element because it is taking into account of bending effect to emerge this behavior in ISF process. However, 3D fully coupled thermal analysis only applies for brick element which describes more accurately the stress state occurring to cross the thickness of sheet. Additionally, it is also used to apply for 3D complex constitutive model that depends on strain rate and temperature. These are main reasons predisposing the use of brick element to this study.

For evaluating the accuracy of thickness and geometry, a 90 mm-deep model (e.g. considering a model with wall angle from 28.25° to 88°) is used the FEM simulation. However, the evaluation of mechanical fracture occurring in the deformed part does not require this large range of wall angle. Thus, the simulation started from the depth of 21.113 mm until 90 mm for saving computational time.

4 Results and Discussion

4.1 Accuracy of Geometry and Thickness

The geometric accuracy of deformed part is an important aspect in ISF process. It is interested in this problem because the sheet is deformed without any die or partial die. Particularly, the sheet became softer when it is heated up to elevated temperature. The sheet deformation occurs far from the contact area of backing plate that is twisted about symmetric axe of product following rotating direction of spindle. It can be difficult to predict in this case. On theoretical view, ISF technique can deform a part with unlimited depth. However, a part with wall angle changing according to the obtaining depth can trigger off the inaccuracy of geometric shape. Thus, the stability of geometric shape should be investigated carefully in this study.

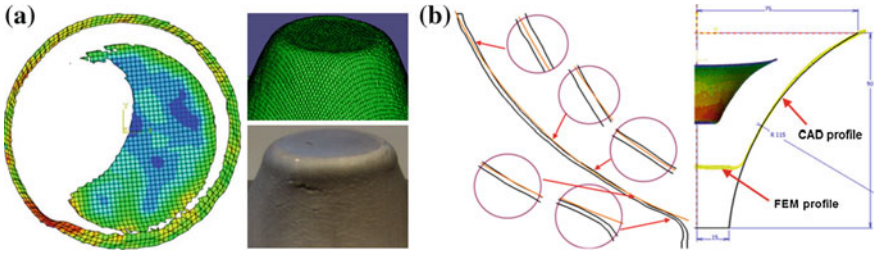

Fig. 6 Comparison between CAD profile and FEM profile

A comparison between the cone-top shape and the practical experiment at maximum achieved depth is also shown in Fig. 6a. The bottom of cone at depth of 61 mm is a concave shape which top of concavity is outward of part. The maximum height of the concavity is 0.02 mm that is very consistent with actual experiment. This result concluded that assuming a partial model for FEM simulation in ISF process for saving computational time could trigger off the inaccuracy in simulated results of the previous results [1, 7]. It should be noted that the part used in FEM simulation is not assumed as symmetric part, although the geometry of product is symmetric. The result showed the difference in both stress-strain state and geometric accuracy.

Figure 6b presented a comparison between CAD profile and a profile extracted from FEM simulation which showed that the section at different heights is not concentric. Thus, the profile is cut along the z-direction at many positions and a profile which has the most inaccuracy to be selected to compare with CAD profile. The measuring results of deformed part from coordinate measuring machine (CMM) are given two profiles of inner and outer surface. Each part is measured at three different positions along the achievable depth. The thickness of deformed part is calculated from measured results in Excel table. For FEM result, ABAQUS allows extracting two profiles of simulated part in wireframe. These profiles are then input into commercial CAD to measure the perpendicular distance between the profiles along the depth of the simulated part. Figures 6b and 7 presented the

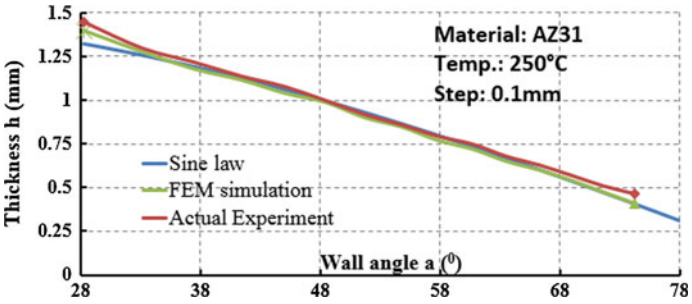

Fig. 7 Comparison of thickness accuracy between simulation and actual experiment

distribution of thickness of actual experiment and FEM simulation with respect to the achievable wall-angle in comparison with sine law. There is a good agreement between experimental result and FEM simulation.

4.2 Validation of Results

FEM simulation of ISF is performed at different processing parameters similar to actual experiments. The simulated results showed a good consistency with one of the actual experiments about the position of fracture and the achieved depth (Fig. 8). They also presented clearly the influences of processing parameters with respect to the experiments.

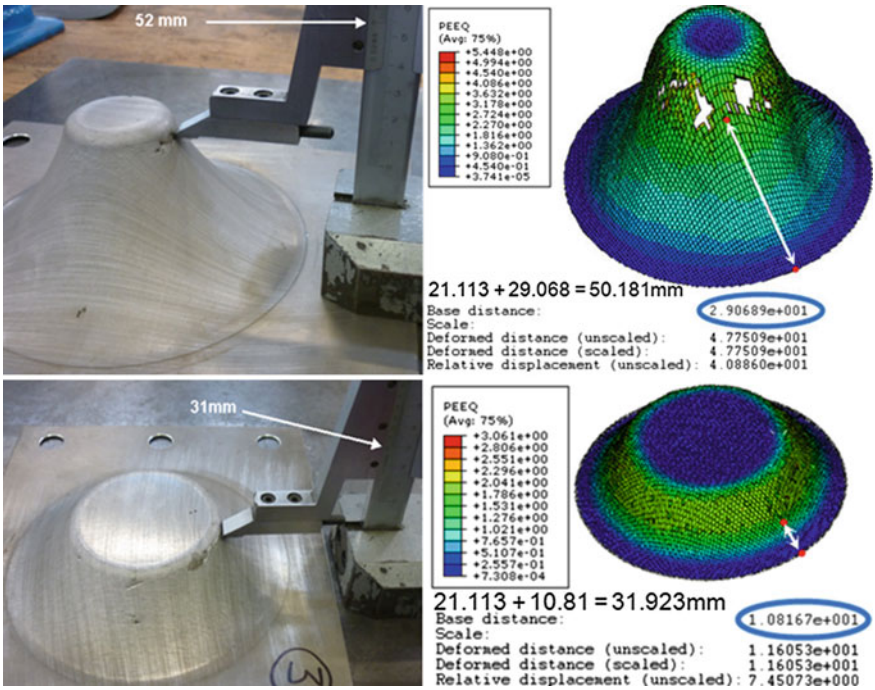

Fig. 8 Validation of simulated result and actual experiment

5 Conclusion

This paper reviewed the deformation and damage mechanics which are the base to choose a suitable fracture criterion for predicting a mechanical failure in ISF process. The damage criterion, called as CrachFEM, have been carried out successfully in this study. This criterion was transformed into a unique space which was convenient to compare together and then to apply for numerical simulation. The key parameter which greatly influenced the amount of plastic deformations, and which a material may undergo before ductile failure occurs, is stress triaxiality. The role of triaxiality for fracture criteria for metal sheet is also presented in this paper. The final aspects relate to the implementation of a progressive damage and failure model on numerical simulation for ductile metals in ABAQUS is mentioned. An excellent agreement between simulated results and the practical experiments was found in predicting the mechanical fractures, thickness and geometric accuracy of the formed part in ISF process.

References

1. Jeswiet J, Allwood J, Micari F, Hirt G, Bramley A, Duflou J (2005) Asymmetric single point incremental forming of sheet metal. CIRP Ann Manuf Technol 54(2):88–114
2. Silva MB, Skjoedt M, Martins PAF, Bay N (2008) Revisiting the fundamentals of single point incremental forming by means of membrane analysis. Int J Mach Tools Manuf 48(1): 73–83
3. Martins PAF, Bay N, Skjoedt M, Silva MB (2008) Theory of single point incremental forming. CIRP Ann Manuf Technol 57(1):247–252
4. Emmens WC, van den Boogaard AH (2009) An overview of stabilizing deformation mechanisms in incremental sheet forming. J Mater Process Technol 209(8):3688–3695
5. Allwood JM, Shouler DR, Tekkaya AE (2007) The increased forming limits of incremental sheet forming processes. SheMet'07, Italy
6. Jackson K, Allwood J (2009) The mechanics of incremental sheet forming. J Mater Process Technol 209(3):1158–1174
7. Eyckens P, Bael AV, Van Houtte Paul (2009) Marciniak-Kuczynski type modelling of the effect of Through-Thickness Shear on the forming limits of sheet metal. Int J Plast 25(12):2249–2268
8. Gese H, Dell H, Werner H, Hooputra H (2004) A comprehensive failure model for crashworthiness simulation of aluminum extrusions. Int J Crashworthiness 9(5):449–464
9. Bao Y, Lee Y-W, Wierzbicki YBT (2005) Calibration and evaluation of seven fracture models. Int J Mech Sci 45(4):719–743

Building Structure Parameter Identification Using the Frequency Domain Decomposition (FDD) Method

Phuoc Nguyen Van

Abstract In recent years, Operational Modal Analysis, also known as Output-Only Analysis, has been used for estimation of modal parameters of the structures such as the buildings, bridges, towers, and mechanical structures. The advantage of this method is that expensive excitation equipment can then be replaced by ambient vibration sources such as wind, wave, and traffic used as input of unknown magnitude, and then modeled as blank interference in the modal identification algorithms. This paper presents an overview of the non-parameter technique based Frequency Domain Decomposition (FDD), dynamic model of n-storeybuilding and method of modal parameters identification using FDD. In addition, using statistical probability to evaluate the results that obtained the stiffness and inter-storey dift of 2-storey building.

Keywords Frequency domain decomposition · Operational modal analysis · Multi-degree of freedom · Single-degree of freedom · Experimental modal analysis · Singular value decomposition

1 Introduction

The experimental determination of structural modes of a structure can be divided into two methods: EMA and OMA. EMA requires knowledge of both input and output, which can be combined to yield stransfer function that describes the system. In recent decades, there are civil structures used OMA method. This method has been developed for many civil engineering structures such as buildings, bridges, rigs, … [1]. Operational modal analysis only requires measurement of the output from the system. In FDD method, spectral density matrix of multi-degree of freedom system is decomposed into a set of auto spectral density functions, each

P.N. Van (✉)
HCMC University of Technical and Education, Ho Chi Minh, Vietnam
e-mail: vanphuocspkt@gmail.com

V.H. Duy et al. (eds.), *AETA 2015: Recent Advances in Electrical Engineering and Related Sciences*, Lecture Notes in Electrical Engineering 371,
DOI 10.1007/978-3-319-27247-4_72

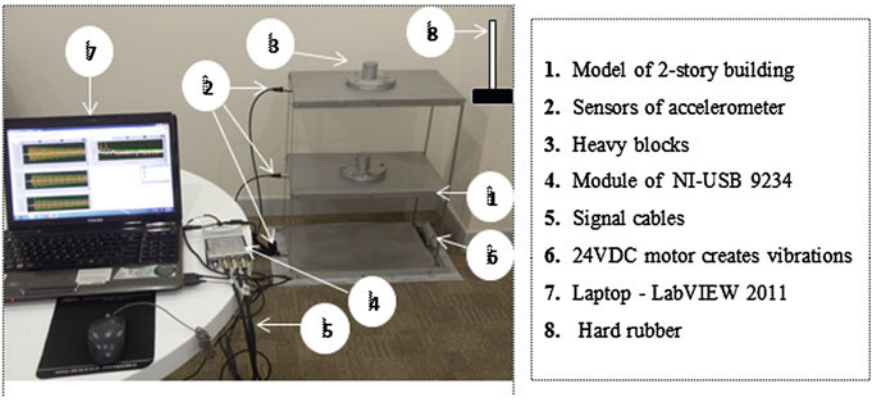

Fig. 1 Data acquisition system with NI-USB 9234 hardware in LabVIEW 2011

corresponding to a single degree of freedom. This method is illustrated by the measurement on a two-storey building model with the excitation source generated by a small hard plastic hammer and a vibration motor. The advantage of using data acquisition hardware NI-USB 9234 of National Instruments is to easily measure responses of accelerometers installed along the height of the building with LabVIEW 2011 as showed in Fig. 1. Then the data continues to be analyzed with Matlab with the support of advanced signal Processing tools. Finally, the modal parameters of the building are obtained as resonant frequency and mode shapes. In addition, the stiffness of each floor is also identified under the shear beam model assume of a two-storey building.

2 Main Content

2.1 Frequency Domain Decomposition (FDD)

The power spectrum density matrices of the input (unknown) and output (recorded) signal as functions of angular frequency ω respectively noted $[X](\omega)$ and $[Y](\omega)$. They are associated to the frequency response function matrix $[H](\omega)$ through the following equations [2, 3, 5, 6, 8, 9]:

$$[Y](\omega) = [H](\omega)^{*}[X](\omega)[H](\omega)^{T}. \tag{1}$$

If r is the number of inputs and m is the number of simultaneous recorded signals, at each angular frequency ω, the size of $[X](\omega)$, $[Y](\omega)$ and $[H](\omega)$ are

$r \times r$, $m \times m$ and $m \times r$, respectively. In OMA, the usual assumption is that the input is white noise. That means the power spectral density matrix is expressed:

$$[X](\omega) = [C] \tag{2}$$

where $[C]$ is constant matrix. The $[H](\omega)$ matrix can be written in a pole (λ_k) and Residue ($[R_k]$) form as:

$$[H](\omega) = \frac{[Y](\omega)}{[X](\omega)} = \sum_{k=1}^{n} \frac{[R_k]}{j\omega - \lambda_k} + \frac{[R_k]^*}{j\omega - \lambda_k^*} \tag{3}$$

$$\lambda_k = -\sigma_k + \omega_{dk} \tag{4}$$

where: n is the total number of interested modes, λ_k is the pole of kth mode and σ_k is the modal damping of the kth mode, ω_{dk} is the damped natural frequency of the kth mode:

$$\omega_{dk} = \omega_{0k}\sqrt{1 - \varsigma_k^2} \tag{5}$$

where: ς_k is the critical damping of the kth mode, ω_{0k} is the undamped natural frequency of the kth mode. $[R_k]$ matrix is expressed as following form:

$$[R_k] = \varphi_k \gamma_k^T \tag{6}$$

where φ_k is the mode shape, λ_k is the modal participation vector. All those parameters are specified for the kth mode. The input assumed to be blank interference with power spectral density is flat (no change) over the entire frequency range, the Eq. (1) becomes:

$$[Y](\omega) = \sum_{k=1}^{n}\sum_{l=1}^{n} \left[\frac{[R_k]}{j\omega - \lambda} + \frac{[R_k]^*}{j\omega - \lambda_k^*}\right] C \left[\frac{[R_l]}{j\omega - \lambda_l} + \frac{[R_l]^*}{j\omega - \lambda_l^*}\right]^H \tag{7}$$

where H denotes complex conjugate and transposition. Multipying the two partial fraction factors and making use of the Heaviside partial fraction theorem, then performing mathematical transformations, output power spectral density can be presented as follows

$$[Y](\omega) = \sum_{k=1}^{n} \frac{[A_k]}{j\omega - \lambda_k} + \frac{[A_k]^*}{j\omega - \lambda_k^*} + \frac{[B_k]}{-j\omega - \lambda_k} + \frac{[B_k]^*}{-j\omega - \lambda_k^*} \tag{8}$$

where:$[A_k]$ is the kth residue matrix. The matrix $[X](\omega)$ is assumed to be a constant C, since the excitation signals are assumed to be uncorrelated zero mean blank

interference in all the measured DOFs. This matrix is Hermitian; its size is $m \times m$ and is described in the form:

$$[A_k] = [R_k]C\left(\sum_{s=1}^{n}\frac{[R_s]^H}{-\lambda_k - \lambda_s^*} + \frac{[R_s]^T}{-\lambda_k - \lambda_s}\right) \tag{9}$$

The contribution to the residue from the kth mode is given:

$$[A_k] = \frac{[R_k]C\left[R_k^*\right]^T}{2\sigma_k} \tag{10}$$

where: σ_k is minus the real part of the pole $\lambda_k = -\sigma_k + j\omega_{dk}$. As it appears, this term becomes dominating when the damping is light, and thus, is case of light damping; the residue becomes proportional to the mode shape vector:

$$\lim_{damping \to light}[A_k] = [R_k]C[R_k]^T = \varphi_k\gamma_k^T C\gamma_k\varphi_k^T = d_k\varphi_k\varphi_k^T \tag{11}$$

where: d_k is a scalar constant. The contribution of the modes at a particular frequency is limited to a finte number. Let this set of modes be denoted by $Sub(\omega)$. Thus, in the case of a lightly damped structure, the response of spectral density matrix can always be written as following final form:

$$[Y](\omega) = \sum_{k \in Sub(\omega)}\frac{d_k\varphi_k\varphi_k^T}{j\omega - \lambda_k} + \frac{d_k^*\varphi_k^*\varphi_k^T}{j\omega - \lambda_k^*} \tag{12}$$

The final form of the matrix $[Y](\omega)$ is decomposed into a set of singular values and singular vectors using the Singular Value Decomposition.

2.2 Singular Value Decomposition

The singular value decomposition of an $m \times n$ complex matrix A is the following factorization:

$$A = U \times S \times V^H \tag{13}$$

where U and V are unitary matrix and S is a diagonal matrix that contains the real singular values:

$$S = diag(s_1, \ldots, s_r) \tag{14}$$

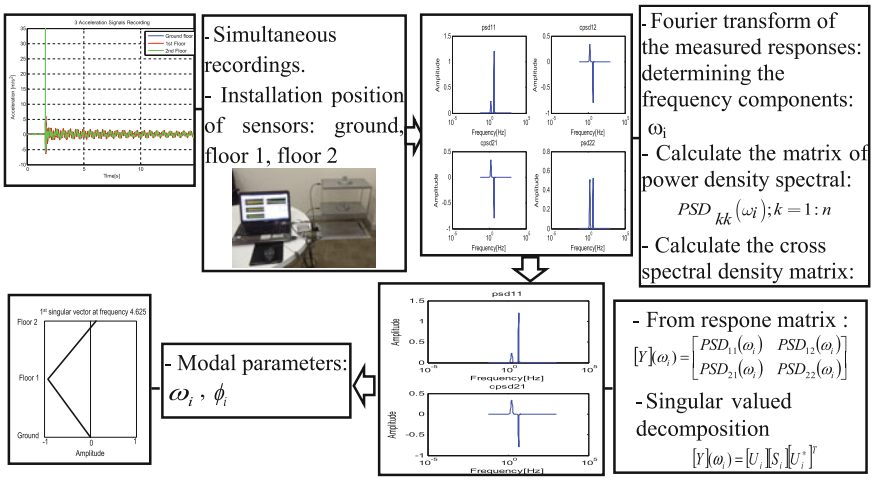

Fig. 2 Experimental flowchart using FDD

The superscript ^{H} on the V matrix denotes a Hermitian transformation. In the case of real valued matrices, the matrix V is only transposed and is denoted ^{T}. The s_i elements in the matrix S are called the singular values and their following singular vectors are contained in the matrix U and V. This singular value decomposition is performed for each of the matrices at each frequency. The experimental flowchart is built by using FDD method and is illustrated through four stages as shown in Fig. 2.

The spectral density matrix is then approximated to the following expression (15) after SVD decomposition:

$$[Y](\omega) = [\Phi][S][\Phi]^{H} \tag{15}$$

$$[\Phi][\Phi]^{H} = [I] \tag{16}$$

Notation $[I]$ is unitary matrix. Where S is a diagonal matrix holding the scalar singular values, $[\Phi]$ is a unitary matrix holding the singular vectors:

$$S = diag(s_1, \ldots, s_r) = \begin{bmatrix} s_1 & 0 & 0 & \cdot & \cdot & 0 \\ 0 & s_2 & 0 & \cdot & \cdot & \cdot \\ 0 & \cdot & s_3 & \cdot & \cdot & \cdot \\ \cdot & \cdot & \cdot & \cdot & \cdot & 0 \\ \cdot & \cdot & \cdot & \cdot & s_r & 0 \\ 0 & \cdot & \cdot & 0 & 0 & 0 \end{bmatrix} \tag{17}$$

$$[\Phi] = [\{\varphi_1\} \quad \{\varphi_2\} \quad \{\varphi_3\} \quad \cdots \quad \{\varphi_r\}] \tag{18}$$

where φ_i are forms of private modes. The number of nonzero elements in the diagonal of the singular matrix corresponds to the rank of each spectral density

matrix. The singular vectors in Eq. (18) correspond to an estimation of the mode shapes and the corresponding singular values are the spectral densities of the SDOF system expressed in Eq. (12).

2.3 Mathematical Model of N-Storey Building

The building will vibrate when it is subjected to external forces exerted by the outside like the wind, stimulated by vehicular traffic, caused by man, even earthquakes. To simplify matters, we assume construction of the mathematical model for n-storey building under the effect of making buildings earthquake vibrations. That means n degrees of freedom system modeled from buildings also fluctuate. The vibration of n degrees of freedom of the form is considered as Fig. 3 [2, 3]. Supposed that the moving is in one direction, according to Newton's second law and D'Alembert principle, the equations of the system oscillate many degrees of freedom under the effect of horizontal x ground acceleration $x_0''(t)$ is described as follows [2, 3]:

$$[M]\left\{x''\right\} + [C]\left\{x'\right\} + [K]\{x\} = -[M]\left\{x_0''\right\} \tag{19}$$

$x_0'' = x_0''(t)$ is ground acceleration. Respectively $x_i(t)$, $x_i'(t)$, $x_i''(t)$ are displacement, velocity, acceleration in the mass concentration at the ith floor, $[M]$ is the mass matrix, $[C]$ is the damping matrix, $[K]$ is the stiffness. We simulatenously

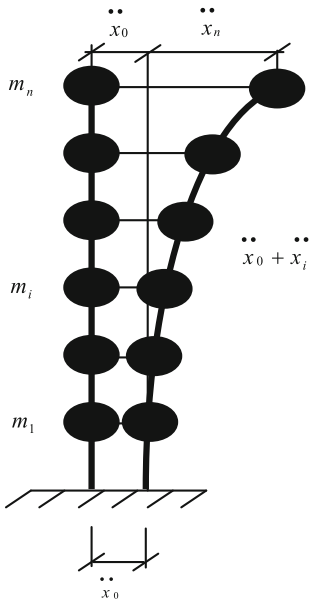

Fig. 3 Mathematical model of n-storey building under the effect of horizontal ground

diagonalize matrices $[M]$ and $[K]$; and assume that $[C]$ is also diagonal with the n damping ratios ξ_i on the diagonal. The n eigenvalues ω_i^2, corresponding eigenvectors $\{\varphi_i\}$ and damping ratios ξ_i are the modal parameters of the system.

All three matrices $[M]$, $[C]$, $[K]$, each with size $(n \times n)$ and is defined as follows:

$$[M] = \begin{bmatrix} m_1 & 0 & 0 & 0 \\ 0 & m_2 & 0 & 0 \\ 0 & 0 & \dots & 0 \\ 0 & 0 & 0 & m_n \end{bmatrix}; \quad [C] = \begin{bmatrix} c_{11} & c_{12} & \dots & c_{1n} \\ c_{21} & c_{22} & \dots & c_{2n} \\ \dots & \dots & \dots & \dots \\ c_{n1} & c_{n2} & \dots & c_{nn} \end{bmatrix};$$

$$[K] = \begin{bmatrix} k_{11} & k_{12} & \dots & k_{1n} \\ k_{21} & k_{22} & \dots & k_{2n} \\ \dots & \dots & \dots & \dots \\ k_{n1} & k_{n2} & \dots & k_{nn} \end{bmatrix}.$$

where m_i is the mass concentration at the ith floor, $i = 1, 2, \ldots n$.

2.4 Construct Stiffness Matrix from Modal Parameters

Shear beam model is assumed that motion in a single floor depends on the displacement of the immediately above and below floors. The assumption is emphasized that the stiffness of the floors is greater than the wall. Stiffness matrix can be written as formula (20):

$$[K] = \begin{bmatrix} k_1 + k_2 & -k_2 & 0 & \dots & \dots & 0 \\ -k_2 & k_2 + k_3 & -k_3 & \ddots & & \vdots \\ 0 & -k_3 & \ddots & \ddots & \ddots & \vdots \\ \vdots & \ddots & \ddots & \ddots & & 0 \\ \vdots & & \ddots & -k_{n-1} & k_{n-1} + k_n & -k_n \\ 0 & \dots & \dots & 0 & -k_n & k_n \end{bmatrix} \tag{20}$$

where: k_j is the stiffness of the storey j.

The equation of the eigenvalues $[K]\{\Phi_i\} = \omega_i^2[M]\{\Phi_i\}$ for the shear beam model can be inverted in order to evaluate the stiffness matrix $[K]$. Where: Respectively ω_i, $\{\Phi_i\}$ are modal frequencies and mode shape vectors corresponding ith. Thus, the relationship between the physical parameters and the modal parameters of the building can be expressed as the Eq. (21):

$$\left([K] - \omega_i^2[M]\right)\{\Phi_i\} = 0 \tag{21}$$

Equation (21) can be written as elementary as the Eq. (22):

$$[K] = \begin{bmatrix} k_1 + k_2 - \omega_i^2 m_1 & -k_2 & 0 & \dots & \dots & 0 \\ -k_2 & k_2 + k_3 - \omega_i^2 m_2 & -k_3 & \ddots & & \vdots \\ 0 & -k_3 & \ddots & \ddots & \ddots & \vdots \\ \vdots & \ddots & \ddots & \ddots & & 0 \\ \vdots & & \ddots & -k_{n-1} & k_{n-1} + k_n - \omega_i^2 m_{n-1} & -k_n \\ 0 & \dots & \dots & 0 & -k_n & k_n - \omega_i^2 m_n \end{bmatrix} \begin{bmatrix} \varphi_{1i} \\ \varphi_{2i} \\ \vdots \\ \varphi_{(n-1)i} \\ \varphi_{ni} \end{bmatrix} = \begin{bmatrix} 0 \\ 0 \\ \vdots \\ 0 \\ 0 \end{bmatrix} \tag{22}$$

Solving the Eq. (22) we find the stiffness from 1th floor to *n*th floor. Therefore, to generalize a corresponding linear system Eq. (22) can be translated into analytical formulas as follows:

$$\Delta\varphi_{ji} = \begin{cases} \varphi_{ji} - \varphi_{(j-1)i} & when \quad j = 2 \div n \\ \varphi_{ji} & when \quad j = 1 \end{cases}; \quad \forall j \in [1, n], k_j = \omega_i^2 \frac{\sum_{l=j}^{n} m_l \varphi_{li}}{\Delta\varphi_{ji}} \tag{23}$$

2.5 *Identificate Modal Parameters and Stiffness of Model of 2-Storey Building*

Geometry of a two-storey building is designed in the pattern of shear beam, painted with software Artemis TestorPro 2011 as in Fig. 4. The material is made entirely of carbon steel.

Acquisition of experimental system is for responses of model two-storey building. The sampling rate f_s = 2048 samples/s, ensuring the Nyquist criterion. Step time retrieving data is 4.8828125×10^{-4} (s). In this experiment, the data was recorded during 15 s. Therefore the amount samples on each channel were 30 720 samples.

Experiment 1 When the 1st and 2nd floor have $m_1 = m_2 = mass = 11.9737$ kg, excitation force generated by a small hard rubber hammer on the 2nd floor in the horizontal x with a random force. Results of from the 4th measurement in a data set with measured 10 times, is shown in Fig. 5 as follows.

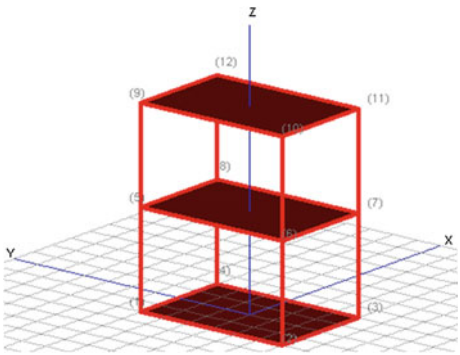

Fig. 4 Geometry two-storey building

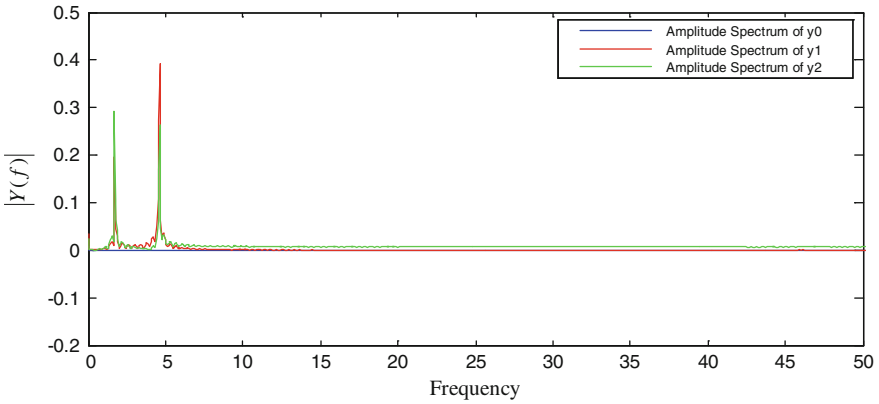

Fig. 5 One side of the spectrum amplitude response ground acceleration, 1st floor and 2nd floor

Through analysis of the spectrum we find out the ground nearly fluctuated. Thus to simplify the problem, we only consider the correlation between 1st floor and 2nd floor. The power spectral density of the system is calculated as a function of physical frequency is shown in Fig. 6.

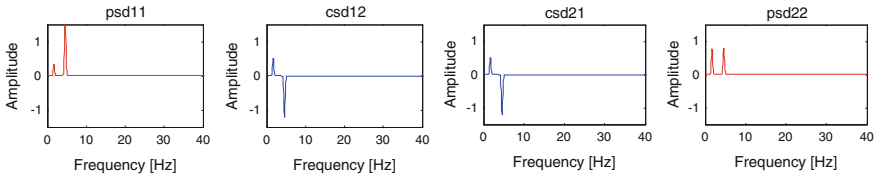

Fig. 6 Power spectral densities of acceleration response and comment on the 1st floor 2nd floor

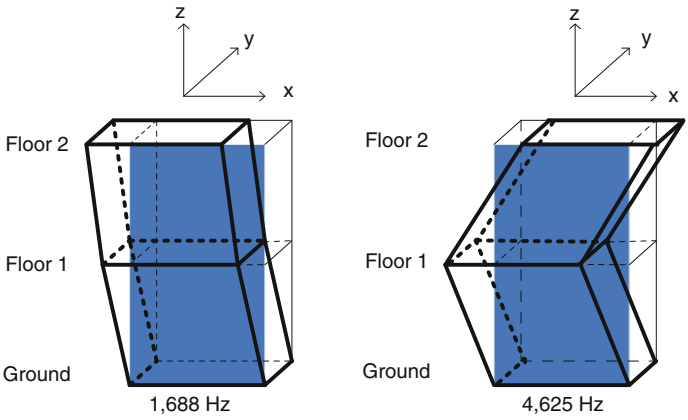

Fig. 7 Bending mode shapes along the identified high building

Table 1 Mode shapes, stiffness identified when we used hard rubber hammer impact with random excitation 2nd floor horizontal x

Mode i	1st	2nd
f (Hz)	1,688	4,625
$\{\varphi_{i1}\}$	−0,55406	−0,83570
$\{\varphi_{i2}\}$	−0,83247	0,54917
The average stiffness of the floor 1, floor 2 [N/m] and the average frequency of two mode shapes of 10 independent measurements	$\overline{k}_1$ = 3317,091 $\overline{k}_2$ = 1326,64 $\overline{f}_1$ = 1,688	$\overline{k}_1$ = 3414,902 $\overline{k}_2$ = 3949,381 $\overline{f}_2$ = 4,625
Standard deviation (d)	d_{k_1} = 1,758 d_{k_2} = 0,0 d_{f_1} = 0,0	d_{k_1} = 7,374 d_{k_2} = 2,669 d_{f_2} = 0,0

In the first mode shape: the 1st and 2nd floor oscillate in phase, its displacement increases with height, floor 2 shifted almost 1.5 times the 1st floor, frequency 10.6060 rad/s. In the second mode shape: 1st and 2nd floor is opposite phase oscillation; a node appears. The 1st inter-story drift 2nd floor is near 1.5 times, frequency 29.0597 rad/s (Fig. 7).

The modal parameters are identified and shown in Table 1: Sketch graphs stiffness and inter storey drift [m/m] between the floors is shown in Figs. 8 and 9.

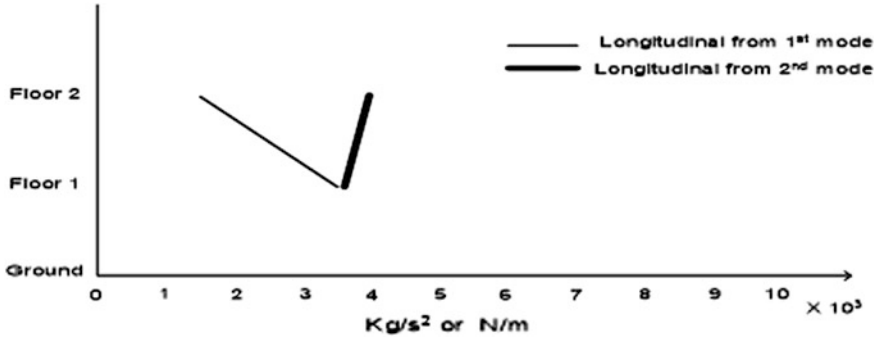

Fig. 8 The stiffness of the floors

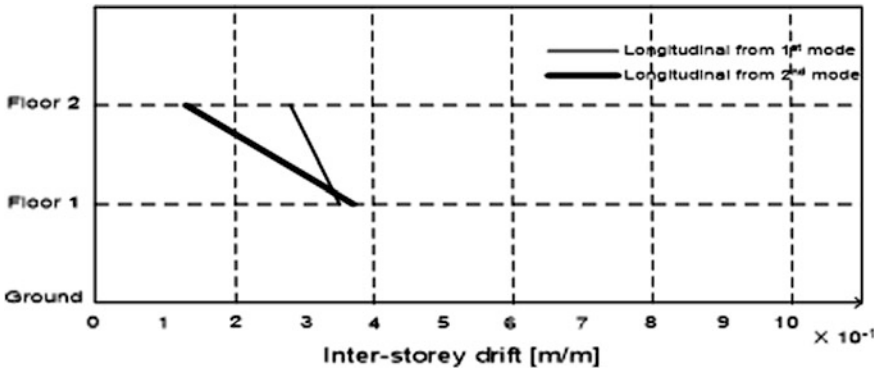

Fig. 9 Inter-storey dirft

3 Conclusion

Recognized results between the two cases with a hard rubber hammer excitation and vibration motor and shock with small deviations are acceptable. Oscillation frequency separately unbiased for both mode shapes. Meanwhile, the stiffness of the 1st floor of mode 1 has deviation with 13.69562 N/m, the 2nd floor stiffness of mode 1 has deviation with 0 N/m; the 1st floor stiffness of mode 2 has deviation with 206,07993 N/m, the 2nd floor stiffness of mode 2 has deviation with 31.62963 N/m.

The analysis of modal with FDD allows us to easily identify the modal parameters quickly and accurately. This was done only with the measurement of the response of the building when it is subjected to the forces excited by the input amplitude regardless even without measuring those excitation forces. This approach provides us with the bending samples. However, it does not affect the calculation results about the stiffness according to the mode shapes. FDD method which was

successfully applied on a model two-storey building was designed and constructed according to the pattern shear beam with identified modal parameters and the stiffness of the floors. The stiffness is one of the main parameters controlling their seismic resistance. The studied results have demonstrated the ability to use the FDD into reality methods for civil engineering structures. It also can be applied to test the health of the structure and the building. This method is a useful contribution to find out the weak floor on the building which is easy affected with earthquake, wind and storm.

References

1. Rainieri C, Fabbrocino G (2011) Operational modal analysis for the characterization of heritage structures, UDC 550.8.013, GEOFIZIKA (vol 28)
2. Nguyễn Đại M (2006) Phương Pháp Phổ Phản Ứng Nhiều Dạng Dao Động Và Tính Toán Nhà Cao Tầng Chịu Động Đất Theo TCXDVN375
3. Ventura C, Liam Finn W, Lord JF, Fujita N (2003) Dynamic characteristics of a base isolated building from ambient vibration measurement and low level earthquake shaking. Soil Dyn Earthquake Eng 313–322
4. Chopra AK (2001) Dynamic of structures. Prentice Hall International, US
5. Peeters B (2000) PhD thesis, Katholieke, System identification and damage detection in civil engineering. Universiteit Leuven
6. Welch PD (1967) The use of fast fourier transform for the estimation of power spectra: method based on time averaging over short, modified periodograms. IEEE Trans Audio Electroacoust AU-15:70–73
7. Brincker R, Ventura C, Andersen P (2003) Why output-only modal testing is a desirable tool for a wide range of practical applications. In: 21st International Modal Analysis Conference (IMAC), Kissimmee, Florida
8. Andersen P, Brincker R, Ventura C, Cantieni R (2010) Modal estimation of civil structures subject to ambient and harmonic excitation
9. Hang J (2011) Operational Modal identification technique based on independent component analysis. In: Electric technology and civil engineering (ICETCE), international conference

Airfoil Selection for Fixed Wing of Small Unmanned Aerial Vehicles

Ngo Khanh Hieu and Huynh Thien Loc

Abstract Vietnam has become a new market for small Unmanned Aerial Vehicles (SUAVs). In the case of SUAVs, the airfoil plays a crucial role in generating lift. This paper presents an approach using opensource/free software to evaluate and choose the airfoil for aircraft designs and suggests a set of criteria used to evaluate the airfoils. The method mentioned in this research can help designers of fixed wing of SUAVs in selecting the most appropriate airfoil from various sources. The obtained airfoil can be modified afterwards for the best performance.

Keywords XFRL5 · Airfoil for suavs · X-foil · Javafoil

1 Introduction

The market of UAVs in Vietnam as well as in other parts of the world is currently very competitive. The challenges that UAVs designers are facing are not only about how to make the aircrafts fly but also how to design an UAV for the best performance and possibly lowest cost.

Normally, in order to select an airfoil, the designers may either use tested data of airfoils or do their own test under the specific working condition of the airfoil. From the testing data acquired, they have to select the the most appropriate airfoil to the criteria needed. However, doing such a test could be time-consuming and costly. Moreover, the errors could be made because the working condition of the selected airfoils will not always be the same as the testing data as the result of the approximation in case of doing a test. In addition, there is no airfoil totally superior

N.K. Hieu (✉) · H.T. Loc
Department of Aerospace Engineering, Ho Chi Minh City University of Technology,
268 Ly Thuong Kiet Street, District 10, Ho Chi Minh City, Vietnam
e-mail: ngokhanhhieu@hcmut.edu.vn

H.T. Loc
e-mail: huynhthienloc0204@gmail.com

V.H. Duy et al. (eds.), *AETA 2015: Recent Advances in Electrical Engineering and Related Sciences*, Lecture Notes in Electrical Engineering 371,
DOI 10.1007/978-3-319-27247-4_73

to others. Therefore, the method of selection and the criteria applied may cause problems to designers.

These difficulties lead to a need of a tool to select the proper airfoils in an effective and trustworthy way. These airfoils then can be selected from the database with the proposed method of selection and optimized afterwards by modifying the airfoil to adapt to the best performance of the SUAVs.

2 Airfoil Selection's Importance

To design an UAV, in general, the designer firstly has to gather all the requirements. After doing the initial sizing to have the operating Reynolds number and gathering the sizing baseline, the designer move to the configuration design where airfoil and aircraft configuration must be chosen, then does many stages of the multidisciplinary analysis and the optimization to give out the optimum configuration. A prototype will be made, based on the former configuration for the flight test. If the prototype meets the requirements, the UAV designed will be commercialized (see Fig. 1).

For UAVs, especially SUAVs, the airfoil is one of the most components to their performance which determine its likelihood of success. The airfoil is normally

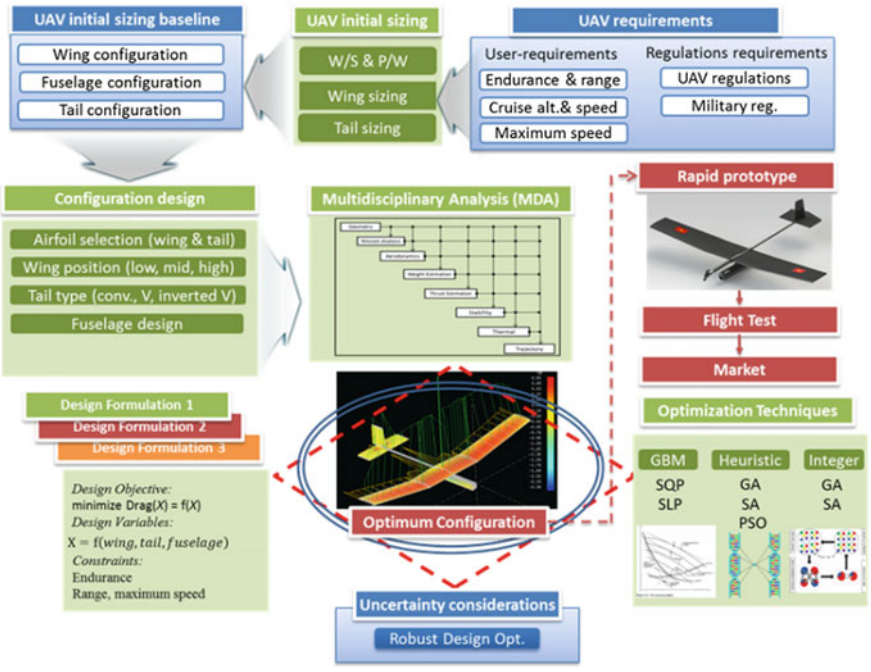

Fig. 1 UAV design flow chart [1]

selected from a database of airfoils operating in the same condition and will be optimized to best fit to the configuration of the SUAVs in the optimization phase.

3 Data Acquisition Method

3.1 Software Utilized

For SUAVs, the working condition is not as critical as other commercial aircrafts, in which many phenomenas may happen including the high flow separation at the trailing edge, the laminar separation bubbles and working beyond the stall angle.

The softwares presented are XFLR5 [2], whose airfoil analysis tool is based on X-Foil [3], and JAVAFOIL [4]. These softwares are medium-fidelity tools which use panel method to give the solution for vorticity and source distributions. From the solutions above, other parameters such as lift, drag and pitching moment coefficients can be computed.

For a shape discretization by N panels, the equation system consists of the matrix of influence coefficients, the unknown circulation strength at each panel corner point and the two vectors representing the conditions for 0° and 90° angle of attack. Each coefficient $C_{i,j}$ represents the effect the influence of the triangular vorticity distribution due to the vortex strength Υi at each corner point on the center point of each panel j. The last row contains the tangential flow condition at the trailing edge which is needed to obtain a solution compatible (see Fig. 2).

3.2 Verifying Software Fidelity

Panel method used in the softwares mentioned above (XFLR5 and JAVAFOIL) has a limitation in predicting boundary layers, flow separation and rotational flows due to its calculation model. The calculation in transonic and supersonic flow and for

$$\begin{bmatrix} C_{1,1} & \cdots & C_{N+1,1} \\ \vdots & \ddots & \vdots \\ C_{1,N} & \cdots & C_{N+1,N} \\ 1 & \cdots 0 \cdots & 1 \end{bmatrix} \cdot \begin{bmatrix} \gamma_{1,0°} & \gamma_{1,90°} \\ \gamma_{2,0°} & \gamma_{2,90°} \\ \vdots & \vdots \\ \gamma_{N+1,0°} & \gamma_{N+1,90°} \end{bmatrix} = \begin{bmatrix} RHS_{1,0°} & RHS_{1,90°} \\ RHS_{2,0°} & RHS_{2,90°} \\ \vdots & \vdots \\ RHS_{N+1,0°} & RHS_{N+1,90°} \end{bmatrix}$$

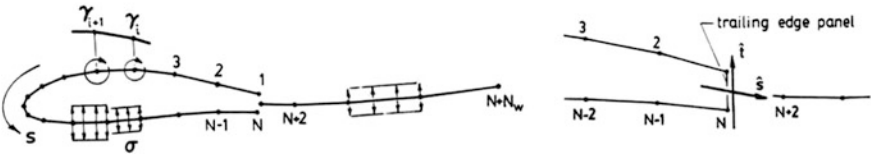

Fig. 2 Visualization of vorticity and source distributions in panel method [3]

airfoils with cusped trailing edges is also not reliable. However, as mentioned, these phenomenas and conditions are not applicable in case of the SUAVs.

To verify the fidelity of the software, the parameters obtained from the analysis of some well known airfoils of the softwares will be compared with the experimental data from University of Illinois Urbana-Champaign [5–7]. The representative airfoils are NACA 2412, NACA 24112 and S 9000 at Reynolds number of 2×10^5 and 5×10^5.

3.3 Airfoil Geometry Analysis

To analyze the reliability of the airfoil geometry, a study on the dependency of the number of points (panels) in the geometry of the airfoil must be conducted. The graph below presents the analysis of the lift and drag coefficients on the geometries having 50–300 points of NACA 2412 versus the data given.

There is a big difference between the parameters analyzed from a 50 point geometry and the others. The parameters received don't differ much from 150 points to 300 points geometries. Therefore, the analysis can be made with airfoil geometries having more than 150 points (panels) (see Fig. 3).

3.4 Fidelity of the Software

The parameters received from the softwares' analysis are compared with the experimental data from [7]. As the summary focus on airfoil in the same Reynolds

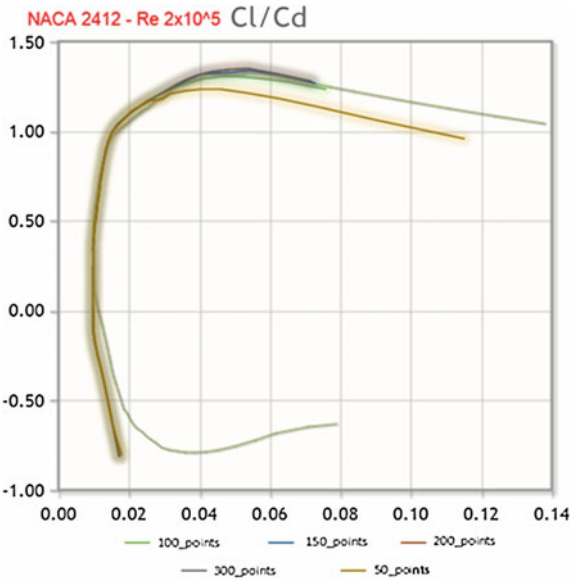

Fig. 3 Fidelity analysis from number of panels in the geometry of airfoils

number as the working condition of the fixed wing of SUAVs, it is for sure a precious reference for the fidelity analysis.

The airfoils tested are CAL 2263 and E 387 (selected randomly from the summary) to verify the fidelity of the software. The drag polars from the analysis versus the experimental data are plotted in the following figures.

As the drag polars plotted, the difference between the parameters acquired, especially XFLR5's calculation is quite precise (about 10 % error on high lift coefficient or below 0 lift coefficient). These error comes from the software unability to predict the high flow separation at trailing edge, laminar separation bubbles and the behavior of airfoil beyond stall angle. Even though XFLR5 gives more accuracy results, sometimes the solutions from XFLR5 can't be acquired due to the divergence of the iterations when Javafoil always manage to get the prediction of the parameters. That is why JavaFoil is also mentioned in this paper.

However, with SUAVs' working condition, these 'critical' cases are normally gone in seconds with an appropriate control reaction thus they won't affect their performance (Figs. 4, 5 and 6).

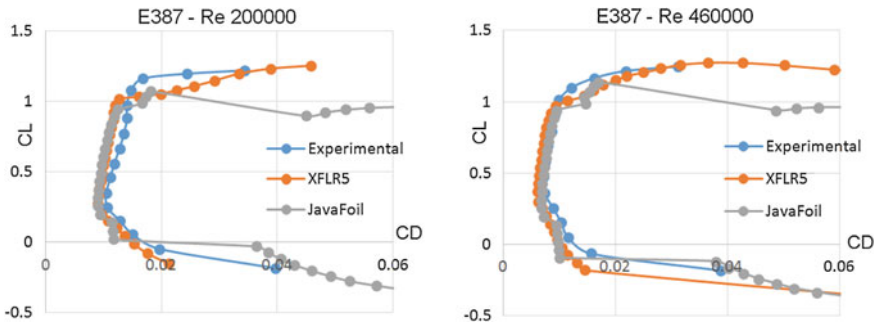

Fig. 4 Drag polars of E 387 airfoil at Reynolds number of 200 000 and 460 000

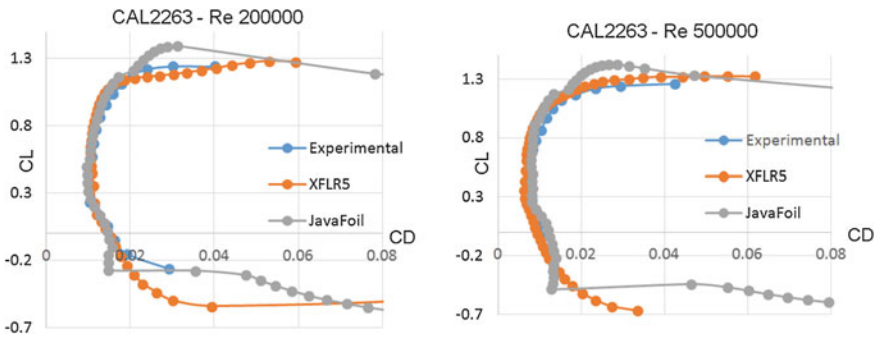

Fig. 5 Drag polars of CAL 2263 airfoil at Reynolds number of 200 000 and 500 000

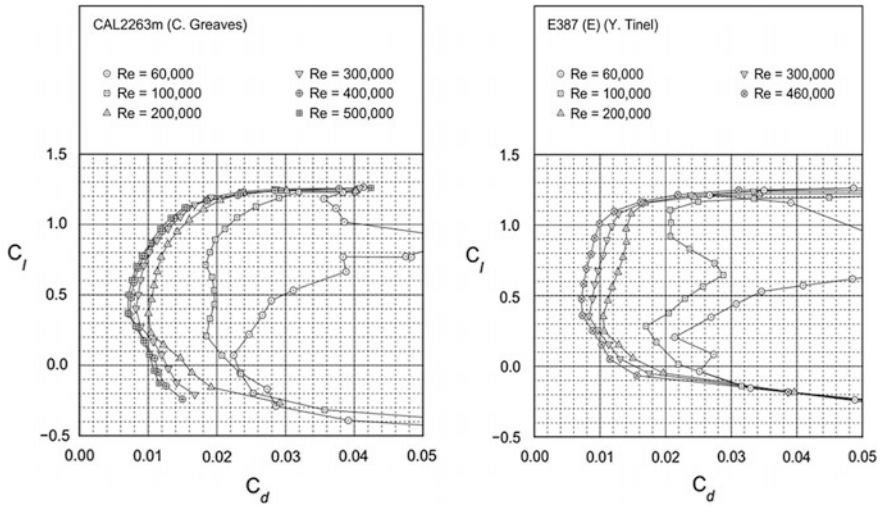

Fig. 6 Data published in summary of low-speed airfoil data, vol 5 about E 387 and CAL 2263

4 Airfoil Selection Method

4.1 Parameters Criteria

A set of criteria for the best performance of the SUAVs have to be set in order to select the best airfoil [8]. The criteria for each parameters is shown in the table below.

Note that there is no 'ultimate' airfoil that can respond to all the criteria as above. Therefore, a selection method is needed to optimize the airfoil selection. Weighted Scoring Method (WSM) is a selection method comparing multi criteria. It includes determining all the criterias related to the selection, giving each criteria a weighted score to reflect their relative importance and evaluation of each criteria.

With: C_{lo}: lift coefficient at angle of attack equal to 0°; C_{l_max}: maximum lift coefficient; α_{stall}: stall angle of attack; C_{d_min}: minimum drag coefficient; C_l/C_{d_max}: maximum of the range parameter; $C_l^{3/2}/C_{d\_max}$: maximum of the endurance parameter and $C_{m,c/4}$: pitching moment coefficient.

WSM consists of the following steps:

- Determining all the criteria.
- Distributing to each criteria a weighted score.
- Evaluating each criteria of an option.
- Multiplying the points evaluated by the weighted score.
- Making sum of all the products and selecting the airfoil with highest total points.

Table 1 Evaluation criteria of each parameter and the weighted scored for SUAVs

Parameter	Evaluation criteria	Weighted scored for fixed wing of SUAVs
C_{l0}	Close to Clcruise is the best	0.15
C_{l_max}	Highest is the best	0.15
α_{stall}	Highest is the best	0.15
C_{d_min}	Lowest is the best	0.15
C_l of C_min	Close to cruise is the best	
C_l/C_{d_max}	Highest is the best	0.15
C_l of C_l/C_{d_max}	Lowest is the best	
$C_l^{3/2}/C_{d\_max}$	Highest is the best	0.2
C_l of $C_l^{3/2}/C_{d\_max}$	Lowest is the best	
$C_{m,c/4}$	Low magnitude is best	0.05

4.2 Proposal of a Set of Weighted Score for Fixed Wing of SUAVs

For most of the fixed wing of SUAVs, the most important criterias are: High endurance/range, Easy to take-off, High performance, Easy to control.

These criterias can be interpreted as parameters as C_{lo}, C_{l_max}, α_{stall}, C_{d_min}, C_l/C_{d_max}, $C_l^{3/2}/C_{d\_max}$ and $C_{m,c/4}$. According to the demand of the customer which focus more on what he wants, a set of weighted score will be determined. Table 1 proposes a set of weighted score focusing more on the high endurance and less on the maneuverability since the design object is the fixed wing of SUAVs [9, 10].

5 Case Study

The recent design project of VSKYLINE Ltd. is for a SUAV having the following requirements: operating velocities from 60 to 100 km/h; take-off by hand-launch; operating altitude of 500 m; flight endurance of 60–90 min; maximum payload of 2 kg.

After the sizing steps (see Fig. 1), the aspect ratio (AR_w) of the SUAV's wing is 8 and the operating Reynolds number is 600 000.

5.1 Airfoil Database

The airfoil set utilized in the selection are the ones performing at the operating Reynolds number. They are gathered from [5–7] (see Table 2).

Table 2 Airfoil database for small UAVs

No.	Airfoil	Thickness (%)	Camber (%)	No.	Airfoil	Thickness (%)	Camber (%)
1	AG12	6.24	1.85	11	RG14	8.47	1.58
2	AG16	7.11	1.87	12	RG15	8.92	1.76
3	AG24	8.41	2.21	13	S7012	8.75	2.02
4	AG35R	8.72	2.38	14	S8064	12.33	1.18
5	CAL1215 J	11.72	2.28	15	S9000	9.01	2.37
6	CAL2263 M	11.72	3.52	16	SA7035	9.19	2.55
7	CAL4014L	10.00	1.84	17	SA7036	9.20	2.79
8	E231	12.33	2.46	18	SD7037	9.20	3.02
9	E374	10.91	2.25	19	SD7080	9.15	2.48
10	E387	9.07	3.80				

The AG airfoils which serve mainly for sailplanes were designed by Dr. Mark Drela from MIT. The CAL airfoils were designed by Christopher Lyon, the former member of the UIUC LSATs team (the University of Illinois at Urbana-Champaign Low-Speed Airfoil Tests team). The Eppler airfoils were designed by the code written by Prof. Richard Eppler, a pioneer of computational aerodynamics. The RG airfoils were designed by Rolf Girsberger based on Prof. Eppler code with some modifications for flexibility in modifying thickness and camber. The S airfoils were designed by Prof. Michael Selig from UIUC. The SD airfoils were designed by Prof. Michael Selig and John Donovan. The SA 7035 and SA 7036 airfoils were designed based on SD 7037 due to its popularity.

5.2 Airfoil Analysis Results

As discussed above, the airfoils are analyzed by XFLR5, the airfoil having the most preferable result in each criteria gets 04 points when the least preferable one gets 01 points. The points for other airfoils are calculated linearly.

The analysis result is shown in Fig. 7. As CAL 2263 M has the highest scoring points among the airfoils analyzed based on the criteria set, this airfoil is chosen for the SUAV. It can be seen that even though CAL 2263 M doesn't have the highest point in the criteria of maximum range and endurance parameter, it is still chosen as the most appropriate airfoil.

From this case study, the Weighted Scoring Method offers clearly a comprehensive way to select the most appropriate airfoil for the best performance of the aircraft.

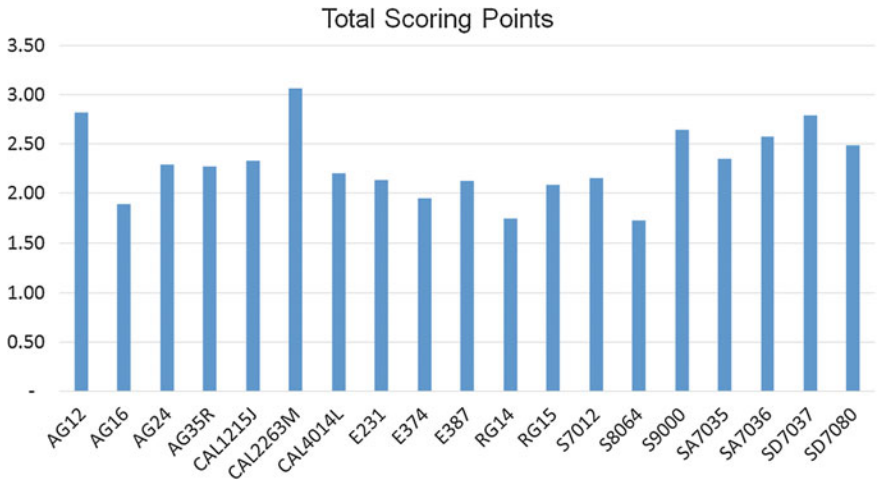

Fig. 7 Total scoring points of each airfoil tested

6 Conclusion

XFLR5 and JavaFoil with the Weighted Scoring Method offers a comprehensive and trustworthy approach for aircrafts designers to select the most appropriate airfoil to the requirements for SUAVs. Moreover, the airfoil selected can be then optimized by higher fidelity tools to ensure the best performance for SUAVs.

The airfoil selection is very important and necessary for designers to move to another steps such as multidisciplinary analysis and optimization.

Acknowledgments This paper is supported by VSKYLINE Ltd. in the project of designing a small unmanned aerial vehicle for surveillance.

References

1. Ngô Khánh H, Nguyễn NV, Huỳnh TL, Đinh AB (2015) VSKYLINE design project of a SUAV for surveillance, VSKYLINE Ltd. research report
2. http://www.xflr5.com/xflr5.htm
3. Drela M (1989) XFOIL: an analysis and design system for low reynolds number airfoils. MIT Dept. of Aeronautics and Astronautics, Cambridge, Massachusetts
4. Hepperle M (2014) JavaFoil User's Guide
5. Selig MS, Lyon CA, Giguère P, Ninham CP, Guglielmo JJ (1996) Summary of low speed airfoil data, vol 2, Department of Aerospace Engineering, University of Illinois at Urbana-Champaign
6. Lyon CA, Broeren AP, Giguère P, Gopalarathnam A, Selig MS (1997) Summary of low speed airfoil data, vol 3, Department of Aerospace Engineering, University of Illinois at Urbana-Champaign

7. Williamson GA, McGranahan BD, Broughton BA, Deters RW, Brandt JB, Selig MS (2012) Summary of low speed airfoil data, vol 5, Department of Aerospace Engineering, University of Illinois at Urbana-Champaign
8. Gundlach J (2012) Designing unmanned aircraft systems: a comprehensive approach. Aurora Flight Sciences, Manassas
9. Park K, Han J-W, Lim H-J, Kim B-S, Lee J (2008) Optimal design of airfoil with high aspect ratio in unmanned aerial vehicles, vol 2. World Academy of Science, Engineering and Technology, 2008-04-28
10. Barnhart F, Cuipa M, Stefanik D, Swick Z (2004) Micro-aerial vehicle design with low reynolds number airfoils

Application of the Dung's Microscopic Damage Model to Predict Ductile Fracture of the Deep Drawn Aluminum Alloy Sheets

Hao H. Nguyen, Trung N. Nguyen and Hoa C. Vu

Abstract In this paper, a mechanistic model to predict failure voided ductile materials is developed based on the Dung's microscopic damage model (Dung, N.L., 1992, Three Dimensional Void Growth in Plastic Materials, Mechanics Research Communications, Vol. 19, No. 3). The model incorporates the Hill's quadratic anisotropic yield criterion (1948) to account for anisotropy of sheet metals. The model is implemented as a vectorized user-defined material (VUMAT) subroutine in the ABAQUS/Explicit commercial finite element code. Predictions of ductile crack behavior based on void nucleation, growth and coalescence by the Dung's model are compared with Gurson–Tvergaard–Needleman (GTN) model and published experimental data.

Keywords Ductile fracture · Sheet forming · Dung's model · Micro-crack mechanism · Anisotropy

1 Introduction

Aluminum alloy materials have been widely applied in automotive and aerospace industry thanks to their light weight and excellent strength characteristics. Sheet metals made from aluminum alloys by rolling process usually exhibit anisotropic

H.H. Nguyen · H.C. Vu (✉)
Department of Engineering Mechanics, Faculty of Applied Science,
HCM City University of Technology, 268 Ly Thuong Kiet Street,
District 10, Ho Chi Minh City, Vietnam
e-mail: vuconghoa@hcmut.edu.vn

H.H. Nguyen
e-mail: hq8087@gmail.com

T.N. Nguyen
School of Mechanical Engineering, Purdue University, West Lafayette IN 47907, USA
e-mail: trungnguye@purdue.edu

V.H. Duy et al. (eds.), *AETA 2015: Recent Advances in Electrical Engineering and Related Sciences*, Lecture Notes in Electrical Engineering 371,
DOI 10.1007/978-3-319-27247-4_74

mechanical response. Although anisotropic yielding of aluminum alloy sheets has been well characterized using sophisticated yield functions [1–5], plastic fracture behavior of the materials still needs further investigation. The metals are considered as matrix materials containing inclusions and second phase particles. Accordingly, upon deformation up to a certain level micro-cracks appear due to void nucleation, growth and coalescences. Gurson [6] proposed a yield function for isotropic matrix materials containing spherical voids. The void volume fraction (f) is defined as a special damage parameter. Tvergaard [7, 8] modified the Gurson model by adding two correction parameters to include interactions of voids and hardening by deformation. Needleman and Tvergaard [9] further extended the model to simulate rapid loss of loading carrying capacity in void materials. To correctly determine void volume fraction growth during deformation of matrix materials, Chu and Needleman [10] proposed a void nucleation criterion. Therefore, the modified Gurson model is also known as Gurson–Tvergaard–Needleman (GTN) model. Applications of the GTN model are limited to anisotropic porous plastic materials. Therefore, in recent years, some researchers have extended the original Gurson model to model anisotropic materials. Liao et al. [11] integrated the Gurson model with Hill quadratic and non-quadratic anisotropic yield criteria to describe the matrix normal anisotropy and planar isotropy. Wang et al. [12] formed a closed-form anisotropic Gurson yield criterion based on an average anisotropy parameter. Tanguy et al. [13] developed a constitutive model based on Gurson model that integrates anisotropic behaviors and ductile damage for a X100 pipeline steel. Grange et al. [14] predicted ductile fracture of Zircaloy-4 sheets based on the GTN model which is extended to take into account plastic anisotropy and viscoelasticity. Chen and Dong [15] developed an implicit stress integration procedure for the GTN model using equivalent stress calculated from the Hill's quadratic anisotropic yield criterion to adapt explicit dynamic solver. Morgeneyer et al. [16] investigated fracture mechanisms of AA2139 Al-alloy sheet by experiments and applied the GTN model to describe and predict deformation behavior, crack propagation and toughness anisotropy of the material. Kami et al. [17] predicted plastic fracture of AA6016-T4 metallic sheet under deep-drawing conditions by using the GTN model and Hill'48 quadratic anisotropic yield function. Based on the work of McClintock [18] on a spheroidal void growth model, Dung [19] developed cylindrical and ellipsoidal void growth models and proposed a yield function which accounts for hardening of matrix materials. Applying the Dung's void growth model to predict failure development at ductile fracture of steel, Schiffmann et al. [20] reported a good agreement between predictions and experimental results.

In this paper, the Dung's model is incorporated with the quadratic yield criterion Hill'48 to account for the anisotropy of matrix materials. The model is then implemented via a vectorized user-defined material (VUMAT) subroutine in the ABAQUS/Explicit commercial finite element code. Applications of the model to investigate ductile fracture of deep drawn aluminum alloy materials are presented. Predictions of the ductile crack behavior resulted from void nucleation; growth and coalescence are compared with the GTN model and experimental results from the literature.

2 The Dung's Microscopic Damage Model for Anisotropic Metallic Materials

The yield function proposed in the Dung's model [19] is given as follows:

$$\Phi = \left(\frac{\sigma_e}{\sigma_f}\right)^2 + 2fq_1 \cosh\left[-\sqrt{3}(1-n)\frac{\sigma_m}{\sigma_f}\right] - 1 - (q_2 f)^2 = 0 \tag{1}$$

where, q_1, q_2 are correction parameters [9], n hardening exponent of matrix material, σ_e equivalent stress, $\sigma_m = -1/3\sigma_{ij}\delta_{ij}$ hydrostatic stress, and δ_{ij} Kronecker delta. Similar to the GTN model, the original Dung's model was constituted with an assumption that matrix material is isotropic and obeys the von Mises yield criterion, i.e.

$$\sigma_e = \sqrt{\frac{3}{2}\sigma' : \sigma'} \tag{2}$$

where σ' is the deviatoric stress tensor. To incorporate anisotropy of matrix materials, the Hill'48 quadratic anisotropic yield criterion [1] is applied. The equivalent stress is then substituted by:

$$\sigma_e = \left[F(\sigma_{22}-\sigma_{33})^2 + G(\sigma_{33}-\sigma_{11})^2 + H(\sigma_{11}-\sigma_{22})^2 + 2L\sigma_{23}^2 + 2M\sigma_{31}^2 + 2N\sigma_{12}^2\right]^{1/2} \tag{3}$$

where σ_{ij} (i, j = 1, 2, 3) are Cartesian components of Cauchy stress tensor. The parameters F, G, H, L, M and N are material constants. For sheet metal materials, these parameters can be calculated by Lankford's coefficients as follows:

$$F = \frac{r_0}{r_{90}(r_0+1)},\ G = \frac{1}{r_0+1},\ H = \frac{r_0}{r_0+1},\ N = \frac{(r_0+r_{90})(1+2r_{45})}{2r_{90}(1+r_0)} \tag{4}$$

The Lankford's coefficients r_0, r_{45} and r_{90} are determined by uniaxial tensile tests at 0^o, 45^o and 90^o to rolling direction. Flow stress of matrix material is given by:

$$\sigma_f = \sigma_f(\bar{\varepsilon}^p) \tag{5}$$

The equivalent plastic strain rate of matrix material $\dot{\bar{\varepsilon}}^p$ is obtained through the following expression of plastic work:

$$(1-f)\sigma_f \dot{\bar{\varepsilon}}^p = \sigma_{ij} : \dot{\varepsilon}_{ij}^p \tag{6}$$

where $\bar{\varepsilon}^p$ is equivalent plastic strain of matrix material, $\dot{\varepsilon}_{ij}^p$ is plastic strain rate tensor. The void volume fraction growth is computed as follows:

$$\dot{f} = \dot{f}_g + \dot{f}_n \tag{7}$$

The void volume fraction growth of present voids in matrix material is calculated:

$$\dot{f}_g = (1-f)\dot{\varepsilon}_{ij}^p \delta_{ij} \tag{8}$$

The nucleated volume void fraction rate in matrix material when deforming is calculated by the following void nucleation law:

$$\dot{f}_n = A\dot{\bar{\varepsilon}}^p \tag{9}$$

where, A is a function of equivalent plastic strain of matrix material $\bar{\varepsilon}^p$:

$$A = \frac{f_N}{s_N\sqrt{2\pi}} \exp\left[-0.5\left(\frac{\bar{\varepsilon}^p - \varepsilon_N}{s_N}\right)^2\right] \tag{10}$$

where, f_n, s_N, ε_N are parameters related to void nucleation during deformation of matrix material.

3 Numerical Analysis

A numerical algorithm based on the Euler backward method has been developed for a class of pressure-dependent plasticity models [21]. By applying the algorithm a VUMAT subroutine in the ABAQUS/Explicit software is implemented for the Dung's model.

3.1 Tensile Tests on Single Element

The subroutine is verified using a single 8-node brick element (C3D8R) for a hydrostatic tensile test and using plane strain element (CPE4R) for a unaxial tensile test. The corresponding boundary and loading conditions are shown in Fig. 1. Initial size of each element edge is 1 mm. The loading velocity for tension is set to 15 mm/s.

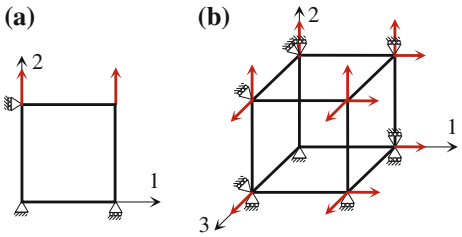

Fig. 1 Single element and boundary conditions: **a** Plane strain tension. **b** Hydrostatic tension

Flow stress of the matrix material obeys:

$$\frac{\sigma_f}{\sigma_0} = \left(\frac{\sigma_f}{\sigma_0} + \frac{3G}{\sigma_0}\bar{\varepsilon}^p\right)^n \tag{11}$$

where σ_0 is initial yield stress of the matrix material, σ_0/E = 1/300, n = 0.1. Parameters of the porous plastic model are $q_1 = q_2 = 1.5$, initial void volume fraction $f_0 = 0$ and $f_0 = 0.04$ for plane strain and hydrostatic tension, respectively, $\varepsilon_N = 0.3$, $s_N = 0.1$, $f_N = 0.04$.

Figure 2a shows the stress ratio (σ_{22}/σ_0) versus logarithmic strain $\varepsilon = \ln(1 + u/l_0)$, where u is the prescribed displacement and l_0 is the initial element length. In the case of isotropic material, the Dung's model (Dung-Mises or Dung-Hill'48 with $r_0 = r_{45} = r_{90} = 1$) coincides with results of GTN model in Abaqus (GTN-Mises) and Chen et al. [15] (GTN Hill'48 $r_0 = r_{45} = r_{90} = 1$). In the case of anisotropic material, results of the Dung's model (Dung-Hill'48) presents a good agreement with those from Chen et al. [15]. For yield function without

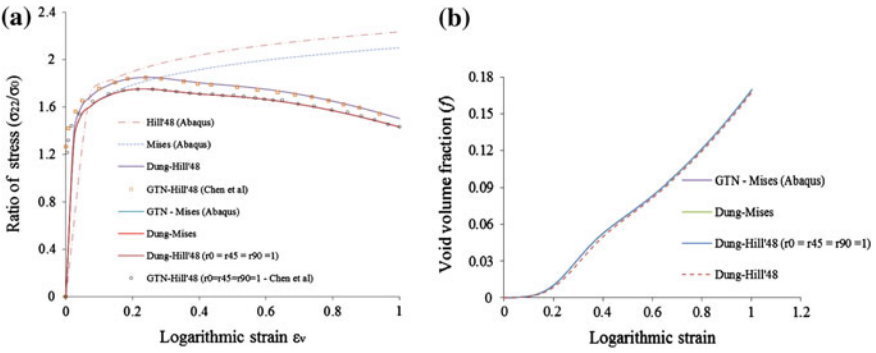

Fig. 2 Plane strain tension: **a** uniaxial stress versus logarithmic strain and **b** void volume fraction versus logarithmic strain

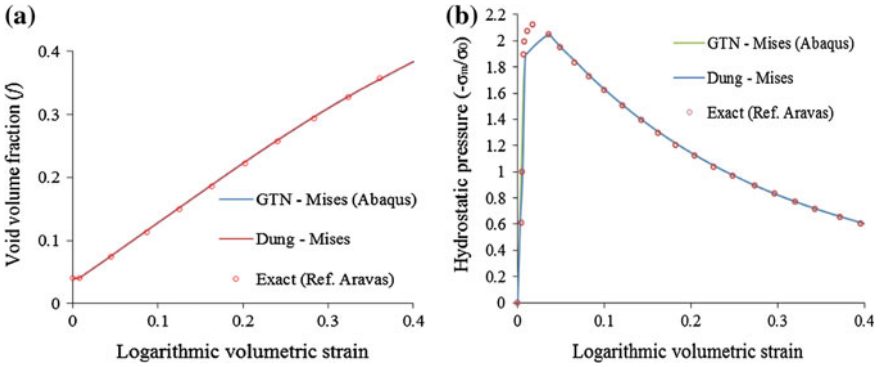

Fig. 3 Hydrostatic tension: **a** void volume fraction versus logarithmic volumetric strain and **b** hydrostatic stress versus logarithmic volumetric strain

damage variable (Hill'48 and von Mises), the axial stress is greater than the Dung's model and GTN model due to damage gradually accumulates by void volume fraction (f) in porous plastic material model. Figure 2b shows the void volume fraction growth with deformation of matrix material. For isotropic material Dung's model (Dung-Mises, Dung-Hill'48, $r_0 = r_{45} = r_{90} = 1$) coincides with GTN model in Abaqus. For anisotropic material, void volume fraction of the Dung's model (Dung-Hill'48) is slightly lower due to the effect of Lankford's coefficients.

In Fig. 3a, the hydrostatic stress is plotted as a function of logarithmic volumetric strain $\varepsilon_v = 3\ln(1 + u/l_0)$. Figure 3b shows void volume fraction as a function of logarithmic volumetric strain. Result from the Dung's model agrees well with that of the GTN model and the exact solution obtained from [22].

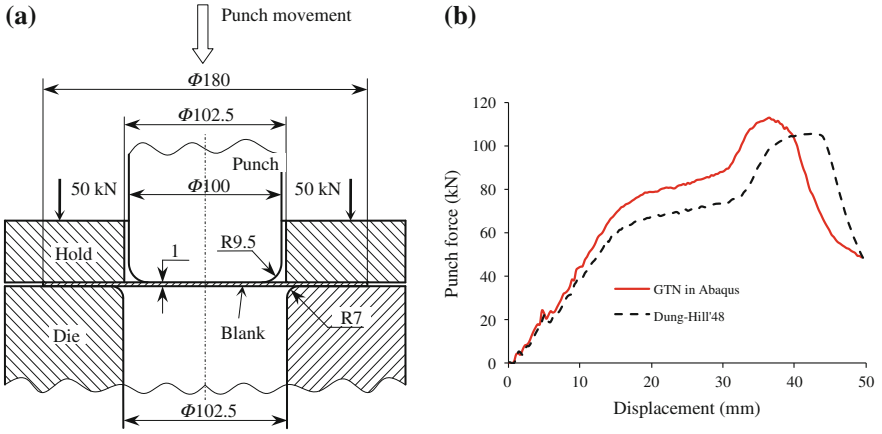

Fig. 4 Cylindrical cup deep drawing: **a** tooling setup for cylindrical cup drawing (NUMISHEET' 2002. Unit: mm) and **b** punch force versus punch displacement

3.2 Deep Drawing

In this section, deep drawing processes of cylindrical and square cups are investigated. Forming behavior predicted by the Dung's damage model is then compared with those by the GTN model and published experimental results.

Cylindrical cup deep drawing

The matrix material is assumed to obey the following isotropic hardening rule:

$$\sigma_f = \sigma_0 + a\left(1 - e^{-b\bar{\varepsilon}^p}\right) \tag{12}$$

where, σ_f is the flow stress of matrix material, $\bar{\varepsilon}^p$ the equivalent plastic strain, σ_0 the initial yield stress, a and b material constants. Figure 4a shows tooling setup for the cylindrical cup drawing. A holding force of 50 kN and a punch stroke of 50 mm are applied. Blank of 1 mm thickness is modeled by eight-node linear brick, reduced integration with hourglass control continuum element (C3D8R) whilst tools are modeled with rigid elements (R3D4). Friction coefficient is set to a value of 0.0096 for all contact surfaces.

The porous material properties of AA6111-T4 aluminum alloy sheet are obtained from [15] and summarized in Table 1.

In Fig. 4b, the punch force is plotted as a function of punch displacement. The Dung-Hill'48 anisotropic plastic damage model predicts a slightly smaller value than that by the GTN model.

Figure 5 shows a comparison of the distribution of void volume fraction between predictions by the Dung-Hill'48 model and the GTN model at a depth of 45 mm of the punch stroke. It can be seen that the Dung-Hill'48 is capable of simulating considerable anisotropy of the blank material which cannot be captured by the GTN model.

Table 1 Damage parameters of AA6111-T4 aluminum alloy for the Dung's model

f_0	0.0
ε_N	0.3
f_N	0.04
s_N	0.1
f_c	0.15
q_1	1.5
q_2	1.5
E (GPa)	70.5
v	0.342
σ_0 (MPa)	180.8
r_0	0.894
r_{45}	0.611
r_{90}	0.66
a (MPa)	274.64
b	6.79

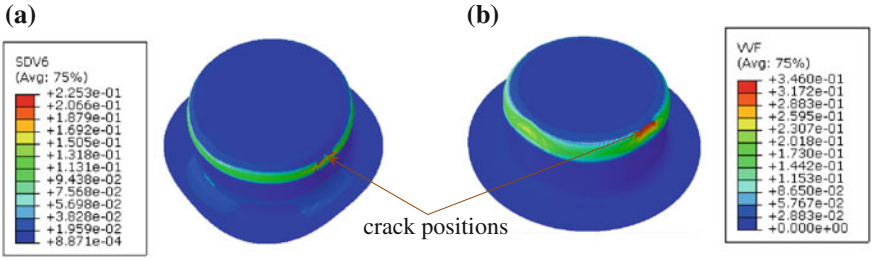

Fig. 5 Distribution of void volume fraction: **a** anisotropic plastic damage model (Dung-Hill'48) and **b** isotropic plastic damage model (GTN)

Square cup deep drawing

The AA6016-T4 aluminum alloy sheet was used to predict plastic fracture in deep drawing process. The material obeys the Swift's hardening rule:

$$\sigma_f = A(\varepsilon_0 + \bar{\varepsilon}^p)^n \tag{13}$$

The parameters of Dung's model given in Table 2.

The deep drawing setup is depicted in Fig. 6a. Diameter of the circular blank is 85 mm. A holding force of 10 kN is applied and the punch stroke is 25 mm. The rigid shell elements (R3D4) were used to mesh punch, die and blank holder, whereas blank was meshed with 8-node hexahedral (C3D8R) solid elements. An average element size of 0.5 mm was applied for the blank. A value of 0.05 was employed for the friction coefficient of all contact surfaces.

Table 2 Damage parameters of AA6016-T4 aluminum alloy for Dung's model [17]

f_0	2.42e-4
ε_N	0.3
f_N	0.042
s_N	0.1
f_c	0.0477
f_F	0.2
q_1	1.5
q_2	1.5
E (GPa)	70
v	0.33
A (MPa)	525.77
r_0	0.553
r_{45}	0.41
r_{90}	0.55
ε_0 (MPa)	0.01125
n	0.27

Figure 6b shows a comparison of the punch force versus displacement curves from the Dung's model and experimental data by Kami et al. [17]. The maximum values of punch force are 35.28 and 34.24 kN for Dung's model and experiment result, respectively. The punch force towards zero at 20.03 mm of depth is predicted by the Dung's model, while that experiment data is 18.7 mm, it is acceptable.

Figure 7 shows a comparison of fracture shape of the blank between simulated results and experiment of Kami et al. [17]. The image show the failed path and position of Dung's model that based on equivalent stress of Hill (1948) is smilar to observation from the experiment.

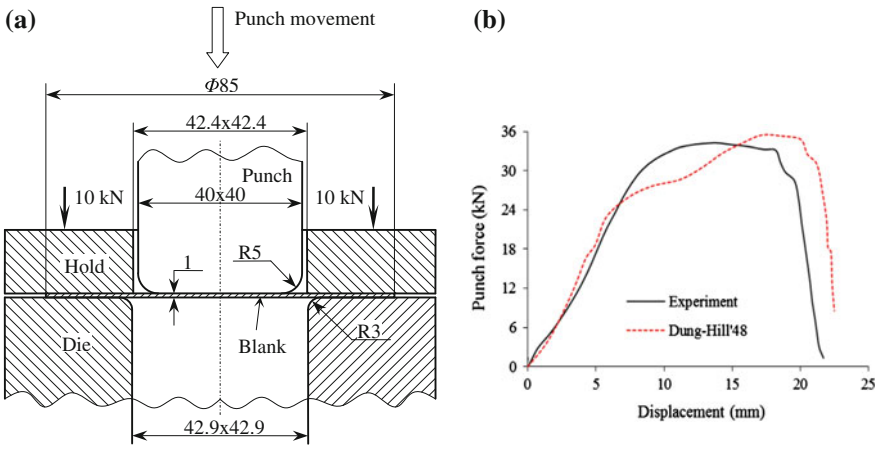

Fig. 6 Square cup drawing: **a** diagram of the tooling setup in square cup drawing (unit: mm) [23] and **b** comparison of forming forces for blank holder of 10 kN

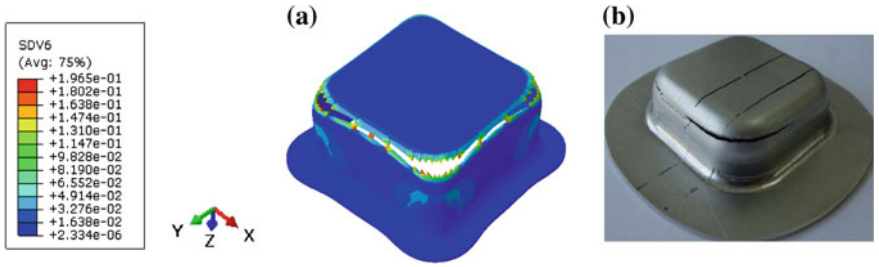

Fig. 7 Failed specimens: **a** Dung-Hill'48 and **b** experiment [17]

4 Conclusions

In this paper, the Dung's model was implemented via a user-defined material (VUMAT) subroutine in the commercial code Abaqus/Explicit. The subroutine is was verified using simple plane strain and hydrostatic tension models. The analysis results have been compared to those using the GTN model in Abaqus and published data. It is shown that the Dung's model that included hardening exponent of matrix material (n) is capacable of predicting damage localization of metallic material.

Two deep drawing processes of cylindrical and square cups have been simulated:

For the first case, fracture positions predicted by the Dung's model is similar to the GTN model. Moreover, the Dung-Hill'48 predicted a lower forming force whilst being capable of simulating earing phenomenon which reflects considerable anisotropy of the blank material.

For the case of square cup deep drawing, comparison with the experiment indicated an identical crack path. It is shown that the forming force and the deep displacement of punch that the punch force toward zero of the Dung's model is higher than that by experiment result with an acceptable accuracy.

References

1. Hill R (1948) A theory of the yielding and plastic flow of anisotropic metals. Proc R Soc Lond A: Math Phys Eng Sci 1948:281–297
2. Hill R (1990) Constitutive modelling of orthotropic plasticity in sheet metals. J Mech Phys Solids 38(3):405–417
3. Barlat F, Lege DJ, Brem JC (1991) A six-component yield function for anisotropic materials. Int J Plast 7(7):693–712
4. Lian J, Barlat F, Baudelet B (1989) Plastic behaviour and stretchability of sheet metals. Part II: Effect of yield surface shape on sheet forming limit. Int J Plast 5(2):131–147
5. Barlat F, Cazacu O, życzkowski M, Banabic D, Yoon JW (2005) Yield surface plasticity and anisotropy. In: Continuum scale simulation of engineering materials. Wiley-VCH Verlag GmbH & Co. KGaA, pp 145–183
6. Gurson AL (1977) Continuum theory of ductile rupture by void nucleation and growth: part I—Yield criteria and flow rules for porous ductile media. J Eng Mater Technol 99(1):2–15
7. Tvergaard V (1982) On localization in ductile materials containing spherical voids. Int J Fract 18(4):237–252
8. Tvergaard V (1981) Influence of voids on shear band instabilities under plane strain conditions. Int J Fract 17(4):389–407
9. Tvergaard V, Needleman A (1984) Analysis of the cup-cone fracture in a round tensile bar. Acta Metall 32(1):157–169
10. Chu CC, Needleman A (1980) Void nucleation effects in biaxially stretched sheets. J Eng Mater Technol 102(3):249–256
11. Liao KC, Pan J, Tang SC (1997) Approximate yield criteria for anisotropic porous ductile sheet metals. Mech Mater 26(4):213–226
12. Wang D-A, Pan J, Liu S-D (2004) An anisotropic Gurson yield criterion for porous ductile sheet metals with planar anisotropy. Int J Damage Mech 13(1):7–33

13. Tanguy B, Luu TT, Perrin G, Pineau A, Besson J (2008) Plastic and damage behaviour of a high strength X100 pipeline steel: Experiments and modelling. Int J Press Vessels Pip 85 (5):322–335
14. Grange M, Besson J, Andrieu E (2000) An anisotropic Gurson type model to represent the ductile rupture of hydrided Zircaloy-4 sheets. Int J Fract 105(3):273–293
15. Chen Z, Dong X (2009) The GTN damage model based on Hill'48 anisotropic yield criterion and its application in sheet metal forming. Comput Mater Sci 44(3):1013–1021
16. Morgeneyer TF, Besson J, Proudhon H, Starink MJ, Sinclair I (2009) Experimental and numerical analysis of toughness anisotropy in AA2139 Al-alloy sheet. Acta Mater 57 (13):3902–3915
17. Kami A, Mollaei DB, Sadough VA, Kami A, Comsa D-S, Banabic D (2014) Application of a GTN damage model to predict the fracture of metallic sheets subjected to deep-drawing. Proc Rom Acad Ser A 15:300–309
18. McClintock FA (1968) A criterion for ductile fracture by the growth of holes. J Appl Mech 35 (2):363–371
19. Dung NL (1992) Three dimensional void growth in plastic materials. Mech Res Commun 19 (3):227
20. Schiffmann R, Wendt U, Dahl W (2001) Damage mechanical investigations at ductile fracture of free-cutting steels by means of microscopy-void growth and fracture surface topography. Le Journal de Physique IV 2001, 11(PR5):Pr5-187–Pr185-193
21. Aravas N (1987) On the numerical integration of a class of pressure-dependent plasticity models. Int J Numer Meth Eng 24(7):1395–1416
22. Aravas N (1987) On the numerical integration of a class of pressure-dependent plasticity models. Int J Numer Meth Eng 24(7):1395–1416
23. Nicodim I, Ciobanu I, Banabic D (2013) Effect of the constitutive law on the prediction of the wall thickness distribution of square cup

Implementation and Application of Dung's Model to Analyze Ductile Fracture of Metallic Material

Hao H. Nguyen, Trung N. Nguyen and Hoa C. Vu

Abstract In this paper, the Dung's microscopic damage model which depicts void growth under plastic deformation is applied to predict ductile fractures in high strength steel API X65. The model is implemented as a vectorized user-defined material (VUMAT) subroutine in the ABAQUS/Explicit commercial finite element code. Notched and smooth round bars under uniaxial tension loading are simulated to show the effect of equivalent plastic strain versus the void volume fraction growth of the material at and after crack initiation. Predictions of the ductile behavior from void nucleation to final failure stage are compared with the built-in Gurson—Tvergaard—Needleman (GTN) model in ABAQUS. Also, comparison with experimental results from the literature is discussed

Keywords Ductile fracture · Void growth · Dung's model · Micro-crack mechanism

1 Introduction

Ductile fracture of metallic material is usually due to void nucleation, growth and coalescence. To investigate this process, the series of experiments are needed to conduct. This is necessary, but it is quite expensive and time cost. For these

H.H. Nguyen · H.C. Vu (✉)
Department of Engineering Mechanics, Faculty of Applied Science,
Ho Chi Minh City University of Technology, 268 Ly Thuong Kiet Street,
District 10, Ho Chi Minh City, Vietnam
e-mail: vuconghoa@hcmut.edu.vn

H.H. Nguyen
e-mail: hq8087@gmail.com

T.N. Nguyen
School of Mechanical Engineering, Purdue University, West Lafayette, IN 47907, USA
e-mail: trungnguye@purdue.edu

V.H. Duy et al. (eds.), *AETA 2015: Recent Advances in Electrical Engineering and Related Sciences*, Lecture Notes in Electrical Engineering 371,
DOI 10.1007/978-3-319-27247-4_75

reasons, finite element ductile failure simulations based on the local approach is considered as the most effective method and quite useful.

Fracture mechanic based on mechanism of void nucleation, growth and coalescences connect between micro structure variables and macro crack behavior of metallic materials. The plastic failure process due to void nucleation, growth and coalescences includes two phases: homogeneous deformation including void nucleation and growth, local deformation for void nucleation [1]. It is usually use a yield function of porous plastic metallic material model for plastic fracture process analyses. The original yield function is proposed by Gurson [2] based on spherical void growth. The Gurson model includes a damage parameter of void volume fraction (f). Tvergaard [3, 4] modified the Gurson model by add two adjusted parameters to consider interaction of the voids and hardening by deformation. Needleman and Tvergaard [5] extended Gurson model to simulate rapid loss of loading carrying capacity in the void materials. Therefore, Gurson model is also known as GTN (Gurson—Tvergaard—Needleman) model. Base on McClintock [6] spheroidal void growth model in 3D space, Dung NL [7] investigated the cylindrical and ellipsoidal void growth and then proposed a yield function similar to the yield function in GTN model. There are differences of Dung's model from GTN model. The first, to consider hardening of matrix material under deformation, Dung have added hardening exponent (n) into yield function. In adding, Dung supposed the initial shape of void is spherical void but when matrix material under deformation then the shape of void become ellipsoidal void. Recently, Schiffmann et al. [8] used the Dung void growth model to predict failure development at ductile fracture of steel, it exhibited good agreement with experiment results. To determine void volume fraction growth during matrix material under deformation, Chu and Needleman [9] supplied the criterions for void nucleation into Gurson model. For the first research about void coalescence criterion: the void coalescences take place only when void volume fraction (f) reaches a critical value (f_c). In the later studies found that, fc strongly depend on initial void volume fraction (f_0), the size of voids, the space of voids in matrix material, stress triaxiality, strain hardening of material [10, 11]. Thomason [12, 13] proposed a critical loading model that describing of the void coalescence. In this model, at start of void coalescence is controlled by mechanism of plastic localization in the spaces of voids. At these positions, the void coalescence can be explained by material and stress states dependences. Bao [14] conducted the series of experiments and finite element analyses in aluminum alloy 2024-T351 and proposed a criterion of void coalescence that based on two parameters of critical equivalent plastic strain (ε_f) and ratio of stress triaxiality (T). When these values reach a critical value then void coalescence occurs, mean micro-crack will form in matrix material.

In this paper, Dung's model is implemented by a VUMAT subroutine in the finite element software (ABAQUS) to consider process of ductile fracture in high strength steel API X65. The notch round bars and smooth round bar is simulated to show the effect of equivalent plastic strain on the void volume fraction growth of the materials. The predictions of ductile behavior in the samples from void

nucleation to final failure in material are compared with GTN model and experiment results of Oh et el [15, 16].

2 Modeling Porous Plastic Metallic Material

The yield function of Dung's model is given [7] as follow:

$$\Phi = \left(\frac{\sigma_e}{\sigma_f}\right)^2 + 2fq_1 \cosh\left[-\sqrt{3}(1-n)\frac{\sigma_m}{\sigma_f}\right] - 1 - (q_2 f)^2 = 0 \tag{1}$$

where, the parameters q_1, q_2 are proposed by Tvergaard [5], n is hardening exponent of matrix material, hydrostatic stress $\sigma_m = -\frac{1}{3}\sigma_{ij}\delta_{ij}$, δ_{ij} is Kronecker delta, equivalent stress vonMises $\sigma_e = \sqrt{\frac{3}{2}\sigma'_{ij} : \sigma'_{ij}}$, σ'_{ij} is deviatoric stress tensor, $\sigma'_{ij} = \sigma_{ij} - \frac{1}{3}\sigma_{ij}\delta_{ij}$, σ_{ij} is Cauchy stress tensor, σ_f is the yield stress of matrix material, $\sigma_f = \sigma_f\left(\bar{\varepsilon}_e^p\right)$. The equivalent plastic strain rate of matrix material $\dot{\bar{\varepsilon}}_e^p$ is dominated by equivalent plastic work:

$$(1-f)\sigma_f \dot{\bar{\varepsilon}}_e^p = \sigma_{ij} : \dot{\varepsilon}_{ij}^p \tag{2}$$

where, $\bar{\varepsilon}_e^p$ is equivalent plastic strain of matrix material, $\dot{\varepsilon}_{ij}^p$ is plastic strain rate tensor.

The void volume fraction growth is computed as follow:

$$\dot{f} = \dot{f}_g + \dot{f}_n \tag{3}$$

Here, the void volume fraction growth of the presence voids in matrix material:

$$\dot{f}_g = (1-f)\dot{\varepsilon}_{ij}^p \delta_{ij} \tag{4}$$

The nucleated void volume fraction growth during matrix material under deformation:

$$\dot{f}_n = A\dot{\bar{\varepsilon}}^p \tag{5}$$

The number of nucleated voids A is a function of equivalent plastic strain of matrix material $\bar{\varepsilon}_e^p$:

$$A = \frac{f_N}{s_N\sqrt{2\pi}} \exp\left[-0.5\left(\frac{\bar{\varepsilon}_e^p - \varepsilon_N}{s_N}\right)^2\right] \tag{6}$$

where, f_n, s_N, ε_N are the parameters relative to the void nucleation during matrix material under deformation.

3 Numerical Implementation

A numerical algorithm based on the Euler backward method has been developed for a class of pressure-dependent plasticity models [17]. By applying the algorithm a VUMAT subroutine in the ABAQUS/Explicit software is implemented for the Dung's model. Steps of the implementation procedures are summarized as follows:

Step1: Initialize variables

$$\sigma_t, \varepsilon_t, f_t, \bar{\varepsilon}_t^p, \Delta\varepsilon_{t+\Delta t}$$

Step 2: Calculate trial state of stresses

- Calculate stress tensor:

$$\boldsymbol{\sigma}_{t+\Delta t}^{trial} = \boldsymbol{\sigma}_t + \mathbf{D} : \boldsymbol{\Delta\varepsilon}_{t+\Delta t} \tag{7}$$

The fourth order tensor $\mathbf{D}$ is the elastic stiffness matrix. Isotropic elasticity is assumed so that

$$D_{ijkl} = \left(K - \frac{2}{3}G\right)\left(\delta_{ij}\delta_{kl}\right) + G\left(\delta_{ik}\delta_{jl} + \delta_{il}\delta_{jk}\right) \tag{8}$$

where K is the elastic bulk modulus and G is the shear modulus.

- Calculate hydrostatic stress:

$$\sigma_m^{trial} = -\frac{1}{3}\boldsymbol{\sigma}_{t+\Delta t}^{trial} : \mathbf{I} \tag{9}$$

where $\mathbf{I}$ is the second order unit tensor

- Calculate equivalent stress:

$$\sigma_e^{trial} = \sqrt{\frac{3}{2}\boldsymbol{\sigma}^{trial\prime} : \boldsymbol{\sigma}^{trial\prime}} \tag{10}$$

for isotropic matrix materials, or

$$\begin{aligned}\sigma_e^{trial} = \Big[&F\left(\sigma_{22}^{trial} - \sigma_{33}^{trial}\right)^2 + G\left(\sigma_{33}^{trial} - \sigma_{11}^{trial}\right)^2 + H\left(\sigma_{11}^{trial} - \sigma_{22}^{trial}\right)^2 \\ &+ 2L\left(\sigma_{23}^{trial}\right)^2 + 2M\left(\sigma_{31}^{trial}\right)^2 + 2N\left(\sigma_{12}^{trial}\right)^2\Big]^{1/2}\end{aligned} \tag{11}$$

for anisotropic matrix materials.

Step 3: Check for plastic yield

$$\Phi^{trial} = \Phi\left(\sigma_m^{trial}, \sigma_e^{trial}, f_t, \bar{\varepsilon}_t^p\right)$$

If $\Phi^{trial} \leq 0$ go to Step 5 and update elastic stress, $\sigma_{t+\Delta t} = \sigma_{t+\Delta t}^{el}$.
If $\Phi^{trial} > 0$ go to Step 4 and calculate plastic correction.

Step 4: Calculate plastic correction

The plastic strain increment is divided into spherical and deviatoric parts:

$$\Delta\boldsymbol{\varepsilon}^p = \frac{1}{3}\Delta\varepsilon_p \mathbf{I} + \Delta\varepsilon_q \mathbf{n} \tag{12}$$

$$\Delta\varepsilon_p = -\lambda\frac{\partial\Phi}{\partial\sigma_m} \text{ and } \Delta\varepsilon_q = \lambda\frac{\partial\Phi}{\partial\sigma_e} \tag{13}$$

where λ is the plastic multiplier, $\mathbf{n} = (3/2\sigma_e)\sigma'$ is the flow direction.

Eliminating λ from Eq. (13) leads to:

$$\Delta\varepsilon_q\left(\frac{\partial\Phi}{\partial\sigma_m}\right) + \Delta\varepsilon_p\left(\frac{\partial\Phi}{\partial\sigma_e}\right) = 0 \tag{14}$$

Using Newton-Raphson iterative method to solve the nonlinear system of Eqs. (15) and (16), the consistency condition Eq. (17) must also be satisfied at the same time.

$$E_1 = \Delta\varepsilon_p^{(k+1)}\frac{\partial\Phi}{\partial\sigma_e} + \Delta\varepsilon_q^{(k+1)}\frac{\partial\Phi}{\partial\sigma_m} = 0 \tag{15}$$

$$E_2 = \Phi\left(\sigma_m^{(k+1)}, \sigma_e^{(k+1)}, \bar{\varepsilon}^{p(k+1)}, f^{(k+1)}\right) = 0 \tag{16}$$

$$\sigma_f^{(k+1)} = H^{(k+1)} \cdot \bar{\varepsilon}^p \tag{17}$$

where $H = \frac{d\sigma_f}{d\bar{\varepsilon}^p}$ is strain hardening modulus of the matrix material.

The iterations is terminated when the values of $|E_1|$ and $|E_2|$ are less than a specified tolerance, e.g. δ = 1E-08.

Step 5: Update of state variables

$$\sigma_m = \sigma_m^{el} + K\Delta\varepsilon_p \tag{18}$$

$$\sigma_e = \sigma_e^{el} - 3G\Delta\varepsilon_q \tag{19}$$

$$\sigma = \sigma^{el} - K\Delta\varepsilon_p I - 2G\Delta\varepsilon_q n \tag{20}$$

$$\Delta\bar{\varepsilon}^p = \frac{-\sigma_m\Delta\varepsilon_p + \sigma_e\Delta\varepsilon_q}{(1-f)\sigma_f} \tag{21}$$

$$\Delta f = (1-f)\Delta\varepsilon_p + A\Delta\bar{\varepsilon}^p \tag{22}$$

4 Application to Tensile Testing Simulations

4.1 Identifying the Parameters for Dung's Model

The properties of material of API X65 steel: Young's modulus E = 210.7 GPa, hardening exponent is chosen n = 0; 0.134; 0.2, Poisson ratio ν = 0.3, initial yield stress σ_0 = 464.5 MPa. The experiment data of yield stress and plastic strain curve is refer to Oh [15].

In order to simulate failure process of metallic materials based on void growth and coalescence model, eight parameters have to identify: two adjustment factors (q_1, q_2), six parameters relative to void growth and coalescence ($f_0, f_c, f_F, \varepsilon_N, s_N, f_N$).

For the Dung's model, Dung [7] proposed $q_1 = q_2 = 1.5$. The void nucleation parameters $\varepsilon_N = 0.3$; $s_N = 0.1$; $f_N = 0.04$ are proposed by Chu and Needleman [9] and widely used by many researchers. For the high strength API X65 steel is the pure steel, during plastic strain process, void nucleation by inclusions and second phase particles is not significant and slow. Therefore, the value f_N is chosen 0.0008.

The initial void volume fraction is calculated based on equation of Franklin [18] as follow:

$$f_0 = 0.054\left(S\% - \frac{0.001}{Mn\%}\right) \tag{23}$$

where, $S\%$ and $Mn\%$ are weight (%) of S and Mn respectively. The content of these chemical elements is referred to Oh et al. [15].

The void volume fraction at fracture f_F is determined from f_0 and based on empirical equation of Zhang [1]:

$$f_F = 0.15 + 2f_0 \tag{24}$$

The critical void volume fraction fc is usually determined by the void coalescence criterions and experiments. In this work, for the API X65 steel, f_c is referred to Oh et al. [16].

Summary, the parameters is chosen and calculated as Table 1:

Table 1 The parameters for Dung's model

ε_N	s_N	f_N	f_0	f_c	f_F	q_1	q_2
0.3	0.1	8.0E-4	1.25E-4	0.015	0.15025	1.5	1.5

4.2 Testing on Single Element

The subroutine is verified using a single 8-node brick element (C3D8R) to simulate uniaxial tension. The boundary conditions and loading as shown in Fig. 1a. The initial size of each element edge is 1 mm. The loading velocity v_2 for tension is set to 15 mm/s.

The Fig. 1b shows void volume fraction versus equivalent plastic strain for the uniaxial tensile test to single element. For hardening exponent $n = 0.134$, the Dung's model coincides with the classical GTN model. Therefore, $n = 0.134$ is chosen to simulate the notched and round bars in Sect. 4.3.

4.3 Application to the Simulation of the Notched Bar and Round Bars

The geometries of tensile specimens as Fig. 2a. Using biaxial symmetry four-node element type with reduce integration (CAX4R). The size of the elements at minimum section are 0.15 × 0.15 mm, the size of the other elements are 0.15 × 0.5 mm. Only 1/4 of bar is used to simulate tensile test. The finite element meshes are presented as Fig. 2b. The velocity loading is applied on top boundary. For each

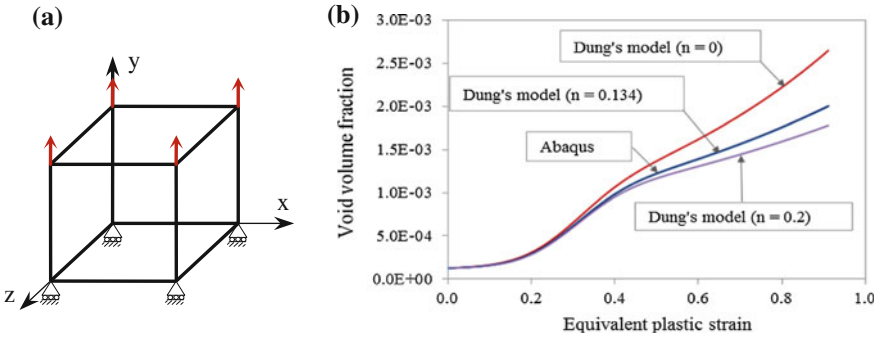

Fig. 1 **a** The single element used to verify subroutine. **b** The void volume fraction versus equivalent plastic strain with hardening exponents in yield function of Dung's model

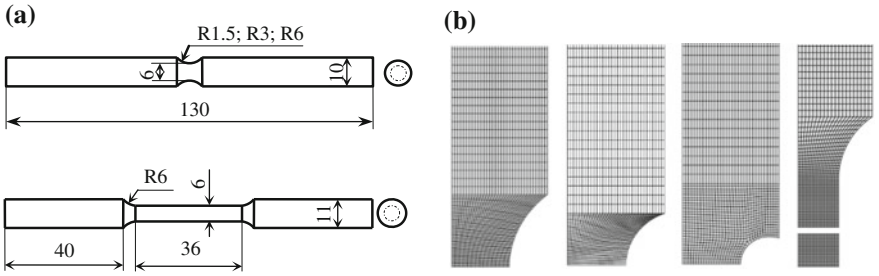

Fig. 2 Geometries of tensile specimens. **a** Notched bars **b** Smooth bar (unit: mm)

specimen, magnitude of load is chosen and controlled via the critical void volume fraction (f_c) or void volume fraction at fracture (f_F), mean the void volume fraction reaches these values, in the matrix material appear initial crack or damage, respectively.

For all the specimens, void volume fraction reaches critical value (f_c) at center of bar earlier than other positions, mean crack initiation occur at these positions before.

The Fig. 3 shows contour of void volume fraction at and after crack initiation of R6 bar. Figure 4a presents void volume fraction growth (from f_0 to f_c) versus equivalent plastic strain of element at center of bars for the Dung's model. For the smooth bar, void volume fraction growth reaches critical void volume fraction (f_c) slower the notched bars. Material fails earlier the R1.5 bar than R3 and R6 bar. Figure 4b shows stress triaxiality versus equivalent plastic strain of center element of bars, the end point of average lines is compared with fracture criterion of Oh [15]

Figure 5 shows comparison between present results and criterion of crack initiation. The fracture strain depend on the stress triaxiality in exponential function [19].

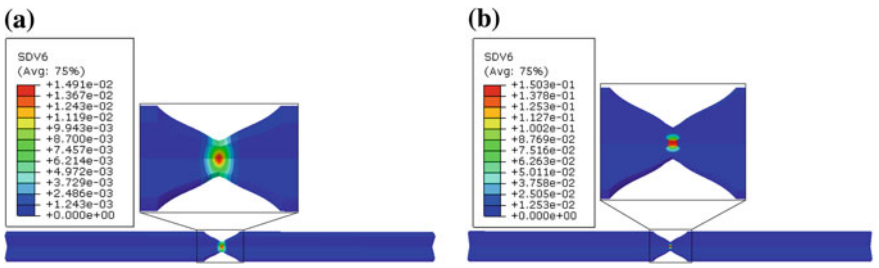

Fig. 3 Contour of void volume fraction of R6 bar. **a** Crack initiation. **b** Failed elements

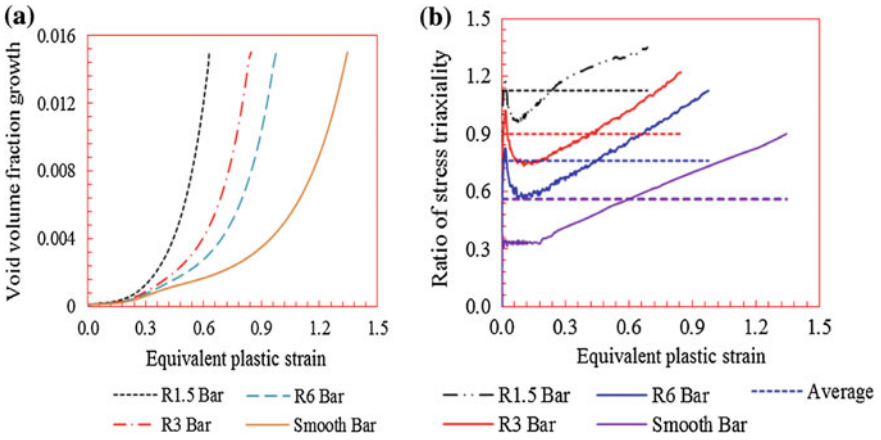

Fig. 4 **a** Void volume fraction growth versus equivalent plastic strain. **b** Comparison crack initiation, true fracture strain as a function of stress triaxiality, between Dung's model and fracture criterion of Oh et al. [15]

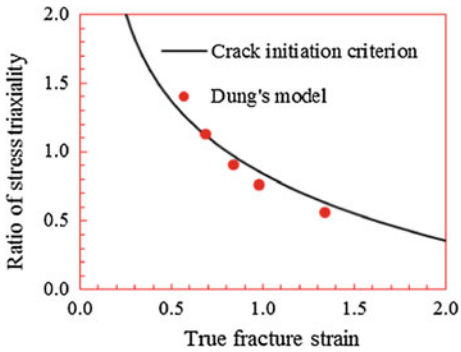

Fig. 5 Ratio of stress triaxiality ($-\sigma_m/\sigma_e$) versus equivalent plastic strain

For API-X65 steel, Oh et al. [15] proposed a critical location criterion that equivalent plastic strain as a function stress triaxiality:

$$\varepsilon_f = 3.29 \exp\left(-1.54 \frac{\sigma_m}{\sigma_e}\right) + 0.1 \tag{25}$$

The analysis results of four bars by Dung's model are able to predict the fracture initiation with an acceptable accuracy.

In the Fig. 6 shows engineering stress versus engineering strain of bars. For all the specimens, the predictions of crack initiation by Dung's model are good agreement with GTN model in Abaqus and experiment results of Oh et al. [15]. For each bar, crack initializes at value of other equivalent plastic strains.

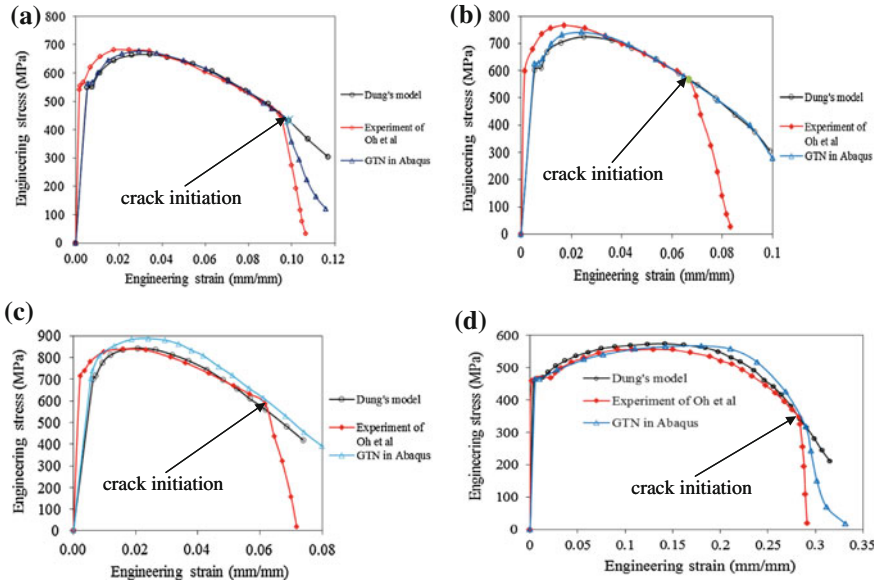

Fig. 6 Comparison between simulated results and experiments of Oh et al. [15]. **a** R6 bar. **b** R3 bar. **c** R1.5 bar. **d** Smooth bar

5 Conclusions

By implemented approach that based on backward Euler method of stress integration for Dung's model succeed in simulating fractured prediction of the notched and round bars. The results provided the predictions of Dung's model are very close to experiment results of Oh et al. [15, 16] and GTN model in Abaqus. This work is also show the fractured predictions as follow: for all the specimens, the crack initializes at center and propagates along minimum section of bars; the different geometries crack initializes at different moment.

References

1. Zhang Z, Thaulow C, Ødegård J (2000) A complete Gurson model approach for ductile fracture. Eng Fract Mech 67(2):155–168
2. Gurson AL (1977) Continuum theory of ductile rupture by void nucleation and growth: part I—Yield criteria and flow rules for porous ductile media. J Eng Mater Technol 99(1):2–15
3. Tvergaard V (1981) Influence of voids on shear band instabilities under plane strain conditions. Int J Fract 17(4):389–407
4. Tvergaard V (1982) On localization in ductile materials containing spherical voids. Int J Fract 18(4):237–252

5. Tvergaard V, Needleman A (1984) Analysis of the cup-cone fracture in a round tensile bar. Acta Metall 32(1):157–169
6. McClintock FA (1968) A criterion for ductile fracture by the growth of holes. J Appl Mech 35(2):363–371
7. Dung NL (1992) Three dimensional void growth in plastic materials. Mech Res Commun 19(3):227
8. Schiffmann R, Dahl W, Bleck W (2013) Different CDM-models and their ability to describe the damage development at ductile fracture of steel. In: ECF13, San Sebastian 2000: 2013
9. Chu CC, Needleman A (1980) Void nucleation effects in biaxially stretched sheets. J Eng Mater Technol 102(3):249–256
10. Pardoen T, Hutchinson JW (2000) An extended model for void growth and coalescence. J Mech Phys Solids 48(12):2467–2512
11. Zhang ZL, Thaulow C, Odegard J (2000) A complete Gurson model approach for ductile fracture. Eng Fract Mech 67(2):155–168
12. Thomason PF (1985) A three-dimensional model for ductile fracture by the growth and coalescence of microvoids. Acta Metall 33(6):1087–1095
13. Thomason PF (1998) A view on ductile fracture modelling. Fatigue Fract Eng Mater Struct 21 (9):1105–1122
14. Bao Y (2005) Dependence of ductile crack formation in tensile tests on stress triaxiality, stress and strain ratios. Eng Fract Mech 72(4):505–522
15. Oh C-K, Kim Y-J, Baek J-H, Kim W-S (2007) Development of stress-modified fracture strain for ductile failure of API X65 steel. Int J Fract 143(2):119–133
16. Oh C-S, Kim N-H, Kim Y-J, Baek J-H, Kim Y-P, Kim W-S (2011) A finite element ductile failure simulation method using stress-modified fracture strain model. Eng Fract Mech 78(1):124–137
17. Aravas N (1987) On the numerical integration of a class of pressure-dependent plasticity models. Int J Numer Meth Eng 24(7):1395–1416
18. Benedetti M, Fontanari V (2013) The transferability of micro-mechanical damage parameters in modern line pipe steel. In: ECF15, Stockolm 2004
19. Rice JR, Tracey DM (1969) On the ductile enlargement of voids in triaxial stress fields∗. J Mech Phys Solids 17(3):201–217

Author Index

A
Ahsan Kazmi, S.M., 3
Aldulaimi, Husam Hasan, 685
Anh, Ho Pham Huy, 399, 411
Anh, Huynh Quoc, 111
Anh, Nguyen Doan Quoc, 283, 299
Anh, Nguyen Duy, 485, 497, 731
Anh, Quyen Huy, 157
Anh, Truong Viet, 249

B
Bark, Hyeon Sang, 293
Bon, Nguyen, 197
Brandstetter, Pavel, 313, 325
Bui, Anh Tuan, 779
Bui, Thanh Luan, 803
Bui, Trong Hieu, 779
Byun, Gi Sig, 237, 441

C
Chen, Chih-Keng, 377
Cho, Sung-Ho, 697
Choe, Yeon Wook, 353, 427
Choi, Hyeung-Sik, 575, 619, 633
Choi, Seung-Bok, 835
Chu, Trung Dung, 541

D
Dang, Duc Ngoc Minh, 63
Dang, Hanh Ngoc, 63
Dao, Nguyen, 197
Dao, Tran Trong, 133, 645
Dinh, Bach H., 721
Dinh, Viet Tuan, 353
Do, Dinh-Thuan, 53
Doan, Phuc Thinh, 337
Dong, Chau, 313, 367
Dong, Chau Si Thien, 325
Dung, Nguyen Quang, 197
Duong, Van Tu, 337
Duong, Viet Anh, 541
Duy, Bui Quoc, 835
Duy, Hung Ha, 53
Duy, Vo Hoang, 133, 367, 645, 671, 685

G
Gulalkari, Amruta Vinod, 603, 655

H
Han, Sung Woo, 237
Hiep, Le Dai, 835
Hieu, Ngo Khanh, 881
Ho, Van Cuu, 185
Hoang, Bach Dinh, 519
Hoang, Khac Anh, 769, 791
Hoang, Minh Doan Vu, 757
Hoang, Tran Ngoc, 731
Hong, Choong Seon, 3, 41, 63
Hong, Sup, 589, 603
Huy, Hung Nguyen, 671
Huynh, Le Minh Thien, 261
Huynh, Van Van, 519, 553

J
Jang, Nakwon, 275
Jeon, M.J., 845
Jeon, Tae-In, 293
Jeong, Jae Hoon, 441, 589, 655
Jeong, Nam Soo, 441
Jeong, Sang-Ki, 633
Jeong, Sang Kwun, 589
Ji, Dae-Hyeung, 575

V.H. Duy et al. (eds.), *AETA 2015: Recent Advances in Electrical Engineering and Related Sciences*, Lecture Notes in Electrical Engineering 371,
DOI 10.1007/978-3-319-27247-4

Ji, Young Bin, 293
Jo, Sung-Won, 619
Jung, Young Seok, 337, 469

K
Kieu, Tam Nguyen, 53
Kim, Dae-Kwang, 697
Kim, Dae Hwan, 337, 469
Kim, Dong Hwa, 367
Kim, Dong Kyu, 685, 697
Kim, Hak-Joon, 697
Kim, Hak Kyeong, 353, 469, 589, 603, 655, 671
Kim, Hwan Seong, 589
Kim, Jin Wook, 469, 603
Kim, Joon-Young, 575, 619
Kim, Min, 237
Kim, Oanh Tran Thi, 41
Kim, Sang Bong, 337, 353, 441, 469, 589, 603, 655, 671, 685
Kim, SangHyun, 275
Kim, SeongGyu, 237
Kim, Young-Bok, 389
Kuznetsov, Nikolay V., 13

L
Le, Anh-Tuan, 377
Le, Ngoc-Bich, 645
Le, Tat-Hien, 823
Le, Trong Nghia, 167
Le Khoa, Dang, 111
Lee, Chung Hwan, 603
Lee, D.H., 845
Lee, D.M., 845
Lee, Hsiao-Yi, 283
Lee, HyunMin, 275
Lee, Jin Han, 237
Lee, Jin Woo, 353
Liu, Yu-Nan, 283
Loc, Huynh Thien, 881
Ly, Pham Huu, 249

M
Ma, Hsin-Yi, 283
Mai, The-Vu, 575
Malčík, Martin, 143
Min, Jung Hu, 337
Minh, Tran Hoang Quang, 175
Moon, Seungil, 3

N
Ngo, Chi Trung, 29
Ngo, Manh-Dung, 457
Ngo, Quynh Tu, 63
Nguyen, Bao Quoc, 213
Nguyen, Duc Chi, 261
Nguyen, Duc-Hoang, 457
Nguyen, Duc Thai, 123
Nguyen, Duy Anh, 709
Nguyen, Hao H., 891, 903
Nguyen, Hoanh, 509
Nguyen, Huu Hieu, 123
Nguyen, Ngoc Au, 167
Nguyen, Ngoc-Duc, 619
Nguyen, Quoc Hung, 835
Nguyen, Tan N., 75
Nguyen, Tan Tien, 441, 745, 757, 769, 791
Nguyen, Thang Trung, 213, 223
Nguyen, Thao Phuong Thi, 509
Nguyen, Thuan Thanh, 223
Nguyen, Tri Dung, 745
Nguyen, Trong Hai, 353
Nguyen, Trung N., 891, 903
Nguyen, V.M., 845
Nguyen, VanDung, 41
Nguyeni, Trong Hai, 685
Nhat, Luong Thanh, 485
Nhat, Tan Nguyen, 53
Noh, Sam Kyu, 293

O
Ochi, Hiroshi, 111
Ock, JaeHeon, 275
Oh, Hoon, 29
Oh, JaeHyeon, 275
Oh, Ji-Youn, 633
Oh, Sea June, 337, 469
Oh, Seung Jae, 293
Ondrejka, Adam, 143

P
Park, Dong Woo, 293
Park, Jae-Ha, 697
Pham, Hiep Ngoc, 223
Pham, Minh Thuy, 29
Pham, Van Anh, 769, 791
Phan, Tan Tung, 757
Phan, Thi Thanh Binh, 167
Phung, Thanh Huy, 779

Phung, Tri Cong, 709
Phung, Tuan Anh, 223
Phuong, Le Minh, 249
Phuong, Nguyen Huu, 111
Phuong, Pham Nhat, 133
Pluhacek, Michal, 563
Pratama, Pandu Sandi, 337, 469, 589, 603, 655, 671, 685

Q
Quang, Nguyen Thanh, 645
Quyen, Huy Anh, 167

R
Rezac, Filip, 99
Rozhon, Jan, 99

S
Saloun, Petr, 143
Senkerik, Roman, 563
Seo, Seung Sam, 237
Seong, Kim Hwan, 731
Sheng, Dong Bo, 671
Shin, Min Saeng, 441
Slachta, Jiri, 99
Son, Hyun-Joong, 575
Son, Nguyen Ngoc, 399, 411
Song, Sung-Jin, 697
Sy, Le Van, 857

T
Thach, Phan Chi, 157
Tho, Tran Quang, 249
Thuong, Tran Ngoc Cong, 497
Tien, Nguyen Tan, 497
Tran, Anh-Minh D., 389
Tran, Cong Thinh, 367
Tran, Minh Hoang Quang, 553
Tran, Ngoc-Huy, 575, 619, 633
Tran, Phuong T., 75, 87
Tran, Thien Phuc, 353, 745
Trang, Nguyen Cong, 541
Trang, Tran Thanh, 261
Tri, Thieu Quang, 299
Trung, Le Quang, 157
Truong, Anh Viet, 223
Tsai, Yao-Wen, 541
Tu Duong, Van, 441
Tuan, Nguyen Anh, 823
Tung, Luu Minh, 133

V
Van, Phuoc Nguyen, 869
Van, Tan Luong, 185, 261
Van Duc, Phan, 541
Van Duong, Tuan, 213
Van Kien, Cao, 411
Van Mui, Nguyen, 3
Van Phan Nhan, Tran, 485
Vo, Dieu Ngoc, 213
Vo, Duy Hoang, 313
Vo, Hau Huu, 325
Vo, Huu Hau, 313
Vo, Thoai Phu, 531
Vo, Tuong Quan, 769, 791
Voznak, Miroslav, 75, 99
Vu, Hoa C., 891, 903

X
Xuan, Xinh Nguyen, 53

Y
Yeu, Tae-Kyeong, 589, 603
Yoo, Hui-Ryong, 685, 697
Yoon, H.K., 845
Yoon, Jung-In, 389

Z
Zelinka, Ivan, 133, 143, 563